Microstructure Related Durability of Cementitious Composites

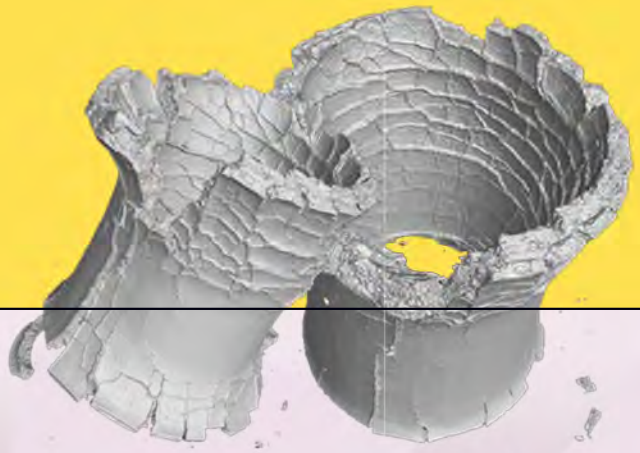

Proceedings
of the 4th International
Rilem Conference

TU Delft

SOUTHEAST UNIVERSITY

aci American Concrete Institute Always advancing

SBT 苏博特 Sobute New Materials Co., Ltd.

fib CEB-FIP

rilem

Edited by:
Guang Ye
Hua Dong
Jiaping Liu
Erik Schlangen
Changwen Miao

4th International RILEM conference on
Microstructure Related Durability of Cementitious Composites

ISSN number: 978-94-6366-422-6

Edited by:

Guang Ye

Hua Dong

Jiaping Liu

Erik Schlangen

Changwen Miao

Cover designed by:

Iris Batterham

Organized by:

Sponsored by:

TABLE OF CONTENTS

Part II: Special Sessions

Preface

The 4th International RILEM conference on Microstructure Related Durability of Cementitious Composites (Microdurability) is held from April to May 2021. Due to Covid-19 the Microdurability conference has been postponed twice, from May 2020 to October 2020, and from October 2020 to April 2021, respectively. Since the ongoing Covid-19 situation continuously prevented us from meeting in person, we have changed the Microdurability conference to 9 webinar series spreading over 5 weeks.

The cement hydration and microstructure development of cementitious materials determine the mechanical properties, durability, and service life of concrete structures. These topics are so important that they are receiving increasing attention. Since the first international conference on Microstructure related durability of cementitious composites was organized in Nanjing in 2008. Up until now, four Microdurability conferences have been successfully held in turn, either in China or in the Netherlands. The Microdurability conferences provide a platform for the researchers to exchange their knowledge and research results.

For the 4th Microdurability conference we have received more than 160 abstracts, and 125 papers have been accepted and published in the proceedings. In total 135 presentations were scheduled to take place during the webinar series. Three special sessions i.e., alkali-activated materials, alkali silica reaction and carbonation were organized. The special session of alkali-activated materials was jointly organized with the midterm workshop of the European ITN-DuRSAAM project. From the presentations and discussions we have learned that the worldwide mission on lowering the global CO2 emission has generated opportunities for researchers to look for new or alternative binders to partially, or fully replace Portland cement in concrete. New binders may alter the hydration mechanism and microstructural development, affecting durability and service life of concrete structures. Smart materials and new technologies (e.g., 3D printing and machine learning) are used more and more in construction. All these open new possibilities to researchers.

The microdurability conferences have received great support from many aspects. We would like to thank our scientific committee for reviewing the papers, chairing sessions, leading discussions and selecting the Best Students Presentations. The valuable efforts of the committee members have ensured scientific quality of the conference. We very much appreciate the keynote speakers for delivering excellent lectures with great scientific value, and for joining the panel discussion to share their views on microstructure, durability of construction materials and trends in future research. Thanks to the supporting staff for their enormous and high-quality support throughout the whole webinar period. We would like to thank authors and presenters for their contribution and knowledge exchange. Finally, RILEM, fib, ACI and Jiangsu Sobute New Materials Company are thanked for their sponsorship.

Hope to see you all in the 5th Microdurability conference in 2024, Nanjing China.

Chairman of conference organization committee

Dr. Guang Ye

Prof. Changwen Miao

Organizing Committee

Guang Ye, TU Delft, the Netherlands (Chair)
Changwen Miao, Southeast University, China
Erik Schlangen, TU Delft, the Netherlands
Jiaping Liu, Southeast University, China
Hua Dong, TU Delft, the Netherlands
Huisu Chen, Southeast University, China
Shizhe Zhang, TU Delft, the Netherlands
Boyu Chen, TU Delft, the Netherlands
Albina Kostiuchenko, TU Delft, the Netherlands
Iris Batterham, TU Delft, the Netherlands (co-ordinator)

Local supporting staff

Jiayi Chen
Zhiyuan Xu
Luiz Miranda de Lima Junior
Yu Zeng
Guilherme da Silva Munhoz
Yun Chen
Zhenming Li
Chen Liu

Scientific Committee Members

Angel Palomo, CSIC, Spain
Camen Andrade, IETcc (CSIC) , Spain
Changwen Miao, Southeast University, China
Chunxiang Qian, Southeast University, China
David A. Lange, UIUC , USA
Doug Hooton, University of Toronto, Canada
Eddy Koenders, Technische Universität Darmstadt, Germany
Edward Garboczi, NIST, USA
Erik Schlangen, Delft University of Technology, The Netherlands
Geert de Schutter, Ghent University, Belgium
Guang Ye , Delft University of Technology, The Netherlands
Frank Dehn, Karlsruhe Institute of Technology, Germany
Huisu Chen , Southeast University, China
Harald Justnes, Norwegian University of Science and Technology, Norway
Ippei Maruyama, Nagoya University, Japan
Jason Weiss, Oregon State University , USA
Jiaping Liu, Southeast University, China
Johann Plank, Technische Universität München, Germany
John Provis, The University of Sheffield , UK
Jorge Dolado, Materials Physics Center, CSIC-UPV/EHU, Spain
Jos Brouwers, Eindhoven University of Technology , The Netherlands
Jueshi Qian , Chongqing University, China
Karen Scrivener, EPFL, Switzerland
Kefei Li, Tsinghua University, China
Klaas van Breugel, Delft University of technology, the Netherlands
Konstantin Kovler, Technion - Israel Institute of Technology, Israel
Ling Wang, China Building Materials Academy , China
Luping Tang, Chalmers University, Sweden
Marios Soutsos, Queen's University, UK
Mark Alexander, University of Cape Town, South Africa
Mette Rica Geiker, NTNU , Norway
Mirja Illikainen, University Oulu, Finland
Nele De Belie , Ghent University, Belgium
Nemkumar Banthia, University of British Columbia, Canada
Ningxu Han, Shenzhen University, China
Ole M. Jensen, Technical University of Denmark, Denmark
Pietro Lura, EMPA, Switzerland
Tetsuya ISHIDA, University of Tokyo, Japan
Qijun Yu, South China University of Technology, China
Tiejun Zhao Qingdao, University of Technology, China
Ueli Angst, ETH Zürich, Switzerland
V. Baroghel-Bouny, IFSTTAR, France
Victor Li, University of Michigan, USA
Vit Smilauer, Czech Technical University in Prague, Czech
Wei Chen , Wuhan University of Technology, China
Weiliang Jin, Zhejiang University, China
Xiaodong Shen, Nanjing Tech University, China

Xing Chen, University of Jinan, China
Yamei Zhang, Southeast University, China
Zhengwu Jiang , Tongji University, China

Keynote speakers

Prof. dr. Ippei Maruyama, Nagoya University, Japan

Microstructure change of concrete under Neutron and Gamma-Ray Irradiation

Dr. Jorge Sanchez Dolado, Materials physics centre, CSIC, Spain

The usefulness of “useless” nanoscience for improving cementitious durability

Prof. dr. Doug Hooton, University of Toronto, Canada

Understanding the differences between chemical and physical degradation mechanisms that can occur in similar exposures

Prof. dr. Liu Jiaping, Southeast University, China

Recently development on Influence of chemical admixtures on microstructure and durability of concrete

Prof. dr. Susan Bernal Lopez, Leeds University, UK

The Materials Science Underpinning the Long-Term Performance of Alkali-Activated Concretes

Prof. dr. Yan Peiyu, Tsinghua University, China

The hydration characteristics of slag in cement-slag complex binder and the microstructural variation of hardened paste under the condition of leaching by soft water

Dr. Ruben Snellings, VITO, Belgium

Reactivity controls on the microstructure development of low clinker blended cements

Prof. dr. Barbara Lothenbach, Senior Researcher, Empa, Switzerland

Effect of chloride and alkalis on the durability of cementitious materials

Prof. dr. Gaurav N. Sant, SAMUELI School of Engineering, UCLA, United States

Machine learning applied to enhance and ensure concrete's durability and engineering performance

Theme 1

Alternative binders, supplementary cementitious materials and industrial or regional wastes used in concrete

APPLICATION OF ULTRA-FINE FLY ASH AS CEMENT REPLACEMENT FOR SUSTAINABLE CONCRETE WITH OPTIMAL PACKING DESIGN

Patricia Kara De Maeijer (1), Bart Craeye (1)(2), Hadi Kazemi-Kamyab (3), Ruben Snellings (3) and Michel Loots (4)

(1) Energy & Materials in Infrastructure & Buildings (EMIB), Faculty of Applied Engineering, University of Antwerp, Belgium

(2) Durable Building in Team (DUBiT), Department of Industrial Sciences & Technology, Odisee University College, Belgium

(3) VITO NV, Belgium

(4) Value Ash Technologies NV, Belgium

Abstract

In the present study, a proprietary 0.2 tonne/h Dusty Cloud Separation (DCS) technology prototype by Value Ash Technologies NV (Belgium) was used to obtain ultra-fine fly ash as a novel by-product. Two types of Class F fly ash were used: separated fly ash (FA1) with particle size < 9.3 μm and ultra-fine fly ash (FA2) < 4.6 μm as sub-fraction of FA1. Two types of cement were used: Portland cement CEM I 52.5 R HES (CEMI) and Blast Furnace Slag Cement CEM III/A 42.5 N LA (CEMIII). The results at paste- and mortar- levels showed that an increased fineness of the fly ash (FA2) contributes to better workability of the mix. For CEMI, the compressive strength of concrete with FA2 with 25% cement replacement was already equal to the reference mix at the age of 28 days. For CEMIII, the compressive strength of concrete mix with FA2 with 25% cement replacement was equal to the reference mix value at the age of 91 days. Regarding the durability, replacing cement with ultra-fine fly ash (FA2) had a positive influence on the chloride migration coefficient and ASR, and a negative influence on the carbonation resistance.

Keywords: concrete, ultra-fine fly ash, compressive strength, corrosion resistance, ASR

1. INTRODUCTION

Concrete is a dominant construction material that is used intensively in the last century. It is a unique material in a way that different wastes and by-products can be utilized in it as a partial substitute for the main components (cement, sand, and aggregates). Moreover, it gives a broad horizon for continuous research of its properties even though a lot of research has been already

performed to substitute cement or aggregates. It is well known that partial substitution or replacement of cement, for example, allows utilizing by-products with a certain impact on concrete properties, in particular, in terms of slower compressive strength development, but in the case of slag an improvement in concrete durability. The pros and cons of the application of different by-products vary from one to another depending on the final target of concrete application. But the question is if any by-product could combine both compressive strength and durability as a positive quality? Which by-product it could be? New advanced technologies could provide a better-quality by-product for further investigation if there is a certain set of investigations done and the pattern of concrete properties is known?

In the present study ultra-fine fly ash, as a novel by-product obtained by means of Dusty Cloud Separation (DCS) technology, is investigated as a cement replacement in concrete as a part of the VASH-project (Value Ash). The aim of this project was not only focused on the development of innovative technology for ultra-fine fly ash application but also aimed for a maximum valorization of fly ash which contributed indirectly to the goal of the separation process of fly ashes. As a result, this process could be exploited internationally on a large scale in the future. The behavior of ultra-fine fly ash was investigated by the upscaling principle in cement-rich environments such as paste, mortar, and concrete. The goal was to determine the influence of fine fractions of ultra-fine fly ash on workability, mechanical properties (compressive strength), and the durability of concrete (ASR, chloride migration, and carbonation). A well-balanced concrete mix composition with ultra-fine fly ashes acting as a cement replacer was developed by means of optimal packing design algorithms.

2. MATERIALS AND METHODS

Two types of cement were used: Portland cement CEM I 52.5 R HES (CEMI) and Blast Furnace Slag Cement CEM III/A 42.5 N LA (CEMIII). Two types of Class F fly ash were used: separated fly ash (FA1) with particle size < 9.3 µm and ultra-fine fly ash (FA2) < 4.6 µm as a sub-fraction of FA1 which was obtained by a 0.2 tonne/h prototype DPS [1]. The chemical composition is shown in Table 1. The particle size distribution is shown in Fig. 1. Aggregates were used: river sand 0/4, limestone 2/6 and limestone 6/20. Superplasticizers were used: Type 1 – PCE-type (polycarboxylic ether), 30 con%; Type 2 – PCE type, 30 con%; Type 3 – PCE-type, 35 con%; Type 4 – PAE-type (polyacrylether), 30 con%.

Table 1: Chemical composition, LOI and density of cements and fly ashes [2]

Constituent	CEMI [%]	CEMIII [%]	FA1 [%]	FA2 [%]
CaO	66.9	57.8	2.7	2.7
SiO_2	17.2	22.6	53.2	53.6
Al_2O_3	3.8	6.5	26.0	26.4
Fe_2O_3	2.5	1.8	8.4	8.6
MgO	1.9	4.0	1.8	1.8
Na_2O	0.2	0.3	1.6	1.6
K_2O	1.8	1.1	3.7	3.7
Na_2O-eq	1.4	1.0	4.0	4.0
SO_3	5.3	5.1	1.1	1.0
Cl^-	0.1	0.1	-	-
LOI	0.5	2.1	4.1	4.3
ρ [kg/m³]	2985	2990	2538	2524

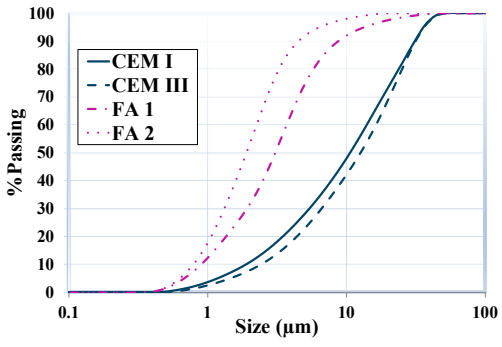

Figure 1: Particle size distribution of fly ashes and cements

2.1. Paste level

Cements were replaced with FA1 and FA2 at five levels: 0%, 15%, 25%, 35% and 50%. The workability of cement pastes was defined by mini-flow table tests in accordance with the standards EN 1015-3 based on determining the consistency of mortars. The mini-flow test setup consisted of a truncated stainless-steel cone (h=60 mm, d_{base}=100 mm, d_{top}=70 mm) placed on a flat, smooth base plate with a diameter of 300 mm. Each paste mix consisted of 500 g of binder (cement with or without fly ash, depending on the replacement level) and 225 g of water. The water/binder factor was always 0.45. Superplasticizer was added in varying amounts to reach the flow diameter in the range of 250-300 mm.

2.2. Mortar level

The mortar compositions were prepared using an automatic mortar mixer in accordance with standard EN 196-1:2016. After 24h the prisms were demolded and placed underwater at a temperature of 20±2°C. The mortar specimens' composition consisted of cement, fly ash, normalized sand and superplasticizer. The choice and dosage of superplasticizer was based on the best flowability of pastes. Mini-slump tests were performed according to the standard EN 12350-2. The mini-slump test setup consisted of a truncated cone (h = 150 mm, d_{base} = 100 mm, d_{top} = 60 mm) placed on a flat, smooth base plate with a diameter of 300 mm. The flexural strength of the hardened mortar prisms (40x40x160 mm) was determined by performing a three-point bending test in accordance with standard EN 196-1:2016. The flexural strength was determined at the age of 28 days after production. The compressive strength tests were carried out at the age of 28 days in accordance with EN 196-1:2016.

2.3. Concrete level

The concrete mix compositions with optimal packing design were partly obtained with the help of software Excel Tool Mix Design (v 1.01) offered by Betonica and optimized in a manual manner by validating the reference mix experimentally. It was decided to produce eight different concrete mixes. The concrete mix compositions are shown in Table 2.

Table 2: Concrete mix compositions with CEM I and CEM III [2]

	CEM REF (kg/m³)	CEM FA1-15% (kg/m³)	CEM FA2-25% (kg/m³)	CEM FA1+FA2-25% (kg/m³)
CEM I 52.5 R / *CEM III/A 42.5N*	360	306	270	270
FA1	-	54	-	36
FA2	-	-	90	54
River sand 0/4	471 / *514*	471 / *514*	471 / *514*	471 / *514*
Limestone 2/6	663 / *641*	663 / *641*	663 / *641*	663 / *641*
Limestone 6/20	755 / *733*	755 / *733*	755 / *733*	755 / *733*
Water	162	162	162	162
Superplasticizer	1.2 / *0.9*	1.2 / *0.9*	1.2 / *0.9*	1.2 / *0.9*
W/B-factor	0.45	0.45	0.45	0.45

Cube and cylinder samples were produced per mix according to EN 206:2013+A1:2016. After demolding, the specimens were cured in a water bath at a temperature of 20±2°C until the age of testing. The slump test was performed in accordance with standard EN 12350-2. The target was to achieve a slump class S3-S4, which should ensure a sufficiently consistent concrete. The flow test was performed to determine the consistency in accordance with standard EN 12350-5. The volumetric mass (density) of the fresh concrete was determined according to the standard EN 12350-6. The air content of fresh concrete was determined with the pressure gauge method according to standard EN 12350-7. The compressive strength of the concrete specimens was determined at the age of 28, 57 and 91 days using an automatic hydraulic press in accordance with standards EN 12390-3 and EN 12390-4.

The ASR test was performed by following RILEM TC 219-ACS AAR-2 test method. The mortar bar specimens with dimensions 25x25x285 mm were cast in prismatic molds and cured for 28 days in a sealed inox container stored in a climatic chamber at 80±2°C for a period of 28 days. In total eight mortars identical to cement replacement levels in the concrete mix composition were prepared. The mortars were mixed in accordance with the mixing procedure EN 196-1:2016. The mortar workability was measured by a flow table test according to EN 12350-2 and a superplasticizer was added to the mortar mixes to achieve the required flow of 205-220 mm. The chloride migration was determined by the chloride migration test according to the NordTest standardized method NT Build 492. Resistance to carbonation was measured on: (1) specimens stored outside protected from rain/snow and exposed to the environment for 13 months and (2) specimens stored for 11 months outside and 2 months in an accelerated laboratory chamber where they were exposed to an environment with 1% CO_2 at a temperature of 20 ± 2 °C and relative humidity of 60 ± 10%. The carbonation depth was measured according to EN 14630 by spraying phenolphthalein (1%) over the axially split specimens.

3. RESULTS AND DISCUSSIONS

3.1. Paste level

The results of the slump [2] and the flow tests (Fig. 2) showed that the more cement is replaced with ultra-fine fly ash, the better is the workability in case of the reference mixes without superplasticizer for both cement types. Superplasticizer (Type 1) made pastes more viscous with an increasing cement replacement. Superplasticizer (Type 2) at some point didn't have any effect / or had a slight effect on the flowability of the pastes with increasing fly ash amount. Superplasticizer (Type 3) gave a very good flowability and required a smaller dosage in comparison to other superplasticizers which had a constant dosage for all cement replacement levels. It can be seen in Fig. 2 that superplasticizer (Type 3) dosage varied depending on the target flowability, when the rest of superplasticizers (SP) had a constant value. Superplasticizer (Type 4) in combination with FA1 made the pastes more viscous, and in combination with FA2 more flowable.

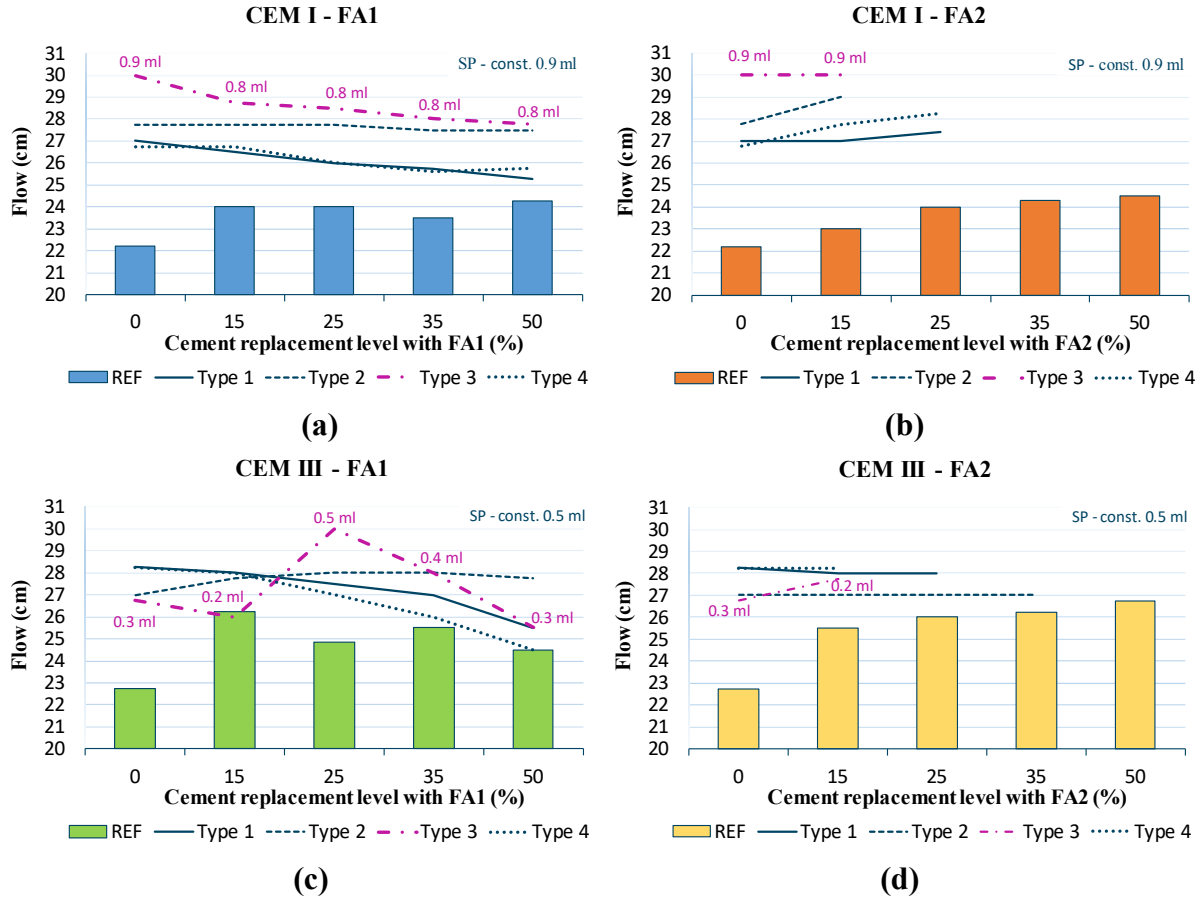

Figure 2: The flowability of the pastes with increasing fly ash amount

Selecting the best suitable superplasticizer, the cost of materials can be limited, which is highly important on a large-scale production. Based on the obtained results, it can be seen that superplasticizer (Type 3) is compatible with both cement types and a lower dosage of it is required. This advantage enables the use of less superplasticizer or the reduction of the water/binder factor, the latter having a favorable effect on the strength and durability of concrete. Also, the results showed that the ultra-fine fly ash (FA2) did have a positive influence on the flowability. FA1, as a slightly coarser ultra-fine fly ash, didn't have such a positive effect on the flowability of the pastes. The higher fineness of the FA2 appeared to have a positive effect on the slump and the flow of the pastes.

3.2. Mortar level

The results of flexural and compressive strength for mortar samples are shown in Fig. 3.

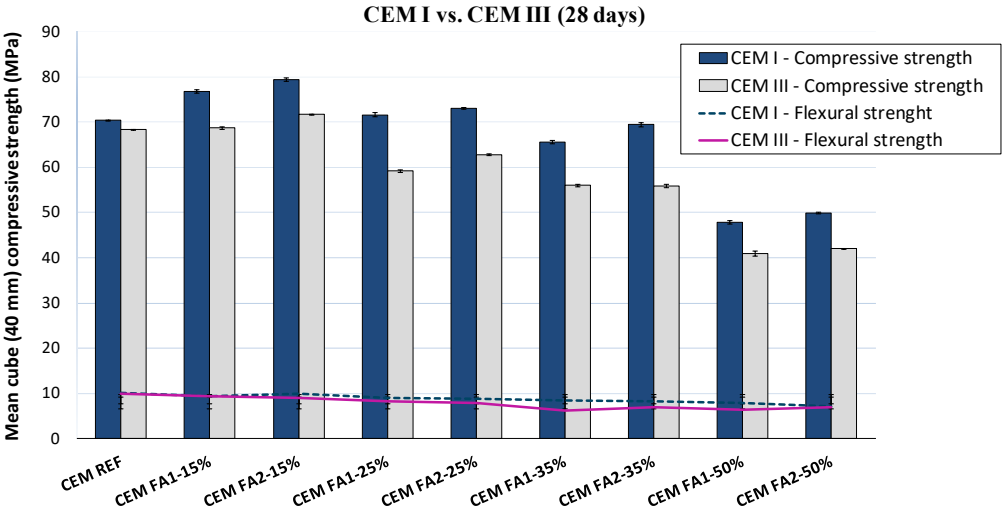

Figure 3: Flexural and compressive strength for mortar samples at the age of 28 days

CEMI – mixes compared to CEMIII – mixes showed a similar but slightly different pattern of flexural strength evolution. At the age of 28 days, the mix CEMI FA2-15% obtained 10% higher compressive strength in comparison to CEMI REF and CEMIII FA2-15% - almost equal compressive strength in comparison to CEMIII REF. The general conclusion from the tests at the mortar-level is that in terms of compressive strength the optimal replacement level of cement with fly ash varies between 15% and 35%, and higher results were achieved with ultra-fine fly ash FA2. The optimum replacement level of cement for mixes with FA2 could be within 15-35% (CEMI) and 15% (CEMIII).

3.3. Concrete level

The results of compressive strength for concrete mixes are shown in Fig. 4.With cement replacement level increase, the slump increased too and concrete mixes had a higher flowability. That was quite good correlated with observations during experiments at the paste level. Concrete with CEMI FA2-25% had a greater slump value than CEMI REF [2]. This indicated that the use of fly ash with a higher fineness (FA2) results in better workability. The densities of the compacted concrete specimens were relatively constant, around 2400 kg/m³. Concrete mixes with FA contained a lower amount of air content in comparison to reference mix: for CEMI FA that difference was lower for 0.4-0.5% and CEMIII FA – for 0.8-1.1%. The air content decreased with an increasing replacement level, which was confirmed by literature [3].

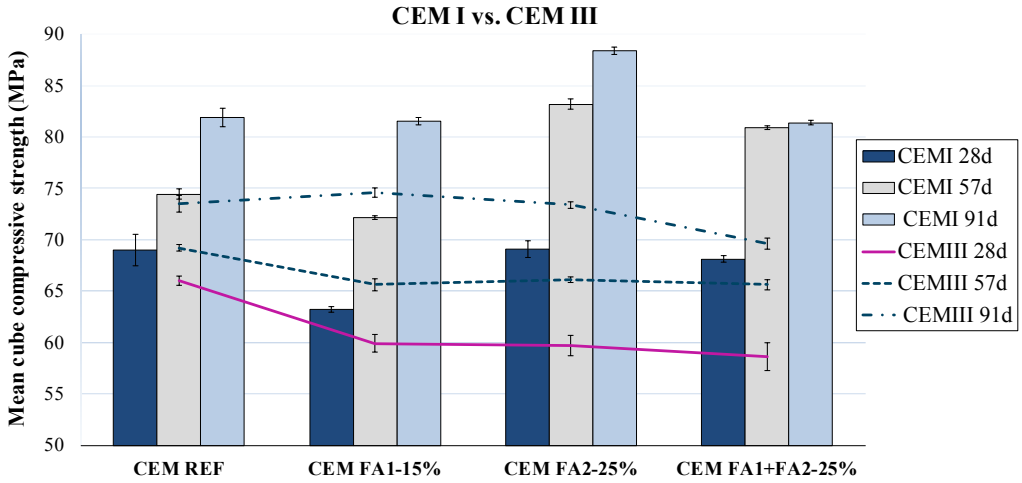

Figure 4: Compressive strength development of concrete mixes

At the age of 28 days, the two concrete mixes with 25% cement replacement (CEMI FA2-25% and CEMI FA1+FA2-25%) approached the reference mix compressive strength value (~70 MPa). From this, it can be inferred that a higher fineness results in a higher pozzolanic reactivity and the reference compressive strength is reached at the age of 28 days and not at the later ages like for conventional fly ash as mentioned in literature [4]. It is known that the pozzolanic activity of fly ash depends upon many parameters such as fineness, amorphous content, chemical and mineralogical composition, and the unburned carbon content or loss on ignition of the fly ash [5]. In an earlier study on the same fly ashes, it was shown that both FA1 and FA2 were enriched in the amorphous phase compared to medium and coarse fractions resulting from post-processing. However, it was concluded from reactivity modeling that at least for early age reactivity fineness was a predominant factor when considering fractions of the same initial fly ash [6]. This is explained by only partial reaction of the fly ash at an early age, resulting in the total amorphous fraction not being a limiting factor, while at the same time the composition of the glassy phase is usually homogeneous over different fly ash size fractions. Concrete mix CEMI FA2-25% obtained compressive strength 7.8% higher in comparison to CEMI REF value at the age of 91 days. The equal compressive strength value to CEMI REF was obtained for CEMI FA1-15% and CEMI FA1+FA2-25% at the age of 91 days.

It was observed that at the age of 28 days the combination of CEMIII with fly ashes gave lower results in comparison to the reference mix. Considering that there is less Portland cement clinker in CEM III producing $Ca(OH)_2$ is needed for the pozzolanic reaction of fly ash, lower results in comparison to concrete mixes with CEMI and fly ashes were noticed. An increase of compressive strength was observed only at the age of 91 days when concrete mix CEMIII FA1-15% reached the value of the reference mix of 74 MPa and CEMIII FA2-25% of 73 MPa. The fineness of the fly ash and the replacement percentage did not affect much compressive strength of the concrete with CEMIII.

ASR expansion tests showed that replacement by ultra-fine fly ash strongly reduced expansion. After 28 days of immersion in the NaOH-solution, the expansion of CEMI REF was significantly greater than the expansion of CEMIII REF, more specifically four times higher. This expansion difference was due to the larger amount of alkalis in CEMI (Portland cement) than in CEMIII. It can be concluded that the choice of cement is an important factor in limiting

the expansion and consequently preventing harmful ASR. The replacement of 25% cement by FA2 was the most optimal to control the expansion after 28 days of immersion. For the mixes with CEMIII, the replacement of 25% cement by the combination of FA1 (10%) and FA2 (15%) performed best [2]. It can be concluded that 25% was the most effective replacement level to limit the risk of harmful ASR. The results for the CEMI- and CEMIII-mixes did not clearly show that the fineness of fly ash influenced the resistance to ASR.

Chloride migration was considerably higher for reference concrete with CEMI. While in the case of fly ash concrete compositions, the migration coefficient was greater for CEMIII (Al_2O_3 – 6.5%) than for CEMI (Al_2O_3 – 3.8%). Concrete specimens with FA2 had a lower chloride migration coefficient (Fig. 5). This was due to the fineness of fly ash that ensured a denser packing. Replacing cement with fly ash was the most effective for CEMI and replacing this cement with 25% FA2.

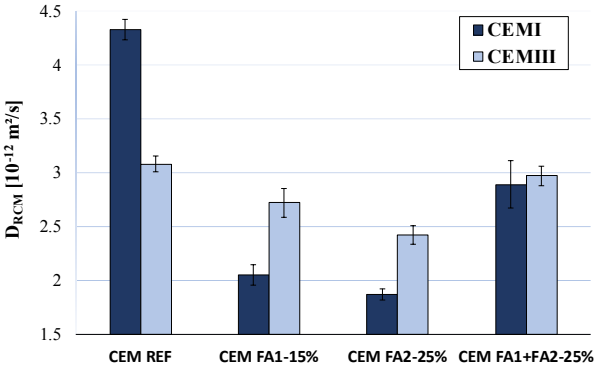

Figure 5: Chloride migration test results

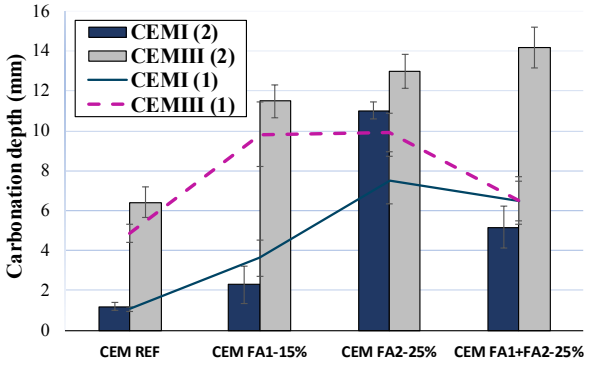

Figure 6: Carbonation test results

It was concluded that carbonation depth was greater for CEMIII compared to CEMI (CEMI - 66.9% CaO and CEMIII - 57.8% CaO). The carbonation depth increased with the increase of the replacement percentage for various concrete compositions (Fig. 6). The finer fly ash also resulted in a greater carbonation depth. The only exception was for CEMI FA2-25%. In terms of concrete microstructure, mainly the $Ca(OH)_2$ content of the cement and to a lesser extent, the pore structure affects the carbonation resistance. The pozzolanic reaction of FA consumes $Ca(OH)_2$, and therefore, also reduces the cement carbonation resistance. The use of FA as a cement component requires careful consideration in the design of concrete mixes and effective curing to produce FA concrete of similar carbonation resistance to reference concrete.

4. CONCLUSIONS

The results at the paste- and mortar- level showed that an increased fineness of the fly ash (FA2) contributed to better workability of the mix. The post-processing of FA into finer fraction by means of DCS technology increased the reactivity of FA and enhanced mechanical properties of concrete. For CEMI, the compressive strength of concrete with FA2 with 25% cement replacement was already equal to the reference mix at the age of 28 days. For CEMIII, the compressive strength of concrete mix with FA2 with 25% cement replacement reached reference mix compressive strength at the age of 91 days. Regarding the durability, replacing

cement with ultra-fine fly ash (FA2) had a positive influence on the chloride migration coefficient and ASR, and a negative influence on the carbonation resistance.

ACKNOWLEDGEMENTS

This work received funding by the VLAIO-MIP program as part of the "VASH – Value ash – classification of fly ashes into valuable fractions" project under grant agreement HBC.2016.0387. The authors would like to thank Willemen Infra NV for providing the cement and aggregates, UAntwerp Mechanics Workshop Team for preparing the setup for ASR and chloride migration experiments, UGent for the performance of accelerated carbonation test. The authors would like to thank master students Lucas Vissers, Cedric van der Waal and Daan van Keijzerswaard for their contribution to the experimental program and specimen preparation/testing.

REFERENCES

[1] Loots M., Snellings R., Maul A., Van den Abeele L. 'Feasibility study report FLAME', 2017, www.valueash.com.

[2] Kara De Maeijer, P., Craeye, B., Snellings, R., Kazemi-Kamyab, H., Loots, M., Janssens, K., Nuyts, G. 'Effect of ultra-fine fly ash on concrete performance and durability', *Constr. Build. Mater.*, **263** (2020) 120493. 10.1016/j.conbuildmat.2020.120493

[3] Jolicoeur, C., To, T. C., Benoit, E., Hill, R., Zhang, Z., Page, M. 'Fly ash-carbon effects on concrete air entrainment: fundamental studies on their origin and chemical mitigation', *In Proc. World of Coal Ash (WOCA2009) Conference*, 4-7 May 2009, Lexington, USA.

[4] Chindaprasirt, P., Jaturapitakkul, C., Sinsiri, T. 'Effect of fly ash fineness on compressive strength and pore size of blended cement paste', *Cem. Concr. Compos*., **27** (4) (2005) 425–428.

[5] Skibsted J., Snellings R. 'Reactivity of supplementary cementitious materials (SCMs) in cement blends', *Cem. Concr. Res*. **124** (2019) 105799. 10.1016/j.cemconres.2019.105799

[6] Snellings, R., Kazemi-Kamyab, H., Joseph, S., Nielsen, P., Loots, M., Van den Abeele, L. 'Pozzolanic reactivity of size-classified siliceous fly ashes', *In Proc. 2nd International Conference of Sustainable Building Materials*, 12-15 August 2019, Eindhoven, The Netherlands, p. 1-18.

COMPRESSIVE STRENGTH AND PORE STRUCTURE STUDIES OF CLAMP-FIRED WASTE POWDERED CLAY BRICK AS A SUPPLEMENTARY CEMENTITIOUS MATERIAL

M. Bediako(1), E. Opoku Amankwah(2) and L. Valentini (3)

(1) Geotechnical and Materials Engineering Department, CSIR-BRRI, Ghana

(2) Development Office, University of Education-Winneba, Kumasi Campus, Ghana

(3)Department of Geoscience, University of Padova, Italy

Abstract

Clamp-firing system is a cost-effective technology used to produce burnt clay bricks in many West African countries including Ghana. However, this firing system generates between 7%-15% of waste in a form of burnt broken bricks and with time creates disposal problems. In this work, burnt clay broken bricks were sampled and pulverised to 75 microns and used as a partial replacement of cement between 10-40 wt. %. Two different sets of mortars were prepared, one from Portland cement as the binder whereas the other set using Portland cement-pulverised bricks as their binders. Compressive strength test was performed on the mortars after moisture exposure at 3, 7 and 28 days. Water absorption test was used to study the pore structure of the optimum mortar mix. The results of the Portland cement-pulverised bricks mortars were compared with the Portland cement mortars. The results of the study indicated that 30 wt.% of the pulverised brick used to replace Portland cement gave the optimum mortar mix. The pore structure of the cement-pulverised brick mortar mixture showed a significant reduction compared to the Portland cement mortars. Si and Al MAS NMR studies revealed that pore structure reduction was due to polymerisation of aluminosilicate hydrates. The study recommends the use of waste powdered burnt clay brick as a supplementary cementitious material and possible means to provide alternative solutions to the disposal of waste burnt broken bricks.

Keywords: Clamp-firing, Broken Bricks, Portland cement, Compressive Strength, Pore Structure

1. INTRODUCTION

Post industrial revolution has brought about enormous changes in the global ecosystem including the depletion of non-renewable natural resources and environmental concerns. The building industry is both a large consumer of some of the earth's finite resources (sand, granite

aggregates, limestone, wood) and also a major contributor of carbon dioxide [1]. The cement industry of which the building industry depends on generate approximately 1 kg per tonne of cement production and 1.5tonnes of natural materials are also use to produce one tonne of cement [2,3]. The depletion of finite resources and the contribution of the cement industry to global carbon emissions has led to sustainable strategies such as selection of materials for buildings and optimization of cement based products (concrete and mortar) incorporating supplementary cementitious materials (fly ash, slag, calcined clays,etc).

Ground powder waste clay brick is generally accepted and used as a supplementary cementitous material [4]. Studies from Wild et al [5], Walker and Parvia [6] and Komnitsas et al [7] have all confirmed the use of ground clay brick powder as pozzolanic materials. Pozzolanic materials as materials that in their powder form reacts with cement in the presence of water and ordinary temperature forming additional cement compounds to enhance cement properties [8]. Analysing the performance of powder brick materials as a pozzolan based on strength analysis criteria have also achieved fairly good number of studies from literature [9]. In many of the works available, 10-20% of powder bricks used to replace cement achieved the maximum strength (Chee et al. 2018). Other studies have investigated and found the positive impact powder bricks have on mortar and concrete mixture in terms of durability, heat of hydration, shrinkage and mitigation of alkali silica reaction [10, 8, 11]

The performance of powder brick as a suitable supplementary cementitiuous material is dependent on the amorphous nature of the material [12]. Though many studies have already been performed on powder clay bricks, the geographical origin of the base material, clay, presents huge chemical and mineralogical variations that influence the amorphousness or reactivity of the powder.

Clamp firing is a firing process used to burn green bricks and it is commonly used in most Western African countries. This process is mostly preferred by the brick producers because it gives them less dependency on expensive electrical energy which is mostly used in developed countries for the same purpose. In most factories in Ghana, approximately 10-15% of the produced bricks are turned into waste in a form of broken and partially baked bricks due to the unevenness of temperature in the clamp. Bediako et al [4] have shown a pictorial view of a clamp set-up. The continuous generation of these waste bricks do create waste disposal problems for many of the factories.

In this work, burnt brick waste generated from the clamp set-up was collected, pulverised and used to replace cement for mortar formation. The objective of the study was to optimise the content of the waste brick powder as a cement replacement material. An earlier study of Bediako et al [4] have shown that powder bricks from clamp-fired set-up is pozzolanic based on chemical composition and strength activity analysis point of view. Compressive strength test was used to optimise the content of waste brick powder in mortar whereas sorptivity test was also performed to understand the pores size refinement. The Magic Angle Spinning (MAS) Nuclear Magnetic Resonance (NMR) tool was used to investigate the silicate and aluminate phases in the optimum paste mixture.

2. MATERIALS AND METHODS

2.1 Materials

The materials that were used for the study were Portland cement, Powder waste clay bricks (PWCB), pit sand, water and a chemical admixture. The Portland cement was Ghacem brand, class 42.4R was obtained from the retail market. Pit sand obtained from the Juaben area in Ashanti region was used. The sand had a maximum size of 2mm, specific gravity of 2.61 and moisture content of 10%. The waste clay brick was obtained from the CSIR-BRRI brick factory located at Fumesua in Ashanti region. The bricks were pulverised into powder with a laboratory ball mill and sieved passing the 75 micrometre sieve size. The chemical admixture used was a sulphonated napthtalene formaldehyde (SNF) water reducing admixture obtained from MC Bauchemie in Accra, Ghana. The solid content of the SNF was 40%. The chemical composition of the cement and the PWCB is shown in Table 1

Table 1: Chemical composition of Portland cement and powder waste clay bricks

Oxide	PC	PWCB
SiO_2 (%)	20.49	67.35
Al_2O_3 (%)	4.26	14.7
Fe_2O_3 (%)	3.14	7.83
CaO (%)	63.48	2.19
MgO (%)	2.11	1.67
SO_3 (%)	2.9	0.15
Na_2O+K_2O (%)	0.49	1.21
SiO_2 (%)+Al_2O_3 (%)+Fe_2O_3 (%)	-	89.88

2.2 Compressive strength determination

Portland cement was replaced by the PWCB and used as binders to formulate mortars. The replacement of cement with PWCB were at 10%, 20%, 30% and 40%. The preparation of the mortars were performed in accordance with the ASTM C109 standards. A three-gang 2inches cubic metallic moulds were used to cast the mortar cubes. The water-to-binder ratio used was 0.485 whereas the binder-to-sand ratio was at 1:2.75. The Hobart mixer was used to mix the mortar constituents and flow determined on a flow table per the ASTM C1437. The addition of PWCB made the mortar less flowable therefore SNF was used to achieve the desired flow. After achieving the desired flow of the mortar, the specimen was cast in the metallic moulds. The mortar specimens cast in the moulds were left in a moist cabinet for 24 hours and then removed and demoulded. The demoulded mortar samples were cured in a saturated lime water in a bath for 3, 7 and 28 days and then crushed for compressive strength test. Compressive strength values were determined on an average of crushed three mortar specimens.

2.3 Sorptivity test

The sorptivity test was performed in accordance with ASTM C1585. 25 mm cube mortar samples cured after 1 and 7 days were conditioned. For the conditioning process, samples were placed in a desiccator containing saturated solution of potassium bromide (KBr) placed at the bottom part inside the dessicator without making any contact with the specimen. KBr was used to maintain a high humidity environment (about 98%). The desiccator and content were placed

in an oven at a temperature of 50˚C for 3 days. After the three days, the dessicator and content were removed from the oven. Mortar samples were placed in sealable transparent plastic containers and placed in an environmental chamber maintained at 50% humidity and 23ºC for at least 15 days. The sealed plastic bags were removed from the chamber after the conditioned period and samples taken out from the sealed plastic bags for their weight measurement. The sides and the top part of the specimens were covered with a black duct tape leaving the side opposite to the top part uncovered. This was done to allow water to flow in one direction. The mass of the covered specimen was recorded as the initial mass of water absorption. A support device was placed at the bottom of a rubber container (shoe box) and filled with tap water up to the height of the of the support device. The uncovered portion of the mortar specimen was placed on the support device whiles the water level was increased to about 2mm above the specimen from the bottom.

The equation used for sorptivity is given below

$$i = S\sqrt{t} \quad (1)$$

S is the sorptivity measured in g per mm^2 (of wetted area) per $sec^{1/2}$. It is easily determined from the slope of the linear part of i versus $t^{1/2}$ curve (Sabir et al, 1998). An average of three mortar specimens were used for the absorption calculations. The gain in mass per unit area over the density of water was plotted versus the square root of the elapsed time. The slope of the line of best fit of these points was taken as the sorptivity value.

2.4 ^{27}Al and ^{29}Si MAS NMR determination

^{27}Al and ^{29}Si MAS NMR were performed on hydrated binder paste of the optimum mortar mixture. Binder paste of normal consistency using the Vicat mould per ASTM C187 was made and compared to that of the cement paste. The test were performed on binder paste samples that were cured for 28 days. The cured specimen was oven dried at 80˚C for about six hours and removed from oven and then milled into fine particles which was sieved through the 75microns sieve size.

Tecmag Apollo Console (Houston, TX) with 8.45 T magnet and homebuilt, single channel, 4 mm wide-bore NMR probe was used to determine ^{27}Al and ^{29}Si spectra. About 90 mg of sample was taken for each analysis and signal represented as chemical shift value; δ: ppm. The ^{27}Al and ^{29}Si Larmor frequencies were 93.074 MHz and 70.958 MHz respectively. ^{27}Al spectra were acquired with MAS spinning frequency, last delay and 90º pulse length of 8 KHz, 1s and 2.5 μs, respectively. 29Si spectra were acquired with MAS spinning frequency, last delay and 60º pulse length of 8kHz, 20s and 5.5 μs, respectively. Aluminum nitrate [$Al(NO_3)$] and Tetramethyl silane (TMS) were used as reference compounds for ^{27}Al and ^{29}Si spectra respectively. All experiments were performed at ambient temperature without any corrections for sample heating.

3. RESULTS AND DISCUSSIONS

3.1 Compressive strength

Figure 1 shows the compressive strength results of the mortars containing the PWCB and the control. The mortar that contained 30% content of PWCB showed higher strength values at the early and the late ages compared the control and the other blended cement mortars. Comparing the 30% PWCB mortar to the control, at 3 and 7 days, strength gained were approximately 11% higher and 9% higher at 28 days respectively. The performance of the 30% PWCB mortar could confirm the fact that there was a pozzolanic reaction that occurred in the

blended mortar. This led to the production extra silicate and aluminate phases known to enhance strength properties (Anderson et al, 2006; Bediako et al 2018).

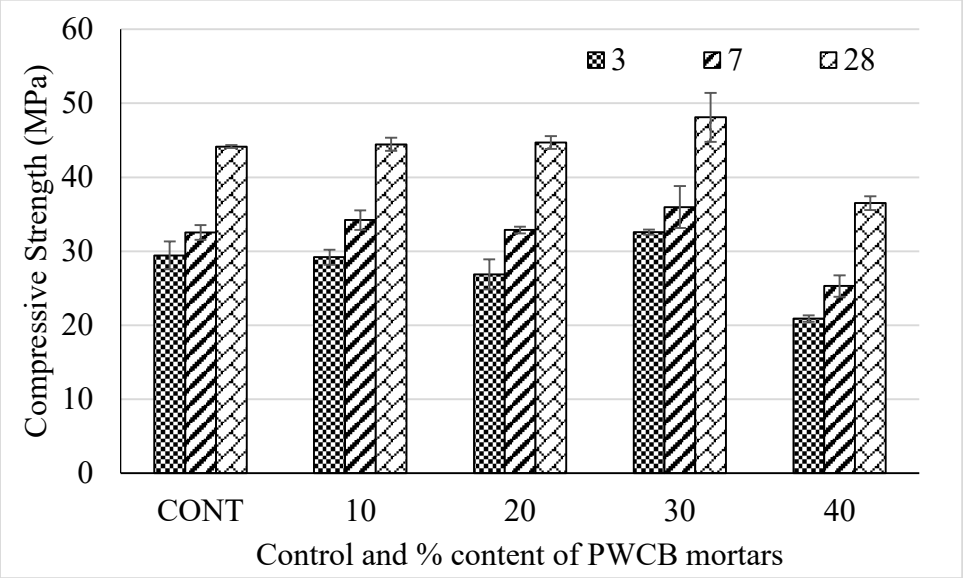

Figure 1: Compressive strength of control and blended mortars

3.2 Water sorptivity

Figure 2 shows the water sorptivity results of the blended mortar that contained 30 wt. % content of PWCB. The initial and the secondary sorptivity of the control mortars were 0.0299 and 0.0083 respectively whereas that of the PWCB incorporated mortars were 0.0055 and 0.0022 respectively. The results indicate that the PWCB mortars had lower sorptivity coefficient values than the control mortars both at the initial and secondary. The lower initial and secondary sorptivity values of the PWCB blended mortar shows that the blended mortars had a more refined pore structure than the control. This has the tendency to resist chemical ingress as posited in the studies of Siddique (2009). The lower sorptivity coefficient value of the blended mortar compared to the control mortar could be attributed to pozzolanic reaction. This argument is supported by the studies of Razak et al (2004).

3.3 ^{27}Al and ^{29}Si MAS NMR

Figure 3 shows the ^{27}Al MAS NMR of the control and the binder paste containing 30wt. % of PWCB. Two distinct shifts are found on the two spectra, 68ppm and 8ppm and they indicate calcium silicate aluminate hydate (CASH) at the tetrahedral region and thermodynamically stable monosulphate phases (AFm) at the octahedral region respectively (Anderson et al, 2006; Brunet et al 2010). The control spectrum showed an intensity of 100% whereas that on the PWCB paste was 108%, a higher intensity than the control. This results at 28 days meant that the inclusion of the PWCB provided more aluminate phases that dissolve in the alkaline environment to form the stable AFm. The stable AFm phases could account for the high strength attainment of the PWCB mortar mixture than the control mortar.

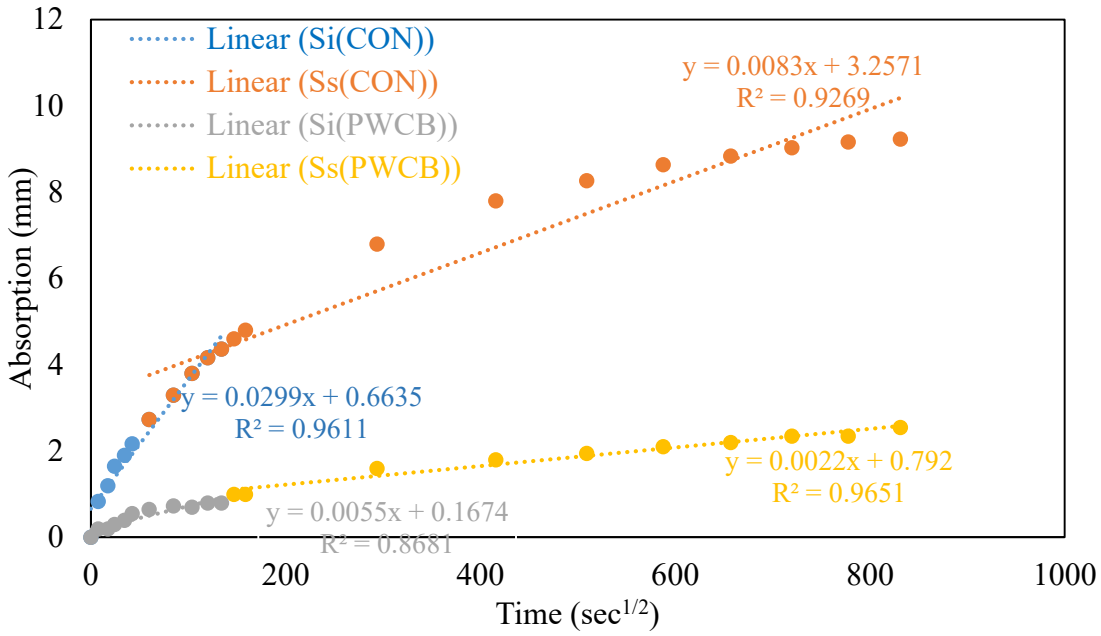

Figure 2: Water Absorption against time

Figure 4 shows the ^{29}Si MAS NMR of the control and the PWCB binder paste. The chemical shift occurred at -90ppm, -97ppm and -103ppm. These chemical shift regions indicate the degree of polymerization of the silicate phases (Mendes et al 2011). The spectrum of the blended paste differed from the control paste at -103ppm which showed a distinct peak formation. The distinct peak indicated that more phases of CSH were formed in the blended paste than the control paste. The increased formation of CSH phases in the blended mixture confirms the reason for the high strength of the mortar than the control.

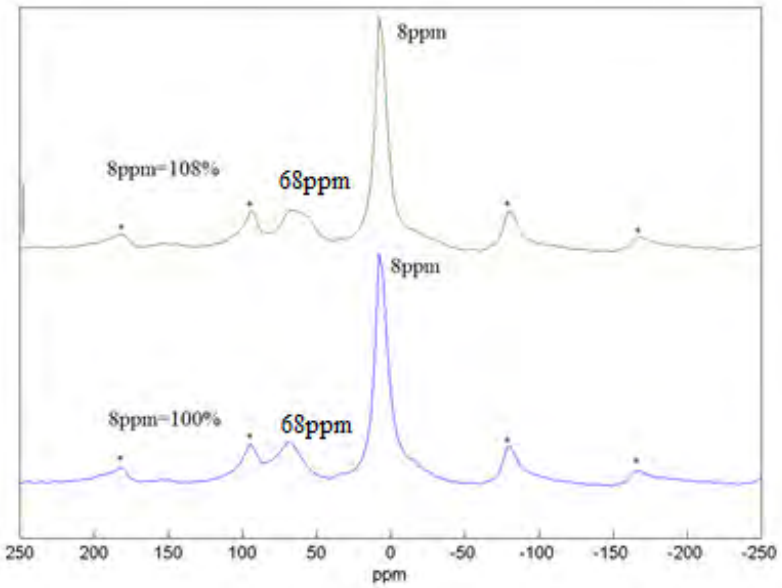

Figure 3: ^{27}Al MAS NMR of control and blended binder paste

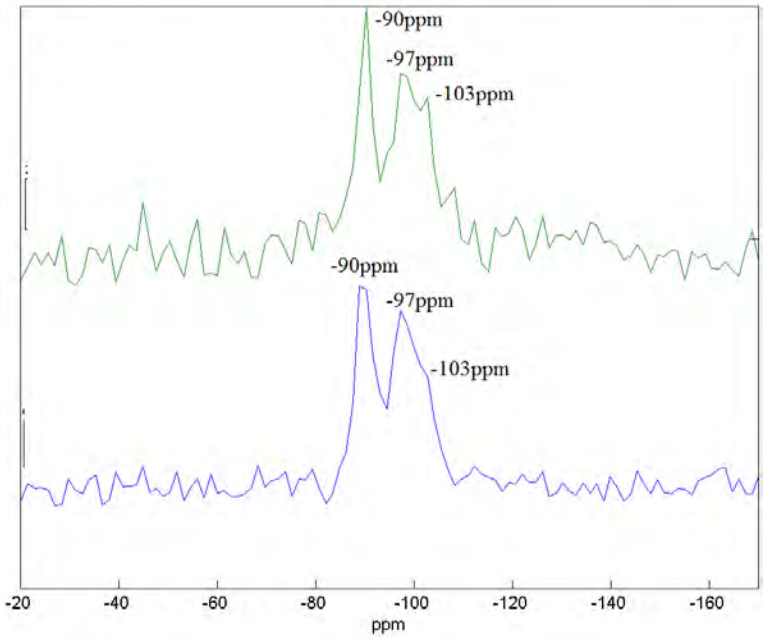

Figure 4:^{29}Si MAS NMR of control and blended binder paste

4. Conclusions

The study investigated the performance of blended cement that contained powder waste clay brick (PWCB) and unblended mortar mixtures. After subjecting the blended and unblended cement mixtures through strength determination, sorptivity studies and MAS NMR studies, the following conclusions could be made

1. PWCB mortar mixture that contained 30wt. % of the material attained the maximum strength at 3, 7 and 28 days. The strength gained over the control mortar at 3 , 7 and 28 days were 11%, 11% and 9% respectively
2. The water sorptivity values (initial and secondary) of the PWCB cement mortar were lower than the control mortar. This shows that the blended mortar mixture could better resist chemical ingress much better than the control mixture.
3. The formation of stable monosulphate (AFm) phases and increased amount of calcium silicate hydrates (CSH) in the blended cement paste than the unblended one at 28 days accounted for the high strength and lower sorptivity values than the control mortar

REFERENCES

[1] Mateus, R., Neiva, S., Braganca, L. Mendonca, P. and Maciera, M. 'Sustainability assessment of an innovative lightweight building technology for partition walls – Comparison with conventional technologies. *Building and Environment* **67**(2013)147-159

[2] Govindan, K., Shankar, K.M., Kannan, D. 'Sustainable material selection for construction industry- A hybrid multi criteria decision making approach. *Renew Sust. Energ.***591 Rev. 55**(2016)1274-1288.

[3] Berndt, M.L. 'Influence of concrete mix design on CO_2 emissions for large wind turbine foundations. *Renew. Energ.* **83**(2015)608-614.

[4] Bediako, M. 'Pozzolanic potentials and hydration behavior of ground waste clay brick obtained from clamp-firing technology. Case Studies in Construction Materials 8(2018)1-7

[5] Wild, S., Gailius, A., Hansen, H., Pederson, L., and Szwabowski, J. Pozzolanic properties of a variety of European clay bricks. *Build. Res. Inf.* **25** (1997)170-175.

[6] Walker, R., & Pavia, S. Physical properties and reactivity of pozzolans, and their influence on the properties of lime–pozzolan pastes. *Mater. Struct.* **44(6)** (2011)1139-1150.

[7] Komnitsas, K., Zaharaki, D., Vlachou, A., Bartzas, G., and Galetakis, M. Effect of synthesis parameters on the quality of construction and demolition wastes (CDW) geopolymers. *Adv. Powder Technol.* **26(2)**(2015)368-376.

[9] Chee, L.W., Kim, H.M., Soon P.Y., U. Johnson, A., Tung-Chai L. Potential use of brick waste as alternate concrete-making materials: A review. *Journal of Cleaner Production* **195**(2018)226-239

[10] O'Farrell, M., Sabir, B., and Wild, S. 'Strength and chemical resistance of mortars containing brick manufacturing clays subjected to different treatments. *Cem. Concr. Compos.* **28**(9) (2006)790-799

[11] Ge, Z., Wang, Y., Sun, R., Wu, X., and Guan, Y. 'Influence of ground waste clay brick on properties of fresh and hardened concrete. *Constr. Build. Mater.* **98**(2015)128–136

[13] Andersen M.D, Jakobsen H.J, Skibsted J. A new aluminium-hydrate species in hydrated Portland cements characterized by ^{27}Al and ^{29}Si MAS NMR spectroscopy. *Cem Concr. Res.* **36**(2006)3-17

[14] Siddique, R. Influence of metakaolin on the properties of mortar and concrete: A review. *Applied Clay Science* **43**(2009)392-400

[15] Razak, H.A, Chai, H.K., Wong, H.S. Near surface characteristics of concrete containing supplementary cementing materials. *Cement Concrete Compos* **26**(2004)883–9

[16] Brunet, F., Charpentier, T., Chao, C.N., Peycelon, H., Nonat, A. Characterization by Solid-state NMR and selective dissolution techniques of anhydrous and hydrated CEM V cement pastes, *Cem. Concr. Res.* **40**(2010)208-219

[17] Mendess, A., Gates, W.P., Sanjayan, J.G., Collins, F. NMR, XRD, IR and synchrotron NEXAFS spectroscopic studies of OPC and OPC/ slag cement paste hydrates. *Materials and Structures* **44**(2011)1773-1791.

DEVELOPMENT OF AN ECOLOGICAL HIGH STRENGTH AND HIGH DUCTILITY CEMENTITIOUS COMPOSITES (ECO-HSHDCC) INCORPORATING GLASS POWDER

Jiandong Wu (1) and Liping Guo (1)
(1) School of Materials Science and Engineering, Southeast University, Nanjing 211189, P.R. China

Abstract

Most of the waste glass, such as flat glass, glass bottle, is buried in the landfill, which is not desirable because it is not biodegradable and is not conducive to the long-term development of the environment. The glass powder (GP) with a certain fineness has excellent pozzolanic effect and can be used as a potential supplementary cementing material in the concrete industry. In this paper, the feasibility of using GP prepared from waste glass as a substitute for cement in the production of an ecological high strength and high ductility cementitious composites (Eco-HSHDCC) was evaluated. Eco-HSHDCC is a unique high performance fiber reinforced cementitious composite with extremely high strength, high tensile strain, and environmental friendliness. The results show that it is feasible to use GP as a partial substitute for cement to produce Eco-HSHDCC. The incorporation of GP can improve the workability of Eco-HSHDCC fresh slurry, which facilitates the dispersion of the fibers in the matrix. In addition, Eco-HSHDCC prepared by incorporating GP has excellent compressive strength and tensile strain capability, reaching 150.0 MPa and 6.0%, respectively. Therefore, the experimental research will provide basic data for the scientific and efficient application of waste glass resource utilization in engineering construction.

Keywords: glass powder, ecological high strength and high ductility cementitious composites (Eco-HSHDCC), workability, compressive strength, tensile strain capability

1. INTRODUCTION

An high strength and high ductility cementitious composites (HSHDCC) is defined as a new type of fiber reinforced cement-based composites with high mechanical properties, high ductility and durability, i.e. tensile ductility is greater than 3% under the condition that compressive strength is higher than 150 MPa. The typical design of HSHDCC mixture is composed of high-strength matrix and super high molecular modulus fiber[1,2]. The high strength of HSHDCC is guaranteed by the very low water-binder ratio and the matrix composed of very high content cement, silica fume, quartz powder and quartz sand[3]. In addition, ultra-high molecular modulus fibers (PE) have hydrophobicity, higher elastic

modulus and tensile strength, which determine their excellent composite effect with extremely dense and high strength cement matrix[4]. During the stress process of HSHDCC, the cracks can expand steadily due to the bridging action of the fibers at the crack site and the transfer stress between the fibers and the matrix. In addition, HSHDCC has a very high energy dissipation capacity before reaching the ultimate tensile strength. Therefore, HSHDCC is not only suitable for the preparation of new structures which must undergo extensive inelastic process under seismic or impact loads[5,6], but also for the reconstruction or reinforcement of old and damaged structures by using thin HSHDCC layers in practical engineering applications[7,8].

In recent years, the construction industry has paid more and more attention to the sustainable development of resource utilization. The research focus has gradually shifted from pursuing mechanical properties of cement-based composites to greening and environmental sustainability of potential infrastructure applications, while maintaining the original performance without degradation as far as possible. However, the cement content used to prepare HSHDCC usually ranges from 900 kg/m^3 to 1500 kg/m^3[1,9,10]. Producing large amounts of cement not only consumes a lot of natural resources and increases production energy consumption, but also releases more carbon dioxide (CO_2) emissions, which will have a serious negative impact on the ecological environment[11]. Therefore, it is urgent to find a new ecological material to optimize and improve HSHDCC matrix system to prepare ecological high strength and high ductility cementitious composites (Eco-HSHDCC).

Most of the waste glass (such as flat glass, glass bottle) produced in industry and life is abandoned to landfills, which is not an environmental management method, because it is a non-biodegradable material and still cause damage to the ecological environment after landfills[12]. In recent years, the research focuses on how to use waste glass as aggregate or cement substitute in concrete and mortar[13,14]. Siad et al.[15] confirmed that waste glass exhibits a significant pozzolanic reaction in the cementitious material, forming a new pozzolanic gel (C-S-H) with low C/S ratio and high amounts of alkalis (Na + K) and aluminum (Al), which contribute to the strength performance and durability of concrete. Therefore, there is an increasing interest in the use of waste glass powder to produce cement-based building materials. However, it is important to notice that there is very limited research focusing on the inclusion or application of GP in Eco-HSHDCC.

The novelty and research contribution of the present work is to develop an Eco-HSHDCC incorporating GP. The objective of this work is to evaluate the potential impact of glass powder on the fresh and hardened characteristics of Eco-HSHDCC. The workability properties of fresh mixtures and uniaxial tensile properties and compressive strength of hardened matrix were carried out.

2. MATERIALS AND METHODS

2.1 Materials

Portland cement (P•II 52.5) and silica fume are selected as the cementitious materials. Besides, glass power (GP) is utilized here to replace part of cement, aiming at developing Eco-HSHDCC. The corresponding the chemical compositions and the particle size distribution of cement, silica fume, and GP are listed in Table 1 and Figure 1, respectively. Silica flour and river sand are utilized as fillers or aggregates. The corresponding the particle size distribution of silica flour and river sand is listed in Figure 1. A polycarboxylate based

super-plasticizer (SP) and ultra-high molecular weight polyethylene (PE) fiber are employed to design Eco-HSHDCC. The properties of PE fiber are presented in Table 2. The water used in the experiment is tap water.

Table 1: Chemical composition of cementitious materials (% by weight)

Material	SiO_2	Al_2O_3	Fe_2O_3	CaO	SO_3	MgO	TiO_2	Na_2O	K_2O	Ignition Loss
Cement	20.72	4.61	3.12	63.95	2.31	1.03	0.22	0.12	0.64	2.84
Silica fume	95.21	1.19	0.13	0.31	0.22	0.92	-	-	0.40	1.16
GP	70.38	1.68	0.38	10.90	0.23	0.91	0.06	13.5	0.50	0.84

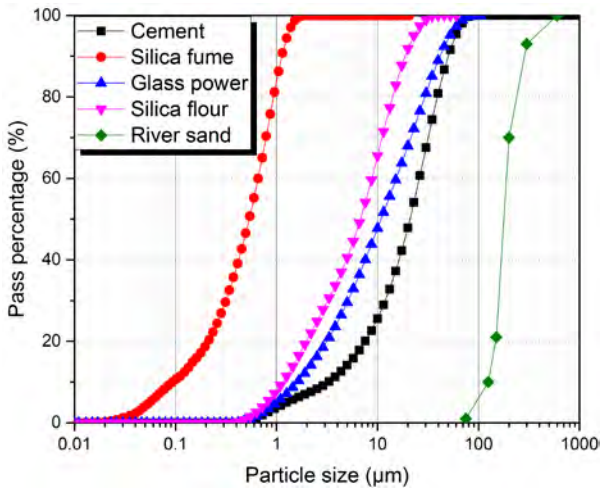

Figure 1: Particle size distribution of cement, silica fume, glass powder, silica flour, and river sand

Table 2: Properties of PE fiber

Diameter d_f, μm	Length L_f, mm	Aspect ratio L_f/d_f	Tensile strength, MPa	Young's modulus, GPa	Density, g/cm^3
24	12	500	2100	116	0.97

2.2 Specimen preparation

Table 3: Mix proportions of Eco-HSHDCC

Mix No.	Composition of mixture							
	Cement	Silica fume	GP	Silica flour	River sand	SP	Water	PE(vol.%)
GP0%	0.8	0.2	-	0.18	0.46	0.012	0.18	2
GP10%	0.7	0.2	0.1	0.18	0.46	0.012	0.18	2
GP20%	0.6	0.2	0.2	0.18	0.46	0.012	0.18	2
GP30%	0.5	0.2	0.3	0.18	0.46	0.012	0.18	2

The mix proportions are given in Table 3. It should be noted that the stirring speed of the whole process is maintained at 140 ± 5 rpm, which avoid the introduction of larger bubbles as far as possible. The fresh Eco-HSHDCC was immediately placed into the greased molds. Finally, the curing temperatures of Eco-HSHDCC specimens before demolding (after curing 24 h) were 22 ± 2 °C in a sealed condition. And then all the specimens after demolding were continued curing at a temperature of 22 ± 2 °C and at RH > 99% to the specified age.

2.3 Methods

The Hägermann cone was employed to measure the fluidity of fresh Eco-HSHDCC mixtures based on EN 1015-3[16]. In the test, the diameters in the two mutually perpendicular directions were measured. Their average values were employed to calculate relative slump.

The compressive strength of Eco-HSHDCC specimens was performed in accordance with ASTM C109[17]. A 3000 kN MTS microcomputer-controlled electro-hydraulic servo universal testing machine was employed to determine the compressive strength of three cube specimens (50 mm × 50 mm × 50 mm) with each composition.

The uniaxial tension tests were performed by means of an electronic universal testing system (MTS 810) machine. Three dumbbell-shaped specimens of each mix proportion were prepared to conduct the stress–strain behavior of Eco-HSHDCC under direct uniaxial tension with a displacement rate of 0.2 mm/min. A linear variable differential sensor (LVDT) was installed at the center of the tensile specimen to monitor the tensile deformation of the specimen with a gauge length of 100 mm during loading.

3. RESULT AND DISCUSSION

3.1 Flowability

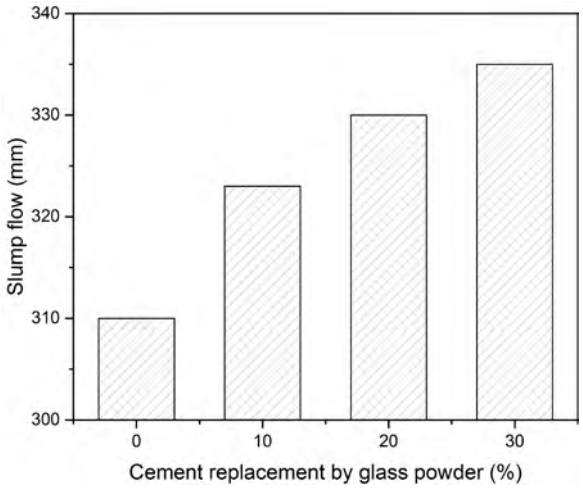

Figure 2: Effect of glass powder on Eco-HSHDCC slump flow

The slump flow of fresh Eco-HSHDCC mixtures versus the content of GP is presented in Figure 2. It can be observed from Figure 2 that the slump flow of fresh Eco-HSHDCC mixtures increases obviously with the addition of GP. For instance, the maximum slump flow value (310 mm) is achieved in mixture without GP, which dramatically increases to 323 mm, 330 mm, and 335 mm when the cement is replaced by 10%, 20%, and 30% of GP,

respectively. The change of slump flow may be attributed to the fact that GP has smoother surface layer and nearly zero water absorption properties, which is beneficial to increase the water demand of cement. As a result, there are not enough hydration products to connect different particles together. Moreover, due to the smooth surface of GP, the interaction between cement paste and glass surface is obviously weakened. Hence, it can be summarized that the addition of GP can improve the flowability of fresh Eco-HSHDCC mixtures, as confirmed by earlier work[18].

3.2 Compressive properties

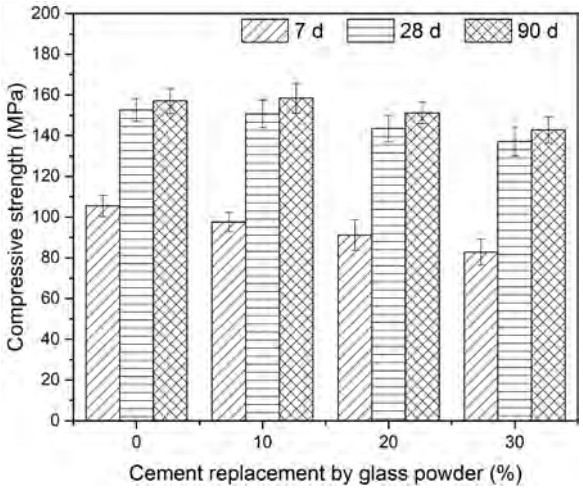

Figure 3: The compressive strength of Eco-HSHDCC at different ages

The effect of cement replacement by glass powder on the compressive strength of Eco-HSHDCC at different ages is illustrated in Figure 3. It can be seen from Figure 3 that the compressive strength of Eco-HSHDCC first increases and then decreases with the increasing content of up to 30% of glass powder at curing 90 d. It is interesting that the compressive strength of Eco-HSHDCC containing glass powder decreased faster at curing 7 d than at curing 28 d and 90 d with the increasing content of up to 30% of glass powder. The reason for this phenomenon is mainly due to the fact that at the early stage of cement hydration, glass powder, as an inert material, can dilute part of cement after being replaced by glass powder, resulting in the decrease of cement content and the increase of water binder ratio. This phenomenon affects the hydration of cement and the mechanical properties of the matrix. With the extension of curing age, the compressive strength of Eco-HSHDCC reached the maximum value of 158.4 MPa when GP substitution was 10%. Compared with pozzolanic materials, glass powder not only keeps the reaction characteristics of pozzolanic, but also has the function of chemical activator. It is generally believed that the dissolution rate of glass powder increases rapidly with the increase of pH value of pore solution. During the dissolution of glass powder, a large amount of alkali is released to act as the active catalyst for the decomposition of cement, silica fume and glass powder in the matrix. The pozzolanic effect of GP can make up for the decrease of cementitious products caused by the loss of cement replaced by GP. However, the compressive strength of UFG decreased when GP replacement increased more than 10%. For example, after 90 d of curing, the compressive

strength of Eco-HSHDCC with 30% GP decreased to 142.8 MPa. The decrease of compressive strength may be attributed to the pozzolanic effect of glass powder is insufficient to make up for the decrease of total hydration products caused by the decrease of cement content with the increase of GP content, resulting the increase of porosity.

3.3 Tensile properties

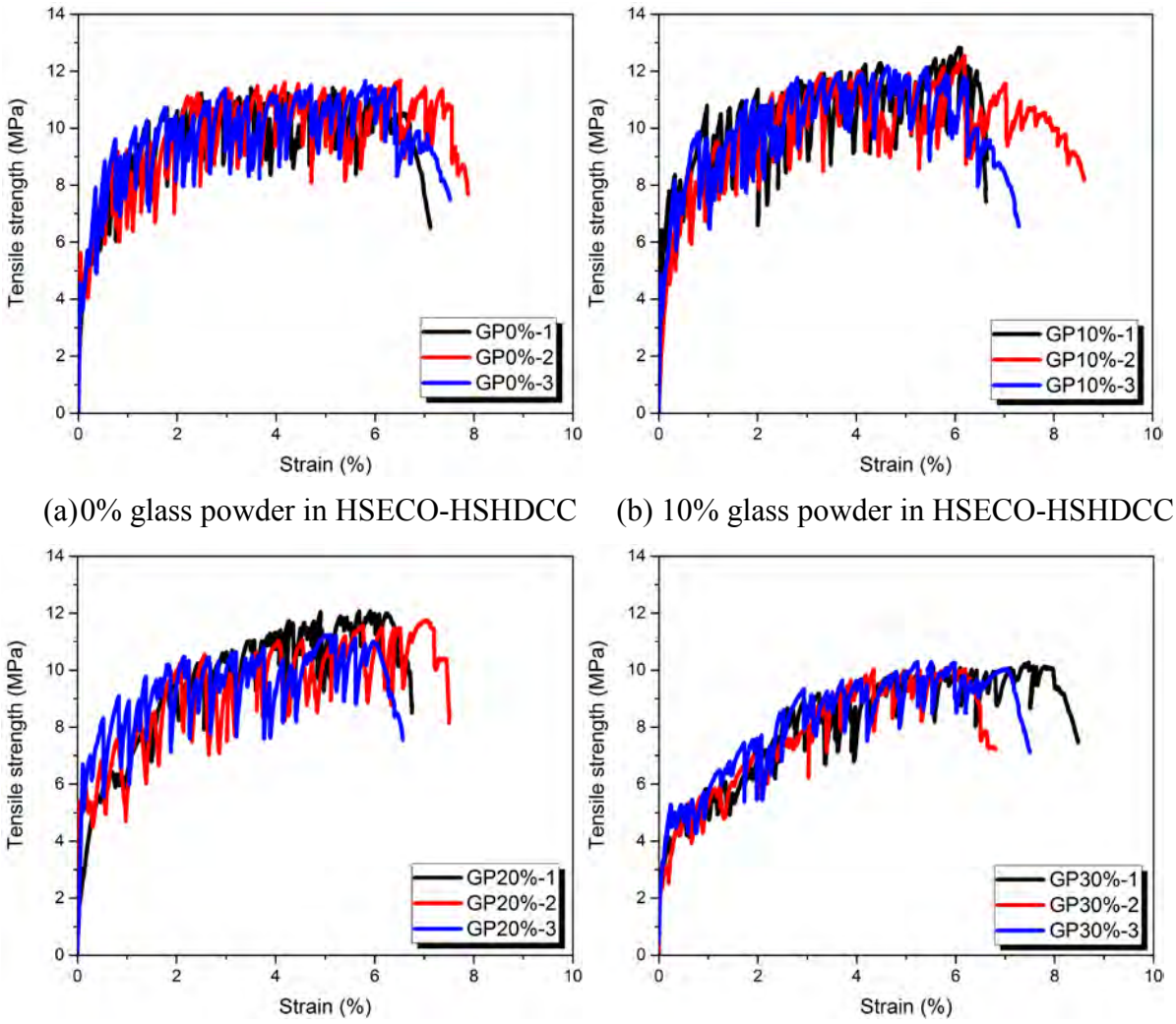

(a)0% glass powder in HSECO-HSHDCC (b) 10% glass powder in HSECO-HSHDCC

(c) 20% glass powder in HSECO-HSHDCC (d) 30% glass powder in HSECO-HSHDCC

Figure 4: The tensile stress-strain curve of Eco-HSHDCC with different cement replacement by glass powder

The tensile stress-strain curves of Eco-HSHDCC with different cement replacement by glass powder are illustrated in Figure 4. All Eco-HSHDCC mixtures undergo four stages in uniaxial tensile process, i.e. linear elastic stage, nonlinear stage, strain hardening stage and strain softening stage. It can be seen from Figure 4 that with the increase of GP content, the ultimate tensile strength of Eco-HSHDCC increases first and then decreases, while the tensile strain shows the opposite trend. When the amount of GP replacing cement is 10%, the

ultimate tensile strength of Eco-HSHDCC mixture reaches the maximum value of 12.47 MPa. It is considered that glass powder contains a large amount of amorphous silica, which can be partially dissolved in high pH environment, showing pozzolanic activity. In other word, amorphous silicon in glass powder reacts with calcium hydroxide (CH) to form low alkalinity hydrated calcium silicate hydrate (C-S-H), which significantly improves the microstructure and compressive strength of Eco-HSHDCC. However, the ultimate tensile strength of Eco-HSHDCC mixture decreased gradually with the increase of GP content. The reason for this phenomenon is that the pozzolanic effect of higher GP content does not play a significant role, and most of its surface is still smooth, which is weak with the interface adhesion of hydration products of surrounding cement. Under tensile stress, the crack is easy to pass through the weak interface, resulting in low strength. In other words, the pozzolanic effect of glass powder with the increase of GP content is not even enough to make up for the decrease of the total amount of hydration products caused by the decrease of cement content, resulting in the decrease of the bond strength of the fiber/matrix interface. However, with the decrease of ultimate tensile strength, the ultimate tensile strain capacity of the mixture increases.

4. CONCLUSIONS

- The effective improvement of the performance of Eco-HSHDCC is achieved by adding waste glass powder, which is conducive to the dispersion of the fiber in the matrix under the condition of very low water cement ratio.
- When the amount of cement replaced by glass powder is 10%, Eco-HSHDCC has the best compressive strength. Although the compressive strength of Eco-HSHDCC decreased with the increase of glass powder substitution, the compressive strength of all samples remained above 140.0 MPa after 90 d of curing, which indicated that ground glass powder could be used effectively in engineering construction.
- With the substitution of glass powder more than 10%, the ultimate tensile strength of Eco-HSHDCC decreased, but the ultimate tensile strain increased gradually. When the amount of cement replaced by glass powder is 10%, the ultimate tensile strength of Eco-HSHDCC is 12.47 MPa and the ultimate tensile strain is 5.88%.

ACKNOWLEDGEMENTS

This work was mainly supported by the National Natural Science Foundations of China (Grant No. 51778133)

REFERENCES

[1] Ranade R, Li V C, Heard W F, B A Williams. Impact resistance of high strength-high ductility concrete. *Cem. Concr. Res.*98(2017)24-35.

[2] Lei D Y, Guo L P, Chen B, et al. The connection between microscopic and macroscopic properties of ultra-high strength and ultra-high ductility cementitious composites (UHS-UHDCC). *Compos. Part B: Eng.*164(2019)144-157.

[3] Ranade R, Li V C, Stults M D, et al. Composite Properties of High-Strength, High-Ductility Concrete. *ACI. Mater. J.*110(4)(2013).

[4] Curosu I, Mechtcherine V, Millon O. Effect of fiber properties and matrix composition on the tensile behavior of strain-hardening cement-based composites (SHCCs) subject to impact loading. *Cem. Concr. Res.*82(2016):23-35.

[5] Mechtcherine V , Millon O , Butler M , et al. Mechanical behaviour of strain hardening cement-based composites under impact loading. *Cem. Concr. Compos.*33(1)(2011)1-11.
[6] Yang E H , Li V C . Strain-rate effects on the tensile behavior of strain-hardening cementitious composites. *Constr. Build. Mater.*52(2014)96-104.
[7] Mechtcherine V. Novel cement-based composites for the strengthening and repair of concrete structures. *Constr. Build. Mater.*41(2013)365-373.
[8] Kamal A, Kunieda M, Ueda N, et al. Evaluation of crack opening performance of a repair material with strain hardening behavior. *Cem. Concr. Compos.* 30(10)(2008)863-871.
[9] Curosu I, Liebscher M, Mechtcherine V, et al. Tensile behavior of high-strength strain-hardening cement-based composites (HS-SHCC) made with high-performance polyethylene, aramid and PBO fibers. *Cem. Concr. Res.* 98(2017)71-81.
[10] Chen Y, Yu J, Leung C K Y. Use of high strength strain-hardening cementitious composites for flexural repair of concrete structures with significant steel corrosion. *Constr. Build. Mater.* 167(2018)325-337.
[11] Ali M B, Saidur R, Hossain M S. A review on emission analysis in cement industries. *Renew. Sust. Energ. Rev.*15(5)(2011)2252-2261.
[12] Jani Y, Hogland W. Waste glass in the production of cement and concrete–A review. *J. Environ. Chem. Eng.* 2(3)(2014)1767-1775.
[13] Khmiri A, Chaabouni M, Samet B. Chemical behaviour of ground waste glass when used as partial cement replacement in mortars. *Constr. Build. Mater.*44(2013)74-80.
[14] Lu J X, Zhan B J, Duan Z H, et al. Using glass powder to improve the durability of architectural mortar prepared with glass aggregates. *Mater. Design.*135(2017)102-111.
[15] H. Siad, M. Lachemi, M. Sahmaran, K.M.A. Hossain, Effect of glass powder on sulfuric acid resistance of cementitious materials, *Constr. Build. Mater.*113(2016)163–173.
[16] BS-EN-1015-3. Methods of test for mortar for masonry - Part 3: Determination of consistence of mixture (by flow table). British Standards Institution-BSI and CEN European Committee for Standardization; 2007.
[17] ASTM C 109. Standard test method for compressive strength of hydraulic cement mortars (using 2-in. or [50-mm] cube specimens). West Conshohocken: ASTM International; 1999.
[18] Taha B, Nounu G. Utilizing waste recycled glass as sand/cement replacement in concrete. *J. Mater. Civil.* Eng.21(12)(2009)709-721.

INFLUENCE OF EXTERNAL ENVIRONMENT ON EARLY-AGE EXPANSION CHARACTERISTICS OF CALCIUM SULFOALUMINATE CEMENT-BASED BINDERS

Vaishnav Kumar Shenbagam (1), Rolands Cepuritis (2) and Piyush Chaunsali (1)

(1) Department of Civil Engineering, Indian Institute of Technology Madras, Chennai, India

(2) Department of Structural Engineering, Norwegian University of Science and Technology, Trondheim, Norway

Abstract

Calcium sulfoaluminate (CSA) cements are widely being promoted as alternative low CO_2 binders. CSA cements can also be expansive and designed to be shrinkage-compensating. The main phase of CSA cement is ye'elimite, which hydrates in the presence of calcium sulfate to form ettringite as the main hydration product. The availability of calcium sulfate can be used to control the hydration kinetics of ye'elimite, which affects the expansion characteristics of CSA cement. Sulfates in the form of gypsum or anhydrite are usually blended with CSA cement in the manufacturing stage. The presence of sulfates in the external environment also affects the expansion characteristics of CSA cement. This study aims to understand the effect of different exposure conditions on the expansion characteristics of CSA-based blended cement. The expansion of the specimens exposed to calcium sulfate solution was found to increase with the amount of calcium sulfate. The addition of CSA cement to Portland cement was found to have a significant influence on the early age expansion characteristics of the system, without affecting the mechanical properties such as compressive strength and dynamic modulus.

Keywords: Calcium sulfoaluminate cement, Expansion, Supersaturation

1. INTRODUCTION

Concrete, the most used human-made material in the world, is a significant contributor to global CO_2 emissions. Portland cement manufacturing process accounts for around 8% of the global CO_2 emissions (1). Hence, reducing the carbon footprint of Portland cement has been an active area of research. To that end, calcium sulfoaluminate (CSA) cement is being promoted as an alternative low CO_2 binder (2). The overall reduction in the CO_2 emissions in the manufacturing of CSA cement can be up to 25–35% compared to OPC, depending on the phase composition of the CSA cement (4).

Ye'elimite ($C_4A_3\hat{S}$), the main phase of CSA cement, was initially developed by Alexander Klein (5) as an expansive cement. Other mineralogical phases present in CSA cement are calcium sulfate ($C\hat{S}$), belite (C_2S), calcium aluminoferrite (C_4AF), and mayenite ($C_{12}A_7$). Hydration of CSA cement mainly results in the formation of calcium sulfoaluminate phases (ettringite or monosulfate) depending on the availability of sulfates. The main hydration

reactions involved in the CSA cement systems are listed below in Eqs. 1–3 (6–8):

$$C_4A_3\hat{S} + 18H \rightarrow C_3A.\ C\hat{S}.\ 12H + 2AH_3 \quad (1)$$

$$C_4A_3\hat{S} + 2C\hat{S}H_2 + 34H \rightarrow C_3A.\ 3C\hat{S}.\ 32H + 2AH_3 \quad (2)$$

$$C_4A_3\hat{S} + 6CH + 8C\hat{S}H_2 + 74H \rightarrow 3C_3A.\ 3C\hat{S}.32H \quad (3)$$

The theoretical water demand for the hydration of pure ye'elimite phase is 0.64 as per Eq. 2 when compared against 0.42 for OPC. As evident from the above-mentioned reactions, the hydration of CSA cement requires higher water content than that of OPC. The $C\hat{S}/C_4A_3\hat{S}$ ratio (by weight) of 1.11 is required for the formation of ettringite according to Eq. 2. When there is a deficit of sulfates, ye'elimite hydrates to form monosulfate and amorphous aluminum hydroxide (Eq. 1). In presence of gypsum, the formation of ettringite (Eq. 2 or Eq. 3) is more favored and faster than the formation of monosulfate as per Eq. 1 (8).

Though ettringite is the main hydration product, metastable phases such as CAH_{10} can also form according to Eq. 4. Belite and calcium aluminoferrite present in the system react to form iron bearing ettringite and strätlingite (Eq. 5 and Eq. 6).

$$C_4A_3\hat{S} + 98H \rightarrow C_3A.\ 3C\hat{S}.\ H_{32} + 6CAH_{10} + 2AH_3 \quad (4)$$

$$3C_4AF + 12C\hat{S}H_2 + 110H \rightarrow 4C_3(A, F).3C\hat{S}.\ 32H + 2(A,F)H_3 \quad (5)$$

$$C_2S + AH_3 + 5H \rightarrow C_2ASH_8 \quad (6)$$

The formation of restrained shrinkage cracks in concrete can be overcome by making the system shrinkage compensating with the creation of expansive stress in the system during the early age of hydration and strength development. The development of expansive stresses can be studied indirectly by monitoring the unrestrained expansion. This expansion can be controlled by understanding the physico-chemical factors influencing it. The expansion characteristics of CSA cement can be attributed to various factors such as the amounts of $C_4A_3\hat{S}$, $C\hat{S}$, water and free lime; the presence of alkali hydroxides; the fineness; and the pore structure features (9). The time of formation of ettringite has a crucial role in governing the final expansion. As the availability of sulfates has a strong influence on the hydration kinetics of ye'elimite, it is important to understand the influence of calcium sulfate on expansion characteristics. The level of expansion increases with the dosage of calcium sulfate until the required stoichiometric amount is reached. With the increasing dosage of calcium sulfate, degree of supersaturation of sulfate is also increased, leading to higher levels of expansion (9,11).

Although, conventionally, expansion is attributed to the formation of ettringite, there is no direct correlation between the expansion and the amount of ettringite formed. Saturation index of ettringite in CSA cement systems has been found to have improved correlation with expansion (12). Using crystallization pressure theory, expansion of CSA cement system could be correlated to the level of supersaturation present in the system (11,13). In a recent study (8), the authors reported that the crystallization pressure due to ettringite and other phases such as AH_3, strätlingite, CAH_{10} and monosulfate might also contribute to expansive stresses in the system.

Expansion of CSA cement is significantly influenced by the environment in which ettringite is formed; that is the pore structure at the time of ettringite formation and the level of supersaturation of sulfate in the system. All other factors mentioned before also directly or indirectly affect either the pore structure or the level of supersaturation which in turn affects the expansion characteristics.

In this work, early-age properties (i.e. expansion, strength and modulus) of OPC-CSA blends

were examined under different environmental conditions. OPC-CSA blends were prepared by blending 10% CSA cement with 90% OPC, and were exposed to saturated lime solution, unsaturated gypsum solution, supersaturated gypsum solution, relative humidity (RH) of 95% and 65% after initial curing period of 7 days.

2. MATERIALS AND METHODS

A commercially available CSA cement and OPC were used for this study. The phase compositions of both cements are given in Table 1. The expansion studies were performed on cement paste specimens prepared at a constant water-to-cement ratio (by weight) of 0.4. Distilled water was used for casting and preparing exposure solutions. Five different exposure conditions were used in the study — drying at 65% relative humidity (65% RH), moist room with 95% relative humidity (95% RH), saturated lime solution (Lime), undersaturated gypsum solution (USCŜ), and supersaturated gypsum solution (SCŜ). Reagent grade calcium hydroxide was used in the concentration of 2g/l to prepare saturated lime solution. Furthermore, gypsum in the concentrations of 1g/l and 5g/l was used to prepare USCŜ and SCŜ solutions, respectively. All the specimens were cast at a controlled temperature and RH of 25°C and 65%, respectively. The specimens were demolded after 24 hours of casting and cured in saturated lime solution (at 25°C) for 7 days before exposing them to various exposure conditions.

Table 1: Mineralogical phase composition of OPC and CSA cement

CSA Cement						
Ye'elimite	Anhydrite	Lime	Dolomite	Belite	Mayenite	
14.1%	43.3%	21.2%	5.5%	10.4%	3.8%	
Portland Cement						
Alite	Belite	Aluminate	Ferrite	Gypsum	Calcite	Portlandite
48.8%	28.1%	6.5%	8.5%	1.9%	3.9%	1.3%

Phase identification and mineralogical examination was performed using X-ray diffraction (XRD), which was carried out in an X'pert Pro PANalytical equipment. The XRD patterns were collected for 2-theta (2θ) range of 5º – 60º for with a step size of 0.02º. Each scan was completed in about 9 minutes. The X'Pert HighScore plus software was used to identify the phase composition and phase quantification using Rietveld refinement. The parameters used for refinement were specimen displacement, scale factor, cell factor, and, if required, the preferred orientation and the profile shape (w value). The background was fitted using a polynomial function with the coefficients 1, 2, 3 and 1/x. The final goodness of fit (GoF) value attained was less than 2.75. Hydration stoppage for the samples was done by solvent exchange with isopropyl alcohol (IPA) followed by vacuum filtration. The samples were crushed and immersed in IPA for an initial period of 30 minutes and washed with IPA under vacuum for about 10 minutes. Diethyl ether was then sprayed on the sample to replace the IPA. The sample was dried and stored in a low-vacuum desiccator for at least 3 days before testing. About 2g of sample was crushed and sieved through a 37-micron sieve (400 number) for characterization.

For the study on dimensional stability, 25 × 25 × 285 mm prismatic paste specimens were cast for binder systems: OPC, OPC with 5% replacement of CSA, and OPC with 10% replacement of CSA.

The mechanical properties of cement paste specimens were determined at different ages of 1, 3, 7 and 28 days. The compressive strength test was done on 50 × 50 × 50 mm cube size specimens, and the dynamic modulus was calculated using the resonant frequency test on the 25 × 25 × 285 mm size prismatic specimen. The Poisson's ratio of the binder matrix was assumed as 0.17.

3. RESULTS AND DISCUSSION

This section reports the results on the hydration progress and strength development of OPC and OPC-CSA blends.

3.1 Hydration of CSA cement

X-ray diffraction was performed to monitor the hydration of OPC-CSA blend. Fig.1 shows the XRD diffractograms of CSA cement and hydration of OPC-CSA blend at early ages.

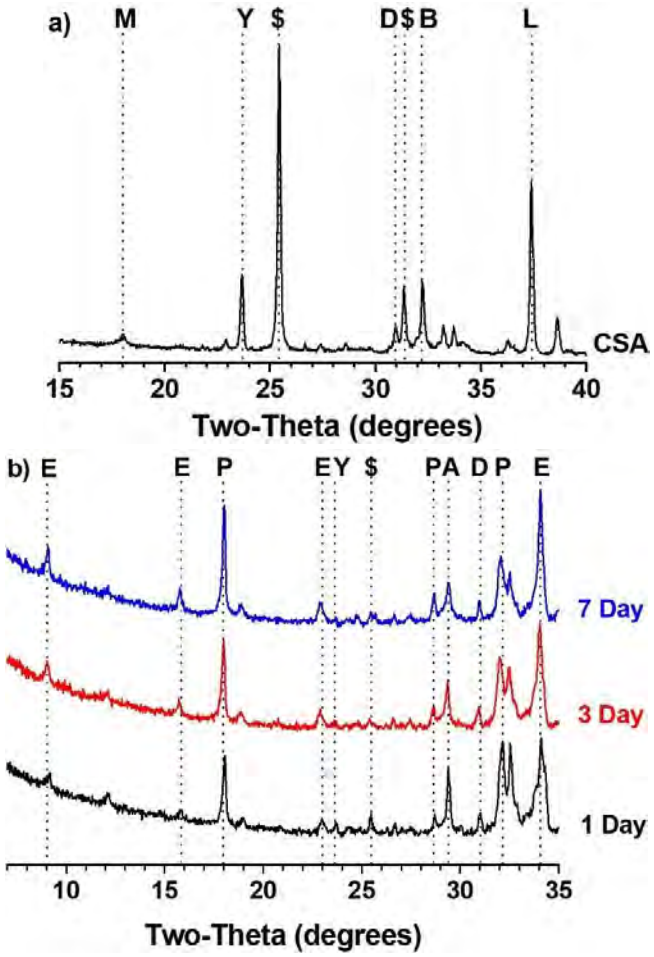

Figure 1: XRD patterns of a) unhyrated CSA cement and b) hydrated OPC-CSA binders after 1, 3 and 7 days

(Note - Y: Ye'elimite, M: Mayenite Ŝ: Anhydrite, A: Alite, B: Belite D: Dolomite, L: Lime, P: Portlandite, E: Ettringite)

It is evident that the ye'elimite phase in CSA cement is completely consumed in 7 days. As the CSA cement hydrates rapidly, the formation of ettringite takes place at early ages. This also influences early-age expansion characteristics of CSA-OPC bleded cements.

3.2 Expansion characteristics of OPC-CSA blends

Initially, expansion characteristics of OPC and OPC-CSA blends were measured in saturated lime water, as shown in Fig.2. The control specimen cast with OPC was found to have expanded to 240 microstrains. With the addition of CSA cement, the expansion was increased to 820 and 4250 microstrains after 28 days for 5% and 10% replacement of CSA, respectively (Fig.2). It is clear that addition of CSA cement corresponds to an increase in the amount of ye'elimite present. With higher levels of ye'elimite present, there is a higher amount of ettringite formed at early ages, which causes expansion. The expansion of OPC-CSA blends

increased with the amount of CSA cement in the system (8,13). It was also observed that most of the expansion occurred within the 7 days, beyond which the curve plateaued. The rate of expansion was also found to increase with the increase in dosage of CSA cement. As the consumption of ye'elimite is completed at within 7 days (Fig.1), the expansion due to the hydration of CSA cement also takes place during this period.

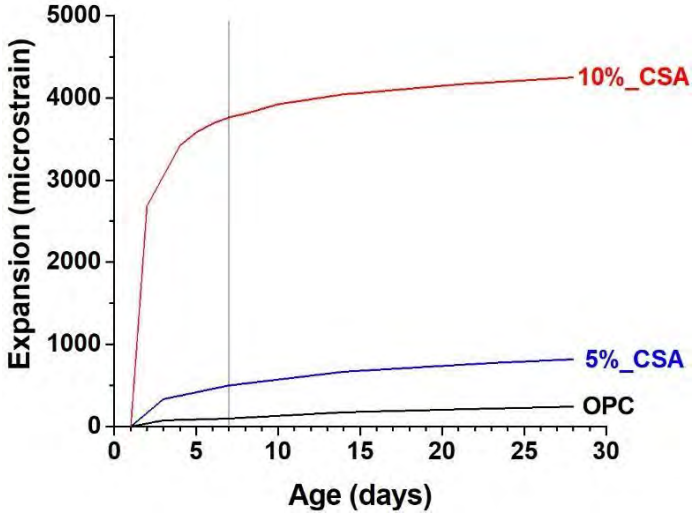

Figure 2: Expansion characteristics of OPC and OPC-CSA blends under lime curing

3.3 Influence of external environment on expansion characteristics

The change in expansion that occurs beyond 7 days can be attributed to the different exposure conditions, as the expansion due to the hydration of ye'elimite is completed within first 7 days. To study the influence of external environments, the specimens cast with 10% CSA cement were exposed to the different exposure conditions after 7 days of curing. The specimens had an expansion of ~3800 microstrains at the time of exposure to different curing environments (Fig.2). The specimens exposed to saturated lime solution and in moist room (~95% RH) had similar levels of expansion (Fig.3). In both cases, there is no loss of moisture from the specimens and leaching of lime is also restricted. This can be considered as the base line to determine the expansion caused due to the presence of external sulfates.

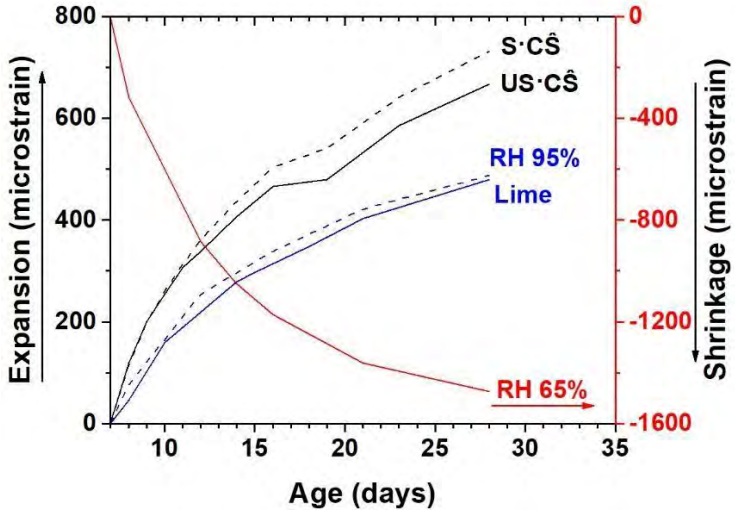

Figure 3: Influence of external environment on expansion and shrinkage Characteristics

When exposed to drying (at 65% RH), ~ 1500 microstrains of shrinkage was recorded at 28

days, which is less than the initial expansion of 3800 microstrains that was attained. This indicates how the CSA based cements can act as a shrinkage compensating agent by inducing additional expansion at early age.

When the specimens were exposed to a sulfate solution, the resultant expansion was found to increase with the increase in the level of sulfates in the solution (14). The increase in sulfate concentration of the solution increased the level of supersaturation with respect to ettringite. This increase led to an increase in the crystallization pressure causing additional expansion. The increase in the level of supersaturation of ettringite has a direct influence on the resultant expansion (10).

3.4 Mechanical characteristics of OPC-CSA blended cement

Compressive strength and dynamic modulus were used as means to evaluate mechanical properties. Figure 4 shows the evolution of dynamic modulus of OPC and OPC-CSA blends with time. The dynamic modulus of all the three binder systems steadily increased with age (Fig.4). This is also an indicator to confirm that the expansion caused due to CSA cement did not lead to cracking of the matrix. A similar trend was also seen with the compressive strength as shown in Fig.5a.The addition of CSA cement did not affect the mechanical properties negatively, whereas the influence of CSA cement on the expansion is evident (Fig.5b). Stiffness of the matrix also affects the extent of expansion. For example, a matrix having lower stiffness will offer reduced resistance to expansion compared to a matrix having higher stiffness. This could potentially play a significant role when there is significant difference in the stiffness.

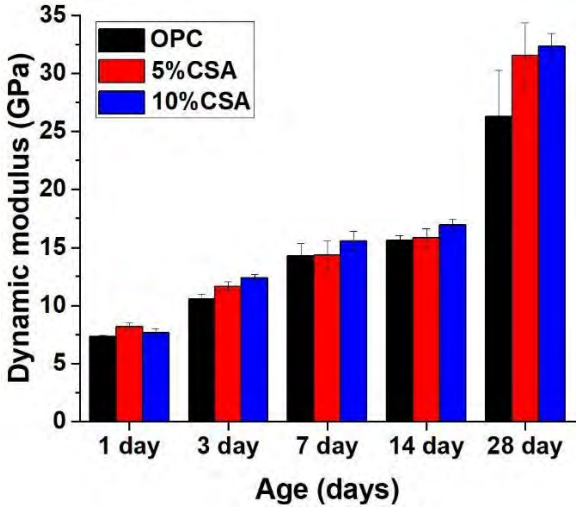

Figure 4: Evolution of dynamic modulus

In this study, the effect of ye'elimite and calcium sulfate (from external environment) on the early-age expansion characteristics of OPC-CSA blend was examined. Increase in ye'elimite and sulfate concentration also increased the expansion. However, the mechanism and the level of expansion attained through them (increase in ye'elimite and sulfate concentration) were different.

The influence of ye'elimite addition on expansion is more prominent in OPC-CSA blend with 10% CSA than the OPC-CSA blend with 5% CSA (9). This increase in expansion was attributed to higher ettringite fraction due to increased ye'elimite content in OPC-CSA blend. However, increase in sulfate concentration resulted in higher supersaturation with respect to ettringite, and thereby, induced higher crystallization pressure resulting expansion (11). Interestingly, when the mature (no ye'elimite present) OPC-CSA paste was exposed to sulfate solution, only ~7% increase in expansion was observed. This indicates the role of curing media

during the formation of ettringite on the extent of expansion. Nonetheless, the change in stiffness of cement matrix will also influence the expansion characteristics. Hence, physico-chemical characterization including pore structure features, pore solution analysis, material stiffness, and phase composition will enable better understanding of expanding cementitious systems based on CSA cement.

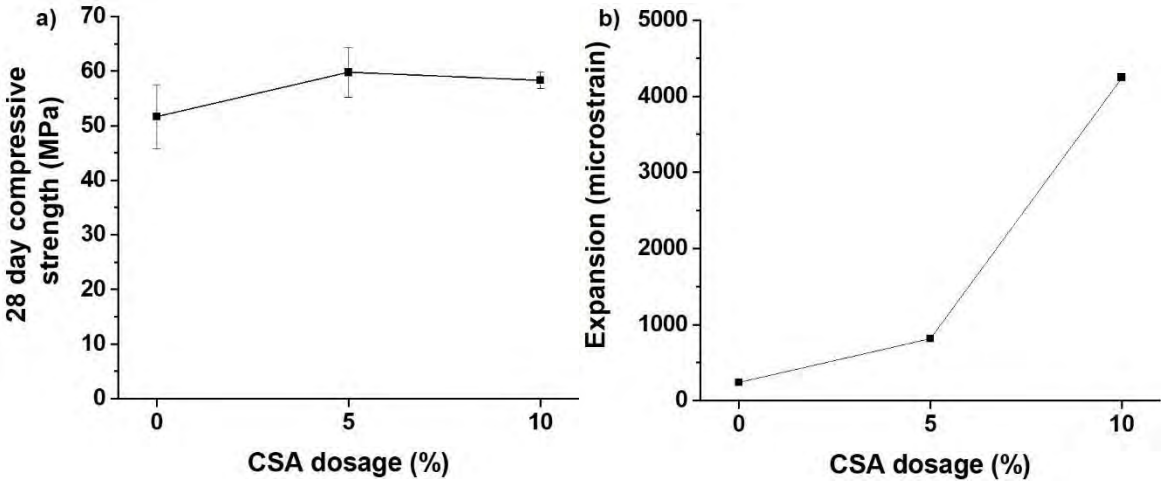

Figure 5: (a) Compressive strength, and (b) expansion of OPC-CSA blends after 28 days

4. CONCLUSION

This study reports the results of the role of different environmental conditions on the expansion characteristics of OPC-CSA blends having 0%, 5%, and 10% CSA cement. The expansion was found to be increasing with the increase in the sulfate concentration of exposure medium. For OPC-CSA blend with 10% CSA cement, the initial expansion during the first 7 days was found to compensate for the drying shrinkage. The addition of CSA cement (up to 10%) with OPC had a strong influence on the expansion characteristics without affecting the strength and dynamic modulus of the system.

Acknowledgements

The first author would like to acknowledge the doctoral scholarship received from the Ministry of Human Resource Development (MHRD), India. All authors would like to acknowledge the financial support of the Department of Civil Engineering at Indian Institute of Technology Madras towards the usage of experimental facilities in this study.

References

1. Andrew RM. Global CO 2 emissions from cement production. Earth System Science Data. 2018;10(1):195.
2. Gartner E. Industrially interesting approaches to “low-CO2” cements. Cement and Concrete research. 2004 Sep 1;34(9):1489-98..
3. Glasser FP, Zhang L. High-performance cement matrices based on calcium sulfoaluminate–belite compositions. Cement and Concrete Research. 2001 Dec 1;31(12):1881-6.
4. Hanein T, Galvez-Martos JL, Bannerman MN. Carbon footprint of calcium sulfoaluminate clinker production. Journal of cleaner production. 2018 Jan 20;172:2278-87.
5. Alexander K, inventor; Chemically Prestressed Concrete Corp, assignee. Expansive and shrinkage-compensated cements. United States patent US 3,251,701. 1966 May 17.
6. Zhang L, Glasser FP. Hydration of calcium sulfoaluminate cement at less than 24 h. Advances in cement research. 2002 Oct;14(4):141-55.

7. Zajac M, Skocek J, Bullerjahn F, Lothenbach B, Scrivener K, Haha MB. Early hydration of ye'elimite: Insights from thermodynamic modelling. Cement and Concrete Research. 2019 Jun 1;120:152-63.8. Hargis CW, Lothenbach B, Müller CJ, Winnefeld F. Further insights into calcium sulfoaluminate cement expansion. Adv Cem Res. 2018;31(4):160–77.
9. Chen IA, Hargis CW, Juenger MC. Understanding expansion in calcium sulfoaluminate–belite cements. Cement and Concrete Research. 2012 Jan 1;42(1):51-60.
10. Winnefeld F, Martin LH, Müller CJ, Lothenbach B. Using gypsum to control hydration kinetics of CSA cements. Construction and Building Materials. 2017 Nov 30;155:154-63.
11. Bizzozero J, Gosselin C, Scrivener KL. Expansion mechanisms in calcium aluminate and sulfoaluminate systems with calcium sulfate. Cement and Concrete Research. 2014 Feb 1;56:190-202.
12. Chaunsali P, Lim S, Mondal P, Tobias DH, Tobias DH. Factors influencing the early-age volume change of expansive cements relevant for bridge deck concrete. InProceedings of the Transportation Research Board 92nd Annual Meeting, Washington, DC, USA 2013 Jan (pp. 13-17).
13. Bullerjahn F, Skocek J, Haha MB, Scrivener K. Chemical shrinkage of ye'elimite with and without gypsum addition. Construction and Building Materials. 2019 Mar 10;200:770-80.
14. Chen IA. Synthesis of Portland cement and calcium sulfoaluminate-belitecement for sustainable development and performance. The University of Texas at Austin; 2009.

MICRO- AND PORE STRUCTURE ANALYSIS OF VOLCANIC ASH BLENDED CEMENT PASTE

Antony J. (1), Al-Bahar S. (1), Jayasree C. (1), Al-Arbeed A. (1), Muntaha H. Behbehani (2) and Zakiah A. Rasheed (2)

(1) Construction and Building Materials Program, Energy and Building Research Centre

(2) Environmental Pollution and Climate Program, Environment and Life Science Research Center

Abstract:

Volcanic ash blended cement based concrete are known for its better performance in terms of strength and durability, especially in marine environments where hot and cold climatic conditions along with chloride and sulphate attacks are detrimental for the construction materials. Since the properties of volcanic ash will vary with region to region, complete knowledge of chemical composition and thorough understanding of the hydration mechanism is unavoidable to find out the optimum dosage of volcanic ash for better performance. Understanding the cement hydration process and characterizing the hydration products in microstructural level is a complex and interdependent process that allows one to design complex mix proportions to produce sustainable concrete materials. Here, the micro- and pore structure of cement paste samples prepared with locally available ordinary Portland cement (OPC) and regionally available volcanic ash (VA) was studied by using Isothermal Calorimetry, N_2-Adsorption analysis, thermogravimetric analysis (TGA), and scanning electron microscopy (SEM). The studies show that, even though the added VA reduces the initial cement hydration process, it could be used as a potential replacement of OPC up to a certain extent for the development of sustainable high performance concrete.
Keywords: cement hydration, volcanic ash, micro- and pore structure, pozzolanic reaction.

1. INTRODUCTION

Concrete, the second most utilized substance in the world, consumes huge quantities of natural resources and energy during its production. Ordinary Portland cement (OPC) is the major binding material used in the concrete. The cement industries account for 6% of global carbon dioxide emissions (CO_2), a greenhouse gas that directly influences global warming and climatic conditions [1]. The World Cement Association (WCA) recently held its first-ever Global Climate Change Forum recently in Paris, France from 27-28 June 2018, where industry leaders and scientists discussed strategies to reduce the carbon footprints of global cement industry. One of the major concerns of the forum was that the existing CO_2 emission mitigation technologies are adopted very slowly, resulting in only a gradual decrease in carbon emissions

associated with production processes and product end-users. So, the WCA urged the global cement industry to increase the efforts to adopt new technologies faster and put greater focus on innovations that make crucial progress on reducing CO_2 emissions. One of the best practices to address this issue is to use the waste/by-product materials such as fly ash, slag, silica fume, and natural pozzolans as a partial or complete replacement for Portland cement in concrete mixtures [2-8].

Supplementary cementitious materials are widely used for the production of durable and sustainable concrete. Volcanic ash blended cement-based concretes are known to show much better performance in terms of strength and durability, especially in areas where sulfate and chloride attacks are a major concern [9-12]. Moreover, the production of green and economical concrete using regionally available volcanic ash creates a sustainable, efficient and simpler route to revalorize large volumes of these natural waste deposits. Many scientists have reported an optimum dosage of 20-30% OPC replacement with volcanic ash gives maximum performance, especially in the later ages. A complete and clear understanding of the hydration mechanism is unavoidable to find out the optimum dosage of supplementary cementitious materials for better performance. Here in this paper, an attempt is made to understand the hydration behavior along with micro and pore structure of cement paste samples prepared with locally available OPC and volcanic ash obtained from regional resources through Isothermal Calorimetry, N_2-Adsorption analysis, thermogravimetric analysis (TGA), and scanning electron microscope (SEM).

2. EXPERIMENTAL METHOD

The experiments were carried out using locally available Ordinary Portland cement (Type I) conforming to ASTM C150 and the volcanic ash obtained from Saudi Arabia. The cement paste samples at a w/c ratio of 0.45 were cast by incorporating varying percentages of volcanic ash (0, 15, 25, and 35%), and the modifications on the microstructure and pore structure of the hardened cement paste matrices after different ages of curing (28 and 90 days) were studied. The samples were cast in miniature molds (1 cm x 1 cm x 1 cm). After being cured for 7, 28 and 90 days in water, the hardened cubes were removed from the water and kept in acetone for arresting the hydration process. Samples were taken from acetone after 24 h and kept under vacuum for the complete removal of acetone. The microstructural and pore structural analysis was carried out using these samples. The early age cement hydration characteristics of cement paste were studied according to ASTM C1679-09 using Calmatrix 1 CAL 4000 Isothermal Calorimeter for a period of 48 hrs. SEM analysis was done using JEOL analytical scanning electron microscope, JSM6010LA. Samples were placed on carbon tape attached to the sample holder with gold coating. Approximately 25 mg of samples were taken in a platinum-rhodium (Pt-Rh) crucible with a pierced lid and heated from room temperature to 900 ^oC at a heating rate of 10 °C per minute using N_2 as a medium under static condition for thermogravimetric analysis. Nitrogen adsorption analysis was performed on chipped solid pieces (approximately 20-30 g) extracted from hardened cement paste samples after 28 and 90 days of curing. The experiments were performed with Adsorption Analyzer Micromeritics ASAP 2020 Plus, manufactured by Micromeritics, Norcross, GA. The adsorption and desorption isotherms, surface area and cumulative intruded volume were calculated using the data from the nitrogen adsorption experiment.

3.1 Isothermal Calorimetry

Early age cement hydration processes are accompanied by thermal changes and it can be monitored by thermal analysis methods like isothermal calorimetry and TGA. The isothermal calorimetric method used to monitor the relative heat changes during the early ages of cement hydration reaction especially up to 48 hours. This helps us to find out the influence of the addition of chemical admixtures or supplementary cementations materials (SCM) on the cement hydration profile. Here, the effect of VA on the hydration characteristics of cement paste was studied according to ASTM C1679-09 using Calmatrix 1 CAL 4000 Isothermal Calorimeter. Cement paste samples were prepared with different percentages of VA (0, 15, 25 and 35%). Raw materials mixed at the water to cement ratio of 0.45 externally in a vortex mixer and then transferred to a vial in the isothermal calorimeter. Tests were performed for a period of 48 hours. The difference in the heat of hydration due to the partial replacement of OPC with VA was analyzed from the thermal power curve. In addition, the total heat of hydration was calculated and plotted in a bar chart for each specimen to study the influence of various percentages of VA on total heat of hydration. The test was repeated for different mixes.

Figure 1 shows the thermal power curve obtained for mixes at 0.45 w/c ratio. According to ASTM C1679–09, the thermal curve showed the different stages of hydration, including initial hydration period, dormant period, and main hydration peak along with accelerated aluminate hydration.

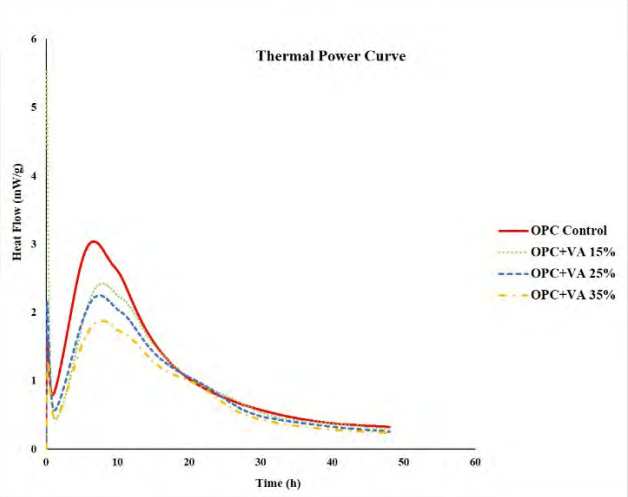

Figure 1: Thermal power curve for cement paste mixes containing different percentages of VA at 0.45 w/c.

The graph also demonstrates how the heat evolved is reduced every time with the increase in the percentage of admixture; however, there is no clear shift in time. Figure 1 show that for w/c 0.45 there is a major reduction in the total heat of hydration as the volcanic ash percentage increases. The reduction in early age hydration reaction can lead to low early age strength and can prevent early age cracking.

Figure 6 shows the total heat of hydration for mixes at 0.45 w/c. The total heat of hydration is the highest for control specimen (53.94 kJ/kg). In addition, comparing the heat of hydration

value of OPC control mix with other mixes, a clear decrease in the total heat of hydration after adding 15% of VA (48.18 kJ/kg) was observed. A further reduction has taken place for the other mixes as the VA percentage increases. Maximum reduction in total heat of hydration has taken place in the sample with the highest percentage of VA, that is, 35%.

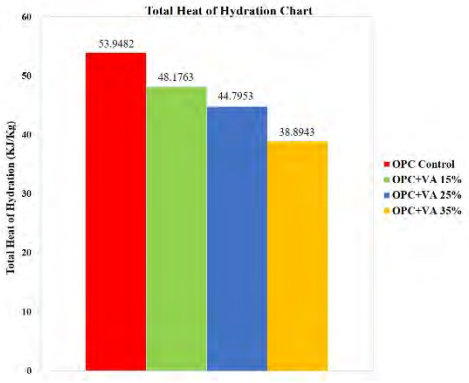

Figure 2: Total heat of hydration for mixes with varying percentages of VA at 0.45 w/c.

3.2 Pore Structure Analysis of Cement Paste Samples by N_2 Adsorption

The characterization of pore structure of the hydrated cement matrix is very important as the engineering properties of concrete such as strength, permeability, diffusivity, shrinkage and creep depends on the porosity and pore size distribution. The influence of different percentages of VA (0-25%) on the surface area and the cumulative pore volume was studied using N_2 adsorption analysis. ASAP 2020 Plus, manufactured by Micromeritics, USA was used for the analysis. The details of adsorption-desorption isotherm, BET surface area and cumulative intruded volume calculated based on the data obtained from gas adsorption experiments are given below in detail. Tests were conducted on solid chips of cement paste samples prepared with 0.45 w/c ratio. The samples were subjected to degassing before analysis and the samples were weighed before and after degassing.

The adsorption-desorption isotherms of different cement paste samples at 0.45 w/c ratio after 28 days of curing is shown in Figure 3. The isotherms were plotted based on the multilayer surface adsorption model developed by Brunauer, Emmett, and Teller (BET). The isotherms are of pseudo Type II with H3 hysteresis loop (Type IIb), indicates that these kind of isotherms are generally formed by the samples with monolayer adsorption followed by multilayer adsorption at ‘point B’ in the Figure 1. The slow rise of the isotherm observed after ‘point B’ is due to the increase in the thickness of the adsorbed layer. However, the sudden increment of the isotherm after ‘point C’ is due to the well-known capillary pore condensation phenomenon [14]. The sample with 25% VA showed higher nitrogen adsorption capacity compared to control and mix with 15% VA replacement, which is in line with the observed BET surface area results shown in Table 1. This is due to an increase in the porosity of the cement paste samples by the incorporation of higher amounts of VA [15].

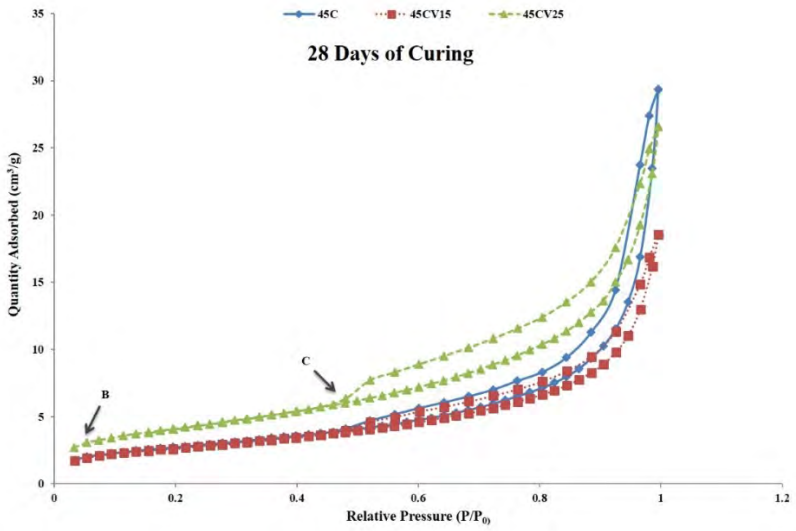

Figure 3. Adsorption-desorption isotherms of different cement paste mixes at 0.45w/c ratio.

Surprisingly, the BET surface area of the cement paste samples (0 and 15% VA replacement) after 28 days of curing was decreased compared to 7 day samples. 45C and 45CV15 showed almost similar BET surface area after 28 days of curing. We have seen in the literature that the increased formation of C-S-H is always accompanied by an increase in the surface area of the cement paste samples [16-18]. As the cement hydration reaction progresses, the large deposits of hydration products along with unreacted materials leads to excess crowding at the pore necks and resulting in the formation of constricted pore entrances (Bottle-neck pores). The formation of these kind of bottle-neck pores and the presence of crowded unreacted starting materials near the entrances of the pores, blocks the passage of gaseous molecules (N_2 gas) in to the pores and hence reduce the BET surface area after 28 days of curing. But in samples with more than 25% VA replacement, an increase in the BET surface area was noticed. Hereafter a greater fraction of the surface area is attributed by the large pore volumes created by the presence of unreacted VA particles in the cement paste.

Table 1: BET Surface Area (m^2/g) of Different Cement Paste mixes

Curing Period	45C	45CV15	45CV25
7 Days	13.6394	9.8793	9.7093
28 days	9.5609	9.2338	14.3990

The cumulative pore volume of nitrogen intrusion verses pore width plot for all the samples after 7 and 28 days of curing is shown in figure 4. 45CV25 showed the lowest nitrogen volume intrusion after 7 days of curing. Whereas, control specimens showed highest nitrogen volume intrusion compared to rest of the specimens. After 28 days of curing, the cumulative nitrogen intruded pore volume of control sample decreased from 0.0184 cm^3/g to 0.01235 cm^3/g;

indicates the densification of the cement matrix by hydration reaction. 45CV15 was also showed a decrease in the cumulative intruded pore volume, while 45CV25 showed an increase after 28 days of curing.

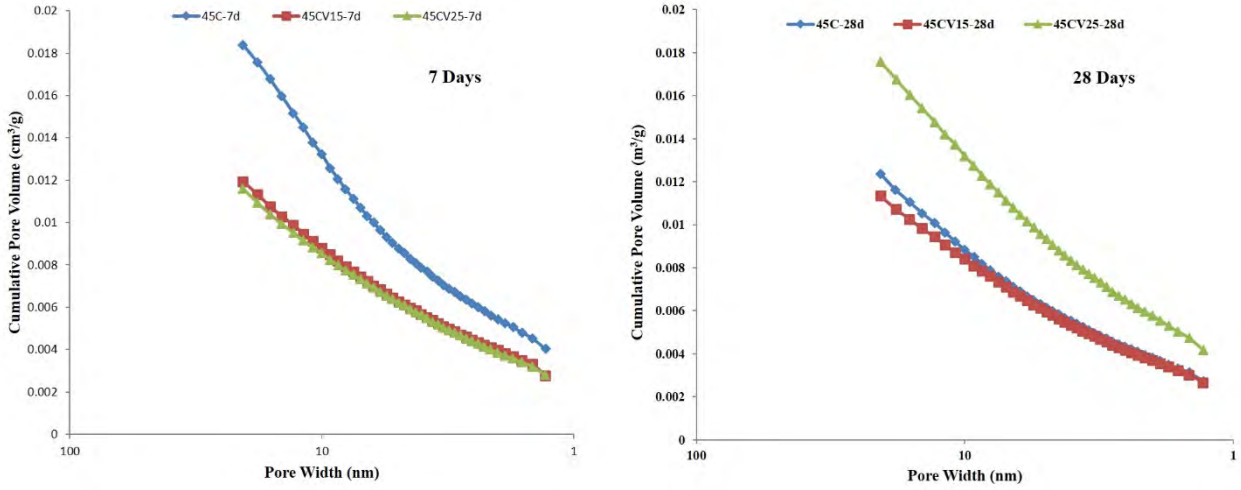

Figure 4: Pore size distribution plots for Cumulative pore volume Vs Pore width for different mixes at 0.45 w/c ratio.

Table 2: Cumulative pore volume (cm^3/g) at median pore width (Å) of different cement paste mixes.

Curing Period	45C	45CV15	45CV25
7 Days	0.018388 (5.4151)	0.011943 (4.4761)	0.011593 (4.2984)
28 days	0.012348 (5.0339)	0.11339 (4.5232)	0.17568 (4.4489)

3.3 Thermogravimetric Analysis

TGA is a method of thermal analysis in which the mass loss of a sample is measured over time as the temperature changes (at a constant heating rate). This analysis provides necessary information about the physical changes such as phase transitions, adsorption and desorption, as well as chemical phenomena like chemisorption, thermal decomposition, and so on [19]. During cement hydration, different components present in the cement reacts with water to form calcium silicate hydrate (C-S-H) and calcium hydroxide ($Ca(OH)_2$) as the major reaction products. TGA could be used to determine the amount of pozzolanic reaction in blended cement pastes by estimating the weight loss due to calcium hydroxide decomposition in a hydrated cement paste [20-22].

Typical TGA plots of the cement paste samples after 28 days of curing (0.45 w/c) are given in Figure 5a. From the TG curves it can be seen that, each curve consists of three different mass loss. The 1st one is between 100 to 350 ^oC corresponding to the dehydration of calcium silicate hydrate (C-S-H), ettringite (Aft) and calcium aluminate hydrate [23]. The 2nd mass loss is

noticed between 420 and 520 °C attributed to the decomposition of calcium hydroxide ($Ca(OH)_2$). $Ca(OH)_2$ decomposition peak is noticed at the same temperature range for all the samples, which clearly indicates that there is no major change in the phase composition. Finally, the 3rd mass loss is noticed in between 620 and 800 °C due to the decomposition of carbonates present in the cement paste sample. Similar graphs are also observed for samples after 90 days of curing as shown in Figure 5b.

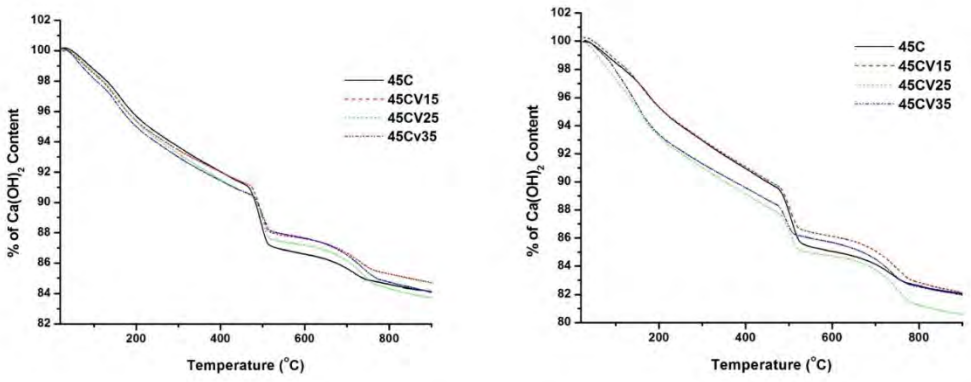

(a) (b)

Figure 5: TG curves of cement paste samples (0.45 w/c ratio) after (a) 28 and (b) 90 days of curing.

The variation of Ca(OH)2 content in cement paste samples with hydration time and VA replacement is given in Figure 6. The figure shows that the Ca(OH)2 content increases with hydration time irrespective of the sample mixtures. But the increase observed in the case of OPC in the early ages is much faster than the blended cement paste samples. This is a clear evidence for the initiation of the pozzolanic reactions in blended cement paste samples due to the presence of VA. The decrease in the $Ca(OH)_2$ content compared to OPC is due to both dilution effect and pozzolanic effect [23]. It can be seen from the graph that the rate of increase of $Ca(OH)_2$ content in blended cement paste samples decreases as the curing ages increases mainly due to pozzolanic reactions.

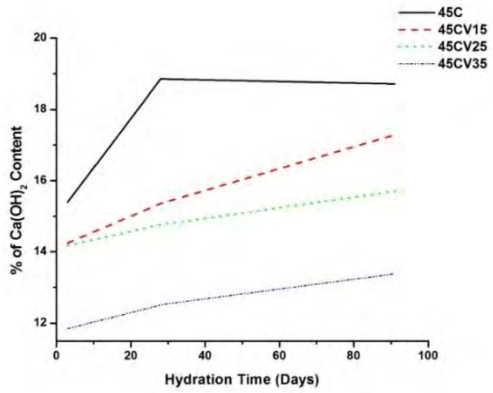

Figure 6: Variation of $Ca(OH)_2$ content with hydration time and VA replacement

3.4 SEM Analysis

The microstructure of cement paste samples with varying VA content (0%, 15%, and 25%) after different ages of curing (28 and 90 days) were studied using Scanning Electron Microscope (Figures 7-8). The prepared cement paste specimens were allowed to cure for the required number of days; and then, the hydration process was stopped by keeping these samples in acetone in an airtight container followed by removing the solvents using a vacuum desiccator. Small samples of size 1 cm x 1 cm x 1 cm were used for SEM analysis. Various hydration products like C-S-H, C-H, $CaCO_3$, and ettringite were identified after 28 and 90 days of curing [23-24].

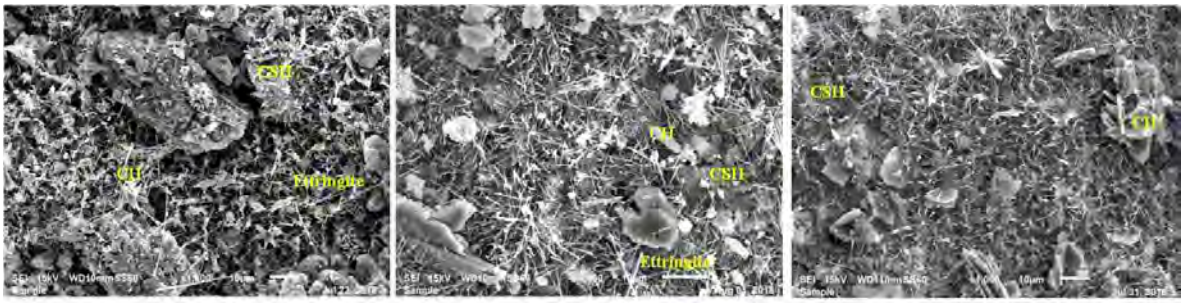

45C 45CV15 45CV25

Figure 7: SEM images of hardened cement paste samples (0.45 w/c ratio) with varying VA content (0-25%) after 28 days of curing

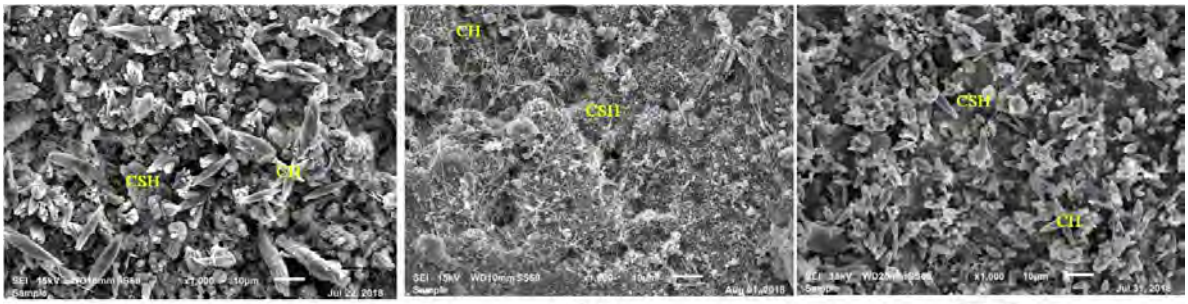

45C 45CV15 45CV25

Figure 8: SEM images of hardened cement paste samples (0.45 w/c ratio) with varying VA content (0-25%) after 90 days of curing

After 28 days of curing, control samples contain harder hydration products with minor amounts of starting materials like alite and belite. The absence of large portlandite crystals in blended cement paste samples was noticed; especially after 90 days of curing. The hydration process in blended cement paste samples is slow compared to control samples. But, the addition of VA provides nucleation site for hydration reaction to initialize and propagate and hence densify the cement paste matrix with uniform distribution of hydration products. The control sample forms much harder hydration products after 90 days of curing (Figure 8). The morphological changes of main cement hydration product C-S-H from gel structure to reticular form can be clearly seen from the SEM images.

4. Summary and Conclusions

A multi-technique approach including SEM, N_2 Adsorption and Thermal analysis methods were used for understanding the effect of VA incorporation on the micro- and pore structure of cement paste samples. Isothermal calorimeter studies show a major reduction in the total heat of hydration of cement paste as the volcanic ash percentage increases. The total heat of hydration was found to be highest for the control samples. As the replacement percentage of OPC with VA increases, heat of hydration was also found to be decreasing and hence the amount of initial cement hydration products also decreases. Thermogravimetric analysis shows an increase in the $Ca(OH)_2$ content with hydration time irrespective of the OPC replacement. The less $Ca(OH)_2$ content in samples with VA when compared to control specimen is due to both dilution effect and pozzolanic effect. The decreased surface area of control specimens after 28 days of curing could be due to the formation of bottle-neck pores which blocks the passage of gaseous molecules (N_2 gas) in to the pores compared to 7-day sample. Whereas, the higher nitrogen adsorption values of cement paste samples with higher VA substitution after 28 days is mainly due to the increased porosity of the cement paste samples by the addition of VA. A decrease in the cumulative nitrogen intruded pore volume of control sample after 28 days of curing was also noticed due to the densification of the cement matrix. The microstructural analysis of hardened cement paste samples using SEM showed different hydration products like C-S-H, C-H, and ettringite after 28, and 90 d of curing. The added VA acts as a nucleation site for the hydration reaction to initialize and densify the cement paste matrix with uniform distribution of hydration products. The control sample forms much harder hydration products after 90 days of curing. Thus, the microstructural analysis of VA blended cement paste helped to understand the formation of hydration products along with its micro- and pore- structure behavior with age, and varying amounts of OPC replacement. Thus the studies show that the incorporation of volcanic ash certainly contributes to the generation of C-S-H and hence the cement hydration progress, especially in the later ages through pozzolanic reactions. The studies further confirm that VA could be used as a potential replacement of OPC for the development of sustainable high-performance concrete.

ACKNOWLEDGEMENTS: -

The research work reported in this paper has been funded and supported by Kuwait Institute for Scientific Research (KISR), under the research activities of the Construction and Building Materials Program. The authors are grateful for KISR's support and for accommodating all the challenges faced during the execution of the project tasks. The authors wish to express their gratitude to Mr. Shamim Ahmad and Ms. Sandhya Ramachandran, technical staffs of Concrete and Material Testing Laboratory, KISR, for their help in casting the cement paste samples and preparing the powder samples for analysis. Finally, we would like to express our sincere thanks to other technical and non-technical staffs of KISR for their constant support and encouragement.

REFERENCES

[1] Robbie, M. A. 'Global CO_2 Emissions from Cement Production'. *Earth Syst. Sci. Data* **10** (2018) 195–217.

[2] Lothenbach, B.; Scrivener, K. and Hooton, R. D. 'Supplementary Cementitious Materials'. *Cem. Concr. Res.* **41** (2011**)** 1244-1256.

[3] Hoffman, G. K. 'Pozzolans and Supplementary Cementitious Materials. *In* Industrial Minerals and Rocks'. 7th Edition; Inc.: Littleton, CO, p. 1161-1172.

[4] ACI 232.1R-00, Use of Raw or Processed Natural Pozzolans in Concrete. American Concrete Institute, Farmington Hills, Michigan, 2001.
[5] Helmuth, R. and Skokie, III. 'Fly Ash in Cement and Concrete' Portland Cement Association, IL, United States, 1987.
[6] Malhotra, V. M. 'Pozzolanic and Cementitious Materials'. Gordon and Breach Publishers, Amsterdam, 1996.
[7] ACI 234R-96, Guide for the Use of Silica Fume in Concrete. American Concrete Institute, Farmington Hills, Michigan, 1996.
[8] Hossain, K. M. A. 'Blended Cement Using Volcanic Ash and Pumice'. *Cem. Concr. Res.* **33** (2003) 1601-1605.
[9] Hossain, K. M. A. 'Volcanic Ash and Pumice As Cement Additives: Pozzolanic, Alkali-Silica Reaction and Autoclave Expansion Characteristics'. *J Mater Civil Eng.* **35** (2005) 1141-1144.
[10] Hossain, K. M. A.; Lachemi, M. and Şahmaran, M. 'Performance of Cementitious Building Renders Incorporating Natural and Industrial Pozzolans Under Aggressive Airborne Marine Salts'. *Cem. Concr. Compos.* **31** (2009) 358-368.
[11] Hossain K. M. A. 'Influence of Extreme Curing Conditions on Compressive Strength and Pulse Velocity of Lightweight Pumice Concrete'. *Comput. Concr.* **6** (2009) 437-450.
[12] Hossain, K. M. A. and Lachemi, M. 'Corrosion Resistance and Chloride Diffusivity of Volcanic Ash Blended Cement Mortar'. *Cem. Concr. Res.* **34** (2004) 695-702.
[13] ASTM C1679-09; *Standard Practice for Measuring Hydration Kinetics of Hydraulic Cementitious Mixtures Using Isothermal Calorimetry*; ASTM International: Pennsylvania, USA, 2009.
[14] Rouquerol, J.; Rouquerol, F.; Llewellyn, P.; Maurin, G. and Sing, K. S. W. 'Adsorption by Powders and Porous Solids: Principles, Methodology and Applications', 2nd ed. Academic Press, Elsevier Science, 2013.
[15] Kupwade-Patil, K., et al. 'Use of Silica Fume and Natural Volcanic Ash as A Replacement to Portland Cement: Micro and Pore Structural Investigation Using NMR, XRD, FTIR and X-Ray Microtomography', *Constr. Build Mater* **158** (2018) 574-590.
[16] Garci Juenger, M.C. and Jennings, H.M. 'The Use of Nitrogen Adsorption to Assess the Microstructure of Cement Paste'. *Cem. Concr. Res.* **31** (2001) 883-892.
[17] PAN, Z., et al. 'Mechanical properties and microstructure of a graphene oxide-cement composite'. *Cem. Concr. Compos.* **58** (2015) 40-147.
[18] Blaine, R. and Valis, H. 'Surface Available to Nitrogen in Hydrated Portland ements, *J. Res. Natl. Bureau Std.* **42** (1949) 257-267.
[19] Vedalakshmi, R.; Sundara Raj, A.; Srinivasan, S. and Ganesh Babu, K. 'Quantification of Hydrated Cement Products of Blended Cements in Low and Medium Strength Concrete Using TG and DTA Technique'. *Thermochim. Acta* **407** (2003) 49-60.
[20] Yogandran, V.; Langan, B.W. and Ward, M. A. 'Hydration of Cement and Silica Fume Pastes'. *Cem. Concr. Res.* **21** (1991) 691-708.
[21] Marsh, B. K. and Day, R. L. 'Pozzolanic and Cementations Reaction of Fly Ash in Blended Cement Pastes'. *Cem. Concr. Res.* **18** (1988) 301-310.
[22] Bakker, R. F. M. 'Permeability of Blended Cement Concretes'. Proceedings of the First CANMET/ACI International Conference on the Use of Fly Ash, Silica Fume, Slag and other Mineral by-Products in Concrete-SP-79, ACI, Detroit, 1983, 589–605.
[23] F.M. Lea. 'The Chemistry of Cement and Concrete'. Fourth ed., Edward Arnold, London, 1974.
[24] Elena, J. and Lucia, M. D. 'X-Ray Diffraction (XRD) Study of Hydration Processes in the Portland Cement'. *J. Appl. Eng. Sci.* **1** (2011) 79-86.

POTENTIAL APPLICATION OF MSWI BOTTOM ASH AS SUBSTITUTE MATERIAL IN PORTLAND CEMENT CONCRETE: FILLER OR BINDER

Yubo Sun (1), Boyu Chen (1), Shizhe Zhang (1), Kees Blom (2), Mladena Luković (3) and Guang Ye (1)

(1) Microlab, Section Materials and Environment, Faculty of Civil Engineering and Geosciences, Delft University of Technology, Stevinweg 1, 2628 CN Delft, The Netherlands

(2) Gemeente Rotterdam, Ingenieursbureau, the Netherlands

(3) Concrete Structures, Faculty of Civil Engineering and Geosciences, Delft University of Technology, Stevinweg 1, 2628 CN Delft, The Netherlands

Abstract

In recent years, the rapid industrialization and urbanization led to the explosive growth of municipal solid waste incineration (MSWI) bottom ashes (BA) production. However, most of them are directly landfilled, which not only brings environmental burden but also results in loss of potential resources. Present researches have proved that MSWI BA could be utilized as a replacement in Portland cement concrete. However, several drawbacks such as volume expansion, leaching behaviour, and relatively lower strength have been reported. In this study, as-received BA was pretreated to remove the metallic aluminium which is responsible for the hydrogen-induced expansion when blended in OPC concretes. Subsequently, the treated BA samples were used as a substitution for cement at the replacement level of 10%. Micronized sand (M300) was selected as reference materials to investigate the role of treated BA in blended cement system, either as filler or binder material. In the experimental program, the hydration process of different mixtures was monitored by isothermal calorimeter and hydration products were determined by X-ray diffraction (XRD) and Thermalgravimetric analysis (TGA). Results showed that the pretreatment effectively removed the metallic aluminum in BA and no severe expansion or strength decrement were detected. The treated BA showed limited reactivity comparing with Portland cement, however, it still worked better than micronized sand as a filler substitution.

1. INTRODUCTION

According to the survey performed by World Bank in 2012 [1], the amount of municipal solid waste (MSW), one of the most typical products of urban lifestyle [2], would be doubled by 2025 (2.2 billion tons per year). The most widely used waste to energy (WtE) process is to

recover the energy in MSW by generating steam and electricity directly through incineration [3, 4]. However, the most important by-product of MSW incineration (MSWI), namely bottom ash (BA), is mainly landfilled at present.

As a result of the increasing landfilling cost and the awareness of resource recovery, MSWI BA is now gaining more attention and regarded as an underutilized material [5]. However, MSWI BA is seldom used directly as a raw material in the industry due to its porous nature and high pollutant content. The primary issue is the leaching problem corresponding to the heavy metal substances and harmful salts in MSWI BA [6-11], which brings a great environmental impact. Numerous studies have been carried out regarding the characterization and potential utilization of MSWI BA in the industry. Several methods of treatment on BA have been proposed to meet the leaching requirement, such as weathering, chemical carbonation and physical stabilization [12].

In more recent years, studies have been carried out to investigate the potential application of MSWI BA. It has been proved that MSWI BA could be used in ordinary Portland cement (OPC) concrete, either as aggregate/filler [13, 14] or cement [15, 16] substitution. However, the application of MSWI BA is quite limited since several significant drawbacks have been frequently reported when used in concrete. For instance, the highly porous and irregular morphology of BA particles [17-20] has been detected, which makes BA easily crushed when used as load-bearing elements. Meanwhile, the relatively low reactivity of MSWI BA has been reported as well, and the addition of BA into concrete resulted in not only the retardation of the hydration process [15, 21] but also the decrement in compressive strength [21-23]. Furthermore, the most undesired issue is the expansion and swelling in concrete structures caused by the addition of MSWI BA. The hydrogen bubbles generated by the dissolution of metallic aluminum content in BA in the concrete mixture was identified as the main cause of the expansion and reduction of strength [14, 16, 22].

According to the present literature, a proper treatment method to improve the properties of MSWI BA is still in scarce before it could be properly used as a substitute material in Portland cement concrete. In addition, the studies corresponding to the hydration properties should be conducted as well to reveal the effect of treated BA samples on the hydration process.

In this study, both chemical and mechanical treatments were performed to reduce the metallic aluminum content in BA samples, followed by a thermal treatment to improve the reactivity of BA. Treated BA samples were then characterized and blended into cement paste to evaluate the effectiveness of different treatment methods. Meanwhile, the hydration process of pastes was measured by the isothermal calorimeter, and the hydration products were detected d by XRD and TG analysis.

2. MATERIALS AND EXPERIMENTAL METHODS

2.1. Materials and pretreatment

The MSWI BA used in this research with a particle size of 0-2 mm was provided by a waste-to-energy (Heros Sluiskil B.V.) in the Netherlands. BA was water quenched and underwent a weathering process. Afterward, proper treatment was performed as well to stabilize the leachable substances within the incineration plant. In this research, different types of pre-treatment were conducted to improve the properties of as-received BA. Details of the treating procedures to derive different types of BA samples are given as follows:

- CBA: BA samples were immersed in 1M sodium hydroxide solution with a solid to liquid ratio of 0.1 for 5 days. Subsequently, the BA particles were washed with running water in vacuum filtration and dried at 105℃ until a constant mass in a ventilated oven. Finally, an extra grinding process was performed to grind BA into fine powders and control the particle size distribution. The BA derived is labelled as CBA.
- MBA: BA samples were ground in Retsch PM100 planetary ball miller at 250 rpm for 30 minutes so that the metallic aluminum with good ductility could be ground into metal plates and easily sieved out. Afterward, the powder in the grinding jar was collected and the finer fraction was separated with a 63 μm sieve and labelled as MBA.
- MTBA: MBA was thermally activated in a ventilated furnace at 1000 ℃ for 1 hour and then cooled down to room temperature to generate new reactive phases and remove unburnt organic matters. The sample derived was labelled as MTBA.

CEM I 42.5N Portland cement from ENCI B.V. the Netherlands was selected as the fundamental cementitious material. Besides, micronized silica sand (M300, pure sand with no reactivity) with a similar particle size distribution as CEM I 42.5N cement was used as reference materials for filler substitution.

2.2. Material characterization

The characterization of BA samples was conducted both before and after each type of treatment. The chemical composition was determined by X-ray fluorescence (XRF). Metallic aluminum content was measured by a dissolving test with alkaline solution as described in [24]. The mineralogical composition of BA was checked by X-ray diffraction (XRD).

2.3. Hydration process

The effect of different types of BA on the cement hydration process was evaluated on paste levels by replacing 10% cement powder with treated BA samples in the cement pastes. The water to cement ratio was kept at 0.5 in each group.

The heat evolution in different pastes was monitored by isothermal calorimeter (TAM-Air-314 thermometric isothermal conduction calorimeter). Meanwhile, the cement pastes containing different BA samples were cast into 20 mm cubic specimens and cured in ambient conditions (room temperature, 95% RH). At the age of 28-day, the specimens were crushed into smaller pieces, and hydration process was terminated by immersing crushed specimens in anhydrous ethanol for 24 hours. Subsequently, the specimens were dried in a vacuum chamber and milled into fine powders. The mineralogical phases in 28-day hydration products were detected by XRD. Thermalgravimetric analysis (TGA) was performed as well to estimate the amount of main hydration products, namely portlandite (CH) and non-evaporable water. The mass percentage of portlandite and non-evaporable water in hardened paste powders was calculated according to [25].

3. RESULTS AND DISCUSSION

3.1. Characterization of BA samples

BA samples were characterized both before and after pre-treatment to reveal the effect of different methods on the properties of BA.

Particle size distribution curves of reference and substitute materials used in this research measured by laser diffraction are given in **Figure 1**. An extra grinding process was performed

on treated BA samples to keep the particle size distribution at the same level as the reference materials.

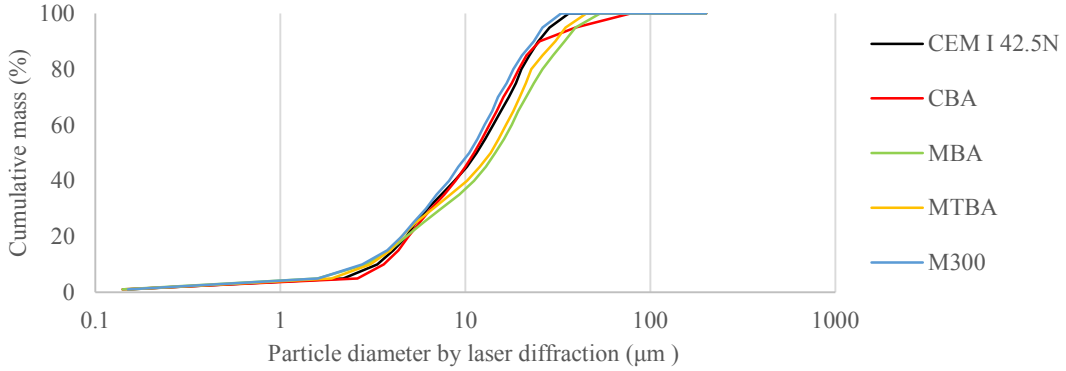

Figure 1: Particle size distribution of reference and substitute materials

As shown in **Figure 2**, the mineralogical compositions of BA samples were detected by XRD. As received BA mainly consists of crystalline phases such as quartz, calcite, magnetite, etc. No significant difference was observed in CBA and MBA. In MTBA, however, much more amorphous phases were detected between 20° and 80° comparing to the narrow peaks referring to crystalline phases in BA, CBA, and MBA. Peaks representing calcite ($CaCO_3$) vanished after thermal treatment which is due to the decomposition of calcite at high temperature.

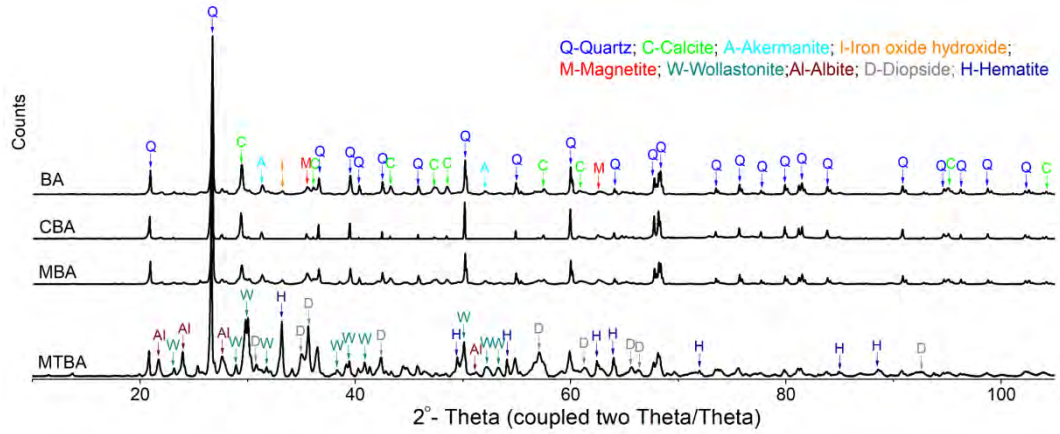

Figure 2: XRD diffractograms of as-received BA and treated BA

The chemical composition of cement and different types of BA samples determined by XRF are given in **Table 1**. Comparing to the reference Portland cement, all BA samples contain much lower content of CaO while the SiO_2 Fe_2O_3 Al_2O_3 and content of MgO are higher than that in cement. All treatments performed in this study did not result in significant changes in the chemical composition of BA. The metallic aluminum content are shown in **Table 1**. The chemical treatment and mechanical treatment effectively reduced the metallic aluminum content in BA by 95% and 84% respectively. Thermal treatment further removed the metallic aluminum by accelerating the oxidation of fine powers at high temperature.

Table 1: Chemical composition of reference cement, as-received BA and treated BA

Chemical composition (wt. %)	CEM I 42.5N	As-received BA	CBA	MBA	MTBA
CaO	64.99	22.39	17.40	18.34	18.70
SiO_2	17.11	48.44	49.82	50.40	43.67
Fe_2O_3	3.59	12.29	10.58	12.94	13.62
Al_2O_3	3.80	11.66	10.20	9.84	10.08
MgO	1.56	2.47	2.52	2.21	2.40
Na_2O	0	0.34	2.96	0.56	0.92
K_2O	0.16	0.94	0.79	0.82	0.82
CuO	0.02	0.62	0.52	0.48	0.48
ZnO	0.15	0.90	1.40	0.75	0.77
P_2O_5	0.63	0.84	0.59	0.67	0.74
TiO_2	0.27	1.30	1.19	1.12	1.20
Cl	0.02	0.16	0.13	0.12	0.03
SO_3	3.96	1.40	0.36	0.86	0.84
other	2.01	1.02	1.54	0.89	0.96
Metallic aluminum	n.m.	0.80± 0.03	0.04±0 .03	0.13±0 .03	0.06±0 .03
n.m.=not measured					

3.2. Hydration properties

Heat flow and cumulative heat curves of different pastes are displayed in **Figure 3**. The paste with CBA was not measured since reactive phases might be already dissolved by chemical treatment.

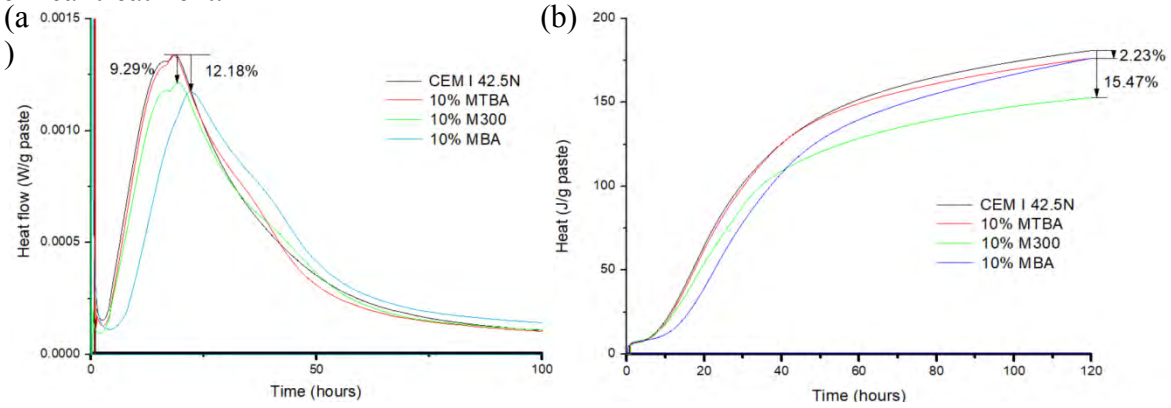

Figure 3: Heat evaluation of paste with treated BA samples. (a) Heat flow (b) Cumulative heat

As shown in **Figure 3 (a)**, there is no significant difference between the maximum heat flow of pure cement and 10% MTBA. However, the maximum heat flow of MBA and M300 decreased by 12.18% and 9.29% respectively. Meanwhile, a remarkable delay of the peak value is observed in the 10% MBA group and the maximum rate of heat release is even lower than 10% M300, which proves that the addition of MBA retarted the early stage hydration. In cumulative heat curve (**Figure 3 (b)**), cement paste with 10% MBA exhibited relatively slow early-stage heat development that the cumulative heat before 40 hours was even lower than

that of 10% M300. However, a reversal occurred at around 40 hours, and after that, the cumulative heat of 10% MBA became higher than that of 10% M300. Therefore, the thermal treatment mainly accelerates the early-stage hydration process.

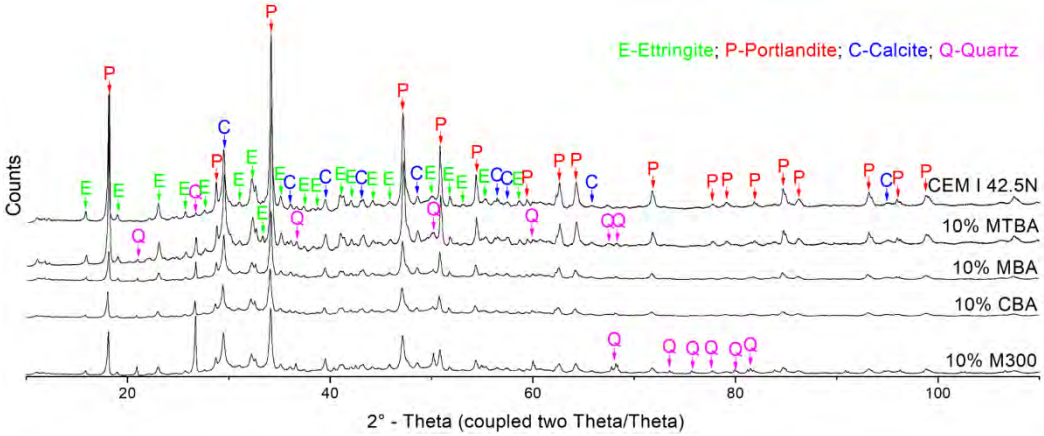

Figure 4: XRD diffractograms of hardened pastes with cement and substitute materials

The mineralogical phases in the hardened pastes were characterized by XRD (as shown in **Figure 4**). The main hydration products detected were ettringite and portlandite distributed over the full XRD detection range. It is also noticed that the profile of cement paste and the paste with 10% MTBA kept almost identical to each other. In pastes with 10% MBA, 10% CBA and 10% M300, dramatic reduction was observed in the intensity of peaks corresponding to calcite, portlandite and ettringite, and some of the peaks even vanished. Accordingly, the addition of MBA, CBA and M300 inhibited the hydration process and less amount of hydration products were generated.

The mass percentage of portlandite and non-evaporable water in hardened paste powders was calculated according to the mass loss along temperature history derived from TGA tests, and the results are given in **Figure 5**. It could be concluded that MTBA is the best cement substitute material in this study with the highest amount of main hydration products. Meanwhile, CBA is the most undesired substitute material in this research which might be attributed to the loss of reactive phases during the chemical treatment. Moreover, MBA exhibited intermediate performance, which is better than micronized sand. The result reveals that MBA could be already regarded as a proper filler substitute material in OPC concrete.

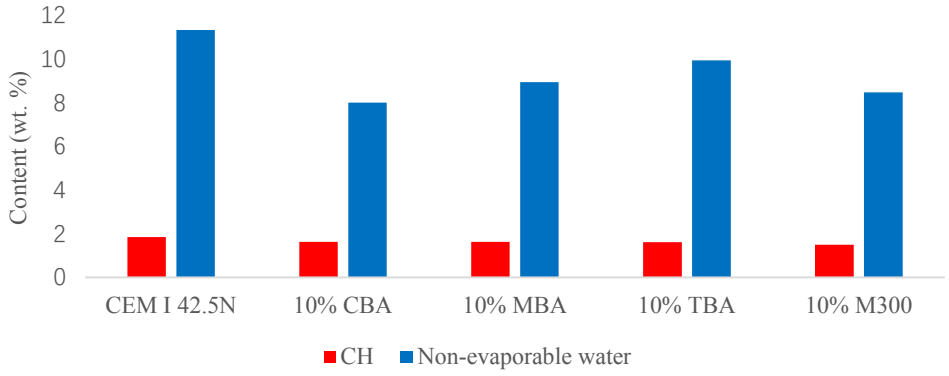

Figure 5: Mass percentage of CH and non-evaporable water in hardened pastes with cement and substitute materials, per unit weight of cement paste

4. CONCLUSIONS

According to the experimental results derived from this study, the following conclusions could be provided :

- Both chemical and mechanical treatments have been proved effective that the metallic aluminum content reduced by 95% and 84% respectively. However, the mineralogical composition characterized by XRD indicates that the soluble amorphous phases might be dissolved during the chemical treatment with alkaline solution.
- More reactive amorphous phases were detected in MTBA, which indicates that thermal treatment increased the reactivity of BA. Meanwhile, according to the result obtained from the metallic Al dissolution test, the thermal treatment further reduced the metallic aluminum content by providing an extreme high-temperature environment which accelerated the oxidization of metallic aluminum powders. MTBA is the best among all cement substitute material derived in this study. However, the thermal treatment might be energy-consuming.
- The hydration product characterized by XRD and TGA reveals that the performance of treated BA samples, when used as substitute material in Portland cement concrete, follows the trend: MTBA > MBA > M300 > CBA. MBA could be regarded as a proper filler substitute material in Portland cement concrete.

REFERENCES

1. Hoornweg, D. and P. Bhada-Tata, *What a waste: a global review of solid waste management*. Vol. 15. 2012: World Bank, Washington, DC.
2. Mian, M.M., et al., *Municipal solid waste management in China: a comparative analysis.* 2017. **19**(3): p. 1127-1135.
3. Cheng, H. and Y.J.B.t. Hu, *Municipal solid waste (MSW) as a renewable source of energy: Current and future practices in China.* 2010. **101**(11): p. 3816-3824.
4. Reddy, P.J., *Municipal solid waste management: processing-energy recovery-global examples*. 2011: CRC press.
5. Verbinnen, B., et al., *Recycling of MSWI bottom ash: a review of chemical barriers, engineering applications and treatment technologies.* 2017. **8**(5): p. 1453-1466.
6. Hjelmar, O., J. Holm, and K.J.J.o.h.m. Crillesen, *Utilisation of MSWI bottom ash as sub-base in road construction: first results from a large-scale test site.* 2007. **139**(3): p. 471-480.
7. Olsson, S., et al., *Environmental systems analysis of the use of bottom ash from incineration of municipal waste for road construction.* 2006. **48**(1): p. 26-40.
8. Su, L., et al., *Copper leaching of MSWI bottom ash co-disposed with refuse: effect of short-term accelerated weathering.* 2013. **33**(6): p. 1411-1417.
9. Heasman, L., H. van der Sloot, and P. Quevauviller, *Harmonization of leaching/extraction tests*. Vol. 70. 1997: Elsevier.
10. Van der Sloot, H., R. Comans, and O.J.S.o.t.T.E. Hjelmar, *Similarities in the leaching behaviour of trace contaminants from waste, stabilized waste, construction materials and soils.* 1996. **178**(1-3): p. 111-126.
11. Chandler, A.J., et al., *Municipal solid waste incinerator residues*. Vol. 67. 1997: Elsevier.

12. Wiles, C. and P. Shepherd, *Beneficial use and recycling of municipal waste combustion residues-a comprehensive resource document*. 1999, National Renewable Energy Lab., Golden, CO (US).
13. Ginés, O., et al., *Combined use of MSWI bottom ash and fly ash as aggregate in concrete formulation: environmental and mechanical considerations.* 2009. **169**(1-3): p. 643-650.
14. Müller, U., K.J.C. Rübner, and C. Research, *The microstructure of concrete made with municipal waste incinerator bottom ash as an aggregate component.* 2006. **36**(8): p. 1434-1443.
15. Li, X.-G., et al., *Utilization of municipal solid waste incineration bottom ash in blended cement.* 2012. **32**: p. 96-100.
16. Pecqueur, G., C. Crignon, and B.J.W.m. Quénée, *Behaviour of cement-treated MSWI bottom ash.* 2001. **21**(3): p. 229-233.
17. Meima, J.A., R.N.J.E.S. Comans, and Technology, *Geochemical modeling of weathering reactions in municipal solid waste incinerator bottom ash.* 1997. **31**(5): p. 1269-1276.
18. Vegas, I., et al., *Construction demolition wastes, Waelz slag and MSWI bottom ash: A comparative technical analysis as material for road construction.* 2008. **28**(3): p. 565-574.
19. Zevenbergen, C., et al., *Weathering of MSWI bottom ash with emphasis on the glassy constituents.* 1998. **62**(1-3): p. 293-298.
20. Izquierdo, M., et al. *Use of bottom ash from municipal solid waste incineration as a road material*. in *International ash utilization symposium, 4th, Lexington, KY, United States*. 2001.
21. Tang, P., et al., *Characteristics and application potential of municipal solid waste incineration (MSWI) bottom ashes from two waste-to-energy plants.* 2015. **83**: p. 77-94.
22. Bertolini, L., et al., *MSWI ashes as mineral additions in concrete.* 2004. **34**(10): p. 1899-1906.
23. Jurič, B., et al., *Utilization of municipal solid waste bottom ash and recycled aggregate in concrete.* 2006. **26**(12): p. 1436-1442.
24. Aubert, J.-E., B. Husson, and A.J.W.M. Vaquier, *Metallic aluminum in MSWI fly ash: quantification and influence on the properties of cement-based products.* 2004. **24**(6): p. 589-596.
25. Zhang, Y.M., et al., *Hydration of high-volume fly ash cement pastes.* 2000. **22**(6): p. 445-452.

RELATIONSHIP BETWEEN THE WATER ABSORPTION AND THE CHLORIDE ION PENETRATION OF BLENDED CEMENT CONCRETE WITH VARIOUS SCMS: A PRELIMINARY EVALUATION ON WHETHER WATER ABSORPTION CAN PROVIDE A RELIABLE ESTIMATION OF OTHER TRANSPORT PROPERTIES

Shiyu Zhuang (1), Qiang Wang (1)

(1) Department of Civil Engineering, Tsinghua University, China

Abstract

Water absorption is an indicator of other transport properties and even durability of concrete since it provides a dominant invasion mechanism for the penetration of aggressive ions. Relationship between the water absorption and the chloride ion penetration of concrete containing fly ash, slag and silica fume at various water-to-binder ratios is investigated in this study. It is found that water absorption can provide a reliable estimation of chloride ion penetration. There is a good correspondence between the initial water absorption rate and the chloride ion penetration grade. The initial water absorption rate of more than 50×10^{-3} mm/s$^{0.5}$, 40-30×10^{-3} mm/s$^{0.5}$, 30-20×10^{-3} mm/s$^{0.5}$ and less than 20×10^{-3} mm/s$^{0.5}$ may correspond to the chloride ion penetration grade of “high”, “moderate”, “low” and “very low”, respectively. The initial water absorption rate can further reflect the transport property and durability of concrete in the same chloride ion penetration grade where the comparison of the specific charge passed values is invalid. Water absorption has the potentiality to act as a deterministic index for the transport properties and the durability of concrete.

Keywords: transport property, durability, water absorption, chloride ion penetration, supplementary cementitious material

1. INTRODUCTION

In recent years, transport properties of concrete have been attached an increasing attention due to their crucial applications in durability evaluation and service life prediction of concrete [1-3]. Since most of the aggressive ions which play important roles in the durability damage and performance degradation access to the interior of concrete through the water absorption process, water absorption should be regarded as a representative and important index of transport properties [4,5]. It can be theoretically applied as a descriptor of other transport properties and even durability of concrete such as chloride ion penetration, sulphate attack, freeze and thaw as well as carbonation, because it provides a dominant invasion mechanism and way for the penetration of hazardous agents [6]. It may also be efficient and

convenient if the information of many other transport properties and durability of concrete can be achieved by measuring only water absorption, especially for engineering practice, given the simplicity of its test method [7-9].

Chloride ion penetration is one of the most significant durability indicators, especially for concrete withstanding aggressive environment. The rapid chloride permeability test such as the electrical conductance test is still the most commonly-used test method to provide an indication of resistance to chloride ion penetration of concrete, in which the permeability grades are just roughly divided and the comparison of the specific charge passed values is invalid, causing great inconvenience and confusion on the evaluation of transport property and durability [10-12]. It provides a new idea whether a reliable estimation of chloride ion penetration can be achieved by water absorption. However, the relationship between water absorption and chloride penetration has not been studied and the feasibility of this idea is lack of research.

In this study, relationship between the water absorption measured by ASTM C 1585 [13]and the chloride ion penetration measured by ASTM C 1202 [14] of concrete with addition of various mineral admixtures such as fly ash, slag and silica fume at various water-to-binder ratios is investigated to comprehensively evaluate whether water absorption can provide a reliable estimation of chloride ion penetration. This study provides a preliminary investigation on the potentiality of water absorption to act as a deterministic index for transport properties and durability of concrete.

2. EXPERIMENTAL PROGRAM

2.1 Raw material and mix proportions

Portland cement (PC) with a grade of P.I 42.5 conforming to the Chinese National Standard GB 175-2020 (equivalent to European CEM I 42.5), fly ash (FA) conforming to the Chinese National Standard GB/T 1596-2017, silica fume (SF) conforming to the Chinese National Standard GB/T 27690-2011, ordinary ground granulated blast furnace slag (OS) and ultra-fine ground granulated blast furnace slag (US) conforming to the Chinese National Standard GB/T 18046-2017 are used in this study. The specific surface areas of PC, FA, OS, US and SF are 376 m^2/kg, 360 m^2/kg, 420 m^2/kg, 3955 m^2/kg and 17650 m^2/kg, respectively. The chemical compositions of these powder materials are shown in Table 1. The mix proportions of concretes are shown in Table 2.

Table 1: Chemical compositions of used materials (%)

Chemical	PC	FA	OS / US	SF
SiO_2	21.10	53.33	31.76	97.34
Al_2O_3	6.33	27.65	14.84	0.34
Fe_2O_3	4.22	6.04	0.60	0.06
CaO	54.86	2.86	36.44	0.17
MgO	2.60	1.35	9.08	0.27
SO_3	2.66	0.45	1.94	0.77
Na_2O_{eq}	0.53	0.64	0.56	0.11
Loss on ignition	2.42	4.71	0.86	0.21

Table 2: Mix proportions of concretes (kg/m3)

Samples	Cement	Slag	Fly ash	Silica fume	Fine aggregate	Coarse aggregate	Water	Curing condition
C-60	350	0	0	0	812	1077	161	60℃/9 h
C-90	350	0	0	0	812	1077	161	90℃/9 h
F30-80	245	0	105	0	812	1077	161	80℃/9 h
F40-80	210	0	140	0	812	1077	161	80℃/9 h
F50-80	175	0	175	0	812	1077	161	80℃/11 h
B30-80	245	105	0	0	812	1077	161	80℃/9 h
B40-80	210	140	0	0	812	1077	161	80℃/9 h
B50-80	175	175	0	0	812	1077	161	80℃/9 h
UF0	350	0	0	0	812	1077	140	
UF6	329	21	0	0	812	1077	140	
UF10	315	35	0	0	812	1077	140	
UF14	301	49	0	0	812	1077	140	
US10-0.35	315	35	0	0	812	1077	122.5	
US15-0.35	297.5	52.5	0	0	812	1077	122.5	
SF10-0.35	315	0	0	35	812	1077	122.5	
SF15-0.35	297.5	0	0	52.5	812	1077	122.5	
US10-0.25	315	35	0	0	812	1077	87.5	
US15-0.25	297.5	52.5	0	0	812	1077	87.5	
SF10-0.25	315	0	0	35	812	1077	87.5	
SF15-0.25	297.5	0	0	52.5	812	1077	87.5	

2.2 Specimen preparation and test methods

Concrete specimens with a diameter of 100 mm and a height of 100 mm were prepared for water absorption test and concrete specimens with dimension of 100 mm × 100 mm × 100 mm were prepared for chloride ion permeability test. After casting, specimens were sealed with plastic film for 3 days and then were demolded and cured at a temperature of 20 °C and a relative humidity (RH) of 95% until testing age. And then specimens were cut into dimension with a diameter of 100 mm and a height of 100 mm and dried to the constant weight in a 60°C oven (the weight change within 24 h is less than 0.1%) to measure the water absorption according to ASTM C1585. Specimens were cut into dimension of 100 mm × 100 mm × 50 mm to measure the charge passed in 6 h to determine the chloride ion permeability according to ASTM C1202.

3. RESULTS AND DISCUSSION

Fig. 1(a) shows the charge passed and the corresponding chloride ion permeability grades of steam-cured plain cement concrete and fly ash concrete. The chloride ion permeability grade of plain cement concrete steam cured at 90°C is “high”, which is two levels higher than the “low” chloride ion permeability grade of plain cement concrete steam cured at 60°C and three levels higher than the “very low” chloride ion permeability grade of fly ash concrete steam cured at 80°C. The chloride ion permeability grade of fly ash concrete with various fly ash content is the same. It is worth noting that although the charge passed is different, it is unfeasible and invalid to evaluate the effect of fly ash content on the chloride ion permeability of concrete by comparing the specific charge passed values according to the mechanism of the electrical conductance test, according to the mechanism of the electrical conductance test, which causes the great inconvenience and confusion. This is a huge deficiency of the electrical conductance test in the transport property and durability evaluation of concrete.

Fig. 1(b) shows the water absorption per unit area of exposed surface versus $t^{0.5}$ and the corresponding initial water absorption rates of steam-cured plain cement concrete and fly ash concrete. The water absorption process can be divided into two stages: initial water absorption stage (1min-6h) and secondary water absorption stage (1-7d). The slopes of the linear fitted lines of two water absorption stage are called the initial water absorption rate and the secondary water absorption rate, respectively, which characterize the speed of water absorption. The initial water absorption stage is generally considered to be the capillary water absorption process, which is attributed to the surface tension of the liquid and the difference between the internal and external pressure of the meniscus. It is related to the porosity, pore size distribution, connectivity and tortuosity. The secondary water absorption stage is generally considered to be attributed to the slow compression, diffusion and loss of the trapped air in the pore structure under the pressure of water, as well as the redistribution of the moisture from the capillary pores towards gel pores and interlayer pores. Therefore, only the initial water absorption stage is considered here. It can be seen that in consistence with the result of chloride ion permeability, the initial water absorption rates of plain cement concrete

steam cured at 90°C, plain cement concrete steam cured at 60°C and fly ash concrete decrease in sequence. The initial water absorption rate of plain cement concrete steam cured at 90°C is higher than 50×10^{-3} mm/s$^{0.5}$, much higher than other groups, which corresponds to its "high" chloride ion penetration grade. The initial water absorption rate of plain cement concrete steam cured at 60°C is approximately 25×10^{-3} mm/s$^{0.5}$, about half of that of plain cement concrete steam cured at 90°C, which corresponds to its "low" chloride ion penetration grade. The initial water absorption rate of fly ash concrete is smaller than 20×10^{-3} mm/s$^{0.5}$, which corresponds to its "very low" chloride ion penetration grade. The initial water absorption rate decreases with the increase of fly ash content. This is because the reaction of fly ash and is much slower than that of cement. Fly ash not only plays a role of nucleation and dilution to promote the hydration of cement and improve the compactness of concrete, but also reacts with Ca $(OH)_2$ to form C-S-H gel to fill the connected pores, refine the pore structure and minimize the ITZ micro-cracks, thereby deteriorating the transport property of concrete. The larger the content of fly ash, the more significant blocking effect on the connected pores. Therefore, the transport property and durability of concrete in the same chloride ion penetration grade can be further evaluated by comparing the initial water absorption rate.

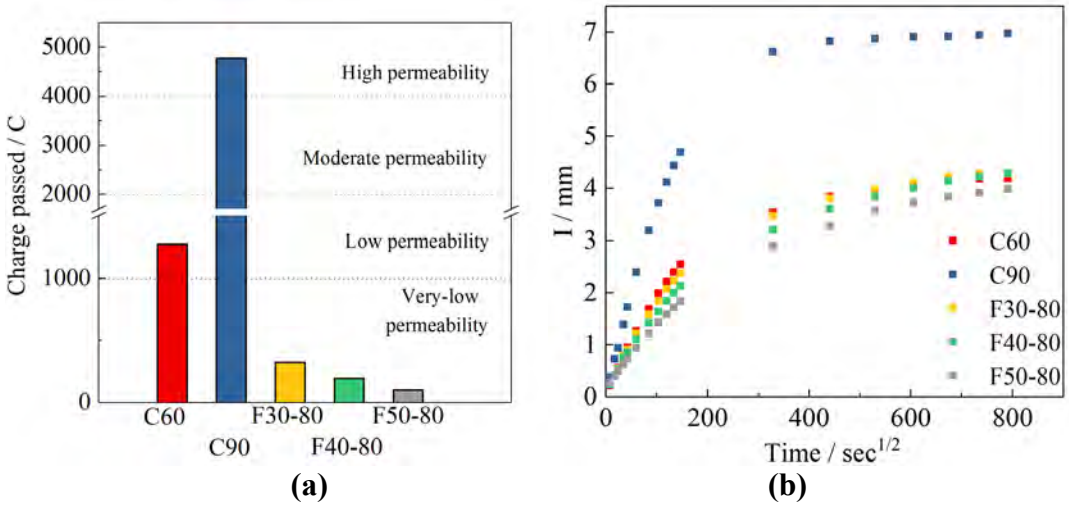

Figure 1: The charge passed and the corresponding chloride ion permeability grades (a) and the water absorption per unit area of exposed surface versus $t^{0.5}$ and the corresponding initial water absorption rates (b) of steam-cured plain cement concrete and fly ash concrete.

Fig. 2(a) shows the charge passed and the corresponding chloride ion permeability grades of plain cement concrete and ordinary slag concrete. The chloride ion permeability grades of both plain cement concrete steam cured at 60°C and ordinary slag concrete with various slag content are “low”, which is two levels lower than the “high” chloride ion permeability grade of plain cement concrete steam cured at 90°C. There is the same problem that it fails to evaluate the effect of ordinary slag content on the transport property and durability of concrete by comparing specific charge passed values, which is unfeasible and invalid.

Fig. 2(b) shows the water absorption per unit area of exposed surface versus $t^{0.5}$ and the corresponding initial water absorption rates of steam-cured plain cement concrete and ordinary slag concrete. It can be seen that in consistence with the result of chloride ion permeability, the initial water absorption rate of plain cement concrete steam cured at 60°C is relatively close to that of ordinary slag concrete, both significantly smaller than that of plain cement concrete steam cured at 90°C. The initial water absorption rates of plain cement concrete steam-cured at 60°C and ordinary slag concrete are between 20×10^{-3} mm/s$^{0.5}$ and 30×10^{-3} mm/s$^{0.5}$, which correspond to their "low" chloride ion penetration grade. The initial water absorption rate of ordinary slag concrete decreases with the increase of ordinary slag content, slightly smaller than that of plain cement concrete. This is because the secondary reaction of slag can also produce C-S-H filling the connected pores and refining the pore structure. It is worth noting that since the blocking effect of the secondary reaction of ordinary slag is not as good as that of fly ash, the effect of ordinary slag on the transport property and durability of concrete is not significant, which cannot be reflected in the chloride ion penetration grade, but can be reflected in the initial water absorption rate.

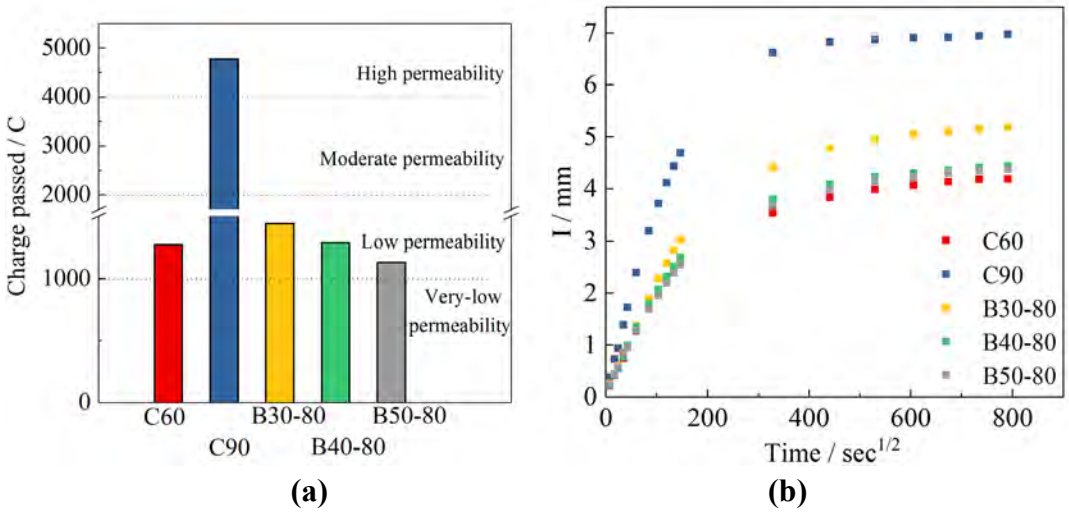

(a) **(b)**

Figure 2: The charge passed and the corresponding chloride ion permeability grades (a) and the water absorption per unit area of exposed surface versus $t^{0.5}$ and the corresponding initial water absorption rates (b) of steam-cured plain cement concrete and ordinary slag concrete.

Fig. 3(a) shows the charge passed and the corresponding chloride ion permeability grades of plain cement concrete and ultra-fine slag concrete. The chloride ion permeability grades of plain cement concrete and ultra-fine slag concrete at both 28d and 60d are all “moderate”. Fig. 3(b) shows the water absorption per unit area of exposed surface versus $t^{0.5}$ and the corresponding initial water absorption rate of plain cement concrete and ultra-fine slag concrete. It can be seen that in consistence with the result of chloride ion permeability, there is not much difference in the initial water absorption rate between plain cement concrete and ultra-fine slag concrete, which are all between 30×10^{-3} mm/s$^{0.5}$ and 40×10^{-3} mm/s$^{0.5}$. And there is almost no difference in the initial water absorption of concrete with various ultra-fine slag content. This may be due to the low content of ultra-fine slag in this experiment and as a

result, the refining effect of ultra-fine slag on the pore structure is not significant, which causes little difference in the chloride ion permeability grade and initial water absorption rate compared with that of plain cement concrete. It reflects that although the ultra-fine slag has a much larger specific surface area and thus higher activity than ordinary slag, it cannot further effectively refine the pore structure compared with ordinary slag, especially with small content.

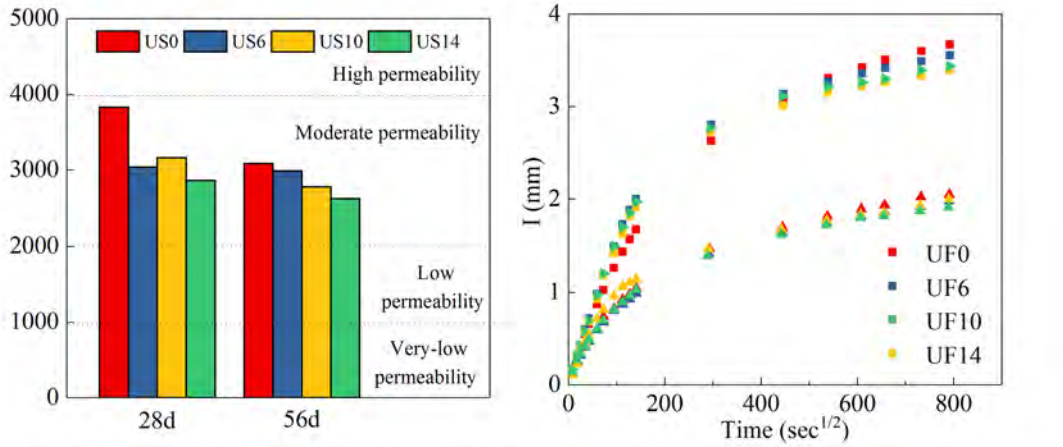

Figure 3: The charge passed and the corresponding chloride ion permeability grades (a) and the water absorption per unit area of exposed surface versus $t^{0.5}$ and the corresponding initial water absorption rates (b) of plain cement concrete and ultra-fine slag concrete.

On the basis of the above experiments, the water-to-binder ratio is further decreased. Fig. 4(a) shows the charge passed and the corresponding chloride ion permeability grades of ultra-fine slag concrete. At a water-to-binder ratio of 0.35, the chloride ion permeability grade of ultra-fine slag concrete with 10% or 15% ultra-fine slag content is "moderate", while at a water-to-binder ratio of 0.25, the chloride ion permeability grade of ultra-fine slag concrete is "very low", decreasing by two levels. However, it fails to evaluate the transport property and durability of concrete with ultra-fine content but the same chloride ion permeability grade by comparing specific charge passed values. Fig. 4(b) shows the water absorption per unit area of exposed surface versus $t^{0.5}$ and the corresponding initial water absorption rate of ultra-fine slag concrete. It can be seen that in consistence with the result of chloride ion permeability, the initial water absorption rates of plain cement concrete and ultra-fine slag concrete at a water-to-binder ratio of 0.35 are close to each other, all between 30×10^{-3} mm/s$^{0.5}$ and 40×10^{-3} mm/s$^{0.5}$, which corresponds to the " moderate " chloride ion penetration grade. The initial water absorption rates of plain cement concrete and ultra-fine slag concrete at a water-to-binder ratio of 0.25 are also close to each other, all less than 20×10^{-3} mm/s$^{0.5}$, which corresponds to the " very low " chloride ion penetration grade. With the increase of the content of ultra-fine slag, the initial water absorption rate decreases, indicating that the transport property of the concrete becomes worse, which cannot be reflected from the chloride ion penetration grade.

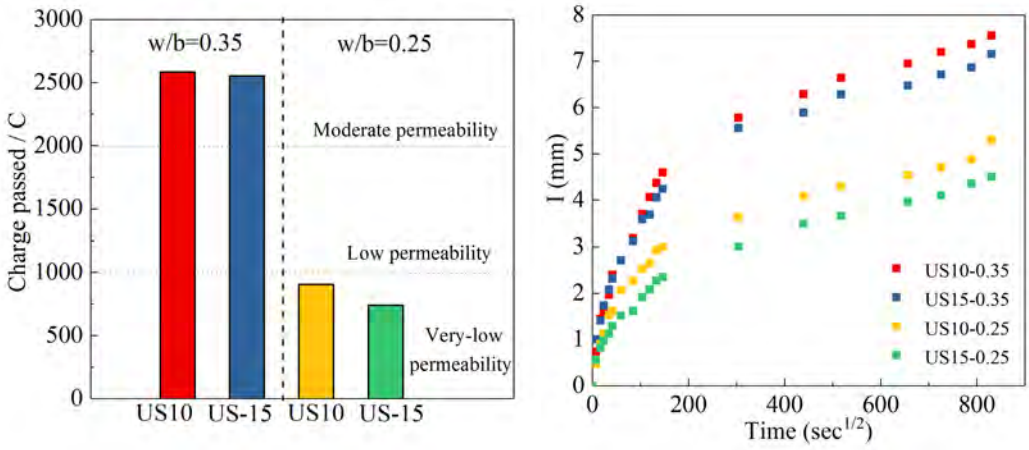

(a) **(b)**

Figure 4: The charge passed and the corresponding chloride ion permeability grades (a) and the water absorption per unit area of exposed surface versus $t^{0.5}$ and the corresponding initial water absorption rates (b) of ultra-fine slag concrete.

Fig. 5(a) shows the charge passed and the corresponding chloride ion permeability grades of silica fume concrete. Regardless of whether the water-to-binder ratio is 0.35 or 0.25, or whether the content of silica fume is 10% or 15%, the chloride ion permeability grade of silica fume concrete is “very low”. It shows that silica fume has a significant refinement effect on the pore structure of concrete, which significantly reduces the transport property of concrete. However, it fails to the effect of ultra-fine slag and silica fume content on the pore structure and even transport property of concrete at a low water-to-binder ratio according to the result of the chloride ion penetration test. Fig. 5(b) shows the water absorption per unit area of exposed surface versus $t^{0.5}$ and the corresponding initial water absorption rate of silica fume concrete. The initial water absorption rates of silica fume concrete at a water-to-binder ratio of 0.35 are between 15×10^{-3} mm/s$^{0.5}$ and 20×10^{-3} mm/s$^{0.5}$, while the initial water absorption rates of silica fume concrete at a water-to-binder ratio of 0.25 are between 10×10^{-3} mm/s$^{0.5}$ and 15×10^{-3} mm/s$^{0.5}$, reflecting that the smaller the water-to-binder ratio, the smaller the initial water absorption rate, due to the lower the porosity of concrete. The larger the content of silica fume, the smaller the initial water absorption, due to the more significant refinement effect on the pore structure of concrete.

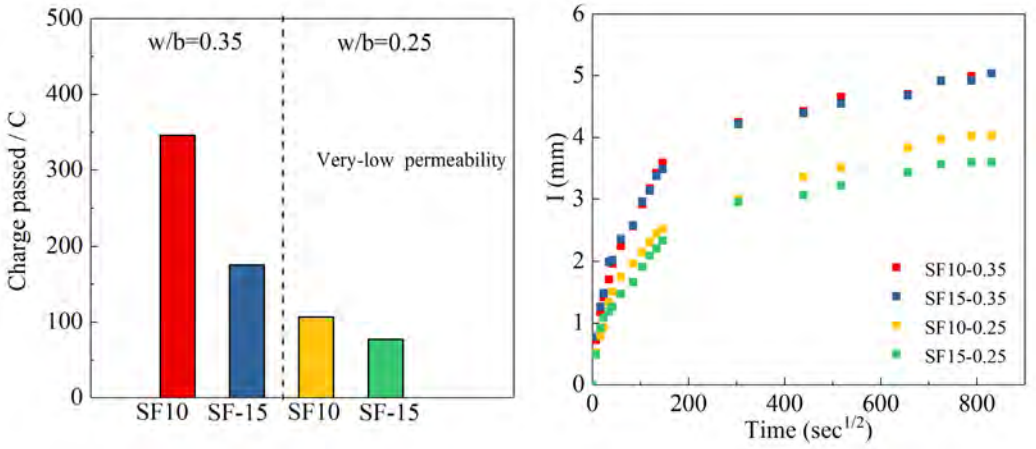

Figure 5: The charge passed and the corresponding chloride ion permeability grades (a) and the water absorption per unit area of exposed surface versus $t^{0.5}$ and the corresponding initial water absorption rates (b) of slica fume slag concrete.

4. CONCLUSIONS

In this study, relationship between the water absorption and the chloride ion penetration with addition of various mineral admixtures such as fly ash, slag and silica fume at various water-to-binder ratios is investigated. It is found that water absorption can provide a reliable estimation of chloride ion penetration. There is a good correspondence between the initial water absorption rate and chloride ion penetration grade. The initial water absorption rate of more than 50×10^{-3} mm/s$^{0.5}$, 40-30×10^{-3} mm/s$^{0.5}$, 30-20×10^{-3} mm/s$^{0.5}$ and less than 20×10^{-3} mm/s$^{0.5}$ may correspond to the chloride ion penetration grade of “high”, “moderate”, “low” and “very low”, respectively. The initial water absorption rate can further reflect the transport property and durability of concrete in the same chloride ion penetration grade where the comparison of the specific charge passed values is invalid. Water absorption has the potentiality to act as a deterministic index for transport properties and durability of concrete.

REFERENCES

[1] J. Bear, Y. Bachmat, Introduction to Modelling Phenomena of Transport in Porous Media, Kluwer Academic Publishers, Dordrecht, 1990.

[2] K. Mehta, Durability of concrete – fifty years of progress? ACI Spec. Pub. 126 (1) (1991) 1–32.

[3] C. Hall, Barrier performance of concrete: a review of fluid transport theory, Mater. Struct. 27 (5) (1994) 291–306.

[4] Maltais Y, Samson E, Marchand J. Predicting the durability of Portland cement systems in aggressive environments – laboratory validation. Cem. Concr. Res. 34(9) (2004) 1579–89.

[5] Hooton RD, Mesisc T, Beal DL. Sorptivity testing of concrete as an indicator of concrete durability and curing efficiency. In: Proceedings of the third Canadian symposium on cement and concrete, Ottawa, Ontario, (1993) 264–75.

[6] Lockington D, Parlange JY, Dux P. Sorptivity and the estimation of water penetration

into unsaturated concrete. Mater. Struct. 32(5) (1999) 342–347.
[7] L. Basheer, J. Kropp, D.J. Cleland, Assessment of the durability of concrete from its permeation properties: a review, Constr. Build. Mater. 15 (2) (2001) 93–103.
[8] Parrot LJ. Water absorption in cover concrete. Mater. Struct. 25(5) (1992) 284–292.
[9] C. Edvardsen, Water permeability and autogenous healing of cracks in concrete, ACI Mater. J. 96 (4) (1999) 448–454.
[10] Henkensiefken R, Castro J, Bentz D, Nantung T, Weiss J. Water absorption in internally cured mortar made with water-filled lightweight aggregate. Cem. Concr. Res. 39(10) (2009) 883–992.
[11] A.A. Ramezanianpour, V.M. Malhotra, Effect of curing on the compressive strength, resistance to chloride-ion penetration and porosity of concretes incorporating slag, fly ash or silica fume, Cem. Concr. Compos. 17 (1995) 125–133.
[12] R.J. Thomas, Erandi Ariyachandra, Diego Lezama et al, Comparison of chloride permeability methods for Alkali-Activated concrete, Constr Build Mater. 165 (2018): 104-111.
[13] ASTM International, ASTM C1585. Standard test method for measurement of rate of absorption of water by hydraulic-cement concretes; 2013.
[14] ASTM International, ASTM C1202. Standard test method for electrical indication of concrete’s ability to resist chloride ion penetration; 2012.

THE EFFECT OF SAP AND SCM ON MICROSTRUCTURE DEVELOPMENT IN EARLY AGE FIBRE REINFORCED MORTARS

R. Rostami (1) and A. J. Klemm (1)

(1) School of Computing, Engineering and Built Environment, Glasgow Caledonian University, UK

Abstract

The use of Supplementary Cementitious Materials (SCMs) in concrete manufacture has significantly increased in the last decades mainly due to their sustainability benefits. Polymeric Fibres (PF) are commonly used in concrete in order to enhance adhesive and frictional bond with a cementitious matrix and improve mechanical properties. Despite these, early age shrinkage of cementitious materials is still a major concern and some form of internal curing is necessary, for example by Superabsorbent polymers (SAP). By providing a continuous supply of water for hydration SAPs influence long term durability and sustainability of mortars. However, the effect of different SAPs on microstructure development in fibre reinforced mortars (FRM) still remains scarce. The current study aims to address this issue. Three commercially available cements: CEM I (PC), CEM II (PC-FA) and CEM III (PC-GGBS) and three types of SAP were analysed. Microstructural features of composites were studied by MIP and SEM techniques. These were accompanied by the elastic modulus analysis of composites. The experimental results showed that application SAP E, with finer particle sizes, results in the lowest total porosities of mortars and greater number of evenly distributed smaller pores (under 20 nm). This subsequently leads to the reduced effect on elastic modulus of FRM. In summary, the smaller SAP particles and more evenly distributed the more efficient in hydration process and more homogenous internal microstructure.

Keywords: Supplementary Cementitious Materials (SCMs), Polymeric Fibres (PF), Superabsorbent polymers (SAPs), Microstructure, Elastic Modulus

1. INTRODUCTION

Worldwide popularity of blended cements, produced by a partial substitution of PC clinker by Supplementary Cementitious Materials (SCMs), is based on their good performance and lower environmental impact [1-2]. In early ages the contribution of SCMs to strength development is generally negligible due to slower reactions [2, 3]. Nevertheless, they have a major effect on hydration kinetics and enhancement of cementitious reactions due to physical effects (filler effect) and chemical reactions (dissolution-precipitation mechanism) during prolonged hydration [3].

However, SCMs are more sensitive to curing regimes and hence more susceptible to early cracking. This is primarily caused by slow pozzolanic reactions in fly ash (FA) [4] and by the limited degree of later reactions in ground granulated blast furnace slag (GGBS) due to a lack of space already filled by early products of PC hydration [5]. Polymeric fibres (PF) are often recommended [6] as a technique to cope with this phenomenon. Unfortunately it is often insufficient and some form of internal curing is still required to decrease self-desiccation and promote cement hydration [7]. Superabsorbent polymers (SAPs) have been proved to be a promising internal curing agent for cementitious materials, which can facilitate hydration process and control water supply in both fresh and hardened state [5, 7-10]. The most remarkable successes of SAPs have been in mitigation of autogenous shrinkage [5] and plastic shrinkage [9] in various types of mortar and concrete. Nevertheless, the effect of different SAPs on microstructure development in imature FRM containing SCM still remains unclear and deficient. Therefore, the main objective of this study is to assess this effect by application of MIP and SEM techniques. The microstructural analyses are supplemented by the analysis of elastic modulus of composites.

2. METHODOLOGY

2.2 Materials

Three types of cement have been used in this study: CEM I 52.5N (Portland cement - PC), CEM II/B-V 42.5N (PC-FA 70-30), and CEM III/A 42.5N (PC-GGBS 50-50). Their chemical and physical characteristics, as provided by manufacturers, are presented in Table 1.

Table 1: Chemical and physical characteristics of PC, PC-FA and PC-GGBS

	SiO_2 (%)	Al_2O_3 (%)	Fe_2O_3 (%)	CaO (%)	MgO (%)	SO_3 (%)	K_2O (%)	TiO_2 (%)	ZnO (%)	LOI (%)
PC	20.1	4.9	2.57	64.3	2.2	3.2	0.27	0.0	0.0	2.39
PC-FA	32.69	13.13	3.29	43.48	1.33	0.4	1.26	0.56	0.02	0.16
PC-GGBS	24.50	8.99	1.76	57.13	5.33	0.0	0.0	0.58	0.0	1.19

The micro polypropylene fibres used in this study had the following characteristics: length of 6-mm, diameter 18μm and density 0.91 kg/m^3. Three types of cross-linked Superabsorbent polymers were used in the experiments; SAP A-copolymer of acrylamide and acrylic acid, SAP C and E-modified polyacrylamide.

2.3 Characterisation of SAPs

Table 2 summarises properties of SAPs, including particle size distribution, their chemical and sorption characteristics. Water absorption capacities have been determined in deionised water and different binder solutions. It should be noted that SAP E has a similar molecular structure to SAP C (modified polyacrylamide) but different particle grading. Predominant particles sizes and mode values for SAP A are 102.51± 0.43 μm, for SAP C 95.19± 0.44 μm and for SAP E 76.74 ± 0.22 μm.

Table 2: Characterisation of SAPs

SAP	Type	Particles size (μm)	WAC[1] Deionized water	WAC PC Solutions	WAC PC-FA Solutions	WAC PC-GGBS Solutions
SAP A	copolymer of acrylamide and acrylic acid	30-140	340 g/g	34 g/g	33 g/g	25 g/g
SAP C	modified polyacrylamide	30-140	290 g/g	36 g/g	37 g/g	33 g/g
SAP E	modified polyacrylamide	20-130	340 g/g	40 g/g	46 g/g	40 g/g

[1] WAC : water absorption capacity

Shapes and size of SAPs have been characterised by SEM image analysis (Figure 1).

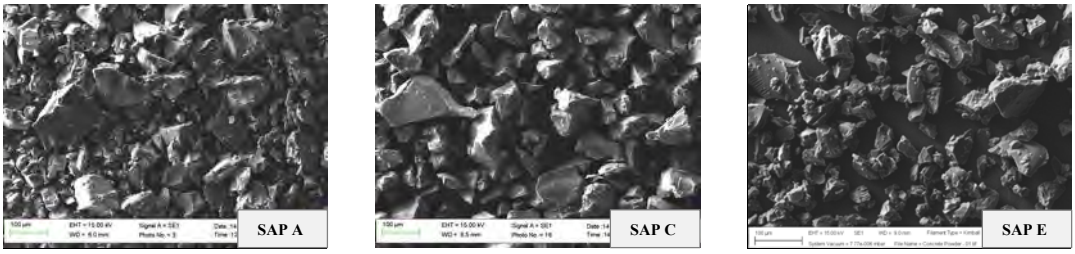

Figure 1: The SEM micrographs of SAP A, C, and E

2.4 Mix Compositions

Fifteen different compositions of FRMs were designed to carry out this study with different water/binder ratios as shown in Table 3. In SAP modified mortars, the water-to-binder ratio (w/b) was increased, in order to compensate for water absorbed by polymer [10].

Table 3: Mix proportion of mortars and water/binder ratios

Cement	Sample Name	SAP type	SAP Content	Fibre Content	W/B ratio
	I	-	-	-	0.48
	I1	-	-	0.50%	0.52
CEM I	I1A	A	0.25%	0.50%	0.58
(PC)	I1C	C	0.25%	0.50%	0.58
	I1E	E	0.25%	0.50%	0.58
	II	-	-	-	0.45
	II1	-	-	0.50%	0.50
CEM II	II1A	A	0.25%	0.50%	0.56
(FA)	II1C	C	0.25%	0.50%	0.56
	II1E	E	0.25%	0.50%	0.57
	III	-	420	-	0.48
	III1	-	-	0.50%	0.52
CEM III	III1A	A	0.25%	0.50%	0.58
(GGBS)	III1C	C	0.25%	0.50%	0.58
	III1E	E	0.25%	0.50%	0.58

All studied mortars were prepared with the proportion of binder to fine sand of 1:2 (by weight). Three types of SAPs were added to mixtures in the proportion of 0.25% by mass of binder. The amount of fibre used was 0.50% by mass of binder. Fine sand had 90% of particles smaller than 0.425mm.

2.5 Microstructure and Elastic Modulus

Microstructural characteristics of FRMs were assessed at 7, 14 and 28 days by the Mercury Intrusion Porosimetry (MIP) and the Scanning Electron Microscopy (SEM) techniques. Porosity and pore size distributions were determined by AutoPore IV 9500 by Micrometrics (with pressure range up to 60000 psi). The elastic modulus in compression were tested on prismatic samples (40 × 40 × 100 mm^3) at 14, 28, 270 and 365 days from the moment of sample preparation, BS EN13412[11].

3. RESULTS AND DISCUSSIONS

Figure 3 shows the total porosity results from the MIP measurements. Generally, the addition of fibre and SAPs increased the total porosity. This effect was reduced over the time for the reference samples (without fibre and SAP). The samples with CEM III (PC-GGBS) had the highest total porosities followed by CEM I (PC) and CEM II (PC-FA). This can be explained by the presence of GGBS (reduction of PC content) and decrease of total volume of hydrates formed [5, 12]. This is also related to low water-to-cement ratio of FA-blended system. As it can be seen in Figure 3, after 7 days, the appearance of a peak of total porosity is closely linked to the presence of bigger pores. With the progress of hydration (at 14 days), the total porosities of SAP samples increased by approximately 8%. However, after 28 days, all total porosities have slightly decreased.

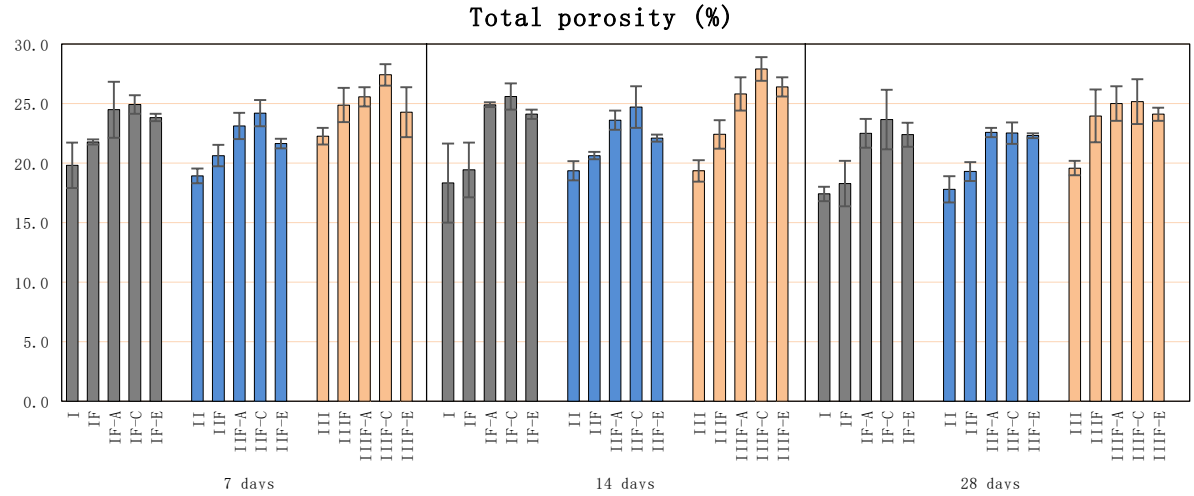

Figure 3: Results of total porosity by MIP

Figure 3 illustrates a clear increase in total porosities of SAP mortars in comparison with corresponding reference samples. The highest total porosity values have been recorded for samples with SAP C, due to its intermediate WAC and larger particle sizes (Table 2). It was also found that SAP E with the similar composition to SAP C, but finer particle sizes had the lowest total porosity values, especially at later age. It appears that the SAP particle sizes notably affect absorption/desorption characteristics.

Different pore size distributions in studied FRMs are shown in Figure 4.

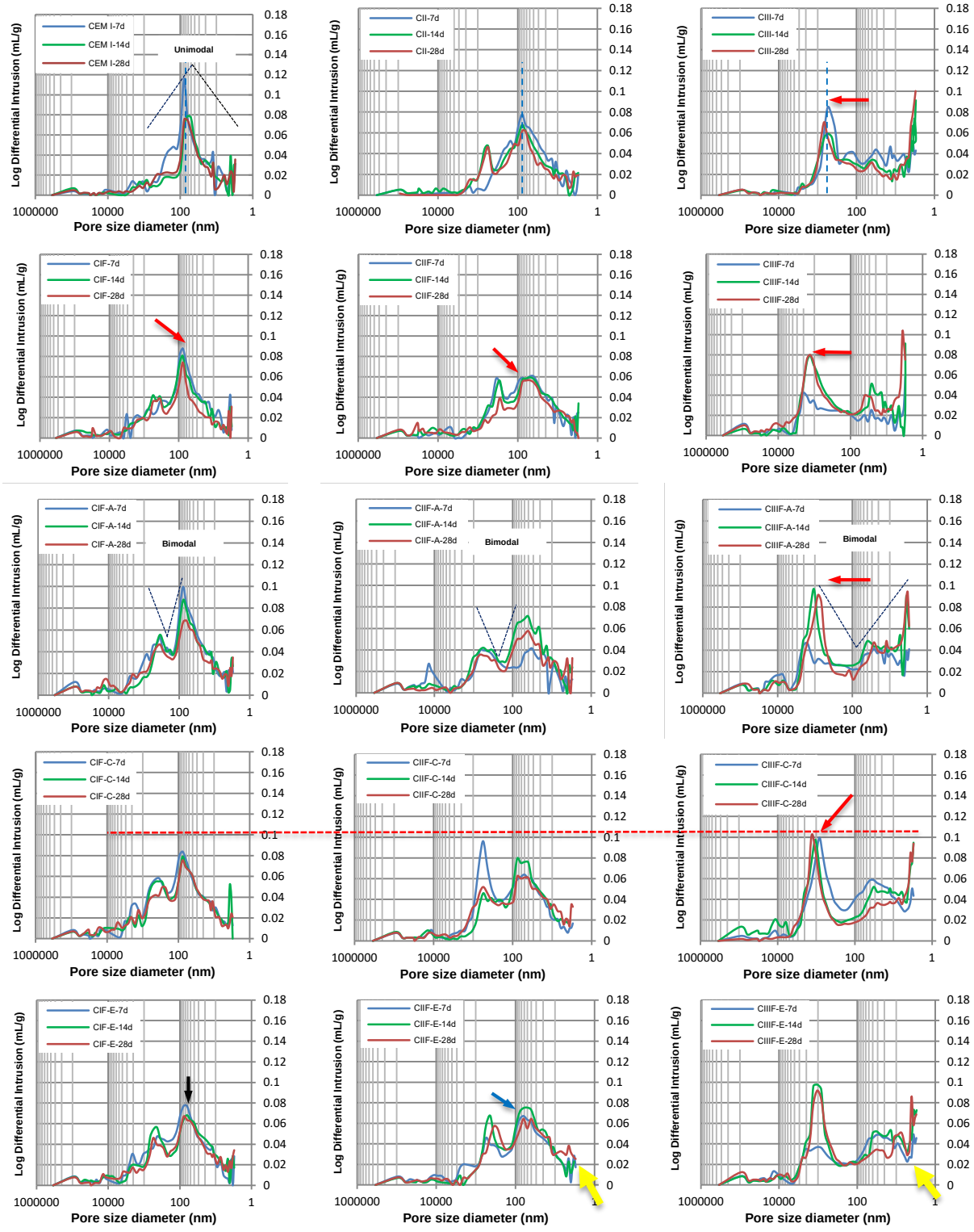

Figure 4: Pore size distributions (by MIP) of mortars

The effects of PF and SAPs on microstructural characteristics differ significantly. Several peaks corresponding to the predominant pore diameters can be identified (red arrows). SAP-

free reference mortars had predominant sizes between 5 to 500 nm and peak around 80 nm, 90 nm and 400 nm for CEM I (PC), CEM II (PC-FA) and CEM III (PC-GGBS) respectively (blue dash line). SAP samples had pore diameters greater than 500 nm, which were formed by collapsing SAPs. The largest pores were recorded for mortars with SAP C (red square dot line).

In early hydration stage, SAP mortars had a similar bimodal PSD pattern compared to the free-SAP samples. However, at about 28 days, the number of smaller pores (under 20 nm) was reduced in SAP mortars; while in the reference sample, this amount has not changed over time. MIP porosity obtained for samples with GGBS is significantly larger than for FA and PC samples. However, as seen on Figure 4, the total porosity values increased during the first 14 days. With the progress of hydration (after the second week), the total porosities slightly decreased. This effect is more evident for SCM samples with SAP E (yellow arrows). Water released from SAPs facilitates formation of hydration products and filling up the existing pores spaces, which in turn results in densified microstructure at later age [5].

Figure 5 shows SEM micrographs of mortars at age of 28 days. The absorption potential of SAPs can be determined by the voids partially filled with hydration products left by the SAP. These voids displayed on the scanned sections can give an estimate of SAPs volumetric fraction. These also can have an impact on the surface roughness, which lead to higher roughness surface [5].

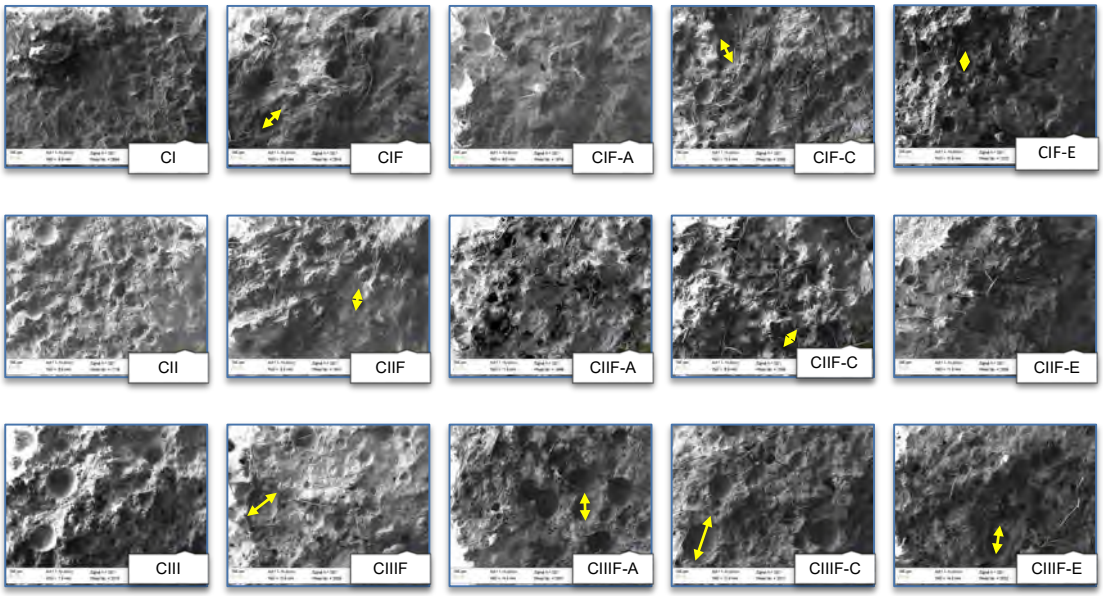

Figure 5: SEM micrographs of mortars at 28 days (100x)

A set of images given in Figure 5 shows clear contrast between macro pores and concaves of all samples. From the SEM analysis of samples at low magnification (100x), it is apparent that big concaves can be clearly identified in samples with CEM III (PC-GGBS) followed by CEM I (PC) and CEM II (PC-FA). The large macro pores observed in all SAP samples contributed to the increased total porosities of mortars. The samples with SAP C seem to have larger (micro and macro) pores, especially for PC-GGBS blends (yellow arrows). It is likely

that the high-water absorption capacity and large particle size for this polymer has caused formation of pores of such big diameters.

The overall trend of elastic modulus up to 360 days is shown on Figure 6. In general, the elastic modulus of mortars increases over time due to the progress of hydration reactions.

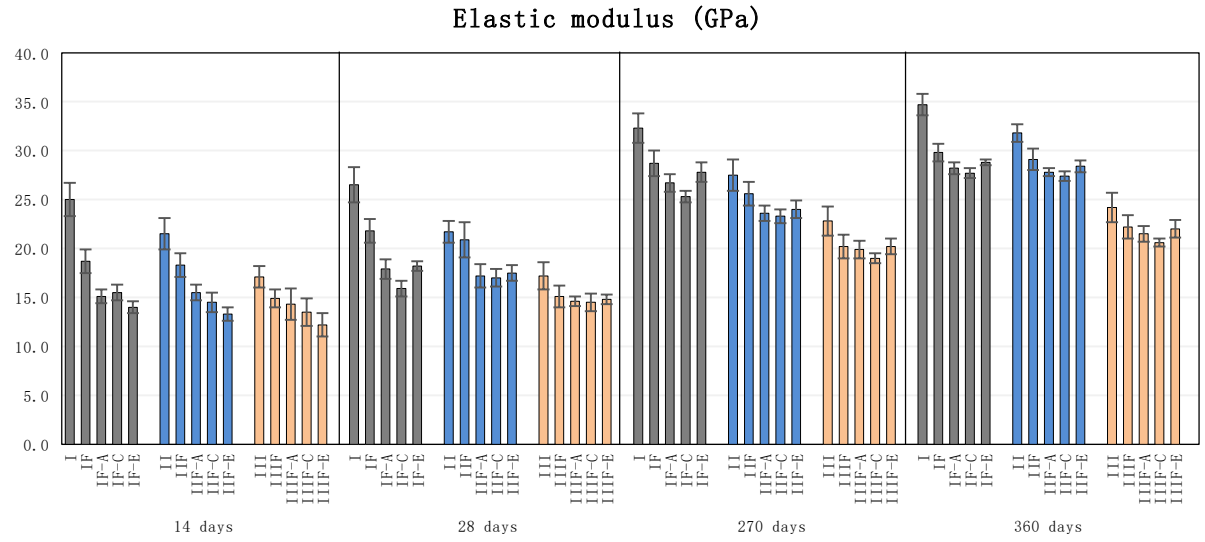

Figure 6: Results of elastic modulus

The results show that elastic moduli for SAP-modified samples are always lower than for the reference mixtures. However, the negative effect of SAP addition is more marked at early age (up to 14 days) and is slightly decreased at 28 days. However, this effect is reduced later due to further hydration facilitated by internal curing of SAP. The decrease in SAP mortars can be related to their higher total porosity at early ages; pores may act as weak spots and influence mechanical behaviour. When comparing mortars containing different binders, it is clear that the higher values were recorded for the CEM I (PC) samples, followed by CEM II (PC-FA) and CEM III (PC-GGBS). Figure 6 also demonstrates that the addition of PF results in a decrease in elastic modulus by comparison with the reference samples. It should be noted that this reduction is more pronounced in matrices with CEM I (PC) cement due to increased porosity of these samples. In majority of samples, SAP A with the lowest water absorption capacity (WAC) had the highest elastic modulus values at early age (up to 14 days). It should be also considered that SAP E with smaller particle sizes had the lowest influence on elastic modulus behavior as smaller particles leave behind smaller voids. Further enhancements (after the second week) were observed in blended cements due to reaction of SCM with portlandite from PC hydration. These new products of the secondary hydration have subsequently filled smaller pores under than 20 nm (Figure 4).

4. CONCLUSIONS

Based on experimental results, the following can be concluded:

- Both MIP and SEM analysis confirm positive effect of finer particle sizes on absorption/desorption characteristics (SAP E).

- After the second week, the number of smaller pores (under 20 nm) was reduced in SAP mortars and this effect is more evident for SCM samples with SAP E.
- SAP E had the lowest influence on elastic modulus as smaller particles left behind smaller voids. Further enhancements (after the second week) were observed in blended cements due to reaction of SCM with portlandite from PC hydration.

REFERENCES

[1] Scrivener, K.L., Juilland, P. and Monteiro, P.J., 2015. Advances in understanding hydration of Portland cement. Cement and Concrete Research, 78, pp.38-56.

[2] Scrivener, K.L., Lothenbach, B., De Belie, N., Gruyaert, E., Skibsted, J., Snellings, R. and Vollpracht, A., 2015. TC 238-SCM: hydration and microstructure of concrete with SCMs. Materials and Structures, 48(4), pp.835-862.

[3] Skibsted, J. and Snellings, R., 2019. Reactivity of supplementary cementitious materials (SCMs) in cement blends. Cement and Concrete Research, 124, p.105799.

[4] De Belie, N., Soutsos, M. and Gruyaert, E., 2018. Properties of Fresh and Hardened Concrete Containing Supplementary Cementitious Materials. Springer.

[5] Almeida, F.C. and Klemm, A.J., 2018. Efficiency of internal curing by superabsorbent polymers (SAP) in PC-GGBS mortars. Cement and Concrete Composites, 88, pp.41-51.

[6] Gong, J., Zeng, W. and Zhang, W., 2018. Influence of shrinkage-reducing agent and polypropylene fiber on shrinkage of ceramsite concrete. Construction and Building Materials, 159, pp.155-163.

[7] Wyrzykowski, M. and Lura, P., 2016. Effect of relative humidity decrease due to self-desiccation on the hydration kinetics of cement. Cement and Concrete Research, 85, pp.75-81.

[8] Mechtcherine, V. and Reinhardt, H.W. eds., 2012. Application of super absorbent polymers (SAP) in concrete construction: state-of-the-art report prepared by Technical Committee 225-SAP (Vol. 2). Springer.

[9] Rostami, R. and Klemm, A.J., Effect of Superabsorbent Polymers on Plastic Shrinkage Cracking and Properties of Fresh State Mortars Reinforced by Polymeric Fibres. 2nd RILEM Spring Convention & International Conference on Sustainable Materials, New Generation of Construction Materials (SMSS2019). Croatia, P606-613.

[10] Snoeck, D., Schaubroeck, D., Dubruel, P. and De Belie, N., 2014. Effect of high amounts of superabsorbent polymers and additional water on the workability, microstructure and strength of mortars with a water-to-cement ratio of 0.50. Construction and Building Materials, 72, pp.148-157.

[11] BS EN, 14630, p.2006. Products and systems for the protection and repair of concrete structures-Test methods-Determination of carbonation depth in hardened concrete by the phenolphthalein method. British Standards Institution.

[12] Lothenbach, B., Scrivener, K., and Hooton, R. D. (2011). Supplementary cementitious materials. Cement and Concrete Research, 41(12), 1244–1256.

[13] Berodier, E. and Scrivener, K., 2015. Evolution of pore structure in blended systems. Cement and Concrete Research, 73, pp.25-35.

THE EFFECT OF SULFATE-RICH SEWAGE SLUDGE ASH ON THE VOLUME DEFORMATION AND MICORSTRUCTURE OF CEMENT PASTE

Chunping Gu (1,2), Yongjie Ji (1), Yang Yang (1,2), Jintao Liu (1,2) and Tongyuan Ni (1,2)

(1) College of Civil Engineering and Architecture, Zhejiang University of Technology, Hangzhou, China

(2) Key Laboratory of Civil Engineering Structures & Disaster Prevention and Mitigation Technology of Zhejiang Province, Zhejiang University of Technology, Hangzhou, China

Abstract

Sewage sludge ash (SSA) is the combustion residue of the sewage sludge obtained from wastewater treatment plants. In China, SSA normally contains high content of SO_3, which may cause detrimental effect on the volume stability of cement-based materials. This study investigated the effect of sulfate-rich SSA (SR-SSA) on the volume deformation and the microstructure of cement paste. The autogenous shrinkage and drying shrinkage of cement pastes incorporating SR-SSA were tested. The microstructure of cement pastes incorporating SR-SSA was studied with mercury intrusion porosimetry (MIP) and scanning electron microscopy (SEM). The results show that the addition of SR-SSA reduced the autogenous shrinkage of cement paste, but increased the drying shrinkage of cement paste. Hence the addition of SSA may cause more serious cracking problem of cement-based materials under drying conditions, but could inhibit the cracking under sealed condition. The SEM and MIP investigations showed that, when SR-SSA was presented, more ettringite was generated in the cement paste and the porosity of the cement paste became higher.

Keywords: cement paste, sulfate, sewage sludge ash, shrinkage, microstructure

1. INTRODUCTION

Due to the increase in sludge production all over the world, the recycling use of SSA has attracted a lot of interest from the government and industry. One of the promising strategies of recycling SSA is to use it as cement replacement in cement-based materials [1,2]. Cement industry is well known for its ability to absorb and recycle different kinds of wastes. If the wastes have binding properties, they could reduce the use of Portland cement, which is indirectly beneficial for the environment because of the reduction of CO_2 emissions.

Many studies have attempted to explore the recycling use of sewage sludge ash (SSA) in cement-based materials. The addition of SSA would reduce the workability of cement-based materials [3,4]. According to the review of Lynn et al. [1], the average rates of decrease in

workability of cement mortar and concrete slump were 6% and 12% respectively for every 10% cement replaced by SSA. Meanwhile, the addition of SSA would retard the initial and final setting of cement-based materials [5]. In addition, the improved content of SSA would cause the reduction of the mechanical properties of cement-based materials [6-8]. Hence, when recycling SSA in cement-based materials, its content should be controlled at a low level for safety reasons. Mix design adjustments, such as increasing cement content, using the water-reducing agent to reduce the water to binder ratio, adding the nano-materials and increasing the fineness of SSA, could be made to improve the mechanical properties the SSA-bleneded cement-based materials [1]. The addition of SSA would also increase the porosity of the cement-based materials [9,10], and thus reduce the carbonation resistance of cement-based materials [10]. Limited studies on the effect of SSA on the volume deformation of the cement-based materials showed that, the drying shrinkage could be reduced when the SSA content was higher than 20%, while the effect of SSA is negligible if the SSA content was lower (i.e. less than 20%) [9-11].

In China, high content of sulfate is normally present in the SSA. Some studies have shown that sulfates presented in SSA are not reactive in cement-based materials [9]. The effect of sulfate-rich SSA (SR-SSA) on the properties of the cement-based materials is not fully studied so far. The presence of high content of SO_3 may cause the formation of ettringite, which would lead to the expansion and cracking of the cement-based materials. Cement degradation caused by internal sulfate attack have been observed when sulfate-rich aggregates are used in concrete [12,13].

The aim of this study was to evaluate the recycling potential of SR-SSA in cement-based materials. The main concern of this paper is to study the effect of SR-SSA on the volume deformation of the cement paste. Moreover, the microstructure of the cement paste with SR-SSA was detected with mercury intrusion porosimetry (MIP), X-ray diffraction (XRD) and scanning electron microscope (SEM).

2. MATERIALS AND METHODS

2.1 Materials and mix proportions

The raw materials for this study included ordinary Portland cement (P·O 42.5) and SR-SSA. The particle size distribution of cement and SR-SSA measured with Mastersizer 3000 laser diffraction system are shown in Figure1. The size of SR-SSA was mainly in the ranges from 1 μm to 100 μm and was a little bigger than the cement particles. The average particle sizes for cement and SR-SSA were 16.3 μm and 24.1 μm respectively. The chemical compositions of cement and SSA are shown in Table 1. The mass content of SO_3 in SR-SSA was 23.2%.

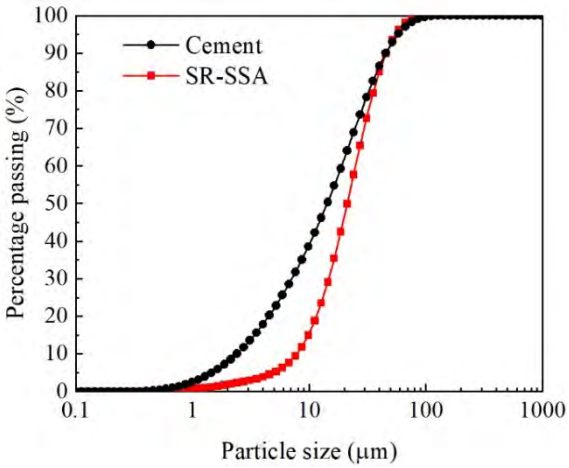

Figure 1: Particle size distributions of cement and SR-SSA

Table 1: Chemical compositions of OPC and SSA

	Cement (wt%)	SSA (wt%)
CaO	55.10	33.19
SiO_2	21.4	12.84
Al_2O_3	6.30	7.00
Fe_2O_3	4.30	15.89
SO_3	2.41	23.20
MgO	2.80	0.90
Na_2O	0.23	0.85
P_2O_5	3.61	---
ZnO	0.69	---
TiO_2	0.42	0.51
K_2O	0.46	0.45

In this study, cement pastes incorporating 0%, 5%, 10% and 15% SR-SSA were prepared, and the water to binder ratio (w/b) of the cement pastes was 0.4. Table 2 shows the mix proportions of the cement pastes.

Table 2: Mix proportions of the pastes

Sample	Cement (wt.%)	SR-SSA (wt.%)	w/b
Control	100	0	0.4
5%SSA	95	5	
10%SSA	90	10	
15%SSA	85	15	

2.2 Autogenous shrinkage and drying shrinkage

The autogenous shrinkage tests were performed according to ASTM C1698-09(2014)[14]. The cement pastes were cast in corrugated plastic tubes. The length change of the corrugated plastic tube was measured with digital dial gauges. The length measurements were started at the time of finial setting, and stopped at the age of 50d. The length data were recorded every 30 minutes with a data acquisition system.

The drying shrinkage tests were performed based on ASTM C596-09(2017) [15]. The size of the cement paste specimens was 25 mm × 25 mm× 285 mm. The specimens were demolded at 1d, and cured in water at 20±2℃ for 2 days. After that，the specimens were placed in a drying chamber with a temperature of 20±3℃ and a relative humidity of 50±4%. The length change of the specimens were monitored with displacement sensors, and the data were recorded with a data log till the age of 28d.

2.3 SEM and MIP

The crashed cement paste pieces were used as the samples for MIP and SEM tests. MIP was used to investigate the pore structure of cement pastes. The tests were carried out with Micromeritics AutoPore IV 9500. The contact angle was set to be 130° and the detected pore size was ranged from 7 nm to 200 nm. The samples at different ages were immersed in the acetone to stop the hydration, and dried in vacuum oven at 50℃ for 3 days before MIP tests. SEM was applied to detect the morphology of the fracture surface of the cement pastes. The samples were coated with gold before SEM observation, and secondary electron images were taken at the fractured surfaces.

3. RESULTS AND DISCUSSION

3.1 Autogenous and drying shrinkage

The autogenous shrinkage of cement pastes with different SR-SSA contents is shown in Figure 2. It can be seen that the addition of SR-SSA led to the expansion of the cement paste for some time depending on the contents of SR-SSA. The more SR-SSA resulted in the longer expensive duration and the higher expensive strain of the cement pastes. The cement paste with 5%, 10% and 15% SR-SSA expanded for 1.0 day, 3.0 days and 18.3 days respectively, and their highest expensive strains were 146.6 με, 505.2 με and 1264.4 με respectively. After the expansion, the cement pastes specimens shrank continuously until the end the test. The control cement paste did not show any expansion at early age and shrank all the time. At the age of 50d, the shrinkage strains of control, 5%SSA, 10%SSA and 15%SSA cement pastes were -1.387.4 με, -1159.7 με, -651.8 με and 452.8 με respectively. The ultimate shrinkage strain was lowered if more SR-SSA was added. 5% SR-SSA slightly reduced the autogenous shrinkage of cement paste, while 10% SR-SSA obviously reduced the autogenous shrinkage of cement paste. If 15% SR-SSA was added, the volume of the cement paste was always higher than the initial state during the tests. The addition of SR-SSA might be capable of reducing the cracking potential of the cement-based materials caused by the autogenous shrinkage, but if a high amount of SR-SSA was used, the cracking caused by the excessive expansion might be occur.

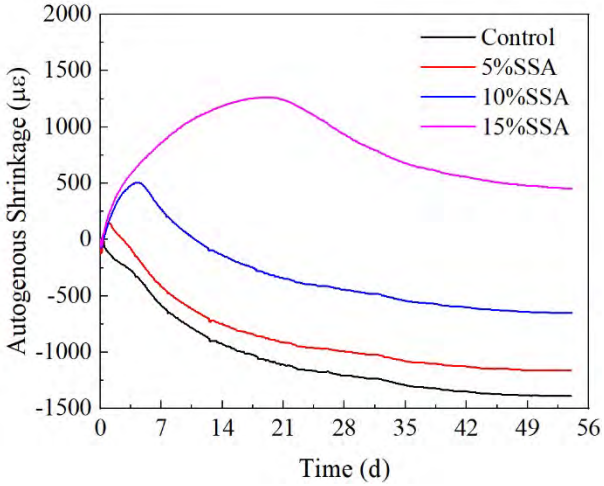

Figure 2: Autogenous shrinkage of cement pastes containing different amounts of SR-SSA (The positive value is for expansion and the negative value is for shrinkage)

The drying shrinkage of cement pastes with different SR-SSA contents is shown in Figure 3. The drying shrinkage increased very fast at the beginning of the tests, and became almost stable after the age of 24 days. When the amount of SR-SSA was 5%, the drying shrinkage of cement paste is similar to that of the control cement paste. When the amount of SR-SSA was 10% and 15%, the drying shrinkage of the cement pastes was lower than that of the control cement paste at early ages. Although the shrinkage caused by the drying was predominate at early ages, the expansion induced by the addition of SR-SSA was still effective. Hence at early age, the addition of SR-SSA reduced the drying shrinkage of cement paste, and the more SR-SSA was added, the lower drying shrinkage was. But afterwards, in spite of the expansion caused by the SR-SSA, the drying shrinkage of cement paste with 10% and 15% SR-SSA became higher than the control cement paste. This should be related to the difference in microstructure of cement pastes with and without SR-SSA. The early age expansion of 15%SSA was higher than 10%SSA, so the total drying shrinkage at 28d of 15%SSA was lower than 10%SSA.

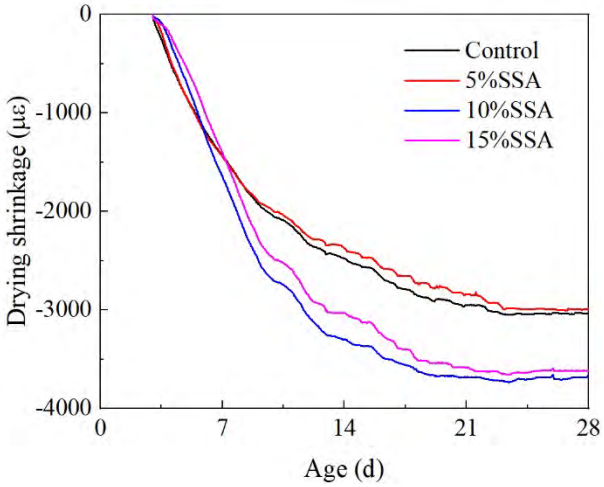

Figure 3: Drying shrinkage of cement pastes containing different amounts of SR-SSA

3.2 Microstructure

SEM was used to observe the morphology of cement pastes with and without SR-SSA. The AFt phase (ettringite) was the main concern of the observation. These images could help to explore the influence of SR-SSA on the microstructure of the cement paste. The SEM images of the Control cement paste and 15%SSA cement paste at the age of 7 days are shown in Figure 4. Needle-like AFt could be found in the control cement paste, but the amount of AFt was relative low. In the cement paste with 15% SR-SSA, more AFt could be fould. Moreover, the cement paste with 15% SR-SSA seemed more porous than the control cement paste.

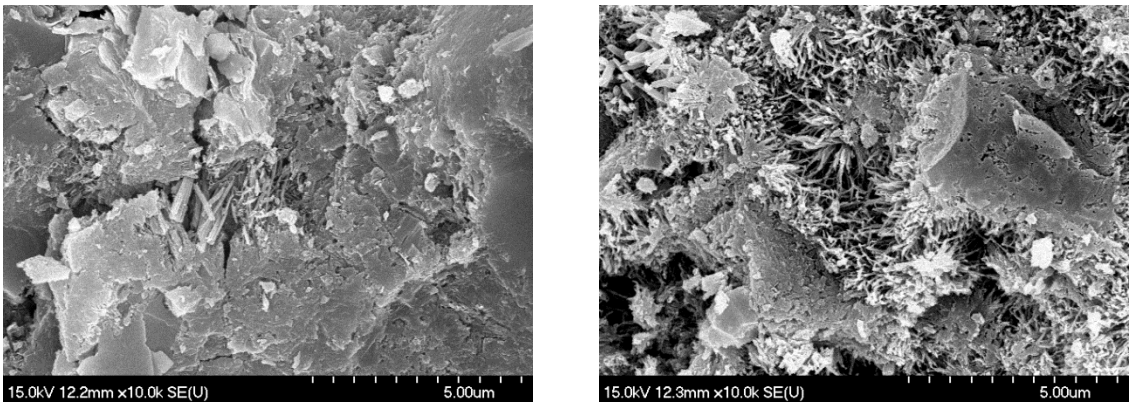

(a) **(b)**

Figure 4: SEM images of (a) Control cement paste (b) cement paste with 15% SR-SSA

MIP was applied to detect the pore structure of cement pastes with and without SR-SSA. Figure 5 shows the cumulative intrusion curve and the pore size distribution of the control cement paste and the cement paste with 15% SR-SSA at 28 days. The total porosity of cement paste with 15% SR-SSA was higher than the control cement paste at 28 days. Moreover, the most probable pore size of cement paste with 15% SR-SSA was much bigger than the control cement paste. Due to the higher porosity of cement paste with 15% SR-SSA, the drying shrinkage was also increased, which may be detrimental to the cracking resistance of cement paste under drying conditions.

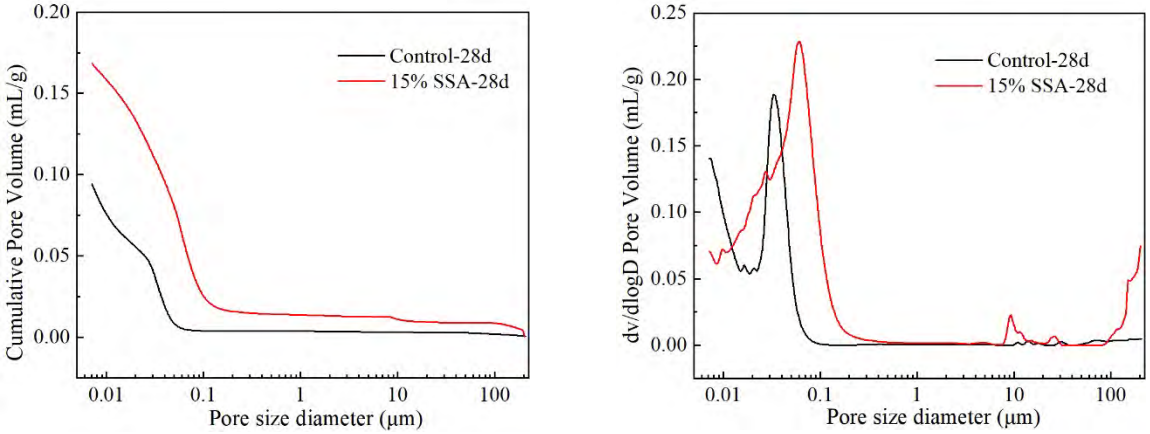

(a) the cumulative intrusion curve **(b) particle size distribution**

Figure 5: pore structures of the control cement paste and cement paste with 15% SR-SSA at 28d

4. CONCLUSIONS

- The addition of SR-SSA caused obvious expansion of the cement paste, hence the autogenous shrinkage was reduced with the increase of the content of SR-SSA in cement paste.
- The addition of 5% SR-SSA did not show much influence on the drying shrinkage of cement. The addition of 10% and 15% of SR-SSA reduced the drying shrinkage at the early age, but increased the drying shrinkage at the late age.
- The SEM and MIP investigations showed that, when SSA was presented, more ettringite was generated in the cement paste and the porosity of the cement paste became higher.
- To replace 5% cement with SR-SSA don't show much influence on the volume deformation of the cement, hence from the volume deformation point of view it is feasible to prepare cement-based materials with up to 5% SR-SSA.

ACKNOWLEDGEMENTS

The authors gratefully acknowledge the National Natural Science Foundation of China (grant numbers 51778583, 51708502) for the financial support of this work.

REFERENCES

[1] Lynn, C.J., Dhir, R.K., Ghataora, S.G. and West, R.P. 'Sewage sludge ash characteristics and potential for use in concrete'. *Constr. Build. Mater.* **98**(2015):767-779.

[2] Swierczek, L., Cieslik B.M. and Konieczka, P. 'The potential of raw sewage sludge in construction industry - a review'. *J. Clean. Prod.* **200**(2018) 342-356.

[3] Pan, S.C., Tseng, D.H., Lee, C.C. and Lee, C., 'Influence of the fineness of sewage sludge ash on the mortar properties'. *Cem. Concr. Res.* **33**(11)(2003)1749-1754.

[4] Chang, F.C., Lin, J.D., Tsai, C.C. and Wang K.S., 'Study on cement mortar and concrete made with sewage sludge ash'. *Water. Sci. Technol.* **62**(7)(2010)1689-1693.

[5] Lin, D.F., Lin, K.L., Chang, W.C., Luo, H.L. and Cai, M.Q. 'Improvements of nano-SiO_2 on sludge/fly ash mortar'. *Waste Manage*. **28**(6)(2008)1081-1087.

[6] Naamane, S., Rais, Z. and Taleb, M. 'The effectiveness of the incineration of sewage sludge on the evolution of physicochemical and mechanical properties of Portland cement'. *Constr. Build. Mater.* **112**(2016) 783-789..

[7] Chen, Z. and Chi, S.P. 'Comparative studies on the effects of sewage sludge ash and fly ash on cement hydration and properties of cement mortars'. *Constr. Build. Mater.* **154**(2017)791-803.

[8] Baeza-Brotons, F., Garcés, P., Payá, J. and Saval J.M. 'Portland cement systems with addition of sewage sludge ash. Application in concretes for the manufacture of blocks'. *J. Clean. Prod.* **82**(2014)112-124.

[9] Garcés, P., Carrión, M.P., García-Alcocel, E., Payá, J., Monzó, J. and Borrachero, M.V. 'Mechanical and physical properties of cement blended with sewage sludge ash'. *Waste Manage*. **28**(12)(2008)2495-2502.

[10] Alcocel, E.G.A., Garcés, P.A., Martínez, J.J., Payá, J., and Andión, L.G.A. 'Effect of sewage sludge ash (SSA) on the mechanical performance and corrosion levels of reinforced Portland cement mortars'. *Mater. Construc.* **56**(282)(2006)31-43.

[11] Tay, J.H. 'Sludge Ash as Filler for Portland Cement Concrete'. *J. Environ. Eng.* **113**(2)(1987)345-351.

[12] Onyang, C., Nanni, A., Chang, W.F. 'Internal and external sources of sulfate ions in Portland cement mortar: Two types of chemical attack'. *Cem. Concr. Res.* **18** (5) (1988) 699–709.

[13] Monzó, J., Payá, J., Borrachero, M.V. and Mora, E.P. 'Mechanical behavior of mortars containing sewage sludge ash (SSA) and Portland cements with different tricalcium aluminate content'. *Cem. Concr. Res.* **29**(1)(1999):87-94.

[14] ASTM C1698-09, Standard Test Method for Autogenous Strain of Cement Paste and Mortar. West Conshokocken: American Society for Testing and Materials, 2014, 8 pages.

[15] ASTM C596-09, Standard Test Method for Drying Shrinkage of Mortar Containing Hydraulic Cement. West Conshokocken: American Society for Testing and Materials, 2017, 4 pages.

THE EFFECT OF MINING WASTE ON THE DURABILITY INDICATORS OF CEMENT-BASED COMPOSITES

Napoleana-Anna Chaliasou (1), Spyridon Michalopoulos (1) and Antonios Kanellopoulos (1)

(1) School of Engineering & Computer Science – Division of Civil Engineering – University of Hertfordshire

Abstract

The need for infrastructure development is of major importance and the projected global infrastructure investment between 2013-2030 is estimated in the excess of £30 trillion to support the rapid growth of societies and economies worldwide (1). This trend puts civil infrastructure industry under immense stress to plan properly, construct fast and deliver resilient structures. Concrete is the dominant construction material and the key element in most infrastructure assets.

However, concrete's manufacture is extremely energy and resource intensive: >4 Billion tonnes of cement are produced annually, accounting to ~8% of global anthropogenic CO_2 and resulting to an annual production of ~2 tonnes of concrete for every person on the planet. The production of concrete is a process associated with very high energy consumption. In Europe, the construction sector alone is responsible for the 36% of CO_2 emissions and the 40% of all energy consumption.

The utilisation of mining waste in cement-based composites is an area of growing interest worldwide, with mining and excavation waste increasing considerably the last decade. Our work focuses on the replacement of cement with mineral wastes and the initial findings suggest that even at 20% replacement, the mechanical properties are marginally affected. This contribution will discuss some preliminary data on the effect of mining waste on the durability indicators of cementitious composites (oxygen permeability, capillary sorption and ion diffusion).

Keywords: Mining waste, Silicates, capillary water absorption,

1. INTRODUCTION

The fabrication of resilient and durable infrastructure is essential to support the rapid growth of societies and economies worldwide. Specifically, the projected global infrastructure investment is estimated to exceed £30 trillion pounds for the period 2013-2030 (1). This trend puts civil infrastructure industry under immense stress to plan properly, construct fast and deliver resilient structures.

Concrete is the key material for infrastructure construction as its properties satisfy the

requirements for fast construction and delivery of resilient elements, while it is abundant and low-cost. The high demand of concrete makes it the second mostly used material in the world (2) but is also associated with high environmental impact. The manufacturing of cement, main component of concrete, is resulting to high energy consumption and natural resource depletion. Furthermore, the CO_2 produced due to fuel consumption for the calcination of limestone and decomposition of calcium carbonate reach up to ~8% of global anthropogenic CO_2, resulting to an annual production of ~2 tonnes of concrete for every person on the planet [2].

The need to address sustainability issues relating to infrastructure development and concrete production has been highly prioritised by the construction industry and the relevant research community over the past decades. Nonetheless, the demand for high performing materials is more pressing to satisfy the growing demands of the society. Replacing part of cement with pozzolanic or mineral materials, has been proven a viable solution to decrease the environmental impact of concrete, while enhancing some of its properties. For example, the addition of silica fume, a by-product of the silicon metal or ferrosilicon alloys production, leads to higher strength and increases resistance to chloride penetration.

The utilisation of mining waste in cement-based composites is an area of growing interest worldwide, with mining and excavation waste increasing considerably the last decade. Mine tailings are a residual product after the separation process of the valuable fraction from the ore (3). Their particle sizes are very small due to the comminution process and they can be used for cement replacement, either directly or with little processing. Therefore, use of such mining wastes does not only add value to a waste product but could also lead to reduction of energy requirement for concrete production.

At the present study, the use of a siliceous by-product from the graphite mining industry in cementitious composites is investigated. The silicate is added in the mortars to replace cement at percentages up to 20% and its effect on the strength the durability indicators of cementitious composites is evaluated.

2. MATERIALS AND METHODS

Materials and mix design

The replacement percentages of cement by silicate mining waste were 0%, 10% and 20% for corresponding mortar mixes REF, Sil10 and Sil20. The cement used was CEM II 32,5R and the mortars were fabricated with binder to sand ratio 1:1.5 and water to cement ratio 0.5.

Table 1: Materials for mortar mix design

Mix label	CEMI (g)	Silicate (g)	Sand (g)	Water (g)
REF	3.00	0	4.5	1.5
Sil10	2.7	0.3	4.5	1.5
Sil20	2.4	0.6	4.5	1.5

Testing methods

The siliceous by-product was characterised by X-ray diffraction (XRD) to obtain chemical composition and estimate the percentage of amorphous material present. The characterisation was performed with a Bruker diffractometer and the parameters used were 2-theta range of 5-80 with step size of 0.02.

The workability of fresh mortars was evaluated immediately after casting, using the flow table method according to BS EN 1015-3 (4). The effect of the silicates on the porosity of the mortars was evaluated indirectly through water absorption by capillary action. The test was performed on half prism specimens (prisms dimension 40x40x160mm) after 28 days of water curing. The specimens were dried to constant mass, then all other sides were sealed with aluminium tape and they were immersed in 3mm water with the 40x40 mm cast side being in contact with water. The mass changes were recorded for a total of 256 minutes (4:16 hours). The compressive and flexural strength of the mortars were tested at 28 days to evaluate the effect of cement replacement by silicate waste, BS EN 1015-11 (5). The compressive strength results are also discussed against those of equivalent mortars with same replacement percentages of silica fume (SF). This is done to highlight the different effect of an amorphous and crystalline fine filler. The nomenclature of the comparative mixes is SF10 and SF20.

3. RESULTS AND DISCUSSION

3.1 Material characterisation

The silicate waste was characterised by XRD and the identified pattern is presented in Figure 1. It appears the waste is mainly composed of crystalline silicon oxide (S) as indicated by the sharpness of the peaks. The hump observed at low 2-theta angles could correspond to a minimal percentage of amorphous material. Also, the peak corresponding to graphite (C) at 26^{o} 2-theta angle was identified. This is expected as the silicate used in the present study is a waste of graphite mining. Even though a separation process is used for the two materials, it is assumed that small amounts of graphite could have remained unseparated. Lastly, the peaks at low angles were attributed to a complex, carbon-containing phase (C'). The two most probable phases are C_{48} H_{62} Cl_{0} Mn N_{60} Na O_{79} and $C_{10.5}$ $H_{7.5}$ $Cl_{0.75}$ $N_{0.75}$ $O_{17.88}$ V_{3}. The particle size distribution of the silicate waste as provided by the supplier is presented in Table 2

Table 2: Physical properties of silicate waste

Properties	Silicate waste
Mean (μm)	8.016
D_{10} (μm)	0.802
D_{50} (μm)	3.611
D_{90} (μm)	18.86

It is expected that the silicate waste could contribute to the cement hydration mainly physically. As seen by the X-ray diffraction analysis in Figure 1, the silicon oxide present in the waste is mainly crystalline and the average particle size of the silicate is around 8 μm according to **Table 2**. Even though it is much smaller compared to that of cement, given the

level of SiO_2 crystallinity the specific surface area might be not sufficient to promote pozzolanic reaction of the material. Therefore, the silicate is considered unlikely to react and contribut chemically in the hydration reaction. Fine materials added in cement, even if they are inert chemically, could contribute to strength development due to the filler effect. This means increase of potential nucleation sites and also more refined porosity (6). Similar inert additions, such as silica powder (3) have been found to favour the strength development of the cementitious matrix in a similar manner; by improving packing, nucleation and refining porosity.

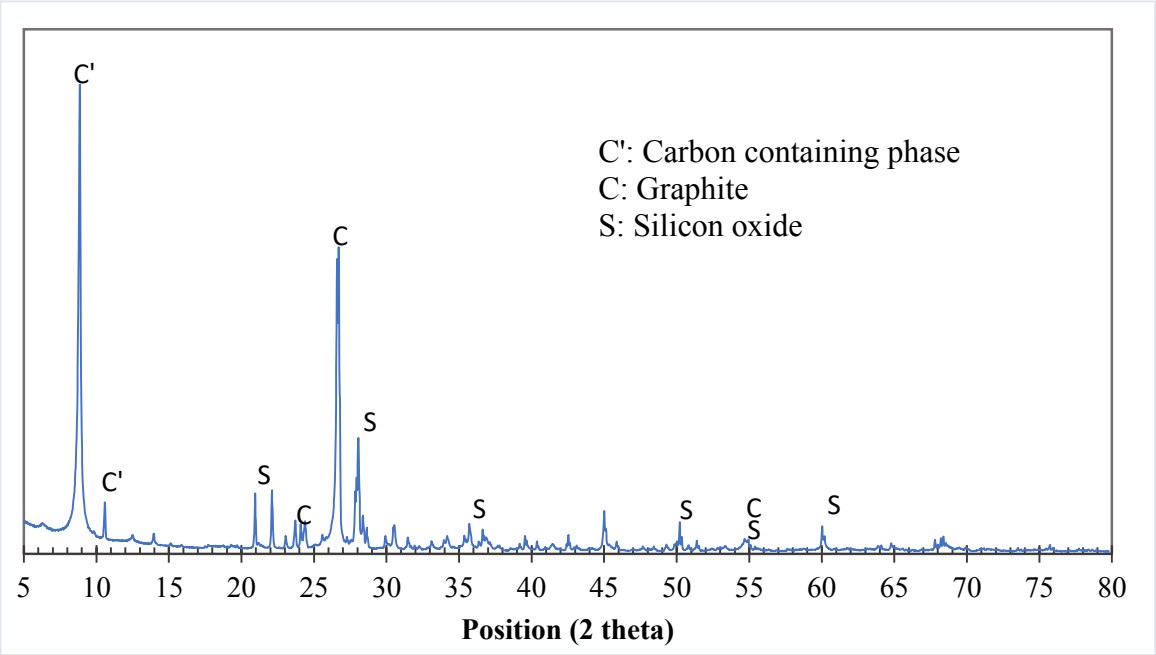

Figure 1 X-ray diffraction pattern of silicate waste

3.2 Workability

The addition of increasing silicate percentages in the mortars resulted to stiffer mixes as seen in **Table 3**. This was expected due to the particle size of the silicate waste which is significantly smaller than that of cement. Also, the shape of the silicate could have contributed to the flow reduction as plate-like or sharply-shaped powders hinder flowability of paste (7). The reduction in flow is not proportional to the replacement percentage, as for 10% silicate waste the reduction is 11% while for double replacement the percentage is 15%.

Table 3: Flow of mortars with silicate replacement

Mix label	Flow (mm)	Reduction percentage
REF	244.5	0%
Sil10	216.5	11%
Sil20	207.0	15%

This reduction would be expected due to the particle size of the silicate waste, as discussed before. Specifically, the addition of a finer particle in the mix is expected to increase water demand due to the increased specific surface area (8). Nonetheless, the reduction exhibited by the mixes did not hinder proper compaction and it is considered that in case of specific requirement for workability level, flow can be maintained by the use of a plasticizer and superplasticizer admixture.

3.3 Capillary water absorption

Water absorption through capillary action was used as an indicator to evaluate effect of silicate waste on mortar durability. The test was performed on mortars cured for 28 days and the results are presented in **Table 4**. It is observed that increasing silicate percentage resulted to reduced water absorption. This could be expected as the increased percentage of finer material leads to stiffer mixes and less porous matrices, due to the filler effect (6). Specifically, addition of fine inert material such as silica powder plays a significant role in refining cementitious matrix porosity and can be used for the production of high-performance mixes (9).

The capillary water absorption results can be associated with the observed reduction of flow and attributed to the particle size of the mineral addition. Specifically, increasing silicate percentages lead to lower flow values. Nonetheless, given that the mix design was performed to ensure a fairly workable mortar, this slight reduction in workability could have led to better compaction and reduced amount of entrapped air in the mix. This alongside with the filler action of the silicate waste are the main reasons the mixes are exhibiting reduction of water absorption by capillary action.

Table 4: Sorptivity coefficient of mortars with silicate replacement

Mix label	Sorptivity Coefficient ($mm/min^{1/2}$)	Reduction percentage
REF	0.8754	0%
Sil10	0.8700	1%
Sil20	0.8506	3%

3.3 Strength of mortars

In order to ensure resilient infrastructure, both durability and strength requirements need to be satisfied. To perform a full preliminary evaluation of silicate mining waste as a it is essential to examine the effect on strength development. The results of 28-day compressive and flexural

strength tests are presented in Figure 2 and Figure 3 respectively. In Figure 2 the strength of equivalent mortars with silica fume is plotted to perform the comparison between the different effects of the two fillers.

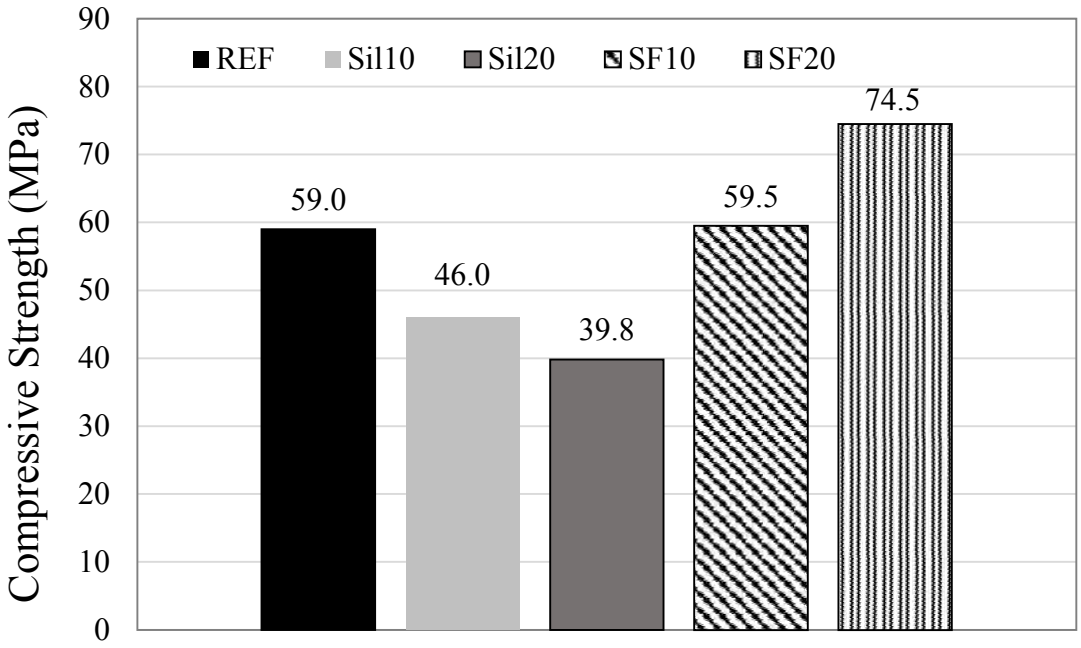

Figure 2: Compressive strength of mortar with silicate waste at 28 days compared to mortars with silica fume

Increasing percentage of cement replacement by silicate is leading to a decreasing trend of compressive strength. Specifically, the Sil10 mortar with 10% silicate waste presents a reduction of about 22% on 28-day strength. The corresponding strength reduction percentage for 20% silicate in the mortar is 32%. In the study of Pyo *et al*. (3), silica powder is replaced by siliceous crystalline mining waste at 50% and 100%, and it was similarly found to reduce workability and strength while no contribution in the hydration products was identified. The reduction of workability was attributed to the particles shape, which was plate-like and the reduction in strength was associated with inert nature of the mining waste. It appears that the silicate waste used here has a similar action, as no contribution on strength development is identified.

Table 5: Strength Activity Index (SAI) for Silicate waste and Silica fume mortars at 28 days

Mix Label	Sil20	SF20
SAI	0.67	1.26

This is further corroborated by examining the quite distinct effect of silica fume addition in the mortars, as increasing percentages lead to increasing strength values. Specifically, the SF10 with 10% silica fume demonstrates a slightly higher value than the REF. The mortar with 20% replacement presents 26% percent increase. Apart from filler effect, silica fume contributes

chemical to the mix resulting to a significant increase of strength due to its strong pozzolanic action. To access pozzolanic reactivity of the silicate waste, the Strength Activity Index of the mortars was calculated and compared to the values for silica fume replacement, as shown in ***Table 5***. The SAI is calculated by diving the unconstrained compressive strength of a pozzolan-containing mortar by that of the control. According to ASTM C618, a SAI greater than 0.75 after 7 and 28 days for FA and natural pozzolans at a cement replacement of 20% is required to indicate positive pozzolanic activity (10). The values for silica fume demonstrate a clear addition to the strength of the mortars. On the contrary the value for 20% replacement of silicate waste is below the threshold. The SAI indicator further supports the hypothesis of the chemical contribution from silicate waste in the mix is not sufficient to enhance strength. Similar observations were made by Donatello *et al*. when the SAI was calculated for mortars with 20% silica sand replacement (10). Nonetheless, the SAI of the silicate waste mortars is not dramatically lower than the threshold values. This could indicate that pozzolanic reactivity of the material could be enhanced by processing such as ball milling for reducing the particle size.

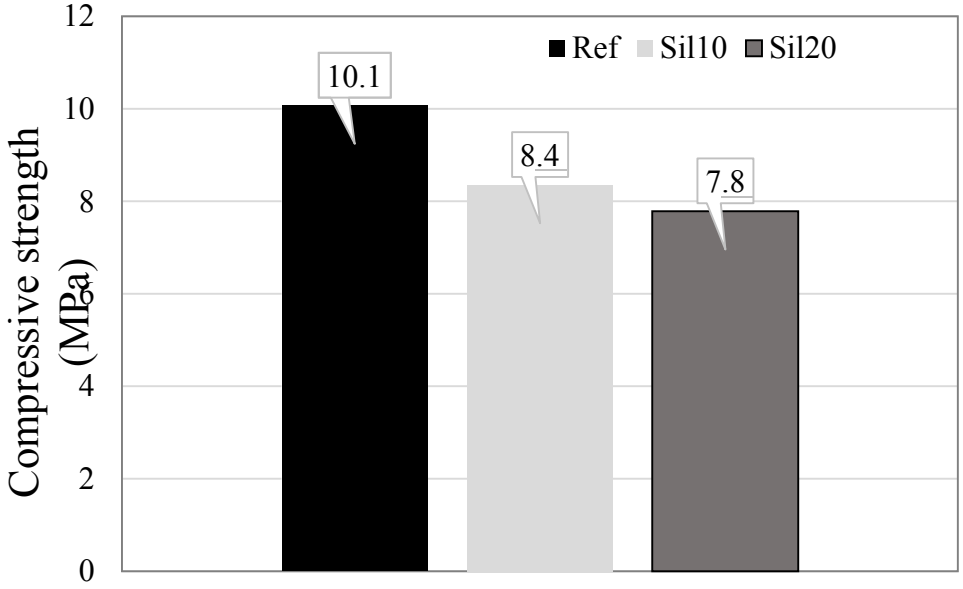

Figure 3: Flexural strength of mortar with silicate waste at 28 days

Regarding the flexural strength, a similar but milder reduction trend is observed. The addition of 10% and 20 % of silicate waste lead to 17% and 23% lower strength values for the 28-day mortars. The reduction in flexural strength could be associated with the increase in the mortars' stiffness and also the overall weaker matrix due to low reactivity of the silicate.

4. CONCLUSIONS

Examination of the silicate mining waste showed that it consists of mainly crystalline silica, with graphite residue and a carbon containing crystalline phase. The high crystallinity of the silicate waste and particle size were associated with low pozzolanic reactivity when added as a cement replacement in mortars. This was confirmed by reduction in compressive and flexural 28-day strength with increasing silicate waste percentages in the mortars. This was further highlighted by comparing the silicate waste effect to that of silica fume, a fine siliceous but mainly amorphous mineral addition.

As expected, the addition of a finer powder reduced the workability of the mortars.

Nonetheless, addition of silicate waste resulted to 1% and 3% reduction of the mortars capillary water absorption. The reduction as associated with the smaller particle size of the silicate waste which resulted to finer pores of the matrix potentially being filled up and the overall filler effect observed.

The results overall demonstrate that addition of the silicate mining waste presents a potential to improve durability of cement mortars through porosity refinement. The impact of the replacement on strength can be addressed by mild processing such as milling to a greater fineness. This would not only enhance the pozzolanic activity of the waste but could lead to further porosity refinement. Further work will be performed on low energy processing of the silicate waste to improve reactivity and optimising the mix design for achieving sufficient strength values while maintaining adequate workability.

REFERENCES

[1] Dobbs R, Pohl H, Lin D-Y, Mischke J, Garemo N, Hexter J, et al. Infrastructure productivity: how to save $1 trillion a year. McKinsey Glob Inst. 2013;88.

[2] Gartner E. Are there any practical alternatives to the manufacture of Portland cement clinker? Struct Concr (excluding steel). 2009;2(1.11):16.

[3] Pyo S, Tafesse M, Kim B-J, Kim H-K. Effects of quartz-based mine tailings on characteristics and leaching behavior of ultra-high performance concrete. Constr Build Mater [Internet]. 2018;166:110–7. Available from: http://www.sciencedirect.com/science/article/pii/S0950061818300953

[4] EN BS. 1015-3: 1999, Methods of Test for Mortar for Masonry—Part 3: Determination of Consistence of Fresh Mortar (by Flow Table). Br Stand Inst London, UK. 1999;

[5] EN BS. 1015-11: Methods of test for mortar for masonry–Part 11: Determination of flexural and compressive strength of hardened mortar. Eur Comm Stand Brussels. 1999;

[6] Scrivener K, Snellings R, Lothenbach B. A Practical Guide to Microstructural Analysis of Cementitious Materials [Internet]. CRC Press Inc; 2016. Available from: https://www.dawsonera.com:443/abstract/9781498738675

[7] Shen W, Cao L, Li Q, Zhang W, Wang G, Li C. Quantifying CO<inf>2</inf> emissions from China's cement industry. Renew Sustain Energy Rev [Internet]. 2015;50:1004–12. Available from:http://www.scopus.com/inward/record.url?eid=2-s2.084930626522&partnerID=40&md5=68ae2ed9dfe7359e55b91444ed392fa2

[8] Massazza F. 10 - Pozzolana and Pozzolanic Cements. In: Hewlett PCBT-LC of C and C (Fourth E, editor. Oxford: Butterworth-Heinemann; 1998. p. 471–635. Available from: http://www.sciencedirect.com/science/article/pii/B9780750662567500229

[9] Alkaysi M, El-Tawil S, Liu Z, Hansen W. Effects of silica powder and cement type on durability of ultra high performance concrete (UHPC). Cem Concr Compos. 2016;

[10] Donatello S, Tyrer M, Cheeseman CR. Comparison of test methods to assess pozzolanic activity. Cem Concr Compos [Internet]. 2010;32(2):121–7. Available from: http://www.sciencedirect.com/science/article/pii/S0958946509001644

UNIDIRECTIONAL SULFATE INGRESS IN LIMESTONE CALCINED CLAY CEMENT (LC^3) PASTES UNDER CYCLIC EXPOSURE

Qiao Wang* (1), William Wilson (1) and Karen Scrivener (1)

(1) École Polytechnique Fédérale de Lausanne, Switzerland

Abstract

If sulfate attack on Portland cement systems has been largely investigated in the last decades, mechanisms of sulfate resistance for systems with new SCMs are still in dim, especially for the emerging materials that are limestone calcined clay cements (LC^3). Using a new semi-immersion approach, we forced the penetration of sulfate ions in just one direction into LC^3 pastes under the capillary rise effect. To enhance the degradation process, highly concentrated sodium sulfate solution of 50 g/L and a cyclic exposure regime (20˚C & 78% RH followed by 40˚C & 33% RH) were employed in this paper. During exposure, lateral expansion was measured over time, showing almost negligible expansion for the LC^3 cement paste even after 56 days of very harsh exposure conditions. Simultaneously, microanalytical studies on the composition of hydration products were carried out by SEM-mapping to explain the expansion mechanisms. The results showed that the novel approach was adequate for cyclic exposure experiments, to investigate the full depth of degradation along the penetrating direction. Based on the analysis of BSE micrographs, phase distribution maps and expansion profiles, the gypsum and the ettringite were found to coexist in the voids resulting in a densified layer which could be associated with the most expansive zone. Overall, this study highlights the potential of the unidirectional semi-immersed method to link the sulfate attack expansion of cement pastes with the underlying mechanisms.

Keywords: LC^3; Sulfate attack; Unidirectional penetration; SEM; Degradation

1 INTRODUCTION

If concrete is considered as a durable construction material in most cases, durability problems may occur when concrete is exposed to deleterious ions, such as chloride and sulfate ions. Sulfate ions often invade inside to react with microstructure phases resulting in structure degradation, including expansion, cracking, spalling and eventually disintegration of concrete material. Even if many studies are available on the subject in literature, there are still open questions regarding this degradation process, such as the misleading nomenclature dividing sulfate attack into “chemical sulfate attack” and “physical sulfate attack”, the mechanisms of this “physical sulfate attack” being not well understood so far. As an example, previous studies

indicated that the gypsum can only precipitate in the already existed cracks which was the result of expansion but not the cause of it [1–3].

The most common conventional method to test the sulfate attack resistance is longitudinal expansion measurement of mortar bars in ponding test, but this approach only considers chemical sulfate attack. Another approach focussing on physical sulfate attack is the semi-immersion test in which a very complicated capillary flow which makes microstructure characterization not practical. Although those approaches were used in several studies (e.g., [4–6]), no obvious relationship was established between expansion and the amount of ettringite formed, which is perhaps due to the sulfate ions ingression in radial and longitudinal directions (eventually not only causing expansion in longitudinal direction). Therefore, the unidirectional test is presumably the most practical and effective approach to know the details along each parallel depth from the solution exposing surface[7,8].

In this paper, the main idea is to use the new established setup with LC³ cement paste exposed to a cyclic exposure regime. By this unidirectional approach, sulfate ions can only invade from bottom to top part under the capillary suction, enabling precise characterization of the structural alteration at different levels. The most competitive point of this investigation approach is that the same sample can be fully characterized over the full depth, i.e., expansion, phase distribution and pore structures. As demonstrated below, the results mainly show that coexistence of ettringite and gypsum in a densified layer in the microstructure causes expansion, in a layered degradation process.

2 MATERIALS AND EXPERIMENTAL APPROACHES

2.1 Materials

- *LC³-50 Cement*

The LC³-50 cement employed in this study was composed of 53 % Portland cement, 30 % calcined clay, 15 % limestone and 2 % gypsum. The chemical composition of Portland cement is displayed in
Table ***1***. A water to binder ratio of 0.6 was used to prepare cement pastes.

Table 1: Chemical composition of PC

Chemical composition (wt%)	SiO_2	Al_2O_3	Fe_2O_3	CaO	MgO	SO_3	Na_2O	K_2O	TiO_2	P_2O_5	LOI
Portland cement	20.4	5.1	1.9	64.2	1.0	2.9	0.4	0.7	0.2	0.2	1.67

- Sodium sulfate

Chemically analytical pure salt contains more than 99 % Na_2SO_4 solid was used as the external sulfate source. A solution of 50 g/L Na_2SO_4 was prepared for exposure of the specimen.

- Sample preparation

Cement pastes were mixed with water using metallic sector shape stirrer for 120 s with a speed of 1600 rpm. Then, they were casted in plastic cylinder containers with diameter of 33 mm, length of 60 mm. After one day, they were demoulded and cured in a slightly bigger container with only small amount of water to avoid leaching. The sample was cut into slices with thickness of 5 mm (both external surfaces with around 3 mm of the sample were removed). The

slices were then ready for installation in the semi-immersion setup, as illustrated in Fig. 1. The setup was place in a 40 ˚C room with relative humidity 33 % and, after one week, the setup was transferred into a 20 ˚C room with relative humidity 78 %. This 2-week cycle was repeated until the age of testing.

(a) (b)

Figure 1: The setup for unidirectional sulfate penetration test

2.2 SEM analyses

The paste samples were examined by scanning electron microscopy (SEM, FEI ESEM XL 30) using backscattered electrons and later on hyper mapping to get the elemental information of each pixel of maps. The elemental information from energy diffraction spectroscopy (EDS) is the foundation of this analysis. The Esprit 1.9 software was used to quantify the mapping data with the Hyper Map Mode after calibration with standards. After the calculation, the matrix of the points on the map of each element can be obtained, as well as the colorful maps of elemental distribution.

The magnification of elemental mappings was ×300, resolution was 1000×750 pixels, corresponding scanning area was about 860×645 μm, high voltage was 15.0 kV, and working distance was 12.5 mm. The images were then quantitatively analyzed using the EDXIA approach developed by F. Georget[9].

2.3 Expansion measurements

The lateral expansion was measured parallel to the degradation front (parallel to the exposed surface). The measurement was carried out as shown in Fig. 2, using 1-mm thick steel rings and a digital slide calliper.

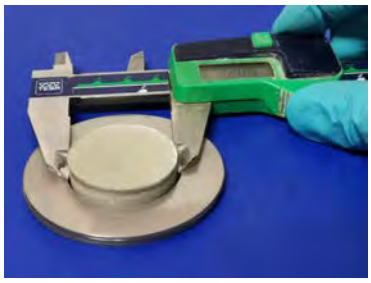

Figure 2: Lateral expansion measurement

3 RESULTS AND DISCUSSION

3.1 Visual inspection

Fig. 3 shows the LC³ cement samples appearance after exposure to sulfate solution. At 28d, samples were intact without any visual damage. At 56d, it was more degraded because the samples were fully penetrated by sulfate ions from bottom to top portion under the flow of capillary rise. The white deposits on the top surface indicates penetration over the full depth of the sample. Because the bottom was directly exposed to the solution, small cracks appeared with longer time of exposure and degradation.

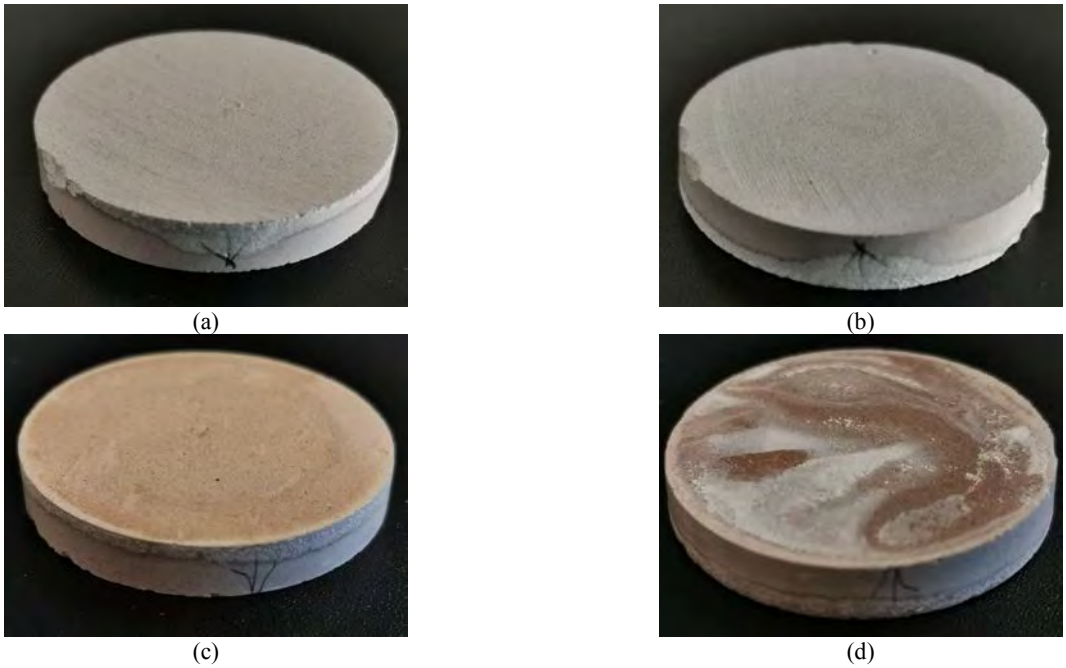

Figure 3: Visual observations of LC³ samples showing (a) bottom surface of 28d sample, (b) top surface of 28d sample, (c) bottom surface of 56d sample, (d) top surface of 56d sample

3.1.1 Expansion vs. depth

The evolution of expansion profiles along the sulfate ions penetrating direction was tracked with time, as shown in Fig. 4. Shrinkage occurred from the top of the LC³ sample with very good resistance to expansion. After 56d of exposure, a slight expansion was measured with a peak at around 0.5 mm. It is of interest to understand why a higher expansion occurred at this point. The comparison with a Portland cement system (PC) in less harsh exposure conditions (w/c=0.6, 30 g/L concentration, constant RH 55 %) shows how the expansion at 28d was much higher than LC³ samples at all ages. It is also interesting to note that the most expanded layers of PC were deeper than LC³ at the same age which illustrates how LC³ system can be more resistant to invading sulfate ions.

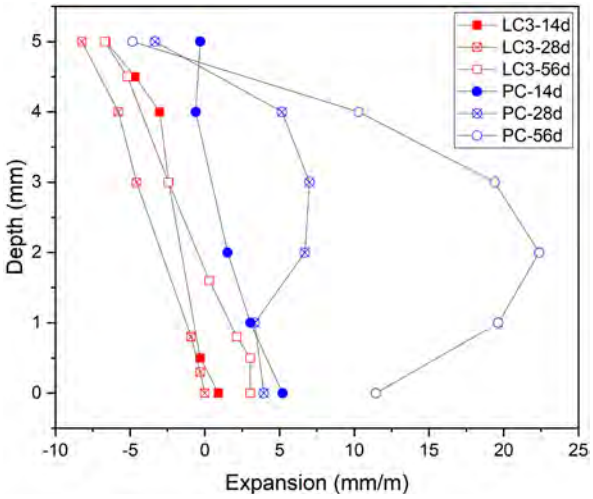

Figure 4: Expansion profile for LC³ cement paste at different ages, in comparison with a PC paste exposed to less harsh conditions [7]

3.1.2 Qualitative analysis of BSE images

When the significant changes according with the expansion are seen, it must be something happening in the microstructure. From a qualitative analysis of BSE images, the porosity variation over depth can be clearly seen in Fig. 5. At 28d of exposure, a bottom layer of approximately 0.5 mm was densified due to the new hydrates precipitating in the cement paste voids. With time, the densified front shifted deeper towards the top of the sample and a porous degraded layer remained below, as seen from the visual evidence at 56d. It is exactly the reason that the sulfate ions can still move inside easily in such a porous material. In later age sample, cracks were observed in most cases parallel to external surface, but it is not clear if cracking occurred from the degradation or during sample preparation, as the cracks were empty at 56d.

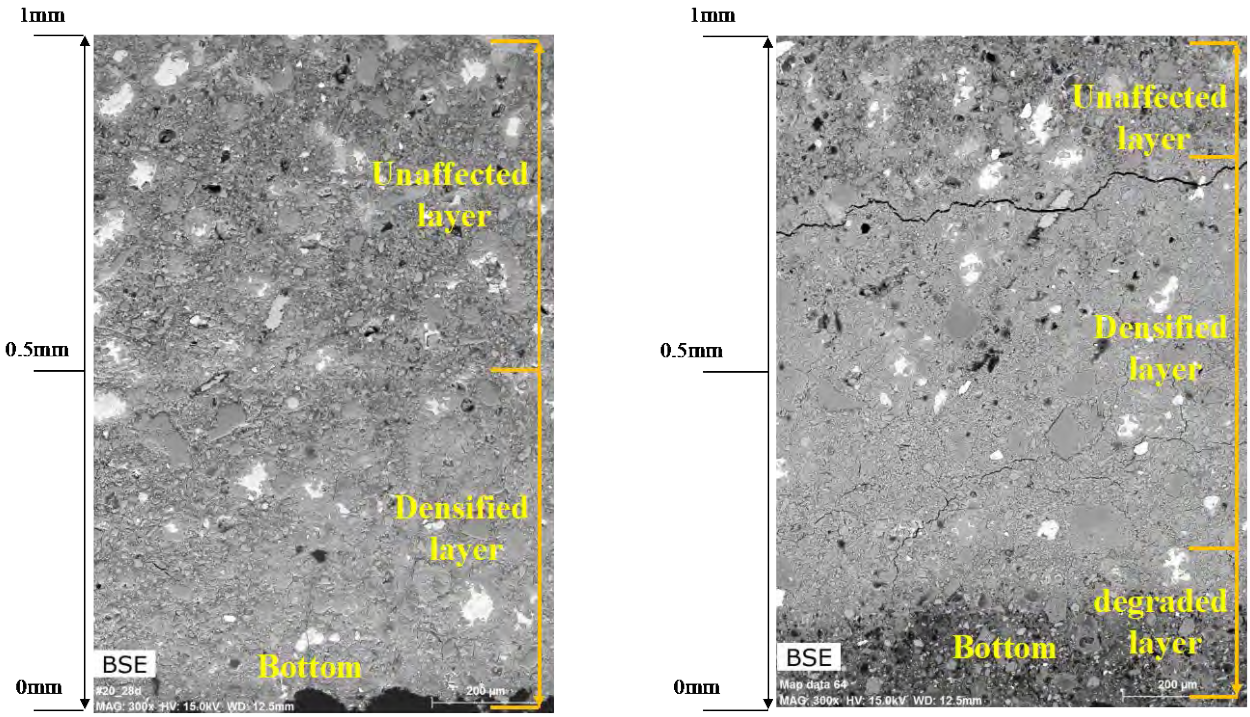

(a) (b)

Figure 5: Comparison of BSE imaging of the bottom of LC³ samples after exposures of (a) 28d and (b) 56d

From a large-scale picture in Fig. 6, the degraded LC³ cement sample consists of three obvious different zones. A fully degraded zone with many pores was noticed in subsurface. Second layer was densified and this region had the highest expansion propagation in contrast with expansion evolution curve. The third layer was the unaffected area and it was a normal porous cement paste matrix. It can be seen that the sulfate attack is a layered-damage process, and the main internal damaging stress was from the crystals growing in the small voids[10,11].

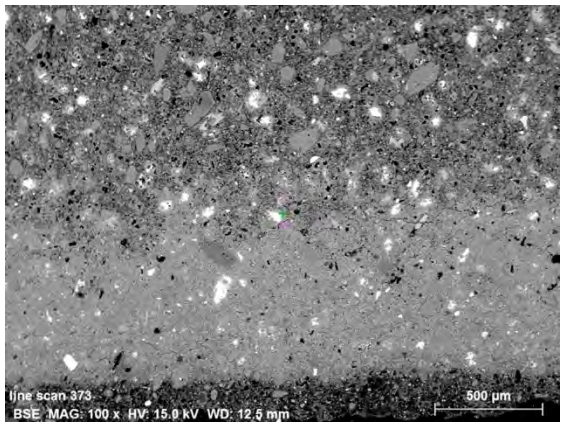

Figure 6: Low-magnification micrography of the bottom part after 56-day exposure

3.2 Quantitative results from SEM-EDS analysis

3.2.1 Phase maps

The phase maps were obtained from the SEM-EDS mappings analysed using the EDXIA framework[9]. Fig. 7 presents phase maps overlaid on BSE micrographs, showing that the gypsum and ettringite hydrates were mainly precipitated in the densified areas. This result further supports that these two phases could cause expansion especially when they coexist[6]. AFm and portlandite phases are the main phases consumed for the formation of ettringite and gypsum, which can be observed from the 56d map. Furthermore, the first 200 micrometres were totally degraded with high porosity at 56d. Above the densified layer, more portlandite and AFm phases were present. However, it was quite difficult to detect the ettringite phase since they were precipitated in very small pores mixed with C-S-H phase, at a scale smaller than the interaction volumes investigated by SEM-EDS.

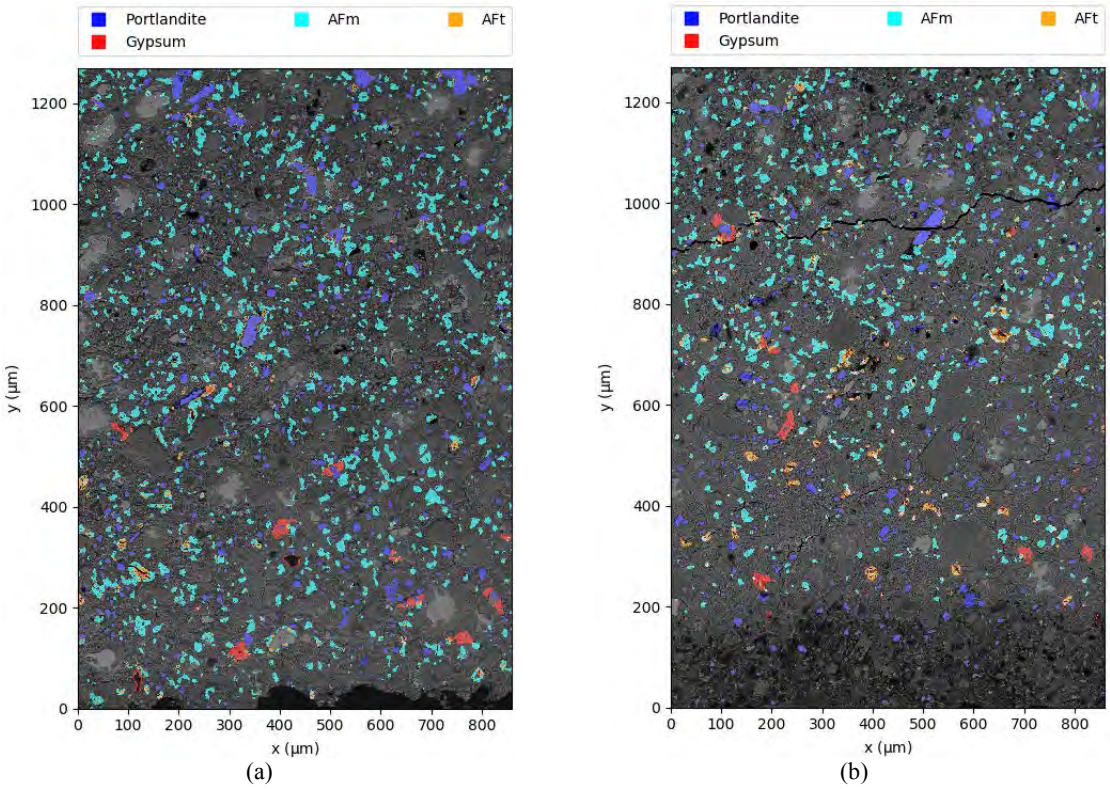

Figure 7: Phase composition maps of LC^3 cement at 28d & 56d. (a) 28d; (b) 56d

3.2.2 Phase profile

The profiles along the depth are displayed for the phases of interest in Fig. 8. It can be visually seen that the gypsum-rich front position can be well correlated with the expansion profile. According to Fig. 8, AFm and Portlandite can be tracked to verify which area is still

intact (the amount of these phases is likely to be higher compared with degraded zones). Therefore, the front of AFm and Portlandite can be used for the estimation of depth of degradation. But there is still one thing missing, ettringite.

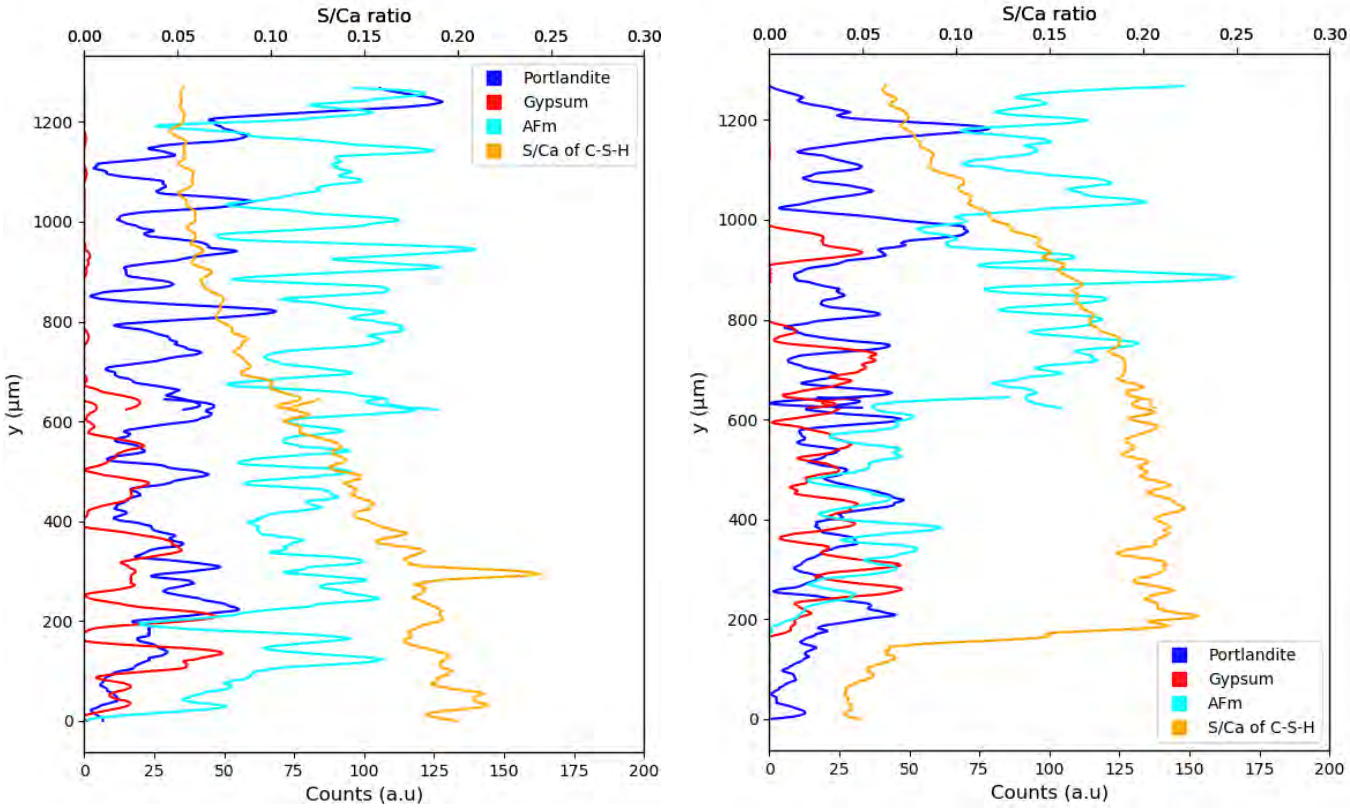

Figure 8: Phase and S/Ca profiles of LC³ pastes exposed to sulfate solution for (a) 28d and (b) 56d.

However, sub-micron sized ettringite presence can be indirectly determined with the profile of atomic ratios of the C-S-H phase. The profile of S/Ca ratio was plotted in Fig. 8 and it proved to enable the identification of ettringite-rich zones of C-S-H. For example, at 56d, the hump from 200 to 800 µm with higher S/Ca value (S/Ca=0.5 for ettringite) than the rest which implies that ettringite was probably intermixed with C-S-H phase. Ettringite precipitated in the shallow depth at 28d and it moved deeper at 56d. The comparison with phase maps, BSE micrographs and expansion measurements showed that a densified layer with coexisting ettringite and gypsum is present, although it does not lead to significant expansion during the length of the test.

4 CONCLUSIONS

This study showed the potential of using a unidirectional semi-immersion approach to simultaneously investigate the expansion and the microstructure degradation due to the chemical sulfate attack in a LC³-50 system. The main findings are the following:

- The novel unidirectional semi-immersion approach was adapted to harsh cycling exposure conditions and provided insights on sulfate attack mechanisms in LC^3 systems;
- LC^3 cement paste showed a good resistance to sulfate attack even in an aggressive environment (cyclic exposure & high solution concentration), showing slow ingress of sulfate ions and slight expansion;
- The results showed that the sulfate attack is a layered-damage process: a densified layer with coexisting ettringite and gypsum penetrates progressively trough the cement paste, potentially leading to expansion.

Overall, this short study showed the microstructure damage near the surface exposed to the sulfate solution, but further work will focus on investigating the salt crystallization mechanisms which are likely taking place at near the surface of the sample exposed to air, due to the evaporation and the reprecipitation of sodium sulfate salts.

REFERENCES

[1] T. Schmidt, B. Lothenbach, M. Romer, J. Neuenschwander, K. Scrivener, Physical and microstructural aspects of sulfate attack on ordinary and limestone blended Portland cements, Cem. Concr. Res. 39 (2009) 1111–1121.

[2] R.S. Gollop, H.F.W. Taylor, Microstructural and microanalytical studies of sulfate attack. I. Ordinary portland cement paste, Cem. Concr. Res. 22 (1992) 1027–1038.

[3] C. Yu, W. Sun, K. Scrivener, Mechanism of expansion of mortars immersed in sodium sulfate solutions, Cem. Concr. Res. 43 (2013) 105–111.

[4] A.R.S. M.L. Nehdi, A.M. Soliman, Investigation of concrete exposed to dual sulfate attack, Cem. Concr. Res. 64 (2014) 42–53.

[5] Z. Shi, S. Ferreiro, B. Lothenbach, M.R. Geiker, W. Kunther, J. Kaufmann, D. Herfort, J. Skibsted, Sulfate resistance of calcined clay – Limestone – Portland cements, Cem. Concr. Res.116 (2019) 238–251.

[6] W. Kunther, Investigation of Sulfate Attack by Experimental and Thermodynamic Means, PhD Thesis, EPFL, 2012.

[7] Qiao Wang, William Wilson, Karen Scrivener, Unidirectional penetration approach for characterizing dual sulfate attack mechanisms on cementitious materials, (In preparation).

[8] W. Qiao, W. William, S. Karen, Investigating dual sulfate attack mechanisms using unidirectional penetration approach, in: Toulouse, France, 2020.

[9] F. Georget, W. Wilson, K. Scrivener, Comprehensive microstructure phase characterization from quantified SEM-EDS maps in cementitious materials (In preparation)

[10] S. Siegesmund, R. Snethlage, eds., Stone in Architecture: Properties, Durability, 5th ed., Springer-Verlag, Berlin Heidelberg, 2014.

[11] E.M. Winkler, P.C. Singer, Crystallization Pressure of Salts in Stone and Concrete, GSA Bull. 83 (1972) 3509–3514.

EFFECT OF FINE AGGREGATE ON RHEOLOGICAL PROPERTIES OF ULTRA-HIGH PERFORMANCE CONCRETE（UHPC）

Siyi Ju (1), Taotao Feng (1), Liguo Wang (1) and Jinyang Jiang(1)

(1) Jiangsu Key Laboratory of Construction Materials, School of Materials Science and Engineering, Southeast University, China

Abstract

In this paper, four kinds of ecological fine aggregates (manufactured sand, recycled sand, aeolian sand and river sand) were used to prepared UHPC, the effects of the fine aggregates on the workability, rheological properties and mechanical properties of UHPC were studied. The results reveal that the type and content of fine aggregate have an effect on the rheological properties and mechanical strength of UHPC. Under the same mix proportion, the yield stress and plastic viscosity of recycled sand UHPC are higher than those of river sand UHPC, manufactured sand UHPC and aeolian sand UHPC, mainly due to its high water absorption. The high intergranular porosity, high surface area and low fineness modulus of aeolian sand contributes to an increase in yield stress, and high rate into thin and irregular shapes of manufactured sand are the major ingredients which affect the workability of UHPC. The yield stress and plastic viscosity of UHPC decrease with the increase of water-binder ratio, and the gap between the four fine aggregate systems is gradually narrowed. The effects of different fine aggregates on the mechanical properties of UHPC are arranged according to the improvement effect: recycled sand > manufactured sand > river sand > aeolian sand.

Keywords: Ultra-high performance concrete, workability, fine aggregate, yield stress, plastic viscosity

1. INTRODUCTION

Due to its excellent mechanical properties (i.e., compressive strength of 120-150MPa, flexural strength of 30-60MPa) [1,2] and durability [3,4], UHPC has attracted a lot of attention during the past decades. High-quality cement, mineral admixtures, well-graded fine aggregates, superplasticizers and steel (or organic) fibers at very low water-to-binder (w/b) ratios are often used to produce UHPC, aiming at improve its homogeneity and packing density [5,6,7]. Low w/b ratios are the key to obtain excellent performance of UHPC, while less water consumption often tends to poor workability. The contradiction between low water consumption and workability has become a major issue in the current mix design of UHPC.

As an important raw material for concrete, river sand resources in some areas have been in a tight supply situation. Confronted with the situation of serious environmental pollution and

increasingly scarce resources, reducing material costs and improving the sustainability of UHPC has become a research hotspot. Therefore, it is imperative to find some suitable substitutes to natural river sands for the construction industry. Several potential substitutes for natural river sands include manufactured sand, recycled sand and aeolian sand [8,9,10,11]. However, there are great differences in particle size, morphology, density and gradation between manufactured sand, recycled sand, aeolian sand and natural river sand, which will make a noticeable impact in the properties of UHPC, under the limitation of low w/b ratio.

At present, research on UHPC at home and abroad mainly focuses on mechanical properties and durability, but little attention has been paid to its fresh properties. The rheological properties of concrete are considered to be the most ideal methods to characterize the workability so far, which can quantitatively reflect the complex work performance of concrete [12]. This paper presents an investigation on the effect of the type and content of fine aggregates on the rheological properties of UHPC.

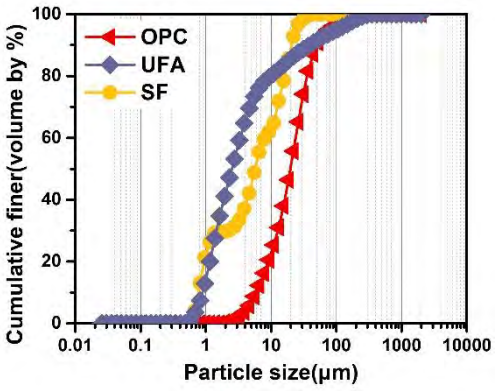

Figure 1: Particle size distributions of cementitious binders.

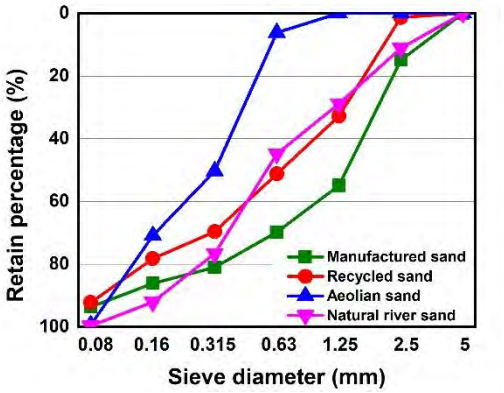

Figure 2: Particle size distributions of fine aggregates.

2. TEST PROGRAM

2.1 Material

The cementitious materials used in this work are Portland cement (P·II 52.5), ultra-fine fly ash (UFA) and silica fume (SF). Fig. 1 presents the particle size distribution of the cementitious materials. The river sand used in this work was provided by a local company, the manufactured sand was crushed by basalt, the recycled sand was generated from low and medium-strength waste concrete and the aeolian sand originated in the Gurbantunggut Desert in Xinjiang, China, some physical properties of them are listed in Table 1. The particle size distributions of fine aggregates are shown in Fig. 2, and Fig. 3 presents the scanning electron microscopy (SEM) images of them. A polycarboxylate-based high-range water-reducing admixture (HRWRA) with 40% solid content by weight was used to obtain satisfactory flowability.

2.2 Mix design

The mix proportion of UHPC mixture is shown in Table 2. When using different kinds of fine aggregate to prepare UHPC, the same mix proportion is used, and the change of water to binder ratio is 0.14, 0.16, 0.18 and 0.20; the change of sand to binder ratio is 0.6, 0.7, 0.8, 0.9, 1.0 and 1.1.

2.3 Specimens preparation

A planetary type mortar mixer was used to prepare UHPC mortars in this study. All mixtures were mixed using the following procedures: first, mix the binders, stir slowly for 60s; second, add the fine aggregate, stir slowly for 60s; third, mix water and water reducer evenly in advance and add the mixed solution in the mixer, stir slowly for 120s and then stir quickly for 120s.

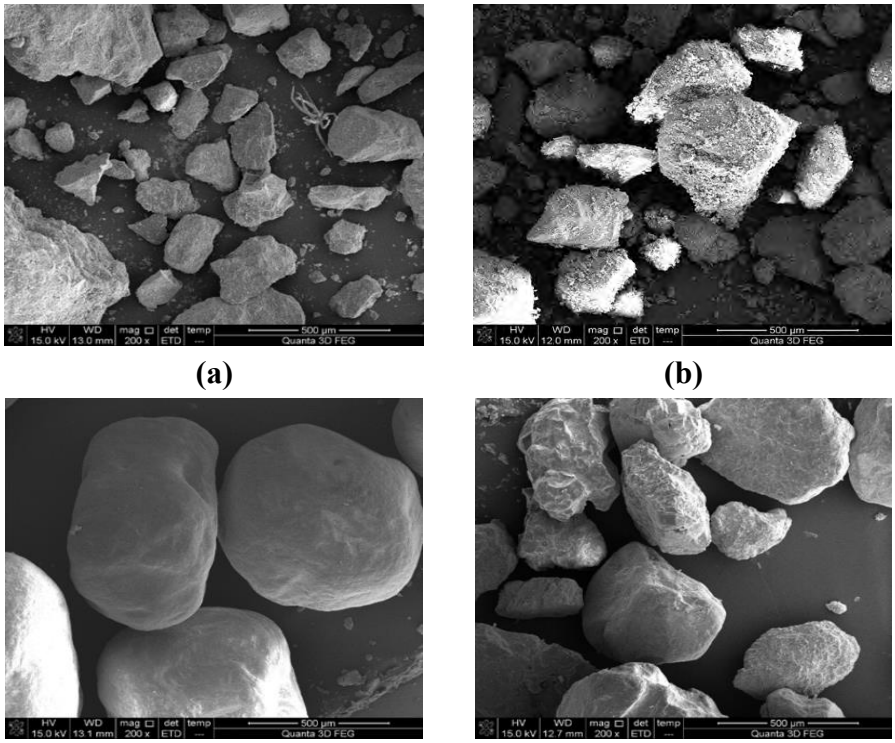

(a) **(b)**

(c) **(d)**

Figure 3: SEM images, (a) manufactured sand; (b) recycled sand; (c) aeolian sand; (d) natural river sand.

3 TEST METHODS

3.1 Flowability

The flowability of the UHPCs were measured refer to the Chinese standard GB/T 175–2005 [13].

3.2 Rheology tests

The rheological properties were tested using a rotational viscometer and the yield stress and plastic viscosity were obtained by applying the rheological model to the registered data at the down curve. The whole test procedure consists of three parts: the pre-shearing, the setting and the data acquisition, as shown in Fig. 4. After initial standing for 30s, the shear rate was increased to $25s^{-1}$ and maintaining the rate within 30-90s. Then the shear rate was rapidly decreased from $25s^{-1}$ to zero and remained up to 150s. Finally, the shear rate was increased again from zero to $25s^{-1}$ within 150-210s and then was decreased to zero within 210-270s. A total of 60 data points during 210-270s were measured to obtain the shear stress-shear rate curve.

Table 1: Physical properties of fine aggregates

Fine aggregate	Fineness modulus	Water adsorption (%)
Manufactured sand	3.1	0.8
Recycled sand	2.4	5.7
Aeolian sand	1.3	1.4
Natural river sand	2.5	1.0

Table 2: Mix proportion of UHPC

OPC	UFA	SF	Sand	Water	Water reducer
0.6	0.3	0.1	1.1	0.18	1.8%

3.3 Angularity tests

The angularity tests of fine aggregates were measured in accordance with the Chinese standard JTG E42-2005 [14].

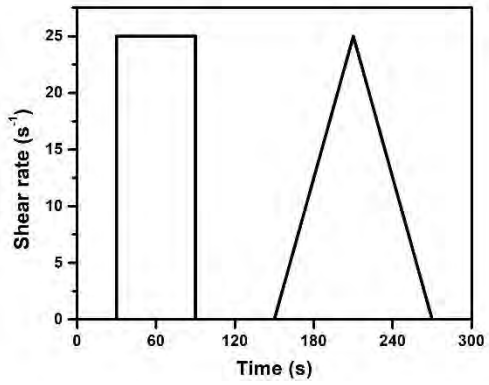

Figure 4: Test program used in rheology test

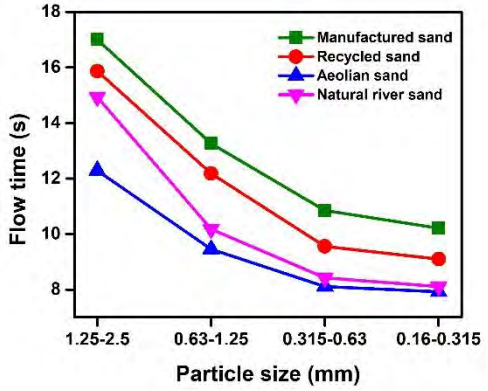

Figure 5: Results of the angular test.

4 TEST AND DISCUSSIONS

4.1 Angularity

Fig. 5 shows the results of flow time of fine aggregates in different particle size intervals. The order of flow time of four kinds of fine aggregates is: manufactured sand > recycled sand > natural river sand > aeolian sand. Longer flow time indicates stronger surface angularity and larger interparticle friction of the fine aggregates. When the particle size is less than 1.25mm, the flow time of river sand and aeolian sand is relatively close. It can be seen from Fig. 3 that the manufactured sand has irregular shape with some micro powder attached to the surface, showing the strongest angularity; the surface of recycled sand is rough with more loose floccules; the aeolian sand is smooth without angularities; the natural river sand has some edges and corners with unsmooth surface. The flow time of fine aggregates is shortened with the decrease of the particle size, and the angularity is obviously reduced, which may be caused by the change of contact area between particles. As the particle size decreases, the interparticle friction area decreases, so the bite force is reduced, leading to lower drop resistance.

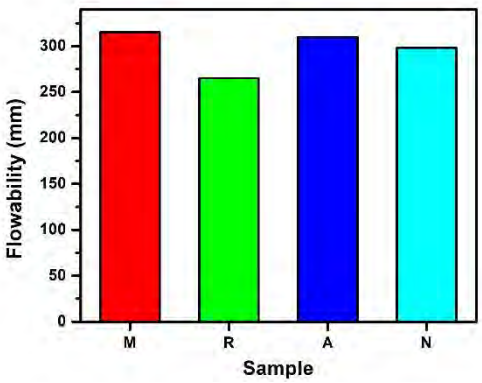

Figure 6: Flowability of UHPC mortars.

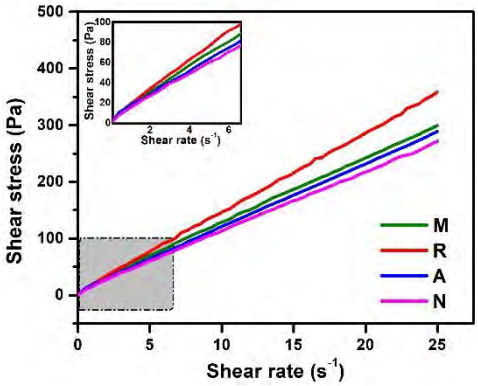

Figure7: Results of the rheology test.

4.2 Flowability

The flowability test results are shown in Fig. 6. Compared with natural river sand, the flowability of aeolian sand and manufactured sand increased, while that of recycled sand decreased. The smooth surface and round shape of aeolian sand make the mortar more uniform and has better flowability; the stone powder attached to the surface of manufactured sand can slightly improve the flowability. For recycled sand, due to the presence of porous and flaky particles, the recycled sand has increased water absorption, causing a significant decrease in the flowability of the mortar, which is mainly related to its source and preparation process [15].

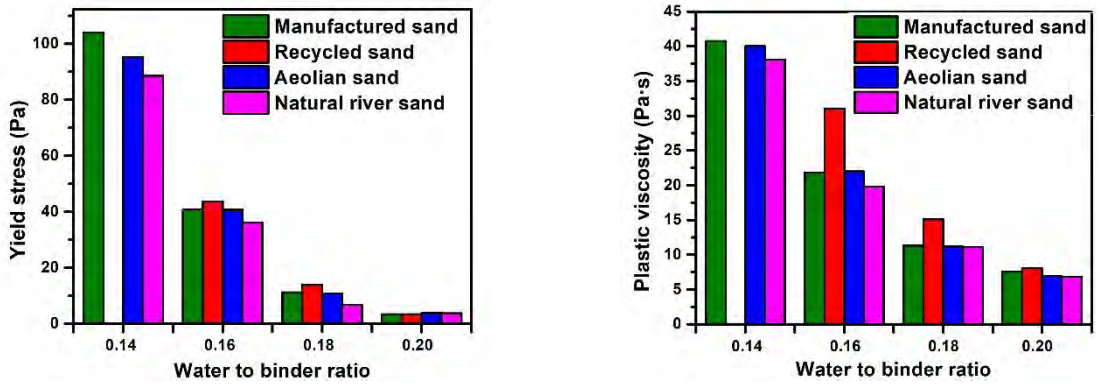

(a) **(b)**

Figure 8: Rheological parameters under different w/b ratios, (a) yield stress, (b) viscosity.

4.3 Rheological properties

Fig. 7 shows the rheological test results of the mixtures with different fine aggregates. The types of fine aggregates have no effect on the fluid type of the mixtures, and all the rheological curves showed higher linearity. By applying the Bingham model (Eq. (1)) to the registered data, the rheological parameters yield stress (τ_0) and plastic viscosity (γ) are obtained, as shown in Fig. 8. The yield stress describes the required shear stress to initiate flow of the mortars, while the plastic viscosity describes how easily the mortar flows. It can be seen from Fig. 8 that in the process of increase the w/b ratio from 0.14 to 0.20, the yield stress and plastic viscosity first decrease substantially, and then decrease by a small margin when the w/b ratio exceeds 0.18. There are two reasons for the above phenomenon: in the case of very low w/b ratio, the available

water in the system is extremely small. On the one hand, the surplus water used to wrap particles to form lubricating layer decreases sharply, and the friction between particles increases, which leads to the increase of the flow resistance. On the other hand, the particles inside the paste are easily agglomerated and overlapped to form a network structure under the action of electrostatic attraction and van der Waals force, which is insufficient to disperse with little water. However, when the lubricating layer between particles reaches a certain thickness, the further increase of w/b ratio will not cause a significant reduction of yield stress and plastic viscosity.

$$\tau=\tau_0+\mu\gamma \quad (1)$$

Under the same mix proportion, the yield stress and plastic viscosity of recycled sand mortars always maintain high, while that of manufactured sand and aeolian sand mortars are slightly higher than river sand mortars. The presence of old mortar makes the recycled sand show strong water absorption and high interparticle bite force. It is prone for manufactured sand to produce multi angular particles due to the uneven stress during crushing, so that the particles overlap each other easily, bring about large resistance to flow. Nevertheless, the main influence on the rheological properties of the mixture is the paste thickness on coated aggregates [16]. The aeolian sands are characterized by a high intergranular porosity and low fineness modulus, which affect the aggregates packing and needs more water to fill the voids, resulting in higher yield stress and plastic viscosity. The difference between the rheological properties of aeolian sand and river sand decreases with the increase of water content in the mortar.

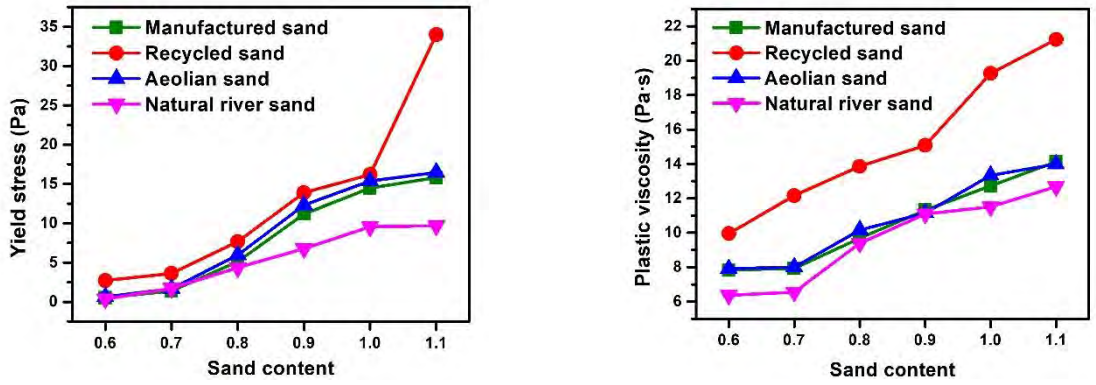

(a) **(b)**

Figure 9: Rheological parameters under different sand contents, (a) yield stress, (b) viscosity.

The effect of the content of fine aggregates on the rheological parameters of UHPC mortars are shown in Fig. 9. As the sand content increased, the yield stress and plastic viscosity of the mixtures all increased. Increasing amounts of fine aggregates increase the required amount of water to wet the particle surfaces adequately and to maintain a specified workability. When the sand content changes from 0.6 to 0.7, the yield stress of the four types of UHPC mortars differ little, which shows that the available water in the mixture slurry is enough to lubricate and wrap the particles. The rheological parameters of manufactured sand UHPC, recycled sand UHPC and aeolian sand UHPC increased significantly compared with river sand UHPC when the sand content increased even further. Meanwhile, the disadvantages of manufactured sand, recycled sand and aeolian sand in particle shape, morphology and grading continue to appear. The plastic viscosity may increase due to the increase of total surface area of fine aggregate.

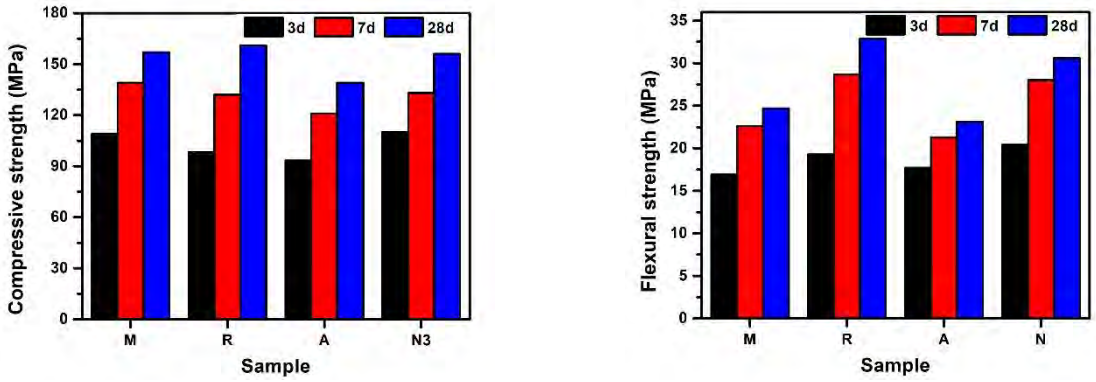

(a) **(b)**

Figure 10: Results of strength test, (a) compressive strength, (b) flexural strength.

4.4 Strength

The measured compressive strengths and flexural strengths of the UHPC mortars are given in Fig. 10. Compared to the UHPC system with natural river sand, the 28d compressive strength and flexural strength of aeolian sand UHPC decreased by 11.4% and 19.4% respectively, mainly due to the spherical shape of aeolian sand, leading to a smaller bite force between aggregates and paste and thus poor mechanical properties. The presence of the lamellar particles makes a larger bite force of manufactured sand so that the compressive strength increased, while its inferior bending resistance makes the flexural strength reduced. The compressive strength of recycled sand UHPC is relatively low in the early stage but relatively large in the later stage. In the early stage, the recycled sand absorbed part of the water, leading to less free water content, lower hydration and slower strength development. In the later stage, as the humidity inside the slurry decreased, the water released in the recycled sand promotes the rehydration of the system, which facilitates a substantial increase in strength. Another factor that may enhance the compressive strength is that the recycled sand inevitably contains partially unhydrated cement during the preparation process [17].

5 CONCLUSIONS

The following conclusions are drawn from the test results and discussion:

- The rheological properties and water demand of mortars are strongly dependent on the properties of fine aggregates. The manufactured sand gives less workability to the UHPC mortars, due to its irregular shape and high interparticle friction. The higher yield stress and plastic viscosity of mortars with recycled sand is believed to mainly originate from the rough surface and high water absorption. High surface area and low fineness modulus of aeolian sand contributes to an increase in yield stress and plastic viscosity.
- Increasing contents of fine aggregates increase the required amount of water to wet the particle surfaces adequately and to maintain a specified workability. The effects of poorly graded and shaped of fine aggregates can be eliminated or reduced by increasing the available water of the mortars.
- In addition to natural river sand, manufactured sand and recycled sand can be used in UHPC, while aeolian sand can reduce the mechanical properties but can basically meet the requirements of high-performance concrete.

ACKNOWLEDGEMENTS

The authors gratefully acknowledge the support from the National Key R&D Program of China（2018YFC0705400）and the National Natural Science Foundation of China (No. 51438003, 51578143).

REFERENCES

[1] Wang, D., Shi, C., Wu, Z., Xiao, J., Huang, Z., & Fang, Z. A review on ultra high performance concrete: part ii. hydration, microstructure and properties. *Constr. Build. Mater.* 96 (2015) 368–377.

[2] Habert, G., E. Denarié., A. Šajna., Rossi, P. Lowering the global warming impact of bridge rehabilitations by using ultra high performance fiber reinforced concretes. *Cem. Concr. Compos.* 38 (2013) 1-11.

[3] Shi, C., Wu, Z., Xiao, J., Wang, D., Huang, Z., Fang, Z. A review on ultra high performance concrete: part i. raw materials and mixture design. *Constr. Build. Mater.* 101 (2015) 741–751.

[4] Pyo, S., Abate, S. Y., Kim, H. K. Abrasion resistance of ultra high performance concrete incorporating coarser aggregate. *Constr. Build. Mater.* 165 (2018) 11–16.

[5] Habel, K., Viviani, M., Denarié, E. Development of the mechanical properties of an Ultra-High Performance Fiber Reinforced Concrete (UHPFRC). *Cem. Concr. Res.* 2006 (36) 1362–1370.

[6] Tayeh, B. A., Bakar, B. H. A., Johari, M. A. M., Voo, Y. L. Mechanical and permeability properties of the interface between normal concrete substrate and ultra high performance fiber concrete overlay. *Constr. Build. Mater.* 36 (2012) 538–548.

[7] Rong, Z., Sun, W., Zhang, Y. Dynamic compression behavior of ultra-high performance cement based composites. *Int. J. Impact. Eng.* 37 (2010) 515-520.

[8] Martins, P., Diane, G., Robert, L. An investigation into the use of manufactured sand as a 100% replacement for fine aggregate in concrete. *Mater.* 9 (2016) 440-448.

[9] Ozbakkaloglu, T., Gholampour, A., Xie, T. Mechanical and durability properties of recycled aggregate concrete: effect of recycled aggregate size and content on the behaviour. *J. Mater. Civ. Eng.* 30 (2017) 04017275.

[10] Zhang, G., Xia, J., Yang, W. The effect of desert sand on the performance of cement mortar and concrete. *J. Ningxia Univ.* 30 (2018) 040180294.

[11] Dong. W., Shen. X., Experimental Study on cement mortar fluidity and compressive strength by different Aeolian sand dosage. *Bull. Chin. Ceram. Soc.* 32 (9) (2013) 1900-1904.

[12] Ferraris, C. F., Obla, K. H., Hill, R. The influence of mineral admixtures on the rheology of cement paste and concrete. *Cem. Concr. Res.* 31(2) (2001) 245-255.

[13] Chinese Standard GB/T 50080, Standard for Test Method of Mechanical Properties on Ordinary Concrete, (2002).

[14] Chinese standard JTG E42, Standard for Test Methods of Aggregate for Highway Engineering, (2005).

[15] Ulsen, C., Kahn, H., Hawlitschek, G., Masini, E. A., Angulo, S. C., John, V. M. Production of recycled sand from construction and demolition waste. *Constr. Build. Mater.* 40 (7) (2013) 1168-1173.

[16] Jiao, D. Quantitative prediction of rheological and mechanical properties of conventional concrete. The 9th International Symposium on Cement and Concrete (ISCC 2017), Wuhan, China, Nov., 2017.

[17] Sagoe-Crentsil, K. K., Brown, T., Taylor, A. H. Performance of concrete made with commercially produced coarse recycled coarse aggregate. *Cem. Concr. Res.* 31(5) (2001) 707-712.

MULTI-LEVEL CHEMICAL CHARACTERIZATION OF DUTCH FINE RECYCLED CONCRETE AGGREGATES: A COMPARATIVE STUDY

Marija Nedeljković (1, 2), Jeanette Visser (2), Timo G. Nijland (2), Siska Valcke (2) and Erik Schlangen (1)

(1) Microlab, Faculty of Civil Engineering and Geosciences, Delft University of Technology, The Netherlands

(2) TNO Buildings, Infrastructure & Maritime Delft, The Netherlands

Abstract

In the Netherlands, beside cement replacement with more green cement types, there is also an urgent need for alternative materials for natural sand in new concrete in order to make it circular. Furthermore, the recyclers have raised questions regarding upscaling and the potential of fine recycled concrete aggregates (fRCA) in structural concrete elements since the availability of recycled construction rubble is increasing. The variations in their chemical and physical properties and lack of standards for their quality evaluation is the main reason for not yet using fRCA in new concrete.

In this paper, an in-depth characterization of different fRCA is performed in order to define their chemical properties. The properties can be eventually related to concrete mix design and performance (next step), so that fRCA can be classified as a material that can be used in more advanced applications. This is achieved with a multi-level chemical characterization of individual and total fractions (0-0.25 mm, 0.25-4 mm and 0-4 mm) for finding type and content of the original sand and cement phases and potential contamination of selected fractions. The tests include quantification of element composition with X-ray fluorescence (XRF), qualitative and quantitative phase analysis with X-ray diffraction (XRD) and Rietveld method. In addition, cement paste content, chlorides and sulfates of each type of fRCA was measured in order to evaluate contamination of studied material. It was shown that fRCA from different origins have similar chemical and mineralogical composition and contain comparative chloride content. The chemical composition testing can provide a first line control regarding composition and potential contamination of fRCA. After that, it can be decided which additional tests are necessary to be done in order to evaluate the suitability of fRCA for replacement of primary natural fine aggregates in new concrete.

Keywords: Fine recycled concrete aggregates, phases, contamination, XRF

1. INTRODUCTION

In the coming decade, sustainable construction materials with low environmental impact will have a crucial role in achieving a circular economy (CE). The Dutch CE strategy aims to make the Netherlands 'fully circular' by 2050 with an interim target of a 50% material reduction of primary raw materials (minerals, fossil fuels and metals) by 2030 [1]. Therefore, in the Netherlands, beside cement replacement with more green cement types, there is also an urgent need for alternative materials for replacement of natural sand. Despite the potential that industrial waste has for concrete production, mainly as replacement for cement, resources for aggregates are not sufficient and concrete rubble is necessary to be included in the stream of alternative raw materials. The largest source of aggregates is the construction and demolition (C&D) waste and its quantity will be significantly increasing due to aging and deterioration of our concrete infrastructure.

The variations in the chemical and physical properties of fine recycled concrete aggregates (fRCA) [2, 3], lack of experience and lack of standards for their quality evaluation are the main reasons for a large quantity of fRCA being mainly used for low grade applications such as road pavements, sub-basements, soil stabilization, improvement of sub-ground [4]. Recent laboratory studies have shown the development of mortars and concretes with different fRCA replacement levels [5, 6]. However, fRCA have not been employed yet in practice. The key question for application as sand replacement in concrete is which properties would hamper the performance of concrete and, related to this, which quality indicators should be used, so that fRCA can be classified as a material that can be used in more advanced applications.

Material characterization is an impotant step in order to understand variations of recycled material and their key properties affecting concrete performance. For example, the type of aggregate, or strictly speaking its modulus of elasticity, influences shrinkage of concrete. Another example; one of the most critical aspects for durability of concrete, are soluble chlorides and sulfates contained in concrete components of which the amount is limited in concrete in order to prevent degradation, in this case initiation of corrosion of reinforcement or sulfate attack. Typically, chlorides can be present in concrete components, i.e. in water, cement, aggregates and in admixtures, but also concrete structures are often exposed to chloride-contaminated environments in the Netherlands, causing chloride ions to penetrate through the concrete cover. After recycling of such a concrete, chemical composition and phase analysis can be an indicator for contamination level of a recycled concrete. X-ray diffraction (XRD) analysis is a powerful tool in this regard, but challenges can arise due to the complex and often varying composition of fRCA. For this reason it is necessary to combine XRD with other characterization techniques such as X-ray fluorescence spectrometry (XRF). Multi-level characterization of Dutch fRCA such as chemical and mineralogical composition, adhered cement paste content and content of Cl^-, SO_4^{2-} in the cement paste, is performed in this study, to demonstrate potential of this material for its use in the new concrete.

2. MATERIALS AND METHODS

2.1 Materials and sample preparation

The fRCA were supplied by three project partners. They were chosen to be representative of major Dutch fRCA. All batches were delivered fresh (no storage in meanwhile). Primary natural river sand with 95 wt.% of SiO_2 was also studied to provide a baseline for comparison.

All fRCA were first dried in an oven at 105 °C. After drying, fRCA were sieved and divided into eight fractions (<0.063 mm, 0.063-0.125 mm, 0.125-0.250 mm, 0.250-0.5 mm, 0.5-1 mm, 1-2 mm, 2-4 mm, >4 mm) using a sieve tower. After evaluation of individual fractions, it was decided to choose two subfractions 0-0.25 mm and 0.25-4 mm and investigate their properties and compare to the properties of total fraction 0-4 mm. The pie charts in Figure 1 show their relative proportions in 0-4 mm in studied materials; where letters refer to primary natural sand (A) and fRCA with different origins (B, C, D).

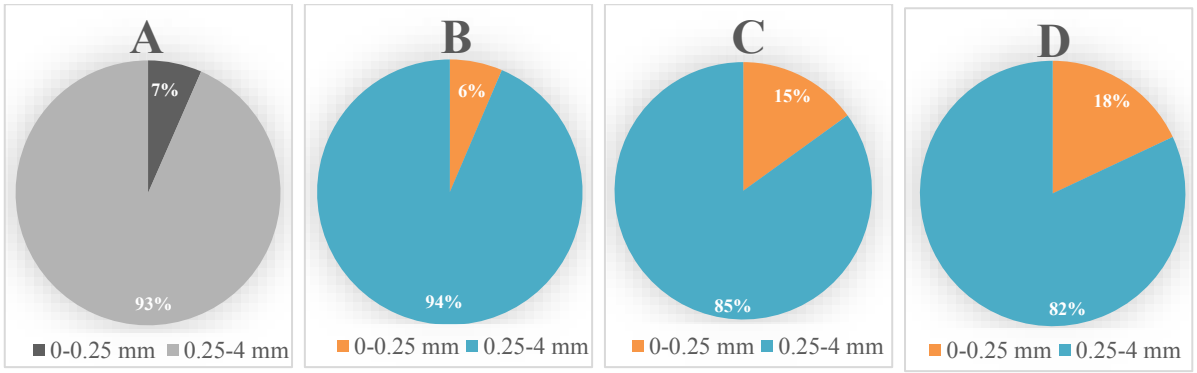

Figure 1: The relative proportions of particle size fractions (0-0.25 mm and 0.25-4 mm) in 0-4 mm (weight %).

The fRCA samples were first ground with a grinding machine, Fritsch pulverizer 5, to an average particle size of 100 µm. The machine has four grinding cups and five steel grinding balls per grinding cup. The maximum sample quantity is 225 ml. After grinding, milling with an Alpine e200 LS air jet sieve of fRCA fractions was done and particles with an average size of 25 µm were obtained. This particle size was necessary for XRD analysis. Finally, manual grinding was applied to obtain particles with an average size of 10 µm for XRF analysis.

2.2 Experimental methods

2.2.1 X-ray fluorescence

The fluorescence spectra of studied materials were recorded with a Bruker S8 Tiger spectrometer. A binding agent, Boreox ($C_{12}H_{22}O_{11}$) from Fluxana, is used during the preparation of pressed pellets. Samples were mixed in a stainless steel grinding cup. The loss on ignition (LOI) was measured by heating the fRCA to 1050 °C. The LOI is expressed in weight percent of the dry matter (EN 15169:2007 (E)). The mass of the sample was 5±0.1 g.

2.2.2 X-ray powder diffraction and Rietveld analysis

The diffractograms of studied materials were recorded using a Bruker D8 Advance X-ray powder diffractometer, equipped with LynxEye detector. The machine was operated with an accelerating voltage of 40 kV and an X-ray beam current of 40 mA. The X-ray source was a Cu-tube working with characteristic Cu-Kα wavelength of 1.54060 Å. The samples were scanned varying the 2-theta angles between 10º and 70º. For quantitative phase analysis, standard reference material (alumina, Al_2O_3, NIST Standard Reference Material 676a) was added and blend was subsequently mixed for about 2 minutes. Phase identification was performed using Bruker Eva 4.2 software and appropriate databases. Rietveld quantitative phase analysis was performed using Bruker Topas 5.1 software.

2.2.3 Acid-soluble chlorides and water-soluble sulfates

The acid-soluble chlorides were obtained by acid dissolution using nitric acid (6 mol/l) according to EN 1744-5. The material was dried in an oven at 105 ºC for 24 h. Samples of approximately 20 grams were used for analysis. Typically, the sample was weighed into a 250 ml beaker in which 100 ml of 6M nitric acid was added subsequently. The mixture was shaken manually for 30 s followed by heating until boiling and boiled for about 5 min under continuous magnetic stirring. After cooling down, the mixture was vacuum filtered using a Buchner filter with a medium grade filter paper 110. The residue on the filter paper was rinsed 4 times with deonized water and 10 ml 1M nitric acid to ensure that all ions had been rinsed. The filtrate was transferred from the filter flask into a volumetric flask. The solution in the volumetric flask was filled up with deionized water to 500 ml. Then 100 ml solution was pipetted into a clean glass cup. Acid-soluble chloride salts content was further determined following Volhard method as described in EN 1744-5. The solid residue left on the filter paper was dried in an oven at 105 ºC for 24 h. This allowed determination of the cement paste content by subtracting the weight of insoluble substances from the initial weight of the oven-dried material.

The water-soluble sulfate content in the fRCA was determined according to EN 1744-1. The sample consisting of 25 g of sand (crushed below 4 mm) was mixed with 1 l of water at 65 ºC under stirring to extract water-soluble sulfate ions. A neat sample is filtered using a Buchner filter with a medium grade filter paper 110, and the filtrate is analyzed by Metrohm 850 ion chromatography system. Sulfate ion was resolved on an anion exchange column and detected by a conductivity detector. Quantification was performed by linear regression analysis of peak areas from the standard sulfate calibration curve containing five points.

3. RESULTS AND DISCUSSION

3.1 Chemical composition

The chemical composition of the investigated primary natural sand (A) and fRCA (B, C, D) fractions (0-0.25 mm, 0.25-4mm, 0-4 mm) is shown in Table 1. As expected, the natural sand is composed mainly of SiO_2 and minor CaO, Al_2O_3, MgO, K_2O, Fe_2O_3, SO_3. In comparison to natural sand, the fRCA contain lower amounts of SiO_2 and higher amounts of CaO, Al_2O_3, MgO, K_2O, Fe_2O_3, SO_3. This is due to presence of cement paste in fRCA, which can be either adhered to original sand particles or form individual grains. The chemical composition of the fRCA is made up mainly by SiO_2 (62-76%), CaO (14-23%), Al_2O_3 (6-10%) and Fe_2O_3 (1.6-3.3%). The chemical composition of fraction D 0-4 mm is very similar to the composition of fraction 0-4 mm studied by Lotfi and Rem [7], which was obtained from recycled concrete based on the use of CEM III/B cement. However, the obtained results in this study are different than that reported by Gomes et al. [2] who reported much lower values for CaO and much higher values for Na_2O and K_2O. On the other hand, the obtained values for CaO are much lower than that reported by Florea et al. [8].

The fraction below 0.25 mm represents between 5% (B) and 17% (C, D) of the total weight of fraction 0-4 mm. This fraction has a different composition compared to 0.25-4 and 0-4 mm with a reduced SiO_2 content (59–67%) and increased CaO (19–27%). The LOI was 8 - 11%.

It is clear that sands are SiO_2-rich material, corroborated with XRD analysis, where it was found that quartz is the main phase in all batches (~60 wt. % material). This was expected, since

river sand, and, therefore, quartz, is a widely used sand type in the Netherlands. The CaO, Al_2O_3, Fe_2O_3 originate from cement which was used in parent concrete. Their contents in studied fractions are much lower than of that of typical cements used in the Netherlands.

Table 1: Chemical composition of different fractions of natural and recycled sands

	SiO_2	CaO	Al_2O_3	MgO	Na_2O	K_2O	TiO_2	Fe_2O_3	SO_3	Cl
A										
0-0.25	93.60	1.08	2.49	0.18	0.49	0.86	0.23	0.88	0.042	0.013
0.25-4	95.60	0.92	1.71	0.12	0.21	0.68	0.06	0.46	0.084	0.007
0-4	96.00	0.46	1.77	0.10	0.22	0.74	0.07	0.49	0.047	0.000
B										
0-0.25	67.80	19.10	5.19	1.20	0.64	1.34	0.37	3.08	0.97	0.03
0.25-4	70.30	17.10	5.09	1.35	0.56	1.33	0.38	2.60	0.98	0.03
0-4	62.80	22.50	5.76	1.54	0.61	1.49	0.47	3.26	1.16	0.03
C										
0-0.25	58.60	27.50	5.14	2.10	0.58	1.47	0.36	2.35	1.32	0.1
0.25-4	62.70	25.80	4.09	1.47	0.42	1.25	0.34	2.38	1.00	0.09
0-4	68.20	20.40	4.44	1.62	0.51	1.24	0.28	2.02	0.91	0.07
D										
0-0.25	59.50	26.70	5.80	1.26	0.46	1.46	0.43	2.36	1.56	0.060
0.25-4	71.70	17.30	4.75	1.06	0.41	1.08	0.30	1.95	1.12	0.043
0-4	75.80	14.40	4.26	0.91	0.41	1.06	0.27	1.67	0.89	0.042

3.2 Phase analysis

Figure 2 shows the X-ray diffractograms of investigated primary natural sand and fRCA, while Table 2 gives an overview of the phases combined with quantification using Rietveld refinement method.

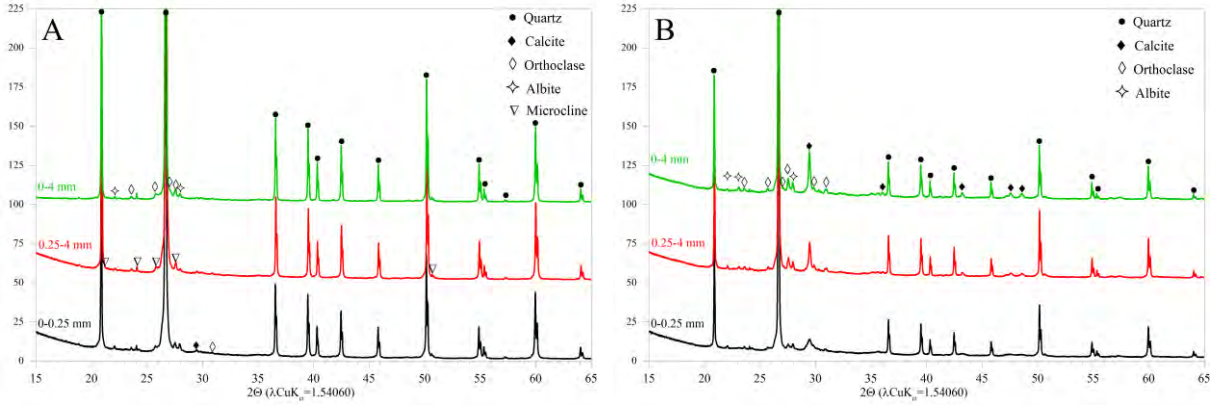

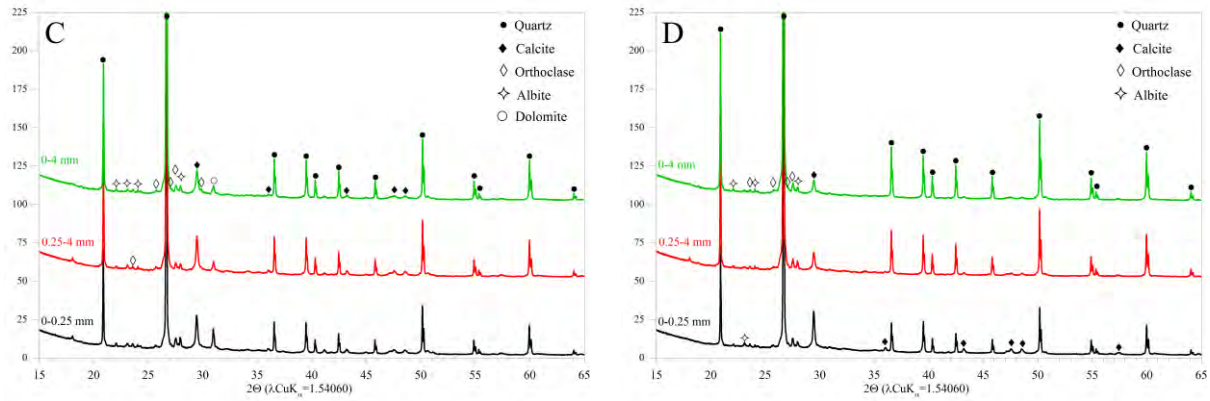

Figure 2: X-ray diffractograms of the natural sand (A) and fRCA (B, C, D).

It is apparent that total fraction and subfractions within each batch contain the same phases. The main phases of fRCA are quartz and calcite. Besides quartz and calcite, albite, orthoclase and microcline are present in all aggregates; quartz makes up 60%. Besides dolomite which is also observed in batch C, there were no other phases present in the fRCA. The amount of quartz is significantly less in the fRCA (B, C, D) compared to natural sand (A) in Figure 2. Each of the phases, their origin and content, is discussed below.

Table 2: Phase quantification by Rietveld refinement method (wt.%).

Phase	Quartz	Albite	Orthoclase	Microcline	Calcite	Dolomite	Amorphous
A							
0-0.25 mm	91.10	2.90	1.30	3.90	0.00	0.00	0.90
0.25-4 mm	95.30	2.50	1.70	0.00	0.00	0.00	0.50
0-4 mm	94.10	1.51	0.84	3.20	0.00	0.00	0.40
B							
0-0.25 mm	58.80	3.50	3.70	0.00	8.58	0.00	25.30
0.25-4 mm	58.20	2.55	5.00	0.00	6.99	0.00	27.30
0-4 mm	57.70	3.63	4.90	0.00	8.70	0.00	25.10
C							
0-0.25 mm	48.50	4.05	4.06	0.00	9.58	3.40	30.40
0.25-4 mm	55.30	2.25	3.50	0.00	10.71	1.81	26.50
0-4 mm	62.70	3.03	4.70	0.00	7.60	0.00	21.90
D							
0-0.25 mm	50.10	3.15	3.12	0.00	9.81	0.00	33.80
0.25-4 mm	62.70	2.45	2.67	0.00	5.05	0.00	27.10
0-4 mm	72.10	2.43	2.62	0.00	3.82	0.00	19.00

Quartz The most common mineral found in all three batches in high quantities is quartz, meaning that origin of fRCA is mainly river sand.

Calcite Potentially, there are four different sources of carbonates:

- from limestone aggregates;
- from limestone filler;
- from carbonation of Ca-rich phases (calcium silicate hydrate gel, $Ca(OH)_2$, ettringite) during concrete service life;
- from carbonation of Ca-rich phases (calcium silicate hydrate gel, $Ca(OH)_2$, ettringite) after crushing of concrete due to storage and weathering.

Amorphous phase Amorphous phases originate from amorphous hydrated phases (e.g. C-S-H-) and unreacted material in amorphous form in cement paste which is usually adhered to fRCA. The amorphous content originating from the raw material (such as unreacted blast furnace slag) can be an indicator about the potential reactivity of the cement.

Anhydrous cement compounds The residual anhydrous cement components (clinkers) were not identified within the XRD detection limit, in agreement with some studies [2, 9, 10] and in disagreement with study of Bordy et al. [11].

3.3 Chlorides, sulfates and cement paste content

Table 3 lists cement paste content, chlorides and sulfates in different fractions. Content of old cement paste adhered to the fRCA ranges from 14.% to 29.8%, depending on the batch (B, C, D) and on particle size range (0-0.25 mm, 0.25-4 mm, 0-4mm). These values are similar to cement paste content estimated by HCl selective dissolution, being between 16.1% and 24.6% for recycled coarse and fine concrete aggregates, respectively [3]. The cement paste concentrates in the finer fraction (0-0.25 mm), in agreement with [12].

Table 3: Cement paste content, acid soluble Cl^- and water soluble SO_4^{2-} in fRCA.

	Cement paste	Acid soluble Cl^-	Water soluble SO_4^{2-}
	[sand wt.%]	[sand wt.%]	[sand wt.%]
A			
0-0.25 mm	0.00	0.00	0.01
0.25-4 mm	0.00	0.00	0.00
0-4 mm	0.00	0.00	0.00
B			
0-0.25 mm	28.91	0.04	0.37
0.25-4 mm	17.86	0.04	0.14
0-4 mm	19.03	0.04	0.16
C			
0-0.25 mm	29.81	0.06	0.18
0.25-4 mm	21.43	0.05	0.09
0-4 mm	25.84	0.04	0.14
D			
0-0.25 mm	22.72	0.04	0.24
0.25-4 mm	14.72	0.04	0.08
0-4 mm	16.16	0.04	0.10

Compared to the primary natural sand (A), in which no chlorides and sulfates are present, fRCA can be a chloride and sulfate source in a concrete mix. The chlorides from fRCA should be considered in total concrete mix design calculations (as is traditionally done for all concrete components) since there is no consensus on the value of the critical chloride content allowed in recycled concrete aggregates. The SO_4^{2-} content in the fRCA is below standard limit value 0.2% (m/m) (EN 12620) for all samples, except for B 0-0.25 mm. The high water soluble SO_4^{2-} of fRCA B 0-0.25 mm and D 0-0.25 mm, might be a result of ettringite dissolution due to carbonated cement paste in these fractions. Brocken and Nijland [13] showed that when ettringite breaks down during carbonation, sulfur is increasing especially in the pore solution.

4. CONCLUSIONS

- Based on multi-level chemical characterization of the different fRCA, it was found that they are mainly made up by crystalline phases (> 70 wt.%), notably quartz (> 60 wt.%), originating from the primary natural sand. In addition, amorphous content varied among the fractions (20-35 wt.%).
- The fRCA (B, C, D) fractions (0-0.25 mm, 0.25-4mm, 0-4 mm) show differences in chemical composition, notably SiO_2 and CaO contents.
- The content of sulfates was below the critical values adopted for aggregates for use in reinforced concrete, with exception for fine fraction 0-0.25 mm. Therefore, from the aspect of chemical properties, the fRCA show a good potential for sand replacement in new concrete.
- Finally, the present work provides new insights for better understanding of the variations among different fRCA batches toward their use in the new concrete mix design.
- In the further study of this project, these chemical results will be combined with the physical characterization and the significance of the results and variations between batches will be studied with respect to appropriate mix design and concrete performance.

ACKNOWLEDGEMENTS

Authors acknowledge funding provided by the Materials innovation institute M2i (www.m2i.nl), Rijkswaterstaat, TweeR Recycling, AVG, Caron Recycling (CRH) and BRBS Recycling.

REFERENCES

[1] Ministry of Infrastructure and the Environment and the Ministry of Economic Affairs in the Netherlands, 'A circular economy in the Netherlands by 2050.' 2016.

[2] Gomes, P. C. C., Ulsen, C., Pereira, F. A., Quattrone, M., and Angulo, S. C. 'Comminution and sizing processes of concrete block waste as recycled aggregates.' *Waste Manage.***45**(2015) 171-179.

[3] Angulo, S. C., Ulsen, C., John, V. M., Kahn, H., and Cincotto, M. A. 'Chemical–mineralogical characterization of C&D waste recycled aggregates from São Paulo, Brazil.' *Waste Manage.* **29**(2)(2009) 721-730.

[4] de Brito, J., F. Agrela, and R.V. Silva, 'Legal regulations of recycled aggregate concrete in buildings and roads.' in New Trends in Eco-efficient and Recycled Concrete, Elsevier. 2019, 509-526.

[5] Nováková, I. and B.-A. Buyle. 'Sand Replacement by Fine Recycled Concrete Aggregates as an Approach for Sustainable Cementitious Materials.' in Proceedings of the International Conference of Sustainable Production and Use of Cement and Concrete. Springer. 2020.

[6] Bouarroudj, M. E., Remond, S., Michel, F., Zhao, Z., Bulteel, D., and Courard, L. 'Use of a reference limestone fine aggregate to study the fresh and hard behavior of mortar made with recycled fine aggregate.' *Mater. Struct.* **52**(1)(2019) 18.

[7] Lotfi, S. and P. Rem, 'Recycling of end of life concrete fines into hardened cement and clean sand.' *J. Environ. Prot. Ecol.* **7**(06)(2016) 934.

[8] Florea, M. and H. Brouwers, 'Properties of various size fractions of crushed concrete related to process conditions and re-use.' *Cem. Concr. Res.* **52**(2013) 11-21.

[9] Evangelista, L., Guedes, M., De Brito, J., Ferro, A. C., and Pereira, M. F. 'Physical, chemical and mineralogical properties of fine recycled aggregates made from concrete waste.' *Constr. Build. Mater.* **86**(2015) 178-188.

[10] Oksri-Nelfia, L., Mahieux, P. Y., Amiri, O., Turcry, P., and Lux, J. 'Reuse of recycled crushed concrete fines as mineral addition in cementitious materials.' *Mater. Struct.* **49**(8)(2016) 3239-3251.

[11] Bordy, A., Younsi, A., Aggoun, S., and Fiorio, B. 'Cement substitution by a recycled cement paste fine: Role of the residual anhydrous clinker.' *Constr. Build. Mater.* **132**(2017) 1-8.

[12] Ulsen, C., Kahn, H., Hawlitschek, G., Masini, E. A., Angulo, S. C., and John, V. M. 'Production of recycled sand from construction and demolition waste.' *Constr. Build. Mater.* **40**(2013), 1168-1173.

[13] Brocken, H. and T.G. Nijland, "White efflorescence on brick masonry and concrete masonry blocks, with special emphasis on sulfate efflorescence on concrete blocks.' *Constr. Build. Mater.* **18**(5)(2004) 315-323.

Theme 2

Hydration and microstructure formation

THE HYDRATION OF SLAG IN COMPLEX BINDER AND THE MICROSTRUCTURAL VARIATION OF HARDENED PASTE UNDER THE CONDITION OF LEACHING OF SOFT WATER

YAN Peiyu (1)

(1) Department of Civil Engineering, Tsinghua University, Beijing 100084; China

Abstract

The hydration of slag in complex binder with different dosage was studied by identifying $Ca(OH)_2$ content in hardened paste and Ca/Si ratio of formed C-A-S-H gel. The results shows that: elevated temperature curing could improve the slag's reaction degree in early ages, but hinder the further hydration in late time. Some $Ca(OH)_2$ is consumed when the outer hydrate is formed in early hydrating time, so the $Ca(OH)_2$ content in the hardened paste decreases and Ca/Si ratio of C-A-S-H gel decreases. In the late hydrating time, the inner hydrate is formed, it no longer consumes a significant amount of $Ca(OH)_2$, then Ca/Si ratio of C-A-S-H gel decreases more and $Ca(OH)_2$ content tends to increase in the hardened paste. The $Ca(OH)_2$ content in pastes is abundant, the Ca/Si ratio of C-A-S-H gel slightly decreases but there is not the decomposition sign of C-A-S-H gel after leaching of soft water for long time. The porosity of cement-slag complex binder pastes is low. The cement-slag complex binder containing no more than 70% slag shows good leaching resistance.

Keywords: slag, $Ca(OH)_2$ content, C-A-S-H gel, Ca/Si ratio, leach

1. INTRODUCTION

Ground granulated blast furnace slag (GGBS) is widely used as a supplemental cemetitious material (SCM) to prepare concrete now. The partial replacement for Portland cement brings many advantages. Firstly, the use of GGBS as an industrial byproduct has economic advantage with no additional clinkering process involved. Secondly, there is environmental benefit with a significant reduction in consume of natural resource and CO_2 emissions during the production of cement [1,2]. Moreover, the appropriate use of slag can bring the technological improvement of concrete, such as the strength at later age and low hydration heat. The higher the content of slag in complex binder, the better the environmental benefit. Liu [3] reported that the compressive strength of motar with up to 70% content of slag is even higher than that of pure Portland cement.

The reaction mechanism of slag with latent activity is different from that of Portland cement. Many studies concerning the hydration of Portland cement blended with GGBS have been carried out in the past few decades. The interaction of the cement and slag will make the

hydration process more complex and also has impact on the microstructure of the hardened binder pastes. Zhou et al. [4] reported that the pores of hardened cement pastes with slag were refined compared with that of pure cement, but the porosity increased. $Ca(OH)_2$ wasn't formed during the reaction of GGBS and it consumed $Ca(OH)_2$ with slag's hydration. As the fraction of GGBS in cement-slag blends increased, the fraction of cement reduced and the content of $Ca(OH)_2$ formed in paste decreased. The content of $Ca(OH)_2$ was less than 6% in the cement paste blended with 70% GGBS [5] and it was probable that the stability of hydration products was affected with higher percentage of GGBS in blended cement paste as a result of the reduction in alkalinity with lower content of $Ca(OH)_2$ and then the durability of concrete would be reduced. Especially in the condition of continuously scouring of soft water, $Ca(OH)_2$ may be leached from concrete prepared with complex binder containing high percentage of GGBS. This effect may result the decomposition of C-S-H gel and influence negatively the mechanical properties and durability of concrete.

In this paper, The hydration characteristics of slag in cement-slag binder with different slag ratio was studied by testing the rariation of $Ca(OH)_2$ content and Ca/Si ratio of formed C-S-H gel in hardened paste during the hydration of complex binder and after leaching of soft water for long time.

2. EXPERIMENT

2.1 Materials

Table 1: Chemical compositions of cement and slag (*w*%)

Composition	SiO_2	Al_2O_3	Fe_2O_3	CaO	MgO	SO_3	Na_2O_{eq}	f-CaO	Cl^-	LOI
Cement	20.55	4.59	3.27	62.50	2.61	2.93	0.53	0.83	0.010	2.08
Slag	34.55	14.36	0.45	33.94	11.16	1.95	0.63	-	-	0.70

$Na_2O_{eq} = Na_2O + 0.658K_2O$; *w*—Mass fraction.

Table 2: Mix proportion of binders

Sample	W/B	Mix proportion (by mass)/%	
		Cement	Slag
B0, C0	0.4	100	0
B1, C1		70	30
B3, C3		30	70

P.I 42.5 Portland cement and S95 ground granulated blast furnace slag were used in the experiment. The chemical composition of cement and slag was shown in Table 1. The specific surface areas of cement and slag are $350m^2/kg$ and $442m^2/kg$, respectively. The mix proportions of cement-slag complex binders were given in Table 2.

2.2 Specimen preparation

The pastes were prepared according to table 2, then cast into PVC tube with the diameter of 45 mm and the length of 15mm. The samples were cured in air at 20±1℃ for 1d. After demolding, Groups B samples was cured for 90d in water at 20±1℃(standard condition) and Group C samples was cured in water at 65±2℃(elevated temperature condition) for 7d, then at 20±1℃ till the testing ages. A piece was taken from the samples at the ages of 3, 7, 28 and 90d and put into acetone to cease further hydration. The samples cured for 90d were immersed in deionized water stirred continuously, to simulate the leaching process of flowing

soft water. Water was renewed at regular intervals (once a day in the first week, then once a week). A piece was taken from the samples at the ages of 90d, 1y and 2y. The surface layer of specimens was cut and put into acetone to cease further hydration at the prescribed age.

2.3 Test methods

The $Ca(OH)_2$ content of the hardened composite binder pastes in different leaching durations was determined by thermogravimetry. Thermogravimetry was carried out from room temperature up to 900°C, at 10°C/min rate.

The micromorphology of hardened binder pastes and the Ca/Si ratio of C-S-H gel in different leaching durations was investigated on a freshly fractured surface of samples using a FEG scanning electron microscope with energy dispersive spectrometer. The sample was coated with carbon. 30 testing areas were measured for each sample. to reduce the error

The cumulative mass loss rate of the hardened composite binder pastes after leaching (φ) can be calculated as follows

$$\varphi = \frac{m_n - m_1}{m_1} \times 100\% \quad (1)$$

Where m_1 and m_n is the weight of specimens before and after leaching, respectively.

Porosity and pore size distribution of the hardened composite binder pastes in different leaching durations were measured with a mercury intrusion porosimeter with the maximum intrusion pressure of 300 MPa.

3. RESULTS AND DISCUSSION

3.1 $Ca(OH)_2$ content in hardened paste

$Ca(OH)_2$ content in the hardened composite binder pastes hydrating for different ages is shown in Fig.1. RB1、RB3、RC1、RC3 is the normalized result based on the cement content in the binders. For the series B cured in the standard condition, the absolute $Ca(OH)_2$ content in the hardened composite binder pastes is lower than that in pure cement paste in all hydration ages. The higher the dosage of GGBS, the lower $Ca(OH)_2$ content. The normalized $Ca(OH)_2$ content in the composite binder pastes is higher than that in pure cement paste at early age. The $Ca(OH)_2$ content in pure cement paste increases slowly in later ages due to the continuous hydration of cement. The $Ca(OH)_2$ content in the composite binder pastes varies a little in later age due to the reaction of GGBS, which consumes some $Ca(OH)_2$.

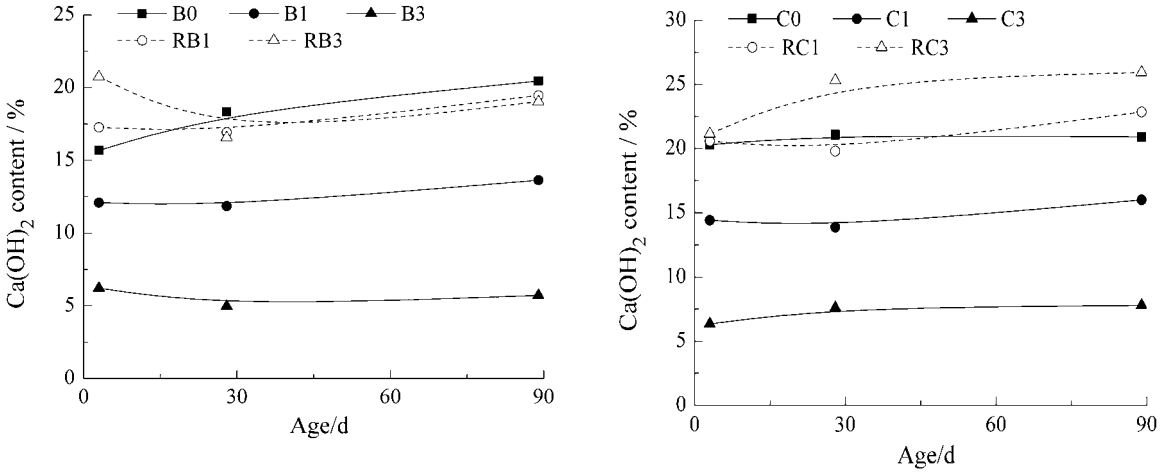

Figure 1: $Ca(OH)_2$ content in complex binders at different hydration ages

For the samples in series B cured in the standard condition, the absolute $Ca(OH)_2$ content for the binders containing GGBS is higher than that for pure cement at 3d. For the samples in series C cured in the elevated temperature condition, the $Ca(OH)_2$ content is higher than 20% at 3d and increases little hereafter in pure cement paste but obviously in the binders containing GGBS due to the very fast hydration of cement and continuous reaction of GGBS stimulated by elevated temperature.

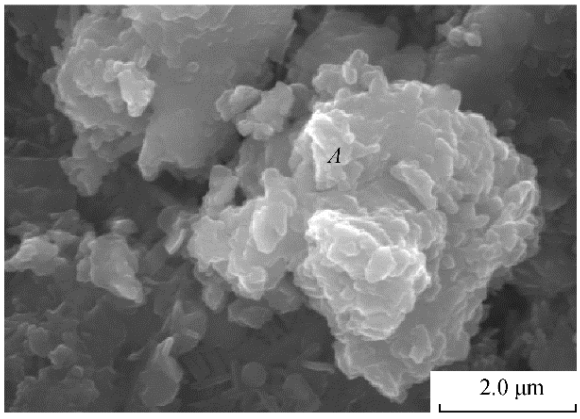

Figure 2: Morphology of hardened binder paste

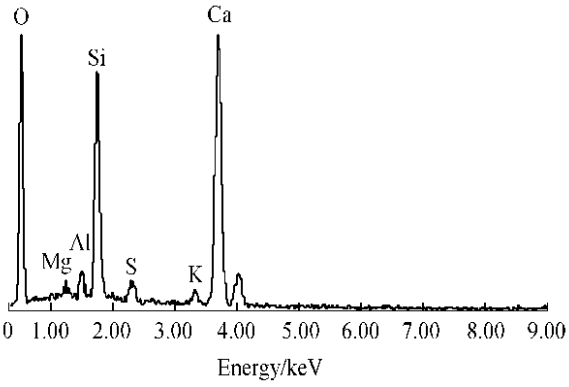

Figure 3: EDS spectrum of C-A-S-H gel at area A in Figure 2

3.2 Ca/Si ratio of C-A-S-H gel

Fig. 2 shows the micromorphology of hardened paste. Fig.3 shows the chemical composition of hydration product in complex binder paste. The main hydration product is C-A-S-H gel. The higher the percentage of GGBS in complex binder, the lower the Ca/Si ratio of C-A-S-H gel (Fig.4). The Ca/Si ratio of C-A-S-H gel in the series B cured in the standard condition decreases less during the period of 3-28 d, but more during the period of 28-90 d than that in the series C cured in the elevated temperature condition. The reaction degree of GGBS cured at elevated temperature is higher than that cured at room temperature in early age. More C-A-S-H gel with low Ca/Si ratio yields. The reaction degree of GGBS cured at room temperature increases continuously with the prolongation of hydration time and

arrives almost same degree of GGBS in the series C. Therefore, The Ca/Si ratio of C-A-S-H gel in the series B is near to, even lower to that in the series C.

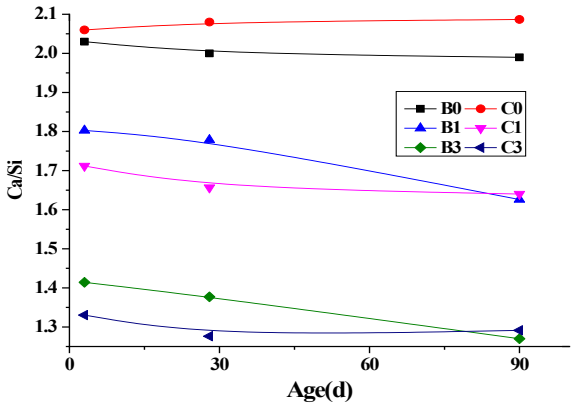

Figure 4: Ca/Si ratio of C-A-S-H gel in hardened paste at different hydration ages

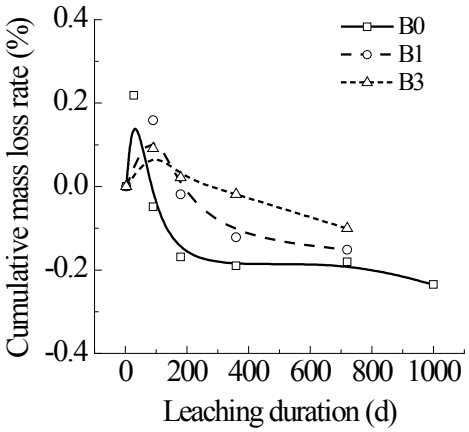

Figure 5: The cumulative mass loss rates of hardened complex binder pastes

3.3 variation of the hydration product and microstructure of hardened paste after long time of leaching by soft water

The cumulative mass loss rates of hardened composite binder pastes in different leaching duration are shown in Fig. 5. The mass of hardened composite binder pastes increases at early leaching age. Half of the cement is still unhydrated in pure cement paste after hydrating for 90 days[6]. Numerous unhydrated cement particles in hardened pastes continues to hydrate and generates more hydration products, the mass of pastes increases. The hardened composite binder pastes shows mass loss after long-term leaching. With the extension of leaching age, the mass loss increases gradually due to the less unhydrated particles existing in the hardened pastes, so the mass loss is more than the mass increase. As the slag content increases, the mass loss rate is lower. This is due to their dense structure and the decreased amount of dissolvable $Ca(OH)_2$.

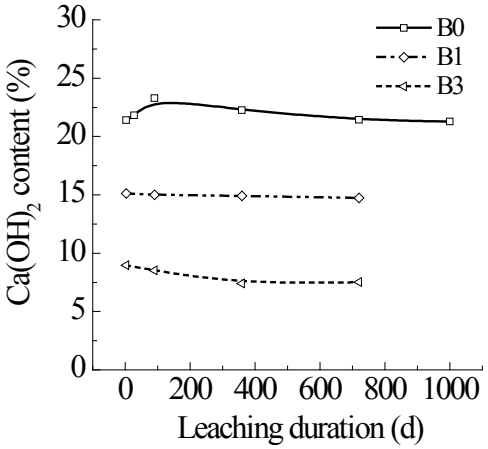

Figure 6: The $Ca(OH)_2$ content in hardened complex binder pastes

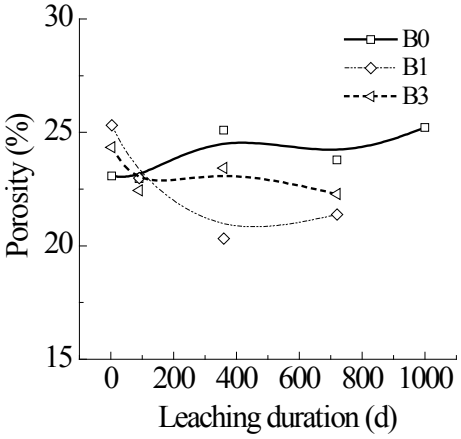

Figure 7: The porosity variation of hardened complex binder pastes

The $Ca(OH)_2$ content in hardened complex binder pastes in different leaching duration is shown in Fig. 6. There is not reduction but a small increase of $Ca(OH)_2$ content in pure cement paste in the early stage of leaching duration. With the prolonged leaching age, the $Ca(OH)_2$ content have a decreasing trend consistent with its mass change rule. The $Ca(OH)_2$ content in complex binder pastes containing slag decreases with the increasing leaching age, but the rate of decrease is gentle. The reaction of slag consumes only a little $Ca(OH)_2$ because it is not entirely pozzolanic reaction. Therefore, the $Ca(OH)_2$ content reduces slightly. For the sample SL70, the $Ca(OH)_2$ content is still above 7% after leaching for 2 years, which could ensure the high alkalinity of pore solution and stability of C-A-S-H gel as well as other hydration product.

The porosity variation of hardened complex binder pastes in different leaching duration is shown in Fig. 7. Their porosity decreases at early leaching stage and increases slightly after long-term leaching duration. The change rule of the porosity is consistent with that of the mass loss. The short-term leaching does not cause the hydration product of complex binder being leached because of the low porosity and dense paste structure of complex binder. More hydration product generated further fills pores to make a decrease of porosity. As the leaching process continues, some hydration product is leached and newly generated hydration product is less and less, so the porosity of paste shows an increasing trend. But the porosity of complex binder pastes remains stable and shows no trend of a great increase after long-term leaching compared with that before leaching. The density of hardened paste is an important factor in the corrosion resistance of concrete. The paste with low porosity and poor pore connectivity made it difficult for water to infiltrate and to dissolve soluble hydration products, so there is only a slight leaching phenomenon in the surface.

Fig.8 shows morphologies of hardened complex binder pastes after leaching for 2y. The paste structure of complex binder is dense and GGBS particles are bonded tightly in matrix, indicating a certain reaction degree of GGBS. There is still a lot of sheet $Ca(OH)_2$ crystal in the hardened paste. The hardened complex binder pastes is still very dense. The Ca/Si ratio of C-A-S-H gel varies little after leaching for 2y. There is not loose decomposition product and the paste structure remained stable after long-term leaching by fresh water.

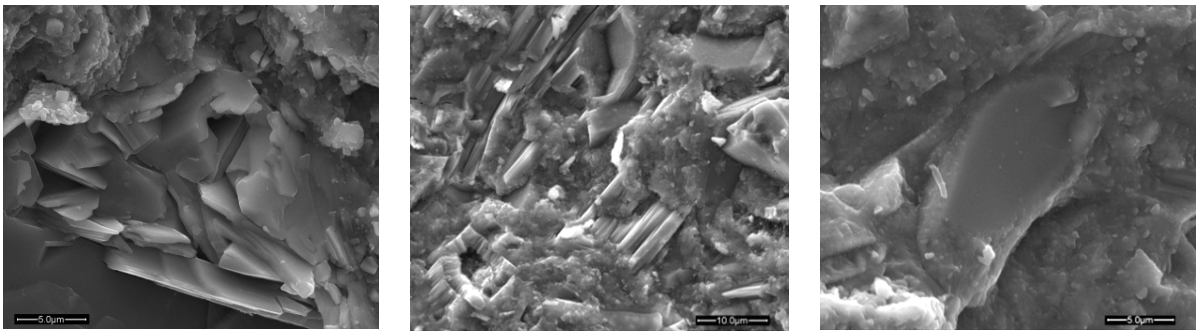

(a) B0 (b) B1 (c) B3

Figure 8: Morphologies of hardened composite binder pastes after leaching for 2y

4. CONCLUSION

Elevated temperature curing could improve the slag's reaction degree in early hydrating ages, but hinder the further hydration in late time. Some $Ca(OH)_2$ is consumed when the outer hydrate is formed in early hydrating time, so the $Ca(OH)_2$ content in the hardened paste decreases and Ca/Si ratio of C-A-S-H gel decreases. In the late hydrating time, the inner hydrate is formed, it no longer consumes a significant amount of $Ca(OH)_2$, then Ca/Si ratio of C-A-S-H gel decreases more and $Ca(OH)_2$ content tends to increase in the hardened paste. The $Ca(OH)_2$ content in pastes is abundant, the Ca/Si ratio of C-A-S-H gel slightly decreases but there is not the decomposition sign of C-A-S-H gel after leaching of soft water for long time. The porosity of cement-slag complex binder pastes is low. The cement-slag complex binder containing no more than 70% slag shows good leaching resistance.

ACKNOWLEDGEMENT

The authors would like to acknowledge National Key R&D Program of China (2017YFB0310101) and National Natural Science Foundation of China (No. 51878381).

REFERENCE:

1. Ekaputri, J.J. Ishida, T, and Maekawa, K. Autogenous shrinkage of mortars made with different types of sag cement. JCI Annual Convention, Saitama, Japan, 2010.
2. Report of ACI Committee 233. S.lag cement in concrete and mortar, ACI 233R-03. American Concrete Institute, Farmington Hills, Mich, 2003.
3. Liu, R.G and Yan, P.Y. Study on Hydration Degree of Portland Cement-slag Complex Binders. Key Engineering Materials. 539(2013)172-177.
4. Zhou, H. Ye, G. and van Breugel, K. Hydration process and pore structure of Portland cement paste blended with blast furnace slag. Proceedings of the 6th International Symposium on Cement & Concrete and CANMET/ACI International Symposium on Concrete Technology for Sustainable Development, Vols 1 and 2. 2006, 417-424.
5. Liu, R.G and Yan, P.Y. Hydration characteristics of slag in cement-slag complex binder (in Chinese). J Chin Ceram Soc. 40(8)(2012)1112-1118
6. Li X. Yan P.Y. and Aruhan. Assessment method of hydration degree of cement in complex binder based on the $Ca(OH)_2$ content (in Chinese). J Chin Ceram Soc. 37(1)(2009)1-5

EFFECT OF CHLORIDE SALTS ON SULFOALUMINATE CEMENT HYDRATION

L. U. D. Tambara Jr (1), J. C. Rocha (1), M. Cheriaf (1), A. Palomo (2) and A. Fernández-Jiménez (2)

(1) Universidade Federal de Santa Catarina - UFSC, Florianópolis, Brazil

(2) Instituto Ciencias de la Construcción Eduardo Torroja - IETcc-CSIC, Madrid, Spain

Abstract

The effect of including 5 % chloride salts (NaCl and $CaCl_2$) on calcium sulfoaluminate cement hydration was studied. The rate of heat release, setting times and mechanical strength were determined in 2 d, 28 d and 90 d cement pastes. The hydration products formed at those ages were identified with XRD and SEM. Hydration reactions were hastened and early age strength heightened with 5 % NaCl. In contrast, 5 % $CaCl_2$ retarded setting times, although it also increased later age compressive strength. The predominant reaction products found in both cases were ettringite and AH_3. Chloraluminates such as Friedel's salt were not observed to form at any of the ages studied. Gypsum precipitation, absent in the reference sample (CSA cement+water), was detected in the presence of chloride salts, however.

Keywords: Chloride, sulfoaluminate cement, hydration, ettringite, X-ray diffraction

1. INTRODUCTION

Calcium sulfoaluminate (CSA) cements are known as eco-friendly materials [1,2] because the sintering temperature required is approximately 200 °C lower than in ordinary portland cement (OPC) and grinding is less energy-intensive [3]. CSA cements also exhibit high early age strength, can offset drying shrinkage and are usable with heavy metals [4].

The predominant phase in CSA is ye'elimite ($C_4A_3\bar{S}$). Others include anhydrite ($C\bar{S}$), belite (C_2S), calcium aluminate (CA), mayenite ($C_{12}A_7$), brownmillerite (C_4AF) and periclase (MgO), to name the most prominent [5]. Depending on the liquid/solid ratio and calcium sulfate content, ye'elimite hydration may induce the formation of calcium monosulfoaluminate (C_4AH_{12}) and gibbsite (AH_3) (Equation 1); ettringite ($C_6A_3H_{32}$), katoite (C_3AH_6) and gibbsite (Equation 2); or ettringite and gibbsite only (Equation 3) [6,7].

$$C_4A_3\check{S} + 18H \rightarrow C_4A\check{S}H_{12} + 2AH_3 \quad \text{(Equation 1)}$$

$$4C_4A_3\check{S} + 80H \rightarrow C_6A\check{S}_3H_{32} + C_4A\check{S}H_{12} + 2C_3AH_6 + 8AH_3 \quad \text{(Equation 2)}$$

$$C_4A_3\check{S} + 2\,C\check{S}H_x + (38-2x)H \rightarrow C_6A\check{S}_3H_{32} + 2\,AH_3 \quad x = 0, 0.5, 2 \quad \text{(Equation 3)}$$

The effect of $CaCl_2$ and NaCl salts on OPC-based binders has been widely studied [8-13] and shown to accelerate calcium silicate and especially C_3S hydration, shortening initial and final setting and hardening times. Chloride ions, in turn, may react with the calcium monosulfoaluminate (AFm) initially formed in OPC hydration to generate AFm-Cl [9,10]. Alternatively, they may be chemically adsorbed onto C-S-H gel [9-12] or induce the formation of chloroaluminates such as Friedel's $[Ca_4Al_2(Cl)_{1.95}(OH)_{12.05}\cdot 4H_2O]$ or Kuzel's $[Ca_4Al_2(Cl)(SO_4)_{0.5}(OH)_{12}\cdot 6H_2O]$ salt [12-13].

The effect of such salts on CSA cement hydration has been less thoroughly researched. Ogawa et al. [2], studying the effect of 20 % NaCl on ye'elimite ($C_4A_3\overline{S}$) formation, reported that the degree of reaction of that predominant phase in CSA was lower in the presence of Cl than in its absence (reference cement). They also detected Friedel's salt and observed that the partial replacement of sulfate with chloride ions changed ettringite morphology, rendering it less expansive.

This study explored the effect of including 5 % chloride salts (NaCl and $CaCl_2$) on calcium sulfoaluminate cement hydration. More specifically, it addressed the effect on paste hydration rate, setting times and mechanical strength development. The reaction products were characterised with XRD and SEM.

2. EXPERIMENTAL PROCEDURE

2.1 Sulfoaluminate cement

The chemical and mineralogical composition of the commercial calcium sulfoaluminate (CSA) cement used, ALICEM©, are given in Table 1. XRD-Rietveld **[17]** mineralogical analysis revealed that the cement contained 52.6 % ye'elimite, 22.1 % anhydrite and 19.9 % calcium silicate (C_2S+Bredigite $[Ca_7Mg(SiO_4)_4]$). Particle size distribution was found on a Coulter LS130 laser diffraction analyser with a measuring range of 0.1 µm to 900.0 µm. Cement density was 2.90 g/cm^3, its Blaine fineness 474.6 m²/kg and its BET specific surface 1373±13 m^2/kg.

Table 1: CSA chemical and physical composition and mineralogical phases

Oxide	**CaO**	**Al_2O_3**	**SO_3**	**SiO_2**	**MgO**	**Fe_2O_3**	**Na_2O**	**Others**	**LoI[1]**
(%)	41.5	23.2	18.4	8.1	3.2	1.1	0.9	1.7	1.5

Phase	**$C_3A_3\overline{S}$**	**$C\overline{S}$**	**C_2S**	**C_3A**	**$Ca_7Mg(SiO_4)_4$**	**MgO**	**$Ca_2Al(AlSiO_7)$**
Content, wt% (R-Bragg)	52.6(4)	22.1(4)	14.9(4)	1.0(2)	5.0(5)	2.8(3)	1.6(5)

[1] Loss on ignition;

2.2 Paste preparation and characterisation

The CSA cement was hydrated with water in the absence or presence of 5 % chloride salts (NaCl and $CaCl_2$). All the pastes were prepared with a liquid/solid ratio of 0.45, by weight, and moulded into specimens cured in a climate chamber at 21±2 °C and >95 % relative humidity until the test date (2 d, 28 d or 90 d). Cubic specimens (1 cm^3) were tested for compressive strength on an Ibertest Autotest 200/100-SW test frame at a load rate of 0.07 kN/s. Twelve specimens per age were tested and the values averaged.

Heat flow and total heat release associated with the hydration reactions were determined with isothermal conduction calorimetry on a TAM AIR calorimeter at a

constant 25 °C. For this analysis the pastes were prepared with 10 g of solid and 5 g of liquid. Immediately after mixing for 3 min 7.5 g were placed in the calorimeter. Some of the fragments and the fine powder (<45 μm) were immersed in isopropyl alcohol to detain hydration. The powder was vacuum filtered and dried in a desiccator at 20 °C to a constant weight for microstructural analysis. Setting times were found as described in European standard EN 196-3.

X-ray diffraction was conducted on a Bruker DS Advance diffractometer under the following conditions: Cu kα1 and kα2 radiation with the secondary monochromator enabled; goniometer radius, 217.5 mm. Measurements were recorded at a 6 mm variable divergence slit (hydrated pastes), 2θ angles of 5° to 60°; a step time of 0.5 s; and a step size of 0.02°. Carbon-coated, vacuum dried samples were observed under a Hitachi S-4800 scanning electron microscope with a maximum resolution of 1.4 nm, fitted with a Bruker XRD detector.

3. RESULTS

3.1 Isothermal conduction calorimetry and setting time

Figure 1 shows the calorimetric curves for pastes REF, 5NCl and 5CCl. The REF material exhibited peaks at 1.6 h, 3.4 h and 6.1 h.

The curve for the NaCl-bearing paste (5NCl) had a single peak at 2.1 h with an intensity of 17.3 mW/g or twice as high as the first REF peak. No difference was observed in the induction period between pastes 5NCl and REF (Figure 1a). The former emitted heat more intensely up to 14.5 h, after which the REF values were higher (Figure 1b). Those findings indicated that the initial reaction was slightly earlier with 5 % NaCl, although the effect was mitigated after 14.5 h.

The pastes with $CaCl_2$ exhibited a first peak at 2.7 h with heat flow of 6.3 mW/g and a second weaker peak (2.1 mW/g) at 17.9 h. Paste 5CCl released total heat at a rate similar to REF up to 6.5 h and more thereafter. At 90 h heat release in REF amounted to 305.4 J/g, in 5NCl to 263.3 J/g and 5CCl to 324.8 J/g.

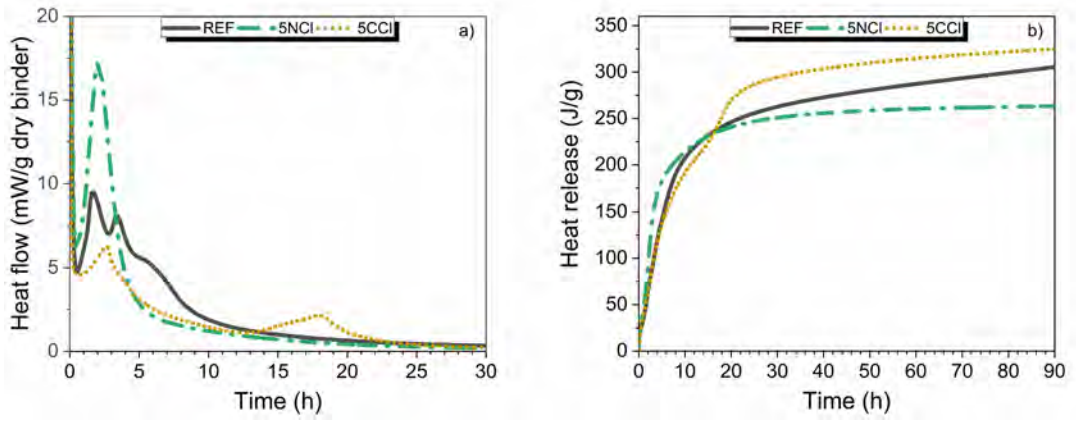

Figure 1: Effect of NaCl and $CaCl_2$ on a) heat flow rate and b) total heat released

As the data given in Table 2 show, initial and final setting times were similar in 5NCl and REF. In contrast, initial setting occurred substantially later in 5CCl, a finding consistent with the longer induction time observed on the calorimetric curves.

Table 2: Initial and final setting times

Sample	Initial setting time (min)	Final setting time (min)
REF	61	161
5NCl	65	150
5CCl	125	170

3.2 Mechanical strength

The 2 d, 28 d and 90 d compressive strength values found for the water-hydrated CSA pastes, with and without chloride salts, are graphed in Figure 2. Although the 5NCl material delivered around 15 % higher 2 d values than REF, the effect reversed at later ages, with strength 8 % lower at 28 d and 16 % lower at 90 d relative to the reference paste. The paste hydrated with water containing calcium chloride (5CCl), in turn, exhibited 2 d and 28 d behaviour similar to REF and higher 90 d strength (63.9 MPa).

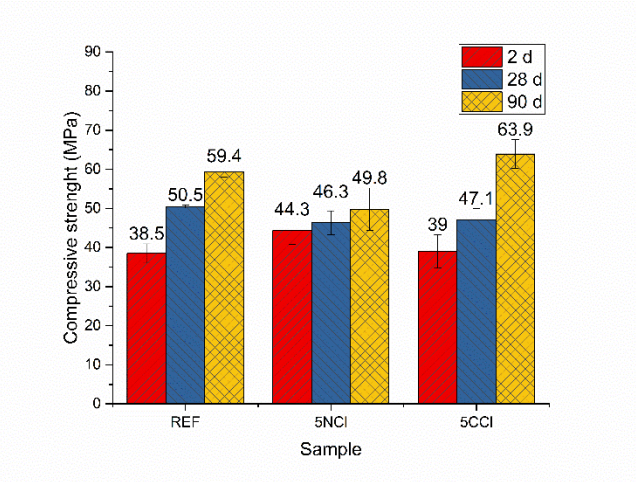

Figure 2: Two-day, 28 d and 90 d compressive strength in CSA pastes hydrated with or without 5 % chlorides

3.3 XRD analysis

The X-ray diffractograms for the anhydrous CSA cement and for the 2 d, 28 d and 90 d REF, 5NCl and 5CCl pastes are reproduced in Figure 3. Diffraction lines for ye'elimite ($C_4A_3\bar{S}$), anhydrite ($C\bar{S}$), ettringite ($C_6A_2\bar{S}_3H_{32}$), AH_3, and calcium carbonate ($CaCO_3$) were generated by all the samples The identification of AH_3 as a series of lines at 2θ values between 18° and 21° was indicative of a semi-amorphous or microcrystalline morphology [18]. Sodium chloride was also detected in the 5NCl samples at all ages.

The intensity of the ye'elimite and anhydrite reflections observed in the anhydrous CSA declined with hydration time. That decline was two-fold steeper for ye'elimite in the 2 d samples bearing chloride salts than in the reference and three-fold after 28 d. Anhydrite intensity also declined more in 5NCl and 5CCl than in REF, especially in the 2 d samples.

Ettringite, which formed as per Equation 3, was the prevalent crystalline hydration product on all the paste XRD patterns Paste 5NCl exhibited lower 2 d ettringite intensity than REF, but higher 28 d and 90 d values than the reference. The AH_3 forming was also observed to be more crystalline in the presence of chloride salts.

The most significant difference in the patterns between the pastes with and without salts was the appearance of gypsum at 28 d and 90 d in the former.

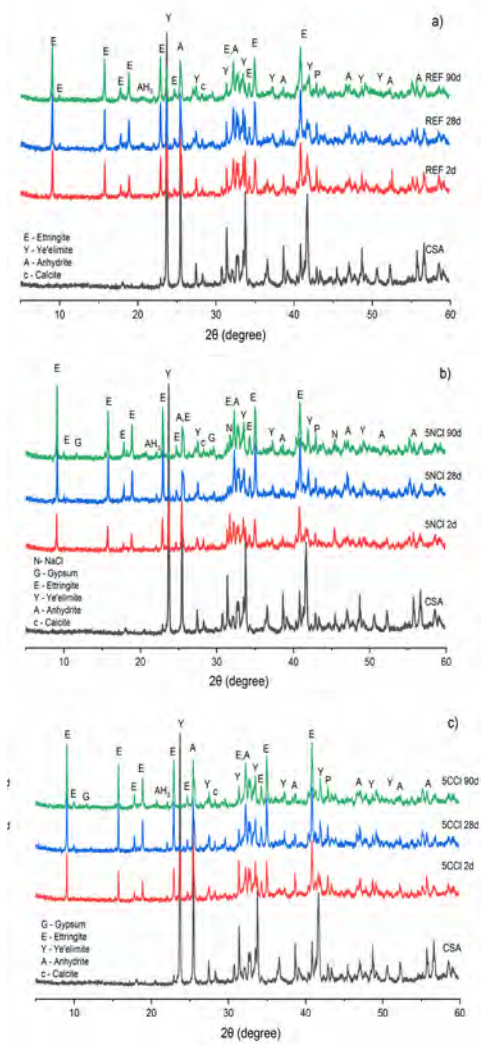

Figure 3: Two-day, 28 d and 90 d diffractograms for a) REF, b) 5NCl and c) 5CCl

3.4 SEM analysis

Micrographs for 28 d REF, 5NCl and 5CCl pastes are reproduced in Figures 4 and 5. The dense REF structure comprised a mix of AH_3 and slender ettringite needles (Figure 4b)). The ettringite phases observed in the chloride salt samples were similar, needle morphology (EDX1 and EDX3), whilst AH_3 was semi-amorphous (EDX4). Ettringite morphology was similar in the salt and non-salt samples, although different in size (Figure 4b). EDX analysis revealed the presence of chloride, although whether it was adsorbed onto the surface or formed part of the hydration products was difficult to discern. Rod-like gypsum crystals were also observed (Figure 5c)).

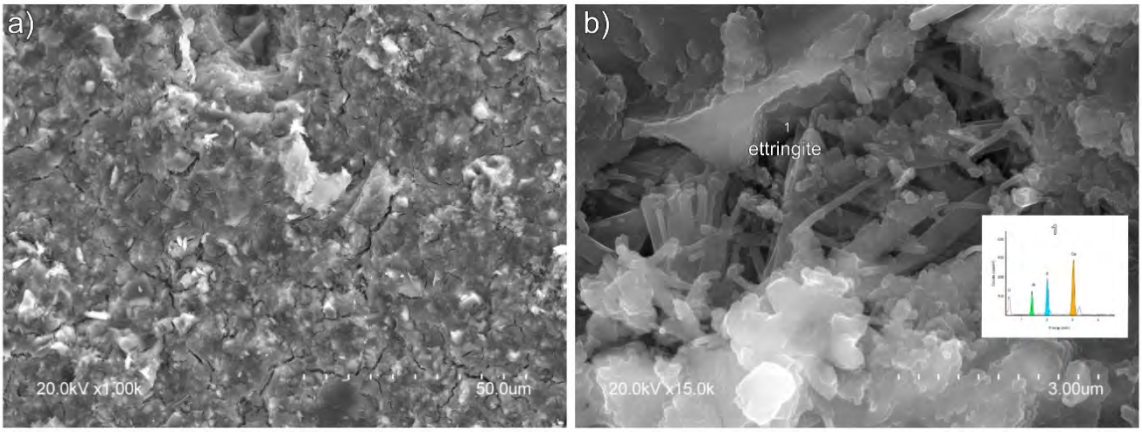

Figure 4: Micrographs and EDX for paste REF

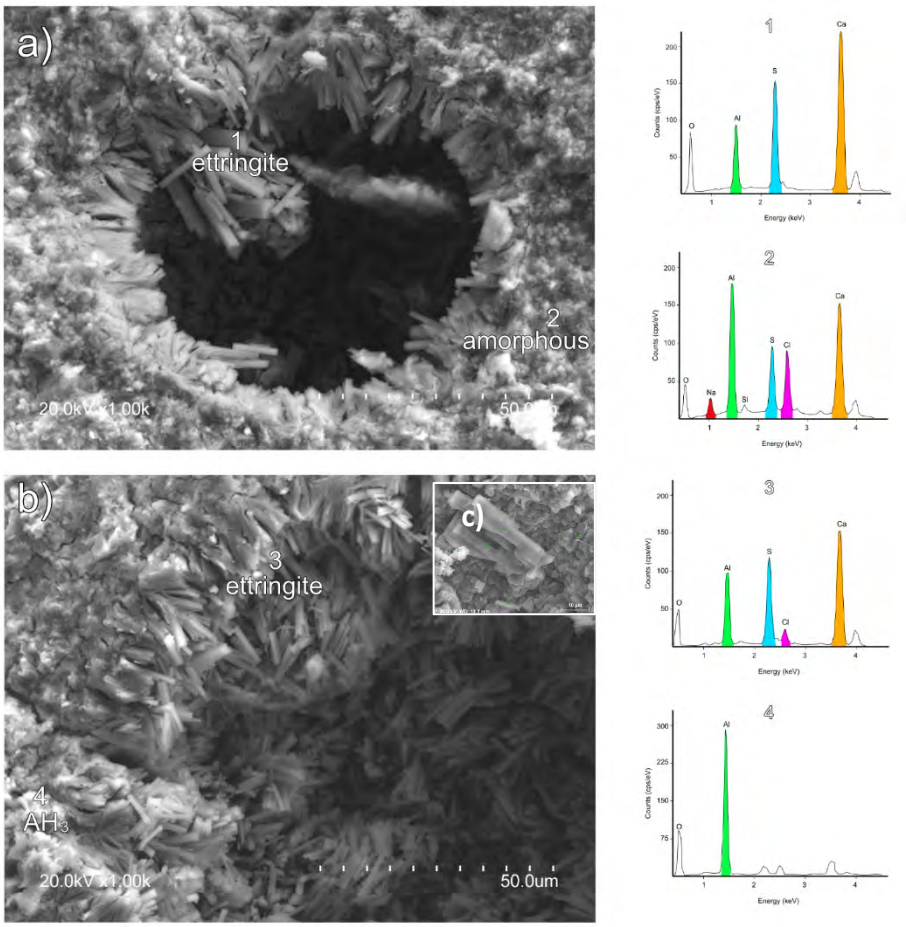

Figure 5: Micrographs and EDX for a) 5NCl and b) 5CCl; (c) gypsum crystals

3. DISCUSSION

Chloride salts shorten setting times in OPC but affect CSA cements differently. At the 5 % concentration studied here, setting times were slightly shorter in the NaCl pastes than in the ones hydrated with water only. In contrast, 5 % $CaCl_2$ retarded setting times, although it also increased later age compressive strength.

At 5 %, NaCl brought initial CSA cement hydration forward slightly, raising initial ye'elimite hydration and initial ettringite precipitation or growth. Ogawa and Roy **[1]** reported accelerated C_4A_3 hydration in an NaCl solution, with saturation taking place in the first few days. Similar behaviour may be attributed to multi-phase CSA cements. The heat release rate curves for 5NCl exhibited a single intense signal associated with the formation of large quantities of initial hydration product, which would explain the higher 2 d strength values. No significant rises in strength were observed in the 28 d or 90 d 5NCl materials, however.

Whilst the XRD findings revealed no AFm-Cl or Friedel's salt -like compounds in the 5 % NaCl pastes, Cl ions were observed in the matrix in the SEM micrographs. Therefore, the possible replacement of SO_4^{2-} with Cl^{1-} ions in AFt hydrate structure cannot be ruled out. In fact, studies currently underway have revealed Friedel's salt formation in pastes bearing 20 % NaCl. A possible working hypothesis is that in the presence of NaCl, Na ions may raise aqueous phase pH slightly. Earlier research [19] showed that pH raises initial ye'elimite dissolution, hastening the reaction (only one intense peak on the calorimetry curves compared to three with water only). That might explain the higher 2 d strength observed here. At 28 d and 90 d, degree of reaction and ettringite content also appeared to be greater with than without the salts (Figure 6), although strength did not rise significantly. That discrepancy was attributed to the possible existence of physical factors related to ettringite needle size and the presence of gypsum. Porosity and dimensional stability studies would be needed to confirm that

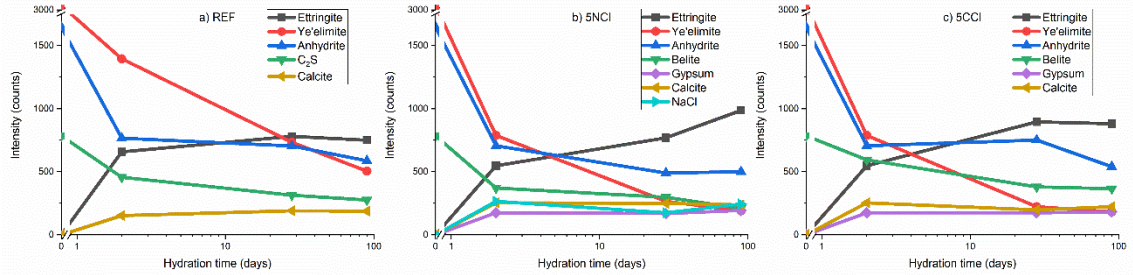

Figure 6: Intensity of the most prominent reflections observed in 2 d, 28 d and 90 d a) water-hydrated, b) 5NCl and c) 5CCl pastes

Initial setting time was retarded by 5 % $CaCl_2$, which also lengthened the induction time on the heat release rate curves. That effect lowered 2 d strength slightly but raised later age values relative to the reference paste. The 2 d XRD patterns showed ye'elimite consumption and ettringite and gypsum formation to be similar in the 5CCl and 5NCl materials, inferring that using one salt or the other has primarily early age implications.

Adding $CaCl_2$ would be expected to lower and adding NaCl to raise pH. $CaCl_2$ detained ye'elimite and other cement clinker phase dissolution, but not the anhydrite reaction. Consequently, gypsum was the sole early age crystalline phase formed. The $CaCl_2$ was consumed (undetected after 2 d). At a sufficiently low 5CCl concentration, ye'elimite would hydrate rapidly, explaining the second peak at 17.9 h and the greater heat of hydration released by this paste at later ages (Figure 1). A more detailed study of early age pastes to verify that hypothesis is currently underway and will be published shortly.

The presence of salts also induced slight variations in ettringite formation and morphology as well as gypsum precipitation, absent in the reference paste. That, in turn, would affect paste microstructure and porosity and consequently their mechanical performance.

4. CONCLUSIONS

This study was conducted as part of a broader research programme on the effect of chloride salts on CSA cement hydration. The preliminary results denote differences in behaviour relative to OPC. At a concentration of 5 %, NaCl hastened hydration, inducing higher initial strength. Conversely, 5 % $CaCl_2$ retarded setting times by up to a full hour and enhanced later age strength development.

In light of the low chloride concentration used in both cases the possible formation of AFm-Cl or Friedel's salt -like phases could not be detected. The presence of chloride salts affected ettringite morphology and formation, however, and induced gypsum formation, not observed in the reference paste. Further studies using higher salt concentrations and earlier age materials will be pursued to acquire a clearer understanding of the effect of chloride salts on CSA cement hydration.

ACKNOWLEDGEMENTS

This study was partially supported by the Brazilian National Council for Scientific and Technological Development (CNPq) under project 208380/2017-5, and CAPES. Financial support was also furnished by the Spanish Ministry of the Economy and Competitiveness and FEDER under research project BIA2016-76466-R. The authors wish to thank Heidelberg Cement Hispania for supplying the cement used in this research.

REFERENCES

[1] Shi, C., Qu, B., and Provis, J.L., 'Recent progress in low-carbon binders', Cem. Concr. Res. 122 (2019) 227–250

[2] Ogawa, K. and Roy D.M., 'C4A3$\bar{S}$ hydration, ettringite formation, and its expansion mechanism: III. Effect of CaO, NaOH and NaCl; conclusions', Cement and Concrete Research. 11 (2) (1982) 247-256 .

[3] Bullerjahn, F., Zajac, M., Ben Haha, M., 'CSA raw mix design: effect on clinker formation and reactivity', Mater. Struct. Constr. 48 (2015) 3895–3911.

[4] Zhang, F.P., Glasser, L., 'Hydration of calcium sulfoaluminate cement at less than 24h', Adv. Cem. Res. 14 (2002) 141–155.

[5] Janotka, I., Krajči, L., Mojumdar, S.C., 'Performance of sulphoaluminate-belite cement with high $C_4A_3\bar{S}$ content', Ceram. - Silikaty. 51 (2007) 74–81.

[6] Winnefeld, F., Martin, L.H.J., Müller, C.J., Lothenbach, B. 'Using gypsum to control hydration kinetics of CSA cements', Constr. Build. Mater. 155 (2017) 154–163.

[7] Jansen, D., Spies, A., Neubauer, J., Ectors, D., Goetz-Neunhoeffer, F., 'Studies on the early hydration of two modifications of ye'elimite with gypsum', Cem. Concr. Res. 91 (2017) 106–116.

[8] Luping, T. Nilsson, L.O., 'Chloride binding capacity and binding isotherms of OPC pastes and mortars' Cem. Concr. Res., 23 (2) (1993) 247-253

[9] Garcia-Lodeiro, I., Carcelen-Taboada, V., Fernández-Jiménez, A., Palomo, A. 'Manufacture of hybrid cements with fly ash and bottom ash from a municipal solid waste incinerator'. Construction and Building Materials, 105 (2016) 218-226

[10] Xu, Y. 'The influence of sulphates on chloride binding and pore solution chemistry', Cem. Concr. Res. 27 (12) (1997) 1841–1850.

[11] Glasser, F.P., Kindness, A., Stronach, S.A., 'Stability and solubility relationships in AFm phases Part I. Chloride, sulfate and hydroxide', Cem. Concr. Res. 29 (1999) 861–866.

[12] Hirao, H., Yamada, K., Takahashi, H., Zibara, H. 'Chloride binding of cement estimated by binding isotherms of hydrates' Journal of Advanced Concrete Technology. 3 (1) (2005), 77-84.

[13] Damidot, D., Glasser, F.P., 'Thermodynamic Investigation of the $CaO-Al_20_3-CaSO_4-H_2O$ System at 50°C and 85°C', Ceme. 22 (1992) 1179–1191

[14] Brown, P. W., Harner, C. L.,Prosen, E. J. 'The effect of inorganic salts on tricalcium silicate hydration'. Cement and Concrete Research. 16 (1) (1986) 17-22.

[15] El-Didamony, H., Sharara, A. M., Helmy, I. M., Abd El-Aleem, S., 'Hydration characteristics of β-C2S in the presence of some accelerators" Cement and Concrete Research, 26(8) (1996) 1179-1187.

[16] Singh, N.B., Ojha, P.N., 'Effect of $CaCl_2$ on the hydration of tricalcium silicate' J Mater Sci, 16 (1981) 2675-2681

[17] Rietveld, H.M., A profile refinement method for nuclear and magnetic structures, J. Appl. Crystallogr. 2 (1969) 65–71.

[18] Zhang, Y., Chang, J., Zhao, J., Fang, Y., 'Nanostructural characterization of $Al(OH)_3$ formed during the hydration of calcium sulfoaluminate cement', J. Am. Ceram. Soc. 101 (2018) 4262–4274.

[19] Tambara Jr, L.U.D., Cheriaf, M., Rocha, J.C., Palomo, A., Fernández-Jiménez, A. 'Effect of alkalis content on calcium sulfoaluminate (CSA) cement hydration', Cement and Concrete Research. 128 (2020) 105953.

EFFECT OF EARLY STRENGTH AGENT ON CEMENT SLURRY CONTAINING RETARDER

Liguo Wang (1), Siyi Ju (1), Lanxin Wang(1) and Jinyang Jiang (1)

(1) Jiangsu Key Laboratory of Construction Materials, School of Materials Science and Engineering, Southeast University, 211189 Nanjing, China

Abstract

Retarders have an important regulation effect on the hydration speed and setting time of cement. However, retarders are not conducive to the early strength development of concrete, so use early strength agents to improve their early performance. In this paper, the effects of different amounts of triethanolamine (TEA) and citric acid (CA) on the hydration dynamics and mechanical properties of silicate cement were investigated. The results showed that, as the CA content increases, the setting time of the cement slurry can be effectively prolonged. And the right amount of TEA can not only make the cement reach the early strength, but also increase the compressive strength in the later stage, and control the setting time of the cement paste. TEA shortens the induction period of CA-incorporated cement and increases the heat release rate during cement hydration induction period.

Keywords: Retarders, early strength agents, retarder, hydration dynamics, mechanical properties

1. INTRODUCTION

The different performance of concrete was required due to the special environment and construction conditions, the regulation of the hydration speed and setting time of cement is one of the research focuses in the field. Typically cement setting is controlled by using retarders or accelerators. Triethanolamine (TEA) and Citric acid (CA) are often used as admixtures to regulate the hydration process of cement. Although the combination of the two can lead to increased flexibility in construction methods, there are rarely used in combination.

Ramachandran and Lowery [1] investigated the effect of citric acid, and citrate on Portland cement hydration process respectively, the results showed by heat evolution rates that the hydration of Portland cement is retarded. Other investigations found that the zeta potential of cement decreases with increasing amounts of citric acid added, which can be

attributed to the adsorption of citrate ions onto the positively charged surfaces of the Portland cement grains[2]. Researchers also studies have been performed to examine the effects of TEA on hydration of cement. TEA acts as a set accelerator at low dosages and evidently enhances the early strength of cementitious materials [3], while in the case of the dosages of TEA higher than 0.1%, the opposite effects of set-retardation and the strength-loss at both early and late stages have been reported [4]. Previous research indicates that: strong accelerating effect on initial setting time caused by relatively high dosages of TEA ascribed to ettringite formation during accelerated tricalcium aluminate (C_3A, $3CaO{\cdot}Al_2O_3$) hydration but retard that of C_3S[5].

The purpose of this work is to investigate the compensation function of different TEA dosage for the excessive retarding caused by CA. The effects of different amounts of TEA (0.06%, 0.12%, 0.18%, 0.3%, 0.5%) and CA (0.2%) on the hydration dynamics and mechanical properties of silicate cement were investigated.

2. EXPERIMENTS

2.1 Materials

The cement used for this experiment was PII 52.5 ordinary Portland cement conforming to the Chinese Standard GB 175-2007，and the composition of Portland cement are shown in Table 1. Citric acid （CA）and triethanolamine（TEA）are provided by Sinopharm Chemical Reagent Co., Ltd. Other parameters such as setting time and compressive strength are shown in table 1.

Table 1: the composition of cement

Type	CaO	SiO_2	Al_2O_3	Fe_2O_3	SO_3	MgO	K_2O	loss
P·II52.5	64.95	18.31	4.21	2.95	4.22	0.64	0.788	3.21

Table 2:Physical properties of Portland cement

Type	density (g/cm^3)	Specific surface area (m^2/kg)	initial /min	final /min	Flexural strength /MPa		Compressive strength /MPa	
					3d	28d	3d	28d
P·II52.5	3.12	372	180	260	5.10	8.15	30.75	54.04

2.2 Mix proportions and methods

In order to investigate the composite effect of TEA and CA on the hydration of the Portland cement, all cement pastes investigated in this study were prepared at a w/c mass of 0.35, the characteristics of several mixes are shown in table 2.

Table 2: Mixes investigated

Mixes designation	% Citric acid	%Triethanolamine
C02T006	0.2	0.06
C02T012	0.2	0.12
C02T018	0.2	0.18

C02T03	0.2	0.3
C02T05	0.2	0.5

2.3 Characterization

Heat evolution over7days was measured in an isothermal calorimeter (TAM AIR Thermometric) for 5g paste samples. And the constant temperature is 20 °C. A 3 g sample is accurately weighed, placed in an ampoule bottle, and then sealed the ampoule bottle and placed into a calorimeter test 7days.

X-ray diffraction (XRD) was used to analyze the hydration products of cement pastes. XRD patterns were recorded at a scanning rate of 2°/min from 2θ=5° to 2θ=80° with Cu Kα radiation (λ=1.5418 Å) on a D max/RB diffractometer.

The setting time was determine according to GB/T1346-2011 “Test methods for Water Requirement of Normal Consistency, accurate to the minute.

Compressive strengths of the cement cement mortar with difference dosage admixture was measured according to the unconfined compression machine. Each compressive strength value represents the average of the results from 6 specimens tested.

3 RESULTS AND DISCUSSION

3.3 Setting time

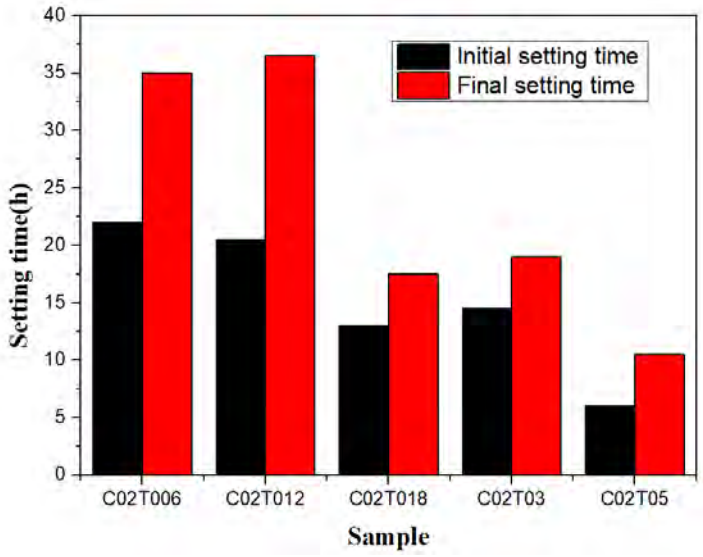

Figure 1: Influence of TEA on the setting time of cement paste containing CA

Fig.1 shows the effects of TEA on the setting time of cement paste containing CA. As can be seen from the figure, CA has obvious delay effect on cement paste, with the increase of TEA, we found the difference trend for the effect of dosage on initial setting time from previous studies[6,7]. When the dosage of TEA is greater than 0.18%, the accelerating effect on setting time are strongly observed. The presence of TEA significantly offset the retarding effect of citric acid. Meanwhile, the setting time is lightly prolong when the TEA dosage reaches 0.3%, However, when the TEA dosage added to 0.5%,the setting time is strongly accelerated and close to the setting time of the control cement paste.

3.2 Compressive strength

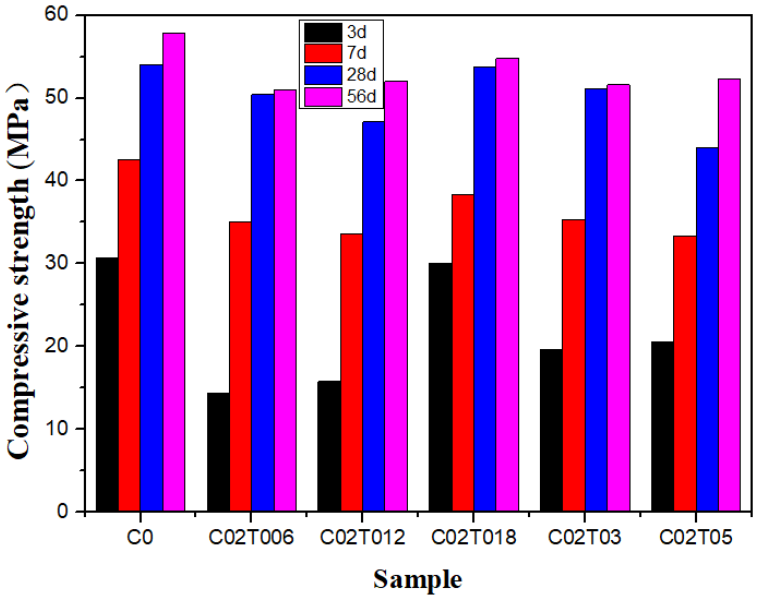

Figure 2: Effect of TEA on compressive strength of cement mortar containing CA

Effect of TEA on compressive strength of cement mortar containing CA is shown in fig.2, CA significantly decreased compressive strength of cement mortar in early age. By 3days of hydration, compare with C0 mortar, the compressive strength of C02T006, C02T012 reduced 53.41%, 48.7%, respectively, and the C02T03, C02T05 also decreased 36.18%, 33.3%. However, it is worth noting that the compressive strength of C02T018 is basically the same as control mortar. At 7 days, the same trend was observed for 3days, C02T018 still has the best mechanical properties among all samples, but the strength of other samples increases rapidly with the passage of hydration time. Ultimately, by 28 days of hydration, all the sample had lightly lower compressive strength than C0 mixture. The relationship between TEA and CA phase content development, reaction kinetics, microstructure, and mechanical properties is a subject of future research.

3.3 Hydration kinetics

Figure 3 shows an example of the relevant impact of addition of CA and variable dosages of TEA on hydration of cement. As shown in fig.3, the exothermic peaks of these samples show different trends to Portland cement hydration process due to TEA and CA added. The heat flow cures of cement is divided into multiple stages with TEA and CA added. The presence of CA significantly retarded the main peak of heat release occurred, Göril Möschner[8] suggested that citrate sorbed onto the clinker surface and formed a protective layer around the clinker grains retarding their dissolution.

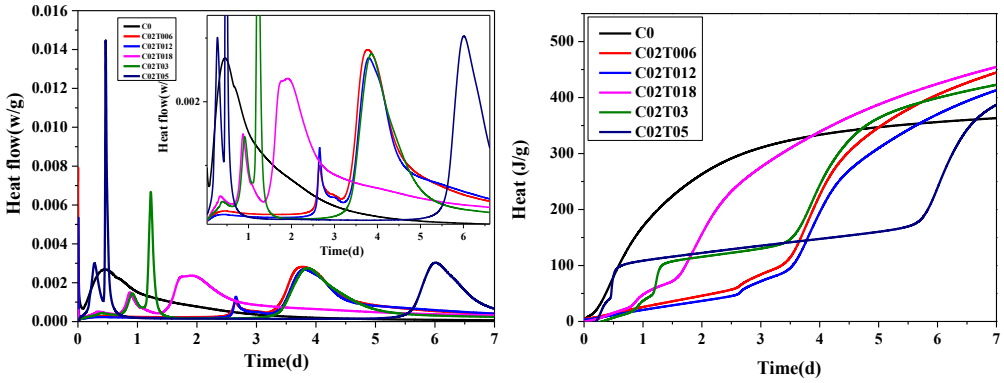

(a) Heat evolution **(b) Accumulative heat released**

Figure 3: Isothermal conduction calorimetry of CA with different TEA dosages

In specimen C02T006, two exothermic peaks are monitored during the hydration process, compare with control sample, CA has a retarding effect on the hydration of cement. The first peak was delayed about 48hours. However，the shape of the heat flow curves is significantly influenced by the presence of TEA, the first peak, in initial reaction period, is mainly resulted from ion dissolution and reaction between C_3A and calcium sulfate, usually resulting in formation of Aft. Previous research indicates that TEA accelerates C_3A hydration and C_3A–gypsum reaction by promoting formation of aluminate hydrate and Aft; The second peak, at the end of acceleration period, is mainly resulted from hydration of C_3S, forming C-S-H and calcium hydroxide (CH)[9]. As the TEA dosage increases, the heat flow cures of sample of C02T012 is similar to that of the C02T006. That means the relatively low TEA dosage has lightly effect on the hydration process of cement paste containing CA. When TEA dosage is higher than 0.18%, the hydration heat release rate in initial reaction period is promoted. Meanwhile, with the TEA dosage increase, the accelerating effect on hydration of cement paste is significantly. As the hydration time goes on, the hydration process of the slurry enters a dormant period, and the time of the dormant period increases with the increase of TEA content. Previous research indicates that: the TEA dosage effect on the cement hydration, at small dosage it acts as setting accelerator, at higher dosage it acts as setting retarder, at more higher dosage it acts as setting accelerator once again[10]

3.4 TG

According to the TG curve, the mass loss in the corresponding temperature range is defined as the dehydroxylation reaction (Ldx), dehydration (Ldh) and decarbonisation (Ldc), and the corresponding temperature range is listed in Table 4[11-13]. According to formula (1) and formula (2), the hydration degree of each sample can be calculated, and the results are listed in Table 4.

$$W_B = L\mathrm{d}h + L\mathrm{d}x + 0.41(L\mathrm{d}c) \quad (1)$$

$$\alpha = \frac{W_B}{0.24} \times 100 \quad (2)$$

Where WB is the total amount of chemical bound water; 0.41 is the conversion of

bound water in calcium hydroxide[13]; α is the degree of hydration of the sample; and 0.24 is the maximum amount of bound water required for cement hydration, generally 0.23-0.25[14,15].

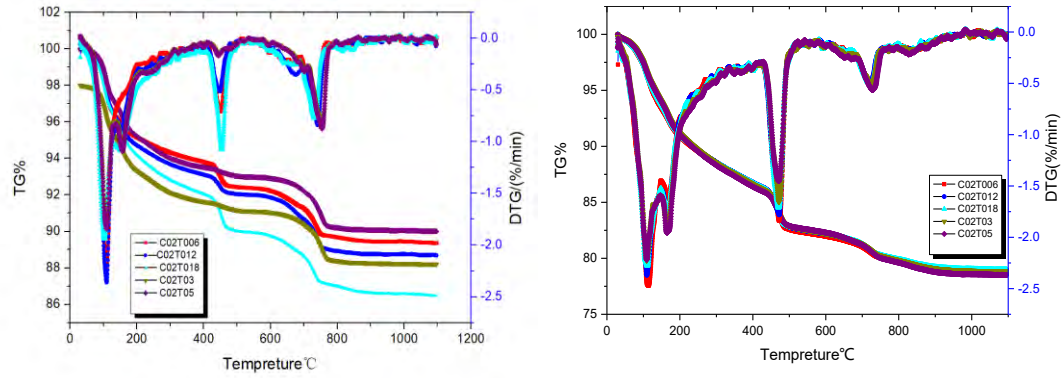

(a) 3days **(b) 28days**

Figure 4: The TG curve of CA with different TEA dosages

Table 3: The chemically bound water and the degree of hydration

	Sample	Ldh % (70-400℃)	Ldx% （400-580℃)	Ldc% （580-1000℃)	WB	a %
3days	C002T006	5.85	1.49	2.85	8.51	35.46
	C002T012	6.60	1.17	3.19	9.07	37.81
	C002T018	7.49	2.19	3.27	11.01	45.90
	C002T03	6.18	0.55	2.84	18.18	32.87
	C002T05	6.31	0.56	2.90	8.05	33.54
28days	C002T006	12.21	4.63	3.34	18.20	75.85
	C002T012	12.21	4.51	3.24	18.04	75.18
	C002T018	12.24	4.38	3.29	17.97	74.87
	C002T03	12.49	4.25	3.49	18.18	75.74
	C002T05	12.66	3.98	3.84	18.22	75.91

The total amount of chemically bound water and the degree of hydration of the sample are shown in Table 3. As shown in table 3, with the TEA dosage increase, the hydration degree of the cement paste showed a trend of first increase and then decrease as the compressive strength in the early age, the hydration degree of C02T018 was up to 45.9%. Ultimately, by 28 days of hydration, all samples have a the same degree of hydration. it indicated that TEA and CA has a greater effect on the early hydration of cement, and a smaller effect on the later stage.

4. CONCLUSIONS

The effects of different amounts of TEA and CA on the hydration dynamics and mechanical properties of silicate cement were investigated. The results as follows:

Proper amount of TEA can offset the delayed effect of CA on hydration. When the TEA dosage is 0.18%, the setting time is lightly delay compare to OPC sample, and the

compressive strength is similar to the same age OPC sample.

The total amount of chemical bound water and the degree of hydration of the sample results show that TEA and CA has a greater effect on the early hydration of cement, and a smaller effect on the later stage.

ACKNOWLEDGEMENTS

The authors greatly acknowledge Key R & D projects in Jiangsu Province (NO.BE2017158).

REFERENCES

[1] V.S. Ramachandran, M.S. Lowery, Conduction calorimetric investigation of the effect of retarders on the hydration of Portland cement, Thermochim. Acta 195 (1992) 373-387.

[2] N.B. Singh, A.K. Singh, S. Prabha Singh, Effect of citric acid on the hydration of Portland cement, Cem. Concr. Res. 16 (6) (1986) 911-920.

[3] J.P. Perez, A. Nonat, S. Pourchet, S. Garrault, M. Mosquet, C. Canevet, Why TIPA Leads to an Increase in the Mechanical Properties of Mortars Whereas TEA Does Not(International Concrete Research & Information Portal) 2003.

[4] Z. Heren, The influence of ethanolamines on the hydration and mechanical properties of Portland cement, Cem. Concr. Res. 26 (1996) 701-705.

[5] Hewlett P. Lea's chemistry of cement and concrete. 4th ed. U.K.: Elsevier; 2004.p. 881-887.

[6] I. Aiad, A.A. Mohammed, S.A. Abo-El-Enein, Rheological properties of cement pastes admixed with some alkanolamines, Cem. Concr. Res. 33(2003) 9-13.

[7] J. Han, K. Wang, J. Shi, Y. Wang, Mechanism of triethanolamine on Portland cement hydration process and microstructure characteristics, Constr. Build.Mater. 93 (2015) 457-462.

[8] G Möschner, B Lothenbach, Figi R, et al. Influence of citric acid on the hydration of Portland cement, Cem. Concr. Res.39(4) (2009)275-282.

[9] Bullard JW, Jennings HM, Livingston RA, et al. Mechanisms of cement hydration. Cem Concr Res 2011;41(12):1208-23.

[10] Gartner E, Myers D. Influence of tertiary alkanolamines on Portland cement hydration. J Am Ceram Soc 1993;76(6):1521-30.

[11] Jinyang J, Sun G, Sun W. Quantitative calculation of hydration products for binary slag-Portland cement system. J Wuhan Univ Technol (Materials Science Edition) 2014, 29(5):972-979.

[12] Pane I, Hansen W. Investigation of blended cement hydration by isothermal calorimetry and thermal analysis. Cem Concr Res 2005; (6):1155-1164.

[13] Monteagudo SM, Moragues A, Gálvez JC. et al. The degree of hydration assessment of blended cement pastes by differential thermal and thermogravimetric analysis. Morphological evolution of the solid phases. Thermochim Acta, 2014;(592): 37-51.

[14] Bhatty JI. Hydration versus strength in a portland cement developed from domestic mineral wastes-a comparative study.Thermochim Acta 1986;(106):93-103.

[15] Fischer P, McDowell C. The infrared absorption spectra of urea–hydrocarbon adducts. Can J Chem 1960;38:187-193.

EFFECT OF SULFATES ON HYDRATION AND PROPERTIES OF BELITE-RICH CEMENT PASTE

Antonina Goncharov (1) and Semion Zhutovsky (1)

(1) Faculty of Civil and Environmental Engineering, Technion - Israel Institute of Technology, Haifa, Israel

Abstract

It is common practice to use gypsum in cement production to control setting time. Traditionally it is believed that sulfate from gypsum combines with aluminates to form ettringite and monosulfate to prevent flash set. However, previous studies have confirmed that sulfates also affect the hydration and mechanical properties of pure alite paste. In view of recent research and development of cements with a low carbon footprint that are rich in belite, the question about the effect of sulfate on hydration and mechanical properties of belite arises. Moreover, this question becomes even more relevant considering the use of raw materials and fuels containing high content of sulfate-bearing impurities. In this work, the influence of the sulfate content on the hydration of belite-rich cement was studied by means of isothermal calorimetry and X-ray diffraction. The effect of sulfate content on compressive strength was also investigated. In the course of this study, an increase in hydration degree of belite with an increase of sulfate content in cement was observed. The compressive strength also increased with the addition of sulfate. The increase in hydration degree of belite and compressive strength of belite-rich paste was associated with the incorporation of sulfate in the cementitious gel as opposed to the ettringite formation.
Keywords: Gypsum, Belite, Cement, Hydration, Clinker

1. INTRODUCTION

Conventionally sulfates are added to a clinker at the last stage of cement production during the grinding process in the form of gypsum (dihydrate or hemihydrate) to control setting time and the speed of the initial hydration reaction of cement [1]. Cement workability is ensured by the presence of sulfates, which prevent the instant reaction between aluminate and water and delay the initial setting time beyond one hour [2]. The optimal content of gypsum depends on the type, fineness and mineral composition of cement and may vary within certain limits. The insufficient gypsum content causes an extremely rapid setting called flash set, while the excessive addition of sulfates in cement may lead to internal cracking due to extended ettringite formation [3]. Ettringite has a lower density (1.73 g/cm^3) in comparison to the average density of other hydration products which is around 2.5 g/cm^3. Ettringite crystals have an elongated needle-like structure that may cause crystalline pressure during formation resulting in volume increase, cracking and consequently deterioration in the hardening cement paste [4]. For this

reason, the concentration of sulfur in cement is regulated by standards. According to the old BS 12 [5], cements are divided into two groups by tricalcium aluminate content: below 7 or more than 7 % of tricalcium aluminate by weight cement with maximum SO_3 content of 2.5 % and 3 % by weight of cement, respectively. ASTM C150 standard [6] has a similar classification with division at 8% of tricalcium aluminate, and SO_3 content limited by 2.3 and 4.5 % by weight of cement, respectively, depending on the cement type. According to EN 197-1 standard [7], the maximum content of sulfur is limited by 4 % of SO_3 by weight of cement. It should be noted that the total sulfur content in the standards is the amount of combined sulfur from added gypsum and from raw materials of clinker. The sulfur trioxide content in clinker of ordinary Portland cement usually less than 1 % by weight.

Since the middle of the last century, scientists have taken a great interest in studying the influence of gypsum not only on setting time but also on mechanical properties of cement pastes and hydrated products [8,9]. In the course of these studies, it was found that gypsum affects the strength and dimensional stability of the cement paste [3,10]. The influence of sulfate on the mechanical properties of hydrated cement namely effect on compressive strength of great interest and requires further more detailed consideration. The previous studies demonstrated that increasing the dosage of sulfate initially increases the strength to a certain maximum and then the strength decreases with the increase of sulfate content in the cement composition.

As was stated above, traditionally, the sulfate content was dictated by the content of tricalcium aluminate in cement. However, previous studies demonstrated that sulfate also has an effect on the hydration of alite. The study conducted by Arnon Bentur [11] revealed that gypsum has a significant effect on the strength of alite pastes. He suggested that with an increase in gypsum content the amount of gel increases, while the quality, or rather its own strength, decreases [11]. In a recent work by Maciej Zajac et al [12], it was suggested that sulfate changes the porosity distribution and phase composition of hydrated cement. According to the authors: “The dilution of calcium- and alumina-silicate phases leads to a reduction of the C-S-H phase content. This reduction has a limited impact on the total amount of hydrates” [12]. At the same time, in another study, it was confirmed that with an increase in the concentration of gypsum, water amount also increases to obtain a normal consistency, which may indicate not only different fineness of cement with different contents of gypsum but also a modification in the hydration process [13]. This may indicate an increase in the number of hydration products in general, and of the C-S-H gel in particular.

It can be seen that different explanations based on various assumptions were given by different researchers to the phenomena of gypsum effect on mechanical properties. These explanations for changes in mechanical properties with change of gypsum content are not always complete and sometimes contradictory. Therefore, further research is required in order to clarify the mechanism of this phenomenon. In addition, the effect of sulfate on hydration and mechanical properties of belite was not systematically studied and calls for further investigation.

Recently, the volume of alternative fuel and raw materials with high sulfur content used in clinker furnaces has been increasing dramatically, which has led to an increase in the level of sulfate in the clinker. This change has affected the mineral composition of clinkers namely reduction of alite content, which led to slower strength development and also higher resistance to sulfate attack [14]. This trend also rekindled the interest to the effect of sulfate on mechanical and durability properties of hydrated cement paste and mortar.

The aim of this work was to study the properties of cement paste prepared using belite-rich cement with various gypsum content. In this paper, we focus on the effect of sulfate on the mineral composition of hydration products and the amount of amorphous phase (namely C-S-H gel), the heat of hydration, and the effect of sulfate content on compressive strength. Tests were carried out using belite clinker produced in the laboratory obtained from oil shale. Eight different contents of trioxide sulfate were studied. Sulfate was added to the clinker in the form of hemihydrate.

2. MATERIALS AND METHODS

2.1 Materials

In this research, a laboratory clinker prepared in the high-temperature bottom-loading furnace was used. Raw meal for clinker was prepared using 76 % wt. of oil shale from Northern Negev, Israel, limestone 18 % wt., quartz sand 6 % wt. Clinker was burned at a temperature of 1250 °C as described in detail in the previous publications [15,16]. The mineral composition of clinker as determined by XRD was 51.3 % wt. belite, 28.9 % wt. alite, 9.5 % wt. apatite, 4.0 % wt. brownmillerite, and 0.4 % wt. anhydrite. Clinker was ground in a disk mill to a size below 75 microns.

For cement preparation, reagent quality calcium sulfate hemihydrate was used ($CaSO_4 \cdot ½H_2O$ with a molar mass of 145.15 and LOI of 4.5-8 % wt.). Cement was prepared by intergrinding clinker with gypsum in a planetary ball mill 8 times for 5 minutes (40 minutes in total). Diethylene glycol was used as a grinding agent to prevent agglomeration and sticking to the mill walls and grinding balls. A total of 8 different cements were prepared with the following sulfur content between 1.5 and 5 % wt. of SO_3 by mass of clinker with steps of 0.5 % wt.

The cement paste for XRD analysis was prepared with water to cement ratio of 0.50 using a blender. The fresh paste was cast into a 50 ml plastic tube vials using vibration for 2 minutes. The paste remained in the sealed vials for 24 hours with constant rotation to prevent bleeding and segregation. At the age of 24 hours, the hardened cement paste was removed from the mold, cut into 5 mm-thick disks and placed in a saturated solution of calcium hydroxide for another 24 hours. After that, the sample was ground without drying and tested in XRD. Paste sample for isothermal calorimetry was prepared directly in glass calorimeter vials.

Mortars with water to cement ratio of 0.50 were prepared for compressive strength test using standard sand with cement to the sand ratio of 1/3. The preparation of samples for compressive strength was performed in accordance with the NF EN 196-1 standard [17], but with different mold size. In the current research cube samples with the side of 25 mm were used for the compressive strength testing. The cubes were demolded at the age of 24 hours and stored in the saturated solution of calcium hydroxide until the test.

2.2 Methods

The total heat of hydration for cements with different amounts of gypsum was determined using isothermal TAM AIR calorimeter. The samples for analysis heat of the hydration were prepared by mixing 3.3 grams of cement with 1.65 grams of distilled water (water-cement ratio of 0.5) directly in the calorimeter glass vial. The duration of the isothermal calorimetry test was 72 hours.

The mineral composition was determined by X-ray diffraction (XRD) using Malvern PANAlytical EMPYREAN X-ray diffractometer with the following configuration: an X-ray

source was CuKα1,2 (λ= 1.5408 Å) with X-Ray generator operated at a voltage of 45 kV and a current of 40 mA; a Goniometer radius was 240 mm; the incident beam optics included 10 mm mask, 0.04 rad Soller slit along with 1/8° divergence and 1/2° anti-scatter fixed slits; the diffracted beam optics consisted of 7.5 mm anti-scatter fixed slit. The detector was PIXcel 3D detector used in a 1D continuous scan mode. The scan was performed using Brag-Brentano geometry, between 5 and 70 °2θ for cement paste without stopping hydration. Time per step was 43.095 s with a step size of 0.007 º2θ were used resulting in a total measurement time of 21.00 min. The quantitative analysis was performed by means of Rietveld refinement using HighScore Plus software.

The compressive strength was determined using 6 25 mm cubes for each SO_3 content. The compressive strength was determined at the age of 48 hours similarly to described in NF EN 196-1 standard [17].

3. RESULTS

The total heat of hydration was determined using isothermal calorimeter for cement with various sulfate content. The total heat of hydration at 24 and 48 hours as a function of sulfate content is presented in Figure 1. Error bars indicate the double standard deviation which corresponds to 95 % confidence bounds. As seen from the graph heat of hydration after 48 hours increases monotonically with the increase of sulfate content in cement. However, this trend is different for the total heat at 24 hours, which demonstrates a maximum of around 3 and 3.5 % of SO_3 content. Apparently, maximum heat indicates the optimal value of gypsum in cement, especially considering that belite has a low heat of hydration. The difference in the trend of the heat of hydration at 24 and 48 hours can be explained by the delay of the sulfate depletion beyond one day at the SO_3 contents of 4 % wt. and above.

The results of the compressive strength test are shown in Figure 2. The compressive strength demonstrates a trend of progression with the increase of sulfate content. The increase in strength is steep between 1.5 and 3 % of SO_3, but between 3 and 5 % of SO_3, the increase becomes only moderate.

The mineral composition of hydrated cements was determined at the age of 48 hours using XRD. The most interesting information can be inferred from ettringite, belite and amorphous phase content. Figure 3 shows the relationship between the content of ettringite, belite and amorphous phase (which generally represents C-S-H gel) and the content of sulfate in cement. The trends in this relationship can be in principle divided into three stages: the first stage from 1.5 to 2% of SO_3, the second stage from 2 to 3.5 % of SO_3 and the third stage from 3.5 to 5 % of SO_3. At the first stage, the content of ettringite grows as fast as the content of belite decreases, while the amorphous phase remains almost unchanged, which may indicate that at the above stage sulfates contribute considerably to the formation of ettringite. At the second stage, the C-S-H gel grows as fast as the content of belite decreases, while ettringite content remains steady. This indicates that sulfate at this stage does not contribute to the formation of ettringite, but rather to the hydration of belite. It is possible that sulfate is involved in the formation of the cementitious gel microstructure, which is consistent with the calorimetry data at 24 hours. At the third stage above 3.5 % of SO_3, the content of the amorphous phase and belite slightly fluctuates around the same values, while the content of ettringite is slightly increased which may indicate the consumption of sulfate by the ettringite formation.

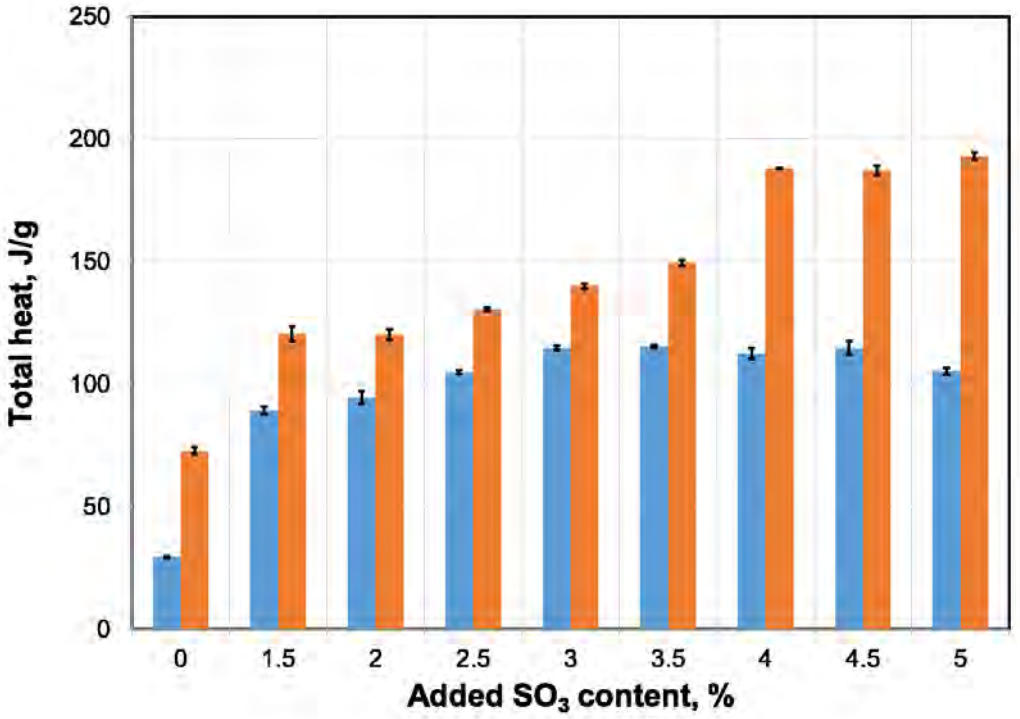

Figure 1: Heat of hydration as a function of sulfate content in cement

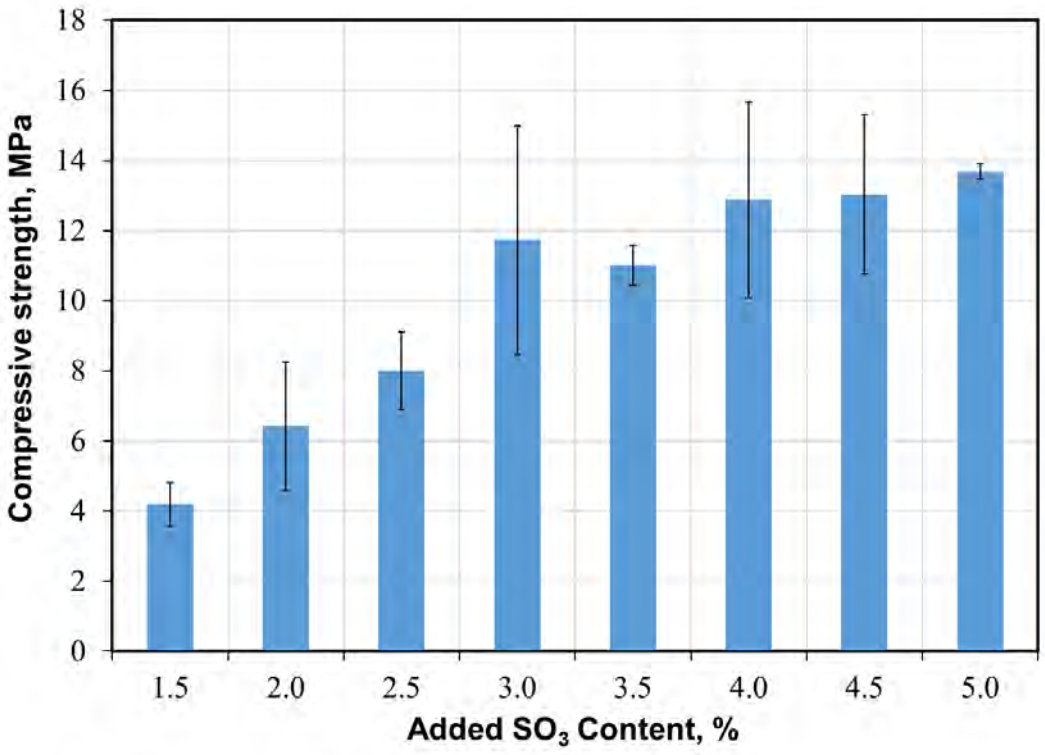

Figure 2: Compressive strength as a function of sulfate content in cement

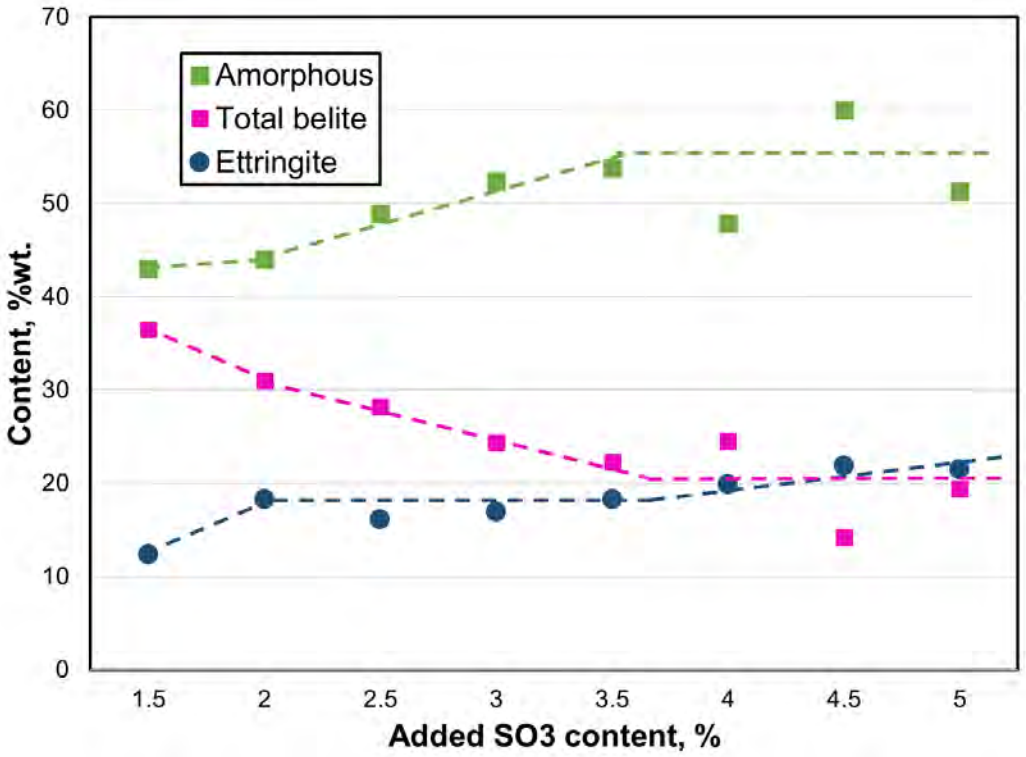

Figure 3: The content of belite, ettringite and amorphous phase in hydrated cement paste as a function of sulfate content in cement

As for the other phases of hydrated cement, they vary slightly with increasing sulfate: apatite is about 2%, alite is practically constant around 1%, brownmillerite is around 2.5%, portlandite is around 3%.

4. DISCUSSION AND CONCLUSIONS

Let us analyze the hydration belite and its connection with the sulfate content and compressive strength. The degree of hydration of belite can be easily calculated based on the content of belite in cement before the hydration, the amount of belite in the hydrated paste for each SO_3 content, and considering the water-cement ratio of 0.50 in cement paste. Figure 4 shows the relationship between the degree of hydration of belite and the content of sulfate in cement. As can be seen from the graph, (disregarding two points at 4 and 5% SO_3), this relationship demonstrates an almost perfect linear relationship, i.e., the degree of hydration of belite increases linearly proportional to the sulfate content in cement.

Similarly, a trend that presents the relationship between the compressive strength and the hydration degree of belite can be clearly seen in Figure 5. In this graph, it is apparent that with increasing degree of belite hydration compressive strength of mortar increases.

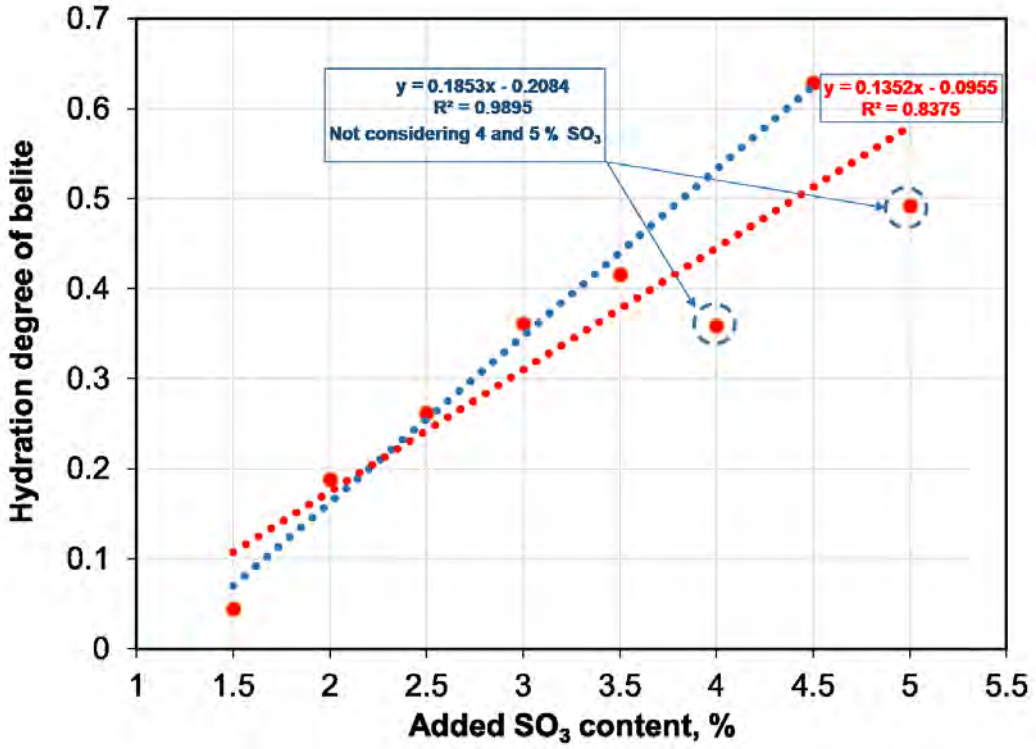

Figure 4: Hydration degree of belite as a function of sulfate content in cement

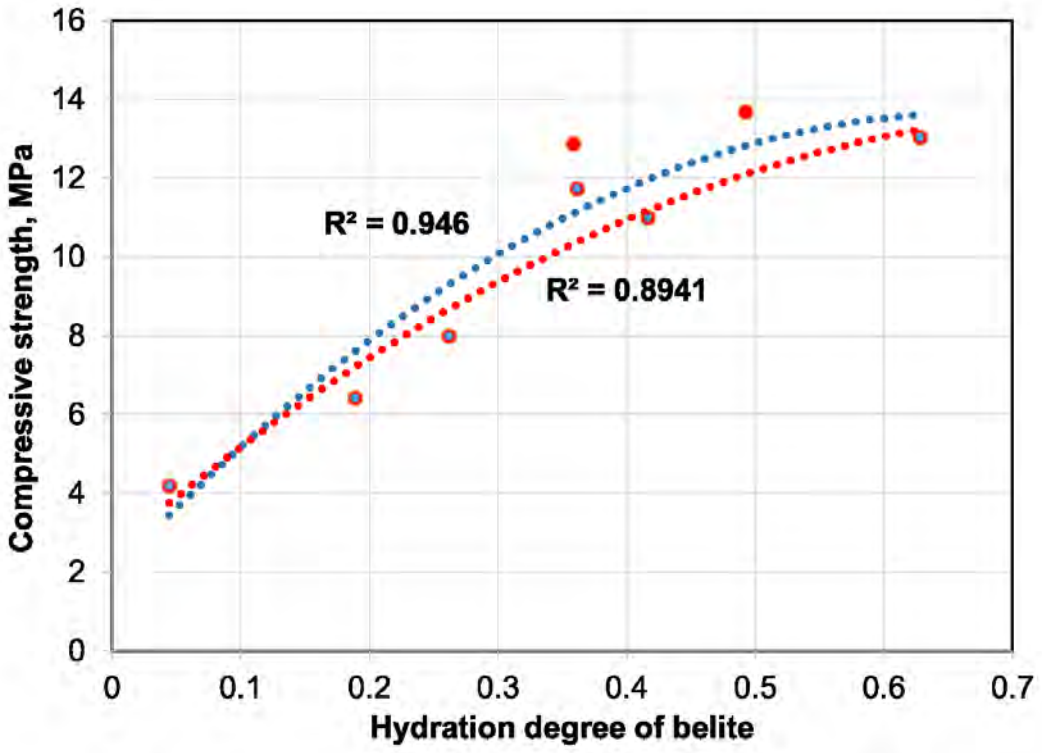

Figure 5: Compressive strength as a function of hydration degree of belite

Accordingly, it can be concluded that, at initial low values of gypsum in cement as well as excessively high contents, sulfates contribute considerably to the formation of ettringite, while at intermediate sulfate contents in cement, sulfate contributes to the hydration of belite and is involved in the formation of C-S-H gel. Thus, the maximum sulfate content that still significantly accelerates the belite hydration and does not contribute additional ettringite can be defined as optimal. This optimal sulfate content also contributes to the development of compressive strength by means of promoting belite hydration. Although it can be concluded that sulfates promote the hydration degree of belite, further research is needed to clarify the mechanism of this effect and better understand the role of sulfate in the formation and microstructure of C-S-H.

4. ACKNOWLEDGMENTS

This study was supported by the Ministry of National Infrastructures, Energy and Water Resources, Israel.

REFERENCES

[1] D.D. Sidney Mindess, J. Francis Young, Concrete, 2005.
[2] H.F.W. Taylor, Cement chemistry, 2nd ed., Thomas Telford, London, 1997.
[3] I. Soroka, M. Abayneh, Effect of gypsum on properties and internal structure of PC paste, Cem. Concr. Res. 16 (1986) 495–504. doi:10.1016/0008-8846(86)90087-6.
[4] I. Soroka, Portland cement paste & concrete, 1979. doi:10.1017/CBO9781107415324.004.
[5] BS 12:1996, Specification for Portland cement, Br. Stand. Inst. (1996).
[6] ASTM C150-12, Standard Specification for Portland Cement, American Society for Testing and Materials, 2012.
[7] BS EN 197-1:2011, Cement Part 1 : Composition, specifications and, British Standard Institution, 2011.
[8] W. Lerch, " The Influence of Gypsum on the Hydration and Properties of Portland Cement Pastes ", Proc. Am. Soc. Test. Mater. (1946).
[9] P. Hewlett, ed., Lea's Chemistry of Cement and Concrete, Butterworth-Heinemann, Oxford, UK, 2003.
[10] I. Soroka, M. Relis, Effect of added gypsum on compressive strength of portland cement clinker, Am. Ceram. Soc. Bull. (1983).
[11] A. Bentur, Effect of Gypsum on the Hydration and Strength of C3S Pastes, J. Am. Ceram. Soc. 59 (1976) 210–213. doi:10.1111/j.1151-2916.1976.tb10935.x.
[12] M. Zajac, J. Skocek, A. Müller, M. Ben Haha, Effect of sulfate content on the porosity distribution and resulting performance of composite cements, Constr. Build. Mater. 186 (2018) 912–919. doi:10.1016/j.conbuildmat.2018.07.247.
[13] S. Mohammed, O. Safiullah, Optimization of the SO3 content of an Algerian Portland cement: Study on the effect of various amounts of gypsum on cement properties, Constr. Build. Mater. 164 (2018) 362–370. doi:10.1016/j.conbuildmat.2017.12.218.
[14] S. Horkoss, R. Lteif, T. Rizk, Influence of the clinker SO3 on the cement characteristics, Cem. Concr. Res. 41 (2011) 913–919. doi:10.1016/j.cemconres.2011.04.015.
[15] A. Goncharov, S. Zhutovsky, Using oil shales for production of low-carbon Portland cement, 1st Int. Conf. Innov. Low-Carbon Cem. Concr. Technol. (2019) 4.
[16] A. Goncharov, S.. Zhutovsky, Comparison of clinkers produced using different layers of oil shale, in: Proc. 3rd Int. RILEM Work. Concr. Durab. Serv. Life Plan., Haifa, Israel, 2020.
[17] BS EN 196-1, Methods of Testing Cement Part 1: Determination of Strength, Br. Stand. Inst. (2016). doi:10.1590/S1413-294X2011000200001.

EFFECTS OF THE FINENESS OF DENSIFIED SILICA FUME ON THE HYDRATION OF PORTLAND CEMENT

Chenxin Ni (1), Zhuqing Yu (1) and Xiaodong Shen (1,2)

(1) College of Materials Science and Engineering, Nanjing Tech University, PR China

(2) The Synergetic Innovation Center for Advanced Materials, PR China

Abstract

As one of the mineral admixtures, silica fume (SF) with high pozzolanic reactivity is generally used to improve the properties of concrete. Most commercial silica fume used in concrete project is dry densified silica fume (DSF). It consists of a good deal of agglomerates of sizes ranging from 10 μm to several millimeters. The size of the undispersed silica fume is usually larger than that of the cement particle. At present, the effect of DSF on the hydration of cement is lack of studied.

In this study, the commercial dry DSF is sifted into three sections (>150 μm, 80 ~ 150 μm, 35 ~ 80 μm) by different sieves. The amount of densified silica fume in mixture is 5% by weight of total binder. The used water/binder ratio (w/b) is 0.5. The effect of the fineness of DSF on the setting time of cement paste is firstly discussed. The hydration process of cement incorporated with different fineness of SF is investigated by a semi-adiabatic calorimetric for 3 days at 20 °C and x-ray diffraction (XRD). The obtained results indicate that the setting time of cement paste increases with the decrease of the fineness of DSF. At the w/b ratio of 0.5, the addition of SF has little effect on the hydration period of cement paste. But the hydration rate of cement is decreased with the increase of the size of DSF particles.

Keywords: Densified silica fume, hydration, fineness

1. INTRODUCTION

Silica fume (SF) is a very fine amorphous silica powder produced in electric arc furnaces as a by-product of the manufacture of alloys with silicon or elemental silicon. Normally, SF is considered as a spherical particle. Actually, SF particle is not isolated each other. It is in the form of linked clusters of adjacent spheres[1, 2]. The size of original SF is between 10 nm and 500 nm. The specific surface area of SF is around 20000 m^2/kg, which is 13 to 20 times higher than that of other pozzolanic materials, determined by Nitrogen adsorption. Due to these characteristics, SF has high pozzolanic reactivity. It can rapidly react with calcium hydroxide produced by the hydration of cement.

The use of SF can improve the properties of concrete, such as strength, porosity and extend the service life of concrete structures. It is generally used in producing high-performance

concrete (HPC). In practice, SF is marketed as densified silica fume (DSF), since it is difficult to transport SF due to its extreme fineness and low density. Dry DSF is the aggregation of many linked clusters of adjacent spheres. The size of these aggregation ranges from tens to hundreds microns. That could results in the change of some physical properties of SF, such as particle size, particle size distribution and bulk density.

The silica fume agglomerations are still observed in the cement pastes and concretes mixed with densified silica fume after 1 year of curing[1, 3, 4]. It is found that the core of agglomeration does not take part in hydration. These undispersed agglomerations sometimes can act as extremely reactive alkali-silica reaction (ASR) aggregates[5-8]. Besides, the effects between raw SF and DSF in the paste, mortar and concrete under low water to binder ratio are different[3, 9, 10]. Raw silica fume always can make more contribution to the compressive strength of paste, mortar and concrete than DSF in the case of same replacing level. In concrete, the fineness of SF has little influence on the content of CH at early ages, whereas the CH contents decreases with the increase of the fineness of SF at 90 days. The particle size distribution of silica fume also has influence on the strength of Portland cement paste[11].

In the view of above, the presence of silica fume agglomeration in concrete seems unavoidable under mixing by ordinary commercial concrete mixers. This work tends to evaluate the capacity of hydration of cement paste mixed with different particle size DSF. In this paper, the commercial dry DSF is sifted into three sections (>150 μm, 80 ~ 150 μm, 35 ~ 80 μm) by different sieves. The amount of densified silica fume in mixture is 5% by weight of total binder. The used water/binder ratio (w/b) is 0.5. The effect of the fineness of DSF on the setting time of cement paste is firstly discussed. The hydration process of cement paste incorporated with different fineness of SF is investigated by semi-adiabatic calorimetric for 3 days at 20 ºC and x-ray diffraction (XRD).

2. EXPERIMENTAL PROGRAMME

2.1 Materials

P.I 42.5 Portland cement with a specific surface area of 340 m^2/kg was used in this study. Densified silica fume was a kind of commercial product from Szechwan, China. The DSF was screened into three particle size ranges, which are >150 μm (DSF I), 80~150 μm (DSF II) and 35~80 μm (DSF III). The chemical compositions of raw materials are shown in Table 1 and Table 2 analysed by X-ray Fluorescence (XRF).

Table 1: Chemical compositions of cement, wt/%.

Composition	SiO_2	Al_2O_3	Fe_2O_3	CaO	MgO	SO_3	Na_2O_{eq}	f-CaO	LOI
Cement	22.37	4.36	3.38	61.08	2.43	2.45	0.506	0.86	1.33

Table 2: Chemical compositions of silica fume, wt/%.

Composition	SiO_2	Al_2O_3	Fe_2O_3	CaO	MgO	P_2O_5	K_2O	Na_2O	LOI
Silica fume	91.53	0.203	0.059	0.218	0.87	0.487	0.436	0.134	5.56

The particle characteristics of DSF are shown in Fig. 1. It can be found that the range of DSF particles size is from a few to hundreds micron range. Each particle is made up of many tens of

nanometers spheres. Its crystalline structure was tested by X-ray diffraction (XRD). From the XRD pattern (Fig. 2), the characteristic diffraction broad peak centered at 23° (2θ) confirms its amorphous nature. The median size d50 of DSF I, DSF II and DSF III was 172 μm, 81.7 μm and 42.8 μm respectively, determined.by laser particle size analyzer (Malvern Masterizer 2000).

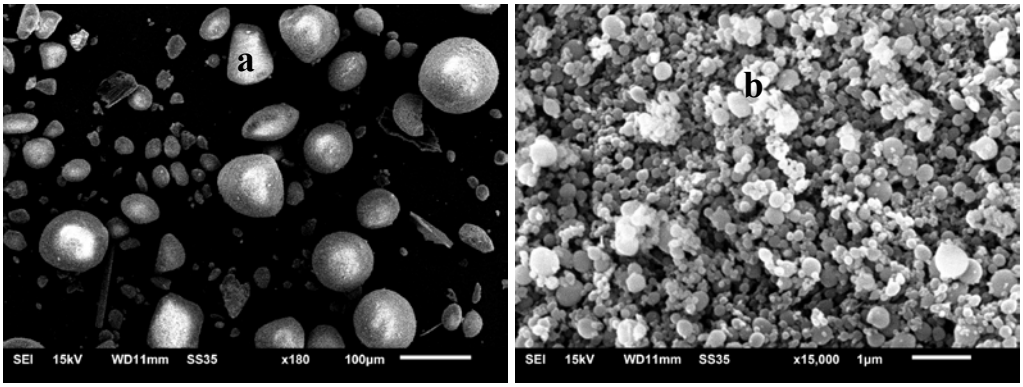

Figure 1: SEM figures of DSF: (a) agglomeration; (b) original SF particle.

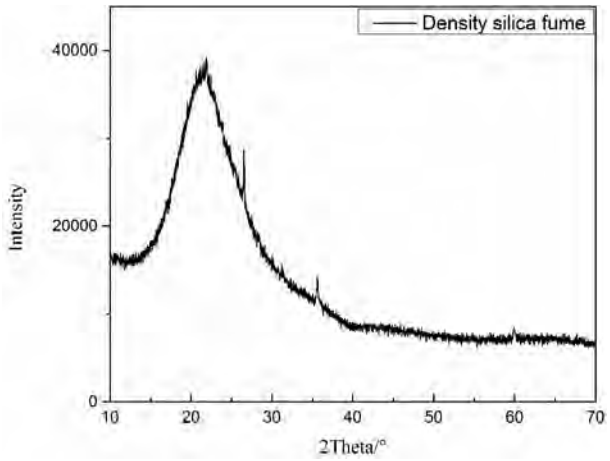

Figure 2: XRD pattern of density silica fume.

2.2 Specimens preparation

The replacement of DSF was 5% by weight of total binder. The water to binder ratio of all mixtures was set as 0.5. All specimens were prepared by overhead stirrers under 800 revolutions per minute, cast in plastic bottles, sealed and cured under 20 ± 1 ºC. At specified time, the sample was soaked in ethanol for 24 h to stop hydration.

2.3 Test methods

The setting time of standard consistency of cement paste was determined according to GB/T1346-2011[12]. The start of hardening of the cement paste after the addition of water to cement is called setting and it is divided into two parts called initial (IST) and final (FST) setting times.

Hydration process of the pastes was measured using an eight-channel isothermal calorimeter (TAM Air; Thermometric AB, Sweden). During the measurement, 4 g of cement and silica fume powder were mixed with 2 g of deionized water for 2 min in a sample vial. Then, the sample vials were loaded into isothermal calorimeter. Heat-flow curves were recorded for 72 h at a constant temperature of 20°C.

For XRD measurement, the specimens were crushed and ground by pestle in a agate mortar, In order to avoid the phase transformation or decomposition, ethanol was poured in the mortar when grinding the hydrated cement pastes. The ground powder was dried at 40 ℃ for 12 h in oven. XRD analysis was performed by using Rigaku SmartLab 3000A diffractiometer with CuKa radiation. All XRD scans were determined in the 2θ angle between 5 ° and 65 ° at the speed of 5° per minute.

3. RESULT AND DISCUSSION

3.1 The setting times of mixture

Water requirements for standard consistencies of cement paste mixed with DSF are given in Fig. 3(a). It is found that the addition of DSF increases the water requirement regardless of the fineness of DSF. The water requirement increases obviously with the decrease of particle size of DSF.

Variations of initial and final setting times are shown in Fig. 3(b). In the presence of 5 % DSF, two setting times are both increased. And the initial and final setting times increase with decreasing the particle size of DSF. It can be concluded that the addition of DSF retards the setting time of cement. This retarding effect is obvious when the size of DSF is in the range of 35 ~ 80 μm.

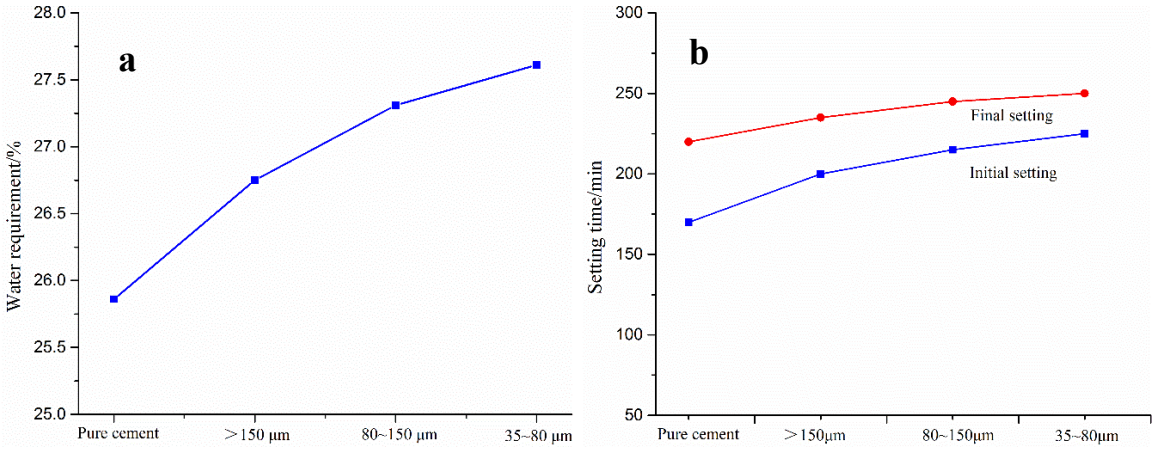

Figure 3: Variation of (a) water requirement and (b) setting time

3.2 Heat evolution

The Isothermal calorimetry data of cement paste are shown in Fig. 4. Four groups (Blank, >150 μm, 80~150 μm, 35~80 μm) are considered.

The hydration process of cement paste can be divided into five stages: the initial reaction period, the induction period, the acceleration period, the deceleration period, and the stable reaction period. As shown in figure 4(a), the addition of DSF does not change the induction process obviously. Due to its large particle, DSF can not provide extra nucleation site to cement

hydration. At early hydration state, DSF does not significantly change the hydration of cement. These experimental results are different from the results of some references because the DSF used are dispersed well by ultrasonic treatment [13,14]. Furthermore, it is clear that the rate of cement hydration tends to decrease when the particle size of DSF increases.

The cumulative heat curves corresponding to the heat flow curves are shown in Figure 4(b). The total hydration heat of blank simple is higher than the samples mixed with DSF. In 72 h, it seems that finer DSF generates more hydration heat.

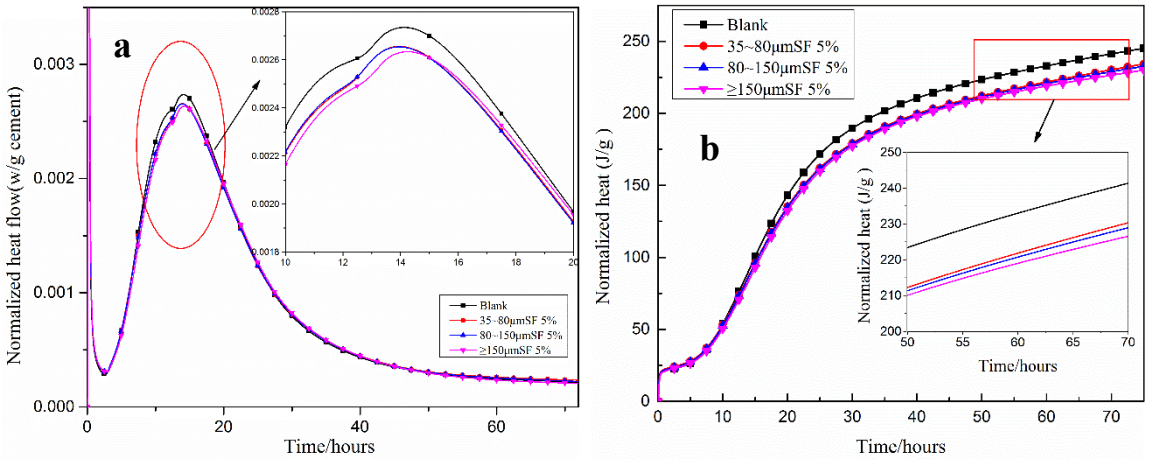

Figure 4: Isothermal calorimetry data of cement paste. (a: heat flow curves; b: cumulative heat curves.)

3.3 X-ray diffraction analyses

X-ray diffraction analysis was conducted to qualitatively investigate the effects of particle size of DSF on the mineralogical composition of cement paste. The experimental results are illustrated in Fig. 5.

Some main phases, such as ettringite, calcium hydroxide (CH), tricalcium silicate (C_3S) and dicalcium silicate (C_2S) are found in all mixtures. That indicates the addition of different sizes of DSF can not change the hydration products during the hydration of cement. However, differences in the intensity of individual peak are observed. For the hydration product, viz. CH, the intensity of characteristic peak ($2\theta = 18^o$) [15-18] increases with the decrease of the particle size of DSF at 15 h. It is clear that the presence of DSF promotes the formation of CH. At this period, it seems that the pozzolanic activity of DSF is not dominant.

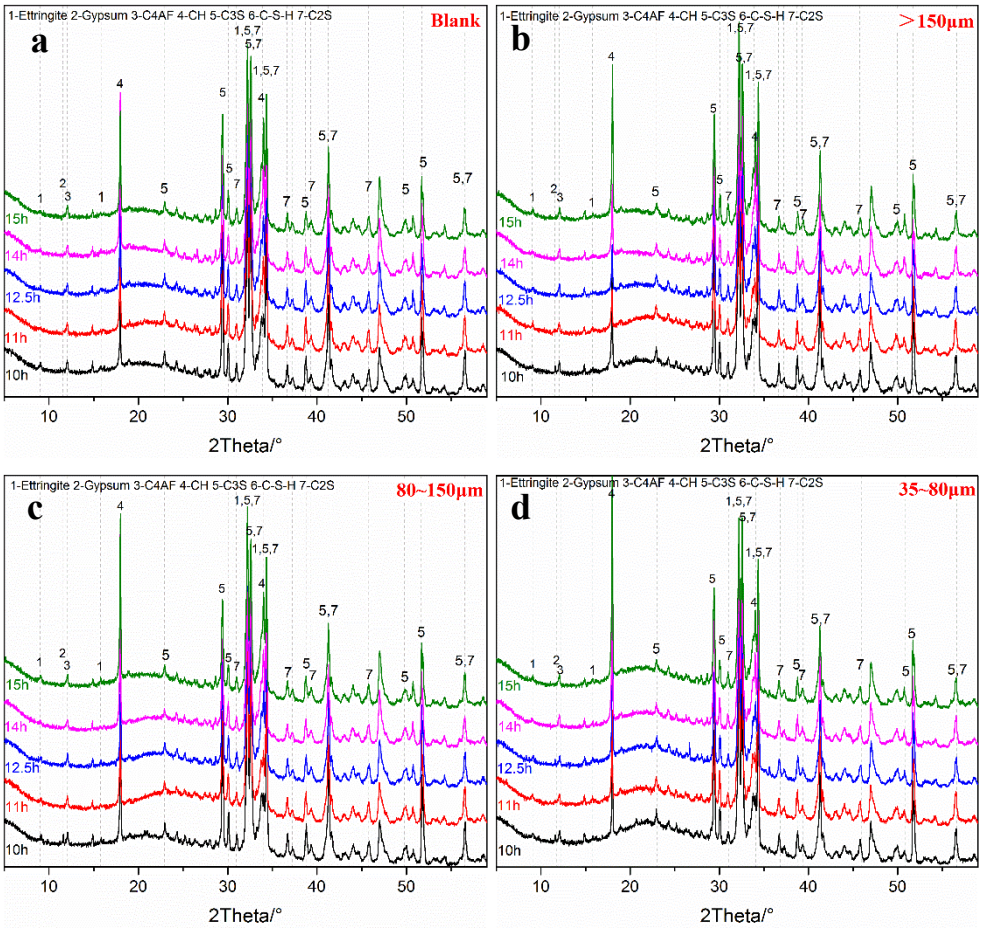

Figure 5: XRD patterns of hydrated cement pastes at different curing ages: (a) Blank cement; (b) ＞150 μm; (c) 80~150 μm; (d) 35~80 μm.

4. CONCLUSIONS

- The addition of DSF increases the setting time of cement. The particle size of DSF smaller, the retarding effect is more significant.
- The fineness of DSF affects the formation of CH during the hydration of cement. More hydration product, CH is generated in the samples mixed with the DSF III (35~80 μm). Meanwhile, in 15 hours, it seems that the pozzolanic activity of DSF is not dominant.

ACKNOWLEDGEMENTS

I hereby express gratitude for the financial support of the National Key R & D Program of China (Grant No. 2017YFB0310002).

REFERENCES

[1] Diamond S, Sahu S. 'Densified silica fume: particle sizes and dispersion in concrete'. *Mater. Struct*.**39**(9)(2006)849-859.

[2] Rodriguez E D, Soriano L, Paya J, et al. 'Increase of the reactivity of densified silica fume by sonication treatment'. *Ultrason. Sonochem*.**19**(5)(2012)1099-1107.

[3] Zhang Z Q, Zhang B, Yan P Y. 'Comparative study of effect of raw and densified silica fume in the paste, mortar and concrete'. *Constr. Build. Mater*.**105(**2016)82-93.
[4] Ji Y J, Cahyadi J H. 'Effects of densified silica fume on microstructure and compressive strength of blended cement pastes'. *Cem. Concr. Res*.**33**(10)(2003)1543-1548.
[5] Marusin S L, Shotwell L B. 'Alkali-silica reaction in concrete caused by densified silica fume lumps: A case study' *Cem. Concr. Aggreg*.**22**(2)(2000)90-94.
[6] Rangaraju P R, Olek J. 'Evaluation of the potential of densified silica fume to cause alkali-silica reaction in cementitious matrices using a modified ASTM C 1260 test procedure'. *Cem. Concr. Aggreg*.**22**(2)(2000)150-159.
[7] Juenger M C G, Ostertag C P. 'Alkali–silica reactivity of large silica fume-derived particles'. *Cem. Concr. Res*.**34**(8)(2004)1389-1402.
[8] Diamond S, Sanu S, Thaulow N. 'Reaction products of densifted silica fume agglomerates in concrete'. *Cem. Concr. Res*.**34**(9)(2004)1625-1632.
[9] Zhang Z Q, Zhang B, Yan P Y. 'Hydration and microstructures of concrete containing raw or densified silica fume at different curing temperatures'. *Constr. Build. Mater*.**121(**2016)483-490.
[10] Yan P, Zhang B. 'Mechanical Properties of High Strength Concrete Prepared with Different Densities of Silica Fume'. *Chin. Chem. Soc.* **44**(2)(2016)196-201.
[11] Ssnju N M Á, Argiz C, G Lvez J C, et al. 'Effect of silica fume fineness on the improvement of Portland cement strength performance'. *Constr. Build. Mater*.**96**(2015)55-64.
[12] GB/T1346-2011, Test method for water requirement of normal consistency, setting time and soundness of the Portland cement. National standardization administration of China, 2011, 8 pages
[13] Meng W N, Lunkad P, Kumar A, et al. 'Influence of Silica Fume and Polycarboxylate Ether Dispersant on Hydration Mechanisms of Cement'. *J. Phys. Chem. C.* **120**(47)(2016)26814-26823.
[14] Ma R, Guo L P, Sun W, et al. 'Well-Dispersed Silica Fume by Surface Modification and the Control of Cement Hydration'. *Adv Civ Eng.* **10**(2018).
[15] Zhu J, Feng C, Yin H, et al. 'Effects of colloidal nanoBoehmite and nanoSiO_2 on fly ash cement hydration'. *Constr. Build. Mater*, **101**(2015)246-251.
[16] Singh L P, Bhattacharyya S K, Shah S P, et al. 'Studies on early stage hydration of tricalcium silicate incorporating silica nanoparticles: Part I'. *Constr. Build. Mater*,**74(**2015)278-286.
[17] Singh L P, Bhattacharyya S K, Shah S P, et al. 'Studies on early stage hydration of tricalcium silicate incorporating silica nanoparticles: Part II'. *Constr. Build. Mater*,**102**(2016)943-949.
[18] Sun J F, Shi H, Qian B B, et al. 'Effects of synthetic C-S-H/PCE nanocomposites on early cement hydration'. *Constr. Build. Mater.***140**(2017)282-292.

EFFECTS OF THE PRE-ABSORPTION OF SUPERABSORBENT POLYMERS AND THE WATER-CEMENT RATIO OF PASTE ON THE ADSORPTION-DESORPTION OF SUPERABSORBENT POLYMERS: AN NMR STUDY

Jingbin Yang (1), Zhenping Sun (1), Ji Yanliang (1), Biyun Li (1) and Min Pang (1)

(1) Key Laboratory of Advanced Civil Engineering Materials of Ministry of Education, School of Materials Science and Engineering, Tongji University, Shanghai, 201804, China

Abstract

As an internal curing material, superabsorbent polymers (SAPs) can effectively reduce the risk of volume shrinkage of cement-based materials. By preparing the cement paste mixed with SAPs, the amount of pre-absorbed water and the water-cement ratio of paste on the water absorption-release behavior in the fresh cement paste were studied by using ^{1}H low-field NMR. The results showed that when the water-cement ratio was 0.30, the SAPs without pre-absorption could absorb the mixing water from the fresh paste and stored the mixing water in the SAPs relatively stable, while the pre-absorbed SAPs released the absorbed water into the paste rapidly, and the more pre-absorbed water, the faster the water released after mixing. When the water-cement ratio was increased to 0.40, the mixing water absorbed by SAPs without pre-absorption was more than that absorbed by SAPs when the water-cement ratio was 0.30, but in the system with super high water-cement ratio of 0.50, the SAPs cannot absorb mixing water from the paste after mixing.

Keywords**:** superabsorbent polymers, ^{1}H low-field NMR, mixing method, water-cement ratio

1. INTRODUCTION

High-performance concrete is produced and cured by modern technology. The main characteristics of high-performance concrete in mix proportion design are to use enough high-efficiency admixtures to ensure a low water-cement ratio. However, when the water-cement ratio is too low, autogenous shrinkage will occur, resulting in cracking[1]. For the high-performance concrete with compact structure, the environmental moisture provided by external curing can hardly enter the interior of concrete and compensate for the water consumed by cement hydration reaction. This means that the traditional curing method cannot guarantee the full hydration and control the autogenous shrinkage. Superabsorbent polymers (SAPs) are cross-linked hydrogel networks consisting of water-soluble polymers, and they can absorb and retain water hundreds of times their own weight[2]. In recent years, many studies have focused on SAPs in cement and concrete, SAPs are effective in reducing the autogenous shrinkage of

high-performance concrete or high-strength mortar, and even self-sealing and self-healing cracks.

There are two mixing methods of the SAPs and concrete in previous literature[3-5]. The first is to mix the SAPs pre-absorbed a certain amount of water before mixing, and control the amount of additional water of SAPs by changing the amount of these pre-absorbed water. However, in this mixing method, whether and how the factors such as the amount of pre-absorbed water affecting the behavior of SAPs in the paste is not fully known. The second is to dry mix the SAPs with cement or supplementary cementing materials before adding water, and control the fluidity of the sample containing SAPs is the same as that of the reference sample, so the difference between the water-cement ratio of the SAPs sample and that of the reference sample is the amount of additional water of SAPs. In the second mixing method, Yang et al.[6] proved that SAPs have different swelling capabilities in the pore fluids with different the water-cement ratios, but the result was evaluated in the filtrate of paste, not in the original paste. Whether these two mixing methods can effectively adjust the amount of additional water of SAPs, and the effects of factors such as the two mixing method and the water-cement ratio of paste on the evolution of SAPs in fresh cement paste are also insufficient.

In this study, a more intuitive method, ^{1}H low-field NMR, was used to monitor the absorption-release behavior of SAPs in the fresh cement paste. The effects of the different mixing methods, the amount of pre-absorbed water and the water-cement ratio on the SAPs in the fresh cement paste were compared. This study can help to better understand the behavior of SAPs in cement and concrete and choose the appropriate mixing method of SAPs.

2. MATERIALS AND METHODS

2.1 Materials

To reduce the interference of paramagnetic substances to the ^{1}H low field NMR signal, the cement used in this study is white Portland cement (P.W. 425, Anqing, China), and its chemical composition (determined by an X-ray Fluorescence Spectrometer, PANalytical Axios, Netherlands) is shown in Table 1. A sodium polyacrylate-based SAPs (Socochem, Qingdao, China) with irregular particle shape were selected, its average particle size was 302.6 μm. The tea-bag method was used to determine that the water absorption ratio of the SAPs in deionized water was about 250 times of its own weight. The water for the cement mixing and the pre-absorbed by the SAPs were deionized water.

Table 1: Chemical composition of the white Portland cement

Component	CaO	SiO_2	Fe_2O_3	Al_2O_3	MgO	SO_3	Na_2O	K_2O	P_2O_5	Others
Mass fraction/ %	60.1	18.2	0.35	2.23	13.5	2.49	0.28	0.48	0.03	2.36

2.2 Preparation of AAS paste

There are two different ways of incorporation of SAPs in this study. In the first way, after mixing cement and deionized water according to the water-cement ratio of 0.3 for 30 seconds, then add the pre-absorbed SAPs (pre-absorbed water-cement ratios are 0.03 and 0.06), and continuously stirred for 30 seconds. The second is to mix the SAPs without pre-absorbed with the cement, then added deionized water according to the water-cement ratio of 0.3, 0.4 and 0.5, and stirred for 1 minute. The dosage of SAPs in all the paste samples is 0.03% (by cement mass).

2.3 ^{1}H low-field NMR test

The ^{1}H low-field NMR instrument (MICRO-MR20, Niumag, Shanghai, China) used for this study has a magnetic field of 0.5 T and a 25 mm Radiofrequency (RF) coil. After mixing, about 20 g of fresh paste was poured into a small glass bottle, which was then sealed by a polytetrafluoroethylene film. The transverse relaxation time (T_2) was measured using CPMG (Carr-Purcell-Meiboom-Gill) sequence and the parameters including the echo time ($\tau 1$ = 0.302 ms) and the number of scans (NS = 4) was kept constant. The T_2 relaxation curve was fitted to a multi-exponential curve by using the inverse Laplace transform algorithm.

3. RESULTS

3.1 Effect of the amount of pre-absorbed water on the behavior of SAPs in the fresh paste

Figure 1 shows the transverse relaxation time (T_2) distribution of cement pastes containing the SAPs without pre-absorption (the total water-cement ratio is 0.30+0), SAPs with 0.03 water-cement ratio of pre-absorption (the total water cement-ratio is 0.30+0.03) and SAPs with 0.06 water-cement ratio of pre-absorption (the total water cement-ratio is 0.30+0.06), respectively. The broad peaks in the T_2 range of about 1-10 ms and the peaks in the T_2 range of about 100-100 ms are attributed to water in the pores of the cement paste and water contained in the SAPs[7-9], respectively.

In Figure 1a, even if the SAPs were not pre-absorbed water, it can be observed that some mixing water was absorbed in the SAPs from paste after 5 minutes after mixing. Between 5 minutes and 1 hour after mixing, the intensity of the T_2 relaxation peaks of SAPs gradually increased, indicating that SAPs continued to absorb free water. And in the following 1 hour to 3 hours, the intensity of the T_2 relaxation peaks of SAPs was relatively stable, indicating that SAPs did not undergo severe water exchange with the fresh paste. In Figure 1b and Figure 1c, the SAPs pre-absorbed a certain amount of deionized water before mixing. However, the intensity of the T_2 relaxation peaks of the SAPs at 5 minutes after mixing was not higher than that of the SAPs at the same time in Figure 1a. And with the increase of the hydration time, the intensity of the T_2 relaxation peaks of the SAPs gradually decreased. In Figure 2b, only a tiny T_2 relaxation peak can be observed at 3 hours after mixing, while in Figure 1c, the T_2 relaxation peak of SAPs was nearly disappeared at 2 hours after mixing. This is, the pre-absorbed SAPs cannot absorb the mixed water from the paste; on the contrary, the pre-absorbed water will gradually release into the paste. Comparing the results in the Figure 1b and Figure 1c, the more pre-absorbed water by the SAPs, the faster the water release in the paste after mixing.

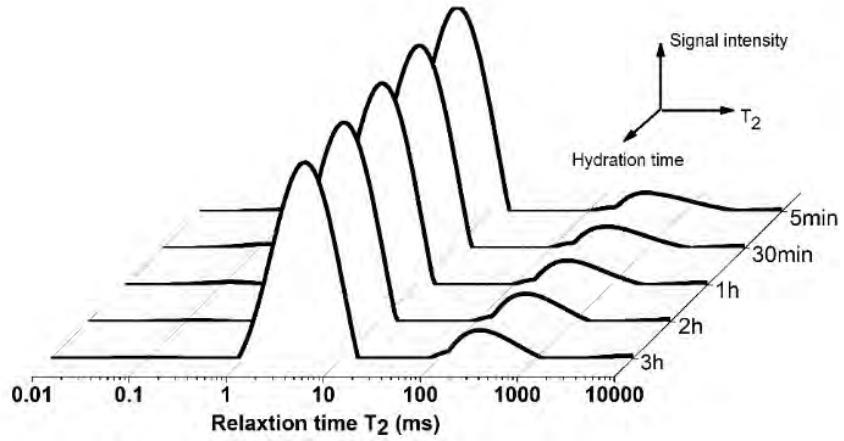

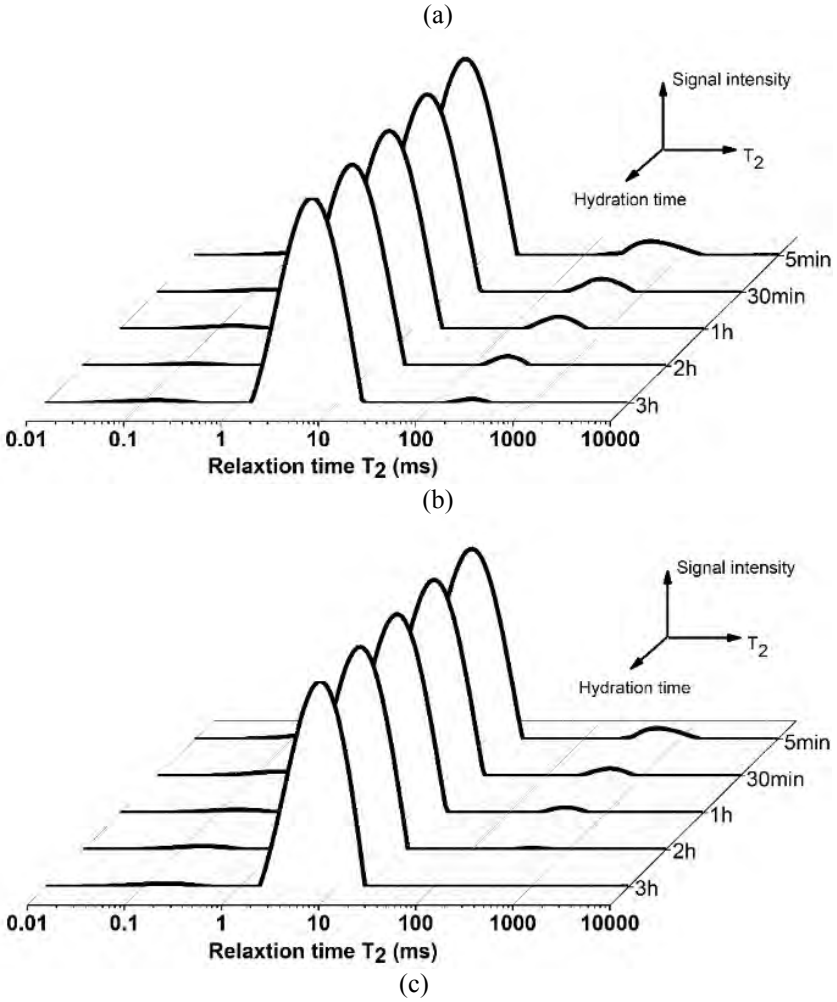

Figure 1: The transverse relaxation time (T_2) distribution of cement pastes containing the SAPs (a: the SAPs without pre-absorption, b: the SAPs with 0.03 water-cement ratio of pre-absorption, c: the SAPs with 0.06 water-cement ratio of pre-absorption)

3.2 Effect of the water-cement ratio on the behavior of SAPs in the fresh paste

To achieve a better internal curing effect, sometimes the water content in the SAPs has to be adjusted. However, the above results showed that it may not be an effective method to change the water content in the SAPs by pre-absorption of a certain amount of water, because the water pre-absorbed by the SAPs before mixing will gradually release into the paste after mixing, and it cannot play a role in adjusting the water content in the SAPs. A better result may be obtained by combining the SAPs without pre-absorption with cement, and it is possible to control the water content in the SAPs by increasing or decreasing the water-cement ratio of the paste.

Figure 2 shows the transverse relaxation time (T_2) distribution of cement pastes containing SAPs without pre-absorption (the total water-cement ratio is 0.40+0) and SAPs without pre-absorption (the total water cement-ratio is 0.50+0), respectively.

When the water-cement ratio of the paste was 0.40, it can be observed that the T_2 relaxation peak of the SAPs at 5 minutes after mixing, and the intensity of this T_2 relaxation peak is higher than that of the T_2 relaxation peak at the same time in Figure 1a. Then, the SAPs continued to

absorb water until the relaxation peak intensity slowly decreased after 1 hour after mixing, and the T_2 relaxation peak of SAPs at each time in the Figure 2a is higher than that at the same time in the Figure 1a, which indicates that increasing the water-cement ratio of the paste from 0.30 to 0.40 does increase the water content in the SAPs.

However, an interesting result is shown in Figure 2b. When the water-cement ratio was further increased to 0.50, except for a tiny T_2 relaxation peak of the SAPs that occurs at 5 minutes after mixing, no T_2 relaxation peak of the SAPs can be observed at other times. The results show that the SAPs do not absorb water from the paste at this water-cement ratio.

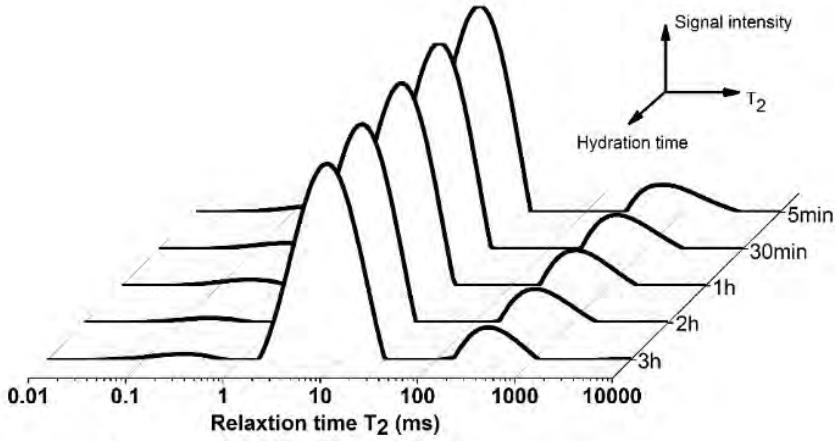

(a)

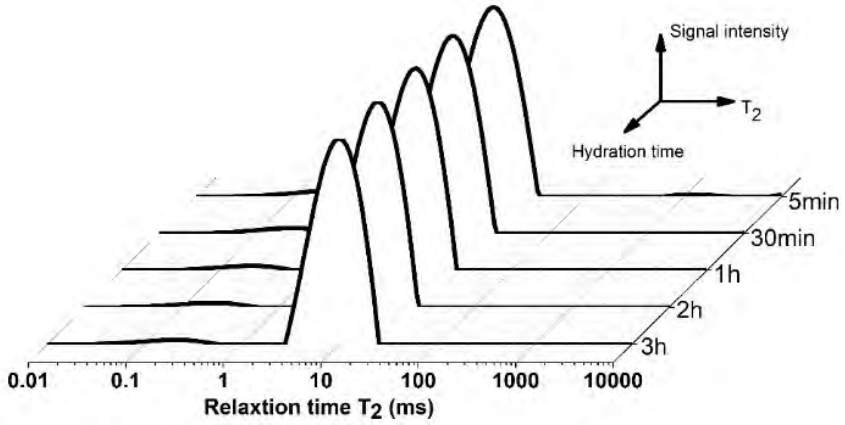

(b)

Figure 2: The transverse relaxation time (T_2) distribution of cement pastes containing the SAPs without pre-absorption (a: the water-cement ratio of paste is 0.40, b: the water-cement ratio of paste is 0.50)

4. DISCUSSIONS

The sodium polyacrylate-based SAPs ionizes in water or solvent, with the increase of ion concentration inside the SAPs, the concentration difference between the inside of the SAPs and the external solution causes reverse osmosis, so that the water enters the SAPs. This is the primary driving force for water absorption.

In the cement paste, the absorption capacity of SAPs is dependent on the external fluid composition and the chemical structure, length and crosslinking degree of the SAPs[5]. When

the SAPs with pre-absorption were added to the cement paste, due to the dissolution of the cement particles, there were a considerable amount of ions (such as Ca^{2+} and Na^{+}) in the liquid phase, which improved the ion concentration of the external solution of SAPs and reduced the concentration difference inside and outside the SAPs. While when the ion concentration of the external solution of SAPs was higher than that of the internal solution of SAPs, the inner solution of the SAPs would be reversely released into the outer solution due to the osmotic pressure. These can explain why after adding the pre-absorbed SAPs to the fresh paste, the SAPs released the pre-adsorbed water instead of absorbing water from the paste. With the increase of pre-absorbed water in the SAPs, the solution in SAP can be considered to be diluted and the internal ion concentration decreased. Therefore, when the water-cement ratio of the external paste was constant, the ion concentration difference inside and outside the SAPs structure was further enlarged, and the release of pre-adsorbed water was accelerated.

It has been known that the swelling capacity of SAPs in a solution is affected by the type and concentration of ions. In the cement paste with a low water-cement ratio generally contains a higher ion concentration, while the paste with a high water-cement ratio has a lower ion concentration in the liquid phase due to dilution[10]. Therefore, when the water-cement ratio of the paste increased from 0.30 to 0.40, the SAPs absorbed more mixing water. However, a high water-cement ratio may also accelerate the dissolution of cement particles, such as accelerating the dissolution of Ca^{2+}[11], while Ca^{2+} can combine the desirable groups in the SAPs structure to form stable complexes, thus reducing the absorption capacity. Therefore, when the water-cement ratio of the paste increased from 0.40 to 0.50, the swelling capacity of SAPs was inhibited, and it could not absorb water in paste with water-cement ratio of 0.5. These results are similar to those obtained by Yang et al.[6] in the filtered slurry, the SAPs achieved the highest absorption in the filtered slurry with water-cement ratio of 0.32, and when the water-cement ratio of the filtered slurry continued to increase to 0.36 and 0.40, the absorption of SAPs decreased. As for the difference of water-cement ratio corresponding to the highest water absorption of SAPs, it may be caused by the filtered slurry and the original cement paste.

5. CONCLUSIONS

In this study, the ^{1}H low-field NMR test was used to determine the water absorption-release behavior of a sodium polyacrylate-based SAPs in the fresh paste. The following conclusions can be drawn:

(1). Different mixing methods have an important effect on the water absorption-release behavior of the SAPs in the fresh paste. When the water-cement ratio of the paste was 0.30, the SAPs without pre-absorption could absorb the mixing water from the paste and stored the mixing water in the SAPs relatively stable, while the pre-absorbed water in the SAPs would quickly release into the paste within 3 hours after mixing, which cannot play an internal curing role. And the more pre-absorbed water, the faster the water release after mixing, it seems that it is not feasible to control the water content in SAPs by adjusting the amount of pre-absorbed water of the SAPs.

(2). When the water-cement ratio of the paste increased from 0.30 to 0.40, the SAPs without pre-absorption absorbed more the mixing water from the paste after mixing. However, when the water-cement ratio of the paste was further increased to 0.50, the SAPs without pre-absorption could not absorb the mixing water from the paste, which may be related to the high water-cement ratio promoting the dissolution of cement particles, increasing the ion

concentration (such as Ca^{2+} and Al^{3+}) in the liquid phase and inhibiting the swelling of SAPs. The water absorption of the SAPs from the paste can be adjusted by changing the water-cement ratio of the paste. However, due to the dissolution of cement particles and the sensitivity of the swelling of SAPs to the ions in the fluid, it is necessary to pay attention to selecting an appropriate water-cement ratio.

ACKNOWLEDGMENTS

This work was funded by the National and Technology Program During the 13th 5-year Plan Period (Grant No.2016YFC0701004), National Natural Science Joint Foundation of China (Grant No. U1534207), National Natural Science Foundation of China (Grant No. 51678441) and Research Project of Shanghai Science and Technology Commission (Grant No. 19DZ1202702 and 19DZ1201404).

REFERENCES

[1] A. Mignon, D. Snoeck, P. Dubruel, S. Van Vlierberghe, N. De Belie, Crack Mitigation in Concrete: Superabsorbent Polymers as Key to Success?, Materials 10(3) (2017).
[2] A. Mignon, G.-J. Graulus, D. Snoeck, J. Martins, N. De Belie, P. Dubruel, S. Van Vlierberghe, pH-sensitive superabsorbent polymers: a potential candidate material for self-healing concrete, J. Mater. Sci. 50(2) (2015) 970-979.
[3] M. Kim, S.-H. Kang, S.-G. Hong, J. Moon, Influence of Effective Water-to-Cement Ratios on Internal Damage and Salt Scaling of Concrete with Superabsorbent Polymer, Materials 12(23) (2019).
[4] D. Snoeck, O.M. Jensen, N. De Belie, The influence of superabsorbent polymers on the autogenous shrinkage properties of cement pastes with supplementary cementitious materials, Cem. Concr. Res. 74 (2015) 59-67.
[5] D. Snoeck, D. Schaubroeck, P. Dubruel, N. De Belie, Effect of high amounts of superabsorbent polymers and additional water on the workability, microstructure and strength of mortars with a water-to-cement ratio of 0.50, Constr. Build. Mater. 72 (2014) 148-157.
[6] J. Yang, F.Z. Wang, Z.C. Liu, Y.P. Liu, S.G. Hu, Early-state water migration characteristics of superabsorbent polymers in cement pastes, Cem. Concr. Res. 118 (2019) 25-37.
[7] Y.L. Ji, Z.P. Sun, X. Yang, C.J. Li, X.B. Tang, Assessment and mechanism study of bleeding process in cement paste by H-1 low-field NMR, Constr. Build. Mater. 100 (2015) 255-261.
[8] Y.L. Ji, Z.P. Sun, C. Chen, L. Pel, A. Barakat, Setting Characteristics, Mechanical Properties and Microstructure of Cement Pastes Containing Accelerators Mixed with Superabsorbent Polymers (SAPs): An NMR Study Combined with Additional Methods, Materials 12(2) (2019).
[9] D. Snoeck, L. Pel, N. De Belie, The water kinetics of superabsorbent polymers during cement hydration and internal curing visualized and studied by NMR, Sci. Rep. 7(1) (2017) 9514.
[10] X.S. Wei, Z.J. Li, Early hydration process of Portland cement paste by electrical measurement, J. Mater. Civ. Eng. 18(1) (2006) 99-105.
[11] P. Mounanga, A. Khelidj, A. Loukili, W. Baroghel-Bouny, Predicting $Ca(OH)_2$ content and chemical shrinkage of hydrating cement pastes using analytical approach, Cem. Concr. Res. 34(2) (2004) 255-265.

FE INCORPORATION IN CEMENT HYDRATES: EXPERIMENTS AND THERMODYNAMIC MODELING

Yogarajah Elakneswaran (1), Natsumi Noguchi (1), Krisnya Siventhirarajah (1), Takashi Chabayashi (2), Hiroyoshi Kato (2) and Toyoharu Nawa (3)

(1) Faculty of Engineering, Hokkaido University, Japan

(2) Cement Business Division, Tokuyama Corporation, Yamaguchi, Japan

(3) Hokkaido University, Japan

*Correspondence E-mail: elakneswaran@eng.hokudai.ac.jp

Abstract

Current understanding of the state of Fe during the hydration of cement is very limited and further studies are necessary to find out the possible incorporation of Fe in cement hydrates. Moreover, it is important to understand the hydration reaction and properties development of ferrite-rich cement. Our previous study [1] reported the hydration reaction and properties of ferrite-rich Portland cement by various experimental techniques and thermodynamic modelling and compared with ordinary Portland cement. However, we could not quantify the Fe-containing hydrates in the cements and the uptake of Fe by C-S-H. Therefore, the objective of this study is to quantify the Fe-containing hydrates during the hydration of ordinary Portland cement and ferrite-rich Portland cement. Ordinary Portland cement and ferrite-rich Portland cement were hydrated for 3 months and the hydration products were quantified with XRD/Rietveld analysis. The selective dissolution was used to determine the amount of Fe-containing phases. It was found that Fe-siliceous hydrogarnet was the primary Fe-containing phase. From the hydration of ferrite and amount of formed Fe-siliceous hydrogarnet, the Fe uptake in C-S-H was determined. The distribution ratio for Fe uptake in C-S-H and chemical composition of Fe-siliceous hydrogarnet were incorporated into the thermodynamic model to predict the hydration reaction of ordinary Portland cement and ferrite-rich Portland cement and the results were compared with experimental data of XRD/Rietveld analysis and selective dissolution. The successful agreement of the experimental results with the model demonstrates the state of Fe in the hydrated cements.

Keywords: Hydration, thermodynamic modelling, C-S-H, Fe-siliceous hydrogarnet

1. INTRODUCTION

It has been reported that the ferrite phase contributes significantly the sintering of the clinker, and the contribution of clinker components to its burnability is in the order of

$C_4AF>C_3A>C_2S>C_3S$ [2-3]. A low-burning-temperature clinker, which sinters at 1350 ºC that is approximately 100 ºC lesser than temperature required for the ordinary Portland Cement (OPC) clinker, was produced by increasing the C_4AF and decreasing the C_2S proportions while targeting a strength equal to that of the conventional OPC [3]. The cement produced using the low-burning-temperature-clinker is called ferrite-rich Portland cement (FC). The manufacturing process of this cement may release 5% lesser CO_2 than that of OPC, thus demonstrating a potential to substitute the OPC [3-4].

Gartner and Myers [5] has reported that higher proportion of ferrite in the cement delays the compressive strength development and admixtures are necessary to enhance the ferrite hydration and thus later strength development [6]. The hydration of ferrite phase induces to form Fe-containing phases [7-8]. However, it is difficult to conclude the kind of Fe-containing phases actually formed in the hydrated cement. In our previous study [1], we have investigated the hydration behaviour of ferrite-rich Portland cement and compared with OPC. However, that study did not identify and quantify the Fe-containing phases in the hydration of cements. Therefore, the present study focuses on the quantification of Fe-containing phases by experiment and compared the data with the hydration model. In addition, a possible Fe incorporation into C-S-H is also investigated.

2. MATERIALS AND METHODS

The ordinary Portland cement (OPC) and ferrite-rich Portland cement (FC) were used in the experiments. The physical properties and the mineral composition by Bogue analysis are listed in Table 1, and the chemical composition of oxide and the proportions of raw materials are given in Table 1 of ref. [1]. The cement paste with a water to cement ratio of 0.5 was prepared and cured at 20 ºC under sealed-condition. The samples that reached the predetermined curing time (1, 6, and 12 h and 1, 2, 3, 7, 14, 28, and 91 days) were ground and immersed in acetone for 1 h to stop hydration. Thereafter, the samples were removed from the acetone solution by suction filtration using an aspirator. Finally, the samples were kept in an oven at 40 ºC until they reached a constant mass. The prepared samples were ground and powdered for XRD and TG measurements. The XRD was performed using a Rigaku MultiFlex X-ray generator with CuKα radiation for the samples blended with 10 wt. % of corundum (α-Al_2O_3). Siroquant Version 4.0, manufactured by Sietronics, was used for quantitative Rietveld analysis. In the Rietveld analysis, monotrinic and triclinic C_3S, α- and β-C_2S, cubic C_3A, C_4AF, Gypsum, Bassanite, Portlandite, Ettringite, Monosulfoaluminate (simply called monosulfate), and Corundum (α-Al_2O_3) were assigned as targets. HITACHI TG/DTA 7220 analyser was used for TG/DTA measurements in nitrogen atmosphere and the measurements were performed at a heating rate of 5 °C/min up to 1000 °C. The selective dissolution experiment was conducted to estimate the Fe-containing phases. According to ref. [8], the phases of C_3S, C_2S, portlandite, C-S-H, ettringite, and monosulfoaluminate will dissolve and ferrite, siliceous-hydrogarnet, and hydrotalcite will remain in the selective dissolution process. The hydrated cement paste of 5 g was dissolved with 300 mL of methanol and 20 g of salicylic acid for 2 hours. Thereafter, the suspension was allowed to settle for 15 minutes and then vacuum filtered thorough 0.08 mm filter paper. The remaining solid was dried at 90 °C for 45 minutes before the solid analysis.

The coupled thermodynamic model developed in our previous work [9] was used to predict the hydrate assemblage of OPC and FC. The thermodynamic properties of various phases including Fe-containing hydrates and minerals in the cement system were collected from

Cemdata18 [10-11], and the data were converted into a format suitable for PHREEQC. The converted data by Elakneswaran [9] along with the PHREEQC default thermodynamic database [12] were used for the calculations.

Table 1: Physical properties and chemical composition of cements used

Cement	OPC	FC
Blaine specific surface area (cm^2/g)	3220	3220
Density(g/cm^3)	3.19	3.20
C_3S	57.6	59.1
C_2S	18.0	8.6
C_3A	9.0	8.5
C_4AF	9.3	17.2

3. RESULTS AND DISCUSSION

Figure 1 shows the effect of selective dissolution on the dissolution of hydrates in both OPC and FC. Although a very small amount of monosulfate and portlandite was observed, the siliceous-hydrogarnet was the main hydration product after the selective dissolution, which is consistent with previous study [8]. It is confirmed that the hydration of both cements produces the siliceous-hydrogarnet from the early age. The chemical composition of siliceous-hydrogarnet was assumed as $Ca_3FeAl(SiO_4)_{0.84}(OH)_{8.64}$ based on the results reported in a previous study [8]. The quantity of siliceous-hydrogarnet remained after selective dissolution was determined by TG and the results are shown in Figure 2 for both cement as a function of hydration time. The data shows that the amount of formed siliceous-hydrogarnet becomes stable after 28 days of hydration. Furthermore, the hydration of ferrite-rich cement forms higher amount of siliceous-hydrogarnet.

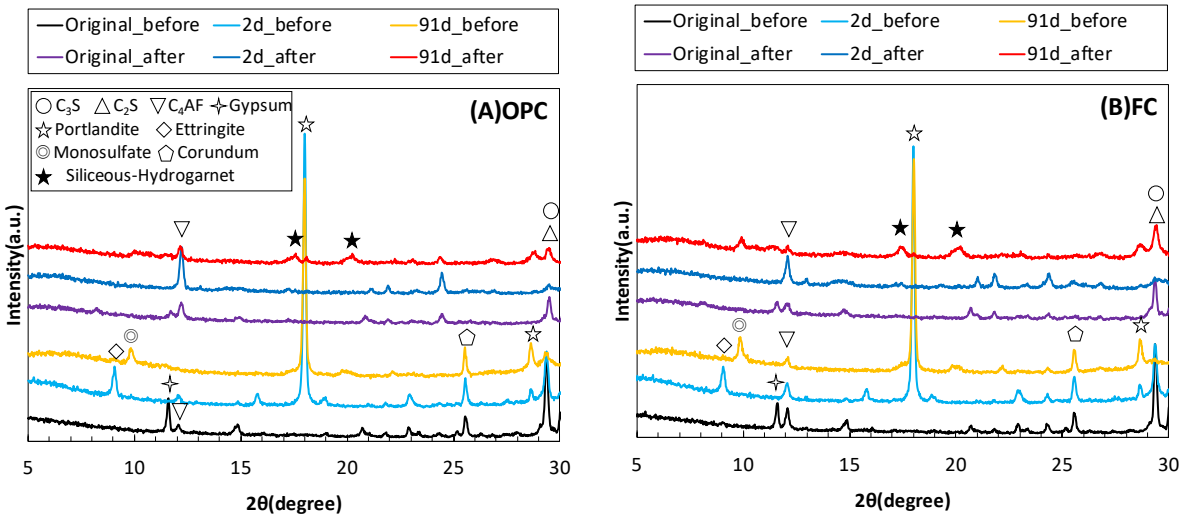

Figure 1: XRD patterns of (A) OPC; (B) FC before and after selective dissolution

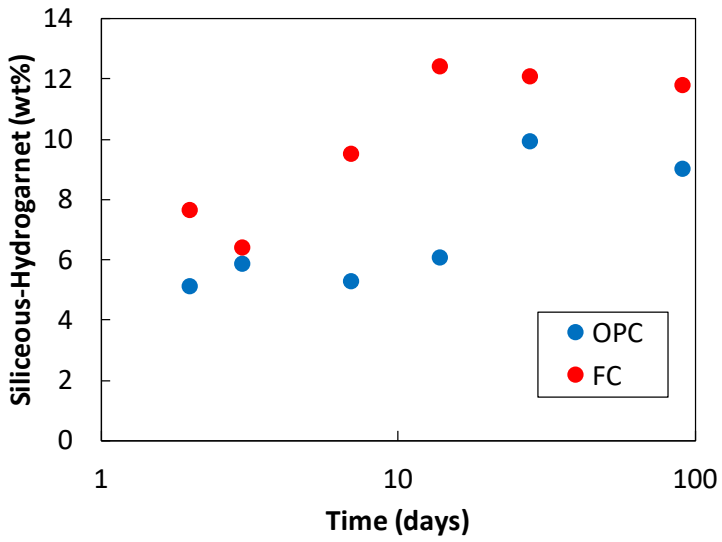

Figure 2: Amount of siliceous-hydrogarnet in the hydrated cements

Fe ions from the ferrite hydration together with aluminium accumulates as siliceous-hydrogarnet, however the Fe ions could accommodate in the C-S-H as well. Mancini et al. has recently highlighted that Fe can incorporate into synthesized C-S-H [13]. Herein, the quantity of Fe incorporate into C-S-H was calculated from the hydration reaction of ferrite and the amount of formed siliceous-hydrogarnet. It has been reported that the concentration of Fe ions in the pore solution is negligible, which leads to determine the amount of Fe uptake by C-S-H. Figure 3 shows Fe incorporation into the siliceous-hydrogarnet and C-S-H as a function of hydration time for both cements. A part of released Fe ions as a result of ferrite hydration incorporates into C-S-H and others precipitates as siliceous-hydrogarnet. After 7 days of hydration, the amount of Fe taken by C-S-H and siliceous-hydrogarnet is reached to a steady state for both cements. A lower hydration degree of ferrite in FC compared to OPC show a nearly equal Fe in the siliceous-hydrogarnet and C-S-H.

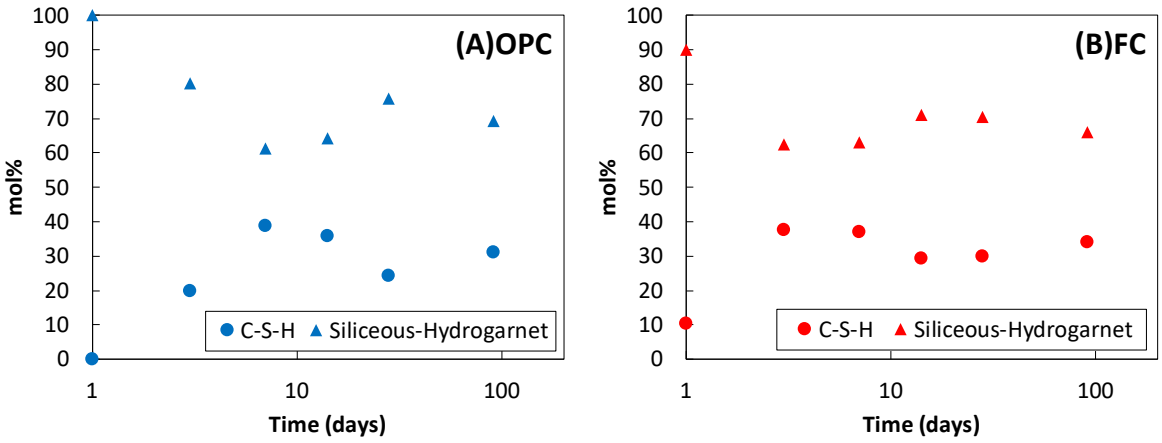

Figure 3: The state of Fe in (A) OPC; (B) FC

The results reported in Figure 3 is an evident in the Fe uptake by C-S-H, but it is difficult to propose a mechanism for uptake as the studies on Fe incorporation into C-S-H are very limited. In this study, the same approach used for Na^+ or K^+ incorporation [14-15] into C-S-H is adopted to quantify Fe uptake by C-S-H. The distribution ratio (R_d) for the uptake is determined and the results are shown in Figure 4. The estimated R_d is a function of Fe concentration and each of OPC and FC show different function for R_d (Figure 4 (A)). The value of R_d tends to decrease as the Fe concentration increases. Further, for the same concentration of Fe, R_d of FC is higher than that of OPC, indicating higher uptake of Fe in ferrite-rich cement. Figure 4(B) shows the R_d relationship irrespective of cement type. From the reported relationship of R_d for alkalis and for the development of model, it is desirable to have a single relationship for R_d regardless of cement type. Although the coefficient of determination (R^2) is low, the relationship derived in Figure 4 (B) is adopted in the hydration model.

The coupled thermodynamic model proposed in our previous study is used to predict hydrate assemblage as a function of hydration time. The model uses chemical composition of cements and mixing conditions as input parameter for the prediction of phase-assemblage composition. The model is applied to predict the hydration of ferrite-rich cement in our previous study [1] and found that Fe-siliceous-hydrogarnet is the main and stable Fe containing phase which forms from the early age. The experimental results obtained in this study is consistent with the model estimation. Furthermore, the experimentally quantified Fe-siliceous-hydrogarnet is compared with model prediction together with other phases in Figure 5 for both cements. Considering the crystallinity of AFm phases, the summation of total amorphous and monosulfate from the experimental results is compared with the addition of modelling results of C-S-H, Fe-incorporated C-S-H (C-F-S-H), monosulfate, and hydrotalcite. Despite some variation in OPC, the predicted Fe-siliceous-hydrogarnet and other hydrates agree well experimental data for both cements. The amount of Fe incorporated C-S-H (C-F-S-H) can be calculated from the moles of Fe uptake by C-S-H given in Figure 3. The modelling results of C-F-S-H are also plotted in Figure 5, which is less than 2% in total weight of hydrated OPC or FC where FC produces slightly higher than OPC.

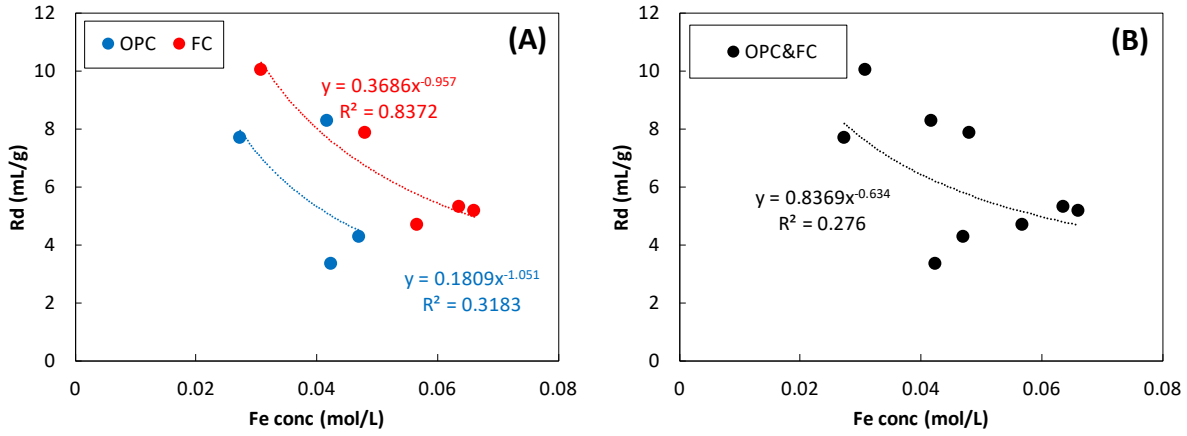

Figure 4: The relationship between distribution coefficient and concentration of Fe: (A) depend on cement type; (B) independent of cement type

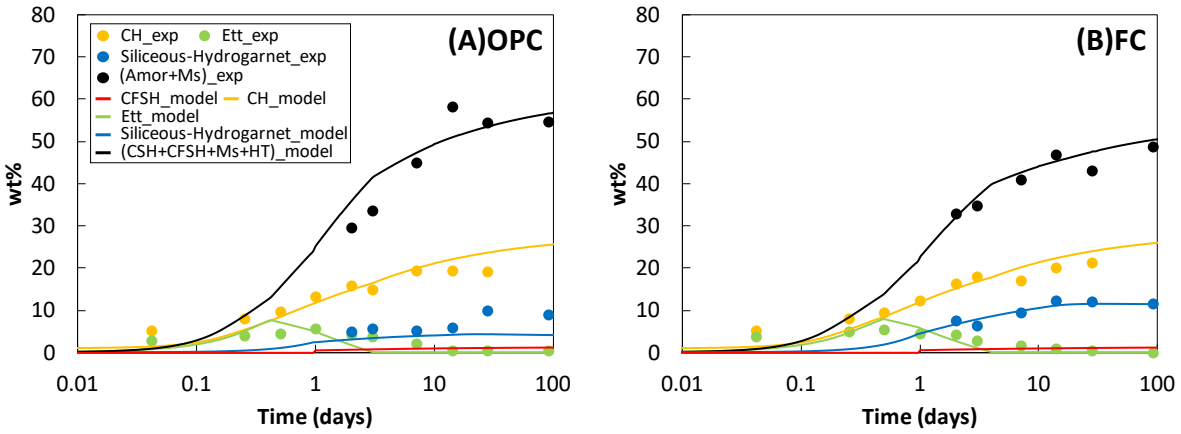

Figure 5: Comparison of calculated hydrates with quantitative value determined by XRD Rietveld analysis and TG/DTA for (A) OPC and (B) FC

4. CONCLUSIONS

In this paper, a combination of experimental and modelling study is conducted to quantify Fe-containing hydrates and Fe-uptake by C-S-H. Based on the results, the following conclusion are made:

- Fe-siliceous-hydrogarnet starts to form from the early age and continue with hydration time, but it reaches to a steady state after 28days of hydration. The high amount of ferrite in FC enhances its formation.
- Hydration of ferrite and the formed Fe-siliceous-hydrogarnet lead to determine Fe uptake in C-S-H. Fe from ferrite hydration can incorporate into C-S-H in addition to the formation of Fe-siliceous-hydrogarnet.
- The distribution ratio (R_d) for Fe uptake in C-S-H is determined as function of Fe^{3+} concentration. A constant relationship is assumed for both cements.
- The thermodynamic model predicts well the hydration reaction of FC. The experimentally determined Fe-siliceous-hydrogarnet agrees satisfactorily with predicted results.
- The hydration model estimates around 2% of Fe incorporated C-S-H (C-F-S-H) in the hydration products.

REFERENCES

[1] Elakneswaran, Y. et al. Characteristics of Ferrite-Rich Portland Cement: Comparison with Ordinary Portland Cement. *Frontiers in Materials 6*, (2019) 97–.

[2] Chabayashi, T. et al., Reduction of burning temperature of cement clinker by adjusting of mineral composition, *Cement Science and Concrete Technology*, 66 (2012), 217-222.

[3] Chabayashi, T. et al., Burning test result of the low burning-temperature type clinker by actual kiln and properties of the cement, Cement Science and Concrete Technology, 69 (2015), 124-130.

[4] Shinmi, T., et al. Long-term strength development, durability and environmental impact assessment of concrete using the low burning-temperature type general-purpose cement. Concrete Engineering, 39, (2017) 1999-2004.

[5] Gartner, E. and Myers, D. Influence of Tertiary Alkanolamines on Portland cement hydration. J. Am. Ceram. Soc 76 (1993), 1521-1530.

[6] Schwarz, W. Novel cement matrices by accelerated hydration of the ferrite phase in Portland cement via chemical activation: Kinetics and cementitious properties. *Advn Cem Bas Mat* 2, (1995). 189-200.
[7] Dilnesa, B. Z., et al. Iron in carbonate containing AFm phases, *Cement and Concrete Research,* 41, (2011) 311-323.
[8] Dilnesa, B. Z., et al. Fe-containing phases in hydrated cements, *Cement and Concrete Research,* 58, (2014) 45-55.
[9] Elakneswaran, Y. et al. Hydration Study of Slag-Blended Cement Based on Thermodynamic Considerations. *Construction and Building Materials* 124, (2016) 615–25.
[10] Lothenbach, B. et al. Cemdata18: A chemical thermodynamic database for hydrated Portland cements and alkali-activated materials. *Cement and Concrete Research* 115, (2019) 472-506.
[11] Lothenbach, B. and Zajac, M., Application of thermodynamic modelling to hydrated cements, *Cement and Concrete Research*, vol. 123 (2019, p. 105779.
[12] Parkhust, D. L., Appelo, C. A. J. A computer program for speciation, batch－reaction, one－dimensional transport and inverse geochemical calculations. USGS report (1999).
[13] Mancini, A. et al.. Interaction of Fe(II, III) with cement phases in anoxic conditions, NUWCEM, (2018) Avignon, France
[14] Hong, S.-Y. and Glasser F. P., Alkali binding in cement pastes Part I. The C-S-H phase, *Cement and Concrete Research*, vol. 29, (1999) pp. 1893–1903.
[15] Chen, W. and Brouwers, H. J. H. Alkali binding in hydrated Portland cement paste, *Cement and Concrete Research*, vol. 40, no. 5, pp. 716–722, May 2010.

HYDRATION BEHAVIOR OF MAGNESIUM AMMONIUM PHOSPHATE CEMENTAND STABILITY ANALYSIS OF ITS HYDRATION PRODUCTS THROUGH THERMODYNAMIC MODELING

Weiwei Han (1), Huisu Chen (1) and Tao Zhang(1)
(1) Jiangsu Key Laboratory of Construction Materials, School of Materials Science and Engineering, Southeast University, Nanjing 211189, P.R. China

Abstract

Magnesium ammonium phosphate cement (MAPC) has been commonly applied in civil engineering. However, the analysis of hydration behavior and composition of solid assemblages still needs further exploration. From thermodynamic simulation, it is shown that the molar ratio between MgO and $NH_4H_2PO_4$ (M/P ratio) determines the final composition of hydration products, When M/P ratio is lower than 0.49, the solid assemblage is $(NH_4)_2Mg(PO_4)_2{\cdot}4H_2O$; When M/P ratio is between 0.49 and 1.00, the solid assemblages are $(NH_4)_2Mg(HPO_4)_2{\cdot}4H_2O$, $MgHPO_4{\cdot}3H_2O$, $MgNH_4PO_4{\cdot}6H_2O$ and unreacted MgO; When M/P ratio is higher than 1.00, the composition of solid assemblages is $MgNH_4PO_4{\cdot}6H_2O$ and unreacted MgO.

Keywords: MAPC, thermodynamic simulation, M/P molar ratio

1. INTRODUCTION

Magnesium phosphate cement (MPC) is a new kind of nonhydraulic cementitious material with ultra-fast setting, hardening and ultra-early strength, usually used for reinforcement of structure and quick repair stabilize/solidify deleterious waste, and treat wastewater [1-3]. MPC are formed through an acid-base reaction between dead-burned MgO and a soluble acid phosphate (typically an ammonium, potassium or sodium phosphate), forming a magnesium phosphate salt with cementitious properties [4].

Magnesium ammonium phosphate cement (MAPC), as one branch of MPC, was first patented by Prosen in 1936 as a binder materials to produce dental casting investment materials via mixing MgO with ammonium phosphate [5].

The performance of materials are intrinsically influenced by the assemblages of hydration products, so it is imperative to put efforts to the hydration products formed to further study the mechanism of cementitious materials. Various hydration products of MAPC have been found in the literature [6-10]. The predominant hydration product of MAPC is usually considered to be MgNH4H2PO4·6H2O (struvite), while other phases such as

MgHPO4·3H2O (newberyite), (NH4)2Mg(PO4)$_2$·4H$_2$O (schertelite), NH$_4$MgPO$_4$·H$_2$O (dittmarite), Mg$_3$(PO$_4$)$_2$·8H$_2$O (bobierrite) and (NH$_4$)$_2$Mg$_3$(PO$_4$)$_4$·8$_{H2}$O (hannayite), are perceived to be intermedia products [6-8].

Previous studies presented experimental results about the assemblage of hydration products, however, to the best of the authors' knowledge, the underlying mechanism for the composition and stability of hydration products remains unclear yet. In this study, thermodynamic calculation was conducted to investigate the mechanism behind.

2. THERMODYNAMIC MODEL

2.1 Model selection

Geochemical specification code PHREEQC is applied here to carry out the thermodynamic simulation of MAPC system. PHREEQC uses an ion-association model to calculate thermodynamic properties. PITZER model [11] is employed to handle the conditions of high ion strength and complicate ion interaction in MAPC solution. Ali et al. [12] and Zhou et al. [13] reported that PITZER model can be used in the modeling of $NH_4H_2PO_4$ and MgO system respectively, which provides preliminary work for MAPC systems. The PITZER equation is given in Eq. (1).

$$\begin{aligned}\frac{1}{2}\sum_i mi\cdot(\phi-1) = {} & \frac{-A^{\phi}\cdot I^{3/2}}{(1+b\cdot I^{1/2})} \\ & + \sum_c\sum_a m_c m_a (B^{\phi}_{ca} + ZC_{ca}) \\ & + \sum_c\sum_{c'} m_c m_{c'} \phi^{\phi}_{cc'} + \sum_a\sum_{a'} m_a m_{a'} \phi^{\phi}_{aa'} \\ & + \sum_c\sum_{c'}\sum_a m_c m_{c'} m_a \psi_{cc'a} + \sum_c\sum_{c'}\sum_a m_a m_{a'} m_c \psi_{aa'c} \\ & + \sum_n\sum_a m_n m_a \lambda_{na} + \sum_n\sum_c m_n m_a \lambda_{nc} \\ & + \sum_n\sum_c\sum_a m_n m_c m_a \psi_{nca}\end{aligned} \tag{1}$$

where Aϕ: Debye–Hückel osmotic parameter, the theoretical expression is given in Eq. (2). b: constant, 1.2, [kg1/2·mol−1/2]. c: cation, a: anion, n: neutral species. ∑c: the sum over all cations in the system; ∑c∑c′: denotes the sum over all the distinguishable pairs of dissimilar cations; analogous definitions apply to the anions. B, C, ϕ, ψ, λ and ζ are the combinations of experimental measured parameters.

$$A^{\phi} = \frac{1}{3}(2\pi N_0 \rho_w / 1000)^{1/2} (e^2 / \varepsilon\kappa T)^{3/2} \tag{2}$$

where ρw: density of water, 997.047 kg/m^{-3} at 25 °C; ε: dielectric constant of water, 78.36 [F·m^{-1}]; κ: Boltzmann constant, 1.3806503 × 10^{-23}, [m^2·kg·s^{-2}]; e: electron volt or charge of an electron, 1.602176565 × 10^{-19}, [C]; N0: Avogadro constant, 6.022 × 10^{23}[mo^{l-1}]. Therefore, A^{ϕ} = 0.39 at 298 K and 0.1MPa.

2.2 Database construction

Thermodynamic data for MAPC system were all collected from critically reviewed literatures. Most of the data were collected from PITZER [11] and MOC [13] database. The data were rewritten in the form recognizable for PHREEQC. Based on the literature review, potential hydration phases of MAPC include, MgHPO$_4$·3H$_2$O, (NH$_4$)$_2$Mg(HPO$_4$)$_2$·4H$_2$O,

$MgNH_4PO_4.H_2O$, and $MgNH_4PO_4 \cdot 6H_2O$. Calculations in this study are based on the assumption that the components in raw material, other than dead burnt magnesia, are not inert in the MAPC reactions. The hydration condition in this study maintains at 25℃, 0.1MPa [14].

2.3 Verification

Ion concentrations and pH value of MAPC suspension are compared with experimental results here to verify the accuracy of the database. The analytical grade dihydrogen phosphate ($NH_4H_2PO_4$), net content >99.0%, magnesium oxide, net content >98% and deionized water were used. The m($NH_4H_2PO_4$)/m (H_2O) is set to 0.024, while the molar ratio of MgO to $NH_4H_2PO_4$ (M/P) changes from 0 to 1 (in 0.1 increments). The prepared MAPC suspension was continuously stirred with an overhead stirrer and placed in a 25 ℃ water bath until the end of testing. The pH data was automatically collected at time steps of 1 min. The measured equilibrium pH value of MAPC suspension is illustrated in Figure 1. Figure 2 exhibits that the calculated pH value and ion concentration of Mg^{2+} and PO_4^{3-} meet well with experimental results conducted in this paper and those from Ronteltap's work [15], which proves that the database used for simulation is reliable.

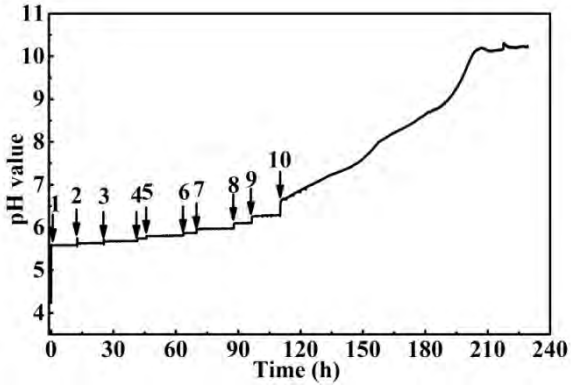

Figure 1: pH value of MAPC suspension with different M/P

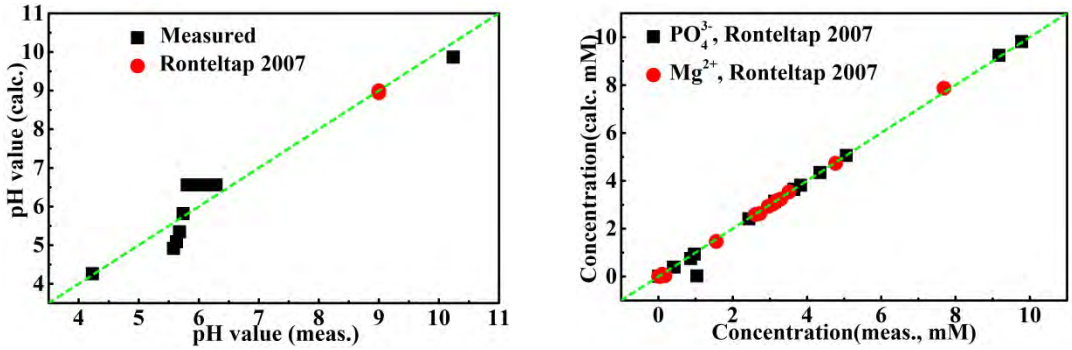

Figure 2: Comparison of measured and calculated pH values and concentration of Mg (Mg^{2+}) and P(PO_4^{3-}) of MAPC suspension.

3. MODELLING RESULTS AND DISCUSSION

Fig. 3 illustrates the assemblage of simulated hydration products and pH values of MAPC suspension with n($NH_4H_2PO_4$) =0.21mol, m (H_2O) =1kg and the M/P(n(MgO)/n($NH_4H_2PO_4$)) molar ratio changes from 0-4. As shown in Fig. 1, when

$NH_4H_2PO_4$ is added to deionized water, pH value drops from 7 to P0. The dissolution of MgO which releases Mg^{2+} to participate in consequent reaction accounts for the pH increase from P0 to P1. As M/P increases, $(NH_4)_2Mg(HPO_4)_2{\cdot}4H_2O$ precipitates from solution first , and the process can be described by Eq. (3). Compared with $NH_4H_2PO_4$, the amount of MgO added at first is relatively small not sufficient. The relatively excess $NH_4H_2PO_4$ reacts with MgO in terms of molar ratio 2:1 to form $(NH_4)_2Mg(HPO_4)_2{\cdot}4H_2O$, as illustrated by Eq. (3). Whereafter, with the increase of M/P, $MgHPO_4{\cdot}3H_2O$ starts to appear in hydration products, corresponding to the increase of pH from P2 to P3(Eq. (4)). After that, the pH value remains unchanged (P3-P4). However, the amount of $(NH_4)_2Mg(HPO_4)_2{\cdot}4H_2O$ is decreasing, and simultaneously $MgNH_4PO_4{\cdot}6H_2O$ starts generating whose content continuously increases with the continued adding of MgO. This phenomenon can be explained through Eq. (5). The generated $(NH_4)_2Mg(HPO_4)_2{\cdot}4H_2O$ reacts with MgO to form $MgNH_4PO_4{\cdot}6H_2O$. This solid phase transformation process does not affect the pH value of investigated MAPC system. The increase of pH from P4 to P5 attributes to the transformation of generated $MgHPO_4{\cdot}3H_2O$ to $MgNH_4PO_4{\cdot}6H_2O$. When M/P molar ratio is equal or greater than 1, the main and the only hydration product is struvite (Eq. (7)). It's worth noting that, the simulation results are the ideal results of a complete reaction in each step.

$$2NH_4H_2PO_4 + MgO + 3H_2O = (NH_4)_2Mg(HPO_4)_2{\cdot}4H_2O \quad (3)$$

$$NH_4H_2PO_4 + MgO + 2H_2O = MgHPO_4{\cdot}3H_2O + NH_3 \quad (4)$$

$$(NH_4)_2Mg(HPO_4)_2{\cdot}4H_2O + MgO + 7H_2O = 2MgNH_4PO_4{\cdot}6H_2O \quad (5)$$

$$MgHPO_4{\cdot}3H_2O + NH_4H_2PO_4 + MgO + NH_3 + 8H_2O = 2MgN_{H4}PO_4{\cdot}6_{H2}O \quad (6)$$

$$NH_4H_2PO_4 + MgO + 3H_2O = MgNH_4PO_4{\cdot}6H_2O \quad (7)$$

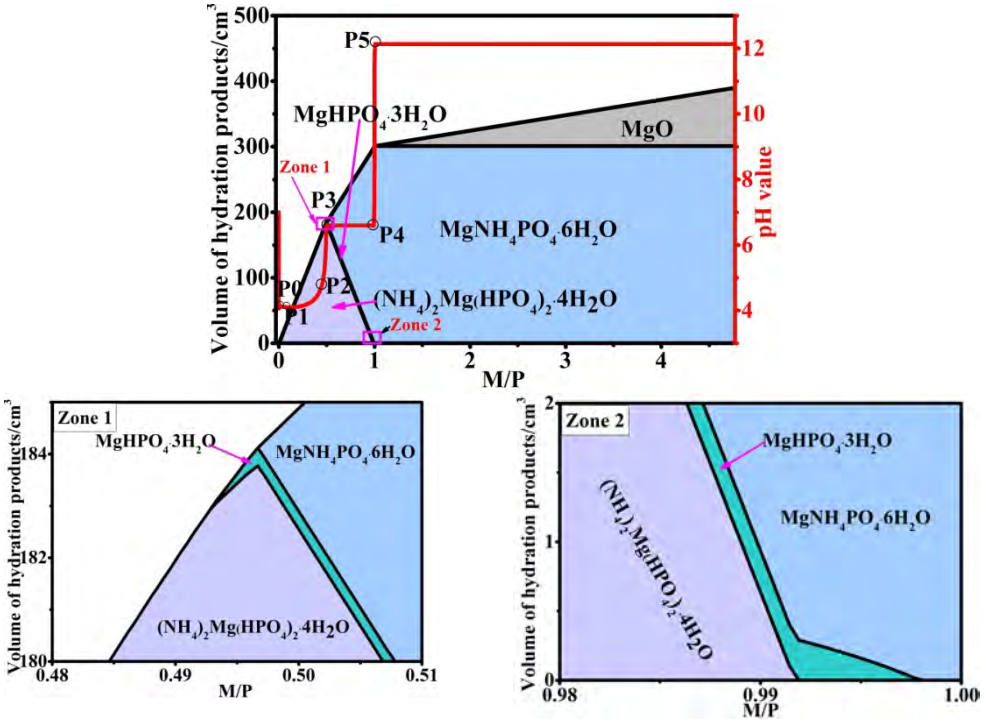

Figure 3: Assemblage of simulated hydration products and pH values of MAPC with different M/P or P/M values:(a):n(NH4H2PO4) =2.1mol, m (H2O) =1kg);(b):n(MgO)=10mol,m(H2O)=1kg.

Fig.3 illustrates the evolution of hydration products with different M/P molar ratio. Following the order of precipitation, $(NH_4)_2Mg(HPO_4)_2{\cdot}4H_2O$, $MgHPO_4{\cdot}3H_2O$ and $MgNH_4PO_4{\cdot}6H_2O$ can precipitate from solution at 25 ℃, 0.1MPa in thermodynamic simulation, which have also been proved by XRD test in recent studies[8]. The precipitation and dissolution condition of hydration products are influenced by $NH_4H_2PO_4$ concentration and M/P ratio. From Fig. 3, it can be found that the formation areas and amount of these hydration products are determined by M/P ratio. When the concentration of ADP is specified, the amount of $(NH_4)_2Mg(HPO_4)_2{\cdot}4H_2O$ precipitated from solution increases firstly and then decreases with the increase of MgO. There is a maximal MgO content where maximum of $(NH_4)_2Mg(HPO_4)_2{\cdot}4H_2O$ can precipitate from the solution(M/P=0.49). The generation of $MgHPO_4{\cdot}3H_2O$ shows similar trend with that of $(NH_4)_2Mg(HPO_4)_2{\cdot}4H_2O$ and the increase rate of $MgHPO_4{\cdot}3H_2O$ amount is slower than that of $(NH_4)_2Mg(HPO_4)_2{\cdot}4H_2O$. With the continue increase of MgO content (M/P>0.49), the amount of $MgNH_4PO_4{\cdot}6H_2O$ increases first and then maintain at a constant value. At the same time, the amount of $(NH_4)_2Mg(HPO_4)_2{\cdot}4H_2O$ and $MgHPO_4{\cdot}3H_2O$ decreases with the increase of M/P. When M/P molar ratio exceeds 1.0, the content of unreacted MgO increases with the increase of M/P molar ratio.

Table 1: Influence of M/P ratio on composition of solid assemblages of MAPC system after hydration

M/P value	Hydration assemblage
<0.49	$(NH_4)_2Mg(HPO_4)_2{\cdot}4H_2O$
0.49<M/P<1	$(NH_4)_2Mg(HPO_4)_2{\cdot}4H_2O$ ， $MgHPO_4{\cdot}3H_2O$，$MgNH_4PO_4{\cdot}6H_2O$
M/P>1	$MgNH_4PO_4{\cdot}6H_2O$

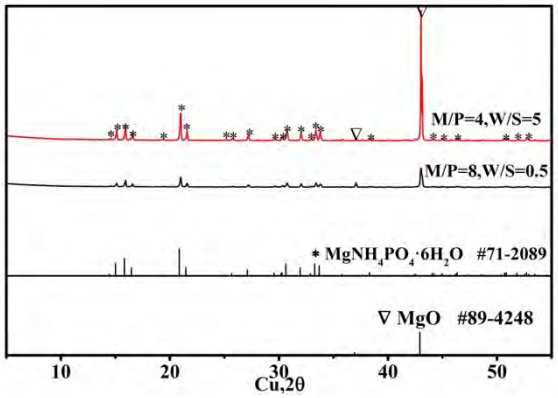

Figure 4: XRD analysis of MAPC system with M/P=8,W/S=0.5 and M/P=4, W/S=5

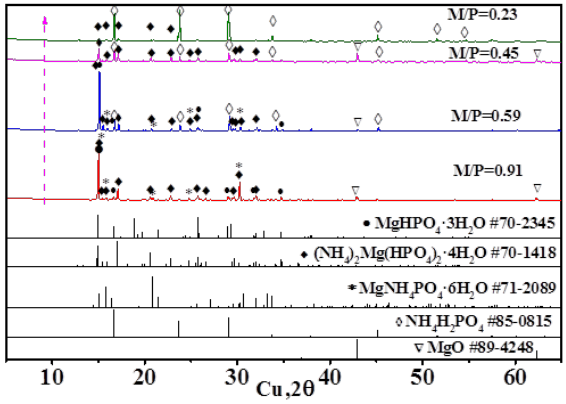

Figure 5: XRD analysis of MAPC system with n(H_2O)/n($NH_4H_2PO_4$)=3.333, P/M= 1.100, 1.692, 2.200, 4.400

4. CONCLUSIONS

- In MAPC system, potential hydration products are $(NH_4)_2Mg(HPO_4)_2·4H_2O$, $MgHPO_4·3H_2O$, $MgNH_4PO_4·6H_2O$, and there are also unreacted MgO.
- The composition and stability of hydration products are determined by M/P ratio. When M/P ratio is lower than 0.49, the final hydration products is $(NH_4)_2Mg(HPO_4)_2·4H_2O$. When M/P ratio is between 0.49 and 1.00, the final hydration products are $(NH_4)_2Mg(HPO_4)_2·4H_2O$, $MgHPO_4·3H_2O$ and $MgNH_4PO_4·6H_2O$. When M/P ratio is higher than 1.00, as intermediate phase, $(NH_4)_2Mg(HPO_4)_2·4H_2O$ can precipitate from the solution at first, and dissolve into solution later, the final hydration products are $MgNH_4PO_4·6H_2O$ and unreacted MgO。

ACKNOWLEDGEMENTS

The authors gratefully thank the financial support from National Natural Science Foundation of China (Grant No.51878152) and Ministry of Science and Technology of China ‘‘973 Project” (Grant No. 2015CB655102)

REFERENCES

[1] Zhang T., Chen H.S., Li X.Y., Zhu Z.G., Hydration behavior of magnesium potassium phosphate cement and stability analysis of its hydration products through thermodynamic modeling. Cem. Concr. Res. 98(2017) 101-110.

[2] Abdelrazig B.E.I., The properties of hardened MPC mortar and concrete relevant to the requirements of rapid repair of concrete pavements, Concr. repair 21 (1987) 25-31.

[3] Yang Q., Zhu B., Zhang S., Wu X., Properties and applications of magnesia phosphate cement mortar for rapid repair of concrete, Cem. Concr. Res. 30 (2000) 1807-1813.

[4] Walling S.A., Provis J.L., Magnesia-based cements: A journey of 150 years, and cements for the future? Chem Rev, 116(2016) 4170-204.

[5] Prosen E.M., Dental investment or refractory material,US Patent No.2152152, 1939.

[6] Yang Q., Wu X., Factors influencing properties of phosphate cement-based binder for rapid repair of concrete, Cem. Concr. Res. 29 (1999) 389-396.

[7] Hipedinger N. E., Scian A. N., Aglietti E. F., Magnesia-ammonium phosphate-bonded cordierite refractory castables: Phase evolution on heating and mechanical properties, Cem. Concr. Res. 34(2004) 157-164.
[8] Abdelrazig B.E.I., Sharp J.H., Ei-Jazairi B., The chemical composition of mortars made from magnesia phosphate cement, Cem. Concr. Res. 18 (1988) 415-425.
[9] Sugama T., Kukacka L., Magnesium monophosphate cements derived from diammonium phosphate solutions, Cem. Concr. Res. 13 (1983) 407-416.
[10] Mousa S., Study on synthesis of magnesium phosphate materials, Phosphorus Res. Bull, 24 (2010) 16-21.
[11] Nordstrom D.K., Munoz J.L., Geochemical Thermodynamics, 2th edition, Blackwell Scientific Publications, Oxford,1994.
[12] Lothenbach B., Zajac M., Application of thermodynamic modelling to hydrated cements, Cem. Concr. Res. 123 (2019) 1-21.
[13] Zhou Z., Chen H.S., Li Z.J., Li H.J., Simulation of the properties of MgO-MgfCl2-H2O system by thermodynamic method, Cem. Concr. Res., 68 (2015) 105-111.
[14] Elizalde M.P., Aparicio J.L., Current theories in the calculation of activity coefcients II. Specifc interaction theories applied to some equilibria studies in solution chemistry, Talanta 42 (1995) 395-400.
[15] Ronteltap M., Maurer M., Gujer W., Struvite precipitation thermodynamics in source-separated urine, Water Res. 41 (2007) 977-984.

IN SITU OBSERVATION OF TRICALCIUM ALUMINATE DISSOLUTION IN WATER

Shaoxiong Ye (1), Pan Feng (1,2), Yao Liu (1) and Jiaping Liu (1,2)

(1) Jiangsu Key Laboratory of Construction Materials, School of Materials Science and Engineering, Southeast University, Nanjing 211189, China

(2) State Key laboratory of High Performance Civil Engineering Materials, Nanjing 210008, China

Abstract

The nanoscale dissolution flux of tricalcium aluminate (C_3A) in flowing water is characterized in situ by Digital Holographic Microscopy (DHM). The pure dissolution of C_3A in flowing water with a flow rate of 34 $ml \cdot min^{-1}$ before the precipitation of hydrated phases only lasted about one quarter of a second, and the pure dissolution rate mostly falls in the range of 500 ~ 1500 $\mu mol \cdot m^{-2} \cdot s^{-1}$. Subsequently, foil shape hydration product formed and rapidly covered the surface of C_3A, leading to the dramatic decrease of the overall dissolution rate to 55 $\pm$ 10 $\mu mol \cdot m^{-2} \cdot s^{-1}$.

Keywords: C_3A, rapid dissolution, DHM

1. INTRODUCTION

Mineral dissolution is a key process in geochemical reactions and environmentally relevant processes[1]. In recent years, the dissolution behaviors of cement clinkers have been obtaining increasing attention[2-5]. Portland cement is a low-cost material with multi minerals, including alite, belite, tricalcium aluminate (C_3A), gypsum, etc. The hydration of cement, which is a complex reaction that combines with mineral dissolution and product precipitation, is the origin of strength and determines other properties of cement paste. According to Julliand et al[2], dissolution plays an important role in alite hydration, and the change of alite dissolution mechanism is responsible for the onset of induction period. Similarly, Nicoleau & Nonat[5] proposed that dissolution of C_3S is the rate controlling step in the early hydration based on the change of saturation index of C_3S.

Besides alite, C_3A is also a key component of Portland cement. Though its content is much lower than alite, it has an important effect on early properties of cement paste, especially for the workability[6]. Because C_3A has a much higher reactivity than alite, it reacts much faster with water than C_3S, which makes it an even bigger challenge to measure its dissolution rate in water. To slow down the dissolution rate of C_3A, Brand and Bullard[7] lowered the water activity by incorporating ethanol in water and measured the dissolution rate in solutions with

high content of ethanol. However, the presence of ethanol is likely to change the dissolution mechanism of C_3A due to its adsorption to the C_3A surface[8-9]. Thus, how the dissolution rate of C_3A in the mixture solutions is related to that in water still remains unresolved.

The Digital Holographic Microscopy (DHM) is a new technique that is able to detect the evolution of surface elevation, which can provide insights about dissolution mechanisms that would be valuable in cement research, like determining the reactivities of clinker and supplementary cementitious materials, exploring the effect of admixtures on cementitious materials, etc. For the purpose of measuring net dissolution rate of C_3A in water, which is helpful in understanding the early age hydration of cement, this paper uses DHM to monitor the surface height change of polished C_3A samples on nano-scale. Because of the unique capability of fast image collection of DHM, the real-time observation of fast dissolution is realized.

2. MATERIALS AND METHODS

2.1 C_3A pellets sintering

C_3A pellets were produced in lab through hot-press sintering method by spark plasma sintering (HP-D5, FCT). A schematic plot of sintering procedure is shown in Figure 1. The detailed information for C_3A pellets sintering is as follows:

Firstly, about 3 g of C_3A powder (purchased from Zibo Ceramic Institute, China) was placed into a graphite die (20 mm in diameter) and pre-pressed by top and down punches. Graphite foil was used to wrap the powder for easy demolding.

Secondly, SPS sintering was carried out to densify the pellet samples. The sintering parameters adopted in this paper was obtained by trial and error. In details, the die was covered by a graphite sleeve and then moved into a vacuum chamber (less than 10 Pa), in which the die was pre-pressed again with a stress of 15 MPa. Then the sample was heated to 1250 °C with a heating rate of 100 °C·min^{-1} and stayed at the maximum temperature for 15 min. Before the temperature reached to 450 °C, the pressure of 15 MPa was applied to the sample, after which the pressure applied was increased at a constant rate from 15 MPa to 40 MPa until the temperature increased up to 1250 °C, and then stayed constantly at 40 MPa at the maximum temperature.

When the heating was done, the sample was rapidly cooled by water cooling system, followed by demolding. The crystal structure of pellet (crushed into powder) was characterized by X-ray diffractometer (Bruker D8, Bruker). The result was shown in Figure 2, indicating the major phase of pellet synthesized was C_3A.

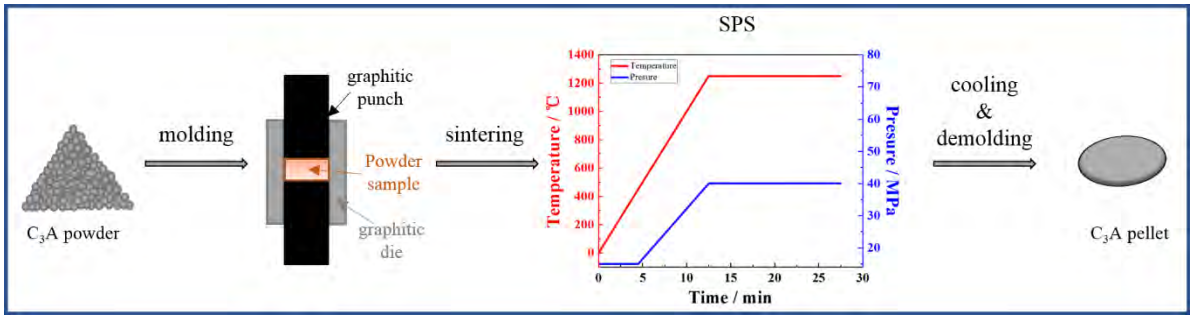

Figure 1: Schematic plot of sintering procedure for C_3A

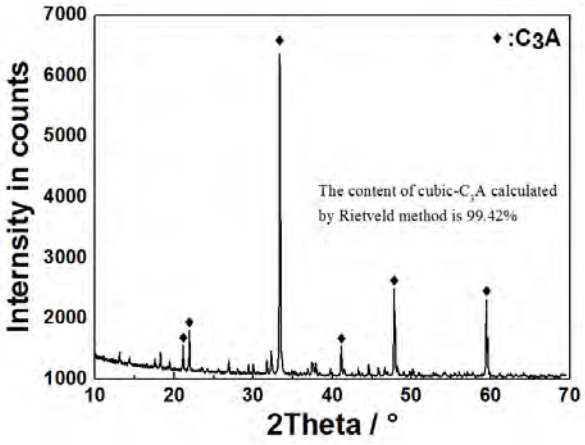

Figure 2: Diffraction pattern of C_3A sample

2.2 DISSOLUTION EXPERIMENTS

C_3A pellets were polished and partially coated with a chemical-inert platinum layer with the thickness of about 20 nm, servicing as a reference plane which is supposed to be unreacted through the whole dissolution measurement. The coating was implemented by applying Turbo-Pumped Sputter Coater (Q150T, JC Nabity). Figure 3 shows one C_3A sample with the coating platinum.

Deionized water was used in all dissolution experiments, and all the experiments were performed following the same method mentioned in [10] at the temperature of 24 ± 1 °C. The DHM (Model R-2203, Lyncée Tec) utilized in this study was operated in the reflection mode. It collected the hologram images of the sample surface at a frequency up to 12.5 s^{-1}. More information about DHM configuration can be found elsewhere[12]. C_3A dissolution was monitored using a 20x immersion objective lens, and the dissolution rate of C_3A, v_{diss}, was determined by dividing the velocity of reactive surface height change by the molar volume of C_3A V_m = 8.91 x 10^{-5} $m^3 \cdot mol^{-1}$

$$v_{diss} = \frac{\Delta h}{\Delta t}\frac{1}{V_m} \quad (1)$$

To reach a condition under which the dissolution is controlled by surface reaction rather than diffusion, the solution was intentionally maintained as diluted as possible by increasing the flow rate of water from 15 up to 55 $ml \cdot min^{-1}$. In this way, conditions far from equilibrium were

obtained. C_3A pellets were produced in lab through hot-press sintering method by spark plasma sintering (HP-D5, FCT). A schematic plot of sintering procedure is shown in Figure 1. The detailed information for C_3A pellets sintering is as follows:

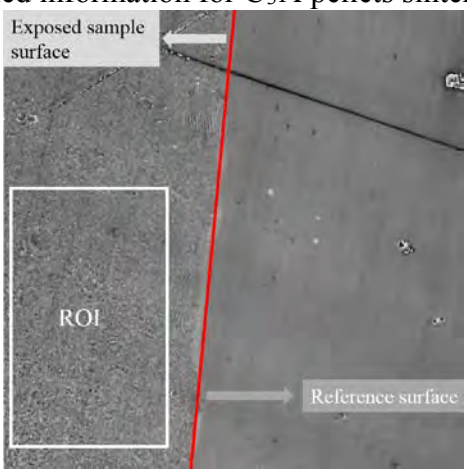

Figure 3: Morphology of partial polished C_3A pellet in phase image obtained by DHM. Reference surface is the surface covered by platinum player. The size of ROI (region of interest) is 220 pixel x 370 pixel, and the size of each pixel is 299 nm x 299 nm

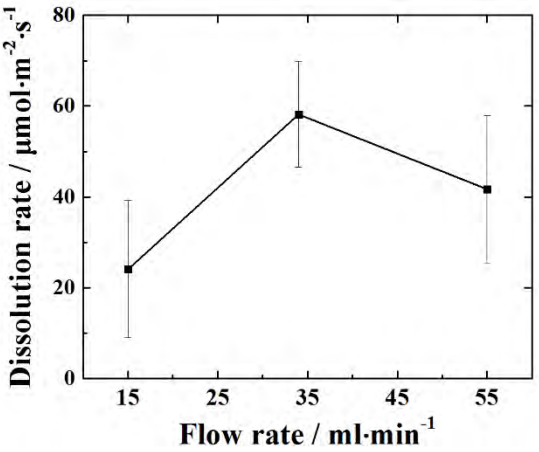

Figure 4: Overall dissolution rate as a function of water flow rate. Error bars are one standard deviation of the average overall dissolution rate for at least three samples at each flow rate

2.3 SURFACE ANALYSIS

Microstructural and morphological characterization of the dissolved surface was carried out using scanning electron microscopy (FEI 3D, FEI). Given that calcium aluminate hydrates form so quickly, C_3A was first dissolved in flowing deionized water with a flow rate of 34 ml·min^{-1} for only about 2 s, and then the surface was washed by ethanol and dried by compacted air as soon as possible. C_3A surface was partially covered with a platinum layer of about 50 nm thickness before immersion as a reference.

3. RESULTS

3.1 FLOW RATE EFFECTS

Figure 4 shows the dependence on flow rate of the overall dissolution rate in the first few seconds. It can be seen that with the increase of flow rate, the measured dissolution rates firstly reach a maximum value at flow rate of 34 ml·min^{-1}, and then drops a little when flow rate continuously increasing. It indicates that when the flow rate is lower than 34 ml·min^{-1}, ionic diffusion may play a more important role than surface reaction in controlling dissolution, and when flow rate is higher, swirls of the water within the flow-through cell might form, resulting the actual flow rate lower than the target value. Therefore, 34 ml·min^{-1} is adopted as the flow rate for the following study.

3.2 SURFACE MORPHOLOGY AFTER INITIAL DISSOLUTION

Surface morphology of C_3A after the contact with water for about 2 s can be seen in Figure 5, in which the right bottom of Figure 5 is the reference surface, and it remains smooth during the measurement, though a few hydration products appears in some local areas. This is due to the incomplete coverage of the platinum player, especially at the regions with deep scratches. Different from reference surface, the surface not covered with chemical-inert layer becomes very rough and a layer of hydration product with crumpled foil shape can be clearly seen, as shown in Figure 6. Similar microstructure changes have been reported by Meredith et al[13]. The thickness of this hydrates layer is measured from the side view of the specimen based on the brightness contrast with the bulk material, as shown in Figure 7. The thickness is about 300 nm.

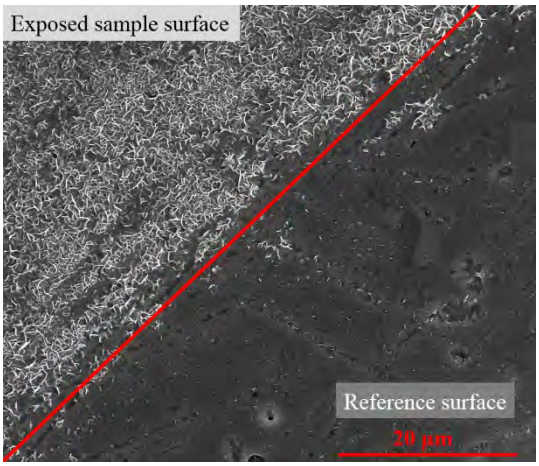

Figure 5: C_3A surface after dissolution

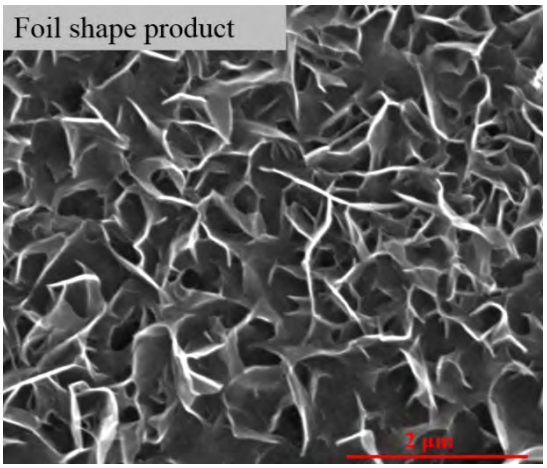

Figure 6: Morphology of hydration product layer

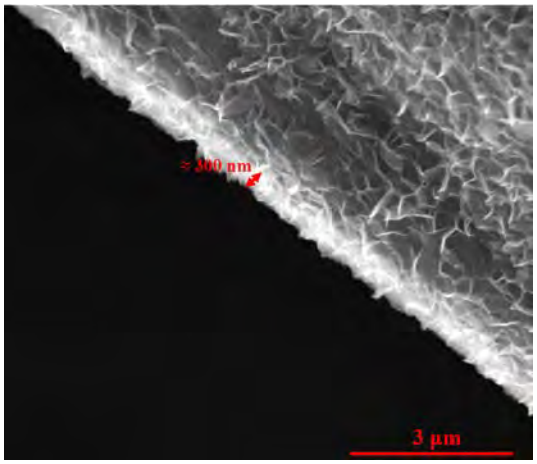

Figure 7: The side view of C_3A surface after dissolution

4. DISCUSSION

4.1 Analysis of C_3A dissolution kinetics

By tracing the average relative surface height change to the reference surface, it is clearly seen in Figure 8 that the surface height changing can be roughly divided into three periods, including the initial fast height reducing, followed by the slow height increasing and the moderate height reducing. It suggests that after the rapid dissolution lasting for about half of a second in the first stage, the surface starts to be gradually covered by the hydration product in the second stage, in agreement with the results shown in Figure 5-7. Though covered by a layer of product, the dissolution continues because the product is with foil shape and not able to stop dissolution completely. Nevertheless, combined by the decreasing effect of dissolution and increasing effect of hydration on surface height change, the average relative surface height decreases at a relative constant rate which is much slower than the initial dissolution. The overall dissolution behavior is similar as the heat flow during C_3A powder hydrates in water[12]. For C_3S and cement, it also can be found in literatures that the heat flow behaves similarly[14-15]. Although it is not completely the same with protective layer hypothesis which assumes a layer formed on the surface can control the hydration reaction for a much longer term, often dozens or hundreds of minutes[16-17], according the DHM measurements, this surface layer was able to decrease the dissolution rate dramatically within the time frame of a quarter of a second.

Figure 9 shows the dissolution rate spectra of region ROI in Figure 3. The rate spectra characterize a frequency distribution of dissolution rates at different locations. They provide much detailed information about the dissolution behavior of a mineral surface and have been widely used in previous studies[10,18]. The positive dissolution rate in Figure 9 means dissolution and the negative means precipitation. Figure 9a shows the overall dissolution rate distribution ranging from -50 to 150 $\mu mol \cdot m^{-2} \cdot s^{-1}$. The precipitation phenomenon is also reported by literature [7], in which the effect of water activity on C_3A dissolution is studied. Different from the overall spectrum, the rates in the first quarter of a second are all positive. More interestingly, the dissolution rates are mostly in the magnitude of 500 ~ 1500 $\mu mol \cdot m^{-2} \cdot s^{-1}$, which are much larger than rates shown in the overall spectrum and the rate extrapolated in literature [7].

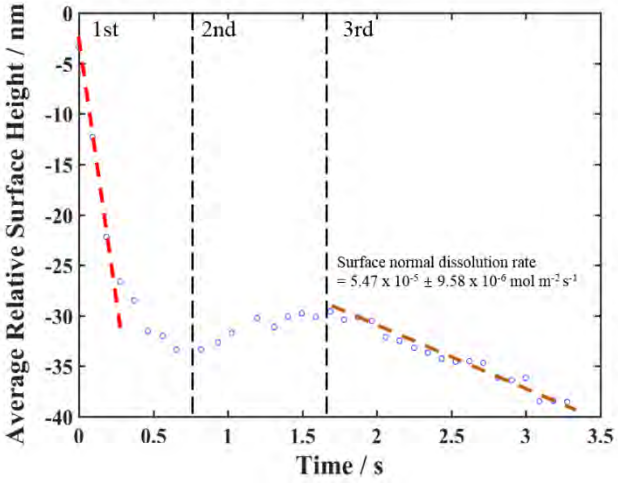

Figure 8: The average surface height change during dissolution

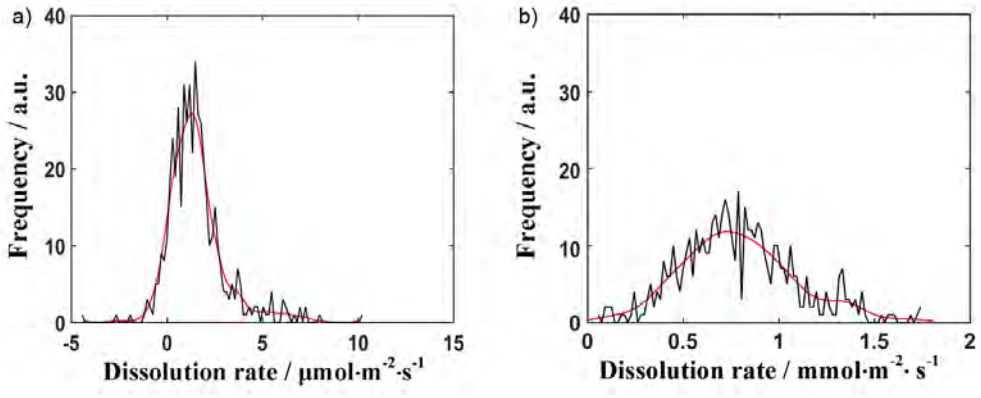

Figure 9: Dissolution rate spectra of region ROI in Figure 3 (a) is the overall dissolution rate spectrum, while (b) is the rate spectrum in the first quarter of a second

4.2 Probable initial dissolution behaviour (a timescale of a few seconds)

As mentioned above, precipitation happens even within the first second of contact with water. Therefore, any dissolution measurement longer than one second is actually a result of the combination of both dissolution and precipitation. By analyzing the data in Figure 8, it can be seen that the average pure dissolution rate of C_3A (in the first quarter of a second) is about 15 to 20 times larger than the rates obtained after two second. So according to Eq. (1) in Section 2.2, the surface height change, $\frac{\Delta h}{\Delta t}$, is about 73.6 ~97.6 nm·s^{-1}. Given the uncertainty of the measurement results shown in Figure 4, the surface height change can reach a maximum value at about 140 nm s^{-1}. If we assume that the pure dissolution rate of C_3A and the pure precipitation rate of hydration product remain constant during the first few seconds, so combined Figure 8 and the value calculated above, the absolute value of precipitation rate should be just slight lower than that of dissolution rate. Within 2 seconds of contact with water, the product layer thickness is estimated to be able to reach 200 ~300 nm. This is close to the value measured under SEM (Figure 7), which is actually slightly higher. This small difference can be attributed to the higher reactivity of the edge region of the sample measured under SEM than the flat regions measured by DHM[19].

5. CONCLUSIONS

- In-situ nanoscale measurement on C_3A dissolution was the first time performed by DHM in flowing deionized water.
- At a flow rate of 34 ml·min^{-1}, C_3A can dissolve at a rate of 500 ~ 1500 mmol·m^{-2}·s^{-1} within the first a quarter of a second after contact with water. After then, crumple foil like hydration product starts to form, which dramatically reduces the dissolution rate of C_3A.

ACKNOWLEDGEMENTS

The authors gratefully acknowledge financial support from National Nature Science Foundation of China via Grant No. U170620242 and 51708108. The authors thank Dr. Jeffrey W. Bullard (Texas A&M University, US) for insightful comments during the preparation of the manuscript.

REFERENCES

[1] Lüttge A. Crystal dissolution kinetics and Gibbs free energy. Journal of Electron Spectroscopy and Related Phenomena, 2006, 150(2-3): 248-259.

[2] Juilland P, Gallucci E, Flatt R, et al. Dissolution theory applied to the induction period in alite hydration. Cement and Concrete Research, 2010, 40(6): 831-844.

[3] Juilland P, Gallucci E. Morpho-topological investigation of the mechanisms and kinetic regimes of alite dissolution. Cement and Concrete Research, 2015, 76: 180-191.

[4] Nicoleau L, Nonat A, Perrey D. The di-and tricalcium silicate dissolutions. Cement and Concrete Research, 2013, 47: 14-30.

[5] Nicoleau L, Nonat A. A new view on the kinetics of tricalcium silicate hydration. Cement and Concrete Research, 2016, 86: 1-11.

[6] Taylor H F W. Cement chemistry. Thomas Telford: London, 1997.

[7] Brand A S, Bullard J W. Dissolution kinetics of cubic tricalcium aluminate measured by digital holographic microscopy. Langmuir, 2017, 33(38): 9645-9656.

[8] Sand K K, Stipp S L S, Hassenkam T, et al. Ethanol adsorption on the $\{10\bar{1}4\}$ calcite surface: preliminary observations with atomic force microscopy. Mineralogical Magazine, 2008, 72(1): 353-357.

[9] Sand K K, Yang M, Makovicky E, et al. Binding of ethanol on calcite: The role of the OH bond and its relevance to biomineralization. Langmuir, 2010, 26(19): 15239-15247.

[10] Feng P, Brand A S, Chen L, et al. In situ nanoscale observations of gypsum dissolution by digital holographic microscopy. Chemical geology, 2017, 460: 25-36.

[11] Brand A S, Feng P, Bullard J W. Calcite dissolution rate spectra measured by in situ digital holographic microscopy. Geochimica et cosmochimica acta, 2017, 213: 317-329.

[12] Alonso M M, Puertas F. Adsorption of PCE and PNS superplasticisers on cubic and orthorhombic C_3A. Effect of sulfate. Construction and Building Materials, 2015, 78: 324-332.

[13] Meredith P, Donald A M, Meller N, et al. Tricalcium aluminate hydration: Microstructural observations by in-situ electron microscopy. Journal of Materials Science, 2004, 39(3): 997-1005.

[14] Ouzia A, Scrivener K. The needle model: A new model for the main hydration peak of alite. Cement and Concrete Research, 2019, 115: 339-360.

[15] Jansen D, Goetz-Neunhoeffer F, Lothenbach B, et al. The early hydration of Ordinary Portland Cement (OPC): An approach comparing measured heat flow with calculated heat flow from QXRD. Cement and Concrete Research, 2012, 42(1): 134-138.

[16] Jennings H M, Pratt P L. An experimental argument for the existence of a protective membrane surrounding Portland cement during the induction period. Cement and Concrete Research, 1979, 9(4): 501-506.

[17] Birchall J D, Howard A J, Bailey J E. On the hydration of Portland cement. Proceedings of the Royal Society of London. A. Mathematical and Physical Sciences, 1978, 360(1702): 445-453.

[18] Fischer C, Luttge A. Beyond the conventional understanding of water–rock reactivity. Earth and Planetary Science Letters, 2017, 457: 100-105.

[19] Arvidson R S, Ertan I E, Amonette J E, et al. Variation in calcite dissolution rates: A fundamental problem?. Geochimica et cosmochimica acta, 2003, 67(9): 1623-1634.

INFLUENCE OF CARBON DIOXIDE AS A MIXTURE COMPONENT ON THE CEMENT HYDRATION

André Silva(1), Rita Nogueira(1), J. Alexandre Bogas(1) and Miguel Rodrigues(2)

(1) CERIS, ICIST, Instituto Superior Técnico, Universidade de Lisboa, Portugal

(2) Centro de Química Estrutural, CERENA, Instituto Superior Técnico, Universidade de Lisboa, Portugal

Abstract

Concrete is the most widely material used in the construction industry. However, it has a great environmental impact, mainly because of cement manufacture and the inherent CO_2 emissions into the atmosphere.

This research intends to contribute to the reduction of the environmental impact of the concrete industry through the uptake of CO_2 during the concrete production phase.

The few research works on this issue report contradictory results regarding the impact of CO_2 when added during the mixing phase. These results report an acceleration of the reactions [1], a reduction of the time setting [2] and either an increase or a decrease in the amount of hydration products, depending on the CO_2 amount [3, 1].

Thus, this research aims at understanding the impact of CO_2 amount on the hydration reactions of cement in order to enable its adoption as a component mixture.

To achieve this purpose, 4 cement pastes were produced with different amounts of CO_2. The pH of the mixture was measured to evaluate the impact of CO_2 on its alkalinity reduction. Compressive strength, XRD and SEM analysis were also performed to assess the influence on the hydration reactions and also on the degree of carbonation. Results suggest that CO_2 can increase the mechanical resistance at early ages if used in a little amount. However, the reduction in pH due to CO_2 appears to compromise this performance at longer ages.

Keywords: Carbonated water, Cement carbonation, Compressive strength, XRD, SEM

1. INTRODUCTION

The ease of application, versatility, good performance and availability of raw materials makes concrete the most widely used construction material, accounting for 70% of all construction materials. Concrete has, however, a high environmental impact due to the emission of carbon dioxide (CO_2) produced during the manufacturing of cement, namely in the calcination of limestone and combustion of fuels. Thus, it is estimated that this industry is responsible for at least 5% of the global CO_2 emission, annually [4, 5].

The reduction of the environmental impact associated with the production of cement has recently been the aim of scientific community and industry, with new strategies focused on capturing and incorporating the CO_2 in cement mixtures [6, 7]. However, these strategies have been mainly focused on the carbonation cure of freshly cast concrete, limiting the applicability of CO_2 usage in the concrete industry.

Although, CO_2 is naturally absorbed by concrete, the carbonation process is slow and only 8% to 28% of the reactive materials are estimated to be carbonated in the end of concrete life cycle [4, 5]. The mechanism of natural carbonation of cement is an extensively documented issue, and can be summarized by Eq. (1) and (2) that show how the two main components in life cycle of cement - portlandite ($Ca(OH)_2$) and calcium silicate hydrate (CSH, in cement chemistry notation) - react with CO_2 to form calcium carbonate ($CaCO_3$) and silica gel (SiO_2) [8, 1]:

$$Ca(OH)_2 + CO_2 \rightarrow CaCO_3 + H_2O \quad (1)$$

$$CSH + 2CO_2 \rightarrow SiO_2 + 2CaCO_3 + H_2O \quad (2)$$

For the carbonation of freshly cast concrete, the mechanisms of early carbonation of cement can be summarized by Eq. (3) and (4), that show the carbonation of the dicalcium and tricalcium silicate (C_2S and C_3S, respectively, both according to the cement chemistry notation), producing a hybrid of calcium-silicate-hydrate and calcium carbonate [8, 1]:

$$C_3S + (3-x)CO_2 + yH_2O \rightarrow C_xSH_y + (3-x)CaCO_3 \quad (3)$$

$$C_2S + (2-x)CO_2 + yH_2O \rightarrow C_xSH_y + (2-x)CaCO_3 \quad (4)$$

Natural carbonation of mature concrete is an undesirable chemical reaction mainly because it decalcifies the concrete and reduces the pH value of the pore solution, leading to the depassivation of the reinforcement and consequently to steel corrosion. However, the carbonation at early ages can be beneficial, as it can be used as an accelerated curing technique [8, 1]. Different studies on carbonation techniques have been developed, mainly based on the curing of fresh concrete, reporting distinct results, namely, an acceleration of the reactions [1], a reduction of the time setting [2] and either an increase or a decrease in the amount of hydration products, depending on the CO_2 amount [3, 1].

The aim of this research is to study the influence of CO_2 on the hydration mechanisms of cement, focusing on the production phase of concrete instead of on the cure phase, strategy widely explored by other authors. For this purpose, CO_2 is provided to the mixing process as a mixture component, by being dissolved in the mixing water. Thus, the pre-carbonation of water provides the carbonate ions needed for the hydration and carbonation kinetics of cement, hence the CO_2 uptake is made during the concrete production instead of its aging.

To achieve this purpose, 4 cement pastes were produced with different amounts of CO_2. The reference sample (R-reference) and three other pastes made with increasing levels of dissolved CO_2 in the water (HC – high carbonated; MC – medium carbonated; and LC – low carbonated). The pH of the mixture was measured to evaluate the impact of CO_2 on its alkalinity reduction. Compressive strength, XRD analysis and scanning electron microscopy were also performed.

2. MATERIALS AND METHODS

2.1. Materials

The Portland Cement CEM I 42,5R used has a mineralogical composition of C_3S=56.7%, C_2S=16.6%, C_3A=10.0%, C_4AF=9.2% and a specific surface (Blaine) of 452 m^2/kg. The chemical composition of cement is CaO=62.76%, SiO_2=19.42%, Al_2O_3=26.00%,

Fe_2O_3=3.00%, Mg0=1.74%, K_20=0.53%, Na_2O=0.12%. The mixing water was provided by the main water supply. The CO_2 gas supply was provided by AirLiquide, at 99.995% purity.

2.2. Pre-carbonation of mixing water

The mixing water was pre-carbonated by pumping CO_2 into an airtight chamber containing water, following the setup illustrated in Figure 1. A container with 1300g of water was placed inside the chamber and the magnetic stirrer was set to give a rotation of 720rpm at a temperature of 25ºC. After closing the chamber, CO_2 was pumped for 20min at a constant flow, until a CO_2 concentration of 80% was reached.

Preliminary tests had determined that the saturation concentration of CO_2 in the water (1.68g/kg of water [9]) could be achieved by this procedure. The CO_2 concentration in the water was monitored by measuring the pH value of water (using a pH probe). The water quickly reached a pH value of ≈4.30, indicating the saturation concentration of CO_2 dissolved in the water previously mentioned [10].

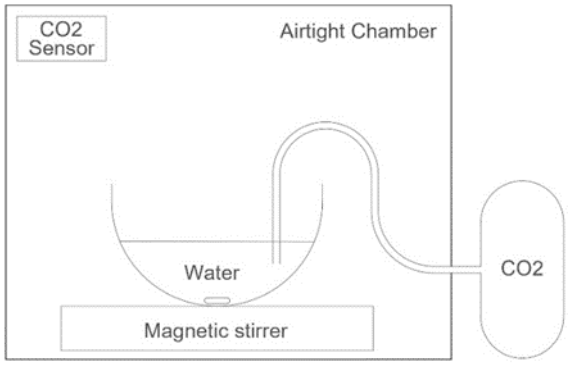

Figure 1: Schematic setup for the carbonation of water

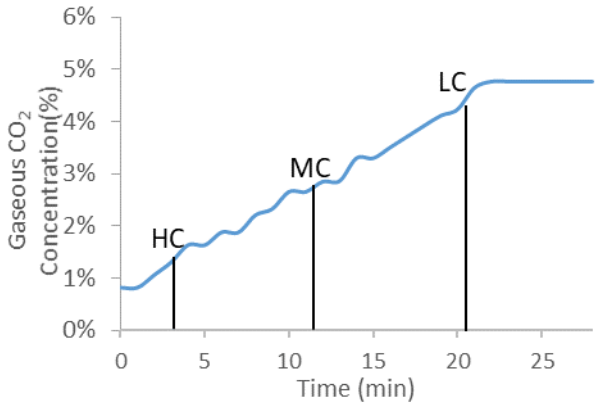

Figure 2: Concentration of gaseous CO2 inside the chamber

Then, the water thus obtained, was left waiting at room environment for defined sets of time, which led to different degrees of carbonation, through CO_2 release. Once the waiting time was over the water sample was mixed with the cement.

Preliminary tests were made to determine the CO_2 release rate, required to establish the diverse degrees of water carbonation and corresponding waiting time sets. Once the CO_2 concentration of 80% was achieved, the flow of gaseous CO_2 was shut and the door of the chamber was open for 1 min. This step allowed to the concentration of CO_2 in the environment

inside the chamber to return to its initial concentration in the atmosphere. Then, the door was closed, and the growing of the CO_2 concentration was monitored (Figure 2). The CO_2 concentration took 21min to stabilize and increased at a constant rate. The aqueous CO_2 concentration over time was determined from gaseous CO_2 concentrations in the atmosphere, by Henry's law [11]. The diverse carbonated water samples are indicated in Figure 2 and in Table 1.

Table 1: Concentrations of the carbonated water samples

Sample	CO_2 concentration (mmol/L)
R	0.01
LC	5.09
MC	15.55
HC	26.01

2.3. Characterization of the cement pastes

Cement pastes were prepared with the diverse water samples, following the standard NP EN 196-1:2006. Specimens were cast in prismatic molds with 4x4x16cm^3, demoulded after 1 day and cured in a moist chamber until testing age. Tests were carried out at 1, 3, 7, 14 and 28 days of curing age.

Hydration and carbonation products formed in cement pastes samples were examined by X-Ray Diffraction (XRD) and Scanning Electron Images (SEM). For XRD and SEM a hydration stoppage method was applied at the different testing ages. The prismatic specimens were cut into smaller samples with 5x5x1cm^3 and put in 50ml of isopropanol for 15 min. Then, the sample was dried in an incubator at 40ºC for 10min and finally put inside a desiccator in vacuum until testing [12, 13].

For each sample, 4 compressive strength tests were performed at different curing ages, following the standard NP EN 196-1:2006.

The pH values of the pore solution were measured by grinding 30g of the sample into fine particles. Then, 30g of distilled water was added, corresponding to a ratio of 1:1, and this mixture was stirred. Finally, the value of the pore solution was measured using a pH probe [14].

3. RESULTS AND DISCUSSION

3.1. Compressive strength

Compressive strength results (Figure 3) show that the mechanical resistance tends to increase with the increasing of CO_2 concentration in the mixing water for the curing age of 3 days, but the opposite happens for the three higher ages (7 days, 14 days and 28 days).

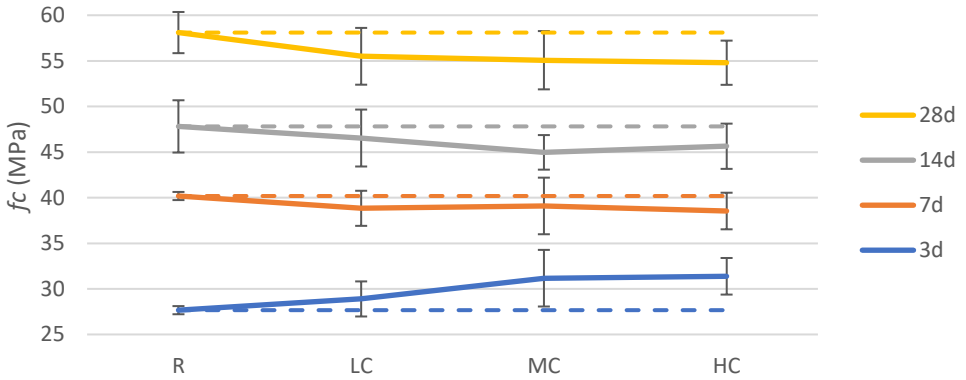

Figure 3: Compressive strength

These results suggest that CO_2 accelerates the cement setting at early ages; however, whichever are the reactions causing this acceleration, it seems that they penalize the development of the mechanical resistance immediately after.

The increase of the mechanical resistance is often explained by the higher amount of calcite returned by carbonation reactions, which tends fill pores, increasing the density of the mixtures [15, 16]. To investigate if this is the explanation for the compressive strength results, XRD analysis were performed to assess, namely, the amount of calcite in the different mixtures.

3.2. X-Ray diffraction (XRD)

Figure 4 shows the XRD results of reference sample (R), low CO_2 sample (LC), and high CO_2 sample (HC) in 4 different ages. XRD results were focused on the patterns of alite, belite, calcite (CC) and portlandite (CH) defined by the peaks 51.7º, 31.1º, 39.4º and 34.1º, respectively, as these peaks were selected as those values are free from peak overlapping [17].

The peak intensity of alite graph shows that, for 1 day, there is a higher consumption of alite for the sample HC and LC when compared with R. This result is also observed in the age of 3 days, but in a lower degree. The analysis of the following ages shows that there is a progressive consumption of alite, an observation also supported by the second smaller peak shown in the peak intensity of CH graph, which corresponds to alite instead of CH.

On the contrary, the peak intensity of belite graph shows a constant amount of belite in every tested age, suggesting that the compound was not consumed throughout the chemical reactions.

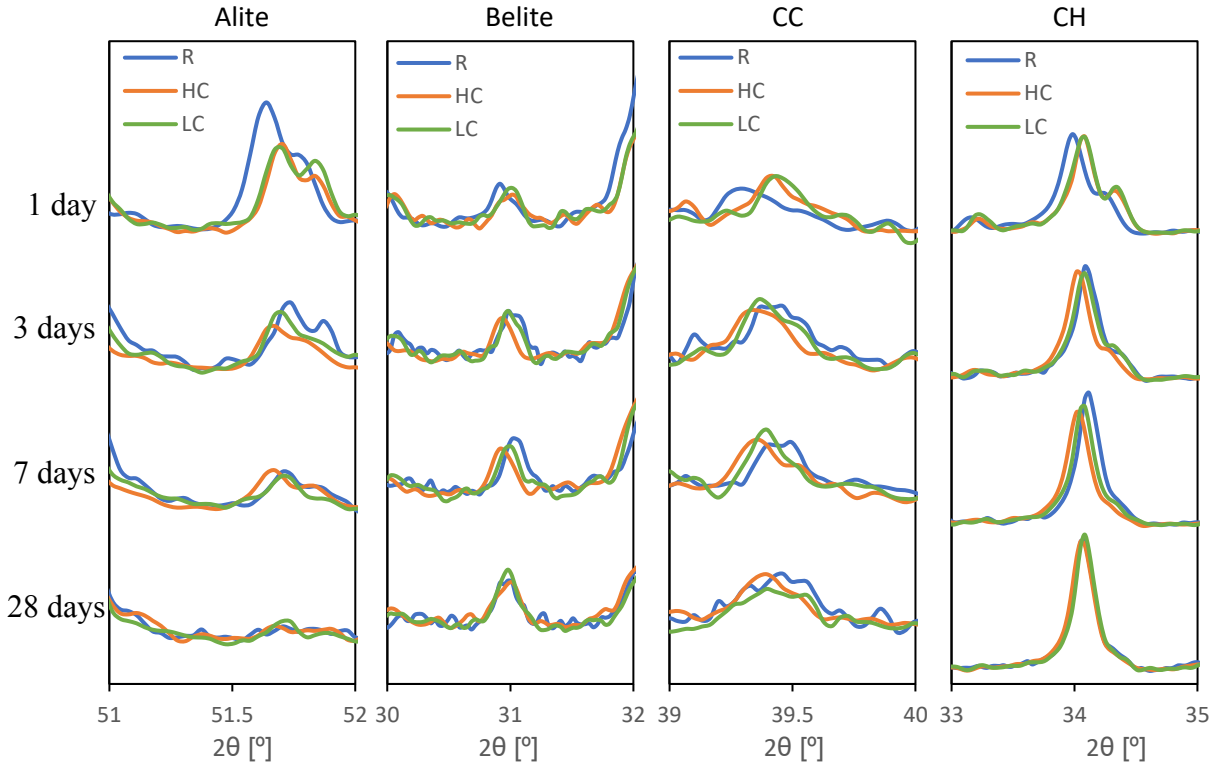

Figure 4: XRD patterns for alite, belite, CC and CH

The peak intensity of CC graph displays a slightly higher peak for HC and LC in comparison with the R sample, for 1 day. However, for the remaining ages, these peaks remain similar, showing that the formation of calcite crystals remains constant for the three samples. Following this result, also the CH shows, in the peak intensity of CH graph, a constant and similar quantity of CH in the three samples, even though the R sample exhibits slightly higher peak in every age, except for the 28 days.

These results suggest that CO_2 contributes to increase the dissolution rate of alite at early ages (1 and 3 days), which might be related with the higher compressive strength obtained in the CO_2-richer pastes with 3 days (Figure 3). In this situation, the dissolution of alite should have contributed to the formation of CC though the Eq. (3), followed by the consequent consumption of CH (Eq. 1). CSH is another product of this reaction and probably the component responsible for the increase in mechanical resistance observed in higher carbonated pastes at lower ages.

However, the mechanisms responsible for the inversion of this rising trend of the mechanical resistance for CO_2-richer pastes at later ages are not evident in the XRD results.

3.3. Scanning electron images (SEM)

SEM images were collected in HC and R pastes for the ages of 1 and 3 days, showed in Figure 5 and Figure 6.

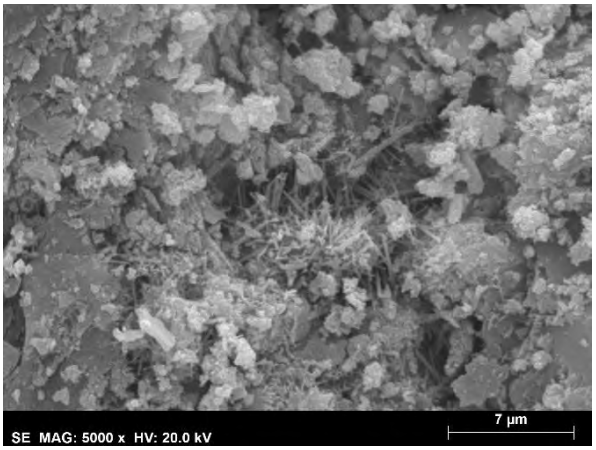

Figure 5:SEM image of a 1 day old HC sample

A macroanalysis of Figure 5 reveals a disperse set of reaction products across the surface of the cement grains with a considerable porosity between them. Figure 5 also shows the presence of needled structures, presumably ettringite, and products of cement chemical reactions of smaller sizes ($\approx 1\ \mu m$) on the surface of unreacted cement grains.

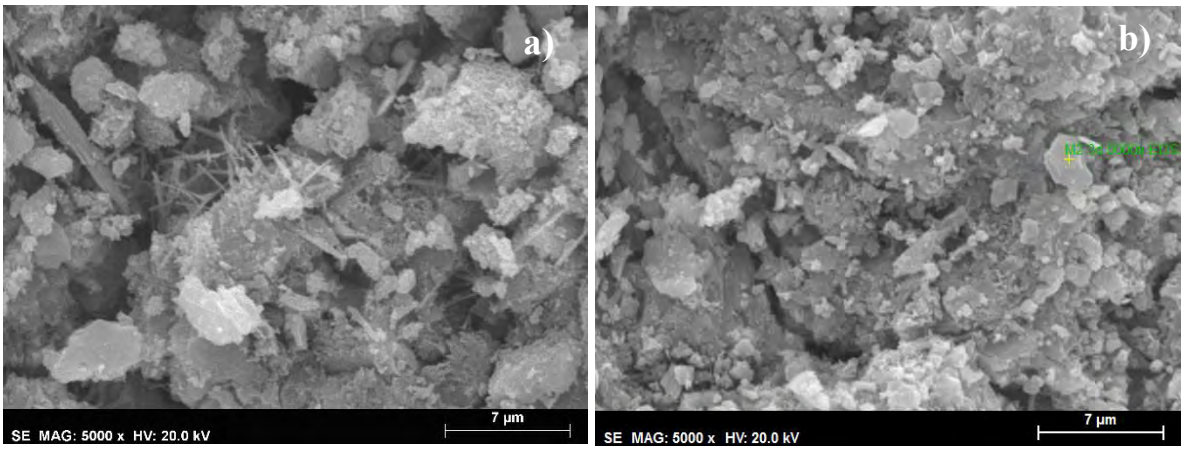

Figure 6: SEM images of a 3 days old R sample (a) and HC sample (b)

The analysis of Figure 6 shows that for the R sample (a) the products of cement reaction exhibit a bigger dimension ($\approx 2\ \mu m\ to\ 3\ \mu m$) than HC paste (b) of 3 days and 1 day (Figure 5). Needled structures were also found in the R sample (a). HC sample also shows the presence of needles, but in a lower amount, and the presence of calcite products identified through EDS (yellow cross in Figure 6b), illustrating the effect of carbonated water on the hydration reactions of cement. The lower presence of needles can be due to a quicker conversion of ettringite into calcium monosulfoaluminate [15]. Conversely the presence of calcite can be attributed to the carbonation of Ca^{2+} ions resulting from the hydration reactions [18, 19].

3.4. pH Measurement

Results from the pH measurement (Figure 7) suggest that for the curing age of 3 days the pH value is higher for LC both in relation to R-paste and CO_2-richer pastes (MC and HC).

However, the pH tends to increase with the curing age, stabilizing for a constant value of 12.7 observed in all the pastes at 28 days.

The pH results also suggest that, for the age of 28 days, each paste presents the same pH value, showing that cement paste carbonation in the early ages can produce specimens with pH values similar to uncarbonated concrete.

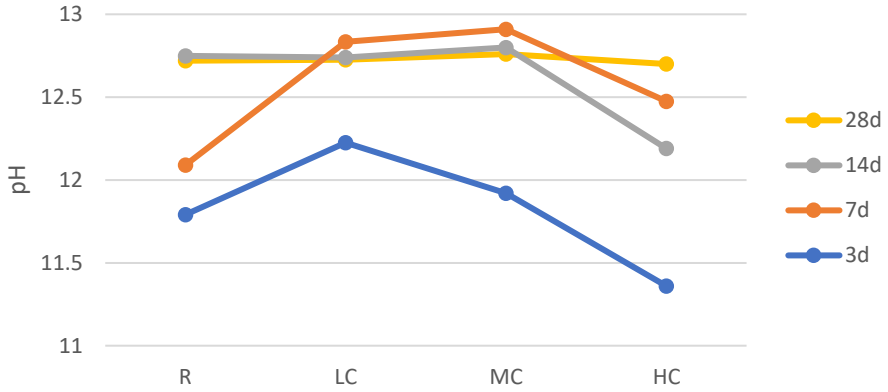

Figure 7: pH measurement results

These results suggest a combination of two opposite effects. On the one hand, the presence of CO_2 in the paste seems to cause an increase of the dissolution of alite at early ages, increasing the hydration and the mechanical resistance (Figure 3). At the same time, the formation of CH also increases, and the pH value rises (case of LC in Figure 7). On the other hand, for higher CO_2 concentrations, there is a consumption of CH (Eq. (5) and (6)) that is not made up by the higher CH release previously mentioned and the pH values drops (cases of MC e HC in Figure 7).

$$CO_{2(aq.)} + OH^- \leftrightarrows HCO^-_{3(aq)} \quad (5)$$

$$HCO^-_{3(aq)} + OH^-_{(aq)} \leftrightarrows H_2O + CO^{2-}_3 \quad (6)$$

These considerations might explain the contradictory trends observed in the compressive strength results for early and later ages. A pH value higher than 11-12 is important to ensure the quality of the hydrated components of cement [20], since the silicate compounds loose reactivity for lower pH values [21].

Hence, it seems that CO_2 gives a positive effect at early ages because it contributes to the hydration of cement, but the effect is negative for later ages, because of the reduction in the pH values.

4. CONCLUSIONS

The impact of CO_2 in cement pastes in the mixing process studied in this article allowed to present the following conclusions:

- The presence of CO_2 in the initial stage of the process of hydration of cement has an effect on the initial compressive strength, leading to higher strengths. However, for the later ages this effected is reversed, leading to lower strengths for carbonated samples.
- The lower peak intensity of alite showed by the XRD results for the carbonated samples suggests that the presence of CO_2 in the mixture promotes an acceleration

of the hydration reactions of cement. Notice that this hydration is supposed to be associated to the production of CH and CSH.

- The SEM images showed the presence of hydration products with smaller dimensions for the carbonated samples and also the presence of calcite products, illustrating the effect of carbonate ions on the cement hydration kinetics.
- The pH results show that the presence of CO_2 increases the pH for early ages and for low CO_2 amounts, and the opposite happens for later ages and higher CO_2 concentrations.
- The results from the tests appear to justify the higher compressive strength for carbonated samples at early ages, due to the faster hydration reactions and the higher quantity of CC. For later ages, the lower compressive strength of the carbonated samples may be justified by the reduction in the pH value of the carbonated water.
- The pH value measurement result showed that even for carbonated samples, it can be achieved a pH value similar to uncarbonated concrete for the 28 days. This is an important result because it shows that problem regarding the depassivation of the reinforcement can be overcome when the carbonation is performed during the mixing process.

The results regarding the influence of CO_2 in the hydration reactions of cement presented in this paper set the base for further studies on this subject. Widening the applicability of the CO_2 usage in concrete production is a research area with a great potential as this paper and others demonstrate [19, 22, 23]. Further work should be focused on the application of the methodology in this paper to mortars and concrete, and the development of new ways to apply the carbonation technology to cementitious products.

5. ACKNOWLEDGEMENTS

This work was supported by the Polish National Agency for Academic Exchange under Grant No. PPI/APM/2019/1/00042/U/00001 and by the CERIS Research Centre, Instituto Superior Técnico, Universidade de Lisboa.

REFERENCES

[1] S. Monkman, M. MacDonald, P. Sandberg and R. Doug Hooton, “Properties and durability of concrete produced using CO2 as an accelerating admixture,” *Cement and Concrete Composites,* no. 74, pp. 218-224, 2016.

[2] F. C. Jorge, C. Pereira and J. M. Ferreira, “Wood-cement composites: a review,” *Holz Roh Werkst,* no. 62, pp. 370-377, 2004.

[3] J. Kwasny, P. Muhammed Basheer and M. Russell, “CO2 Sequestration in Cement-Based Materials During Mixing Process Using Carbonated Water and Gaseous CO2,” *4th International Conference on the Durability of Concrete Structures,* 2014.

[4] P. K. Metha, “Reducing the environmental impact of concrete: concrete can be durable and environmentally friendly,” *Concrete International,* vol. 10, pp. 61-66, 2001.

[5] C. Pade and M. Guimaraes, “The CO2 uptake of concrete in a 100 year perspective,” *Cem. Concr. Re,* vol. 37, pp. 1348-1356, 2007.

[6] L. Haselbach and Thomle J., "An alternative mechanism for accelerated carbon sequestration in concrete," *Sustainable Cities and Society,* vol. 12, pp. 25-30, 2014.

[7] P. He, C. Shi, Z. Tu, C. Sun Poon and J. Zhang, "Effect of further water curing on compressive strength and microstructure of CO2-cured concrete," *Cem. Concr. Compos.,* vol. 72, pp. 80-88, 2016.

[8] V. Rostami, Y. Shao, A. Boyd and Z. He, "Microstructure of cement paste subject to early carbonation curing," *Cem. Concr. Res.,* vol. 42, pp. 186-193, 2012.

[9] J. A. Dean, Lange´s Handbook of Chemistry, 15º ed., University of Tennessee, Knoxville: McGraw-Hill, Inc., 1999.

[10] S. E. Manahan, Environmental Chemistry, 9º ed., Boca Raton: CRC Press, 2010.

[11] R. Sander, "Compilation of Henry's law constants (version 4.0) for water as solvent," *Atmospheric Chemistry and Physics,* no. 15, pp. 4399-4981, 2015.

[12] J. Zhang and G. W. Scherer, "Comparison of methods for arresting hydration of cement," *Cement and Concrete Research,* no. 41, pp. 1024-1036, 2011.

[13] K. Scrivener, R. Snellings and B. Lothenbach, A Pratical Guide to Microstructural Analysis of Cementitious Materials, CRC Press, 2016.

[14] A. Behnood, K. V. Tittelboom and N. D. Belie, "Methods for measuring pH in concrete: A review," *Construction and Building Materials,* no. 105, pp. 176-188, 2016.

[15] X. Qian, J. Wang, Y. Fang and L. Wang, "Carbon dioxide as an admixture for better performance of OPC-based concrete," *Journal of CO2 Utilization,* no. 25, pp. 31-38, 2018.

[16] E. Possana, W. Thomazc, G. Aleandric, E. Felixa and A. Santos, "CO2 uptake potential due to concrete carbonation: A case study.," *Case Studies in Construction Materials,* vol. 6, pp. 147-161, 2017.

[17] J. Jang and H. Lee, "Microstructural densification and CO2 uptake promoted by the carbonation curing of belite-rich Portland cement," *Cem. Concr. Res.,* vol. 82, pp. 50-57, 2016.

[18] N. Lippiatt and T.-C. Ling, "Rapid hydration mechanism of carbonic acid and cement," *Journal of Building Engineering,* no. 31, p. 101357, 2020.

[19] D. Zhang, Z. Ghouleh and Y. Shao, "Review on carbonation curing of cement-based materials," *Journal of CO2 Utilization,* vol. 21, pp. 119-131, 2017.

[20] W. K. W. Lee and J. S. J. v. Deventer, "The effect of ionic contaminants on the early-age properties alkali-activated fly ash-based cements," *Cement and Concrete Research,* no. 32, pp. 577-584, 2002.

[21] F. Pacheco-Torgal, J. Castro-Gomes and S. Jalali, "Alkali-activated binders: A review Part 1. Historical background, terminology, reaction mechanisms and hydration products," *Construction and Building Materials,* no. 22, pp. 1305-1314, 2008.

[22] M. F. Bertos, S. J. R. Simons, C. D. Hills and P. J. Carey, "A review of accelerated carbonation technology in the treatment of cement-based materials and sequestration of CO2," *Journal of Hazardous Materials,* no. B112, pp. 193-205, 2004.

[23] J. Jang, G. Kim, H. Kim and H. Lee, “Review on recent advances in CO2 utilization and sequestration technologies in cement-based materials,” *Constr. Build. Mater.,* vol. 127, pp. 762-773, 2016.

MICROSTRUCTURAL INVESTIGATION OF NANOCELLULOSE ADDITION ON THE PERFORMANCE OF CEMENTITIOUS MATERIALS CURED IN AGGRESSIVE ENVIRONMENTS

E. G. Deze (1), E. Cuenca* (2), M. Iakovlev (1), S. Sideri (1) and L. Ferrara (2)

(1) API Europe, Athens, Greece

(2) Department of Civil and Environmental Engineering, Politecnico di Milano, Italy

Abstract

During the last years, incorporation of nano-constituents into cement-based construction materials has been increasingly spreading thanks to their unique physicochemical properties which enable both nano- and micro-mechanical improvement of cementitious composites. It has been well established that besides increasing concretes strength, refinement of pore size occurs causing a significant reduction in total porosity values and improvement in specimens durability. The present work aims at the analysis and performance evaluation of nanocellulose (NC) enriched Ultra High Durable Concretes (UHDC) exposed to aggressive environmental conditions (i.e. chemical attack - XA environmental exposure class). To this purpose, two reference UHDC materials containing crystalline admixtures and steel fibers were compared with mixes holding also cellulose nanocrystals (CNCs) and cellulose nanofibrils (CNFs) into their structures. In all cases, NC loading remained constant and equal to 0.15% (by %wt of cement amount).The excellent reinforcing capabilities of NCs are demonstrated by the enhanced fracture resistance properties of the cementitious matrix. Additionally, microstructural analysis results of as derived specimens suggest that the use of NCs can lead to the development of materials with advanced textural and morphological characteristics and therefore widen their application prospects to aggressive environmental conditions.

Keywords: Nanoadditives, Nanocellulose (CNFs, CNCs) Ultra-High Durable Concretes

1. INTRODUCTION

Cement based materials are generally characterized as quasi-brittle due to their low tensile strength and fracture toughness. At the material level, typical reinforcement may be accomplished through the incorporation of dispersed fibers into the matrix. In that way, crack formation and propagation are being delayed to a great extent resulting into improved mechanical performance

[1,2]. The ultimate goal of this research is to modify the properties of concretes at the nanoscale and develop nano.engineered materials with improved macroscopic properties.

It has been reported that integration of cellulosic fibers into cementitious composites (C-FCCs) impart an adequate bonding capacity to the matrix resulting in substantial improvements in toughness, ductility, flexural strength and impact resistance [3]. Indeed, cellulose is characterized by superior mechanical properties (tensile strength up to 700MPa), low density and an internal curing ability due to the high water retention capacity. Moreover, cellulose is considered as non-toxic, renewable, cost effective and abundant compared to other fibers (e.g. asbestos, polyvinyl-alcohol PVOH, polypropylene) satisfying the need for the development of novel, biodegradable and non-petroleum materials with low environmental impact. However, several drawbacks arose in the performance of C-FCCs, which mainly lay on fibers mineralization, low durability and low biopolymer loading dictated from poor dispersion issues and the formation of inhomogeneous regions in more cellulose concentrated materials [3,4].

A likely feasible alternative for enhancing cellulose reinforcement capacity without increasing its loading in cementitious mix-designs is to utilize biopolymer at the nanometer scale. Incorporation of nanocellulose (NCs) has opened a new field for nanosized reinforcement within cementitious composites and the development of materials with improved performance [5,6]. Several reasons can be attributed to NCs reinforcement activity. Their high specific surface area and chemical reactivity derived from the high population of hydroxylic and carboxylic surface groups, significantly promotes interactions between materials components (e.g. PVOH fibers, SiO_2 etc.) also favoring the formation of an extensive NCs-matrix network [7]. The latter, improves bonding strength and act as stress boundary uniformly distributing stress in a bridge-like pattern and inhibiting fiber pull out phenomena [8]. More than that, during cement hydration the small sized NCs tend to interlock with each other and accumulate along with the precipitated hydration products into structure defects contributing to the reduction of porosity and micro-cracking activity. NCs hydrophilic nature also play an important role during cement hydration process. Acting as nuclei, NCs promote the formation of hydration products (especially CSH), whereas the already formed NCs-matrix network operates as water reservoir that gradually releases water to the matrix in dry environment. In this way, the matrix is able to undergo continuous hydration with partially replenished porosity and low micro-crack formation.

Summarizing, there is a significant potential for NCs (CNFs or CNCs) in improving the properties of cementitious composites. In this study, that was performed under the scope of H2020 ReSHEALience project, the effect was investigated of NCs on the macro- to micro- to nano-scale mechanical properties of cementitious composites. The main objective is the development of Ultra High Durability Concretes (UHDC) with improved strength, toughness and durability performance in aggressive environmental conditions (chemical attack exposure-XA). To this goal, specimens containing crystalline admixtures, steel fibers and cellulose nanocrystals (CNCs) or cellulose nanofibrils (CNFs) were produced. Incorporation of different NC species into cementitious mixtures will offer a side-by-side performance comparison between CNCs and CNFs leading to a better understanding of particle morphology impact on composite properties.

2. MATERIALS & METHODS

In an attempt to evaluate the microstructural characteristics and mechanical properties of nanocellulose enriched concretes exposed in XA environmental conditions, three different High-Performance Fiber Reinforced Cementitious Composites (HPFRCCs) were cast (Table 1). Among them, HPFRCCs mixture containing CEM I and slag as binder, sand, crystalline admixtures and steel fibers was used as reference material (labeled as XA-CA). The adopted mixing procedure and the employed dosages of constituents were formulated in order to guarantee self-compacting properties. Following the same experimental protocol two additional mixtures were produced containing also cellulose nanocrystals (XA-CA-CNC) and cellulose nanofibrils (XA-CA-CNF). Nanocellulose polymers used were derived from softwood biomass using AVAP® biorefinery technology and were supplied as 10%wt aqueous suspension. Prior to their addition to cement, both NC additives were further dispersed in water down to 1.5%wt in order to achieve a final NC loading equal to 0.15%wt (by %wt of cement) at concretes. Slag, crystalline admixtures and cellulose nanoadditions have been added in the mixes to improve the mechanical and durability performance of the concretes when are exposed to chemical attack targeting to the new concept of "Ultra-High Durable Concrete (UHDC)". The water to cement ratio in the mix was set at 0.33. Following mixing, the mixtures were casted in appropriate molds to produce prismatic 40x40x160 mm beam specimens, for flexural and compressive strength testing. After demolding (one day after casting) the specimens were cured in moist (20ºC, 95% RH) and geothermal water conditions until testing. The geothermal water used for specimen immersion, originates from the cooling basins of a geothermal plant owned by Enel Green Power (Tuscany, Italy). Chemical analysis results indicate the presence of both sulfate (SO_4^{-2}) and chloride (Cl^-) ions at of 2678ppm and 441 ppm, respectively.

Table 1 : mix-composition of investigated UHDCs

Constituents	XA-CA	XA-CA+CNC	XA-CA+CNF
CEM I 52.5R	600	600	600
Slag	500	500	500
Water	200	200	200
Steel fibers (l_f = 20 mm; d_f = 0.22 mm)	120	120	120
Sand 0-2mm	982	982	982
Superplasticizer	33	33	33
Crystalline admixtures (CA)	4.8	4.8	4.8
Cellulose nanocrystals (CNC)	-	0.15*	-
Cellulose nanofibrils (CNF)	-	-	0.15*

**by % wt cement*

Morphological investigation of materials was conducted with a Jeol JSM 7401F Field Emission Scanning Electron Microscope equipped with Gentle Beam mode and EDAX analyser. The applied acceleration voltage was 2 kV and samples were mounted on metallic (brass) substrates using a double coated carbon conductive tape. Prior to their observation, nanocellulose polymers and the fracture surface of the specimens were sputter coated at a 20nm thick layer of gold-palladium

(Au/Pd). Specimens were tested at For X-ray diffraction measurements, NC samples were prepared on microscope glass slides and allowed to dry in a silica designator for 72h. The corresponding patterns were acquired using a Rigaku rotating anode X-ray generator (operating at 50kV, 100mA, nickel filtered CuKa1 radiation) and a R-AXIS IV imaging plate. Thermogravimetric analysis was performed on a SETARAM SETSYS Evolution 18 Analyser, at a heating rate of 10 °C/min, in an alumina crucible using dried air as the carrier gas.

The mechanical performance of as prepared specimens was evaluated by flexural toughness (3-point bending) and compressive strength tests. Flexural tests were performed according to EN 1015-11:1999 on prismatic specimens (40x40x160mm). To this purpose, a 7 mm deep notch was cut at mid-span of the specimens. Three-point bending tests were performed in displacement control by measuring the Crack Mouth Opening Displacement (CMOD) at the tip of the notch. Then, once each specimen was completely tested in flexure and broken in two halves, compressive strength tests were performed also according to EN 1015-11. Tests were performed after 28, 56 and 84 days curing the specimens in both a climate room (T = 20°C and 95%) and in the geothermal water as above.

3. RESULTS AND DISCUSSION

3.1 Physicochemical and Morphological characterization of NC additives

3.1.1. Fourier-transform infrared spectroscopy (FT-IR)

Fourier Transform Infrared spectroscopy (FT-IR) provided a quantitive estimation of the presence of hydroxyl, sulphate and carboxylic groups attached on nanocellulose polymeric chains, as well as the existence of residual lignin amount. Recorded FT-IR spectrums of the examined NC samples along with a summary of transmittance signals associated with the corresponding bond vibrations are illustrated in **Errore. L'origine riferimento non è stata trovata.** and Table 2, respectively.

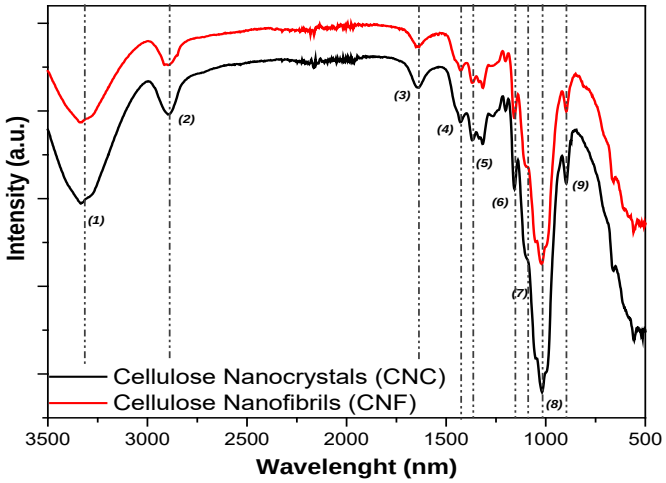

Figure 1: FT-IR spectrums of NC fibrils (CNF) & crystals (CNC).

As seen, all samples exhibit similar FTIR spectrums with analogous stretching-bending bond vibrations and signal intensities, displaying all characteristic α-cellulose peaks. These data are constituent with analogues results for NCs found in the literature (Figure 1, Table 2). The intense band noted at ~1025cm^{-1} (Label 8) is related to the glycosidic ^{4}C1 ring conformation deformation and β-glycosidic linkages between glucopyranose rings in cellulose. On the other hand, the band located at ~1430cm^{-1} (Label 4) is associated with the amount of crystalline structure within cellulose, while the band at ~895cm^{-1} (Label 8) is generally assigned to the amorphous regions of cellulose. Characteristic bands attributed to lignin functional groups (~3570cm^{-1}, ~1715-1675cm^{-1}, ~1602-1502cm^{-1}), carboxylic (~1729cm^{-1}) or sulphate (~1376cm^{-1}) compounds could not be distinguished in the spectrums, signifying the absence of these groups in NC polymers.

Table 2: Infrared band assignments for NC materials.

Wavenumber (nm)	Characteristic bands
(1) - 3320	OH stretching
(2) - 2890	Aliphatic C-H stretching
(3) - 1630	OH bending (absorbed water)
(4) - 1430	C-H symmetric bending (CH_2)
(5) - 1370	C-H & C-O pyranose ring bending
(6) - 1160	C-O-C stretching
(7) - 1100	Out of phase bending
(8) - 1025	C-C, C-OH, C-H pyranose ring & side groups
(9) – 895	C-O-C, C-C-O, C-C-H deformation & stretching

3.1.2. X-Ray Diffraction analysis (XRD)

Both nanocellulose polymers exhibit a single broad peak at low angle region centered between 15º and 15.5º, accompanied with a higher order Bragg reflection located at 22.5º assigned to crystallographic planes (110^{-}) and (200), respectively (Figure 2). These polymorphs correspond to cellulose I structure, which consider as the polymorph of cellulose with the highest mechanical integrity [9]. A low intensity peak can also be observed at 2θ=34°, which corresponds to (004) cellulose plane, whereas (110) diffraction peak is convoluted under the broad peak at 15º.

Crystallinity index (CI) of NC samples was estimated from the empirical Segal equation using the height ratio between the intensity of crystalline peak and total intensity after baseline subtraction. CI equal to 94% was obtained in the case of CNC sample, whereas its value decreased to 85% regarding CNF signifying also the presence of a higher amorphous cellulose fraction.

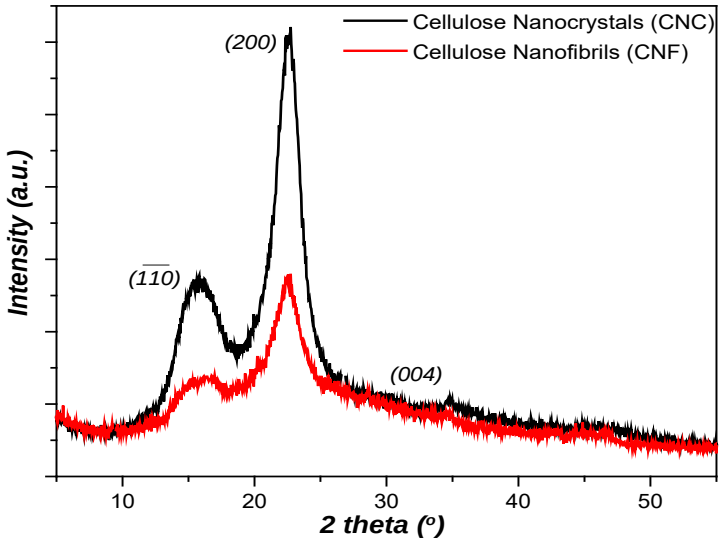

Figure 2: X-ray diffraction patterns of NC fibrils (CNF) & crystals (CNC).

3.1.3 Thermal Stability

Thermogravimetric weight changes were recorded in order to evaluate the onset and crystal decomposition temperatures of NC samples. The respective TGA/DTG profiles along with DSC curves are presented in Figure 3. As seen, all samples exhibit analogous TGA degradation patterns demonstrating an initial weight loss at around 70°C related to the desorption of physically absorbed water and volatile compounds. Likewise, the major steep weight loss displayed in the range 245-350°C can be assigned to onset and maximum rate of crystal decomposition, accompanied with the complete removal of the organic contend at higher temperatures. In addition, the TGA curve of CNC sample is slightly shifted towards higher temperatures, signifying a moderately delayed onset of decomposition temperature due to the higher CI, as obtained from XRD analysis. These results are further validated from dTG curves, in which crystal decomposition at 325±5°C is also assigned. Differential scanning Calorimetry (DSC) was also performed in order to elucidate the onset of melting and crystallization temperature (Figure 3). Similar patterns appear also in this case, demonstrating a sharp and well defined exothermic peak located at 325±5°C indexed to crystal decomposition phenomena, in accordance to TGA/DTG results. In the area of endothermic activity, peaks of different intensity are illustrated at low temperature values, which could be regarded as an indication of different bounded water amounts.

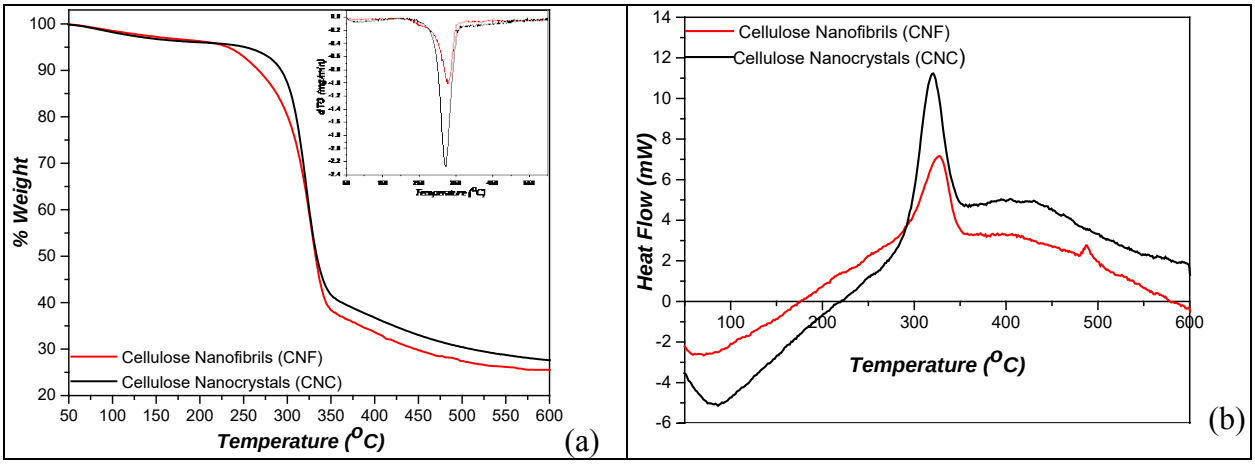

Figure 3: Thermogravimetric analysis (a) & Differential Scanning Calorimetry curves (b) of NC fibrils (CNF) and crystals (CNC) [1].

[1] TGA/DSC experimental conditions: Ar, Flow=50ml/min, T_{max}=600°C, T_{rate}=5°C/min, isotherm=40°C/ 20min.

3.2. Thermal, Morphological & Mechanical characterization of NC UHDCs

3.2.1. Thermo-gravimetric analysis

TGA/DTGA analyses of samples extracted from UHDC specimens cured under both aforementioned conditions showed, for all the investigated mixes, absolutely similar trends, highlighting delayed hydration (CSH peak) and carbonation (CaCO3 peak) as the main reactions responsible of healing (Figure 4).

It can be interestingly observed, in the curves of the samples reinforced with both cellulose nano-fibrils and nano-crystals, the presence of a small peak in correspondence of the decomposition temperature of the same nano-cellulose, observed as above. This can be called as a confirmation for good dispersion, given the randomness of sampling material for TGA analysis, of the nano-constituent and hence of the effectiveness of the employed mixing procedure as well as of the actions on the mechanical performance of the composite, ad further elucidated. Higher intensity of peaks in correspondence of CSH decomposition also confirms the effects of NC as seed for hydration of cement, as hypothesized.

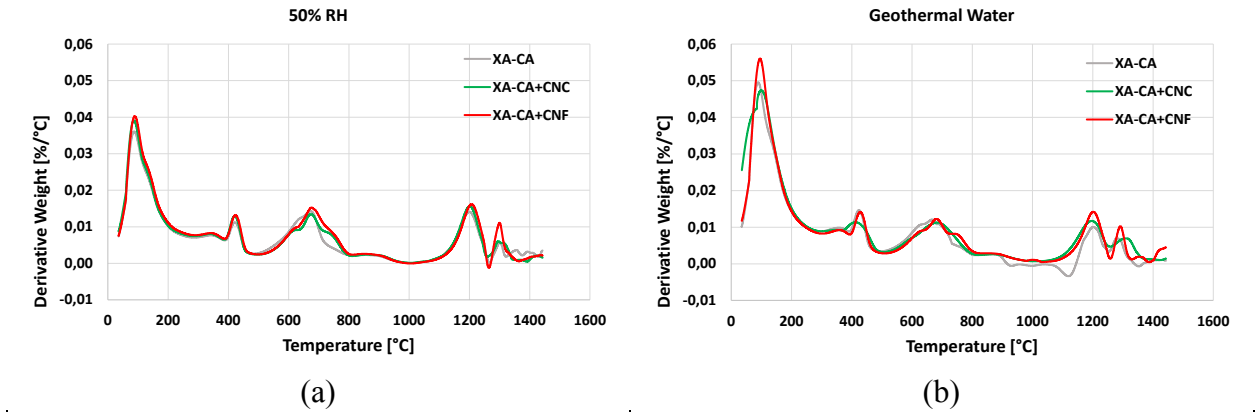

(a) (b)

Figure 4: DTGA curves of samples extracted in the vicinity of cracks healed in different regimes: a) 50%RH and b) geothermal water.

3.2.2. Mechanical characterization: Compressive & Flexural strength tests

Table 3 summarizes the average values of six (compression strength) and three (flexural strength) tests on nominally identical specimens cured under moist room and geothermal water (GW).

According to the results, the presence of NCs positively affects the performance of specimens in both curing environments, with those exposed to GW treatment demonstrating better results. One possible reason could evolve interactions between NCs and defects existing on the matrix at the very onset of their formation. Specifically, after curing in GW, XA-CA-CNF and XA-CA-CNC samples exhibit 43% and 29% increase in flexural strength values respectively at 28 days and 27% for XA-CA-CNC at later ages (84 days). On the other hand, materials efficiency cured under moist environment is much lower as flexural strength values range between 8% and 16% increase at 28d and 56d, with the percentage raising up to 27% only in the case of CNF at the later age (84d). Based on these results, it could be hypothesized that the beneficial role of NC presence into cementitious mixtures under XA conditions is actually a synergetic effect of NCs particle size and crystalline structure. In particular, the small size of nano-cellulose (CNC: 4-5nm width & ~300nm length, CNF: 5-200nm width & 500nm to several μm length, as from SEM measurements) allow their accumulation into matrix defects that originally are filled with water contributing to the refinement of micro-porosity. Beyond that, the hydrophilic nature of NCs and their tendency to interact with cementitious constituents facilitate hydration reactions and the formation of insoluble products (C-S-H) that also fill the pore network leading to further pore refinement [6, 8, 10,11]. The latter, as also indicated from MIP measurements [12], demonstrate reduction of pore size values when NC is also present in the matrix. Considering both porosity of specimens and XRD analysis results that highlight the presence of a higher amorphous fraction in CNF structures it could be suggested that the enhanced efficiency of XA-CA-CNF samples, especially in earlier stages, is due to the higher diffusivity of water molecules through the amorphous regions of the nano-consituent. In that way, hydration of cement particles is facilitated increasing the number of hydration loci and the population of inorganic hydration products.

On contrary to what stated for flexural strength efficiency, compressive strength tests demonstrate that increasing in the performance in both curing environments is negligible. A

maximum of 10-12% at the age of 28 and 56 days is revealed for mixes cured in RH which turns to zero at later cement ages. Similar trend is followed from the materials cured under GW conditions.

Table 3: Influence of curing exposure on compressive/flexural strength values

Mix	Curing	Compressive strength [MPa]			Flexural strength [MPa]		
		28 d	56 d	84 d	28 d	56 d	84 d
XA-CA	Moist room	127,0 (1.0)	142,9 (12.2)	166,3 (1.5)	24,4 (15.4)	28,9 (17.1)	29,0 (41.3)
XA-CA+CNC		147,6 (1.0)	157,0 (12.5)	170,5 (2.6)	27,3 (9.1)	31,4 (15.6)	30,4 (6.5)
XA-CA+CNF		137,7 (1.4)	145,0 (13.3)	152,3 (7.6)	29,1 (25.2)	32,5 (27.0)	40,0 (12.5)
XA-CA	Immersion in geothermal water	140,4 (11.1)	152,8 (4.1)	161,4 (3.6)	26,1 (6.5)	26,2 (5.4)	27,5 (17.8)
XA-CA+CNC		137,3 (15.6)	147,0 (11.6)	169,2 (2.0)	33,7 (17.2)	34,9 (17.4)	32,2 (14.7)
XA-CA+CNF		152,8 (4.1)	158,7 (5.9)	164,5 (1.0)	33,6 (8.9)	32,2 (13.5)	30,3 (5.2)

** CoV (%) in brackets*

3.2.3. Morphological characterization: SEM/BS/EDAX analysis

Morphological characteristics NC-enriched specimens and reference materials were investigated through SEM measurements. Preliminary results of the samples treated under geothermal water conditions are illustrated in Figure & 6.

All materials demonstrate the typical' morphology of cementitious composites. At low magnifications, regions of different morphologies could not be distinguished, whereas small cracks and pore openings prevail in the surface of reference sample. On contrary, at higher magnifications different morphologies can be distinguished attributed to the presence of hydration products (mainly C-S-H and CaOH to a lesser extent) (Figure 6). SEM micrographs of NC loaded samples reveal that hydration products exist in a much higher degree, justifying the improved strength properties and the enhanced hydration rhythm. The beneficial role of CNF presence into cementitious mixture with respect to facilitation of hydration reactions and increase of microstructure consistency ("bridging effect") is well evident in the micrograph of Figure Figure D. In this case, nano-fibrilated cellulosic components appear to act as nuclei for hydration reactions and as bridge binding inorganic constituents covered with hydration products.

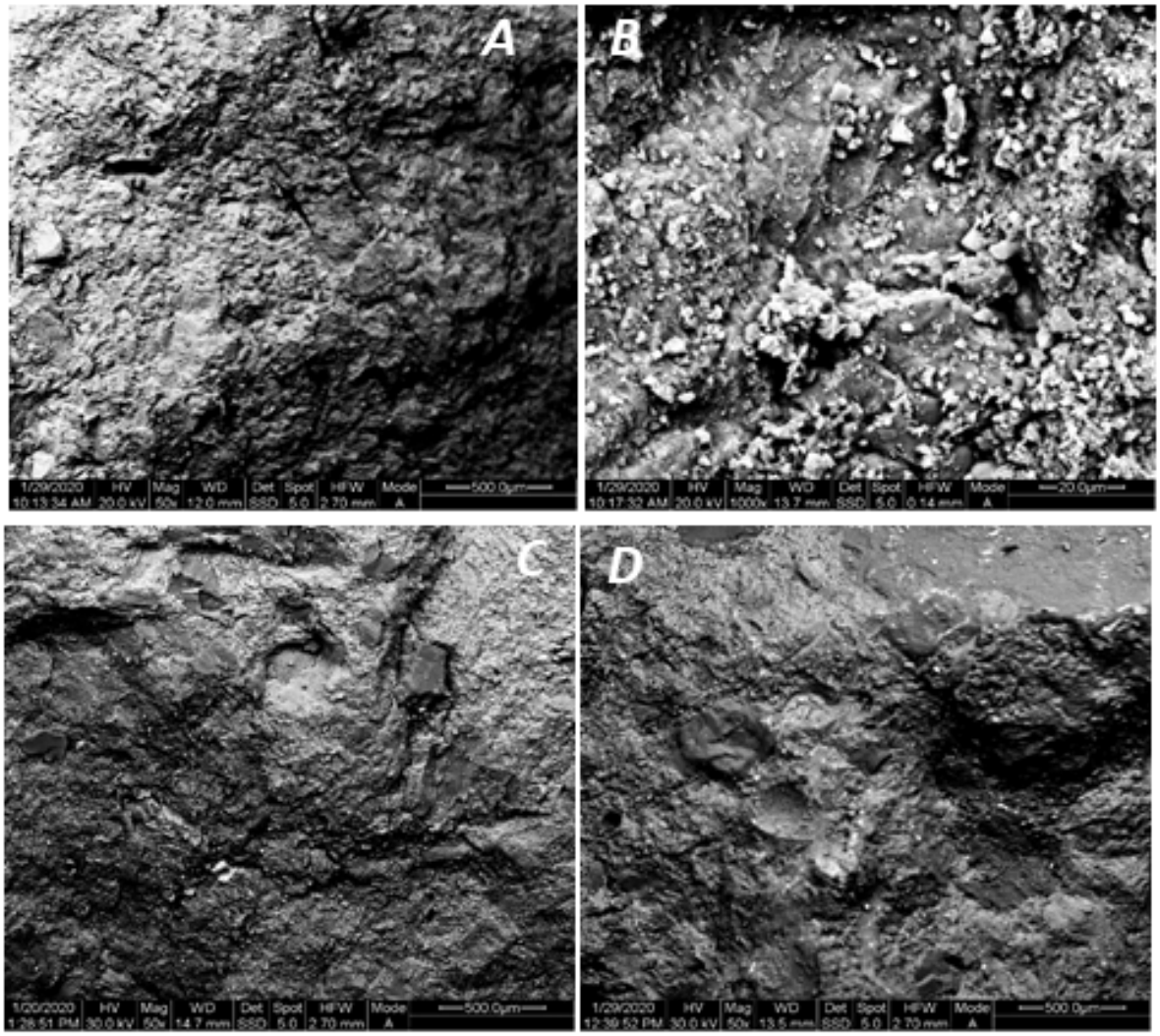

Figure 5: BS-SEM micrographs at low magnifications of specimens treated under GW (A, B) Reference (C) XA-CA-CNC & (D) XA-CA-CNF.

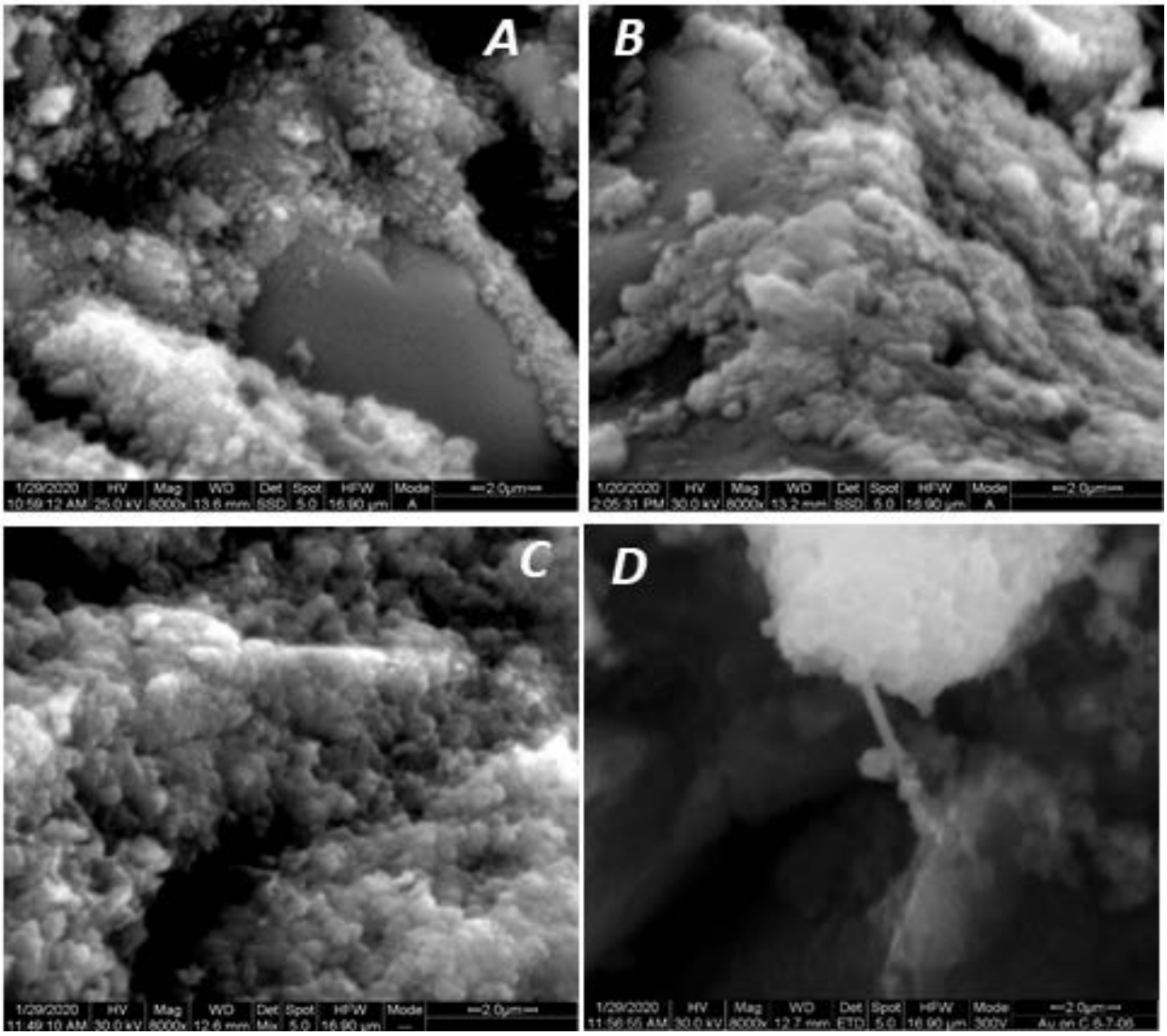

Figure 6: BS-SEM micrographs at high magnifications of specimens treated under GW (A,B) Reference, (C) XA-CA-CNC & (D) XA-CA-CNF.

4. CONCLUSIONS

The effect of Nanocellulose (NCs) on the nanostructure, as well as the macro-scale mechanical properties of UHDCs containing nanocellulose and cured under aggressive XA environmental conditions has been investigated. Flexural strength test results indicate that fracture properties of NC-cement matrix have been enhanced when materials are cured in GW conditions. In particular, an increase up to 43% has been achieved using CNFs and 29% when CNCs are added in the mixture at a constant 0.15%wt loading. Characterization analysis results suggest that CNs can strongly modify and reinforce cement paste matrix at the nanoscale by increasing the amount of high stiffness hydration products and decreasing the porosity. It has been hypothesized that

incorporation of CNFs is more effective also due to the higher amorphous fraction that facilitates the diffusion of water molecules and hydration reactions. Further characterization tests such as XRD, N_2 adsorption/desorption porosimetry and H_2O diffusion measurements will be performed in order to clarify CNs reinforcement mechanisms.

5. ACKNOWLEDGEMENTS

The research activity reported in this paper has been performed in the framework of the ReSHEALience project (Rethinking coastal defence and Green-energy Service infrastructures through enHancEd-durAbiLity high-performance cement-based materials) which has received funding from the European Union's Horizon 2020 research and innovation program under grant agreement No 760824. The information and views set out in this publication do not necessarily reflect the official opinion of the European Commission.

UHDC characterization tests were held at the facilities of Civil & Environmental engineering Department of Politecnico di Milano. CNs characterization tests were performed at the Laboratory of Materials & Membranes for Environmental Separations (INN) at NCSRD "Demokritos", Athens.

REFERENCES

[1] Li, G.Y., Wang, P.M., Zhao, X.: Mechanical behavior and microstructure of cement composites incorporating surface-treated multi-walled carbon nanotubes. Carbon 43, 2005, 1239–1245.
[2] Z. Chen, X. Zhou, X. Wang, P. Guo, Mechanical behavior of multilayer GO carbon-fiber cement composites. Construction and Building Materials 159, 2018, 205–212.
[3] H. Savastano, P.G. Warden, R. Coutts, Mechanically pulped sisal as reinforcement in cementitious matrices. Cement and Concrete Composites 2003, 25, 311–319.
[4] M. Ardanuy, J. Claramunt, J.A García-Hortal, M. Barra, Fiber-matrix interactions in cement mortar composites reinforced with cellulosic fibers. Cellulose 2011, 18, 281–289.
[5] T. Fu, F. Montes, P. Suraneni, J. Youngblood, J. Weiss, The Influence of Cellulose Nanocrystals on the Hydration and Flexural Strength of Portland Cement Pastes, polymers, 2017, 1-16.
[6] Y. Cao, N. Tian, D. Bahr, P. D. Zavattieri, J. Youngblood, R. J. Moon, J. Weiss, The influence of cellulose nanocrystals on the microstructure of cement paste, Cement and Concrete Composites, 2016
[7] A. Balea, E. Fuente, A. Blanco, C. Negro, Nanocelluloses: Natural-Based Materials for Fiber-Reinforced Cement Composites. A Critical Review, Polymers, 11, 2019, 518, 1-33
[8] O. Onuaguluchi, L Panesar, M. Sain, Properties of nanofibre reinforced cement composites, Construction and Building Materials 63 , 2014, 119–124
[9] S. Kyle, Z. Jessop, A. Al-Sabah, K. Hawkinsc, A. Lewis, T. Maffeis, C. Charbonneau, A. Gazze, L. W. Francisc, M. Iakovlev, K. Nelson, S. J. Eichhorn, I. S. Whitaker, Characterization of pulp derived nanocellulose hydrogels using AVAP® Technology, Carbohydrate Polymers, 198, 2018, 270–280
[10] R. Mejdoub, H. Hammi, J. Sunol, M. Khitouni, A. Mnif, S. Boufi, Nanofibrillated cellulose as nanoreinforcement in Portland cement: Thermal, mechanical and microstructural properties, Journal of Composite Materials, 2016, 1–13
[11] M. Ardanuy, J. Claramunt, R. Arevalo, F. Pares, E. Aracri, T. Vidal, Nanofibrillated cellulose (NFC) as a potential reinforcement for high performance cement mortar composites, Bioresources 7(3), 2012,3 883-3894.
[12] E.Cuenca, M. Criado, M. Giménez, E. Gastaldo-Brac, S. Sideri, A. Tretjakov, M. Alonso, L. Ferrara, Concept of Ultra High Durability Concrete for improved durability in chemical environments: Preliminary

results. In: Proceedings of the LORCENIS Conference on Durable Concrete for Infrastruc-ture under Severe Conditions - Smart admixtures, self-responsiveness and nano-additions, Ghent, Belgium.
[13] E. Cuenca, A. Mezzena, L. Ferrara, Synergy between crystalline admixtures and nano-constituents in enhancing autogenous healing capacity of cementitious composites under cracking and healing cycles in aggressive waters, *submitted to Construction and Building Materials, April 27, 2020.*

NACL INTERACTION DURING HYDRATION AS STUDIED BY NMR

L. Pel (1), Yanliang Ji (2) and Zhenping Sun (2)

(1) Eindhoven University of Technology, Eindhoven, the Netherlands

(2) Key Laboratory of Advanced Civil Engineering Materials, Tongji University, Shanghai, China

Abstract

With freshwater getting scares seawater, i.e., water containing NaCl, can become the only viable option for making concrete. Although a lot of research had been directed to understanding the role of water in cement hydration, not much is known about the interaction of the Na^+ and Cl^- with cement paste during drying. A problem is that available techniques like, i.e., XRD, SEM, and EDX, for measuring the microstructure and the methods for determining the concentration of Na+, Cl- ions in pore solutions are either indirect or invasive and moreover often destructive, which consequently may lead to inadequate interpretations. Using a specially designed Nuclear Magnetic Resonance (NMR) setup, the ^{1}H, ^{23}Na and ^{35}Cl content in cementitious materials can be measured quasi-simultaneously and hence give us direct information on the interaction of the ions and the microstructure development. We have studied the influence factor, i.e., the water-cement ratio, on the microstructure development and the binding of Cl^- and Na^+. It was found that during the initial hydration stage more Cl^- is bound in comparison to Na^+ . This is reversed during the acceleration period after which there is a preference for binding of Na^+ in comparison to Cl^-. Increase of W/C ratio results in less binding capability of Na^+ and Cl^-.

Keywords: Cement-based materials; NMR; Hydration process; Sodium chloride

1. INTRODUCTION

When considering Alkali-Silica Reaction (ASR) or chloride attack, there are strict limits on the concentration of both Na^+ and Cl^- ions, in reinforced concrete, pre-stressed concrete and plain concrete [1-3]. However, it can still be that in special cases sodium chloride (NaCl) is introduced in the preparation of concrete. One can think of job sites where there is a lack of natural fresh water, e.g. islands, seacoasts and places near saline lakes, and hence in these cases often water containing NaCl is the most viable option for producing concrete. Therefore a better understanding of the microstructure development during cement hydration process with NaCl solutions may lead to an improved design for cement-based materials.

However, available techniques like i.e., XRD, SEM, and EDX, for measuring the microstructure and the methods for determining the concentration of Na^+, Cl^- ions in pore

solutions, e.g., pore solution compression method, are either indirect or invasive and moreover often destructive, which consequently may lead to inadequate interpretations. Hence the influence of these ions on hydration is not only poorly understood, but there has also a lack of non-destructive techniques to systematically study the interaction of ions during hydration. Using Nuclear Magnetic Resonance (NMR) one can probe the microstructure in cement-based materials, and various studies [4-8] have focused on microstructure evolution and water consumption in cement paste during hydration. Despite the lower sensitivity of NMR for ^{23}Na and ^{35}Cl NMR can be used to study the ion transport/interaction in cement [9,10].

We will first present the specialized NMR as used in this study, which allows us to quasi-simultaneously measure the ^{1}H, ^{23}Na and ^{35}Cl. Next, we will discuss the measurements of the hydration with NaCl solutions followed by discussion and conclusions.

2. NMR SETUP

Nuclear Magnetic Resonance (NMR) is a non-destructive technique for quantitatively mapping certain elements. During an NMR experiment, the magnetic moments of the nuclei are manipulated by suitably chosen Radio Frequency (RF) fields. The resonance condition for the nuclei is given by:

$$f = \gamma B \tag{1}$$

Where f is the frequency of the alternating field, γ is the gyromagnetic ratio of the nuclei, and B is the magnitude of the externally applied static magnetic field. Hence according to the resonance condition, the measurement can be made only sensitive to ^{1}H, ^{23}Na or ^{35}Cl.

In an NMR experiment the magnetic moments of hydrogen nuclei are manipulated by suitably chosen alternating RF pulses, leading to a so-called Hahn spin-echo signal. The spin-echo signal will give information about the rate at which this magnetic excitation of the spins decays. The system will return to its equilibrium by two mechanisms: interactions between the nuclei themselves, causing the so-called spin-spin relaxation, and interactions between the nuclei and their environment, causing the so-called spin-lattice relaxation. Assuming that both mechanisms give rise to a single exponential relaxation and that spin lattice relaxation is much slower than the spin-spin relaxation, the magnitude of the NMR spin-echo signal is given (see, e.g., [11]):

$$S \sim G\rho \left[1 - \exp\left(-\frac{TR}{T_1}\right)\right] \exp\left(-\frac{TE}{T_2}\right) \tag{2}$$

where G is the relative sensitivity (G=1 for ^{1}H, 0.0925 for ^{23}Na and 0.0035 for ^{35}Cl), ρ the density, T_1 is the spin-lattice relaxation time, TR is the repetition time of the spin echo experiment, T_2 is the spin-spin or transverse relaxation time and TE is the so-called spin-echo time. In general, the repetition time is chosen as TR ~ $4T_1$ and hence the signal will only depend on the T_2 relaxation and short-spin echo times are preferred.

As the nuclei are moving randomly because of Brownian motion during an NMR experiment, they are also probing the pore-space. By Brownstein and Tarr [12] it was shown

that both the T_1 and T_2 relaxation of water in the pores of a material can be related to the pore size:

$$\frac{1}{T_{1,2}} = \frac{1}{T_{bulk}} + \rho_{1,2}\frac{S}{V} \quad (3)$$

Where $\rho_{1,2}$ is the so-called surface relaxivity for the T_1 and T_2 relaxation respectively. As T_{bulk} is in general quite large in comparison to the surface relaxation, the first term can in most cases for porous building materials, like cements, be neglected. Hence the relaxation time can give information on the V/S, which is proportional to the pores size, where the nuclei are present.

In this study an NMR setup was used which is specially designed for measuring ions in porous building materials. This setup makes use of a vertical Oxford 4.7 T superconducting magnet with a vertical 200 mm bore. As the gyromagnetic ratios and hence the resonance frequencies of the selected nuclei are too far apart to be covered by one insert, a specially designed insert was constructed. This insert is a combination of three RF inserts, which can be moved through the magnet with the help of a 3-stepper motor. In Fig. 1 the principle of the setup is given. There are three separate RF setups corresponding to ^{1}H, ^{23}Na and ^{35}Cl.

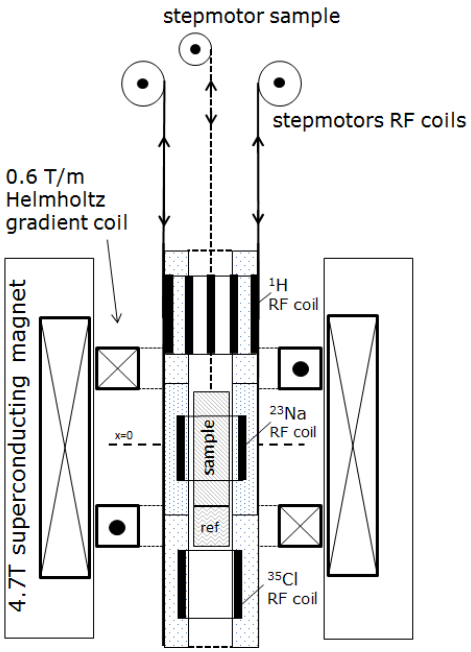

Figure1: A schematic diagram of the NMR setup for measuring the ^{1}H, ^{23}Na and ^{35}Cl signal during the hydration of cement paste. The main field is provided by a 4.7 T superconducting magnet, equipped with an 0.6 T/m anti-Helmholtz gradient coil set. Using a step motor the sample can be moved through the setup.

3. MEASUREMENTS

3.1 Materials

The types of cement used in this study (supplied by HEIDELBERG Group, ENCI B.V. Netherlands) was Ordinary Portland Cement (OPC) which have specific area of 340 m^2/kg In this study the water-to-cement (W/C) was varied from 0.45 to 0.60 at a fixed concentration of 1 M NaCl.

3.2 Hydrogen

The results for the measured longitudinal (T_1) relaxation time and normalized signal of hydrogen as a function of the hydration time are given in Fig. 2. For comparisons we have also shown the results for an experiment for W/C=0.5 made with only water. As can be seen in first order the evolution of the curves in Fig. 2 looks very similar: T_1 relaxation time and the normalized signals of hydrogen first remain stable and after about 1 hour they start to decrease. Whereas the T_1 relaxation time reaches a stable plateau after about 10 hours, the hydrogen signal keeps on decreasing. As can be seen both the T_1 relaxation time and the signals of hydrogen increase with W/C ratio reflecting the increased porosity and pore-size with increasing W/C.

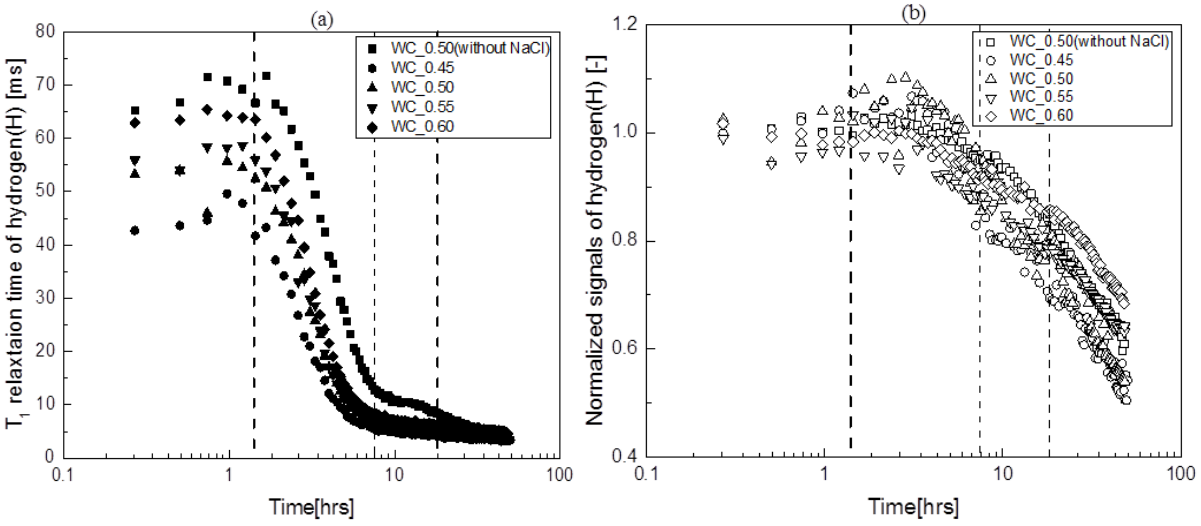

Figure 2: The T_1 relaxation time(a) and normalized signal (b) of hydrogen(H) as the function of time as measured for Portland cements samples with water-to-cement ratio from 0.45 to 0.60 and made with a 1 M NaCl solutions.

Based on the study by P.F. Faure et al.[13], in which they combined NMR and hear flow evolution of hydrating cement, the T_1 evolution correlates with the four stages of cement hydration. The initial reaction and induction period are reflected in the initial constant T_1 relaxation. A second acceleration period where the setting takes place and is reflected in the sharp decrease of the T_1 relaxation. A third stage of deceleration, i.e., the transition from chemical to diffusion controlled reaction, can be observed as the small shoulder as also seen in our experiment with only water. In the final fourth stage the reaction is diffusion controlled

and there is a slow continuation of the reaction and the relaxation almost remains constant. These boundaries of the hydration stages are indicated by the dashed lines in the figures.

3.3 Na and Cl

The corresponding measured normalized signals for both Na^+ and Cl^- as a function of time are given in Fig 3. Here we have indicated the various stages again in accordance with the T_1 relaxation in time measured for hydrogen.

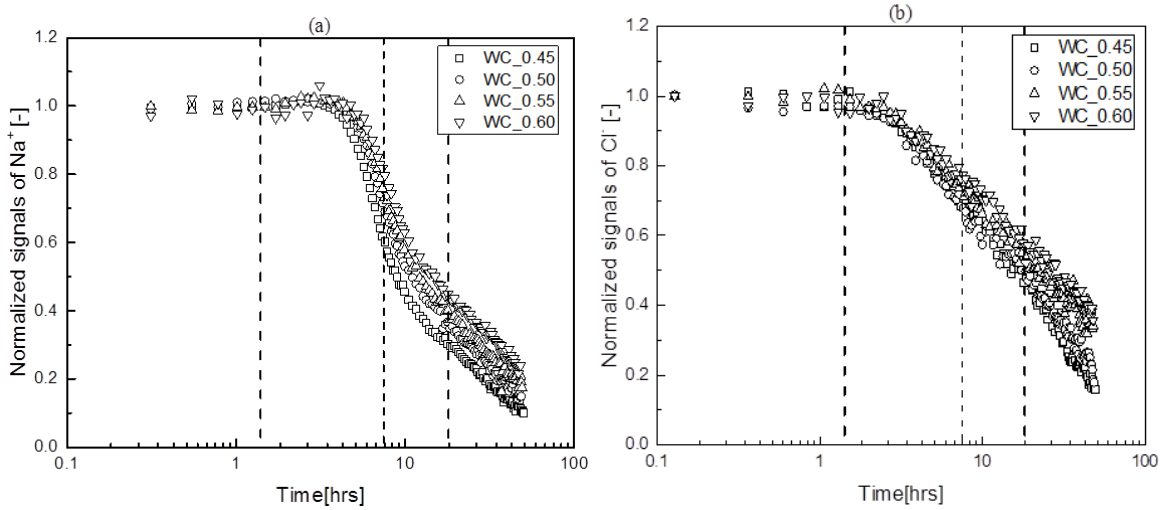

Figure 3: The normalized signals of (a) sodium ions(Na^+) and (b) chloride ions(Cl^-) as function of time as measured for Portland cements samples with a water-to-cement ratio from 0.45 to 0.60 made with a 1M NaCl solutions.

We can see that with an increase of the W/C ratio of cement paste, i.e., as bigger pores are formed and therefore less surface area, there is less binding of Na^+ and Cl^- ions. However if we compare the signal intensity as a function of time, which reflecting the decrease of ion concentration some clear differences between Na^+ and Cl^- can be observed. Initially in stage I, i.e., the initial reaction and induction period, the concentration of Na^+ and Cl^- remains constant. As soon as stage II, i.e., the acceleration period starts a clear difference can be observed. Whereas the Cl^- concentration immediately start to decrease at the beginning of stage II, for Na^+ it is observed that this only starts to decrease near the end of stage II and at the beginning of stage III, i.e., the deceleration stage. In contrast to Cl^- we also observe for Na^+ that the decrease in concentration slows down during stage III.

In order to have a clearer understanding of decrease we have plotted in Fig 4 the relationship between the measured Na^+ and Cl^- concentration, i.e., we have plotted the normalized measured Cl^- concentration as the function of the normalized measured Na^+. As can be seen independent of the W/C ratio all the measurements seem to fall on one master curve. Initially, the Cl^- concentration decreases at first as the Na^+ concentration remains constant values (approximately 1.0 M) and then continues to decrease with the decrease of Na^+ concentration.

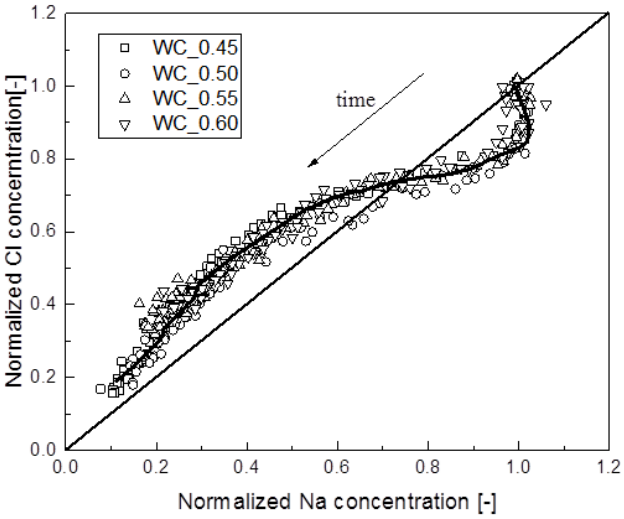

Figure 4: The normalized Cl^- concentration as a function of the normalized Na^+ concentration of cement paste sampled prepared with water-to-cement ratio from 0.45 to 0.60 made with 1 M NaCl solution (see fig 3)

The binding mechanisms for Cl^- can be characterized as both chemical and physical binding [2,3,14]. The AFm compounds ($3CaO{\cdot}(Al, Fe)_2O_3{\cdot}CaSO_4{\cdot}nH_2O$) formed during the hydrations are generally known to be able to chemically bind the Cl- ions directly to form Friedel`s salt ($3CaO{\cdot}Al_2O_3{\cdot}CaCl_2{\cdot}10H_2O$) [15, 16]. Additionally it is known that the C_3A has a rapid reaction speed in comparison with the other mineral phases (i.e., C_3S and C_2S) and its products include these AFm phases. Also, the Cl^- ions can be physically bound to the porous hydrates, i.e., C-S-H gels can absorb the Cl^- ions on the surface and inside the pores due to its high specific areas [17]. However, it is generally considered there is only as physical adsorption as a binding mechanism for the Na^+. Therefore binding capacity for Na^+ of the sample depends on the hydrate properties (i.e., amount of the porous hydrates and their permeability) formed during hydrations.

The reasons for the observed initial preference for binding of Cl^- (compared with Na^+) could be due to the quickly formed AFm phases (compared with C-S-H phases) during hydration. With the amount of AFm phases decrease and more porous hydrates are formed, the physical binding becomes dominant. Hydrates formed later (after the acceleration period) will bind more the Na^+ ions than the Cl^+ ions in pore solutions.

5. CONCLUSIONS

It has been shown that by using a specially designed NMR setup of the binding of Na^+, Cl^- during can be studied during the hydration of cement pastes made with NaCl solutions. It is observed that the binding of the Na and Cl is closely linked to the hydration process. The initial hydrations could bind more Cl^- ions compared with Na^+ ions during the acceleration period and the later binding preference on Na^+ ions. The increase of W/C ratio results in less binding capability on Na^+ and Cl^- ions.

ACKNOWLEDGEMENTS

We like to thank Jef Noijen, Hans Dalderop for their assistance in performing these experiments.

This study was funded by Dutch Technology Foundation STW, which is part of the Netherlands Organisation for Scientific Research (NWO), and which is partly funded by the Ministry of Economic Affairs. In addition financial support was provided by the 13th Five-Year Plan (2016YFC0701004) and the National Natural Science Foundation of China (Project no. 51678441 and Project no. U153420040) and the China Scholarship Council.

REFERENCES

[1] L. Struble, S. Diamond. Influence of cement alkali distribution on expansion due to alkali-silica reaction, ASTM International, Alkalies in Concrete (1986) 31-45.

[2] C. Arya, N.R. Buenfeld, J.B. Newman, Factors influencing chloride-binding in concrete [J], *Cem. Concr. Res.* **20** (1990) 291-300

[3] M. Balonis, B. Lothenbach, G. Le Saout, F.P. Glasser, Impact of chloride on the mineralogy of hydrated Portland cement systems, *Cem. Concr. Res.* **40** (2010) 1009-1022.

[4] S. Bhattacharj, M. Moukwa, F. D'Orazio, J.Y.r Jehng, W.P. Halperin, Microstructure determination of cement pastes by NMR and conventional techniques, *Advanced Cement Based Materials* **2** (1993) 67-76.

[5] R. Valckenborg, L. Pel, K. Hazrati, K.Kopinga and J. Marchand, Pore water distribution in mortar during drying as determined by NMR, *Mat. and Struc.* **34** (2001) 599-604.

[6] P. J. McDonald, J.P. Korb, J. Mitchell, and L. Monteilhet, Surface relaxation and chemical exchange in hydrating cement pastes: A two-dimensional NMR relaxation study, *Phys. Rev.* **72** (2005) 011409.

[7] D. Snoeck, L. Pel and N. De Belie, The water kinetics of superabsorbent polymers during cement hydration and internal curing visualized and studied by NMR, *Scientific reports*, 2017

[8] A.C.A. Muller, K.L. Scrivener, A reassessment of mercury intrusion porosimetry by comparison with 1H NMR relaxometry, *Cem. Concr. Res.* **100** (2017) 350-36.

[9] F.de J. Cano, T.W. Bremner, R.P. McGregor, B.J. Balcom, Magnetic resonance imaging of ^{1}H, ^{23}Na, and ^{35}Cl penetration in Portland cement mortar, *Cem. Concr. Res*. **32** (2002) 1-4.

[10] L. Pel, P.A.J. Donkers, K. Kopinga, J.J. Noijen, ^{1}H, ^{23}Na and ^{35}Cl imaging in cementitious materials with NMR. *App. Mag. Res.* **47** (2016) 265-276.

[11] E. L. Hahn, Spin echoes, *Phys. Rev*. **80** (1950) 580-594.

[12] K.R. Brownstein, C.E. Tarr, Importance of classical diffusion in NMR studies of water in biological cells, *Phys. Rev.A* **19** (1979) 2446-2453.

[13] P.F. Faure, S. Rodts, Proton NMR relaxation as a probe for setting cement pastes, *Mag. Reson. Im*. **26** (2008) 1183-1196.

[14] J. Tritthart, Chloride binding in cement II. The influence of the hydroxide concentration in the pore solution of hardened cement paste on chloride binding, *Cem. Concr. Res.* **19** (1989) 683-691.

[15] E. Nielsen, D. Herfort, M. Geiker, D. Hooton, Effect of solid solution of AFm phases on chloride binding, Proceedings, 11th Int. Congress on the Chemistry of Cement, South Africa, 2003.

[16] A. Delagrave, J. Marchand, J.P. Ollivier, S. Julien, K. Hazrati, Chloride binding capacity of various hydrated cement paste systems, *Adv. Cem. Based Mater* **6** (1997) 28-35.

[17] D. Sugiyama, Chemical alteration of calcium silicate hydrate (C-S-H) in sodium chloride solution, *Cem. Concr. Res*. **38** (2008) 1270-1275

PORE SOLUTION CHEMISTRY OF EXPANSIVE HEAT CURED CEMENTITIOUS SYSTEMS

Yogesh K. Ramu (1), Paul Thomas (2) and Vute Sirivivatnanon (1)

(1) School of Civil and Environmental Engineering, University of Technology Sydney, Australia

(2) School of Mathematical and Physical Science, University of Technology Sydney, Australia

Abstract

Heat cured cement mortars may result in linear expansion due to later age ettringite precipitation, popularly termed as delayed ettringite formation (DEF). However, later age ettringite precipitation may not result in expansion always. To differentiate the expansive and non-expansive nature of heat-cured cementitious systems, in this research pore solution chemistry of various cementitious systems cured at 90°C for 12 hours were studied. Linear expansion of mortar bars was measured periodically. Besides, ettringite precipitation was studied using X-ray diffraction (XRD) and thermal gravimetric analysis (TGA). The XRD, TGA results show the absence of early age ettringite and its delayed precipitation in all the heat-cured cementitious systems irrespective of expansive or non-expansive mortars. However, the pore solution ionic concentration reveals that sulphate ion concentration at the end of heat curing is vital to predicting whether the mortar will expand or not in the future. The curing temperature increased the solubility of sulphates and total alkalis present in the pore solution. The expanded mortars had a relatively higher amount of sulphates in the pore solution at the age of 30 hours, compared to the non-expansive mortars. Further, at the age of 7 and 30 days, a drop in sulphate, sodium, potassium ions concentration in pore solution was noticed, suggesting the leaching of alkalis and consumption of Sulphate for the precipitation of ettringite.
Keywords: Pore solution, durability, ettringite, DEF, heat curing

1. INTRODUCTION

The curing of cementitious systems at elevated temperatures accelerates the hydration reactions [1], thereby reducing the setting time and faster the strength achievement [2]. However it is not a mere acceleration in hydration reactions, as it results in changing the hydration products (monosulphate in place of ettringite), alter the properties of hydrates (lower density C-S-H, differences in ettringite morphology), modifies the pore structure of cementitious systems and transport properties [3]. As curing at elevated temperatures has

practical relevance in precast concrete production, implications on durability due to microstructural changes caused by high-temperature curing needs to be studied. Already many research works studies the various implications of heat curing in cementitious systems/concrete. Among all, the delayed ettringite formation (DEF) is one of the important research area spanning over three decades. Considering the DEF reaction mechanisms are extensively investigated by various researchers, in this research, changes in pore solution chemistry due to heat curing is studied along with expansion behaviour. It is noteworthy to mention, similar works already been done by [4]–[6], however, few gaps have been left. For instance, [5] deals with studying the pore solution chemistry of ASTM Type III cement and the impact of supplementary cementitious (SCMs) systems in it, thus creating expansive and non-expansive systems. However, the pore solution chemistry of non-expansive systems in the absence of SCMs to compare the expansive systems was not studied. In [6], changes in ettringite peak intensity and morphology along with changes in pore solution chemistry due to temperature was studied in detail. However, the maximum temperature taken was only 50°C and also no expansion data available. In this research, expansive and non-expansive systems were created by varying the sulphate, alkali content of cement and curing temperature and changes in pore solution chemistry was studied.

2. EXPERIMENTAL

2.1 Materials

An Australian cement conforming to AS 3972:2010 is used in this research. The cement contains 7.5% limestone as a mineral additive and has a specific surface area of 395 m^2/kg. The main oxides (in %) are CaO-64.18, SiO_2-19.67, Al_2O_3-4.78, Fe_2O_3-3.1, MgO-0.91, Na_2O-0.23, K_2O-0.41 and SO_3-2.37. Clinker composition was estimated using a modified Boque calculation [7], and the results (in %) are C_3S - 49.9, C_2S - 18.3, C_3A – 7.4, C_4AF – 9.4. Analytical grade gypsum and sodium hydroxide were used to alter the sulphate and alkali content of the cement. Distilled water used to make mortar and paste specimens.

2.1 Design and methods

Three different cementitious systems were developed by varying the original sulphate, alkali content of cement and exposed to two different curing temperature (23, 90°C), thus forming six different mixes as given in Table 1.

Table 1: Different mixes used in this study

Sl No	Cement's overall		Curing temperature (°C)	Mix ID
	SO_3 (%)	Na_2O_{eq} (%)		
1	2.37	0.49	23.00	C-23°C
2	4.00	0.49	23.00	C-S-23°C
3	4.00	1.00	23.00	C-SN-23°C
4	2.37	0.49	90.00	C-90°C
5	4.00	0.49	90.00	C-S-90°C
6	4.00	1.00	90.00	C-SN-90°C

Mortar prisms (cement: sand: water = 1:2:0.45) were prepared as described in AS 2350.12-2006 and cast in steel moulds of size 40 X 40 X 160 mm. Besides, cement pastes (cement: water = 1:0.4) were made with and cast in 50 mm φ X 150 mm cylindrical container for pore solution extraction and in 10 ml vial for studying the development of crystalline phase using X-ray diffraction (XRD) and thermogravimetric analysis (TGA). Prepared mortars and cement paste specimens were exposed to different curing regimes; (i) for curing at 23°C specimens were kept in a humidity chamber at 90% relative humidity (ii) for heat curing, a programmable oven was used and specimens were cured at 90°C for 12 hours with 4 hours pre-cure. After the initial curing ~ 25 hours, specimens were transferred to saturated lime water for further curing. Length changes of mortar prisms were noted with a digital length comparator, up to 600 days considering 7^{th} day reading as initial. Cement paste specimens were powdered, and hydration stopped at 1, 7 and 30 days using the solvent (isopropanol) replacement method. XRD patterns were collected using Bruker D8-discover diffractometer in Bragg-Brentano geometry at an angular scan of 5 to 20° 2θ with 0.02 step size. TGA curves were collected using Netzsch Jupiter F5 STA instrument with helium flowing at 40 mL/min on 20 ± 0.3 mg cement powder placed in open alumina crucible over the temperature range of 40 to 1000°C. Pore solution was extracted from paste specimens at the age of 4 hours, 1, 7 and 30 days using an extractor; by applying a load of 800 KN at the rate of 2000 N per second. For 4-hour old specimens, a maximum load of 50 KN was sufficient to extract pore solution. Obtained pore solution filtered using a 0.2 μm micro-filter and diluted with ultra-pure water, and acidified using 69% concentrated nitric acid (total dilution ratio was 1:10) and stored under 5°C until testing. The prepared solution was tested for ionic concentrations using Perkin Elmer Optima 5300 DV inductively coupled plasma optical emission spectroscopy (ICP-OES).

3. RESULTS AND DISCUSSIONS

Linear expansion results are shown in Figure 1. The results show all the mixes cured at 23°C did not expand at all irrespective of sulphate and alkali content in cement. This result suggests the chemistry of cement had no significance concerning DEF related expansion when subjected to ambient temperature curing. In the mix C-90°C, with no additional sulphate or alkali, irrespective of heat curing no significant linear expansion was noticed. The mix with 4% sulphate (C-S-90°C), expanded at a very late stage of hydration and reached 0.1% expansion after a year. However, from [8], [9] specimens showed microstructural cracks only when the expansion was at least 0.4%. Hence, the expansion noticed in C-S-90°C shall be considered insignificant. The mix C-S-N-90°C (4% sulphate. 1% sodium equivalent) had expanded (more than 0.7%) significantly and shall be treated as deleterious and have the potential to cause micro-cracks in the system.

The expansive nature of heat-cured cementitious systems often linked with ettringite suppression at the end of heat curing and its precipitation at later age hydration [10], [11]. Though the mechanism of later age ettringite precipitation in heat-cured cementitious systems is well established, the correlation between ettringite formation and expansion was not obtained at all times [12], [13]. For instance, Figure 2 & 3 shows absence of ettringite (AF_t) peaks in XRD, TGA at day 1 for all heat cured cementitious systems and Figure 4 & 5 shows the ettringite reformation at the age of 30 days. However, not all the heat-cured mixes experienced significant expansion as discussed above. Though the intensity of reformed ettringite peaks

(Figure 4 & 5) can be an argument to explain expansion, however even that holds well only to differentiate C-90°C with the other two mixes.

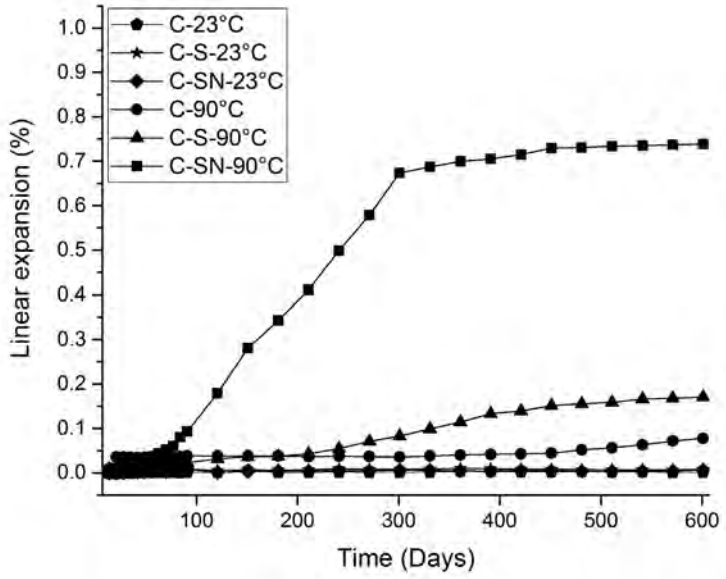

Figure 1: Linear expansion of mortar prisms exposed to curing at 23°C and 90°C

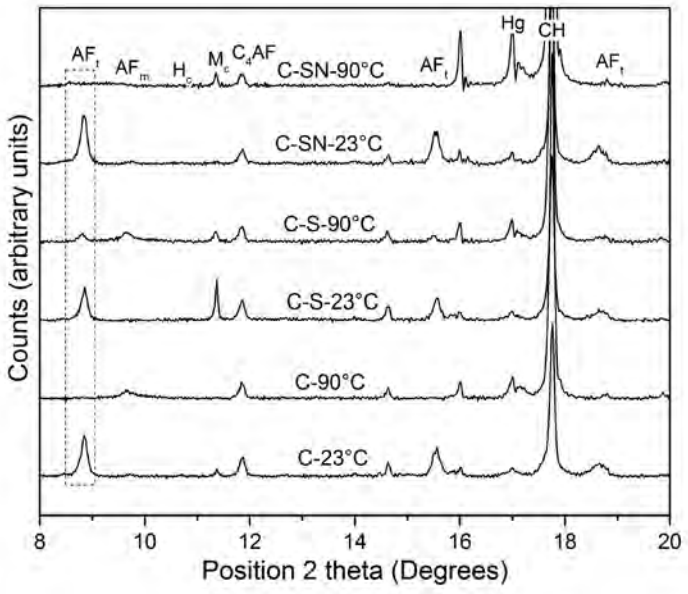

Figure 2: XRD patterns of 1-day old cement pastes

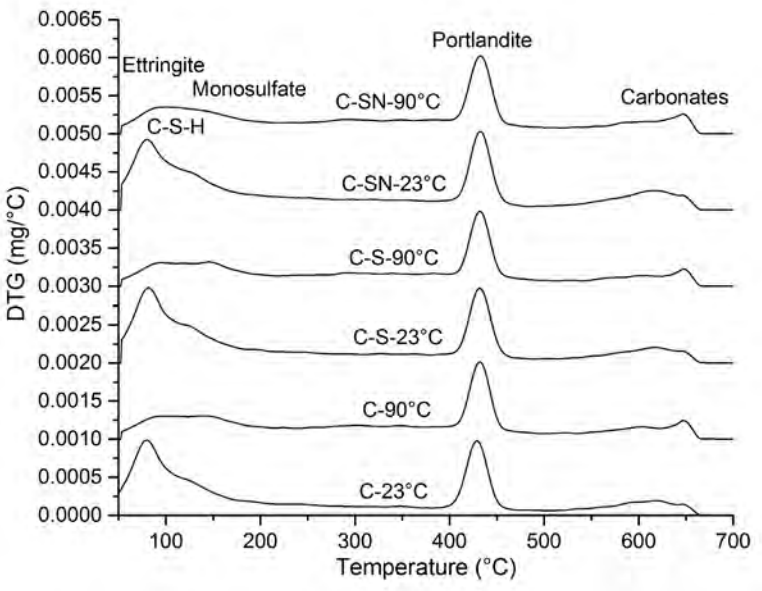

Figure 3: DTG curves of 1-day old cement pastes

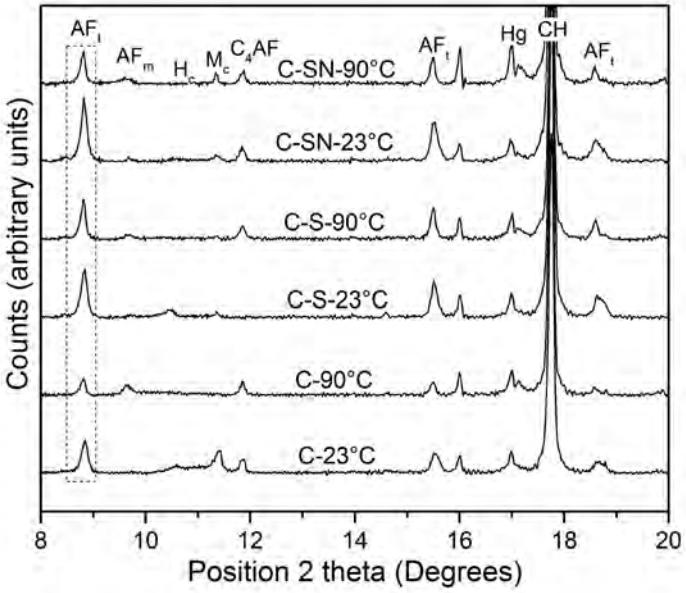

Figure 4: XRD patterns of 30 days old cement pastes

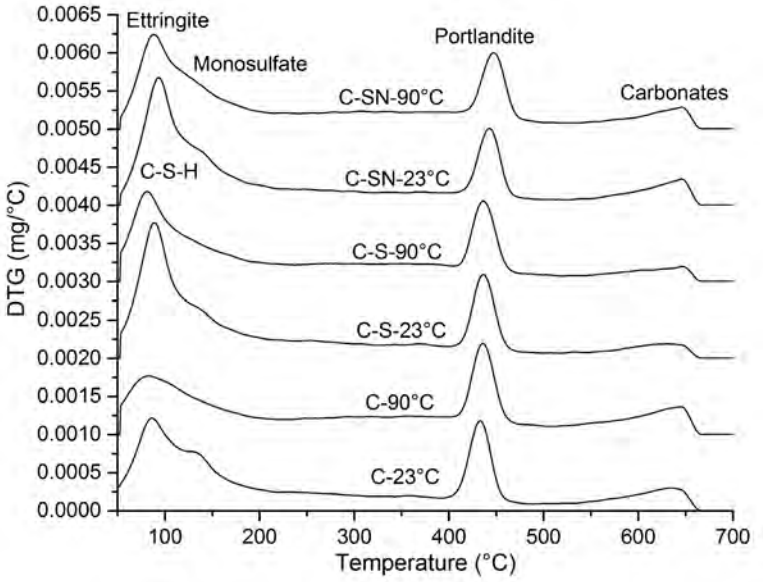

Figure 5: DTG curves of 30 days old cement pastes

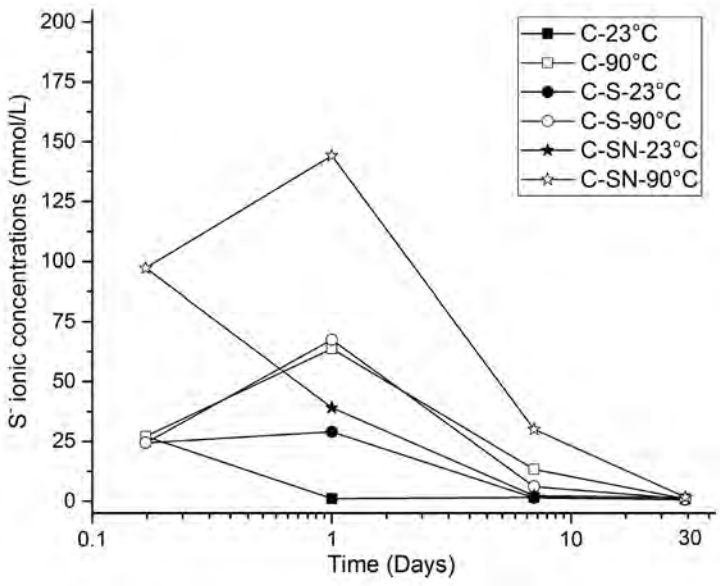

Figure 6: Pore solution S^- ion concentration at different ages

To differentiate between the expansive and non-expansive nature of cementitious systems, the chemistry of the pore solution was studied from 4 hours to 30 days. Ionic levels of sulphur (S) and total alkali (K+Na) is presented in Figure 6 & 7. At the end of day 1, sulphur and alkali ion concentrations show a contrast difference between heat and ambient cured cementitious systems, shows the impact of temperature in the dissolution of ions. At 23°C, sulphur ions in the systems could have reacted with calcium and alumina forming ettringite, resulting in low concentration in pore solution and this correlates with the steady ettringite peaks in XRD and

TGA (Figure 2 & 3). However, at 90°C, alkali ions concentration increased (refer to Figure 8) in the pore solution due to the impact of temperature in dissolution. An increase in alkali ions in the pore solution can lead to an increase in dissolution of sulphur ions [4], thus increasing the sulphur ions concentrations in the pore solution as clearly evident in Figure 7.

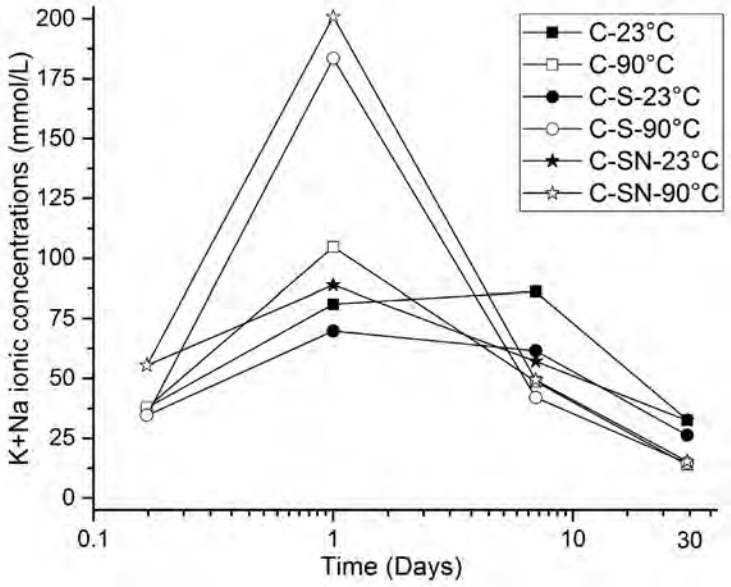

Figure 7: Pore solution k+Na concentration at different ages

Thus not sufficient sulphates to form ettringite (during or at the end of heat curing) and hence monosulphate formed instead as noticed in XRD and TGA patterns (refer Figure 2 & 3). At later ages, the drop in alkali ions shall be attributed to the leaching during storage in saturated lime water [14] leaving the sulphate ions to react with monosulphate, forming ettringite. This correlates with ettringite peaks noticed in 30 days XRD and TGA peaks (Figure 4 & 5). Among the heat-cured cementitious systems, the expansive/non-expansive systems can be differentiated from the sulphur ions dissolution difference at the end of day 1. For the non-expansive (~ 0.2% max. expansion) heat cured cementitious systems C-90°C, C-S-90°C the sulphur ions concentration at day 1 are 63.72 and 67.47 mmol/L respectively; leaving only a difference of 3.74 mmol/L. However, for the expansive cementitious system C-SN-90°C (~ 0.74% expansion), the sulphur ion concentration at day 1 is 144.23 mmol/L, which is more than two folds of other systems, thus suggesting the early age dissolution of ions can help predict long term expansion behaviour

4. CONCLUSIONS

1. Later age ettringite precipitation may not be able to explain the expansion behaviour of heat-cured cementitious systems.
2. Sulphur and alkali ions concentration in pore solution increased with respect increase in the curing temperature.
3. Among heat-cured cementitious systems, later-age expansion resulted only when early-age sulphur dissolution tremendously increased by the combined effect of temperature and high alkali concentration.

ACKNOWLEDGEMENTS

Financial support from Humes (Holcim), Australia, for conducting this research project, is gratefully acknowledged.

Technical guidance from Prof. Manu Santhanam, IIT Madras and Mr Yuvaraj Dhandapani, graduate student, IIT Madras to do pore solution experiment are gratefully acknowledged.

Construction materials research laboratory, IIT Madras, India is acknowledged for providing laboratory support to do part of this research work.

REFERENCES

[1] J. I. Escalante-García and J. H. Sharp, "Effect of Temperature on the Hydration of the Main Clinker," *Cem. Concr. Res.*, vol. 28, no. 9, pp. 1259–1274, 1998.

[2] R. Day, "The effect of secondary ettringite formation on the durability of concrete: A literature analysis," 1992.

[3] Y. Dhandapani, K. L. Scrivener, and M. Santhanam, "Temperature Effects on Performance of Cementitious Systems : Microstructure and Transport Properties," no. September 2017.

[4] M. D. A. Thomas, R. D. Hooton, and T. Ramlochan, "Use of pore solution analysis in design for concrete durability," *Adv. Cem. Res.*, vol. 22, no. 4, pp. 203–210, 2010.

[5] T. Ramlochan, M. D. A. Thomas, and R. D. Hooton, "The effect of pozzolans and slag on the expansion of mortars cured at elevated temperature: Part II: Microstructural and microchemical investigations," *Cem. Concr. Res.*, vol. 34, no. 8, pp. 1341–1356, 2004.

[6] B. Lothenbach, F. Winnefeld, C. Alder, E. Wieland, and P. Lunk, "Effect of temperature on the pore solution, microstructure and hydration products of Portland cement pastes," *Cem. Concr. Res.*, vol. 37, no. 4, pp. 483–491, 2007.

[7] H. F. W. Taylor, "Modification of the Bogue calculation," *Adv. Cem. Res.*, vol. 2, no. 6, pp. 73–77, 1989.

[8] A. S. Silva *et al.*, "Influence of Mineral Additions in the Inhibition of Delayed Ettringite Formation in Cement Based Materials – A Microstructural Characterization," *Mater. Sci. Forum*, vol. 636–637, pp. 1272–1279, 2010.

[9] K. Tosun, "Effect of SO3 content and fineness on the rate of delayed ettringite formation in heat cured Portland cement mortars," *Cem. Concr. Compos.*, vol. 28, pp. 761–772, 2006.

[10] H. F. W. Taylor, C. Famy, and K. L. Scrivener, "Delayed ettringite formation," *Cem. Concr. Res.*, vol. 31, no. 5, pp. 683–693, 2001.

[11] R. Yang, C. D. Lawrence, C. J. Lynsdale, and J. H. Sharp, "Delayed ettringite formation in heat-cured Portland cement mortars," *Cem. Concr. Res.*, vol. 29, no. January 1997, pp. 17–25, 1999.

[12] K. Scrivener and M. Lewis, "A microstructural and microanalytical study of heat cured mortars and delayed ettringite formation," in *Proceedings of the 10th International Congress on the Chemistry of Cement, Gothenburg, Schweden*, 1997, vol. 4, p. 4iv061.

[13] K. L. Scrivener and H. F. W. Taylor, "Delayed ettringite formation : a microstructural and microanalytical study," *Adv. Cem. Res.*, vol. 5, no. 20, pp. 139–146, 1993.

[14] J. Aubert and G. Escadeillas, "Five year monitoring of curing solutions of heat-cured mortars affected by delayed ettringite formation," *Adv. Cem. Res.*, vol. 25, no. 3, 2013.

RESEARCH ON PREPARATION AND PROPERTIES OF C-S-H /PEG1000 PHASE CHANGE COMPOSITE

Chen Chen (1), Qi Zheng (1) and Jinyang Jiang *(1)

(1) School of Materials Science and Engineering, Southeast University, China

Abstract

In this paper, composite material C-S-H/PEG1000 was prepared by multi-scale porous material C-S-H as support and phase change material (PCM) PEG1000 by melt blending, so that it can reduce hydration heat of cementitious system utilizing the characteristics of releasing and storing energy of PCM. TEM, IR, DSC-Tg, BET, MIP and various other characterization methods were used to discuss the feasibility of C-S-H as carrier and investigate the morphology, pore structure and stability of the C-S-H/PEG1000 composite. The change of hydration heat and feathers of pore structure as while as its effect on compressive strength were also tested when the composite was added into the cementitious system. Study shows that the PEG1000 can be well embedded into the hollow inside space of C-S-H to form dense blocks in the form of physical adsorption, with good bonding state and thermal stability, which can decrease heat releasing rate and total heat of the hydration process in cementitious system. The early strength was pretty influenced with different addition of C-S-H/PEG1000, however, the later strength was improved.

Keywords: calcium silicate hydrate; phase change material composite; pore structure; hydration heat; thermal stability

1. INTRODUCTION

In recent years, PCMs has been widely applied in various fields owing to their high latent heat storage density, small volume changes and fixed phase change temperature range [1]. For constructions, this feature has great potential in terms of saving energy [2], such as concrete walls and insulating layers. Generally speaking, the integratation of PCMs and supports into architectural fabrics can effectively exert this characteristic [3,4]. Similarly, suitable phase change materials can also be used to solve the problem of thermal stress caused by the massive release of hydration heat in short term.

Due to the large thermal stress caused by internal temperature difference, mass concrete and other projects demand extremely low thermal cement based materials. The ABAQUS simulation illustrated in the Fig.1 demonstrates the concrete adiabatic temperature rise and thermal stress distribution, in which the highest initial internal temperature is up to 70℃ and nearly 40 hours are costed to cool down completely, similar to existed works [5]. It shows that it is in urgent need of phase change energy storage material with a certain temperature, so the proposed research of C-S-H/PEG1000 is of importance and necessity in building materials field.

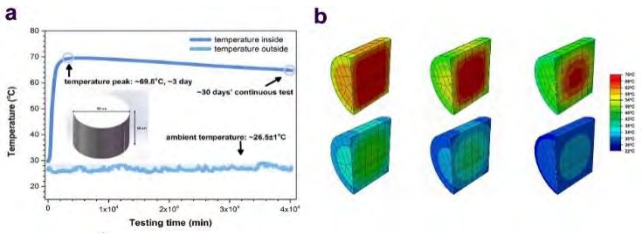

Figure 1: ABAQUS simulation of adiabatic temperature rise [(a)] and thermal stress distribution [(b)].

PEG1000 is PCM with a large latent heat capacity, 152.9 J/g measured in this work. Combining PEG with other porous materials, such as porous silica [6], MCS [8] and LA [12], is an effective way to use thermal properties to produce new smart materials and avoid leakage. Zhang et al. [10] studied the phase change properties of PEG blends with PP, PET or ethylene vinyl acetate, while the materials tend to lose their phase change characteristics after several heating cooling cycles due to the loss of PEG. Hu et al. [9] prepared a solid-solid PCM by poly-PEG. However, even the maximum enthalpy was still low. Therefore, in order to apply it stably and efficiently in cement, it is necessary to ensure the combination stability and chemical stability with appropriate support.

CSH is a kind of material with multi-scale pore structure. The pores of CSH can be divided into three parts [14]: the pores caused by the accumulation of large particles (> 200nm), medium particles (50-200 nm) and small particles (< 50nm), the intrinsic pores inside the particles, and the interlayer pores at the level of C-S-H structure. C-S-H is a common and readily available hydration product of porous cement.

In this work, a phase change composite material C-S-H/PEG1000, which can effectively reduce the heat of hydration, was prepared by combining cement basic hydration product C-S-H with PEG1000 innovatively. The feasibility and rationality of the support were deduced through simulation model and experimental characterization, and the properties of the phase change composite were characterized, including morphology, pore structure, stability, etc., which were mutually verified with the experimental results of hydration heat and compressive strength on the macro level. To sum up, we provided some new insights to C-S-H design and application of energy absorption and storage performance of PCMs for cement-based materials.

2. EXPERIMENTAL

2.1 Materials

Tricalcium silicate (C_3S), Polyethylene glycol (PEG1000), were purchased from Sinopharm Chemical Reagent Co., Ltd. All these chemicals were used as received without further purification. Deionized water (Ω > 18MΩ cm, 25°C) and ethanol (99.7%) were used throughout.

2.2 Methods

2.2.1 Preparation of C-S-H

C-S-H was prepared by hydration of C_3S at room temperature. C_3S powder was dissolved in deionized water with the mass ratio of water to solid by 125:1 in the beaker. After suspension for 72h with continuous stirring on magnetic mixer, the precipitates were collected and separated by vacuum filtration over a 0.45μm membrane. The filter cake was re-dispersed and filtered and repeated for times to remove salts and unwanted ions like the by-product $Ca(OH)_2$. The final filter cake was dried at 150°C, and C-S-H was obtained by grinding and sieving.

2.2.2 Preparation of C-S-H/PEG1000

After the synthesis of C-S-H, thermal-stabilized phase change materials composite was prepared by a facile blending and impregnating method. PEG were intercalated into C-S-H porous structure in specific procedures. Firstly, C-S-H and PEG1000 were proportionally mixed in a mass ratio of 1:1.6, and then the mixture was processed at 70℃ for 2h with stirring. Ultimately, the C-S-H/PEG1000 was cooled, grinding and sieving for further characterization.

2.2.3 Analysis methods

The particle size distribution was measured by laser diffraction particle size analyzer. The morphology was investigated by SEM and TEM. XRD patterns were collected at a scanning rate of 0.15 s/step with 0.02° step size in the 2θ range 5~60° using Ni-filtered CuKα radiation and operating at 40 kV and 30 mA. The BET surface areas and BJH pore-size distributions were measured with analyzer. MIP was also adopted to calculate the pore volume and pore-size distributions. Different phase distribution was investigated by a high resolution 3D X-ray microscope. The FT-IR spectra were recorded in the wavenumber region between 400 cm^{-1} and 4000 cm^{-1}. The phase change temperature and enthalpy were obtained by using DSC-TG. Zeta potential was investigated to explain the stability of C-S-H/PEG1000.

3. RESULTS AND DISCUSSION

3.1 Simulation of C-S-H

The model construction of C-S-H was based on the procedures proposed by Pellenq, Manzano and Qomi [7,13]. The calcium to silicon ratio was controlled at 1.5 according to experimental results. The multi-scale pore structure of C-S-H was obtained by building a C-S-H model between particles and atoms at different scales, as shown in Fig. 2, which provided theoretical basis for its rationality as a carrier.

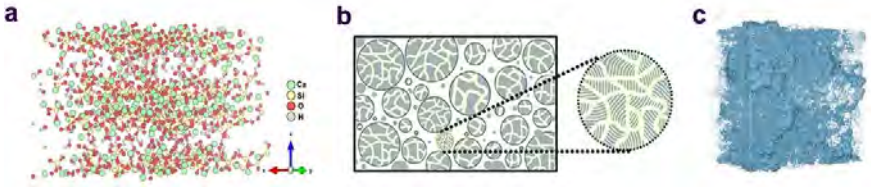

Figure 2: Construction multi-scale pore structure models of C-S-H including the micro model (a), mesoscopic model (b) and macro model (c).

3.2 Characterization of C-S-H/PEG1000

Particle size analysis was carried out and the average size of monodispersity C-S-H is 21.89μm approximating to a normal distribution shown in Fig. 3. For composite, part of PEG1000 enters and fills the internal pores and part is wrapped on the surface. As a result, the particle size of the composite material after grinding becomes thicker and larger, and shows a bimodal distribution with the average size of 45.01μm. The value of two peaks appears at approximately 13μm and 115μm, related to the uniformity of the wrapping.

SEM and TEM images exhibited in Fig. 4 show the morphology of C-S-H and C-S-H/PEG1000. Fig. 4(a, b) shows the cluster morphology of C-S-H composed of sheets of nanometers. Randomly oriented hydration products are staggered and stacked, showing stratified pores between clusters, forming a 3D network structure.Moreover, a typical high resolution TEM image in Fig. 4 (e) shows C-S-H is amorphous thin-layer structure similar to

'silica gardens' structure of Double. These nanosheets are likely to fold, crinkling and stacking, corresponding to the results of SEM.

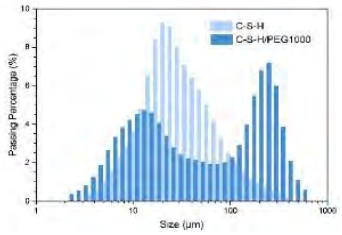

Figure 3: Particle size distribution of synthetic C-S-H and C-S-H/PEG1000.

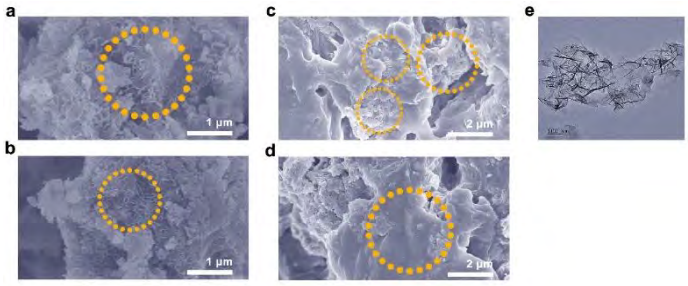

Figure 4: Micrographs of C-S-H (a, b) and C-S-H/PEG1000 (c, d) obtained by SEM (a-d) and C-S-H by TEM (e). Scale bars are 1μm, 2μm and 100 nm, respectively.

Subsequently, it could be found in Fig. 4(c, d) that PEG1000 change the morphology of C-S-H when cooperated into it. The morphology presented in the yellow circle can be seen that PEG1000 molecules embedded in the hollow space of C-S-H perfectly. Namely, PEG1000 is loaded on the multi-scale pore structure of C-S-H to form a compact and dense C-S-H/PEG1000 block by blocking and filling the pores. Due to the coating effect of PEG1000 on the surface of C-S-H, the surface of composite becomes more smooth than C-S-H. Most importantly, no leakage of PEG1000 is observed in Fig. 4(c, d), confirming the stability of C-S-H/PEG1000 composites. Even after dozens of thermal-cold cycling treatment, there was little leakage of PEG1000 can be seen, suggesting that the PEG1000 is well impregnated into C-S-H pores and C-S-H/PEG1000 is successfully synthesized as a composite.

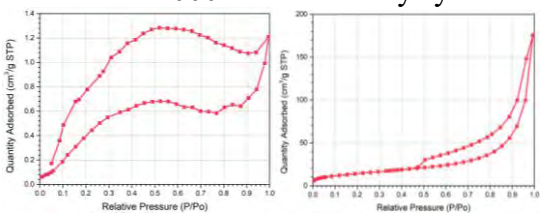

Figure 5: N_2-adsorption–desorption isotherms of C-S-H (a) and C-S-H/ PEG1000 (b).

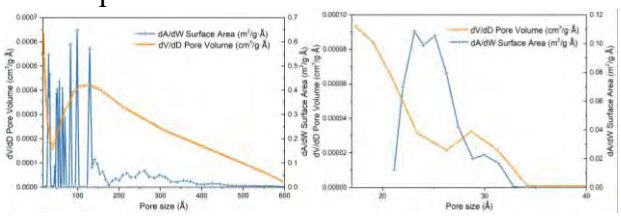

Figure 6: BJH-desorption pore-size-distribution curves of C-S-H (a) and C-S-H/ PEG1000 (b)

The porous characteristics of the C-S-H and C-S-H/PEG1000 is examined by BET. As Fig.5 presents, the N_2 adsorption-desorption isotherm of C-S-H matches the type III isotherm in the Brunauer classification corresponding to a solid material with large pores. And it exhibits type H3 hysteresis loop according to IUPAC, which is commonly found in layered aggregates, forming mesoporous or macroporous materials in the shape of slits. Demonstrated characteristic features is in good accordance with SEM and TEM observations. The pore size distribution of C-S-H is reflected by BJH model. As is shown in Fig.6 (a), the results suggest abundant specific surface area about 52.5 m^2/g measured by BET and a wide range of pore size distribution ranging from 17 to 600Å of C-S-H, the most probable pore size of which is at 125.17Å. This multi-scale pore structure enables C-S-H to carry amount of PCM of different particle sizes.

The multi-scale pores of C-S-H can be divided into three parts: pores caused by the accumulation of large particles (>200nm), medium particles (50-200nm) and small particles (<50nm), intrinsic pores inside the particles, and interlayer pores on the C-S-H structure level.

Fig. 5 (b) and Fig.6 (b) provide that the specific surface area of C-S-H/PEG1000 decreases more than 90% which is 3.3075m^2/g measured by BET method, and the mean pore size of BJH-desorption is 25.787Å dropping around 80%. Moreover, BJH Desorption cumulative volume of pores between 17Å and 3,000Å diameter of C-S-H and C-S-H/PEG1000 are 0.27 cm^3/g and 0.0020 cm^3/g, respectively. When PEG is introduced into C-S-H, the pores of C-S-H larger than 4 nm are almost completely contained by PEG1000 molecules, resulting in a high proportion of pores at the center of 2 nm. The steep decrease in specific surface area, pore volume, and pore size combined with the electron microscopy results proves that the PEG1000 could indeed fill the multi-scale pores of C-S-H. combination with the support can change the texture and morphology of the PCM, providing convenience for the incorporation of PCM, so that many problems of incorporation of single PCM are avoided. Therefore, it is necessary to introduce PCM support into the cement based composite material.

As mentioned above, porous characteristics and multi-scale pore structure of c-s-h were clearly illustrated by means of electron microscopy imaging and pore structure analysis. The structure feasibility of composite using C-S-H as a support is proved, which provides a premise for the perfect filling and stable composite to achieve the aim of efficient energy storage. In addition, as one of the main hydration products of cement, the incorporation of c-s-h can avoid unknown adverse reactions, and at the same time, C-S-H can prevent the leakage of phase change materials during energy absorption and energy release, so that the composite material has excellent working performance and high energy absorption efficiency.

3.3 Stability of C-S-H/PEG1000

The weak characteristic peak of C-S-H (I) around 30° in XRD patterns in Fig.7 shows that the sample is amorphous gel of low crystallinity degree. The main characteristic peaks (d=0.303nm, 0.277nm and 0.192nm) are basically consistent with the literature[11]. Furthermore, $Ca(OH)_2$ characteristic peak (d = 0.488nm, 0.261nm, 0.192nm) can be seen around 18°, which is the residual hydration products after washing. The XRD of C-S-H/PEG1000 is superposition of C-S-H and PEG1000. No obvious characteristic peak of new phase is found, meaning it is probably a simple physical combination between them.

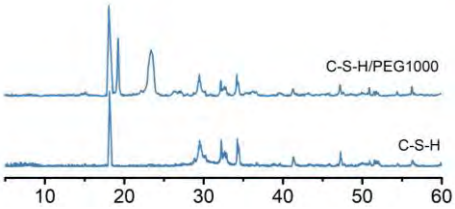

Figure 7: XRD of C-S-H and C-S-H/PEG100

The chemical compatibility of composite is shown in Fig. 8. From bottom th top, spectra nanometers stretching vibration at 1480 and 960 cm^{-1}. The peak at 1355 cm^{-1} is caused by C-O-C, while peaks of C-O is also found at 1650 cm^{-1} and 1110 cm^{-1}. In addition, the characteristic peaks for stretching vibration of -OH at 3450 cm^{-1}.

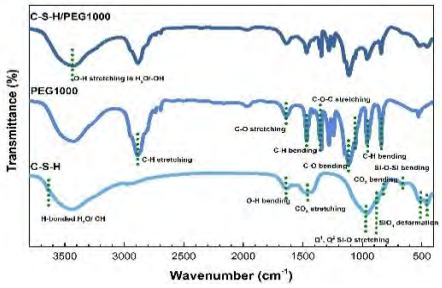

Figure 8: IR of C-S-H/PEG1000

From the perspective of C-S-H, the peaks of O-H, Si-O-Si and SiO_4 tetrahedrons are found Peaks at 870 and 970 cm^{-1} could be ascribed to the stretching vibration of Si-O groups in Q^1 or Q^2 states. Compared with PEG1000 and C-S-H, no obvious new peaks generating in the spectra

of composite. The physical binding between them is controlled by weak Vanderwals force without other obvious chemical interactions. Based on the vulnerable physical sorption, the PEG1000 molecules can accommodate in C-S-H pore structures recyclable and sustainable. It reveals the chemical compatibility between the C-S-H and PEG1000 conforming to the XRD.

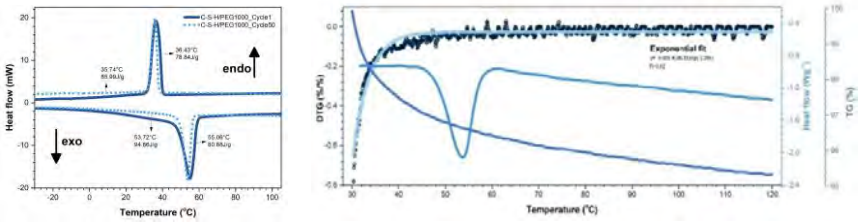

Figure 9: DSC-TG curves of C-S-H/PEG1000 after thermal-cold cycles

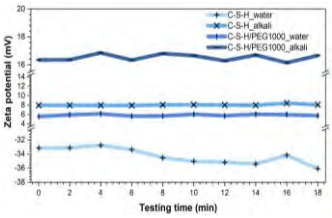

Figure10: Zeta potential of C-S-H and composite.

DSC and TG are conducted to investigate long-term thermal stability in variable temperature environment to ensure the its effective service. The phase change temperature ranges from 30 to 60℃ in Fig. 9, equivalent to hydration heat. The loss of weight and phase change enthalpy are within reasonable value, and DTG curve follows the equation y=-0.025-4386.55exp(-0.29x). Until temperature raised to 120 ℃, the mass loss rate of composite is less than 5%, showing good thermal stability. The thermal stability properties were performed by 50 thermal-cold cycles. The peak temperature of endothermic and exothermic are 35.74 and 53.72℃ now, while the latent heat are 85.99 and 80.68 J/g, closed to data of first cycle. It is remarkably noted that the form-stable C-S-H/PEG1000 shows good thermal reliability and bonding stability regarding to its slight change in phase change temperatures and latent heat. These strong evidence suggest that composite is chemically, thermally and structurally stable during working.

As a complement, the Zeta potential are relatively stable in alkali and aqueous solution with the extension of testing time. There are no significant fluctuations, therefore the combination stability and chemical stability of the support C-S-H and the new prepared composite are verified. C-S-H/PEG1000 composite can work in cement based materials steadily and well.

Various characterization of the performance of C-S-H/PEG1000 indicate that PEG1000 can be well loaded on c-s-h, and it has good adaptability and stability in cement system.

3.4 Performance analysis of C-S-H/PEG1000 in cement system

3.4.1 Hydration heat

Phase change composite is added into the PII 525 cement replacing 0% to 20% binding material (W/C=0.5). Fig. 11 shows the change of hydration heat of cement system with the increase of C-S-H/PEG1000 to explore the effect of energy absorption and storage. With the content of composite raised up to 20%, the peak height of rate decrease significantly, meanwhile the peaks move right and become wider obviously, indicating that hydration rate slows down. Total amount of hydration heat decreases, which is reduced to half under the condition of 20%, indicating that C-S-H/PEG1000 could play a good role in energy absorption and energy storage. The existence of PCM reduces the hydration heat and slowed down the hydration process.

3.4.2 Compressive stress

The compressive strength of blocks with different dosage of the C-S-H/PEG1000 curing for 3d to 28d is shown in the Fig.12, as well as the contrast added in pure PEG. With the increase

of C-S-H/PEG1000, the compressive strength shows a downward trend at all age. The influence on early strength is relatively great, however, the later strength rises distinctly. And the later strength after 14d is almost not affected at low dosage of the composite. Compared with blocks with PEG1000 alone, strength decreases to the half. The results indicate that the combination with C-S-H and PEG1000 improves the compressive strength when used in cement system at the same dosage and curing age. Hence, taking advantage of C-S-H as support is necessary.

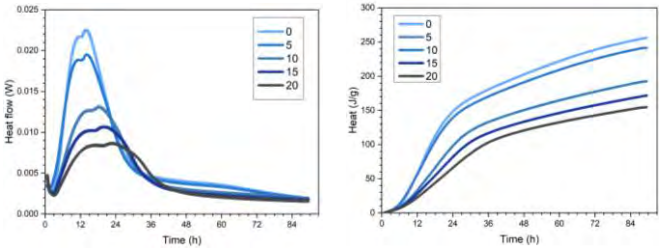

Figure 11: Hydration heat of cement incorporated with C-S-H /PEG1000.

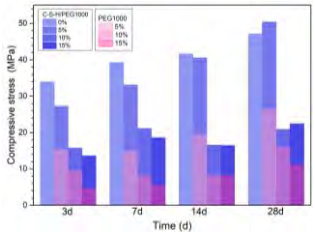

Figure 12: Compressive stress of different cement blocks.

3.4.3 Microstructure

SEM images in Fig.13 show the morphology of blank samples and blocks incorporated in 15% composite. The former is denser with a large number of needle-like hydration products overlapping. C-S-H has lost its cementitious property in composite due to complete hydration. In contrast, the cementitious products in the pores and micro-cracks are reduced (orange circles) and the texture was more loose (green circles) for C-S-H/PEG1000 replaced cement blocks.

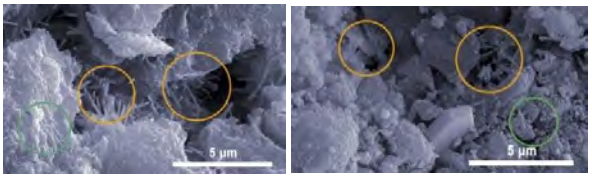

Figure 13: SEM of blocks incorporated with 0% and 15% C-S-H/PEG1000

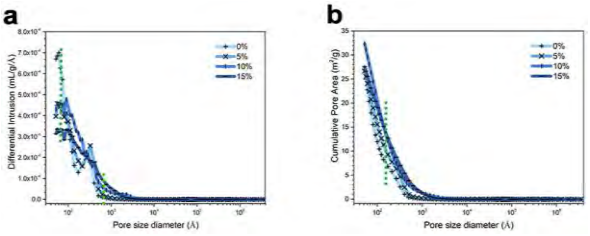

Figure 14: Pore size distribution and pore area of blocks with different amount of C-S-H/ PEG1000 curing for 28d

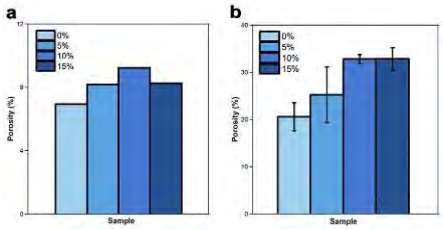

Figure 15: Porosity of cement blocks obtained by MIP (a) and 3D computed tomography segregation (b) curing for 28d

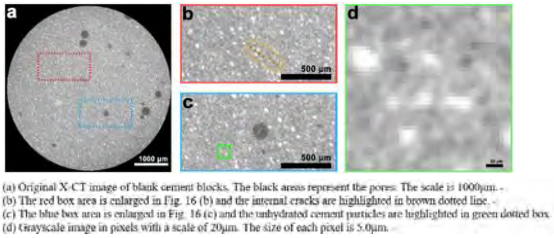

Figure 16: Schematic diagram of computed tomography obtained by 3D microscope

MIP results reflect the pore structure of the cement blocks and the gray value obtained from high resolution 3D X-ray microscope can be used to analyze the distribution of different phases, including pores, cracks and unhydrated cement particles in Fig.16. Accordingly, the internal microstructure is explored. in Fig. 14 and Fig. 15, the blocks gain more pore volume and area

when composite gradually increases from the results calculated by MIP and CT. Consistent with the regular of SEM, the porosity increases and the compactness is affected with the improvement of composite, reflecting the damage of compressive strength at the macro level.

4. CONCLUSIONS

- A preparation method of C-S-H/PEG1000 phase change composite was introduced.
- The multi-scale and rich pore structure of C-S-H is analysed through simulation and experiments, and its feasibility and rationality as a support for PCM are demonstrated.
- C-S-H/PEG1000 phase change composite material has not only the suitable phase change temperature range and large latent heat, but also the good chemical and thermal stability.
- Composite can effectively slow down the hydration rate and reduce the total heat in cement system. Moreover, direct incorporation of PEG1000 will greatly damage the compressive strength compared with C-S-H/PEG1000, for which the early strength is influenced to a certain extent while and the later strength will gradually increase.

REFERENCES

[1] Pellenq J M, Kushima A, Shahsavari R, et al. A realistic molecular model of cement hydrates[J]. Proceedings of the National Academy of Sciences, 2009, 106(38):16102-16107.

[2] Memon SA. Phase change materials integrated in building walls: a state of the art review. Renew Sustain Energy Rev 2014; 31:870 906.

[3] Frédéric Kuznik, David D, Johannes K, et al. A review on phase change materials integrated in building walls[J]. Renewable and Sustainable Energy Reviews, 2011, 15(1):379-391.

[4] Ramakrish S, et al. Thermal performance of buildings integrated with phase change materials to reduce heat stress risks during extreme heatwave events[J]. Applied Energy, 2016, 194:410-421.

[5] Han F, et al. Study on mix proportion optimization and performance of mass concrete [J]. Concrete world, 2014(3):66-69.

[6] Wang J, Yang M, Lu Y, et al. Surface functionalization engineering driven crystallization behavior of polyethylene glycol confined in mesoporous silica for shape-stabilized phase change materials[J]. Nano Energy, 2015, 19:78-87.

[7] Pellenq RJ-M, Kushima A, Shahsavari R, Van Vliet KJ, Buehler MJ, Yip S, et al. A realistic molecular model of cement hydrates. Proc Natl Acad Sci 2009; 106:16102 7.

[8] Qian T, Li J, Min X, et al. Polyethylene glycol/mesoporous calcium silicate shape-stabilized composite phase change material: Preparation, characterization, and adjustable thermal property[J]. Energy, 2015, 82:333-340.

[9] Hu J, Yu H, Chen Y, et al. Study on Phase Change Characteristics of PET‐PEG Copolymers[J]. Journal of Macromolecular Science, Part B, 2006, 45(4):615-621.

[10] Liang X H, Guo Y Q, Gu L Z, et al. Crystalline-Amorphous Phase Transition of Poly (ethylene Glycol)/Cellulose Blend[J]. Macromolecules, 1995, 28(19):6551-6555.

[11] Zhao X. Synthesis of calcium silicate hydrate and its composition, structure and morphology [D]. Wuhan university of technology, 2010.

[12] Jiang J, Zheng Q, Yan Y, et al. Design of a novel nanocomposite with C-S-H@LA for thermal energy storage: A theoretical and experimental study[J]. Applied Energy, 2018, 220:395-407.

[13] Manzano H, et al. Confined water dissociation in microporous defective silicates: mechanism, dipole distribution, and impact on substrate properties. J Am Chem Soc 2012; 134:2208 15.

[14] Wenzel O, Schwotzer M, Müller E, Chakravadhanula VSK, Scherer T, Gerdes A. Investigating the pore structure of the calcium silicate hydrate phase. Mater Charact 2017; 133:133 7.

STRENGTH DEVELOPMENT AND HYDRATION PROGRESS OF A CEMENT-BASED SOLIDIFYING AGENT USED IN CEMENT-TREATED SOIL CONTAINING VOLCANIC MINERAL COMPONENTS

Izuru Segawa (1), Yuya Takahashi (1) and Go Igarashi (1)

(1) Department of Civil Engineering, The University of Tokyo, Japan

Abstract

This study investigates the relationship between the strength development and hydration progress of cement-based solidifying agents (CBSAs) in cement-treated soil with volcanic mineral components. A CBSA is a cement-based material used as a soil stabilizer. It is known that the strength development of cement-based materials is inhibited by volcanic mineral components, e.g., allophane, and CBSAs are specially controlled against hydration inhibitions. Previous studies showed that allophane might be the governing factor for the inhibition of cement hydration, and its response to the hydration properties should be investigated.

In this study, cement-paste and cement-treated–soil specimens are made with three types of binder (ordinary Portland cement, blast-furnace slag cement, and a CBSA) to investigate the hydration progress and strength development. Uniaxial compression tests were conducted, and the strength development was measured with the different binder types. It was found that the strengths of the cement-paste specimens at day 28 were almost the same with the three binders, while they differed in the mortar specimens that contained allophane. X-ray diffraction/Rietveld analyses were conducted to measure the hydration properties. From the results, it was supposed that, owing to the lack of $Ca(OH)_2$, the pozzolanic reaction was stagnant. Considering the ion concentration of the pore water in the solidified materials, quantitative estimations of the strength development affected by allophane should be possible in the future.

Keywords: Cement-based solidifying agents, cement-treated soil, XRD Rietveld, ettringite, allophane

1. INTRODUCTION

A cement-based solidifying agent (CBSA) is a material for soil improvement. Components that are effective for hardening soil are added to the base cement material. The CBSA composition is designed to produce the appropriate amount of ettringite during its hydration. Ettringite should improve the ground through its capacity to absorb large amounts of water

and decrease the moisture content in the ground; it also acts like a bridge to firmly connect the soil particles.

CBSAs are widely used in various places for structure-foundation stabilization, roadbed improvements, etc. About 8-million tons of CBSAs are used annually in Japan. However, when soil containing volcanic ash is treated, the strength is often lower than in other soil cases. Because volcanic-ash soils are distributed all over Japan, understandings of the mechanism and future prediction models are anticipated in the engineering field.

Allophane, a mineral contained in volcanic-ash soil, is thought to be one of the main causes of the insufficient strength development in cement treatments. Allophane is the weathered phase of volcanic glass or pumice, and its chemical composition can be represented as $(SiO_2)_n \cdot Al_2O_3 \cdot (H_2O)_m$, where n = 1.3–2.0 and m = 2.5–3.0. The amorphous phase of allophane in the soil inhibits the cement-solidification reaction by adsorbing the calcium ions.

Experiments by the Japan Cement Association showed a correlation between the amount of allophane and the uniaxial compressive strengths of cement-treated soils, as well as a correlation between the amount of allophane and a reduction in the calcium-hydroxide solution concentrations [1]. It was assumed that the strength development was inhibited because of the insufficient hydration progress. However, no studies have been conducted to quantify the hydration progress against the solidification inhibition.

Thus, in this study, the degree of solidification inhibition by allophane in cement-treated soil was investigated by preparing cement-treated soil specimens and quantitatively measuring the clinker consumption and the hydrate production. The study attempts to clarify the contribution of each hydrate to the strength development.

2. EXPERIMENTAL SETUP

Cement-paste and cement-treated–soil specimens were prepared and subjected to compressive-strength tests, X-ray diffraction tests (XRD), and thermal gravimetric analysis tests (TGA). Three types of binder were used: ordinary Portland cement (OPC), blast-furnace slag cement (type B in accordance with Japanese Industrial Standard JIS R 5211 [2]) (BB), and a cement-based solidification agent (CBSA).

Table 1 shows the physical properties and clinker compositions of the binders. Cement-paste specimens were prepared at two water-to-binder ratios (W/B): 0.5 and 1.0. For the cement-treated soil, the particle sizes of commercial sand from Kanuma, Japan (*Kanuma*-soil) were adjusted and used in this study.

Table 2 shows the physical properties of the soil. The allophane content in the soil was estimated by XRD. It should be noted that the estimated allophane content includes other inorganic amorphous materials. Table 3 shows a series of cement-treated soil specimens. The cement-treated soil was prepared according to the method in the Japanese Geotechnical Society's JGS 0821-2009 [3].

Table 1: Binder properties

Binder type	*Ig. Loss* (%)	Chemical composition (mass %)						Density (g/cm^3)	Specific surface area (cm^2/g)
		SiO_2	Al_2O_3	Fe_2O_3	CaO	MgO	SO_3		
OPC	2.47	13.89	3.74	3.47	75.12	0.97	1.94	3.15	3550
BB	1.88	19.63	7.27	1.76	62.99	3.30	3.27	3.02	3800
CBSA	1.38	22.23	7.13	2.01	55.77	2.61	6.87	3.06	3630

Table 2: **Physical soil properties**

Moisture content	Density	Amount of allophane
26.1%	2.7 g/cm^3	82%
Gravel	Sand	Clay& Silt
12%	87%	1%

Table 3: Mix proportions of cement-treated soil specimens

W/B	S/B	Unit (kg/m^3)		
		W	B	S
1.75	2.50	585	334	835
2.33	3.33	601	257	858
3.50	5.00	617	176	882

W/B	S/B	Unit (kg/m^3)		
		W	B	S
1.13	2.50	475	422	1056
1.50	3.33	491	328	1092
2.25	5.00	509	226	1131

Three cylindrical specimens (φ5 × 10 cm) were prepared for each cement-paste or cement-treated–soil case. The top surface of each specimen was covered with plastic wrap until the test-material age after casting (sealed curing), and the specimens were placed at a constant temperature of 20 °C.

The specimens were subjected to uniaxial compression tests at their material ages of 1, 3, 7, and 28 days. After the compression tests, some specimen pieces were collected and subjected to XRD and TGA tests. The test pieces were pulverized to about 5 mm and immersed in isopropanol for one week to stop their hydration. Next, one week of vacuum drying was applied. They were pulverized again and sieved to 100-μm particle sizes for the TGA and XRD tests.

The TGA measurements were conducted with an STA 2500 Regulus thermal analyzer (NETZSCH) under nitrogen-flow conditions with a temperature-increase rate of 15 °C/min. The ignition-loss (*Ig. Loss*) value is defined as the value of the mass lost from 105 °C to 950 °C divided by the mass at 950 °C. XRD analyses were conducted using the LabX XRD-6100 X-ray differential system (Shimadzu). The hydrated and dried powder samples were analyzed under the following conditions: The X-ray source is Cu-Kα, the tube voltage is 40.0 kV, the tube current is 30.0 mA, the scanning range is 2θ = 5–70°, the step width is 0.02°, and the scanning speed is 2.0°/min.

XRD Rietveld analyses were conducted on the XRD results with SIROQUANT software ver. 3.0. The following phases were considered in the quantifications as cement minerals or hydration products: C_3S, C_2S, C_3A, C_4AF, MgO, CaO, $CaCO_3$, $CaSO_4 \cdot 2H_2O$ (gypsum), $CaSO_4 \cdot 0.5H_2O$ (basanite), $CaSO_4$ (anhydrite), $Ca(OH)_2$ (CH), $C_3A \cdot 3CaSO_4 \cdot 32H_2O$ (ettringite), $C_3A \cdot CaSO_4 \cdot 12H_2O$ (monosulfate), $3CaO \cdot Al_2O_3 \cdot 0.5Ca(OH)_2 \cdot 0.5CaCO_3 \cdot 12H_2O$ (hemicarbonate), $3CaO \cdot Al_2O_3 \cdot CaCO_3 \cdot 11H_2O$ (monocarbonate), and α-Al_2O_3. α-Al_2O_3 of 10 wt% of the samples was mixed as the internal standard.

For the cement-treated–soil specimens, albite, anorthite, and quartz were added to the phases for the quantifications. The amorphous-substance content was calculated according to Eq. (1) from the quantified value of the internal standard α-Al_2O_3 [4]. The amounts of unhydrated clinkers and hydrated products in the samples were calculated by correcting the quantitative values obtained from the XRD Rietveld analyses with the *Ig. Loss* and the amorphous content, according to Eq. (2).

$$A = \{100 \times (S_R - S)\} / \{S_R \times 100 - S) / 100\} \quad (1)$$

$$Q = Q_R \times (100 - A) / (100 - L), \quad (2)$$

where A is the amorphous-material content, S is the mixing ratio (%) of α-Al_2O_3, S_R is the quantified value of α-Al_2O_3 (%), Q_R is the quantitative value of each phase (%), and L is *Ig. Loss.*

3. EXPERIMENTAL RESULTS OF CEMENT-PASTE SPECIMENS

Figure 1 shows the results for the compression tests of the cement-paste specimens. The legend in the figure represents the (Binder Type)-(W/B). From the results in Fig. 1, BB and CBSA showed strengths similar to OPC at day 28, while their initial strength developments were slower than OPC in both the 0.5 and 1.0 W/B cases.

Table 4 and Figure 2 show the phase compositions of the mass calculated by the XRD Rietveld analyses. The W/C 0.5 cases of the OPC and CBSA specimens are displayed in Fig. 2. There was no significant difference in the C_3S hydration rate between OPC and CBSA, which is considered to contribute the most to the strength in the early ages. Regarding the other clinkers, CBSA had a slower hydration rate than OPC. In CBSA, anhydrite was consumed at almost the same rate as C_3S, and an accordingly large amount of ettringite was produced.

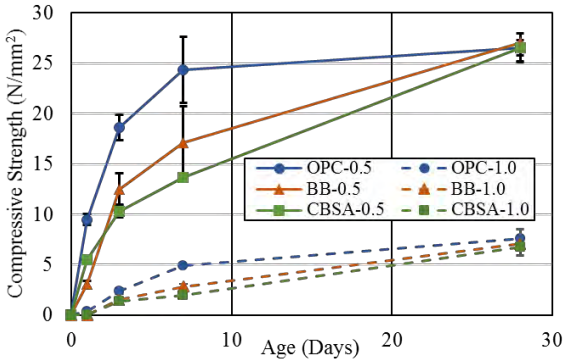

Figure 1: Strength development of paste

Table 4: Mineral composition of binders

	C3S	C2S	C3A	C4AF
OPC	68	12.2	10.2	5.3
BB	57.3	13.9	6.6	4.4
CBSA	56.1	10.7	5.4	5.9
	Bassanite	Anhydrite	Gypsum	Others
OPC	0.4	0.1	0.5	3.3
BB	1.9	0.5	3.7	11.7
CBSA	0.7	14.3	2.1	4.8

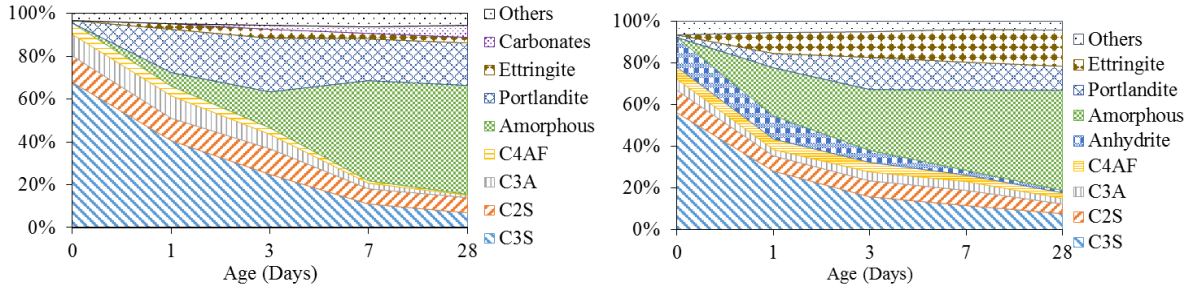

OPC-0.5 case CBSA-0.5 case

Figure 2: Calculated mass of phase compositions

Using the density of each cement mineral and the hydrate phase from previous research [4, 5] (Table 5), the phase compositions in the volume basis were calculated [5, 6]. Figure 3 shows the calculated volume of the phases of the cement-paste specimens. The volume of ettringite in the CBSA case is larger than that of the OPC case. In addition, the theoretical porosities of the cement pastes were estimated from the calculated phase volumes. The porosities of the cement-paste specimens (Φ_{cp}) were calculated by Eq. (3):

$$\Phi_{cp} = V_{pore} / V_{total.ini}, \quad (3)$$

where V_{pore} is the volume of free-water and blank spaces and $V_{total.ini}$ is the volume of the cement paste at day 0.

Table 5: Density of each phase in kg/m^3

phase	C_3S	C_2S	ettringite	monocarbonate	portlandite	anhydrite	gypsum
density	3150	3310	1778	2175	2251	2968	2311
phase	C_3A	C_4AF	calcite	hemicarbonate	monosulfate	amorphas	water
density	3030	3740	2710	1985	2015	2410	1000

Figure 4 shows the estimated porosities of the cement-paste specimens. A correlation between porosity and strength was shown in previous research [7]. However, in this study, the CBSA and OPC cases showed almost the same porosity decrease rates, while the strength developments were different, as shown in Fig. 1.

From these results, the following process can be assumed for the strength development of CBSA. In the early stage, large quantities of ettringite are produced, owing to the extensive anhydrite content. Because the cement-paste skeletons are not very stiff yet, the cement paste itself expands or is destroyed, due to the expansion pressure of the ettringite. Hence, the strength of CBSA can be lower than the strength of OPC at the early stage. A similar tendency was observed in previous research [8].

After the paste has stiffened, the ettringite formation can contribute to the strength, as well as other hydrates. Previous research has shown that the expansion pressure changes, depending on the shape of the ettringite, and the shape changes depend on the Ca^{2+} concentration in the pore solution [9]. In this study, neither the expansion nor the void distribution was measured. Measuring the volume changes or pore-size distributions can help researchers better understand the CBSA hydration characteristics.

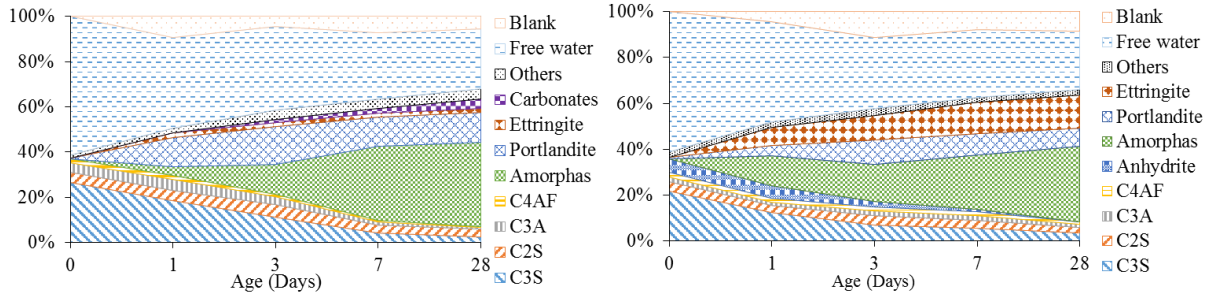

Figure 3: Calculated volume of the phase compositions

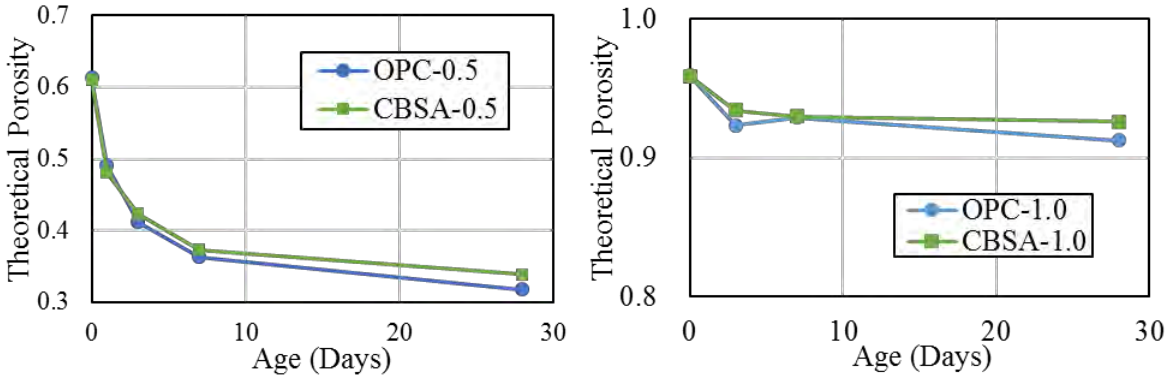

Figure 4: Theoretical porosity of the cement-paste specimens

4. EXPERIMENTAL RESULTS OF CEMENT-TREATED–SOIL SPECIMENS

Figure 5 shows the compressive strengths of the cement-treated–soil specimens. The strength-development tendencies in the early stages vary, depending on the W/B. The OPC and CBSA cases have almost the same strength transitions at higher W/Bs (more than 2.25); these are an available mix-proportion range in actual soil-improving methods. On the other hand, for lower W/B specimens, the CBSA specimens initially have a higher strength than the OPC, while the OPC specimens have a higher strength at day 28. The tendency of the cement-treated–soil specimens is different from the cement-paste specimens. The BB specimens have significantly lower strength than the rest of the series.

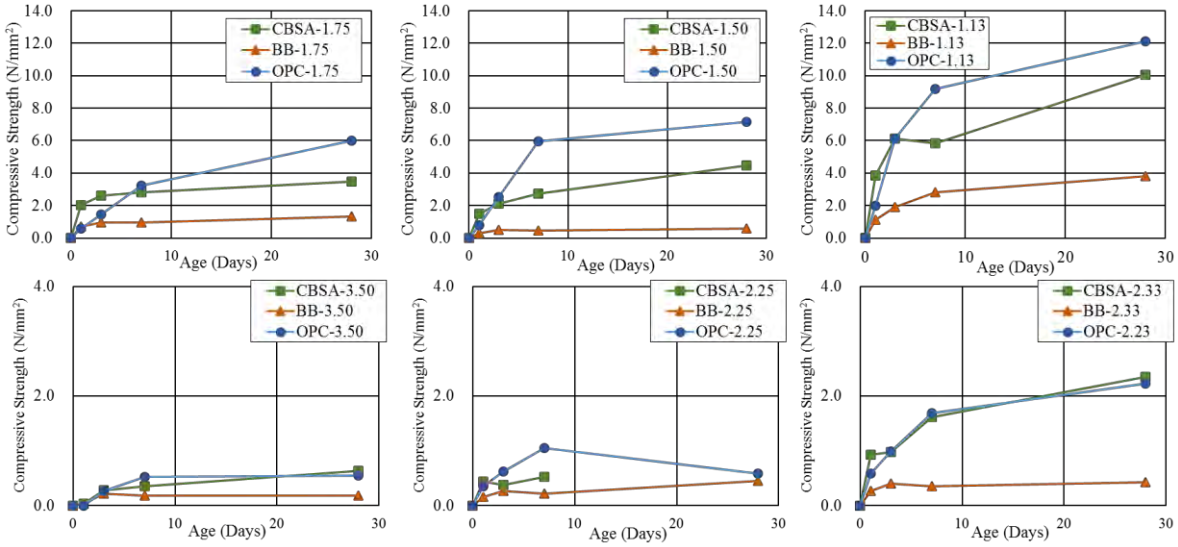

Figure 5: Strength development of cement-treated–soil specimens

Figure 6 shows the XRD profiles of the cement-treated–soil specimens. Each result is a profile of a corundum mixture. The data for day 0 show the results of *Kanuma*-soil that does not contain cement, and the other charts show the results of the cement-treated–soil specimens of the W/B 1.75 cases for the OPC and CBSA cases. A gentle broad peak around 20–30°, which is unique to allophane, is observed; however, the height of this peak decreases in the cement-treated–soil specimens.

In OPC, peaks for hemicarbonate and monocarbonate are observed around 10.7 ° and 11.7 °, respectively. In CBSA, ettringite peaks are observed at around 9.1 °, for example. In both the OPC and CBSA cases, no CH peaks can be observed.

Previous studies have reported that ettringite can be produced by adding $Ca(OH)_2$ and gypsum to allophane [10]. It is supposed that the following reaction occurs between allophane and the cement system in cement-treated soils:

$$(SiO_2)_n \cdot Al_2O_3 \cdot (H_2O)_m + 3Ca(OH)_2 + 3(CaSO_4 \cdot 2H_2O) + (23\text{-}m)H_2O \quad (4)$$
$$\rightarrow 3(CaO \cdot Al_2O_3) \cdot 3CaSO_4 \cdot 32H_2O + nSiO_2$$
$$2SiO_2 + 3Ca(OH)_2 + H_2O \rightarrow 3CaO \cdot 2SiO_2 \cdot 4H_2O. \quad (5)$$

These reactions are assumed to be pozzolanic reactions, and they might be effective for long-term strength development. With these reactions, large amounts of CH, which are generated by clinker hydration, are almost completely consumed.

Figure 7 shows the calculated masses of the phases in the cement-treated–soil specimens, based on the XRD results. Regarding the clinkers' consumption rates, there is no significant difference between the cement-treated soil specimens (Fig. 7) and the cement-paste specimens (Fig. 2).

From these results, the following strength-development mechanisms for CBSA in cement-treated soil containing allophane can be assumed. Large amounts of ettringite are produced in the early stage and absorb the moisture. Then, the moisture content in the soil decreases and the connection between the soil particles can be strengthened, which can contribute to an increase in strength, as opposed to the OPC case.

On the other hand, after the early stage, because a large amount of gypsum is present, a large amount of CH is consumed to produce ettringite, and the allophane's pozzolanic reaction does not occur sufficiently. In addition, CBSA produces only about half of the CH that OPC does in cement paste. As a result, the amount of calcium-silicate-hydrate (C-S-H) in the CBSA case is less than that in the OPC case. These phenomena could be the cause of the strength-development slowdown in the CBSA case. This assumption can also explain the lowest strength of the BB case. The calcium concentrations in the pore water decrease in the presence of allophane, and the reaction of the blast-furnace slag can stagnate.

In this research, it was not possible to separate the allophane-derived amorphous phase and the cement-derived C-S-H amorphous phase in the XRD results. By studying the clear-phase composition and the theoretical porosity, a strength prediction should be achieved in the future. In addition, it is thought that the mechanism's hypothesis can be confirmed by measuring the ion concentrations of the pore solutions to discuss the phase equilibrium of the pore water and hydrates.

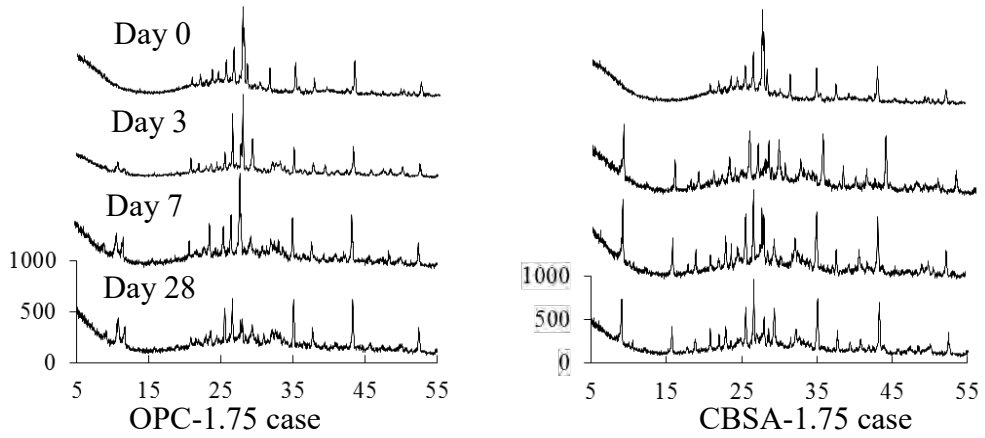

Figure 6: XRD profiles of cement-treated–soil specimens

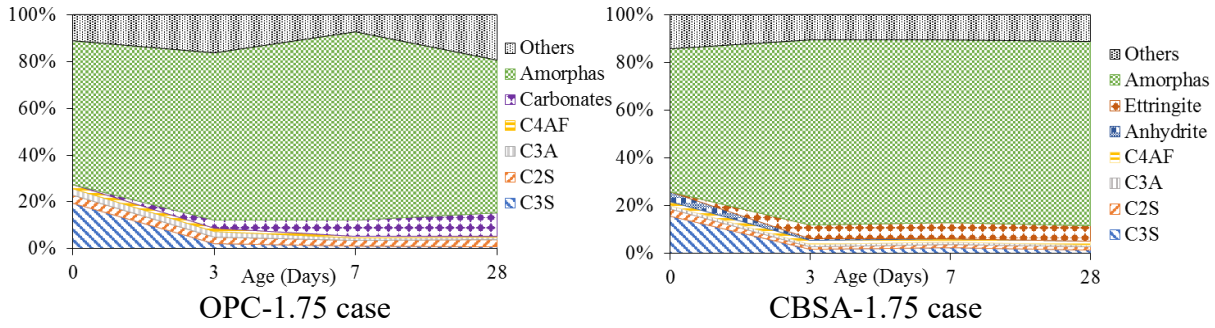

Figure 7: Calculated mass of phase compositions of cement–treated–soil specimens

5. CONCLUSIONS

To investigate the hydration characteristics of CBSA, cement-paste specimens and cement-treated soil specimens were prepared, and uniaxial compression, TGA, and XRD tests were conducted. The relationships between the compressive strengths and the quantitative values of the hydrate phases were investigated.

The early-stage strengths of the CBSA cement pastes were smaller than those of OPC. A large amount of anhydrous gypsum was present and a large amount of ettringite was produced in CBSA. After the stiffness development of the cement-paste systems, it is supposed that the ettringite contributes to the strength, as other hydrates do.

The early-stage strengths of the CBSA cement-treated–soil specimens were almost equal to or slightly higher than those of OPC. On the other hand, the subsequent strength of CBSA did not increase much. In the early-stage strength development, a large amount of ettringite can contribute to changing the moisture state of the soil, which can increase the initial strength. The subsequent slow strength developments can be explained by the stagnation of the pozzolanic reaction, due to the lack of $Ca(OH)_2$.

ACKNOWLEDGMENTS

This study was financially supported by JSPS KAKENHI grants numbers 17H01284 and 18KK0120.

REFERENCES

[1] Japan Cement Association. 'A study of strength development of volcanic cohesive soil using geocement: influence of allophane.' *Cement and Concrete*, **780** (2012) 3–8. (in Japanese)

[2] JIS R 5211: 2009. https://kikakurui.com/r5/R5211-2009-01.html.

[3] JGS 0821-2009. 'Practice for making and curing stabilized soil specimens without compaction.' The Japanese Geotechnical Society: JAPANESE GEOTECHNICAL SOCIETY STANDARDS. Laboratory Testing Standards of Geomaterials (vol. 2), 2009, 426-435.

[4] Bish, D.L. and Howard, S.A. 'Quantitative phase analysis using the Rietveld method.' *Journal of Applied Crystallography* **21**(2) (1988) 86–91.

[5] Balonis, M. and Glasser, F.P. 'The density of cement phases.' *Cement and Concrete Research* **39**(9) (2009) 733–739.

[6] Maruyama, I. and Igarashi, G. 'Cement reaction and resultant physical properties of cement paste.' *Journal of Advanced Concrete Technology* **12**(6) (2014) 200–213.

[7] Chen, X., Wu, S., and Zhou, J. 'Influence of porosity on compressive and tensile strength of cement mortar.' *Construction and Building Materials* **40** (2013) 869–874.

[8] Halaweh, M. 'Effect of alkalis and sulfates on Portland cement systems.' (2006).

[9] Mehta, P.K. 'Mechanism of sulfate attack on Portland cement concrete—Another look.' *Cement and Concrete Research* **13(**3) (1983) 401–406.

[10] So, E. and Ying, C. 'Influence of Allophane Content on Lime-Gypsum Stabilized Volcanic Cohesive Soils.' *Soils and Foundations* **34** (1994) 97–107.

THE INFLUENCE OF HYDRATION ON THE MICROSTRUCTURE DEVELOPMENT OF CEMENT PASTE WITH BLEEDING: AN NMR STUDY

Yanliang Ji (1)(2)(3), Zhenping Sun (1)(2) *Leo Pel (3) and Min Pang (1)(2)

(1) Key Laboratory of Advanced Civil Engineering Materials, Ministry of Education, Tongji University, Shanghai 201804, China;

(2) School of Materials Science and Engineering, Tongji University, Shanghai 201804, China;

(3) Eindhoven University of Technology, Department of Applied Physics, Transport in Permeable Media, P.O. Box 513, 5600 MB Eindhoven, The Netherlands

Abstract

Bleeding can be described as water coming out from fresh cement paste, which not only affects the homogeneity at fresh stage but also decides the hardened state structure. Previous studies have focused on the determination or simulation of the bleeding extent of fresh cement paste and give objective conclusions. However, there are rare researches about the influence of bleeding on the final structure of cement paste. In this study we have monitored the cement paste with various bleeding caused by water cement ratio and slag replacement. The microstructure development of cement paste from top to bottom was measured by using low-field NMR with Hahn spin sequence from 6 h to 72 h. Results showed that within 4.4 mm bleeding thickness the bleeding will decrease the slope of the void ratio as a function of distance which suggests a homogeneous structure is formed. However, when the bleeding water thickness is higher than 4.4 mm, hydration would lead to a heterogeneous structure. Detailed discussions on the connection between the bleeding and the final structure are also presented in this paper.

Keywords: Bleeding, Cement paste, NMR, Hydration, Microstructure

1. INTRODUCTION

Bleeding of cement-based materials is a water-related behavior which can be simply defined as water coming from cement -based materials to their surface. Bleeding has different impacts on cement-based materials in different period of its lifecycle [1-2]. The settlement cracks in early stage of cement-based materials, a weaker layer in construction and deterioration of durability are all considered to be related to the bleeding process. It is also known that bleeding

can lead to inhomogeneity of fresh cement paste and instability for commercial application of cement-based products, i.e., self-compacting concrete and grouting materials.

Previous studies [2-4] focused on the prediction of bleeding process by various models and confirmed that the bleeding process is a consolidation process rather than a sedimentation one. However, for the influence of hydration on the microstructure development of cement paste with bleeding, there are rarely reported in literature. In fact, hydration characteristics at different position of cement-based materials with bleeding theoretically directly decides the final performance of the cement-based materials who have bleeding. Therefore further study on hydration characteristics of cement-based materials with bleeding are needed.

As a nondestructive and noninvasive method, NMR can quantitatively study the water distribution and structure of a sample. It can provide important insights into the microstructure development from fresh to hardened state [3, 5]. In our previous study, the Nuclear Magnetic Resonance (NMR) has been used to investigate the microstructure development of cement paste during bleeding [2]. Here in this study, we have monitored the cement paste with various bleeding caused by water cement ratio and slag replacement. The microstructure development of cement paste from top to bottom was measured by using low-field NMR with Hahn spin sequence from 6 h to 72 h. Analysis and discussion about the experimental results are also given in this paper.

2 MATERIALS AND METHODS

2.1 Materials

The cements used in this study (HEIDELBERG Group, ENCI B.V. Netherlands) are Ordinary Portland cement (OPC), which has specific area of 340 m^2/kg. The specific density for the cements is 3.1 g/cm^3. The slag used in this study has a specific area 501 m^2/kg and a specific density 2.93 g/cm^3. In this study various parameters were systematically changed of which an overview of the used mix designs and identification codes are given in Table 1.

Table 1: Mix design and identification codes of the cement paste samples

No.	Water	Cement	Slag	Water reducer/%	Final bleeding[mm]
WC_0.60	0.60	1	-	-	3.1
WC_0.65	0.65	1	-	-	3.6
WC_0.70	0.70	1	-	-	5.5
SL_0 %	0.65	1	-	-	3.6
SL_30 %	0.65	0.7	0.3	-	2.3
SL_60 %	0.65	0.4	0.6	-	5.7

2.2 Method

In an NMR experiment, the signal intensity *S* of a Hahn spin-echo sequence [5] is proportional to the amount of hydrogens and can be described by [5, 6]:

$$S(t_E) = \rho \exp\left(-\frac{t_E}{T_2}\right)\left(1 - \exp\left(-\frac{t_R}{T_1}\right)\right) \tag{1}$$

where ρ is the density of the hydrogen nuclei, T_1 is the spin-lattice relaxation time, T_2 is the spin-spin relaxation time and t_R is the repetition time and t_E is the echo time. Assuming the pores are saturated, the signal intensity $S(t_E)$ will be proportional to the porosity, i.e., it will give us a direct indication of the void ratio (e). It has been well established [2, 5] that the relaxation rate can be correlated with the pore size. In the so-called fast diffusion regime, both T_1 and T_2 are related to the surface-to-volume ratio of pores as:

$$\frac{1}{T_{1,2}} = \frac{1}{T_{bulk}} + \rho_{1,2}\frac{S}{V} \tag{2}$$

where $\rho_{1,2}$ is the surface relaxivity for T_1 and T_2 relaxation respectively, which reflects a sink at the surface of the pores. As T_{bulk} for water at room temperature is in the order 3 seconds the first term for many porous building material with sufficient small pore can be neglected [2,3]. For measuring a complete profile using Hahn spin-echo sequence during hydration (6-72 h), approximately 92 seconds are needed. In all the NMR experiment, the sampling parameters such as the echo time (280μs) and repetition time (500 ms) were kept constant.

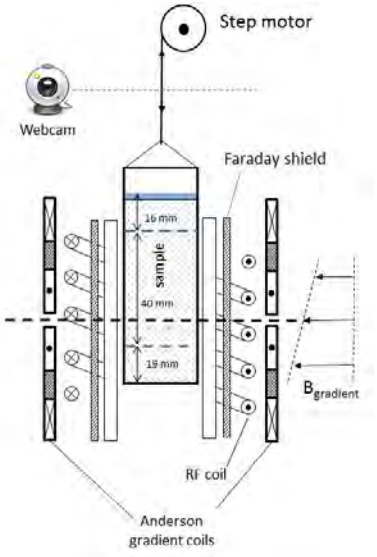

Figure 1: A schematic representation of the NMR set up for measuring the microstructure changing of fresh cement paste. The sample holder is a Perspex cylindrical tube with a diameter of 27 mm, which with the help of a step motor is moved through the NMR. A webcam has been added as to measure free moisture content on top to the sample, i.e., the bleeding. After 6 hours the complete profile is measured

3 RESULTS AND DISCUSSION

3.1 Profiles of the cement paste with bleeding

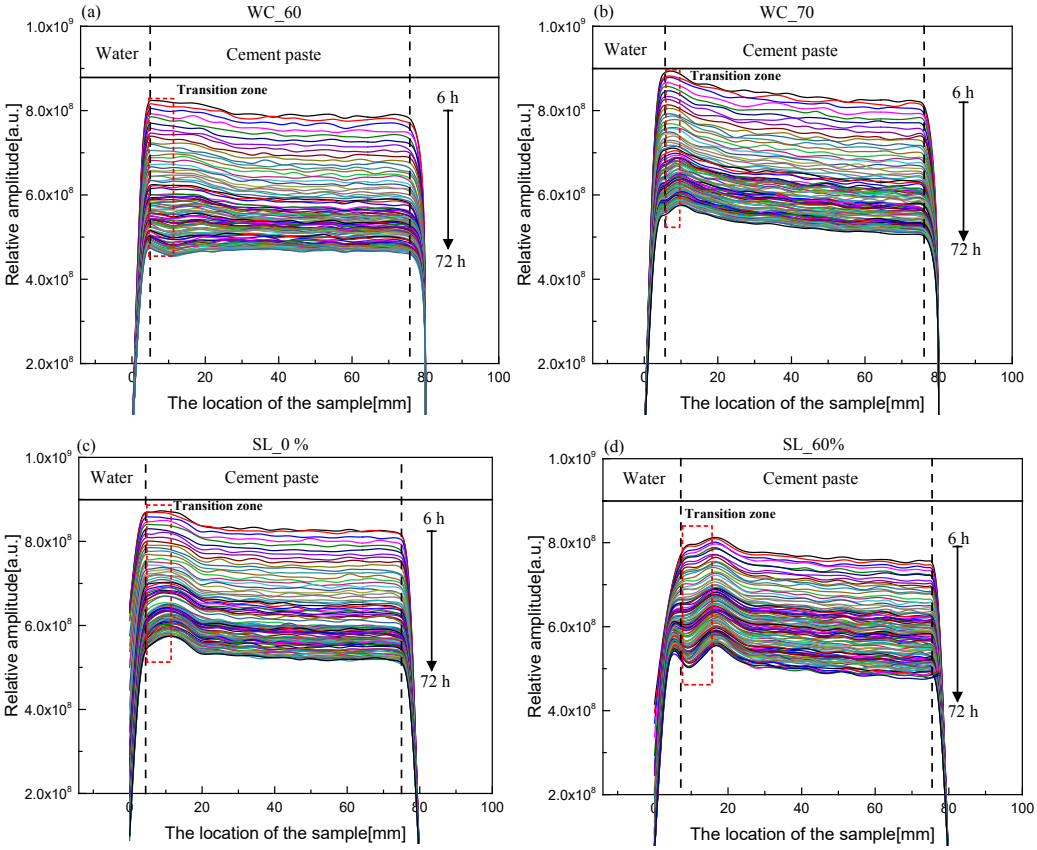

Fgure 2: The NMR profiles of typical cement pastes with bleeding water measured during hydration 6-72 h (a: WC_60, b: WC_70). The vertical dash line was placed to differentiate the bleeding water and cement paste

In Fig. 2, the measured profiles during hydration (6 h-72h) are given for typical cement paste with bleeding. It can be seen that bleeding water has different relative amplitude which has a range altering from 8×10^{-9} to 9×10^{-9}. Here special attention has to be paid to NMR profiles of cement paste part below the bleeding water. The presence of bleeding water ensures that the pore in cement paste is saturated during the whole NMR method. Thus the water amount expressed as relative amplitude (Hahn spin) linearly correlated with the porosity at different locations in theory [6].

As expected, the moisture profile generally decrease as function of hydration time from 6 h to 72 h, and during the whole hydration process the moisture exhibit different values with the distance from the bleeding surface. To be specific, the part close to the bleeding surface (named as transition zone) has shown an opposite trend (increasing relative amplitude with distance) compared to the rest of the cement paste sample. One possible reason for the existence of transition zone may correlate with uneven distributed gypsum during the sediment process. The large distance between particles during sediment process allows more gypsum particles stay in utter section of a cement paste because they have a comparably lower density and smaller particle size [7]. This would therefore lead to more SO_4^{2-} existing in this part and may facilitate

the formation of hydration products such as ettringite (Aft) and calcium hydroxide (CH). The transition zone of a cement paste with bleeding has more crystalline products and can weaken the surface integrity and mechanical property in practical engineering, and it needs more systematic to investigate this point. In addition, the majority of the sample showed that the moisture signals decrease with the distance from surface.

3.2 The microstructural homogeneity during hydration

In this study, the slope of the relative amplitude versus depth(the transition zone are not taken into consideration) was used to evaluate the influence of sediment and consolidation on the heterogeneous property during hydration. Using the Eq. 3, the slope was calculated and the results are shown in Fig. 3.

$$K = (\frac{N\Sigma LA - \Sigma L\Sigma A)}{N\Sigma L\hat{}2 - (\Sigma L)\hat{}2} \tag{3}$$

where N is the number of the data, L is the distance from the transition zone boundary to bottom and A is the relative amplitude. Results in the Fig. 3 indicated that the hydration have different influence on the heterogeneous cement paste with bleeding in the control factors of water cement ratio, slag powder replacement and PCEs dosage.

As expected, higher water cement ratio will lead to an uneven pore structure from the top to bottom and the hydrations in 72 hours will aggravate the heterogeneous property because an even larger slopes were found for the sample WC_65 and WC_70. For the sample WC_60, the slope kept on increasing after a short time decreasing, during the hydration may due to the water supplied from the surface have curing effect on the system which then in turn reduce the heterogeneous property. In Fig.3 b, compared with the reference sample, the 60% slag replacement sample has a trend that absolute slope value will continue to increase. The slope curve for the SL_30% has a same pattern which first decrease then increase during hydration. This suggest the high slag replacement mixing sample will form an even more heterogeneous structure after the hydration. Reason for this may be due to the that the lower density particles (slag) may pass through the space between the particle during sediment process, then lead to more slag powder existing in the top section of a paste. The slag powders are poor activity materials [8]. High amount of slag means less products are formed in the pore structure, thus it would increase the inhomogeneity during the hydration.

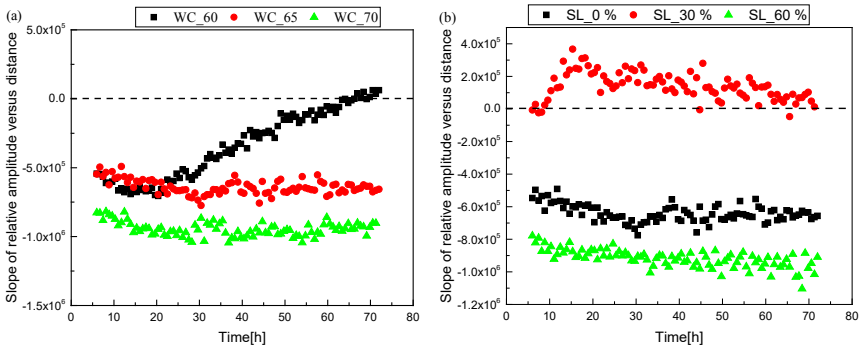

Figure 3: The slope of the relative amplitude versus depth derived from the cement paste sample with bleeding (a: Water cement ratio, b: Slag powder replacement)

3.3 The impacts of bleeding extent on microstructural homogeneity

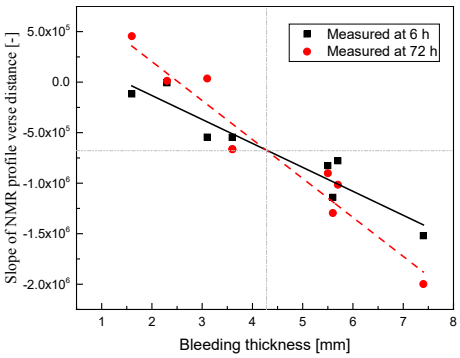

Figure 4: Relationship between the bleeding thickness and the slope of the NMR with distance at 6 h and 72 h

In Fig.4, the relationship between the bleeding thickness and the slope of the NMR with distance at 6 h and 72 h is shown. It was found that the bleeding thickness decrease with the slope of the NMR with distance, and the bleeding thickness is linearly correlated to the slope. In addition, compare the results at 6 h and 72 h, it can be seen that the within 4.4 mm bleeding thickness the hydration will decrease the slope of the void ratio as a function of distance which suggests a homogeneous structure is formed. However, when the bleeding water thickness is higher than 4.4 mm, hydration would lead to a heterogeneous structure.

4 CONCLUSIONS

The microstructure development of cement paste from top to bottom as well as a transition zone of the cement paste can be measured by using low-field NMR with Hahn spin sequence. The majority of the sample showed that the moisture signals decrease with the distance from surface. It was found the bleeding thickness decrease with the slope of the NMR with distance, and the bleeding thickness is linearly correlated to the slope. Within 4.4 mm bleeding thickness the bleeding will decrease the slope of the void ratio as a function of distance which suggests a homogeneous structure is formed. However, when the bleeding water thickness is higher than 4.4 mm, hydration would lead to a heterogeneous structure.

ACKNOWLEDGEMENTS

The authors acknowledge the financial support provided by the 13th Five-Year Plan (2016YFC0701004), the National Natural Science Foundation of China (Project no. 51678441 and Project no. U153420040), the Science and Technology Commission of Shanghai Municipality (Grant No. 19DZ1202702 and 19DZ1201404), Shanghai "super postdoctoral" incentive program, the China Scholarship Council.

REFERENCE

[1] Y. Peng, S. Jacobsen, Influence of water/cement ratio, admixtures and filler on sedimentation and bleeding of cement paste, Cem. Concr. Res. 54(2013), pp. 133-142

[2] Y.L. Ji, P. Leo, Z.P. Sun, The microstructure development during bleeding of cement paste: An NMR study, Cem.Concr. Res., 125(2019), 105866, ISSN 0008-8846
[3] Y.L. Ji, Z.P. Sun, X. Yang, C.J. Li, X.B. Tang, Assessment and mechanism study of bleeding process in cement paste by ^{1}H low-field NMR, Constr. Build. Mater., 100(2015), pp. 255-261
[4] P.H. Morris, P.F. Dux, Analytical solutions for bleeding of concrete due to consolidation, Cem. Concr. Res. 40(10) (2010), pp. 1531-1540
[5] M. T. Vlaardingerbroek, J.A. Den Boer, Magnetic Resonance Imaging. Theory and Practice, Springer, Berlin, Heidelberg, 1996
[6] C.P. Slichter, Principles of Magnetic Resonance, Springer Verlag, Berlin (1989)
[7] Jianguo Han, Kejin Wang, Influence of bleeding on properties and microstructure of fresh and hydrated Portland cement paste, Construction and Building Materials. 115 (2016), pp. 240-246.
[8] P.J. Wainwright, H.A. Aider, The influence of cement source and slag additions on the bleeding of concrete, Cement and Concrete Research, 25(7)(1995),pp. 1445-1456.

Theme 3

Transport properties in cracked and uncracked concrete

ADVANCED CHARACTERIZATION OF CHLORIDE BINDING IN OPC AND LC³ PASTES

Julien Nicolas Gonthier (1), William Wilson (1), Fabien Georget (1) and Karen Scrivener (1)

(1) École Polytechnique fédérale de Lausanne (EPFL), Lausanne VD, Switzerland

Abstract

The incorporation of supplementary cementitious materials (SCMs) in cement pastes enables both decreasing CO_2 emissions and increasing the concrete durability, notably with a better resistance against chloride ingress and thus retarding the chloride-induced corrosion of steel rebars. Nevertheless, a better understanding of the chloride fixation in cement pastes is required to build an accurate model for the transport of chlorides in new types of cementitious systems with SCMs. The purpose of this study is to characterize the chloride binding capacity of Limestone Calcined Clay Cement (LC³) pastes compared to Ordinary Portland Cement (OPC) pastes.

The binding of chlorides was investigated in hardened cement pastes equilibrated with 0.5M NaCl and 0.5M NaCl + 0.3M NaOH solutions whose chloride concentration is similar to that of sea water. The total chloride content was determined by acid dissolution of the paste after exposure, while chemically and physically bound chlorides were determined by X-Ray Diffraction (XRD) coupled with Rietveld analyses, Scanning Electron Microscopy with Electron Dispersive Spectroscopy (SEM-EDS) and water dissolution of the pastes.

The results showed that the higher content of AFm phases in LC³-50 pastes at 28 days did not lead to a higher chloride binding capacity compared to the reference OPC pastes, for both investigated chlorine solutions. XRD and SEM-EDS provided coherent estimates of chemically bound chlorides into AFm phases for each system (i.e., different solid solutions of Hemicarboaluminate and Friedel's salt). These chlorides fixed in AFm were found to be lower than the difference between total acid-soluble chlorides and water-soluble chlorides (by 0.4 to 2.3 mg of fixed chlorides per gram of paste, depending on the system), suggesting other mechanisms of chloride binding such as physical binding on the C-A-S-H. Overall, the findings in this study suggest that the amount of the different kinds of chlorides fixed in cement pastes can be evaluated with relatively straightforward methods such as XRD/Rietveld and acid-soluble chloride titration.

Keywords: Chloride binding, AFm, Friedel's salt, limestone calcined clay cement

1. INTRODUCTION

In the search for a more accessible and durable binder for concrete with a lower carbon footprint, the addition of calcined clay and limestone to Portland cement was found to be a sustainable alternative while maintaining similar mechanical properties as 100 % Portland cement [1,2]. Chloride transport in cement pastes is a key parameter to predict the durability of the concrete, previous studies have shown significant increase of the resistance capacity against chloride ingress in LC³ systems compared to OPC systems, consequence of denser microstructure and porosity refinement in LC³ pastes [2-5].

Complete modelling of chlorides transport requires to consider the capacity of the hardened cement paste to fix chlorides in two ways: either by chemical binding in AFm by the replacement of the carbonate counter-ion by $2Cl^-$ (forming Friedel's salt), either by physical binding in C-A-S-H [6]. Chemically bound chlorides in AFm have been quantified in OPC by researchers using notably XRD [7] and previous work showed that carboaluminates and Friedel's salt can coexist within a solid solution [8,9]. The compounds released from calcined clays and limestone during hydration lead to higher content of carboaluminates [10] and thus to a potentially higher binding capacity of LC³ systems.

In this study, the total, chemically and physically fixed chlorides were quantified in OPC and LC³-50 hardened pastes equilibrated with a 0.5 M NaCl solution (chloride ingress in marine environment can be estimated using NaCl solutions [11]) at two different pH during 8 months with no renewal of the solution. XRD, SEM-EDS and titration of acid/water-soluble chlorides were employed to investigate the effect of both the binder and the pH on the amount of Friedel's salt. A further aim was to provide insights on the comparability between acid-soluble (total chlorides) and water-soluble (not bound chlorides) chloride contents in the studied systems in relation to the amount of chemically bound chlorides.

2. MATERIALS AND METHODS

The raw materials used in this study to produce the cement pastes are listed as follows: an industrial cement CEM I 42.5, an Indian calcined clay containing 45% of calcined kaolinite, fine limestone powder and gypsum of chemical grade. Chemical grade NaCl and NaOH were employed to prepare the exposure solutions. All the samples were prepared at the same water-to-binder ratio of 0.4 by mass and were cured in their pore solution for 28 days at room temperature.

2.1 Sample preparation

A series of OPC pastes was prepared by mixing CEM I with distilled water and a series of LC³-50 pastes was prepared by mixing 53 % of CEM I, 30 % of calcined clay, 15 % of limestone and 2 % of gypsum. The powders were homogenized using a paint mixer with ceramic balls for 10 minutes before mixing with distilled water. A high-shear mixer was used to mix the pastes at 1600 RPM for 2 min in air, followed by 1 min under vacuum at 450 RPM. A superplasticizer (polycarboxylate-based) was added to ensure a good workability. The fresh pastes were cast into cylindrical polypropylene recipients (Ø = 33 mm, h = 55 mm) sealed and left at room temperature for the first 24 hr. The hardened pastes were then cured at room temperature in slightly larger recipients filled with the lowest possible amount of water. A few grams of sacrificial finely ground sample (from the same batch) was added into each curing container to act as a leaching buffer and allow the curing in "pore solution".

After 28 days of curing, the cylinders were removed from the curing solutions and slices of about 2 mm thick were cut out using a water-lubricated saw, dismissing the first 2 mm of the cylinder's top and bottom. Slices were kept in a wetted tissue before being transferred in a slightly larger polypropylene cylindric container (Ø = 36 mm, h = 60 mm) filled with 40 ml of the host solution (0.5 M NaCl or 0.5 M NaCl + 0.3 M NaOH). Two slices were inserted per recipient along with two small polypropylene pieces inserted between slices to ensure the whole surface of the slices was in contact with the solution. Samples were stored at room temperature for about 8 months to reach equilibrium.

2.2 XRD and SEM-QEDS

The phase assemblage in the cement pastes was quantified by XRD coupled with Rietveld refinements on a 28-day cured sample as a reference and on the two samples exposed to high and low pH NaCl solutions. A slice was wet polished using its host solution for about 1 min with a 1200 carbide paper on both sides, it was then gently wiped with a wet paper and its Saturated Surface Dry (SSD) mass was recorded as well as its diameter and thickness. The slice was analyzed on a X'Pert PANalytical diffractometer in the Bragg-Brentano geometry using a CuKα source operated at 45 kV and 40 mA with a X-Celerator detector. The beam was constrained by fixed divergence and anti-scatter slits of 0.5 °, with a mask of 15 mm. The 2θ range was [5 °, 70 °] with a step size of 2θ = 0.02 ° and the scan lasted for 14 min. The external standard method was employed with a rutile standard. The phase assemblage quantification was carried out considering a Friedel's salt solid solution (Fs_{ssol}) between the Hemicarboaluminate (Hc) and pure Friedel's salt (Fs) phases, whose chemical composition was extracted from the position of the Friedel's salt peak, as illustrated in Figure 1 and described in [9].

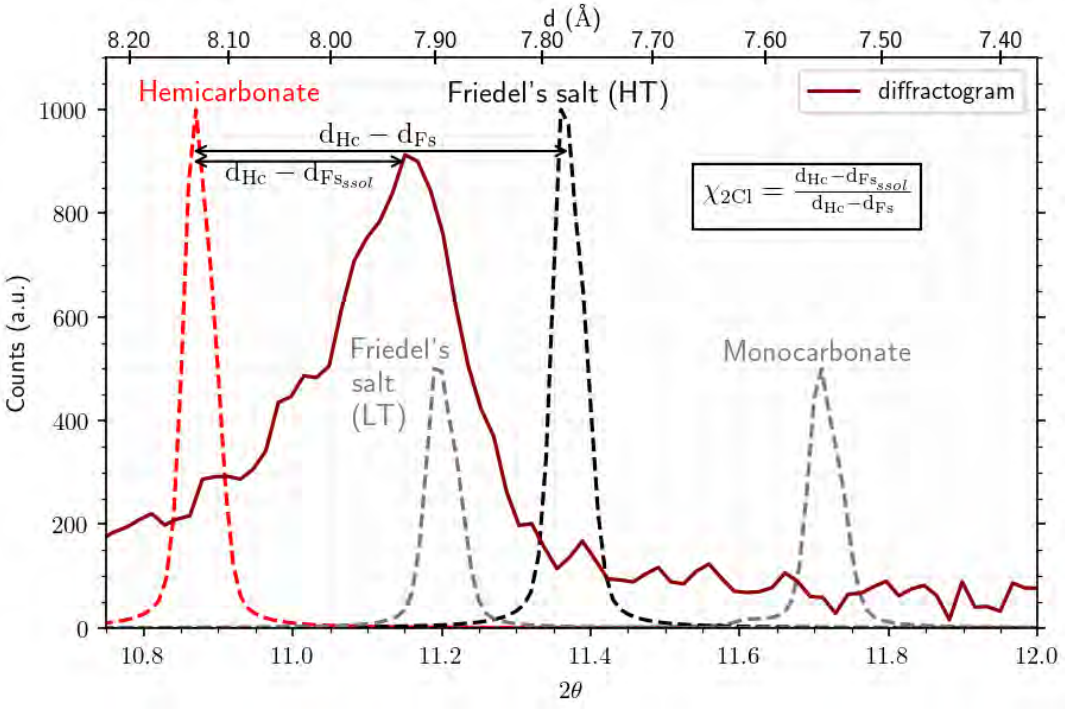

Figure 1: Determination of the chloride content within the Friedel's salt solid solution

The weight fraction of chemically fixed chlorides in AFm was calculated with Eq. (1):

$$\%Cl\,[\%wt] = f_{Fs_{ssol}} \cdot \frac{d_{Hc} - d_{Fs_{ssol}}}{d_{Hc} - d_{Fs}} \cdot \frac{2M_{Cl}}{M_{Fs_{ssol}}} \cdot 100 \quad (1)$$

where $f_{Fs_{ssol}}$ is the mass fraction [-] of the Friedel's salt solid solution obtained from the Rietveld refinement, d_X is the basal spacing of the phase X [Å] and M_{Cl} and $M\ \ Fs_{ssol}$ are the molar mass of Cl and the Friedel's salt solid solution [g/mol].

After the analysis, the slice was dried using the solvent exchange method [12]: isopropanol was changed two times during the first 24 hr, then the sample was removed after 5–7 days of immersion and placed in a desiccator for at least 48 hr. A piece of the sample was then impregnated using a low viscosity epoxy resin. The sample's surface was polished using diamond suspensions (9 µm, 3 µm and 1 µm). The carbon-coated polished section was studied using by scanning electron microscopy on a Zeiss Cross Beam FEI equipped with an Oxford Ultim Max 170 energy-dispersive spectrometer. The EDS analyses were calibrated with standard reference materials ($CaCO_3$ for C, $CaSiO_3$ for O & Ca, Jadeite for Na, MgO for Mg, Al_2O_3 for Al, SiO_2 for Si, $CaSO_4$ for S, KCl for Cl & K, TiO_2 for Ti, and Fe_2O_3 for Fe). Quantitative chemical mappings were averaged from 12 frames at a resolution of 1024 x 768 with a pixel width of 0.0682 nm and a pixel dwell time of 256 µs.

The maps were analyzed with the *edxia* framework [13,14]. Representative points are extracted from the maps using a SLIC segmentation of a Si-Al-Ca composite image. These points are then analyzed using the Cl/Ca vs. Al/Ca ratio plots as described by Sui et al. [9], i.e. the composition of the pure AFm is given by the extrapolation of the mixture line between the C-S-H and the AFm to Al/Ca=0.5.

2.2 Acid-soluble and water-soluble chlorides

The second slice exposed to each host solution was wiped with a paper wetted with the host solution and broken up into two half disks by hand. The protocol described in ASTM C1152 [15] was adapted to determine the amount of acid-soluble chlorides in one half, whereas the amount of water-soluble chlorides in the second half was determined with a protocol adapted from ASTM C1218 [16]. Both protocols are described on a basis of 10 g of concrete, but given the homogeneity and the size of the cement paste specimens used in this study, the weight of each half-slice was only around 2 g. Therefore, every quantity of chemicals employed were scaled accordingly. In ASTM C1218 (water-soluble chlorides), filtration was performed through a PA 0.2 µm paper using a syringe rather than by gravity or by vacuum.

The weight fractions of acid-soluble and water-soluble chlorides were determined using Eq. (2):

$$\%Cl\,[\%wt] = V_{AgNO_3} \cdot c_{AgNO_3} \cdot M_{Cl}/m_{sample} \cdot 100 \quad (2)$$

where V_{AgNO_3} is the volume [L] resulting from titration, c_{AgNO_3} is the concentration of the $AgNO_3$ solution [mol/L] and m_{sample} is the mass of the powder used [g].

3. RESULTS AND DISCUSSION

3.1 Phase assemblage from XRD

Fig. 2 presents the mass fractions of the phases identified from Rietveld refinement in the investigated systems. The comparison of 28d samples and samples after equilibrium shows further hydration during the 8-month exposure in the NaCl solution, especially for the OPC system. As expected, the presence of calcite in both systems results in AFm in the form of carboaluminates instead of monosulfoaluminates [17]. Also, the Portlandite content was reduced during exposure, which can be explained with the leaching into the host solution. Moreover, the additional alumina, carbonate and calcium respectively released by calcined clays, limestone and portlandite in the LC³-50 system led to about twice the amount of carboaluminates compared to the OPC system. After exposure to chloride environment, carboaluminates were mostly transformed into a Friedel's salt solid solution, although non-negligible amount of carboaluminates remained in all systems except the LC³-50 system at a low pH (which also lost all its portlandite).

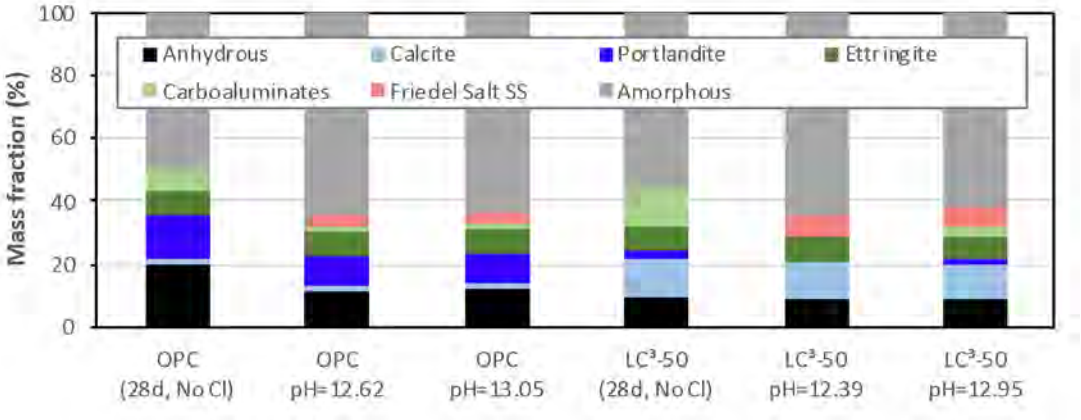

Figure 2: Phase assemblage from XRD coupled with Rietveld analysis

3.2 Chloride chemical binding in Friedel's salt solid solution

In all systems, "pure" Friedel's salt was not found for the NaCl concentrations investigated in this study, but solid solutions (Fs_{ssol}) were rather observed with different relative contents of Friedel's salt (Fs) and Hemicarboaluminate (Hc). The stoichiometry of Fs_{ssol} was investigated both from basal spacing of XRD patterns and from SEM-QEDS mappings (Fig. 3). The stoichiometry of the solid solution is given as the amount of chloride in the AFm phase. It is defined as $\chi 2Cl=2Cl/Ca$. Notably, the two methods provided very coherent estimates of the AFm chloride content for both LC³-50 and OPC systems. This good agreement suggests that XRD basal-spacing analyses can be used to quantify the chemically bound chlorides in Fs solid solutions, allowing sustainable saving of time compared to SEM-QEDS mappings. The initial quantity of AFm in 28-days pastes is insufficient to estimate chloride binding in AFm phases after the exposure to the NaCl solution, given different equilibrium states and AFm chloride contents are reached despite identical protocols.

In addition, the lower pH of the host solution led to higher $\chi 2Cl$, with a greater effect for LC³-50 than for OPC. The lowest value was obtained for the LC³-50 system at high pH. Moreover, $\chi 2Cl$ is higher for OPC at the same pH. XRD phase assemblage showed lower

amounts of carboaluminates in OPC pastes (Fig. 2), meaning there is less AFm to bind, eventually leading to a higher fraction of Friedel's salt per AFm than in LC³-50 pastes. However, the refined porosity in the latter limits significatively the chloride ingress as shown in [3]. Therefore, it cannot be excluded that the chloride transport properties of the porous network play a role in the chemical binding in AFm, by restricting the amount of chlorides in contact with the AFm.

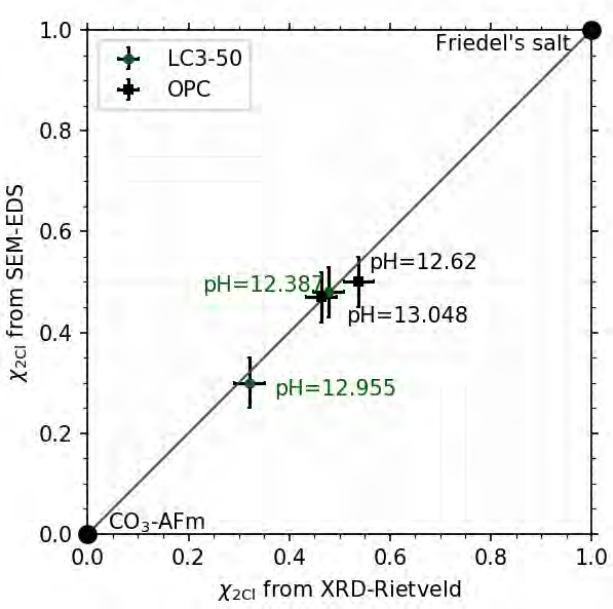

Figure 3: Comparison of the stoichiometry of the Fs + Hc solid solution (χCl) between XRD and SEM-QEDS

3.3 Repartition of total chlorides between free chlorides and bound chlorides

Chloride content weight ratios obtained using Eq. (2) from acid-soluble and water-soluble chloride experiments were plotted in Fig. 4 along with the amount of chemically fixed chlorides in AFm determined with Eq. (1) from Rietveld refinements. Due to the complexity of the protocols, the analyses were performed on only one sample per system, therefore error bars cannot be provided.

LC³-50 systems showed lower water-soluble chloride content compared to OPC systems, which is consistent with previous studies on the chloride fixation in C-A-S-H in limestone-substituted binders [4]. The total amount of chlorides (acid-soluble chlorides) in LC³-50 appeared to be strongly dependent on the pH. Also, it is equal or lower than for OPC, although LC³-50 systems showed the highest content of AFm phases at 28 days. The chlorides bound in AFm represent about 25 % to 45 % of the total fixed chlorides, the highest fraction corresponding to LC³-50 systems and the cumulation of the chloride content in AFm with the water-soluble chlorides correspond to 78 % to 92 % of the total chloride amount, there is therefore in each system remaining chlorides that are not related to the chemical binding in AFm. Despite the fact the standard deviation of both ASTM 1152 and 1218 is negligible (~ 0.04 %), it cannot be excluded that this gap comes from experimental errors of the various experiments. However, these remaining chlorides may be fixed in other hydrates like C-A-S-H, suggesting that they are not water-soluble although being physically fixed. The latter

statement is beyond the scope of the current study, although it is part of ongoing work on characterization of the capacity of C-S-H and C-A-S-H to bind chlorides.

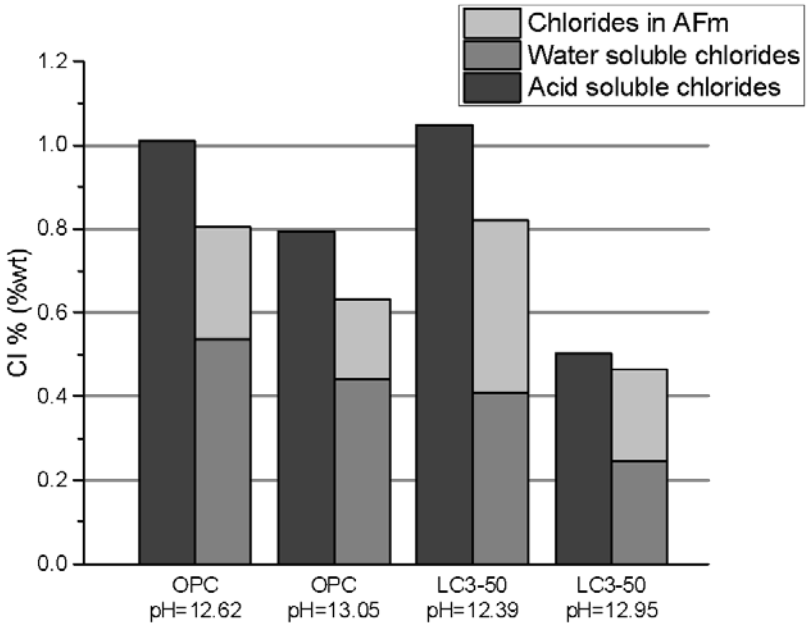

Figure 4: Acid/water-soluble chlorides + chlorides in AFm (XRD) weight fractions

4. CONCLUSIONS

Based on 8-month exposure of LC³-50 and OPC pastes to chlorine solutions, this study showed how chlorides were present in different quantities and bound with different mechanisms depending on the system and pH. Notably, chlorides were chemically bound in solid solutions of Fs and Hc (with variable χCl) and most chlorides occurred as non-bound chlorides (water-soluble chlorides). The main findings of this study can be summarized as follows:

- No direct link was observed between the higher AFm content in LC³-50 pastes at 28 days (compared to OPC) and its capacity to chemically bind chlorides in Friedel's salt;
- The stoichiometry of Friedel's salt solid solutions was determined both from XRD patterns and from SEM-EDS mappings in very concordant estimations;
- The total binding capacity of LC³-50 pastes was found to be equal or lower that of OPC pastes and strongly dependent on the pH of the chloride solution;
- The sum of chemically fixed chlorides in Friedel's salt and water-soluble chlorides was found to be lower than the total chloride content (acid-soluble) for both LC³-50 and OPC systems at both pH, suggesting non-negligible contents of chlorides are bound by other mechanisms (e.g., physical chloride binding).

In order to support and complete the presented characterization approach relying on acid/water-soluble chloride determinations and on the Rietveld refinement method, further ongoing investigation focusses on the physical binding capacity of C-A-S-H.

REFERENCES

[1] Ramezanianpour, A.M. and Hooton, R., D., 'A study on hydration, compressive strength, and porosity of Portland-limestone cement mixes containing SCMs', *Cem. Concr. Compos.***51**(2014) 1-13.

[2] Dhandapani, Y., Sakthivel, T., Santhanam, M., Gettu, R., Pillai, R.G., 'Mechanical properties and durability performance of concretes with Limestone Calcined Clay Cement (LC^3)', *Cem. Concr. Res.***107**(2018) 136-151.

[3] Maraghechi, H., Avet, F., Wong, H., Kamyab, H. and Scrivener K., 'Performance of Limestone Calcined Clay Cement (LC^3) with various kaolinite contents with respect to chloride transport', *Mater. Struct. Constr.***51**(2018).

[4] Sui, S., Georget, F. and Scrivener, K., 'Developing a generic approach to durability: Factors affecting chloride transport in binary and ternary cementitious materials', *Cem. Concr. Res.***124**(2019).

[5] Wilson, W., Gonthier, J.N., Georget, F. and Scrivener, K., 'Tortuosity as a Key Parameter of Chloride Diffusion in LC^3 Systems'. In: Bishnoi, S. (eds.), 3rd International Conference on Calcined Clays for Sustainable Concrete III. New Delhi, India: RILEM Bookseries by Springer, 2019, 13-20, in press.

[6] Beaudoin, J.J., Ramachandran, V.S. and Feldman, R.F., 'Interaction of chloride and C-S-H', *Cem. Concr. Res.***20**(1990) 875-883.

[7] Gbozee, M., Zheng, K., He, F. and Zeng, X., 'The influence of aluminum from metakaolin on chemical binding of chloride ions in hydrated cement pastes', *Appl. Clay Sci.***158**(2018) 186-194.

[8] Balonis, M., Lothenbach, B., Le Saout, G. and Glasser, F.P., 'Impact of chloride on the mineralogy of hydrated Portland cement systems', *Cem. Concr. Res.***40**(7)(2010) 1009-1022.

[9] Sui, S., Wilson, W., Georget, F., Maraghechi, H., Kazemi-Kamyab, H., Sun, W. and Scrivener, K., 'Quantification methods for chloride binding in Portland cement and limestone systems', *Cem. Concr. Res.***125**(2019) 105864.

[10] Antoni, M., Rossen, J., Martirena, F. and Scrivener, K., 'Cement substitution by a combination of metakaolin and limestone', *Cem. Concr. Res.***42**(12)(2012) 1579-1589.

[11] De Weerdt, K., Lothenbach, B. and Geiker, M.R., 'Comparing chloride ingress from seawater and NaCl solution in Portland cement mortar', *Cem. Concr. Res.***115**(2018) 80-89.

[12] Scrivener, K., Snellings, R., and Lothenbach, B., 'A Practical Guide to Microstructural Analysis of Cementitious Materials Edited', 2016.

[13] Georget, F., Wilson, W. and Scrivener, K., 'Comprehensive microstructure phase characterization from quantified SEM-EDS maps in cementitious materials' (In preparation)

[14] Georget, F. and Wilson W. (2019, June 15). edxia. Zenodo. http://doi.org/10.5281/zenodo.3246902

[15] ASTM C1152-12, Standard Test Method for Acid-Soluble Chloride in Mortar and Concrete. West Conshokocken: American Society for Testing and Materials, 2012, 4pages

[16] ASTM C1218-17, Standard Test Method for Water-Soluble Chloride in Mortar and Concrete. West Conshokocken: American Society for Testing and Materials, 2017, 3pages

[17] Lothenbach, B., Le Saout, G., Gallucci, E. and Scrivener, K., 'Influence of limestone on the hydration of Portland cements', *Cem. Concr. Res.***38**(2008) 848–860.

ADVANCES IN CHLORIDE DIFFUSION OF CONCRETE EXPOSED TO MARINE FIELD ENVIRONMENT

Haiwei Zhu (1), Hongfa Yu (1), Haiyan Ma (1), Bo Da (1), Qiquan Mei (1) and Liming Yang (2)

(1) Department of Civil and Airport Engineering, Nanjing University of Aeronautics and Astronautics, China
(2) Guangxi Communications Design Group Co., Ltd., China

Abstract

For elaborating the research significance, goal, content and representative results of the concrete marine field exposure experiments all over the world, we have collected a large number of research literature since 1905. The longest exposure test for concrete has reached 62 years and, most importantly, concrete exposure experiments have made great contributions to the establishment of three classical chloride diffusion models such as DuraCrete model, Life-365 model and ClinConc model. And the comparison with foreign countries shows that concrete marine field exposure sites in China should adhere to long-term research with continuous tracking tests, for purpose of improving the durability evaluation method and life design theory of concrete structures in the harsh marine environment. Moreover, by analyzing the chloride content in the RC components after 42 months of exposure in the submerged zone in South China Sea, the diffusion depth of the chloride exceeds 40 mm, and the distribution of chloride content with diffusion depth is quite consistent with the chloride diffusion model established by Yu.

Keywords: concrete, marine environment, field exposure, durability, chloride diffusion models

1. INTRODUCTION

The durability of concrete structures exposed to a harsh marine field environment is very complex. Common methods to assess the concrete durability include the laboratory durability experiments, field exposure experiments and engineering project tracking tests. Although field exposure experiments are time consuming, they can most truly reflect the performance degradation law of concrete. Therefore, conducting the field exposure experiments is a basic and necessary research method for investigating the long-term performance of concrete structures. Moreover, the field exposure experiments offer effective verification of laboratory results, and are the indispensable basic research work in infrastructure construction. At the beginning of the 20th century, a handful of countries, led by the United States and Japan, first began to conduct concrete marine field exposure experiments to investigate the failure mechanism of concrete structures in different marine environments. In 1970s, the Chinese government began to set up permanent concrete marine field exposure sites in Tianjin Port,

Lianyungang Port and Zhanjiang Port; then, other organizations made sites scale up and distribute more widely. This paper focuses on the research significance, research goal, research content, construction mechanisms and main achievement of the concrete marine field exposure experiments. Furthermore, it introduces the most representative exposure experiments and sites which have made outstanding contribution to the concrete science in the world, as well as the exposure experiments in South China Sea.

1.1 Research significance and goal of concrete marine field exposure experiments

The coupling effects of freezing and thawing, chemical corrosion, dry and wet alternation, wave erosion, steel corrosion and atmospheric carbonation are the main factors that affect the durability of concrete. Because it is difficult to simulate the actual natural environment in laboratory durability tests, the research results of laboratory durability tests have limitations and even deviate from the actual projects. Thus, experiments of concrete exposed to marine field environments are important.

Setting up concrete marine field exposure sites is an important method to study the durability of reinforced concrete structures in marine engineering, which can construct a transitional bridge between the laboratory durability test and practical engineering application. Through the long-term test of the durability of concrete material and structure, the durability parameter that is consistent with the practical environment can be obtained to determine or adjust the relevant parameters in the durability degradation model of concrete and provide the scientific basis to design and construct the engineering of concrete marine structures.

The purposes of concrete marine exposure experiments are as follows: (1) determining the effect of various factors in the marine environment on the durability of concrete materials and structures and exploring the corresponding protection measures; (2) assessing the durability, adaptability and life degradation of concrete prepared with different materials and methods in marine environments; (3) providing basic verification for artificially accelerated simulation test methods in the laboratory.

1.2 Research contents and results of concrete marine field exposure experiments

Concrete marine field exposure experiments usually perform the following research work:

(1) Climatic conditions of concrete marine field exposure sites, such as the ocean tidal flow, seawater spatter, composition and concentration of seawater as the erosive medium, chloride deposition in the atmosphere at different atmospheric altitudes and coastal distances, are collected and monitored. These environmental parameters are the basis for selecting the etch parameters of artificially accelerated tests in the laboratory and are necessary for the durability design of concrete marine engineering.

(2) The long-term evolution of mechanical properties of cement with different mineral compositions in marine environments was investigated to supply a scientific basis to the mineral composition design of cement.

(3) The effects of ordinary concrete, high-performance concrete, fiber-reinforced concrete, prestressed concrete, polymer concrete and reactive powder concrete on the long-term evolution of concrete mechanical properties and chloride diffusion permeability in marine environments were investigated to provide a basis for the material design of concrete in marine construction engineering.

(4) The research on the long-term performance of concrete structures protected by various coatings in marine environments offers a basis for additional protective measures.

(5) Concrete marine field exposure experiments examine the long-term performance degradation of structures of reinforced concrete and prestressed reinforced concrete and the stress corrosion and hydrogen brittleness of prestressed reinforcements to supply the verification basis for the durability design of concrete structures in marine construction engineering.

(6) Artificially accelerated simulation tests in the laboratory and field exposure tests were simultaneously performed to study the correlation of concrete structure durability between the artificially simulated marine environment and the marine field environment, which laid the foundation for further improvement of accelerated tests in the laboratory.

(7) Researches on the chloride diffusion behavior in concrete during the long-term exposure in marine environments and the correlation among parameters (surface chloride ion content, chloride diffusion coefficient, raw material, mix ratio, exposure zone and duration) have a very important role to perfect and verify the theory and life prediction model of concrete based on Fick's second diffusion law, such as the DuraCrete model [1] verified by the long-time exposure experiments of concrete in 10 field sites in Europe, ACI Life-365 model [2] verified by the long-time exposure experiments of concrete in Treat Island, the Unite States, and in Thames Estuary, Britain, and ClinConc model [3, 4] verified by the longtime exposure experiments of concrete in Träslövsläge, Sweden.

2. CONCRETE MARINE FIELD EXPOSURE SITES IN THE WORLD

Figure 1: Distribution of concrete marine field exposure sites in the world

Fig.1 shows the geographical distribution of 50 concrete marine field exposure sites reported in the world, and details of these sites are listed in Table 1. Yu et al. [5] investigated the temporal change in chloride diffusion coefficient of concrete collected from 2207 marine field exposure experiments. The longest concrete marine exposure experiment has been

conducted for more than 60 years. And exposure experiments investigated the durability of materials and structures, such as mineral admixtures, concrete strength grades, admixtures, reinforcement methods and outer coatings, as well as the deterioration law of concrete structures exposed to the harsh marine field environments.

Table 1: Details of concrete marine field exposure sites represented by the serial numbers in Fig.1

Number	Continent	Country	Exposure site	Period	Longest exposure /year	Object	Exposure zone	Local climate	Annual air temperature / ℃
1	Asia	JAP	Sakata Port [6]	1980-2000	20	RC beams & columns	AT & SU	TEMO	12
2	Asia	JAP	Niigata [7-9]	1999-2004	5	RC beams	AT	SUMO	17
3	Asia	JAP	Izu Peninsula [10-13]	1983-2007	15	RC structure & beams	AT & TI	SUMO	16
4	Asia	JAP	Miura Peninsula [14-22]	1983-2019	30	RC cylinders	AT, TI & SU	SUMO	16
5	Asia	JAP	Shimizu Harbor [23-25]	1984-1996	10	RC beams & columns	AT, SP & SU	SUMO	15
6	Asia	JAP	Nagoya [26]	1982-1987	5	RC prisms	AT	SUMO	16
7	Asia	JAP	Ishikawa [27]	1989-1996	7	Cubes	TI	SUMO	16
8	Asia	JAP	Kagoshima [6, 28]	1980-2000	20	RC beams & columns	AT & SU	SUMO	17
9	Asia	JAP	Okinawa [9, 29-38]	1981-2005	10	Cylinders & RC structure	AT	SUMO	23
10	Asia	JAP	Naha Port [39, 40]	1988-2004	15	RC beams	SP	SUMO	20
11	Asia	THA	Chonburi [41-49]	2002-2012	10	RC cubes	TI	TRMO	30
12	Asia	IND	Tuticorin [50]	1987-2017	10	RC cubes	AT, SP & SU	TRMO	30
13	Asia	IRA	Bandar Abbas [51-56]	2005-2010	7	Prisms	TI	TECO	27
14	Asia	IRA	Qeshm Island [57-59]	2012-2016	4	Prisms	AT	TECO	26
15	Asia	KSA	Al-Jubail [60]	1999-2003	4	Cubes & RC walls	AT	TRDE	25
16	Asia	KSA	Khobar [61]	2003-2013	10	RC blocks	SP, TI & SU	TRDE	23
17	Asia	KUW	Kuwait [62, 63]	1996-2003	7	Cubes, RC beams & slabs	AT	TRDE	26
18	Europe	NOR	Trondheim [64]	1983-2004	21	Blocks	TI	TEMA	5
19	Europe	SWE	Träslövsläge [65-70]	1992-2015	21	RC slabs	AT, SP & SU	TEMA	8
20	Europe	DEN	Rodbyhavn Port [71]	2010-2020	10	RC blocks	SP & SU	TEMA	6
21	Europe	GER	Baltic Sea coast [72]	1991-2012	21	RC slabs	SP, TI & SU	TEMA	6
22	Europe	GER	North Sea coast [73]	1991-2012	21	RC slabs	SP, TI & SU	TEMA	9
23	Europe	NED	North Sea coast [73]	1976-2002	16	RC prisms	SU	TEMA	10
24	Europe	FRA	Rance's dam [74]	1960-1976	16	RC beams	TI	TEMA	11
25	Europe	FRA	Sainte Anne de Portzic [74]	1976-2000	24	RC beams	TI	TEMA	11
26	Europe	GBR	Dornoch Firth [75, 76]	1997-2015	18	Pier-stems	AT, SP & TI	TEMA	9
27	Europe	GBR	Thames Estuary [77]	1988-1994	10	RC prisms	TI	TEMA	11
28	Europe	GBR	Folkestone [78, 79]	1987-1995	8	RC blocks	SP	TEMA	12
29	Europe	POR	Setubal Peninsula [80, 81]	1992-1997	4	Panels	AT, SP & TI	METE	17
30	Europe	POR	Cascais Bay [82]	2015-2018	3	RC slabs	AT, SP, TI & SU	METE	16
31	Europe	CRO	Krk Bridge [83]	2008-2010	3	RC columns	AT, SP & SU	TECO	13

32	Europe	GRE	Santorin Island [84]	1991-1994	3	RC prisms	SU	METE	20
33	Europe	ISL	Hvalfjörður	2000-2001	1	Cubes	SU	TEMA	4
34	North America	USA	Treat Island [85-90]	1936-2020	30	Blocks, Slabs, Columns & RC Prisms	TI	TECO	7
35	North America	USA	Los Angeles Harbor	1905-1967	62	Blocks	TI	METE	18
36	North America	USA	ST. Augustine [85]	1940-1970	30	Columns & Prisms	TI	SUMO	23
37	Oceania	USA	Honolulu Harbor [91-95]	2004-2012	7	RC panels	TI	TRMO	26
38	North America	MEX	Progreso Port [96]	1993-1997	4	Cylinders	AT	TRSA	27
39	South America	BRA	João Pessoa [97-100]	2006-2014	4	RC cubes	AT	TRSA	25
40	Oceania	AUS	Fremantle [101]	1982-2001	19	RC beams	SP	TRSA	15
41	Asia	CHN	Jinzhou Port [102]	1990-2020	5	Cubes	AT, SP, TI & SU	TEMO	8
42	Asia	CHN	Dagang District [103-105]	1992-2009	17	RC columns	AT	TEMO	12
43	Asia	CHN	Tianjin Port [106-108]	1964-2020	20	RC prisms	SP & TI	TEMO	12
44	Asia	CHN	Xiaomai Island [109, 110]	1983-2020	2	RC prisms & structure	AT, SP, TI & SU	TEMO	13
45	Asia	CHN	Lianyun Port [107]	1961-2003	20	Prisms	SP & TI	SUMO	14
46	Asia	CHN	Shanghai Port [108, 111]	1973-1983	10	Prisms	SP & TI	SUMO	17
47	Asia	CHN	Zhanjiang Port [107, 108, 112-116]	1961-2020	20	RC prisms	AT, SP, TI & SU	SUMO	23
48	Asia	CHN	Basuo Port [107, 117]	1992-2006	4	RC prisms	SP	TRMO	25
49	Asia	CHN	Xisha Islands [118, 119]	2013-2020	6	Prisms, RC beams & columns	AT, SP, TI & SU	TRMO	26
50	Asia	CHN	Nansha Islands	2016-2020	4	Prisms & RC beams	AT, SP, TI & SU	TRMO	27

Note: AT, SP, TI and SU mean the atmospheric zone, splash zone, tidal zone and underwater zone, respectively. TEMO, SUMO, TRMO, TECO, TRDE, TEMA, METE, TRSA mean the temperate monsoon climate, subtropical monsoon climate, tropical monsoon climate, temperate continental climate, tropical desert climate, temperate marine climate, mediterranean climate, tropical savanna climate, respectively.

Fig.2(a) shows the geography distribution of the 50 concrete marine field exposure sites in five continents of the world. It can be seen that the sites are mainly distributed in Asia and Europe, accounting for 86% of the total number, and that a few are distributed in North America, South America and Oceania. However, the two remaining continents on earth, Antarctica and Africa, have not yet reported marine field exposure experiments of concrete. Due to the wide geographical distribution of concrete marine field exposure sites, the climate of sites is also very diverse, including the tropical monsoon climate, the tropical savanna climate, the tropical desert climate, the subtropical monsoon climate, the temperate monsoon climate, the temperate continental climate, the temperate marine climate and the Mediterranean climate, as showed in Fig.2(b), and basically covers all the climates in the coastal areas of the earth.

Fig.2(c) shows how the number of concrete marine field exposure sites varies with the timeline since 1905. It can be seen that the number of sites increased slowly from 1905 to 1980, and peaked at 26 in 2000, but then began to decline rapidly. Furthermore, the statistical results of the longest marine field exposure experiments at each site are shown in Fig.2(d). It can be seen that the duration decreases with the extension of exposure time and mainly focuses on less than 10 years.

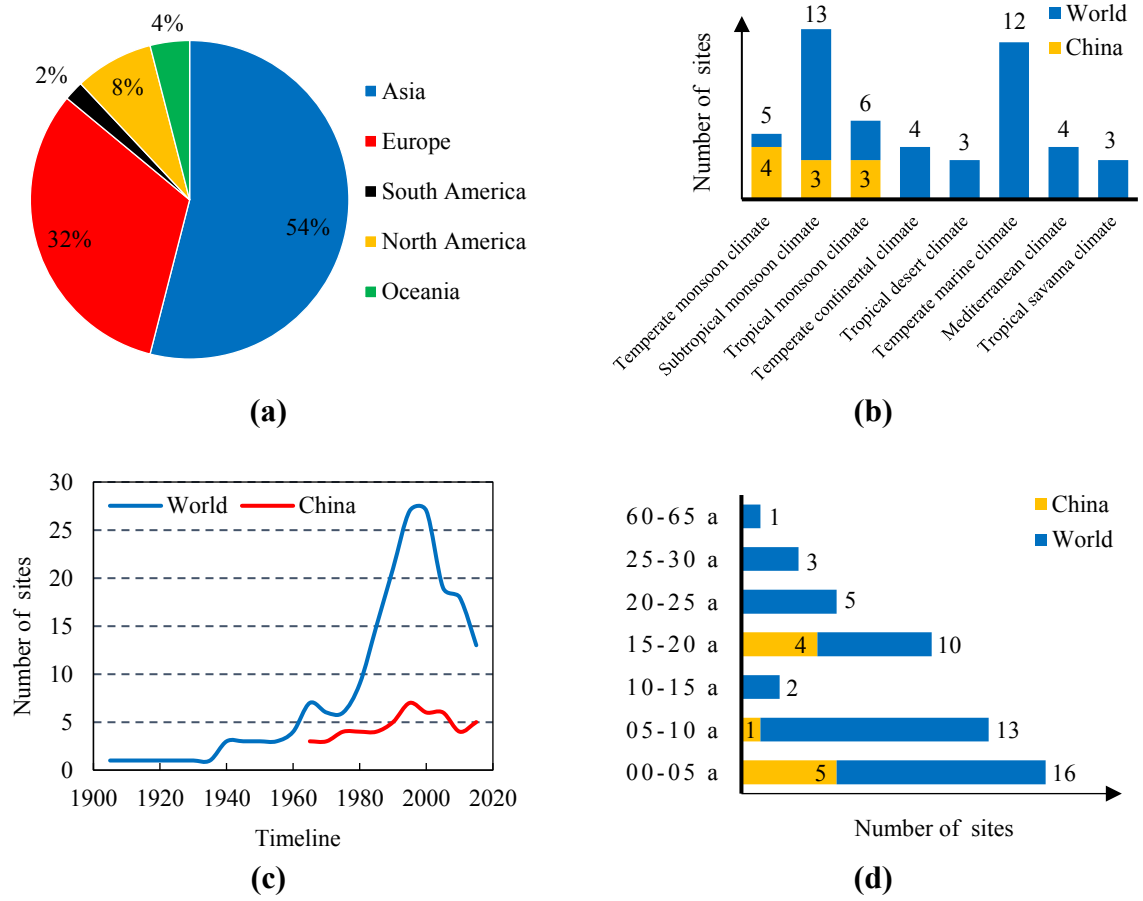

Figure 2: Statistical analysis of the concrete marine field exposure experiments

3. MARINE FIELD EXPOSURE EXPERIMENTS OF CONCRETE IN THE WORLD

3.1 Typical marine field exposure experiments of concrete in Japan

In 1984, Ryukyu University built a full-scale reinforced concrete structure at the atmosphere zone on the coast of East China Sea in Okinawa, as showed in Fig.3. By continuously testing the corrosion potential (E_{corr}) and polarization resistance (R_p) of the RC structure, the corrosion area of reinforcement and the diffusion distribution of chloride from atmosphere in concrete for 10 years, the researchers established a corrosion evaluation method of RC structure, and mastered the deterioration law of RC structures caused by chloride corrosion [37]. Therefore, the influence of chloride corrosion on the mechanical properties of RC structures is also investigated, and it is found that corrosion will lead to the deterioration of seismic performance of RC structures, such as the reduction of fracture strength and fracture strain [38]. In addition, it is also proved that the application of acrylic rubber waterproof material on the concrete

surface has a good blocking effect on the diffusion of chloride from the atmosphere in the concrete [36].

Figure 3: RC structure exposed in Okinawa [35]

Figure 4: Concrete cubes exposed in the Gulf of Thailand [47]

In 1983, Japan Port and Airport Research Institute built a tidal pool of seawater circulation on the coast of the Pacific Ocean in Miura Peninsula. The influence of joint treatments on reinforcement corrosion in concrete structure in marine environment was investigated, and it was found that brushing of laitance to the joints can only reduce the corrosion rate of the reinforcement in the early stage in the tidal zone, and the corrosion rate of reinforcement could be reduced by 10 % in the atmosphere zone, but there was no difference in the influence of joint treatments on reinforcement corrosion in the submerged zone [22]. By testing the carbonation depth, chloride diffusion and electrochemical characteristic values of the reinforcement and analyzing the mineral composition, microstructure, reinforcement-concrete interface of the RC cylinders made with ordinary Portland cement, high early strength Portland cement, slag cement and alumina cement, after 30 years exposure in the tidal zone, it was found that external microstructure of slag cement concrete was good and could most effectively improve the durability of concrete structures in the harsh marine environment [18, 19].

3.2 Typical marine field exposure experiments of concrete in Thailand

Based on chloride diffusion test, compressive strength test and corrosion status analysis of the RC cubes exposed for 10 years in the tidal zone in the gulf of Thailand (Fig.4), it is found that the concrete with water cement ratio of 0.45 and fly ash content of 15-35 % (mass ratio) shows excellent durability performance in the marine environment [50]. By water-soluble tracking the free chloride distribution of concrete cubes exposed in the tidal zone as long as 10 years, the relationship between the threshold diffusion depth of chloride and the initial corrosion time was determined, and it was found that chloride threshold diffusion depth in the five years before at a higher rate of growth, after growth rate drop, and high content fly ash greatly prolongs the initial corrosion of concrete [48].

3.3 Typical marine field exposure experiments of concrete in Britain

In 2015, S V Nanukuttan [75] established a method to predict the long-term performance of concrete in the marine environment, namely the the relationship between the steady state migration coefficient (D_{ssm}) and the Wenner four-probe resistivity ($1000/\rho_{Wenner}$):

$$D_{ssm} = \frac{260}{\rho_{Wenner}} \quad (1)$$

Where ρ_{Wenner} is in ohm·m and D_{ssm} is in m^2/s (without the multiplier 10^{-12}).

As well as the relationship between the migration coefficient ($D_{in\ situ}$) and the Wenner four-probe resistivity ($1000/\rho_{Wenner}$):

$$D_{in\ situ} = \frac{160}{\rho_{Wenner}} \quad (2)$$

Where ρ_{Wenner} is in ohm·m and $D_{in\ situ}$ is in m^2/s (without the multiplier 10^{-12}).

And the model was verified with the chloride diffusion testing data from the concrete pier-stems exposed for 18 years on the coast of the North Sea, as shown in Fig.5.

Figure 5: Concrete pier-stems exposed in Dornoch Firth [75]

Figure 6: Concrete prisms and RC components exposed on Treat Island [87]

3.4 Typical marine field exposure experiments of concrete in the Unite State

The famous field exposure site in Treat Island was set up in 1936 to study concrete durability in the marine environment, as shown in Fig.6. Considering the unique geographical and climatic condition there, concrete specimens exposed to the tidal zone experience approximately 100 freeze-thaw cycles per year. Through the chloride test on the concrete prisms exposed in the tidal zone on Treat Island for 25 years, it is found that the chloride diffusion resistance of the lightweight concrete can be significantly improved by adding silica fume and fly ash [87], and the chloride diffusion coefficient can be significantly reduced by adding slag [88]. In addition, it is also found that the *W*/*C*, kinds and dosage of mineral admixtures have important influence on the durability of concrete in the marine environment, and the chloride diffusion resistance of concrete increases with the increase of mineral admixture content. However, under the freezing condition, mineral admixtures with high content may easily cause concrete surface scaling [90].

In 2001, ACI TC-365 [2] established the empirical model of chloride diffusion which utilizes Fick's second law of time-dependent diffusion as the transport function with the total chloride content (*C*) as the driving force:

$$\frac{\partial C}{\partial t} = D(t)\frac{\partial^2 C}{\partial x^2} \tag{3}$$

$$D(t) = D_{\text{ref}}\left(\frac{t_{\text{ref}}}{t}\right)^m \tag{4}$$

Where D_{ref} is the apparent diffusion coefficient at the reference time of exposure t_{ref} ; m is a constant. Then, in 2002, the field exposure experiments in Honolulu Harbor was conducted, as shown in Fig.7, where 25 reinforced concrete slabs were placed in the tidal zone. And the feasibility of ACT Life-365 model was verified by chlorine test of the RC slabs exposed in tidal zone for 7 years [95].

Figure 7: RC slabs exposed in Honolulu Harbor [92]

Figure 8: Concrete prisms and RC slabs exposed in Träslövsläge [66]

3.5 Typical marine field exposure experiments of concrete in Sweden

The Träslövsläge marine field site, located on the west coast of Sweden, was found in 1992, as shown in Fig.8. The RC slabs were vertically mounted on the side of three pontoons and carry more than 50 concrete specimens with various cement varieties and mineral admixtures. And in the middle of 1990's, based on the results of chloride test of the RC slabs and concrete specimens exposed for 10 years, the ClinConc model was first developed by Tang [3, 4]. ClinConc model consists of two main procedures: (I) Simulation of free chloride penetration through the solution in concrete using a genuine flux equation based on the principle of Fick's law with the chloride concentration as the driving potential; (II) Calculation of the distribution of the total chloride content in concrete using the mass balance equation combined with non-linear chloride binding. The free chloride concentration in the concrete at depth, x, is determined using the following equation:

$$\frac{c - c_{\text{i}}}{c_{\text{s}} - c_{\text{i}}} = 1 - erf\left\{\frac{x}{2\sqrt{\frac{\xi_{\text{D}} D_{\text{6m}}}{1-n}}\cdot\left(\frac{t_{\text{6m}}}{t}\right)^n \cdot\left[\left(1+\frac{t_{\text{ex}}}{t}\right)^{1-n} - \left(\frac{t_{\text{ex}}}{t}\right)^{1-n}\right]\cdot t}\right\} \tag{5}$$

Where c, c_{i} and c_{s} are the concentration of free chloride in the pore solution at depth x, at the

surface of the concrete and initially in the concrete, respectively, D_{6m} = the diffusion coefficient measured by the rapid chloride migration test, at the age of t_{6m}, ξ_D is the factor bridging the laboratory measured D_{6m} to the initial apparent diffusion coefficient for the actual exposure environment, n is the age factor accounting for the diffusivity decrease with age, t_{ex} is the age of concrete at the start of exposure and t is the duration of the exposure.

3.6 Typical marine field exposure experiments of concrete in China

In the 1950s, the Chinese government first built three permanent concrete marine field exposure sites in Lianyun Port in east China, Tianjin Port in north China and Zhanjiang Port in south China, but the relevant research results about concrete exposure in the sites are very few. Among them, the most significant research achievement is that Wang, et al. [107] established a durability life prediction model for marine concrete structures by conducting chloride tests on concrete specimens exposed for about 20 years and successfully applied it in the durability design of Hongkong-Zhuhai-Macao Bridge. As shown in Fig.3, the climate distribution of concrete marine field exposure sites in China includes three major typical climates of coastal areas, namely, temperate monsoon climate, subtropical monsoon climate and tropical monsoon climate. However, it can be seen from Fig.2(c) and Fig.2(d) that the total number of field exposure sites in China is relatively small and the exposure time is relatively short.

In 1983, Qingdao Institute of Technology and Qingdao Institute of Marine Corrosion [28-29] placed the concrete specimens in Xiaomai Island in order to investigate the chloride diffusion rule of concrete in different zones and within different durations in a harsh marine environment. [109]. Then, in 2005, a 12.8-meter RC bridge coated with strain hardening cementitious compounds and waterproof materials was built, and dozens of 2.5-meter RC beams with bending loads were exposed to investigate the chloride distribution and steel corrosion, as shown in Fig.9(a). Since 2009, the strength grades of C30, C50 and C80 concrete specimens with special specimens used for the submarine tunnel in Jiaozhou bay have been exposed there. Meanwhile, a three-story frame structure of reinforced concrete built by Zhejiang University and Tongji University was exposed to the field site, as shown in Fig.9(b).

(a) **(b)**

Figure 9: RC structures, RC beams and concrete prisms exposed on Xiaomai Island

3.7 Marine field exposure experiments of concrete conducted by this research group

With the National Key Basic Research Development Plan of China as the guide, the concrete marine field exposure sites in the Xisha Islands and Nansha Islands in South China Sea, were established in 2013 and 2016. In total, 200 RC beams and columns with 600 concrete specimens (strength grades of C30, C50 and C80) were exposed to the submerged zone, tidal zone, splash zone and atmosphere zone to examine the deterioration law of RC and chloride diffusion in the harsh environment of the South China Sea, as shown in Fig.10.

Figure 10: RC columns, RC beams and concrete prisms exposed on the island

Some concrete specimens and components exposed for 42 months were retrieved, as shown in Fig.11, and the concrete durability and structural properties were tested. The RC components, which were used for the chloride diffusion testing, adopted P·O 42.5 cement with a specific surface area of 360 m^2/kg, river sand with a fineness modulus of 2.55, stone with continuous grading of 5-20 mm, ground granulated blast furnace slag (GGBFS) with a specific surface area of 450 m^2/kg, fly ash (FA) with a specific surface area of 350 m^2/kg, the carboxylic acid high performance water reducing agent with a solid content of 20 %, and tap water. The mix ratio and basic mechanical properties of concrete are shown in Table 2.

Table 2: Mix ratio and basic mechanical properties of concrete

Compressive strength Grade	Materials/kg·m^{-3}							*W/B*	Slump /mm	28d Standard compressive strength /MPa
	Cement	GGBFS	FA	Water	Sand	Stone	Water reducing agent			
C50	342	157	0	156.1	675	1122	9.98	0.32	175	75.4
C80	408	157	79	141.6	683	1025	16.10	0.23	190	94.9

RC beams had a rectangular cross section with a size of 1500 mm×150 mm×200 mm. The longitudinal tensile reinforcement was two HRB500 ribbed bars with a diameter of 16 mm, and the standing reinforcement was two HPB235 plain bars with a diameter of 12 mm, and the hoop was HPB235 plain bars with a diameter of 10 mm and a spacing of 100 mm. The thickness of concrete cover was 25 mm.

RC columns had a rectangular cross section with size of 1500 mm×200 mm×240 mm. According to the symmetric reinforcement, the tensile reinforcement and the standing

reinforcement were both HRB335 ribbed bars with a diameter of 20 mm, and the hoop was HPB235 plain bars with a diameter of 6 mm and a spacing of 100 mm (encryption zone) and 200 mm (non-encryption zone). The thickness of concrete cover was 25 mm.

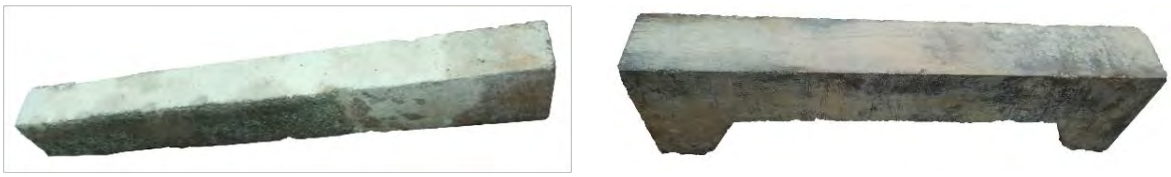

(a) **(b)**

Figure 11: Appearance of RC components after 42 months exposure

In 2002, Yu et al. [120-122] established a new diffusion equation based on Fick's second law of diffusion and deduced the effect of chloride diffusion, the time dependence of chloride ion diffusion coefficient and the effect of micro-defects of concrete structure:

$$\frac{\partial c_f}{\partial t} = \frac{KD_o t_o^m}{1+R} \cdot t^{-m} \cdot \frac{\partial^2 c_f}{\partial x^2} \tag{6}$$

The initial condition for the above equation is $c_f = c_o$ for t=0, x>0 and $c_f = c_s$ for t>0, x=0 for the boundary conditions. Under this initial and boundary conditions, the theoretical model for obtaining concrete chloride diffusion is as follows:

$$c_f = c_o + (c_s - c_o)\left[1 - erf\frac{x}{2\sqrt{\frac{KD_o t_o^m}{(1+R)(1-m)} \cdot t^{1-m}}}\right] \tag{7}$$

Where c_o is the initial chloride concentration in the concrete; c_s is the chloride ion concentration on the exposed surface of the concrete, which is equal to the chloride concentration in the exposed environment medium; *erf* is the error function.

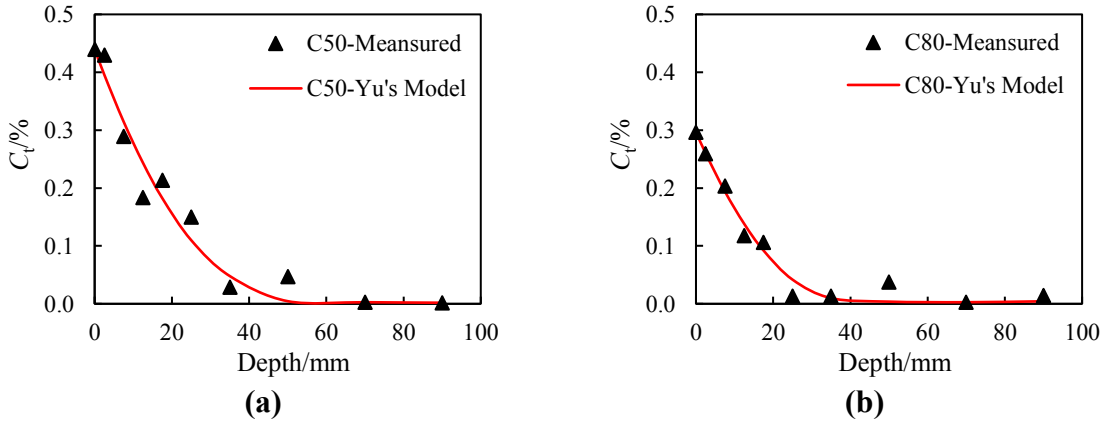

(a) **(b)**

Figure 12: Comparison between predicted by the Yu's model and measured profiles

Fig.12 shows the total chloride profiles determined from retrieved RC columns after 42 months exposure with the predicted profiles from the Yu's model. And the test data is quite consistent with Yu's model, indicating that the model has good applicability and high accuracy.

4. CONCLUSIONS

Research results of concrete marine field experiments overseas have comprehensively covered the raw materials such as the cement varieties, admixtures, mineral admixtures, concrete coatings and steel coatings, mix ratios and structures. The studies accumulated a mass of valuable long-term tracking experimental data to build reliable concrete life analysis models, which offer theoretical and technical support for marine construction projects. Because the running time of Chinese marine field exposure experiments is short and the research content is not systematic, reasonable planning and scientific distribution should be performed. In addition, studies on the multi-layered concrete specimen-component-structure and additional protection technology should adhere to long-term tracking to obtain continuity data on chloride diffusion, electrochemical corrosion, and steel corrosion, among other factors. Hence, the test database of field sites will primarily improve the durability assessment method of marine concrete structures and the life design theory system, which provide the selection basis of new concrete materials and life analysis software of concrete structures for Chinese marine development projects.

After exposure for 42 months in the submerged zone in the South China Sea, the diffusion depth of chloride in C50 and C80 RC components exceeds 40 mm and the chloride content gradually decreases with the increasing diffusion depth. Discriminately, C50 has a larger diffusion depth and a higher chloride content than C80. In addition, by comparing the distribution of chloride ion content in C50 and C80 with Yu's model, it is found that the degree of agreement between the two is quite high, which proves the feasibility of this model.

ACKNOWLEDGEMENTS

The authors gratefully acknowledge the financial support from the National Natural Science Foundation of China No. 11832013, No. 51878350 and No. 51678304.

REFERENCES

[1] Engelund, S., Edvardsen, C. and Mohr, L. 'General guidelines for durability design and redesign'. *European Union-Brite EuRamIII*.(2)(2000)90-95.

[2] Thomas, M.D.A. and Bentz, D. 'Life-365: computer program for predicting the service life and life-cycle costs of reinforced concrete structures exposed to chlorides', Fairfax: Silica Fume Association, 2001.

[3] Tang, L. and Nilsson, L.O. 'A numerical method for prediction of chloride penetration into concrete structure//The Modelling of Microstructure and its Potential for studying transport properties and durability', Dordrecht: Kluwer Academic Publisher, 1994, 539-552.

[4] Tang, L. 'Chloride transport in concrete - Measurement and prediction'. Gothenburg: Chalmers University of Technology, 1996.

[5] Yu, H., Tan, Y. and Feng, T. 'Study of Temporal Change in Chloride Diffusion Coefficient of Concrete'. *ACI Materials Journal*.(116)(2019)103-112.

[6] Hiroko, W., Hidetoshi, O., Hiroshi, Y., *et al*. 'Long-term behavior of concrete and reinforcement in concrete under marine environment'. *Concrete Engineering Annual Proceedings*.(22)(2000)91-96.

[7] Ryo, T., Manabu, F., Hirotaka, K., *et al*. 'Resistance to chloride permeation of HPC'. *Concrete Engineering Annual Proceedings*.(23)(2001)517-522.
[8] Hideaki, T., Hiroshi, W., Hirotaka. K., *et al*. 'Evaluation of chloride permeability and reinforcement corrosion of HPC after exposure'. *Concrete Engineering Annual Proceedings*.(6)(2004)826-830.
[9] Hidetoshi, N., Hiroshi, W., Hirohisa, K., *et al*. 'Chloride permeability and reinforcement corrosion of concrete with cracks'. *Concrete Engineering Annual Proceedings*.(30)(2008)735-740.
[10] Toshio, H. and Kento, U. 'Permeation of chloride into carbonated concrete exposed to marine environment'. *Concrete Engineering Annual Proceedings*.(17)(1995)847-852.
[11] Toshio, H., Kento, U. and Kazuyoshi, K. 'Durability and anticorrosion effect of RC beams using epoxy resin-coated reinforcement and galvanized reinforcement exposed for 15 years under marine environment'. *Concrete Engineering Annual Proceedings*.(19)(1997)883-888.
[12] Osamu, K., Masanori, I., Hiroyuki, K., *et al*. 'Effect of chloride migration on reinforcement corrosion of repaired concrete structure'. *Concrete Engineering Annual Proceedings*.(27)(2005)955-960.
[13] Takayuki, S., Koji, N., Tomio, H., *et al*. 'Chloride diffusion of repaired concrete under marine environment'. *Concrete Engineering Annual Proceedings*.(29)(2007)1113-1118.
[14] Mohammed, T.U., Yamaji, T. and Hamada, H. 'Chloride diffusion, microstructure, and mineralogy of concrete after 15 years of exposure in tidal environment'. *ACI Materials Journal*.(99)(2002)256-263.
[15] Toru, Y., Mohammed, T.U., Toshiyuki, A., *et al*. 'Effect of exposure environments and type of cements on concrete durability under marine concrete'. *Concrete Engineering Annual Proceedings*.(23)(2001)577-582.
[16] Mohammed, T.U. and Hamada, H. 'Durability of concrete made with different water-reducing chemical admixtures in tidal environment'. *ACI Materials Journal*.(100)(2003)194-202.
[17] Mohammed, T.U., Hamada, H. and Yamaji, T. 'Marine durability of 30-year old concrete made with different cements'. *Journal of Advanced Concrete Technology*.(1)(2003)63-75.
[18] Mohammed, T.U., Hamada, H. and Yamaji, T. 'Concrete after 30 years of exposure - part I: mineralogy, microstructures, and interfaces'. *ACI Materials Journal*.(101)(2004)3-12.
[19] Mohammed, T.U., Hamada, H. and Yamaji, T. 'Concrete after 30 years of exposure - part II: chloride ingress and corrosion of steel bars'. *ACI Materials Journal*.(101)(2004)13-18.
[20] Mohammed, T.U., Hamada, H. and Yamaji, T. 'Performance of seawater-mixed concrete in the tidal environment'. *Cement and Concrete Research*.(34)(2004)593-601.
[21] Yoshikazu, A., Hidenori. S., Nobuaki, O., *et al*. 'Diffusion coefficient of chloride infiltrated from the side of cylindrical specimens'. *Concrete Engineering Annual Proceedings*.(27)(2005)613-618.
[22] Ukishima, F., Otsuki, N., Nishida, T., *et al*. 'Influence of joint treatment on corrosion of steel bars in concrete exposed in marine environment for 25-years'. In: The 30th Conference on Our World in Concrete and Structures. Singapore: CI-Premier PTE LTD, 2005.
[23] Keizo, S., Masanori, T. and Shigeyuki, T. 'Chloride penetration and corrosion of concrete under marine environment'. *Concrete Engineering Annual Proceedings*.(10)(1988)487-492.
[24] Akinori, T., Shinzo, S. and Shigeyuki, T. 'Aging of RC exposed for 10 years under marine environment'. *Concrete Engineering Annual Proceedings*.(18)(1996)753-758.
[25] Keizo, S., Masanori, T., Shigeyuki, T., *et al*. 'Properties of light-weight aggregate concrete exposed for 10 years under marine environment'. *Concrete Engineering Annual Proceedings*.(19)(1997)343-348.
[26] Shin, T., Kentaro, N. and Takeshi, M. 'Effect of acrylic rubber coating material on preventing chloride corrosion to concrete'. *Concrete Engineering Annual Proceedings*.(9)(1987)411-416.

[27] Teruhiko, K., Kazuyuki, T., Miki, K., *et al*. 'Chloride penetration into concrete exposed for a long time under marine environment'. *Concrete Engineering Annual Proceedings*.(18)(1996)957-962.
[28] Yamaguchi, T., Takewaka, K. and Mori, S. 'Durability monitoring on RC structures using "Shirasu concrete" in marine environment', London: Taylor and Francis Group, 2010, 209-216.
[29] Takeshi, O., Shin, T. and Kentaro, N. 'Performance of RC structures after exposure'. *Concrete under Severe Conditions*.(8)(1986)193-196.
[30] Takeshi, O., Shin, T. and Kentaro, N. 'Performance of RC structures after exposure'. *Concrete Engineering Annual Proceedings*.(10)(1988)547-552.
[31] Takeshi, O. and Shin, T. 'Corrosion of reinforcement in concrete due to chloride diffusion'. *Concrete Engineering Annual Proceedings*.(11)(1989)569-574.
[32] Takeshi, O., Hitoshi, S. and Tadahiro, K. 'Corrosion evaluation of RC structures damaged by chloride diffusion'. *Concrete Engineering Annual Proceedings*.(14)(1992)649-654.
[33] Takeshi, O. and Shin, T. 'Exposure experiment of RC structure under marine environment (7 years exposure)'. *Concrete Engineering Annual Proceedings*.(14)(1992)855-890.
[34] Takeshi, O., Hiroshi, I., Tadahiro, K., *et al*. 'Deterioration process of RC structure under marine environment'. *Concrete Engineering Annual Proceedings*.(16)(1994)947-952.
[35] Shin, T., Takeshi, O., Nobuhiro, G., *et al*. 'Deterioration evaluation of RC structures exposed to marine environment'. *Concrete Engineering Annual Proceedings*.(16)(1994)953-958.
[36] Takeshi, O., Yoshitomo, Y. and Shin, T. 'Long-term exposure test of full-scale RC structure under marine severe environment'. *Concrete Engineering Annual Proceedings*.(17)(1995)961-966.
[37] Shin, T., Yoshitomo, Y. and Takeshi, O. 'Accumulation of chloride in concrete under marine environment'. *Concrete Engineering Annual Proceedings*.(18)(1996)939-944.
[38] Shigeru, U., Tetsuo, Y., Hiroka, N., *et al*. 'Seismic performance of chloride-corroded RC columns naturally exposed on the coast of Okinawa'. *Concrete Engineering Annual Proceedings*.(27)(2005)1483-1488.
[39] Toru, Y., Kenichi, K. and Hidenori, K. 'Effects of surface coatings on chloride corrosion in concrete exposed to marine environment for 15 years'. *Concrete Engineering Annual Proceedings*.(25)(2003)833-838.
[40] Toru, Y., Kenichi, K. and Hidenori, K. 'Relationship between oxygen diffusion properties and renforcement corrosion in concrete exposed to marine environment'. *Concrete Engineering Annual Proceedings*.(26)(2004)813-818.
[41] Chalee, W., Teekavanit, M., Kiattikomol, K., *et al*. 'Effect of w/c ratio on covering depth of fly ash concrete in marine environment'. *Construction and Building Materials*.(21)(2007)965-971.
[42] Chalee, W. and Jaturapitakkul, C. 'Effects of w/b ratios and fly ash fineness on chloride diffusion coefficient of concrete in marine environment'. *Materials and Structures*.(42)(2009)505-514.
[43] Chalee, W., Jaturapitakkul, C. and Chindaprasirt, P. 'Predicting the chloride penetration of fly ash concrete in seawater'. *Marine Structures*.(22)(2009)341-353.
[44] Petcherdchoo, A. 'Time dependent models of apparent diffusion coefficient and surface chloride for chloride transport in fly ash concrete'. *Construction and Building Materials*.(38)(2013)497-507.
[45] Chalee, W., Sasakul, T., Suwanmaneechot, P., *et al*. 'Utilization of rice husk–bark ash to improve the corrosion resistance of concrete under 5-year exposure in a marine environment'. *Cement and Concrete Composites*.(37)(2013)47-53.
[46] Cheewaket, T., Jaturapitakkul, C. and Chalee, W. 'Long term performance of chloride binding capacity in fly ash concrete in a marine environment'. *Construction and Building Materials*.(24)(2010)1352-1357.
[47] Chalee, W., Ausapanit, P. and Jaturapitakkul, C. 'Utilization of fly ash concrete in marine environment for long term design life analysis'. *Materials and Design*.(31)(2010)1242-1249.

[48] Cheewaket, T., Jaturapitakkul, C. and Chalee, W. 'Initial corrosion presented by chloride threshold penetration of concrete up to 10 year-results under marine site'. *Construction and Building Materials*.(37)(2012)693-698.
[49] Cheewaket, T., Jaturapitakkul, C. and Chalee, W. 'Concrete durability presented by acceptable chloride level and chloride diffusion coefficient in concrete: 10-year results in marine site'. *Materials and Structures*.(47)(2014)1501-1511.
[50] Kwon, S.J., Lee, H.S., Karthick, S., *et al*. 'Long-term corrosion performance of blended cement concrete in the marine environment - A real-time study'. *Construction and Building Materials*.(154)(2017)349-360.
[51] Dousti, A., Rashetnia, R., Almotahari, A., *et al*. 'Effect of different marine exposure conditions on chloride diffusion in concrete'. In: The 2nd International Conference on Microstructural-related Durability of Cementitious Composites. Amsterdam: 2012.
[52] Shekarchi, M., Rafiee, A. and Layssi, H. 'Long-term chloride diffusion in silica fume concrete in harsh marine climates'. *Cement and Concrete Composites*.(31)(2009)769-775.
[53] Farahani, A., Taghaddos, H. and Shekarchi, M. 'Prediction of long-term chloride diffusion in silica fume concrete in a marine environment'. *Cement and Concrete Composites*.(59)(2015)10-17.
[54] Moradllo, M.K., Shekarchi, M. and Hoseini, M. 'Time-dependent performance of concrete surface coatings in tidal zone of marine environment'. *Construction and Building Materials*.(30)(2012)198-205.
[55] Sadati, S., Arezoumandi, M. and Shekarchi, M. 'Long-term performance of concrete surface coatings in soil exposure of marine environments'. *Construction and Building Materials*.(94)(2015)656-663.
[56] Sadati, S., Moradllo, M.K. and Shekarchi, M. 'Long-Term Performance of Silica Fume Concrete in Soil Exposure of Marine Environments'. *Journal of Materials in Civil Engineering*.(29)(2017)04017126.
[57] Valipour, M., Pargar, F., Shekarchi, M., *et al*. 'In situ study of chloride ingress in concretes containing natural zeolite, metakaolin and silica fume exposed to various exposure conditions in a harsh marine environment'. *Construction and Building Materials*.(46)(2013)63-70.
[58] Valipour, M., Yekkalar, M., Shekarchi, M., *et al*. 'Environmental assessment of green concrete containing natural zeolite on the global warming index in marine environments'. *Journal of Cleaner Productio*.(65)(2014)418-423.
[59] Tadayon, M.H., Shekarchi, M. and Tadayon, M. 'Long-term field study of chloride ingress in concretes containing pozzolans exposed to severe marine tidal zone'. *Construction and Building Materials*.(123)(2016)611-616.
[60] Bader, M.A. 'Performance of concrete in a coastal environment'. *Cement and Concrete Composites*.(25)(2003)539-548.
[61] Bhutta, M.A.R., Maruya, T. and Tsuruta, K. 'Use of polymer-impregnated concrete permanent form in marine environment: 10-year outdoor exposure in Saudi Arabia'. *Construction and Building Materials*.(43)(2013)50-57.
[62] Haque, N. and Al-Khaiat, H. 'Strength and durability of lightweight concrete in hot marine exposure conditions'. *Materials and Structures*.(32)(1999)533-538.
[63] Haque, N., Al-Khaiat, H. and Kayali, O. 'Long-term strength and durability parameters of lightweight concrete in hot regime: importance of initial curing'. *Building and Environment*.(42)(2007)3086-3092.
[64] Skjølsvold, O., Justnes, H., Hammer, T.A., *et al*. 'Long-term chloride intrusion in field-exposed concrete with and without silica fume'. In: The 9th CANMET/ACI International Conference on Fly ash, Silica Fume, Slag, and Natural Pozzolans in Concrete. Warsaw: 2007.
[65] Tang, L. 'Engineering expression of the ClinConc model for prediction of free and total chloride ingress in submerged marine concrete'. *Cement and Concrete Research*.(38)(2008)1092-1097.

[66] Sandberg, P., Tang, L. and Andersen, A. 'Recurrent studies of chloride ingress in uncracked marine concrete at various exposure times and elevations'. *Cement and Concrete Research*.(28)(1998)1489-1503.
[67] Tang, L. and Nilsson, L.O. 'Modeling of chloride penetration into concrete - Tracing five years field exposure'. *Concrete Science and Engineering*. (2)(2000)170-175.
[68] Tang, L. and Gulikers, J. 'On the mathematics of time-dependent apparent chloride diffusion coefficient in concrete'. *Cement and Concrete Research*.(37)(2007)589-595.
[69] Tang, L. and Utgenannt, P. 'A field study of critical chloride content in reinforced concrete with blended binder'. *Materials and Corrosion*.(60)(2009)617-622.
[70] Tang, L., Utgenannt, P. and Boubitsas, D. 'Durability and service life prediction of reinforced concrete structures'. *Journal of The Chinese Ceramic Society*.(43)(2015)1408-1419.
[71] Sørensen, H.E., Jönsson, U. and Munch-Petersen, C. 'Chloride penetration into concrete - comparison of results from field exposure tests and laboratory tests'. In: The 2nd International Congress on Durability of Concrete. New Delhi: 2014.
[72] Rahimi, A., Gehlen, C., Reschke, T. and Westendarp, A. 'Approaches for modelling the residual service life of marine concrete structures'. *International Journal of Corrosion*.(2014)432472.
[73] Polder, R.B. and Larbi, J.A. 'Investigation of concrete exposed to North Sea water submersion for 16 years'. *TNO Building and Construction research*.(40)(1995)31-56.
[74] Poupard, O., Hostis, V.L., Catinaud, S., *et al*. 'Corrosion damage diagnosis of a reinforced concrete beam after 40 years natural exposure in marine environment'. *Cement and Concrete Research*.(36)(2006)504-520.
[75] Nanukuttan, S.V., Basheer, P.A.M., McCarter, W.J., *et al*. 'The performance of concrete exposed to marine environments: Predictive modelling and use of laboratory/on site test methods'. *Construction and Building Materials*.(93)(2015)831-840.
[76] Kim, J., McCarter, W.J., Suryanto, B., *et al*. 'Chloride ingress into marine exposed concrete: A comparison of empirical- and physically- based models'. *Cement and Concrete Composites*.(72)(2016)133-145.
[77] Thomas, M.D.A. and Bamforth, P.B. 'Modelling chloride diffusion in concrete Effect of fly ash and slag'. *Cement and Concrete Research*.(29)(1999)487-495.
[78] Thomas, M.D.A. 'Chloride thresholds in marine concrete'. *Cement and Concrete Research*.(26)(1996)513-519.
[79] Thomas, M.D.A. and Matthews, J.D. 'Performance of pfa concrete in a marine environment - 10-year results'. *Cement and Concrete Composites*.(26)(2004)5-20.
[80] Costa, A. and Appleton, J. 'Chloride penetration into concrete in marine environment - Part I: Main parameters affecting chloride penetration'. *Materials and Structures*.(32)(1999)252-259.
[81] Costa, A. and Appleton, J. 'Chloride penetration into concrete in marine environment - Part II: Prediction of long-term chloride penetration'. *Materials and Structures*.(32)(1999)354-359.
[82] Real, S. and Bogas, J.A. 'Chloride ingress into structural lightweight aggregate concrete in real marine environment'. *Marine Structures*.(61)(2018)170-187.
[83] Serdar, M., Bjegovic, D. and Stipanovic-Oslakovic, I. 'Corrosion resistant steel reinforcement - laboratory and field testing'. In: The 6th International Conference on Concrete under Severe Conditions. Merida Yucatan: 2010.
[84] Kouloumbi, N., Batis, G. and Malami, C. 'The anticorrosive effect of fly ash, slag and a Greek pozzolan in reinforced concrete'. *Cement and Concrete Composites*.(16)(1994)253-260.
[85] Roshore, E.C. 'Cement durability program, long-term field exposure of concrete columns', Vicksburg: US Army Engineer Waterways Experiment Station, 1972.
[86] Kondratova, I.L., Montes, P. and Bremner, T.W. 'Natural marine exposure results for reinforced concrete slabs with corrosion inhibitors'. *Cement and Concrete Composites*.(25)(2003)483-490.

[87] Moffatt, E.G. and Thomas, M.D.A. 'Performance of 25-year-old silica fume and fly ash lightweight concrete blocks in a harsh marine environment'. *Cement and Concrete Research*.(113)(2018)65-73.
[88] Thomas, M.D.A. and Bremner, T. 'Performance of lightweight aggregate concrete containing slag after 25 years in a harsh marine environment'. *Cement and Concrete Research*.(42)(2012)358-364.
[89] Alexander, M. and Thomas, M.D.A. 'Service life prediction and performance testing - Current developments and practical applications'. *Cement and Concrete Research*.(78)(2015)155-164.
[90] Thomas, M.D.A. and Scott, A.C.N. 'Sustainable Concrete in a Marine Environment'. In: The 2nd International Conference on Sustainable Construction Materials and Technologies. Ancona: 2010.
[91] Robertson, I.N. 'Prediction of chloride ingress into concrete in a marine environment'. In: Strategies for Sustainable Concrete Structures. Aix-en-Provence: 2012.
[92] Uno, J., Robertson, I.N. and Newtson, C.M. 'Corrosion susceptibility of concrete exposed to a marine environment'. In: University of Hawaii College of Engineering/Department of Civil and Environmental Engineering. Hawaii: 2004.
[93] Cheng, H. and Robertson, I.N. 'Performance of admixtures intended to resist corrosion in concrete exposed to a marine environment'. In: University of Hawaii College of Engineering/Department of Civil and Environmental Engineering. Hawaii: 2006.
[94] Robertson, I.N. and Newtson, C. 'Performance of corrosion inhibitors in concrete exposed to marine environment'. In: The 2nd International Conference on Concrete Repair, Rehabilitation and Retrofitting. Cape Town: 2008.
[95] Robertson, I.N. 'Improving concrete durability through the use of corrosion inhibitors'. In: The 3rd International Conference on Concrete Repair, Rehabilitation and Retrofitting. Cape Town: 2012.
[96] Castroa, P., Rinconb, O.T.D. and Pazini, E.J. 'Interpretation of chloride profiles from concrete exposed to tropical marine environments'. *Cement and Concrete Research*.(31)(2001)529-537.
[97] Meira, G.R., Andrade, C., Padaratz, I.J., *et al*. 'Chloride penetration into concrete structures in the marine atmosphere zone - Relationship between deposition of chlorides on the wet candle and chlorides accumulated into concrete'. *Cement and Concrete Composites*.(29)(2007)667-676.
[98] Meira, G.R., Andrade, C., Alonso, C., *et al*. 'Modelling sea-salt transport and deposition in marine atmosphere zone - A tool for corrosion studies'. *Corrosion Science*.(50)(2008)2724-2731.
[99] Meira, G.R., Andrade, C., Vilar, E.O., *et al*. 'Analysis of chloride threshold from laboratory and field experiments in marine atmosphere zone'. *Construction and Building Materials*.(55)(2014)289-298.
[100] Meira, G.R., Andrade, C., Alonso, C., *et al*. 'Durability of concrete structures in marine atmosphere zones - The use of chloride deposition rate on the wet candle as an environmental indicator'. *Cement and Concrete Composites*.(32)(2010)427-435.
[101] Aldred, J.M. and Castel, A. 'Chloride penetration after field exposure compared with estimates from service life prediction models'. In: The RILEM International Workshop on Performance-Based Specification and Control of Concrete Durability. Zagreb: 2014.
[102] Kang, B. 'Design and building of CHEC's engineering material exposure testing station in northeast China (port of Jinzhou) '. *China Harbour Engineering*.(129)(2004)35-38.
[103] Qiu, X., Ma, X. and Sun, X. 'Study on Corrosion Rules of Reinforced Concrete Buried in Seaside Salt Soil'. *Building Science*.(17)(2001)41-43.
[104] Ma, X., Qiu, X. and Sun, X. 'Corrosion law of RC piles exposed naturally in coastal saline soil environment'. *China Concrete and Cement Products*.(1)(2002)23-24.
[105] Leng, F., Ma, X,, Dong, W., *et al*. 'Durability analysis of RC piles exposed naturally in coastal saline soil environment for 17 years'. *Building Structure*.(41)(2011)148-151.

[106] Kang, B. 'Design and construction of north China (Tianjin) laboratory for seaside atmospheric exposure testing'. *China Harbour Engineering*.(2)(2002)52-55.
[107] Wang, S., Tian, J. and Fan, Z. 'Research on theory and method of service life prediction of marine concrete structures based on exposure test and filed investigation'. *China Harbour Engineering*.(169)(2010)67-74.
[108] Chen, B., Hong, D., Guo, H., *et al*. 'Durability of RC used for harbor engineering after 10 years field exposure'. *Journal of Nanjing Hydraulic Research Institute*.(4)(1982)1-11.
[109] Sun, P., Zhao, T., Jin, Z., *et al*. 'Rules of chloride iron ingression in concrete under marine environment'. *Tunnel Construction*.(31)(2011)573-576.
[110] Xue, H., Jin, Z. and Wang, X. Chloride ion penetration into concrete exposed to marine environment for a long period. *The Ocean Engineering*.(33)(2015)60-65.
[111] Li, S., Fan, W., Xu, N., *et al*. 'Design and application of offshore field exposure station (Donghai bridge)'. *Port and Waterway Engineering*.(6)(2011)30-38.
[112] Fan, Z., Yang, F., Huang, J. *et al*. 'Experimental study on long-term exposure test of marine concrete'. *Port and Waterway Engineering*.(9)(2005)45-48.
[113] Fan, Z., Pan, J. and Wang, S. 'Long term and medium-term exposition test and research for materials in south china region'. *South China Harbour Engineering*.(2)(2008)13-18.
[114] Wang, S., Su, Q., Fan, Z., *et al*. 'Durability design principle and method for concrete structures in Hong Kong-Zhuhai-Macau sea link project'. *China Civil Engineering Journal*.(46)(2014)1-8.
[115] Pang, L. and Li, Q. 'Service life prediction of RC structures in marine environment using long term chloride ingress data: Comparison between exposure trials and real structure surveys'. *Construction and Building Materials*.(113)(2016)979-987.
[116] Zeng, J., Fan, Z., Xiong, J., *et al*. 'Research on durability of metakaolin concrete based on long-term exposure experiment at in-situ marine splash zone'. *Journal of South China University of Technology (Natural Science Edition)*.(46)(2018)53-60.
[117] Li, Z., Zhu, Y., Cai, W., *et al*. 'Coastal exposure test of corrosion of rebar in concrete'. *Concrete*.(2)(2010)25-28.
[118] Da, B., Yu, H., Ma, H., *et al*. 'Investigation of durability of ordinary concrete structures in the South China Sea'. *Journal of Harbin Engineering University*.(37)(2016)1034-1040.
[119] Da, B., Yu, H., Ma, H., *et al*. 'Factors Influencing Durability of Coral Concrete Structure in the South China Sea'. *Journal of the Chinese ceramic society*.(44)(2016)253-260.
[120] Yu, H., Sun, W., Yan, L., *et al*. 'Study on prediction of concrete service life I - Theoretical model'. *Journal of The Chinese Ceramic Society*.(30)(2002)686-690.
[121] Yu, H., Sun, W., Ma, H., *et al*. 'Study on prediction of concrete service life II - Model's examination and application'. *Journal of The Chinese Ceramic Society*.(30)(2002)691-695.
[122] Yu, H., Sun, W., Ma, H., *et al*. 'Study on prediction of concrete service life III - Evaluation of influencing factors and service life'. *Journal of The Chinese Ceramic Society*.(30)(2002)696-701.

DIFFUSION OF CHLORIDES IN CRACKED STRAIN-HARDENING CEMENT-BASED COMPOSITES (SHCC)

Philipp Kunz (1) and Viktor Mechtcherine (1)

(1) Institute of Construction Materials, Technische Universität Dresden, Germany

Abstract

Strain-hardening cement-based composites (SHCC) are high-performance fiber-reinforced composites with promising durability properties due to their considerably enhanced crack control under tensile load conditions. The knowledge of the transport properties of such composites in cracked state are crucial for estimating their durability characteristics. In the project at hand, chloride diffusion tests were performed and their results were related to crack widths and crack distances in SHCC specimens under investigation. SHCC specimens were first subjected to uniaxial tension under deformation-controlled loading regime in order to achieve formation of multiple cracks. Optical investigations provided a basis for evaluating the crack pattern. Eventually the cracked specimens were exposed to chloride solutions. Qualitative and quantitative chloride evaluations were conducted and discussed with particular respect to the recorded crack pattern. The results obtained within the project for chloride diffusion in cracked and crack-free areas enlarge the basis for assessing durability characteristics of SHCC and for further developing existing durability concepts and approaches.

Keywords: crack distribution, chloride diffusion, SHCC, durability

1. INTRODUCTION

Strain-hardening cement-based composite (SHCC) was developed at the beginning of the 1990s by Victor C. Li [1] under the name of ECC (Engineered cementitious composites). Both terms refer to the same material. Due to its strain-hardening tensile behaviour, SHCC was originally used as a repair material applied in thin layers to cover cracked members of reinforced concrete. Such layer impedes the penetration by harmful substances through narrow cracks typical for SHCC and herewith ensures a more resistant and durable member. SHCC has been continuously used in rehabilitation of reinforced concrete structures or as a replacement for concrete in reinforced concrete members [2] [3]. Therefore, the performance of SHCC with respect to the protection of reinforcement plays a crucial role in the research on this material [3] [4]. The characteristic stress-strain diagram of SHCC in

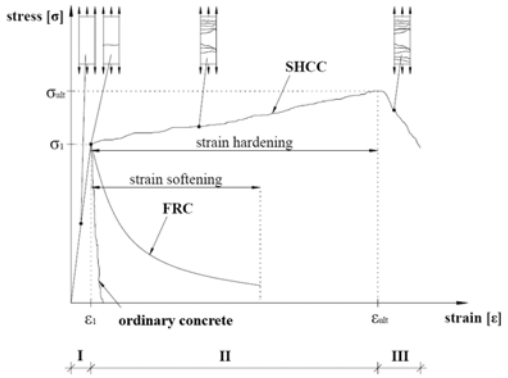

Figure 1: Typical stress-strain behaviour and crack pattern of SHCC under uniaxial tensile loading.

comparison to conventional fibre-reinforced concrete (FRC) and ordinary concrete are shown in Fig. 1

To investigate the durability behavior properly a broad range of tests for the various environmental factors must be performed. Due to the promising tensile strain characteristics SHCC is very suitable to be used together with steel reinforcement as presented by Fisher et al. [5], the durability investigations need to consider not only the deterioration of SHCC as such but also the corrosion protection of the steel reinforcement. A reinforced SHCC member is subjected to a variety of aggressive environmental factors. Damage processes are thereby often initiated by a pollutant which is carried into the component by liquids, especially water. Such ingress is accelerated by cracks and increases with growing crack widths. Since a long time crack width regulating proofs are used for this reason in standards for the serviceability design. Since SHCC has significantly lower crack widths as ordinary concrete, it is considered a promising material with respect to durability [6]. Water is mostly acting as a carrier for harmful pollutants, e.g. in connection with chlorides and sulfates, it is reasonable to perform permeability tests on cracked construction components. In the project at hand, a series of experiments were performed to enlarge the data base for the durability related properties of SHCC. The main focus was on the behaviour of SHCC with respect to liquid-based, durability-influencing transport mechanisms. Special attention was directed to the crack width effect on the transport of chlorides. While a variety of transport processes may occur usually in combinations (cf. Fig. 2), this paper focusses on the diffusion-based process only. To separate this process from other ones, a complete water saturation of the specimens under investigation must be attained before starting actual diffusion tests. The experiments were based on a broad experience collected at the Institute of Construction Materials of the TU Dresden [7] [8] [9] [10].The data base developed will be the basis in further research to assess the crack-related material behaviour and to verify the durability concept for SHCC presented by Altmann [11] [9].

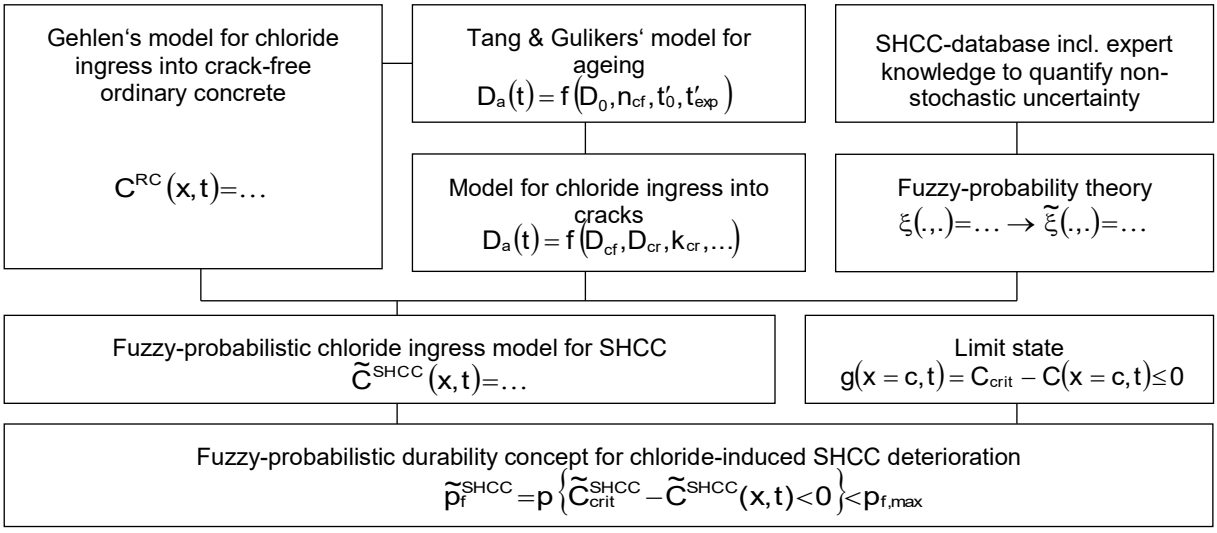

Figure 2: Schematic model for chloride ingress according to Altmann [9]

2. EXPERIMENTAL PROGRAMM

To evaluate effect of the crack width on the chloride diffusion in SHCC a series of experiments were designed and performed. The experiments were based on a mechanical preloading to generate multiple crack patterns. For this purpose, dumbbell shaped specimens were produced and subjected to monotonic, uniaxial tensile loading after 28 days to achieve the SHCC typical cracking pattern. Subsequently, the specimens

were cut, coated and subjected to concentrated different saline solutions with various exposure times. To ensure a good comparability between the results of this project with former findings, in particular those from Altmann [9], the recommendations derived from his work served as basis for the experimental setup and evaluation procedure.

2.1 Materials and specimen preparation

The SHCC mixture under investigation was developed at the Institute of Construction Materials, TU Dresden and yielded already promising results in earlier studies. The mixture composition is given in Table 1. It has a fibre content of 2.0% by volume, the fibres are made of polyvinyl alcohol (PVA) and have a length of 12 mm and a diameter of 40 µm. The mixing was performed following the procedure described by Jun [12].

Table 1: Composition of SHCC under investigation [13]

Cement	CEM I 42,5 R-HS	505	kg/m³
Coal fly ash	Powerment HKV / Kreament alt	621	kg/m³
Water	H_2O	398	kg/m³
Aggregate	Sand 0,06-0,2	536	kg/m³
Add1	FM GlenAce 30	10	kg/m³
Add2	UW-Comp	3	kg/m³
Fibre	PVA	26	kg/m³

2.2 Uniaxial tensile loading

After taking the specimens out of the water tank, they were wrapped in foil at the mid-section. Both dumbbell shaped ends were briefly dried and subsequently glued in the universal testing machine Instron by means of a two-component adhesive, see also Fig. 3.

All 15 specimens were subjected to the uniaxial tension at the age of 28 to 30 days. The loading was performed under deformation-controlled low-cyclic tension regime with a loading speed of 0.01 mm/s and 0.25 mm increase in deformation per cycle, which corresponds to a strain increase by 0.1% per cycle, cf. Fig. 4. The deformations were measured by two inductive displacement transducers fixed to the respective opposite sides of the specimen. The final state of damage was determined by 1% residual strain after unloading. After tensile loading, each specimen was cut in two bars with the dimensions of 250 mm x 48 mm x 60 mm.

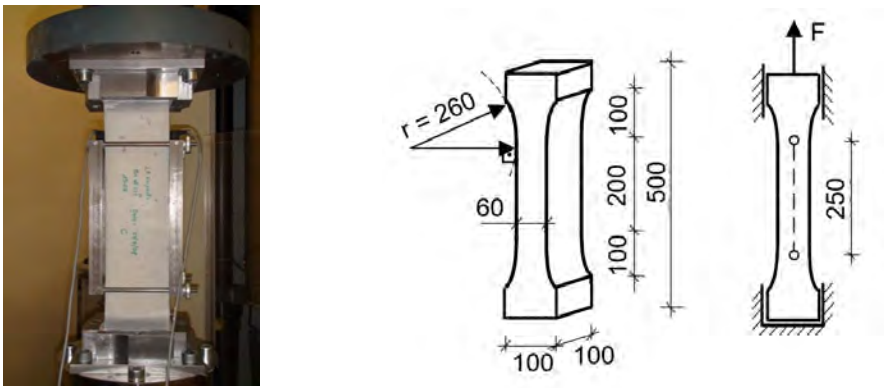

Figure 3: Uniaxial tensile loading: (a) test setup and (b) geometry of the specimen

2.3 Crack evaluation and quantification

The crack pattern of each specimen was recorded directly after the cutting works using a high resolution scanner (3600 dpi). This resolution enables pictures with a pixel size of 7.06 µm by 7.06 µm. On this bases, cracks could be theoretically observed starting by a crack width of 14.1 µm. The crack widths and crack distances were evaluated using image editing software and counted specifically along one central axis, according to the recommendations of JSCE (Japan Society of Civil Engineering) [14] (Fig. 5).

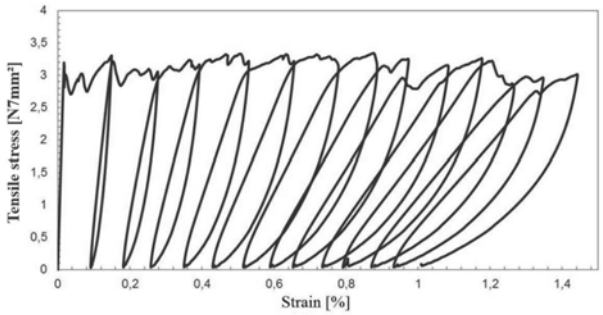

Figure 4: Stress-strain curve of deformation-controlled low-cyclic tensile loading of the specimens

(a)

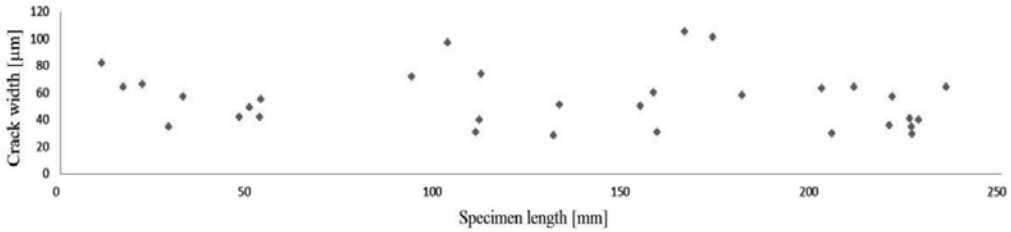

(b)

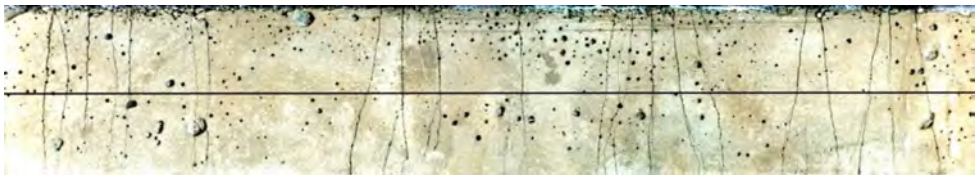

Figure 5: (a) Crack width distribution along the length of a specimen after tensile loading and (b) corresponding specimen with line at which crack measurements were performed

(a) b)

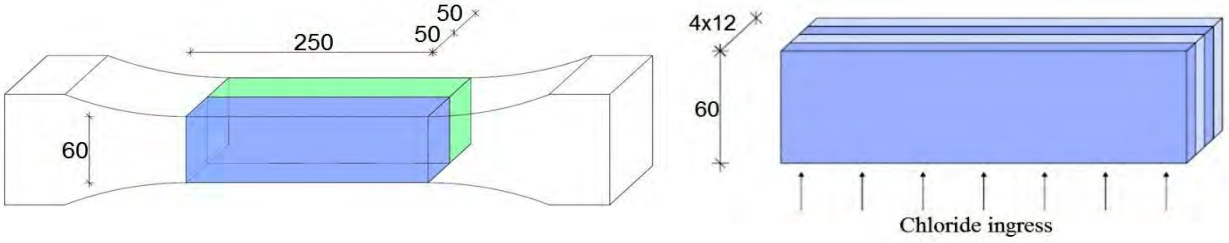

Figure 6: Specimen with cutting regime before chloride penetration

2.4 Chloride diffusion test

Different concentrated sodium chloride solutions were produced. One solution was prepared according to NT BUILD 443 with a sodium chloride concentration of 165g/l. The second solution with a concentration of 30g/l [15] [9]. Both sodium chloride solutions were stored at 20°C and fully sealed to minimize evaporation effects. The cracked and non-cracked specimens were subjected to the different chloride solutions and different exposure from 3 to 7 days as shown in Fig. 7. Complete water saturation was ensured by an aluminum butyl coating which prevented specimen from evaporation.

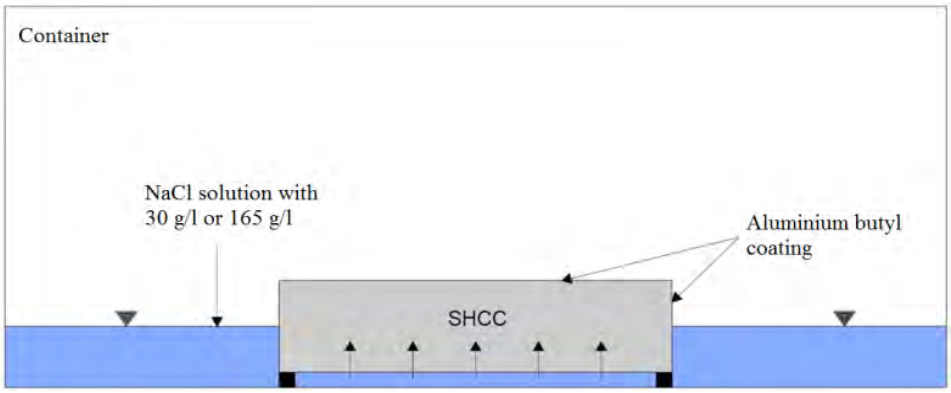

Figure 7: Test setup for chloride ingress experiments

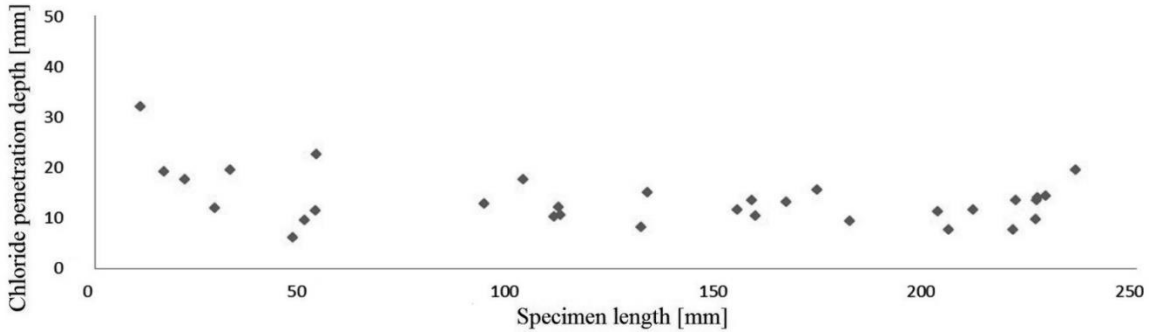

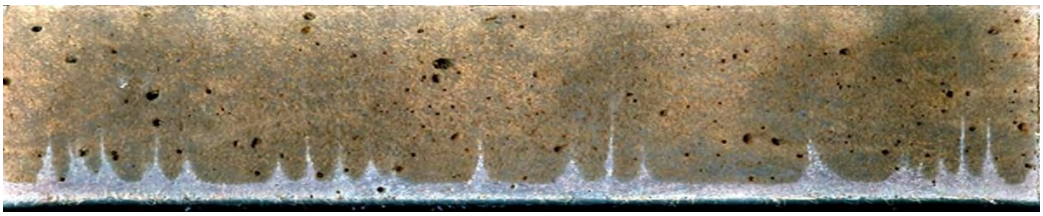

Figure 8: (a) Chloride penetration depths and (b) appearance of chloride ingress on a slice surface upon spaying AgNO3 solution

2.5 Silver nitrate test

After removing the samples from sodium solution the silver nitrate test was conducted, in which a 0.1 M $AgNO_3$ solution was used [15]. Silver nitrate reacts on a freshly fractured surface with unbound chlorides to silver chloride which can be seen on the surface due to its silver-gray reaction product. The visual analysis of the colour change enables qualitative evaluation of chloride ingress in cement based materials, cf. Fig. 8b. Due to high fibre content of SHCC and subsequently it high ductility, it was not possible to split SHCC specimens to produce fresh fracture surfaces, the way it is usually done for concrete or mortar. Instead, all specimens were cut, which led to four slices of approximately 10 mm thickness (cf. Fig. 6). Subsequently, silver nitrate solution was sprayed on each surface. Half an hour later silver nitrate was sprayed for the second time. After drying each surface was scanned and the chloride penetration depth measured as shown in Fig. 8 and afterwards related to the crack width.

2.6 Quantitative chloride determination

While the silver nitrate test only provides qualitative statements for chloride ingress, the quantitative analysis of chloride concentration was performed following the recommendations

described in NT BUILD 443 by abrade thin layers of each specimen. For chloride concentration investigation the crack-free specimens which were subjected to 28 days exposure in sodium solution were used exclusively. A minimum of 6 layers of each specimen were abraded to define the particular chloride concentration for this layer. The thickness of each abraded layer was 1 mm to 2 mm. In order to conduct the chemical analysis for the test material, the powdered material was given in 18% diluted nitric acid (HNO3). The filtrate was afterwards investigated by using a photometer which provided the exact chlorid concentration per layer.

3. EXPERIMENTAL RESULTS

3.1 Crack evaluation

Crack width distributions were evaluated combining all specimens investigated and grouped by their widths, while for each group a range of 0.01 mm was set. Fig. 9 shows the empirical density function for crack widths. This probability density function shows a similarity to a lognormal distribution as described by Wang et al. [17]. However, a precise statistical description of this function was not scope of this project.

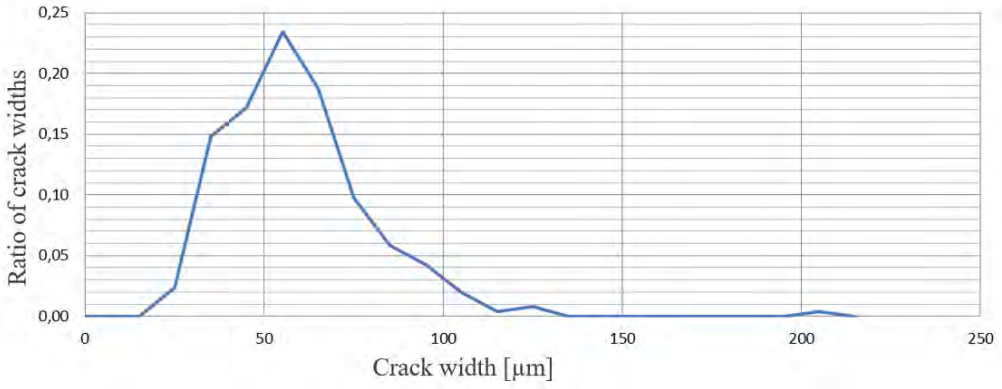

Figure 9: Empirical density function of crack widths

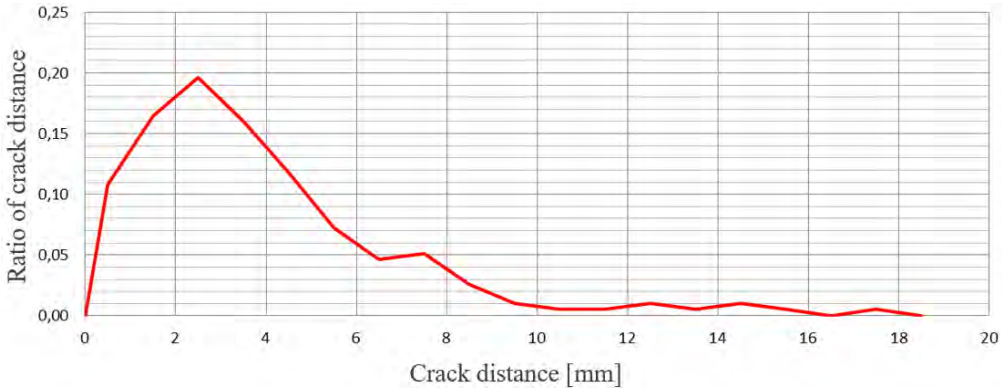

Figure 10: Empirical density function of crack proximity

Evaluating the crack distances turned out to be more challenging due to the fact that they are only relevant and harmful with respect to durability in situations of mutual crack influence of two neighboring cracks. For this reason a general statement regarding specific distances relevant from the durability perspective would be to uncertain. Within the framework of this project the evaluation of crack distances was conducted after the chloride tests. The measurements were performed for all specimens but only the distances which appeared to clearly accelerate the chloride transport were taken into consideration.

3.2 Qualitative chloride evaluation

After analysing the chloride penetration depth every crack was related to certain amount of chloride penetrated into SHCC. None accelerated chloride ingress could be observed in non-cracked areas. Based on this founding, the authors assume that for crack widths below 25 µm no acceleration of chloride diffusion occurs measurable by the applied techniques. The chloride penetration increases with increasing crack width and chloride concentration gradient. The conducted silver nitrate tests however only enable finding free, unbound chlorides in SHCC and give no indication on physically and chemically bounded chlorides. This must be considered when evaluating the mechanisms compromising durability. In particular so, knowing that chloride binding is a reversible process and that already bounded chlorides can easily be released again with increasing solution concentration or as a result of another chemical deterioration process. As mentioned before also the crack distances plays a significant role on the chloride penetration depths. Thus, Fig. 12 relates chloride penetration to specific crack distances. As expected the chloride ingress increases with growing crack width and decreases with growing crack distance.

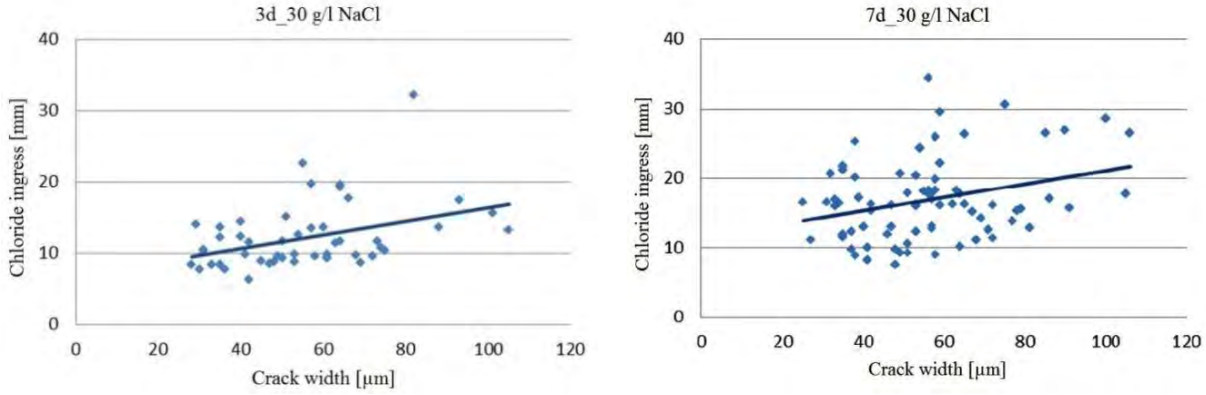

Figure 11: Evaluation of chloride ingress in relation to crack widths for different exposure times and concentration of NaCl solution: 3d with 30g/l NaCl (left) and 7d with 30g/l (right)

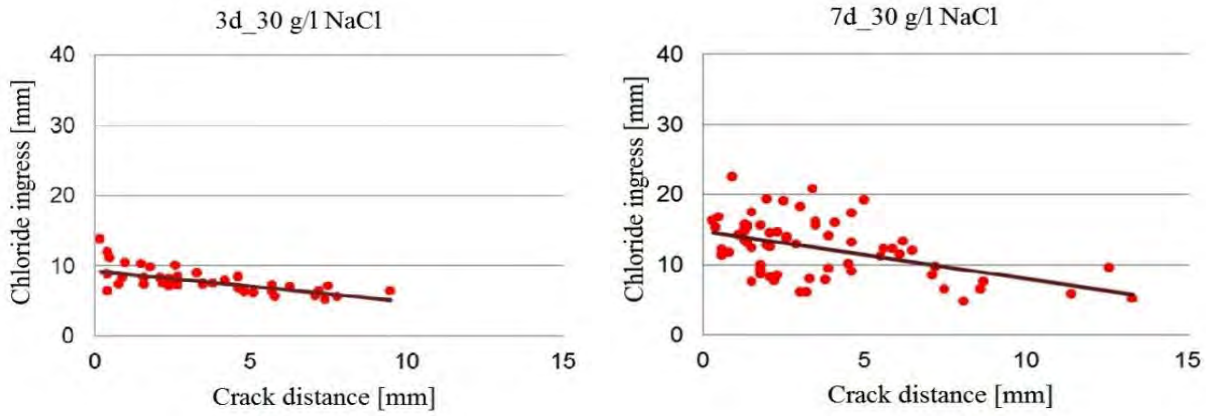

Figure 12 : Evaluation of chloride ingress in relation to crack proximity for different exposure times and concentration of NaCl solution: (a) 3 d and 30 g/l NaCl, (b) 7 d and 30 g/l NaCl, (c) 3d and 165 g/l NaCl

3.3 Quantitative chloride evaluation

The quantitative chloride evaluation was performed on un-cracked specimens. It must be kept in mind that the quantitative chloride evaluation considers bound and unbound chlorides, while the qualitative one captures the unbound chlorides only. The quantitative analysis provided various chloride profiles over penetration depth, see Fig. 13. The results obtained from the photometer tests gave the chloride concentration per mass of SHCC.

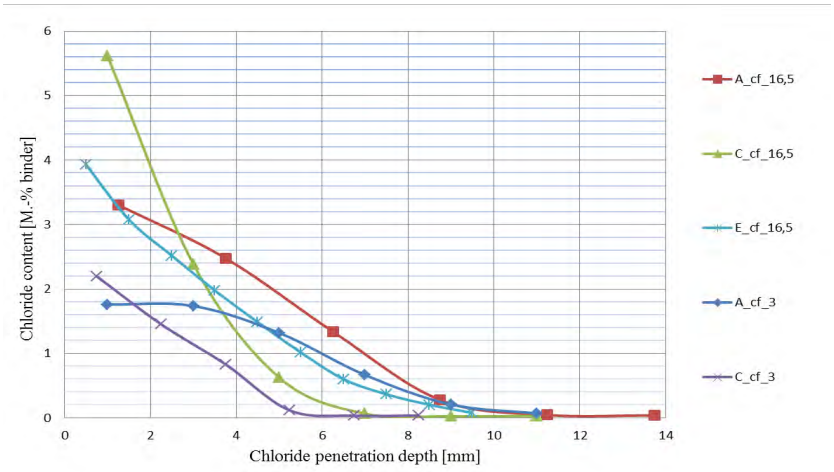

Figure 13: Chloride profiles, chloride content is given in mass % of binder

4. SUMMARY AND CONCLUSIONS

Chloride diffusion tests were performed no non-cracked and cracked specimens made of SHCC. First, crack width distributions were assessed showing that the most crack widths were in the range between 50 µm and 60 µm, while 96% of all cracks evaluated had widths below 100 µm. The smallest crack distance recorded was 200 µm, the most crack distances in multiple crack patterns amounted between 2 mm and 3 mm. In the investigation at hand, 95% of all crack distances leading to noticeable acceleration of chloride diffusion were under 10 mm. Based on the qualitative chloride profiles as observed in the silver nitrate test, it could assured that beside diffusion no noticeable other transport processes took place. It was found that the specimen dimension chosen for the experimental investigations were suitable for chloride exposures upto 14 days. Chloride diffusion tests on cracked material have shown to be an order of magnitude faster process compared to chloride diffusion in crack-free regions.

The qualitative tests yielded to no accelerated chloride diffusion in crack-free regions. Thus, it can be assumed that crack widths below 25 µm do not course any acceleration of diffusion. Referring also to similar findings by Djerbi et al. [18] a certain lower limit of crack width can be suggested to be set at 25 µm postulating that more narrow cracks do not contribute significantly to the higher ingress of chlorides by diffusion processes. It should be however underlined that the silver nitrate test only considers free, unbound chlorides. The quantitative tests, however, consider both bound and unbound chlorides [16]. This must be taken into account when relating a certain chloride concentration to the moment of colour changing in the silver nitrate test. Within the framework of this project specific magnitudes of chloride binding capacity, surface chloride concentration and diffusion coefficient were calculated. Based on this data further investigations can be conducted to verify particular durability concepts [19]. The described experimental approach provides suitable procedure to achieve information on durability indicators and to lower uncertainties that come along with handling new materials.

REFERENCES

[1] Li, V. C. From micromechanics to structural engineering - The design of cementitiouscomposites for civil engineering applications. JSCE J. of Struc. Mechanics and EarthquakeEngineering. 1993, S. 37-48.

[2] Li, V. C.; Wang, S.; Wu, C. Tensile Strain-hardening Behavior of PVA-ECC. ACI Materials Journal. 2001, S. 483-492.

[3] Mechanical behaviour of slabs made of strain-hardening cement-based composite and steel reinforcement subject to uniaxial tensile loading. Mündecke, E. und Mechtcherine, V. Montreal : FRC 2014 Joint ACI-fib International Workshop Fibre Reinforced Concrete: From Design to Structural Applications, Polytechnique Montreal, 2014.

[4] Mechtcherine, V. Novel cement-based composites for the strengthening and repair. Construction and Building Materials. 2012.

[5] Fischer, G.; Li, V.C. Influence of matrix ductility on the tension-stiffening behavior of steel reinforced Engineered Cementitious Composites (ECC). s.l. : ACI Structural Journal, Vol. 99, No.1, 2002. S. 104-111.

[6] C. Schröfl, V. Mechtcherine, A. Kaestner , P. Vontobel, J. Hovind ,. Transport of water through strain-hardening cement-based composite (SHCC) applied on top of cracked reinforced concrete slabs with and without hydrophobization of cracks – Investigation by neutron radiography. 2014.

[7] Wagner, C.; Villmann, B.; Slowik, V.; Mechtcherine, V., Water permeability of cracked strain-hardening cement-based. Cement and Concrete Composites 82, 234-241, 2017

[8] Wagner, C.; Villmann, B.; Slowik, V.; Mechtcherine, V., Capillary absorption of cracked strain-hardening cement-based. Cement and Concrete Composites 97, 239-247, 2019

[9] Altmann, F. Sickert, J.U.; Mechtcherine, V.; Kaliske, M., A fuzzy-probabilistic durability concept for strain-hardening cement-based composites (SHCCs) exposed to chlorides. Cement & Concrete Composites : Cement & Concrete Composites Vol. 34, 754–770, 2012

[10] Lieboldt, M. Mechtcherine, V., Permeation of water and gases through cracked textile reinforced concrete: Cement and Concrete Composites Vol.33, 725-734, 2011.

[11] F. Altmann, V. Mechtcherine. Durability design strategies for new cementitious materials. Cement and Concrete Research. 2013.

[12] Jun, P. Behaviour of strain-hardening cement-based composites (SHCC) under monotonic and cyclic tensile loading. Dresden : Technische Universität Dresden, 2011. Doktorarbeit. Schriftenreihe des Institutes für Baustoffe. Heft 2011/1. 978-3-86780-229-1.

[13] Brüdern, A.-E.; Mechtcherine V. Multifunctional use of SAP in strain-hardening cement-based composites. International RILEM Conference on Use of Superabsorbent Polymers and Other New Additives in Concrete. s.l. : RILEM Publications SARL, 2010.

[14] Rokugo, K. Recommendations for design and construction of High Performance Fiber Reinforced Cement Composites with multiple fine cracks (HPFRCC). [Buchverf.] Japan Society of Civil Engineering (JSCE). Concrete Engineering Series 82. Tokyo : s.n., 2008.

[15] NT BUILD 443. Concrete, hardened: Accelerated chloride penetration. s.l. : Nordtest method, 1995.

[16] Baroghel-Bouny, V.; Belin, P.; Maultzsch, M.; Henry, D. Advantages, weakness, and various applications to quantify chloride ingress into concrete. Part: Non-steady-state diffusion tests and exposure to natural conditions. Matrials and Structures. 2007, S. 783-799.

[17] Wang, P.; Wittmann, F. H.; Zhao, T.; Huang, W. Evolution of crack patterns on SHCC as function of imposed strain. Strain Hardening Cementitous Composites (SHCC2 - Rio). Rio de Janero, Brazil : Rilem, 2011, S. 217-232. Proceedings of the 2nd international RILEM Conference.

[18] Djerbi, A.; Bonnet, S.; Khelidj, A.; Baroghel-Bouny, V. Influence of traversing crack on chloride diffusion into concrete. Cement and Concrete Research. 2008, 38, S. 877-883.

[19] Mechtcherine, V. Towards a durability framework for structural elements and structures made of or strengthened with high-performance fibre-reinforced composites. Construction and Building Materials. 2011.

EFFECT OF THE TEMPERATURE ON THE WATER TRANSPORT BY CAPILLARITY INTO THE CONCRETE POROSITY

X. Chen (1), T. Sanchez (1), D. Conciatori (1), H. Chaouki (1), L. Sorelli (1), B. Selma (2), and M. Chekired (2)

(1) CRIB-Department of Civil Engineering, Laval University, Québec, Canada

(2) Institut de recherche d'Hydro-Québec, Montréal, Canada

Abstract

This paper presents a new 2D water transport model considering capillary suction to predict the water content evolution in the concrete porosity. The basic formulations of the model are illustrated, and a switching algorithm is introduced to simulated wet-drying effects. Two specific absorption tests are studied to validate this model. The first test conducted under room temperature allows to observe that capillary effects play an important role in the concrete material sorptivity and this phenomenon was well captured by the numerical model. The second test conducted under different temperatures highlight that temperature has significant effect on the capillary suction process and it has been considered in the model as an important input parameter.

Keywords: Capillary suction, concrete porosity, transport model, finite element method, absorption test

1. INTRODUCTION

Over the past decades, concrete structures have suffered from corrosion induced by chloride ions, decreasing both their durability and sustainability [1,2]. When the concrete is unsaturated and exposed to aggressive environment (tides, mist, splash), it is commonly admitted that the capillary suction of salt water will significantly accelerate the penetration of chloride ions in the concrete structure [3-6], compared to the speed of chloride diffusion. Many transport models using traditional Fick's diffusion law in the literature [7-9], however, failed to capture this physical nature and kinetics of capillarity. More elaborated multiphase transport models [10-12] can explain capillarity by introducing a "capillary pressure" on liquid-vapor interface in its formulation, yet applications of these models on water absorption tests have not been found. Water transport with presence of capillarity in concrete porosity is still poorly understood and modelled. To address this problem, the 1D FEM software TransChlor® [6,13] was developed considering the coupling between temperature [14], carbonation, water transport, ion diffusion and chloride isothermal adsorption [15] during the concrete corrosion process. Water and chloride diffusion equations from Bazant et al. [7] coupled with a kinetic term driven by

capillarity [6] were implemented in TransChlor®, to simulate water transport in porosity with capillary suction effect. Based on the simulation results from TransChlor®, Sanchez et al. [16] developed a new numerical model on a geochemical software PhreeqC [17, 18] and simulated the capillary suction impact on chloride transport at ambient temperature. However, few studies can be found about the impact of different temperatures, especially low temperature, on the capillary suction process in concrete, and till now, not many models exist. In addition, most of existing numerical models with capillarity effect are quite limited to a 1D framework [6, 12,13] and are only able to simulate tests with laboratory exposure conditions [17, 18] (constant temperature, fixed salt solution concentration, constant boundary relative humidity, 1D drying or wetting…). Higher dimensional transport simulations considering capillarity, with real environmental exposures as boundary conditions, are still absent in the literature.

The objective of this paper is then to present a better concrete pore water transport model that models the influence of the temperature on capillary process and that is developed in 2D to further consider real complex exposure conditions. This model (TransChlor2D®) was formulated by integrating the effect of vapor diffusion and liquid suction with Fick's and Darcy's law, respectively and was implemented in the architecture of TransChlor® (Fig. 1).

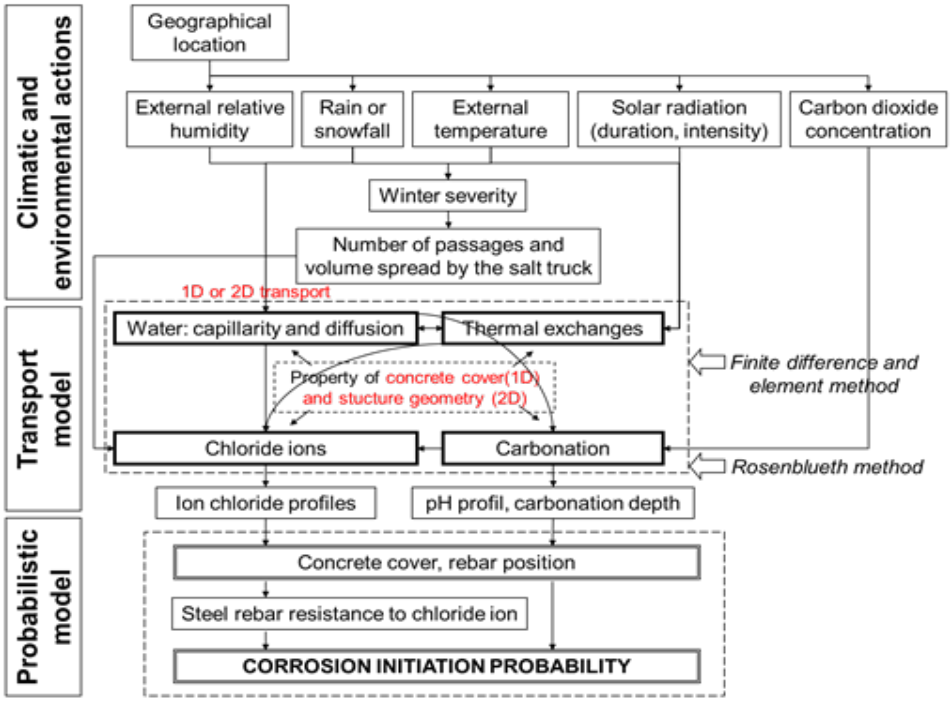

Figure 1: Implementation of a new 2D water transport module in the TransChlor® software architecture

A 2D Finite Element Method (FEM) algorithm was implemented to solve the nonlinear differential equations. The transport parameters in this new transport model were calibrated with various durability tests [19-22] while in this paper, only the simulation results on water absorption tests [20,21] were discussed since they are most relevant to capillary suction phenomenon.

2. MODELLING WATER TRANSPORT INTO CONCRETE POROSITY CONSIDERING CAPILLARY EFFECTS

Water movement in porous medium can be considered as a multiphase transport process.

Considering concrete as a homogeneous porous medium and no presence of liquid water inside, the whole water transport process can be generally represented by "vaporized water" diffusing through an interconnecting pore network [7]. In this case, the "Bazant-Najjar" diffusion model [8,9] is commonly used to represent the mass balance of non-wetting phase (water vapor + air). Using saturation degree as state variable and by introducing porosity, the expression of mass balance on water vapor yields to [8,9]:

$$\rho_{nw} \cdot \emptyset \cdot \frac{\partial S_{nw}}{\partial t} = -\nabla . \overrightarrow{J_{nw}} \tag{1}$$

ρ_l is the density of water vapor ($kg.m^{-3}$), $\emptyset$ is the porosity of medium and S_{nw} is the pore saturation of water vapor. The massive flux of water vapor $\overrightarrow{J_{nw}}$ ($kg.m^{-2}.s^{-1}$) is driven by saturation gradient in space with the massif water vapor diffusion coefficient D_{nw} ($kg.m^{-1}.s^{-1}$),

$$\overrightarrow{J_{nw}} = -D_{nw} \cdot \boldsymbol{\nabla} S_{nw} \tag{2}$$

The coefficient D_{nw} can be further modelled with a nonlinear "S-Shape" mathematical function [8] and coupled with an Arrhenius law [6]:

$$D_{nw} = \rho_{nw} \cdot D_{nw0} \cdot \left(\alpha_0 + \frac{1-\alpha_0}{1+\left(\frac{1-S_{nw}}{1-S_{cr}}\right)^n} \right) \cdot e^{\frac{Q}{R}\left(\frac{1}{T_0}-\frac{1}{T}\right)} \tag{3}$$

with D_{nw0} the asymptotic diffusion coefficient at 100% pore relative humidity, α_0 a minor non-zero constant, S_{cr} the turning point in $(D_{nw} - S_{nw})$ relationship and n governing the curvature of function curve. For vapor diffusion, the Arrhenius par Q refers to the activation energy (Q=32000 kJ/mol) and R refers to the gas constant (R=8.314) [7]. T_0 is the referential temperature (usual laboratory temperature, 293K) and T is the actual ambient temperature.

However, not only vaporized water engaged in water transport. With the presence of wetting phase (liquid) in concrete pores and contact surfaces, the capillary suction phenomenon comes from the capillary pressure difference on liquid-air interface on thermodynamic equilibrium state [12]. According to some research [11,12] and by neglecting the non-wetting phase (since liquid capillarity becomes dominant in transport process), the governing equation for wetting phase driven by capillary pressure can be expressed as simple as:

$$\rho_w \cdot \emptyset \cdot \frac{\partial S_w}{\partial t} = -\boldsymbol{\nabla} . (D_w(T, S_w) \cdot \boldsymbol{\nabla} S_w) \tag{4}$$

The transport coefficient of wetting phase D_w can be modelled with a Darcy's law [10] upon pressure gradient combined with an Arrhenius law of temperature variation:

$$D_w(T, S_w) = \left(\rho_w(T) \cdot \frac{\partial P_c(S_w)}{\partial S_w} \cdot \frac{K \cdot k_{rw}(S_w)}{\eta_w(T)} \cdot f_w(S, \emptyset) \right) \cdot e^{\frac{Q}{R}\left(\frac{1}{T_0}-\frac{1}{T}\right)} \tag{5}$$

where $P_c(S_w)$ is the capillary pressure (function of saturation) derived from material's main isotherm curves [23]. K is the intrinsic permeability of medium, k_{rw} is the pore relative

permeability to wetting phase, η_w is the viscosity of wetting phase and f_w is the tortuosity factor related to the complexity of pore microstructure.

To decide the appropriate D coefficient to use in different transport modes, a 'hybrid model' was introduced here. Let us introduce a general pore saturation degree S and the density ρ as state variable (may be different according to temperature), we can have one single equation for all scenarios:

$$\rho \cdot \emptyset \cdot \frac{\partial S}{\partial t} = -\nabla.(D \cdot \nabla S) \quad (6)$$

The 'hybrid model' interprets how to determinate the right equation to integrate with the correct transport coefficient by the following switching algorithm based on local element hygroscopic state. Whenever local material element is in contact with wetting front (on its adjacent position/element, water saturation changes with a positive rate ≥ 0 and saturation passes the liquification threshold level $S \geq 0.95$ [24]) (Fig. 2)

$$\begin{cases} S = S_w, \rho = \rho_w, D = D_w \; if \; \dot{S} \geq 0 \; and \; S \geq 0.95 \; (liquid \; capillary \; suction) \\ S = S_{nw}, \rho = \rho_{nw}, D = D_{nw} \; if \; \dot{S} < 0 \; or \; S < 0.95 \; (water \; vapor \; diffusion) \end{cases} \quad (7)$$

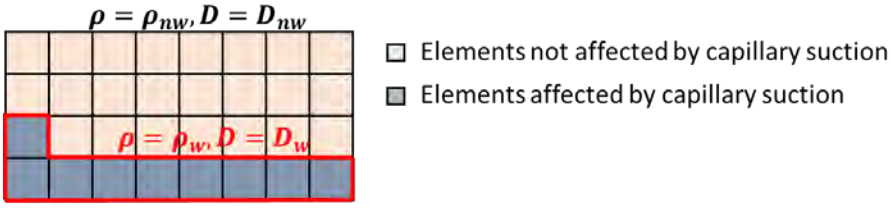

Figure 2: Numerical interpretation of the "Hybrid model"

The integrated form of Eq. (6) was then discretized and solved with a FEM computation program TransChlor2D ® [25] with given initial and boundary water saturation conditions.

3. SIMULATION RESULTS ON WATER ABSORPTION TEST AT AMBIANT TEMPERATURE

A unidimensional water absorption test from Lunk [20] was simulated in this paper to validate the performance of the implemented hybrid transport model algorithm.

Table 1 provides some important properties and transport parameters used for the simulation of the studied samples. Cement type used for all concrete samples were Portland CEM I 42.5R with properties and compositions in accordance with norm SN EN 197-1 [26].

Table 1: Water transport properties of the Lunk samples [20].

Properties	**A**	**B**	**C**
Cement type	CEM I 42.5	CEM I 42.5	CEM I 42.5
Cement (kg/m^3)	400	350	310
Water (kg/m^3)	160	175	186
Density (kg/m^3)	2445	2412	2388

Porosity	0.1024	0.119	0.133
D_{nw0} **(m²/s)**	5E-11	1.27E-10	1.7E-10
K **(m²)**	1.5E-21	3.7E-21	5.5E-21

The test consists in merging three different cuboid concrete samples with different formulation in brine container and measuring their water content evolution inside and alongside over time (2h, 24h, 72h), as shown in Fig. 3a). Samples were initially dried and kept at 75% RH and their lateral surfaces were sealed by resin. Only the bottom faces are immerged into a 3% NaCl solution. The chamber temperature was maintained at 20°C during the test.

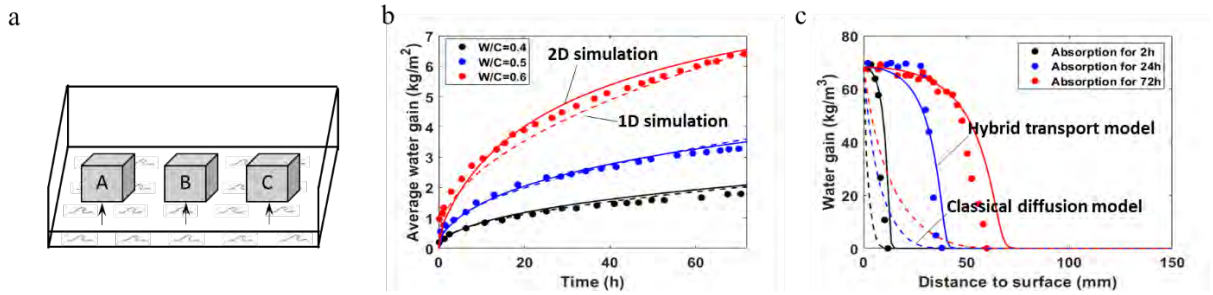

Figure 3: Simulation results on Lunk's water absorption test at 20°C (273K): a) test setup b) average mass water gain c) water gain distribution over height.

The numerical simulation results on average water gain in concrete porosity, with 2D implementation of transport equations, are compared with experimental data from all three concrete mixtures (Fig. 3b). A good correlation was observed between model prediction and real results. Additionally, the simulation results with 1D implementation of same equations were also compared, showing very similar tendency. The very little difference between 1D and 2D simulations should come from the different mesh densities and integration schemes (1D:2 Gauss points and 2D: 4 Gauss points) chosen for FEM computation.

In particular, the water saturation profiles at 2h, 24h, and 72h were extracted from simulated saturation field values and compared with results measured in laboratory (Fig. 3c). The simulated profile matches quite well the experimental data set and captures well the rapid water penetration into concrete especially during the first few hours of absorption. Then, a comparative transport model, with only diffusion equations, was also implemented and the simulation results are far from satisfying. By comparison we can tell it is impossible to obtain a concave water profile with only a diffusion law and calculation based on it will lead to signification underestimation in water content variation, whereas our implementation of capillarity part into the governing equation of TransChlor2D® compensated this systematical error successfully.

4. SIMULATION RESULTS ON WATER ABSORPTION TEST AT DIFFERENT TEMPERATURES (-20°C TO 10°C)

Experimental results from Conciatori [21] showed that the external temperature has a significant impact on the capillary suction process. One of the concrete mixtures casted

(referred by sample A in [21]) is composed with 375 kg/m^3 of cement CEM I 42.5 and 154 kg/m^3 of water. The density is 2450 kg/m^3, the porosity is 0.12, the diffusion coefficient D_{nw0} (m^2/s) is 6E-11 m^2/s and the permeability K is 8.5E-22 m^2. Cylindric concrete specimens were merged in a temperature and humidity-controlled basin filled with salt solution (27%) for 7 days (Fig. 4a). Lateral and top surfaces of cylinders were sealed by resin to have only 1D capillary suction along height. Four different temperatures were applied on each group of samples (-20°C, -10°C, 0°C, 10°C) and the mass samples were registered every 15 mins. Temperature dependent parameters of salt solution are given here in Table 2.

Table 2: Transport properties related to temperature impact.

Properties	**10°C**	**0°C**	**-10°C**	**-20°C**
ρ_w **(kg/m^3)**	1207	1208	1208	1208
Q (kJ/mol)	75216	5477.1	16804	-361840
Porosity ϕ	0.12	0.12	0.12	0.12/0.018*

* porosity after correction

Experimental results on samples A showed the significant impact of temperature on capillary suction process and our capillary model equipped with Arrhenius law correctly predicted it (Fig. 4b). Above -10°C, salt solution remains liquid and its movement into porosity obeys an ordinary Darcy's law. Higher external temperature leads to a higher transport coefficient thus a higher water suction rate, as observed from the simulated curves. At -20°C, however, a sharp decrease of the amount of water absorbed by capillarity was observed in experimental data points. This requires a correction factor applying on material's porosity since formation of freezing ice in pores will largely reduce porous space. An abnormal negative activation energy at this temperature was also observed. Comparing to real data, a slight overestimation on the amount of water absorbed can be also found in model prediction, this may be due to some minor effects neglected in numerical assumptions such as: 1) Cement hydration or other chemical reactions that consume water 2) Phase change of water (liquid to vapor, liquid to ice). Besides that, the new TransChlor2D® exhibits good performance in capturing the temperature impact while modelling capillary suction in the transport process.

a

b

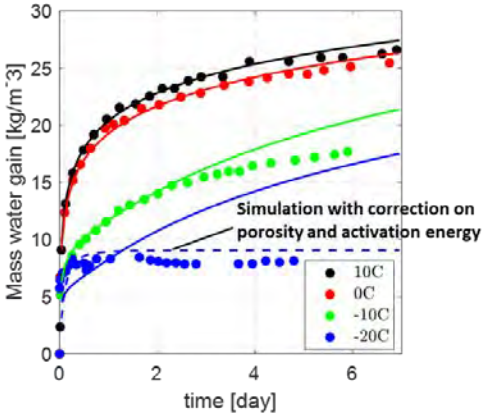

Figure 4: a) Experimental setup for capillary absorption test in temperature-controlled basin [10] b) results on water mass gain at different temperatures.

5. CONCLUSIONS

In this paper, a new FEM pore water transport model for unsaturated concrete was presented, as an extension to the previous chloride corrosion prediction computation program TransChlor ®. In this model, the wetting phase transport in concrete pore structure was modelled with a Darcy's law and the non-wetting phase transport was modelled with a classical Fick's law of diffusion. The combination of the two constitutive laws was realized with a switching algorithm, based on material's hygroscopic state (whether affected or not by capillary suction). Temperature effect on capillarity was modelled with an Arrhenius law.

Two water absorption tests were studied here to validate the model: one at room temperature and the other one at different temperatures. The model showed good overall performance in simulations and an excellent capacity in capturing the capillary suction as well as the temperature impact on it.

The following conclusions can be drawn from numerical analysis:

- Capillary suction happens quite faster than normal diffusion process. In transport model, capillary suction should be coupled with a traditional diffusion model and a switching algorithm.
- Compared to the Fick's law used in most transport models, Darcy's law better captures the capillary suction
- Temperature has an important impact on capillary suction. Higher temperature tends to accelerate the capillary suction process and this effect was considered with an Arrhenius law coupled with capillary transport coefficient. Specifically, at -20°C, the freezing effect in concrete pores will lead to a huge reduction in concrete's sorptivity. This effect was considered in capillary model by a reduction of the overall material porosity.
- The use of a 2D model allows to treat more ambitious exposure conditions, such as underground water, splash/tide zone and floating structures.

To improve the simulation results, further model refinement should be done to consider the chemical reactions, physical binding and phase change models involving the water participation. As the whole transport model presented in this paper was developed in a 2D framework, the

simulation of structures under more complex exposure conditions could be considered and simulated properly.

REFERENCES

[1] F. Pruckner, Corrosion and Protection of Reinforcement in Concrete Measurements and Interpretations, *na*, (2001).
[2] S. Qian, D. Cusson, Electrochemical evaluation of the performance of corrosion-inhibiting systems in concrete bridges, *Cem. Concr. Compos*. 26 (2004) 217–233.
[3] M.H.F. Medeiros. P. Helene, Surface treatment of reinforced concrete in marine environment: Influence on chloride diffusion coefficient and capillary water absorption, *Construction and Building Materials*, 23 (2009) 1476–1484.
[4] Nicos S. Martys, Chiara F. Ferraris, Capillary transport in mortars and concrete, *Cem. Concr. Res*, Volume 27, Issue 5, 1997, Pages 747-760.
[5] Ilker Ustabas, The effect of capillarity on chloride transport and the prediction of the accumulation region of chloride in concretes with reinforcement corrosion, *Construction and Building Materials*, 28 (2012) 640–647.
[6] D. Conciatori, H. Sadouki, E. Brühwiler, Capillary suction and diffusion model forchloride ingress into concrete. *Cem. Concr. Res.*138 (2008) 1401–1408.
[7] Bazant, Z.P.; Najjar, L.J. *Matériaux et Construction*, 1972, 5, 3-20.
[8] Xi, Y., Bazant, Z. P., and Jennings, H. M. (1994a), Moisture diffusion in cementitious materials. Moisture capacity and diffusivity, *Advanced Cement Based Mat*., 1, 258–266.
[9] Xi, Y., Bazant, Z. P., and Jennings, H. M, Moisture diffusion in cementitious materials Adsorption isotherms, *Advanced Cement Based Mat*., 1, 248-257.
[10] Coussy, O., Mechanics of porous continua, Wiley, New York, 2010.
[11] M. Mainguy, O. Coussy, V. Baroghel-Bouny, Role of air pressure in drying of weakly permeable materials, *J. Eng. Mech*. 127 (2001) 582–592.
[12] Zhidong Z., Mickaël T., Véronique B. Numerical modelling of moisture transfers with hysteresis within cementitious materials: Verification and investigation of the effects of repeated wetting–drying boundary conditions. *Cem. Concr. Res*, 68 (2015) 10–23
[13] D. Conciatori, F. Laferrière, E. Brühwiler, Comprehensive modeling of chloride ion and water ingress into concrete considering thermal and carbonation state for real climate, *Cem. Concr. Res*, 40 (2010) 109–118
[14] D. Conciatori, E. Denarié, E. Brühwiler, Influence of microclimate on the probability of initiation of chloride induced corrosion in reinforced concrete, 4th Int. PhD Symp. Civ. Eng., Munich, Germany, 2002 (p. 7p).
[15] T. Luping, L.-O. Nilsson, Chloride binding capacity and binding isotherms of OPC pastes and mortars, *Cem. Concr. Res*. 23 (1993) 247–253.
[16] T. Sanchez, D. Conciatori, F. Laferriere, L. Sorelli, Modelling capillary effects on the reactive transport of chloride ions in cementitious materials, *Cem. Concr. Res*. 131 (2020) 106033.
[17] D.L. Parkhurst, C.A.J. Appelo, Description of Input and Examples for PHREEQC Version 3 – A Computer Program for Speciation, Batch-reaction, One-dimensional Transport, and Inverse Geochemical Calculations, (2013).
[18] D.L. Parkhurst, C.A.J. Appelo, User's Guide to PHREEQC (Version 2): A Computer Program for Speciation, Batch-reaction, One-dimensional Transport, and Inverse Geochemical Calculations, (1999).
[19] Taheri-Motlagh A., *Durability of reinforced concrete structures in Aggressive marine environment*, Delft University of Technology, 194, Delft, Hollande, November 1998.
[20] P. Lunk. Penetration of Water and Salt Solutions into Concrete by Capillary Suction. Internationale Zeitschrift für Bauinstandsetzen 4. Jahrgang. 399-422. (1998).
[21] D. Conciatori. Essai d'absorption capillaire à basses températures appliqué à des bétons de différentes perméabilités. Rapport d'essai n° 02.09-01

[22] L. Chunqiu，L. Kefei. Moisture transport in concrete cover under drying-wetting cycles: theory, experiment and modeling. *Journal of the Chinese Ceramic Society*. Vol. 38 No.7 July 2010.
[23] Véronique Baroghel-Bouny. Water vapour sorption experiments on hardened cementitious materials Part I: Essential tool for analysis of hygral behaviour and its relation to pore structure. *Cem. Concr. Res*, 37 (2007) 414–437
[24] Meiqian Wang, Jian Zhang, Qiang Xu,* and Kuyen Li, Thermodynamic-Analysis-Based Energy Consumption Minimization for Natural Gas Liquefaction, *Ind. Eng. Chem. Res*, 2011, 50, 12630–12640
[25] X. Chen., T. Sanchez., D. Conciatori, H. Chaouki, Numerical modelling of 2D water transport in unsaturated concrete with capillary effect, in review preparation, *Cem. Concr. Res*
[26] CAN Fiches techniques, *Ciment selon la norme SN EN 197-1:2011*, www.crb.ch

INFLEUNCE OF THE POROUS NETWORK ON CHLORIDE DIFFUSION IN PRESENCE OF SULPHATE

M. Saillio (1), V. Baroghel-Bouny (2), M. Bertin (2), B. Mohamed (2), J. Vincent (1) and J.B. D'Espinose de Lacaillerie (3)

(1) CPDM, IFSTTAR – Paris-Est University, France

(2) FM2D, IFSTTAR – Paris-Est University, France

(3) SIMM – ESPCI Paris, France

Abstract

The main cause of premature deterioration of reinforced concrete structures is the corrosion of steel bars, induced by chloride ions (for example in marine environment). At the same time, environmental-induced degradations of concrete can also affect the structure, such as external sulphate attack leading to the formation of ettringite, inducing expansion inside the materials and finally degradation.

In this paper, chloride ingress are studied for concretes and cement pastes or/and in presence of sulphate in chloride contact solution. The mixtures contain OPC alone or with SCM. SCMs are here pozzolanic materials (Fly Ash or Metakaolin) or alkali-activated materials such as ground granulated blast furnace slag (GGBS). The materials are put in contact with chloride solutions in presence of sulphate. This study focuses on the influence of the porous network on the apparent chloride diffusion coefficients, as well as on chloride binding isotherms which are obtained by the profile method. Various aspects of the microstructure and of the pore structure are investigated, by using Mercury Intrusion Porosimetry and ^{27}Al NMR, in order to better understand the results obtained relatively to the apparent chloride diffusion coefficients and to the chloride binding.

Results show the difference between the various microstructures of the materials and their consequences on chloride/sulphate ingress. In addition, chloride ingress increases when sulphates are present in the contact solution for all cement materials tested. It appears that presence of sulphate decrease chloride binding, thus explaining the results.

Keywords: Durability, Sulphate, Chloride, SCM, Porous network

1. INTRODUCTION

Corrosion of steels bar is one of the main causes of reinforced concrete degradation [1-3]. This corrosion can be induced by chloride ingress in marine environments or in the presence of deicing salts. In addition, local environment can contain sulphate which may react with the cementitious matrix leading to the formation of ettringite. Thus, this can induce expansion and

finally degradation inside the materials [4]. Numerous studies describe these two phenomena separately but a few studies state a possible coupling [5-6].

There are few parameters which influence these ingress and in particular, the porous network. In addition, Chloride ingress is delayed by interactions between chlorides and the cementitious matrix [7-9] and the same for sulphate ingress. Consequently, both sulphate and chloride react with the same cementitious phases (C-S-H or aluminates phases) and a competition between these two ions can occur in marine environment [5-7].

These coupled phenomena should be taken into account particularly when the concrete mixture contains supplementary cementitious materials (SCMs). Binders which contain, for example, ground granulated blast furnace slag (GGBS) are used in marine environment since the chloride diffusion coefficient of GGBS-mixtures is significantly reduced which is mainly due to the modification of the porous network [2] as also expected for binder with fly ash (FA) and métakaolin (MK) [8-9]. However, in general, these concrete need a longer water curing time to reach their full performances. In addition, the phase assemblage is quite different as function of the SCM used in the concrete. Competition between chlorides and sulphates are not very well known in these binders [10]. With regard to chemical binding, since the aluminates phase content is different in the mixture, the reactions between ions and these phases should be different. The type of C-S-H produced during hydration is a function of the composition of the mixture (C/S, substitution to Si by Al,…). Consequently, physical binding should also be different between cementitious materials with or without SCMs.

The aim of this research is first to investigate the porous network of cement pastes (OPC alone or with SCMs) in order to then, understand the chloride ingress in presence of sulphate in NaCl contact solutions. In particular, chloride diffusion tests were performed in presence or not of sulphate in contact solution. The microstructure is investigated here by Mercury Intrusion Porosimetry (MIP), thermogravimetry (TGA-DTG), and ^{27}Al NMR spectroscopy. In addition, an experimental campaign has been carried out on a concrete with fly ash, which is exposed during 20 years at marine conditions.

2. EXPERIMENTAL

Various concretes were designed with the same clinker and granular squeleton using siliceous aggregates. The main constituents of the clinker are given in table 1. The water-to-binder ratio (w/binder) is equal to 0.50 for all cement paste. Studied binders are CEM I (OPC with 97% clinker), CEM III/A (with 62% GGBS) denoted CEM III GGBS(62%), CEM III/C (with 82% GGBS) denoted CEM III GGBS(82%), CEM I + 20% FA denoted CEM I FA(20%), CEM I + 30% FA denoted CEM I FA(30%), CEM I + 40% FA denoted CEM I FA(40%), CEM I + 10% MK denoted CEM I MK(10%) and CEM I + 25% MK denoted CEM I MK(25%). Various water-curing times are chosen (7 days to 1 year) in order to take into account the evolution of the microstructure as a function of the age.

After water curing, slices of materials are covered with aluminum sheets except one face (unidirectional tests). They are put in contact with various NaCl solutions. Contact solutions are denoted P1 (0.5 M NaCl + 0.1 M NaOH) , P2 (2.8 M NaCl) and P3 (0.5 M NaCl + 0.06 M Na_2SO_4). The profile method is used in order to obtain the apparent chloride diffusion coefficients ($D_{app,Cl}$) and the chloride binding isotherms (CBIs) [9,11].

In addition, a “real” concrete, denoted M30CV (with CEM I and fly ash, W/B=0.52 and limestone aggregates), was exposed to marine environment (La Rochelle) during 20 years in

order to compare natural exposure and accelerated procedure. The microstructure of the cement pastes and the concrete is characterized by MIP, TGA-DTA and ^{27}Al nuclear magnetic resonance magical angle spinning spectroscopy (NMR MAS) [8-10].

Table 1: Chemical composition of the cement and SCM tested (%).

	CaO	SiO_2	Fe_2O_3	Al_2O_3	TiO_2	MgO	Na_2O	K_2O	MnO	SO_3
CEM I	62.5	19.5	2.9	4.9	0.3	0.8	0.3	0.8	0.0	2.9
CEM III/A	49.7	29.8	1.2	8.1	0.4	4.6	0.4	0.5	0.1	2.2
CEM III/C	45.7	32.0	1.0	9.9	0.5	5.8	0.6	0.5	0.2	2.0
MK	2.00	66.2	4.2	21.3	1.1	0.2	0.8	0.4	0.0	0.1
FA	4.30	51.5	6.5	23.7	1.0	0.4	1.0	3.0	0.1	3.1

3. RESULTS AND DISCUSSION

Figure 1 shows the pore size distribution (S) of various cement pastes after 365 days of water curing. The main peak of this distribution observed for CEM I is reduced and/or shifted to smaller pore when cement pastes contain SCM as also observed on the average porous diameters (D_p). Filler effect, slag activation and pozzolanic reactions are responsible of these results [12-13]. In addition, figure 1 and figure 2 indicate a strong effect of water curing time on S, D_p and the porosity (P_{Hg}) for all cement paste. The main peak of S is reduced and/or shifted to smaller pores and both D_p and P_{Hg} values decrease. However, this effect depend on the SCM. For CEM I, stabilization occurs between 7 and 28 days. For the other cement pastes, it continues to evolve until 365 days. In general, it is considered that slag activation and pozzolanic reactions have slower kinetics than clinker hydration explaining the results [12-14].

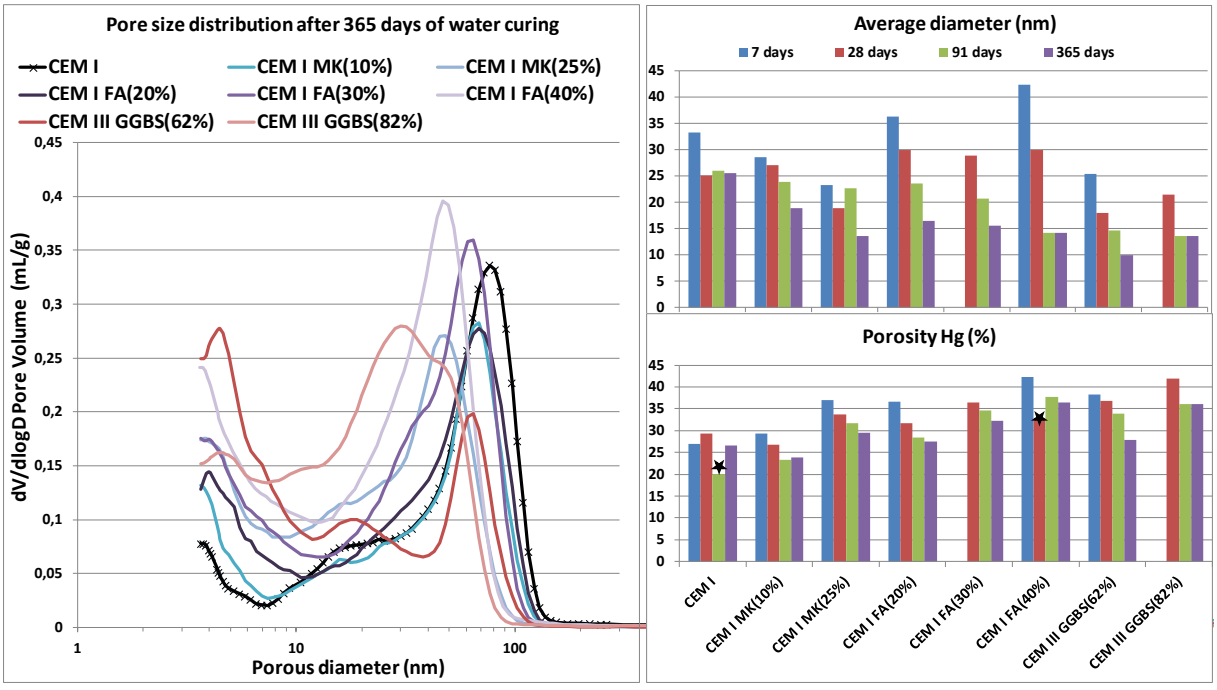

Figure 1: Pore size distribution, average pore diameter and porosity obtained by MIP. *: aberrant values.

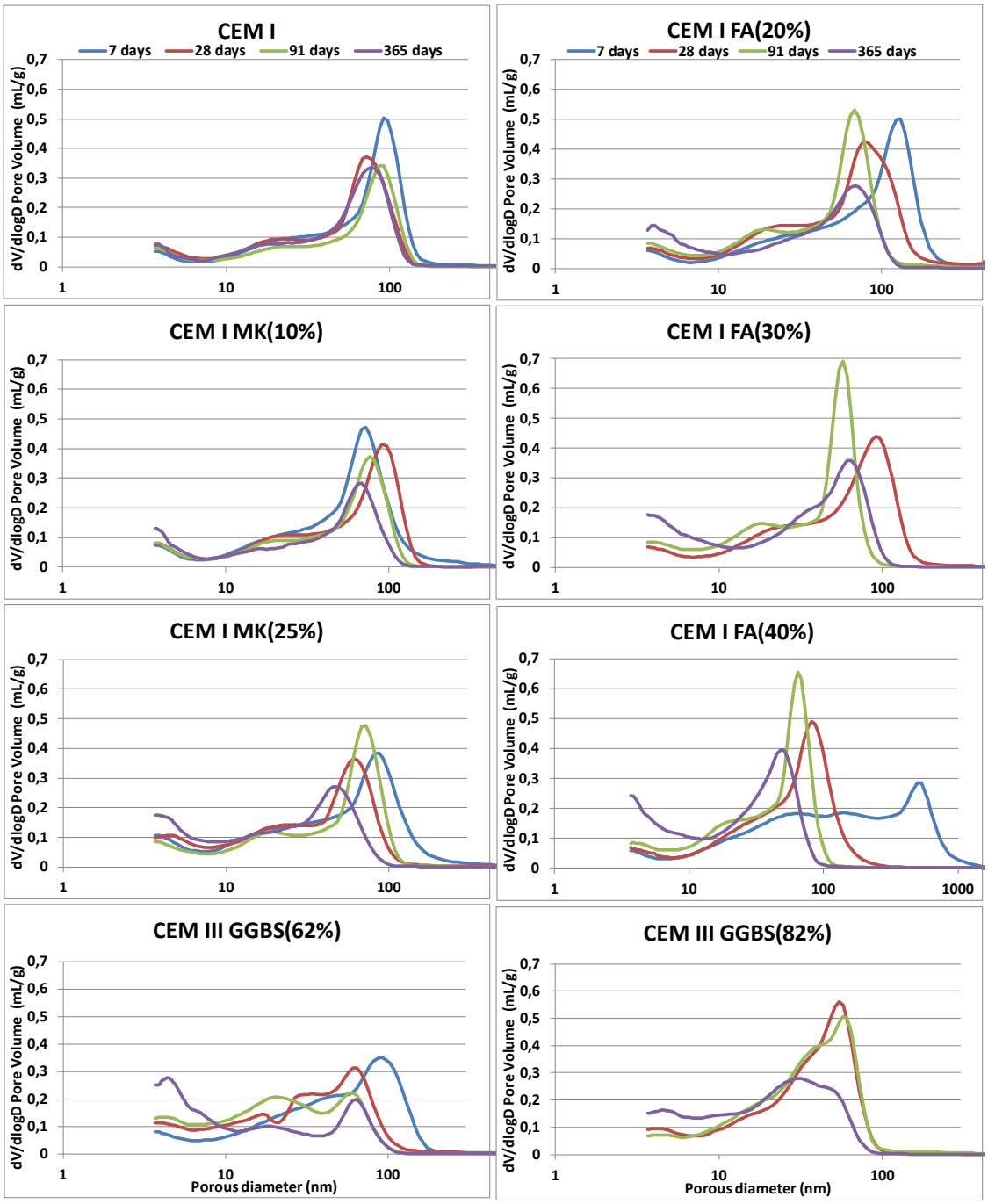

Figure 2: Pore size distribution as a function of water curing time obtained by MIP

The effect on S and D_p is more marked for cement paste with fly ash than the other materials meaning that hydration of fly ash has a slower kinetic in comparison to slag or metakaolin ones.

Fig. 3 shows $D_{app,Cl}$ results obtained by the profile method without or with sulphate in the contact solution. Without sulphate (P1 and P2), $D_{app,Cl}$ decreases when materials contain SCM as already observed [2]. These observations can be directly link to the results obtained by MIP.

In fact, a filler effect and a lower D_p mean that the connectivity decreases and the tortuosity increases, explaining why $D_{app,Cl}$ of cement paste with SCM are lower than these of CEM I. However, the results presented here are obtained on materials after 365 days of water curing. Since the porous network continues to evolve until 365 days for cement pastes with SCM, $D_{app,Cl}$ evolve too depending of the state of hydration. In addition, some cementitious matrices with SCM can bind more chloride than CEM I which also decreases the $D_{app,Cl}$ [8].

Comparing P1 with P3, $D_{app,Cl}$ increases in presence of sulphate. In addition, comparing P3 with P2, the $D_{app,Cl}$ values obtained are generally superior to those obtained for a contact solution with a very higher chloride content (except for cement paste with GGBS where the values are equal). This means that the presence of sulphate is highly detrimental regarding the durability against chloride ingress. There is no visible crack at the surfaces of the cylindrical samples, after contact with P3 solution but previous studies [4,6] reported possible microcraks which can explain the increase of chloride ingress. In addition, the cementitious matrix binds more chloride in the case of P1 than in presence of sulphate in the NaCl contact solution as shown by CBIs (see Fig. 3). There is a higher binding capacity of cementitious matrix for sulphate than for chloride [7] explaining the results of the present study. In addition, ^{27}Al NMR profiles of the exposed materials were obtained and specially on the surface of the sample in contact with P1 and P3 solutions (see Fig. 4). These samples are assumed to be at the equilibrium between the cementitious matrix and the contact solution. Samples in contact of P3 exhibit more AFt phases (ettringite) than samples in contact of P1. This increase affects all other aluminates phases (but depending on the SCM type) and especially, these aluminates phases are needed to form Friedel's salt. Chloride chemical binding is thus limited with the presence of sulphate in the contact solution. Chloride physical binding decreases too as shown in other studies [5,7].

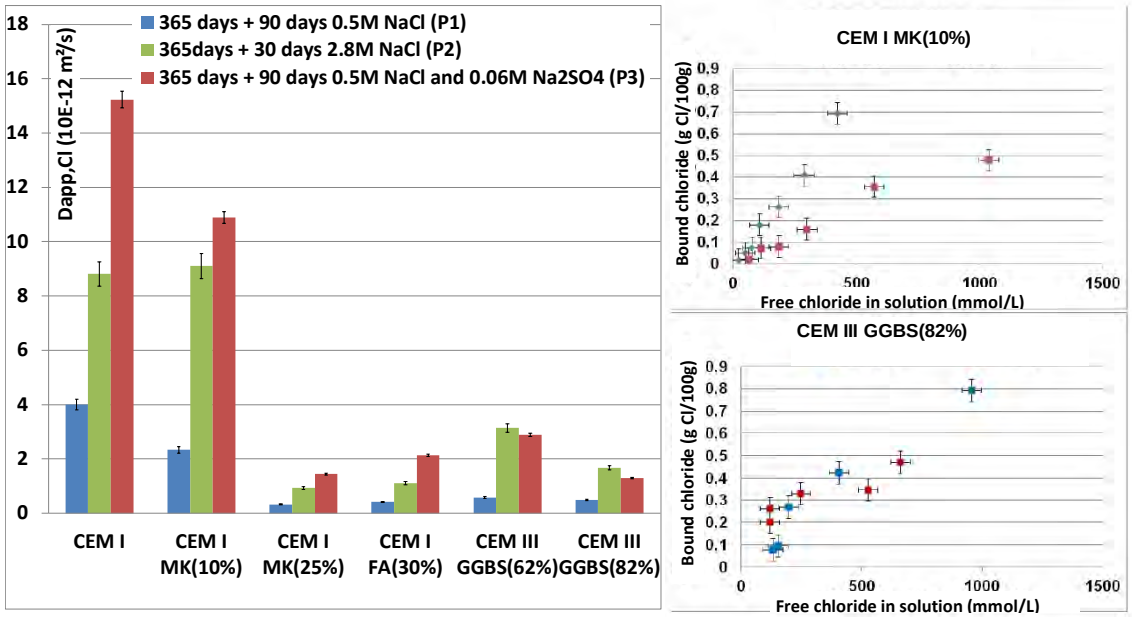

Figure 3: Chloride apparent coefficients (Dapp,Cl) (in left) and CBIs obtained by profile method on cement pastes after 365 days of water curing and contact with solutions.

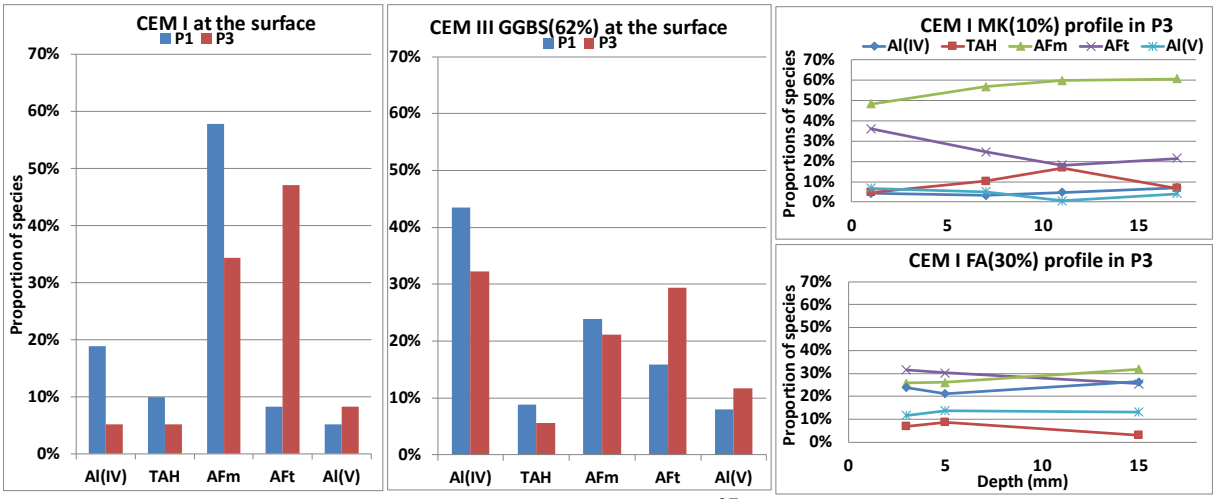

Figure 4: Proportion of Al species obtained by ^{27}Al MAS NMR after exposition to contact solution P1 and P3. Al(IV) and Al(V): aluminum substituted in C-S-H chains. TAH: amorphous/disordered aluminate phase.

This competition between these two ions can explain the good result for CEM I MK(25%). As a matter of fact, this cementitious material has the highest binding capacity as reported in the literature [8] and consequently more chloride can be bound despite the presence of sulphate. The increase of chloride ingress is thus limited in this last case. In addition, CEM III GGBS(82%) have one of the best performance in this diffusion test. A lower porous connectivity (due to filler effect and slag activation) can explain this results for this materials.

Finally, profile of a concrete (M30CV), which is exposed during 20 year to natural sea environment, is characterized by various technics (Fig. 5). The evolutions observed give similar results for all technics used. Close to the surface (0-11mm), there is of course ettringite but also the presence of Friedel's salt, however the ratio free Chloride on bound chloride is the highest measured of all depth and moreover, SO_3 concentration is the highest. This means a competition between chloride and sulphate to bind to cementitious matrix and consequently cementitious matrix bind less chloride in presence of sulphate. Deeper inside the concrete (13-23mm), ettringite amount is considerably reduced (as well as SO_3 concentration) and amount of Friedel's salt seem to be higher confirmed by elementary analysis showing the highest amount of bound chloride. At 34-44mm, ettringite amount is equal to its surface amount and it seems there is solid solution between Friedel's salt and hemicarboaluminate. At 55-60mm, there is still traces of Friedel's salt, which is in accordance with chloride front measured at 93mm, but the main AFm phases are hemicarboaluminate and monocarboaluminate. The presence of these two phases deep inside is due to aggregates used ($CaCO_3$) in concrete which can react with the aluminates of the cement during hydration and form these type of AFm phases. At 117-132mm, there is no sign of Fridel's salt. In resume, most of the results on these concrete are in accordance with results obtained by accelerated measured. However, there are differences (e.g. aluminates equilibrium for the point at the surface) which is due to variable exposure conditions in sea comparing to controlled conditions in lab. In fact, in sea, there is other ions such Mg^{2+}, which can react with cementitious matrix and influence the transport of chloride and sulphate inside the materials.

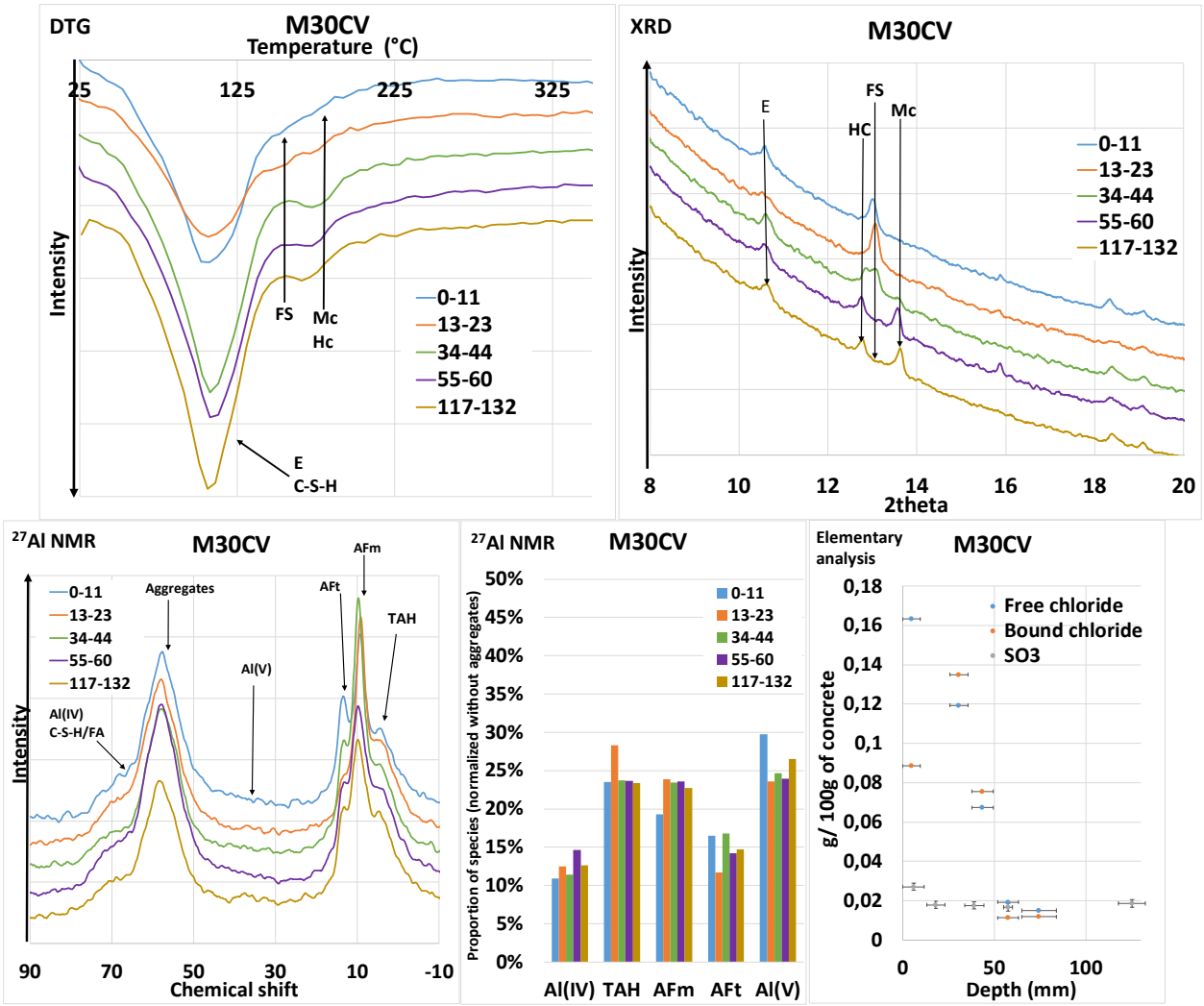

Figure 5: DTG, XRD, ^{27}Al NMR and elementary profiles (mm) of a concrete exposed to sea during 20 years. E: ettringite, FS: Friedel's salt, Mc: monocarboaluminate and Hc: hemicarboaluminate. Chloride front (measured by $AgNO_3$) is equal to 93mm.

4. CONCLUSIONS

This research aimed to investigate the effect of the porous network on diffusion properties and also the combined effects of sulphate on chloride ingress for various concretes and cement pastes.

The experimental results demonstrated that the porous network is different as SCM is used in the mixture. At long term, using SCM in cement paste upgrades the porous network (Average diameter decreases and tortuosity probably increases) despite the increases of the global porosity for some materials. In addition, the water curing time is fundamental for the development of the porous network in order to obtain the best performance of the materials, in particular for concrete with SCM.

Consequently, Chloride ingress is less marked in cement pastes with SCM. In addition, chloride ingress is accelerated by the presence of sulphate in contact solution. This increase is

explained by a change in the microstructure and the pore solution but also by a lower chloride binding. With regard to chloride ingress, there are differences between the various cementitious matrices. Cementitious matrixes with high metakolin or slag content are more resistant to the effect of the presence of sulphate in the contact solution.

Finally, comparison of these results with a concrete in real sea conditions is difficult since the presence of other parameters such pH, temperature, contact solution with other ions (Mg^{2+}, …). However, it is quite promising because the different technics used (XRD, TGA and ^{27}Al NMR) in order to establish a profile, show the same results.

REFERENCES

[1] Villain, G., Thiery, M. and Platret, G. 'Measurement of carbonation profiles in concrete: Thermogravimetry, chemical analysis and gammadensimetry'. *Cem. Concr. Res*.**37**(2007)1182-1192.

[2] Bouteiller V., Cremona C., Baroghel-Bouny V. and Maloula, A. 'Corrosion initiation of reinforced concretes based on Portland or GGBS cements: chloride contents and electrochemical characterizations versus time'. *Cem. Concr. Res*.**42**(2012)1456-1467.

[3] Castellote, M., Fernandez, L., Andrade, C. and Alonso, C. 'Chemical changes and phase analysis of OPC pastes carbonated at different CO2 concentrations'. *Cem. Concr. Res*.**42**(2009)515-525.

[4] El-Hachem, R., Rozière, E., Grondin, F. and Loukili A. 'New procedure to investigate external sulphate attack on cementitious materials'. *Cem. Concr. Comp*.**34**(2012)357-364.

[5] Balonis, M., Lothenbach, B., Le Saout, G. and Glasser, F.P. 'Impact of chloride on the mineralogy of hydrated Portland cement systems'. *Cem. Concr. Res*.**40**(2010)1009-1022.

[6] Maes, M. and De Belie, N. 'Resistance of concrete and mortar against combined attack of chloride and sodium sulphate'. *Cem. Concr. Comp*.**53**(2014)59-72.

[7] Henocq, P. *Modeling Ionic Interactions on the Surface of Calcium Silicate Hydrates, in French*. PhD. Thesis, Laval University, 2005.

[8] Saillio, M., Baroghel-Bouny, V. and Barberon F. 'Chloride binding in sound and carbonated cementitious materials'. Construction and Building Materials.**68**(2014)82-91.

[9] Baroghel-Bouny, V., Wang, X., Thiery, M., Saillio, M. and Barberon F. 'Prediction of chloride binding isotherms of cementitious materials by analytical model or numerical inverse analysis'. *Cem. Concr. Res*.**42**(2012)1207-1224.

[10] Geng, J., Easterbrook D., Li L.Y. and Mo L.W. 'The stability of bound chlorides in cement paste with sulfate attack'. *Cem. Concr. Res*.**68**(2015)211-222

[11] Baroghel-Bouny, V., Kinomura, K., Thiery, M. and Moscardelli, S. 'Easy assessment of durability indicators for service life prediction or quality control of concretes with high volumes of supplementary cementitious materials'. *Cem. Concr. Comp*.**33**(2011)832-847.

[12] Saillio, M., Baroghel-Bouny V., Bertin, M., Pradelle, S. and Vincent, J. 'Phase assemblage of cement pastes with SCM at different ages'. *Construction and Building Materials.***224**(2019)144-157.

[13] Bullard, J.W. et al. 'Mechanisms of cement hydration'. *Cem. Concr. Res.***41**(12)(2011)1208-1223.

[14] Kolani, B. et al. 'Hydration of slag-blended cements'. *Cem. Concr. Comp*.**34**(9)(2012)1009-1018.

INFLUENCE OF THE RELATIVE MOLECULAR MASS OF VISCOSITY ENHANCERS ON CHLORIDE DIFFUSION IN MORTARS: A PERLIMINARY STUDY

Lixiao Zhao (1), Pan Feng(1)(2)

(1) School of Materials Science and Engineering, Southeast University, China

(2) State Key Laboratory of High Performance Civil Engineering Materials, China

Abstract

Chloride diffusion in concrete is one of the key parameters of durability design for structure. Existing methods of reducing the chloride diffusion such as decreasing water-cement ratio and adding mineral admixtures often lead to increase the risk of concrete cracking. In this study, we focused on mitigating the permeation of chloride ions in concrete by adding viscosity enhancers to improve the viscosity of concrete pore solution, without densifying the pore structure of concrete. A comparative study was conducted among the conductivity of KCl solutions with the addition of polyethylene glycol (PEG) with 11 different relative molecular masses. The results show that the chloride diffusion can be most effectively reduced when the relative molecular mass remains in the range of 400-1500.

Keywords: Viscosity enhancer, Chloride diffusion, Relative molecular mass, Conductivity

1. INTRODUCTION

As one of the most widely used building materials in the world, the durability of cement-based materials has attracted extensive attention. It is well known that steel corrosion is the biggest threat to the durability of reinforced concrete [1-2]. Corrosion of reinforcement is generally caused by electrochemical process which is triggered by chloride ions from the external environment to the surface of reinforcement passing through concrete matrix, which serves as the protective layer. Therefore, the permeability of chloride ions in concrete is one of the key parameters that affect the service life of reinforced concrete structures [3-4].

Currently, to reduce the permeability of chloride ions in concrete, we usually decrease the water-cement ratio or add mineral admixtures [5]. But these methods inevitably increase the compactness of concrete, accordingly, these will increase the risk of concrete cracking and the dead load of the structure. Is there a way to reduce the permeability of chloride ions without increasing the density of the structure? The literatures published in 2008 [6] and 2010 [7] proposed an innovative way to reduce the diffusion coefficient of chloride ions by increasing the viscosity of pore solution of cement-based materials, by adding nanomolecule viscosity enhancers. Kenneth et al. [8] extended for the research in [7], and through a year's exposure

experiments, it was found that after adding small molecular viscosity enhancer, the effective diffusion of chloride ions in the mortar can be reduced by nearly a factor of two, and the method that adding prewetted fine lightweight aggregate with viscosity enhancer can achieve a better effect. Bentz et al. [9] clarified the influence of several different ways of adding viscosity enhancer on chloride ions penetration in concrete mixed with fly ash and slag, as well as its adverse influence on the strength development of concrete. Qiao et al. [10] explored the effects of shrinkage-reducing agent (SRA) on isothermal drying, ion diffusion and water permeability of concrete, and perceived that chloride ions permeation was reduced for concrete with higher SRA content. In fact, SRA is also one of the viscosity enhancers.

Almost all studies have shown that adding appropriate viscosity enhancer have the ability to restrain chloride ions diffusion in concrete. We can regard the diffusion rate of ions in solution as being inverse proportional to the viscosity of the solution based on the Stokes-Einstein equation [6, 11]. However, it is noticeable that, limited by the coverage of Stokes-Einstein equation [12-13], the key to whether a viscosity enhancer can effectively reduce chloride diffusion is the relative molecular mass, which must be small, as Bentz et al [6] also pointed out. In the previous studies, the appropriate range of relative molecular mass of viscosity enhancer used to reduce the diffusion coefficient of chloride ions has not been paid much attention, and most researchers have only used commercial shrinkage-reducing agent as viscosity enhancers for their projects.

In this paper, we used polyethylene glycol (PEG) with different relative molecular mass as viscosity enhancers to preliminarily study the resistance to chloride diffusion in aqueous solution. Here, the diffusivity of chloride ions was estimated by the conductivity of 0.1mol/L KCl solution, using the direct proportional relationship between solution conductivity and ion diffusion rate [14]. On trial, to get approximately equal viscosity, the dosage of PEG with different relative molecular mass was determined first, based on which, the conductivity of KCl solutions were tested. By the end, an appropriate range of relative molecular mass of viscosity enhancer for reducing chloride ion diffusion was given.

2.Materials and experiment

In this study, there were 11 kinds of PEG, corresponding to different relative molecular mass, PEG200, PEG400, PEG600, PEG1000, PEG1500, PEG2000, PEG4000, PEG6000, PEG8000, PEG10000 and PEG20000, respectively. Here, the number after PEG represents the relative molecular mass. As the monomer of PEG, we tested ethylene glycol as a minimum relative molecular mass viscosity enhancer. KCl, ethylene glycol and all PEG used in this test were analytical reagent and purchased commercially. And the water used was deionized water.

The viscosimeter used in this test was rotary viscosimeter, it works by driving a rotor to rotate continuously in the fluid through a verified spring. The rotating torque sensor measures the degree of torsion of the spring, namely the torque. The torque is proportional to the resistance caused by viscous drag of the rotor immersed in the sample, based on which the viscosity can be obtained. In this test, ultra-low viscosity adapter and rotor 0# were selected, and the rotation speed was set at 60 RPM. This collocation can accurately measure the viscosity range of 1-10 mpa·s. The two-plate conductance electrode was used in the conductivity test, and it's measuring range was 0-20000 uS/cm.

Since the temperature directly affects the viscosity and conductivity of the solution, all of our solution tests were carried out in the low-temperature thermostatic tank with the

temperature constant at 20.2℃. Depending on the research results in literature [6], when the concentration of KCl in the solution is lower than 0.001mol/kg, the addition of additives will have a significant impact on the conductivity of the solution. The concentration of KCl solution used in this paper was 0.1 mol/L, so the influence of the viscosity enhancers on the conductivity of the solution was not considered in this test.

3.Results and discussion

3.1 Viscosity in solutions of different additive concentration

The mix proportions of ethylene glycol and its polymers (relative molecular mass range 200-20000) solution for 2, 3, 4, 5 (±0.05) mpa·s were determined through trial preparation. The mass fraction of PEG with different relative molecular mass and the viscosity of solutions are plotted in Figure 1. In Figure 1, it is clearly indicate that the solution viscosity increase exponentially with the increase of mass fraction of PEG under different relative molecular mass conditions. Further, with the increase of relative molecular mass of PEG, the increasing trend of the solution viscosity with the increase of mass fraction was more intense. In other words, as has been indicated in many literatures [6, 15], if it is only to increase the viscosity of the solution, then the viscosity enhancer with higher relative molecular mass would be the better choice.

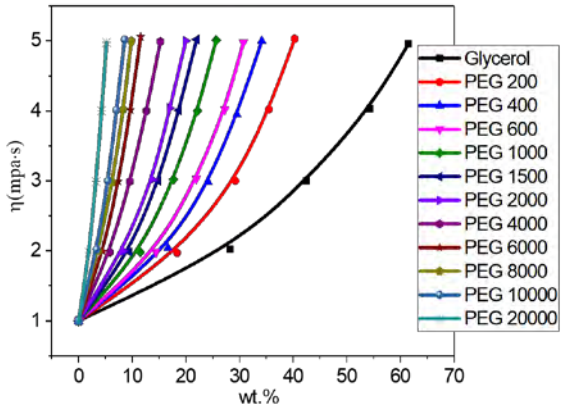

Figure 1: The relationship between mass fraction of PEG with different relative molecular mass and solution viscosity

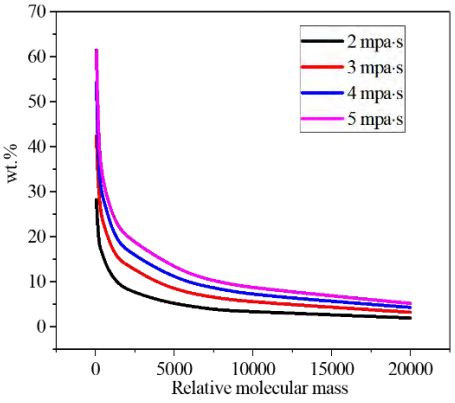

Figure 2: The relationship between relative molecular mass and mass fraction of PEG under different solution viscosity

As presented in Figure 2, the larger the relative molecular mass, the smaller the amount of PEG required to improve the viscosity. In Figure 2, we can also observe that the amount of PEG required to improve the unit viscosity (1 mpa·s) is decreasing under the same relative molecular mass. This might be due to the increasing possibility for molecules to attract or entangle with each other, under the condition of the increasing number of polymer molecules in a certain volume.

3.2 Conductivity of KCl in solutions of different viscosity

As recorded in Figure 3, we obtained the relationship between solution viscosity and solution conductivity with different relative molecular masses of PEG. Figure 3 shows that the conductivity of solution decrease with the increase of solution viscosity, indicating that PEG has the ability to improve solution viscosity and reduce chloride ions diffusion. It was explicit,

however, that the PEG with lower relative molecular mass was much efficient in reducing the conductivity of KCl solution than that of the PEG with higher relative molecular mass. And our results also confirm that the size of the relative molecular mass proposed in the literature [6, 11] is the key to whether the viscosity enhancer can effectively reduce the ion diffusion in solution.

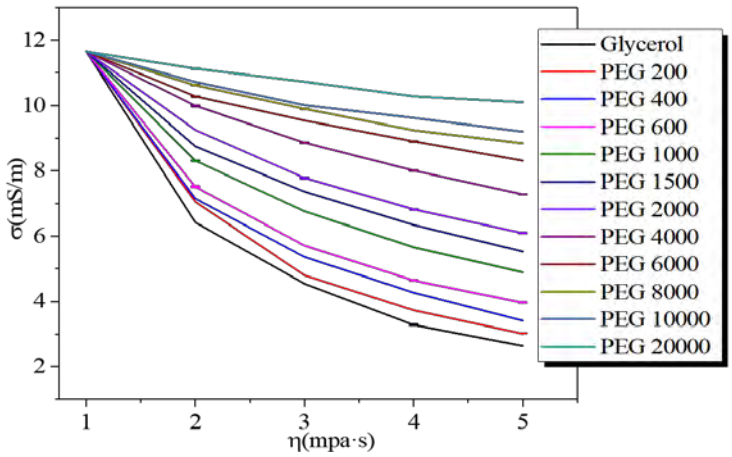

Figure 3: The relationship between viscosity and conductivity of PEG solutions with different relative molecular mass

3.3 The potential boundary of relative molecular mass for viscosity enhancer to reduce the conductivity

To further reveal the relationship between relative molecular mass of viscosity enhancer and solution conductivity, Figure 3 was deformed to obtain Figure 4, which is the relationship among relative molecular mass, mass fraction and conductivity of solution under different viscosity. Clearly, when the optimal limit is exceeded, excessive addition of admixture will reduce the properties of cement-based materials. In other words, too much added admixture may be not well. As exhibited in Figure 4, under different viscosity, the relationship curve among relative molecular mass, mass fraction and solution conductivity can be roughly divided into two parts. One part of it is a straight line, the other part of it is a curve, and all this inflection point occurs at a relative molecular mass of 400. In order to reveal the best solution conductivity reduction effect with the lowest dosage, the linear part of the curve in Figure 4 was taken as an ideal relationship curve between the relative molecular mass and the solution conductivity. Therefore, relative molecular mass 400 is regarded as the lower limit of the appropriate relative molecular mass range for the viscosity enhancer used to reduce ion diffusion.

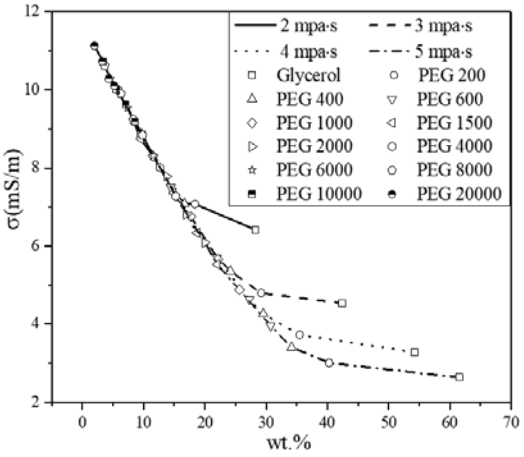

Figure 4: The relationship among relative molecular mass, mass fraction and conductivity of solution under different viscosity

Further treatment of Figure 3 is necessary to determine the appropriate upper relative molecular mass limit. Firstly, we need to define a parameter, as shown in Equation (1):

$$\varphi = \frac{\sigma_w - \sigma_r}{wt.\%} \quad (1)$$

Where φ is the decrease in the conductivity of the solution with a unit mass viscosity enhancer; σ_w is the conductivity of KCl in pure water; σ_r is the conductivity of KCl in solution; $wt.\%$ is the mass fraction of the viscosity enhancer in solution.

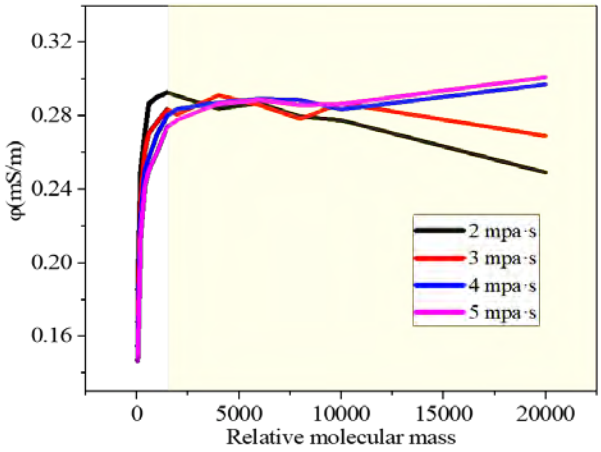

Figure 5: The relationship between the decrease of unit mass viscosity enhancer solution conductivity and the relative molecular mass under different viscosity.

In Figure 5, with the increase of the relative molecular mass of the viscosity enhancer, the decrease of the solution conductivity by unit mass viscosity enhancer will reach a plateau when the relative molecular mass reaches 1500. In other words, when the relative molecular mass of the viscosity enhancer is greater than 1500, the increase of relative molecular mass for viscosity enhancer at the same dosage will not cause the solution conductivity to decrease significantly. Whereas, as we have mentioned before, at the same dosage, increasing the relative molecular mass of the viscosity enhancer will increase the viscosity of the solution. In our original purpose, this type of viscosity enhancer was applied to reduce the diffusion of chloride ions rather than

simply increase the viscosity of the solution. Hence, relative molecular mass 1500 is regarded as the upper limit of the appropriate relative molecular mass range for the viscosity enhancer used to reduce ion diffusion. Of course, if you want to greatly increase the viscosity of the cement paste while reducing the chloride diffusion, you can also increase the upper limit of the relative molecular mass appropriately.

4.Conclusions

In this study, by using PEG with different relative molecular mass as viscosity enhancer and KCl solution conductivity as a means of characterizing chloride diffusion, we preliminarily concluded that the appropriate relative molecular mass range of viscosity enhancer which used to reduce ion diffusion was 400-1500. At the same time, we also proved that the size of relative molecular mass is the key for viscosity enhancer to reduce the diffusion of ions.

ACKNOWLEDEGMENTS

The authors would like to acknowledge the financial support from National Natural Science Foundation of China (No. 51890904, 1706222, No. 51708108), and State Key Laboratory of High Performance Civil Engineering Materials Open Fund (No. 2018CEM001).

REFERENCES

[1] Alexander, M.; Beushausen, H., Durability, service life prediction, and modelling for reinforced concrete structures – review and critique. *Cement. Concrete. Res* **2019,** *122*, 17-29.
[2] Kumar, M. P.; Mini, K. M.; Rangarajan, M., Ultrafine GGBS and calcium nitrate as concrete admixtures for improved mechanical properties and corrosion resistance. *Constr. Build. Mater* **2018,** *182*, 249-257.
[3] Zhang, P.; Cong, Y.; Vogel, M.; Liu, Z.; Müller, H. S.; Zhu, Y.; Zhao, T., Steel reinforcement corrosion in concrete under combined actions: The role of freeze-thaw cycles, chloride ingress, and surface impregnation. *Constr. Build. Mater* **2017,** *148*, 113-121.
[4] Hassani, M. S.; Asadollahfardi, G.; Saghravani, S. F.; Jafari, S.; Peighambarzadeh, F. S., The difference in chloride ion diffusion coefficient of concrete made with drinking water and wastewater. *Constr. Build. Mater* **2020,** *231*, 117182.
[5] Al Menhosh, A.; Wang, Y.; Wang, Y.; Augusthus-Nelson, L., Long term durability properties of concrete modified with metakaolin and polymer admixture. *Constr. Build. Mater* **2018,** *172*, 41-51.
[6] Bentz, D. P.; Snyder, K. A.; Cass, L. C.; Peltz, M. A., Doubling the service life of concrete structures. I: Reducing ion mobility using nanoscale viscosity modifiers. *Cement. Concrete. Comp* **2008,** *30* (8), 674-678.
[7] Bentz, D. P.; Snyder, K. A.; Peltz, M. A., Doubling the service life of concrete structures. II: Performance of nanoscale viscosity modifiers in mortars. *Cement. Concrete. Comp* **2010,** *32* (3), 187-193.
[8] Snyder, K. A.; Bentz, D. P.; Davis, J. M., Using viscosity modifiers to reduce effective diffusivity in mortars. *Journal of Materials in Civil Engineering* **2012,** *24* (8), 1017-1024.
[9] Bentz, D. P.; Snyder, K. A.; Peltz, M. A.; Obla, K.; Kim, H., Viscosity Modifiers to Enhance Concrete Performance. *ACI Materials Journal* **2013,** *110* (5).
[10] Qiao, C.; Ni, W.; Weiss, J., Transport due to diffusion, drying, and wicking in concrete containing a shrinkage-reducing admixture. *Journal of Materials in Civil Engineering* **2017,** *29* (9), 04017146.
[11] Shimizu, T.; Kenndler, E., Capillary electrophoresis of small solutes in linear polymer solutions: Relation between ionic mobility, diffusion coefficient and viscosity. *ELECTROPHORESIS: An International Journal* **1999,** *20* (17), 3364-3372.

[12] Zia, R. N., Active and passive microrheology: Theory and simulation. *Annual Review of Fluid Mechanics* **2018,** *50*, 371-405.
[13] Cussler, E. L.; Cussler, E. L., *Diffusion: mass transfer in fluid systems*. Cambridge university press: 2009.
[14] Snyder, K. A.; Ferraris, C.; Martys, N.; Garboczi, E. J., Using impedance spectroscopy to assess the viability of the rapid chloride test for determining concrete conductivity. *Journal of research of the National Institute of Standards and Technology* **2000,** *105* (4), 497.
[15] Pierre, A.; Perrot, A.; Picandet, V.; Guevel, Y., Cellulose ethers and cement paste permeability. *Cement. Concrete. Res* **2015,** *72*, 117-127.

THE AIR PERMEABILITY, CARBONATION AND CHLORIDE CONTENT ALONG A CONCRETE HIGHWAY UNDERPASS

C. Paglia(1) and S. Antonietti (1)

(1) University of Applied Sciences of Southern Switzerland, DACD, Trevano,

CP 12, 6952 Canobbio, Switzerland

Abstract

In reinforced concrete structures carbonation and chloride ingress are two main phenomena that induce rebar corrosion. Agents such as CO_2 gas or water containing chloride enter the cementitious material mainly throughout the pore system. The air permeability was measured with a non-destructive rapid test method. The aim of the present work was to identify a relation between the carbonation, chloride ingress and the permeability to air of a reinforce concrete underpass. Concrete cores were drilled from a 40 years old in service highway underpass located in the South alpine region. The carbonation values were between 11-25 mm after 40 years exposure to the atmosphere. They corresponded to the conventional carbonation rate, in spite of the cyclic exposure condition of the artefact. In general, the wing wall east and west exhibited lower values as compared to the shoulders. This also indicated the importance of the geometry, orientation and exposition of the structure. The chloride content were generally well beyond 0.025 % referred to the concrete mass. This was due to the location of the structure close to the Alps at 1000 meters above sea and the spreading of the deicing salts during winters. The chlorides were leached from the concrete surface, so that higher contents were sometimes found with concrete depth. A correlation existed between the carbonation (CO_2 entrance) and the permeability to air. The higher the permeability, the deeper the carbonation. At concrete depths 0-20 mm chloride ingress and carbonation seemed to be antagonist phenomena. They could not occur simultaneously to a great extent. When humidity is present, gas penetration is lowered. While from 30 to 40 mm chloride ingress, transport and carbonation appeared to be both present. Keywords: concrete, air permeability, carbonation, chloride

1. INTRODUCTION

In cementitious artefacts the material quality and the rebar concrete cover thickness largely control the extent and the velocity of infrastructure surface damage. The concrete permeability

controls the entrance of substances such as gases or liquids. Transport takes place by diffusion with concentration gradient (CO_2 in air), or by capillary adsorption with chloride containing water adsorbed. In low and moderate strength concrete, the air permeability is greatly affected by curing [1]. It is also known that, the air permeability is affected by the concrete moisture content, which is not always homogeneous within the material [2]. Air contains CO_2 gas, which induces carbonation within the cementitious material, and the rate of carbonation increases with the concentration [3]. The process reduces the pH of the pore solution [4] resulting in uniform rebar corrosion. Another detrimental agent for reinforced concrete is chloride. Alternating wetting and drying cycles promote the ions ingress, in particular within the first 40 mm from the surface. The content can be higher than the sea water concentration after 10 years exposure [5]. chloride induces localized rebar corrosion and a limit of 0.025 % referred to concrete mass is set for reinforced concrete structures [6]. In tidal zones, a relatively high humidity is present. The humidity might reduce the entrance of gases, such as CO2 within the material. Therefore, chloride might enter the structures, while a reduction in the gas entrance might be detected [7]. Nevertheless, it was found that, both carbonation and chlorides may be present, because of the relative high humidity [8]. Furthermore, both phenomena were present in bridge abutments in cold regions [9].

The objective of the work is to identify a relationship between the air permeability, measured with a non-destructive technique directly on site on the artefact, the carbonation and the chloride content of a still in service 40 years old highway underpass.

2. EXPERIMENTAL

The in service highway underpass 40 years old located at 1000 meters above Sea is analyzed. In the last decades, the mean temperature of the January-March period was -0.7 ^{o}C. The mean temperature of the June-August period was 13.8 ^{o}C. The mean rain / snow fall of January-February-March was 82 mm, while the mean rain / snow fall in the period June-July-August was 154 mm. The sheltered underpass is located in a South alpine clima, close to the Alps.

The air permeability is measured with a Torrent permeability Tester, a rapid non- destructive method [10]. The equipment consists of a test chamber with an external ring applied on concrete surface. An under pressure is created. During the measurement, the external ring pressure is maintained the same as the pressure in the test chamber. Within the test chamber the pressure variation with time is registered (air flux from concrete to test chamber). The air permeability is calculated from the pressure change with time. The test chamber allows a unidimensional air flux. The air comes only from the internal part of the concrete cover (Fig. 1).

Figure1: Test chamber and external protection ring of the Torrent permeability tester.

To define the air permeability and the relation to the humidity, it is necessary to determine the electric specific resistance of the surface. This is done with a four electrode Wenner method. Between the external electrode a current (alternate current 50-1000 Hz) is applied and between the internal points a resistance is measured. The involved concrete depth corresponds to the electrode distance of 5 cm.

The carbonation front is determined on drilled concrete cores (diameter 50 mm) and the minimum, maximum and average values are presented by using a basicity indicator i. e. phenolphtalein [11]. Concrete cylinders are cut in 10 mm thick disks and pulverized and the chloride content is determined to a depth of 40 mm [12].

3. RESULTS AND DISCUSSION

The concrete is generally a high quality concrete used for highway structures with an expected life duration of at least 60 years. The carbonation values vary depending on the quality of the material and degree of exposition (temperature, humidity) of the parts of infrastructure, in particular shoulders or wing walls. The main values are located between 11 and 25 mm. The highest rate of carbonation occurs at relative humidity between 50 and 70 %. According to the conventional equation, the depth of carbonation in millimeters increases with the square root of time [13]. Assuming a carbonation coefficient variable between 3-4 and a time exposure of 40 years, the carbonation front may vary between 18 and 25 mm. Most measured values on the underpass vary exactly within this range, even though the equation applies with steady state condition. But on site, the condition are not stable and varies daily and upon winter or summer time. Nonetheless, on the artefact, the mean carbonation also assumes different values that changes from 1-5 mm to 26-30 mm. This is also accounted for a different exposition condition of the part of the artefact. The carbonation of the shoulder South is only slightly higher as compared to the shoulder North. The values of the wing wall east and west are generally lower as compared to the shoulders (Fig. 2).

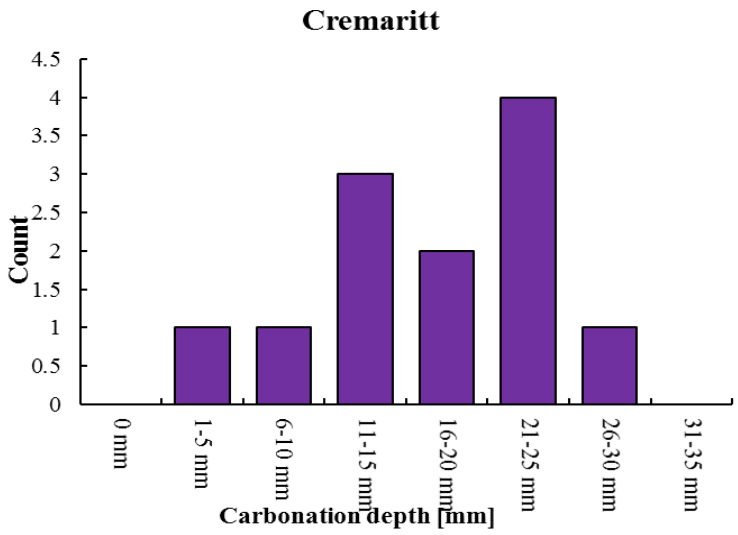

Figure 2: Mean carbonation distribution and occurrence on the underpass.

The region of the underpass is located close to the alps. During the winters, a relatively high amount of NaCl salt is spread along the highway. The underpass generally exhibits a high amount of chlorides exceeding to the limit established for reinforced concrete of 0.025 % referred to the concrete mass [6]. The underpass reaches values up to 0.400 % by concrete mass, and below 40 mm depth the chloride content was still higher than the established limit. The chloride content is higher at the surface compared to the deeper regions, but the total chloride presence can be higher with depth down to 40 mm. In particular high chloride total concentration is observed at depths between 20 and 40 mm. This is likely to be linked to the water leaching of the surface. (Fig. 3). It is also important to notice that, a variation of the chloride content and concentration is observed. This may be caused by a different exposition of the artefact to the degrading or atmospheric agents (insulation, wind, thermal excursions) and by the geometry of artefacts, snow accumulation during winter or different removal of the salt containing waters form the lanes.

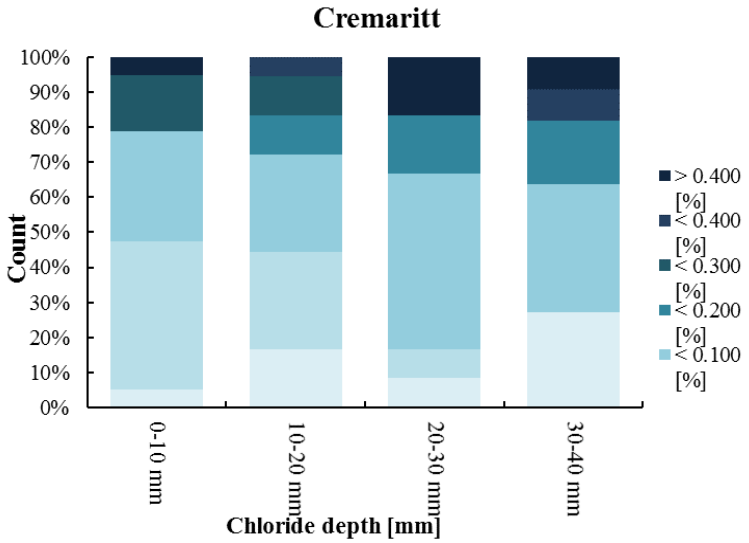

Figure 3: Chloride distribution with depth along the underpass.

The porosity influences the strength of cementitious materials, but also represents a preferential way for the substance to enter the concrete. The entrance of CO_2 gas has a detrimental effect on the rebar [3, 4]. In addition, the entrance of chlorides in concentration above 0.025 % referred to the concrete mass promotes the localized rebar corrosion [6]. A slight general correlation is observed between the air permeability of the cementitious material and the carbonation depth (Fig. 4). That means, the higher the permeability, the more air, i. e. CO_2 gas, can enter the concrete.

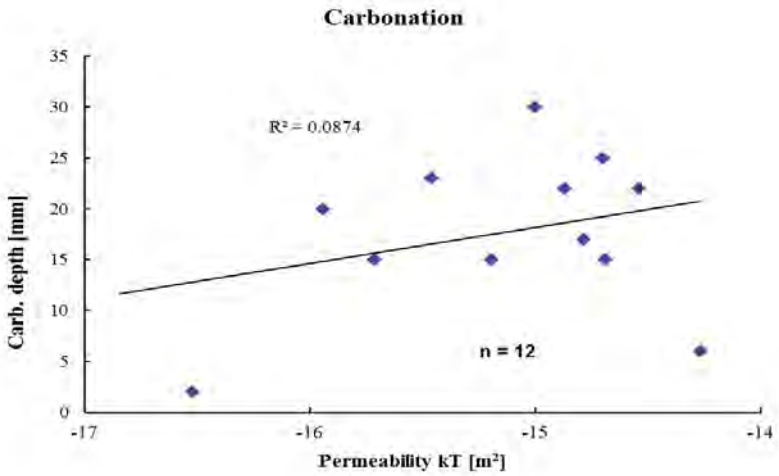

Figure 4: Correlation between carbonation depth and air permeability.

Contrary to the relationship between the air permeability and the CO_2 gas penetration, i. e. the carbonation depth, a negative correlation exists between the chloride content in the first 20 mm depth and the air permeability. This is particularly observed for the first 10 mm below the concrete surface. That means, low air permeability corresponds to high chloride content. This may correlate with the reverse relationship between carbonation and chloride ingress. Chloride is relatively present within the first 20 mm depth. Humidity is present and carbonation, i.e. CO_2 gas permeation, is lowered [7]. Between 20 to 40 mm the relation is more variable (Fig. 5). A slight trend with increased air permeability and chloride content is seen. This indicates that, at lower levels within the concrete, both phenomena, chloride ingress, transport and carbonation, may be detected [8, 9]. While in the upper levels, surface effects, such as water leaching, direct exposition to the atmosphere may also influence the phenomena.

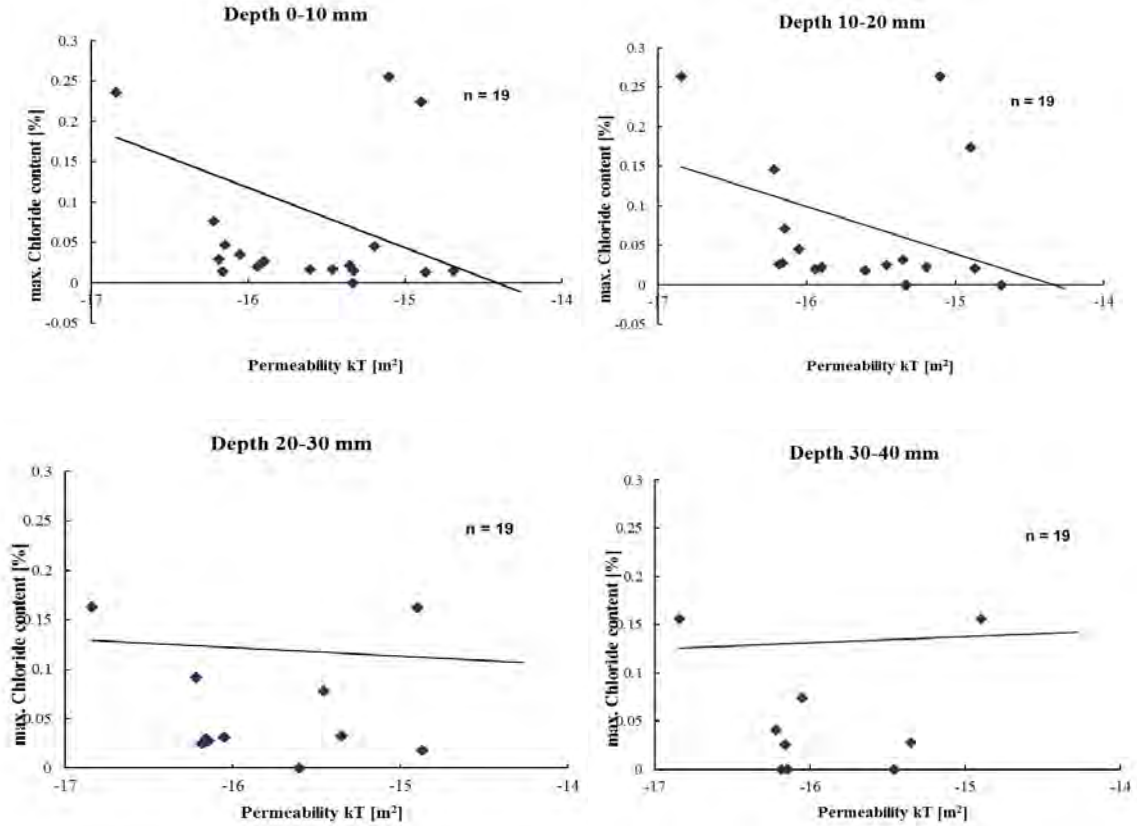

Figure 5: Correlation between chloride content with depth and air permeability.

4. CONCLUSIONS

The carbonation and chloride content of concrete cores withdrawn from a highway underpass have been analyzed and correlated with the air permeability. The carbonation values were between 11-25 mm after 40 years exposure to the atmosphere. They corresponded to the conventional carbonation rate, in spite of the non-steady state condition. In general, the wing wall

east and west exhibited lower values as compared to the shoulders. The chloride content was generally well beyond the limit of 0.025 %, due to the location of the structure close to the Alps at 1000 meters above sea and the spreading of the deicing salts during winters. Sometimes the chlorides were leached from the concrete surface, so that higher contents were sometimes found with concrete depth. A correlation existed between the carbonation (CO_2 entrance) and the permeability to air. At concrete depths 0-20 mm, chloride ingress and carbonation seemed to be antagonist phenomena, while from 30 to 40 mm chloride ingress, transport and carbonation appeared coexisting.

ACKNOWLEDGEMENTS

The authors would like to thank A. Salmina for the data support, M. Mezzetti and E. Pesenti for samples withdrawal.

REFERENCES

[1] P. B. Bamforth, The relationship between permeability coefficients for concrete obtained using liquid and gas, Mag. Concr. Res. 39, No. 138, 1987.
[2] L. Tang and L. O. Nilsson, Effect of drying at an early age on moisture distributions in concrete specimens used for air permeability tests, Nordic concrete research, 13/2/93, Oslo, 1993.
[3] P. Schubert and K. Wesche, Einfluss der Karbonatisierung auf die Eigenschaften von Zementmörtel, Resear report No. F 16, Institut für Bauforschung BWTH, Aachen 1974.
[4] V. G. Papadakis, M. N. Fardis and C. G. Vayenas, Effect of composition environmental factors and cement-lime mortar coating on concrete carbonation, Materials and Structures, 25, No. 149, 1992.
[5] S. Nagataki et al, Condensation of Chloride ions in hardened cement matrix materials and on embedded steel bars, ACI Materials Journal, 90, No. 4, 1993.
[6] SN EN 206-1, Concrete, specification, performance, production, conformity, 2013.
[7] Concrete Science and Engineering, Vol. 3, December 2001, pp 242-249.
[8] Costa, J. Appleton, Concrete carbonation and chloride penetration in a marine environment, Concr. Sci. Eng. 3 (2001) 242–249.
[9] R.R. Aveldano, N.F. Ortega, Characterization of concrete cracking due to corrosion of reinforcement in different environments, Constr. Build. Mater. 25 (2) (2011) 630–637.
[10] SIA 262/1 Concrete construction, complimentary specifications, appendix E, 2016.
[11] SN EN 14630 norm, determination of carbonation depth in hardened concrete by the phenolpthalein method, 2006.
[12] SN EN 14629 norm, products and systems for the protection and reparation of concrete structures, measurements of the concrete Chloride content, 2007.
[13] R. J. Currie, Carbonation depth in structural-quality concrete, Building research establishment report, Watford, U. K. 1986.

THE COMPETITIVE DIFFUSION PROCESS OF CHLORIDE INTO MORTAR IMMERSED IN CHLORIDE-SULFATE SOLUTION

Yuanzhang Cao (1), Liping Guo (1, 2, 3)

(1) School of Materials Science and Engineering, Southeast University, Nanjing, 211189, China

(2) Jiangsu Key Laboratory of Construction Materials, Nanjing 211189, China

(3) Collaborative Innovation Center for Sustainable Civil Engineering Materials & Structures, Nanjing 211189, China

Abstract

The chloride and sulfate exist together in real environment, no matter marine or salts lakes, and the ratio of the chloride to sulfate is varied. To precisely predict the concrete durability under real environment, this paper mainly investigated the influence of sulfate on chloride ions diffuse into hardened cement paste. The Minitab software was used to calculate and design the content of compound impregnating solution in order to fully understand the effect of the concentration of chloride and sulfate on the chloride diffusion depth. The $AgNO_3$-based colorimetric method and acid-soluble chloride test were used to determine the chloride diffusion depth and the chloride penetration profile. The evolution phase distribution from the outer to the inner were characterized by SEM, EDS and XRD. The results showed that chloride diffusion generally increased with increasing concentration of chloride. The presence of sulfates promoted chloride diffusion initially, while it delayed the chloride diffusion in the later. Chloride ions diffused into mortar mainly through ITZ and pores, and reacted with the hydration products to produce Friedel's salt. Although the diffusion rate of sulfate ions is slow, it can alter the stability of the Friedel's salt and block the pores, which has a long-term effect on chloride ion diffusion.

Keywords: Chloride, Sulfate, Diffusion, Attack production

1. INTRODUCTION

Chloride-induced corrosion of steel reinforcement is a dominant factor on durability of

concrete structures which exposed to marine and salts lake environments. Many studies have been focused on the chloride attack and simulated the process of chloride diffusion into the cement-based materials [1-5]. However, the real service environment is usually a combination with chloride and sulfate. For example, Maes [6] reported that the presence of sulfates decreased the chloride binding capacity and the effect of sulfate on the chloride diffusion depended on the exposure time.

As we all known, the formation of ettringite and gypsum causes the damage of concrete after sulfate ions ingress into the pore structure [7, 8]. However, the phase distribution in cement paste is a complicated problem when chloride-sulfate solution involved [9-12]. The penetrated chloride reacted with hydration products to produce Friedel's salt. However, sulfate can release the bound chloride easily [13-15]. In general, chloride ions penetrate much deeper in the mortar than sulfate ions. With the ingress of sulfate ions, the bound chloride will be decomposed into pore solution again. At this point, the diffusion process of chloride ions becomes complex and the laws of chloride diffusion will be broken by the presence of sulfate ions.

The purpose of this paper is to investigate the diffusion of chloride ions under combined exposure conditions of chloride and sulfate. The impact of sulfate on the entire chloride ion diffusion process is still unclear. Besides, the compound solution used in previous studies are limited into several groups, such as 165 g/l NaCl + 50 g/l Na_2SO_2 in [6] and 3.5% NaCl + 5% Na_2SO_4 in [16], or the simulation of sea water [9]. It is still unknown that the influence of sulfate concentration on the chloride diffusion. To reveal the effect of chloride and sulfate concentrations on the diffusion process, the Minitab was used to design a compound salt solution, in which the concentration range of the chloride salt was 0-25% and the sulfate was 0-5% in this study. This concentration range contains almost all of real chloride-sulfate environment.

2. MATERIALS AND METHODS

2.1 Materials

Cement (P II 52.5) was used to prepare the cement mortars and the detailed chemical composition of the cement is presented in **Table 1**. Combined chloride-sulfate corrosion was simulated under laboratory conditions by dissolve NaCl and Na_2SO_4 in designed concentrations.

Table 1: Chemical composition of the cement (%)

SiO_2	Al_2O_3	Fe_2O_3	CaO	MgO	SO_3	K_2O	Na_2O	LOI
20.87	4.87	3.59	64.47	2.13	2.52	0.65	0.11	0.77

2.2 The design of compound salts solution

The Minitab is helpful to intuitively understand the relationship between the factors and the response, and it was usually used to optimize the mix design for desired responses and to find the synergistic effect between factors since it provided continuous features of the image analysis

[17-19]. In this study, chloride and sulfate in the compound salts solution are equivalent attack factors which should satisfy the equation (1):

$NaCl\ (wt/\%) + Na_2SO_4\ (wt/\%) + H_2O\ (wt/\%) = 1$ (1)

The detail of the compound ratio is shown in Table 2. 25% NaCl (Cl25) was selected as single chloride solution, while 25% NaCl+5% Na_2SO_4 (Cl25S5) was the chloride-sulfate compound salts solution.

Table 2: The proportion of compound salt solutions (wt/%)

Number	H_2O	NaCl	Na_2SO_4
Cl25	75	25	0
S5	95	0	5
Cl6S3	89.375	6.875	3.75
Cl19S1	79.375	19.375	1.25
Cl25S5	70	25	5
Cl5	95	5	0
Cl19S3	76.875	19.375	3.75
Cl9S1	89.375	9.375	1.25
Cl13S2	83.75	13.75	2.5

2.3 Test methods

The mortars with dimension of 40*40*160 mm were prepared at water-to-cement of 0.48. The sand to binder ratio was maintained at 1.5 by weight. After standard curing for 28 days, the specimens were sealed with epoxy on around to ensure one-dimensional diffusion. Then, the specimens were immersed in the compound salts solution above.

The $AgNO_3$-based colorimetric method was used to determine the depth of chloride diffusion [20]. After immersing for different times, the specimens are split and sprayed with $AgNO_3$.

The total chloride content (acid-soluble chloride) along the depth of the specimen was test according to Chinese standard (JTJ 270-1998). The chloride content at each depth of the specimen and various designated time was tested in order to determine the chloride profile according to the depth and the time.

3. RESULTS AND DISCUSSION

3.1 Chloride penetration depth

Fig. 1 demonstrates the chloride diffusion depth immersed in chloride and chloride-sulfate, respectively. For immersion periods before 120 d, chloride diffusion depth in chloride solution was shorter than that in the compound salts solution. After 120 d immersion, the chloride penetration depth immersed in chloride-sulfate solution was less than that in single chloride environment. The results revealed that the presence of sulfate promoted chloride diffusion initially, with the prolongation of immersion time, the sulfate has an inhibitory effect on

chloride ion diffusion. Therefore, the influence of sulfate on the chloride diffusion mechanism changes in a function of the exposure time.

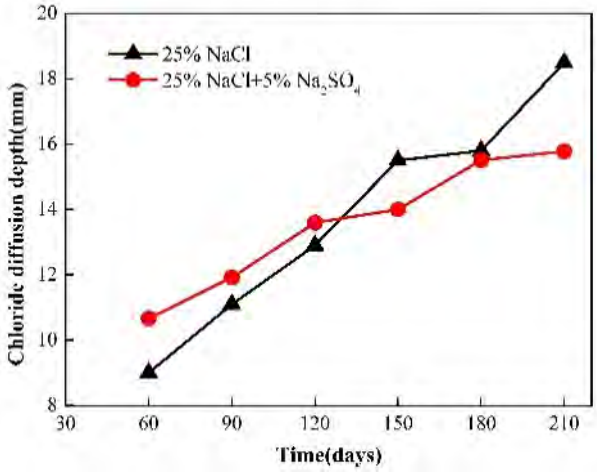

Figure 1: Chloride diffusion depth for exposure to Cl25 and Cl25S5 solution

3.2 Chloride penetration profile

The chloride content in the mortars at different depth when subjected to chloride and chloride-sulfate are shown in Fig. 2. In the outermost layer, when immersed in 25% NaCl for 60 d, the chloride content was 1%, and it had reached up to 1.55% after 210 d. For immersion time from 60 d to 210 d, the longer immersion time, the more chloride contents diffusion into the mortars. The presence of sulfate can promote more chloride ions into the mortars at every depth, when the immersion time was 60 d. However, after immersion time up to 210 d, the chloride contents of mortars immersed in single chloride environment were more than that immersed in chloride-sulfate solution, especially in the outmost layer.

The distribution of chloride content in the mortar are present in Fig. 3, from which it can draw the conclusion that the interaction effect between chloride and sulfate on chloride diffusion. The abscissa is the concentration of the chloride salt, and the ordinate is the concentration of the sulfate. The most obvious rule was that the higher the concentration of the chloride salt, the more chloride content entered into the mortar. After immersion for 210 d, the change trend of counter was upward as shown in Fig. 3(a), which demonstrated that the presence of sulfate reduced the amount of chloride content within 0-5 mm. In the range from 5 to 10 mm, the effect of the sulfate was not obvious shown in Fig. 3(b), but, this level can be considered as the region where the role of sulfate begin to transform. From Fig. 3(c) and Fig. 3 (d), it can be found that sulfate was helpful to increase the chloride content in the range of 10-20 mm, which was different from Fig. 3(a).

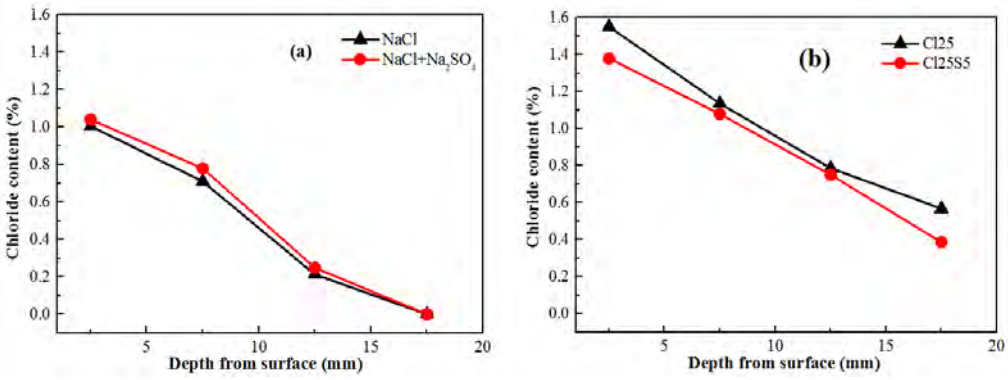

Figure 2: Chloride penetration profile along the depth at: (a) 60 d and (b) 210 d

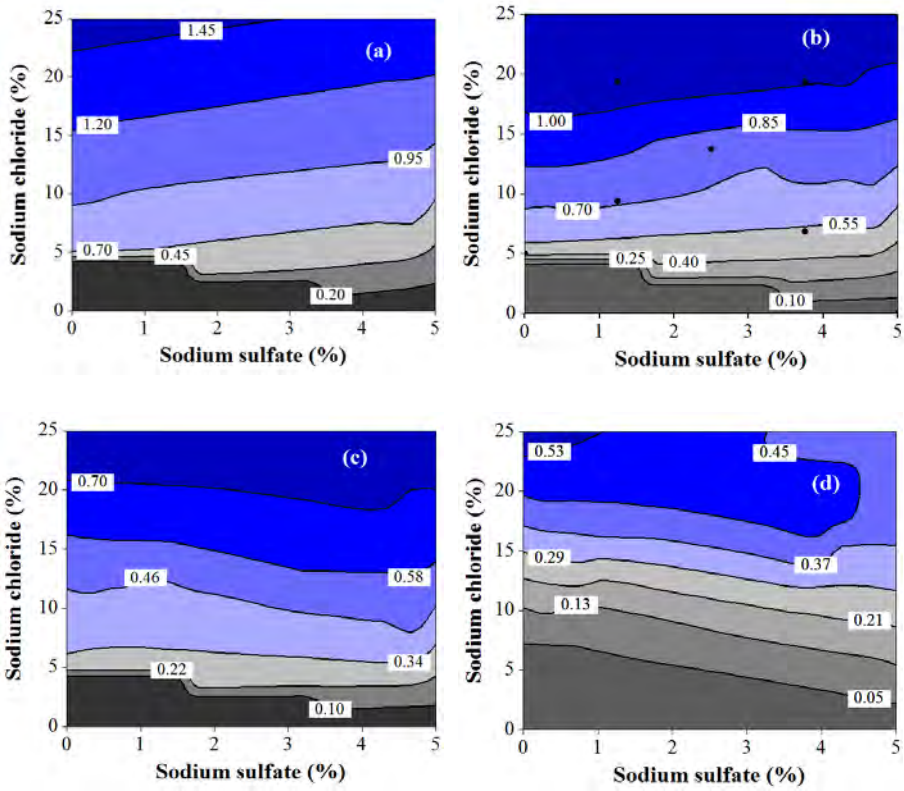

Figure 3: The distribution of chloride content in the mortar (a) 0-5 mm; (b) 5-10 mm; (c) 10-15 mm; (d) 15-20 mm

3.3 XRD analysis

The phase distribution inner the mortar is shown in **Fig. 4**. There are two hydration products which are best known to bind chloride ions, the CSH phase and AFm phase. When immersed in 25% NaCl+5% Na_2SO_4 for 60 d, Friedel's salt was still present at the outmost layer. However, it disappeared after 210 d immersion because of sulfate invasion. It is reported that the SO_4^{2-}

can replace the Cl^- in Friedel's salt to form ettringite, which can also be confirmed by **Fig. 4**. At the same immersion time for 60 d, the Friedel's salt subjected to 25% 25% NaCl + 5% Na_2SO_4 was more than that subjected to NaCl at the depth of 15 mm to 20 mm. It can be considered that the sulfate can promote the chloride diffusion before 60 d. On the contrary, the rule was reversed when the immersion time was up to 210 d.

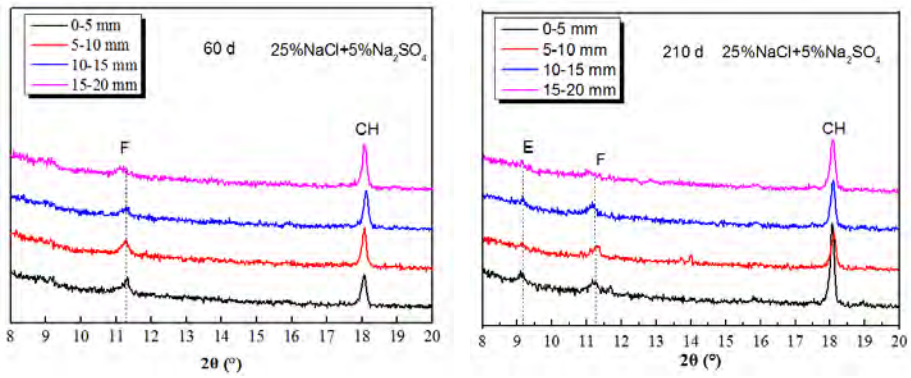

Figure 4: XRD pattern of mortar immersed in NaCl and NaCl + Na_2SO_4 for different immersion age (E: ettringite, F: Friedel's salt, CH: $Ca(OH)_2$)

3.4 SEM analysis

Fig. 5 gives the distribution of sodium chloride inner mortar by SEM analysis. There was a large amount of sodium chloride crystals, determined by EDS analysis, in the vicinity of the sands. The diffusion properties of the ITZ has a significant impact on chloride ingress in concrete [21]. Therefore, the ITZ and pores are the main paths for chloride diffusion. **Fig. 6** is the SEM images of ettringite crystals after 210d immersion in 25% NaCl+5% Na_2SO_4. The ettringite crystals have perfect needle-shape with hexagonal cross section [22] and usually form in cracks.

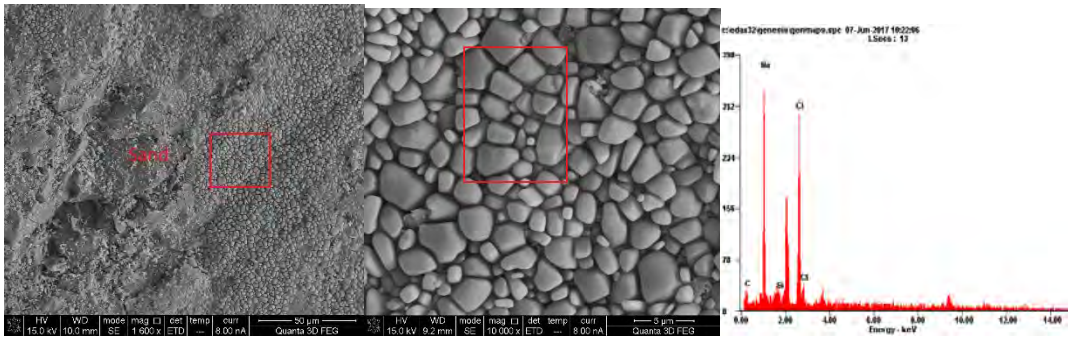

Figure 5: SEM images of NaCl crystals growing inside pores and ITZ after 210d immersion in NaCl

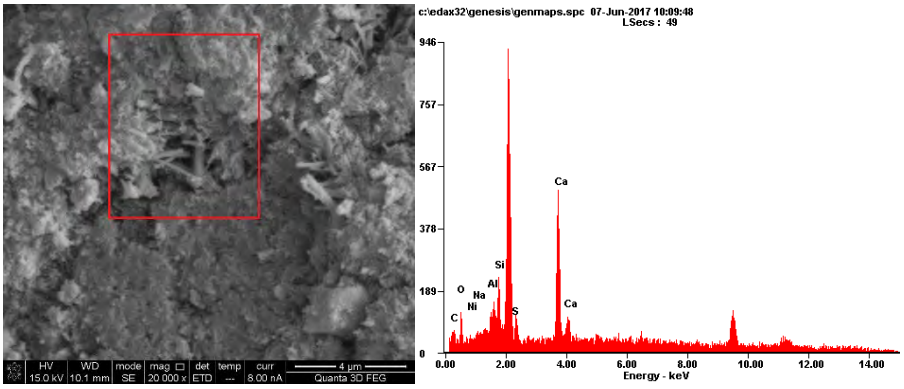

Figure 6: SEM images of ettringite crystals after 210 d immersion in 25% NaCl+ 5%Na_2SO_4

When the mortar was immersed in chloride-sulfate solution, chloride and sulfate ions diffused into the interior of the mortar simultaneously. Because of the fast diffusion rate of chloride, it can be considered that hydration products have reacted with chloride completely. However, the sulfate has a significant effect on the stability of the Friedel's salt, which can convert the Friedel's salt into ettringite. It is also reported that there is a binding competition between chloride and sulfate and the competition should start from the outmost layers [6]. This implies that the presence of sulfate will decrease the amount of chloride bound by hydration products and accelerate the chloride diffusion. After immersion for 210 d, the sulfate also entered into the mortar and filled in the pores and ITZ as the sodium chloride shown in **Fig. 4**. In other words, sulfate ions maybe an unfavorable factor for chloride diffusion for a long term.

4 CONCLUSIONS

(1) The influence of sulfates on the chloride diffusion in function of not only the exposure time, but also the concentration.

(2) The stability of bound chlorides is susceptible to Na_2SO_4 attack, so the presence of sodium sulfate in a chloride solution aggravates the diffusion of free chlorides at early/short exposure.

(3) The ITZ and pores are main paths for chloride and sulfate diffusion. The formation of ettringite and gypsum caused by sulfate act as a favorable factor to delay chloride diffusion in the long term.

ACKNOWLEDGEMENTS

This work was supported by China Ministry of Science and Technology (Grant No.: 2015CB655102).

REFERENCES

[1] Song Z, Jiang L, Zhang Z, *et al.* Distance-associated chloride binding capacity of cement paste

subjected to natural diffusion [J]. Construction and Building Materials, 2016, 112: 925-932.
[2] Loser R, Lothenbach B, Leemann A*, et al.* Chloride resistance of concrete and its binding capacity – Comparison between experimental results and thermodynamic modeling [J]. Cement and Concrete Composites, 2010, 32(1): 34-42.
[3] Cheewaket T, Jaturapitakkul C, Chalee W. Concrete durability presented by acceptable chloride level and chloride diffusion coefficient in concrete: 10-year results in marine site [J]. Materials and structures, 2014, 47(9): 1501-1511.
[4] Spiesz P, Ballari M, Brouwers H. RCM: a new model accounting for the non-linear chloride binding isotherm and the non-equilibrium conditions between the free-and bound-chloride concentrations [J]. Construction and Building Materials, 2012, 27(1): 293-304.
[5] Neithalath N, Jain J. Relating rapid chloride transport parameters of concretes to microstructural features extracted from electrical impedance [J]. Cement and Concrete Research, 2010, 40(7): 1041-1051.
[6] Maes M, Mittermayr F, Belie N. D. The influence of sodium and magnesium sulfate on the penetration of chlorides in mortar [J]. Materials and Structures, 2017, 50(2): 153.
[7] Müllauer W, Beddoe R. E, Heinz D. Sulfate attack expansion mechanisms [J]. Cement and Concrete Research, 2013, 52: 208-215.
[8] Lothenbach B, Bary B, Bescop P. L, *et al.* Sulfate ingress in Portland cement [J]. Cement and Concrete Research, 2010, 40(8): 1211-1225.
[9] Maes M, Belie N. D. Resistance of concrete and mortar against combined attack of chloride and sodium sulphate [J]. Cement and Concrete Composites, 2014, 53(10): 59-72.
[10] Weerdt K. D, Justnes H, Geiker M. R. Changes in the phase assemblage of concrete exposed to sea water [J]. Cement and Concrete Composites, 2013, 47(3): 53-63.
[11] Yoon S, Ha J, Chae S*, et al.* Phase Changes of Monosulfoaluminate in NaCl Aqueous Solution [J]. Materials, 2016, 9(5): 401.
[12] Brown P. W, Badger S. The distributions of bound sulfates and chlorides in concrete subjected to mixed NaCl, MgSO 4 , Na 2 SO 4 attack [J]. Cement and Concrete Research, 2000, 30(10): 1535-1542.
[13] Xu J, Zhang C, Jiang L*, et al.* Releases of bound chlorides from chloride-admixed plain and blended cement pastes subjected to sulfate attacks [J]. Construction and Building Materials, 2013, 45: 53-59.
[14] Geng J, Easterbrook D, Li L.-Y*, et al.* The stability of bound chlorides in cement paste with sulfate attack [J]. Cement and Concrete Research, 2015, 68: 211-222.
[15] De Weerdt K, Orsáková D, Geiker M. The impact of sulphate and magnesium on chloride binding in Portland cement paste [J]. Cement and Concrete Research, 2014, 65: 30-40.
[16] Jin Z, Wei S, Zhang Y*, et al.* Interaction between sulfate and chloride solution attack of concretes with and without fly ash [J]. Cement and Concrete Research, 2007, 37(8): 1223-1232.
[17] Moseson A. J, Moseson D. E, Barsoum M. W. High volume limestone alkali-activated cement developed by design of experiment [J]. Cement and Concrete Composites, 2012, 34(3): 328-336.
[18] Ghafari E, Costa H, Júlio E. Statistical mixture design approach for eco-efficient UHPC [J]. Cement

and Concrete Composites, 2015, 55: 17-25.

[19] Zaitri R, Bederina M, Bouziani T*, et al.* Development of high performances concrete based on the addition of grinded dune sand and limestone rock using the mixture design modelling approach [J]. Construction and Building Materials, 2014, 60(9): 8-16.

[20] He F, Shi C, Yuan Q*, et al.* $AgNO_3$ -based colorimetric methods for measurement of chloride penetration in concrete [J]. Construction and Building Materials, 2012, 26(1): 1-8.

[21] Du X, Jin L, Ma G. A meso-scale numerical method for the simulation of chloride diffusivity in concrete [J]. Finite Elements in Analysis and Design, 2014, 85(4): 87–100.

[22] Ragab A. M, Elgammal M. A, Hodhod A. G*, et al.* Evaluation of field concrete deterioration under real conditions of seawater attack [J]. Construction and Building Materials, 2016, 119: 130-144

Theme 4

Chemical and physical degradation under coupled loading conditions

ANALYSIS OF MICROCRACKING FORMATION DURING BASIC AND DRYING CREEP IN CEMENTITIOUS MATERIALS

Aliaksandra Tsitova (1,2)*, Fabien Bernachy-Barbe (1), Benoît Bary (1) and François Hild (2)

(1) DEN-Service d'Etude du Comportement des Radionucléides (SECR), CEA, Université Paris-Saclay, 91191 Gif-sur-Yvette, France

(2) LMT (ENS Paris-Saclay, CNRS, Université Paris Saclay), 61 avenue du Président Wilson, 94230 Cachan, France

* Main author. E-mail: aliaksandra.tsitova@cea.fr

Abstract

The safety of double wall Concrete Containment Buildings (CCBs) in the French nuclear fleet primarily depends on the level of prestress applied to concrete. The delayed strains in concrete induced by creep and shrinkage cause a loss of prestress in the inner wall that may increase the risk of potential leaks in accidental conditions. The creep rate in concrete depends on multiple factors among which microcracking is of major significance. In this paper, an experimental approach is being developed for the qualitative and quantitative characterization of creep/damage coupling. The creep behaviour in compression of matured cement paste and mortar is characterised at the macroscale for different hygro-mechanical loadings. A non-destructive Impulse Excitation Technique (IET) is applied for damage evaluation after creep tests by measuring the degradation of the dynamic elastic modulus. The comparison of creep compliances allows creep and shrinkage mechanisms along with microcracking formation to be assessed in the matrix and at matrix-inclusion interfaces. The acquired data will then help to gain insight into the general coupling mechanisms between drying, creep and damage in cement-based materials.

Keywords: basic creep, drying creep, microcracking, mortar, cement paste.

1. INTRODUCTION

The Concrete Containment Buildings (CCBs) are commonly called the third containment barrier for French reactors as they must provide confinement of radioactive species in the event of failure of fuel rod cladding (first barrier) and reactor coolant system (second barrier).

The double wall CCB is a widespread design of containment vessels in the French nuclear fleet (i.e., 24 out of 58 nuclear reactors). This construction ensures the confinement function with the prestressed concrete inner wall.

The inner wall of CCBs undergoes accelerated creep and shrinkage kinetics due to the particular environmental conditions (heated air of the reactor, absence of rehydration from outside). The consequence of creep and shrinkage is an increased risk of potential leaks under proof-testing or accidental high internal pressure [1]. As the safety of double wall CCBs primarily depends on the prestress applied to concrete, the prediction of delayed strains and subsequent mechanical property degradation is of major interest.

The creep rate in concrete depends on multiple factors among which microcracking is of major importance [2]. In uniaxial compression, the creep strain is linearly related to stresses at loadings under about 40% of compressive strength [3]. At higher stress levels, creep strains become nonlinear with more pronounced nonlinearity at higher stresses. It is considered that most of nonlinear creep can be attributed to microcracking. To investigate the role of microcracking in cement-based materials, compressive creep tests are conducted on mature cement paste and mortar specimens at different hygro-mechanical loadings.

2. EXPERIMENTAL PROGRAM

2.1 Materials

Formulations for cement and mortar are derived from the VeRCoRs concrete formulation [4] that is used for laboratory tests. Mortar and cement paste were mixed with W/C=0.525. The material compositions are given in Table 1.

Table 1: Material constituents

Constituents	Proportion, kg	Density, kg/m^3
Mortar:		
Cement CEM I 52.5 N CE CP2 NF Gaurain	320	3100
Sand 0/4 REC LGP1 thresholded to 2 mm	681	2600
Sikaplast Techno 80	2.6	1060
Addition water	170	1000
Total water	172	1000
Cement paste:		
Cement CEM I 52.5 N CE CP2 NF Gaurain	320	3100
Total water	168	1000

Mortar and cement paste cylinders are molded in vertical plastic tubes 30 mm in diameter. Specimens are demolded after 24 hours and stored at 100% relative humidity. The initial height of cast specimens is ca. 100 mm. Before testing, the upper and lower parts of cylinders are cut with a wire saw to eliminate volumes with non-homogeneous properties (due to varying W/C ratio). The final dimensions are Ø 30 × h 60-65mm. Boundary faces are rectified to ensure orthogonality and planar surfaces for compression testing. Caution is exercised during specimen preparation to protect them from drying and cracking by rewetting their surfaces and wrapping with a waterproof coating.

The minimum age of specimens at the start of all tests is 90 days. Carrying out the test on the matured material allows the ageing effects on viscous behavior to be neglected.

2.2 Experimental set-up

The experimental campaign aims to investigate and decouple the influence of several factors on the creep behavior:

- Loading level,
- Heterogeneity (effect of aggregates),
- Drying (Pickett's effect).

The loading levels are defined as the ratio of compressive strength evaluated at 90 days on similar specimens (geometry, fabrication and preparation protocol). Two levels of loadings are chosen, namely, 30% f_c^{90} corresponding to the linear creep range for concretes, and 60% f_c^{90} corresponding to the nonlinear range (Table 2).

Table 2: Loading levels

Material	f_c^{90}, MPa	Loading level, MPa
Cement paste	32	$0.3f_c^{90} = 9.6$
		$0.6f_c^{90} = 19.2$
Mortar	45	$0.3f_c^{90} = 13.4$
		$0.6f_c^{90} = 26.8$

Axial and lateral strains are measured via HBM® foil prewired strain gauges. The strain gauges are glued with X60 HBM® adhesive that provides a good adhesion for strain measurements. The longitudinal strain is measured by linear strain gauges with a 20 mm measuring grid and lateral strain is measured by linear strain gauges with 10 mm grid. Loadings are applied by a hydraulic system where the pressure is controlled by a dead weight. Before load application, specimens are preloaded with ca. 1kN. Then, the main loading is applied instantaneously.

Basic creep tests

Basic creep is the delayed strain occurring under a sustained load without moisture exchange with the environment. Therefore, several actions are taken to prevent specimens from drying during the test. First, specimens are sealed with two layers of adhesive aluminum foil. Second, loading cells are placed in isolated chambers where the elevated relative humidity is controlled by a saturated saline solution. The saturated saline solution of barium dichloride ($BaCl_2$) is used to obtain RH = 90-95%. Performing tests at 100% RH is avoided because of water condensation that may interfere with the normal operation of strain gauges.

Drying creep tests

Drying creep is the delayed strain occurring under simultaneous drying and sustained load. Two specimens were subjected to simultaneous loading and drying at two different stress levels and one specimen was subjected only to drying to measure the drying shrinkage strains.

The tests were carried out in a ventilated climate-controlled chamber with controlled temperature and relative humidity (T = 20.3 ± 0.2°C and RH = 70.7 ± 0.5%. Ventilation in the

chamber ensures permanent humidity profiles on the surfaces of specimens for a stable drying process.

3. EXPERIMENTAL RESULTS AND DISCUSSION

3.1 Basic creep of cement paste

Uniaxial compliances for low and medium loading levels are presented in Figure 1a). First, different dependences of short-term creep and medium-term creep on stress levels are noticed. The specimen at higher stress level exhibits increased creep growth only during the short-term phase.

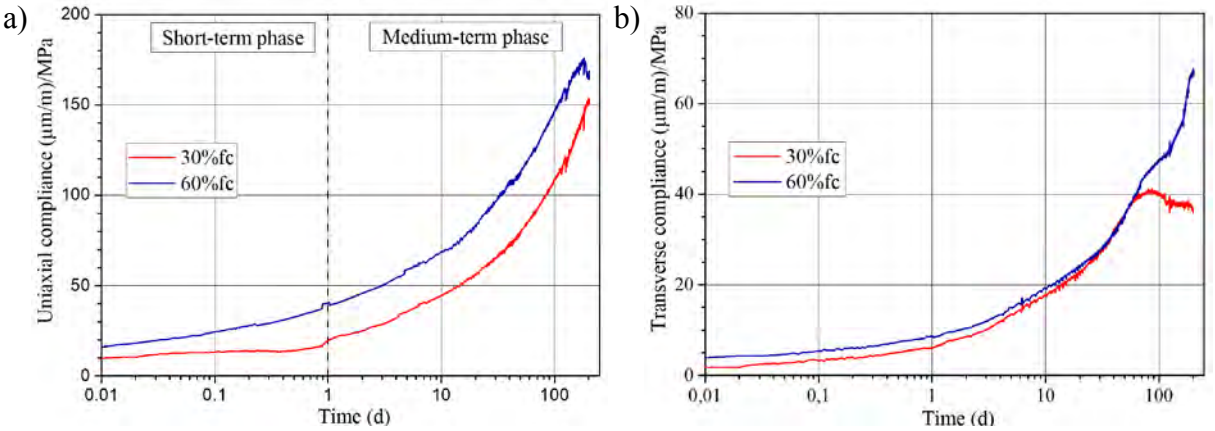

Figure 1: Basic creep of cement paste a) uniaxial compliance b) transverse compliance

For the presented experimental results, it is assumed that most of the damage is occurring during a short time after load application as delayed propagation of the microcracks formed during the loading step. The propagation of microcracks after load application in concrete during stress relaxation was demonstrated by Acoustic Emission (AE) [5]. After approximately one day after load application, the creep rate of both specimens follows the same trend. Consequently, no pronounced nonlinearity manifested itself between low and medium stresses at long-term.

The transverse compliance reveals creep linearity as a function of stress for both short-term and long-term creep in the stress range up to 60%f_c (Figure 1b)). Starting from a certain instant, both curves deviate from the initial trend. The transverse compliance of the 30% loaded specimen decreases down to a constant value while the compliance of the 60% loaded specimen exhibits an increasing rate. In the case of the 30% loaded specimen, the decrease of lateral creep rate may indicate drying or autogenous shrinkage. For the 60% loaded specimen, the increase of creep rate may be an indicator of damage propagation in the specimen. It was confirmed on a tomographic scan that displayed a network of angled cracks that could be the result of shear sliding in the cement paste.

3.2 Basic creep of mortar

Unlike the case of basic creep in cement paste, uniaxial compliance of basic creep of mortar (Figure 2a)) displays a non-linearity dependent on stress level between 30% and 60% of failure

loading. As it is assumed that microcracks growth in the cement paste matrix at long-term does not affect significantly the creep kinetics, nonlinearity in mortar is assumed to be influenced by microcracking on the aggregate-matrix interfaces. It was proposed, based on AE monitoring of creep tests on mortar and concrete that most of the detected acoustic events corresponded to cracking of Interface Transition Zones (ITZ) [6]. Despite the nonlinearity of axial creep strains, lateral creep strains show the same trend for low and medium levels (Figure 2b)).

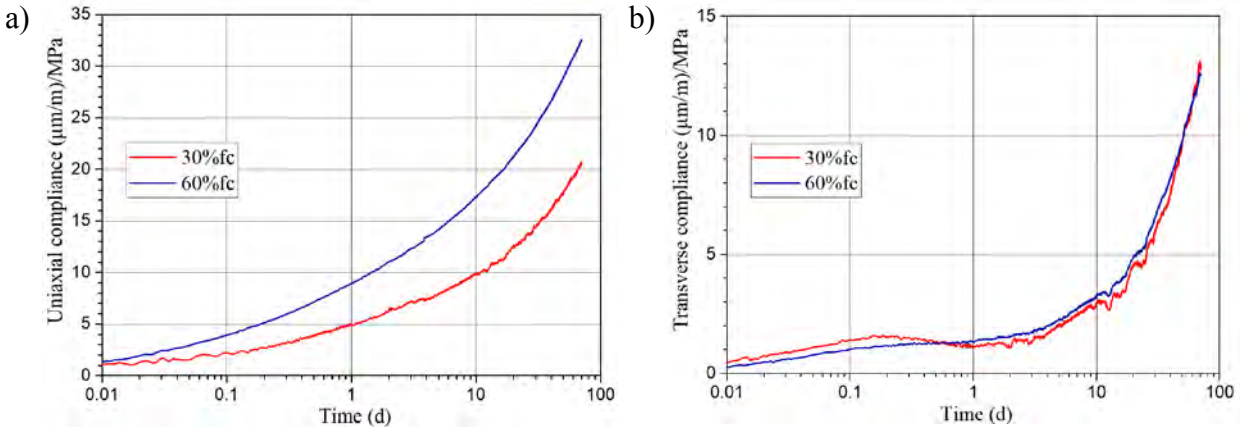

Figure 2: Basic creep of mortar, a) uniaxial compliance, b) transverse compliance

3.3 Drying creep of cement paste

Uniaxial compliances of cement paste in drying and basic creep are presented in Figure 3a). The Pickett's effect is fully manifesting itself after approximately one day after load application when the total creep rate is increasing fast. Unlike the case of basic creep, total creep strains are nonlinear wrt. the stress level in the range from low to medium stresses. Therefore, the Pickett's effect may be influenced by the stress level.

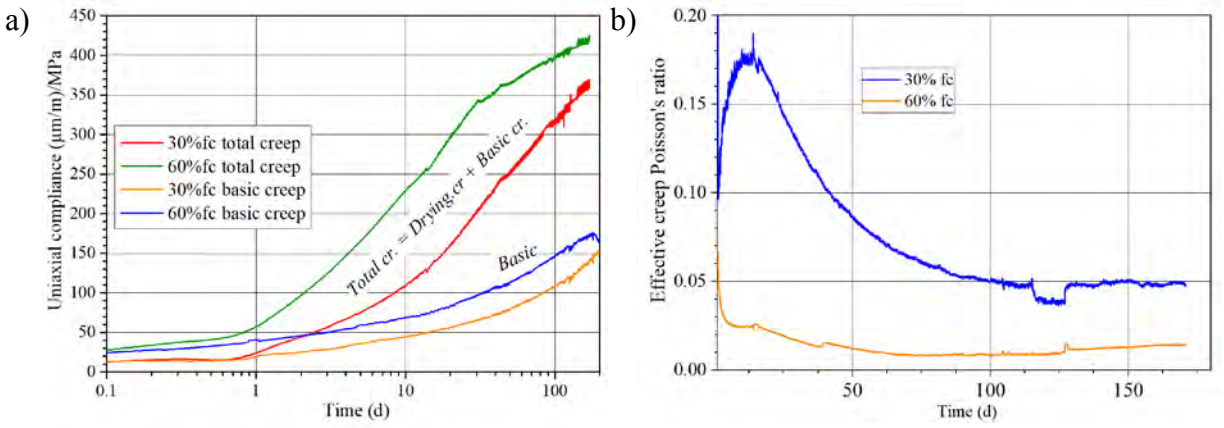

Figure 3: a) Uniaxial compliance of drying and basic creep of cement paste, b) effective creep Poisson's ratio of drying creep

Further, it is observed that the total creep rate of the specimen loaded at 60% f_c starts decreasing ca. 40 days after load application. The specimen loaded at 30% f_c exhibits a similar behavior after ca. 130 days. From this statement, it can be assumed that under higher

compressive loadings the drying kinetics is faster than at lower loadings. The calculation of lateral creep strains gives abnormally low values of the effective creep Poisson's ratio. One likely explanation is that the specimens under compressive loading exhibit elevated drying shrinkage strains.

A comparison of strains of loaded specimens and the companion (unloaded) specimen reveals that the total creep strain at 30% f_c is of the same order of magnitude as the drying shrinkage strain (Figure 4a)). Their relationship is almost linear with a slope close to 1 (Figure 4b)). For medium stress level, this dependence is nonlinear during the drying phase but then it converges to a linear trend (Figure 4b)).

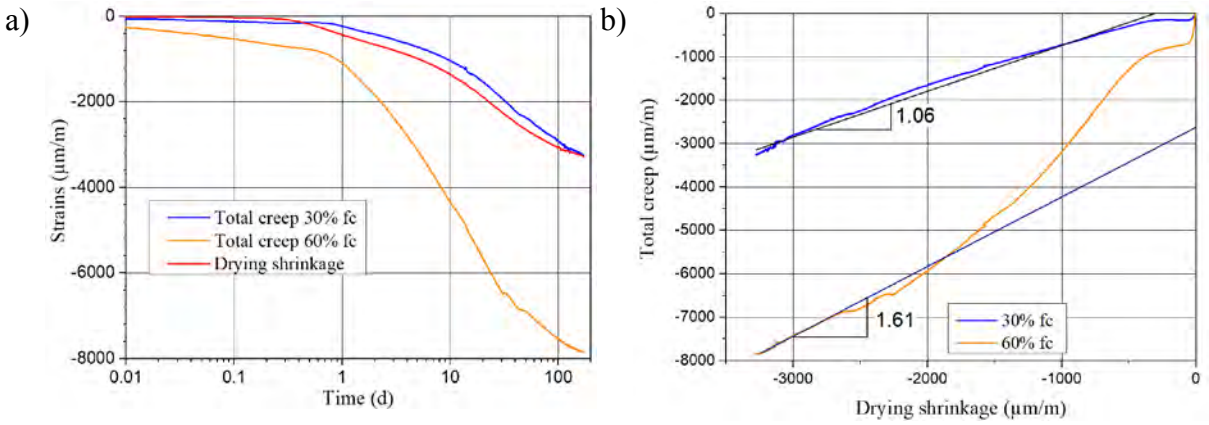

Figure 4: a) Total creep and drying shrinkage strains, b) total creep as a function of drying shrinkage

The Impulse Excitation Technique (IET) was applied to measure the dynamic modulus of elasticity before and after drying creep tests. Relationships between dynamic modulus and strength were observed by several authors [7], but the exact correlation between static and dynamic properties has not yet been established. Therefore, IET is used not to measure the exact static properties, but to observe the variation of stiffness before and after creep tests.

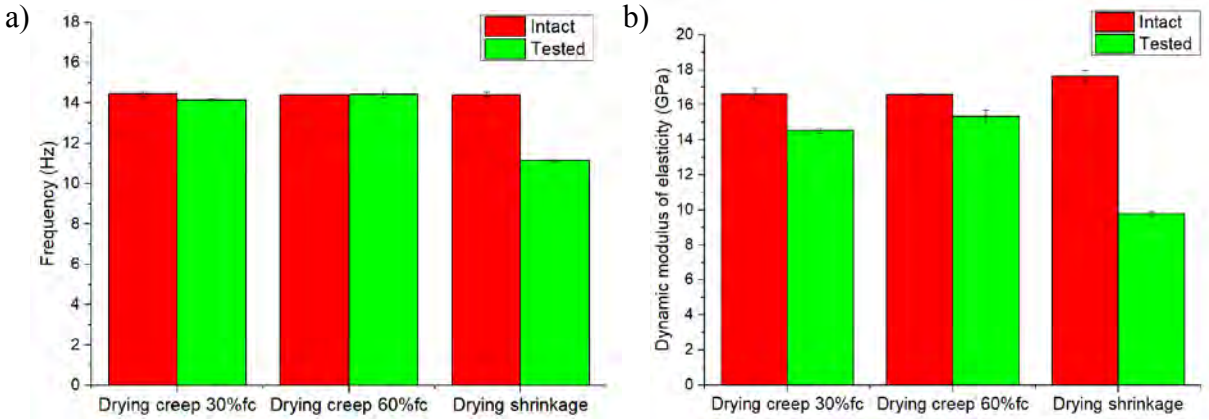

Figure 5 : Evolution of parameters before and after drying creep tests. a) Natural frequency, b) dynamic modulus of elasticity

The natural frequencies of flexural vibration modes are measured with the GrindoSonic® device. The dynamic modulus of elasticity in flexure is calculated according to an ASTM standard [8] as a function of specimen dimensions, mass and Poisson's ratio assuming that the material is homogeneous, isotropic and perfectly elastic.

Figure 6a) shows the change of natural frequencies before and after drying creep. The frequencies of specimens subjected to drying creep do not considerably evolve, while those of the companion specimen dropped from 14 Hz to 11 Hz. The dynamic modulus of elasticity of specimens after drying creep has decreased as their masses have decreased due to drying (Figure 6b)). However, as their natural frequencies have not changed, no significant positive effect (due to cement paste consolidation) nor negative effect (due to microcracking) of creep is observed. The drastic decrease of the natural frequency of the companion specimen subjected to drying is attributed to microcracking in the vicinity of the surfaces. In further studies, the specimens will be examined and subjected to destructive tests to measure the elastic modulus and strength.

4. CONCLUSION AND PERSPECTIVES

The presented experimental results give an insight into delayed strains of homogeneous and heterogeneous materials and the role of damage in the viscous response. Basic creep of cement paste is observed to be linear at medium term in the range of stresses up to $0.6\,f_c$. Thus, it is assumed that there is no progressive damage propagation after the short-term. Mortar exhibits a nonlinear behavior from $0.3\,f_c$ to $0.6\,f_c$. As the basic creep of the cement paste in this stress range is mostly linear, it is hypothesized that non-linearity of mortar is attributed to microcracking accumulation at the aggregate-matrix interfaces.

In drying creep tests, the specimen subjected to higher loading ($0.6\,f_c$) exhibits faster drying kinetics in comparison to the one subjected to low compressive stress ($0.3\,f_c$). To check the hypothesis about drying shrinkage/sustained stress coupling, periodic weighting and mass comparison of specimens subjected to drying shrinkage and to drying creep at low and high stresses are required. The low magnitude of calculated lateral creep strains indicates that simultaneous loading and drying can lead to increased drying shrinkage strains.

In a further study, tomographic investigations will be used to estimate damage in the tested specimens. Basic creep tests of mortar and cement paste stabilized at RH = 70% and drying creep of mortar at RH = 70% will be carried out to complete the necessary data for the estimation of microcracking influence on the creep kinetics.

REFERENCES

[1] E. Gallitre, P. Labbe, G. Pastor, and Y. Le Pape, 'Durée de vie des enceintes de confinement', *Revue Générale Nucléaire*, pp. 43–47, Mar. 2014.

[2] Z. P. Bažant and Y. Xi, 'Drying creep of concrete: constitutive model and new experiments separating its mechanisms', *Materials and Structures*, vol. 27, no. 1, pp. 3–14, Jan. 1994.

[3] M. F. Ruiz, A. Muttoni, and P. G. Gambarova, 'Relationship between Nonlinear Creep and Cracking of Concrete under Uniaxial Compression', *Journal of Advanced Concrete Technology*, vol. 5, no. 3, pp. 383–393, 2007.

[4] S. Huang, 'Comportement vieillissant du béton en fluage : application au béton VeRCoRs', PhD thesis, Université Paris-Est, 2018.

[5] E. Denarié, C. Cécot, and C. Huet, 'Characterization of creep and crack growth interactions in the fracture behavior of concrete', *Cement and Concrete Research*, vol. 36, no. 3, pp. 571–575, Mar. 2006.
[6] J. Saliba, 'Contribution of the Acoustic Emission technique in the understanding and the modelling of the coupling between creep and damage in concrete', Theses, Ecole Centrale de Nantes (ECN), 2012.
[7] V. M. Malhotra, V. Sivasundaram, and N. J. Carino (Eds.), 'Resonant Frequency Methods.', in *Handbook on Nondestructive Testing of Concrete*, West Conshohocken: CRC Press LLC (ASTM International), 2004, pp. 7–1 – 7–21.
[8] ASTM E1876-15, 'Standard Test Method for Dynamic Youngs Modulus, Shear Modulus, and Poissons Ratio by Impulse Excitation of Vibration'. ASTM International, West Conshohocken, PA, 2015.

EFFECT OF YOUNG'S MODULUS ON THE DEGRADATION OF REPAIR MORTARS CHLORIDE MIGRATION RESISTANCE UNDER COUPLED LOADING CONDITIONS

Stefan Ullmann (1), Dirk Lowke (1)

(1) Institute of Building Materials, Concrete Construction and Fire Safety, Technische Universität Braunschweig, Germany

Abstract

The chloride migration coefficient is the most important material parameter for the service life prediction of reinforced concrete structures in exposure to chloride. For a comprehensive and precise prediction of the service life, however, further effects such as load-induced microcracks must be taken into account. Currently coupled effects like chloride exposure in connection with the formation of load-induced microcracks cannot be predicted adequately. In the past years, research was done to develop test set-ups for coupled loading conditions. Mostly the performance of concrete was tested and described.

This paper focusses on the performance of loaded repair mortar samples under chloride attack. For concrete samples, a load-related increase of the chloride migration coefficient is widely known. It is pointed out, that repair mortars behave differently. Especially in dependency on the materials Young's modulus. Furthermore, details of the used test set-up and the resulting fracture pattern are discussed. The results indicate that also the size and amount of aggregates may affect the performance of a cementitious mortar under coupled loading conditions.
Keywords: Young's modulus, chloride migration, microcracks, repair mortar, durability

1. INTRODUCTION

Whereas probability-based service life design is an established tool to ensure the required durability of new concrete structures, models for service life design of repaired structures have not been available. The work of Rahimi [1] and von Greve-Dierfeld [2] focused on the adoption of existing models and on the inclusion of aspects related to concrete repair, such as the application of thin layers of repair mortar in order to extend a buildings remaining lifetime. However, these models are valid for uncracked concrete or repair mortar only. At the same time, numerous researchers proved [3] that mechanical load above 50 % of the ultimate load capacity causes microcracks, which consequently reduce durability related resistances. Thus, coupled effects, such as service loading and chloride attack, and the interaction between old concrete

and repair mortar need to be investigated, to determine the remaining lifetime of a concrete structure after repair precisely. Along others, an important influencing variable within these investigations is the difference in Young's modulus of old concrete and repair mortar.

As part of this work, this paper is focusing on the degradation of the chloride migration coefficient under load and in dependency on certain levels of Young's modulus. Therefore the test set-up according to Wang et al. [4] a was modified in order to mount certain stress-levels to the standardized specimen (cylinders of 100 mm diameter and a height of 50 mm) and run the migration tests under constant loading conditions. The technical requirements of NT Build 492 [5] and the German leaflet for the determination of the chloride migration coefficient of concrete (BAW-Merkblatt MDCC [6]) were therefore taken into account. Along with that, the design of the loading frame was done in accordance to calculations regarding the stress-distribution within the specimen.

2. THEORETICAL BACKGROUND

Various researchers already proved the effect of microcracks on the resistance of concrete against ingress of fluids or gases. The publications listed in the RILEM report043 [3] indicate, that load-induced microcracks reduce the resistances against ingress, such as e.g. chloride and CO_2-ingress (carbonation). It is also shown, that tensile stresses immediately decrease concrete's resistances whereas compressive stresses within the elastic part of the stress-strain-relationship even increase values like the chloride migration coefficient. At a load level beyond 40 % - 50 % (within the plastic deformation region), the resistances start to decrease. The intensity of this effect is strongly dependent on the concrete mix.

According to [4] the determination of a load-affected chloride migration coefficient is possible. Following [7], the design of the loading frame would lead to mostly compressive stresses within the cross-section. Within the middle of the round surface of the disk, also small values of tensile stresses will occur because of the lateral extension of the specimen. They will lead to vertical microcracks (crack-width <0.1 mm) at the surface and within the disk and finally affect the resistance of the sample against the ingress of chloride ions. Therefore, the loading frame used for the research presented in this paper was designed to cover 95° of the disks circumference on top and on the bottom of the sample, respectively.

Wang [4] showed the effect of occurring microcracks using different concrete mixes and aggregates (basalt) up to 20 mm. The occurrence of the cracks was validated using an ultrasonic pulse velocity device. The cited paper also shows that cracks will vertically occur on the base surface of the cylindrical specimen.

The presented work focussed on the three questions, (1) whether this test set-up is also appropriate for repair mortar specimen, (2) whether the mentioned effect can also be detected for repair mortars (smaller aggregates) and (3) whether its appearance and intensity is dependent on the Young's modulus. Furthermore, the results of unloaded specimen tested in the developed loading frame will be compared with results of the same material tested under conditions according to [6].

3. MATERIALS AND METHODS

Three repair mortars (one Cement Concrete mortar (CC) and two Polymer Cement Concrete mortars (PCC1 + 2)) were investigated. Table 1 shows the proportion for the mixtures. Both

PCC mortars are based on an Ordinary Portland Cement (CEM I 42.5 R according to EN 197-1 [8]) and contain PP-fibres of 4 mm length. While the maximum diameter of the aggregates (sand) of PCC1 was 2 mm, PCC2 contains fine sand with a maximum diameter of 0.8 mm. The CC mortar contains a CEM I 52,5 N and sand with a maximum diameter of 3,15 mm. The hardened properties of the three mortars, determined on prismatic samples after 28 days according to EN 12190 [9] and EN 13412 [10], are summarised in Table 2.

Table 1: Mixture proportion of CC and PCC repair mortars

Materials	CC	PCC1	PCC2
Sand [kg/dm³]	1.255	1.129	942
Limestone powder / Filler [kg/dm³]	100	156	130
Cement [kg/dm³]	600	584	487
Water [kg/dm³]	270	253	276
Superplasticizer	0.3 % bwoc	-	-
Additives/PP-Fibres [kg/dm³]	-	78	65

Table 2: Hardened properties of the three repair mortars

Material	Slump [mm]	Bulk density [g/cm³]	Young's modulus [GPa]	Compressive strength [MPa]	Bending tensile strength [MPa]
CC	23.3	2.22	35	43.9	6.7
PCC1	15.0	2.21	25	54.6	10.5
PCC2	12.9	2.05	13	23.2	5.2

The specimen were casted in cylindrical molds with a height of 200 mm and a diameter of 100 mm. After demolding the cylinders were cured in water at a temperature of 20°C until the day of testing (28 days). Seven days before testing, the cylinders were sawn for the testing. The first 10 mm were discarded. Subsequently, three disks with a height of 50 mm were cut out of the remaining cylinder. By the time, this paper had to be submitted, the work is based on the results of 18 disks of CC, 23 disks of PCC1 and 20 disks of PCC2.

A loading frame was designed according to Wang [4] to conduct the chloride migration tests at certain stress levels equivalent to 0 %, 40 %, 60 % and 80 % (in case of PCC2 also 100 %) of the ultimate compressive load. The ultimate load for each mix was determined in a compression test. Therefore the specimen were placed in the loading frame and then placed into a testing machine. Up to six specimen were loaded until failure. According to [7] and [11], the average load was converted into stress related to the chord length covered by the loading frame and the depth of the specimen. The ultimate load of CC and PCC1 was 165 kN, i.e. 40 MPa. The ultimate load of PCC2 was 60 kN, i.e. 15 MPa. The water curing (standard curing for RCM tests) and the different loading regime in the frame explain the lower compressive strength of the two PCC mortars compared to the compressive strength testing according to [9] (Table 2).

A torque wrench was used to apply the load to the specimen in the frame. The load that needs to be applied can be transferred into a torque by multiplying the pitch of the steel bold, which is 2.5 mm using a M20 thread. The calculations were validated using a load cell.

After loading, the migration cells were attached to the frame (Figure 1 left). Silicone was used to ensure water tightness at the lateral surface and along the edges of the loading frame. The chloride migration tests were conducted at a constant voltage of 30 Volt. The duration of testing was set to 24 hours for CC samples and 48 hours for the PCC samples.

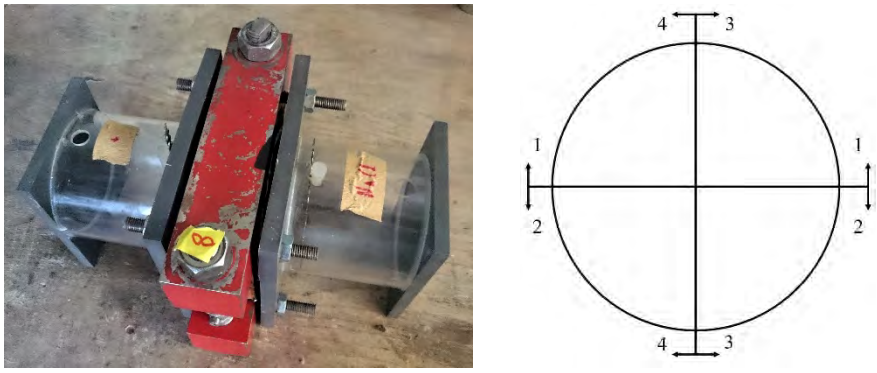

Figure 1: Test set-up for the determination of D_{nssm} under load (left) and sketch to visualise the directions of splitting (right)

For the analysis of the depth of ingress the sample was split into quarters, horizontally (cross-sections 1 + 2) and vertically (cross-sections 3 + 4), in order to detect potential differences in dependency in the direction of loading and cracking (Figure 1 right). The calculation of the D_{nssm} value was done according to [6].

4. RESULTS

4.1 Formation of cracks and fracture pattern

To fully understand the results presented in this paper it is important, to describe the formation of cracks and the fracture pattern of the specimen after applying the ultimate load in a loading frame. Differences between the three repair mortars became clearly visible.

Figure 2 left shows a sample of the CC mortar after failure. It seems that the inside of the cylinder received compressive stresses only in vertical direction, as there is the classical “sand clock-shape” known from cubes and cylinders in compressive strength testing (1). Within the contact area between the loading frame and the sample, lateral extension was hindered. Before reaching the ultimate load, the first visible cracks (crack-width 0.1 mm) appeared at the left and right edge of the cylinder starting at the edge of the internal radius of the loading frame (2l and 2r, white arrows right figure, further on named “edge region”). Followed by a plate-like detachment of the front and end face of the cylinder (Fig. 2, 3f and 3b). A PCC1 sample showed similar behaviour. Due to the PP fibres, however, the samples did not fall to pieces as strongly. The two large cracks occurred less strongly in the edge area and were instead distributed in finer cracks over the entire surface. The PCC2 samples (not shown here) did not show any visible cracks at all after reaching the ultimate load. Only if stopping the testing machine was prevented, the specimen was destroyed. The specimen then showed a similar fracture pattern to the other samples.

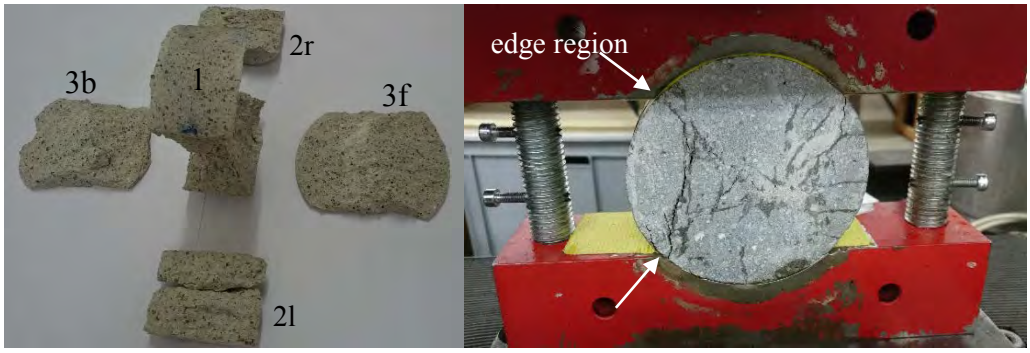

Figure 2: Fracture pattern of a specimen after applying the ultimate load, CC sample left, PCC1 sample right

The formation of one or two cracks at the edge region did not occur immediately but during the rapid chloride migration tests and only if a load level of 80 % was applied. After finishing the tests, the cracks were clearly visible at the surface, especially after splitting the samples (Figure 3). As these areas do not represent a micro-cracked area and as these cracks do intensively affect the determination of the D_{nssm} value, two characteristic values were determined for further evaluation: The "original" uncorrected D_{nssm} value (as shown in Figure 3) and a corrected D_{nssm} value, excluding the areas affected by the cracks at the edge region of the cylinder. It is worth noting, that only cross-sections 1+2 are taken into consideration, as cross-sections 3+4 did not show any noticeable differences in the depth of ingress compared to unloaded samples. This could be explained by a rather vertically formation of the microcracks.

Figure 3: Chloride ingress into cross-sections 1 + 2 for CC-sample (lighter colour), D_{nssm} value affected by cracks

3.2 Chloride migration coefficient under load

For comparison, Table 4 shows the effect of the test set-up on the D_{nssm} value. Each value is an average of at least two and up to four single values. It seems that the test set-up according to [4] generally overestimates the chloride migration coefficient and thus underestimates the resistance of the repair mortar against chloride-ingress in comparison to the test setup according to **[6]**. The measured values are up to 20 % higher than the values determined according to [6] (Table 4, columns 2 and 3). The reasons for differences between the D_{nssm} values determined according to [6] and in the unloaded frame have to be clarified as part of ongoing investigations. The fact that the preparation of a set-up in a loading frame takes up to 90 minutes may cause a certain drying of the repair mortar sample at the surface what might initially lead to capillary sorption. For this reason, the values according to [6] were not taken into consideration for further presentations in this paper as it focusses on the effect of loaded and unloaded samples in the loading frame only.

Table 4: Comparison between D_{nssm} determined confirming [6] and in an unloaded frame

	D_{nssm} acc. to [6] [m²/s]	D_{nssm} unloaded frame [m²/s]	Difference [%]
CC	10.2×10^{-12}	12.2×10^{-12}	16
PCC1	4.0×10^{-12}	4.5×10^{-12}	11
PCC2	5.7×10^{-12}	7.2×10^{-12}	21

The results of CC (2 × 0%, 4 × 40%, 2 × 60% and 1 × 80%), PCC1 (3 × 0%, 3 × 40%, 2 × 60% and 3 × 80%) and PCC2 tests (2 × 0%, 1 × 40%, 1 × 60% 2 × 80% and 1 × 100%) are shown in Figure 4. The left part shows the uncorrected D_{nssm} value (absolute value on top, relative on the bottom). The corrected D_{nssm} value is visualised the same way on the right side.

A chloride migration test at a load-level of 100 % was only possible for the PCC2 sample due to the low Young's modulus. It has to be mentioned, that as a result of relaxation, the PCC2 sample lost up to 20 % of the initially applied torque while the test was running.

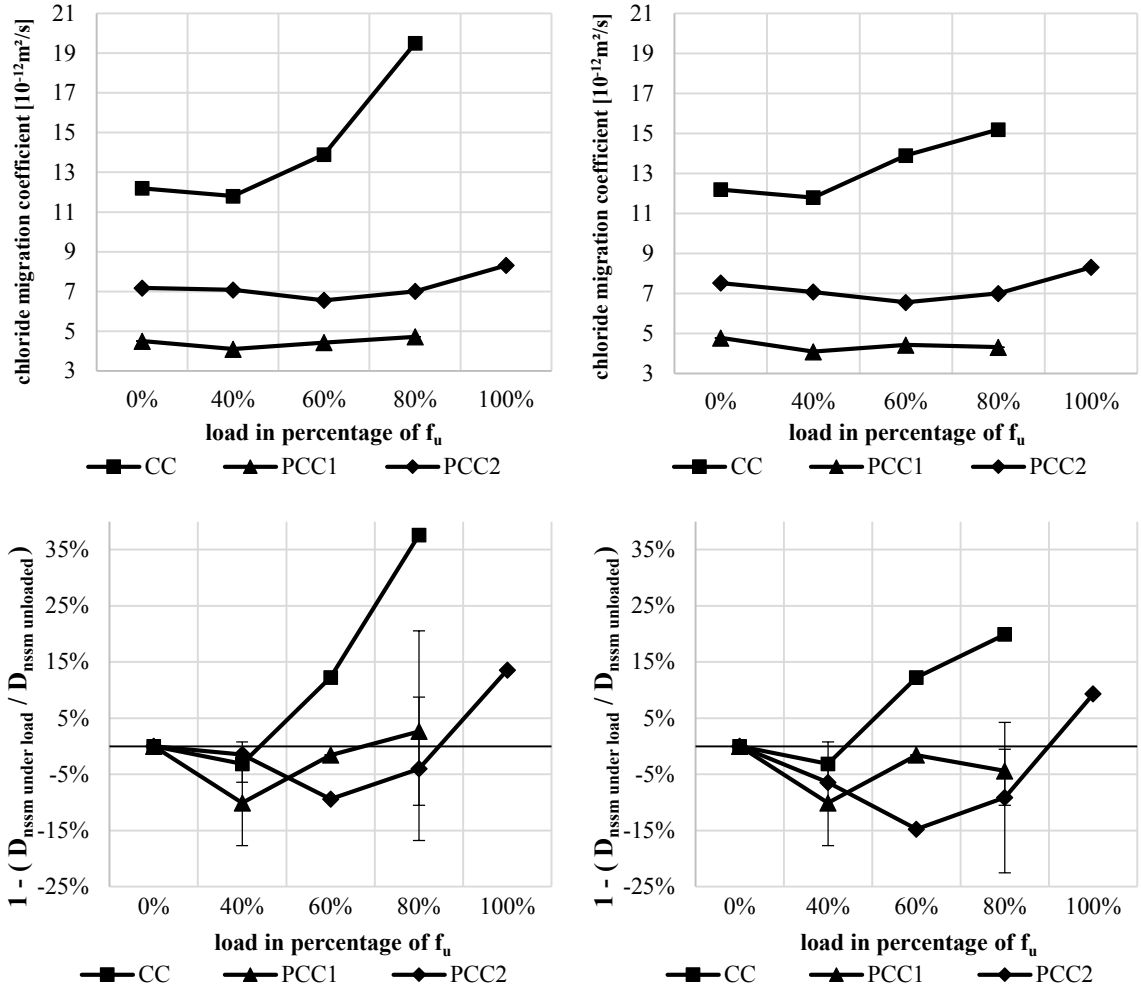

Figure 4: D_{nssm} determined for three repair mortars under certain load levels - uncorrected values including macro cracks (top left), corrected values excluding areas with macro cracks (top right) and load-dependent change of D_{nssm} [%] related to unloaded sample including (bottom left) and excluding macro cracks (bottom right)

5. DISCUSSION

Compared to [4] only the CC mortar showed a significant load-related increase of D_{nssm}, i.e. a decrease of the resistance against ingress of chlorides, as the concrete samples of Wang [4] did. The effect is still visible (even though the increase of D_{nssm} is less obvious), if the corrected D_{nssm} values (no consideration of macro-cracks) are compared (Figure 4, top left and right). At a load level of 40 % the CC mortar also showed a slight decrease of the chloride migration coefficient. The same effect was observed by Wang and referred to the compression of the pore structure within the elastic region of the stress strain relationship [4].

In contrary, PCC1 and PCC2 did not show any load-related increase of the D_{nssm} value between 0 % and 80 % of the ultimate load. In contrary, the values noticeably decreased up to 15 %. A load-level of 60 % for PCC1 and respectively 80 % of the ultimate load for PCC2 still caused lower chloride migration coefficients compared to the unloaded samples. In addition, the difference between the uncorrected and the corrected values becomes less significant.

Obviously the Young‘s modulus as well as the PP-fibres have an effect on the formation of microcracks and the corresponding chloride migration coefficient. The capability of crack-free deformation is limited for repair mortars with a rather high Young’s modulus, like CC (35 GPa). In contrary, a material like PCC2 (Young’s modulus of 13 GPa) behaves softer. It seems that a higher stress-related strain and the related compression of the pore structure leads to a higher resistivity against the formation of microcracks and the ingress of chloride ions. A decrease of the chloride migration coefficient is only visible, if the specimen is loaded until failure (100 %).

The graph of PCC1 (25 GPa) logically fits the observations pointed out so far as it behaves like a “mixture” of the CC mortar and PCC2 mortar regarding the sensitivity to external loading.

Furthermore, the formation, the size and the shape of microcracks between the cement matrix and the aggregates (interfacial transition zone (ITZ)) might be significantly affected by the size and the amount of aggregates. Larger aggregates (as an example Wang used 20 mm basalt) might also lead to larger microcracks. That could be an explanation, why the chloride migration coefficient of concrete is more affected by external loading than the D_{nssm} value of repair mortar. The PCC2, that showed no load-related increase of the chloride migration coefficient within these investigations contained aggregates with a maximum size of 0.8 mm only.

However, further investigations are necessary to support this hypothesis. It appears as if the results by Wang cannot be transferred to repair mortar systems, as there is an effect of Young’s modulus and as there might be a correlation between the formation of microcracks and the maximum size and amount of the aggregates in the mixture.

6. CONCLUSION

The following conclusions can be drawn from the results presented in this paper:

- The effect of load-induced microcracks on the degradation of concrete’s resistance against chloride ingress was observed for a CC repair mortar. Beyond a load-level of around 50 % of the ultimate load, the D_{nssm} value increased.
- Using a repair mortar with low Young’s modulus (such as PCC mortar), the effect disappeared and external loading even improved the resistance to chloride ingress.

- The size and amount of the aggregates seems to have an influence on the formation of microcracks, which might be why mortar samples behave differently from concrete samples.
- For the evaluation of the D_{nssm} value in visibly cracked samples, careful decisions have to be made, as the larger cracks strongly affect the value but do not represent the influence of the microcracks throughout the cross-section.

ACKNOWLEDGEMENTS

This work is financed by the German Research Foundation (DFG) within the Research Training Group 2075 at Technische Universität Braunschweig (project no. 255042459). The authors would furthermore like to thank the researchers at the Department of Sustainable Built Environment of Queens University Belfast and StoCrete GmbH Germany for the kind support.

REFERENCES

[1] Rahimi, A. *Semiprobabilistisches Nachweiskonzept zur Dauerhaftigkeitsbemessung und -bewertung von Stahlbetonbauteilen unter Chlorideinwirkung*. Ph.D. Thesis, Munich: Technische Universität Munich, 2016.

[2] von Greve-Dierfeld, S. *Bemessungsregeln zur Sicherstellung der Dauerhaftigkeit XC-exponierter Stahlbetonteile*, Ph.D. Thesis, Munich: Technische Universität Munich, 2015.

[3] Yao, Y., Wang, L., Wittmann, F. H. 'Publications on Durability of Reinforced Concrete Structures under combined mechanical loads and Environmental Actions: An Annotated Bibliography', RILEM report 043, Aedificatio Publishers, 2013

[4] Wang, J., Basheer, P.A.M., Nanukuttan, S.V., Long, A.E., Bai, Y. 'Influence of service loading and the resulting micro-cracks on chloride resistance of concrete'. *Construction and Building Materials* **108** (2016) 56-66.

[5] Nordtest. NT Build 492 Approved 1999-11, Concrete, mortar and cement-based repair materials: Chloride migration coefficient from non-steady-state migration experiments, 1999.

[6] Bundesanstalt für Wasserbau BAW, Merkblatt MDCC - Dauerhaftigkeitsbemessung und -bewertung von Stahlbetonbauwerken bei Carbonatisierung und Chlorideinwirkung, 2017.

[7] Zhang, W. Drescher, A. Newcomb, D.E. 'Viscoelastic analysis of diametral compression of asphalt concrete'. *Journal of Engineering Mechanics* **108** (1997) 596-603.

[8] EN 197-1, Cement - Part 1: Composition, specifications and conformity criteria for common cements, European Committee for Standardization, 2011.

[9] EN 12190, Products and systems for the protection and repair of concrete structures - Test methods - Determination of compressive strength of repair mortar, European Committee for Standardization, 1998.

[10] EN 13412, Products and systems for the protection and repair of concrete structures - Test methods - Determination of modulus of elasticity in compression, European Committee for Standardization, 2006.

[11] Hondros, G. 'The evaluation of Poisson's ratio and the modulus of materials of a low tensile resistance by the Brazilian (indirect tensile) test with particular reference to concrete'. *Australian Journal of applied science* **10** (3) (1959) 243-268.

Theme 5

Effect of time-dependent phenomena and ageing on microstructure and durability

AGEING COEFFICIENT OF FLY ASH CONCRETE

M.M.R. Boutz (1), G.J.L. Van Der Wegen (1), A. J. Sarabèr (2)

(1) SGS INTRON, Sittard, The Netherlands

(2) Vliegasunie, Culemborg, The Netherlands

Abstract

The time dependency of the chloride diffusion coefficient, the so-called ageing coefficient, of fly ash concrete has been investigated. The effect of origin of the fly ash as well as the origin and strength level of the cement combined with the fly ash, has been determined. Results obtained using the RCM-method on samples aged up to 5 years under ambient conditions in The Netherlands are presented in detail. Our research shows that the ageing coefficient of the fly ash concrete is in good agreement with the values mentioned in the Dutch guideline for service life design of structural concrete.

Keywords: chloride diffusion, ageing coefficient, concrete resistivity, fly ash concrete.

1. INTRODUCTION

The service life of reinforced concrete structures exposed to high concentrations of chlorides is mainly determined by the thickness of the concrete cover and its resistance to chloride ingress [1,2]. The cumulative ingress of chlorides in time is of course related to the initial value of the chloride diffusion coefficient, but it is much more affected by the so-called ageing coefficient of the concrete [1,2]. Concrete in which part of the cement has been replaced by fly ash is known to have an initial (28 days) chloride diffusion coefficient significantly higher than the same concrete without fly ash. However, due to the pozzolanic behaviour of the fly ash the chloride diffusion coefficient will decrease more rapidly in time than the concrete without fly ash. Hence, the ageing coefficient of fly ash concrete is much higher.

Based on the principle of equivalent concrete performance, concrete compositions with low cement content (down to 200 kg/m^3) and high fly ash content (up to 100 kg/m^3) have been used successfully in The Netherlands on a large scale for more than 25 years now [3]. Although the benefits of such fly ash concretes are generally well recognized, there is some discussion on the actual value of their ageing coefficient [4].

The effect of ageing of concrete on the chloride diffusion coefficient is generally described by:

$$D_t = D_0 (t_0/t)^n \quad (1)$$

in which D_t is the chloride diffusion coefficient at time t, D_0 is the chloride diffusion coefficient at reference time t_0 (usually 28 days) and n is the ageing coefficient.

In the CEB-FIP Model code for service life design [2] a value of 0.60 is given for the ageing coefficient of Portland fly ash cement concrete. The Dutch guideline for service life design [5] gives higher values: 0.70 for XS3/XD2 and 0.80 for XS1/XD1/XD3. In more recent literature values up to 0.90 were reported [6][7] for the ageing coefficient. Such differences in the n-value have a tremendous impact on the calculated service life.

Therefore, a long term research programme has been performed to examine the effect of different origins of fly ash and different origins as well as strength levels of ordinary Portland cement on the value of the ageing coefficient of fly ash concrete. A typical Dutch CEM I 52.5N cement was combined with 3 fly ashes originating from different Dutch coal fired power stations; one of the fly ashes was additionally combined with 2 other CEM I 52.5N cements of different origin and strength level. As a reference Dutch CEM III/B cement was used, which is known for its high resistance against chloride ingress [3]. The chloride migration coefficient and the electrical resistivity of concrete specimens prepared with these binders have been tested at different ages up to 5 years. In order to be close to practical conditions, the specimens were exposed outdoors (unsheltered) until testing. The final results are presented and discussed in this paper.

2. MATERIALS AND METHODS

2.1 Materials and properties

The chemical composition of the fly ashes and the compressive strength of the cements, are shown in Tables 1 and 2. Cement C2 clearly has the slowest strength development from the 3 Portland cements. Dutch river sand (0-4 mm) and gravel (4-16 mm) were used as aggregate. The maximum grain size is limited to 16 mm in order to lower the variation in chloride migration coefficient.

Table 1: Composition (wt.%) of fly ashes

Code	FA1	FA2	FA3
SiO_2	58.6	61.0	61.0
Al_2O_3	20.7	20.6	21.1
Fe_2O_3	7.6	6.8	6.8
CaO	4.5	4.7	3.5
MgO	2.0	1.8	2.2
Na_2O-eq	2.5	3.0	2.7
TiO_2	0.88	0.86	0.94
P_2O_5	0.55	0.38	0.34
LOI	2.7	0.72	2.0
<45 µm	77.9	79.6	84.8

Table 2: Compressive strength development cements (EN 196-1)

Code	Cref	C1	C2	C3
Compressive strength (MPa)	CEM III/B 42.5N ENCI	CEM I 52.5N ENCI	CEM I 52.5N CBR Lixhe	CEM I 52.5N Seibel Erwitte
2 days	11.8	30.1	23.2	30.0
7 days	33.3	47.9	38.7	51.1
28 days	56.4	61.8	55.0	63.0

The concrete mixes were produced with local tap water. A superplasticizer (Tillman ON-S5000) was applied to establish good workability. Table 3 shows the composition of the concrete mixes investigated. All mixes possess the same binder content (cement + fly ash = 360 kg/m^3), same water/binder ratio (= 0.45) and same dosage of superplasticizer. In Table 4 the properties of the fresh concretes are shown.

Table 3: Composition of concrete mixes (kg/m^3)

Component	Cref	C1FA1	C1FA2	C1FA3	C2FA1	C3FA1
CEM III/B 42.5N	360	0	0	0	0	0
CEM I 52.5N	0	240	240	240	240	240
Fly ash	0	120	120	120	120	120
River sand	800	793	793	793	793	793
River gravel	1015	1006	1006	1006	1006	1006
Water (effective)	162	162	162	162	162	162
Superplasticizer	1.8	1.8	1.8	1.8	1.8	1.8

Table 4: Fresh concrete properties

Property (unit)	Cref	C1FA1	C1FA2	C1FA3	C2FA1	C3FA1
Slump (mm)	155	150	210	220	65	155
Density (kg/m^3)	2350	2370	2350	2370	2370	2330
Air content (vol.-%)	2.0	2.1	1.0	1.0	1.9	1.9

2.2 Preparation of concrete specimens

After mixing for 4 minutes, the concrete mixes were cast in 150 mm cube moulds, covered with plastic sheets and stored in a moist cabinet at 20°C for 24 hours. Subsequently the specimens were demoulded and cured in saturated lime water of 20°C for 6 days. At the age of 7 days the specimens were taped in airtight plastic foils (i.e. no evaporation of water) and stored in a moist cabinet at 20°C until the age of 91 days. At that age the plastic foils were removed and the specimens were exposed outside (unsheltered) until the moment of testing.

2.3 Test methods

The compressive strength of the cement is measured according to EN 196-1. The compressive strength of the concrete is tested according to EN 12390-3.

The Rapid Chloride Migration (RCM) test was conducted to determine the chloride migration coefficient of the concrete according to NT Build 492. A core Ø100 mm was drilled from the cubes and 2 specimens 50 mm thick were prepared from the central 100 mm of the core. One specimen is tested with the surface originally located at 75 mm depth in the cube exposed to the chloride solution. The 2nd specimen is kept as spare. Measurements were performed on 3 specimens per concrete mix and age.

The specific resistivity of the specimens was determined according to the Two Electrode Method (TEM) described in [5]. The resistivity of the concrete specimen is measured by clamping stainless steel plates on opposite (mould) sides of the concrete cubes and in between a wet sponge for proper electrical contact. An AC (1 kHz) current passes between the two electrodes (passing through the entire concrete specimen) while the voltage drop is measured, from which the specific resistivity is calculated.

After 3 years curing an additional investigation was performed on 2 mixes (Cref, C1FA1) to determine the chloride diffusivity following EN 12390-11. For each mix 3 cubes were immersed in a 3 wt.% NaCl-solution (20°C) during 90 days. After removing the cubes from the solution 7 parallel layers 1.0 mm thick were dry ground and the chloride content of each layer was determined according to EN 14629. The non-steady state chloride diffusion coefficient (D_{nss}) is then determined from the profile by the regression method described in the standard.

3. RESULTS

3.1 Compressive strength

The development of the compressive strength with time of the concrete mixes is shown in Figure 1. The fly ash concrete mixes have a slower strength development than the reference mix, but reach similar strength level after 6 months. A closer look at Figure 1 and Table 2 also reveals that the strength development of the fly ash mixes is predominantly determined by the strength development of the Portland cement and to a lesser extent by the quality of the fly ash.

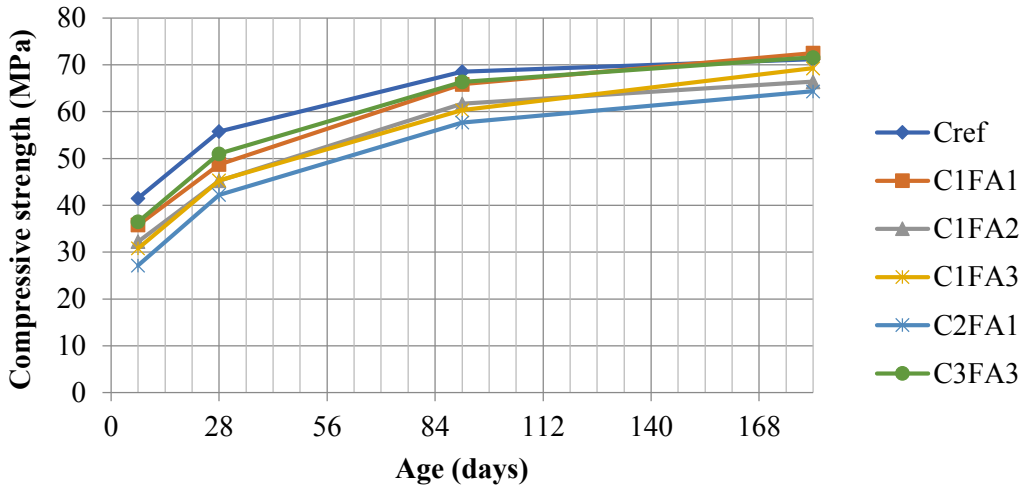

Figure 1: Development of cube compressive strength with time

3.2 Chloride migration coefficient

Table 5 gives the values of the chloride migration coefficient D_{RCM} at ages between 28 days and 5 years. At 28 days, the D_{RCM} of the mixes with fly ash is one order of magnitude higher than for the reference concrete with CEM III/B. However, after 1 year the RCM values are similar and after 3 years even lower than that of the reference mix.

The D_{RCM} of all fly ash mixes is around 0.5×10^{-12} m^2/s after 3 years. Unexpectedly, after 5 years the D_{RCM} increases again for all fly ash mixes. By contrast, D_{RCM} of the reference mix remains constant from 3 to 5 years. After 3 years the fly ash concrete is so dense that the RCM test has to be performed at the outer limit of the test conditions (maximum voltage 60 V, maximum test duration 96h) of NT Build 492. However, after 5 years the required test conditions were one step lower (60 V, 48h). It was therefore decided to run the RCM test again with the same test conditions as after 3 years (60V, 48h). The 2 fly ash mixes C1FA2 and C1FA3 were selected, because they show the largest increase in RCM-value from 3 to 5 years. The RCM-values of this 2nd test after 5 years are almost identical to those after 3 years (Table 5).

Because of the good correlation between RCM and 1000/TEM (see §3.5), RCM-values can be calculated from the TEM-values. The RCM-values calculated in this way agree well with the 2nd test result after 5 years for the 2 fly ash mixes and differ significantly from the first test result after 5 years. It is therefore concluded that D_{RCM} of the fly ash mixes does not increase between 3 and 5 years. Based on the 2nd test after 5 years, D_{RCM} remains unchanged. The increase of TEM-values for all fly ash mixes (see §3.4) indicates that RCM continues to decrease, even after 3 years.

Table 5: Chloride migration coefficient (x10^{-12} m^2/s) at increasing ages

Mix	28d	91d	182d	365d	3y	5y	5y (2^{nd} test)
Cref	2.1		1.1	1.1	0.9	0.9	
C1FA1	16.7	4.0	2.1	1.2	0.5	0.7	
C1FA2	18.0	4.6	2.2	1.4	0.4	1.6	0.5
C1FA3	18.3	4.9	2.8	1.4	0.4	1.0	0.4
C2FA1	22.9	6.0	3.5	1.8	0.4	0.9	
C3FA3	17.1	6.0	3.2	1.7	0.5	0.8	

3.3 Ageing coefficient

Figure 2 shows D_{RCM} as a function of age on a double logarithmic scale for all mixes. The 2^{nd} test result after 5 years was used for C1FA2 and C1FA3. From the slope of the curve fits the ageing coefficient (n) has been calculated (Table 6, method 1). The n-value of the fly ash mixes varies between 0.80 and 0.95 and is much higher than that of the reference mix (0.20).

Accurately determining the very low RCM-values of fly ash concrete mixes at ages of 3 years and more has proven difficult (see §3.2). Therefore a second method (method 2) has been used to determine the ageing coefficients for the fly ash mixes. In this method the RCM-values at 3 and 5 years were calculated from the TEM-values. The K-value (see §3.5) obtained from the RCM and TEM test results up to 1 year was used for this purpose. The n-values obtained with method 2 vary between 0.72 and 0.83 and are lower than those obtained with method 1 (see Table 6). These n-values are in excellent agreement with those mentioned in the Dutch guideline CUR Leidraad 1.

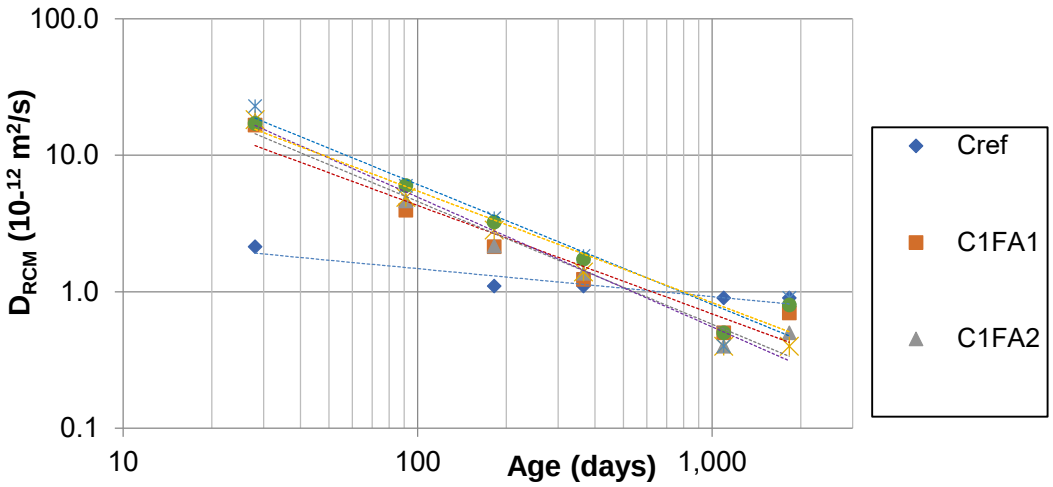

Figure 2: D_{RCM} as a function of age (log-log scale).

Table 6: Ageing coefficient n (−) calculated by 2 methods

	Cref	C1FA1	C1FA2	C1FA3	C2FA1	C3FA1
Method 1	0.20	0.80	0.90	0.95	0.88	0.82
Method 2	–	0.73	0.72	0.80	0.83	0.73

3.4 Electrical resistivity

The development with time of the TEM-value of all mixes is shown in Figure 3. The TEM-value continuously increases with time for all mixes during the full test period of 5 years. Up to 1 year the fly ash mixes have lower resistivities, but from 3 years onwards all fly ash mixes have a resistivity comparable or higher than the reference mix.

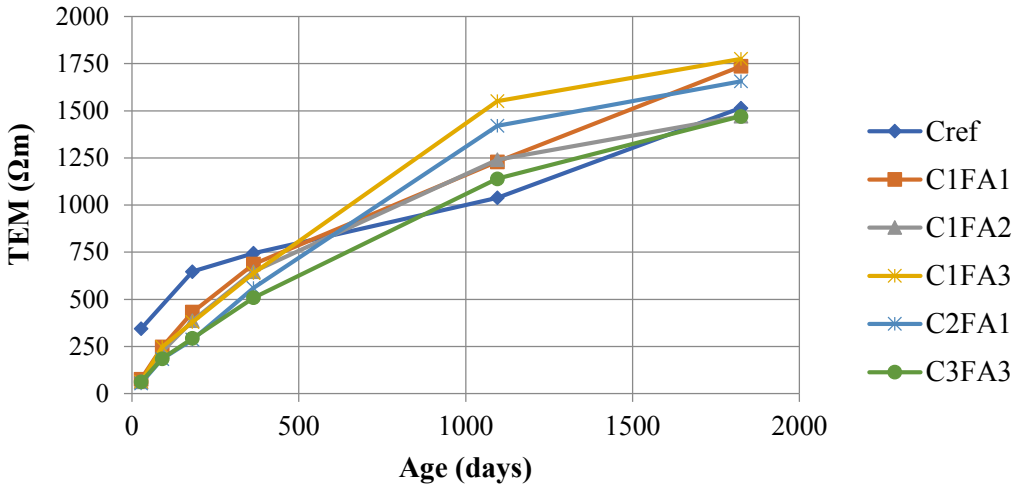

Figure 3: Development of TEM-value with time

3.5 Relation between D_{RCM} and TEM

In Figure 4 the relation between D_{RCM} and 1000/TEM is shown for all individual test results. Both parameters are highly correlated. The product of the RCM and TEM value is therefore a constant (K) and can be calculated from the slope of the trendline. The obtained value equals 1173×10^{-12} $\Omega m^3 s^{-1}$. This value is quite similar to the value of 1000×10^{-12} $\Omega m^3 s^{-1}$ reported in [8] for concrete mixes with water/cement ratio 0.45 produced with 6 different cement types.

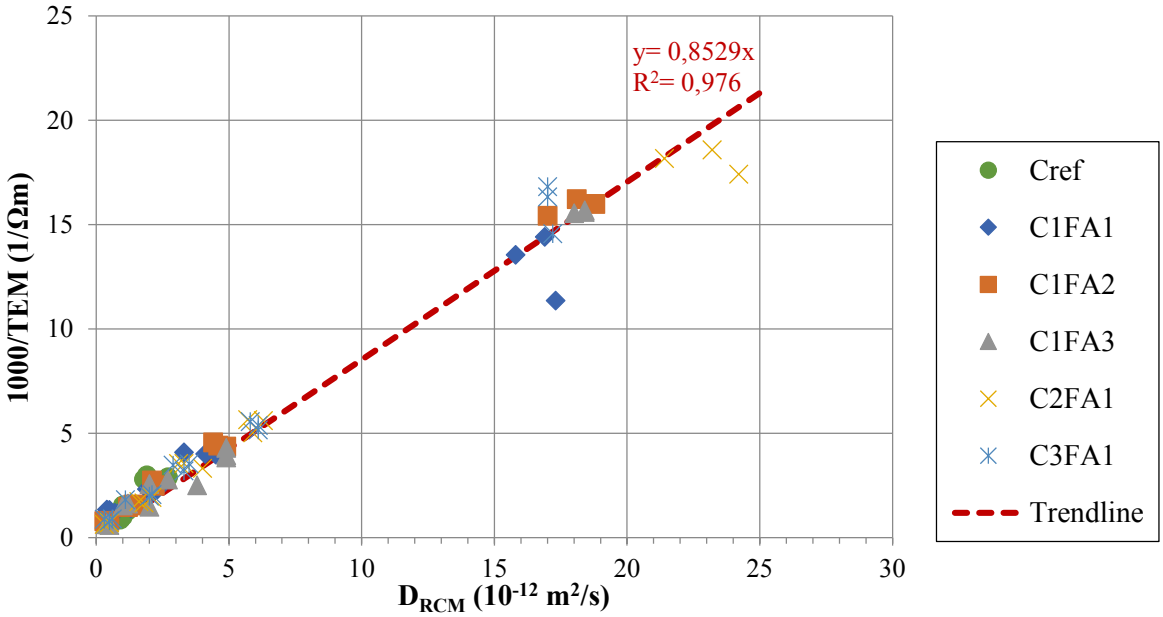

Figure 4: 1000/TEM versus RCM for all individual test results up to 5 years

3.6 Chloride diffusivity at age 3 years

The RCM tests demonstrate that at ages higher than 1 year fly ash concrete shows comparable or lower values than the reference mix. To verify this important result, it was decided to measure the chloride diffusivity by the immersion method described in EN 12390-11 for the reference mix and one fly ash mix at an age of 3 years. The test results (Table 7) are almost identical for both mixes. So, both the accelerated and the 'natural' method show that at higher ages the chloride penetration resistance of fly ash concrete is comparable or better than that of the reference mix with CEM III/B.

Table 7: Chloride diffusivity (Dnss) at age 3 years

Mix	D_{nss} (10^{-12} m^2/s)				
	Sample 1	Sample 2	Sample 3	Average	St.dev.
Cref	0.52	0.85	0.75	0.71	0.17
C1FA1	0.63	0.60	0.75	0.66	0.08

4. COMPARISON WITH PRACTICE

In the current investigation the development of D_{RCM} with time has been measured up to 5 years. Between 3 and 5 years D_{RCM} shows little or no decrease anymore for fly ash concrete. In the same period the TEM-value continues to increase, which would correspond to a further decrease of D_{RCM}. To obtain more certainty about the long term behaviour, the results of an investigation of a 14 year old concrete highway in the Netherlands were used [9]. The concrete

was made with 350 kg/m^3 Portland fly ash cement and w/c 0.42. From a curvefit of the chloride profile a value of $0.1x10^{-12}$ m^2/s was derived for the diffusion coefficient [3]. Inserting this value in Figure 2 shows that it is in good alignment with the curve fits through the RCM-values up to 5 years of the fly ash concrete mixes.

5. CONCLUSIONS

The following conclusions are drawn:

- D_{RCM} of fly ash concrete is much higher at 28 days than that of the reference mix with CEM III/B. However, after 1 year the RCM values are similar and after 3 years even lower than that of the reference mix.
- Both the accelerated method (RCM) and the non-accelerated immersion method confirm that the chloride penetration resistance of fly ash concrete is equal or better than the reference mix.
- The quality of the fly ash only has a limited effect on the ageing coefficient of D_{RCM}.
- The value of the ageing coefficient varies between 0.72 and 0.83 for fly ash concrete. These values are comparable to those mentioned in [8].

REFERENCES

[1] Duracrete Final Technical Report (2000) Document BE95-1347/R17, The European Union – Brite EuRam lll, DuraCrete – Probabilistic performance based durability design of concrete structures.

[2] "Model Code for Service Life Design", CEB-FIP, fib bulletin 34, 2006.

[3] Wegen van der, G, Lichtmann, M. and Polder, R. ‘Beton mit hohem Chlorid-eindringwiderstand. Erfahrungen aus den Niederlanden. *Beton* **5** (2018) 166-171.

[4] “Development of guidelines for durability design of reinforced concrete structures”, J. Gulikers, RWS, in: proceedings of the conference Service Life Design for Infrastructure, Delft, 2010.

[5] “Duurzaamheid van constructief beton met betrekking tot chloride-geïnitieerde wapeningscorrosie.”, CUR-Leidraad 1, 2009.

[6] “Concrete binder performance evaluation in service life design”, J.H.M. Visser & R.B. Polder, pp. 330-340 in ConcreteLife’06, proceedings of the International Rilem-JCI Seminar on Concrete Durability and Service Life Planning (2006).

[7] “New perspective of service life prediction of fly ash concrete”, Z. Yu & G. Ye, Construction and Building Materials 48 (2013) 764-771.

[8] "Measurements with the Rapid Chloride Migration Test (VC81-99)", A. Cheizoo, ENCI, 2007.

[9] “Duurzaamheid van beton met poederkoolvliegas in de praktijk.”, CUR-rapport 2000-2, 2000.

ANALYSIS OF THE DURABILITY OF HIGH STRENGTH CONCRETE WITH SUPERABSORVENT POLYMER

Carolina M. de Azambuja (1), Eugênia F. Silva (1) and Valdirene M. S. Capuzzo (1)

(1) UNB, University of Brasília, Brasília/DF, BR

Abstract

The High Strength Concretes (HSC) provided significant advances in civil construction, due its superior strength, efficiency and durability. Due to the high content of cement, low water/cement ratio and mineral additions, it is essential to avoid the emergence of tensile stresses generated autogenous shrinkage and consequently the cracking of structural elements and, therefore, losses in the durability. One strategy to mitigate autogenous shrinkage of HSC is the use of superabsorbent polymers (SAP) as internal curing agent. However, the use of SAP increases the porosity, leaving unconnected voids in the hardened material, which can reduce the durability of it.

This research aims to analyse the influence of the addition of superabsorbent polymer on the durability of Portland cement microconcrete.

In order to compare the influence of the use of shrinkage mitigation agents in durability, the experimental program consists of two mixtures of high strength microconcretes with water/cement ratio equal to 0.35: one used as reference and another one containing 0.3% of SAP. The behaviour of concrete in the hardened state was evaluated by performing the tests: resistance to simple axial compression, modulus of elasticity, migration of chloride ions and absorption by capillarity.

It was verified that the dense microstructure, characteristic of HSC, was preserved even in the presence of pores created by the SAP desorption process, because they are larger and disconnected instead of smaller and continuous pores. In conclusion, the SAP is a promising strategy to mitigate autogenous shrinkage, with a low prejudice to the mechanical properties and even improving the durability.

Keywords: *High Strength Concretes (HSC), Superabsorbent Polymers (SAP), Durability*

1. INTRODUCTION

The development of high strength concrete has provided numerous advances on the productive and economic aspects for civil construction. With the use of plasticizing additives and, later, superplasticizers (SP), it was possible to reduce the water/cement ratio (w/c) of concretes, achieving increasingly higher compressive strengths, without compromising on workability.

Due to the dense and refined microstructure, the low w/c ratio, the mineral additions and the high cement consumption, this concrete is less permeable and more resistant to attack by aggressive agents such as chlorides – sulphates and CO_2 – and presents higher abrasion resistance. However, one of the main factors limiting the use of HSC is the occurrence of a great increase in autogenous shrinkage to which they are susceptible - is especially prominent in concrete with low water-cement ratio below 0.4 - (WYRZYKOWSKI et al., 2018), due to the low w/c, which can cause early cracking that compromises the stability, durability and aesthetics of the structure.

To mitigate this shrinkage, several solutions have already been idealized, but the use of internal cure water with porous materials (such as superabsorbent polymer - SAP - or light aggregates) has been consolidating as the best alternative.

Polymers are superabsorbent and fine synthetic particles capable of absorbing a large amount of liquid from the environment, allowing the formation of water-filled macropores in the cement paste, thereby retaining water within its structure without dissolution (JENSEN and HANSEN, 2001). In a publication derived from the Rilem TC 260-RSC working group, Wyrzykowski et al. (2018) defines SAP as reticulated polyelectrolytes that swell in contact with water or aqueous solutions, resulting in the formation of a hydrogel.

Internal curing using SAP occurs effectively due to the rapid absorption of water by the polymer, which then gradually releases it, reducing the internal moisture content of the concrete. This process occurs over several days or week, with the major portion occurring within the first's days of hardening.

According to HASHOLT and JENSEN (2015) this internal healing water participates in the hydration process, increasing the degree of hydration of the paste. Thus, hydration reactions are controlled by the total w/c ratio rather than the initial basic w/c ratio of the cement paste. Therefore, the comparison of SAP effectiveness should be based on the same total w/c ratio.

That said, the w/c ratio, by neglecting the water stored in SAP, is called the basic w/c ratio (w/c_b). The incorporated cement water ratio (w/c_{inc}) refers to SAP internal cure water. Therefore, the total w/c would be the sum of the basic water/cement ratio with the incorporated water cement ratio. Agostinho (2019) also concluded that the comparison on SAP efficiency should be based on the same total a/c ratio.

Although a lot of research is underway, there are still gaps about the long-term effects of these polymers on the durability of high strength cementitious materials and whether this internal cure water (w/c_{inc}) actually participates in hydration reactions.

2. MATERIALS AND METHODS

This research aims to analyse the influence of superabsorbent polymer (SAP) addition on the durability of Portland cement microconcrete. It was measured the interference of SAP addition on the mechanical properties of microconcretos by performing the tests: compressive strength and modulus of elasticity. The chloride ion migration assay and the absorption by capillarity was performed to evaluate the interference of SAP addition on durability.

The premise of the research is to maintain the fixed spread of (215 ± 20) mm (based on ABNT NBR 13276: 2016, without applying beats to the table); and the variable SP content. The total w/c ratio used in the present study was constant of 0.35 for both mixtures, the first

being the reference admixture and the second containing 0.3% SAP in relation to the cement mass. Table 1 shows the nomenclature of de microcretes used in this research.

Table 1: Nomenclature of the microconcretes

Name	Description
035 REF	Reference mixture with total w/c = 0.35
035 SAP 03	Mixture SAP/C = 0.3% with total w/c = 0.35)

2.1 Materials

For this study, CPV-ARI cement was used, due to its amount of clinker and the fact that it is a cement widely used in HSC. The fine aggregate used in this research is natural and washed river sand from the Corumbá alluvial deposit in the Pires do Rio – Goiás/BR.

The active silica used is of non-densified national origin, from DOW CHEMICAL®. The addition content of 10% in relation to the cement mass was fixed, as recommended by the TC 225-SAP Committee (RILEM, 2012).

The chemical additive GLENIUM® 51, of the high efficiency water reducing type (superplasticizer type II - SPII-N) was the superplasticizer used. Such additive is based on a modified polycarboxylic ether chain that acts as a dispersant of cementitious material.

The superabsorbent polymer used in the work was supplied by Professor Ole Mejlhede Jensen and developed at the Technical University of Denmark (DTU) and is supplied as a dry white powder with spherical particles. It is a covalent crosslinked acrylic acid/acrylamide type polymer produced by the reverse suspension polymerization technique (JENSEN and HANSEN, 2001). The use of 0.3% was enough to mitigate autogenous shrinkage in HSC, not justifying a higher content, as exposed by MANZANO (2016), SANTOS (2016), BORGES and AIDAR (2016).

2.2 Mixtures compositions

The w/c ratio of 0.30 is usual for HSC, which is suggested by the TC 225-SAP organizing committee (RILEM, 2012). However, the mixtures that have internal curing water have a basic w/c ratio (w/c_b) of 0.30 and incorporated w/c ratio (w/c_{inc}) of 0.054, considering the SAP absorption value of 18 g/g. Summing the w/c_b with the w/c_{inc} gives a value of 0.354. By approximation criteria and practicality of execution, total w/c ratio of 0.35 will be used in both mixtures. Details of the composition of the traces can be found in Table 2.

Table 2: Composition of the microcretes (kg/m^3)

Name	Cement	Sand	Active silica	SAP	SP	Water		
						Water (measured)	SAP internal curing eater	Water contained in SP
035 REF	700	1265	70	-	6.3	240.59	-	4.41
035 SAP 03	700	1265	70	2.1	15.4	234.22	31.5	10.78

The mixing script was based on the recommendations presents by the TC 225-SAP Committee (RILEM, 2012). The sand was used in the wet condition, so it is essential in the

production process to perform the moisture correction for the dry surface saturated condition (SSS). The determination of this surface moisture was performed by the Chapman Bottle (ABNT NBR 9775: 2011) moments before the production of microconcretes.

2.3 Methods

To evaluate the **compressive strength**, 50 x 100 mm cylindrical specimens were used and the tops of the specimens were adjusted by grinding. The method was performed according to ABNT NBR 5739:2018 and the specimens were tested at the ages of 1, 7 and 28 days.

Regarding the **modulus of elasticity** test, the methodology used followed the ABNT NBR 8522: 2017, at 28 days of age. Initially, the tensile strength (Fc) of two specimens was determined and an upper limit stress equal to 30% Fc and a lower limit of 0.5 MPa was established. Then three other specimens were subjected to four loading and unloading cycles at a rate of 0.45 ± 0.15 MPa/s.

For the **chloride ion migration** test, the methodology proposed by NT BUILD 492: 2011 – Chloride migration coefficient from non-steady-state migration experiments – was followed. The specimens measuring 100 x 200 mm, were cut into four equal 100 x 50 mm parts after 28 days of curing, and the two central parts were used in the test. The samples underwent vacuum preconditioning. After this preconditioning, the samples were transferred to the test apparatus. Fig. 1 shows the schematic drawing suggested by the standard for the construction of the test apparatus and the apparatus made according to the normative specifications.

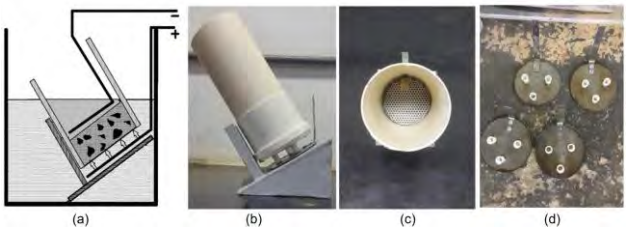

Figure 1: (a) Schematic drawing of the chloride migration test apparatus suggested by NT BUILD 492: 2011; (b) Side view of the migration test apparatus; c) Top view of the migration test apparatus; d) Lower plate used to position the test apparatus.

The plastic containers are filled with 10% sodium chloride cathodic solution by mass of water. Each apparatus was filled with an anodic solution of sodium hydroxide in distilled water (1.2g NaOH for every 100g water). From this, all devices were connected in parallel and initially the voltage was set to 30 volts, as can be seen in Fig. 2.

Figure 2: Chloride chloride migration test in progress

At the end of the test, the samples were ruptured by diametral compression and a 0.1 molar silver nitrate solution was sprayed onto the fractured surface of the specimen. The chemical reaction between silver nitrate and chloride impregnated in concrete results in silver chloride salt, being possible to measure chloride penetration. Concluding the measuring, it becomes possible to calculate the non-steady state chloride diffusion/migration coefficient.

The **capillary water absorption** test was performed according to the recommendations of ABNT NBR 9779: 2012, using 3 cylindrical specimens measuring 50 x 100 mm. The test was performed on the specimens at 28 days of age.

3. RESULTS AND DISCUSSION

Figure 3 shows the **compressive strength** results of the microconcrete containing 0.3% SAP addition to the reference mixture for ages 1, 7 and 28 days. It is observed that the SAP causes a decrease in compressive strength with 1 day cure, promoting a reduction of around 35% over the reference. At this early age, the reference microconcrete obtained a resistance value of 40.16 MPa and the mixture containing SAP a value of 25.92 MPa.

However, at 7 days, it is observed that SAP no longer brings damage to the resistance. The reference mixture obtained a value of 57.96 MPa and the mixture containing SAP showed 57.29 MPa, representing a difference of about 1%. At 28 days, the reference microconcrete obtained 72.87 MPa, compared to 72.59 MPa of the superabsorbent polymer mixture. Again, the difference between the observed values was 1%, which cannot be considered a reduction. That is, at 7 days and at 28 days, SAP did not harm the mechanical properties of concrete.

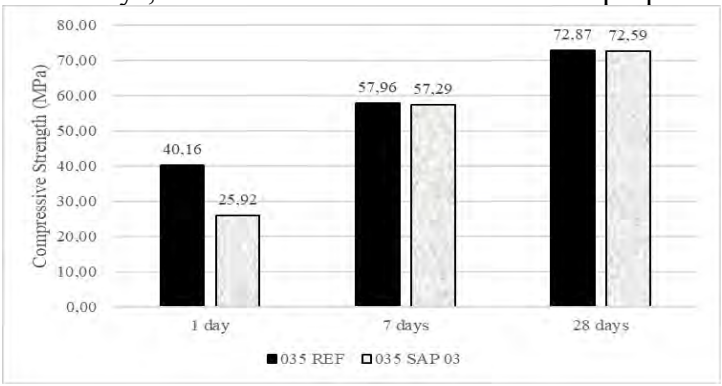

Figure 3: Results of simple compressive strength at ages 1, 7 and 28 days.

It is important to emphasize that several studies report the loss of mechanical resistance caused by SAP, among them DUDZIAK and MECHTCHERINE (2010); SILVA (2014) and SANTOS (2016). Though, all the above authors added extra water to the SAP-containing mixtures; so they compared traits with even basic w/c.

Nevertheless, the results obtained in this research corroborate the theory that in fact SAP internal healing water is part of the hydration process. Thus, the initially observed reduction in resistance is probably due to an increase in microconcrete porosity due to the introduction of SAP particles, since when they come into contact with water they absorb and increase in volume. Over time, there is the desorption of the polymer particle. During cement hydration, when the external relative humidity becomes lower, SAP releases the water inside the cement into the cementitious medium and reduces in volume.

Figure 4 shows the results of **modulus of elasticity** of microconcrete containing 0.3% SAP addition to the reference mixture at 28 days. The use of SAP triggered a 9% increase over the reference microconcrete. The reference mixture obtained a modulus value of 34.9 GPa and the mixture containing SAP, 38.1 GPa. This increase is probably due to advanced cement hydration, which may compensate for the reduction in strength caused by the high porosity left by the polymer (SANTOS, 2016).

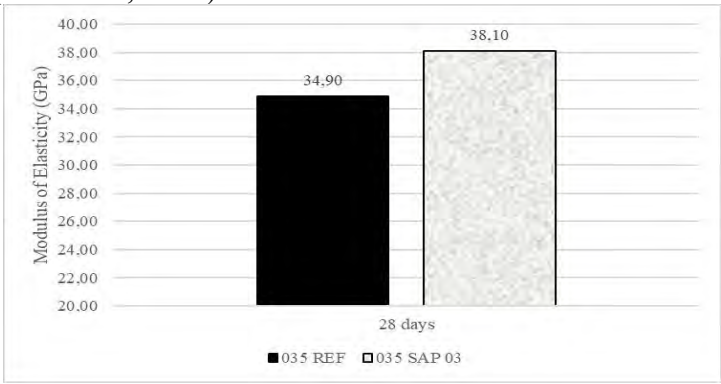

Figure 4: Results of modulus of elasticity at 28 days.

Figure 5 shows the results of **chloride ion migration** test containing 0.3% SAP addition to the reference mixture for the age of 28 days. The reference mixture obtained a migration coefficient value of 2.78 (10^{12} m^2/s) and the mixture containing SAP a value of 1.61 (10^{12} m^2/s). Thus, the value found in the mixture containing SAP is 58% lower than the value found for the reference microconcrete.

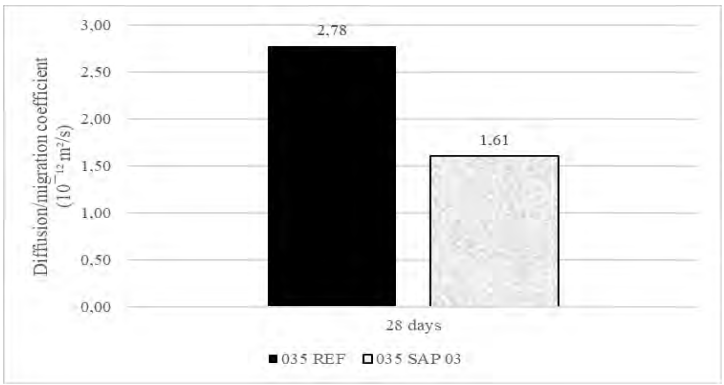

Figure 5: Results of chloride ion migration test at 28 days.

NILSSON, NGO and GJØRV (1998) *apud* NEGREDO (2018) proposed a classification of the concrete resistance to chloride penetration as a function of the diffusion/migration coefficient in the non-steady state regime. By this classification, the reference microconcrete has a very high chloride penetration resistance. Demonstrating that the w/c ratio equal to 0.35 already promotes a pore refinement and a denser microstructure, precisely because it is a high strength concrete.

Figure 6 shows the **capillary absorption results as a function of time** to the two studied mixtures. It is noticeable that in the first hours of the test, the trace containing only SAP had higher absorption values, however over the course of the test, the reference trace reached

higher absorptions. When analyzing the absorption after the end of the test, the 035 SAP03 trait, compared to the REF trait, had a 12% lower absorption value.

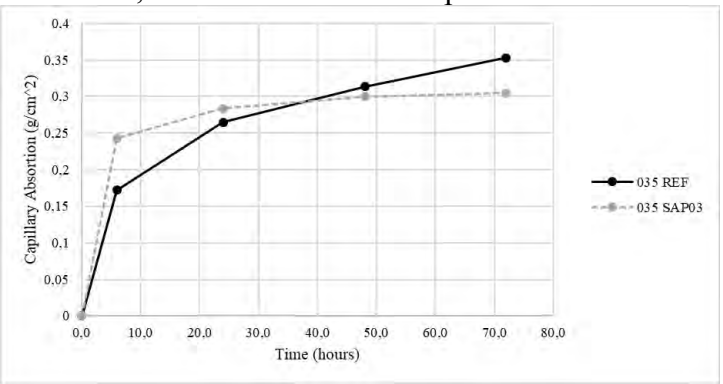

Figure 6: Capillary absorption results as a function of time.

To explain a lower absorption of trace 035 SAP03 when compared to the reference two hypotheses are raised. The first of these is that the additional porosity caused by polymer detachment is poorly interconnected, positively influencing the absorption property, that is, decreasing it by creating a tortuous, disconnected network. The second hypothesis is related to the reduction of self-drying due to the addition of superabsorbent polymer, thus reducing the microfissure of the composite, thus creating a more integral cementitious matrix and thus presenting a lower absorption capacity.

4. CONCLUSIONS

- Regarding mechanical properties, a small reduction (35%) of resistance was observed at the age of 1 day, which is justified by the rapid absorption of SAP upon contact with water. However, at the age of 28 days, the SAP-containing mixture recovered the resistance initially lost, reaching the resistance observed in the reference trait. In addition, adding 0.3% SAP represented a 7% increase in elasticity modulus. Given the above, SAP does not harm such mechanical properties.
- In the capillarity absorption test, the mixture cointaining SAP had a higher performance, that is, it presented lower absorption values (12%). Improvement in chloride ion migration results by adding SAP (42% reduction in diffusion/migration coefficient) reiterates that the addition of polymer results in the maintenance of dense microstructure.
- The voids left by the desorption process form a tortuous, discontinuous and barely permeable net. Therefore, SAP does not harm the durability of microconcretes, promoting even a certain improvement, which should be further investigated and evaluated. It is recommended to perform the accelerated carbonation, electrical and surface resistivity, immersion absorption tests.
- Finally, the data collected in this research reiterate that the most appropriate comparison of SAP effects when added to mixtures as an internal curing agent is in fact using a reference composition with the same total w/c rather than w/c basic, as it is currently widespread in the academic community.
- Therefore, it is observed that dense microstructure, characteristic of CAR, was preserved even in the presence of pores created by the use of SAP, because they are larger and disconnected pores instead of smaller and continuous pores.

REFERENCES

Articles in Conference Proceedings or Edited Books:

[1] DUDZIAK, L. e MECHTCHERINE, V. Enhancing early-age resistance to cracking in highstrength cement-based materials by means of internal curing using superabsorbent polymers. In: Brameshuber W (ed) Additions improving properties of concrete, RILEM Proceedings PRO 77, 2010, pages 129–139.

[2] HASHOLT, M. T.; JENSEN, O.M. Chloride migration in concrete with superabsorbent polymers. Elsevier. Department of Civil Engineering, Technical University of Denmark, Building 118, Brovej, DK-2800 Lyngby, 2015.

[3] RILEM. State-of-the-art report of the Rilem Technical Committee 225-SAP: Application of superabsorbent polymers (SAP) in concrete construction. Mechtcherine, V. & Reinhardt, H.W. (Eds.). London: Ed. Springer, 2012.

[4] SILVA, E. F.; MANZANO, M. A. R. LOPES, A. N. M.; TOLEDO FILHO, R. D. Effect of SAP on the Autogenous Shrinkage and Compressive Strength of High-Strength Fine-Grained Concrete. In: International RILEM Conference on Application of Superabsorbent Polymers and Other New Admixtures in Concrete Construction, Dresden, 2014, p. 211-219.

[5] WYRZYKOWSKI, M., IGARASHI, S., LURA, P., MECHTCHERINE, V. Recommendation of RILEM TC 260-RSC: using superabsorbent polymers (SAP) to mitigate autogenous shrinkage. RILEM TC 260-RSCSAP, Dubendorf, Switzerland, 2018.

Thesis:

[6] AGOSTINHO, L. B. *Monitoramento da Hidratação de Pastas de Cimento Portland contendo Polímero Superabsorvente e Nanosilica*. Qualificação de Doutorado em Estruturas e Construção Civil, Universidade de Brasília, Brasília, DF, 2019, 116 pages.

[7] BORGES, J. G.; AIDAR, L. A. G. *Avaliação da adição de polímero superabsorvente e nanossílica no tempo zero de concretos de alta resistência pela técnica do ultrassom.* Monografia de Projeto Final, Universidade de Brasília, Brasília, DF, 2016, 56 pages.

[8] MANZANO, M. A. R. *Estudo Experimental de Materiais Cimentícios de Alta Resistência modificados com Polímeros Superabsorventes (PSAs) como Agentes de Cura Interna.* Tese de Doutorado em Estruturas e Construção Civil, Universidade de Brasília, Brasília, DF, 2016, 324

[9] SANTOS, T. A. C. E. *Estudo da adição de polímero superabsorvente e nano partículas de sílica para melhorar propriedades de concretos de alta resistência.* Dissertação de Mestrado em Estruturas e Construção Civil, Universidade de Brasília, Brasília, DF, 2016, 145 pages.

[10] JENSEN, O. M. e HANSEN, P.F. Water-entrained cement-based materials I. Principles and theoretical background. In: Cement and Concrete Research, v. 31, n. 6, 2001, pages 647-654.

Standards:

[11] ABNT NBR NBR 5739, Concreto - Ensaios de compressão de corpos-de-prova cilíndricos. Rio de Janeiro: Associação Brasileira de Normas Técnicas, 2018, 9 pages.

[12] ABNT NBR NBR 8522, Concreto - Determinação do módulo estático de elasticidade à compressão. Rio de Janeiro: Associação Brasileira de Normas Técnicas, 2017, 16 pages.

[13] ABNT NBR NBR 9775, Agregado miúdo – Determinação do teor de umidade superficial por meio do frasco de Chapman – Método de ensaio. Rio de Janeiro: Associação Brasileira de Normas Técnicas, 2017, 16 pages.

[14] ABNT NBR NBR 9779, Argamassa e concreto endurecidos 0 Determinação da absorção água por capilaridade. Rio de Janeiro: Associação Brasileira de Normas Técnicas, 2012, 3 pages.

[15] ABNT NBR NBR 13276, Argamassa para assentamento e revestimento de paredes e tetos - Preparo da mistura e determinação do índice de consistência. Rio de Janeiro: Associação Brasileira de Normas Técnicas, 2016, 2 pages.

[16] NT BUILD 492, Chloride migration coefficient from non-steady-state migration experiments. Northern Territory Legislative Assembly, 2011, 8 pages.

CHLORIDE BINDING ASSESSMENT IN C_3S SYSTEMS WITH CALCINED CLAY

Shiyu Sui (1), Fabien Georget (2), Jinyang Jiang (1) and Karen Scrivener (2)

(1) Jiangsu Key Laboratory of Construction Materials, School of Material Science and Engineering, Southeast University, Nanjing 211189, China

(2) Laboratory of Construction Materials, LMC, EPFL-STI-IMX, Station 12, CH-1015 Lausanne, Switzerland

Abstract

Chloride binding is an important factor for chloride transport in cementitious materials, which can fix the chloride on the solid phase and decrease the free chloride content. As an alumina-rich supplementary cementitious material, calcined clay can be applied to improve the binding capacity of the system. While the contribution of calcined clay to chemical binding (through the formation of Friedel's salt) is clear, its influence on physical binding (adsorption on hydration products) is still under debate. In this study, pure C_3S instead of cement was used to assess the binding capacity on the presence of calcined clay. In addition, extra limestone was added to investigate the synergetic effect between calcined clay and limestone on binding capacity. Binding capacity was evaluated by an equilibrium method between free chloride in the solution and bound chloride in the solid phase. The evolution of the phase assemblage was analyzed using XRD-Rietveld, the pore structure, and the specific surface area were measured with the nitrogen adsorption method. It was observed that the systems with calcined clay present higher binding capacity than the reference. In addition, the binary system demonstrates similar bound chloride content compared to the ternary system. Characterization results were used to correlate the microstructural properties of cementitious materials to chloride binding capacity. Results showed that the calcined clay contributes to the chemical binding and, that there is no clear relation between specific surface area and physical binding in cementitious materials.

Key words: Chloride binding, Calcined clay, C_3S

1. INTRODUCTION

Supplementary cementitious materials (SCMs) incorporated in cements and concrete are by far the most realistic means to increase the performance [1]. The “classic” SCMs are fly ash (FA), slag, silica fume and so forth. Nowadays, kaolinitic clay, calcined at 700-850°C, is an important source of additional SCMs. However, the performance of samples with calcined clay has not been comprehensively investigated.

Steel corrosion, caused by chloride ingress, is one of the most serious durability issue for cementitious materials. A high chloride binding capacity can fix the chloride ions on solid phase to avoid chloride ions reaching steel [2]. There are two kinds of chloride binding: chemical binding and physical binding. Alumium-rich AFm phase (monosulfoaluminate (Ms), Monocarboaluminate (Mc) or Hemicarboaluminate (Hc)) can react with chloride to form Friedel’s salt or Kuzel’s salt, which is called chemical bound chloride [3]. Some other chloride ions can be adsorbed on the surface of hydration products like C(-A)-S-H, which is treated as physical bound chloride [4,5].

For the calcined clay, there is abundant aluminum in the materials and calcined clay is a pozzolanic material [6]. Therefore, calcined clay has the potential to improve the chloride binding of cementitious materials. This work focused on the chloride binding capacity of C_3S and the mechanism of calcined clay to improve chloride binding capacity. Microstructure characterization was made to get a better understanding of the factors affecting chloride binding.

2. MATERIALS AND METHODS

This study used a C_3S powder, a limestone powder (LS) and an industrial calcined clay (calcined kaolinite content is 48%). The chemical composition is shown in Table 1.

Table 1: Chemical composition (wt. %) of cementitious materials

	CaO	SiO_2	Al_2O_3
C_3S	73.4	26.6	
Calcined clay		54.5	45.5
Limestone	55		

Four paste mixtures were studied, with the name of C_3S 0.5, C_3S 1.0, C_3S+Clay, C_3S+Clay+LS. The water to solid (w/s) ratio for all the systems is 0.5, except for the C_3S 1.0, which is 1.0. In binary system, calcined clay was used to replace 30% of C_3S while in ternary system, extra limestone was employed to substitute a further 15% of C_3S. The paste preparation procedure included blending of the dried powders, followed by mixing with deionized water for 2 min at 1600 rpm. Fresh paste was sealed for 24 h and after that submerged in water (minimum amount of water to avoid leaching) for further curing. For the water to C_3S ratio of 1.0 system, rotation was used for the first 24 hours to avoid bleeding.

The following methods are used to characterize the performance of the samples.

Binding capacity: After 28 days of curing, approximately 25g samples were weighed and placed in 100 ml of 0.1, 0.3, 0.5, 1, 3 M NaCl solution for 10 weeks until the equilibrium between free chloride and bound chloride was reached. The host solutions were then analyzed for chloride concentration by means of potentiometric titration using 0.05 M $AgNO_3$.

XRD analysis, coupled with Rietveld refinement, was employed to quantify the main phases in 28 days fresh paste samples. A PANalytical X'Pert Pro MPD diffractometer in a θ–θ configuration using Cu-Kα source (λ=1.54 Å) with a fixed divergence slit size of 0.5° was used.

Mass balance: Along with the XRD analysis, a simplified mass balance calculation was used to quantify the C(-A)-S-H content in hydrated pastes:

(1) Total amounts of reacted oxides are quantified from reaction degrees of C_3S and $CaCO_3$, by using XRD Rietveld analysis.

(2) The $Ca(OH)_2$ (CH), AFt, AFm and calcite content are taken directly from XRD-Rietveld refinement, and the CaO included in them are subtracted from the initial reacted oxides.

(3) All CaO in remaining oxides is incorporated into C(-A)-S-H ($CaO.aAl_2O_3.bSiO_2.4(a+b)H_2O$, in this work a=0 and b=0.55 for pure C_3S system, a=0.065 and b=0.67 for systems with calcined clay from previous research [7]), assuming the molar ratio of H_2O/(Si+Al) to be 4 [8].

Nitrogen adsorption (N_2 adsorption): nitrogen adsorption with Barrett Joyner Halenda (BJH) model and Brunauer Emmett Tellerwas (BET) model were used for finding the pore size distribution and surface area of hydrated samples, respectively.

3. RESULTS

3.1 Binding capacity

Binding isotherm curves are shown in Fig. 1. Freundlich isotherm ($C_b = \alpha \cdot {C_f}^{\beta}$) was used to fit the experimental data. The parameters are provided in Table 2. Since several binding modes may coexist (physical and chemical binding), these parameters are only mathematical parameters without physical meaning. However, these parameters can be used to compare the binding capacity of different systems. C_3S+Clay system exhibits the highest bound chloride content among all the systems. When limestone is added, bound chloride content decreases a bit compared to the C_3S+Clay system. Systems with pure C_3S presents the lowest bound chloride content. In addition, pure C_3S systems demonstrate similar bound chloride content with the w/s ratio of 0.5 and 1.0, which means that the w/s shows little effect on chloride binding capacity. In Table 2, C_3S+Clay system shows the highest values of α, while C_3S 1.0 presents the lowest values. The higher values of α, the higher the binding capacity. Besides, the fitting curves for pure C_3S systems seem not as good as other systems. However, as a binding capacity evaluation indicator, the parameters from the Freundlich isotherm fitting can still be used.

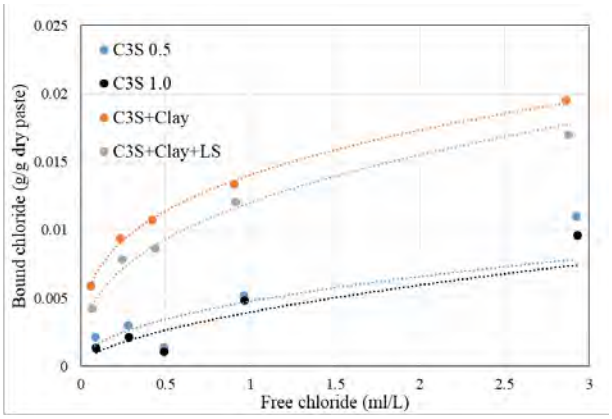

Figure 1: Binding isotherm of the investigated systems

Table 2: Binding coefficients for Freundlich isotherm

	α	β	r^2
C_3S 0.5	0.0048	0.467	0.5802
C_3S 1.0	0.0040	0.586	0.6915
C_3S+Clay	0.014	0.303	0.9975
C_3S+Clay+LS	0.012	0.370	0.9861

3.2 XRD/Rietveld analysis and mass balance results

Fig. 2 presents the XRD spectrums for C_3S and C_3S+Clay+LS. For C_3S 0.5 and C_3S 1.0 systems, the main hydration products are C(-A)-S-H and $Ca(OH)_2$. In C_3S+Clay+LS system, Hc and Mc were found thanks to the limestone reaction with the aluminum phase.

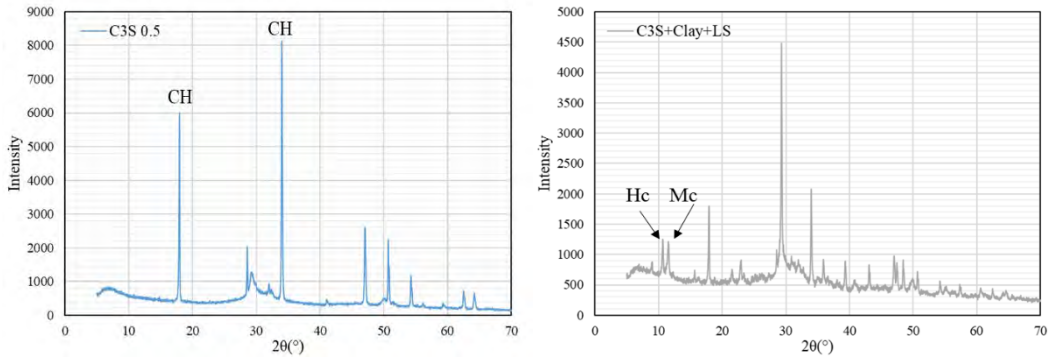

Figure 2: XRD spectrum for part of the investigated systems

Table 3 is a summary of the phase assemblage of the investigated systems from XRD/Rietveld analysis and mass balance calculation. It is clear that higher w/s ratio leads to higher degree of hydration in pure C_3S systems. For systems with calcined clay, AFt and AFm

were formed because of the Al and impurities of clay. Therefore, in C_3S+Clay and C_3S+Clay+LS systems, when NaCl solution is added, chemical binding of chloride may happen.

Table 3: Phase assemblage from mass balance (g/100g solid)

	CH	C(-A)-S-H	Calcite	AFt	Mc	Hc	Other phases	Free water
C_3S 0.5	39.32	95.98	0	0	0	0	0	10.01
C_3S 1.0	30.32	107.12	0	0	0	0	0	61.15
C_3S+Clay	13.16	104.36	2.42	5.29	0	0	7.07	14.50
C_3S+Clay+LS	6.28	89.50	12.52	2.68	7.68	2.97	3.55	23.72

3.3 N_2 adsorption analysis

N_2 adsorption method was used for pore structure and surface area comparison. Fig. 3 shows the pore size distribution of the investigated systems. For the pure C_3S system, there is a peak around 5nm. However, when calcined clay is added, the peak shifts to bigger size and becomes wider. Systems with calcined clay and limestone exhibits similar pore size distribution to the one with only calcined clay. This suggests that when supplementary cementitious materials are added to C_3S system, the pore size will become bigger. In addition, Table 4 presents the pore volume from N_2 adsorption method. The result shows that C_3S+Clay+LS shows the highest pore volume while the pure C_3S displays the lowest pore volume.

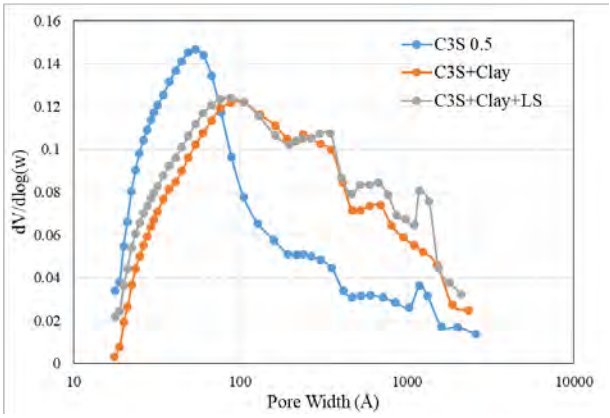

Figure 3: Pore size distribution from N2 adsorption for 28d samples

Table 4: Pore volume from N_2 adsorption for the investigated systems

	C_3S 0.5	C_3S+Clay	C_3S+Clay+LS
Pore volume (cm^3/g)	0.138	0.169	0.184

Surface area is very important for the physical binding capacity. It is found in some literature that when the surface area is higher, there are more chloride ions bound on C(-A)-S-H [9]. Fig.

4 is the surface area distribution curves for the investigated systems. The critical pore size are quite similar, around 2-4 nm, which may come from the representative pore size of C(-A)-S-H. However, it is clear that the total surface area decreases when calcined clay is present. In addition, sample with calcined clay and limestone exhibits higher surface area than the one with calcined clay in Table 5. Therefore, from the N_2 adsorption results, the addition of calcined clay increases the pore volume while decreases the surface area.

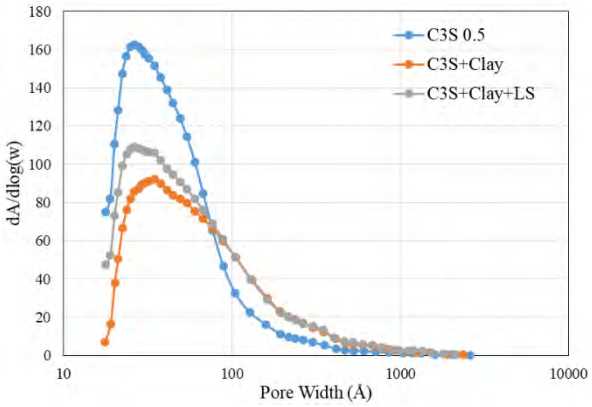

Figure 4: Surface area distribution from N_2 adsorption for 28d samples

Table 5: BET surface area from N_2 adsorption for the investigated systems

	C_3S	C_3S+Clay	C_3S+Clay+LS
BET surface area (m^2/g)	77.12	59.08	66.44

4. DISCUSSION

From the results session, when calcined clay was added to the system, binding capacity increases. In pure C_3S systems, only physical binding exists. However, for C_3S+Clay+LS system, physical binding and chemical binding both happen because of the C(-A)-S-H and AFm phases. For C_3S+Clay, even though no AFm was found in XRD spectrum, the Friedel's salt could still be formed in the presence of Al from the pore solution.

Since the Al content in C_3S+Clay and C_3S+Clay+LS systems are similar, we assume that the Friedel's salt in these two systems are same. Therefore, the values for chemical bound chloride could be estimated from the AFm content in C_3S+Clay+LS system. Fig. 5 correlates the surface area with physical bound chloride in 3M NaCl solution. The physical bound chloride content is from the total bound chloride subtracting the chemical bound chloride, under the assumption that all the AFm transformed to Friedel's salt. In Fig. 5, there is no clear relation between surface area and the physical bound chloride. There are two possible reasons for this: the Ca/Si of C(-A)-S-H ratio are different; the pH values of the NaCl solution are different. The Ca/Si ratio for pure C_3S system is 1.82 while it is 1.49 for systems with calcined clay. From previous study , the higher Ca/Si ratio, the higher binding capacity of C(-A)-S-H [10]. Table 6 shows the final pH of the NaCl solutions. The pure C_3S system presents lower pH values compared to the

systems with calcined, which is good for physical binding [11[]. However, the reason for C_3S+Clay showing higher bound chloride than C_3S+Clay+LS is not clear. The reason may come from the higher C(-A)-S-H content in the former system. Therefore, the physical binding is a complicated process. More research is needed for the mechanism.

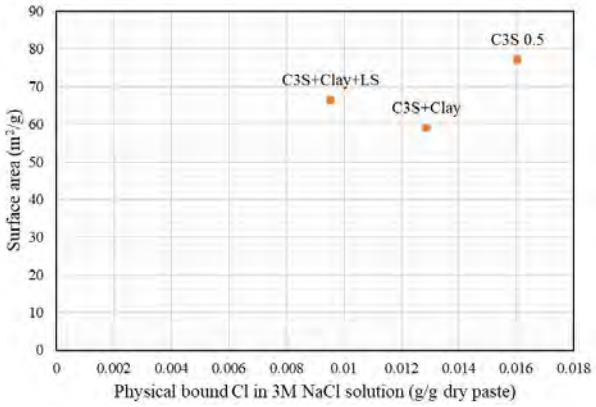

Figure 5: Relationship between N_2 adsorption results and physical bound Cl

Table 6: pH values of the NaCl solution after equilibrium

	C_3S 0.5	C_3S 1.0	C_3S+Clay	C_3S+Clay+LS
0.1M	12.622	12.61	12.695	12.658
0.3M	12.585	12.533	12.69	12.628
0.5M	12.568	12.523	12.624	12.59
1M	12.47	12.391	12.564	12.504
3M	12.188	12.092	12.257	12.249

5. CONCLUSION

This study investigated the chloride binding of C_3S systems in related to calcined clay. It is found that the presence of calcined clay can improve the chloride binding capacity, which comes from the improved chemical binding capacity; The W/C ratio shows little effect on chloride binding; There is no clear relation between the surface area and physical bound chloride. Surface area, Ca/Si ratio of C(-A)-S-H, pH of the final NaCl solution and C(-A)-S-H content could affect the physical binding of chloride.

ACKNOWLEDGEMENTS

The financial support from Key R&D projects in Jiangsu province (BE2017158) and National Natural Science Foundation of China (51578143) is gratefully acknowledged. The authors are grateful to Construction Material Lab of EPFL for the experimental process.

REFERENCES

[1] Scrivener, K.L., Options for the future of cement, *Indian Concr. J.* (2014).

[2] Tang, L.P., Nilsson, L.O., Chloride binding capacity and binding isotherms of OPC pastes and mortars, *Cem. Concr. Res.* **23** (1993) 247–253.

[3] Thomas, M.D.A., R.D., Hooton, Scott, A., Zibara, H., The effect of supplementary cementitious materials on chloride binding in hardened cement paste, *Cem. Concr. Res.* **42** (2012) 1–7.

[4] Beaudoin, J.J., Ramachandran, V.S., Feldman, R.F., Interaction of chloride and CSH, *Cem. Concr. Res.* **20** (1990) 875–883.

[5] Plusquellec, G., Nonat, A., Interactions between calcium silicate hydrate (C-S-H) and calcium chloride, bromide and nitrate, *Cem. Concr. Res.* **90** (2016): 89-96.

[6] Avet, F., Scrivener, K., Investigation of the calcined kaolinite content on the hydration of Limestone Calcined Clay Cement (LC3), *Cem. Concr. Res.* **107** (2018): 124-135.

[7] Avet, F., Boehm-Courjault, E., Scrivener, K., Investigation of C-A-S-H composition, morphology and density in Limestone Calcined Clay Cement (LC3), *Cem. Concr. Res.* **115** (2019): 70-79.

[8] Muller, A.C.A., Scrivener, K.L., Gajewicz, A.M., McDonald, P.J., Densification of C-S-H measured by 1H NMR relaxometry, *J. Phys. Chem. C.* **1** (2012): 403-412.

[9] Guo, Y., Zhang, T., Tian, W., Wei, J., Yu, Q., Physically and chemically bound chlorides in hydrated cement pastes: a comparison study of the effects of silica fume and metakaolin, *J. Mater. Sci.* **3** (2019): 2152-2169.

[10] Zibara, H., Hooton, R.D., Thomas, M.D.A., Stanish, K., Influence of the C/S and C/A ratios of hydration products on the chloride ion binding capacity of lime-SF and lime-MK mixtures, *Cem. Concr. Res.* **38** (2008) 422–426.

[11] Shi, Z., Geiker, M.R., De Weerdt, K., Østnor, T.A., Lothenbach, B., Winnefeld, F., Skibsted, J., Role of calcium on chloride binding in hydrated Portland cement–metakaolin–limestone blends, *Cem. Concr. Res.* **95** (2017) 205–216.

COMPRESSIVE STRENGTH AND CHLORIDE ION PERMEATION RESISTANCE OF MORTAR CONTAINING CLINKER WITH DIFFERENT MINERAL COMPOSITION AS AN AGGREGATE

Kotaro Ishikawara (1), Shintaro Miyamoto (2), Kensuke Hayashi (3), Hiroshi Minagawa (2), Makoto Hisada (2)

(1) TOHOKU University student

(2) TOHOKU University

(3) TAIHEIYO CEMENT CORPRATION

Abstract

The purpose of this study is to clarify the performance of cement hardenings containing clinkers which are utilized as aggregate by evaluating the compressive strength and chloride ion penetration resistance of the mortars. Here, the fine aggregate used in this study were the ordinary portland cement clinker and the clinker with more waste as an alternative raw material. In addition to this, we discussed on the effect of the clinkers on the compressive strength and chloride ion penetration resistance of mortar based on the weight loss on ignition and void structure. The results showed that the compressive strength of the mortars containing clinker aggregate was equal to or more than the mortar used an ISO standard sand, and the apparent diffusion coefficient of chloride ion decreased by using clinker. The reason why improving compressive strength and chloride ion penetration resistance might be attributed to the densification of the voids in the range of 50 nm to 2 μm, which is considered to be the void diameter represented by the interfacial transition zone, by hydration of clinker itself.

Keywords: cement clinker aggregate, compressive strength, chloride ion permeation resistance

1. Introduction

In Japan, the shortage of final disposal sites has been aggravated in recent years due to the discharge of large amounts of waste. The cement industry is playing an important role as a venous industry by utilizing waste as an alternative raw material for cement clinker and contributes to recycling waste. However, it is extremely difficult to increase the amount of waste utilized for producing cement more than the amount currently utilized because the quality of cement should be controlled at a certain level. In addition to this, the cement production tends to decrease in Japan. Therefore, it is necessary to explore other applications of cement clinker such as aggregate in order to ensure the future capacity of dealing with waste and recycle it. Here, it is becoming more difficult to obtain quality concrete aggregates such as natural gravel and natural sand such as river gravel and sea sand or crushed stone and crushed sand produced by crushing hard rock from the viewpoint of environmental protection and natural resource

protection. Therefore, applying cement clinker as a concrete aggregate has a possibility to contribute to environment preservation and the construction of a sustainable society.

Until now, there are many studies evaluating the performance of cement hardenings improved by using cement clinker aggregate and considering the mechanism of it. Previous studies reported that applying cement clinker as fine aggregate encouraged to produce hydrate formation and densify in the interfacial transition zone between aggregate and cement paste by hydration of cement clinker itself [1][2]. Here, in consideration of the relationship between mass transfer in cement hardening and void structure including interfacial transition zone [3], mass transfer resistance can be expected to improve by using cement clinker. In addition, they also reported that compressive strength of cement hardenings containing clinker as an aggregate became higher than that of cement hardenings containing an ISO standard sand because interfacial transition zone densified by using cement clinker aggregate. In this way, using cement clinker as an aggregate instead of ISO standard sand enable to improve compressive strength and mass transfer resistance.

On the other hand, the cement industry in Japan can produce various types of clinkers to accept more industrial waste and industrial by-products. The typical example is the eco cement clinker which is produced from a large amount of waste such as incineration ash of city garbage that is difficult to treat. Similarly, belite gehlenite clinker is also a promising one because it can treat industrial waste more than ordinary portland cement clinker. From the above, it can be pointed out that applying cement clinker aggregate can contribute to constructing a sustainable society by producing more durable concrete and environment preservation. Here, there are few studies on cement hardenings containing clinker aggregates at the long-term age, and studies on cement hardenings containing eco cement clinker aggregate and belite gehlenite clinker aggregate. Consequently, in regard to cement hardenings containing various clinker aggregates, it is necessary to examine in the long term that there is no problem in strength and durability or whether it contributes to improvement of these performances. Therefore, the purpose of this study is to evaluate the basic physical properties and mass transfer resistance of the mortars with the clinker fine aggregates. In addition to this, we discussed on the effect of the clinker aggregates on the compressive strength and the apparent diffusion coefficient of chloride ion of the mortars based on the loss of ignition and void structure.

2. EXPERIMENTAL PROCEDURES

2.1 Materials

In this study, the ordinary portland cement conforming to JIS R 5201: 2015 and JCAS K-03 was used as a binder. The fine aggregates were an ISO standard sand defined according to JIS R 5201 (hereinafter called “SS”), an ordinary portland cement clinker (hereinafter called “NCL”), an eco cement clinker (hereinafter called “ECL”), and two types of belite gehlenite clinker with different mineral compositions (hereinafter called “V1CL and V2CL”) for the purpose of evaluating the effect of clinker types on compressive strength and chloride ion penetration resistance of the mortars. Table 1 shows the density in oven-dry condition, the water absorption and the mineral composition of various clinkers. These clinkers as fine aggregates had the same particle size distribution as SS by crushing and sieve classification.

Table 1 : Absolute dry density, water absorption and mineral composition of the fine aggregates

Clinker	Absolute Dry Density (g/cm^3)	Water Absorption (%)	Content Ratio (%)					
			C_3S	C_2S	C_2AS	C_3A	C_4AF	f.CaO
NCL	2.66	4.20	54.2	25.2	0.0	9.2	11.2	0.0
ECL	2.78	3.39	55.6	16.5	0.0	11.8	15.0	0.3
V1CL	2.94	2.38	0.0	75.7	19.2	0.0	5.1	0.0
V2CL	2.88	1.35	0.0	47.7	52.1	0.0	0.1	0.0

2.2 Sample Preparation

The water cement ratio (hereinafter called "W/C") was held at 50 percent and the fine aggregates cement ratio (hereinafter called "S/C") was held at 2.5 at all levels. Table 2 shows the mix proportions of the mortars. The mortars were mixed in accordance with JIS R 5201. The fresh mortar was mixed until the bleeding was settled, and was put into a plastic disposable mold with an internal dimension of ϕ 50 × 100 mm. After 24 ± 2 hours, the mold was removed, and hardened mortar was performed water curing for up to 91 days in a saturated aqueous solution of calcium hydroxide. However, the samples for the measurement in 1 day of the material age were tested immediately after demolding. Besides, the mortars containing SS, NCL, ECL, V1CL and V2CL as fine aggregates are referred to as SS-M, NCL-M, ECL-M, V1CL-M and V2CL-M respectively.

Table 2: Mix proportion of mortar made with SS and cement clinker aggregates

	Water/Cement (-)	aggregate/Cement (-)	Water (kg/m^3)	Cement (kg/m^3)	Aggregate (kg/m^3)
SS-M	0.5	2.5	284	567	1418
NCL-M			285	569	1423
ECL-M			291	583	1457
V1CL-M			300	600	1500
V2CL-M			297	594	1484

2.3 Testing Procedure

Using the samples in up to 91 days, the measurement of ignition loss (measurement range: 105 °C) by thermogravimetry differential thermal analysis (hereinafter called "TG-DTA"), the measurement of total porosity and pore size distribution by mercury intrusion porosimetry (hereinafter called "MIP"), the observation of aggregate interface by scanning electron microscope (hereinafter called "SEM"), the compressive strength test and the salt water immersion test were carried out. In addition, ignition loss is the total amount of bound water and calcium carbonate.The compressive strength test was performed 3 times per each case and the average of the three measurement results was defined as the testing result. The immersion test was carried out as the following. The mortar sample of ϕ 50 × 100 mm at a material age of 28 days was cut 10 mm from the top and the bottom. The cut sample was covered with an epoxy resin paint excepted one flat surface. The covered sample was immersed in 3 percent NaCl solution for 28 days so that the solid-liquid ratio was 1 : 20. After that, the measurement sample for chloride ion concentration distribution in the mortar was obtained by cutting the immersed

sample so that the measurement sample dimension was 40 × 40 × 10 mm and the sample has the exposed surface. Figure 1 shows sample preparation procedure.

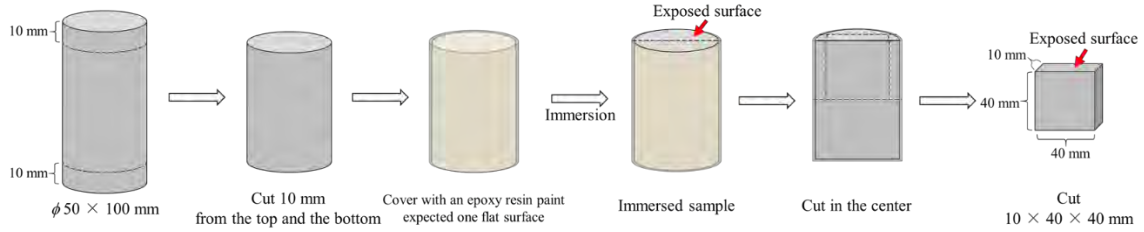

Figure 1: Sample preparation procedure

The surface analysis of the chloride ion concentration distribution in the sample was performed by an electron probe microanalyzer (hereinafter called "EPMA"). After that, the apparent diffusion coefficient of chloride ion was calculated by applying the concentration distribution of chloride ion obtained from EPMA to diffusion equation based on Fick's law shown in Eq.(1) and regression analysis of the total chloride ion concentration by each depth of the sample:

$$C(x,t)-C_i = C_{a0}\left\{1-erf\left(\frac{x}{2\sqrt{D_{ap}\cdot t}}\right)\right\} \tag{1}$$

where t is immersing period, $C(x,t)$ is total chloride ion concentration of mortar per unit volume at x meter deep in t year, C_{a0} is total chloride ion concentration of mortar per unit volume on the surface by the immersion test, C_i is total chloride ion concentration of mortar per unit volume contained originally, D_{ap} is apparent diffusion coefficient.

3. RESULT AND DISCUSSION

3.1 Effect each clinker aggregate on compressive strength

Figure 2 shows the relationship between the porosity of voids in the range of 50 nm to 2 μm and the ignition loss, Figure 3 shows the compressive strength in each day and Figure 4 shows the relationship between the increasing rate of compressive strength to the material age of 1 day and the decreasing rate of the porosity of voids in the range of 50 nm to 2 μm to the material age of 1 day. Here, these rates were calculated from the following Eq. (2) and Eq. (3):

$$\Delta F_n = \frac{F_{nd}-F_{1d}}{F_{1d}}\times 100 \qquad (n=7,\ 28,\ 56) \tag{2}$$

$$\Delta P_n = \frac{P_{nd}-P_{1d}}{P_{1d}}\times 100 \qquad (n=7,\ 28,\ 56) \tag{3}$$

where ΔF_n is the increasing rate of compressive strength to the material age of 1 day, F_{1d} is compressive strength at the material age of 1 day, F_{nd} is compressive strength at the material age of n days, ΔP_n is the decreasing rate of the porosity of voids in the range of 50 nm to 2 μm to the material age of 1 day, P_{1d} is the porosity of voids in the range of 50 nm to 2 μm at the material age of 1 day and P_{nd} is the porosity of voids in the range of 50 nm to 2 μm, which is the void constituting the tranzisiton zone, at the material age of n days.

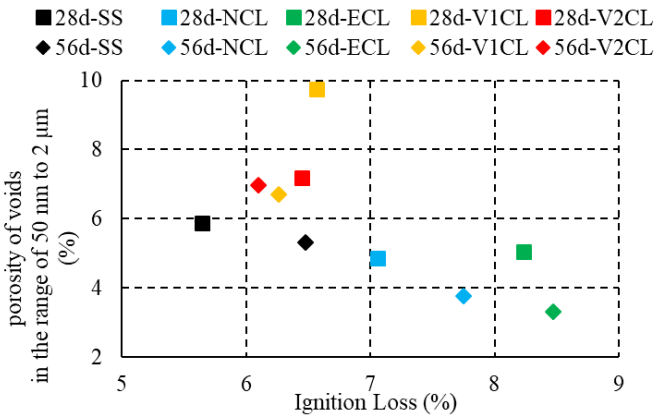

Figure 2: the relationship between the porosity of voids in the range of 50 nm to 2 µm and the ignition loss

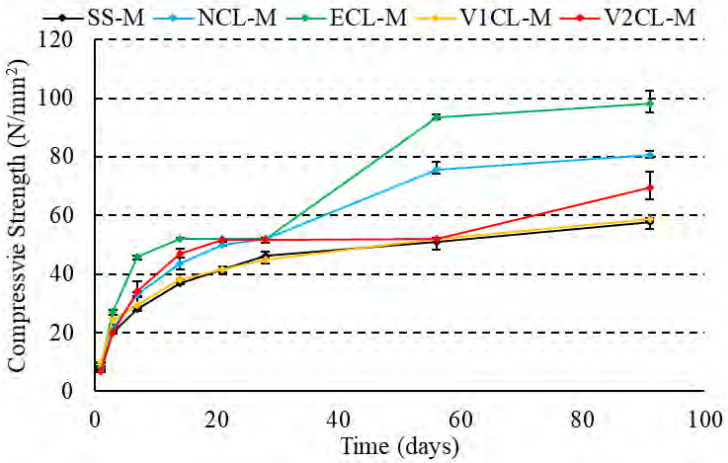

Figure 3: the compressive strength in each days

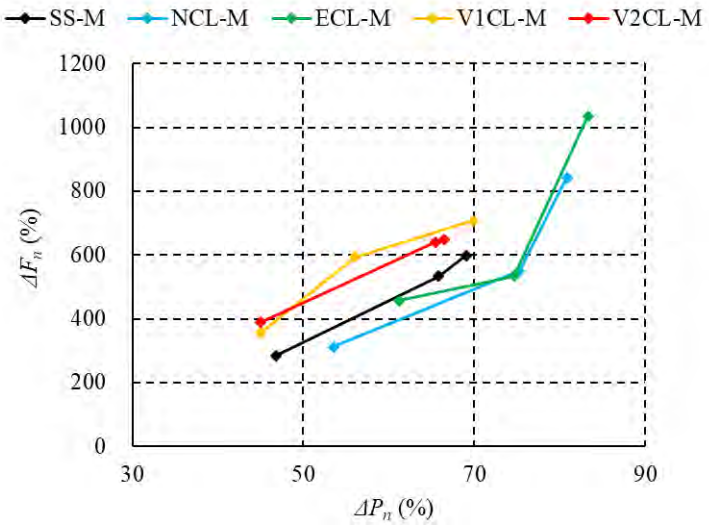

Figure 4: the relationship between ΔF_n and ΔP_n

Figure 2 is a graph focusing on the relationship between the porosity of the voids in the range of 50 nm to 2 μm, and ignition loss in order to investigate the change in the content of hydrate affect porosity. As shown in Figure 2, in regard to SS-M, NCL-M and ECL-M, the porosity decreased with increasing ignition loss. In contrast, V1CL-M and V2CL-M didn't show this tendency. However, in regard to V1CL-M, ignition loss at a material age of 28 days was 7.4 percent and increased from a material age of 28 days to that of 91 days. Considering these results, it was suggested the possibility that the increase in ignition loss has contributed to the decrease in porosity of voids in the range of 50 nm to 2 μm. Besides，NCL-M and ECL-M had more ignition loss and fewer voids in this range than SS-M. As a reason for this, it is mentioned that since NCL and ECL contain a relatively large amount of alite and aluminate phase, which have high hydration activity, the transition zones around NCL-M and ECL-M were densified by themselves hydration reaction [4]. In contrast, it was inferred that V1CL and V2CL contain belite and gehlenite as the main mineral, which has low hydration activity, the porosity of this range of V1CL-M and V2CL is not as small as SS-M.

Figure 3 shows the change with time in compressive strength. As shown in Figure 3 in regard to the material age of 91 days, the mortars containing clinker fine aggregates showed equal or higher compressive strength than SS-M. NCL-M and ECL-M in particular, showed higher compressive strength than SS-M.

Figure 4 shows the relationship between ΔF_n and ΔP_n. As shown in Figure 4, all cases showed that the more decreasing rate of the porosity of voids in this range, more the rate of increase in compressive strength. As mentioned above, the void in this range is regarded as the transition zone, and it is reported that the smaller the void in this range, the higher the compressive strength [3]. Therefore, in this study, it is possible that the densification of the transition zone has contributed to increasing the increasing rate in compressive strength. It was suggested that NCL-M and ECL-M had more increasing rate of compressive strength than SS-M, because they particularly had the more decreasing rate of the porosity of the void in this range.

From the above, it was suggested the possibility that the compressive strength of mortars containing V1CL and V2CL, which is considered to have low hydration activity, was comparable to that of mortar containing SS. Similarly, it was also suggested the possibility that the compressive strength of mortars containing NCL and ECL, which is considered to have high hydration activity, were high than that of mortar containing SS.

3.2 Effect each clinker aggregate on the apparent diffusion coefficient of chloride ion

Figure 5 shows the concentration distribution of chloride ion in mortar immersed for 28 days and Figure 6 shows the apparent diffusion coefficient of chloride ion. As shown in Figure 5, in regard to chloride ion penetration depth, V2CL-M was comparable to SS-M, and NCL-M, ECL-M and V1CL-M were lower than SS-M. Therefore, the apparent diffusion coefficient of chloride ion at each case was calculated and shown in Figure 6. As shown in Figure 6, focusing on the relationship between the difference in fine aggregate and the apparent diffusion coefficient of chloride ion, the apparent diffusion coefficient of chloride ion was smaller in the order of ECL-M, NCL-M, and V1CL-M, and these of SS-M and V2CL-M were almost the same. Considering this point, chloride ions move through the voids in the cement hardening, and gaps in the transition zone have a significant effect on mass transfer [5]. Therefore, it is suggested that the densification of the transition zone contributed to suppressing chloride shift with clinker, which is considered to have high hydration activity.

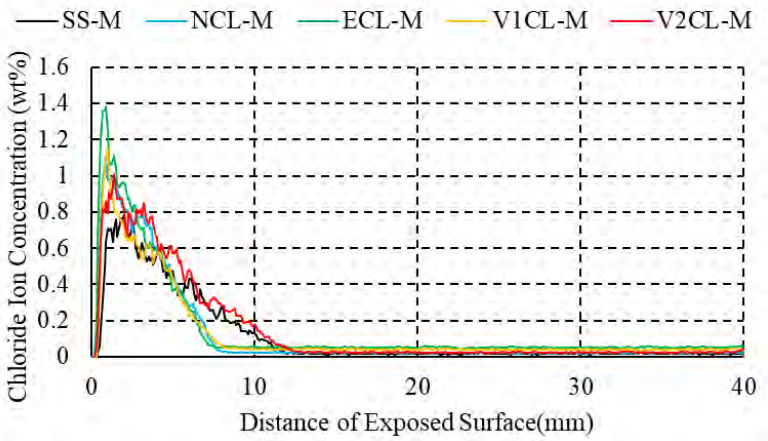

Figure 5: the concentration distribution of chloride ion in mortar immersed for 28 days

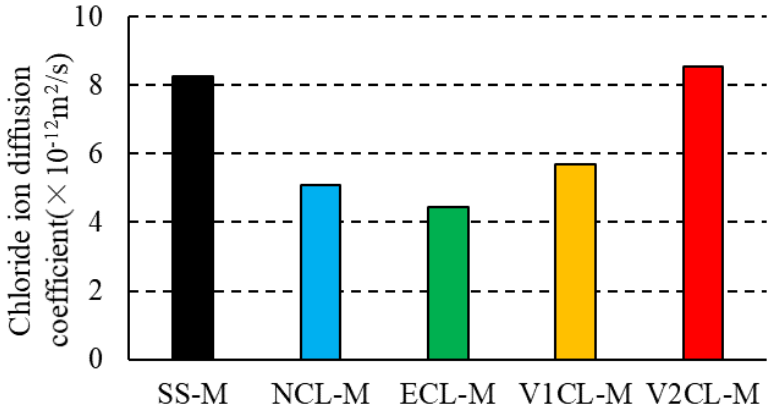

Figure 6: the apparent diffusion coefficient of chloride ion

It was previously inferred that the transition zone was densified form the relationship with ignition loss, porosity and compressive strength with clinker, which is considered to have high hydration activity. By contrast, here, chloride ion penetration resistance was evaluated by acquiring a backscattered electron image with SEM and observing the condition around the transition zone for each aggregate. Figure 6 shows the backscattered electron images. As shown in Figure 7, in regard to NCL-M and ECL-M, there was no gaps around the transition zone and precipitate such as hydrate were observed. In contrast, in regard to SS-M, V1CL and V2CL-M, there were gaps with different width. Similarly, from this result, it was suggested the possibility that the densification of the transition zone caused by precipitation of hydrate contributes to the improvement of chloride ion penetration resistance with clinker, which is considered to have high hydration activity.

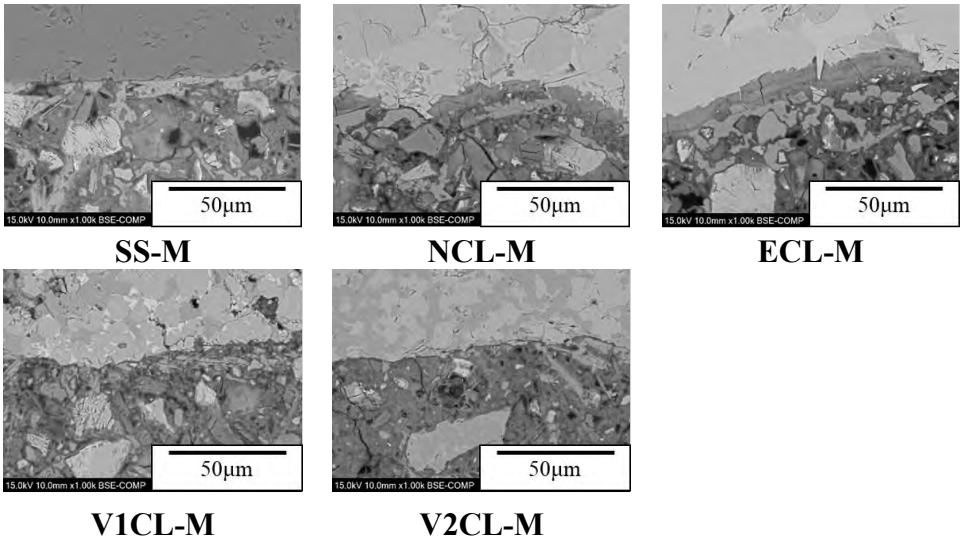

Figure 7: the backscattered electron images

4. Conclusions

In this study, focusing on the basic physical properties and mass transfer resistance of mortars containing clinkers which are utilized as aggregate, the effects on these properties were evaluated. These results showed that mortar containing clinker fine aggregate performed equal or higher compressive strength and equal or lower apparent diffusion coefficient of chloride ion than SS-M. Besides, the results obtained from the compressive strength test showed the tendency to improve compressive strength in the long term. It was suggested that the main reason that the clinker fine aggregates contributed to the improvement in compressive strength and chloride ion penetration resistance was the densification of the transition zone by the hydration reaction of clinker, which is considered to have high hydration activity.

References

[1] R. L. Berger, PROPERTIES OF CONCRETE WITH CEMENT CLINKER AGGREGATE, Cement and Concrete Research, 4, 1974, 99-112.

[2] S. Miyamoto, H. Inada, H. Minagawa, M, Hisada, Influence of using cement clinker as fine aggregate on the properties of mortar (in Japanese), Cement Science and Concrete Technology, 69, 2015, 169-175.

[3] S. Hanehara, D. Sawaki, Void structure and physical properties of hardened concrete, Gypsum & Lime, 1992(240)(1992)314-323.

[4] K. Hayashi, R. Soga, S. Uchida, H. Fujiwara, M. Maruoka, Study on Physical Properties and Interfacial Transition Zone Improvement Effect of Mortar Using Clinker Aggregate, TAIHEIYO CEMENT KENKYU HOKOHU, 173, 2017, 19-26.

[5] H. Uchikawa, Influence of cement paste and the structure of aggregate interface on concrete quality, concrete technology, 33(9)(1995)5-17.

CHARACTERISTICS OF FLY ASH BLENDED MORTARS UNDER AMMONIUM CHLORIDE SOLUTION LEACHING

Min Pang (1,2), Zhenping Sun (1,2), Yanliang Ji (1,2), Jingbin Yang (1,2), Peiming Wang (1), Yaling Xu (3), Huanhuan Li (3), Jiaying Liu (3), Fei Li (4)

(1) School of Materials Science and Engineering, Tongji University, Shanghai 201804, China

(2) Key Laboratory of Advanced Civil Engineering Material of Ministry of Education, Tongji University, Shanghai 201804, China

(3) Shanghai Urban Construction Material Co., Ltd., Shanghai, 200063, China

(4) Shanghai Fupei New Material Technology Co., Ltd., Shanghai, 201804, China

Abstract

Characteristics of fly ash(FA) blended mortars (50%, 70% and 90%) at different curing ages (28 days and 180 days) under ammonium chloride solution(ACS) leaching were investigated. Mass loss under leaching, initial CaO content, $Ca(OH)_2$ content(CH), content of chemical bonded water, and hydration degree of blended pastes were tested by XRF and DSC-TG. Based on correlations between initial CaO content and CH content in blended pastes, correlations between mass loss under leaching and initial CaO content were analyzed, as well as effects of hydration degree of blended pastes and chemical bonded water in blended pastes. Results showed that FA blended mortars experienced a mass-loss period along with immersion in ACS, either 28-day curing regime or 180-day curing regime, and FA could minimize this mass loss obviously. Effects of hydration degree of FA blended pastes on this mass loss were feeble, but remarkable fluctuations could be made by chemical bonded water of FA blended pastes. Effect of FA against ACS leaching should be owed to its pozzolanic reaction which might neutralize attacks from ACS. However, this effect of FA against ACS leaching would weaken as long as alkaline environment increasingly extinguished. Therefore, excessive dosages of FA should be careful for structures and buildings experiencing solution leaching attacks. According to correlations with mass loss under solution leaching attacks, characteristic of initial CaO content in FA blended pastes could be regarded as one effective evaluation against solution leaching attacks.

Keywords: fly ash blended pastes; initial CaO content; Ca(OH)2 content; mass loss under leaching

1. INTRODUCTION

Leaching attacks are quite common for cement-based materials in their service life, which have been investigated by a few researchers. Based on modeling calculations of Van Eijk et al[1], leaching rate strongly depended on characteristics of cement pastes(i.e. $Ca(OH)_2$ content(CH), hydration degree, water/cement ratio). Carde et al[2] believed on their leaching model of cement pastes that effects of CH was more important than C-S-H during this situation. Bentz et al[3] and Garboczi et al[4] had used CH-dissolution as an effective indicator in leaching model of cement-based materials. Initial CaO content was also regarded as an indispensable factor in leaching dynamic equation for mortars during leaching situations [7]. It had been reported by [8,9]that slag(50%～70%) and fly ash (FA, 40%)could strengthen leaching resistance by changing initial CaO content and CH content in cement pastes.

In the previous experiments, we had already confirm good performance of slag blended mortars against leaching attacks and there were indeed certain correlations for blended mortars between mass loss under leaching and initial CaO content. But what correlations for FA blended mortars against leaching attacks is still uncertain. Hence, this paper has presented investigations about FA blended mortars under ammonium chloride solution leaching(accelerating situations) through microstructure transformations.

2. MATERIALS AND METHODS

Chemical compositions of Type-P.I portland cement(none of additives) and FA were showed in Table 1. Mix proportions of FA blended mortars were listed in Table 2. Initial CaO content of plain cement pastes and FA blended pastes were listed in Table 3, which were calculated according to Table 1 and Table 2. Fineness of Type-P.I portland cement and FA were 350 m^2/kg and 365 m^2/kg. Sand in mortars was Chinese National Standard Sand according to ISO 679 and deionized water was used for sample mixing and curing.

Table 1: Chemical compositions of raw materials

	CaO	SiO_2	Al_2O_3	Fe_2O_3	MgO	MnO	f-CaO	SO_3	Na_2O	K_2O	TiO_2	loss
Cement	62.0	21.9	4.2	3.4	2.6	-	0.6	2.9	0.35	-	1.7	1.7
Fly ash	8.0	48.9	26.6	5.0	0.8	0.08	-	0.6	0.64	1.0	0.96	7.0

Table 2: Mix proportion of cement mortars

Sample	Cement	Fly ash	Sand	Water
P	450	0	1350	225
F50	225	225	1350	225
F70	135	315	1350	225
F90	45	405	1350	225

Table 3: Initial CaO content in cement pastes

Sample	P	F50	F70	F90
CaO/%	62.0	35.0	24.2	13.4

Chemical accelerating method was used in this experiment similar like [10] and the accelerating solution was ammonium chloride solution(ACS). Mortars were made along with

regular procedures in GB/T 17671-1999(CHN Standard: method of testing-determination of strength ISO). All of making and curing procedures about samples were stably kept at 20±1°C. Samples were cured at the standard environment in GB/T 17671-1999 for one day and then divided into two groups. The first group of samples were cured under water for 28 days and then immersed into ACS at PH value-5.6, this PH value maintained firmly(Notification: solubility of $CaCl_2$ was 0.745 g/ml, much more than solubility of CH-0.0026 g/ml, so no disturbing from Cl^- to CH). Mass changing of samples was tested during immersion period. Differently, the second group of samples were cured under water for 180 days and then also immersed into ACS, with their mass changing recorded as the first group. Mass loss was calculated by Equation (1), in which M_0 representing the original mass of sample, M_t representing the mass of sample under ACS at immersion period t(day), ΔM representing mass loss.

$$\Delta M\ (\%) = (M_0 - M_t)/M_0 \times 100\% \quad (1)$$

In order to detect phase transformation during ACS immersion, paste samples were made according to Table.2 without sand and regular procedure in GB/T 17671-1999(CHN Standard: method of testing-determination of strength ISO). Paste samples were also cured under water for 28 days and 180 days, respectively. After ACS immersion, hydration of pastes samples were stopped by alcohol, dried under 105℃ until constant-weight stage, grinded into powders(through stiffer of 0.08m) and stored for investigations. Extra paste samples theoretically called "completed-hydration samples" were made based on Table.2, at special w/c=10. Its mixing procedure during fresh state was done by manual grinding in one agate crucible to make sure cement hydration fully and freely happening. Completed-hydration samples were dried and stored on the same way as others.

Hydration degree of paste samples in this experiment was calculated by contents of chemical-bonding water as Equation (2). Contents of chemical-bonding water in paste samples and "completed-hydration samples" depended on weight difference between samples from 105℃ to 1050℃. Heating regime was carried out by one Netzsch STA-449C TG-DSC equipment and at heating rate of 20℃/min under nitrogen environment (flowing rate at 100 cm^3/min). CH contents in paste samples were also recorded by the same equipment so that one more factor to describe characteristics inside paste samples. In Equation (2), α_t represented hydration degree at the curing age t, W_t represented certain content of chemical-bonding water in hardened cement pastes at the curing age t, W_∞ represented content of chemical-bonding water in "completed-hydration pastes".

$$\alpha_t = W_t/W_\infty \times 100\% \quad (2)$$

3. RESULTS AND DISCUSSION

2.1 Mass loss

Figure 1 showed mass loss of plain mortars and FA blended mortars under ACS immersion, both 28-day water curing regime and 180-day water curing regime before exposure to ACS solutions. From Figure 1a, mass loss of plain mortars increased as curing ages prolonged while mass loss of FA blended mortars changed similarly but in smaller scopes. From Figure 1b, mass loss of plain mortars became larger clearly without turning points among the whole immersion, but mass loss of FA blended mortars presented

complicated changing rules. All of them enlarged rapidly before 14 days and then grew smoothly. Comparatively, mass loss of FA blended mortars in Figure 1a and Figure 1b have demonstrated that improvement of FA bringing into mass loss of plain mortars. Efficacy of FA against leaching attacks increased with its replacement levels. Mass loss of plain mortars under 28-day water curing regime was bigger than that under 180-day water curing regime before 42 days, the latter took its revenge until 56 days. It is quite simple for FA blended mortars that mass loss under 180-day water curing regime always higher than that under 28-day water curing regime.

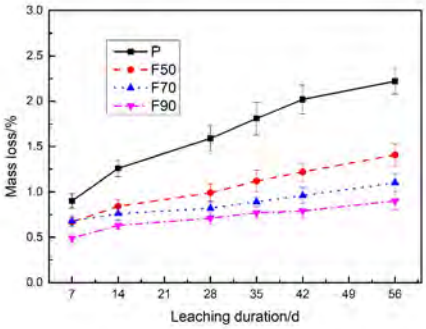

(a)28-day water curing regime

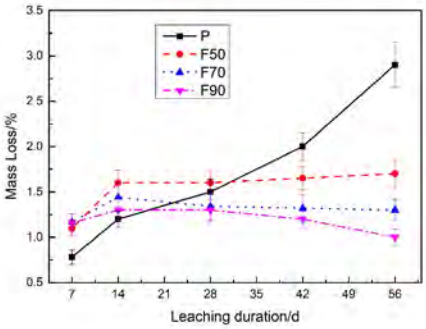

(b)180-day water curing regime

Figure 1: Mass loss of FA blended mortars under two curing regimes against leaching attacks

2.2 Phase transformation

Characteristics of plain pastes and FA blended pastes against leaching attacks were listed in Table 4. It could be seen that CH content and content of chemical bonded water of FA blended pastes under 28-day water curing regime decreased following increase of FA dosages. Hydration degree of FA blended pastes was lower than that of plain pastes, showing successive downside oppositely to FA dosages. Under 180-day water curing regime, CH content of FA blended pastes(70% and 90%) were zero, but content of chemical bonded water was more than that under 28-day water curing regime, hydration degree of other paste samples also rising substantially.

Figure 2 show correlations between CH content and mass loss under ACS immersion at 56 days in the exposure period. There was a good linear relationship between CH content and mass loss in Figure 2, whose equation of linear regression was y=0.1119x+0.7074 (x>0), R^2=0.9697。

Table 4: Characteristics of Portland cement and fly ash blended cement pastes

Sample	Content of CH /%		Content of Bound water /%			hydration degree	
	28d	180d	28d	180d	Extremity hydration situation	28d	180d
P	15	18.6	21.7	24.1	35.6	60.9	71.3
F50	7.4	7.2	14.6	18.3	26.9	54.3	68.4
F70	3.5	0	11.6	14.2	20.6	53.3	65
F90	1.8	0	5.5	8.9	11.2	49.1	57.1

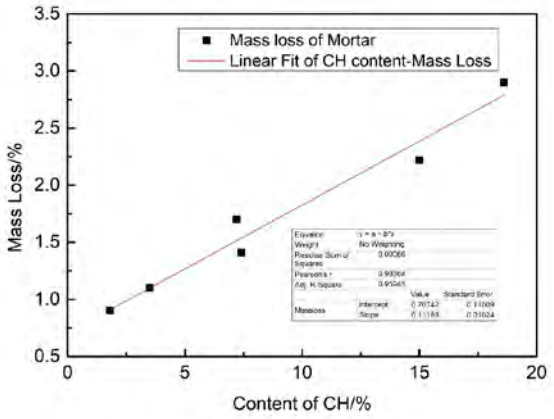

Figure 2: Correlation between CH content and mass loss against leaching attacks

CH content of FA blended pastes was the result from adder-subtractor between cement hydration and FA pozzolanic reaction, but initial CaO content of FA blended pastes could consistently represent all of Ca^{2+} in cement hydration. Following with increasing of FA dosages, initial CaO content of blended pastes became less and less. Therefore, there might be one dynamic equilibrium between initial CaO content of plain pastes as well as FA blended pastes and CH content which could be found in Figure 3. Under 28-day water curing regime, the equation of linear regression was y=0.02724x-2.4517, x ∈(42，62), R^2=0.9803. Under 180-day water curing regime, the equation of linear regression was y=0.0059x^2-0.0481x-0.9117, x ∈(42，62), R^2=0.9857.

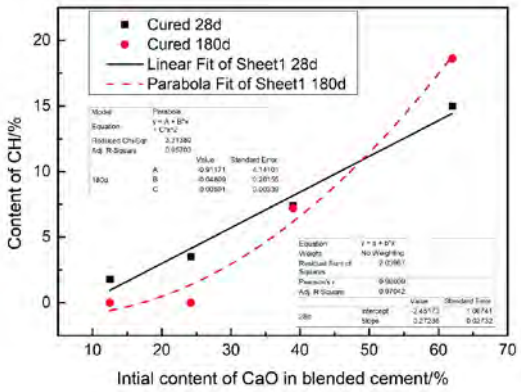

Figure 3: Correlation between initial CaO content and CH content against leaching attacks

Based on Figure 2 and Figure 3, it could be assumed that there were indeed correlations between initial CaO content and CH content in blended pastes and there also correlations between CH content and mass loss. Hence, there must be correlations between initial CaO content and mass loss in certain extent which was Figure 4. Under 28-day water curing regime, the equation of linear regression was y=0.0268x+0.4833 $x \in (42, 62)$, R^2=0.99. Under 180-day water curing regime, the equation of linear regression was y=0.0005x^2+0.0026x+0.9141 $x \in (42, 62)$, R^2=0.973.

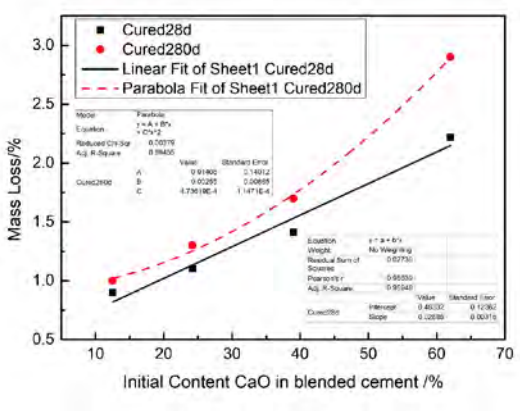

Figure 4: Correlation between initial CaO content and mass loss against leaching attacks

Moreover, unhydrated cement grains and unhydrated FA particles would still go on cement hydration and pozzolanic reaction meanwhile leaching attacks going on outside, so there might be some interactions between these situations. Figure 5 showed correlations between hydration degree and mass loss in blended pastes. Figure 6 showed correlations between chemical bonded water and mass loss in blended pastes. From Figure 5, correlations between hydration degree and mass loss were not linear, its equation of linear regression was y=0.0024x^2-0.2238x+6.2347, R^2=0.59. According to R^2, these correlations could only be evaluated as medium association. From Figure 6, relationships between chemical bonded water and mass loss were also not linear , its equation of linear regression was y=0.006x^2-0.0781x+1.1859, $x \in (42, 62)$, R^2=0.98. According to R^2, these correlations could be evaluated as premier association.

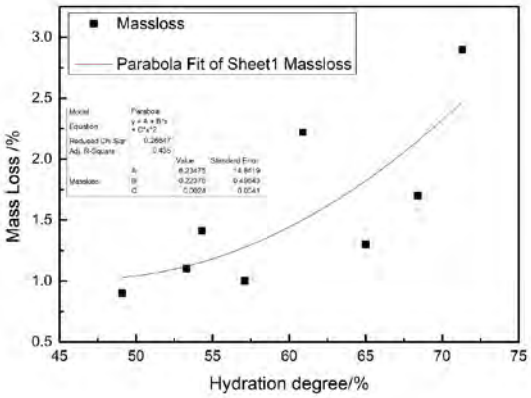

Figure 5: Correlation between hydration degree and mass loss against leaching attacks

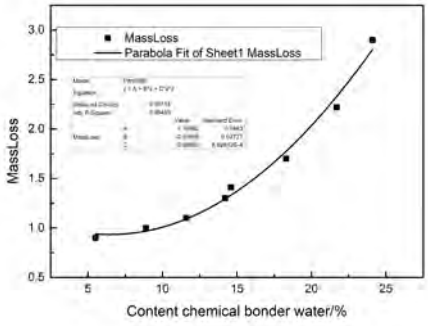

Figure 6: Correlation between chemical bonded water and mass loss against leaching attacks

2.3 Mechanism discussion

According to mechanism in leaching model proposed by Van Eijk et al[1] and results from other researchers[11–13] , dissolution of CH was much higher than Ca^{2+} dissolving from C-S-H during leaching attacks and it was suggested by [14] that leaching attacks would begin with dissolution of CH and then decalcification of C-S-H. From Figure 1, one can see that performance of high volume FA blended mortars were better than that of plain mortars, effect of 28-day water curing regime was also better than that of 180-day water curing regime. But there might be different roles for cement hydrates, unhydrated cement grains, unhydrated FA particles against leaching attacks.

Firstly, CH would continuously dissolve, resulting in mass loss during leaching attacks, this cement hydrates should be regarded as top-class disadvantage. Decalcification of C-S-H would also lead to mass loss, whose dissolving rate slower than CH, and should be regarded as second-class disadvantage. Unhydrated cement grains would bring into new hydrates which could repair damages caused by leaching attacks at first and their products would continue dissolving and decalcification. These phases should also be regarded as disadvantage at third-class. Unhydrated FA particles were difficult to evaluate. When plenty of CH, unhydrated FA particles could process pozzolanic reactions which would consume top-class disadvantage of CH and produce C-S-H to strengthen matrix partly. When lack of CH in matrix(low hydration degree or CH dissolved much already), pozzolanic reaction willful consuming CH might cause decline of alkalinity in solution-environment and this also might

diminish repairing effects of FA against leaching attacks. This is why effect of 28-day water curing regime was better, because of less CH and C-S-H to minimize damages from leaching attacks, more unhydrated cement grains and unhydrated FA particles to repair damages in a certain extent.

From Figure 2, one can see that linear correlations between CH content and mass loss were clear. But it would be different for relationships between initial CaO content and mass loss in Figure 3. Under 28-day water curing regime, linear correlations between initial CaO content and mass loss were also obvious. This situation owed to low pozzolanic reactivity of FA at early ages(0～28 days). High volume FA could not begin their pozzolanic reaction and nearly none of CH consuming. Under 180-day water curing regime, correlations between initial CaO content and mass loss were nolinear totally. This situation originated from facts that many CH have been reacted with high volume FA. Consequently, correlations between initial CaO content and mass loss in Figure 4 might be an effective indicator for cement pastes and mortars against leaching attacks.

According to another article from our laboratory(unpublished yet), correlations between mass loss and hydration degree in slag blended mortars against ACS leaching attacks were good linear, which meant that more higher degree of hydration and more mass loss. As these correlations evaluated as medium association for FA blended mortars and nolinear, reasonable explanations could be given that FA was one SCM with low reactivity which constituted of inert substances as quartz and mullite. These inert substances might resist percentages of mass loss only at data line but no real effects during ACS leaching attacks. Thus, dosages of FA should be controlled under certain ranges, not as many as possible.

4. CONCLUSIONS

Fly ash blended mortars could show better performance compared to plain mortars against ammonium chloride solution leaching attacks. Effects of fly ash depended on their replacement levels. 28-day water curing regime in advance was an improvement method for fly ash blended mortars which need refinement against solution leaching attacks. Mass loss of fly ash blended mortars was highly related to their initial CaO content. Higher content of initial CaO content, more mass loss of fly ash blended mortars experiencing. Data of initial CaO content could be used as theoretical evaluation against leaching attacks. Pozzolanic reaction of fly ash could decrease leaching rate and repair matrix partly. But excessive fly ash could lead to overbalanced consuming of $Ca(OH)_2$ which would degenerate alkalinity inside matrix and finally hinder their effects. Dosage of fly ash against leaching attacks should be suitably under control.

ACKNOWLEDGEMENTS

The authors express their thanks for financial supporting this investigation from the National Key Technology R&D Programs in the 13th Five-year Plan of China(2016YFC0701004), the Social Development Science and Technology Field Projects of Shanghai Science and Technology Commission(19DZ1201404, 19DZ1202702), Special Fund Project of Shanghai Economic and Information Technology Commission(Shanghai CXY-2016-012), and Shanghai "Alliance Plan" Project in 2019 (LM201947). The authors also wish to appreciate warming help from colleagues in Professor Zhenping Sun’s Group for daily experiments and discussions and useful suggestions from Professor Peiming Wang in Department of Civil Engineering Materials in Tongji University.

REFERENCE

[1] Van Eijk R J, Brouwers H J H. Study of the relation between hydrated portland cement composition and leaching resistance [J]. Cement and Concrete Research, 1998, 28(6): 815-828.
[2] Carde C, Francois R, Torrenti J M. Leaching of both calcium hydroxide and C-S-H from cement paste: modeling the mechanical behavior [J]. Cement and Concrete Research, 1996, 26(8): 1257-1268.
[3] Bentz D P, Garboczi E J. Modelling the leaching of calcium hydroxide from cement paste: effects on pore space percolation and diffusivity [J]. Materials and Structures, 1992, 25(9): 523-533.
[4] Garboczi E J, Bentz D P. Computer simulation of the diffusivity of cement-based materials [J]. Journal of Materials Science, 1992, 27(8): 2083-2092.
[5] Yang H, Jiang L H, Zhang Y, et al. Predicting the calcium leaching behavior of cement pastes in aggressive environments[J]. Construction and Building Materials, 2012(29): 88-96.
[6] Bernard F, Bernard S K. Performance simulation and quantitative analysis of cement-based materials subjected to leaching[J]. Computational Materials Science, 2010(50): 218-226.
[7] Segura I, Molero M, Aparicio S, et al. Decalcification of cement mortars: characterization and modelling[J]. Cement and Concrete Composites, 2013, 35(1):136-150.
[8] Huo J X, Song H Z, Guo Y Q, et al. Investigation on different cement-based materials in contact leaching under deionized water environment [J]. Journal of Hydroelectric Engineering, 2013, 32(1): 242-247.
[9] Liu R G, Zhang B, Yan P Y. Microstructural variation of hardened cement-slag pastes leached by soft water [J]. Journal of the Chinese Ceramic Society, 2013, 41(11): 1487-1492.
[10] Christophe Carde, Raoul Francois, Jean-Michel Torrenti.. Leaching of both calcium hydroxide and C-S-H from cement pastes: Modeling the mechanical behavior[J]. Cement and Concrete Research, 1996, 26(8): 1257-1268.
[11] Yang H, Jiang L H, Zhang Y, et al. Summary of researches on chemical damage of concrete based on leaching process [J]. Advances in Science and Technology of Water Resources, 2011, 31(1):83-89.
[12] P. Faucon, P. LeBescop, F.Adenot et al. Leaching of cement: Study of the surface layer[J]. Cement and Concrete Research, 1996, 26(11):1707-1715.
[13] Buil M, Revertegat E, Oliver J A. A model of the attack of pure water or undersaturated lime solutions on cement, Stab. Soild. Hazard. Radioact. Wastes, 2nd Vol. STP 1123, T.M. Gilliam, and C.C. Wiles, (eds), ASTM, Philadelphia, 1992: 217-226.
[14] Feng P, Miao C W, Bullard J W. A model of phase stability, microstructure and properties during leaching of Portland cement binders[J]. Cement and Concrete Composites, 2014(49): 9-19.

DETERIORATION OF CEMENT MORTARS WITH DIFFERENT WATER CEMENT RATIO PARTIALLY IMMERSED IN SULFATE

Zhenhai Xu (1), Jianming Gao* (1,2), Fei Chen (1,2)

(1) School of Materials Science and Engineering, Southeast University, Nanjing 211189, China

(2) Jiangsu Key Laboratory of Construction Materials, Nanjing 211189, China

Abstract

Cement-based materials in sulfate rich areas will suffer from serious corrosion after semi-immersion. To study the degradation of cement mortars with different water cement ratio (w/c) partially exposed to sulfate solution, the mass change were employed to reveal damage progress. Moreover, porosity, erosion products and SO_4^{2-} content were monitored to study the damage mechanism. Results indicate that the porosity, SO_4^{2-} content and erosion products of mortars show an augment as the w/c increases. Correspondingly, high w/c leads to more severe mass change. XRD results reveal that the deterioration of drying portion is attributed to both chemical and physical sulfate corrosion. In addition, the water-soluble SO_4^{2-} content in drying portions is higher than that in immersed portion, implying more serious sulfate attack in drying portion.
Keywords: Sulfate attack; Partial immersion; Water cement ratio (w/c); Porosity; Erosion products

1. INTRODUCTION

Durability, the most important properties of cement-based materials, fails prematurely due to sulfate attack, which causes the dramatic life-span shortening of cement-based materials [1-3]. Over the few decades, many researches [4-6] have been done to describe the degradation behavior of cement-based materials under sulfate environment. Most studies focus on full immersion [7-9] and only a few researches concentrate on partial immersion [10, 11]. Under the condition of full sulfate immersion, sulfate can diffuse into the interior of cement-based materials and react

* Corresponding author.
E-mail address: xuzhenhaimail@foxmail.com (Z. Xu), jmgao@seu.edu.cn (J. Gao).

with hydration products (hydrated calcium aluminate, $Ca(OH)_2$, C_3A, etc.) to form AFt and gypsum, resulting in expansion and cracking [4]. This is the most acceptable mechanism of chemical sulfate attack in full immersion. However, there are two main controversies about the mechanism of partial immersion. According to researches from Nehdi [12] and Harvey [13], concrete partially submerged in sulfate solution suffers from both chemical and physical attack (i.e., salt crystallization). This is in accord with the field experience that concrete partially immersed in sulfate suffers from surface scaling above ground level. On the contrary, Zanqun Liu [14] finds that Na_2SO_4 crystallization can't occur in the Portland cement concrete. Therefore, it's an important work deeply investigating the deterioration driving force of cement-based materials partially immerged in sulfate solution.

The performance of cement-based materials depends largely on w/c. According to the Jurlin's law [15], capillary absorption height is inversely proportional to the pore radius. Cement mortar with lower w/c has fine pore radius and stronger capillary absorption, which is conducive to the transport of sulfate solution and finally causes more serious erosion. Nehdi [16] has investigated the sulfate attack resistance of mortars with 0.3, 0.45 and 0.6 w/c. The results show that mortars with 0.45 w/c have the highest amount of crystal salt. On the contrary, other researchers [17, 18] get the opposite conclusion. Consequently, the degradation of cement-based materials with different w/c still needs investigation.

Contradictory data and theories still exist regarding the deterioration of cement-based materials partially immerged in sulfate solution. In present work, mass change, porosity, erosion products as well as SO_4^{2-} concentration have been studied to figure out the damage process and deterioration mechanism of cement mortars with different w/c partially immerged in sulfate solution.

2. MATERIALS AND METHODS

2.1. Materials and samples preparation

Portland cement (P·I 52.5) conforming to Chinese standard (GB 175-2007) was used for this investigation. The chemical composition and physical properties of cement are shown in Table 1. Tap water and river sand (<5 mm) with the fineness modulus of 2.6 were used.

Table 1: Chemical composition and physical properties of cement

Chemical composition (wt%)								Specific surface area (m^2/kg)	Specific gravity (g/cm^3)
CaO	SiO_2	Al_2O_3	Fe_2O_3	MgO	SO_3	K_2O	Na_2O		
64.47	20.87	4.87	3.59	2.13	2.52	0.65	0.11	368.90	3.11

The water cement ratio (w/c) of cement mortars varies from 0.35 to 0.65 and the detailed mixing proportions of the samples are shown in Table 2. Cement and sand were added to a blender and stirred for 60 s, then the water was added to the blender and another 60 s was used for agitation, finally the mixture was blended with a high speed for 120 s. The fresh mortar was made into 40 mm × 40 mm × 160 mm samples.

All samples were cured at 20 ± 1°C and 90% RH for 60 days before testing.

Table 2: Mixing proportions of samples

Sample	Cement (g)	Sand (g)	Water (g)	w/c
W35	1000	3000	350	0.35
W53	1000	3000	530	0.53
W65	1000	3000	650	0.65

2.2. Partial sulfate immersion

Following 60 days curing, the mortar specimens were placed in room temperature environment to remove the extra water on the surface of mortars. After drying, the mortar simples were put into a plastic box containing 5 wt% Na_2SO_4 solution, the height of the solution is 60 mm. Besides, each container has a lid with six 40 mm × 40 mm holes to reduce water evaporation and the pH value of the solution was controlled based on Chinese standard (GB/T 50082-2009, the Na_2SO_4 solution was replaced every month). The container details are depicted in Fig. 1. In addition, containers were placed in a temperature of 35°C and relative humidity of 50%, which can accelerate the sulfate attack and simulate the environment of South China Sea.

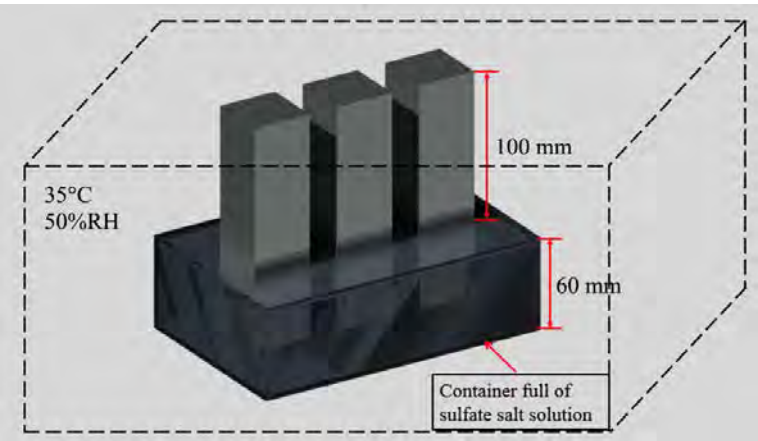

Figure 1: Diagrammatic drawing of partial sulfate immersion.

2.3. Test methodology

2.3.1. Mass

The mass of mortars were tested monthly during sulfate immersion. The crystalline substances and corrosion products on mortars surface were removed used a lint brush, then put mortars at room temperature for 6 h to release the excess water on the surface of mortars. Following that, an electronic balance (range: 5 kg, accuracy: 0.01 g) was employed to detect mass of mortars.

2.3.2. Mercury intrusion porosimetry

Mercury intrusion porosimetry (MIP, Micrometrics, AutoPore IV 9500, USA)

technique was used to quantitatively evaluate the porosity of the samples after 6 months erosion. The pressure ranges from 0.5 to 60000 psia and the detectable pore diameter ranges from 3.6 nm to 400 μm. After being eroded for 6 months, the core portions were extracted from the drying part (under the efflorescence) with a deep of 5 mm - 10 mm. All samples were vacuum dried at 60 °C for 24 h before MIP tests to avoid structural damage.

2.3.3. X-ray diffraction analysis (XRD)

The X-ray diffraction data from 5° to 40° was collected by an X-ray diffractometer (Bruker, D8 Discover, Germany). The accelerating voltage, accelerating current, step size and dwelling time of tests were 40 kV, 30 mA, 0.02° and 0.15 s, respectively. Powders from drying part (under the efflorescence) was grounded to pass 200 mesh fineness to conduct the test.

2.3.4. SO_4^{-2} concentration

The water-soluble SO_4^{-2} concentration of mortars were measured by ICP (inductive coupled plasma emission spectrometer). Powders from drying portion (under the efflorescence) and immersed part (the bottom of the specimens) were collected and passed 200 mesh fineness and dried at 60°C to a constant weight. Subsequently, 3g dried powder was added to 100 mL distilled water and settled for 1 day, and the supernatant was diluted by distilled water to 0.1-100 ppm for ICP test.

3. RESULTS AND DISCUSSION

3.1. Mass change

The mass change of mortars after partial immersion in 5% Na_2SO_4 is presented in Fig. 2. Results show that the mass change of mortars includes two stages, i.e., slow decline and accelerated rise stages. The weight loss is attributed to the evaporation of water under lower RH. The weight starts to increase after a slow decline stage. The increment of weight is mainly due to the accumulation of erosion products. The weight of W65 and W53 starts to increase from the second and fifth corrosion months, respectively. However, the weight of M35 reduces all the time. In addition, W65 and W53 specimens rupture after corrosion for 7 and 9 months. Physical and chemical erosion leads to expansion and surface peeling of mortars, then causes the fracture of mortars. W35 mortar, however, has shown a constant reduction in weight during the 12 months and the mass of W35 decreases 1.33% after 12 months corrosion. The mass change results reveal that high w/c leads to more severe corrosion partially exposed to 5% Na_2SO_4.

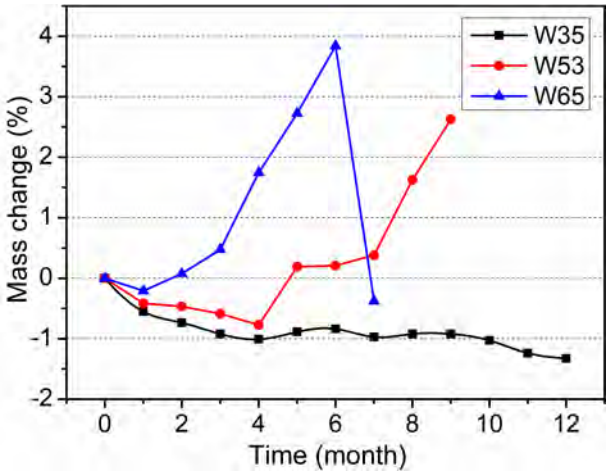

Figure 2: Mass change of mortars with different w/c partially immersed in 5% Na_2SO_4 solution.

3.2. Porosity of specimens

After 6 months corrosion, the drying portions were selected and the porosities were detected by MIP to estimate the effect of w/c on mortars partially immersed in sulfate solution.

The cumulative porosity of mortars after partially exposed to 5% Na_2SO_4 solution for 6 months in Fig. 3 shows that the porosity of cement mortars increases as the w/c augments. The porosities of W35, W53 and W65 are 9.09%, 11.90% and 20.45%, respectively. The high porosity caused by large w/c leads to a undesirable pore structure, increasing the connection of the pores, improving the capillary absorption and more sulfate ions penetrating into the drying portion (section 3.2) when cement mortar partially exposed to Na_2SO_4 solution. Besides, more sulfate ions will react with cement paste and crystallize to thenardite (section 3.2), finally causing more severe mass change (section 3.1).

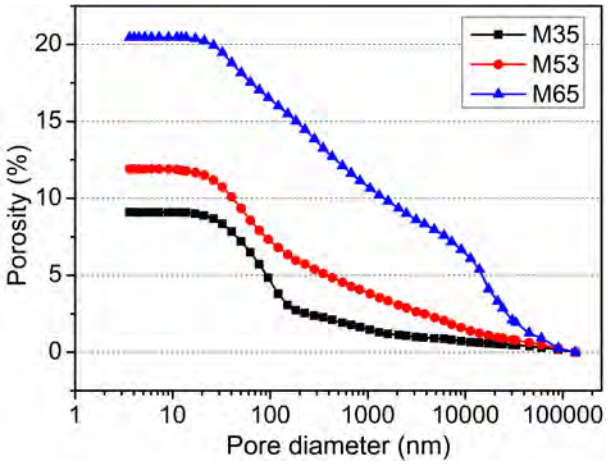

Figure 3: Porosity of mortars after partially exposed to 5% Na_2SO_4 solution for 6 months.

3.3. Erosion products

The XRD test has been employed to investigate the erosion products in drying portion (under the efflorescence zone) after 6 months erosion and the results have emerged in Fig. 4.

It can be observed from Fig. 4 that the erosion products (i.e., ettringite (AFt), gypsum and thenardite) are observed in all mortar specimens. AFt and gypsum are generated due to the chemical reaction between cement paste and Na_2SO_4. With respect to thenardite, it's mainly owing to the crystallization of Na_2SO_4 transported from the immersed portion. The results illustrate that the degradation of cement mortars partially exposed to sulfate solution is ascribed to both chemical and physical attack, which is in agreement with the Ref. [12]. Besides, the content of corrosion products shows an augmentation with the increased w/c. It's attributed to the large porosity caused by high w/c (section 3.2).

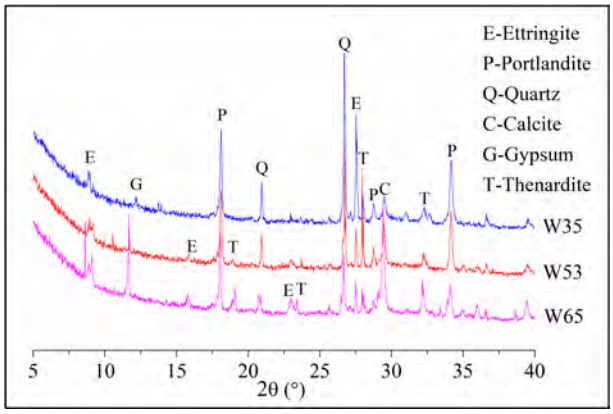

Figure 4: XRD patterns of mortar specimens with different w/c.

3.4. SO_4^{2-} diffusion

In order to evaluate the SO_4^{2-} diffusion of mortar under partially immersed in sulfate solution, the SO_4^{2-} concentration of mortar in drying portion (under the efflorescence) and immersed portion (the bottom of the specimens) after 6 months immersion has been tested and the results are presented in Fig. 5.

As can be obviously seen in Fig. 5 that the water-soluble SO24- concentration in drying portion is higher than that in immersed portion for all mortars. The reason is that SO 24- ions can transport from immersed part to drying part with water transportation by the capillary absorption, while the water can evaporate and SO24- ions will accumulate in drying part. It can be concluded that the drying portion with higher SO24- concentration suffers from more severe sulfate attack (both chemical and physical attack according to section 3.3). Besides, Fig. 5 also shows thatthe water-soluble SO24- concentration in both drying and immersed parts presents a gradually increment with the w/c increasing. Mortars with high w/c have larger

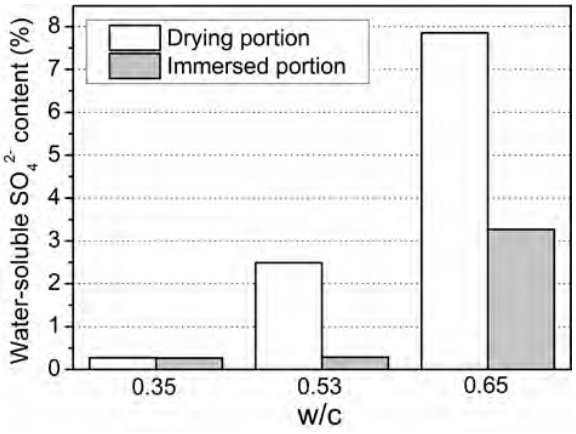

Figure 5: Water-soluble SO_4^{2-} content in drying/immersed portions of mortars with different w/c.

porosity (section 3.2) and better pore connection, leading to the enhanced capillary effect and finally resulting in higher sulfate concentration. This result is accord with the mass change observation.

4. CONCLUSIONS

This paper focuses on the deterioration behavior of cement mortars with different water cement ratio partially immersed in sulfate. From the experimental results obtained, the following conclusions are advanced:

(1) High w/c can increase the porosity of mortar, leading to more severe mass change;
(2) Both chemical and physical sulfate attacks are contributed to the degradation of drying part and the content of corrosion products (i.e., AFt, gypsum and thenardite) show an increase with the augmentation of w/c;
(3) The water-soluble SO_4^{2-} content in drying portions is higher than that in immersed portion, which can lead to more serious sulfate attack in drying portion.

ACKNOWLEDGEMENTS

This work has been made possible thanks to financing from National Natural Science Foundation of China (No. 51578141), National Basic Research Program of China (973 Program, No. 2015CB655102) and National Key R&D Program of China (NO. 2017YFB0309904-04).

REFERENCES

[1] N.M. Al-Akhras, Durability of metakaolin concrete to sulfate attack, Cement and Concrete Research 36(9) (2006) 1727-1734.
[2] K. Sotiriadis, E. Nikolopoulou, S. Tsivilis, Sulfate resistance of limestone cement concrete exposed to combined chloride and sulfate environment at low temperature, Cement and Concrete Composites 34(8) (2012) 903-910.
[3] A. Skaropoulou, K. Sotiriadis, G. Kakali, S. Tsivilis, Use of mineral admixtures to improve the resistance of limestone cement concrete against thaumasite form of sulfate attack, Cement and Concrete Composites 37 (2013) 267-275.
[4] A. Neville, The confused world of sulfate attack on concrete, Cement and Concrete Research 34(8) (2004) 1275-1296.

[5] D. Sun, K. Wu, H. Shi, S. Miramini, L. Zhang, Deformation behaviour of concrete materials under the sulfate attack, Construction and Building Materials 210 (2019) 232-241.
[6] T. Ikumi, I. Segura, Numerical assessment of external sulfate attack in concrete structures. A review, Cement and Concrete Research 121 (2019) 91-105.
[7] W.-y. Ouyang, J.-k. Chen, M.-q. Jiang, Evolution of surface hardness of concrete under sulfate attack, Construction and Building Materials 53 (2014) 419-424.
[8] M. Zhang, J. Chen, Y. Lv, D. Wang, J. Ye, Study on the expansion of concrete under attack of sulfate and sulfate–chloride ions, Construction and Building Materials 39 (2013) 26-32.
[9] Z. Zhang, X. Jin, W. Luo, Long-term behaviors of concrete under low-concentration sulfate attack subjected to natural variation of environmental climate conditions, Cement and Concrete Research 116 (2019) 217-230.
[10] F. Chen, J. Gao, B. Qi, D. Shen, Deterioration mechanism of plain and blended cement mortars partially exposed to sulfate attack, Construction and Building Materials 154 (2017) 849-856.
[11] Z. Liu, D. Deng, G.D. Schutter, Z. Yu, Chemical sulfate attack performance of partially exposed cement and cement+fly ash paste, Construction and Building Materials 28(1) (2012) 230-237.
[12] M.L. Nehdi, A.R. Suleiman, A.M. Soliman, Investigation of concrete exposed to dual sulfate attack, Cement and Concrete Research 64 (2014) 42-53.
[13] H. Haynes, R. O'Neill, M. Neff, P.K. Mehta, Salt weathering distress on concrete exposed to sodium sulfate environment, Aci Materials Journal 105(1) (2008) 35-43.
[14] Z. Liu, X. Li, D. Deng, G. De Schutter, L. Hou, The role of $Ca(OH)_2$ in sulfate salt weathering of ordinary concrete, Construction and Building Materials 123 (2016) 127-134.
[15] D. Quéré, F. Brochard-Wyart, P.-G.d. Gennes, Capillarity and Wetting Phenomena, Springer, New York, 2004.
[16] M. Nehdi, M. Hayek, Behavior of blended cement mortars exposed to sulfate solutions cycling in relative humidity, Cement and Concrete Research 35(4) (2005) 731-742.
[17] M.T. Bassuoni, M.M. Rahman, Response of concrete to accelerated physical salt attack exposure, Cement and Concrete Research 79 (2016) 395-408.
[18] D. Stark, Performance of concrete in sulfate environments, Cement Content (2002).

DURABILITY INVESTIGATIONS OF MICRO AND NANO SILICA BLENDED CEMENTITIOUS SYSTEMS IN SELF-COMPACTING CONCRETE UNDER ADVERSE CONDITIONS

Nandhini K (1) and Ponmalar V (2)

(1) Department of Civil Engineering, National Institute of Technology Tiruchirappalli, India

(2) Division of Structural Engineering, Anna University, Chennai, Tamil Nadu, India

Abstract

The colossal magnification of industrialization in recent years led to the snags of squandering materials that harm the environment. To employ the industrial debris into the concrete, can contribute to lower the carbon footprint to some extent. For this purpose, the M60 grade of self-compacting concrete was designed with industrial waste products. Fly ash was used as a constant cement substitute product of 20% of the cementitious systems. Further, silica of micro and nano-sized particles are used as a cementitious replacement in varying percentages from 5% to 15% and 1% to 3% respectively. A total of eight mixes including the reference mix and the combined mix of micro and nano silica were prepared and examined for the fresh state property. The slump flow test, J-ring test, and Orimet test were performed in the fresh state of concrete. Concrete specimens in the hardened state were tested for compression strength and durability characteristics like water absorption, acid attack, and sulphate attack at 7, 28, and 90 days respectively. Further, investigations were carried out on the microstructural behavior when exposed to acid and sulphate attack using a scanning electron microscope (SEM). The hardened state properties of SCC showed positive durability results for the combined mix of 10% micro and 2% nano silica, where better hiking of calcium silicate hydrate gel was observed by the inclusion of binary and ternary blending materials.

Keywords: Flowability, hardened property, particle packing density, SEM

1. INTRODUCTION

Concrete plays a lead role in the building industry to that of a heart in a human body. Nowadays, the employment of the traditional concrete faces the complication of concreting in highly reinforced concrete structures, narrow members, and complex shaped sections. Therefore, Self-Compacting Concrete (SCC) has emerged to fill the concrete members under its self-weight. SCC carries three major crediting properties of filling ability, passing ability, and resistance to segregation [1]. The recommended mix design procedure with a set of tests

conducted for fresh concrete properties of SCC has been included in "Specifications and guidelines for SCC" Europe Federation (EFNARC) [2]. In 2016, the global market of SCC was almost around 8.74 billion USD and by 2023, it would reach 11.67 billion USD [3]. Numerous research activities on various aspects of SCC are being pursued due to its rising demand of SCC production. The advantage of SCC includes less labor, saves construction time and noise reduction at the work site [4]. The global patterning of urbanization and industrialization is mounting vigorously each day. The development and disposal of numerous by-products from industries like fly ash, rice husk ash, silica fume, etc. are the major challenges faced. To overthrow this issue, the industrial by-products could be utilized in concrete as cementitious materials. The SCC when blended with these filler materials improved the mechanical and durability properties [5]. SCC containing blended materials like fly ash and blast furnace slag enhanced the passing and filling ability of fresh SCC [6]. The investigation of adopting fly ash at 10%, 15%, 20%, 25%, and 30% while silica fume at 10%, 15%, and 20% as partial cement substitute in SCC containing 450 kg/m^3 of cement was conducted. The fly ash with 20% replacement to cement was found to perform better in terms of workability and mechanical strength [7].

This study investigates the fresh concrete property and durability characteristics of SCC using micro and nano silica as partial cement replacement. The concrete was exposed to an acid and sulphate environment and investigation was carried out using SEM analysis.

2. MATERIALS AND MIX DESIGN

Ordinary Portland Cement (OPC) of grade 53 was used in the study. The Fly Ash (FA) procured from the Ennore Thermal Power plant was used as a constant replacement of cement at 20%. The Microsilica (MS) from Corniche Chemicals, Mumbai and Nanosilica (NS) from Astra Chemicals, Chennai were used as partial cement substitute materials at 0%, 5%, 10%, 15% and 0%, 1%, 2%, 3% respectively. The coarse aggregate used for the study was crushed stones of a maximum of 12.5mm and the fine aggregate used was natural river sand. The bulk densities of coarse and fine aggregates are presented in Table 1. The water-binder ratio for the M60 grade of SCC was maintained constant at 0.38. Table 2 represents the mix proportions of SCC. The superplasticizer and the viscosity modifying agent were increased for the increasing contents of MS and NS as listed in Table 2.

Table 1: **Properties of coarse aggregate**

Materials	Specific gravity	Compacted bulk density (kg/m^3)	Loose bulk density (kg/m^3)	Fineness modulus	Maximum size (mm)
Fine aggregate	2.635	1636	1510	2.77	4.75
Coarse aggregate	2.725	1539	1329	-	12.5

3. EXPERIMENTAL INVESTIGATION

The experimental study consist of arriving at the suitable mix proportions that satisfied the fresh properties of self-compacting concrete as per EFNARC specifications. The main objective of this project is to study the strength and durability effects of self-compacting concrete using FA, MS and NS with various percentages.

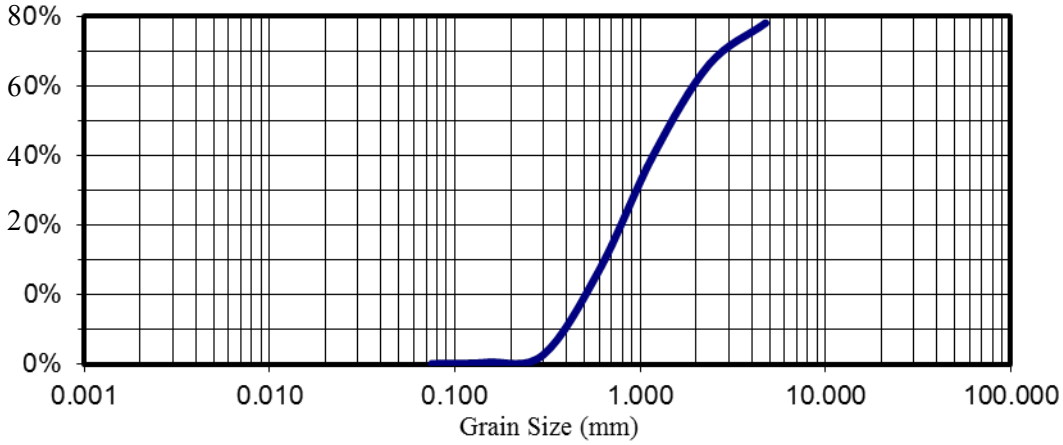

Figure 1: S-Curve for fine aggregate

Table 2: SCC mix proportions

Mix ID	Mix proportions (kg/m^3)							Dosage (%)	
	Cement	FA	MS	NS	Water	Aggregates		SP	VMA
						Fine	Coarse		
M1	424.0	106	-	-	200	940	850	1.2	0.12
M2	402.8	106	21.2	-	200	940	850	1.5	0.15
M3	381.6	106	42.4	-	200	940	850	1.8	0.18
M4	360.4	106	63.6	-	200	940	850	2.0	0.20
M5	419.8	106	-	4.2	200	940	850	1.5	0.15
M6	415.5	106	-	8.5	200	940	850	1.8	0.18
M7	411.3	106	-	12.7	200	940	850	2.0	0.20
M8	373.1	106	42.4	8.5	200	940	850	1.8	0.18

3.1 Fresh properties of SCC

The slump flow was used to calculate the horizontal spread of fresh concrete without any blockages. The slump flow test method was evaluated using the Abrams cone. The diameter of the concrete in a circular pattern indicates the measure of the filling ability of the concrete. In the slump flow test, the cone is filled with concrete and then lifted vertically and to measure the flow diameter (mm).

The J-ring flow test was conducted to determine the passing ability of SCC. It is used for the examination of quality control for the developed fresh concrete. The J-ring test can be used to determine the passing ability of self-consolidating concrete. The difference in height of the concrete just inside the bars and just outside the bars was measured in mm.

The determination of the filling ability of SCC was identified using the orimet apparatus. The orimet apparatus consists of a steel pipe of 120mm diameter with 80 mm orifice at the bottom and it was fabricated as suggested by the EFNARC guidelines.

3.2 Durability properties

3.2.1 Water absorption test

The water absorption test on concrete samples was conducted as per BS 1881 – Part 122 (2011) and ASTM C642-13 standards. This test was carried out on SCC samples containing FA, micro silica, nano silica, and steel fibres. Three cubes of size 100 mm × 100 mm × 100 mm were cast to determine the water absorption test at the age of 28 days.

3.2.2 Acid attack test

This test was performed based on ASTM C 267-01 (2012). Cubes of size 100 mm × 100 mm × 100 mm were cast and water cured at 20° C for 28 days. The cube specimens were removed from the water and their weight was noted. The cubes were immersed in a plastic tub containing the water diluted with 5% hydrochloric acid. HCl was chosen for the most aggressive environment and maintained at 5%. The response of specimens to acid was assessed through the modified appearance, weight loss, and strength reduction. The acid attack on SCC is shown in Figure 2.

3.2.3 Sulphate attack test

Cubes of size 100 mm × 100 mm × 100 mm were cast using SCC and allowed for 28 days of water curing. Then the cubes were weighed and immersed in water containing 5% Magnesium Sulphate ($MgSO_4$). This test was performed as recommended by ASTM C 452. The effect of the $MgSO_4$ attack on SCC blended with micro and nano silica and its deterioration were analyzed visual inspection and strength reduction. The specimens exposed to sulphate attack is shown in Figure 3.

Figure 2: Acid attack

Figure 3: Sulphate attack

4. RESULTS AND DISCUSSIONS

4.1 Fresh properties of SCC

The slump flow values for M60 grade of SCC containing MS and NS as cement replacement values as shown in Figure 4. The slump flow ranged from 720 mm to 670 mm. As per EFNARC standards, the minimum slump flow value is 650 mm where all the mixtures from M1 to M8 satisfied the minimum criteria. M7 showed marginal slump flow compared to all other mixers this was due to a high amount of NS got agglomerated and clumped in the cementitious systems which restricted the flow.

The J-ring flow test values showed 710 to 652 mm. The J-ring flow properties are also indicated in Figure 4, where the increased dosages of micro and NS showed a linear decrease in trend for slump flow values. The higher difference in flow diameter derived from slump flow and the J-ring slump flow test showed that M4 and M7 exhibited a greater difference of about 20 mm other mixes assured a lesser value and which are admissible as per EFNARC standards. The European guidelines stated that the accepted limits, the flow diameter difference is allowed up to 30 mm.

Figure 4 represents the Orimet flow time taken for SCC investigations. The time taken for SCC to flow through the Orimet increased gradually for increasing the dosages of MS from 5% to 15% and NS from 1% to 3% respectively. Mix M8 containing 10% MS and 2% NS took 3.8 seconds time to pass through the orifice of the Orimet apparatus. Mix M4 took greater time to pass through the Orimet test and due to the excess of silica particles made the concrete to be stiff and decrease the workability.

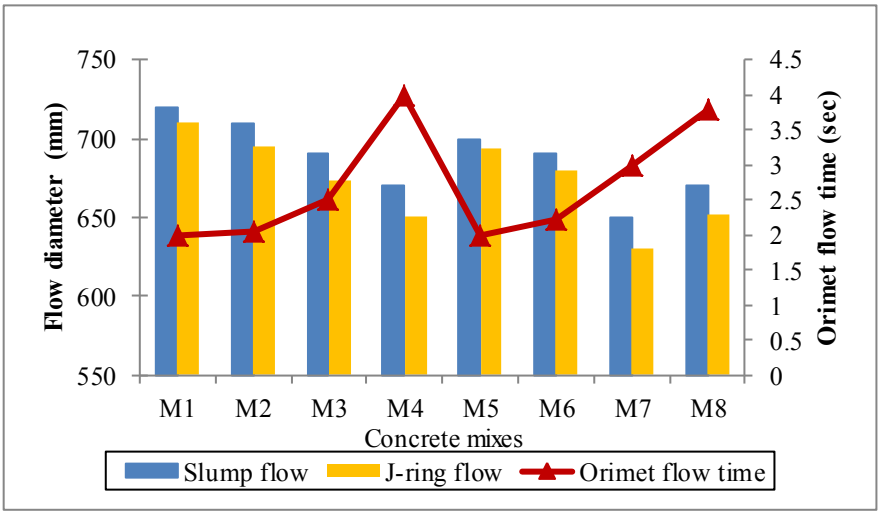

Figure 4: Fresh properties of SCC

4.2 Durability properties

4.2.1 Water absorption test

The water absorption test was conducted on self-compacting concrete was reported in Figure 5. The addition of micro particles and nanoparticles lower the permeability of concrete. From figure 5, the addition of 10% MS and 2% NS showed lesser water absorption of 2.348% and 2.055% at 7 days, 2.467% and 2.127% at 90 days respectively. Mix 8 which consists of 10 % MS and 2% is NS as partial cement replacement exhibited the lower water absorption of 2.28% at 90 days.

4.2.2 Acid attack test

Figure 6 represents the compressive strength test results of acid and sulphate attack on SCC. The 90 days compressive strength difference between water curing and hydrochloric acid solution for control SCC was 4.73 MPa. For MS replacement of 5% to 15%, the difference varied from 3.14 MPa to 3.11 MPa where 10% MS produced 1.72 MPa difference. For NS utilization, the strength variation was 3.16 MPa for 2% NS and greater for both 1% and 3% NS.

4.2.3 Sulphate attack test

There was an increase in compressive strength when micro silica was added initially in 5% and 10% M60 SCC. Further inclusion of NS from 1 to 3% slightly lowered the compressive strength test exposed to acid as the micro-level pores still exist and penetrates the acid solution into the concrete. The combined mix M8 containing 10% MS and 2% NS showed higher strength due to the less voids in the mix as the micro and nano silica enhanced the pozzolanic activity thereby making concrete impermeable.

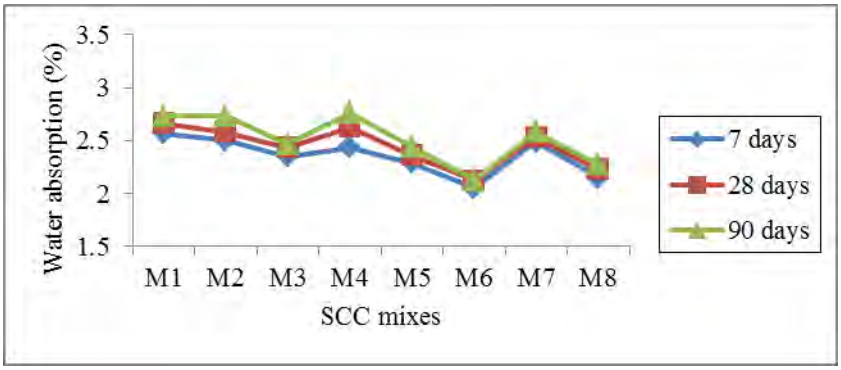

Figure 5: Water absorption of SCC

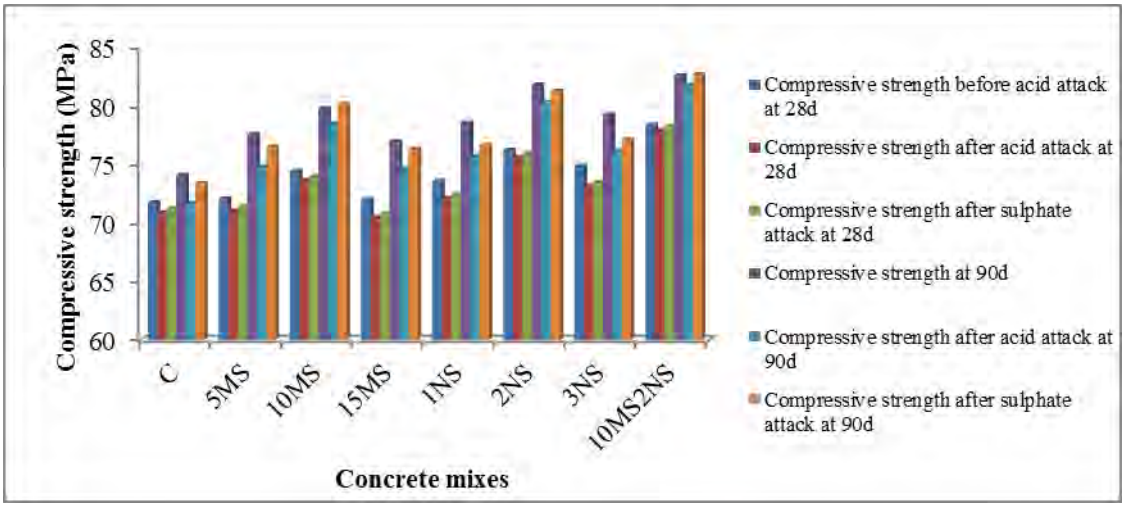

Figure 6: Acid and sulphate attack on SCC.

The SEM analysis of acid and sulphate attack at 90days on M60 SCC of mixes M1, M3, M6 and M8 are shown in Figures 7 and 8 respectively. The acid attack shows that initial development of needle like ettringite was developed in M1 and further growth of calcium silicate hydrate gels were observed in M3 and M6. The fly ash particles were visible along with the encirlement of CSH gel where MS and NS comparitively densified the structure.

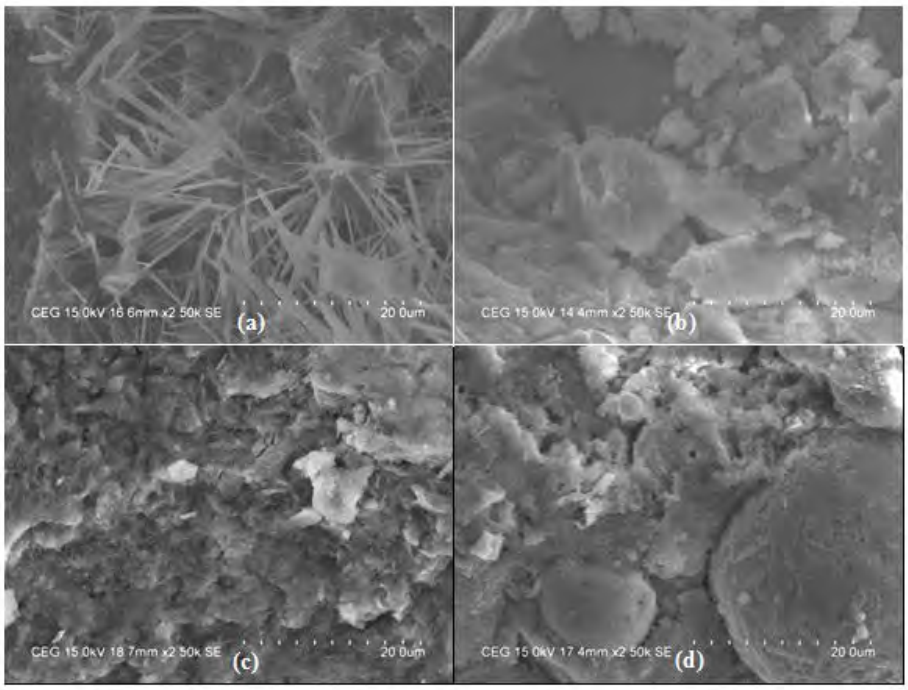

Figure 7: SEM analysis of acid attack on (a)M1 (b) M3 (c) M6 and (d) M8

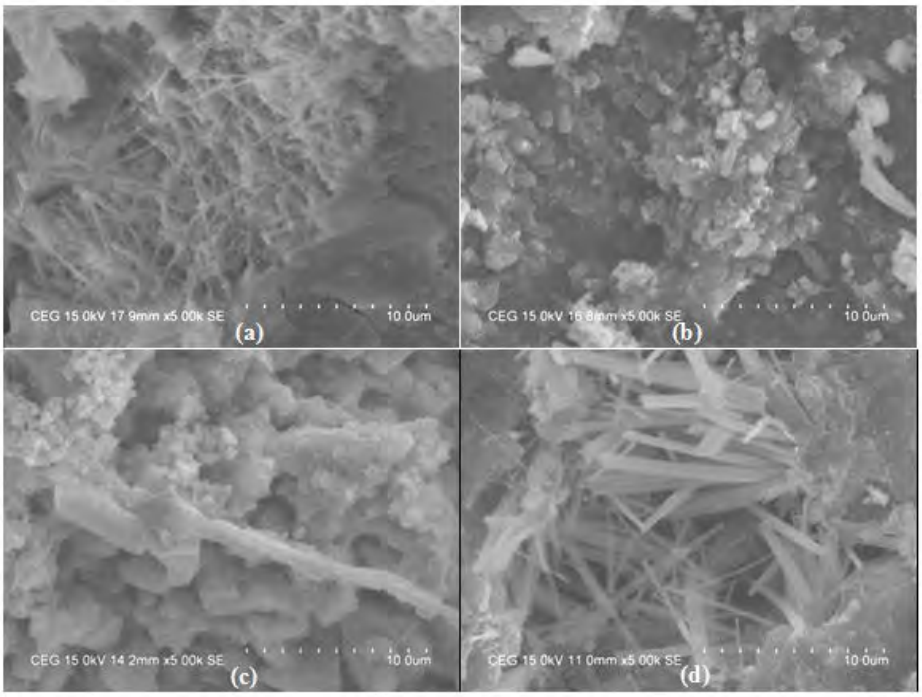

Figure 8: SEM analysis of sulphate attack on (a) M1 (b) M3 (c) M6 and (d) M8

The sulphate attack of SCC for mixes M1, M3, M6 and M8 showed the ingress attack of magnesium sulphate. The web like structures in M1 mix showed more amount of sulphate attack which small sugar crystals like structures and tubular like structures were observed in M3 and M6 respectively. M8 showed less sulphate attack on SCC with MS and NS.

5. CONCLUSION

- SCC can be adopted in all types of construction sectors nowadays because of the easy placing of concrete in congested areas of reinforcements. The SCC mixes with the addition of various combinations of micro and nano-silica satisfied the fresh properties as per EFNARC specifications. The addition of FA improved the workability characteristics.
- The concrete shows a densified microstructure with fewer pores and a better arrangement of particles in a mix. Besides, the silica contributes more on the hydration products especially the calcium silicate hydrate gel products directly influencing strength improvement.
- SCC mixes with 10% micro-silica and 2% nano-silica as a replacement of cement content to give higher values of concrete compressive strength. The combination of 10% micro silica and 2% nano silica showed better compressive strength at 28 days and 90 days.

REFERENCES

[1] EFNARC, Specification and guidelines for self-compacting concrete, European federation of specialist construction chemicals and concrete systems, Syderstone, Norfolk, UK (2002).

[2] EFNARC, The European guidelines for self-compacting concrete, (2005). http://www.efnarc.org/pdf/SCCGuidelinesMay2005.pdf

[3] Markets and Markets (2017) Self-compacting concrete market b type (powder, viscosity, combination), application (drilled shafts, columns, metal decking, concrete frames), end user (oil & gas construction, infrastructure, building & construction), region- global forecast to 2026, Mark. Res. Rep. https://www.marketsandmarkets.com/Market-Reports/self-compacting-concrete-market-226178048.html.

[4] Jeevetha, T. Krishnamoorthi, S., Rampradheep, G.S., 'Study on strength properties of self-compacting concrete with microsilica', *Int. J. Innov. Res. Sci. Eng. Tech.* **3** (2014) 11239-11244.

[5] Barluenga, G, Palomar, I, Puentes, J, 'Early age monitoring of Self Compacting Concrete with mineral additions', *Constr. Build. Mater.* **77** (2015)66–73.

[6] Gesoglu, M, Güneyisi, E, Asaad, D.S., Muhyaddin, G.F, 'Properties of low binder ultra-high performance cementitious composites: Comparison o nanosilica and microsilica', *Constr. Build. Mater.* **102** (2016) 706-713.

[7] Mohamed, HA 2011, 'Effect of fly ash and silica fume on compressive strength of self-compacting concrete under different curing conditions', *Ain. Sh. Eng. J.* **2**,79-86.

ELECTROCHEMICAL REACTIONS BETWEEN IRON SULFIDE MINERALS AND THEIR IMPLICATIONS FOR CONCRETE DURABILITY

Nafiseh Ebrahimi (1), Amin Ghaziaskar (1) and Jon M. Makar (1)

(1) Construction Research Centre, National Research Council Canada, Ottawa, ON Canada

Abstract

It is well known that iron sulphides such as pyrite (FeS2) and pyrrhotite ((Fe1-xS, 0<x<0.125) are unstable in presence of oxygen and moisture, oxidizing to produce sulfuric acid and iron sulphate. Further reactions in concrete cause the formation of expansive reaction products such as ettringite and thaumasite, potentially leading to structural failure. However, the possibility of accelerated oxidation when pyrite and pyrrhotite come to contact with each other or with a steel rebar has not yet been investigated.

This type of accelerated oxidation is more commonly known as corrosion when it happens in metals such as steel reinforcements. Since both pyrite and pyrrhotite are semiconductors and therefore sources of electrons, they can, however, promote this type of electrochemical reaction. Using electrochemical techniques, the electrochemical properties of pyrite, pyrrhotite, and steel and their open-circuit potentials were measured at different pH values. A zero resistance ammeter was also used to investigate the possibility of an accelerated oxidation reaction when any two of pyrite, pyrrhotite or steel are in electrical contact. The results show that pyrrhotite oxidation is accelerated in the presence of pyrite and both minerals could lead to an increased corrosion rate for steel rebar.

These results are particularly significant as the Maskimo aggregate that was responsible for over $400 million dollars in damage to concrete in the Trois Rivières region of Quebec, Canada contains significant quantities of both pyrite and pyrrhotite. While pyrrhotite alone will cause damage to concrete through expansive reaction products, the combination of the two minerals may have contributed to both the extent of the damage and the small amount of pyrrhotite that was necessary to cause the damage. In addition to the results of the electrochemical studies, on-going work to investigate the electrochemical behaviour of the two minerals in concrete will also be outlined.

Keywords: Iron sulphide, pyrrhotite, pyrite, electrochemical reaction, concrete

1. INTRODUCTION

Sulfide sulfur has been identified as a potential source of adverse chemical reactions in concrete that produce expansive reaction products since at least the 1970s [1]. Early work focused on the effects of pyrite (FeS_2), often in the bedrock below concrete foundations and basements. In the early 1990s, pyrrhotite ($Fe_{1-x}S$, $0<x<0.125$) was identified as the cause of

cracking in a dam in Spain [2-4]. While considerable research was done to investigate this incident, analysis of the unaltered concrete showed high levels of calcium aluminate hydrate [2], suggesting that the cement used in the dam may not have had a standard composition.

More recently, significant problems related to pyrrhotite in concrete have developed in the Trois Rivières region of Quebec, Canada and in northern Connecticut and southern Massachusetts in the U.S.A. These problems have resulted in an estimated $400 million worth of damage to date in Canada and have affected more than 1000 home owners. Some estimates from the victim's association in Connecticut suggest 10x the number of households will eventually be affected in the United States. Further details of the damage are given elsewhere [5]. The incident in Trois Rivières resulted in considerable research in terms of understanding pyrrhotite induced failure mechanisms [5] and developing new test methods [6-8].

The adverse reactions that cause pyrrhotite induced cracking in concrete are complex and multi-stage. While the final reaction products associated with pyrrhotite damage in concrete are ettringite [3,4] and thaumasite [4,5], the first reaction is the oxidation of the pyrrhotite in the presence of water, which forms iron hydroxide (goethite, FeOOH) and sulfuric acid. The iron hydroxide is itself expansive and may itself contribute to the cracking. Damage to basements and foundations typically starts with cracking at corners, possibly due to oxygen and water vapour entering the concrete in two directions, rather than one.

While there has been considerable work on the underlying behavior that produces pyrrhotite damage, it has been assumed that the damage to the concrete is solely driven by the presence of the pyrrhotite. The aggregate in Trois Rivières contains, however, both pyrrhotite and pyrite. The two minerals are both semi-metallic and can have very low resistivities, raising the possibility that one mineral might accelerate the oxidation of the other or of steel rebar. The initial results from an on-going investigation of this study are presented here, along with a brief summary of the next steps in the research.

2. MATERIALS AND METHODOLOGY

Pyrite and pyrrhotite cores were taken out of mineralogical samples purchased from Ward's Science (NY, USA). Synchrotron XRD measurements were taken of material from the same samples at the Canadian Light Source in Saskatoon, Saskatchewan, Canada (Table 1), with results quantified by Rietveld analysis. These measurements showed that samples were approximately 70-80% composed of the mineral of interest, but that no pyrite was present in the pyrrhotite sample or vice-versa.

Table 1: Mineralogical composition of pyrite and pyrrhotite samples

Mineral	Pyrite Sample (wt.%)	Pyrrhotite sample (wt.%)
Pyrite	81.4	0.0
Quartz	17.1	0.0
Muscovite-2M1	1.4	0.0
Galena	0.1	0.0
Pyrrhotite-6C	0.0	74.3

Dolomite	0.0	20.2
Sphalerite	0.0	2.2
Chalcopyrite	0.0	1.9
Clinochlore	0.0	1.4

The extracted cylindrical samples were 1.176 cm in diameter with length varying from 1 to 3 cm. The end of the cylindrical samples was attached to 30 cm long conductive copper wires using a conductive carbon adhesive paste. The sample wire assembly was then coated with 3MTM Scotchkote^{TM} liquid epoxy coating 323 in order to limit the electrolyte contact with an area of 1.086 cm^2.

Prior to each experiment, the exposed surfaces of the electrodes were ground and polished with wet SiC papers (BUEHLER, IL, USA) from 120 to 600 and 1200 grit finish, washed by de-ionized water and degreased by acetone and dried at room temperature.

The carbon steel rebar sample was passivated by keeping in saturated calcium hydroxide ($Ca(OH)_2$) solution (pH= 12-13), for at least 48 hours, prior to testing. The passivation process simulates the effect of the concrete pore solution on rebar before exposure to experimental conditions. The elemental composition of carbon steel rebar is presented in Table 1.

Table 2: Chemical composition of the carbon steel provided by the manufacturer (wt%)

C	Si	S	P	Mn	Cr	Mo	Ni	Fe
0.26	0.27	0.03	0.01	1.1	0.05	<0.01	0.07	Balance

Three different solutions with acidic, neutral and basic pH were selected in this experiment. The solutions were 0.1 wt. % NaCl in distilled water (pH 6), saturated $Ca(OH)_2$ with addition of 0.1 wt.% NaCl (pH 12) and distilled water solution with added H_2SO_4 (pH 4). While the saturated calcium hydroxide solution approximates the pH conditions typically associated with concrete pore water, the other two solutions were included as H2SO4 is expected to be produced during oxidation of pyrrhotite, raising the possibility that local conditions in the concrete have a lower than expected pH.

A straightforward and easily measurable electrochemical parameter is the free corrosion potential (E_{CORR}). E_{CORR} was obtained by measuring the potential of a freely corroding specimen with respect to the reference electrode. The potential of specimens in the selected solution was measured against a Fisher brand^{TM} accumet^{TM} epoxy body mercury-free reference electrode (-45 mV vs. Saturated Calomel Electrode). Corrware software (Scribner Associates Inc, NC, USA) was used to set up the electrochemical experiments.

The galvanic corrosion experiments were carried following the basic principles of ASTM G71 (G71 2009) [9]. Galvanic corrosion of two dissimilar specimens can occur if their E_{Corr} values are more than 100 mV apart [10]. This may lead to the accelerated electrochemical reaction between the two specimens. The pyrite and pyrrhotite, pyrite and carbon steel, and pyrrhotite and carbon steel were coupled to investigate their possibility of galvanic corrosion among them. The two selected specimens were connected through a zero-resistance ammeter, and their galvanic corrosion current (I_{Couple}) and galvanic corrosion potential (E_{Couple}) against standard reference electrode were monitored once the two samples were electrically connected.

3. RESULTS AND DISCUSSION

E_{Corr} values are indicative of the level of activity of samples, a more positive E_{Corr} value, indicates a more "noble" material that is less likely to oxidize while a more negative value indicates a more active specimen that will oxidize preferentially when connected with a specimen with a more positive potential [10]. As can be seen in figure 1, pyrite shows the most positive E_{Corr} value of 0.25 V while pyrrhotite has a value of -0.14 V and carbon steel shows the most negative value of -0.20 V. Based on E_{Corr} measurements alone the activity of the measured specimens rank as follows pyrite < pyrrhotite< carbon steel.

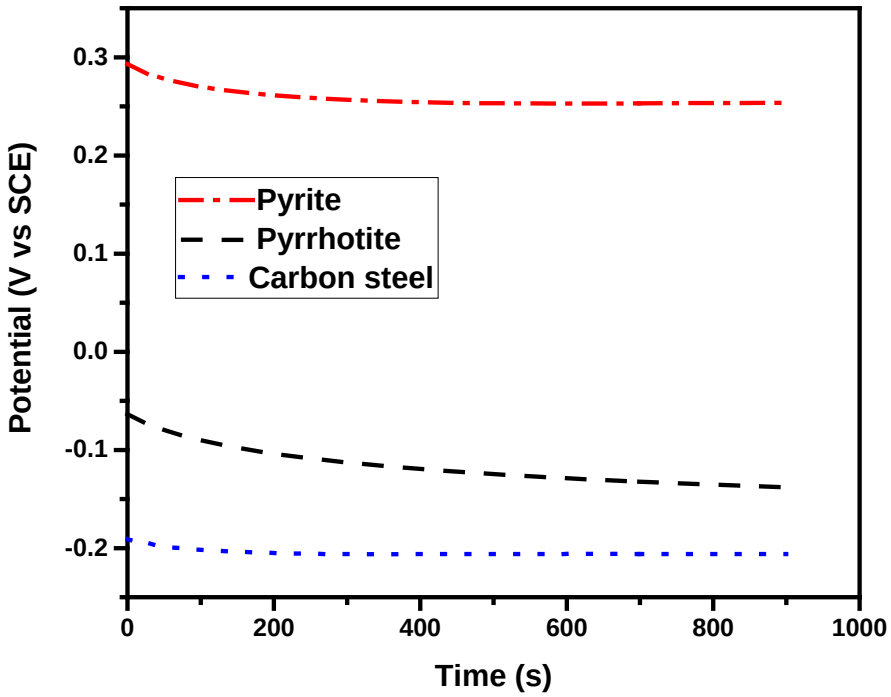

Figure 1: The corrosion potential of alloys measured in saturated $Ca(OH)_2$ solution containing 0.1 wt.% NaCl for 30 minutes.

The other important information obtained from Figure 1 is the possibility of galvanic corrosion between the specimens. The E_{CORR} difference between pyrite and pyrrhotite is as much as 0.39 V, and the difference between pyrite and carbon steel is about 0.45 V. Both differences would produce a significant driving force for galvanic corrosion to occur, as the pyrite would accelerate the oxidation of both carbon steel and pyrrhotite [11,12]. The E_{CORR} difference between pyrrhotite and carbon steel is, however, only 0.06 V, a potential difference that is often too low to accelerate the corrosion of carbon steel in connection.

The E_{Couple} and I_{Couple} measured while coupling pyrite and pyrrhotite in the pH 12 solution are shown in Figure 2. It is clearly seen that two regions of change are observed. The first phase lasts for about 75-80 hrs, where the E_{Couple} starts at a negative value of -0.1 V, close to the E_{CORR} of pyrrhotite, and gradually increases and reaches 0.056 V, a value between E_{CORR} of pyrite and pyrrhotite. In this phase, initially the I_{Couple} starts at 0.03 mA and over time drop to 0.0.002 mA in 80 hrs. In the second phase from 80 h to 150 h, both E_{Couple} and I_{Couple} reach a stable value of 0.056 V and 0.0015 mA respectively.

The coupling measurement shown in figure 2 indicates that when pyrite and pyrrhotite are in contact with each other in a conductive environment, an electrochemical reaction can occur between them, the rate of this reaction is high at the beginning as measured by a current of 0.03 mA and it will slow down about 20 times to the negligible rate of 0.0015 mA. The final current indicates almost no ongoing reaction between the coupled specimens.

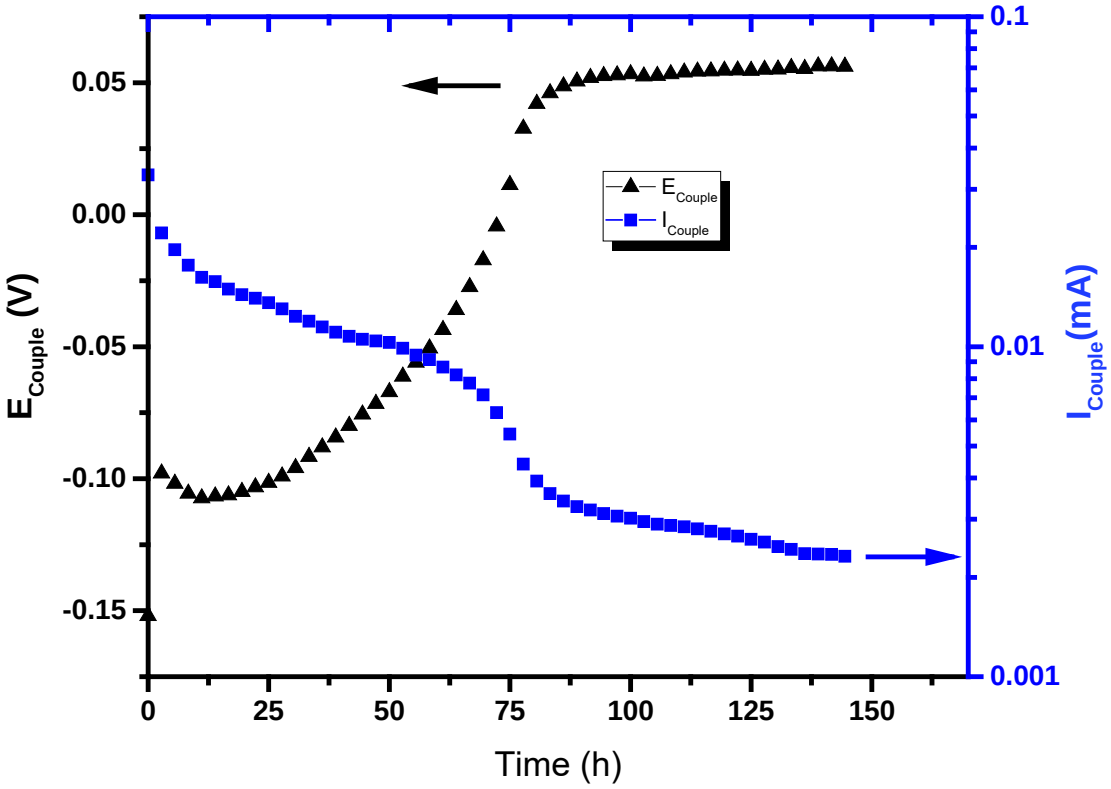

Figure 2: E_{Couple} and I_{Couple} from coupling of pyrite and pyrrhotite in saturated $Ca(OH)_2$ solution containing 0.1 wt.% NaCl (pH12).

The same coupling measurements were performed for other couples of pyrite/carbon steel and pyrrhotite/carbon steel at pH 12, and for the pyrite/pyrrhotite couple at different pH values. The results are summarized in Table 3.

Table 3: Activity of coupled specimens in varying pH values.

pH	Coupled specimens	Initial I_{couple} (mA)	Final I_{couple} (mA)
4	Pyrite/ Pyrrhotite	2.2E-3	1.2E-3
6	Pyrite/ Pyrrhotite	6.4E-3	1.8E-3
12	Pyrite/ Pyrrhotite	3.3E-2	1.5E-3
12	Pyrite/carbon steel	4.5E-4	5.7E-6
12	Pyrrhotite/carbon steel	1.7E-5	2.4E-6

As seen in Table 3, the magnitude of current measured between pyrite and pyrrhotite depends on the pH, the basic pH of 12 shows the highest initial coupling current of 3.3 E-2 mA. By decreasing the pH to 6, the current drops 5 times to 6.4 E-3 and at pH 4 it reaches 2.2 E-3. The final current however is independent of pH and is close to 1.5 E-3 in all different pH values confirming close to no activity between the couples.

The coupling of carbon steel rebar with pyrite also increases the oxidation of carbon steel with an increased rate of 4.5E-4 mA. The optical examination of carbon steel samples after coupling with pyrite shows signs of corrosion. However, the connection of pyrrhotite and carbon steel did not increase the activity of carbon steel to a level that corrosion be detected. This is in agreement with the E_{corr} measurements shown in Figure 1, where the free corrosion potential difference between pyrrhotite and carbon steel was only 0.06 V.

The pyrite and pyrrhotite specimens prior and post coupling at pH 12 solution are shown in Figures 3 (a) and 3 (b) respectively. The color change on both minerals is clear in the images.

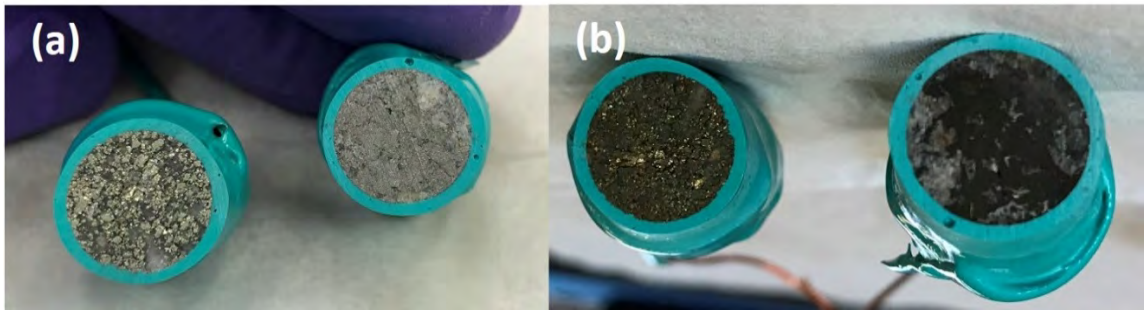

Figure 3: Pyrite (on the left) and pyrrhotite (on the right) electrodes before (a) and after (b) coupling experiment at pH 12.

After coupling, the pyrite and pyrrhotite electrodes were analyzed using Secondary Electron Microscopy (SEM) as shown in Figures 4 (a) and (b) respectively. The pyrrhotite shows an inhomogeneous structure after coupling that is indicative of preferential dissolution of species on the surface, consistent with the results of Figures 2 and 3. Energy Dispersive X-Ray Spectroscopy (EDS) (not shown) were also performed on both electrodes after coupling, with the analysis primarily showing iron, oxygen and sulfur, along with trace elements as seen in Table 1. These results were also consistent with the oxidization seen in Figure 3. Further surface analysis is required to confirm the nature of structure formed on the two electrodes after coupling and exposure to electrolyte.

4. CONCLUSIONS

The results presented here show that the presence of pyrite in concrete aggregate may accelerate the oxidation of both pyrrhotite and reinforcing steel. While the observed effects between pyrrhotite and pyrite are most prominent in the samples measured at a pH of 12, tests at lower pH show the same behaviour. The possibility of acceleration is therefore likely independent of the local pH in concrete samples. It should be noted, however, that the work here was done using standard electrochemical research methods and may not represent the behaviour that actually occurs in concrete in the field.

If the same behaviour does in concrete, then the rate of oxidation of pyrrhotite in concrete aggregate would depend on whether pyrite is present in the same aggregate. It is also possible that other semi-metallic minerals would have the same effect. In this case the production of expansive reaction products would be expected to accelerate as well, causing more rapid deterioration of the concrete. It is also possible that the presence of pyrite would mean that deterioration would occur at lower levels of pyrrhotite content then would otherwise be the case.

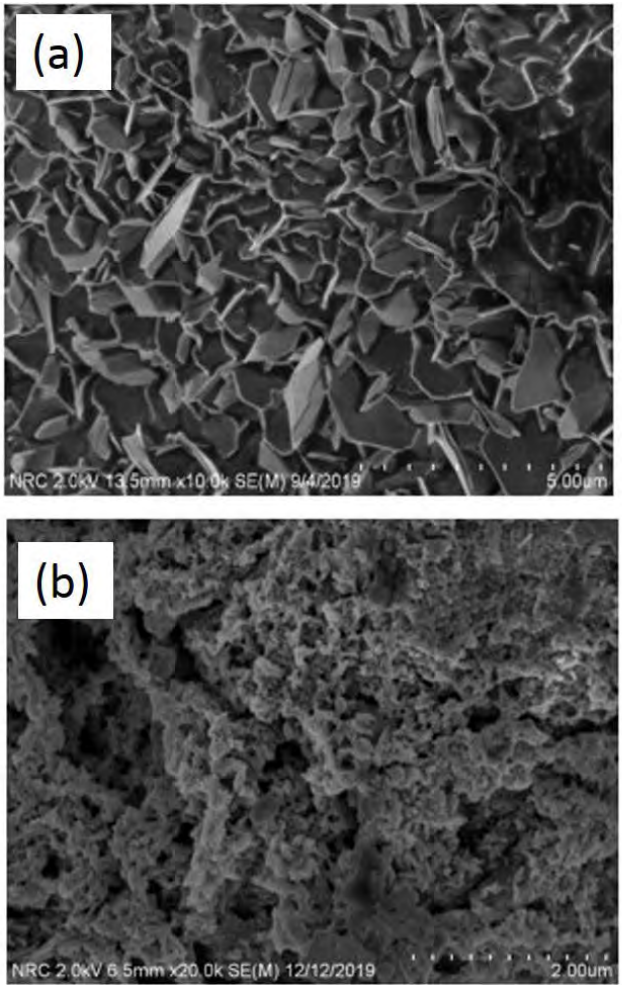

Figure 4 SEM imaging of (a) Pyrite and (b) Pyrrhotite electrodes after coupling at pH 12 electrolyte.

Considerable additional work is underway to explore whether the observed behaviour does occur in the field. Instrumented samples of pyrite and pyrrhotite connected with carbon paste have been placed in concrete and are currently being monitored to see how their potential changes over time. Additional work looking at the coupling of pyrrhotite and other minerals such as chalcopyrite and magnetite are planned. A number of other experiments are also under consideration, including further investigations of the impact of the presence of pyrite on the corrosion of rebar. Once this work is completed the role of mineral-mineral coupling in concrete deterioration will be clarified, potentially supporting changes in North American concrete standards.

ACKNOWLEDGEMENTS

This research was funded by the National Research Council Canada (NRC) and the Regie du Batiment du Quebec as part of the project "Impact of Aggregates Containing Pyrrhotite and Other Sulfides on Canadian Concrete Structures". The authors would also like to thank Mr. Bruce Baldock and Ms. Olga Naboka for their help with the experiments carried out at NRC. The XRD data was produced and analysed at the Canadian Light Source by Joel Reid. The authors gratefully acknowledge discussions with Prof. Benoit Fournier of the Université Laval, who originally posed the question about whether the presence of pyrite would affect the pyrrhotite deterioration mechanisms in concrete.

REFERENCES

[1] Grattan-Bellew, P.E. and Eden, W.J., 'Concrete Deterioration and Floor Heave Due to Biogeochemical Weathering of Underlying Shale', *Can. Geotech. J.,* **12**, (1975) 372-378.

[2] Ayora, C., Chinchon, S., Aguado, A., Guirado, F., 'Weathering of iron sulfides and concrete alteration: Thermodynamic model and observation in dams from central Pyrenees, Spain', *Cem. Conc. Res.***28** (9) (1998) 1223-1235.

[3] Casanova, I., Aguado, A., Agullo, L., 'Aggregate Expansivity due to Sulfide Oxidation – II. Physico-chemical modelling of sulfate attack', *Cem. Conc. Res.* **27** (11)(1997)1627-1632.

[4] Chinon-Paya, S., Agaudo, A., Chinon, S., 'A comparative investigation of the degradation of pyrite and pyrrhotite under simulated laboratory conditions', *Eng. Geo.* **127** (2012) 75-80.

[5] Rodrigues, A., Duchesne, J., Fournier, B. Durand, B., Rivard, P., Shehata, M., 'Mineralogical and chemical assessment of concrete damaged by the oxidation of sulfide-bearing aggregates: Importance of thaumasite formation on reaction mechanisms', *Cem. Conc. Res.* **42** (2012) 1336-1347.

[6] Rodrigues, A., Duchesne, J., Fournier, B., 'A new accelerated mortar bar test to assess the potential deleterious effect of sulfide-bearing aggregate in concrete', *Cem. Conc.Res.* **73** (2015) 96-110.

[7] Ramos, V., Rodrigues, A., Fournier, B. Duchesne, J., 'Development of a quick screening staining test for detecting theoxidation potential of iron sulfide-bearing aggregates for use in concrete', *Cem. Conc. Res*. **81** (2016) 49-58.

[8] Rodrigues, A., Duchesne, J., Fournier, B., 'Quantitative assessment of the oxidation potential of sulfide-bearing aggregates in concrete using an oxygen consumption test, *Cem. Conc. Comp.* **67** (2016) 93-100.

[9] ASTM G71-81, Standard Guide for Conducting and Evaluating Galvanic Corrosion Tests in Electrolytes. West Conshokocken: American Society for Testing and Materials, 2019**,** 5pages.

[10] Soltis.J, Lichti. K.A, “Galvanic corrosion of carbon steel coupled to antimony”. *Corrosion science*, 68(2013)162-167.
[11] Jones, D. A. Principles and Prevention of Corrosion. Prentice Hall, Upper Saddle River, NJ. 1992
[12] Cecı´lia M.V.B., Almeida, B., Giannetti, F., “The electrochemical behavior of pyrite/pyrrhotite mixtures” *Journal of Electroanalytical Chemistry,* 553 (2003) 27-34

QUANTITATIVE ANALYSES OF AGING STATUS OF DAM CONCRETE FOR A 25-YEAR-OLD DAM

Shuguang Li (1), Jinsheng Jia (1), Yaoqun Xu (1), Xiangjun Zhai (2), Xiulin Li (1), Gaixin Chen (2)

(1) State Key Laboratory of Simulation and Regulation of Water Cycle in River Basin, China Institute of Water Resources and Hydropower Research, Beijing, China

(2) PowerChina Kunming Engineering Corporation Limtied, Kunming, China

Abstract

In order to evaluate the aging status of the dam concrete for a 25-years-old concrete dam, the internal concrete and surface layer of the dam were tested by elastic wave computerized tomography (CT) and spectral analysis of surface wave (SASW). Also mechanical strength and elastic wave velocity were tested for the concrete cores from the dam. The CT results show that the elastic wave velocities of the three dam sections are basically around 4400~4500m/s and no obvious low-speed zone could be detected, indicating the quality of the internal concrete is good without aging signs. The SASW results show that the Rayleigh wave velocity of the surface layer (deeper than 25cm) is about 2500 m/s (the corresponding P wave velocity is 4500 m/s) which is basically consistent with the CT results. The average compressive strength of the concrete cores is over 40 MPa (higher than the design values) while the elastic wave velocities are between 3600 and 4400 m/s. Microstructural analysis results show that the a few microcracks could be observed in all the 16 cores from the upstream, the downstream, the gallery and the spillway. The overall results indicate that the dam concrete is of good quality and no obvious aging signs could be found.

Keywords: Dam concrete; Aging status; CT test; SASW; Microcrack analysis

1. INTRODUCTION

Most of the concrete dams built between over a decade ago in China are inevitably aging and the ageing status of these old dams is becoming the focus of the society. The first step to evaluate the aging status of old dams is to quantitatively evaluate the aging status of the dam concrete.

To evaluate the quality and aging status of a concrete dam in south China which was built 25 years ago, elastic wave CT test, spectral analysis of surface wave (SASW) test were performed on selected dam blocks as well as the dam outer layer. Mechanical tests, elastic wave tests and quantitative microcrack analysis were also performed on typical concrete cores to get a comprehensive evaluation of the dam quality.

2. COMPUTERIZED TOMOGRAPHY (CT) TEST AND SPECTRAL ANALYSIS OF SURFACE WAVE (SASW) TEST

2.1 CT test by elastic wave

Seismic Tomography (CT) test by elastic wave is conducted between the upstream and downstream faces of selected dam blocks (#3 and #16), to show the distribution of elastic wave (P-wave) velocities inside the dam block, and then to reflect the physical property (such as the modulus of elasticity) of each unit cell of the dam body [1]. Details of the CT test could be found on Ref. [1].

2.2 SASW test

SASW is a powerful method when only a single side access is available. Unlike CT test which employs P-wave velocity, Rayleigh wave (surface wave, or shear wave) is employed to reflect the physical property such as modulus of elasticity of concrete [1].

SASW test was performed on the upstream outer layer of the dam. The schematic of the test and the location of the sensors on the dam surface are shown in Figure 1 and Figure 2.

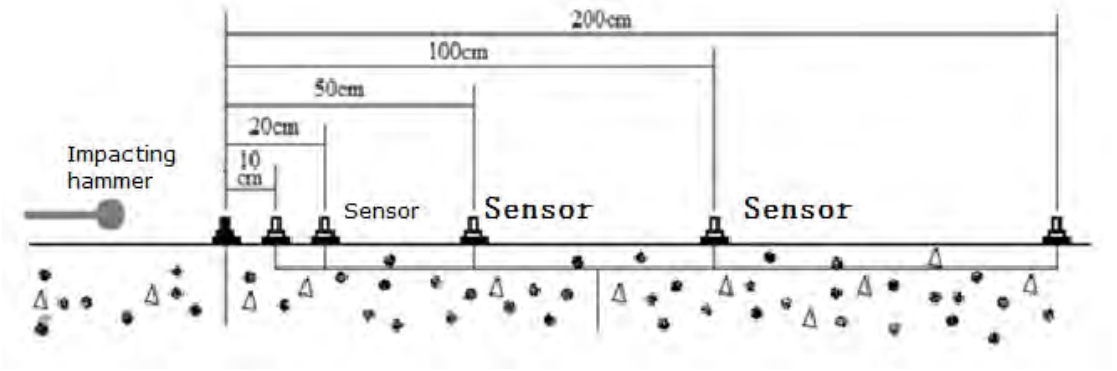

Figure 1: Schematic of SASW test

Figure 2: Sensor location on the dam surface (pointed by red arrow)

2.3 Tests on concrete cores

(1) Coring location

Cores were extracted from the upstream, the downstream, the gallery and the spillway, respectively. The depths of the cores drilled from the upstream and downstream are both 24 m, while the depths of the cores from the spillway and gallery are both 2m. Diameters of the cores are 219mm.

(2) Mechanical tests

The cores were cut and grounded according to test codes for hydraulic concrete in China (SL352-2006) [2] and mechanical tests were performed on the cylindrical cores whose height was the same with diameter.

(3) Elastic wave velocity tests

Previous studies have revealed that quadratic correlation could be established between the dynamic modulus of elasticity of concrete and the P-wave velocity [3]. It suggests that P-wave velocity can be used to quantify damage extent in concrete like the resonant frequency method.

The elastic wave velocity testing system is composed of five components, the sensor, the hammer, the data collecting device and the controlling computer, as shown in Figure 3.

Figure 3: Elastic wave velocity testing device

(4) Microcrack analysis

An automated panoramic fluorescent microscope was designed and developed to get a panoramic image of the microcrack pattern in the concrete automatically.

The cores are sliced into 2cm thick disks and cut into square slices 10cm*10cm in dimension as microscopic specimens. Once the impregnated microscopic specimen (by fluorescent epoxy resin) is put on the stage, the stage will automatically move in two directions in the range of 10cm x 10cm. All the clear microscopic image will be captured and stored in the computer. More than 4000 images will be obtained for a slice 10cm*10cm in dimension and the images can be stitched into one panoramic mega-image automatically by DIP technique. The specimens are scanned automatically on the stage at a magnification of 40x which was sufficient to detect microcracks as thin as 2 μm in width. Typical microscopic image of the concrete slice can be seen in Figure 4.

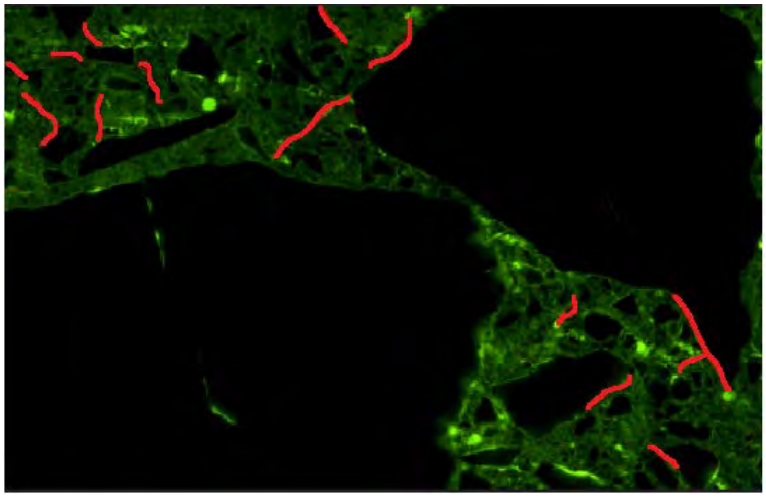

Figure 4: Microscopic image of core from the gallery (2cm*2cm in dimension, microcracks are highlighted by red lines)

A program called QUANSMIC is developed to extract microcracks on the panoramic mega-image and quantify microcrack patterns. Microcrack length density is used to quantify the microcrack structure and it is calculated by the following equation,

$$D=L/A \quad (1)$$

Where, D is the microcrack length density, L is the total length of the extracted microcracks in the slice image, and A is the total area of the slice. Details of the processing chart and the program could be found in Ref [4] and [5].

3. RESULTS AND DISCUSSION

3.1 CT test results

After reconstruction, the velocity distributions in each dam block section is shown in Figure 5.

For concrete with good quality, the P-wave velocity is between 3600 m/s and 4500 m/s [1]. As seen from Figure 5, the velocity in each dam section is around 4400~4500m/s and the minimum value is greater than 4023 m/s. It indicated that the dam concrete in these two blocks are in good quality and no defects could be found.

3.2 SASW results

Eight locations were tested by SASW in the upstream of the dam. The frequency dispersion curve of the Rayleigh-wave for the eight locations were shown in Figure 6 (only two were shown because of the page limit).

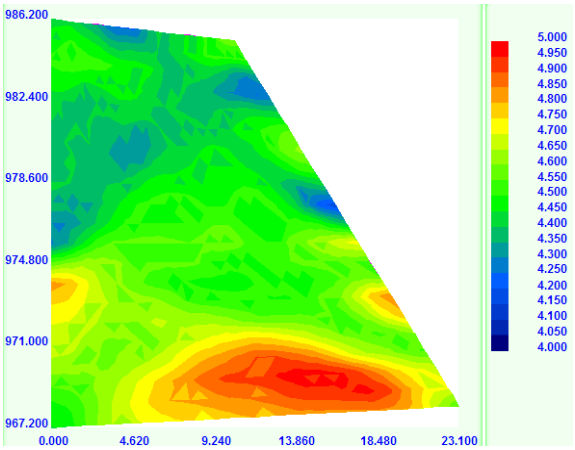

(a) #3 dam block, P-wave velocity: average value 4541 m/s, maximum value 4983 m/s, minimum value 4172 m/s

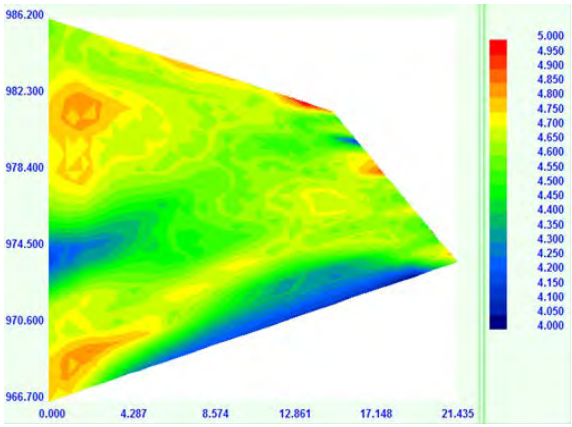

(b) #16 dam block, P-wave velocity: average value 4596 m/s, maximum value 4974 m/s, minimum value 4023 m/s

Figure 5: Elastic wave velocity distribution in dam blocks

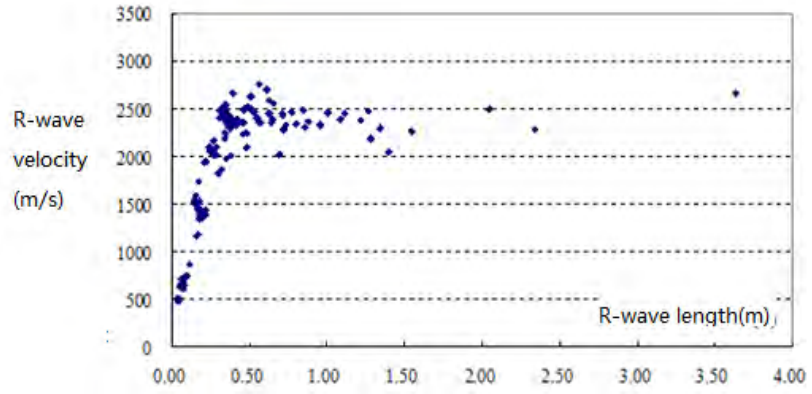

(a) Location 1 (#18 dam block)

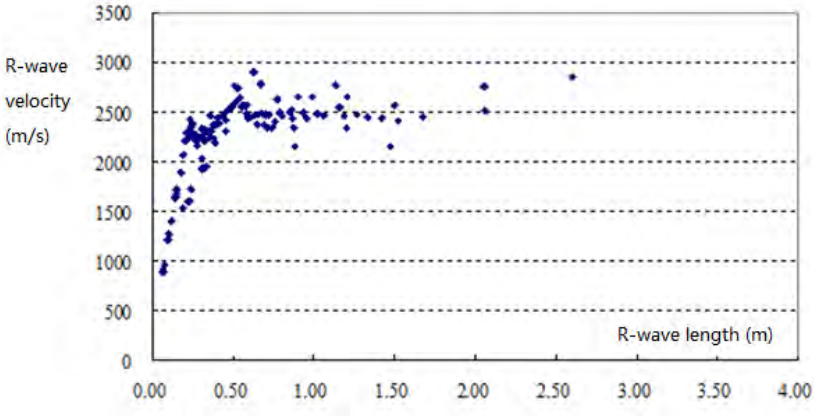

(b) Location 2 (#17 dam block)

Figure 6: R-wave frequency dispersion curve

As seen from Figure 6, the variation of the R-wave frequency dispersion curve is similar. When the wave length is greater than 50cm, the velocity is fluctuating around 2500m/s. The velocity decreases as the wave length decreases when the wave length is smaller than 50cm. It indicated that the superficial layer (about 25cm thick) of the concrete in the upstream is weathered and aging, so it's not as dense as the concrete inside. According to the relationship between the P-wave velocity and the R-wave velocity[1], the corresponding P-wave velocity is around 4500m/s and it is consistent with the testing results obtained by elastic wave CT. Also we can see from Figure 6 that the internal concrete whose depth is bigger than 2.0m is of good quality and no aging sign could be found.

3.3 Analysis for the cores

(1) Mechanical tests

The compressive strength of the cores are obtained and compared with the design value as well as the testing values right after the completion, as shown in Figure 7.

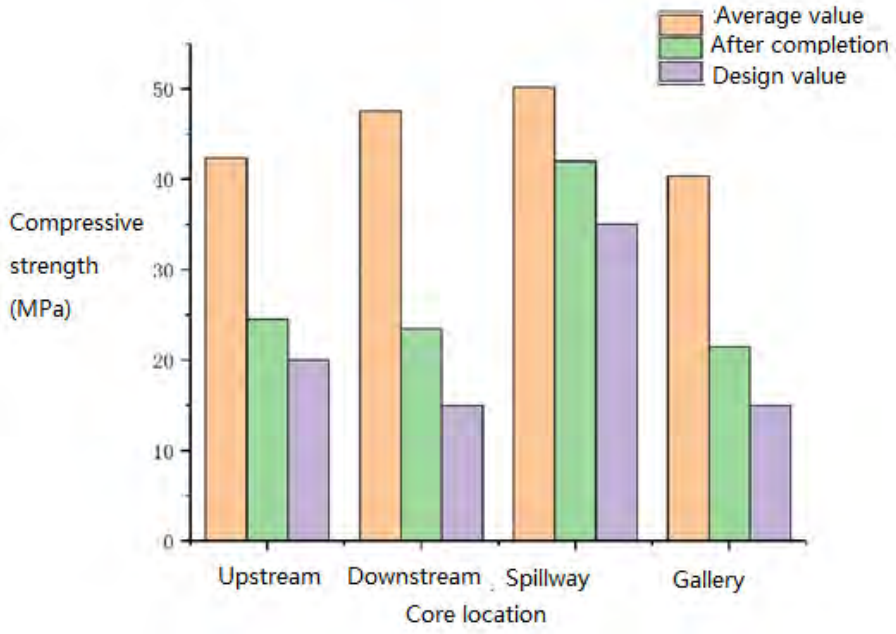

Figure 7: Comparison of the compressive strength of the dam concrete cores

As seen from Figure 7, the average compressive strength of the concrete cores from the upstream, the downstream, the spillway and the gallery is 42.3MPa, 47.5MPa, 50.2MPa and 40.4MPa, respectively. And the compressive strength values are all much higher than the design values as well as the values obtained right after the completion of the dam 25 years ago.

(2) Elastic wave velocity

The elastic wave velocities of the cores are shown in Table 1.

Table 1 Elastic wave velocities of the concrete cores

Upstream		Downstream		Gallery		Spillway	
NO.	Velocity (m/s)	NO.	Velocity (m/s)	NO.	Velocity (m/s)	NO.	Velocity (m/s)
S1	4133	X1	4408	L1	3952	Y1	4301
S2	3629	X1	4580	L2	4222	Y2	4164
S3	3735	X3	3890	L3	3349		
S4	3894	X4	4376	L4	3762		
S5	4198	X5	3337				

As seen from Table 1, the P-wave velocity values of the cores are mostly between 3600 m/s and 4400 m/s, indicating most of them are of good quality (only two values are lower than 3600). It is also in good agreement with the CT results shown in Section 3.1.

(3) Microcrack analysis

The microcrack density of the concrete cores from different locations are shown in Table 2.

Table 2 Microcrack density for different specimens

Upstream		Downstream		Gallery		Spillway	
NO.	Density/ mm/mm^2	NO.	Density/ mm/mm^2	NO.	Density/ mm/mm^2	NO.	Density/ mm/mm^2
S1	0.0124	X1	0.0740	L1	0.0916	Y1	0.1029
S2	0.0558	X1	0.0875	L2	0.0665	Y2	0.0620
S3	0.0615	X3	0.0353	L3	0.0303		
S4	0.0101	X4	0.0282	L4	0.0388		
S5	0.0188	X5	0.0335				
Average	0.0317	Average	0.0517	Average	0.0568	Average	0.0824

As seen from Table 2, microcracks could be observed on all the 16 concrete core slicess and the microcrack density varies from 0.0101 mm/mm^2 to 0.1029 mm/mm^2. The average density value for the concrete cores from the spillway is the highest, 0.0824mm/mm^2 , while the average density for the upstream is the smallest, 0.0317 mm/mm^2. The reason is perhaps that concrete from the spillway has low water/cement ratio, high compressive strength and complicated loading conditions resulted from discharging.

4. CONCLUSIONS

Comprehensive inspecting tests were performed on a 25-years-old concrete dam. The CT results as well as the SASW results show that the superficial layer of the upstream (25cm thick) is weathered and degraded. For the internal concrete (whose depth is greater than 2.0m) the elastic wave is around 4400~4500m/s and no low-speed zone could be detected. The average compressive strengths of the 16 concrete cores from the upstream, the downstream, the gallery and the spillway are over 40 MPa (all are higher than the design values) while the

elastic wave velocities are between 3600 and 4400 m/s. Microstructural analysis results show that the a few microcracks could be observed in all the cores. The overall results indicate that the dam concrete is of good quality and no obvious aging signs could be found.

ACKNOWLEDGEMENTS

Financial support from the National R&D Program of China (Grant No. 2018YFC0406700), the National Natural Science Foundation of China (Grant No. 51879286), State Key Laboratory of Simulation and Regulation of Water Cycle in River Basin (SKL2018TS09) and IWHR are gratefully acknowledged.

REFERENCES

[1] Olson, L.D. and Sack, D. A.. 'Nondestructive Evaluation of Concrete Dams and Other Structures'. In: Nondestructive Evaluation of Aging Infrastructure, sponsored by SPIE, The International Society for Optical Engineering, Oakland, CA, June 6-8 1995.

[2] SL352-2006, Test code for hydraulic concrete. China Institute of Water Resources and Hydropower Research, 2006,380pages [in Chinese].

[3] Lv, X. and Wu, J. 2016, 'Impact elastic wave theory and application'. China Water & Power Press, 2016. (in Chinese)

[4] Li, S., Chen, G., Ji, G., et al. 'Quantitative damage evaluation of concrete suffered freezing–thawing by DIP technique'. *Constr. Build. Mat.*, **69**(11) (2014) 177-185.

[5] Li, S., Chen, G., Lu, Y.. 'Quantitative damage evaluation of AAR-affected concrete by DIP technique'. *Mag. Conc. Res.*, **65**(5)(2013) 332-342.

Theme 6

New techniques for evaluation of hydration, microstructure, and service life

USING MACHINE LEARNING TO PREDICT CONCRETE'S STRENGTH: LEARNING FROM SMALL DATASETS

Boya OUYANG (1, 2), Yuhai LI (1), Yu SONG (1), Feishu WU (1), Huizi YU (1), Yongzhe WANG (1), Mathieu BAUCHY (1, 4) and Gaurav SANT (2, 3, 4)

(1) Physics of AmoRphous and Inorganic Solids Laboratory (PARISlab), Department of Civil and Environmental Engineering, University of California, Los Angeles, CA 90095, USA

(2) Department of Materials Science and Engineering, University of California, Los Angeles, CA, USA

(3) Laboratory for the Chemistry of Construction Materials (LC^2), Department of Civil and Environmental Engineering, University of California, Los Angeles, CA, USA

(4) Institute for Carbon Management, University of California, Los Angeles, CA, USA

Abstract

Despite previous efforts to relate concrete proportioning and strength, a robust knowledge-based model for accurate concrete strength predictions is still lacking. As an alternative to physical or chemical-based models, machine learning (ML) methods offer a new solution to this problem. Although ML can handle the complex, non-linear, non-additive relationship between concrete mixture proportions and strength, it requires large datasets. This is a concern as reliable strength data is rather limited, especially for industrial concretes. Here, based on a large dataset (>10,000 observations) of measured compressive strengths from industrially-produced concretes, we compare the ability of select ML algorithms to "learn" how to reliably predict concrete strength as a function of the size of the dataset. Based on these results, we discuss the competition between how accurate a given model can eventually be (when trained on a large dataset) and how much data is actually required to train this model.

Keywords: concrete, strength prediction, machine learning, modeling

1. INTRODUCTION

The 28-day compressive strength is one of the most widely used metrics to characterize concrete's performance. Indeed, although this standardized index is primarily used to evaluate the ultimate strength of concretes [1], it can also be used to infer other critical mechanical properties, e.g., stiffness or tensile strength [2]. Accurate concrete strength predictions have a profound impact on construction projects since an insufficient concrete strength can be the culprit of a catastrophic failure of civil infrastructures. Conversely, concretes exhibiting an

overdesigned strength leads not only to higher material expenses [3], but also to additional environmental burdens (e.g., CO_2 emissions) [4].

Over the past decades, substantial efforts have been devoted to developing predictive models for correlating a given concrete mixture proportion to its associated strength [5]. Beyond this, an ideal predictive model would also provide important insights for designing new concrete with better constructability and durability, and/or at a lower cost [6,7]. Conventional approaches often seek to achieve these goals using physics or chemistry-based relationships [8–10]. Although the role played by major proportioning parameters (e.g., water-to-cementitious ratio, w/cm, aggregate fraction, and air void content) has been extensively investigated, the influence of many other factors is not always negligible, e.g., chemical and mineral admixtures or aggregates gradation [11]. Due to the limited understanding of these complex property-strength correlations, it is still extremely challenging to get a robust and universal concrete strength model using conventional approaches [12].

As an alternative pathway, the recent development of machine learning (ML) techniques provides a novel data-driven approach to revisit the strength prediction problem. Importantly, ML-based predictions have been shown to significantly outperform those of conventional approaches, especially for non-linear problems [13]. As such, recent studies have established ML as a promising approach to predict concrete strength [14–17]. However, ML approaches often require a large dataset to "learn" the relationship between inputs and outputs [18,19]. This is a major concern for concrete strength applications, as strength data for industrial concretes are often difficult to access (i.e., data is not publicly available). In addition, reported concrete strength data are often incomplete (some important features are often missing, e.g., curing temperature, additives, types of aggregates, etc.). More generally, ML approaches require accurate and self-consistent data—which is often questionable for concrete strength data due to non-standardized measurements or inconsistencies in data recording [20]. For example, the strength of a given concrete can significantly vary when the testing protocol or specimen size is changed [21–23]. Although such difficulties can be filtered out with sufficiently large datasets, their significance tends to be exacerbated in the case of small datasets. For all these reasons, it is critical to assess how the reliability of ML approaches for concrete strength prediction applications depends on the number of training data points.

This study revolves around two core questions: (i) how much data is sufficient for training a ML model and (ii) which ML algorithms are better suited to deal with small datasets. By building on our previous studies [17,24], we explore these questions by taking the example of three archetypal ML algorithms, i.e., polynomial regression (PR), artificial neural network (ANN), and random forest (RF). We compare the ultimate accuracy of these algorithms and their learning efficiency as a function of data volume. These results are insightful for facilitating the adoption of ML for small datasets—as relevant to concrete engineering.

2. BACKGROUND AND METHODS

2.1 Machine learning algorithms

We assess the performance of three archetypical ML algorithms (PR, ANN, and RF) as a function of the number of training data points. These methods are chosen as they belong to three distinct families of ML models, i.e., polynomial, network-based, and tree-based [25,26]. All the hyperparameters of the ML models considered herein were optimized in a previous

study so as to achieve an optimal balance between under- and overfitting [16]. First, we consider PR, which is essentially based on linear regression, wherein the model parameters designate an *n*-degree polynomial function [27]. Based on our previous work [16], the PR model adopted herein features a maximum polynomial degree of 3. Second, we explore the potential ANN, which is a computational structure consisting of an input layer, an output layer, and one or several hidden layers bridging the two formers—wherein each layer comprises a collection of artificial neurons (i.e., computational units) [28]4/18/2021 4:16:00 PM. Based on our previous work [16], the present ANN model exhibits 7 neurons in a single hidden layer. We adopt the sigmoid function as activation function to prioritize the importance of the input data and we use the backpropagation algorithm to optimize the model parameters [29]. Third, we consider RF, which is an enhanced bagging method since, by using the majority-voting concept, this approach is typically more predictive than conventional decision trees [30]. Here, based on our previous work [16], our RF model comprises 16 trees. Despite the different nature of these algorithms, their common goal is to predict a variable y (i.e., the 28-day strength) as a function of the input variables x (i.e., mixing proportions of concrete), while minimizing the difference between measured and predicted strength values (see Ref. [16] for details).

2.2 Feature selection

The dataset used in this study includes the 28-day compressive strength of 10,264 commercial concretes and associated mixture proportions [17]. All the mixtures were cast using ASTM C150 compliant Type I/II cement [31] and Class F fly ash compliant with ASTM C618 [32]. The seven most influential features are considered in this study, namely, (1) w/cm, (2) cement %, (3) fly ash %, (4) fine aggregate %, (5) air-entraining admixture (AEA) dosage, and (6) water-reducing admixture (WRA) dosage. For normalization purposes, the features from (2) to (4) are taken as the solid weight fractions, wherein the fraction of coarse aggregates is excluded as it is redundant (i.e., the sum of all the weight fractions is 100%).

2.3 Model training

Following common practices, 70% of the strength observations are randomly selected and used for model training (i.e., "training set"). The remaining 30% of the data are kept hidden to the model and assess the ability of the model to predict the strength of unknown concretes (i.e., "test set"). The hyperparameters of each mode are optimized by five-fold cross-validation [33]. In detail, the training set is randomly split into five smaller folds (each made of 20% of the training data). In each of the five rounds of analysis, the model is iteratively trained based on four folds and validated based on the remaining fold (i.e., "cross-validation set").

2.4 Accuracy evaluation

We evaluate the accuracy of each model based on their mean-square error (MSE) and coefficient of determination (R^2), wherein the MSE is the averaged Euclidian distance between predicted and measured strength data. The relative MSE (RMSE) is calculated as the square root of the MSE. The R^2 factor further quantifies the accuracy of the model predictions in terms of the degree of scattering around the fitted input-output relationship (a perfect prediction is associated with $R^2 = 1$. We analyze the deviation between strength predictions and measurements by computing the error distribution—that is, the distribution of the

differences between predicted and measured strength values for each concrete mixture in the test set. The error distribution yielded by each model then serves to calculate the 90 and 95% confidence intervals of a predicted strength falling into these ranges (see Ref. [16] for details).

2.5 Evaluation of the learning efficiency

To investigate how each model "learns" how to predict concrete strength as it exposed to more training examples, we compute their "learning curve" [34]. This approach consists of plotting the accuracy of the model as it is exposed to an increasing number of training examples. Here, we compute the MSE (for the training and validation sets) while gradually increasing the size of the training set by 10% increments. To ensure consistent comparison, all the models are trained and evaluated based on identical training and validation sets.

3. RESULTS AND DISCUSSION

3.1 Accuracy of the machine learning models

We first compare the final accuracy offered by each ML model when trained based on the entire training set. Figure 1 shows for each model the predicted vs. measured strengths for the entire test set and the associated error distributions. The accuracy analysis is summarized in Tab. 1. In detail, we find that RF features the highest degree of accuracy, which manifests itself by a minimum RMSE, maximum R^2, and minimum confidence intervals.

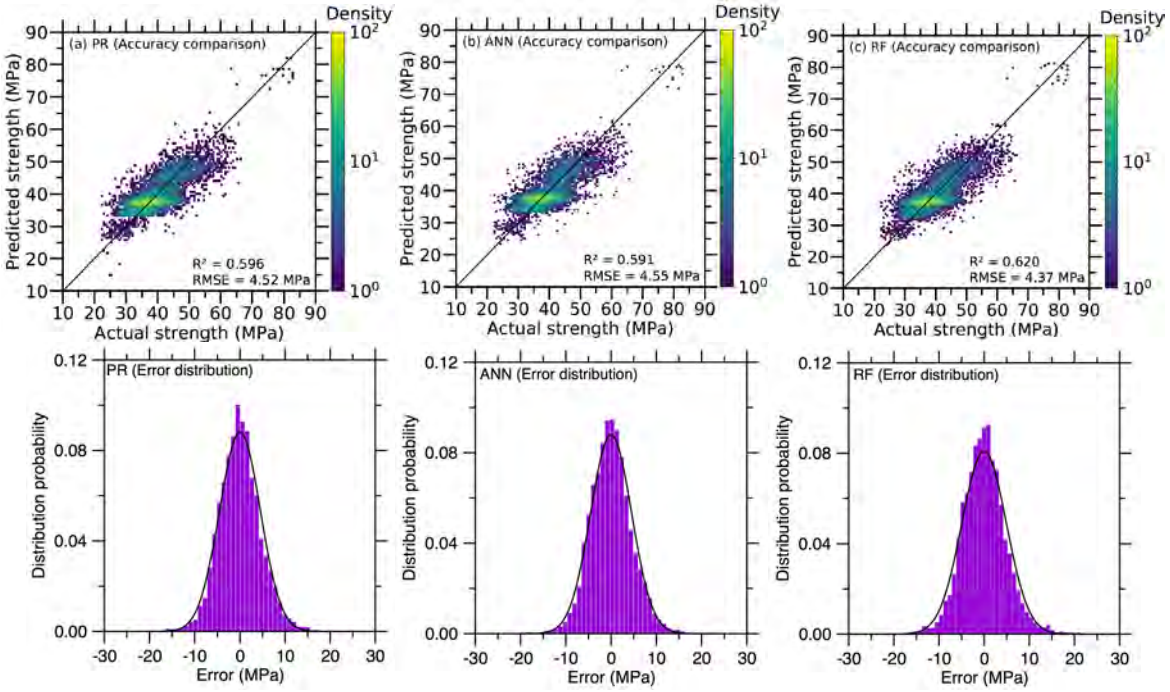

Figure 1: Comparison between predicted vs. measured (ground-truth) strengths (top) and error distribution (bottom) for the (a) PR, (b) ANN, and (c) RF models. The pixel colors in the left plots indicate the number of overlapped points. The error distributions are fitted by a Gaussian distribution function.

3.2 Gradual learning upon increasing training set size

Having shown that RF offers the best final accuracy when trained based on the entire training set, we now focus on the learning curve exhibited by each model—to assess their ability to quickly learn the input-output relationship as they become exposed to a gradually increasing number of training examples, as shown in Fig. 2. As expected, all the models exhibit a fairly similar trend, that is, (i) the MSE of the training set increases with increasing training set size since it becomes increasingly difficult from the model to perfectly interpolate the training set and (ii) the MSE of the cross-validation set decreases with increasing training set size as the model gradually manages to learn the input-output relationship and, hence, eventually shows an increased ability to predict the strength of unknown concretes.

Table 1: Values of R^2 and confidence intervals over the test set for each model (when trained based on the entire training set) and minimum number of training data that is needed for each model to achieve an average validation set MSE that is less than one standard deviation away from its final validation set MSE.

Model type	Accuracy analysis			Learning analysis
	R^2	Confidence interval (MPa)		Minimum number of training data points to reach maximum accuracy
		90%	95%	
PR	0.596	± 7.43	± 8.86	2680
ANN	0.591	± 7.45	± 8.88	3010
RF	0.620	± 7.22	± 8.60	4070

Nevertheless, we find that, although the final accuracy offered by the models shows only minor differences (see Tab. 1), their learning curves exhibit more significantly distinct features. In detail, in agreement with the data presented in Tab. 1, we find that RF eventually features the lowest MSE for the validation set, as well as for the training set. However, we note that the MSE of the validation set exhibits a faster decrease in the case of PR and ANN. We further quantify this behavior by computing the minimum number of training data points that is needed for the model to achieve an average validation set MSE that is less than one standard deviation away from its final validation set MSE (i.e., when trained based on the entire training set), wherein the standard deviation is calculated based on the MSE obtained for each validation fold in cross-validation. Overall, we find that PR and, to a lesser extent, ANN features an increased ability to quickly learn how to predict concrete strength from small datasets as compared to RF (see Tab. 1).

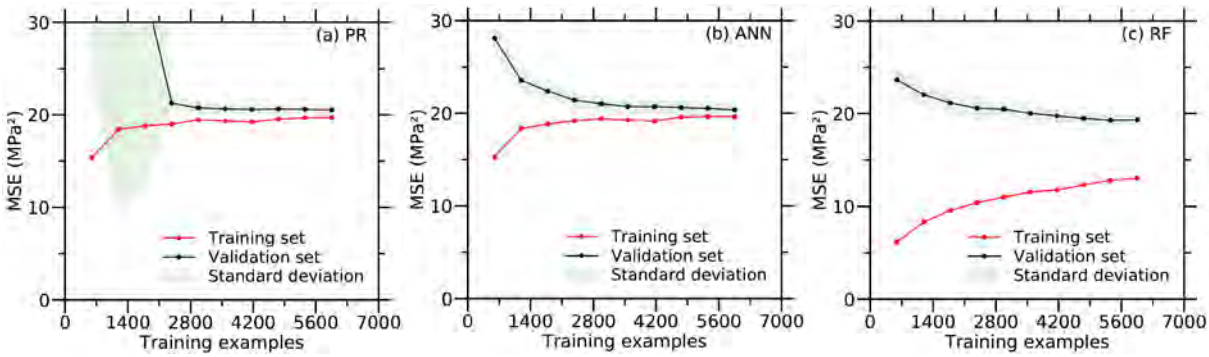

Figure 2: Learning curves showing the MSE of the training and cross-validation sets as a function of the size of the training set for the (a) PR, (b) ANN, and (c) RF models.

3.3 Competition between model accuracy and need for large dataset

Overall, we find that the model offering the highest final degree of accuracy (i.e., RF) requires the largest training set to be trained, whereas, in turn, the models presenting the lowest final accuracy (i.e., PR and ANN) require the smallest training set. These results suggest the existence of competition between (i) the ability of a model to accurately learn the input-output relationship when trained based on an excess of training examples and (ii) the ability of a model to quickly learn this relationship when trained based on a small dataset. This competition can be rationalized in terms of the intrinsic "flexibility" of the model.

On the one hand, PR and ANN are constrained, poorly-flexible models—since PR relies on a fixed analytical form, while the present ANN model exhibits a limited ability to capture complex input-output relationships as it comprises a single hidden layer. This lack of flexibility limits the final accuracy that is achievable by these models. Although the degree of complexity of these models (i.e., maximum polynomial degree for PR and number of hidden neurons for ANN) is already tuned to achieve the best balance between under- and overfitting [16], the fact that the MSE of the training and validation sets both plateau toward the same value suggests that these models are too simple and lack some degrees of freedom. For a given amount of data, this limitation could potentially be mitigated by carefully increasing the complexity of these models (while avoiding overfitting)—for instance, by increasing the number of hidden layers in ANN [35]. In turn, the constrained nature of these models allows them to quickly achieve their maximum accuracy—since only a limited number of parameters (i.e., polynomial coefficients for PR and neuron-neuron connection weights for ANN) need to be parameterized [36]. This makes it possible for these algorithms to handle small datasets. However, it is clear from Fig. 2 that these models have already achieved their maximum accuracy and, hence, would not benefit from being trained with any additional data.

On the other hand, RF is, in contrast, more flexible as it is not constrained by any analytical formulation. Indeed, in contrast to PR (which intrinsically yields a smooth, continuous, and differentiable relationship between inputs and output due to its analytical form), the tree-based structure makes it possible for the RF model to capture rough, less continuous/differentiable functions [37]. This flexibility enables RF to eventually reach a higher final degree accuracy once trained based on the entire training set. In turn, such complexity comes at a cost, namely, a large number of training data points is needed to properly parameterize the RF model. This is well illustrated by the facts that, unlike the cases

of PR and ANN, (i) the validation set MSE of the RF model does not reach a plateau and continues to decrease upon increasing training set size and (ii) the final validation set MSE is significantly higher than the final training set MSE. Both of these learning curve features suggests that the RF model has not yet finished its training and, hence, could further by improved if exposed to an increased number of data—that is, unlike the PR and ANN models, the RF model still features some room for improvement

5. CONCLUSIONS

- Machine learning offers a promising pathway to predict concrete strength.
- Simple, more constrained models (e.g., PR) offer limited final accuracy, but can quickly achieve their maximum accuracy while trained based on a small training set.
- Less constrained, more flexible models (e.g., RF) require larger training sets, but can eventually feature a higher final prediction accuracy.

ACKNOWLEDGEMENTS

The authors acknowledge some financial support for this research provided by the U.S. Department of Transportation through the Federal Highway Administration (Grant #: 693JJ31950021) and the U.S. National Science Foundation (DMREF: 1922167).

REFERENCES

[1] Rodríguez de Sensale, G. ‘Strength Development of Concrete with Rice-Husk Ash’. Cem. Concr. Compos.**28**(2)(2006)158–160.
[2] Ashour, S. A. and Wafa, F. F. ‘Flexural Behavior of High-Strength Fiber Reinforced Concrete Beams’. Struct. J.**90**(3)(1993)279–287.
[3] Purnell, P. and Black, L. ‘Embodied Carbon Dioxide in Concrete: Variation with Common Mix Design Parameters’. Cem. Concr. Res.**42**(6)(2012)874–877.
[4] Vance, K. Falzone, G. Pignatelli, I. Bauchy, M. *et al.* ‘Direct Carbonation of Ca(OH)2 Using Liquid and Supercritical CO2: Implications for Carbon-Neutral Cementation’. Ind. Eng. Chem. Res.**54**(36)(2015)8908–8918.
[5] Moutassem, F. and Chidiac, S. E. ‘Assessment of Concrete Compressive Strength Prediction Models’. KSCE J. Civ. Eng.**20**(1)(2016)343–358.
[6] Biernacki, J. J. Bullard, J. W. Sant, G. *et al.* ‘Cements in the 21st Century: Challenges, Perspectives, and Opportunities’. J. Am. Ceram. Soc.**100**(7)(2017)2746–2773.
[7] Provis, J. L. ‘Grand Challenges in Structural Materials’. Front. Mater.**2**(2015)31
[8] Powers, T. C. ‘Physical Properties of Cement Paste’, Skokie: Portland Cement Assoc R & D Lab Bull Publishers, 1960, 577-609.
[9] Popovics, S. ‘History of a Mathematical Model for Strength Development of Portland Cement Concrete’. Mater. J.**95**(5)(1998)593–600.
[10] Zain, M. F. M. and Abd, S. M. ‘Multiple Regression Model for Compressive Strength Prediction of High Performance Concrete’. J. Appl. Sci.**9**(1)(2009)155–160.
[11] Wild, S. Sabir, B. B. and Khatib, J. M. ‘Factors Influencing Strength Development of Concrete Containing Silica Fume’. Cem. Concr. Res.**25**(7)(1995)1567–1580.
[12] Burris, L. E. Alapati, P. Moser, R. D. *et al.* ‘Alternative Cementitious Materials: Challenges and Opportunities’. International Workshop on Durability and Sustainability of Concrete Structures, Bologna : ACI Publishers, 2015, 27.1-27.10.
[13] Yeh, I.-C. ‘Modeling of Strength of High-Performance Concrete Using Artificial Neural Networks’. Cem. Concr. Res.**28**(12)(1998)1797–1808.

[14] Rafiei, M. H. Khushefati, W. H. Demirboga, R. *et al.* 'Neural Network, Machine Learning, and Evolutionary Approaches for Concrete Material Characterization'. ACI Mater. J.**113**(6) (2016)781-789.
[15] DeRousseau, M. A. Kasprzyk, J. R. and Srubar III, W. V. 'Computational Design Optimization of Concrete Mixtures: A Review'. Cem. Concr. Res.**109**(2018)42–53.
[16] Ouyang, B. Li, Y. Wu, F. Yu, H. *et al.* 'Computational Modeling – Predicting Concrete's Strength by Machine Learning: Balance between Accuracy and Complexity of Algorithms'. ACI Mater. J. (2020)
[17] Young, B. A. Hall, A. Pilon, L. *et al.* 'Can the Compressive Strength of Concrete Be Estimated from Knowledge of the Mixture Proportions?: New Insights from Statistical Analysis and Machine Learning Methods'. Cem. Concr. Res.**115**(2019)379–388.
[18] Liu, H. Zhang, T. Krishnan, N. M. A. *et al.* 'Predicting the Dissolution Kinetics of Silicate Glasses by Topology-Informed Machine Learning'. Npj Mater. Degrad.**3**(1)(2019)1–12.
[19] Bishnoi, S. Singh, S. Ravinder, R. *et al.* 'Predicting Young's Modulus of Oxide Glasses with Sparse Datasets Using Machine Learning'. J. Non-Cryst. Solids.**524**(2019)119643.
[20] Pani, A. K., Amin, K. G., and Mohanta, H. K. 'Data Driven Soft Sensor of a Cement Mill Using Generalized Regression Neural Network'. International Conference on Data Science Engineering (ICDSE), Cochin : IEEE Publishers, 2012, 98–102.
[21] Rejeb, S. K. 'Improving Compressive Strength of Concrete by a Two-Step Mixing Method'. Cem. Concr. Res.**26**(4)(1996)585–592.
[22] Hemalatha, T. Sundar, K. R. Murthy, A. R. *et al.* 'Influence of Mixing Protocol on Fresh and Hardened Properties of Self-Compacting Concrete'. Constr. Build. Mater.**98**(2015)119–127.
[23] Elhakam, A. A. Mohamed, A. E. and Awad, E. 'Influence of Self-Healing, Mixing Method and Adding Silica Fume on Mechanical Properties of Recycled Aggregates Concrete'. Constr. Build. Mater.**35**(2012)421–427.
[24] Oey, T. Jones, S. Bullard, J. W. *et al.* 'Machine Learning Can Predict Setting Behavior and Strength Evolution of Hydrating Cement Systems'. J. Am. Ceram. Soc.**103**(1) (2020)480–490.
[25] Anoop Krishnan, N. M. Mangalathu, S. Smedskjaer, M. M. *et al.* 'Predicting the Dissolution Kinetics of Silicate Glasses Using Machine Learning'. J. Non-Cryst. Solids.**487**(2018)37–45.
[26] Liu, H. Fu, Z. Yang, K. *et al.* 'Machine Learning for Glass Science and Engineering: A Review'. J. Non-Cryst. Solids X.**4**(2019)100036.
[27] Sinha, P. 'Multivariate Polynomial Regression in Data Mining: Methodology, Problems and Solutions'. Int. J. Sci. Eng. Res.**4**(12)(2013)962–965.
[28] Wasserman, P. D. 'Advanced Methods in Neural Computing', New York: John Wiley & Sons, Inc. Publishers, 1993, 16-40.
[29] Li, J., Cheng, J., Shi, J., *et al.* 'Brief Introduction of Back Propagation (BP) Neural Network Algorithm and Its Improvement'. In: Jin D., Lin S. (eds.), Advances in Computer Science and Information Engineering. Berlin, Heidelberg: SPRINGER Publishers, 2012, 553–558.
[30] Liaw, A. and Wiener, M. 'Classification and Regression by Random Forest'. R News.**2**(3)(2002)18–22.
[31] ASTM C150-07, Standard Specification for Portland Cement. West Conshokocken: American Society for Testing and Materials, 2017, 8pages.
[32] ASTM C618-19, Standard Specification for Coal Fly Ash and Raw or Calcined Natural Pozzolan for Use in Concrete. West Conshokocken: American Society for Testing and Materials, 2019, 5pages.
[33] Stone, M. 'Cross-Validatory Choice and Assessment of Statistical Predictions' J. R. Stat. Soc. Ser. B Methodol.**36**(2)(1974)111–133.
[34] Anzanello, M. J. and Fogliatto, F. S. 'Learning Curve Models and Applications: Literature Review and Research Directions'. Int. J. Ind. Ergon.**41**(5)(2011)573–583.

[35] Ravinder, R. Sreedhara, K. H. Bishnoi, S. *et al.* 'Deep Learning Aided Rational Design of Oxide Glasses'. ArXiv191211582 Cond-Mat Physics (2019).

[36] Liu, H. Fu, Z. Li, Y. Sabri, N. F. A. and Bauchy, M. 'Balance between Accuracy and Simplicity in Empirical Forcefields for Glass Modeling: Insights from Machine Learning'. J. Non-Cryst. Solids.**515**(2019)133–142.

[37] Yang, K. Xu, X. Yang, B. Cook, B. Ramos, H. Krishnan, N. M. A. Smedskjaer, M. M. Hoover, C. and Bauchy, M. 'Predicting the Young's Modulus of Silicate Glasses Using High-Throughput Molecular Dynamics Simulations and Machine Learning'. Sci. Rep.**9**(1)(2019)8739.

DEVELOPPING A GENERIC APPROACH TO DURABILITY

Karen Scrivener, Fabien Georget, William Wilson, Shiyu Sui

École polytechnique fédérale de Lausanne (EPFL), Lausanne VD, Switzerland

Abstract

Cementitious Materials become more diverse. In particular, to reduce the CO2 emissions associate with production, it is necessary to increase the levels of replacement of clinker by other materials. A critical consideration is to know how durable different materials will be. Most forms of degradation involve the ingress of different species into the cement paste. The rate of ingress will be controlled by the concrete microstructure. Therefore, in order to predict the durability of new materials we need to understand how the microstructure controls durability: to develop a generic approach.

This presentation summarizes a large research programme ongoing at EPFL to identify the features of the microstructure which determine durability. A wide range of materials with different SCMs and at different w/c ratios are investigated. Both the solid phases and porosity are characterized using a combination of analytical methods (XRD, SEM, 1H NMR, MIP). Various experimental techniques are used to investigate transport properties (resistivity, diffusion cells, electrochemically induced migration, etc). Modelling approaches are also used. The initial focus is on ingress of chloride ions.

The work, so far, indicates that a least 3 factors affect the rate of ingress of chloride ions:(1) Solid phases (binding), (2) Pore structure and (3) Pore solution composition.

The interaction of these 3 factors means that materials with very similar pore structure may show dramatically different resistance to the ingress of chloride ions. This work has very important implications for the choice of materials in aggressive environments and for modelling durability

Keywords: Durability, Chloride ingress, Microstructure, Supplementary Cementitious materials

1. INTRODUCTION

Traditional study to understand the impact of microstructure are usually limited to a few system with varying water to cement ratio. These studies put the emphasizes on the porosity effect. However, porosity is just one of the many properties that can affect durability issues. The connectivity, chemical binding, tortuosity can all have an impact. This is crucial when considering supplementary cementitious materials (SCMs). To better understand the impact of the SCMs, it is thus important to solve two challenging problems: (1) understand how the SCMs impact the microstructure and (2) understand how the microstructure is related to the

macroscopic durability indicators. Unfortunately, it is not possible to separate these two steps in experiments. Therefore, carefully designing the experiment plan is crucial.

In this article, we demonstrate these effects on a simple study of chloride ingress. The standard bulk diffusion test is used to obtain the macroscopic durability indicators on mortars made from a variety of cement blends. In addition, microscopic indicators are measured independently on cement pastes. The common and new relationships are investigated and the implications for reactive transport modelling are discussed.

2. MATERIALS AND METHODS

2.1 Materials

This study used a type I ordinary Portland cement, a limestone powder (LS), a slag, a siliceous fly ash (FA) and an industrial calcined clay (the calcination temperature is around 800 °C). Seven paste and mortar mixtures were studied, with different levels and combinations of SCMs, as shown in figure 1, with a water to binder ratio of 0.5. In the binary systems, calcined clay, slag or FA was used to replace 30% of clinker. In the ternary systems, extra limestone was employed to substitute a further 15% of clinker. 1.96% gypsum was added to the systems containing calcined clay. A sand to cement blend ratio of three was used for the mortars. The paste preparation procedure included blending of the dried powders, followed by mixing with deionized water for 2 min at 1600 RPM. Fresh paste was cast in plastic containers (3 cm diameter and 5 cm height), sealed for 24h and after that submerged in water (minimum amount of water to avoid leaching) for further curing. For mortars, the EN 196 procedure was followed. After 1 d of curing in molds, mortar samples were cured in a fog room (>95% RH) prior to testing. More details for the cement preparationa re available in Sui et al. [1].

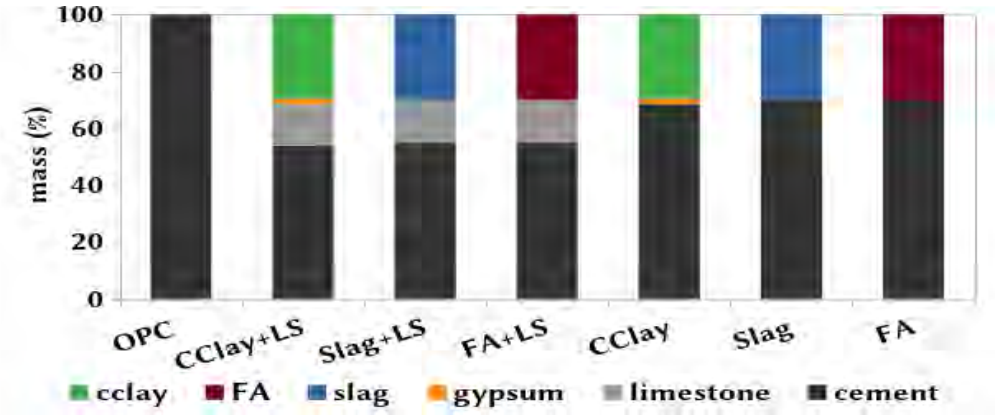

Figure 1: Mix design of the cement blends

2.2 Methods

Compressive strength was measured after on mortars 1, 4, 7, 28, 90 and 180d of moist curing in accordance with EN 196. After 28d of moist curing, cylindrical mortar samples were cut into two halves, each being 11 cm diameter and 10 cm height. All surfaces of the samples were sealed using epoxy resin except the saw cut face and submerged in 0.5 M NaCl solution at 23 °C. After 6 months of exposure, the specimens were removed from the solution and the total chloride content profiles were measured after drilling using nitric acid dissolution and $AgNO_3$

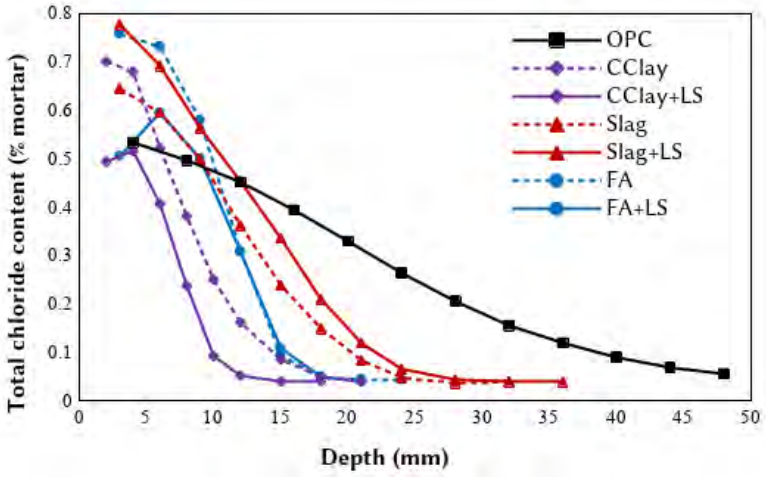

Figure 2: Bulk diffusion at one year

titration following the ASTM C1152 method [2]. The data collected was used to calculate the apparent diffusion coefficient of the mortars in accordance to ASTM C1552[2].

After 28d of curing, cylindrical paste samples were taken out from the curing water bath, and central portion cut into 3-5 mm thick slices[3]. The slices were vacuum dried for around 1 month in a vacuum desiccator containing silica gel. After storage, the 3-5 mm thick discs were broken into small fragments and samples, weighing approximately 25g samples whose size are between 1-2 mm and placed them in 100 ml of 0.5M NaCl solution, sealed and stored at 23 ℃. The samples were stored for 10 weeks; from preliminary tests, this duration was found to be sufficient to ensure that equilibrium was reached between the pore solution of the samples and the host solution. The host solutions were then analyzed for chloride concentration by means of potentiometric titration using 0.05 M $AgNO_3$. XRD analysis, coupled with Rietveld refinement, was employed to quantify the Friedel's salt on the binding cement paste samples. At 28d of curing. A PANalytical X'Pert Pro MPD diffractometer in a θ–θ configuration using Cu-Kα source (λ=1.54 Å) with a fixed divergence slit size of 0.5° was employed[3].

Mercury intrusion porosimetry (MIP) (Porotec GmbH Pascal 140-440 instruments) with up to a pressure of 400 MPa was employed to measure the porosity distribution of the pastes, cured for 90 days[3]. A solvent exchange with isopropanol was employed to dry the samples prior to the analysis. Thin paste slices were saw cut and submerged in alcohol for 7 days, followed by further curing under vacuum for at least another week. Finally, the elemental composition of the pore solution was measured using a high pressure extraction die method, with applying 1000kN load on paste sample cured in sealed container for 28 days. The concentrations of ions were measured using ICP method on samples, after 10, 100 or 1000 times dilution.

3. RESULTS AND DISCUSSION

3.1 Bulk diffusion

The bulk diffusion results at one year are presented in figure 2. As expected systems with supplementary cementitious materials are more resistant to chloride ingress. The main challenge is to try to understand why some blends are more resistant than others. All results are presented as function of the penetration depth at one year. It is a stronger numerical descriptor

of the chloride ingress than the apparent diffusion coefficient as it less subject to the surface values.

3.2 Strength

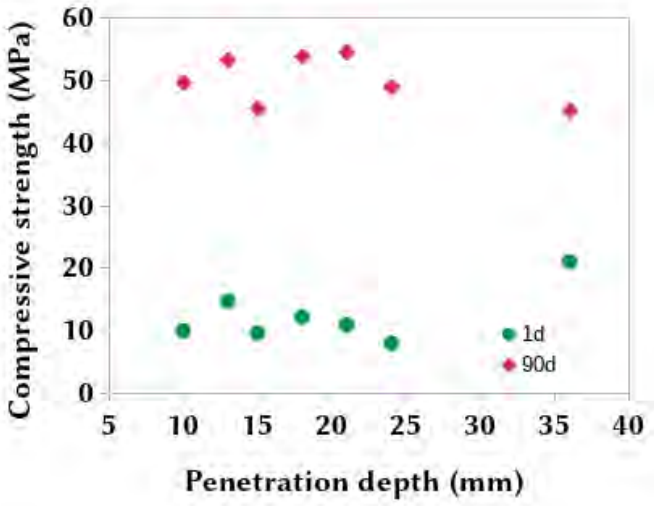

Figure 3: Compressive strength as a function of the penetration depth

Figure 3 presents the compressive strength at 1 and 90d as function of the penetration depth is studied. At late age, all systems have a similar compressive strength (50 MPa +/- 5). There is no clear correlation between the strength and the penetration depth.

Strength and transport properties are often expected to relate. Bigger pores leads to lower strength and to higher transport properties. Similarly, more AFm phases means that more of these big pores are filled (higher strength) but also that more Friedel's salt can form (lower penetration depth). Finally a better connected C-S-H network means more surface contacts (higher strength) and lower capillary porosity in favour of gel porosity (lower transport). Many models are relatively good at predicting the strength of cementitious materials [4]. Given the expected correlations, many attempts have been made to extend these models to predict the diffusion coefficient. These attempts have not been successful outside a few selected systems. Our results highlights these problems. It is possible to have similar strengths with very different chloride resistance.

3.3 Porosity

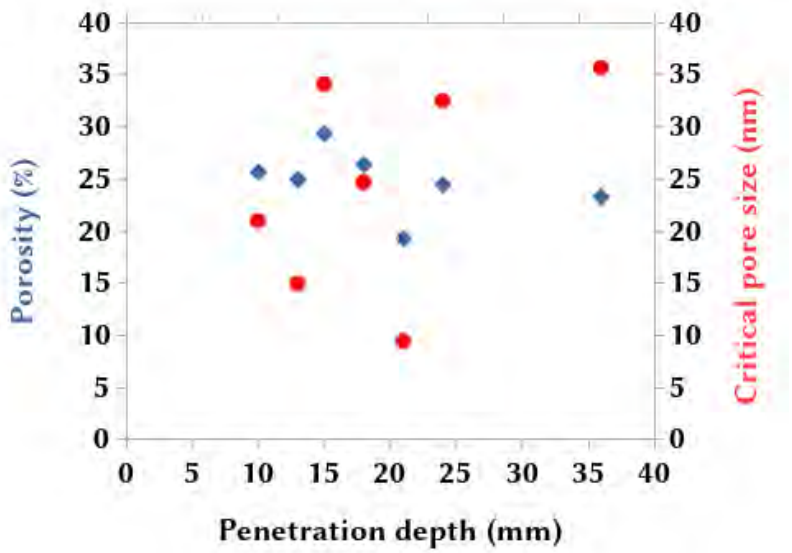

Figure 4: Porosity and critical pore size as function of the penetration depth

Figure 4 presents the pore structure descriptors (MIP total porosity, and MIP critical pore size) as function of the penetration depth. No clear trend is observed between porosity and penetration depth. If any, the penetration depth increases slightly when the porosity increases. The picture is even more confusing with the critical pore size.

The diffusion coefficient is a function of the porosity and the pore size distribution. As porosity and pore size increases, the diffusion also increases. Higher diffusivity would correlate to higher penetration depth. This is however not observed in figure 4. Two reasons could explain it. (1) The measure might not be correct for practical [5] or physical reasons. For example, the apparent diffusion was measured on mortars, while cement paste samples were used for MIP. Hydration process or interfacial transition zone (ITZ) might modify the process. This problem highlights the needs for methods that can measure both the durability issue and the microstructure of the sample. (2) And other effects could be more important and mask the trend. The other effect commonly investigated is the binding of chloride.

3.4 Chloride binding

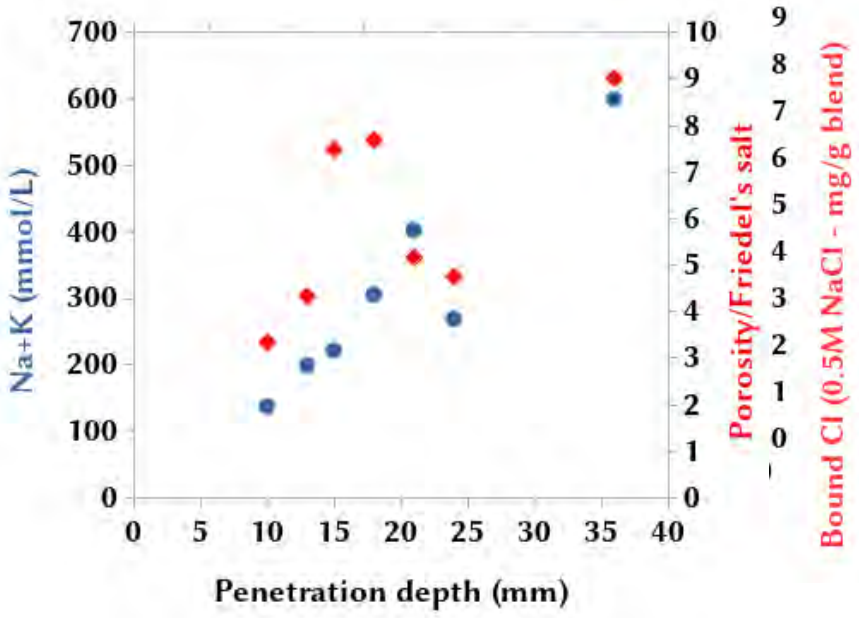

Figure 5: Alkali content and Porosity/Friedel's salt as function of the penetration depth

Figure 5 presents the Friedel's salt content(by XRD) and the bound chloride (at 0.5M NaCl) as function of the penetration depth. The Friedel's salt content is quite similar in all samples and it is not correlated to the penetration depth. The bound chloride also does not correlate with the carbonation depth. However, it is interesting to note that the bound Cl do not correlate with the Friedel's salt amount either. The same two reasons could be used to explain the lack of correlation. (1) Either the binding experiments do not represent the bulk diffusion coefficient . This could be explained by the leaching of ions or the effect of the co-ions [6]. (2) Or other factors mask the trends. In most models, the porosity and the binding capacity are the two main factors [7].

3.5 Other factors

Figure 6 shows the alkali content and φ/Fs (Porosity/Friedel's salt) as function of the penetration depth. Unlike the previous results a clear correlation can be found between the alkali content and the penetration depth. Similarly, a trend is observed between the penetration depth and the φ/Fs indicator.

A porosity increase and a Friedel's salt amount decrease would both lead to an increase in penetration depth. Combining the parameters in the φ/Fs make the expected correlations appear. However, the trend is not perfect and systems are grouped together. This is an indication that these parameters are important but not the complete story. It is interesting to note that the same trend cannot be observed when porosity/bound chloride is plotted. The φ/Fs indicator is similar to the w/[Ca] indicator that have been proposed for carbonation [8].

The missing factor might be the alkali content. Several explanations might be advanced for the correlations. First, the alkali is directly related to the pH of the pore solution. Higher pH will reduce the binding and thus, it will increase the penetration depth. Secondly, higher pH also means higher concentration of high mobility ions (HO^-) [9]. This higher concentration might help chloride ingress due to ionic exchange. Thirdly, higher alkali content means a higher ionic strength. The higher ionic strength means that the surface charges are going to be screened

more strongly. Therefore, the chloride ions will interact less with the charged surfaces. All these mechanisms would lead to higher penetration depth with higher alkali content. This is the trend observed in figure.

4. CONCLUSION

The relationships between the macroscopic durability indicators and the microstructure properties were investigated for chloride ingress in cement blends with various Supplementary Cementitious Materials. It was shown that expected straightforward correlations between porosity, chemical binding and the chloride penetration are not respected due to the complex effect of the supplementary cementitious materials on the microstructure. Combination of indicators such as the porosity over the Friedel's salt content are not sufficient to remove the effect of the SCMs. Instead, other not well understood relationships can be found, such as the effect of the alkali concentration. These effects are not explicitely taken into account in most service-life prediction models.

This study demonstrate that a more generic and systematic approach is needed to understand and quantify the effect of supplementary cementitious materials.

ACKNOWLEDGEMENTS

The China Scholarship Council (CSC) and the Construction Material Lab of EPFL provided financial support for Shiyu Sui.

REFERENCES

[1] Sui, Shiyu, Georget, Fabien, Maraghechi, Hamed, Sun, Wei, Scrivener, Karen: Towards a generic approach to durability: Factors affecting chloride transport in binary and ternary cementitious materials , Cement and Concrete Research 124, 105783, 2019

[2] ASTM C1152 / C1152M-04(2012)e1, Standard Test Method for Acid-Soluble Chloride in Mortar and Concrete , ASTM International

[3] Scrivener, K., Snellings, R., Lothenbach, B.: A Practical Guide to Microstructural Analysis of Cementitious Materials , Taylor & Francis, 201

[4] Bary, B., Béjaoui, S.: Assessment of diffusive and mechanical properties of hardened cement pastes using a multi-coated sphere assemblage model , Cement and Concrete Research 36(2), 245–258, 2006

[5] A.C.A. Muller, K.L. Scrivener, A reassessment of mercury intrusion porosimetry by comparison with1H NMR relaxometry, Cem. Concr. Res. (2017). doi:10.1016/j.cemconres.2017.05.024.

[6] Weerdt, K. De, Colombo, A., Coppola, L., Justnes, H., Geiker, M.R.: Impact of the associated cation on chloride binding of Portland cement paste , Cement and Concrete Research 68, 196–202, 2015

[7] B. Martín-Pérez, H. Zibara, R.. Hooton, M.D.. Thomas, A study of the effect of chloride binding on service life predictions, Cem. Concr. Res. (2000). doi:10.1016/S0008-8846(00)00339-2.

[8] Leemann, Andreas, Nygaard, Peter, Kaufmann, Josef, Loser, Roman: Relation between carbonation resistance, mix design and exposure of mortar and concrete , Cement and Concrete Composites 62, 33–43, 2015

[9] Tang, Luping: Concentration dependence of diffusion and migration of chloride ions: Part 2. Experimental evaluations , Cement and Concrete Research 29(9), 1469–1474, 1999

A STUDY OF THE ELASTIC MODULI AND CHEMICAL COMPOSITION OF CORROSION PRODUCT NATURALLY-GENERATED DUE TO CHLORIDES THROUGH NANO-INDENTATION AND ENERGY DISPERSIVE X-RAY SPECTROMETRY (EDS)

Emanuele Rossi (1), Hongzhi Zhang (2), Timo G. Nijland (3), Oğuzhan Çopuroğlu (1), Rob B. Polder (4) and Branko Šavija (1)

(1) Delft University of Technology, Faculty of Civil Engineering & Geosciences - Department of Materials & Environment,Stevinweg 1, 2628 CN Delft, The Netherlands

(2) Shandong University, School of Qilu Transportation, 25002 Jinan, , PR China

(3) TNO Buildings, Infrastructures and Maritime, PO Box 155, 2600 AD Delft, The Netherlands

(4) RPCP, Fluwelensingel 106, 2806 CH Gouda, The Netherland

Abstract

An important input parameter for numerical models that simulate cracking of the concrete cover due to reinforcement corrosion is the Elastic modulus of corrosion product (E_{cp}). Despite its relevance, E_{cp} is subject of significant variations according to the values reported in the literature, which vary from less than 100 MPa up to 360 GPa. Furthermore, E_{cp} values proposed in most of the present literature are representative of the corrosion product generated by anodic accelerated corrosion or extracted from the steel/concrete interface (SCI), which might differ from that formed in real corroding structures. Therefore, this study aims to investigate the Elastic modulus of naturally-generated corrosion product present at the SCI through nano-indentation conducted on six reinforced concrete polished sections. The polished sections were obtained from six 20-year-old reinforced concrete prisms cast with different cement type (CEM I, CEM II/B-V, CEM III/B, CEM V/A), same water/binder ratio (0.55) and which were previously exposed to NaCl solution wet/dry cycles. This study revealed that the range of E_{cp} did not considerably vary between corrosion products formed in different concrete mixes. However, corrosion product was microscopically found to consist of overlapping bands with different E_{cp}, varying for up to around 70 GPa between each other. Through Environmental Scanning-Electron Microscopy (ESEM) and Energy Dispersive X-ray Spectrometry (EDS) analysis of the indented locations, it was found that E_{cp} is highly dependent on the presence of interfacial cracks and inversely proportional to the concentration of Si and Ca, representative for corrosion product mixed with the surrounding concrete.

Furthermore, higher concentration of Fe leads to higher E_{cp}. Based on this study, an average range of values for E_{cp} between 80-100 GPa can be suggested for use in numerical models for corrosion induced cracking, regardless of cement type of the structure under investigation.
Keywords: nano-indentation, corrosion products, reinforcement corrosion

1. INTRODUCTION

Chloride-induced corrosion of reinforcement is one of the major degradation mechanisms affecting reinforced concrete structures. It involves the dissolution of iron due to ingress of harmful agents from the outside environment, which penetrates the concrete matrix and reach the reinforcement. In presence of oxygen and an electrolyte, formation of corrosion products (i.e. iron oxides and hydroxides) occurs, which generate tensile stresses inside the matrix that cause cracking of concrete, whilst reducing the effective cross-section of the reinforcement itself. Cracks enable harmful ions (such as chloride ions) to penetrate the structure more easily and accelerate the steel corrosion rate [1]. When occurring in practice, corrosion results in unforeseen maintenance and repair costs and, eventually, in faster structural failures. Therefore, predicting the cracking of concrete due to corrosion is an important topic, as suggested by the number of relevant numerical models proposed during the last decades to assess the mechanical and durability consequences of corrosion [2-6]. In these models, the elastic modulus of corrosion product (E_{cp}) is an important parameter to accurately predict the cracking time of the concrete cover since corrosion products at the steel/concrete interface (SCI) participate in the mechanical interaction between reinforcement and concrete when corrosion occurs [7]. Depending on the model, the used E_{cp} can have significant impact on the accuracy of the predicted time to cracking [8].
Many studies have been conducted to determine the most likely value of E_{cp} to be used in concrete cracking models. However, the values of E_{cp} proposed in the literature vary up to a factor of 10^6, as already pointed out by other researchers [7-8]. Furthermore, the dependency of E_{cp} on the chemical composition of corrosion products naturally-generated in different concrete mixes has rarely been investigated. Therefore, the aim of this study is to investigate the mechanical properties of corrosion products formed at the SCI in different concrete mixes and to evaluate the relation between E_{cp} and corresponding elemental concentrations of individual corrosion products through ESEM (Environmental Scanning Electron Microscope) observations and EDS (Energy Dispersive Spectrometry) semi-quantitative spot analysis.

2. MATERIALS AND METHODS

2.1 Specimen preparation

In this study, six reinforced concrete polished sections have been analyzed through nano-indentation, ESEM observations and EDS elemental mapping and spot analysis. The polished sections were obtained from 20-years-old prisms cast in 1998 by Polder et al. [9]. The prisms were cast with four different cement types (CEM I, CEM II/B-V, CEM III/B, CEM V/A), same water/binder ratio (0.55) using siliceous river sand and gravel with a maximum diameter (D_{max}) of 8 mm as aggregate. After casting, prisms were exposed to 3% NaCl solution wet/dry cycles for 6 months and otherwise left directly exposed (unsheltered) to the outside environment in Delft, the Netherlands.

One core of 20 mm in diameter was drilled from each prism parallel to the reinforcement and containing one steel bar, as described elsewhere [10]. The steel bar had 10 mm of cover depth. The cores were vacuum impregnated with fluorescent epoxy and carefully sawn perpendicularly to the bars, obtaining one 5-mm-high section per each core which was then grinded and polished prior to microscopic analysis. The composition and label of each polished section are summarized in Table 1.

Table 1: Specimen label and cement type (w/c = 0.55; D_{max} = 8 mm)

Specimen label	1550-S1	1550-S3	2550-S3	3550-S2	5550-S1	5550-S2
Cement type	CEM I	CEM I	CEM II/B	CEM III/B	CEM V/A	CEM V/A

2.2 Nano-indentation, Environmental scanning Electron Microscopy (ESEM) and Energy Dispersive Spectroscopy (EDS) analysis

Nano-indentation was conducted on the corrosion product formed at the SCI with an Agilent Nano Indenter G200 with diamond Berkovich tip (i.e. a three-side pyramidal diamond). Each polished section was subjected to one grid-like series of 100 indents (5 rows and 20 columns), with spacing between each indent of 20 μm. E_{cp} was determined through the Continuous Stiffness Method (CSM) developed by Oliver and Pharr [11]. The output E_{cp} was the average of the values measured between 1000 nm and 1800 nm in depth, while the Poisson's ratio of corrosion product was set at 0.25 [7-8].

For the microanalysis of the indented corrosion products, a Philips XL30 ESEM in hi-vac chamber conditions was used. Backscattered electron (BSE) images were acquired at 20 kV. To investigate the relation between the chemical composition and E_{cp}, EDS semi-quantitative spot analysis was conducted for around 25 spots of indented corrosion product for each specimen. For each spot, X-rays spectra were collected for 60 seconds. The spots analyzed through EDS coincided to the circular portion of corrosion product passing through all the three vertices of the triangular indenter's footprint, as graphically shown in Figure 1.

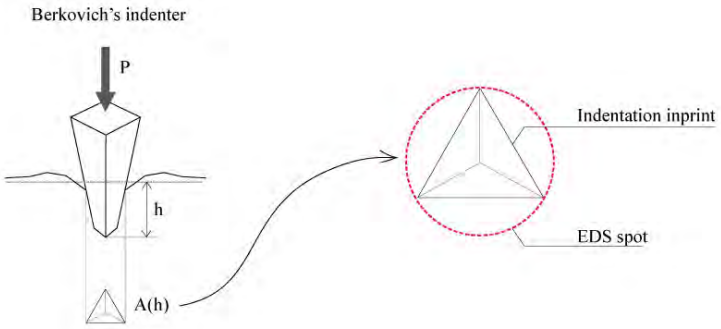

Figure 1: (left) footprint of Berkovich's indenter (P=applied load; h=penetration depth; A=inprint surface); (right) EDS spot around indenter's footprint.

3. RESULTS

In Figure 2, BSE images of the indented locations at the SCI are reported. The indented locations are overlapped by a map showing the E_{cp} of each indent (divided in 5 rows and 20 columns; column #1, #5, #10, #15 and #20 of the E_{cp} map are highlighted in each Figure).

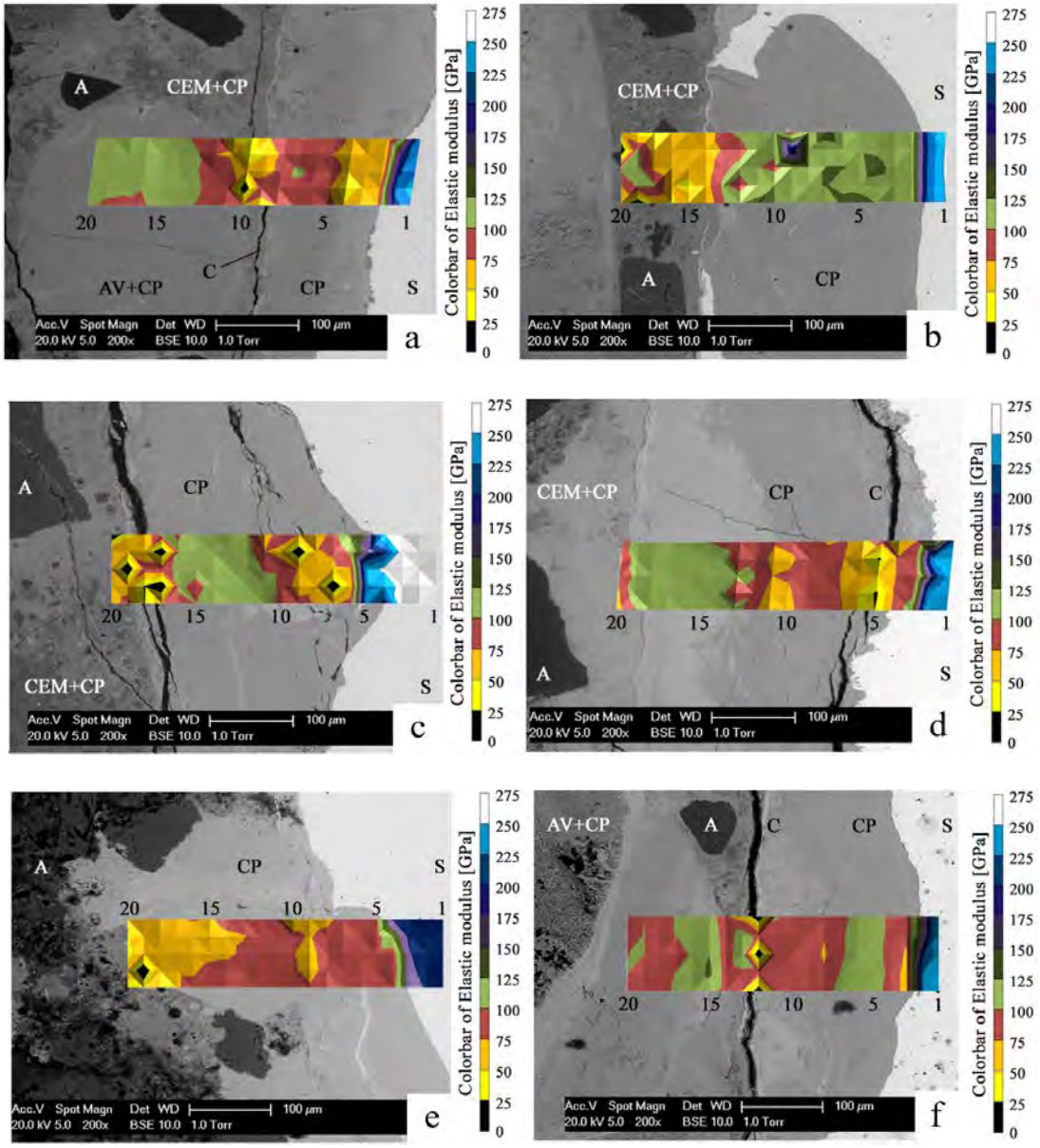

Figure 2: BSE image of indented location with overlapped E_{cp} map (S=steel; CEM=cement paste; CP=corrosion products; A=aggregate; AV=air void; C=crack). (a=1550-S1; b=1550-S3; c=2550-S3; d=3550-S2; e=5550-S1; f=5550-S2).

For 1550-S1 and 5550-S2 (Figure 2a and 2f), an air void filled by corrosion product separated by a thin cement paste interlayer (around 20 µm) is visible. A cracked alongside to this interlayer is also observed for both specimens. An interfacial void filled by corrosion product is also visible for 1550-S3 (Figure 2b), separated by a cement paste interlayer of around 80

μm. In these cases, the interlayers between interfacial air voids and the reinforcement are completely filled by corrosion products. In 2550-S3, 3550-S2 and 5550-S1 (Figure 2c, 2d and 2e, respectively) no interfacial voids are observed and corrosion products penetrated the concrete matrix for more than 100 μm. A thin and bright layer (5 to 10 μm) is visible around the reinforcement for all the specimens, which is thought to represent a mill scale layer as reported by other studies [12]. This layer was found intact around the reinforcement for 1550-S3 and 3550-S2, coincident to a crack around the steel in 1550-S1, 2550-S3 and 5550-S2, while it is not intact for 5550-S1. For 2550-S3 and 3550-S2 a cracked portion of corrosion products is visible at the steel interface, with cracks parallel to the reinforcement.

According to ESEM analysis, areas of corrosion product with different grey intensity in the BSE images (hence suggesting that corrosion products have different atomic weights on average) and E_{cp} can be distinguished. A clear example of the different micro-structure of corrosion products is visible for 3550-S2, in which three corrosion product layers are visible: a cracked portion close to the reinforcement (column 1-7), a denser dark-grey portion (column 7-13) and a compact light-grey layer close at the interface between surrounding cement paste (column 13-19). Layered corrosion products are also clearly visible for 1550-S1, 2550-S3 and 5550-S2. In 1550-S1, 2550-S3 and 3550-S2 a three-layered increase of E_{cp} from the reinforcement towards the surrounding cement paste is visible. E_{cp} ranging between 25-75 GPa at the steel interface for 2550-S3 and 3550-S1 was most likely due to the presence of visible cracks rather than due to the composition of the corrosion products themselves. More variable progress of E_{cp} was found for 5550-S2. At the steel interface E_{cp} increases from 75 GPa to 125 GPa in two distinct layers. A decrease of E_{cp} (column 12-13) is coincident to an interfacial portion of corrosion products mixed with cement paste. More further away from the reinforcement, E_{cp} decreases from 125 GPa to 75 GPa when approaching an interfacial void partially filled by corrosion products. For 1550-S3 and 5550-S1, corrosion products appear more uniform and compact, with no layered structure. Consequently, E_{cp} of undisturbed corrosion product was less variable than for the other specimens, overall ranging between 100-125 GPa and 75-100 GPa, respectively. The samples investigated do not show any systematic pattern of corrosion product layers with regard to their E_{cp} and to their appearance is visible from the steel to the surrounding cement paste.

The E_{cp} ranges between 75-125 GPa (red-green), with a few areas between 50-75 GPa (orange) visible for 1550-S1 and 5550-S1. Lower E_{cp} (0-50 GPa, black-yellow) was measured for portions of cracked corrosion products as well as for corrosion products mixed with cement paste.

4. DISCUSSION

In Figure 9 the range of E_{cp} measured for each specimen is reported.

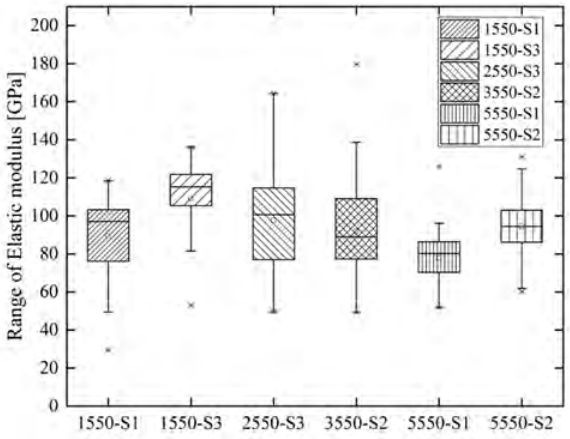

Figure 3: Range of E_{cp} of corrosion products per specimen. The top, middle and bottom line of the boxes correspond to the 75-, 50- and 25-percentile value (x_{75}, x_{50} and x_{25}) respectively. The whiskers show the minimum and maximum values.

The range of E_{cp} of undisturbed corrosion products formed in different concrete mixes does not considerably change depending on the cement type of the mixture, since average values of E_{cp} between 80-100 GPa have been measured in all specimens. This range of E_{cp} is similar to what was found by Hosemann et al. [12] (70-100 GPa) and slightly different from the E_{cp} studied through nano-indentation by others [7-8]. Šavija et al. [8] found that E_{cp} ranged between 49.4-67.9 GPa, while Zhao et al. [7] measured E_{cp} of two distinct corrosion product layers. In this latter case, they found that the inner layer (formed due to degradation of the reinforcement) had E_{cp} of 47-86 GPa, while the outer layer (mill scale-related) had 98-122 GPa. Differences with previous studies might be addressed to the different preparation of samples. Both of these studies investigated the E_{cp} of anodically-formed corrosion products. Anodic corrosion tends to influence the formation and further distribution of corrosion products [8]. The corrosion current density at which corrosion is accelerated might influence the micro-structure of corrosion products, such as its density and crystallinity, which likely influence the resulting micro-mechanical properties. Further specimens nano-indented by Zhao et al. [7] included portions of corrosion product previously peeled from a corroding bar, thus excluding the potential effect that the steel/concrete interface might have on the corrosion product's microstructure (due to constrain from the surrounding concrete). The influence that boundary conditions (i.e. presence of cracks and cement paste) were already pointed out by Šavija et al. [8], who observed that the elastic modulus of cracked corrosion products was lower than the E_{cp} of undisturbed products. This is because the presence of defects and lack of surrounding boundaries would offer accommodating area for the deformation of the material while being indented, as it was also observed in the present study. Differently to previous researches [7-8], in this study corrosion product was naturally-generated over 20 years, avoiding any potential influence of anodic acceleration of corrosion. Also, nano-indentation was performed on corrosion products still constrained by the surrounding steel and concrete, which is more representative for a real case scenario than extracted portions of corrosion product. Nevertheless, the range of E_{cp} measured in this study is overall comparable to the one analysed through nano-indentation by previous studies [7, 8, 12].

In Figure 4, the relation between E_{cp} and elemental concentration (Ca, Si, Fe) resulting from EDS spot analysis is shown. During the nano-indentation test, the location that is indented might be a cluster of different components, and not corrosion product only. Higher concentrations of Ca and Si suggests that corrosion product was partially mixed with cement paste, with consequent lower concentration of Fe. In agreement with Šavija et al. [8], corrosion products mixed with cement paste have lower Elastic modulus than the E_{cp} of undisturbed corrosion product, which generally contained no more than 2 wt% of Ca and Si. Figure 4 shows that E_{cp} is proportional to the Fe concentration of corrosion products. One possible explanation might be that the Elastic modulus of the indented cluster is proportional to its inter-atomic bonding energy, which is inversely proportional the inter-atomic distance and directly proportional to the ionic valency of the cluster. Since (Fe^{III}) iron oxides have lower inter-atomic distance and higher ionic valency than CaO and SiO_2 respectively, it is reasonable to find E_{cp} rather than that of corrosion product mixed with cement paste. Zhao et al. [7] observed that E_{cp} of the mill scale layer was higher than that of electrochemical corrosion products, and they concluded that this was due to the higher Fe/O of the former one, as reported by Cook [13]. This relation was recently confirmed by Jiang et al. [14]. In principle, the results of Figure 4 might suggest the same relation. However, since significant scatter of E_{cp} with 55-65 % Fe is visible, it may be the case that E_{cp} of corrosion product layers is more precisely dependant on the mineralogy of the corrosion products (i.e. different phases or polymorphs), as widely investigated by Dehoux et al. [15].

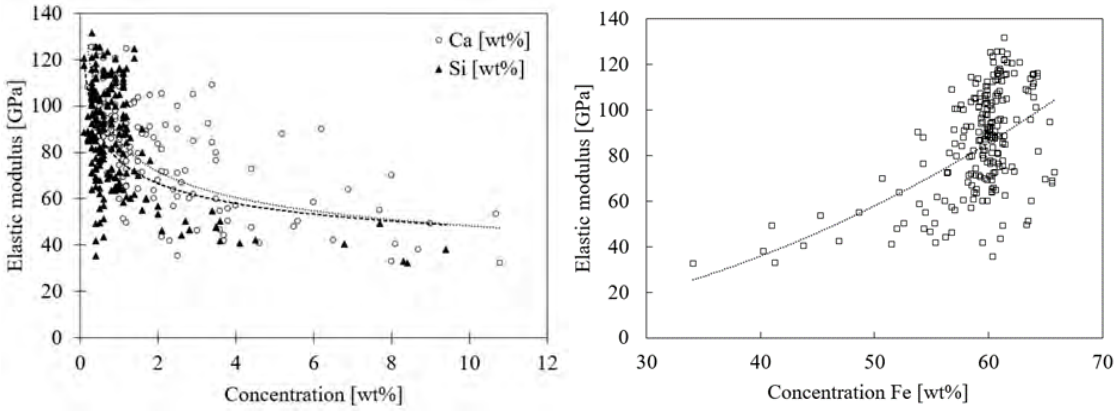

Figure 4: Influence of concentration of Ca, Si [wt.%] (left) and Fe [wt.%] (right) on E_{cp}

In line with previous studies [7, 16], corrosion products formed at the SCI were found to be made up by successive layers. Corrosion product layers for which the BSE image indicates a (slightly) different chemical composition also show different E_{cp}, as clearly visible for 1550-S1, 3550-S2 and 5550-S2. Nevertheless, the samples do not show a systematic pattern of corrosion product development from the reinforcement to the surrounding cement paste in terms of BSE appearance and E_{cp}. Through SEM and Raman spectroscopy analysis of corrosion product, both Dehoux et al. [15] and Demoulin et al. [16] found that layers of corrosion products with a different appearance under BSE were representative for different mineralogy of corrosion products. In this study, the mineralogical characterization was not carried out. It is likely, however, that differences in mineralogical composition provide an explanation for the different ranges of E_{cp}.

5. CONCLUSIONS

- From nano-indentation tests on natural corrosion products generated over 20 years due to chlorides, an average E_{cp} ranging between 80-100 GPa is obtained for use in numerical models for corrosion induced cover cracking. On average, no significant variations have been observed between E_{cp} of corrosion products generated in mixes cast with different cement types (CEM I, II/B-V, III/B and V/A).
- E_{cp} of corrosion products determined in this study is overall comparable to the E_{cp} found in previous studies in which nano-indentation was performed [7-8, 12, 14-15]. Slight differences with previous studies might be due to the different preparation of the samples and of the test set-ups. Nevertheless, the order of magnitude of E_{cp} is overall comparable to the one proposed by other authors.
- No systematic pattern of corrosion product layers from the reinforcement towards the surrounding cement paste with regard to its appearance and Elastic modulus was found.
- EDS spot analysis revealed that E_{cp} is inversely proportional to the presence of cracks and the concentration of cement-related components (i.e. Ca and Si). Furthermore, corrosion products with higher concentration of Fe show higher E_{cp}.

ACKNOWLEDGEMENTS

The authors would like to thank Mr. Arjan Thijssen and Mr. Willem Duvalois for their assistance with the microscope analysis.

REFERENCES

[1] Bertolini L, Elsener B, Pedeferri P, Redaelli E, Polder RB (2013). Corrosion of steel in concrete: prevention, diagnosis, repair. JohnWiley & Sons.

[2] Bazant Z (1979) Physical model for steel corrosion in concrete sea structures—theory. J Struct Div ASCE 105(6):1137–1153.

[3] Molina J, Alonso C, Andrade C (1993) Cover cracking as a function of rebar corrosion: Part 2—Numerical model. Mater Struct 26:532–548.

[4] Liu Y, Weyers RE (1998) Modeling the time-to-corrosion cracking in chloride contaminated reinforced concrete structures. ACI Mater J 95(6):675–680.

[5] Ozbolt J, Orsanic F, Balabanic G, Kuster M (2013) Modeling damage in concrete caused by corrosion of reinforcement: coupled 3D FE model. Int J Fract 178(1–2): 233–244.

[6] Savija B, Lukovic M, Pacheco J, Schlangen E (2013) Cracking of the concrete cover due to reinforcement corrosion: a two-dimensional lattice model study. Constr Build Mater 44:626–638.

[7] Zhao Y, Dai H, Jin W (2012). A study of the elastic moduli of corrosion products using nanoindentation techniques. Corros Sci 65:163-168.

[8] Savija B, Lukovic M, Hosseini SAS, Pacheco J, Schlangen E (2015). Corrosion induced cover cracking studied by X-ray computed tomography, nanoindentation and energy dispersive X-ray spectrometry (EDS). Mater. Struct. 48 (2043-2062).

[9] Polder RB, Russo P (1998) Concrete resistivity, corrosion potential and corrosion rate at young age as a function of cement type. 98-BT-R1664. TNO Building and Construction Research. Rijswijk, TNO.

[10] Rossi E, Nijland T, Çopuroğlu O, Polder RB, Šavija B. (2019). The influence of defects at the steel/concrete interface for pitting corrosion initiation studied through X-ray Computed Tomography and image analysis. In MATEC Web of Conferences (Vol. 289, p. 10011). EDP Sciences.

[11] Oliver WC, Pharr GM (2004) Measurement of hardness and elastic modulus by instrumented indentation: advances in understanding and refinements to methodology. J Mater Res 19:3–20.
[12] Hosemann P, Swadener JG, Welch J, Li N (2008). Nano-indentation measurement of oxide layers formed in LBE on F/M steels. J. Nucl. Mater. 201-205.
[13] Cook DC (2005). Spectroscopic identification of protective and non-protective corrosion coatings on steel structures in marine environments. Corros. Sci. 2250-2570.
[14] Jiang B, Doi K, Tsuchiya K, Kawano Y, Kori A, Ikushima K (2019). Micromechanical properties of steel corrosion products in concrete studied by nano-indentation technique. Corros. Sci.
[15] Dehoux A, Bouchelaghem F, Berthaud Y (2015). Micromechanical and microstructural investigation of steel corrosion layers of variable age developed under impressed current method, atmospheric or saline conditions. Corrosion Science 97:49-61.
[16] Demoulin A, Trigance C, Neff D, Foy E, Dillmann P, L'Hostis V (2010). The evolution of the corrosion of iron in hydraulic binders analysed from 46- and 260-year-old buildings. Corrosion Science 52:3168–3179.

ASSESSING PROPERTIES OF HYDRATING CEMENT PASTE USING X-RAY COMPUTED TOMOGRAPHY CHARACTERISATION

H.Zhang (1,2), E. Schlangen (1), Z. Ge (2) and B. Šavija (1)

(1) Materials & Environment, Delft University of Technology, The Netherlands

(2) School of Qilu Transportation, Shandong University, China

Abstract

Properties of concrete are, to a large extent, dependent on the properties of its binding constituent, hydrated cement paste. Therefore, knowledge of properties of hydrated cement paste is crucial for predicting concrete behaviour. This paper presents an experimentally informed approach for modelling elastic and transport properties of cement paste. The models used realistic microstructural information-obtained by X-ray computed tomography-as input for property determination. The properties were then determined using discrete numerical models, namely, models based on a lattice approach. Modelling results were compared with literature data, showing excellent correlations. Furthermore, dependence of properties of cement paste on the total porosity, based on the modelling results, was explored. Finally, a correlation between elastic and transport properties for the explored range of Portland cement pastes was established. It is seen that the models can be used for property prediction, but also for exploring correlations between different parameters.

Keywords: Cement paste, Young's modulus, Chloride diffusion; Lattice model, X-ray computed tomography

1. INTRODUCTION

Understanding properties of concrete and their development in time is of great interest. Properties of concrete are, to a great extent, determined by the properties of its main constituent – cement paste [1]. This is valid for the mechanical properties, such as strength [2] and elastic modulus [3], but also for the durability, measured through e.g. transport properties such as permeability [4]. Simulation and prediction of property development in cement pastes is therefore a major topic of research in the field of cementitious materials.

In the past decade or so, numerous approaches for simulating property development of cement paste have been proposed. In general, these approaches comprise two parts: simulation of hydration and microstructure development, and simulation of the property (e.g. elastic modulus, strength, or diffusivity) itself.

In this work, experimentally obtained microstructures are used as input for simulating transport (diffusivity) and mechanical (elastic modulus) properties of cement pastes of various

ages. Simulation results are first validated by comparing them to experimental observations. Then, properties of cement pastes for different w/c ratios and ages are determined. This work has two aims: first, it tries to establish the experimentally-informed modelling procedure as a viable option for obtaining properties of multi-phase porous materials such as cement paste and second, it explores relationships between mechanical and transport properties (chloride diffusivity) of cement paste.

2. EXPERIMENTS

X-ray computed tomography was performed on micro-beam specimens with 500 μm × 500 μm cross section. Specimens were prepared for w/c ratio of 0.3, 0.4 and 0.5 and testing age of 7, 28 and 60 d. The specimen preparation procedure and scanning set-up are described in detail in [5]. The resulting digital material structure has a resolution of 2 μm/voxel. Image segmentation was then processed to segment the material structure into different phases: pore phase, the outer hydration product phase, the inner hydration product phase, and unhydrated cement phase. From each scanned image, 10 cubic subsamples of 100 × 100 × 100 μm3 (i.e. 50 × 50 × 50 voxels) were extracted to be used for numerical simulations. Examples of the microcubes are shown in Fig. 1 for 7 days of hydration, respectively. Properties of each micro-cube were simulated in 3 orthogonal directions, to capture the anisotropy in the material behavior. This provided 30 measures for the elastic modulus and chloride diffusivity for each w/c ratio and testing age.

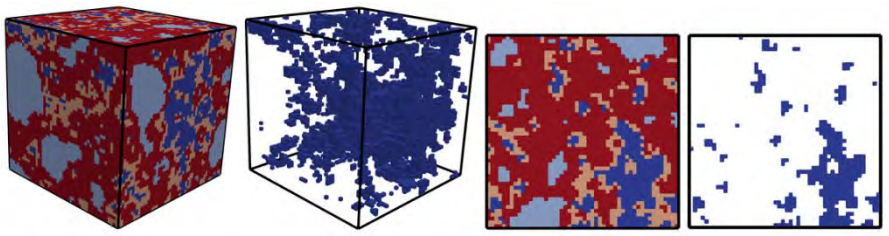

(a) w/c=0.3

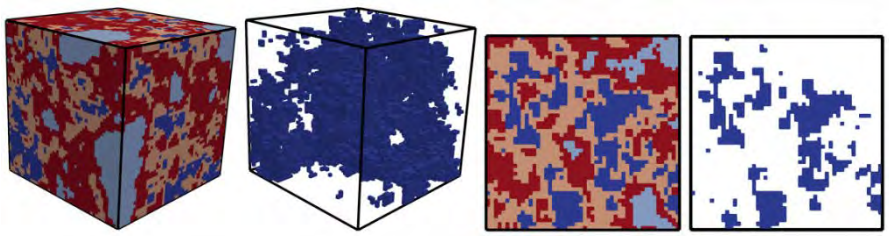

(b) w/c=0.4

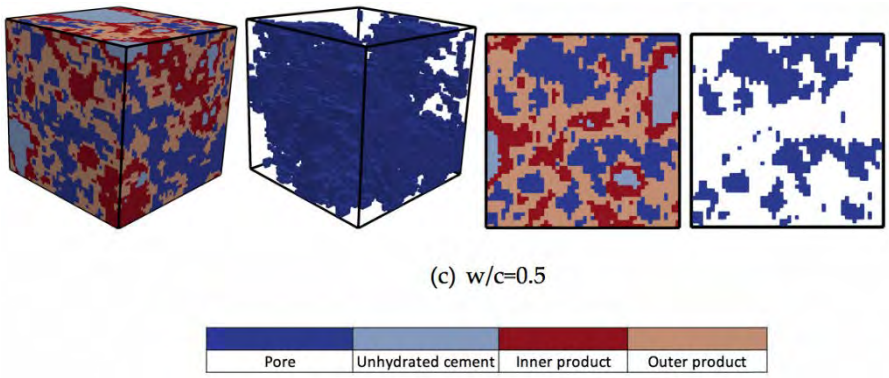

Figure 1: Examples of 100 × 100 × 100 µm^3 cement paste microcubes obtained from X-ray computed tomography after 7 days of hydration and subsequently segmented. Left to right: complete microstructure; only pores; 2D of the microstructure; 2D slice showing only the pores

3. MODELLING

In recent years, discrete models have been used to simulate transport processes in concrete [6-8]. Furthermore, coupled mechanical and transport models, which consider the effect of cracking on transport, have been developed [9-12]. In the mechanical lattice model, the continuum is discretized as a set of truss or beam elements that can transfer forces. On the other hand, in the transport lattice model, the continuum is discretized as a set of one dimensional conduit ("pipe") elements through which the transport takes place. In the current study, the approach described in [13] was used to calculate the Young's modulus and chloride diffusion coefficient of the microcubes.

4. RESULTS

In Fig. 2, simulated Young's moduli for all microcubes are plotted as a function of the total porosity. The Young's modulus of cement paste is approximately an exponential function of the porosity, i.e. of the following form:

$$E = ae^{bP} \quad (1)$$

Here, E is the Young's modulus of cement paste (GPa), a and b are the fitting parameters, and P the porosity (%). For the considered cement pastes, the fitting coefficients are a=38.76 and b=-0.04418 and the coefficient of determination is R^2=0.9337. Note that the linear fit is valid for all w/c ratios and ages: in other words, the Young's modulus of considered cement pastes is dominantly a function of porosity. Relative amounts of solids (i.e. unhydrated particles and hydration products) in the skeleton is of secondary importance for the Young's modulus of the composite according to the model since the Young's moduli of individual hydration phases are relatively similar, especially the inner and the outer product, while the amount of unhydrated cement is small. An exponential relation between porosity and Young's modulus has been proposed previously in the literature. For example, Spriggs [14] showed that the relation is valid for refractory materials. Note that this relation is purely empirical and, although it is valid for a practical range of porosities, it does not satisfy the physical condition that, for a 100% porosity, a zero elastic modulus should be obtained [15].

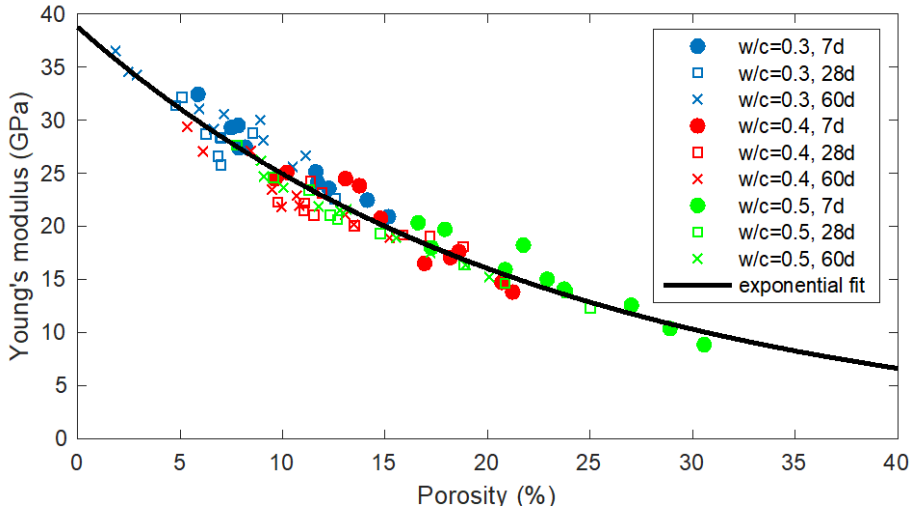

Figure 2: Young's modulus as a function of total porosity

In Fig. 3, chloride diffusion coefficient for all microcubes is plotted as a function of total porosity. It can be seen from Fig. 3 that the chloride diffusion coefficient of hydrated cement paste is dependent on the porosity in an approximately exponential way. An exponential relation between the porosity and the chloride diffusion coefficient is determined through regression analysis as follows:

$$D = ae^{bP} \quad (2)$$

where D is the diffusion coefficient (in 10^{-12} m^2/s), a and b fitting parameters, and P the porosity (%). For the considered cement pastes, a=1.192 and b=0.07852, with a coefficient of determination R^2=0.9164. The exponential fit is also shown in Fig. 3.

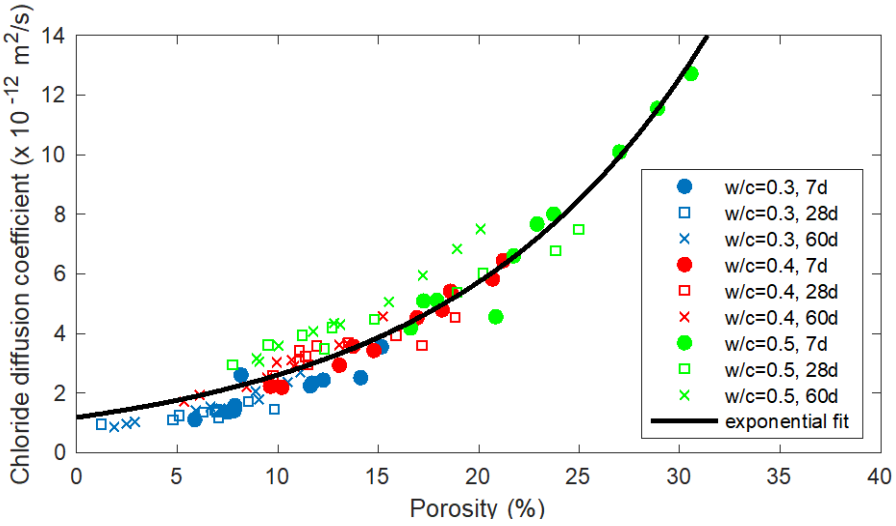

Figure 3: Chloride diffusion coefficient as a function of total porosity

It is clear that both the Young's modulus and the chloride diffusivity of hydrated Portland cement paste are dependent on the microstructure, especially the porosity. However, while Young's modulus decreases exponentially with increasing porosity (Fig. 2), the chloride diffusion coefficient shows an exponential increase with increasing porosity (Fig. 3). Therefore,

for the ordinary Portland cement pastes considered, it may be possible to define a relationship between the Young's modulus and the chloride diffusion coefficient. In Fig. 4, a relationship between the calculated Young's modulus and calculated chloride diffusion coefficient for each microcube is plotted.

It can be seen that an approximately power relation exists between the two variables. This relation can be written as:

$$D = kE^m \quad (3)$$

where k and m are fitting parameters. For the microstructures considered, k=429.3 and m=-1.564, and the power fit has a coefficient of determination R^2=0.8534. The fitting relation is also shown in Fig. 4.

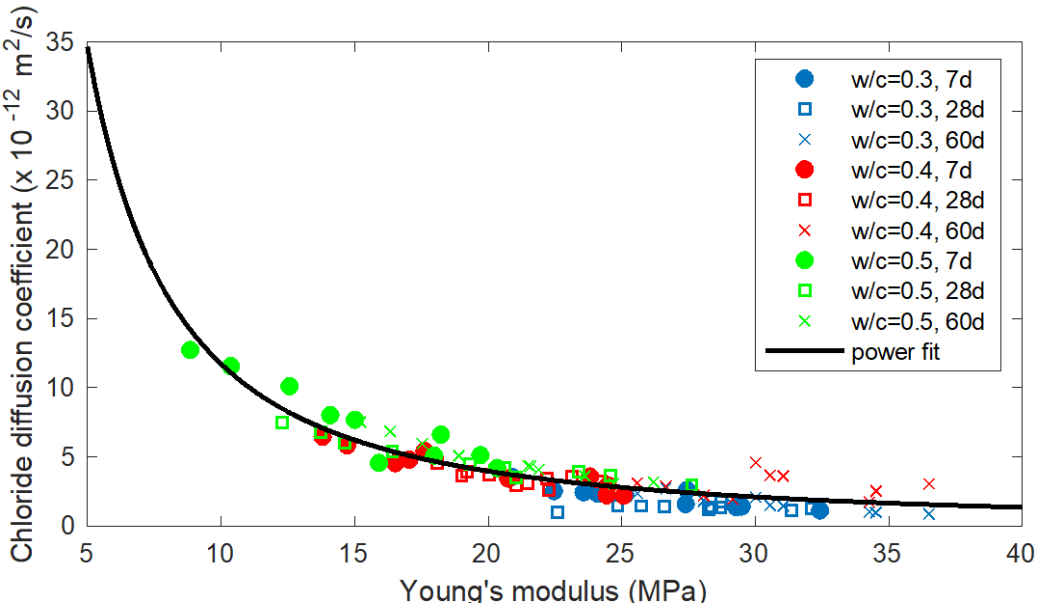

Figure 4: Relationship between the Young's modulus and the chloride diffusion coefficient for hydrated cement pastes considered.

5. CONCLUSIONS

In this work, an experimentally-informed modelling approach for determining elastic (Young's modulus) and transport (chloride diffusivity) properties has been proposed. The models use X-ray computed tomography data as microstructural input. Both the mechanical and the transport model use a discrete (lattice) approach to discretize the material domain and simulate different phases in the microstructure. Microstructure-property relationships and their time dependence were explored. Finally, a correlation between Young's modulus and chloride diffusivity in ordinary Portland cement pastes has been discussed.

ACKNOWLEDGEMENTS

This work has been financially supported by a European Union Horizon 2020 project InnovaConcrete (Innovative Materials and Techniques for the Conservation of 20th Century Concrete-Based Cultural Heritage), Grant Agreement Number 760858. H. Zhang would like to acknowledge the financial support of China Scholarship Counsil (CSC) under the grant CSC No.201506120067 and Taishan Scholars Program of Shandong province under the grant

number tsqn201909032. Arjan Thijssen has performed the X-ray computed tomography experiments and his assistance is gratefully acknowledged.

REFERENCES

[1] T.C. Powers, T.L. Brownyard, Studies of the physical properties of hardened Portland cement paste, Journal Proceedings, 1946, pp. 101-132.
[2] H.A. Toutanji, T. El-Korchi, The influence of silica fume on the compressive strength of cement paste and mortar, Cement Concrete Res 25(7) (1995) 1591-1602.
[3] T.J. Hirsch, Modulus of elasticity of concrete affected by elastic moduli of cement paste matrix and aggregate, Journal Proceedings, 1962, pp. 427-452.
[4] G. Ye, Experimental study and numerical simulation of the development of the microstructure and permeability of cementitious materials, TU Delft, Delft University of Technology, 2003.
[5] H. Zhang, B. Šavija, S.C. Figueiredo, E. Schlangen, Experimentally validated multi-scale modelling scheme of deformation and fracture of cement paste, Cement Concrete Res 102 (2017) 175-186.
[6] S.D. Abyaneh, H. Wong, N. Buenfeld, Computational investigation of capillary absorption in concrete using a three-dimensional mesoscale approach, Comp Mater Sci 87 (2014) 54-64.
[7] B. Šavija, M. Luković, E. Schlangen, Lattice modeling of rapid chloride migration in concrete, Cement Concrete Res 61 (2014) 49-63.
[8] L. Wang, T. Ueda, Mesoscale modeling of water penetration into concrete by capillary absorption, Ocean Eng 38(4) (2011) 519-528.
[9] D. Asahina, J.E. Houseworth, J.T. Birkholzer, J. Rutqvist, J. Bolander, Hydro-mechanical model for wetting/drying and fracture development in geomaterials, Comput Geosci 65 (2014) 13-23.
[10] P. Grassl, J. Bolander, Three-dimensional network model for coupling of fracture and mass transport in quasi-brittle geomaterials, Materials 9(9) (2016) 782.
[11] M. Luković, B. Šavija, E. Schlangen, G. Ye, K. van Breugel, A 3D lattice modelling study of drying shrinkage damage in concrete repair systems, Materials 9(7) (2016) 575.
[12] N. Benkemoun, M.N. Hammood, O. Amiri, A meso-macro numerical approach for crack-induced diffusivity evolution in concrete, Constr Build Mater 141 (2017) 72-85.
[13] B. Šavija, H. Zhang, E. Schlangen, Assessing Hydrated Cement Paste Properties Using Experimentally Informed Discrete Models, J. Mater. Civ. Eng. 31(9) (2019) 04019169.
[14] R. Spriggs, Expression for effect of porosity on elastic modulus of polycrystalline refractory materials, particularly aluminum oxide, J Am Ceram Soc 44(12) (1961) 628-629.
[15] D. Hasselman, On the porosity dependence of the elastic moduli of polycrystalline refractory materials, J Am Ceram Soc 45(9) (1962) 452-453.

ASSESSMENT OF FREEZE-THAW RESISTANCE OF CEMENT BASED CONCRETE WITH GROUND GLASS – POZZOLAN THROUGH X-RAY MICRO TOMOGRAPHY

Marija Krstic (1), Julio F. Davalos (1), Emanuele Rossi (2), Stefan C. Figueiredo (2) and Oguzhan Copuroglu (2)

(1) Department of Civil Engineering, the City College of New York, the City University of New York, 160 Convent Avenue, New York, 10031 NY, USA

(2) Microlab, Faculty of Civil Engineering and Geosciences, Delft University of Technology, Stevinweg 1, 2628CN Delft, the Netherlands

Abstract

Over the last few years, the United States has experienced a shortage of fly ash and slag that consequently created a need for an alternative material that is locally available, sustainable, and provides desirable concrete properties. Recent studies have shown that Ground Glass Pozzolan (GGP) offers favorable attributes as a supplementary cementitious material (SCM) for concrete. However, there are limited studies demonstrating freeze-thaw (FT) resistance of concrete with GGP, as well as assessing the FT resistance in relation with the air-void system of GGP mixtures. In response, this study aimed to evaluate both macro- and micro-level behavior of GGP on FT resistance, and characterize mixtures with different contents of GGP. Six concrete mixtures were evaluated: three mixtures with 20, 30, and 40% GGP as cement replacements and three other reference mixtures with 30% fly ash and 40% slag and 100% Ordinary Portland cement (OPC). Following ASTM standards, concrete beam samples were tested for accelerated FT resistance and dynamic modulus of elasticity up to 1000 cycles. All concretes showed high FT resistance with a durability factor over 90% and, consequently, minimal deterioration and scaling. Core samples extracted from the FT conditioned beams were scanned with the X-ray micro-tomography (CT-scan) to identify air-void parameters. Through image analysis a quantification of air-void parameters was obtained, and their relationship to FT resistance was established. Using CT scan analysis, we demonstrated that concretes with the highest cement replacement with GGP and slag developed the most desirable spacing factor and specific surface for FT resistance.

Keywords: ground glass pozzolan (GGP), freeze-thaw resistance, durability factor, X-Ray micro tomography, air-void analysis

1. INTRODUCTION

Supplementary cementitious materials (SCMs), such as fly ash and granulated blast-furnace slag, are commonly used worldwide to produce more sustainable concrete with better mechanical and durability properties. The availability of fly ash in the USA has declined significantly due to recent environmental protection rules [1-2]. Slag is generally produced outside the USA and imported what makes it relatively expensive [3]. The shortage and cost of SCMs in the USA are of concern to the concrete industry. Consequently, there is a need for an alternate SCM to overcome the reduced supply of fly ash, particularly in the USA's Northeastern region. In recent years, the recycled soda-lime glass has received increased attention in the concrete industry since it can be effectively and economically transformed into pozzolanic material for concrete [4-7].

Freezing and thawing resistance is an essential durability property of concrete in inclement weather environments. Concrete structures are, besides mechanical loads, also exposed to environmental effects (e.g., low-temperature weather conditions), which can be damaging to porous brittle materials such as concrete. The durability of concrete is affected when subjected to repetitive freezing and thawing (FT) cycles, leading to accelerated deterioration and loss of stiffness and strength. Considering the freeze–thaw response, the most important factor of air void properties is pore interconnectivity. In normal concrete, the capillary pores (usually between 5 nm and 1 mm) are responsible for creating a network of voids [8]. Capillary forces in such small volumes are very important for allowing the water transport inside the paste matrix. One of the severe types of deterioration in concrete structures is associated with the cyclic volume expansion and contraction due to internal water freezing and thawing [9]. The volume expansion results in pressure build-up inside the pores if not accommodated with sufficient pore space and inter-connectivity in the matrix [10]. When the pressure exceeds the tensile strength of the cement paste at any point, it will lead to local cracking; hence the strength of concrete will decrease after several FT cycles [11].

Adding air-entraining agents is a well-known technique to improve the FT resistance. Compared to accidental entrapped air, entrained air bubbles are intentional and range from 1 μm to 100 μm [12]. Apart from increased air void content, it is believed that it is vital for freeze–thaw resistant concrete to have a spacing factor smaller than 0.2 mm (200 μm) and a specific surface of air void system greater than 24 1/mm [13]. Air void analysis is usually carried out as conventional testing method ASTM C457 [14], and it requires a tedious preparation of large samples dependent on aggregate size. Firstly, samples are viewed in 2D through an optical microscope or flatbed scanner [15], and then a standardized stereological method is applied (linear traverse method or point counting). X-ray computed tomography (CT-scan) can be also applied to characterize the air void system of cementitious materials, and it is a nondestructive method that uses high resolution for the characterization of materials in 3D [16]. It does not require elaborate sample preparation, however the limitation of micro CT is the size of samples that can fit into the machine and still accomplish an appropriate resolution to see the air voids [17].

There are limited studies [18] that have evaluated the freeze–thaw resistance of concrete with GGP replacements. Hence, this study aims to establish correlations among freeze–thaw resistance and air void parameters for concrete with different cement replacements with GGP. After the macroscopic characterization was completed, air void analysis was conducted using micro CT-scan to correlate macro and micro-evaluations. This work demonstrates a multiscale understanding of concrete durability properties with GGP as SCM, and the results contribute to practical implementations of concrete in inclement weather environments.

2. MATERIALS AND METHODOLOGY

This study evaluated six mixtures of air-entrained concrete for FT resistance up to 1000 cycles and air void system properties: three mixtures with 20, 30, and 40% GGP as cement replacements per weight, and three other reference mixtures with 30% fly ash (FA) and 40% slag (S) and 100% Ordinary Portland cement (OPC). The particle size distribution of cementitious raw materials, is presented in Table 1, and median particle size of OPC, S, FA and GGP is 14, 11, 15, and 10 μm respectively. Chemical composition (oxides and total alkalis) of raw cementitious materials was obtained with x-ray fluorescence (XRF) (see Table 2).

Table 1: Particle size distribution of raw materials

		OPC	**S**	**FA**	**GGP**
Mean:	μm	19.8	13.9	25.9	11.8
Median:	μm	14.2	11.3	14.9	10.0
S.D.:	μm	19.1	10.7	34.2	8.4
d10:	μm	2.9	2.1	3.3	2.3
d50:	μm	14.2	11.3	14.9	10.0
d90:	μm	45.7	30.0	65.4	24.2

Table 2: Chemical compositions of raw materials obtained through XRF.

Chemical Composition	**Ordinary Portland Cement (PC)**	**Slag (S)**	**Fly Ash Class F (FA)**	**Ground Glass Pozzolan (GGP)**
SiO_2, %	20.2	38.00	47.58	72.5
Na_2O, %	0.19	0.32	1.5	13.7
CaO, %	61.9	39.84	5.54	9.7
Al_2O_3, %	4.7	7.52	26.42	0.4
MgO, %	2.6	10.54	0.9	3.3
K_2O, %	0.82	0.38	1.9	0.1
Fe_2O_3, %	3.0	0.31	12.19	0.2
SO_3, %	3.9	0.16	1.08	0.1
Total alkalis Na_2O + 0.658K_2O, %	0.73	0.6	2.75	13.77

All six concretes were tested simultaneously for dynamic modulus and freeze-thaw resistance according to ASTM standards [19, 20]. X-ray micro computed tomography (Micro CT) was used to evaluate air-void properties of the same concrete mixtures (samples not exposed to freeze-thaw cycles). Micro CT- scanner was (Phoenix Nanotom, Boston, MA, USA), with digital GE DXR detector, and 3-D reconstruction was carried out with the software Phoenix datos|x 2.0. Core samples for air-void analysis (23 mm tall and 20 mm in diameter) were scanned with the voxel resolution of 10 µm, and the voltage and current of 140 kV and 170 µA respectively. The image analysis was performed with open source ImageJ [21], and there were two different approaches applied for calculating the air-void content for comparison of results. The first approach consisted of 2-D images equally spaced, 1 mm apart along the entire image stack (Figure 1 image 1.b). The assumption was made that air voids are not larger than 1 mm in vertical direction. For quantification of air void parameters; air content, spacing factor, specific surface, the linear-traverse method (ASTM C457 and EN 480-11) [14, 22], was downsized as shown in the Figure 1, (images 1.c through 1.f). The second approach was based on converting the entire stack of 1100 images into binary images and applying a threshold, black value for voids (0 GV) and white for everything else (256 GV). The area of voids was calculated as per each 2D image, and they were generated throughout the entire height of the image stack, 3D (see Figure 1, images 2.a through 2.d).

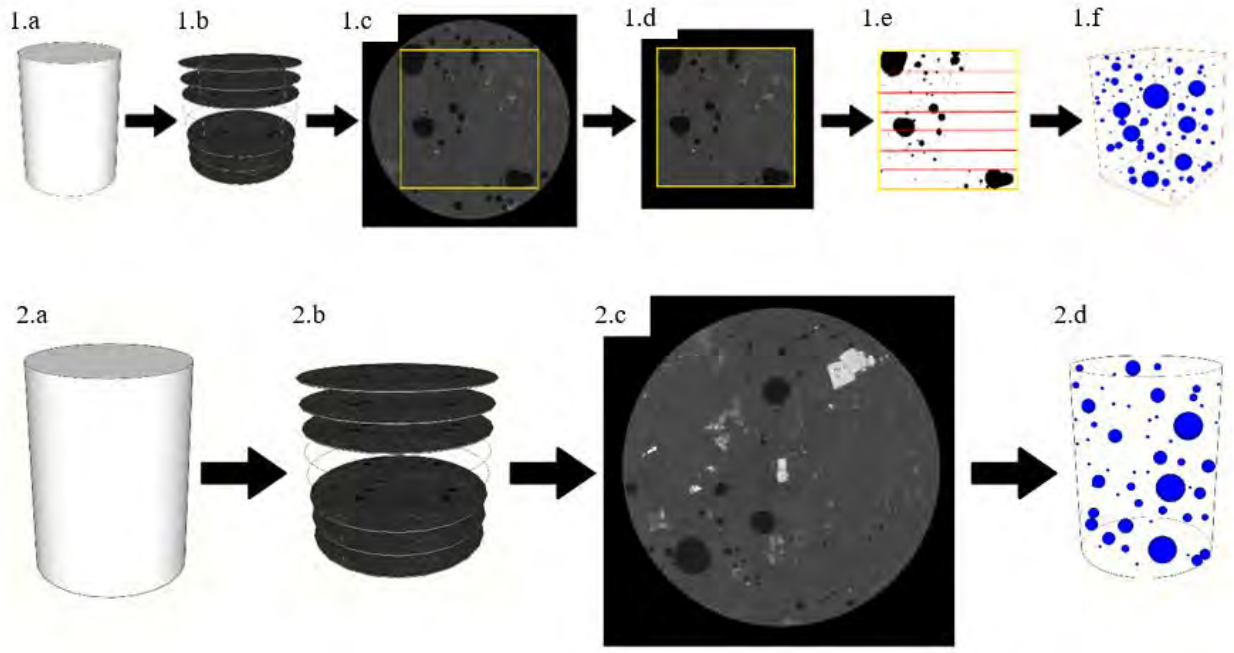

Figure 1: Approach 1.a-f: Downsized linear traversed method (2D), Approach 2.a-d: Threshold method of entire stack (3D). [23 24]

3. RESULTS AND DISCUSSION

3.1 Freeze-thaw resistance and dynamic modulus

The mass loss and durability factor are presented in Table 3. The mass loss was less than 1% for all concretes except for CM (1.6%). The durability factor was above 90% for all six concretes (0.9 for CM, and 0.94 for S-40 and G-40). The results indicate there was negligible deterioration of specimens, partly due to entrained air of ~6%. Although, it is widely recognized that air-entrainment enhances the freeze–thaw resistance of concrete, it was observed that the mixes with the highest cement replacement of 40% by S and GGP showed the highest durability factor and least mass loss of concrete (0.56, and 0.52 for S-40 and G-40 respectively).

Table 3: Durability properties.

	CM	G-20	G-30	S-40	G-40	FA-30
Mass Loss %	1.58	0.75	0.6	0.56	0.52	1.01
Durability factor	0.90	0.920	0.93	0.94	0.94	0.91

3.2 Air-void analysis of hardened concrete using x-ray computed tomography

Air content of fresh concrete and air-void content of hardened concrete by both approaches were compared for all six concrete mixtures and summarized in Figure 2. The difference in results could be due to numerous reasons, a slightly different geometry of a sample considered for calculating air content, or in the case of a linear traverse method it is possible that human error can likely occur. The Threshold method of an entire stack did not account for any voids smaller than 50 µm, while the linear traverse method did. The linear traverse method applied through micro CT-scan is a tedious procedure and it is difficult to make a decision as to whether the air voids are smaller than 50 µm, so it is easier to account for all of them. Therefore, it is reasonable that the linear traverse method gives a slight overestimation of the air void content [24].

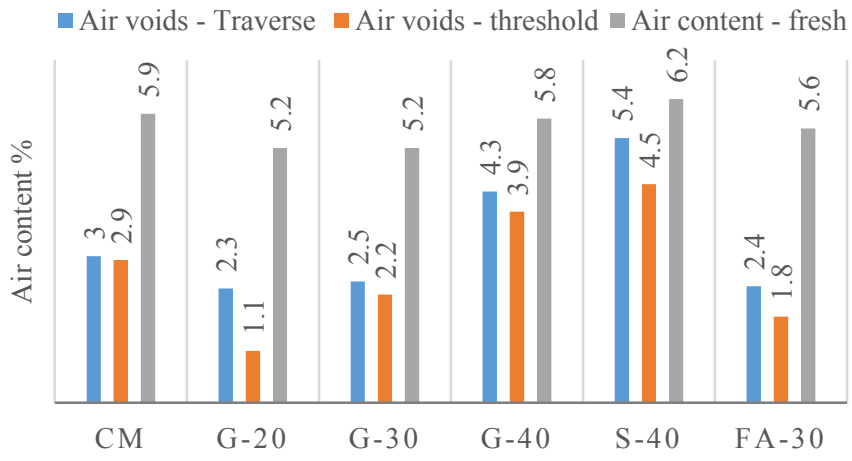

Figure 2: Summary of air void content obtained with different methods.

The spacing factor L (mm) is presented in Figure 3, and shows that all concretes had smaller than 0.3 mm except for CM (0.45 mm). Both S-40 and G-40 had the spacing factor smaller than recommended 0.2 mm (0.15 mm and 0.19 mm, respectively). Results for specific surface α, are presented in Figure 4. CM had only 11.9 1/mm, while S-40 had 26.2 1/mm. Both G-20 and FA-30 had ~21 1/mm, while G-30 and G-40 measured ~24 1/mm. The linear traverse method, showed negligibly higher percent air void content than the approach completely based on Threshold of an entire stack (see Figure 2). From the air void analysis it was also demonstrated that G-40 and S-40 showed the most desirable parameters prescribed for freeze–thaw resistant concrete as measured by spacing factor smaller than 0.2 mm and specific surface greater than 24 1/mm [13]. According to this study 40% GGP replacement showed that it is as successful as 40% S to improve the FT resistance of concrete, by maintaining a recommended spacing factor and specific surface which are crucial parameters.

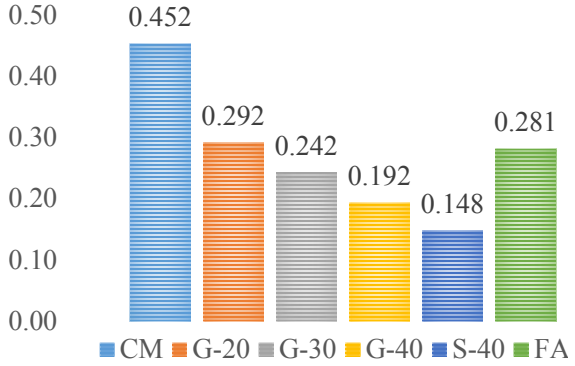

Figure 3: Spacing factor of all concretes L (mm)

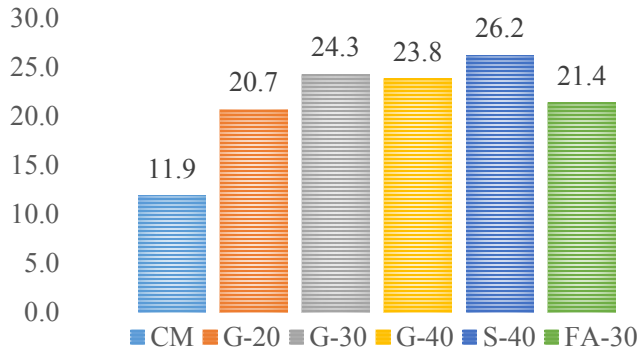

Figure 4: Specific surface of all concretes α (1/mm)

4. CONCLUSION

This study is a succinct summary [24] of an assessment of the freeze–thaw resistance of concretes containing cement replacement by GGP of up to 40% by weight, and comparing the performance with fly ash and slag. Macroscopic properties such as air content of fresh concrete, mass loss, and durability factor were attained through standard ASTM methods. The air void properties of hardened concretes that were not exposed to freeze-thaw cycles, were evaluated with X-ray computed tomography, and the image analysis was performed with ImageJ. Based on the combined macro and micro-evaluations of concretes with GGP in this study, the following conclusions can be drawn:

- A mass loss of ~1%, and durability factor of above 90%, for all concretes except for CM, indicated improved freeze–thaw resistance with increased cement replacements by GGP regardless to air-entraining agent, due to its pozzolanic activity, and perhaps consuming more CH for C-S-H formation.

- Using GGP as an alternate SCM, serves as nucleation for air bubbles due to its angular particle shape and finer particle size than CM, and subsequently its larger specific surface area. With higher cement replacement with GGP, spacing factor decreases and specific surface increases, which are favorable for FT resistance.
- The air void analysis by micro CT-scan coupled with ImageJ can be successfully utilized for evaluating the microstructure of cementitious materials. It is a nondestructive method, and it can provide 3D information that is especially useful for air void analysis. This method requires minimum sample preparation, unlike the standard method ASTM C457; however, it has a limitation on a sample size.

ACKNOWLEDGEMENTS

We gratefully acknowledge the collaboration and supply of commercial GGP *Pozzotive* by Urban Mining Northeast. We thank the contributions and input from Building Product Ecosystems, LLC. We appreciate the generous help and guidance from the technical team at the Microab at Delft University of Technology in the Netherlands. We also thank the DURST Organization for partial funding of the project.

REFERENCES

[1] Roston E.; and Migliozzi, B. "Obama's EPA Rule Is Redrawing the U.S. Coal Map," *Bloomberg New Energy Finance-US coal retirements database*, 2015: http://www.bloomberg.com/graphics/2015-coal-plants/.

[2] Sheikh, V. Limited Availability of Cementitious Materials Could Impact the Value Chain. *Appl. Sci. Sustain. Coal Ash* **2018**, 34–36.

[3] Ober, J.E. U.S. Geological Survey, "Mineral Commodity Summaries," 2017: https://www.usgs.gov/centers/nmic/arsenic-statistics-and-information#mcs.

[4] Kamali, M.; Ghahremaninezhad, A. An investigation into the hydration and microstructure of cement pastes modified with glass powders. *Constr. Build. Mater.* **2016**, *112*, 915–924.

[5] Krstic, M.; Davalos, J.F. Field application of recycled glass pozzolan for concrete. *ACI Mater. J.* **2019**, *116*, 123–131.

[6] Krstic, M.; Davalos, J.F. Macro-and Micro-structure Evaluations of Recycled Post-consumer Glass Cementitious Material for Concrete. In *Proceedings of the Interdisciplinary Approaches for Cement-based Materials and Structural Concrete: Synergizing Expertise and Bridging Scales of Space and Ti*me; Miguel, A., Dirk Schlicke, F.B., Jędrzejewska, A., Eds.; RILEM Publications: Madeira Island, Portugal, 2018; pp. 261–266.

[7] Kaminsky, A.; Krstic, M.; Rangaraju, P.; Hamou, A.T.; Thomas, M. Ground-Glass Pozzolan for Use in Concrete, Members of ASTM Subcommittee C09.24 summarize industry context behind new ASTM standard specification. *Concr. Int.* **2020** *42*, 24-32.

[8] Pawlowicz, J. Evaluation of Air Entraining Behaviour in Concrete Using Computer Aided Methods on Hardened Samples. Master's Thesis,TU Delft University, Delft, The Netherlands, 2019.

[9] Hanjari, K.Z.; Utgenannt, P.; Lundgren, K. Experimental study of the material and bond properties of frost-damaged concrete. *Cem. Concr. Res.* **2011**, *41*, 244–254.

[10] Neville, A.M. *Properties of Concrete*; Pearson Education Limited: London, UK, 2011; ISBN 978-0-273-75580-7.

[11] Shang HS, S.Y. Experimental study of strength and deformation of plain concrete under biaxial compression after freezing and thawing cycles. *Cem. Concr. Res.* **2006**, *36*, 1857–1864.
[12] Gagne; R *Science and Technology of Concrete Admixtures*; Elsevier: Amsterdam, The Netherlands, 2016; ISBN 9780081006931.
[13] Saucier, F., Pigeon, M., Cameron, M. Air-void stability-part V: Temperature, general analysis, and performance index. *ACI Mater. J.* **1991**, *88*, 25–36.
[14] ASTM C 457-12 Standard Test Method for Microscopical Determination of Parameters of the Air-Void System in Hardened Concrete 1. *ASTM Int.* **2013**, *05*, 15 pages.
[15] Peterson, K.W.; Anzalone, G.C.; Nezami, S.; Oh, C.Y.S.; Lu, H. Robust Test of the Flatbed Scanner for Air-Void Characterization in Hardened Concrete. *J. Test. Eval.* **2016**, *44*, 20140432.
[16] Kim, K.Y.; Yun, T.S.; Choo, J.; Kang, D.H.; Shin, H.S. Determination of air-void parameters of hardened cement-based materials using X-ray computed tomography. *Constr. Build. Mater.* **2012**, *37*, 93–101.
[17] Lanzón, M.; Cnudde, V.; De Kock, T.; Dewanckele, J. X-ray microtomography (μ-CT) to evaluate microstructure of mortars containing low density additions. *Cem. Concr. Compos.* **2012**, *34*, 993–1000.
[18] Omran, A.; Tagnit-hamou, A. Performance of glass-powder concrete in field applications. *Constr. Build. Mater.* **2016**, *109*, 84–95.
[19] *ASTM C215*; *Standard Test Method for Fundamental Transverse, Longitudinal, and Torsional Resonant Frequencies of Concrete Specimens,* ASTM: West Conshohocken, PA, USA, 2015; volume 4.02, 7 pages.
[20] *ASTM C666*; *Standard Test Method for Resistance of Concrete to Rapid Freezing and Thawing* ASTM: West Conshohocken, PA, USA, 2015.
[21] Rueden, C.T.; Schindelin, J.; Hiner, M.C.; DeZonia, B.E.; Walter, A.E.; Arena, E.T.; Eliceiri, K.W. ImageJ2: ImageJ for the next generation of scientific image data. *BMC Bioinformatics* **2017**, *18*, 1–26.
[22] NEN-EN 480-11, Admixtures for concrete, mortar and grout- Test methods Part 11: Determination of air void characteristics in hardened concrete. TU Delft, The Netherlands,**2005**; Volume 11, European Committee for Standardization, Brussels, Belgium, 25 pages.
[23] Krstic, M. Macro- and Micro-structure Evaluations and Field Applications of Concrete with Recycled Glass. Ph.D. Thesis, The CIty College of New York: CUNY, New York, NY, USA, 2020.
[24] Krstic, J. F. Davalos, E. Rossi, Stefan C. Figueiredo, O. Copuroglu, "Freeze-Thaw Resistance and Air-Void Analysis of Concrete with Recycled Glass – Pozzolan Using X-Ray Micro Tomography," MDPI Materials Journal, (2021)

A PROBABILISTIC APPROACH FOR ESTIMATING CORROSION POSSIBILITY OF REINFORCED CONCRETE STRUCTURE CONSIDERING CRACK DEVELOPMENT

Tiao Wang (1)*, Yao Luan(2)

(1) Department of Civil Engineering, School of Engineering, The University of Tokyo, 7-3-1 Hongo, Bunkyo-ku, Tokyo, 113-8656, Japan.

(2) Civil and Environmental Engineering, Saitama University, Saitama, 338-8570, Japan

Abstract

Reinforcement corrosion induced by chloride ingress is one of the major threats of reinforced concrete (RC) structures exposed to chloride attack. The cracks of concrete cover provide additional paths of chloride ingress and facilitate the reinforcement corrosion. Current information regarding the influence of crack development on corrosion possibility is insufficient due to lack of proper analytical approach. On this account, a rapid numerical approach (RNA) is developed in this study to study the chloride ingress of cracked concrete. It could consider the crack development and chloride biding effect. This approach is validated through comparisons with the FEM analysis. Based on this approach, it becomes feasible to estimate the corrosion possibility of cracked RC structures.

Keywords: Chloride content; Crack Development; Rapid numerical approach; Corrosion possibility

1. INTRODUCTION

Reinforcement corrosion induced by chloride ingress is one of the principle threats of reinforced concrete (RC) structures exposed to marine environments. Concrete structures undergo continuous deterioration due to combined environmental and loading actions from concrete mixing, such as thermal- or shrinkage -induced cracking. These cracks provide additional diffusion path of chloride ingress and facilitate the reinforcement corrosion [1-5]. On the other hand, the microstructure of cement matrix become denser because of continuous hydration [6, 7]. The cement matrix also chemically absorbs free chloride as Friedel's salt and bound chloride of the diffuse layer of calcium-silicate-hydrate (C-S-H) gel [8, 9]. These two effects enhance the chloride resistance of concrete and suppresses the corrosion possibility of RC structures. Considerable efforts have been made to study these two effects during last decades [1-5, 8, 9]. However, there is little information regarding the influence of cracks and

chloride binding on the corrosion failure time of RC structures. More importantly, chloride ingress of concrete structure involves a lot of uncertainties and randomness, which arise from the variability of material properties (e.g. the diffusion coefficient); the variability of structure geometry (e.g. concrete cover) and the random nature of the marine environment (e.g. the surface chloride content). It is therefore more reasonable to adopt a probabilistic approach to estimate the corrosion failure time of RC structures. Finite element method (FEM) is a possible way to solve these problems. However, probabilistic analysis usually needs millions of samples (e.g. Monte Carlo simulation) to obtain convergent results, which makes the FEM is actually inapplicable. Engineering practices therefore demand a method to optimize design method and maintenance strategy of RC structures. An explicit diffusion solution of two-layer material had been developed in previous study [5, 10]. Based on this two-layer diffusion solution, this study presents a rapid numerical approach (RNA) for estimating the corrosion possibility of cracked RC structures. This approach could consider the crack development and chloride biding effect. This approach is validated through comparisons with the FEM analysis. A case study of an actual structure will be presented in the end of this paper.

2. EXPLICIT DIFFUSION SOLUTION OF TWO-LAYER MATERIAL

Figure 1 shows the diffusion model in a two-layer material. The thicknesses of first layer and second layer are h_1 and h_2, respectively, and their diffusion coefficients are $D_{t_0,1}$ and $D_{t_0,2}$ at age of t_0, respectively.

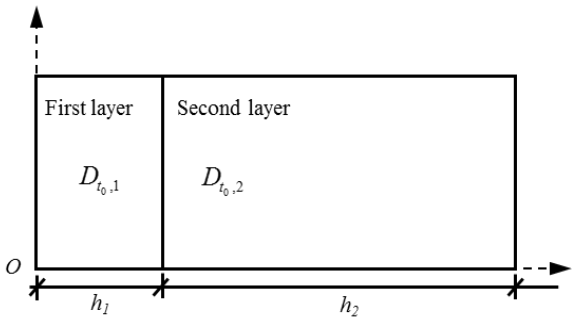

Figure 1: Diffusion model of two-layer material

$$\frac{\partial C(x,T)}{\partial T} = D_{t_0,1}\frac{\partial^2 C(x,T)}{\partial x^2} \text{ for } 0 \le x \le h_1 \tag{1}$$

$$\frac{\partial C(x,T)}{\partial T} = D_{t_0,2}\frac{\partial^2 C(x,T)}{\partial x^2} \text{ for } h_1 \le x \le h_1 + h_2 \tag{2}$$

where $C(x,T)$ is the chloride profile; x is the interested concrete depth; and T is the interested exposure time.

An explicit solution for two-layer material was developed in previous study [5, 10].

$$C(x,T) = C_T^{x=0} + \sum_{n=1}^{\infty} A_n' f_n(x,\lambda_n)\exp(-\lambda_n^2 T) \tag{3}$$

where $C_T^{x=0}$ is the surface chloride content; and $f_n(x,\lambda_n)$ is defined as

$$f_n(x,\lambda_n)=\begin{cases}\dfrac{\cot\left(\lambda_n h_2/\sqrt{D_{t_0,2}}\right)}{\sin\left(\lambda_n h_1/\sqrt{D_{t_0,1}}\right)}\sin\left(\lambda_n x/\sqrt{D_{t_0,1}}\right) & 0\le x\le h_1\\ \dfrac{1}{\sin\left(\lambda_n h_2/\sqrt{D_{t_0,2}}\right)}\cos\left[\lambda_n\left(x-h_1-h_2\right)/\sqrt{D_{t_0,2}}\right] & h_1\le x<h_1+h_2\end{cases} \tag{4}$$

A_n' is determined by Eq. (5)

$$A_n'=\int_0^{h_1+h_2}[\bar{C}(x)-C_T^{x=0}]f_n(x,\lambda_n)dx\Big/\int_0^{h_1+h_2}f_n^2(x,\lambda_n)dx \tag{5}$$

where $\bar{C}(x)$ is the exited chloride content; and

$$\begin{aligned}\int_0^{h_1+h_2}f_n^2(x,\lambda_n)dx=&\frac{\cot^2\left(\lambda_n h_2/\sqrt{D_{t_0,2}}\right)}{2\sin^2\left(\lambda_n h_1/\sqrt{D_{t_0,1}}\right)}\left[h_1-\frac{\sqrt{D_{t_0,1}}}{2\lambda_n}\sin\left(\frac{2\lambda_n h_1}{\sqrt{D_{t_0,1}}}\right)\right]\\&+\frac{1}{2\sin^2\left(\lambda_n h_2/\sqrt{D_{t_0,2}}\right)}\left[h_2+\frac{\sqrt{D_{t_0,2}}}{2\lambda_n}\sin\left(\frac{2\lambda_n h_2}{\sqrt{D_{t_0,2}}}\right)\right]\end{aligned} \tag{6}$$

Characteristic roots λ_n are determined by Eq. (7)

$$\tan(\lambda_n h_1/\sqrt{D_{t_0,1}})\tan(\lambda_n h_2/\sqrt{D_{t_0,2}})=\sqrt{D_{t_0,1}/D_{t_0,2}} \tag{7}$$

3. RAPID NUMERICAL APPROACH FOR CRACK DEVELOPMENT, CHLORIDE BIDING AND

3.1 Simulation approach of crack development

The concrete cover always cracks due to combined loading and environmental actions. These cracks facilitates the chloride ingress by two effects : (1) developing crack length (e.g. Figure 2 (a)) ; and (2) increasing diffusion coefficient of cracked concrete (e.g. D_1 in Figure 2 (b)).

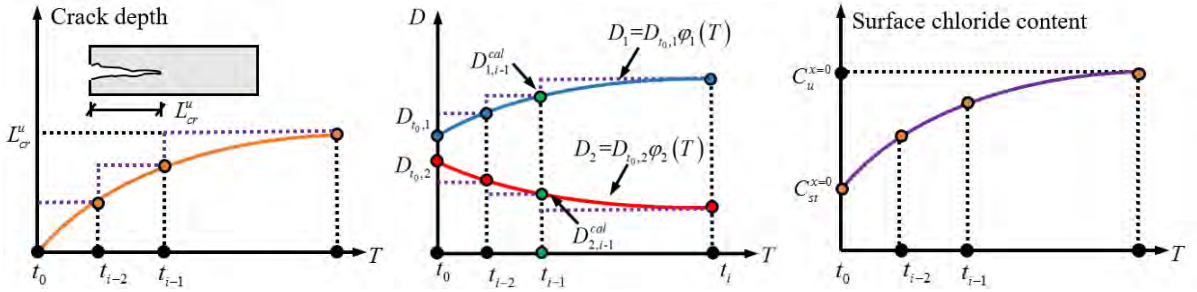

(a) Crack length (b) Diffusion coefficients (c) surface chloride content

Figure 2: Crack development model and simulation approach

To simulate these two effects, a feasible and practical way is to approach the crack length development and increasing diffusion coefficients with the step functions, as shown in Figure 2 (b). Since the crack length and chloride diffusion coefficient are approximated as a constant

in each step, the analytical solution is approached to accurate result as the number of steps increases.

3.2 Simulation approach of time-dependency of uncracked concrete

As mentioned previously, the porosity and chloride diffusion coefficient of uncracked concrete decreases as cement hydration proceeds. The diffusion properties of uncracked concrete shows opposite trend of cracked concrete. This effect should be considered. Because the time-dependency of crack length and diffusion coefficient of cracked concrete are simulated by step functions, the same approach can be used for uncracked concrete as well (e.g. D_2 in Figure 2 (b)).

3.3 Simulation approach of time-dependency of surface chloride content

Considerable researches reported that the surface chloride content is time-dependent as well. Like the crack length and chloride diffusion coefficient, the surface chloride content is approximately represented with the step function with the same time steps, as shown in Figure 2 (c).

3.4 Simplified chloride binding model

Liu et al. [11] proposed a simplified model for chloride binding effect. They assumed the the varication of total chloride C_t along depth is same as the variation of free chloride C_f . Therefore, the chloride binding effect can be considered by an apparent diffusion coefficient (i.e. Eq. (8))

$$D^* = \frac{D}{1+\partial C_b/\partial C_f} \tag{8}$$

where C_b is bound chloride. Liu et al. [11] further assumed that the binding ratio ϕ is constant (i.e. Eq. (9)) when the free chloride concertation is not high

$$\partial C_b/\partial C_f = \phi \tag{9}$$

Thus, the apparent diffusion coefficient can be determined by Eq. (10)

$$D^* = D/(1+\phi) \tag{10}$$

4. VALIDATION OF THE PROPOSED NUMERICAL APPROACH

To validate this rapid numerical approach (RNA) for predicating the chloride ingress for cracked concrete, 4 case studies were carried out in this study. The time-dependency of cracked concrete and uncracked concrete are described by power functions (Eqs. (11) and (12)). The surface chloride content is described by Eq. (13). The crack developments are described by 10 points step function (e.g. Figure 3 (b)). All values of the parameters used in the analyses are summarized in Table 1.

$$D_1 = D_{t_0,1}\left(\frac{t_{st}+T}{t_0}\right)^{-\alpha_1} \tag{11}$$

$$D_2 = D_{t_0,2}\left(\frac{t_{st}+T}{t_0}\right)^{-\alpha_2} \tag{12}$$

$$C_T^{x=0} = C_{st}^{x=0} + C_u^{x=0}(1-e^{-\beta T}) \tag{13}$$

where $D_{t_0,1}$ and $D_{t_0,2}$ are the chloride diffusion coefficient of the cracked and uncracked concrete at age t_0 ; α_1 and α_2 are the time-dependent coefficients of cracked and uncracked concrete; t_0 is the curing age of specimens, t_{st} and t_{ex} are the initial and final exposure times ; and $C_{st}^{x=0}$ is the initial surface chloride content, $C_u^{x=0}$ is the ultimate surface chloride content, and β is the ageing factor of the surface chloride content.

Table 1: Values of parameters used for validation of RNA.

Case	L_{cr}^u (mm)	$D_{t_0,1}$ (mm²/d)	$D_{t_0,2}$ (mm²/d)	$C_{t_{st}}^{x=0}$ (%)	$C_u^{x=0}$ (%)	α_1	α_2	β	ϕ	t_0 (d)	t_{st} (d)	t_{ex} (year)
C1	8.0	2.5×10^{-2}	2.5×10^{-2}	2.0	3.5	-0.20	0.25	0.25	0.15	120	180	30
C2	8.0	2.0×10^{-2}	2.0×10^{-2}	2.0	3.5	-0.15	0.20	0.20	0.18	100	180	40
C3	8.0	2.0×10^{-2}	2.0×10^{-2}	1.5	3.5	-0.20	0.20	0.15	0.18	90	180	50
C4	8.8	2.0×10^{-2}	2.0×10^{-2}	1.5	3.5	-0.20	0.20	0.15	0.18	90	180	50

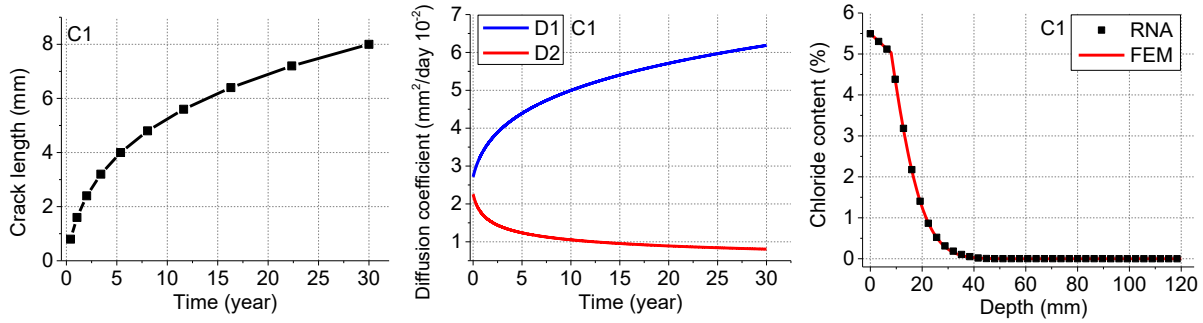

(a) Crack length (b) Diffusion coefficients (c) comparison

Figure 3: Verification of simple case C1

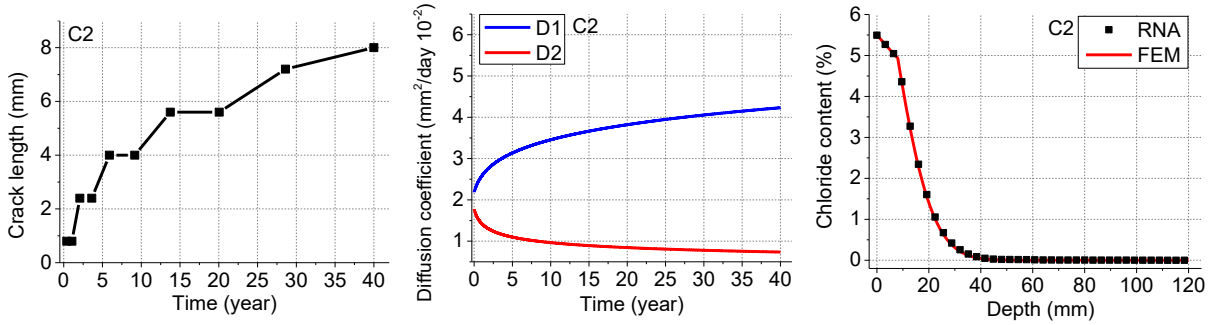

(a) Crack length (b) Diffusion coefficients (c) comparison

Figure 4: Verification of simple case C2

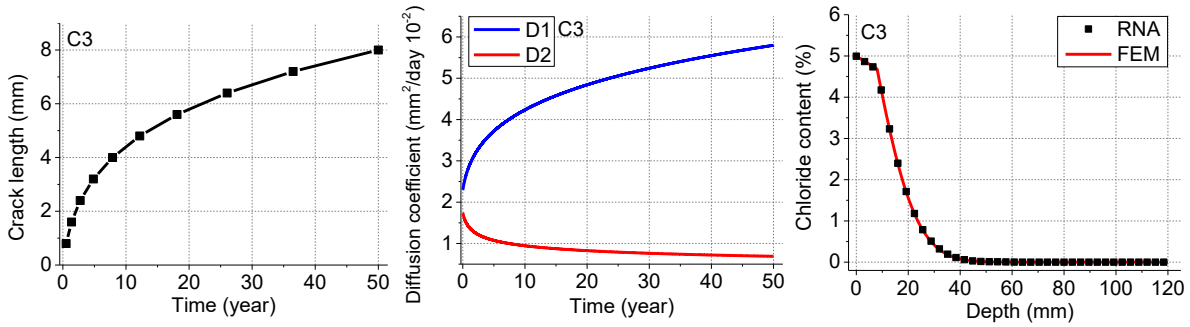

(a) Crack length (b) Diffusion coefficients (c) comparison

Figure 5: Verification of simple case C3

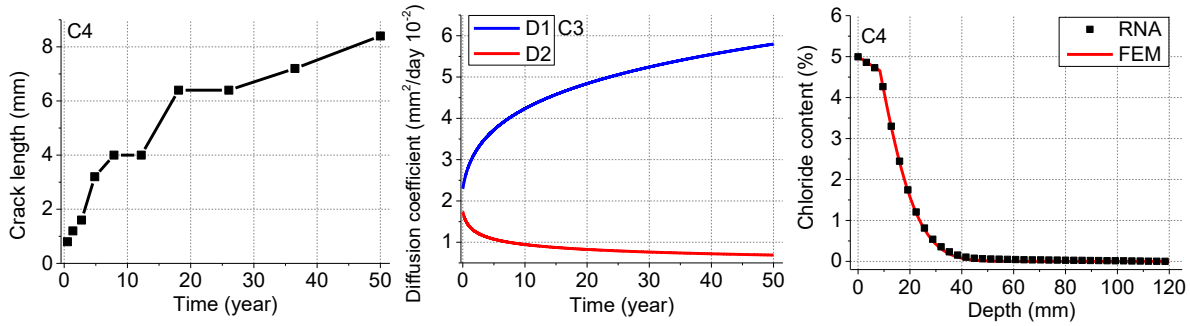

(a) Crack length (b) Diffusion coefficients (c) comparison

Figure 6: Verification of simple case C4

The crack length development of these four cases are shown in Figure 3~6 (a). The time-dependencies of diffusion coefficient are shown in Figure 3~6 (b). Both are simulated by 10 steps. The analytical prediction is compared with the FEM [24], where the element length and the time step are 0.4 mm and 0.1 day, respectively. Figure 3~6 (c) shows the comparisons between the result of RNA and FEM. The number of characteristic root and the interval of depth is 10 and 0.4 mm, respectively. A perfect agreement is presented between them, which validate the reliability of the proposed numerical approach. The computation times of RNA and FEM are shown in Table 2. The computation time enormously decreases (e.g. almost one-hounded thousand times in case C4). It makes the probabilistic estimation of corrosion failure time of RC structures feasible.

Table 2: Comparison of computation time for FEM and RNA.

Time (s)	C1	C2	C3	C4
FEM	8602	20099	23702	23689
RNA	0.2543	0.2651	0.2475	0.2567
Comparison	3.38×10^4	7.58×10^4	9.58×10^4	9.23×10^4

5. A CASE STUDY OF AN ACTUAL CONCRETE STRUCTURES

A case study of an actual port is conducted to show the application of RNA on predicting the corrosion possibility of cracked RC structure. This port structure is located at Shenzhen City, Mainland China and exposed to a severe marine environment. The concrete cover depths were extensively measured and the statistical information is shown in Figure 7 (a). The

parameters used for simulation are summarized in Table 3. The effects of the chloride binding effect and crack development are investigated. The number of time steps and characteristic roots are both 10. The interval of depth is 1 mm. The sample size of Monte-Carlo simulation is two million and the calculation were completed in 12 hours.

Figure 7 are analysis results of corrosion possibility of cracked concrete structures. Figure 7 (b) studies the influence of crack development on the corrosion possibility. The crack length increases $L_{cr}^{u}/10$ every ten year (L_{cr}^{u} is the ultimate crack length). The corrosion possibility increases as the ultimate crack length L_{cr}^{u} increases and degradation ratio of diffusion coefficient α_1 increases. Comparing to the ultimate crack length, the degradation ratio of diffusion coefficient has more significant effect on the corrosion possibility. Figure 7 (c) shows the chloride binding effect. The corrosion possibility decreases as the chloride biding effect increases. It shows that chloride binding effect cannot be ignored. It should be noted that the chloride binding effect is considered by a simplified model in this study. More accurate model should be developed in the future to study the chloride binding effect. In conclusion, this proposed rapid numerical approach can be used to study the corrosion possibility of cracked RC structures.

Table 3: Parameters for Monte Carlo simulation.

Parameter	Mean	COV	Distribution
Ultimate crack length (mm)	0, 10, 20	0.10	Lognormal distribution
Concrete cover (mm)	61.49mm	0.17	Normal distribution
Binding ratio ϕ	0, 0.10, 0.15	0.10	Normal distribution
$D_{t_0,1}$ (mm²/day)	0.20	0.20	Normal distribution
$D_{t_0,2}$ (mm²/day)	0.20	0.20	Normal distribution
α_1	-0.25	0.20	Normal distribution
α_2	0.2	0.20	Normal distribution

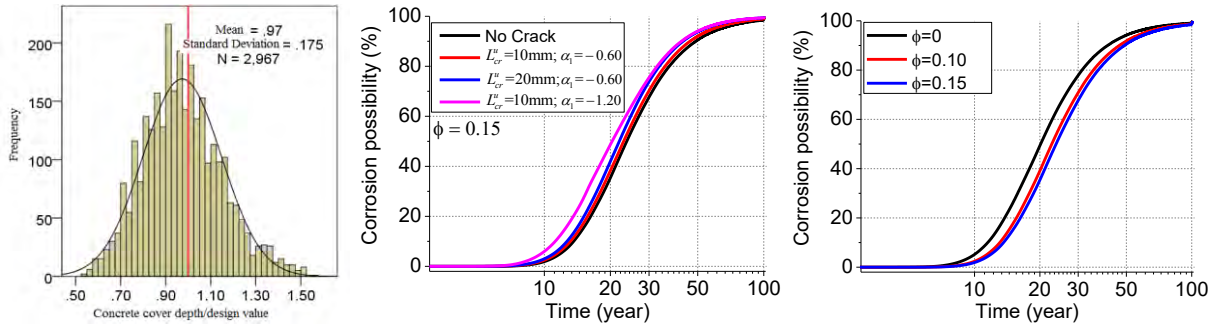

(a) Concrete cover depth (b) Crack development (c) Chloride binding

Figure 7: Corrosion possibility of concrete port

6. CONCLUSION

A rapid numerical approach is developed for the chloride diffusion of cracked concrete. In this approach, the crack development and chloride binding ratio are both taken into account. Based on numerical results, it has been confirmed that the RNA is in excellent agreement with

the FEM for simple and complicated cases. More importantly, the RNA can improve the computational efficiency enormously. With the RNA, the Monte-Carlo simulation can be implemented to estimate the corrosion possibility of cracked RC structures in marine environments. The analysis results show the crack development and chloride biding both have significant influence on the corrosion possibility.

ACKNOWLEDGEMENTS

The authors are grateful for the financial support from Japan Society for the Promotion of Science (Project code: 19K15059).

REFERENCES

[1] Prezzi M., P.J Geyskens and P. Monteiro, "Reliability approach to service life prediction of concrete exposed to marine environments", *ACI Mater.* 93(6) (1996) 544-552.

[2] Saad, A. "Effectiveness of concrete surface treatment materials in reducing chloride-induced reinforcement corrosion", *Constr Build Mater.* 1997, 11(7-8): 443-451.

[3] Val D.V. and Trapper P.A. "Probabilistic evaluation of initiation time of chloride-induced corrosion", *Reliab Eng Syst Safe.* 93(3) (2008) 364-372.

[4] Bertolini L., Elsener B., Pedeferri P., Redaelli E. and Polder R.B, "Corrosion of steel in concrete: Prevention, diagnosis, repair", John Wiley & Sons, 2013.

[5] Dai J. and Wang T. "Probabilistic model for service life prediction of water repellent rc structures in marine environments", Proceeding of the 7th Asia Pacific Young Researchers and Graduates SymposiumMalaysia, 2015.

[6] Pack, S.W., Jung M.S., Song H.W., Kim S.H., Ann K.Y. "Prediction of time dependent chloride transport in concrete structures exposed to a marine environment", *Cem. Concr. Res.* 40(2) (2010) 302-312.

[7] Maekawa K., Ishida T., Kishi T. "Multi-scale modeling of structural concrete", CRC Press, 2008.

[8] Tang L.P. and Nilsson L.O., "Chloride binding capacity and binding isotherms of opc pastes and mortars", *Cem. Concr. Res.* 23(2) (1993) 247-253.

[9] Shi Z., Geiker M.R., De Weerdt K., Østnor T.A., Lothenbach B., Winnefeld F. and Skibsted J. "Role of calcium on chloride binding in hydrated portland cement–metakaolin–limestone blends", *Cem. Concr. Res.* 95 (2017) 205-216.

[10] Wang T., Zheng J., Ishida T. and Dai J. "A rapid numerical approach for time-dependent chloride diffusion in surface-treated concrete", *Cem. Concr. Comp.(submitting)*.

[11] Liu J., Xing F., Dong B.Q., Ma H.Y. and Pan D. "New equation for description of chloride ions diffusion in concrete under shallow immersion condition", *Mater. Res. Innovat.* 18(sup2) (2014) S2-265-S262-269.

EARLY CRACKING OF CEMENTITIOUS MATERIALS BASED ON THE ECCENTRIC RING TEST

Cong Tian(1), Xiaosheng Wei(2)

(1) School of Civil and Hydraulic Engineering, Huazhong University of Science and Technology, Wuhan 430072, China

Abstract: An improved method based on the ring test called eccentric ring test is used to study the cracking of cementitious materials. The water-cement ratios were 0.25, 0.30, 0.35, 0.4 and the aggregate mass fractions were 10%, 30%, 50%, respectively. It was found that with the increase of water-cement ratio and aggregate, the cracking time of the sample will be prolonged. There will always be just one single complete-through crack in the pure cement paste sample. With further increase of the water-cement ratio and aggregate volume, there will be several fine and undeveloped cracks appearing symmetrically, from the thin sides to the thick sides. Humidity field simulation was accomplished by use of MATLAB and the simulation results showed that the isohume lines on the thinner sides of the sample are denser the thicker sides.
Keywords: the eccentric ring test, crack, humidity field, simulation.

1. INTRODUCTION

Concrete tends to crack at the early hydration age under the restraint condition. The test methods related to restraint cracking can be divided into three main categories: the uniaxial constraint tests[1-3], the flat plate tests[4-6]and the ring tests[7-9]. The ring test is a widely used test method, which can be used to test the problems of shrinkage cracking, cracking sensitivity, creep and stress relaxation of cement-based materials[10]. In recent years, the researches and applications of the ring test are endless and the traditional ring test has been studied quite well. Gao[11] considered the influence of the thickness of the inner steel ring on the cracking time which was obtained precisely by recording the hoop strain at different positions on the inner ring. Zachary[12] derived approximate solutions for internal relative humidity and tangential stress gradients considering viscoelastic and solidification effects comprehensively. The problem of the stress distribution in the ring shape concrete has been solved by Swamy[13] and Weiss[14]. However, there is still a big barrier for the ring test: the random distribution of cracks' positions. In order to eradicate these two problems, some improved tests are emerging: the elliptical ring test, the square-eccentric ring test and the eccentric ring test.

Zhou and Dong[15-16] found that the cracking time of cementitious materials could be shortened by use of the elliptical ring test. Zhu[17] made a preliminary comparison between the eccentric ring tests and the square-eccentric ring test. The double ring method was proposed by Weiss and colleagues[18]. In order to evaluate the volumetric deformation of the expanded paste, the inner and outer surfaces of the annular test piece were covered by a steel ring. At present, the development of the eccentric ring test and the elliptical ring test is still in the initial stage. The theoretical analysis and experimental standards of the two methods are not perfect enough, so they are only used by a small number of people.

This paper focuses on cracking caused by dry shrinkage of the cement surface based on the eccentric ring test. Some significant cracking indicators like cracking time, cracking position were included. The effects of w/c ratios and aggregate volume on the cracking time are demonstrated, as well as the crack pattern of the pure cement paste and the samples added aggregate. The humidity field simulation was accomplished by use of MATLAB to find out the relationship between the humidity diffusion and the cracking.

2. THE ECCENTRIC RING TEST

2.1 The mold of the eccentric ring test

Fig.1 shows the actual mold of the eccentric ring test. The mold consists of four parts: a metal base, two outer semi-circular metal rings for cement-based material setting, and a metal inner ring designed to provide restraint and one piece of metal strip. The thickness of the groove is same as the inner ring so that inner ring is fixed without any movement when paste is poured into the mold.

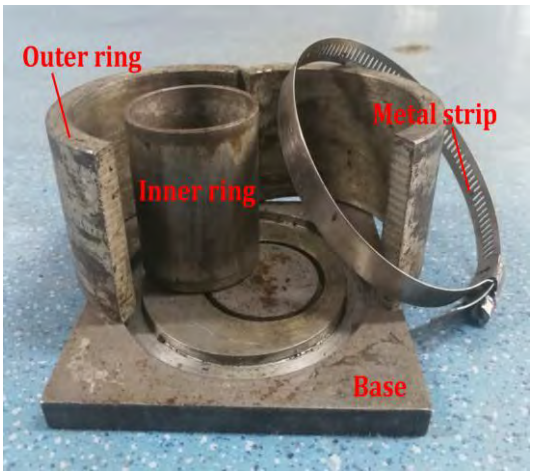

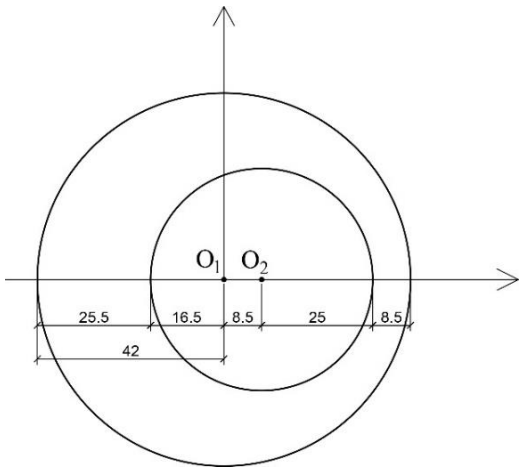

Figure 1: Actual mold of the eccentric ring test (left)
Figure 2: Plane dimensions of the mold (right)

Fig.2 shows the size of the device. Both the inner and outer rings have a height of 50 mm. Since the cracking positions are relatively fixed on the thinner sides, it is possible to focus on the part where the crack is to be generated, and a more accurate record can be made for the final cracking time. However, it should be noted that due to the thickness

limit of the thinnest part of the mold, the maximum plane size of the added aggregate should not exceed 8.5 mm.

2.2 Experimental materials and mixtures

Ordinary Portland Cement P•O42.5 was used in all the test groups, which met Chinese standard GB175-2007. Gravel with diameters of 5mm to 10mm was sieved to provide coarse aggregate. The density of gravel was 2.436g/cm^2. The tap water from the Wuhan Water Group was used in the mixing.

The ambient relative humidity (RH) was kept around 35%. For the convenience of referring to each experimental group hereinafter, the label P0.3-35 stands for the sample with water-cement ratio of 0.3 in RH of 35% and P0.4G30-35 refers to sample with water-cement ratio of 0.4 and aggregate mass fraction of 30% in RH of 35%. Other labels have similar meanings. 0.2% water reducer (naphthalene water reducer) was added to the samples with water-cement ratio of 0.25 to improve the workability of the cement paste. The environmental temperature was controlled at 20 ±2 °C. The amount of experimental mix and materials is shown in **Table.1**, where Ma is aggregate content.

Table 1: Experimental groups under different environmental humidity

Temperature	20±2℃	**Relative humidity(RH)**		35%	
Sample	**W/C**	**Cement/g**	**Water/g**	**Coarse aggregate/g**	**Ma**
P25-35	0.25(0.2%sp)	350	87.5	0	0%
P30-35	0.30	350	105	0	0%
P35-35	0.35	300	105	0	0%
P40-35	0.40	300	120	0	0%
P40G10-35	0.40	300	120	30	10%
P40G30-35	0.40	250	100	75	30%
P40G50-35	0.40	250	100	125	50%

2.3 Experiment procedures

The cement paste was put in standard curing room after the pouring into the mold to cure for 24-hours. Then the sample was taken out and outer ring was removed. Later when outer ring was detached from the sample, the side surface was exposed to the air. Some Vaseline or wax was applied on the top surface of the sample and the sample was considered to be in a circumferential drying condition. Four displacement meters were used to automatically record the shrinkage displacement of the samples. Four displacement curves of a sample can be obtained in a single experiment. The sudden change point of a shrinkage displacement curve corresponds to the cracking time accurately.

3. THE EXPERIMENTAL RESULTS

3.1 The cracking time

The cracking time in this paper is defined as the point at which the first crack is extending from top to bottom for the pure cement paste sample. For the sample added aggregate, there may be multiple cracks. The time point when the last crack appears was defined as the relative cracking time. **Fig.3** shows cracking time of different w/c ratios and aggregate volumes with 35%RH. It can be seen that all of the samples cracked within three days. For pure cement pastes, the cracking time is increasing with the increase of w/c. For samples with the same w/c, adding more aggregate can increase the cracking time.

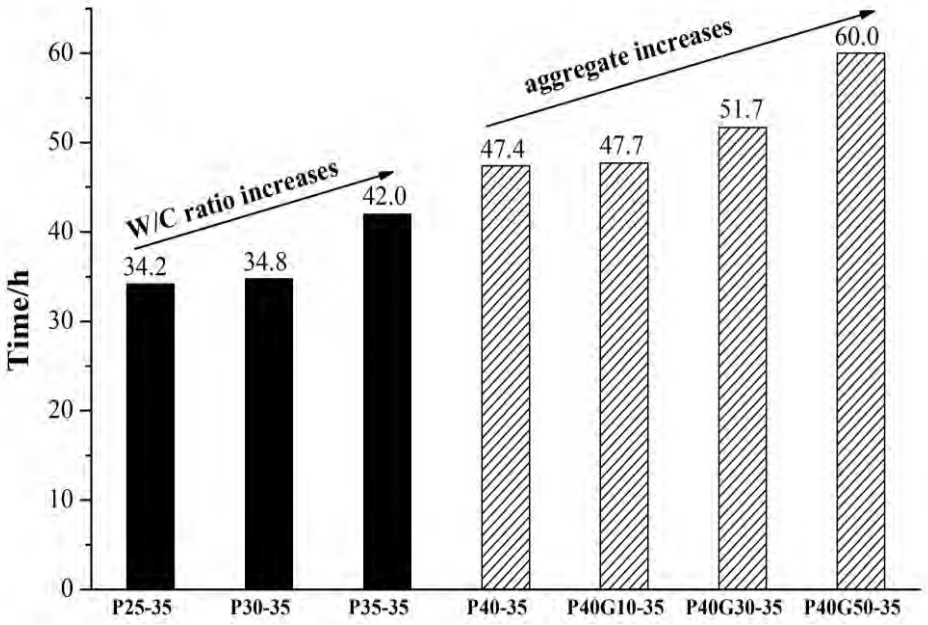

Figure 3: The cracking time with RH of 35%

In terms of humidity, the samples with low w/c ratios have more cement particles and the water is relatively less, so the shrinkage value during hydration is larger. More cement particles hydrating means more water will be consumed, which leads to a lower internal relative humidity. The dry shrinkage value of the sample with a lower w/c is larger. The samples with a low w/c ratio has bigger shrinkage and the internal stress is accumulated earlier under the condition of inner ring constraint, causing the low w/c samples cracking earlier. Adding aggregate reduces the total amount of cement, which in turn has an important effect on reducing porosity and reducing capillary stress, thereby reducing the overall drying shrinkage. Since the elasticity and the stiffness of aggregate is bigger than the cement matrix, the presence of aggregate can prolong the path that the cracks develop through, making the development of cracks is more difficult. Therefore, the aggregates have a beneficial effect on the resistance against cracks. Adding aggregates can affect the development of cracks and it prolongs the cracking time.

3.2 The difference between cracks in pure and aggregate cement paste

Fig.4 shows the morphology of cracks and the width of cracks in P30-35. **Fig.5** shows

the morphology of cracks and the width of cracks in P40G30-35. Pure cement samples tend to produce only one completely through crack from top to bottom. For samples added aggregate, the morphology of the crack depends on the w/c and the amount of aggregate. With the increase of the w/c and aggregate volume, there will be several fine and undeveloped cracks appearing symmetrically, from the thin side to the thick side. By using a 100x magnification microscope, it is easy to find significant differences between a straight crack and fine cracks in width. The width of a completely through crack can be as large as 0.12mm while a part-through crack is just 0.02mm.

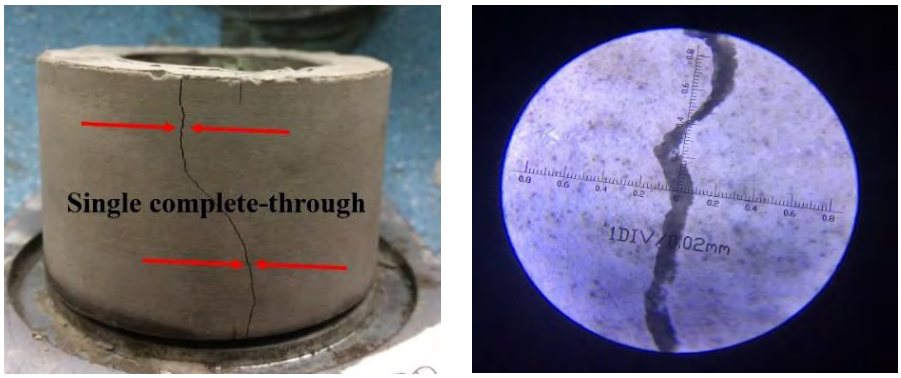

Figure 4: (a) Macroscopic crack in paste P30-35 (left), (b) Magnified crack in P30-35 (right)

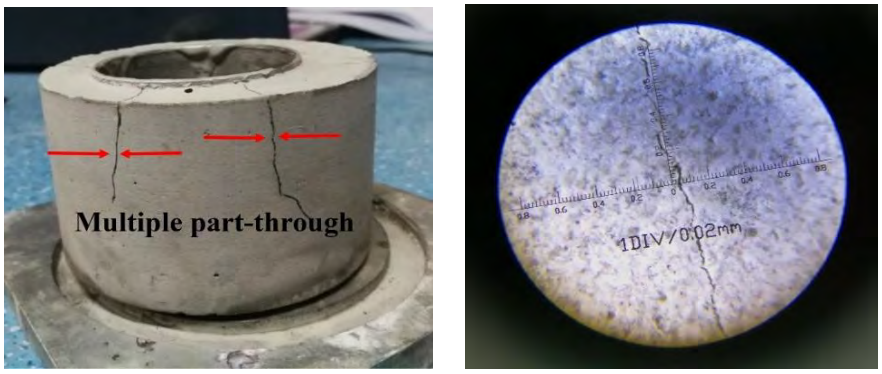

Figure 5: (a) Macroscopic cracks in concrete P40G30-35 (left), (b) Magnified crack in P40G30-35 (right)

The fine cracks in the samples with more aggregates are not easy to develop completely. Aggregates in concrete can be considered as intrinsic constraints. If the developing crack extends to a location where the proportion of aggregate is high, it is difficult for the cracks to continue to develop along its original path. Further, the presence of other cracks releases some of the strain energy, making the first crack more difficult to continue. As a result, more addition of aggregate is more likely to indicate smaller cracks.

4. HUMIDITY FIELD SIMULATION

The cracking in the eccentric ring test is mainly affected by the humidity exchange with the environment. The humidity diffusion coefficient D is of great importance in the humidity field. In this paper, the compressive strength is used to approximate the humidity diffusion coefficient. According to CEB-FIP (2010)[19], the relationship between humidity diffusion coefficient D and humidity h is:

$$D(h) = D_{sat}\left(\alpha + \frac{1-\alpha}{1+[(1-h)(1-h_c)]^n}\right) \tag{1}$$

where α, n, h_c are empirical coefficients, the specification recommends α= 0.05, n=15, h_c= 0.8, D_{sat} is the maximum value of the humidity diffusion coefficient D, h is the sample humidity. D_{sat} can be estimated by:

$$D_{sat} = \frac{D_0}{f_{ck}/f_{ck0}} \tag{2}$$

where D_0 is an empirical value of the humidity diffusion coefficient, f_{ck} can be calculated by average compression strength, f_{ck0}=10MPa. The differential governing equation describing the unsteady humidity field is:

$$\frac{\partial h}{\partial t} = D_x\frac{\partial^2 h}{\partial^2 x} + D_y\frac{\partial^2 h}{\partial^2 y} + D_z\frac{\partial^2 h}{\partial^2 z} \tag{3}$$

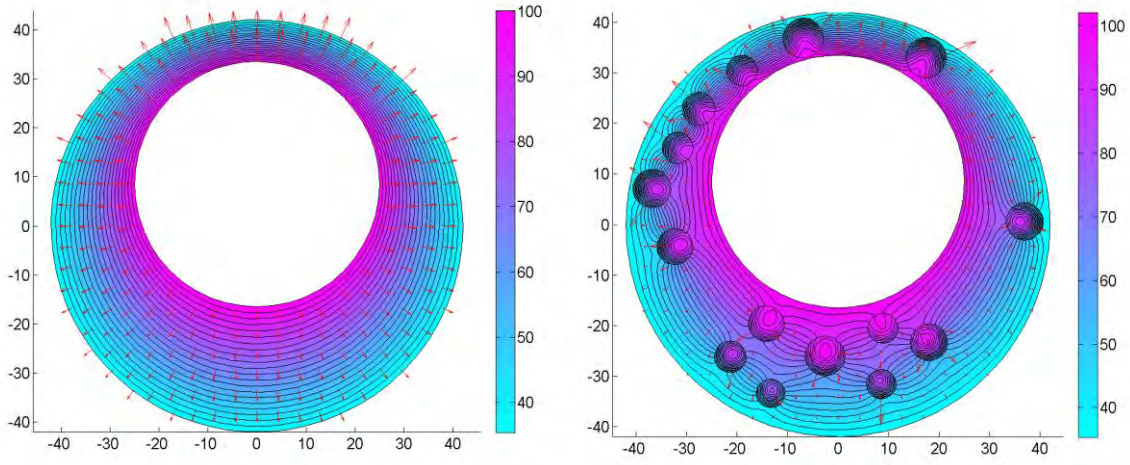

Figure 6: (a) Humidity diffusion in pure cement paste after 24 hours (left), (b) Humidity diffusion in the sample P40G30 after 24 hours (right)

Fig.6(a) is a simulation image based on the eccentric cross-section of the actual sample. When the ambient humidity is 35%, the water inside the sample spreads out, forming a lot of isohume (similar to isotherm). From the distribution of the isohume, the isohume on the thinner side of the sample is denser while the isohume on the thicker side of the sample is sparse. So the humidity gradient in the thinner side is bigger. It can be inferred that the intensity of the isohume and the locations of the crack are related. The big humidity gradient indicates a big shrinkage strain[20]. Therefore, the intensity of the isohume lines is positively related to the probability of cracking. That means the thinner

side is more likely to crack in the condition of drying shrinkage.

Fig.6(b) shows the humidity diffusion process in the samples added aggregate. It can be seen from the figure when the humidity is diffusing around the aggregate, the humidity diffusion process begins to become uneven. Due to the low moisture diffusion coefficient of the aggregate, the moisture in the aggregate diffuses slowly so that the relative humidity beneath the aggregate is lower than other parts on the same horizontal line.

5. CONCLUSIONS

Compared to the ring method, the biggest advantage of the eccentric ring test is that the cracking positions of the samples are easy to be determined. Setting a small eccentricity between the centers of the inner ring and the outer ring can artificially produce a large change in the thickness of the samples at different positions, thus creating a weak position in the thinner side and inducing the occurrence of the cracking. For the experimental groups added aggregate, the cracking time is determined by the amount of aggregate as well as the w/c. In this study, the following conclusions can be drawn through the eccentric ring experiment:

1. With the increase of water-cement ratio and aggregate, the cracking time of the sample will be prolonged.
2. A single completely through crack tends to appear on the thin side of the pure cement paste while several fine cracks are likely to appear symmetrically on the samples containing aggregate, depending on the volume of the aggregate, indicating that aggregate is beneficial in resisting the development of cracks.
3. The humidity simulation results show that the isohume on the thinner side of the sample is denser while the isohume on the thicker side of the sample is sparse.

ACKNOWLEDGMENT

This paper refers to some contents from published paper: Tian Cong, Wei Xiaosheng. Early shrinkage cracking of cementitious materials based on the eccentric ring method. Construction and Building Materials. 216(2019):599-611. The authors wish to express their gratitude and sincere appreciation to the National Natural Science Foundation of China (grant number 51778257).

REFERENCE

[1] Springenschmid R. Prevention of thermal cracking in concrete at early ages: state-of-the-art report presented by RILEM Technical Committee 119, Avoidance of Thermal Cracking in Concrete at Early Ages[M]. E & FN Spon, 2004.

[2] Xin J, Zhang G, Liu Y, Wang Z, Wu Z. Evaluation of behavior and cracking potential of early-age cementitious systems using uniaxial restraint tests: A review[J]. Construction and Building Materials. 231(2020):117146.

[3] Wei Y , Hansen W . Early-age strain–stress relationship and cracking behavior of slag cement mixtures subject to constant uniaxial restraint[J]. Construction and Building Materials, 2013, 49:635-642.
[4] Soroushian P , Ravanbakhsh S . Control of plastic shrinkage cracking with specialty cellulose fibers[J]. Aci Materials Journal, 1998, 95(4):429-435.
[5] Kraai P P. Proposed test to determine the cracking potential due to drying shrinkage of concrete. Concrete Construction - World of Concrete, 1985, 30(9), 775-778. [J]. Concrete Construction - World of Concrete. 30(9)(1985):775-778.
[6] Cai J, Li G, Yang C, Lin F. Tests on Unbonded Post-Tensioned Concrete Flat Plate with T-shaped Column Connections[J]. Advances in Structural Engineering. 2006,9(5):671-85.
[7] R.N. Swamy, A.K. Bandyopadhyay,H. Stavrides, The ring method of measuring restrained shrinkage in mortar and concrete, Cem. Concr. Aggregates, 1979, 1(1):13-20.
[8] Burrows R W. The visible and invisible cracking of concrete[M]. American Concrete Institute, 2012.
[9] Gao Y , Zhang J , Han P . Determination of stress relaxation parameters of concrete in tension at early-age by ring test[J]. Construction & Building Materials, 2013, 41:152-164.
[10] Kanavaris F, Azenha M, Soutsos M, Kovler K. Assessment of behaviour and cracking susceptibility of cementitious systems under restrained conditions through ring tests: A critical review[J]. Cement and Concrete Composites. 2019, 95:137-53.
[11] Gao Yuan, Zhang Jun. Evaluation of Cracking Behavior of Concrete at Early-Age Based on Ring Test[J]. Journal of Building Materials. 2012, 15(5):618-623.
[12] Grasley, Zachary C, D'Ambrosia, Matthew D. Viscoelastic properties and drying stress extracted from concrete ring tests[J], Cement and Concrete Composites. 2011, 33(2):171-178.
[13] S. Timoshenko. Strength of materials. Part II. Advanced theory and problems. 1958, New York.
[14] A.B. Hossain, J.W. Weiss. Assessing the residual stress development and stressrelaxation in restrained concrete ring specimens[J]. Cement and Concrete Composites. 2004, 26(5):531-540.
[15] W. Dong,W. Yuan,X. Zhou,F. Wang, The fracture mechanism of circular/elliptical concrete rings under restrained shrinkage and drying from top and bottom surfaces[J]. Eng. Fract. Mech.2017, 189:148-163.
[16] W. Dong,X.M. Zhou,Z.M. Wu,H. Luo,G. Kastiukas, Quantifying the influence of elliptical ring geometry on the degree of restraint in a ring test[J]. Comput. Struct. 2018, 207:111-120.
[17] H. Zhu, H.R. Li, X.C. Zhu, On concrete restrained eccentric ring and square eccentric ring shrinkage test methods[J]. Construct. Build. Mater. 2015, 84:239-244.
[18] J. Weiss, P. Lura, F. Rajabipour, G. Sant. Performance of shrinkage-reducing admixtures at different humidities at and early ages. ACI Mater.J. 2008, 105(5):478-486.
[19] Kang J Y, Park J S, Jung W T, et al. Connection between Concrete Layers with Different Strengths[J]. Engineering. 2015, 7(7):365-372.
[20] Jae Heum Moon, Jason Weiss. Estimating residual stress in the restrained ring test under circumferential drying. Cement and Concrete Composites. 2006, 28:486-496.

INFLUENCE OF DIFFERENT CORROSION SOLUTIONS ON REINFORCED CONCRETE BY DIC AND TRADITIONAL STRAIN TEST

XiaoX Wang (1), JiaP Liu* (1) (2) (3), PeiH Zhong (1)

(1) School of Materials Science and Engineering, Southeast University, Nanjing 211189, China

(2) State Key Laboratory of High Performance Civil Engineering Materials, Jiangsu Research Institute of Building Science, Nanjing 210008, China

(3) Jiangsu Sobute New Materials Co., Ltd, Nanjing 210003, China

Abstract

When the corrosion expansion stress of the steel reinforcement exceeds the ultimate tensile strength of the concrete, the concrete will crack and eventually cause structural damage. Therefore, direct characterization methods of steel corrosion expansion stress can help predict the concrete cracking time, prevent corrosion expansion and repair the reinforcement concrete in advance. In this paper, by using the digital image correlation technology (DIC) to monitor the surface strain of concrete, and using the hollow steel bar to catch the strain of the steel bar under the condition of constant potential acceleration, the experiment and theory are established to characterized the relationship between the corrosion expansion stress and the concrete surface deformation. Besides, different corrosion solutions were applied to the specimens to investigate the effect of the corrosion solution on the corrosion rate of the steel bars in the concrete. The results show that the corrosion rate is seawater > 3% NaCl solution > 3% NaCl + 5% Na_2SO_4 composite solution. Among them, sulfate ions inhibited the promotion of chloride ions corroding on steel bars to a certain extent.

Keywords: Reinforced concrete, Corrosion, Corrosion expansion stress, DIC

1. INTRODUCTION

Since the appearance of Portland cement in 1824 and the patent for reinforced concrete in France in 1867, reinforced concrete structures, as a composite material, has fully exerted to the compressive properties of concrete materials and the tensile properties of reinforcement, forming the complementary synergy. Because of its low cost performance, easy access to raw materials, it has become the most mainstream materials used in various types of construction facilities. American researchers have said the "five-fold law" to vividly describe the durability of reinforced concrete structures [1]. Obviously, it can be seen that the decline in the durability of reinforced concrete structures and the premature attenuation of service life have become

important scientific and engineering problems that need to be solved nowadays, which has attracted close attention from the scientific and engineering community in the domestic and overseas[2-3].

Under the action of corrosion ions, Steel bars in concrete have de-passived and gradually be corroded, and the volume of corrosion products is 2~4 times of the corresponding steel bars [4]. With the increase of the corrosion degree of reinforcement, the corrosion expansion stress will augment. Accordingly, when the corrosion expansion stress exceeds the concrete tensile strength, the concrete protective layer will crack [5]. Apparently, it is significant to accurately investigate the corrosion degree of steel bars and obtain the change of corrosion expansion stress stage of steel bars to predict the cracking caused by corrosion expansion stress and durability issues of reinforced concrete [6-7].

At present, the detection of the reinforcement corrosion in concrete mainly uses electrochemical methods, such as semi-battery potential method, linear polarization method, constant voltage method, resistance probe method, etc. [8]. Based on these methods, we can see that the reflection of the averaging corrosion state of the whole steel bar by measuring the electrochemical characteristic information. It is unable to reflect the local pitting phenomenon of the reinforcement. The methods for detecting cracks in reinforced concrete structures include manual observation method, ultrasonic inspection method, sensor detection method, strain gauge, and extensometer [9-10]. The artificial observation method is subjective, and the results produced vary from person to person. In addition, the observation of micro-cracks by human eyes cannot reach the accuracy of industrial cameras. Ultrasonic testing cannot carry out long-term continuous monitoring of the whole process of steel corrosion. The sensor detection method cannot monitor the stress-strain on the surface of the specimen in real time, and it is easy to be damaged by the corrosion ions because it is placed inside the specimens. And strain gauges, extension gauges cannot detect cracks in the specimen (cracks caused by the reinforcement corrosion expansion stress) [9-10]. Therefore, how to accurately monitor the corrosion expansion stress of reinforcement and the crack growth caused by corrosion expansion, then establish the quantitative relationship between them is a major difficulty in the monitoring system of reinforced concrete structures. These problems can be solved by the digital image correlation technology (DIC) method, which can monitor the crack propagation process of reinforced concrete specimens in real time. DIC is a non-destructive, non-contact optical measurement method. Yamaguchi[10] and Peters[11] first introduced this method, and it has gradually been used by researchers to measure the displacement and surface deformation characteristics of objects in three-dimensional space.The method has high precision, low requirements on environmental conditions, less economic investment of the equipment, and can continuously monitor the whole process of the specimens in real time. Thus, DIC is easy to implement and cost-effective, and is widely used to monitor mechanical damage and structural health of materials [12-13].

In this paper, the combination of DIC method and traditional strain collection method is used to continuously track the deformation and cracking effect of reinforced concrete specimens under constant potential acceleration conditions. Based on this method, the corrosion stages of reinforced concrete specimens are monitored in real time. The process provides a new method for the study of corrosion of reinforcement concrete cracking.

2. EXPERIMENT

2.1 Raw materials and mix proportion

PI.52.5 Portland cement is used according to Chinese standard GB 175-2007. The chemical composition of the cement is shown in Table 1. Class I FA, specific surface area is 380~400 m^2/kg, S95 GGBS, specific surface area is 430~450 m^2/kg, coarse aggregate is granite, continuous grading of 5~20 mm, crushing value is 13.8%. The fine aggregate is river medium sand, the fineness modulus is 2.7. The polycarboxylate based superplasticizer is JM-PCA(I) type with a water reduction rate is about 30%, the dosage is 5.58kg/m^3, air-entraining agent content is 0.22kg/m^3, adopting H700 type super absorbent resin (SAP), which is pre-absorbed and mixed into the concrete. The water absorption ratio is taken as SAP: water=1: 30 by mass (SAP water consumption is a part of the total water consumption in the concrete mix ratio), and the water is tap water. Q235 carbon steel bar is used and their specific chemical compositions is shown in Table 2. The mixture ratio of concrete is prepared with the effective water cement ratio (w/c) of 0.33. The mixture proportions for the reinforced concrete is shown in Table 2-3. The compressive strength of concrete is 30.03Mpa and 37.14Mpa after standard curing for 7d and 28d respectively.

Table 1: Chemical compositions of P.I 52.5 cement

Constituent	SiO_2	LOI	Fe_2O_3	Al_2O_3	MgO	CaO	K_2O	SO_3	Na_2O
Wt%	20.87	0.77	3.59	4.87	2.13	64.49	0.65	2.52	0.11

Table 2: Chemical compositions of Q235 carbon steel bar

Fe	C	Si	Mn	P	S	V	Cr	Ni	Al	Mo
Bal.	0.22	0.35	1.4	0.04	0.05	-	-	-	-	-

Table 3: Concrete mix ratio (kg/m^3)

Name	Cement	GGBS	FA	Sand	Aggregate	Water	SAP
LF50SP1	250	145	75	730	1095	130	1

2.2 Preparation of reinforced concrete specimens

The size of reinforced concrete specimens are 100*100*250 mm^3, and the size of upper prepared corrosion solution tank is 15*20*150 mm^3. After curing for 24h in mould, the reinforced concrete specimens are placed in a standard curing room (temperature (20±3) ℃, relative humidity RH≥95%) for curing to 28 days. In order to ensure that the strain gauge is not affected by external corrosion ions, the Q235 carbon steel bar with a diameter of 20 mm is split into two halves, internal processing diameter of 15 mm grooves, decorated in the steel bar inside groove section 7 points, points as shown in Figure 1. Among them, the leftmost point is the strain gauge compensation point, and the remaining points are strain collection points. The formed reinforced concrete specimen is shown in Figure 2. The thickness of concrete protective layer designed in this experiment is 25 mm.

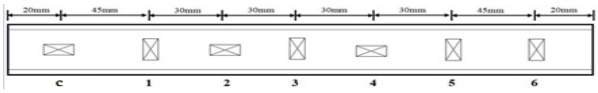

Figure 1: Position of resistance strain gauges

Figure 2: Reinforced concrete specimen

2.3 Principle of DIC method

The DIC method, also known as the digital speckle method (DSCM), is a non-contact deformation measurement method that uses the randomly distributed spots on the surface of the object to give the deformation field [9]. In this method, the deformation information is obtained by correlation processing of two speckle images on the object surface before and after deformation. The basic idea of the DIC method is to compare the images before and after the deformation of the object, and identify the specific sub-regions to "track" the deformed position of the points on the surface of the object, and then obtain the displacement and strain values.

3. RESULT AND DISCUSSION

3.1 Micro-strain of reinforcement

Figure 3 shows the variation of the micro-strain value of point 3 on the inner surface of reinforcement under electrical acceleration of three different corrosion solutions, the micro-strain values of the three specimens gradually increase with time at first, especially for the specimen under the action of 3% NaCl solution, which indicate a very obvious strain growth trend. This phenomenon indicates that chloride ions promote the corrosion reaction of reinforcement and accelerate the process of the corrosion reaction. At the later stage of the corrosion reaction, the micro-strain values of the specimens gradually decreases under the action of 3%NaCl solution and 3%NaCl+5%Na_2SO_4 composite solution, while the concrete specimen under the seawater solution still showed an increasing trend. It is indicated that high concentration of chloride ions causes pitting corrosion phenomenon, then the corrosion products only appeared in the area of point 3. After reaching the ultimate tensile strength of the concrete, then micro-cracks are generated, the stress unloading occur. As sulfate ions can inhibit the corrosion of steel bars, the change of micro-strain values from beginning to end is not obvious, and it is consistent with the phenomenon described in previous literature [14]. As a composite solution of various ions, seawater causes extensive corrosion of steel bars, and its micro-strain continue to increase and causes concrete corrosion and cracking.

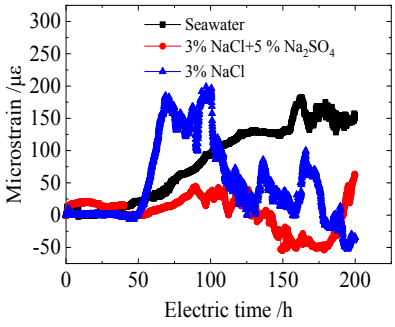

Figure 3: The internal micro-strain value of reinforcement in concrete varies with time

3.2 Strain evolution analysis based on DIC test

The square section of the reinforced concrete side is as 100×100 mm^2. The calibration result of this section is 0.076 mm/pixel, and the area size is 122×166 pixels. The evolution process of the strain field is shown in Figure 4.This figure shows that the change of strain field with time is consistent with the information in Figure 3. In the early stage of the experiment, the degree of corrosion reaction is: seawater > 3%NaCl solution > 3%NaCl+5%Na_2SO_4 solution, and in the middle and late stage of the experiment, the degree of corrosion reaction is: 3%NaCl solution > seawater > 3%NaCl+5%Na_2SO_4 composite solution.

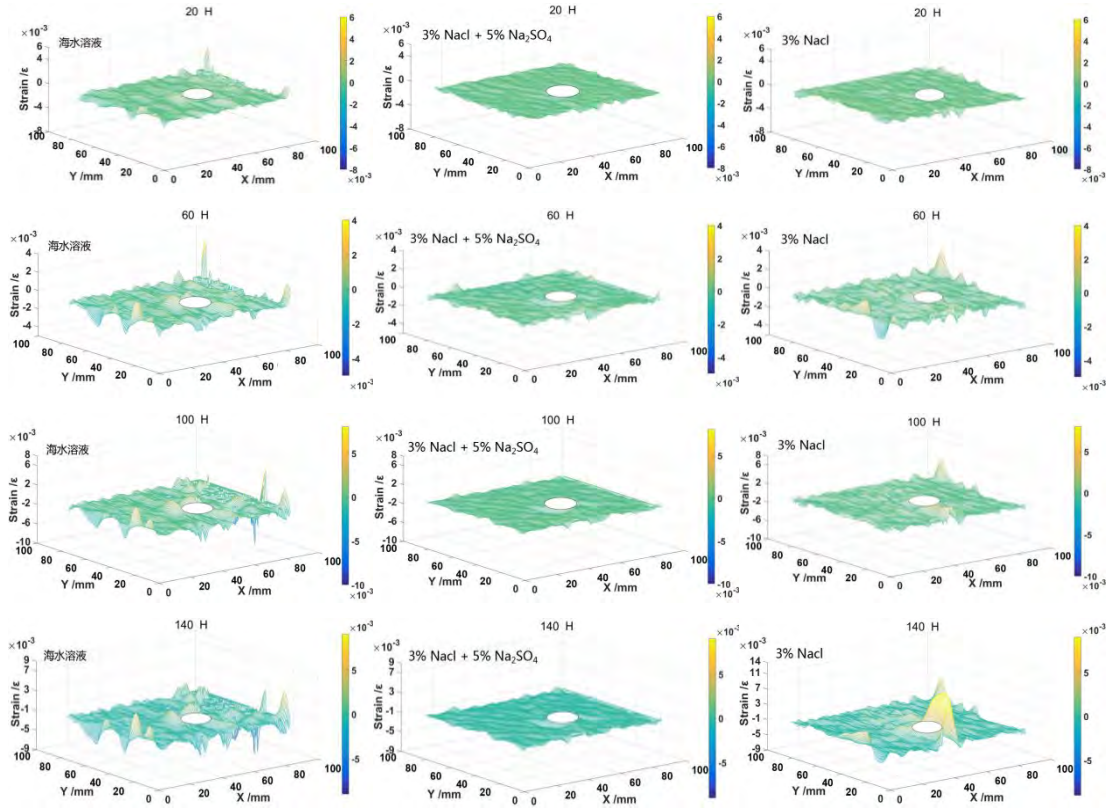

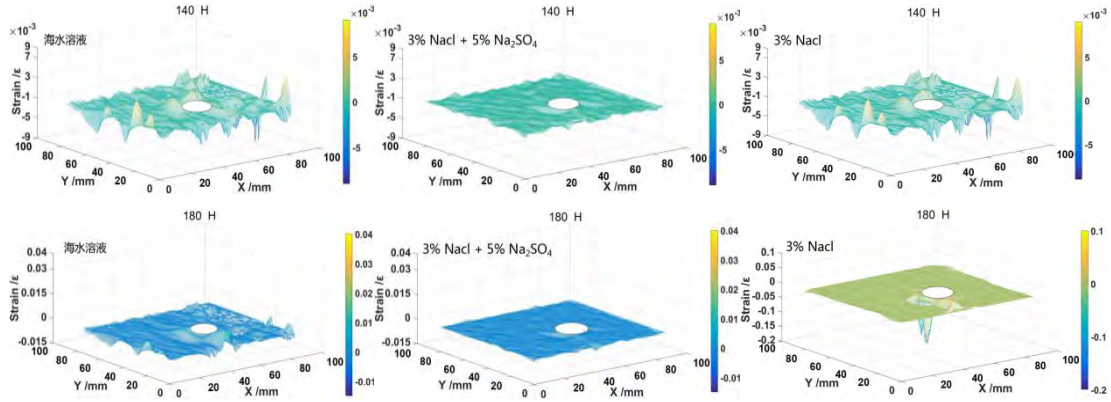

Figure 4: The strain field on the side of reinforced concrete changes with time

According to Figure 5, the strain variation of upper side reinforcement (x=25 mm, y= 20 mm) of the three specimens is shown in Figure 5. Figure 5(b) shows that the reinforced concrete specimens under the action of seawater and 3% NaCl solution gradually increase the lateral strain at first stage due to the corrosion expansion stress. At 120 h, the specimen subjected to seawater show a small degree of stress unloading phenomenon, indicating that the cracks spread to the concrete surface, so the corrosion products overflow with the corrosive solution, and a significant sudden increasing occurs at 160h. After that the strain show increases till the end of the experiment, indicating that the corrosion effect of seawater on steel bars is continuous, and the incremental volume of corrosion products are much larger than the volume of overflow, resulting in more and more obvious cracks on the concrete surface and increasing the crack width. For the specimen under the action of 3% NaCl solution, although the growth trend of the strain curve is consistent with that of seawater at first, the micro-strain value is much smaller than that of the seawater, which further confirms that the influence of seawater on steel corrosion is more serious. At 160 h, the specimen also appears obvious stress unloading phenomenon due to the pitting corrosion of chloride ions, which indicates that the volume of corrosion products is much smaller than the volume of corrosion products under seawater. For the specimen corroded by 3%NaCl+5%Na_2SO_4 composite solution, during the whole experimental time, although there is a certain trend of micro-strain variation, the micro-strain value is relatively small, and the maximum micro-strain value is 300 με, which cannot reach the ultimate tensile strength of concrete. The above results further illustrate that seawater has the greatest effect on the corrosion of steel bars in concrete, while sulfate ions can inhibit the corrosion of steel bars by chloride ions.

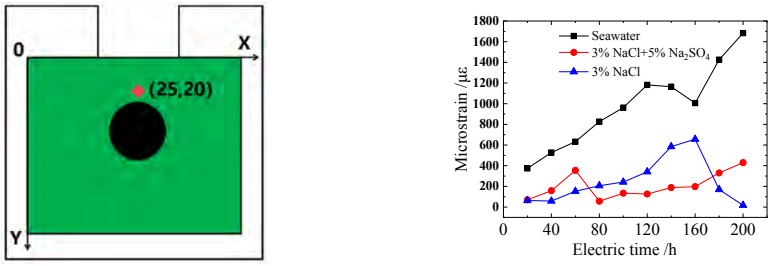

(a) Schematic diagram **(b) Micro-strain contrast diagram**

Fig. 5 Comparison of the points on the side of reinforced concrete

4. CONCLUSIONS

(1) The strain gauge inside the steel bar can effectively monitor the variation of the steel corrosion expansion stress with time. Besides, the DIC technology can realize the real-time monitoring of the reinforced concrete surface strain field and the cracking process.
(2) Through the method of full-field strain monitoring combining DIC technology and hollow steel bar strain gauges, the real-time monitoring of the internal and external reinforced concrete specimens can be effectively carried out to estimate the corrosion expansion stress caused by reinforcement corrosion of concrete specimens. In addition, it can also catch the damage form and evolution process of cracking.
(3) The effect of different types of corrosive solutions on the corrosion rate of steel in concrete is seawater > 3% NaCl solution > 3%NaCl+5%Na_2SO_4 composite solution. Moreover, the single chloride salt solution causes obvious pitting corrosion phenomenon of the steel bars. The seawater containing multiple ions causes the large-area continuous corrosion reaction of the steel bars, and the presence of sulfate ions can mitigate the corrosion of the steel bars caused by the chloride salts to some extent.

REFERENCES

[1] Zhang, X.Y., Ou, J.P. 'Durability of FRP bars in concrete structures.' Science and Technology Forum on the Durability of Concrete Structures in Coastal Areas and the National Conference on Concrete Durability. 2004.

[2] Jin, W.L., Lv, Q.F., Zhao, Y.X., Gan, W.Z. 'Research progress on the durability design and life prediction of concrete structures'. *Journal of Building Structures*. **28**(1) (2007)7-13.

[3] Zhang, L., Yan, J.J., Li, X. 'A Review on the Durability of Concrete Structure'. *Materials Review*. **27**(S1) (2013)294-297.

[4] Niu, D. T., Wang Q. L., Wang, L.K. 'Pre-determinate Modle of Steel Corrosion Extent in Reinforced Concrete Structures before Reproducing Corrosion Crack'. *Industrial Construction*. **26**(4) (1996)8.

[5] Liu, Y. 'Modeling the time-to-corrosion cracking of the cover concrete in chloride contaminated reinforced concrete structures [electronic resource]'. *ACI Materials Journal*. **95**(6) (1998) 675-681.

[6] Bazant, Z. P. 'Physical model for steel corrosion in concrete sea structures-application'. *Journal of Structural Divison*. **105**(6) (1979)1155-1166.

[7] Andrade, C., Alonso, C., Molina, F. J. 'Cover cracking as a function of bar corrosion: Part I-Experimental test'. *Materials & Strictures*. **26**(8) (1993) 453-464.

[8] Chen, L. T., Zh/ang, S. P., Zou, G. J., et al. 'Reinforced concrete corrosion monitoring technology and its application'. *Materials Protection.* **40**(5) (2007)52-55.

[9] Destrebecq, J. F., Toussaint, E., Ferrier, E. 'Analysis of Cracks and Deformations in a Full Scale Reinforced Concrete Beam Using a Digital Image Correlation Technique'. *Experimental Mechanics*. **51**(6) (2011)879-890.

[10] Yamaguchi, I. 'A laser-speckle strain gauge'. *Journal of Physics E Scientific Instruments*. **14**(11) (2000)1270.

[11] Peters, W. H. 'Digital image techniques in experimental stress analysis'. *Optical Engineering*. **21**(3) (1982) 213427.

[12] Iskander, M. 'Digital Image Correlation'. *Materials Today*. **13**(12) (2010) 52-54.

[13] Gencturk, B., Hossain, K., Kapadia, A., et al. 'Use of digital image correlation technique in full-scale testing of prestressed concrete structures'. *Measurement*. **47**(1) (2014)505-515.

[14] Jin, Z. Q., Sun, W., Zhang Y. S., et al. 'Interaction between sulfate and chloride solution attack of concretes with and without fly ash'. *Cement and Concrete Research.* **37**(8) (2007) 1223-1232.

NUMERICAL ANALYSIS OF CALCIUM LEACHING ON THE DURABILITY OF DAM CONCRETE

Ding Nie (1), Feng Shang (1) and Xun Han (2)

(1) China Institute of Water Resources and Hydropower Research, Beijing, China

(2) Nanjing Hydraulic Research Institute, Nanjing, Jiangsu, China

Abstract

Concrete dams are subjected to soft water penetration of a high water head during their long service lives. Degradation due to calcium leaching will decrease the durability of the concrete and affect dam safety. The long-term performance of concrete dams due to calcium leaching should be evaluated and predicted accurately to complete the reinforcement work in a timely manner, ensuring long-term safety of concrete dam. In this paper, sediments and seepage water from corridors of a concrete dam located in southeastern China were first collected on-site. The components of the sediments and seepage water were detected by X-ray photoelectron spectroscopy, scanning electron microscopy and inductively coupled plasma mass spectrometry. Through a comprehensive analysis of the components, a certain degree of calcium leaching was found in the concrete inside the dam. In order to predict the long-term degradation of concrete, a multi-scale model of calcium leaching considering the micro-pore structure of cement hydrates was used and finite element analysis were carried out to simulate the durability of dam concrete. The simulated results using the calcium leaching model showed a good agreement with the experiments. Finally, the long-term durability of the dam concrete was predicted. It implies that the proposed method could provide calculation and theoretical basis for the durability analysis of concrete dams due to long period calcium leaching.

Keywords: concrete, calcium leaching, multi-scale model, numerical analysis, dam precipitate detection

1. INTRODUCTION

Concrete dams are designed to store water, mostly soft water throughout their lifetime. At macro-level, these concrete structures are prone to problems such as loss of strength, performance degradation and shortened service life under long-term soft water erosion [1]. Especially when the dams have existed damages, such as inner crack and leakage of water, the calcium leaching dissolution would be more serious. At mirco-level, this phenomenon is due to calcium ions in the concrete pore solution diffuse into the soft water under the concentration gradient, causing cement hydration products such as calcium hydroxide ($Ca(OH)_2$), ca-silicate-hydrate gel (CSH) and other solid calcium to dissolve and lose. As time passes by, the calcium

concentration and the alkalinity of the pore solution inside the concrete decrease, while the porosity increases, causing the loss of strength and impermeability of concrete [2]. For concrete dams, according to the Chinese national standard, the design lifetime often exceeds 100 years or more. Calcium leaching over such long service life become one essential issue to be considered in the design, operation and maintenance period of such projects. Therefore, it is of great importance to estimate and predict the properties of the concrete at a later stage after construction to complete the reinforcement work in a timely manner, ensuring dams' long-term safety. Recently, many researchers have investigated experimental study on calcium dissolution process of hardened cementitious materials in deionized water or purified water. Jain et al.[3] studied the calcium leaching behavior of hardened cement pastes modified with a high-alkali fine glass powder, silica fume, and fly ash, exposed to deionized water to accelerate calcium leaching.

However, calcium leaching rate of cementitious materials under soft water is quite a slow process according to inspection results of real projects. Thus, the prediction and analysis of this phenomenon is difficult just through normal or accelerated experiments. Experimental methods need to be taken into consideration combined with numerical methods for more accurate evaluation of concrete properties, since real-time scale tests are almost unrealistic. Some researchers have proposed calcium leaching models to calculate the degradation of cement-based materials. Samon et.al[4] presents a multi-ionic transport model for saturated and unsaturated cementitious materials. Li et.al[5] developed an one dimension model of calcium ion transportation. These models provide numerical methods to analyze and simulate the long-term calcium leaching process. However, the micropore structures are assumed to be constant through all the leaching process in these models, while calcium leaching and the evolving microstructure are strongly coupled with each other and both need to be simulated especially over extremely long periods of time. Hence, a multi-scale model integrating a calcium ion transport model with a statistical micro-structural model of chemophysics proposed by Nakarai et al.[6] is used in this study.

In this paper, this calcium leaching model and its numerical system were first introduced comprehensively. Verifications of the immersion tests have been proved that this model shows a good agreement with the experiments. At last, in a real dam inspection project, by detecting the components of sediments and seepage water, calcium leaching dissolution had been proved inside the concrete. Long-term durability prediction of the dam concrete was performed and reasonable advices were given according to the numerical analysis results.

2. METHODOLOGY OF ANALYSIS CALCIUM LEACHING

2.1 Numerical analytical system, DuCOM

According to former researchers' study, calcium leaching from cement hydrates has a strong relationship with the process of cement hydration, microstructure formation and moisture distribution. All these chemo-physical processes are highly time-dependent. Based on the theoretical study, a computational method has been developed by Maekawa et al. [7] for numerical simulation and it's computer code named DuCOM. This scheme is used in this study to verify the calcium leaching model and analyse the long-term properties of dam concrete. Through several verifications, this system can also simulate microstructure of hydrate formed by both cement and admixture such as fly ash and slag, which makes DuCOM more widely used.

2.2 Modeling of calcium leaching proposed by Nakarai

Based on the scheme of DuCOM, Nakarai developed a new model of calcium leaching. This model follows the law of mass conservation and combines the equilibrium of calcium in the solid and liquid phases with the calcium ion transport of both diffusion and advection.

The mass conservation equation is applied in terms of the total calcium ions in the pore solution and the solid-phase calcium, in reference to the equation by Gerard et al.[8].

$$\frac{\partial}{\partial t}\left(\phi \cdot S \cdot C_{ion}\right)+\frac{\partial C_{solid}}{\partial t}-divJ_{ion}=0 \tag{1}$$

where ϕ is porosity, S is degree of saturation, C_{ion} is the concentration of calcium ions in the liquid phase, C_{solid} is the amount of calcium in the solid phase, and J_{ion} is the flux of calcium ions. The porosity and the saturation are calculated in the DuCOM system. The next step is try to calculate the solid calcium and the liquid calcium ions.

The mathematical formulation adopted by Gerard et al.[8] and latter be modified was referred as,

$$C_{solid}=f\left(C_{ion}\right)=AC_{CSH}\left(\frac{C_{ion}}{C_{satu}}\right)^{1/3}+B \tag{2}$$

$$A=\begin{cases}-\frac{2}{x_1^3}C_{ion}^3+\frac{3}{x_1^2}C_{ion}^2 & \left(0\le C_{ion}\le x_1\right)\\ 1 & \left(x_1\le C_{ion}\right)\end{cases},\ B=\begin{cases}0 & \left(0\le C_{ion}\le x_2\right)\\ \frac{C_{CH}}{\left(C_{satu}-x_2\right)^3}\left(C_{ion}-x_2\right)^3 & \left(x_2\le C_{ion}\right)\end{cases} \tag{3}$$

where, C_{CSH} is the amount of calcium in the solid phase of the C-S-H gel, C_{CH} is the amount of calcium in the solid phase of the calcium hydroxide, C_{satu} is the saturated liquid phase calcium ion concentration. According to Nakarai's research, x_1 and x_2 are 0.3 mmol/L and (C_{satu} – 0.7) mmol/L, respectively. All the parameters are calculated as time-dependent variables under the scheme of DuCOM.

Nakarai's study shows that the flux of calcium ions transported in a porous media is written as,

$$J_{ion}=-\left(\frac{\phi \cdot S}{\tau}\cdot\delta\cdot D_{ion}\right)\cdot\nabla C_{ion}+\phi\cdot S\cdot\mathbf{u}\cdot C_{ion} \tag{4}$$

where, τ is tortuosity, δ is constrictivity, D_{ion} is the diffusion coefficient of a calcium ion, and $\mathbf{u}$ is the velocity vector of a calcium ion transported by solution flow. The calculation of tortuosity factor and constrictivity factor can be found in Maekawa's study.[7]

3. VERIFICATION OF THE CALCIUM LEACHING MODEL

In order to verify the calcium leaching model, besides the verifications from their own study, another verification by simulating cement pastes immersion tests conducted by Samson et al.[4] was provided in this paper.

3.1 Cement pastes immersion tests

In Samson's experiment, cement pastes were prepared at a water/cement ratio of 0.6 by mass and then cast in cylinders with diameter of 7 cm and height of 20 cm. After hydration period, the cylinders were sawn in disks with height of 2 cm. Before immersed in water, the disks were

sealed on the side and on one face with silicon. All the test disks were immersed in deionized water for at least 3 months. After the pre-processing procedure, the degradation states of test samples, including the total calcium contents, were analyzed with a microprobe.

3.2 Numerical simulation

The input parameters including mixture proportions and mineral compositions of cement are listed in Table 1. Among them, C_3A represents tricalcium aluminate, C_3S represents tricalcium silicate, C_2S represents dicalcium silicate, and C_4AF represents tetracalcium iron aluminate. A one-dimensional FE model was established to simulate the calcium ion (dissolved) migration and leaching from $Ca(OH)_2$ and C-S-H gel. The boundary conditions were set the same as the experiment. The exposed face of the disk (at $x = 0$) was set to transfer heat, humidity and calcium ions, and all concentrations are set to 0 either. The rest faces were set to transfer only heat. The time steps of 30 min were used and total calculation time is 90 days.

Table 1: Mixture proportions and mineral composition of cement

Properties	Mixture proportions (kg/m^3)			Cement composition (% mass)				
	Water	Cement	Aggregates	C_3A	C_3S	C_2S	C_4AF	Gypsum
Values	653.3	1088.8	0	8.8	49.7	23.9	9.4	3.4

In Figure 1, the numerical simulation profiles of total calcium content are plotted, together with the experimental profiles. The simulation demonstrates slightly less deterioration than obtained from the experiment. Given that the sealed side surfaces may have slightly leaching of calcium ions, accelerating the deterioration in experiment. This little discrepancy is considered to be accepted. For more accurate estimate, it would be necessary to modify the boundary conditions and improve the parameters in the model. This comparison and the former verifications all showed good applicability of the model for calculating and analysing calcium leaching from cementitious materials.

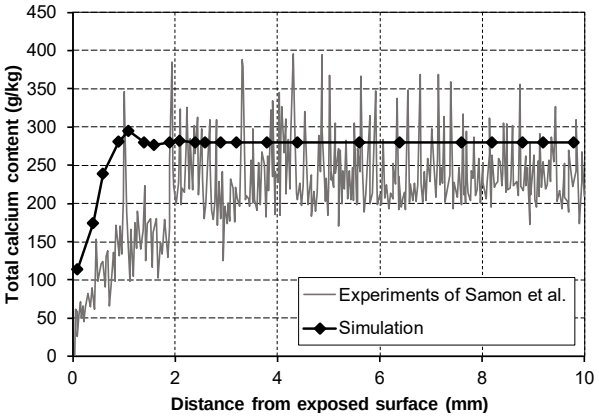

Figure 1: The experimental and simulated profiles of calcium distribution

4. NUMERICAL ANALYSIS OF DAM CONCRETE

In this section, precipitates from a concrete gravity dam was detected and analyzed. The calcium leaching model and DuCOM system were applied to carry out numerical analysis and prediction of the long-term properties of dam concrete.

4.1 Detection and analysis of dam precipitate

The concrete dam of HK hydropower station is located in Southeastern China. After 10 years of operation, precipitates including sediments and seepage water were found in the corridors inside the dam, as shown in Figure 2. In order to evaluate long-term deterioration of dam concrete, the precipitates inside the dam need to be detected and analyzed first.

Both the up stream and corridor seepage water was collected and analyzed according to the Chinese national standards. The dosages of calcium and pH value were detected quantitative using inductively coupled plasma mass spectrometry and glass electrode method, respectively. The average calcium ion dosages and pH values of up stream water and corridor seepage water were 1.45 mg/L and 21.37 mg/L, respectively. The relevant average pH values were 6.58 and 10.42, respectively. Increases in calcium ion and pH value were observed from up stream to the corridor.

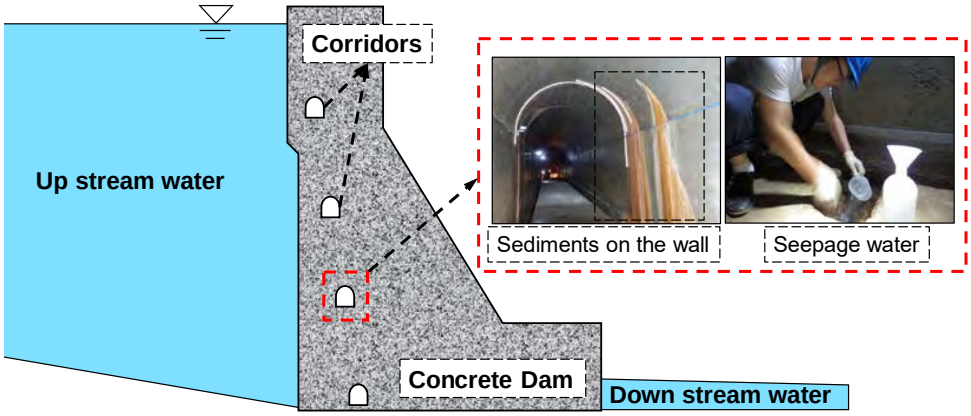

Figure 2: The experimental and simulated profiles of calcium distribution.

The components of the solid sediments collected from the corridors were detected by X-ray photoelectron spectroscopy (XPS) and scanning electron microscopy (SEM) tests, the results were shown in Figure 3.

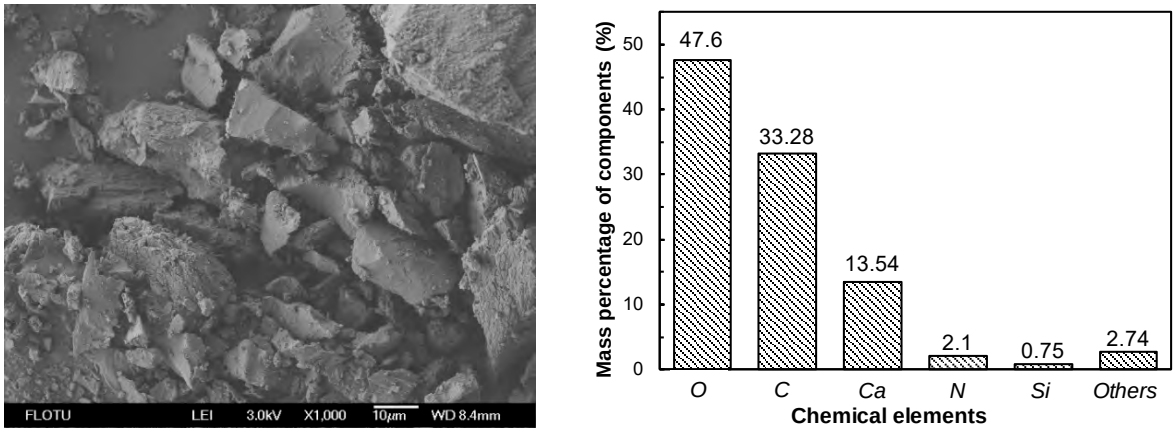

(a) Micromorphologies of the solid sediments

(b) Mass percentage of main components

Figure 3: The detection results of solid sediments.

Combined the micromorphologies and the elements mass percentage of the components, solid precipitates might be consisted of calcium carbonate and grouting materials. The calcium carbonate probably be formed by calcium hydroxide caused by calcium leaching dissolution. According to the repair record, the grouting material was polyurethane, which is mainly composed of carbon and oxygen. The detection and analysis of liquid and solid precipitates all indicate that a certain degree of calcium leaching dissolution existed in the concrete inside the dam.

4.2 Numerical analysis of long-term properties of dam concrete

Based on the DuCOM system and material parameters from the design reports, the long-term properties of dam concrete were numerically analyzed. The mineral compositions of cement including C_3A, C_3S, C_2S, C_4AF, and Gypsum were 15.50%, 54.76%, 14.16%, 5.47%, and 3.40% by mass, respectively. The mixture proportions of concrete varied during construction. To simplify calculations, upper limit and lower limit mixture proportions were applied for simulation, as shown in Table 2.

Table 2: Mix proportions of dam concrete during construction period

Type	Mixture proportions (kg/m^3)					
	Water	Cement	Fly ash	Slag	Fine Aggregates	Coarse Aggregates
Upper limit	85.2	86.9	161.4	0	732	1314
Lower limit	85.2	63.3	173.8	11.2	732	1314

The simulated compressive strength and adiabatic temperature rise were compared with the experiments, as show in Figure 4. The results indicate that the values of experiments are just between the simulated upper and lower limit cases. Therefore, the application of using upper and lower limit mix proportions to simulate the long-term properties of the concrete inside dam is reasonable to some extend.

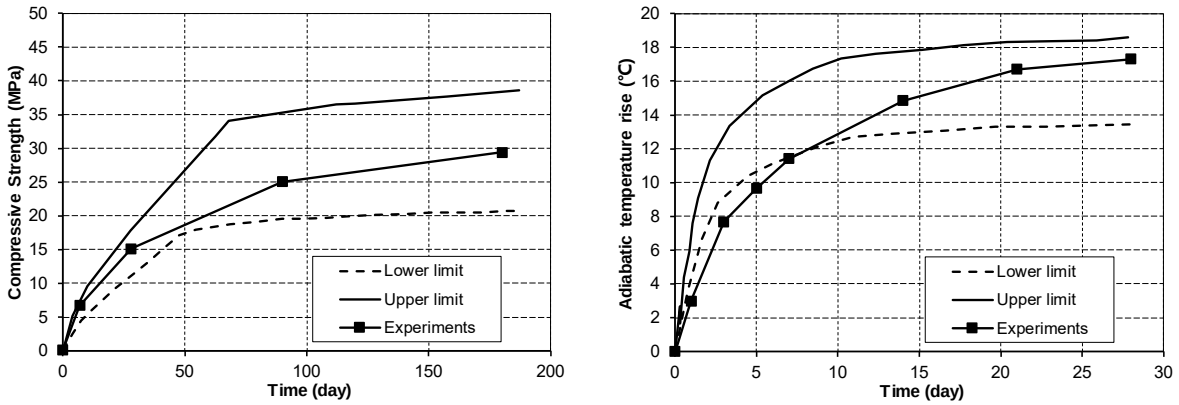

(a) Simulation results of compressive strength (b) Simulation results of adiabatic temperature rise

Figure 4: Comparison between experimental and simulated results.

The water seeping from the cracks takes more calcium ions away and accelerates the dissolution of concrete. This phenomenon will cause the crack width to increase and most seriously endanger the dam safety. Considering the above possibility, an one-dimensional FE model was set to simulate the process and used to predict the long-term properties of dam concrete, as show in Figure 5 (a). The boundary conditions were set as below. The crack side (at $x = 0$) was set to transfer heat, humidity and calcium ions. The concentration is set to 1.45 mg/L, just the same value with it in the up stream reservoir. The time steps of 1 day were used in the first year and increase to 10 days after that. Total calculation time is 36,500 days. For the dissolution of C-S-H is after the loss of $Ca(OH)_2$. The damage rate of C-S-H gel was used to represent the long-term durability of concrete, as shown in Figure 5 (b).

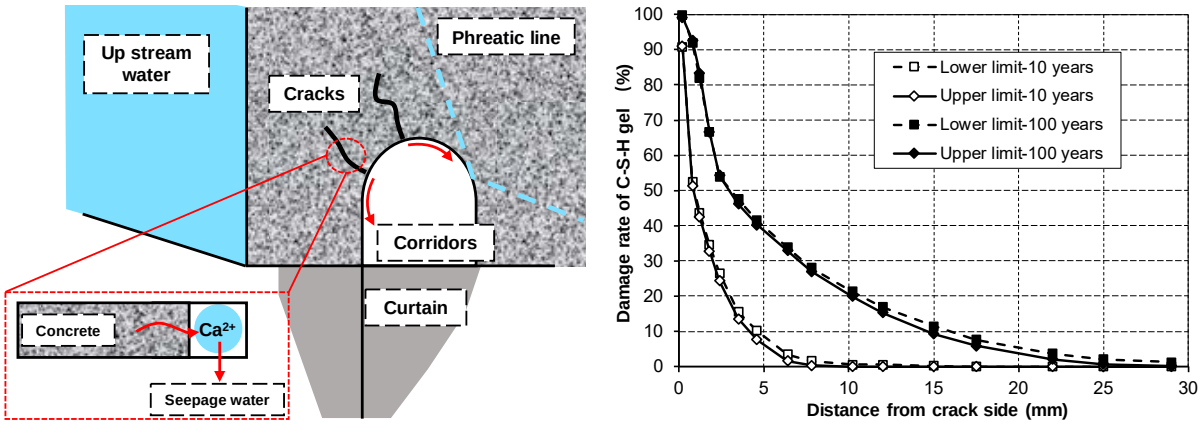

(a) Principle of calcium leaching in corridor (b) Simulated long-term properties of concrete

Figure 5: Analysis of long-term properties of dam concrete.

The contents of C-S-H gel in concrete have a strong relationship with strength and porosity. According to the simulated results, both the damage rate and depth are increased as time goes on. The numerical predictions indicate that after construction 10 to 100 years, the dam the damage depth increases from about 7 mm to 25 mm. A comprehensive numerical simulation

could be performance if it is needed and the managers would complete the reinforcement work including grouting and sealing of cracks in a timely manner to ensure dam's long-term safety.

5. CONCLUSIONS

- Through a comparison with the experimental results, the calcium leaching model and the relevant computational system used in this paper showed reasonable prediction results. Long-term calcium leaching process of concrete could be numerically simulated by using this method.
- Through the analysis of the precipitates of concrete dam, the calcium dissolution degree of the concrete in the dam can be obtained. Using the computational system described in this paper, it is also possible to achieve long-term predictions of concrete properties. This method provides calculation and theoretical basis for the durability analysis of concrete dams due to long period calcium leaching.

ACKNOWLEDGEMENTS

This work was supported by the National Natural Science Foundation of China (No. 51909280) and the Fundamental Research Funds for China Institute of Water Resources and Hydropower Research (No. SS0145B612017).

REFERENCES

Articles in Conference Proceedings or Edited Books:

[1] Chen, H.S., Ye, G., and Stroeven, P. 'Computer simulation of structure of hydrated cement paste enclosed by interfacial transition zones in concrete'. In: Setzer, M.J. and Palecki, S. (eds.), Proceedings of International Conference on Durability of High-Performance Concrete and Final Workshop of CONLIFE. Freiburg: AEDIFICATIO Publishers, 2004, 133-144.

[2] Pathak, R. P., Sharma Pankaj, and Murari Ratnam. 'Characterisation of leachate material from dam concrete by X-ray diffractometer and FTIR.' *International Journal of Research in Chemistry and Environment* 2.4 (2012): 58-63.

[3] Han, Fanghui, Rengguang Liu, and Peiyu Yan. 'Effect of fresh water leaching on the microstructure of hardened composite binder pastes.' *Construction and Building Materials* 68 (2014): 630-636.

[4] Jain, Jitendra, and Narayanan Neithalath. 'Analysis of calcium leaching behavior of plain and modified cement pastes in pure water.' *Cement and Concrete Composites* 31.3 (2009): 176-185.

[5] Samson, E., and J. Marchand. 'Modeling the transport of ions in unsaturated cement-based materials.' *Computers & Structures* 85.23-24 (2007): 1740-1756.

[6] LI, Xin-yu, and Kunhe FANG. 'Numerical Simulation of Ca-ion Transportation during Concrete Leaching Dissolution.' *Journal of Yangtze River Scientific Research Institute* 6 (2008).

[7] Nakarai, Kenichiro, Tetsuya Ishida, and Koichi Maekawa. "Modeling of calcium leaching from cement hydrates coupled with micro-pore formation." *Journal Of advanced concrete technology* 4.3 (2006): 395-407.

[8] Maekawa K, Ishida T, Toshiharu K. 'Multi-scale modeling of structural concrete', *London and New York: Taylor & Francis*, 2009, 256-290.

[9] Gérard, B., C. Le Bellego, and O. Bernard. 'Simplified modelling of calcium leaching of concrete in various environments.' *Materials and Structures* 35.10 (2002): 632-640.

QUANTIFIYING WATER PERMEABILITY AND PORE SIZE THROUGH CAPILLARY ABSORPTION

C. Andrade (1), E. Coppens (2)

(1) CIMNE- Madrid- Spain

(2) ONDRAF/NIRAS, the Belgian National Agency for Radioactive Waste and Enriched Fissile Materials, Kunstlaan 14, 1210 Brussels

Abstract

In Belgium the construction of a repository for low and intermediate short living radioactive waste is in preparation. The safety is, among other aspects, based on engineered barriers of cementitious materials preventing release of radionuclides to the atmosphere or to the surrounding soil. Relatively low water infiltration through these concrete constructions for a significant time period is important aspect to assure a safe disposal of these wastes. In this context it can be interesting to test multiple candidate concretes for water permeability. However testing for water permeability is a difficult task because of the relative high hydraulic pressures needed to percolate water through high quality dense concrete. In the present paper we are presenting results of the water permeability flows obtained at different pressures. These clearly indicate the measurement is greatly affected by the pressure applied. Therefore another type of measurement which does not involve a pressure head was developed. Indeed capillary absorption was used to deduce pore size distribution and water permeability. Not only is this method very easy to bring into practice, the conditions are also close to the real environmental conditions of these concrete structures due to the absence of a pressure head. A good fit can be made with mercury intrusion porosity. This is illustrated in the paper for two different concretes.

Keywords: concrete, nuclear, permeability, absorption, porosimetry

1. INTRODUCTION

Concrete is a very suitable material for being engineering barrier for nuclear waste storage due to its high pH, which lowers de solubility of most radionuclides and due to its physical confining ability. ONDRAF/NIRAS in Belgium is designing a repository for low and intermediate radioactive waste where cementitious materials will be employed as engineering barriers for limiting release of radionuclides to the atmosphere or to the surrounding soil. The confining materials should exhibit relative low water infiltration, which has been traditionally assessed through the determination of the permeability coefficient which is named “intrinsic” when it is made independent of the type of percolating fluid and is considered a “material

property". This coefficient is introduced into mathematical models to assess the saturation factor and possible migration routes of the radionuclides [1].

In general the test, to assess the intrinsic permeability coefficient, consists in the application of an hydraulic pressure head: at pressures above 1 bar [3-4] and measure the flow of liquid in the down-stream face of the specimen in order to apply Darcy's law for the calculation of the permeability coefficient. This practice, which find his origin in the publication of Powers [2] is well-known and often applied [3-8]. This method however, is difficult to perform in dense materials where the percolation of water takes too long or needs too high pressure heads with the risk to damage the specimen. An often used alternative is the simple scoring of the unidirectional water penetration depth inside the concrete [5]. This test consist in injecting water at one face a specimens, breaking the specimen and measure visually the depth of water penetration. In what follows the first test is referred to as the *water percolation* test, the second one is referred to as the *water penetration* test.

Attempts to relate the water transport to concrete microstructure (critical pore diameter) or durability [3,4,6] have been made, although without general acceptance on the conclusions. In the present paper we present data resulting from these tests two, gathered at different pressures heads for the same materials. Also a different method is developed based on a capillary suction, as demonstrated in [7]. This new method, which is very easy to apply by a simple capillary suction experiment, is based on theoretical considerations of the velocity of the water and the total flow rising up. In present paper a methodology is presented to measure the permeability coefficient and of the pore size distribution. This last one is compared with MIP measurements to validate the approach.

2. EXPERIMENTAL

For the first set of experiments, being the *percolation test* at different pressure heads, two different dense concrete types named O and E and a standardized mortar, named M, were fabricated. The composition, compressive strength and volumetric weight are given in Table 1. For a second set of tests, consisting only on the capillary water absorption a new set of concretes were fabricated whose composition is given in Table 2 and are equal or close to concrete O from Table 1. For the water permeability tests, specimens of 15 cm in diameter and 30 cm in height were poured and cured at 20±2ºC and >95% RH for 28 days. Cores, 5 cm in diameter and 8 cm in height were drilled from these cylinders for the *percolation tests* after the cores were used as-such for *water penetration* tests.

The *Percolation* test was performed with varying pressure up to 2.5 bars by water (equipment in figure 1-left). The flow is recorded through the weighing of the percolated water with time. The *water penetration* test (equipment in figure 1-right) was applied at higher pressure heads, varying up to pressures of 70 bar. The device used was a commercial one, in which the water is injected from the bottom face of the cylindrical specimens of 15 cm in diameter and 30 cm in height.

Table 1: The materials used in this paper

Dosage concrete [kg/m^3]	CONCRETE O	CONCRETE E	MORTAR M
Amount of cement	350	400	1 part in weight
Type of cement	CEM I 42.5 N	CEM I 42,5 SR	CEM I 42,5 SR
Calcarous filler	50	-	-
Superplastifier	3.92 (Rheobuild 1100 con. 30%)	4.8 (Superplastifier Melcret 222)	-
sand (0/4)	Calcareous 721	Siliceous 297	3 parts in weight Siliceous
aggregates (2/6)	Calcareous 417	Siliceous 614	-
aggregates (6/14)	Calcareous 200	Siliceous 949	-
aggregates (6/20)	Calcareous 472	-	-
W/C ratio	0.47	0.45	0.5
Volumetric weight [kg/dm^3]	2.4	2.5	-
Average compressive strength at 28 days [MPa]	55,27	61	34

Table 2: Second set of experiments: Mix composition of the concretes

DOSAGE CONCRETE (kg/m^3)	BCR	BCG
CEM I 42.5 N LA HSR LH	350	350
Calcitec 2001 MS	50	50
Admixture	3.92 (Rheobuild 1100 con. 30%)	2.45 (Glenium 27)
Limestone sand (0/4)	721	721
Calcareous aggregates (2/6)	417	417
Calcareous aggregates (6/14)	200	200
Calcareous aggregates (6/20)	472	472
W/C ratio	0.47	0.47

For the alternative test, the capillary water absorption test, specimens were prepared by cutting a slice 5 cm in height from the center of a cylinder of 15x30 cm in size. After wet curing during 28 days, they were left to dry at laboratory conditions RH ~ 60% and 20 ± 2ºC until constant weight. Further, they were submitted to a capillary suction experiment (figure 2) in which the specimens were introduced in a container having in the bottom a rack in plastic and water until the specimens were covered only 1 cm in height (figure 2 right). The specimens were periodically weighed until constant weight.

Figure 1: Left: Arrangement for percolation tests from the upper surface with pressures until 2,5bar. Machine for tests until 7 bars with water introduced by the lower face of the specimens

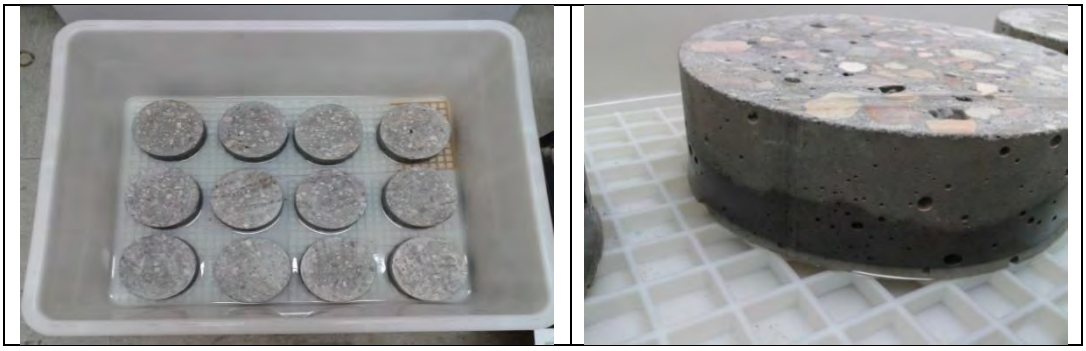

Figure 2: Left: samples submitted to water absorption. Right: detail of the rack and the level of the water

The Mercury porosity has been measured by means of a PORESIZER - MICROMERITICS device which operates until 30.000 Psi (207 MPa) able to measure pore sizes from 360 µm until 0,006 µm. The velocity of mercury penetration is of 10 s for each step. The sample used is around of 2 gram and is previously degasified in vacuum. The equation used for the calculations are given in Table 3 below.

Table 3: Equations used for the calculations

AUTHOR	EQUATIONS	PARAMETERS
Darcy's equation	$\boldsymbol{k = \frac{Q \cdot l \cdot \eta}{t \cdot A \cdot \Delta p}}$ [1]	Q = volume of liquid flowing [m^3] l =thickness of penetrated section [m] η =viscosity [Ns/m^2] t =time [s] A =cross area [m^2] k= intrinsic permeability coefficient

Hagen-Poiseuille	$Q = \Delta P * \pi * R^4 / (8 * L * \mu)$ [2]	Q [m^3/s] = volume flow ΔP [Pa] = differential of pressure between inlet and outlet. R [m] = internal radius L [m] = distance between inlet and outlet μ [Pa*s] = dynamic viscosity of the fluid

3. RESULTS

The results of the permeability coefficient calculated through Dracy's law, by making use of the data from the *water percolation* test are represented in figure 3. The mortar specimens logically show a higher coefficient of permeability than the concretes that gave rise to similar results. It is evident that in general by applying higher pressures, especially for the concretes, the coefficient of permeability seems to decrease. For the mortars indication of what might be a maximum can be observed, but the lack of sufficient data points at intermediate pressures makes it difficult to confirm this observation.

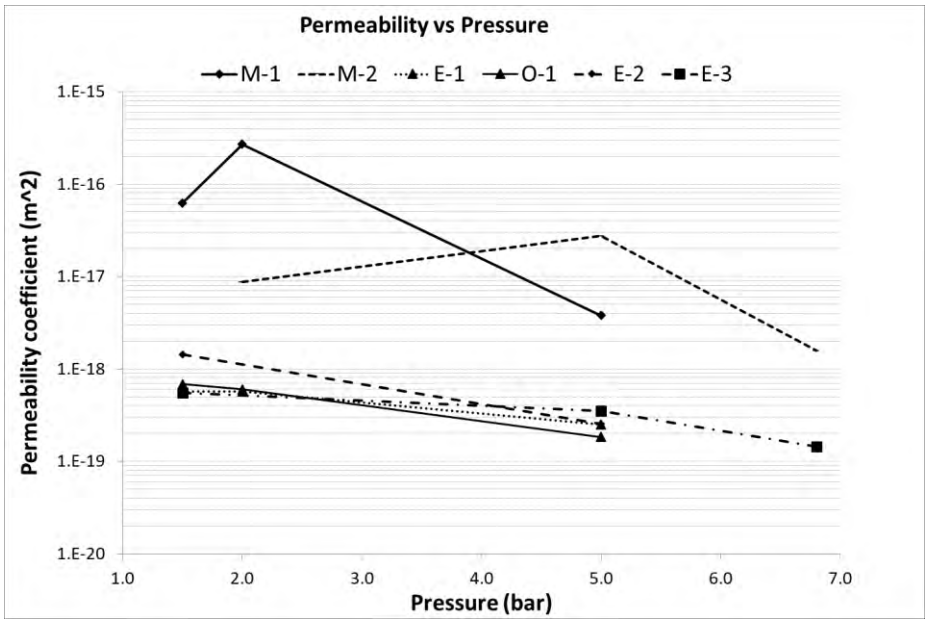

Figure 3: Coefficient of Permeability versus Pressure at several RH of pre-conditioning of the specimens

In addition to Darcy's equation, Hagen-Poiseuille equation was applied to the measurement results of *water percolation* test, to calculate a sort-of average pore diameter. The results are given in Figure 4 and are consistent with those derived from Darcy's law, being larger pores in the mortar specimens with respect to concretes. But, they do not seem to be much influenced

by the applied pressure. It is important to observe absolute values of the calculated pore radius, which is ranging from 5 to more than 20 microns. It must be stated, the equation only applies to straight pipes and conditions are: laminar flow, steady state, incompressible fluid, uniform viscosity and a constant circular section. Its application to porous materials and in particular concrete, seems very ambiguous.

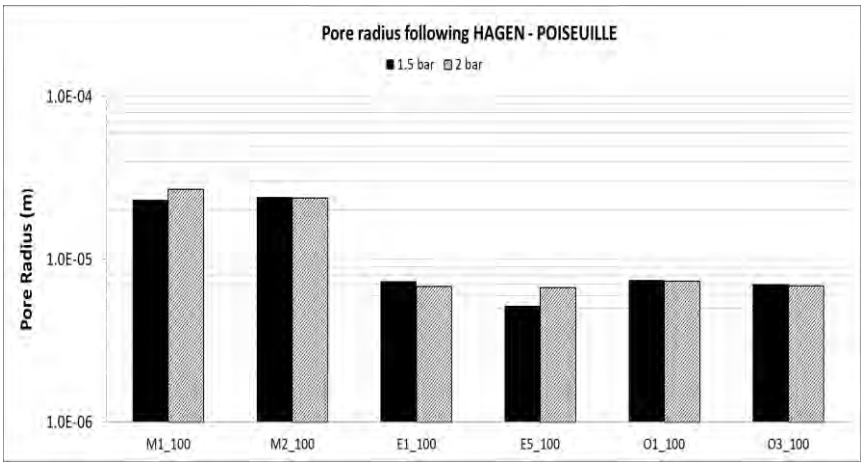

Figure 4: Radius of "equivalent" pore according Hagen – Poiseuille

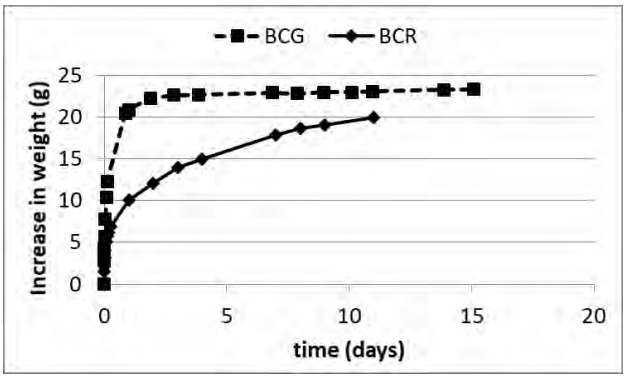

Figure 5: Increase in weight by absorption with time of concretes of second set of experiments

The data from the capillary absorption experiment, being the increase in weight of the specimens in function of time, is plotted in figure 5. The pattern of the absorption trend are very different for the two concretes, nevertheless they have a similar composition. This is confirmed by the MIP porosity values, which were of 1.03 % in volume for BCR and of 5.09% for BCG.

4. DISCUSSION

In the water percolation and in the water penetration tests, it seemed to us logical to expect higher flow for the higher pressures applied, because not only is the water pressed in with more fore, a higher external pressure could overpasses the capillary pressures of smaller pores. Pores with capillary pressures above the applied ones will not enable water to percolate throughout

them. However, this was not the observed as such in the results, on the contrary, the water permeability coefficient deviated from the *percolation* test by Darcy's Law was mostly smaller for higher pressures. The unexpected result might be explained by an increase in friction against pore walls, but this is still a hypothesis to be confirmed. In any case, the findings demonstrates the water *percolation test* cannot be regarded adequate for permeability testing of very dense concretes as those under study in this paper. In addition, it has to be emphasized that the coefficient of permeability, k, cannot be a material parameter (intrinsic value) as it is dependent on the pressure applied.

On the other hand, the calculation through Hagen-Poiseuille equation also failed, because it gives the equivalent radius of a virtual single pore in the material whose numerical value has doubtful any meaning, especially when compared to MIP measurements of similar concretes.Therefore we developed another approach based on the capillary absorption test that was advanced in [7]. This new approach is based in the relation between time of absorption and pore radius and on the velocity of capillary rising. In a capillary absorption test, all the pores absorb water at the same time, but the water in the larger pores will reach the upper face of the specimens earlier than the water in the smaller pores. Therefore by taking into account the theoretical velocity of water rising by capillary forces and from the derivative of the data gained by the capillary absorption test, it is possible to calculate the pore size distribution that should give rise to the observed gain weight in function of time [7]. This porosity distribution is in the following being referred to as WAPP (Water Absorption Porosity and Permeability). The permeability coefficient can be calculated through Darcy's law from the increase in weight (total rising flow of water). As a result the permeability coefficient of a concrete specimen is the equal to the weighted sum of the intrinsic permeability coefficients of the pores in the concrete. The effect of additional external hydraulic pressure can be easily calculated in a similar manner.

Figure 6 present the data obtained from MIP and from WAP, by applying equation from [7], for both concrete BCR and BCG. The pore size distribution is in the same order of magnitude than MIP, which confirms that the WAP method is reproducing correctly the microstructure. At this respect, it has to be taken into account that the water pore size distribution can be slightly different than the mercury one, as the wetting capacities of both fluids are different. In most cases, it can be argued water is the more representative medium. The Permeability coefficients k (m/s) are given in Table 4.

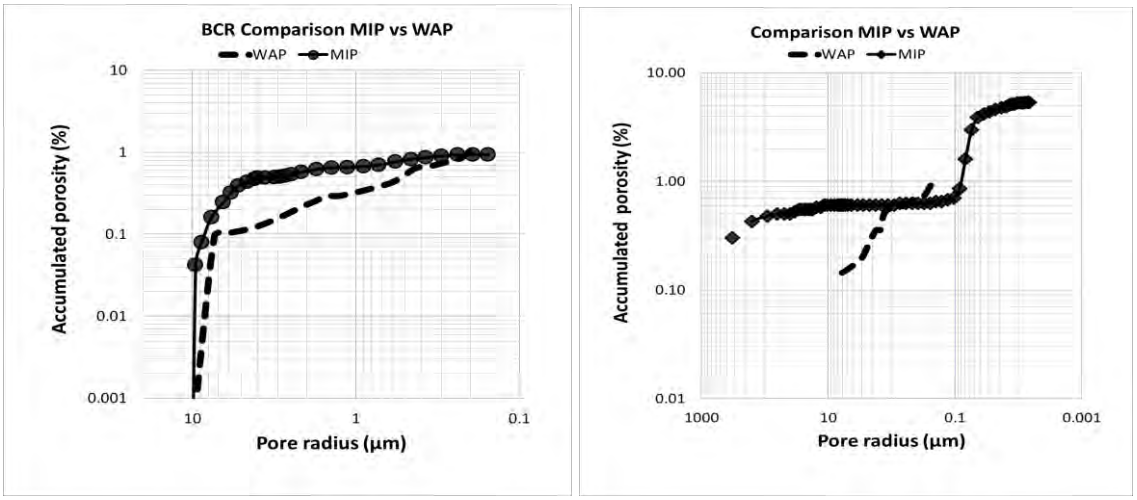

Figure 6: Total (cumulative) porosity of BCR and BCG samples. The dashed line is WAP method and the symbols are the values of MIP.

Table 4: Permeability coefficients and comparison of WAPP and MIP porosity

CONCRETES	Permeability coefficient (no Pressure applied)		Permeability coefficient (with 2 bars Pressure)		Total Porosity (%volume)		
	m/s	m2	m/s	m2	MIP	WAP	ε
BCR	8,26E-10	8,26E-17	7,55E-11	7,55E-18	1.03	5.2	4.40
BCG	2,87E-09	2,87E-16	2,62E-10	2,62E-17	5,09	7.76	3.62

5. CONCLUSIONS

The result shows that the use of Darcy's law or Valenta expression cannot be applied to concretes except that the material is very porous due to only larger pore size enable the water percolation. The calculation through Hagen- Poiseuille assumes the existence of a single pore in the material which is not logical. The paper presents the new method named WAPP based in the absorption test to calculate the permeability coefficient and the pore size distribution.

REFERENCES

[1] Zuloaga P. (2007). "Modelo de comportamiento de barreras de hormigón para el aislamiento de residuos radiactivos de baja actividad (Performance model of concrete barriers for the isolation of wastes of low radiactivity)". Doctoral Thesis. Industrial Engineers Faculty. Bilbao-Spain.

[2] Powers, T. C. Structure and physical properties of hardened portland cement paste. Journal of the American Ceramic Society 41,1, (1958) 1-6.

[3] Kropp J. (1995). "Relations between transport characteristics and Durability. Performance criteria for concrete Durability". Edit. J. Kropp and H.K. Hilsdorf. Published by E&FN SPON. Results of Rilem TC 116.

[4] Hooton, R.D. (1986). "Permeability and Pore Structure of Cement Pastes Containing Fly ash, Slag and Silica Fume". Blended Cements, ASTM STP 897, G.Frohnsdorff, Ed., American Society for Testing and Materials, Philadelphia, pp. 128-143.

[5] Valenta, O., "General Analysis ot the methods of testing the durability of concrete", Rilem Symposium of Durability of Concrete, Paper A-3, Vol. 1 (1969).

[6] Dullien F. A. L. (1975). "Invited Review. Single Phase Flow Through Porous Media and Pore Structure". The Chemical Engineering Journal. Vol. 10, p. l-34.

[7] Saucedo-Mora L., Andrade C., Cabeza S., Meinel D. (2017). "Physical model of the capillary absorption in cementitious materials, new approach to calculate analytically the pore size distribution from the gravimetric test". International Conference of Advances in Construction Materials and Systems. RILEM. Chennai-India. September.

REAL-TIME CHLORIDE DIFFUSION COEFFICIENT IN CONCRETE USING EMBEDDED RESISTIVITY SENSORS

Ameya Kamat (1), Yawar Abbas (1), Andrija Blagojević (1) Toine van Casteren (1) and Joost Walraven (2)

(1) Concrefy B.V., Venlo, The Netherlands

(2) Em. Prof. Delft University of Technology, Delft, The Netherlands

Abstract

Service life of concrete infrastructure is severely compromised because of chloride-induced corrosion and measuring the chloride content is crucial to determine the remaining service life. DuraCrete provides a chloride ingress model based on Fick's 2nd law. Although the diffusion coefficient is modelled as a time-dependent variable, the DuraCrete solution averages it to a constant value. This simplification leads to inaccurate estimation of the chloride content. A new analytical solution that addresses the underlying mathematical discrepancy has been proposed. However, the time-dependent diffusion coefficient is still based on an empirical factor. In this study, a real-time durability monitoring system has been developed using remotely operated resistivity sensors. Such a system is able to monitor the time dependent diffusion coefficient without the need to incorporate empirical factors. Additionally, a numerical technique to find an approximation of the proposed improved analytical solution is presented using real-time resistivity measurements from laboratory and real structures. The results show that the discrete sensor data measurements over time provide a good approximation of the proposed analytical solution. The system developed in this study is used as a data-driven input parameter to supplement the existing chloride models.

Keywords: Real-time resistivity sensors, time-dependent chloride diffusion coefficient, DuraCrete, service life monitoring, concrete durability.

1. INTRODUCTION

Chloride-induced corrosion is arguably one of the most common degradation mechanisms that affects the durability and consequently the service life of concrete infrastructure. The ingress of chlorides in concrete can lead to pitting corrosion, spalling of concrete and an eventual structural failure. Thus, monitoring chloride ingress is crucial for estimating the service life. The current practice of condition assessment is by visual inspections which often miss the early corrosion symptoms. Other techniques often involve drilling concrete cores to measure the chloride profiles and the chloride diffusion coefficient [1]. DuraCrete provides guidelines to a probabilistic method to design a structure for a designated service life [2].

In DuraCrete, the models to predict the ingress of chlorides in concrete are based on the Fick's 2nd law of diffusion. The solution to determine the chloride ingress assumed the diffusion coefficient to be a constant parameter [3]. However, the time dependency of diffusion coefficient has been reported by many publications [4, 5] and an attempt is made to incorporate this in the DuraCrete model. Some mathematical discrepancies were reported pertaining to the inclusion of time-dependent diffusion [6,7]. Therefore a re-derived analytical model for chloride ingress is used in this study [8].

The aforementioned prediction models still heavily depend on the early age Rapid Chloride Migration (RCM) test and empirical ageing coefficients to model the time-dependency of diffusion coefficient. Making predictions based on a single input from a laboratory test may not give reliable predictions in the long term. Additionally, performing rapid chloride test is laborious and expensive. The idealised functions used in the models are not able to capture the effects due to varying environments in real structures. Electrical resistivity of concrete has been reported in the literature as a key parameter for concrete durability [9, 10]. In the past researchers have tried to correlate the electrical resistivity of concrete to chloride migration coefficient as an alternative to the RCM test [11, 12]. In this study, the sensor technology using electrical resistivity is used not only to determine the chloride migration coefficient but also as a monitoring tool to supplement the aforementioned models with a realistic dataset.

2. THEORETICAL BACKGROUND

Chloride transport in a porous medium like concrete is strongly dependent on the microstructure and its underlying permeability. The most widely known equation to model the chloride transport is based on the solution to the Fick's 2nd law of diffusion. The solution of Fick's 2nd law as presented by Collepardi et al.[3] is presented in Eq. 1.

$$C(x,t) = C_s - C_s.\,\mathrm{erf}\left\{\frac{x}{2\sqrt{D.t}}\right\} \quad (1)$$

Where, C_s is the surface chloride concentration assumed to be a constant value. In Eq. 1, the diffusion coefficient, D, is the constant of proportionality. D is indicative of the ability of concrete to transport chloride ions via diffusion. It was shown experimentally that the diffusion coefficient is a time dependent phenomenon and decreases with time [5, 13]. In the DuraCrete model, this time-dependency has been modelled as shown in Eq. 2 [2].

$$D(t) = D_0.\left(\frac{t_0}{t}\right)^{n_{cl}} \quad (2)$$

Where, t_0: reference time; 28 days, n_{cl}: ageing factor determined empirically and D_0 = RCM coefficient at reference time t_0. D_0 for modelling the time-dependent diffusion coefficient is based on RCM concept developed as an accelerated non-steady-state chloride migration test and standardised as NT Build 492 [14]. The time dependent-function as seen in Eq. 2 has been directly substituted in the solution presented in Eq. 1 which results in Eq. 3 and does not satisfy the Fick's 2nd law of diffusion. This erroneous substitution by DuraCrete is partially compensated using an empirical factor 'K_{tot}'. This mathematical discrepancy has been acknowledged in many studies [6–8].

$$C(x,t) = C_s - (C_s - C_i).\,\mathrm{erf}\left\{\frac{x}{2\sqrt{K_{tot}.D_0.\left(\frac{t}{t_0}\right)^{n_{cl}}.t}}\right\} \quad (3)$$

Where, $C(x,t)$ = chloride content at x depth and time t, and C_i= initial chloride content. This results in an over-simplification. The diffusion coefficient in Eq. 3 is treated as a constant at a particular instance in time. This results in an averaged value of the instantaneous diffusion coefficient over the whole service life giving erroneous estimations. A mathematically appropriate way of approaching the problem was presented by Gaal [6]. This required re-solving the differential equations as proposed in [15] but with a time-dependent diffusion coefficient function modelled as per Eq. 2. This resulted in an evaluation of a definite integral of the diffusion function $D(\tau)$ over time, see Eq. 6. A generalised solution is presented by Tang and Gulikers [8]. The solution takes into account the history of diffusion coefficient and provides an analytical solution that satisfies Fick's 2nd law, presented in Eq. 4-5.

$$C(x,t) = C_{s,0}\text{erfc}\left\{\frac{x}{2\sqrt{T(t)}}\right\} \tag{4}$$

$$T(t) = \int_{t_{ex}}^{t+t_{ex}} D(\tau)d\tau = \frac{D_0}{1-n_{cl}}.\left[\left(1+\frac{t_{ex}}{t}\right)^{1-n_{cl}} - \left(\frac{t_{ex}}{t}\right)^{1-n_{cl}}\right]\left(\frac{t_0}{t}\right)^{n_{cl}}.t \tag{5}$$

Here, t_{ex} is the concrete age at first exposure to chlorides. The model is simplified further by assuming $t \gg t_{ex}$ which implies $t_{ex} \approx 0$. This reduces the model further to Eq. 6.

$$T(t) = \int_0^t D(\tau)d\tau = \frac{D_0}{1-n_{cl}}.\left(\frac{t_0}{t}\right)^{n_{cl}}.t \tag{6}$$

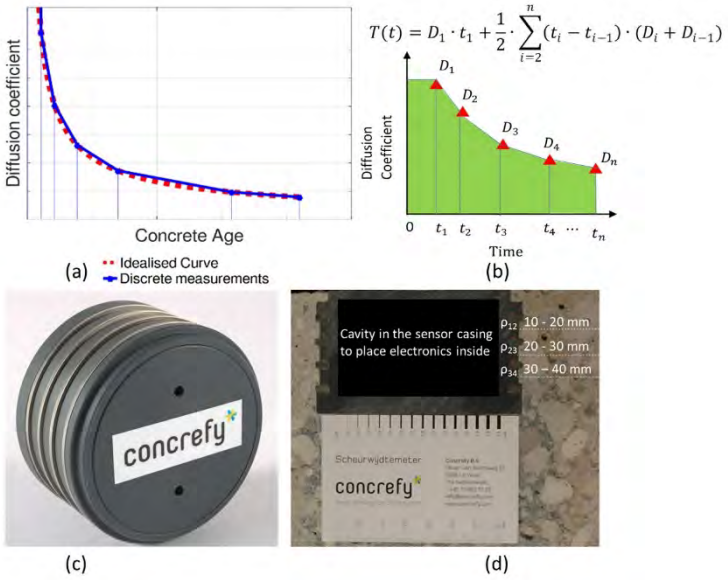

Figure 1: (a) Discrete data schematic (b) Concept to evaluate the area under the curve by trapezoidal rule (c) Durability sensor (d) Cross-section of the durability sensor.

The electrical resistivity is a parameter that is closely associated with the ionic transport of species in concrete. It can be correlated to the moisture content and tortuosity of concrete microstructure [9]. The chloride ingress models need RCM coefficient as an input. The test is time intensive. As an alternative, researches have proposed electrical resistivity to evaluate the RCM test with success. As a part of Brite EURam III, different resistivity methods were compared with the RCM test results conducted in the laboratory and a good correlation was found [11]. The resistivity and the RCM coefficient are inversely proportional under saturated

conditions with similar regression coefficients [9, 12, 16–18]. Under non-saturated conditions, resistivity was proven to be a good indicator of diffusion [19].

In this study, electrical resistivity is used as a parameter to evaluate the time-dependent diffusion coefficient by providing real-time data. For this purpose, a multi-ring impedance sensor is developed at Concrefy that remains embedded in concrete and send resistivity data remotely. The correlation based on DuraCrete [11] is used to relate electrical resistivity measured in concrete using embedded sensors to RCM. The obtained diffusion coefficient from the resistivity measurements is combined with Eq. 4 and Eq. 6 to evaluate chloride ingress in concrete. In Eq. 4 a new term $T(t)$ was introduced as a correction to the DuraCrete model and integrated in Eq. 6. Since $D(\tau)$ can be described as a continuous function modelled using an ageing coefficient, it was possible to evaluate a definite integral. However, resistivity measured by the sensors results in a set of discrete points in time. Thus, an integration over the time domain is undefined. The variable $T(t)$ is the area under the diffusion-time curve presented in Eq. 2. The data points can be used to approximate $T(t)$ by discretising them further as trapezoids, see Fig. 1a. The scheme to approximate $T(t)$ is presented in Fig. 1b. The discrete points are marked in red which measure D_i at time t_i. The vertices of the points serve as boundaries for trapeziums. The approximation of $T(t)$ is thus a cumulative sum of the discrete trapeziums as seen in Fig. 1 b. The function is updated for every new measurement in time. The applied numerical technique is called 'Trapezoidal-rule'.

3. EXPERIMENTAL

The schematic of the real-time durability sensor and its cross-section is shown in Fig. 1c and d. The sensor has four stainless steel rings 10 mm apart with a geometric constant of 0.2 and excitation frequency of 108 Hz. The resistivity is measured at 3 zones within the concrete cover depth as shown in Fig. 1d. For the evaluation of diffusion coefficient in DuraCrete, the resistivity of Two Electrode Method (TEM) is used. The DuraCrete also reported the correlation between the multiple-ring electrode (MRE) sensors and the TEM method. The resistivity of TEM was found to be 1.07 times as the MRE with negligible variance [11]. This implies that the TEM-MRE correlation can be directly applied. The experiment involves regular resistivity measurements and translating them to diffusion coefficients. The measurements are obtained in the laboratory conditions as well as an engineering structure used in the case study.

Table 1: Concrete mix design and properties for lab experiments

Mix Tag	Binder type	Binder Content (Kg/m^3)	w/b	Exposed Environment	$D_{RCM\ @\ 28\ days}$ [x10^{-12} m^2/s]	Ageing Coefficient [n_{cl}]
I	CEM I	400	0.4	95% RH, 20ºC	11	0.3 [2]
II	CEM III/B	340	0.48	95% RH, 20ºC	10.8	0.71 [2]
III	CEM I	280	0.65	95% RH, 20ºC	33	0.3 [2]
MG	CEM IIB-S+CEM IIA-S	340	0.5	Atmospheric	10	0.65 [12]

Three different mixes were prepared by changing the binder type as well as the water-binder (w/b) ratio. The details of the mix are presented in Table 1. CEM I and CEM III/B were used since they are the most prevalent binder types in the Netherlands. Concrete was cast for the purpose of sensor measurements and for evaluating the standard RCM coefficient. For every mix, 3 cubes were casted in situ with embedded sensors and 3 cubes were cast without sensors.

The cubes were cast in the laboratory and maintained in the climate room at 95% RH and 20 ºC condition. Mix MG was cast on the construction site as part of the case-study bridge in Mönchengladbach, Germany. Sensors were embedded in the bridge. The sensor installation is presented in Fig. 2a and b.

The diffusion coefficient derived from resistivity measurements are compared with the time-dependent idealised curve used in chloride ingress models, presented in Eq. 2. The idealised curves depend on the RCM coefficients at a reference age of 28 days and the ageing coefficient (n_{cl}) adopted from DuraCrete [2]. RCM test is conducted as per [14]. Submerged condition is assumed since it was closest to the condition in the climate room. For the casestudy, n_{cl} is adopted from CUR-81 for the specific binder type that was used [12]. The parameters are presented in Table 1.

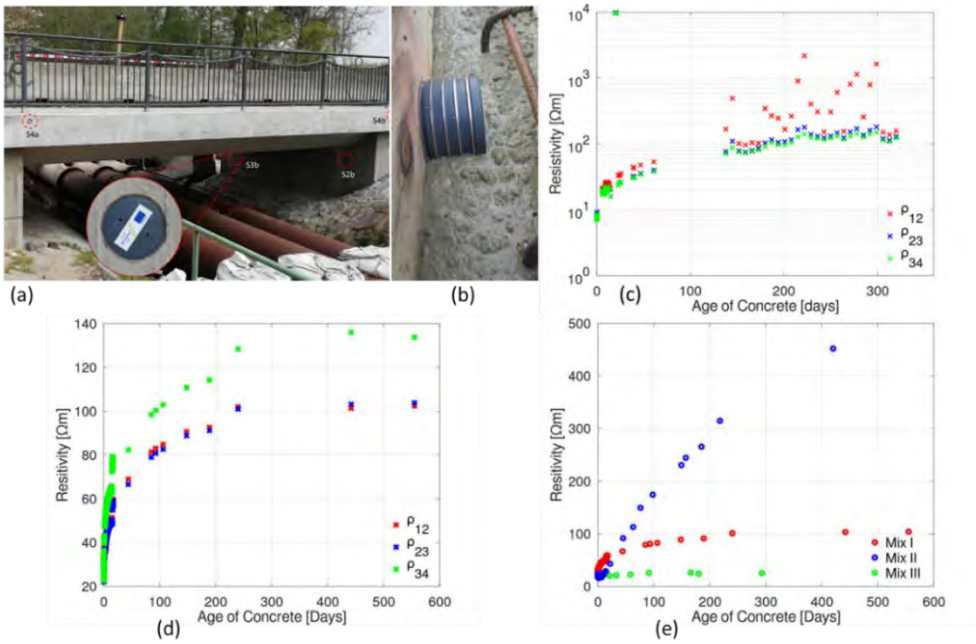

Figure 2: (a) and (b) Durability sensor in a bridge from the case study (c) Resistivity measurements of sensor from the case study (d) Resistivity measurements of Mix I at three depths in the climate room (e) Comparison of the resistivity measurements.

4. RESULTS AND DISCUSSION

The results of the resistivity measurements in the lab and the case-study are presented in Fig. 2. In Fig. 2c, the resistivity at the top zone (ρ_{12}) is relatively different than the resistivity at the inner depths (ρ_{23} and ρ_{34}). The top surface is sensitive to the environmental changes compared to the inner layers and thus exhibits different transport properties compared to the internal layers as seen in Fig. 2c. This is called 'skin effect' and is one of the reasons for inaccuracies while modelling chloride transport using Fick's second law of diffusion [20]. In this study, the diffusion coefficient is calculated based on the average across the depth. This partially captures the skin effect and its role in the transport properties of concrete. The electrical resistivity of concrete is related to its degree of saturation [21]. Thus, monitoring electrical resistivity provides insights in the transport properties. This dependency is visible in Fig. 2d (see ρ_{12}) which results in steady resistivity values for a wet environment and Fig. 2c where the drier

environment results in an increasing resistivity (see ρ_{12}). The continuous monitoring of the resistivity is also able to capture the fluctuations in the transport properties arising from the changes in the ambient RH. Moreover, the electrical resistivity shows a strong dependence on the type of binder as seen in Fig. 2e.

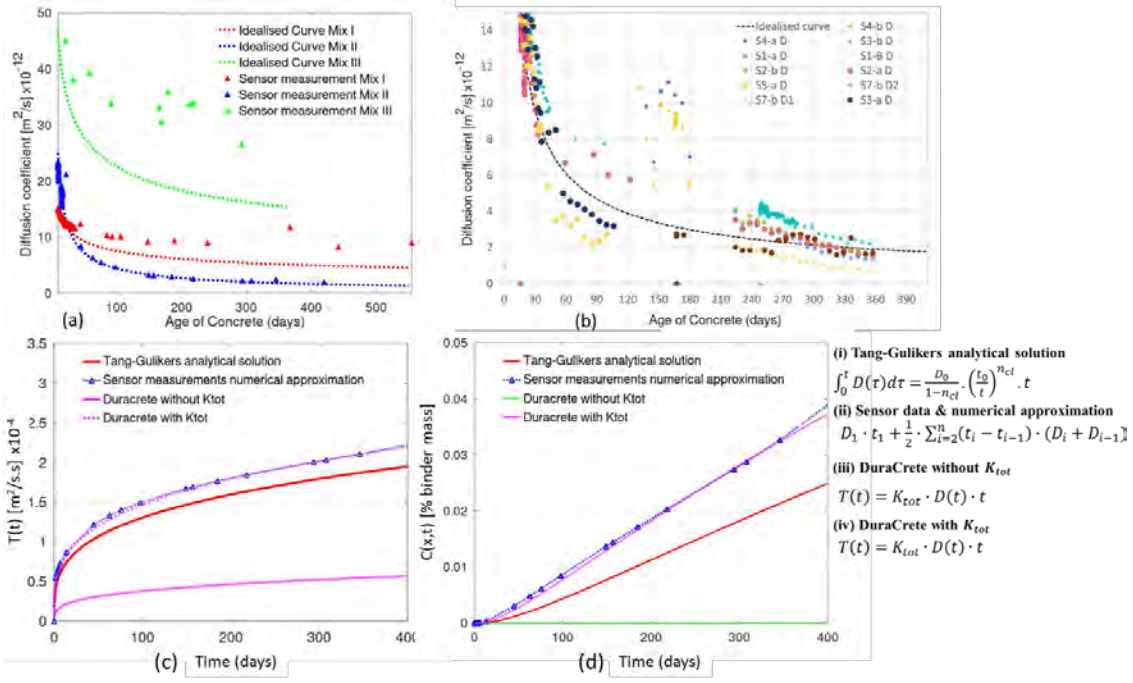

Figure 3: (a) Comparison of the diffusion coefficient measured by the sensors in the lab conditions (b) Diffusion coefficient measured in the case-study (c) Comparison of different approaches to evaluate T(t) (d) Comparison of chloride content calculation.

The results for the diffusion coefficients using sensor measurements in the lab as well as case-study are presented in Fig. 3a and b. These are compared against their respective idealised curves. The sensor results are in case of Mix I and Mix II. Both the mixes are composed of different binder types as well as water-binder ratios. In spite of different chemical compositions, the sensor results are able to correspond to the ideal curves. As a result, a mix-specific calibration is not necessary. The real-time data thus provides better insights in the ageing and offers a possibility to monitor transport properties without a need to incorporate an empirical ageing factor. Moreover, the diffusion coefficients calculated from the case study as presented in Figure 3b are also comparable to its respective idealised curve. The low scatter results from the variation in local concrete properties and the environment. The bulk results still lie in an acceptable range. The measurements do not correspond to the idealised curve when it comes to Mix III. Mix III has a higher w/b ratio compared to Mix I. Possibly, Mix III forms a microstructure with a high pore connectivity resulting in a much higher diffusion coefficient compared to the idealised curve. It is plausible, water-binder ratio is not taken into account while modelling the idealised curves.

A comparison of different approaches to estimate chloride content is carried out. Different approaches differ in the calculation of the variable $T(t)$. This is elaborated in Fig. 3d. The analytical solution by Tang and Gulikers is used as a reference [8] (see Eq. 6). Mix II data is presented for comparison. It can be inferred from Fig. 3c that the sensor measurements

evaluated using numerical approximation slightly overestimate the analytical solution. However, they are comparable. The deviation occurs only in the initial stages because of large time steps in the sensor measurements. However, after the initial deviation, the slope of the analytical solution and the approximation using sensors remains similar. This implies the error does not accumulate over time. The initial deviation can thus be overcome by assigning shorter time steps in the initial period.

From Fig. 3c, it is also evident that the DuraCrete model without the factor K_{tot}, underestimates $T(t)$. This is because at every instance of time this approach approximates $T(t)$ to a rectangle using the diffusion coefficient at a particular time t. The diffusion coefficient is averaged over the entire time period without taking into account the history of diffusion coefficient. This results in an underestimation. The error increases with each time step. However the rate of error decreases with each time step since the long term diffusion coefficient tends to a constant value. Over the service life of a structure, the error may not be significant. However, it is quite significant in the first few years and thus cannot be used for monitoring. DuraCrete compensates this error by introducing an empirical factor K_{tot}. With that, the DuraCrete model comes close to the analytical model. However, the underlying mathematical lapse is not addressed. The introduction of an empirical factor is flawed as the solution is not generalised. As the error accumulation decreases in time, inclusion of a constant factor in the long would result in an overcompensation making the service life model too conservative.

Having calculated *T(t),* the chloride content is calculated as per Eq. 6 where $T(t)$ is defined and the result presented in Fig. 3d. The sample calculation assumes the parameters listed for Mix II in Table 1; $C_{s,0}$=2.2 % of the binder weight; K_{tot}=3.88 based on DuraCrete; Cover depth=50 mm. It is evident that DuraCrete without the K_{tot} factor underestimates chloride ingress. The error between the analytical model and measurements is due to the early deviation.

5. CONCLUSIONS

Embedded durability sensor using remote real-time resistivity measurements is shown to estimate the changing diffusion coefficient of concrete irrespective of the type of binder and without defining an empirical ageing coefficient. As a result, additional calibrations may not be required thereby providing a generalised approach. The sensor results were comparable to the laboratory as well as the full-scale case study. These measurements capture local variations in diffusion coefficient due to changes in the ambient conditions contrary to the current modelling practices. Thus, the sensor technology offers a potential to overcome some modelling limitations by providing a realistic dataset. Integrating sensor data to the existing chloride ingress models require some modifications. This is achieved by employing a numerical method to approximate the analytical solution using sensor readings as an input parameter. This method is able to provide a comparable approximation in relation to the time-dependent analytical model mentioned in the literature. The mathematical discrepancy in the DuraCrete approach in relation to the time-dependent diffusion coefficient and its potential overcompensation due to the use of a constant empirical factor K_{tot}, is also discussed. A deterministic approach is followed as a first step to develop the methodology. However, owing to the potential of significant data collection, spatial variation in diffusion properties can be included in the model. Subsequently, the model can be extended to a robust probabilistic model. Finally, to conclude, the data-driven approach presented in this study is a significant step towards development of a valuable tool that can extend the existing chloride ingress models.

ACKNOWLEDGEMENTS

The work was supported by EU-Interreg Deutschland-Nederland. We would also like to thank Umlaut and Ibac, RWTH University Aachen for their contributions pertaining to sensor.

REFERENCES

[1] NT-Build:443 ,*Concrete, Hardened: Accelerated Chloride Penetration*. Espoo NordTest 1995, p. 1–5.

[2] BE95-1347/R17: *DuraCrete-Final Technical Report: Probabilistic Performance based Durability Design of Concrete Structures*. 2000.

[3] Collepardi, M. et al.: Penetration of chloride ions into cement pastes and concrete. *J. Am. Ceram. Soc.*, **55** (10), 1972, p. 534–535.

[4] Mangat, P.S., Molloy, B.T.: Prediction of long term chloride concentration in concrete. *Mater. Struct.*, **27** (6), 1994, p. 338–346.

[5] Takewaka, K., Mastumoto, S.: Quality and cover thickness of concrete based on the estimation of chloride penetration in marine environments. *Am. Concr. Inst.*, **109** (17), 1988, p. 381–400.

[6] Gaal, G.C.M.: *Prediction of Deterioration of Concrete Bridges: Corrosion of Reinforcement due to Chloride Ingress and Carbonation*. PhD. thesis, Delft University Of Technology, 2004.

[7] Frederiksen, J.M. et al.: *Fick's 2nd law - Complete solutions for chloride ingress into concrete - with focus on time dependent diffusivity and boundary condition*. Lund Institute of Technology Division of Building Materials, 2008.

[8] Tang, L., Gulikers, J.: On the mathematics of time-dependent apparent chloride diffusion coefficient in concrete. *Cem. Concr. Res.*, **37** (4), 2007, p. 589–595.

[9] Andrade, C., Andrea, R.: Electrical resistivity as microstructural parameter for modelling of service life of reinforced concrete structures. *2nd Int. Symp. Serv. Life Des. Infrastructure, Delft, Netherlands*, (October), 2010, p. 379–388.

[10] Polder, R. et al.: RILEM TC 154-Electrochemical Techniques For Measuring Metallic Corrosion. *Mater. Struct.*, **3**, 2000, p. 603–611.

[11] BE95-1347/R8: *DuraCrete: Compliance Testing for Probabilistic Design Purposes*. 1999.

[12] CUR-81: *Duurzamheid van constructief beton met betrekking tot choloride-geiniteerde wapeningscorrosie*. 2007.

[13] Tang, L., Nilsson, L.-O.: Chloride diffusivity in high strength concrete at different ages. *Nord. Concr. Res.*, **11** (1), 1992, p. 162–171.

[14] NT-Build:492: *Concrete, Mortar and Cement-Based Repair Materials - Chloride Migration Coefficient From Non-Steady-State Migration Experiments*. NordTest, 1999.

[15] Crank, J.: *The Mathematics Of Diffusion*. Oxford: Oxford University Press, 1975.

[16] Denis, P. et al.: *Use of resistivity as a routine concrete quality control tool . Outcomes of records gathered during 2-year for the New Coastal Road on Reunion Island (France) offshore viaduct*. In: The International Federation for Structural Concrete 5th International fib Congress. Australia, 2018.

[17] Van Noort, R. et al.: Long-term chloride migration coefficient in slag cement-based concrete and resistivity as an alternative test method. *Constr. Build. Mater.*, **115**, 2016, p. 746–759.

[18] Andrade, C.: Calculation of chloride diffusion coefficients in concrete from ionic migration measurements. *Cem. Concr. Res.*, **23** (3), 1993, p. 724–742.

[19] Climent, M.A. et al.: A test method for measuring chloride diffusion coefficients through nonsaturated concrete. *Cem. Concr. Res.*, **32** (7), 2002, p. 1113–1123.

[20] Andrade, C. et al.: Chloride ion penetration in concrete: The reaction factor in the electrical resistivity model. *Cem. Concr. Compos.*, **47**, 2014, p. 41–46.

[21] Brameshuber, W. et al.: *Non-destructive determination of the water-content in the concrete cover using the multiring-electrode*. In: International Symposium on Non-Destructive Testing in Civil Engineering. 2003.

THE INFLUENCE OF LIGHTWEIGHT FUNCTIONAL AGGREGATES ON THE ACIDIFICATION DAMAGE IN THE EXTERNAL ANODE MORTAR DURING CATHODIC PROTECTION FOR REINFORCED CONCRETE

Wenhao Guo (1), Jie Hu (1), Yuwei Ma (2), Haoliang Huang (1), Jiangxiong Wei (1) and Qijun Yu (1)

(1) School of Materials Science and Engineering, South China University of Technology, Guangzhou 510640, Guangdong, China

(2) Guangzhou University - Tamkang University Joint Research Center for Engineering Structure Disaster Prevention and Control, Guangzhou University, Guangzhou 510006, Guangdong, China

Abstract

Impressed current cathodic protection (ICCP) is an effective corrosion protection and prevention technique for reinforced concrete structures served in chloride-contaminated environment. The acidification damage in the external anode mortar caused by the anodic reactions significantly influences the efficiency of ICCP for reinforced concrete. Therefore, improving the acidification resistance of the external anode mortar is of great importance for the successful application of ICCP treatment. In this study, a novel type of lightweight functional aggregates was proposed to mitigate the acidification damage in the external anode mortar. The influence of the prepared lightweight functional aggregates both on the electrochemical performance of the primary anode and morphology, mineral compositions and microstructure of the secondary mortar were investigated.

The results indicated that the lightweight aggregates efficiently mitigated the damage of MMO coating on the primary anode surface, thus maintaining the high stability and catalytic activity of the primary anode. Severe acidification damage happened in the mortar matrix within a distance of 300 μm from the primary anode; beyond this region, the acidification damage was mainly propagated along the interfacial transition zone around the aggregates. Because the lightweight functional aggregates maintained the high alkalinity in the secondary mortar, the acidification damage both in the vicinity of the primary anode and ITZ around aggregates was significantly halted. Therefore, the prepared lightweight functional aggregates can be potentially used for preparing the high performance external anode mortar, further improving the stability and efficiency of ICCP treatment and durability of reinforced concrete structures.

Keywords: Cathodic protection, External anode mortar, lightweight functional aggregates, acidification damage, reinforced concrete

1. INTRODUCTION

Impressed current cathodic protection (ICCP) is proved to be an effective corrosion mitigation and rehabilitation technique for reinforced concrete structures under chloride-contaminated environment [1, 2]. The basic theoretical principle for ICCP treatment is to negatively polarize the embedded reinforcement (generally more cathodic than -850 mV vs saturated calomel electrode (SCE) [3]), thus thermodynamically inhibiting the electrochemical reactions related to corrosion damage of the reinforcement.

During ICCP treatment, the following anodic reactions will occur mainly on the surface and vicinity of the primary anode [4-6]:

$$2OH^- \rightarrow 1/2O_2+2e^-+H_2O \quad (1)$$

$$H_2O \rightarrow 1/2O_2+2e^-+2H^+ \quad (2)$$

$$2Cl^- \rightarrow Cl_2+2e^- \quad (3)$$

$$Cl_2+H_2O \rightarrow Cl^-+ClO^-+2H^+ \quad (4)$$

The above reactions consume OH^- ions in the vicinity of the primary anode, thus leading to a pH drop of mortar pore solution. After the pH drop of mortar pore solution, the stability of hydration products at the primary anode/secondary mortar interface is reduced due to the altered micro-environment. The above process is known as acidification damage caused by the applied external current. The acidification damage of the external anode mortar can lead to more porous microstructure [4] and reduced adhesion at the primary anode/secondary mortar interface [7, 8], and also reduce the catalytic activity and subsequently increase the potential of the primary anode [9]. Therefore, improving the acidification resistance of the external anode mortar is of great importance for the successful application of ICCP treatment.

The preparation and optimization of the external anode mortar were widely investigated for decades. However, the optimization of the external anode mortar was mainly focused on improving either its conductivity or mechanical properties [10, 11]. To our best knowledge, the improvement related to the acidification resistance of the external anode mortar was not reported. To this end, the objective of this present paper is to apply lightweight functional aggregates (LFA) to prepare the high performance external anode mortar and investigate their mitigation effect on the acidification damage of the external anode mortar during ICCP treatment.

2. EXPERIMENTAL

2.1 Materials

Ordinary Portland cement (PII 42.5, China Resources Cement Holdings Ltd) and local tap water were used to prepare the mortar specimens. Two types of aggregates were applied for the preparation of the external anode mortar: the lightweight functional aggregates (LFA) and ordinary aggregates (NA). Commercially available porous ceramsites within the particle size of 3.5-4.0 mm were used for the preparation of LFA, and ordinary quartz river sands in the same size range were used as NA. The chemical composition of Portland cement is presented in Table 1. The sample designations in this study are as follows: specimens NA-20, NA-30

and NA-40 were the reference mortar specimens prepared with ordinary river sands with the volume fraction of 20 vol. %, 30 vol. % and 40 vol. %, respectively; specimens LFA-20, LFA-30 and LFA-40 were the mortar specimens prepared with lightweight functional aggregates with the volume fraction of 20 vol. %, 30 vol. % and 40 vol. %, respectively.

Table 1: Chemical composition of P Ⅱ 42.5 Portland cement used in this study (wt. %)

Composition	SiO_2	Al_2O_3	Fe_2O_3	CaO	MgO	K_2O	Na_2O	SO_3	TiO_2	LOI
Content	21.86	4.45	2.35	63.51	1.67	0.55	0.26	2.91	0.11	2.33

*LOI is the loss on ignition

Agar powders $(C_{12}H_{18}O_9)_n$ used in this study were plant tissue culture grade with a gel strength of 1300 g/cm^2 (code: H8145). Analytical grade reagents (e.g. NaOH, $Ca(OH)_2$, KOH and NaCl) and deionized water were used for the preparation of LFA and simulated concrete pore solution. Carbon fibers used in this study were isotropic Polyacrylonitrile (PAN)-based series chopped carbon fibers (Jiangsu Elda Composite Material Co., Ltd).

The primary anode used in this study was mixed metal oxide (MMO) coated Ti wire (with a diameter of 2.0 mm and length of 60 mm). Q 235 construction steel reinforcement (with a diameter of 8 mm and length of 110 mm) was used as cathode. The working surface area of the reinforcement was 28.14 cm^2.

2.2 Sample preparation

(1) Preparation of the simulated concrete pore solution

In this study, simulated concrete pore solution was prepared based on the reported studies [12-14]: the concentration of $Ca(OH)_2$, NaOH and KOH was 0.002 mol/l, 0.06 mol/l and 0.18 mol/l, respectively; the pH of the simulated concrete pore solution was 13.29. Furthermore, 3 wt. % NaCl was added in the simulated concrete pore solution to simulate the chloride-contaminated environment.

(2) Preparation of the lightweight functional aggregates

The lightweight functional aggregates (LFA) were prepared by impregnating the modified agar gel solution into dry and preheated porous ceramsites and the specific parameters and proportion of all components for the preparation of the modified agar gel solution are presented in Table 2. The impregnation procedure and related details for the preparation of LFA were similar to our previous study, and the resistivity of the prepared LFA was about 0.5 Ω·m [15].

Table 2: Mixture and preparation procedures of the modified agar solution in this study

Steps	Stirring speed (r/min)	Material added (wt. % per water weight)	Time (min)/Temp (℃)
1	30	Water/-- --	--/100.0
2	30	Agar powders/6.00	10.0/100.0
3	30	NaOH/0.33	0.5/90.0
4	30	KOH/1.40	0.5/90.0
5	60	$Ca(OH)_2$/8.62	1.0/90.0
6	120	Graphite powders/5.00	1.0/80.0~90.0

(3) Preparation of the external anode mortar specimen

In order to investigate the influence of the lightweight functional aggregates (LFA) on the acidification damage of the external anode mortar, cylindrical external anode mortar specimens with a height of 30 mm and diameter of 30 mm were prepared with the carbon fibers content of 0.75 vol. %. The volume fraction of aggregates (both NA and LFA) was 20 vol. %, 30 vol. % and 40 vol. %, respectively. MMO coated Ti wire (as the primary anode) with a length of 60 mm and diameter of 2 mm was placed in the axial center of the specimen, and the working surface area of the primary anode was 1.89 cm^2. The external anode specimens were cured at 20 ± 2 ℃ and 95 % relative humidity for 28 days before the accelerated acidification tests.

The positive and negative terminal of the external power supply (galvanostat, Corrtest CS1002) was connected to the primary MMO Ti anode and steel reinforcement, respectively. The surface area ratio of the secondary mortar and primary anode was 15:1. A constant current of 566 μA was applied, corresponding to a current density of about 200 mA/m^2 per surface area of the secondary mortar.

2.3 Methods

(1) Electrochemical measurements of the primary anode

Electrochemical impedance spectroscopy (EIS) and potentio-dynamic polarization (PD) measurements were performed for the external anode mortar specimen before and after the accelerated acidification test. The specimen was depolarized for 24 h before the electrochemical measurements, and three-electrode system was used for all electrochemical measurements, in which the external anode mortar specimen was the working electrode (WE), saturated calomel electrode (SCE) was used as the reference electrode (RE) and Ti mesh with a surface area of 200 cm^2 was used as the counter electrode (CE). The frequency range for EIS measurement was 100 kHz-10 mHz, and the amplitude was ±10 mV vs. open circuit potential (OCP) of the primary anode. The scanning rate of potentio-dynamic polarization was 0.5 mV/s in a potential range of -0.2 to 1.0 V vs. OCP of the primary anode.

(2) Optical fluorescence microscopy observation (OFM)

In order to investigate the acidification damage in the secondary anode mortar, the cross section of the external anode mortar specimen was observed by using optical fluorescence microscopy (OFM, Zeiss Discovery V12) with a excitation wavelength of 590 nm and magnifications range of 20× to 50×. After the accelerated acidification test, the cross section was cut from the middle part of the external anode mortar specimen and dried in vacuum oven at 40 °C until the weight of the cross section maintained constant. The fluorescent dye-containing epoxy (EpoFix pack, Struers Ltd) was then vacuum impregnated into the cross section specimen. The impregnated cross section specimen was polished with no.220, no.320, no.500, no.800, no.1200, no.2000 and no.3000 grinding papers, respectively.

(3) SEM observation

Scanning electron microscopy (SEM, EVO 18, Germany) was applied to investigate the morphology alterations at the primary anode/secondary mortar interface after the accelerated acidification test. SEM images with backscattered electron (BSE) mode were obtained for the

cross section specimen with an accelerating voltage of 20 kV and magnifications of 100× and 500×.

3. RESULTS AND DISCUSSIONS

3.1 The influence of LFA on the electrochemical performance of the primary anode

(1) Potential-dynamic polarization of the primary anode

The potentio-dynamic (PD) polarization curves for all specimens after the accelerated acidification test are shown in Fig.1. It was observed that after the accelerated acidification test, the anodic current density for specimen LFA was higher than specimen NA with the same aggregates content when the same polarization potential was applied. Furthermore, a lower polarization potential was needed to obtain an anodic current density of 400 mA/m^2 (per surface area of the primary anode) which was normally used for ICCP treatment [2, 3, 5]. For example, the potential for obtaining the above anodic current density was 728 mV for specimen LFA and 1105 mV for specimen NA with the aggregate content of 40 vol. %, respectively. The above results confirmed that the lightweight functional aggregates were beneficial for maintaining the high catalytic activity and stability of the primary anode embedded in the external anode mortar.

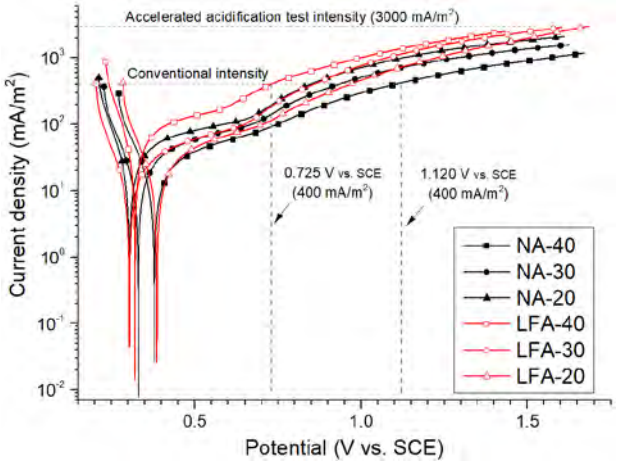

Figure 1: Potentio-dynamic (PD) polarization curves of all specimens after the accelerated acidification test

(2) The impedance response of the primary anode embedded in the external anode mortar

Fig.2 presents the impedance response of the specimens before and after the accelerated acidification test. In this study, EIS response was fitted by the equivalent circuit ($R_s((R_{ct}Z_w)Q_{dl})$) in this study. The physical meanings of the elements in the above equivalent circuit were as follows: R_s was the mortar matrix resistance, including the electrolyte resistance; R_{ct} was the charge transfer resistance of the primary anode, which represented the catalytic activity of MMO Ti anode for oxygen evolution; Q_{dl} was related to the property of the electrical double layer; Z_w was Warburg impedance.

The derived mortar resistance (R_s) and Warburg impedance (Z_w) of different specimens are shown in Fig.3. It was observed in Fig.3 (a) that before the accelerated acidification test, the mortar resistance for all specimens was at the similar level. After the accelerated

acidification test, R_s for specimen NA was significantly increased. When the lightweight functional aggregates were used, R_s for specimen LFA was also increased; however, specimen LFA presented lower R_s value, compared to specimen NA. The lower R_s for specimen LFA was mainly attributed to the mitigation effect of the lightweight functional aggregates on the acidification damage of mortar matrix at the primary anode/secondary mortar interface, leading to a better adhesion between mortar matrix and carbon fibers/LFA and subsequently higher conductivity of the external anode mortar. It was also observed from Fig.3 (b) that Z_w of all specimens was dramatically reduced after the accelerated acidification test.

Fig.4 presents the derived charge transfer resistance (R_{ct}) and related electrical double layer capacitance (Q_{dl}) of different specimens. All the specimens presented very low R_{ct} and high Q_{dl} before the accelerated acidification test, indicating the good catalytic activity of the primary anode. After the accelerated acidification test, R_{ct} of all specimens increased and the related Q_{dl} was slightly reduced. The beneficial effect of the lightweight functional aggregates was evidenced by the lower R_{ct} of specimen LFA compared to specimen NA, indicating a better catalytic activity of specimen LFA after the accelerated acidification test.

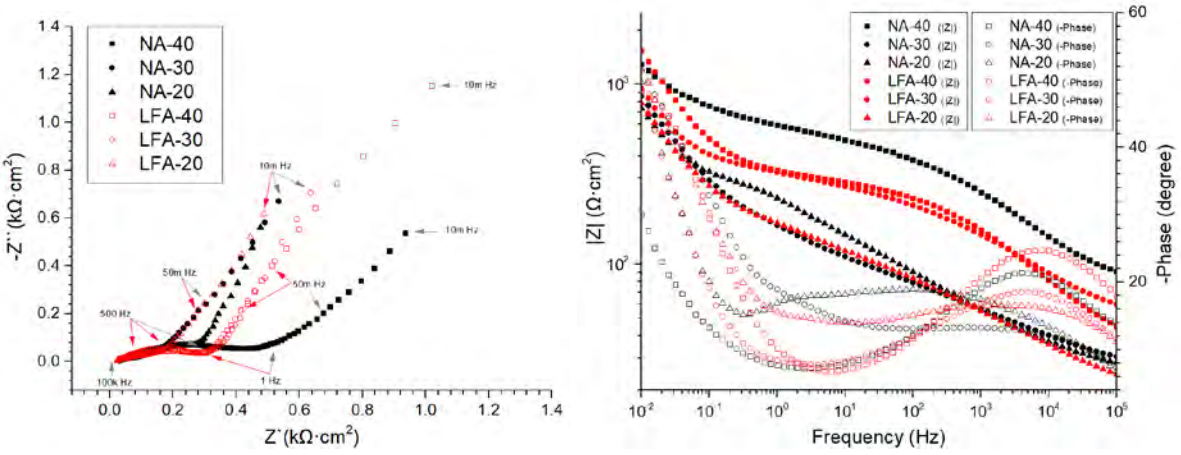

(a) Before the accelerated acidification test

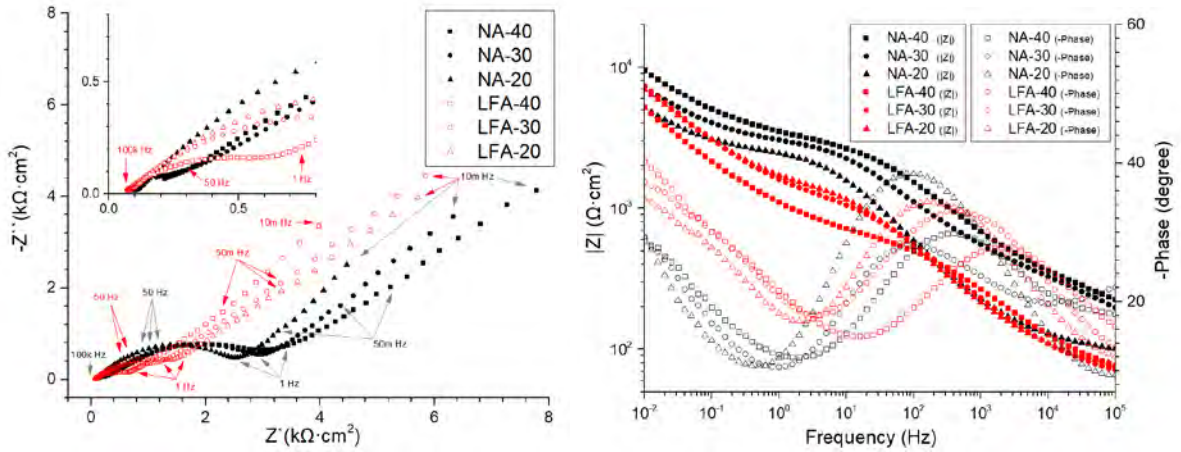

(b) After the accelerated acidification test

Figure 2: EIS responses in Nyquist and Bode format for the specimens before and after the AAT

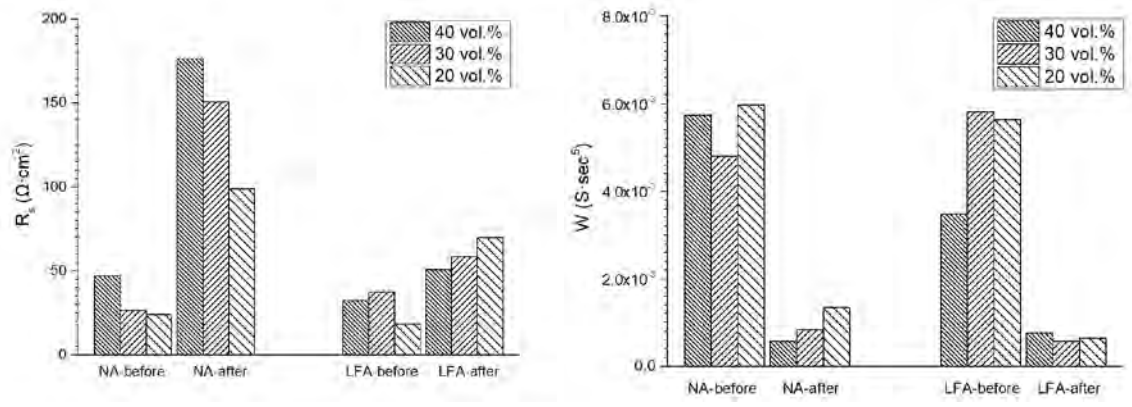

(a) Mortar resistance **(b) Warburg impedance**

Figure 3: The derived mortar resistance (R_s) and Warburg impedance (Z_w) for different specimens before and after the accelerated acidification test

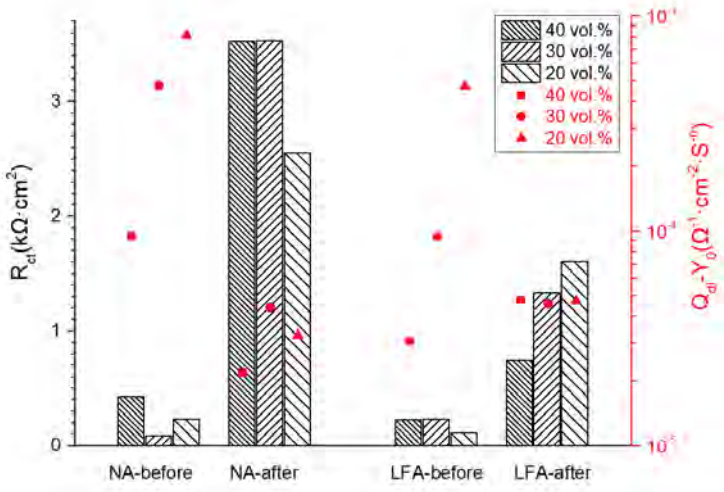

Figure 4: The derived charge transfer resistance (R_{ct}) and related electrical double layer capacitance (Q_{dl}) of different specimens before and after the accelerated acidification test

3.2 The influence of LFA on the acidification damage in the secondary mortar

(1) Acidification damage regions in the external anode mortar

The fluorescence microscopy images for specimens with 40 vol. % NA/LFA before and after the accelerated acidification test are shown in Fig.5.

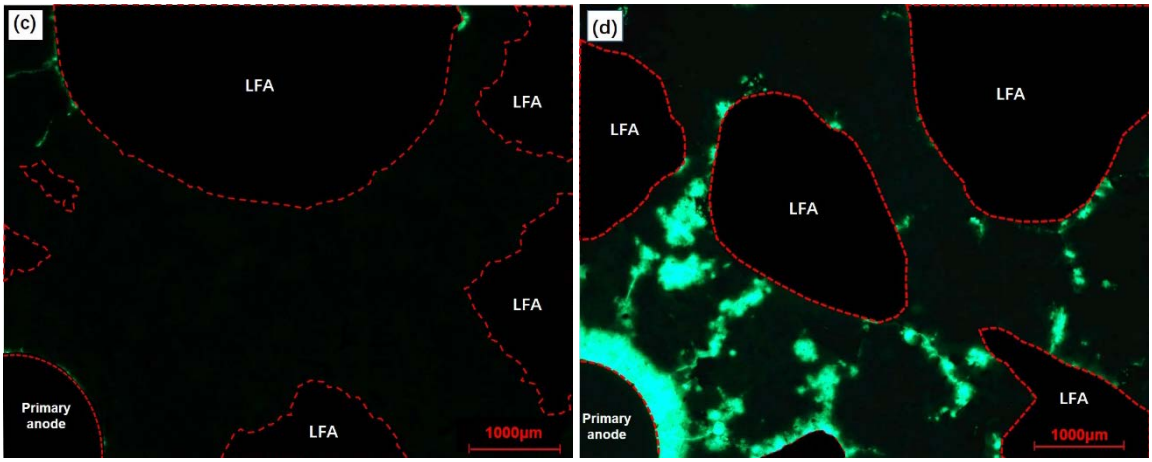

(a) Specimen LFA before AAT **(b) Specimen LFA after AAT**

Figure 5: The fluorescence microscopy images for specimen with an aggregate content of 40 vol. % NA/LFA before and after the accelerated acidification test (AAT)

After the accelerated acidification test, the acidification damage of the secondary mortar can be divided into two different regions. The first region was within the distance of about 300 μm from the primary anode surface. The most severe acidification damage happened in the vicinity of the primary anode, leading to porous microstructure in this region. Therefore, this region presented very bright colour in the fluorescence microscopy images. In this region, no obvious effect of the lightweight functional aggregates was observed, evidenced by the similar thickness of this region in the fluorescence microscopy images. Beyond the distance of about 300 μm from the primary anode surface, the acidification damage mainly occurred around the aggregate/mortar matrix interfacial transition zone (ITZ) and resulted in cracks in the mortar matrix. In this region, the lightweight functional aggregates halted the further propagation of the acidification damage, evidenced by the denser microstructure in ITZ and less cracks in the mortar matrix.

(2) Acidification damage in the vicinity of the primary anode

Fig.6 presents SEM images at the primary anode/secondary mortar interface for specimens with 40 vol. % NA/LFA after the accelerated acidification test. Two distinct acidification damage regions were also observed in SEM images, which was consistent with the fluorescence microscopy results. Compared to specimen NA, specimen LFA presented a denser microstructure in the severe acidification damage region (within a distance of 300 μm from the primary anode); furthermore, the cracks in the mortar matrix were also significantly less for specimen LFA. The above results indicated that the acidification damage degree in the external anode mortar was reduced by the lightweight functional aggregates.

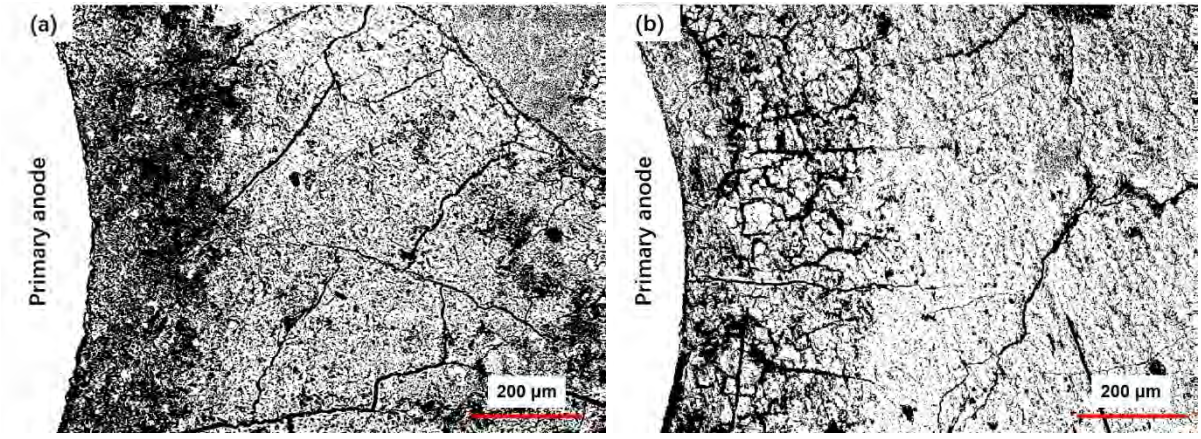

(a) Specimen NA **(b) Specimen LFA**

Figure 6: SEM images at the primary anode/secondary mortar interface after the accelerated acidification test: (a) specimen NA with the aggregate content of 40 vol. %; (b) specimen LFA with the aggregate content of 40 vol. %

(3) Acidification damage in the vicinity of the primary anode

SEM images and EDS analysis results in the vicinity of the aggregates with a distance larger than 1000 μm from the primary anode are shown in Fig.7. It was observed that specimen LFA presented a denser ITZ, compared to specimen NA; Ca/Si ratio in ITZ was significantly higher for specimen LFA (in the range of 0.58-1.64 for specimen NA and 1.97-4.82 for specimen LFA). The acidification damage area was also reduced by the lightweight functional aggregates, evidenced by the denser microstructure in the region with a distance larger than 50 μm from the aggregate. In this region, the difference in Ca/Si ratio of mortar matrix was small; however, specimen LFA still presented slightly higher Ca/Si ratio (in the range of 1.83-2.44), compared to specimen NA (1.74-2.28).

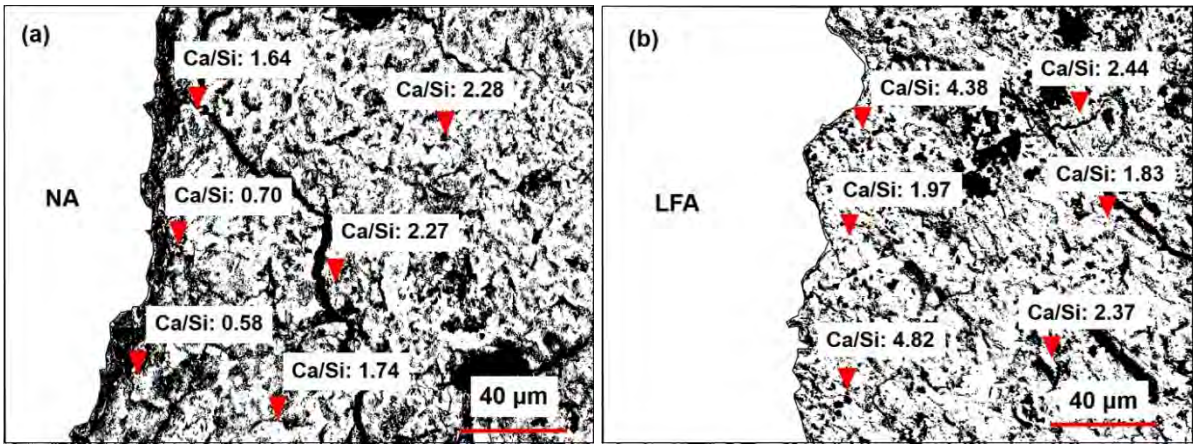

Figure 7: SEM images and EDS analysis results in the vicinity of the aggregates with a distance larger than 1000 μm from the primary anode after the accelerated acidification test: (a) specimen NA with the aggregate content of 40 vol. %; (b) specimen LFA with the aggregate content of 40 vol. %

4. CONCLUSIONS

In this study, a novel type of the external anode mortar was design and prepared based on lightweight functional aggregates and the influence of the lightweight functional aggregates on the acidification damage resulted from the applied external current during ICCP treatment was investigated. Based on the experimental results, the main conclusions in this study are summarized as follows:

(1) The lightweight aggregates efficiently mitigated the damage of MMO coating, thus maintaining the high stability and catalytic activity of the primary anode, e.g. lower anodic potential and charge transfer resistance of the primary anode.

(2) In this study, severe acidification damage happened in the mortar matrix within a distance of 300 μm from the primary anode; beyond this region, the acidification damage was mainly propagated around the interfacial transition zone around the aggregates.

(3) Because the lightweight aggregates maintained the high alkalinity in the secondary mortar by release OH^- from the aggregates, the acidification damage both in the vicinity of the primary anode and ITZ around aggregates was significantly halted. Therefore, the external anode based on the prepared lightweight functional aggregates presented excellent durability during ICCP treatment under chloride-contaminated environment.

ACKNOWLEDGEMENTS

This work was financially supported by Key Research and Development Program of China (Project No.2017YFB0309904), National Natural Science Foundation of China (No. 51572088, and 51602050), Pearl River S&T Nova Program of Guangzhou (No. 201806010188) and State Key Laboratory of Silicate Materials for Architectures (Wuhan University of Technology, No. SYSJJ2017-05). Their financial supports are gratefully acknowledged.

REFERENCES

[1] US Federal Highway Administration, Memorandum on FHWA Position on Cathodic protection System in, 1982.
[2] P. Pedeferri, Cathodic protection and cathodic prevention, Construction and Building Materials, 10 (1996) 391-402.
[3] EN12696:2016, Cathodic protection of steel in atmospherically exposed concrete, European Committee for Standardization, 2016.
[4] C.J. Weale, Cathodic Protection of Reinforced Concrete: Anodic process in cements and related electrolytes, in, Aston University, 1992, pp. 40-41.
[5] J.P. Broomfield, Corrosion of steel in concrete: understanding, investigation and repair, 2nd ed., Taylor & Francis, London and New York, 1997, pp. 142-153.
[6] J.E. Bennett, J.J. Bartholomew, J.B. Bushman, K.C. Clear, R.N. Kamp, W.J. Swiat, Cathodic Protection of Concrete Bridges: A Manual of Practice, in, Strategic Highway Research Program National Academy of Science, Washington, DC, 1993.
[7] C.L. Page, G. Sergi, Development in cathodic protection applied to reinforced concrete, Journal of Materials in Civil Engineering 12 (2000) 8-15.
[8] K. Wilson, M. Jawed, V. Ngala, The selection and use of cathodic protection systems for the repair of reinforced concrete structures, Construction and Building Materials, 39 (2013) 19-25.
[9] S.D. Cramer, B.S. Covino, G.R. Holcomb, S.J. Bullard, W.K. Collins, R.D. Govier, R.D. Wilson, H.M. Laylor, Thermal sprayed titanium anode for cathodic protection of reinforced concrete bridges, Journal of Thermal Spray Technology, 8 (1999) 133-145.

[10] X. Fu, D.D.L. Chung, Carbon fiber reinforced mortar as an electrical contact material for cathodic protection, Cement and Concrete Research, 25 (1995) 689-694.
[11] S. Wen, D.D.L. Chung, Carbon fiber-reinforced cement as a thermistor, Cement and Concrete Research, 29 (1999) 961-965.
[12] K. Andersson, B. Allard, M. Bengtsson, B. Magnusson, Chemical composition of cement pore solutions, Cement and Concrete Research, 19 (1989) 327-332.
[13] Leemann, B. Lothenbach, C. Thalmann, Influence of superplasticizers on pore solution composition and on expansion of concrete due to alkali-silica reaction, Construction and Building Materials, 25 (2011) 344-350.
[14] F. Puertas, A. Fernández-Jiménez, M.T. Blanco-Varela, Pore solution in alkali-activated slag cement pastes. Relation to the composition and structure of calcium silicate hydrate, Cement and Concrete Research, 34 (2004) 139-148.
[15] W. Guo, J. Hu, Y. Wang, Z. Zhang, S. Yin, J. Wei, Q. Yu, Preparation and performance of conductive mortar based on lightweight conductive aggregates, Construction and Building Materials, 156 (2017) 340-350.

Theme 7

Development and application of smart cementitious materials for enhanced durability

BASIC PROPERTIES OF CEMENT PASTE MIXED WITH CALCIUM HYDROXIDE-ETTRINGITE COMPOSITE TYPE EXPANSIVE ADDITIVE

Kohsuke Handa (1), Guang Ye (2)

(1) Fujita Technology Center – Fujita Corporation, Japan

(2) Delft University of Technology, The Netherlands

Abstract

In this study, we targeted a calcium hydroxide and ettringite composite-type expansive additive (EA) and obtained the basic characteristics of the EA mixed cement paste in order to create a method for calculating volume expansion based on the hydration reaction of the PC-EA system. Expansion strain, setting time, and compressive strength were measured. In addition, we observed the state of EA after hydration using a micro-CT scanner and scanning electron microscope, and elucidated the expansion mechanism.

Our results show that strain rapidly increased and the compressive strength decreased when the replacement ratio of the EA (C_{rep}) exceeds 6.4%. At the same time, radial cracks were generated from the hydrated EA particles, suggesting that the EA itself grew to expand the cement paste. Although no ettringite was confirmed inside the EA when the C_{rep} was 5.1%, when the C_{rep} was 10.3%, ettringite was formed vertically from the surface of C_3A with a large amount of pores. These results show that simultaneous formation of ettringite and pores causes rapid expansion.

Keywords: Expansive additive, Calcium hydroxide, Ettringite, micro-CT scanning, SEM

1. INTRODUCTION

In order to maintain the durability and aesthetics of reinforced concrete structures over a long period of time, it is necessary to prevent the occurrence of cracks such as drying shrinkage cracking. For example, reducing drying shrinkage strain is effective at preventing cracks, and expansive additive (EA) can be used for this purpose. Although there are many types of EA, calcium hydroxide-ettringite composite type EA is an admixture for concrete that has long been used, and its components are mainly composed of free-lime (f-CaO), anhydrite (CS) and hydraulic minerals such as calcium aluminate (C_3A) or calcium aluminoferrite (C_4AF) [1]. These minerals change into calcium hydroxide (CH) and ettringite (AFt) respectively. They have a large volume evolution, and thus give a cement paste (CP) a macroscopic volume expansion that compensates for shrinkage.

Up to now, regarding studies on the volume change mechanism of CP mixed with EA, Yamamoto et al. proposed the radius evolution of the EA from measurement data such as reaction degree of each mineral and volume of CH and AFt [2]. In addition, Choi calculated the expansion strain of CP by mathematical modeling based on Yamamoto's data [3]. However, some challenges remain, such as the radius evolution proposed by Yamamoto is not a value calculated based on the chemical reaction formula, and the particle size distribution is not taken into consideration.

This study aims to create a method for calculating the volume expansion of CP based on the hydration reaction and radius evolution of the calcium hydroxide-ettringite composite type EA. In this study, experiments were conducted to measure the basic properties of CP mixed with EA. These included expansion strain, setting time, compressive strength and static modulus of the CP mixed with EA. In addition, the state of EA after the hydration was observed using a micro-CT scanner and scanning electron microscopy (SEM) to elucidate the expansion mechanism.

2. EXPERIMENTS

2.1 Sample preparation

All samples were prepared using moderate-heat Portland cement (PC) adapted JIS R 5210 [4] as Japanese standard, EA (powder), Polycarboxylic acid-based super plasticizer (Ad) and deionized water. The water-binder ratio was 0.45. The applied CP mix design is shown in Table 1. All samples were cured at room temperature (20 °C). The CP for micro-CT scanning and SEM was casted in a cylindrical resin bottle with 24mm diameter and 39mm height.

Table 1: Mix-design for cement paste specimen and compressive strength

Name	Replacement ratio for cement Crep (weight.%)	Water-Binder ratio (%)	Composition					Compressive strength [MPa]		
			Water (g/L)	PC (g/L)	EA (g/L)	Ad (mL/L)	Ad (B×%)	1 day	3 days	7 days
Reference	0%	45%	590.9	1313.2	0.0	7.2	0.55	4.42	12.1	21.7
EA26	2.57%		590.6	1278.7	33.7			3.97	14.2	23.8
EA51	5.14%		590.3	1244.3	67.5			5.71	15.6	23.6
EA64	6.43%		590.2	1227.2	84.3			6.98	14.1	23.7
EA103	10.29%		589.7	1175.7	134.8			4.10	8.7	13.2
EA109	10.93%		589.6	1167.1	143.2			5.11	8.4	11.7
EA129	12.86%		589.4	1141.4	168.4			Not conducted		

2.1 Setting time

In the expansion by EA, the force caused by the expansion is, unless it is a completely enclosed space, transmitted to the rebar or restrained member only when the mortar matrix is hardened and transmits the expansion pressure. That is, even if the unhardened paste expands, no stress is generated, so that it has no meaning in the structural design. Therefore, in this study, we focused the expansion that occurs after hardening of CP begins.

The modified initial setting time determined by the modified Vicat Needle test was adopted for the starting age of hardening. Instead of the water-cement ratio that produces the “normal

consistency" paste proposed in JIS R 5201 [5], water-binder ratio was kept constant at 0.45 and the test was conducted. This standard is almost the same as ASTM C191-13 [6], with slightly different conditions. The diameter of the needle for initial setting is 1.13mm. For the modified initial setting time, the material age when the penetration depth of the Vicat needle was 1 mm from the bottom was adopted.

2.2 Expansion strain

Expansion strain of CP is measured using 50 x 400(X axis direction) x 10mm specimen. A 10 mm square aluminum bar was installed to the end of the specimen, and the change in length of x axis was measured by a non-reaction force LVDT. In order to reduce the frictional force, the CP was casted into the polyester film, and a Teflon sheet was installed between the form on the bottom and the specimen.

2.3 Compressive strength

Compressive strengths were measured using a cylindrical specimen 50(diameter) x 100(height) mm. 24 hours after casting, the CP specimens were carefully removed from their plastic moulds, sealed in polyethylene plastic film.

2.4 Observation by micro-CT scanning

Slices with a thickness of 2-3 mm were cut from the sample in resin bottle and then ground using a thin sectioning machine. Next, micro dicing machine was used and slices were processed into square bars. The length of bar was approximately 0.92 to 1.02 mm. The bars were immersed in isopropanol until testing. Phoenix Nanotom m was used for the test.

2.5 Observation and elemental analysis by E-SEM

On the 3 days of age, the sample was crushed with a hammer to a size of about 5-10 mm, and hydration was stopped with liquid nitrogen. The sample was immediately placed in a freeze-dryer and dried for 1 month. One month later, the sample was impregnated with epoxy resin while performing vacuum defoaming and cured. After the resin has hardened, each sample was grinded and polished on a lapping table with 6 µm, 3 µm, 1 µm and 0.25 µm diamond paste. In between each paste the samples were submerged in ethanol and ultrasonicated to remove debris. Following polishing samples were kept in a desiccator until testing. Philips XL 30 ESEM was used for testing.

3. RESULTS

3.1 Setting time

Test results of setting time are shown in fig 1. The setting time tended to be faster when the C_{rep} was up to 6.4%, but when the C_{rep} exceeded 6.4%, the setting time became slower as C_{rep} increased.

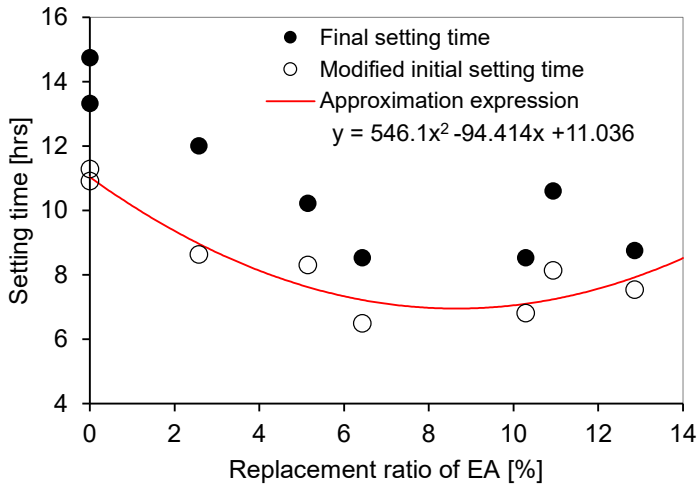

Figure 1: Relationship between C_{rep} and modified initial setting time

3.2 Expansion strain

Test results of expansion strain at 7 days of age are shown in fig 1. For all strains, the strain at the modified initial setting time was set to 0. The strain increases sharply when the replacement ratio of EA (C_{rep}) exceeds from 6.4%.

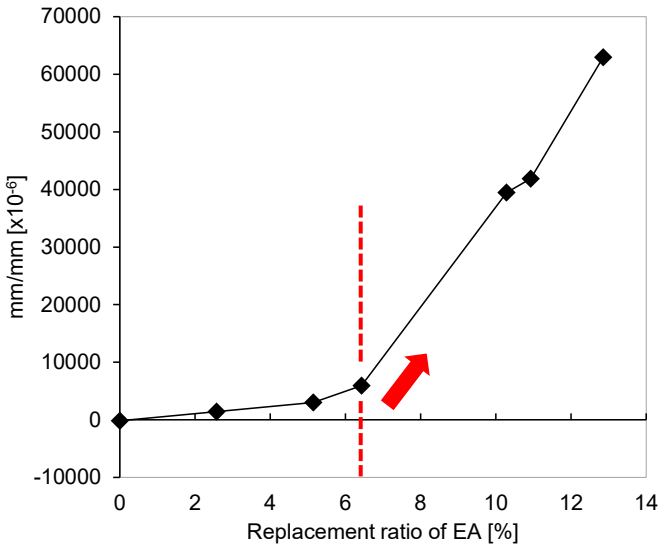

Figure 2: Relationship between C_{rep} and expansion strain at 7 days of age

3.3 Compressive strength

Test results of compressive strength at 1day, 3days and 7 days of age are shown in table 1 and strength ratio compared to reference is shown in fig 3. Compressive strength tended to decrease when the C_{rep} exceeded 6.4%.

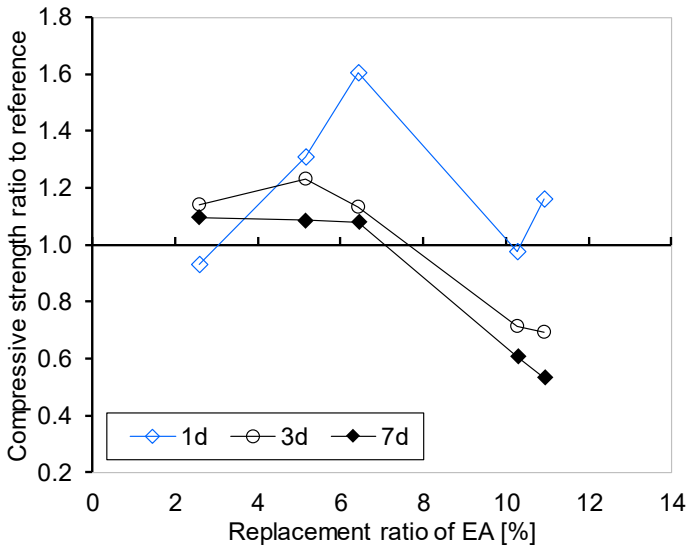

Figure 3: Relationship between C_{rep} and compressive strength

3.4 Observation by micro-CT scanning

A cross section image obtained by CT scanning is shown in Fig 4. Microcracks are radially generated from the aggregated portion of the hydration products. Hydration products such as this is not generated in the case of PC alone, and it is considered that the EA particle have grown. This result shows that the strength decreasing is caused by the expansion of the EA particles themselves.

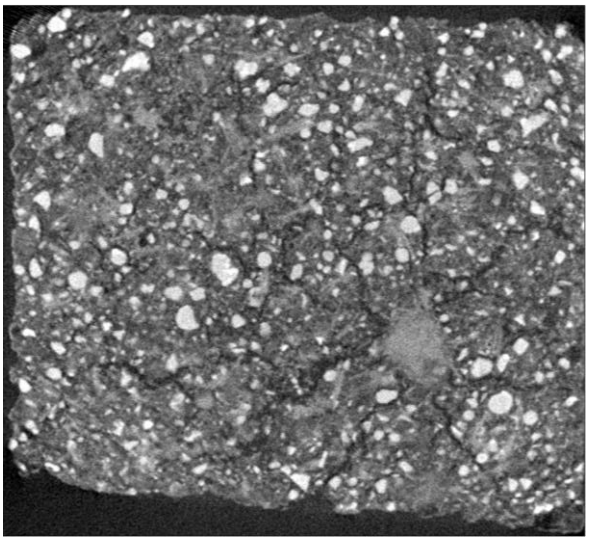

Figure 4: CT scanning image of hardened cement paste bar (C_{rep} = 10.3%)

3.5 Observation and elemental analysis by E-SEM

Fig 5 shows BSE images of raw EA particle and hydrated EA particle at 3 days of age. The EA particles have a structure in which f-CaO is the main constituent mineral, and the gaps are filled with C_3A, C_4AF and anhydrite.

From observation results of EA C_{rep} = 10.3% (b), we confirmed a larger amount of AFt was produced than in 5.1% (c). (For example, a part surrounded by the red dash line in (b))

The enlarged image of the formation location of AFt is shown in (d). Mono-sulphate (AFm) exists on the surface of C_3A, and needle-like AFt grows vertically from above. In addition, a large quantity of pore was simultaneously formed around the AFt. This result shows that rapid strain expansion occurring near C_{rep} exceeding 6.4% is caused by vertical generated AFt with pores. Also, as with Delayed Ettringite Formation, we have concluded that anhydrite dissolves in water once and AFt can be produced only when the sulphate ion concentration exceeds a certain threshold.

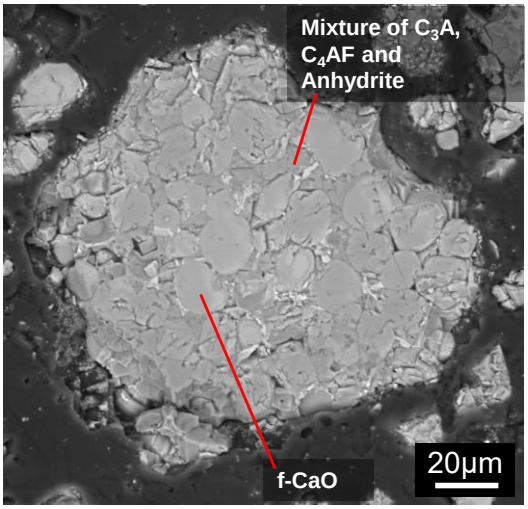

(a) Raw EA particle

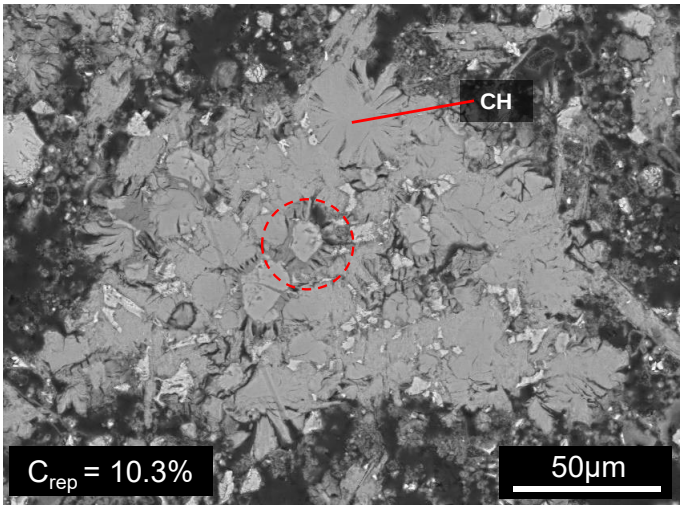

(b) Hydrated EA particle at 3 days of age (C_{rep} = 10.3%)

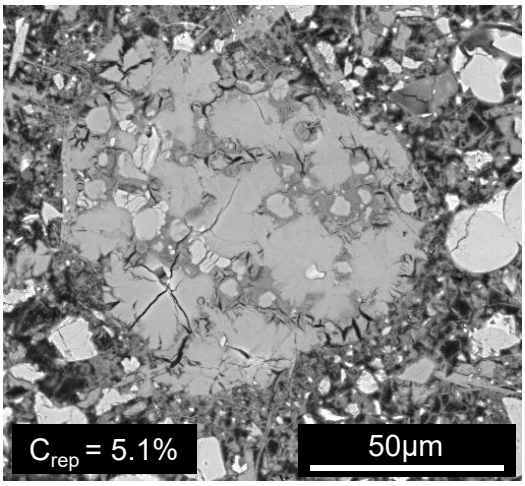

(c) Hydrated EA particle at 3 days of age (C_{rep} = 5.1%)

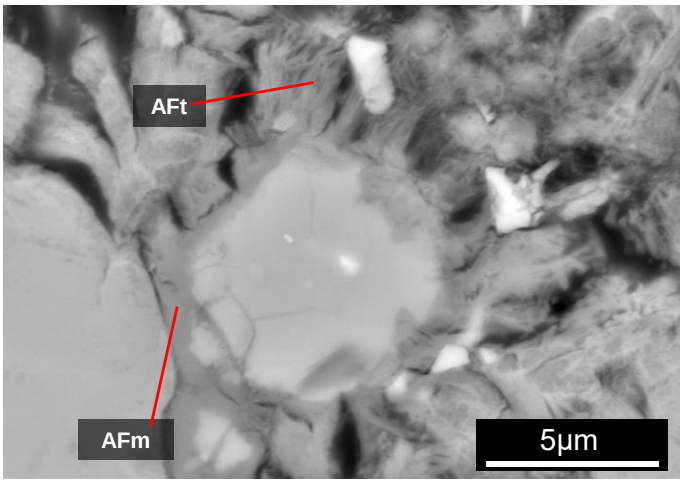

(d) Ettringite and pores generated around C_3A in EA at 3 days of age

Figure 5: BSE images of raw EA material and HCP mixed with EA

4. CONCLUSIONS

- The expansion strain increases sharply when the replacement ratio of EA (C_{rep}) exceeds from 6.4%.
- The setting time tended to be faster when the C_{rep} was up to 6.4%, but when the Crep exceeded 6.4%, the setting time became slower as C_{rep} increased.

- Compressive strength tended to decrease compared to reference when the C_{rep} exceeded 6.4%.
- From the cross-section image of C_{rep} 10.3% obtained by CT-scanning, microcracks are radially generated from the aggregated portion of the hydration product. This result shows that the strength decreasing is caused by the expansion of the EA particles themselves.
- From the image of the formation location of AFt in EA particle of C_{rep} 10.3% paste, AFm exists on the surface of C_3A, and needle-like AFt grows vertically from above. In addition, a large quantity of pore was simultaneously formed around the AFt. This result shows that rapid strain expansion occurring near C_{rep} exceeding 6.4% is caused by this vertical generated AFt with pores. Also, as with Delayed Ettringite Formation, we have concluded that anhydrite dissolves in water once and AFt can be produced only when the sulphate ion concentration exceeds a certain threshold.

REFERENCES

Journal Paper:

[1] Minoru MORIOKA, Yasuhiro NAKASHIMA, Takayuki HIGUCHI, Masataka EGUCHI, Etsuo SAKAI and Masaki DAIMON, 'Characteristics of Expansive Additives in the System of Free Lime-Hydraulic Compound-Anhydrite', Tokyo: Journal of the Society of Inorganic Materials, Japan, 2003, Vol.10, 225-232

[2] Kenji YAMAMOTO, Minoru Morioka, Etsuo SAKAI and Masaki DAIMON 'Expansion Mechanism of Cement Added with Expansive Additive', Tokyo: Concrete Research and Technology, 2003, Vol.14, No.3, 23-31

[3] Hyeonggil Choi, Heesup Choi, Myungkwan Lim, Takafumi Noguchi, Ryoma Kitagaki, ' Modeling of volume changes of concrete mixed with expansive additives', Construction and Building Materials, 2015, 266-274

Standards:

[4] JIS R 5210, Portland cement, 2009, 22pages.

[5] JIS R 5201, Physical testing methods for cement, 1997, 46pages.

[6] ASTM C191-13, Standard Test Methods for Time of Setting of Hydraulic Cement by Vicat Needle. West Conshokocken: American Society for Testing and Materials, 2013**,** 8pages.

CONTACT BETWEEN CEMENTITIOUS MATRIX AND FIBRES INFLUENCED BY THE MODIFICATION OF THEIR PARAMETERS

Anna Antonova (1), Marika Eik (1), Jouni Punkki (1) , Ville Jokinen (2) and Jari Puttonen (1)

(1) Department of Civil Engineering, Aalto University, Finland

(2) Department of Chemistry and Materials Science, Aalto University, Finland

Abstract

The performance of fibre reinforced cementitious composites depends on the interaction between the cementitious matrix and the fibres on the micro-scale. This interaction is affected by the material and surface properties of the fibre and the micro-scale characteristics of the cementitious matrix close to the fibre surface, creating the interfacial transition zone (ITZ). However, the discussions regarding the effect of the surface properties of fibres on the formation of the ITZ and, as a result, the bond strength between the matrix and the fibres are limited. The present paper reports the progress of the ongoing research project, which concentrates on investigating the contact created by the steel fibres with different characteristics of the surface roughness and cementitious matrix. The results of this study can support the development of efficient fibre reinforced cementitious composites.

Keywords: contact, roughness, wetting, fibre reinforced cementitious composites

1. INTRODUCTION

The inclusion of fibres into the cementitious matrix can help to restrict the propagation of cracks and improve the ductile performance of the fibre reinforced cementitious (FRC) composites. However, the behaviour of FRC composites at the structural level depends on the stress transferring from the cement-based matrix to the fibres on the micro-scale. The stress is transferred from the matrix to the fibre by the interfacial contact. This contact is provided by the interfacial transition zone (ITZ), that is known to have porous microstructure with precipitation of calcium hydroxide (CH), whose binding property is lower than that of the calcium-silicate-hydrate (C-S-H) phase [1]. The increased porosity in the ITZ is governed by the poor packing of the cement clinker grains [2]. Since fibre is several orders of magnitude larger than the cement clinker grains, it acts as a wall, and the cement grains that are located at the surface of the fibre cannot efficiently fill the space available. Those empty spaces created between the cement grains also may contribute to increased porosity close to the fibre surface, as it was discussed in [3] by comparing the measured roughness of the fibre and the size of the particles that can fill the surface grooves. Authors in [4] discussed that the wetting of the fibre

surface can affect the distribution of cement hydrates near the fibre. The relation between the wetting and the roughness of the fibre surface and the quality of contact between the fibre and water-based geopolymer matrix was also observed in [5]. At a more general level, the roughness of the surface is known to have an impact on the wetting properties of a material, as was reported in [6, 7]. The ongoing research work is aimed to investigate the influence of the steel fibre roughness on its wetting properties and their mutual effect on the contact characteristics between the steel fibre and the cementitious matrix, such as packing of cement-based matrix around the fibre and mechanical resistance of fibre to the pull-out from a matrix.

2. MATERIALS AND METHODS

2.1 Materials

Steel fibres with a diameter of 1 mm with different roughness of the surface were examined. The fibres were divided by types of the processing technique applied to receive the different roughness profiles: electro-polished – R1; non-processed (reference) – R2; coarsened with sandpaper – R3 (Fig. 1). The cement-paste was prepared from the ordinary Portland cement (OPC) CEM I 52,5 N.

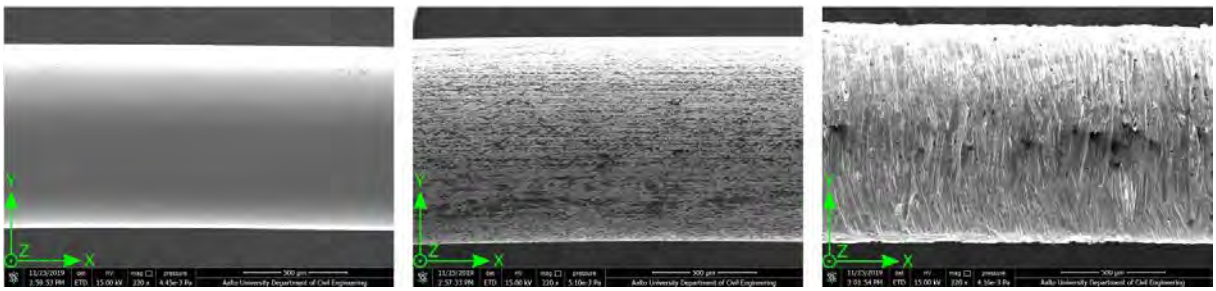

(a) R1 (b) R2 (c) R3

Figure 1: SEM images of the fibres with different roughness of the surface.

2.2 Methods

The atomic force microscope (AFM) and stylus profilometer were used to quantify the three different surface profiles of the steel fibre. Contact angle goniometry will be implied to examine the wetting properties of the steel fibres with different surface profiles by studying advancing (water spreading along the surface) and receding (adhesion of the water to the surface) water contact angles of the surface. The packing of the cementitious matrix will be examined with the scanning electron microscope (SEM) and the energy dispersive X-ray (EDX) analysis. The performance of the contact between the steel fibres with different surface profiles and the cement-based matrix will be studied with the pull-out test.

3. PRELIMINARY RESULTS AND DISCUSSION

3.1 Roughness profile of the steel fibres

AFM was used to measure epy fibres with the surfaces R1 and R2. The fibres with the surface R3 were measured with stylus profilometer since the size of this roughness exceeded the

measuring limits of the AFM. The measurements were performed in the longitudinal direction of the fibres.

Figure 2 represents the surface profiles of the fibres with different types of roughness. The apparent grooves on the surfaces of the fibres with roughness R2 and R3 may contribute to the

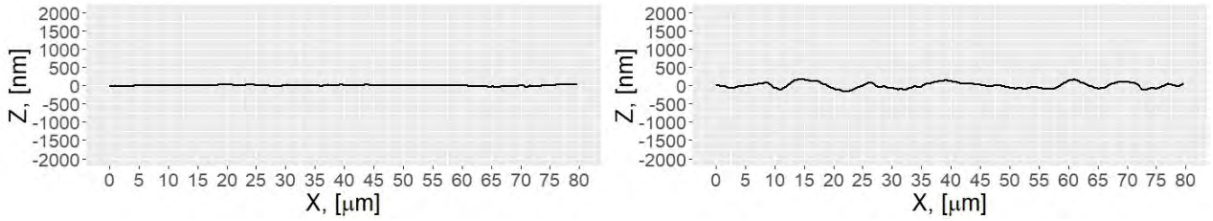

mechanical interlocking between the fibre and the cement-based matrix. The mechanical interlocking was noticed previously in [8] between the cement hydrates and the aggregates with a rough surface.

(a) R1 (b) R2

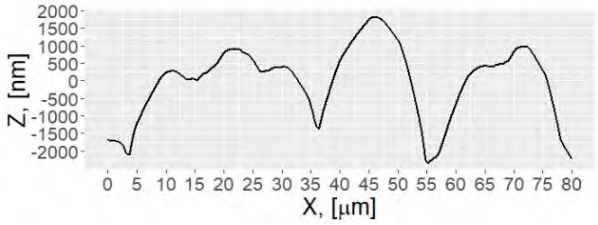

(c) R3

Figure 2: Surface profiles of the steel fibres with different types of roughness.

The surface profiles R2 and R3 may also affect the spreading of the water, that can be captured by the grooves of the surface. The abrupt spreading of the water along the rough surface was explained before in [9] as the "slip-stick" behaviour of the water droplet on the rough surfaces. The peaks of the surface profile work as barriers, which block further movements of the water and capture water in surface grooves. The spreading and sticking of the water at the surface of the steel fibre is crucial for the formation of the hydrates and the micro-bleeding, i.e. packing of the cement-based matrix in the close vicinity to the fibre.

3.2 Packing of the cementitious matrix around the steel fibres

Sufficient packaging of the cementitious matrix around the fibre, especially decreased porosity, promotes lower permeability, thus decreasing the possible corrosion of the steel fibres. In addition, the denser cement-based matrix in the vicinity of the fibre is contributing to better contact between mentioned constituents, therefore increasing the resistance to the cracking of the FRC composite and reducing the subsequent destruction of the material.

In the scope of the on-going study, the packing of the cementitious matrix near the steel fibre is planned to be investigated as follows. The point EDX analysis will be applied to identify the CH and unhydrated cement clinker grains, such as alite, belite, aluminate and ferrite, on the backscattered electron (BSE) images based on the chemical composition. Then the grey-level

values of the identified cement phases will be measured with the BSE images. The measured grey-level values will be used to segment pores, CH and unhydrated cement clinker grains on the BSE images, as it is demonstrated in Figure 3(b). The image segmentation techniques based on the grey-level histogram, such as overflow criteria and minimum between the peaks, are also considered to verify the measured grey-level values. The distributions of the three mentioned cement-paste phases will be examined with a distance of 100 µm from the fibre surface. The volume fraction of pores, CH and unhydrated cement clinker grains will be calculated with the step of 10 µm (Fig. 3(b)).

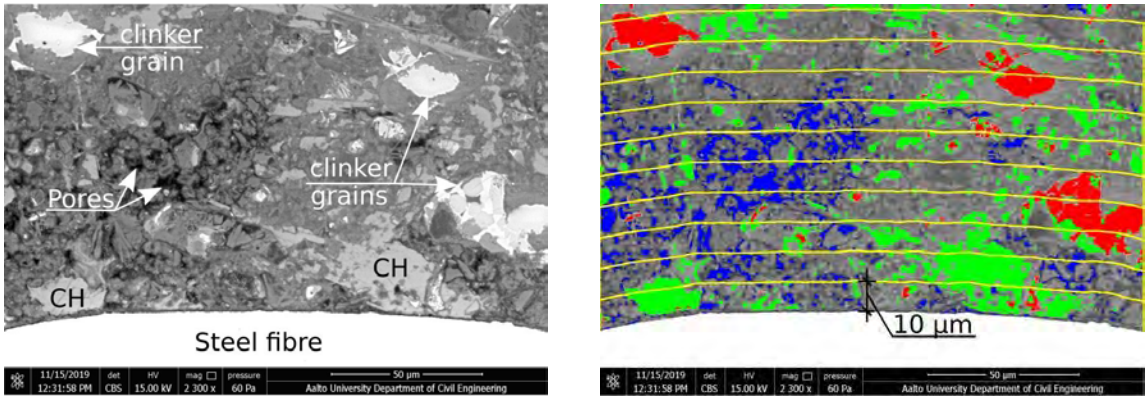

(a) (b)

Figure 3: (a) Example of SEM image. (b) Example of the segmented SEM image. The distributions of pores (blue), CH (green) and unhydrated clinker grains (red) will be analyzed with the step of 10 µm stripe-wise, which are marked with yellow lines.

3.3 Single fibre pull-out test

The quality of the packing of the cementitious matrix around the fibre, i.e. contact, can be also defined with the performance of the pull-out test.

The steel fibre with a total length of 50 mm was cast into the cement-paste cylinder with a diameter of 45 mm. The cracks that are initiated in FRC composite can reach the fibre, which is bridging the crack, any point of the fibre length. For this reason, the several embedded fibre lengths of 10 mm, 20 mm, 30 mm and 40 mm were selected to study the range of the load-bearing capacities of the fibre. The setup of the pull-out test was designed to eliminate the influence of possible compressive stress, that may occur from the fixation of fibre or cement cylinders (Fig. 4 (a)). The load was applied with the rate of 0.1 mm/min. Figure 4 (b) illustrates the results of the preliminary pull-out tests of the non-processed fibre (R2) with the embedded length of 20 mm.

Figure 4 (b) illustrates the occurrence of the varying hardening behaviour after the adhesion breakage during slippage. This behaviour may be attributed to the additional mechanical anchorage provided by the roughness of the fibre surface and non-uniform ITZ structure, which result in the interlocking between the cementitious matrix and the steel fibre. This response is typical for the general contact of rough surfaces, that was discussed previously in [10]. The possible occurrence of the slip softening or hardening behaviour during the slippage of fibre

from the cementitious matrix was explained in [11] by the nature of the interaction and the damage developed along the interface during the slip.

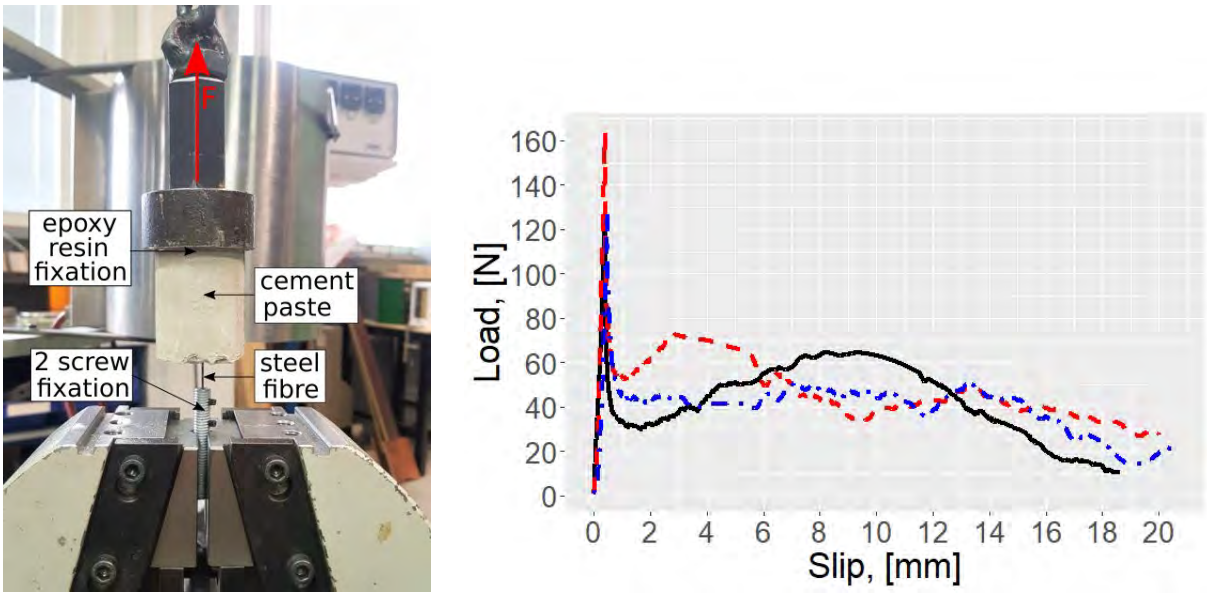

(a) (b)

Figure 4: (a) Setup for single fibre pull-out test. (b) Example of the load-slip curve obtained with single fibre pull-out test. The embedded length was 20 mm and the type of fibre roughness was R2 – non-processed.

4. CONCLUDING REMARKS

The combination of several measuring techniques are used in the present study to examine the relation between roughness, packing of the cement-based matrix in the vicinity of the fibre and mechanical performance of the contact between the cement-paste and fibre. This research has the potential to increase understanding of the interaction between the cementitious matrix and steel fibres considering the filling effect and interlocking between the fibre grooves and the cement hydrates and water spreading affected by the roughness of the fibre on the micro-scale.

ACKNOWLEDGEMENTS

The research leading to these results received funding from the Doctoral program of the School of Engineering, Aalto University.

REFERENCES

[1] Lee, S.F., Jacobsen, S. 'Study of interfacial microstructure, fracture energy, compressive energy and debonding load of steel fiber-reinforced mortar'. *Mat. and Str.* **44** (2011) 1451 – 1465.

[2] Scrivener, K. L., Crumbie, A. K. and Laugesen, P. 'The Interfacial Transition Zone (ITZ) Between Cement Paste and Aggregate in Concrete'. *Interface Sci.* **12** (2004) 411 – 421.

[3] Eik, M., Antonova, A. and Puttonen, J. 'Roughness of steel fibre and composition of cement paste close to fibre surface'. *Journal of Adv. Concr. Tech.* **17** (2019) 628 – 638.

[4] Xu, L., Deng, F. and Chi, Y. 'Nano-mechanical behavior of the interfacial transition zone between steel-polypropylene fiber and cement paste.' *Constr. and Build. Mat.* **145** (2017) 619 – 638.

[5] Ranjbar, N., Talebian, S., Mehrali, M., Kuenzel, C., Metselaar, H. S. C. and Jumaat, M. Z. 'Mechanisms of interfacial bond in steel and polypropylene fiber reinforced geopolymer composites'. *Comp. Sci. and Tech.* **122** (2016) 73 – 81.

[6] Wenzel, R. N. 'Resistance of solid surfaces to wetting by water'. *Industrial and Eng. Chem.* **28** (1936) 988 – 994.

[7] Kubiaka, K.J., Wilsona, M.C.T., Mathia, T.G. and Carval Ph. 'Wettability versus roughness of engineering surfaces'. *Wear.* **271** (2011) 523 – 528.

[8] Qudoos, A., Rehman, A. U., Kim, H. G. and Ryou, J. S. 'Influence of the surface roughness of crushed natural aggregates on the microhardness of the interfacial transition zone of concrete with mineral admixtures and polymer latex'. *Constr. and Build. Mat.* **168** (2018) 946 – 957.

[9] Shanahan, M. E. R. 'Simple theory of "stick-slip" wetting hysteresis'. *Langmuir* **11** (1995)1041-1043.

[10] Jiménez, A.-E. and Bermúdez, M.-D. 'Friction and wear'. In: Davim, J. P. (eds.), Tribology for Engineers. Woodhead Publishing, 2011, 33-63.

[11] Bentur, A. and Mindess, S. 'Fibre reinforced cementitious composites'. Crc Press, 2006, 31 – 97.

DETERIORATION OF ORGANIC COATINGS ON CONCRETE UNDER ARTIFICIAL AGING

Haochuan Wang(1), Pan Feng(1)(2), Zifan Geng(1), Qi Liu(1)

(1) Jiangsu Key Laboratory of Construction Materials, School of Materials Science and Engineering, Southeast University, Nanjing, Jiangsu 211189, China

(2) State Key Laboratory of High Performance Civil Engineering Materials, Nanjing 210008, China

Abstract

The deterioration of organic coatings on concrete is closely linked to the efficiency in the protection process of reinforced structures. In the present work, polyurea resin and epoxy resin, which are widely used engineering coatings, were selected to measure and compare the performance under artificial aging. Fourier Transform infrared spectroscopy, water contact angle and scanning electron microscope were used to determine the deterioration of coatings. X-ray fluorescence method was used to measure chloride content passing through the coatings, which represent the efficiency of protection. Test results demonstrate that both deterioration and resistance to corrosion are important in assessment of the organic coatings under aging.
Keywords: organic coating, concrete, artificial ageing, efficiency

1. INTRODUCTION

Reinforced concrete structures in harsh environments, such as hypersaline environments or circumstances with large difference in temperature or humidity, have already drawn special attention worldwide. The corrosion of steel materials, embedded in alkaline concrete with a passivation film, are considered as the significant part in structure failure. On the other hand, various durability improvements are proposed in order to prevent this essential position from the erosion outside.

Amelioration of reinforced structure can be divided into three main types focusing on different parts. First, fiber-reinforced polymer bars[1], epoxy coated reinforcement[2], or corrosion inhibitors[3] were adopted to enhance the quality of bars. Second, various methods were used in order to improve the performance of concrete, mainly aiming at a better hole

structure and enhanced compactness, including employing better raw materials or mineral admixtures, using high performance admixtures or other active control of properties of concrete[4]. Third, surface treatments including organic or inorganic coatings, hydrophobic impregnation or pore-blocking surface treatment are aiming at establishing a barrier resisting the corrosion[5]. Under comprehensive consideration of economy, construction convenience and repeatable implementation, organic coatings have great advantages in durability enhancement of situ reinforced concrete. Almusallam A. A. et al[6] showed that the chloride diffusion coefficient for polyurethane coated concrete was about 10 times smaller than uncoated concrete.

However, as mentioned in[7], the service life of organic coating is much shorter than that of structures. Organic materials are more vulnerable to severe environment including ultraviolet light irradiation, temperature variation, water invasion or other environmental factors. Also, decreased interface properties or more serious de-bonding will result in descending properties of coating efficiency. Many researches have focused on deterioration of organic coatings under different situations[8, 9, 10]. Researches are limited concentrating on the relations between different deterioration degree and efficiency.

In order to reflect the influence of deterioration under artificial aging on the protective performance, two kinds of organic coatings are used in this research. After being treated in artificial ageing environment, various changes of coatings including chemical structures and physical properties are measured and analyzed. Efficiency of resistance to chloride content, or called protective performance of organic coatings are also studied mainly focus on the resistance to chloride ions.

2. EXPERIMENTAL

2.1. Materials and mix proportions

Two kinds of commercial organic coatings were employed in this research, epoxy resin and polyurea resin produced by SOBUTE NEW MATERIALS CO.,LTD, and both of these types are widely used concrete coatings. Coatings were applied on the paste surface or the metal base for the convenience of different tests respectively. The water-to-cement ratio of paste samples is 0.35 and commercial PII.52.5 Portland cement, tap water and polycarboxylic acid type superplasticizer were used in the paste casting. Mix design was shown in Table 1. Paste samples of size 40mm×40mm×160mm were made to measure chloride content. After 28-days standard curing, paste samples were treated to surface dry condition and polished with sandpaper for coating. Metal base used in this paper were 10mm×10mm×1mm sized 304 stainless steel square plates, which were used to evaluate the self-structure changes of organic coatings. Coatings were applied to cleaned concrete or metal base by SZQ-400 film equipment and cured at 23 ± 1℃ and 40% relative humidity for 144h until weight constant.

Table 1: Concrete mix design

Mix components	Water	Cement	Water reducer
Weight (kg/m^3)	156	450	2

2.2. Artificial aging process

Accelerated aging tests for coatings samples were carried out by using a home-made ageing box shown in Fig.1, in which irradiation intensity in different parts has been tested to be uniformly distributed. In order to avoid rapid temperature changing, spray humidification was employed in the condensation system rather than direct water cooling. Remote status monitoring and remote control are available for this ageing box. The ageing process included 4 hours of UVB lamp irradiation and 4 hours of condensation. Irradiation wavelength concentrated at 340nm with average radiation intensity was 12 W/m^2. During the weathering process, the temperature increased from room temperature (RT) to 49℃ in the irradiation stage and decreased to RT in the condensation stage periodically.

Figure 1: The home-made ageing box

2.3. Performance assessment

A series of tests were carried out to characterize the degradation process of organic coatings during aging and test can be divided into three parts: chemical changes, physical changes and efficiency changes.

To determine the chemical changes over aging, Fourier Transform infrared spectroscopy (FTIR) was conducted using Thermo Scientific Nicolet iS10 under Attenuated Total Refraction (ATR) mode. Pieces of coatings around 1 cm2 were used and FTIR spectra were recorded in a range of 400 cm^{-1} to 4000cm^{-1}, with 4 cm^{-1} as scanning resolution.

Hydrophilicity of the coating surfaces was tested by observing the wettability of the methyl

blue aqueous solution on coatings. Nikon D7200 N1406 with a 25mm f/2.8 2.5-5X Ultra-Macro lens was adopted to take photographs. Then water contact angles were measured according to these photographs.

The morphology of both surface and cross-section of coatings was observed using FEI Quanta 3D scanning electron microscope (SEM). Samples less than 1cm^2 were cleaned by compressed clean air and sprayed gold particles on observed side with. It is worth mentioning that cross-section samples were made by dip organic coatings into liquid nitrogen and broken with tweezers. This step of sampling was to obtain natural fracture cross-sections.

In order to evaluate the efficiency of coatings, paste samples which applied coatings (all other surfaces are sealed using epoxy resin) were immersed into 10wt% sodium chloride solution for 960 hours. After immersion, coatings were removed and powders were obtained by milling the paste samples (within 1mm). X-ray fluorescence method was used to measure chloride content in paste samples by using ThermoFisher ARL Perform X 4200.

3. RESULTS AND DISCUSSION

3.1. Deterioration

3.1.1. Chemical structure changes

Figure 2 shows the FTIR of coatings before and after aging. From Fig. 2, chemical structures were nearly unchanged in polyurea resin before and after aging. This suggest that polyurea has kept its stability of functional groups under ultraviolet aging. As shown in Fig. 2, it is illustrated that the transmittance around 3300cm-1 of epoxy resin becomes border and lower after aging 1440 hours, which represents the increased hydroxyl group. During the aging process, epoxy resin shows a worse chemical stability than polyurea resin and then a worse resistance.

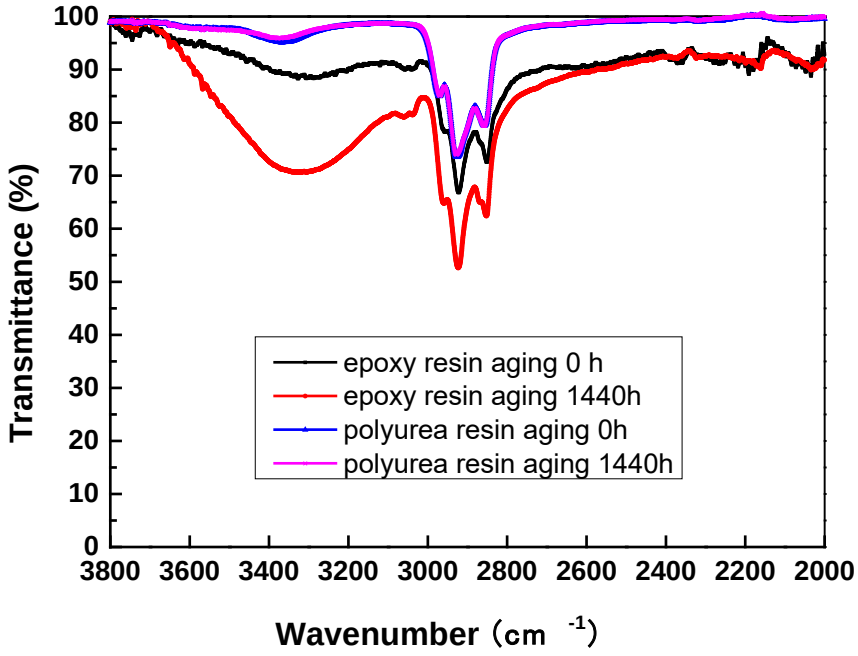

Figure 2: ATR-FTIR measurements in transmittance of coatings over aging

Table 2: Water contact angle of coatings over aging

	Aging 0h	Aging 1440h
Polyurea resin	80.1°	50.2°
Epoxy resin	53.6°	17.1°

3.1.2. Hydrophilicity test

Table 2 shows the water contact angle of coatings before and after aging. The water contact angle of both polyurea coatings and epoxy resin coatings decreased after aging 1440 hours. This demonstrates that the hydrophobicity of coating decreased and water will enter into coatings easier. The hydrophobicity of epoxy resin decreased quicker, which can be associated with the worse chemical stability (increased polar functional groups) observed by FTIR.

3.1.3. Scanning electron microscope

Figure 3. shows the SEM morphology pictures of coating surface exposed to UV agin environment. It can be observed that after 1440 hours aging, defects appear obviously and the surface of epoxy resin turns to be rougher with some chalking phenomenon. The vulnerable surface of epoxy resin is consistent with its fragile chemical structure.

On the opposite situation, there is no obvious change of polyurea resin over aging under the SEM shown in Fig. 3 (b).

Figure 4. demonstrates the morphology pictures of cross-section of coatings. The same as the surface observation, polyurea resin keeps its stability before and after aging while deterioration occurs in epoxy resin. Defects are obvious in the epoxy resin, especially at the exposed side of the epoxy coating (right side in Fig. 4(d)), which may resulting in poor corrosion-resisting performance.

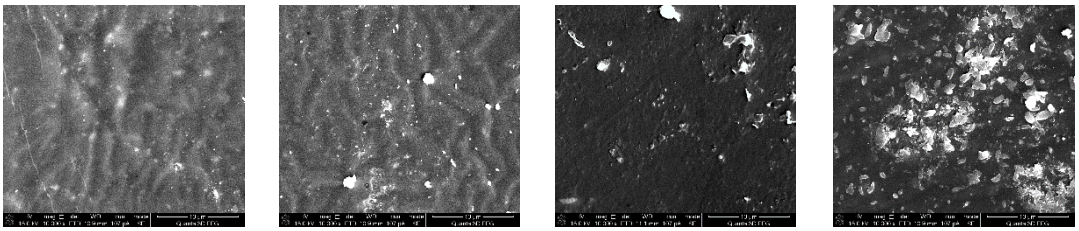

(a) 0 hours aged (b) 1440 hours aged (c) 0 hours aged (d) 1440 hours aged

Figure 3: SEM images of coating surface
(a)(b): Polyurea resin; (c)(d): Epoxy resin

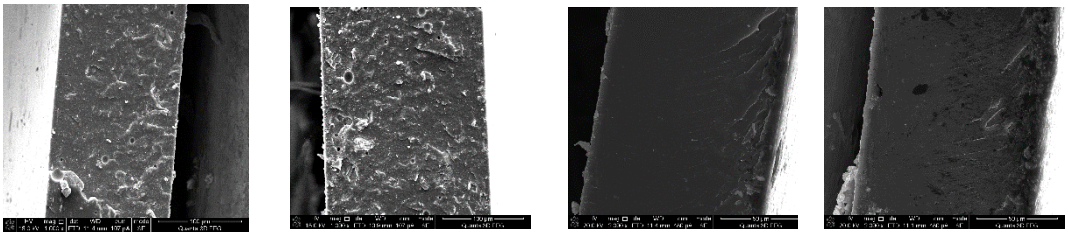

(a) 0 hours aged (b) 1440 hours aged (c) 0 hours aged (d) 1440 hours aged

Figure 4: SEM images of coating cross-section
(a)(b): Polyurea resin; (c)(d): Epoxy resin

3.2. Chloride resistance

Table 3 shows the chloride content in paste near the surface. It is obvious that coatings (whether aging or not) can reduce the chloride content significantly. Polyurea resin exhibits worse after aging which is different from the performance in the deterioration characterize. This can be explained by the weak-interface between polyurea and samples. On the other side, the slight decreases of chloride content in aged epoxy resin sample may associate with the radical recombination[11].

Table 3: The chloride content in paste surface tested by XRF

Paste	No coating	Epoxy	Epoxy	Polyurea	Polyurea
samples		resin (0h)	resin(960h)	resin (0h)	resin(960h)
The chloride content (wt%)	3.580	0.127	0.117	0.017	0.369

4. CONCLUSIONS

In this study, deterioration and efficiency of coatings under artificial aging is being studied. Two kinds of coatings including epoxy resin and polyurea resin were used in order to make comparison. Under the aging process consisting ultraviolet irradiation, thermal-cycle and wet-dry-cycle, the rate of degradation of polyurea resin is slower than epoxy resin, indicating that polyurea resin is more suitable for top layer coating. However, in the chloride resistance test, aged polyurea resin exhibits poor resistance to chloride. While combining the results of deterioration and protective performance experiments, both sides should be taken into consideration in evaluation the coatings under aging on concrete surface.

REFERENCES

[1] Hollaway, L. C., A review of the present and future utilisation of FRP composites in the civil infrastructure with reference to their important in-service properties. *Construction and Building Materials* **2010,** *24* (12), 2419-2445.

[2] Kondratova, Ş. E. T. W. B. I. L., Accelerated testing of plain and epoxy-coated reinforcement in simulated seawater and chloride solutions. *Cement and Concrete Composites* **2001,** *31* (6), 861-867.

[3] Ormellese, M.; Berra, M.; Bolzoni, F.; Pastore, T., Corrosion inhibitors for chlorides induced corrosion in reinforced concrete structures. *Cement and Concrete Research* **2006,** *36* (3), 536-547.

[4] De Schutter, G.; Lesage, K., Active control of properties of concrete: a (p)review. *Mater Struct* **2018,** *51* (5), 123.

[5] Pan, X.; Shi, Z.; Shi, C.; Ling, T.-C.; Li, N., A review on concrete surface treatment Part I: Types and mechanisms. *Construction and Building Materials* **2017,** *132*, 578-590.

[6] Almusallam, A. A.; Khan, F. M.; Dulaijan, S. U.; Al-Amoudi, O. S. B., Effectiveness of surface coatings in improving concrete durability. *Cement and Concrete Composites* **2003,** *25* (4-5), 473-481.

[7] Rodrigues, M. P. M. C.; Costa, M. R. N.; Mendes, A. M.; Marques, M. I. E., Effectiveness of surface coatings to protect reinforced concrete in marine environments. *Materials and Structures* **2000,** *33* (234), 618-626.

[8] Bhargava, S.; Kubota, M.; Lewis, R. D.; Advani, S. G.; Prasad, A. K.; Deitzel, J. M., Ultraviolet, water, and thermal aging studies of a waterborne polyurethane elastomer-based high reflectivity coating. *Progress in Organic Coatings* **2015,** *79*, 75-82.

[9] Gheno, G.; Ganzerla, R.; Bortoluzzi, M.; Paganica, R., Accelerated weathering degradation

behaviour of polyester thermosetting powder coatings. *Progress in Organic Coatings* **2016,** *101*, 90-99.

[10] Yang, X. F.; Li, J.; Croll, S. G.; Tallman, D. E.; Bierwagen, G. P., Degradation of low gloss polyurethane aircraft coatings under UV and prohesion alternating exposures. *Polymer Degradation and Stability* **2003,** *80* (1), 51-58.

[11] Liu, F.; Yin, M.; Xiong, B.; Zheng, F.; Mao, W.; Chen, Z.; He, C.; Zhao, X.; Fang, P., Evolution of microstructure of epoxy coating during UV degradation progress studied by slow positron annihilation spectroscopy and electrochemical impedance spectroscopy. *Electrochimica Acta* **2014,** *133*, 283-293.

EFFECT OF ULTRA-FINE FLY ASH ON THE MECHANICAL AND SHRINKAGE PROPERTIES OF ULTRA-HIGH PERFORMANCE CONCRETE

Taotao Feng (1), Jinyang Jiang (1), Hongyan Chu (2), Liguo Wang (1)

(1) School of Materials Science and Engineering, Southeast University, China

(2) College of Civil Engineering, Nanjing Forestry University, China

Abstract

This paper reports on a study to determine the possibility of using ultra-fine fly ash (UFA) for partial or total replacement of normal fly ash (NFA) in ultra-high performance concrete (UHPC). Workability, microstructure, porosity, drying shrinkage as well as mechanical properties were comprehensively studied to investigate the influence of UFA on UHPC. The fly ash, which was a compound of NFA and UFA with various mass fractions, had a total content of 30 wt%. The results demonstrated that compressive strength is enhanced if NFA is partially or totally replaced with UFA. Compared to the reference mixture containing 100 wt% NFA, incorporating UFA into UHPC has been shown to improve its workability. Contrarily, adverse effects on drying shrinkage were discovered when NFA is substituted with UFA.

Keywords: Ultra-fine fly ash; ultra-high performance concrete; compressive strength; drying shrinkage

1 INTRODUCTION

Ultra-high-performance concrete is a kind of cementitious composite material that has superior mechanical and durability properties [1]. Compared to ordinary concrete, UHPC has an outstanding compressive strength (greater than 150 MPa) due to its denser microstructure [2].

Ultra-fine fly ash is a kind of fly ash with an average particle size less than 10μm or a specific surface area greater than 600m^2/kg. Compared with NFA, UFA has lower water requirement, higher density and higher reactivity. With the partial replacement of cement by UFA, the second reactivity will occur under the effect of $Ca(OH)_2$ in the later stage [3]. Therefore, adding UFA can effectively reduce the setting time of mixture, as well as the hydration heat. Some studies show that the total quantity of heat release and heat release of the composite cementitious material mixed with ultra-fine fly ash at each moment is significantly lower than that of the pure cement group, and in the early hydration stage of cement-UFA binary composite cementitious material system, UFA particles can promote the hydration of cement to some extent.

Steve et al. [4] found UFA could increase the workability of fresh concrete. The superfine mineral admixture particles filled in the matrix, which can replace the filling water between the particles. Some studies have shown that the replacement effect is more obvious when mixed with efficient superplasticizer under the condition of low water-cement ratio. Adding UFA is an important way to improve the mechanical property and durability of concrete. UFA can play a good filling role in the matrix, greatly increasing the compactness of concrete. Furthermore, the pozzolana reaction of UFA with cement could generate much denser C-S-H gel, which increases the compactness of the concrete as well. Gao et al. [5] presented a study on the influence of UFA on the hydration shrinkage of cement paste. Compared with paste without the UFA, the shrinkage ratio of paste was reduced by between 23.4% and 39.7% when the UFA replacement was between 20% and 50%.

The previous studies mainly focused on ordinary concrete or high performance concrete, and the purpose of this work is to investigate the influence of UFA on the fresh, mechanical and shrinkage properties of UHPC. In the current study, NFA was partially or totally replaced with UFA in UHPC, with a total fly ash mass fraction of 30%. Workability tests were performed to evaluate the fresh properties of UHPC improved by UFA. Compressive strength were studied to investigate the influence of UFA on the mechanical properties of UHPC. In addition, drying shrinkage behaviours of concrete containing different content levels of UFA was also researched.

2 TEST PROGRAM

2.1 Materials

The materials used in this study were ordinary Portland cement (OPC), silica fume (SF), NFA and UFA. Particle size distribution of the raw materials is presented in Fig. 1.

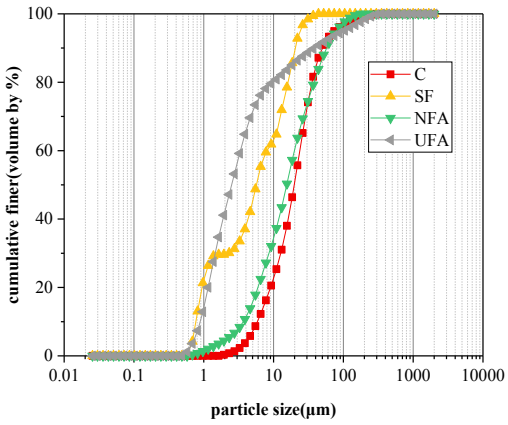

Figure1: Particle size distribution of the raw materials.

Natural river sand was used as fine aggregate, and its maximum particle size was 5 mm, the fineness modulus of which is 2.5. Straight steel fibres with a length of 13 mm and diameter of 0.2 mm was incorporated at 2.5 vol%, and the tensile strength of the fibres was about 3000 MPa. A polycarboxylate-based superplasticizer (PC) with 35% solid content by weight was used to obtain a satisfactory fluidity.

2.2 Mix design

The mix proportions of UHPC are shown in Table 1. The mixtures in Table 1 were designed based on the reference U0N100 mixture by taking into account the NFA replacement with UFA. The total fly ash content accounts for 20% of cementitious materials. The names of the mixtures are a combination of NFA percentage and UFA percentage, and the letters represent the NFA and UFA used in the mixture. For example, the U25N75 label means UFA and NFA constitute 25% and 75% of the total amount of fly ash, respectively.

Table 1: Mix proportions of UHPC

Relative weight ratios to binder								
Sample	c	NFA	UFA	SF	w	sand	PC	Steel fiber(V_f)
U0N100	0.7	0.2	0	0.1	0.16	1.1	1%	2.5%
U25N75	0.7	0.15	0.05	0.1	0.16	1.1	1%	2.5%
U50N50	0.7	0.10	0.10	0.1	0.16	1.1	1%	2.5%
U75N25	0.7	0.05	0.15	0.1	0.16	1.1	1%	2.5%
U100N0	0.7	0	0.2	0.1	0.16	1.1	1%	2.5%

Where, V_f = volume fraction of fiber to concrete.

2.3 Specimens preparation

In order to achieve a homogeneous mixture, all of the powdered materials were mixed using a mixer for 3 min, and the river sands were added mixing for another 5 min. Then the water and HRWRA were gradually added to the mixer over 5 min of mixing time, and the high-strength steel fibres were finally added to the mixer, and mixed for 3 min.

The fresh concrete was placed into moulds after mixing. The compressive strength of the UHPC was measured by compression tests using cubic specimens with a length of 100 mm. To monitor the drying shrinkage of the UHPC, 100 × 100 × 515 mm prism specimens were used. All test specimens were then covered with plastic sheets and cured at room temperature for the first 48 h prior to demoulding. After demoulding, the specimens were cured in a standard room with a temperature of 21±1ºC and a relative humidity above 95%.

3 TEST METHODS

3.1 Workability

The flowability of UHPC mixtures was measured in accordance with the Chinese standard GB/T 2419-2005 [6].

3.2 Compressive strength

When the curing age reached 28 days, mechanical tests were performed. For the compressive test, a constant loading rate of 1.0 MPa/s was employed according to the standard [6].

3.3 Drying shrinkage

After curing under standard conditions for 3 days, the prisms were stored in a drying room where the temperature was 20±3°C, and the relative humidity (RH) was 60±5%. Three specimens were prepared to obtain the drying shrinkage data for each group. The initial length

of the prisms was measured immediately after standard curing. The length of the prisms was measured every other day for the first 28days, and thereafter, every three days. Drying shrinkage values were calculated at 43 days when all the specimens showed relatively constant lengths.

3.4 Microstructure

In order to detect the microstructure of the specimens, a 3D ESEM (produced by FEI Company and named Quanta 3D FEG) was used to take micrographs of UHPC. After curing treatment, the specimens were crushed into small fragments and soaked in alcohol to stop hydration. Subsequently, the samples were dried and stored in a vacuum drier before testing.

4 TEST AND DISCUSSIONS

4.1 Workability of fresh mortar

Figure 2 presents the fluidity of mortars with different replacements of UFA. It could be seen that UFA lead to significant improvement on the workability, with slump flow values of 235mm, 238mm, 264mm, 279mm, 250mm for the U0N100, U25N75, U50N50, U75N25, and U100N0 mixtures, respectively. As shown in Fig.1, the mean particle size of fine UFA was much less than that of NFA, which means higher water absorption. However, the use of UFA as a substitute for NFA had an positive effect on the workability of UHPC. It could be attributed to the nature of spherical geometry, which significantly contributes to the workability of fresh pastes [7]. It should note that the fluidity showed downward trend when the substitution rate of NFA exceeded 75%. This could be attributed to the negative effect of ultra-fine particle sizes, namely high water absorption, playing a more outstanding effect compared with the morphological features.

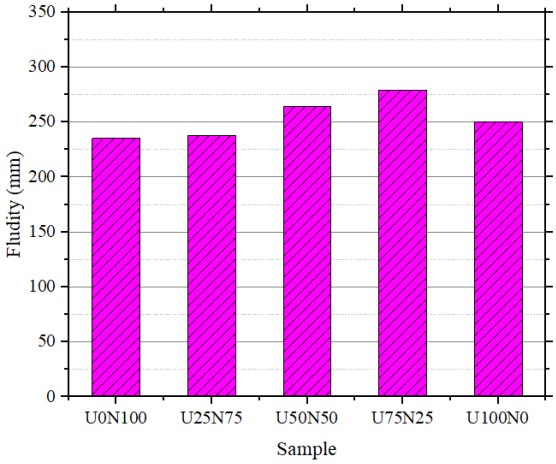

Figure 2: Fluidity of different kinds of mixtures.

4.2 Mechanical properties

As depicted in Fig. 3, partial replacement of NFA by UFA enhanced the compressive strength of the mixtures, and the greater the amount of substitution, the higher the strength was. The compressive strength of U0N100, U25N75, U50N50, U75N25, and U100N0 at a curing age of 28 days was 145.3 MPa, 154.9 MPa, 162.7 MPa, 167.8 MPa, and 174.5 MPa respectively. The compressive strength reached the maximum when all the NFA was replaced

with UFA. This may be attributed to the reduced porosity of UHPC due to the addition of UFA. Ravina [8] found that mortars possessed higher compressive strength when NFA was substituted with UFA due to the reduction in porosity. By comparison, UFA favoured a denser microstructure as well as compressive strength due to its smaller-size particles. These results were in agreement with the research of Long [9], where the incorporation of UFA into cement mixtures could increase the packing density of matrix, consequently, improving the compressive strength of concrete.

For the ordinary concrete or high performance concrete, the enhancement was mainly attributed to the filler effect of ultra fine particles, as well as the secondary hydration reaction with portlandite to produce additional C-S-H gel. Fig. 4 shows the ESEM images of the mixture U0N100 and U100N0. It could be found that two kinds of fly ash are both smooth, indicating that the improvement of UFA to UHPC is mainly due to the filling effect, instead of the secondary hydration reaction.

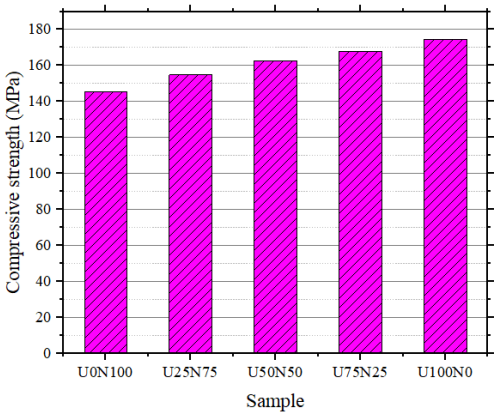

Figure 3: Compressive strength of UHPC.

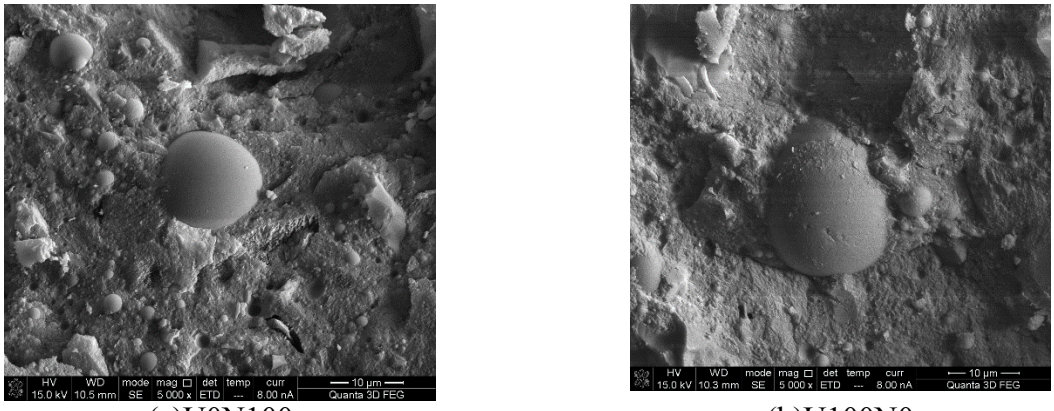

(a)U0N100 (b)U100N0

Figure 4: Microstructures of U0N100 and U100N0.

4.3 Drying shrinkage

The measured drying shrinkage is shown in Fig. 5 for different mixtures. All concrete containing UFA had higher drying shrinkage than the U0N100 concrete, and the higher the UFA replacement percentage, the higher the drying shrinkage. After 28 days of curing, the drying shrinkage of U50N50 and U100N0 was 30.7% and 68.0% greater, respectively, than

that of U0N100. Zhao et al. [10] reported that the inclusion of NFA in high-performance concrete can lead to a great decrease in drying shrinkage. Chindaprasirt [11] investigated the shrinkage behaviour of mortar containing five different fineness values of fly ash, and found that all of the fly ashes reduced the drying shrinkage of the mortars with relatively high water-to-binder ratios. Contrary to the findings of Chindaprasirt, UFA resulted in an enhancement of drying shrinkage in this study.

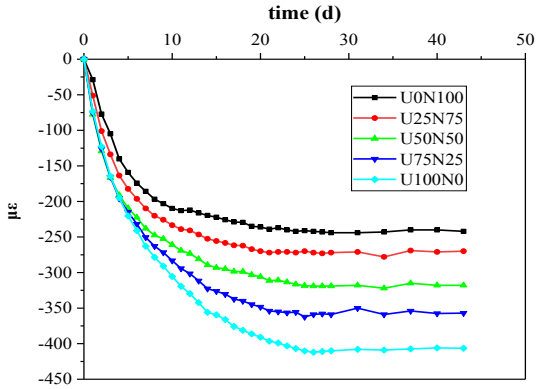

Figure 5: Drying shrinkage of UHPC.

This can be explained as follows: microstructures ware denser if the NFA is replaced by UFA, and the capillary pore pressure by water and air menisci, which is the driving force for shrinkage, is inversely proportional to the size of the capillary pores [12,13]. With the increase in UFA content, the filling effect of admixtures turns big pores in the structure into small voids. In addition, UFA may contribute further to accelerating the hydration of cement due to its higher reactivity than NFA, which can enhance chemical shrinkage [14,15]. Hence, the amount of shrinkage is more pronounced in the sample containing a higher volume fraction of UFA due to the finer pore structures.

5 CONCLUSIONS

In this study, the ability of ultra-fine fly ash to be used as replacement of normal fly ash in UHPC was evaluated. In total, 20 wt% fly ashes content was involved which was compounded of normal fly ash and ultra-fine fly ash with various mass fraction. Effects of ultra-fine fly ash on the shrinkage and mechanical properties of UHPC were comprehensively studied. The main conclusions are drawn as follows:

- Ultra-fine fly ash has a more significant effect on the overall workability of UHPC than normal fly ash.
- The compressive strength showed an increasing trend as the replacement of normal fly ash by ultra-fine fly ash enhanced, which reached the maximum when all the NFA was replaced with UFA.
- Drying shrinkage behaviours differed at different ultra-fine fly ash substitution rates. The shrinkage values increased with the increase of ultra-fine fly ash content and need more time to be steady.
- The physical effect of ultra-fine fly ash to UHPC could yield denser microstructures, which were of great importance to the shrinkage and mechanical properties of UHPC.

ACKNOWLEDGEMENTS

The authors greatly acknowledge the support from the National Key R&D Program of China (No.2018YFC0705400), and the Science and Technology Program of Jiangsu Province (No. BE2017158).

REFERENCES

[1] Yalcinkaya C, Yazici H. Effects of ambient temperature and relative humidity on early-age shrinkage of UHPC with high-volume mineral admixtures. *Constr. Build. Mater*. **144** (2017) 252-259.
[2] Lee NK, Koh KT, Kim MO, Ryu GS. Uncovering the role of micro silica in hydration of ultra-high performance concrete (UHPC). *Cem. Concr. Res*. **104** (2018) 68-79.
[3] Xiao Han, Jinbo Yang, Jingjing Feng, Cuiling Zhou, Xiaoqing Wang. Research on hydration mechanism of ultrafine fly ash and cement composite. *Constr. Build. Mater.* **227** (2019).
[4] Steve W.M. Supit,Faiz U.A. Shaikh,Prabir K. Sarker. Effect of ultrafine fly ash on mechanical properties of high volume fly ash mortar. *Constr. Build. Mater*. **51** (2014) 278-286.
[5] Gao YL, Zhou SQ. Influence of ultra-fine fly ash on hydration shrinkage of cement paste. J. Cent. South. Univ. T. **12**(5) (2005) 596-600.
[6] GB2419-2005, Chinese National Standard, Test methods for flowability of cement paste, 2005.
[7] Cyr M, Lawrence P, Ringot E. Efficiency of mineral admixtures in mortars: Quantification of the physical and chemical effects of fine admixtures in relation with compressive strength. *Cem. Concr. Res*. **36**(2) (2006):264-277.
[8] Ravina D. Optimized determination of PFA (fly-ash) fineness with reference to pozzolanic activity. *Cem. Concr. Res*. **10**(4) (1980) 573-580.
[9] Long G, Wang XY, Xiao R, Xie Y. The influences of ultra-fine powders on the compatibility of cement and superplasticiser with very low water/binder ratio. Adv. Cem. Res. **15**(1) (2003)17-21.
[10] Zhao Y, Gong J, Zhao S. Experimental study on shrinkage of HPC containing fly ash and ground granulated blast-furnace slag. *Constr. Build. Mater*. **155** (2017)145-153.
[11] Chindaprasirt P, Homwuttiwong S, Sirivivatnanon V. Influence of fly ash fineness on strength, drying shrinkage and sulfate resistance of blended cement mortar. *Cem. Concr. Res*. **34**(7) (2004) 1087-1092.
[12] Soliman AM, Nehdi ML. Effect of drying conditions on autogenous shrinkage in ultra-high performance concrete at early-age. *Mater. Struct*. **44**(5) (2011) 879-899.
[13] Kovler K, Zhutovsky S. Overview and future trends of shrinkage research. *Mater. Struct*. **39**(9) (2006) 827-847.
[14] Ghafari E, Ghahari SA, Costa H, Julio E, Portugal A, Duraes L. Effect of supplementary cementitious materials on autogenous shrinkage of ultra-high performance concrete. *Constr. Build. Mater*. **127** (2016) 43-48.
[15] Bouasker M, Mounanga P, Turcry P, Loukili A, Khelidj A. Chemical shrinkage of cement pastes and mortars at very early age: Effect of limestone filler and granular inclusions. *Cem. Concer. Compos*. **30**(1) (2008)13-22.

EXPLORING THE POTENTIAL OF NANO-SIO2 TO PREVENT EARLY-AGE FROST DAMAGE IN PORTLAND CEMENT PASTE

Shuai Bai (1), Xinchun Guan (1), Hui Li (1), Jinping Ou (1)

(1) School of Civil Engineering, Harbin Institute of Technology, China

Abstract

The purpose of this study is to explore the potential of nano-SiO_2 (NS) to prevent early frost damage, and the effect of nano-SiO_2 (NS) on cement pastes subjected to early-age freezing was investigated regarding the macro properties (strength and durability) and micro properties (hydration and microstructure). The specimens were prepared with NS content of 0%, 0.6%, 0.9% and 1.2% by weight of cement. The results indicated that nano-SiO_2 has a positive impact on the macro properties of cement pastes frozen at early ages, compared with reference specimen. The cement pastes containing 0.9% NS achieved the best enhancements of 22.6% and 30.9% in compressive strength and chloride ion penetration, respectively. The TG results indicated that the additional nano-SiO_2 particles can increase the hydration degree of cement paste and the MIP data indicated that nano-SiO_2 particles reduced the total porosity and other pore structure parameters. This is because the additional C-S-H gels produced by the pozzolanic effect of nano-SiO_2, and nano-filling of nano-SiO_2 particles refine the pore structure of cement matrix. Moreover, XRD results showed that nano-SiO_2 also reduce the $Ca(OH)_2$ orientation in cement matrix.

Keywords: Cement paste, Nano-SiO_2, Early-age frost damage, Strength, Microstructure

1. INTRODUCTION

In the north of China, the climate is characterized by the duration of wintertime up to 5 months a year and the minimum temperature in winter can reach approximately -30 ~ -40 °C. In the construction industry, this extremely cold environments require development of technologies for preventing the frost damage.

Nanomaterial is being adopted to improve the performance of cement-based building materials, such as nano-metakaolin [1], nano-TiO_2 [2], nano-Fe_2O_3 [3], nano-Al_2O_3 [4]. Among them, nano-SiO_2 has been gaining increasing attention and turned into an effective material to improve the properties of cement-based building materials. Due to the high specific surface areas and activities of nano-SiO_2 [5, 6], it can significantly improve the mechanical and durability properties of cement-based material, even at small dosage [7,8,9,10,11,12,13]. Zhang et al. [14] suggested that the 2.0% addition of nano-SiO_2 achieved the maximum increase of strength. The compressive strengths increased 48.1% and 48.7% at the age of 3d and 28d,

respectively. Salemi and Behfarnia [15] used 5% nano-silica to achieve 84% reduction in deterioration of concrete after 300 cycles of freezing and thawing. Quercia et al. [16] proposed that nano-SiO_2 modified self-compacting concrete has a high resistance to the freeze-thaw cycles, owing to the formation of highly stiff C-S-H gel and the refined pore structure. Moreover, Nano-SiO_2 can also behave as a filler to improve microstructure, as an activator to accelerate pozzolanic reaction and as the nuclear agent to tightly bond with hydration products [17,18,19]. The size and amount of calcium hydroxide ($Ca(OH)_2$) crystals are significantly decreased by means of pozzolanic reaction [20]. And forming additional C-S-H phase make the cement paste more stable and more strongly bonded [21]. These improvements lead to a longer lifespan of concrete structures, thus reduce the cost of repairing such structures. Considering the excellent performance of nano-SiO_2 in improving the properties, it is expected that nano-SiO_2 can improve the performance of cement composites to prevent the early frost damage.

Accordingly, this paper explored the effect of nano-SiO_2 on the mechanical properties and durability of cement pastes suffered early-age frost damage. Using the XRD, TG, and MIP techniques, the influence of the nano-SiO_2 on microstructure and cement hydration was investigated. The results provide the experimental and theoretical support for applying nano-SiO_2 in concrete structures serving in extremely cold environments.

2. MATERIALS AND EXPERIMENTAL METHODOLOGY

2.1 Material

P.O.42.5 used as binder material was provided by Harbin Yatai Cement Company. The nano-SiO2 were purchased from Taihong Yuda New Material Co., Ltd. The properties of nano-SiO2 are listed in Table 1.

Table 1: Properties of nano-SiO_2

Item	Purity (%)	Diameter (nm)	SSA (BET) (m^2/g)	Density (g/cm3)
Target	99.0	20	100.53	≤0.12

2.2 Mix procedures

A Scientz SB-5200DT sonicator (40 KHz, 300 W) was applied to disperse the nano-SiO_2 particles in the water. The sonication process was carried out three times, with the duration of each stage being 60 mins. The suspensions needed to be placed in ice water after each sonication stage in order to eliminate the heat and foam caused by sonication. Mixing procedures were carried out in a multifunctional mixer (TZJBJ-001, Wuxi City Construction Test Equipment Co., Ltd.), as follows:

1. Weighed all raw materials according to the mixture proportions.
2. Added the 4/5 of prepared nano-SiO2 suspensions into cement and simultaneously stirred at a low speed of 72 r/min for 2 min, then held for 1 min.
3. Added the remaining suspensions into mixture and mixed at a high speed of 200 r/min for 4 min.
4. Put the mixtures into molds and demold after 24 hours.

2.3 Curing method

The samples were immediately stored in automatic temperature-controlled freezer at -15 ℃ for 7 days, and then were cured in standard curing room (20 ℃) for 28 days to carry out macro performance tests, so as to reflect the warming conditions encountered after winter. The normal cement paste and cement paste with nano-SiO_2 (nano-SiO_2 cement paste) are referred to as "Freezing-PC'' and ''Freezing-NS", respectively. In the nano-SiO2 cement paste, nano-SiO2 is added at the amounts of 0.6%, 0.9% and 1.2% by the weight of cement, as shown in Table 2.

Table 2: Experimental design

Sample Name	Weight Fraction /(wt.%)	Water-cement ratio	Freezing ages /(d)	Standard curing ages /(d)
Freezing-PC	0	0.35	7	28
Freezing-NS06	0.6	0.35	7	28
Freezing-NS09	0.9	0.35	7	28
Freezing-NS12	1.2	0.35	7	28

2.4 Testing methods

The compressive strength was evaluated on cubic samples, 40-mm side and the average strength of six samples was used as an index according to the Chinese standard GB/T 17671-1999 [22]. The test was performed using a 2000 kN compression testing machine (WHY-2000) under displacement control and the rate of loading was kept as 0.6 kN/s. And the non-steady state migration test in accordance with NT BUILD 492 [23] were used to evaluate the chloride-ion penetration.

The AutoPore IV 9500 Mercury Porosimeters, able to determine a broad pore size distribution (0.003 to 1100 μm), was used for mercury intrusion porosimetry (MIP). By assuming a contact angle of 130° and a mercury surface tension of 485 dynes/cm, the minimum pore access diameter reached is about 5.65 nm. The MIP samples were taken from the fracture pieces of the prism. To stop the hydration, samples were soaked in ethanol for 7 days, and then were further oven-dried at 60 ℃ until the weight of samples were accurate to 0.001 g.

Thermal analysis was investigated by a thermogravimetric apparatus (TG; NETZSCH STA449F3). All experiments were performed from 60 up to 1000 ℃ and with a 10 ℃/min heating rate under flowing nitrogen.

The X-ray diffraction analysis (X'PERT, PANalytical B.V.)) were applied for determining the amount and change tendency of calcium hydroxide crystal. The samples were scanned from 5° to 90° at a scanning speed of 8°/min.

3. RESULTS

3.1 Compressive strength

The compressive strengths of cement pastes with nano-SiO_2 and reference sample are presented in Fig. 1. It is found that the compressive strengths of Freezing-NS samples are higher than the reference samples (Freezing-PC). Especially, the compressive strength of Freezing-NS sample at dosage of 0.9 wt.% reached the maximum, which increases by 22.6%/10MPa.

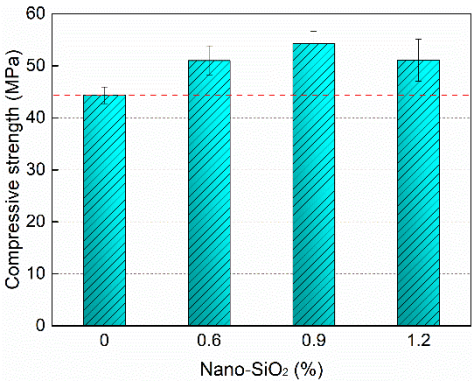

Figure 1: Compressive strengths of the samples.

3.2 Chloride ion penetration

The 35-day D_{nssm} (Fig. 2) indicate the addition of the nano-SiO_2 can effectively enhance the resistance of cement matrix to the intrusion of chlorides. At 0.6 wt.%, 0.9 wt.%, and 1.2 wt.% nano-SiO_2 content, the non-steady-state migration coefficient (D_{nssm}) were decreased by 18.2%, 30.9%, and 29.7%, respectively, compared with the reference samples (Freezing-PC).

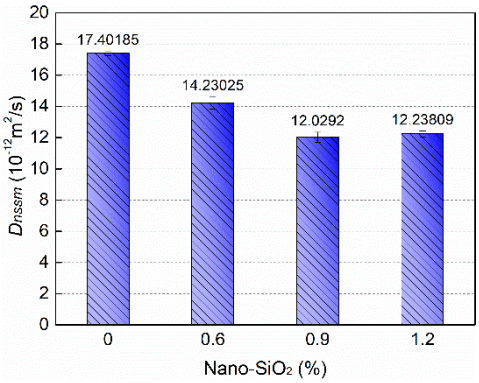

Figure 2: The non-steady-state migration coefficient (D_{nssm}) of the samples.

3.3 Pore structure

The MIP results are shown in Table 3 and it can be seen that the addition of nano-SiO_2 obviously decreased the median pore diameter (by volume), which is reduced from 106.2 nm (for the reference, Freezing-PC) to 73.6. The average pore diameter and the critical pore diameter were decreased and the reductions of 7.4 nm and 100.8 nm was found in the average pore diameter and critical pore diameter, respectively.

Table 3: MIP data

Parameters	Freezing-PC	Freezing-NS09
Median pore diameter (volume) (nm)	106.2	73.6
Median pore diameter (area) (nm)	10.1	9.8
Average pore diameter (4V/A) (nm)	38.8	31.4
Critical pore diameter (nm)	283.9	183.1
Porosity (%)	20.3	18.1

3.4 Hydration degree

Based on the TG results (Fig. 3), non-evaporable water contents of the hydrated cement pastes were calculated to estimate the hydration degree. As shown in Table 4, the hydration degrees of Freezing-NS09 sample is higher than that of Freezing-PC sample.

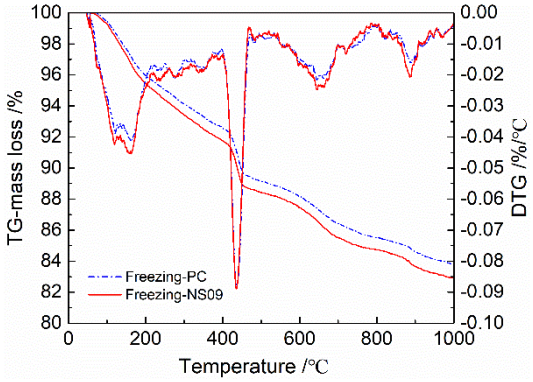

Figure 3: TG and DTG curves of cement paste with 0.9 wt.% nano-SiO_2 (Freezing-NS09) and reference sample (Freezing-PC).

Table 4: Hydration degree (%)

Sample	Freezing-PC	Freezing-NS09
Hydration degree	61.0	63.9

3.5 XRD

The X-ray diffraction analysis (XRD) were used to qualitatively determine the pozzolanic activity of nano-silica. The X-ray patterns of cement pastes containing 0% and 0.9% nano-SiO_2 contents are shown in Fig. 4. The $Ca(OH)_2$ consumption, which is obtained by the intensity change of the main diffraction peaks, was used as an indicator to the pozzolanic activities. As shown in Table 5, the intensity of main diffraction peaks of $Ca(OH)_2$ in cement paste with nano-SiO_2 (Freezing-NS09) is significantly lower than those in reference specimen (Freezing-PC), which means that nano-SiO_2 can consume calcium hydroxide to some extent. And nano-SiO_2 can also reduce the $Ca(OH)_2$ orientation in cement matrix. Moreover, it is found that no special

diffraction peaks appear in Freezing-NS09 samples compared with Freezing-PC sample, which means the addition of nano-SiO_2 cannot produce new substances.

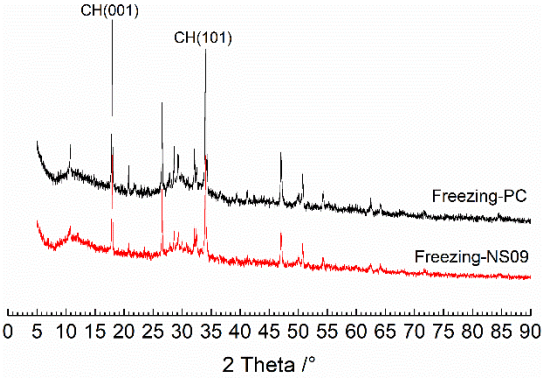

Figure 4: XRD patterns of Freezing-PC and Freezing-NS09.

Table 5: Diffraction intensity

Sample Name	CH (001)	CH (101)	CH orientation
Freezing-PC	2066	1784	1.56
Freezing-NS09	1275	1274	1.35

4. DISCUSSION

For the compressive strength of cement pastes suffered early-age freezing, it is found that the incorporation of nano-SiO_2 can significantly enhance the compressive strength of the matrix. In terms of cement hydration, TG results show that the addition of nano-SiO_2 increases the degree of hydration of cement due to the ultra-high specific surface of nano-SiO_2 particles [24]. Using quantitative (TG) and qualitative (XRD) methods, it is proved that nano-SiO_2 can consume $Ca(OH)_2$ to reduce the weak points Moreover, additional C-S-H gel, produced by the chemical reaction of nano-SiO_2 with $Ca(OH)_2$, is the main constituent for strength improvement of cement matrix. It is called pozzolanic reaction. It is known that strength is also closely related to the compactness of pore structure. The denser the pore structure form, the less internal defects are, and the higher the strength gains. These additional C-S-H gels make hydration products formed more compact with less voids, which generate higher strength. According to the Fig. 2, it can be observed that nano-SiO_2 can improve the permeability, thus enhancing the durability of cement paste. It is widely known that the pore structure is a critical factor to influence the durability of cement-based materials. MIP results indicate that the incorporation of nano-SiO_2 reduces the total porosity and other pore structure parameters. In other word, the incorporation of nano-SiO_2 can refine the pore structure of cement matrix.

5. CONCLUSIONS

The incorporation of nano-SiO_2 can significantly improve the macro properties of cement pastes suffered early-age frost damage. This improvement is due to the pozzolanic activity of nano-SiO_2, which can consume calcium hydroxide to reduce the weak points in the matrix and produce additional C-S-H gels to increase the compactness of pore structure.

ACKNOWLEDGEMENTS

This research is supported by the National Natural Science Foundation of China with Grant No. 51778189 and the National key research and development program of China with Grant No. 2018YFC0705601.

REFERENCES

[1] Norhasri M S M, Hamidah M S, Fadzil A M, et al. 'Inclusion of nano metakaolin as additive in ultra high performance concrete (UHPC)'. Construction & Building Materials, 2016, 127:167-175.

[2] Mohseni E , Naseri F , Amjadi R , et al. 'Microstructure and durability properties of cement mortars containing nano-TiO2 and rice husk ash'. Construction and Building Materials, 2016, 114:656-664.

[3] OLTULU, Meral, SAHIN, et al. 'Single and combined effects of nano-SiO2, nano-Al2O3 and nano-Fe2O3 powders on compressive strength and capillary permeability of cement mortar containing silica fume'. Materials Science & Engineering A, 2011, 528(22):7012-7019.

[4] NAZARI, Ali, RIAHI, et al. 'Improvement compressive strength of concrete in different curing media by Al2O3 nanoparticles'. Materials Science & Engineering A, 2011, 528(3):1183-1191.

[5] Land G , Stephan D . 'The influence of nano-silica on the hydration of ordinary Portland cement'. Journal of Materials Science, 2012, 47(2):1011-1017.

[6] Björnström J, Martinelli A, Matic A, et al. 'Accelerating effects of colloidal nano-silica for beneficial calcium–silicate–hydrate formation in cement'. Chemical Physics Letters, 2004, 392(1):242-248.

[7] Shih J Y, Chang T P, Hsiao T C. 'Effect of nanosilica on characterization of Portland cement composite'. Materials Science & Engineering A, 2006, 424(1):266-274.

[8] Li H , Xiao H G , Yuan J , et al. 'Microstructure of Cement Mortar with Nano-Particles'. Composites Part B, 2004, 35(2):185-189.

[9] Givi A N , Rashid S A , Aziz F N A , et al. 'Experimental investigation of the size effects of SiO2 nano-particles on the mechanical properties of binary blended concrete'. Composites Part B: Engineering, 2010, 41(8):673-677.

[10] Li G . 'Properties of high-volume fly ash concrete incorporating nano-SiO2'. Cement & Concrete Research, 2004, 34(6):1043-1049.

[11] Said A M , Zeidan M S , Bassuoni M T , et al. 'Properties of concrete incorporating nano-silica'. Construction and Building Materials, 2012, 36(none):838---844.

[12] Li L G , Zhu J , Huang Z H , et al. 'Combined effects of micro-silica and nano-silica on durability of mortar'. Construction and Building Materials, 2017, 157:337-347.

[13] Ghafari E , Arezoumandi M , Costa H , et al. 'Influence of nano-silica addition on durability of UHPC'. Construction and Building Materials, 2015, 94:181-188.

[14] Zhang, L. , Ma, N. , Wang, Y. , Han, B. , Cui, X. , & Yu, X. , et al. 'Study on the reinforcing mechanisms of nano silica to cement-based materials with theoretical calculation and experimental evidence'. Journal of Composite Materials, 2016, 0021998316632602.

[15] Salemi, N. , & Behfarnia, K. 'Effect of nano-particles on durability of fiber-reinforced concrete pavement'. Construction & Building Materials, 2013, 48(11), 934-941.

[16] Quercia, G., Spiesz, P., Hüsken, G., & Brouwers, H. J. H. 'Scc modification by use of amorphous nano-silica'. Cement & Concrete Composites, 2014, 45(1), 69-81.

[17] Jo B W , Kim C H , Lim J H . 'Investigations on the development of powder concrete with nano-SiO2particles'. KSCE Journal of Civil Engineering, 2007, 11(1):37-42.

[18] Mohammad B , Alireza J , Fadi A . 'Nano-SiO 2, contribution to mechanical, durability, fresh and microstructural characteristics of concrete: A review'. Construction and Building Materials, 2018, 181:27-41.

[19] Ji T . 'Preliminary study on the water permeability and microstructure of concrete incorporating nano-SiO2'. Cement and Concrete Research, 2005, 35(10):1943-1947.
[20] Rai S , Tiwari S . 'Nano Silica in Cement Hydration. Materials Today: Proceedings', 2018, 5(3):9196-9202.
[21] Gaitero J J , Campillo I , Guerrero A . 'Reduction of the calcium leaching rate of cement paste by addition of silica nanoparticles'. Cement and Concrete Research, 2008, 38(8-9):1112-1118.
[22] GB/T 17671–1999. Method of testing cements: determination of strength. Beijing; 1999.
[23] NT Build 492, Concrete, Mortar and Cement-Based Repair Materials: Chloride Migration Coefficient from Non-Steady-State, Migration Experiments, 1999.
[24] Lavergne, F. , Belhadi, R. , Carriat, J. , & Ben Fraj, A. 'Effect of nano-silica particles on the hydration, the rheology and the strength development of a blended cement paste'. Cement and Concrete Composites, 2018.

INFLUENCE OF AMBIENT TEMPERATURE ON THE MECHANICAL PROPERTIES OF MACRO FIBRE REINFORCED CONCRETE

Feilian Deng (1), Chenjia Zuo (1), Yanbo Liu (1) and Xianpeng Liu (2)

(1) College of Shipbuilding Engineering, Harbin Engineering University, China

(2) Tianjin Research Institute for Water Transport Engineering, China

Abstract

The incorporation of macro fibers have been an effective method to improve the mechanical and durability properties of concrete. As the mechanical properties of Macro fiber reinforced concrete are mostly tested at room temperatures, the effect of ambient temperature on the mechanical properties have been rarely reported. In this investigation, concrete specimens were prepared with three types of Macro fibers including steel fiber (SF), modified polypropylene (PP) fiber and polyvinyl alcohol (PVA) fiber. Compressive strength and flexural strength tests were performed on specimens with temperature ranging from -30°C and 30°C. Test results show that both the compressive strength increase with decreasing ambient temperature. The toughness of SF concrete was found to increase with increasing ambient temperature, while the toughness of PP and PVA fiber concrete was found to decrease with increasing ambient temperature.

Keywords: Compressive Strength, Flexural Strength, Macro Fibers, Ambient Temperature

1. INTRODUCTION

Concrete is the most widely used building material in the world. Adding proper amount of fibers is widely recognized as one of the effective methods to improve the crack resistance, tensile properties of concrete.[1,2] Compared with micro fibers, macro-fiber not was found not only provide resistance for early crack, but also improve the impact resistance, flexural toughness and fracture properties.[Zongcai Deng*and Jianhui Li] Environmental temperature is known to have a great impact on the mechanical properties of fiber-reinforced concrete (FRC) and these properties trend to change at low temperatures. In most research, mechanical properties of concrete are conducted at room and high temperatures; [3,4] however, the mechanical performance of FRC at low temperature environment have been rarely reported. Due to the trend of constructing of concrete projects which possibly serve at low temperatures, such as concrete LNG storage towers and concrete structures in cold and arctic regions, it is necessary to study the mechanical performance of Macro fiber reinforced concrete under various ambient temperatures.

Published researches reported that the compressive strength increases with decreasing temperature.[5] However, most of these studies focus on concrete without fibers, and the flexural behavior have rarely been investigated. In this investigation, concrete specimens with three types of macro steel fibers (SF), polypropylene (PP) fibers and polyvinyl alcohol (PVA) fibers were prepared. Compressive strength and flexural strength tests were tested on specimens with temperatures ranging from -30℃ to 30℃.

2. EXPERIMENTAL

2.1 Materials

Thirteen mixtures were prepared in this investigation including specimens that contained only OPC and specimens with three types of fibers, as shown in Fig.1. Details of physical and mechanical properties of Macro fibers are listed in Table 1. Fibers were mixed into the concrete according to the volumetric method and the content is 1.5%. Additionally, 20% Class I fly ash, 30% Class F slag powder and 0.5% water reducer were added. P·O 42.5 cement was used for all the mixes and the *w*/*cm* was 0.43. Limestone with size range ranging from 5 to 20 mm was used as coarse aggregate. River sand from the local Songhua River was used as fine aggregate. Details of the mixture designs are listed in Table 2.

(a) Steel fiber (b) PP fiber (c) PVA fiber

Figure 1: Appearance of Macro fibers

Table1: Physical and mechanical properties of different Macro fibers

Macro fibers	Density (g/cm^3)	Tensile Strength (MPa)	Elastic Modulus (GPa)	Length (mm)	Diameter (μm)
SF	7.8	1000.0	154.0	50.0	620.0
PP	0.9	530.0	7.1	50.0	910.0
PVA	1.3	254.0	15.9	30.0	646.4

Table 2: Mix properties of concrete

Mix	Cement (kg/m³)	Fly Ash (kg/m³)	Slag (kg/m³)	Fine agg (kg/m³)	Coarse agg (kg/m³)	Fibers		
						Type	Mass	Volume
							(kg/m³)	Content (%)
OPC	215.1	86.1	129.1	624.7	1160.1	-	-	-
SF	215.1	86.1	129.1	624.7	1160.1	SF	117.0	1.5
PP	215.1	86.1	129.1	624.7	1160.1	PP	16.4	1.5
PVA	215.1	86.1	129.1	624.7	1160.1	PVA	19.5	1.5

3.2 Experimental Methods

Two geometries of specimens were prepared. Φ10 cm×20 cm (4×8in) cylinders specimens were prepared for compressive strength tests. 10 cm×10 cm×40cm rectangular specimens were prepared for flexural test according to ASTM C1609 [6]. As the large amount of mineral admixtures added in the concrete reduces the hydration rate, an elevated temperature curing regime was used to accelerate the curing rate of specimens. The specimens were demoulded 48 hours after casting and then immersed in 40°C saturated lime water for curing until the age of 28 days. A maturity method according to ASTM C1074 [7] was employed to calculate the equivalent age of specimens cured at 20°C. The calculated equivalent age is listed in Table 3. It is noted that the concrete age presented in this paper is the actual age but not the equivalent age.

At the age of 28 days, specimens were removed from the curing tanks and then stored in various chambers to obtain specimens with difference temperatures. Specimens stored in water baths of 10°C, 20°C and 30°C to obtain the specimens with temperature between 10°C to 30°C. A refrigerator with capacity of -40°C minimum temperature was used to obtain specimens with temperature ranging from -30°C to 0°C. The specimens were stored in the water bath or refrigerator for more than 24 hours to assure the targeted temperature of the specimens were obtained. Type K thermocouples were cast in some specimens to measure the inner temperature of the specimens before tested.

Both the compressive and flexural strength tests were performed immediately after removing the specimens from the water bath or refrigerator to minimize the effect of temperature change of specimens during testing.

Table 3: Equivalent Age

Curing age at 40℃	Equivalent Age at 20℃
7d	25d
14d	50d
28d	101d

3. RESULTS AND DISCUSSION

3.1 Compressive strength

The compressive strength of specimens from the four mixtures at various temperatures are presented Fig. 2. It shows that the compressive strength of four kinds of concrete increases with the decrease of temperature. The trends are as follows, 30℃~10℃, the compressive strength increases slowly and steadily; 10℃~0℃, the compressive strength decreases slightly; 0℃~-

20℃, the compressive strength increases greatly. The largest increase in strength is PVA reinforced concrete with an increase of 83.9%. The smallest increase is SF reinforced concrete with an increase of 35.3%. This shows that the decrease of temperature has the greatest influence on PVA reinforced concrete and the least on SF reinforced concrete. The incorporation of PP fibers reduces the compressive strength of the concrete.

From the damage at two extreme temperatures in Fig. 3. It can be found that the SF reinforced concrete has little change in the failure form at 30°C and -30°C, and the failure modes of other groups have changed greatly. However, the integrity of the failure is better than that of OPC concrete group, which indicates that the incorporation of fibers limits the generation of cracks and improves the integrity of the concrete under compression, especially steel fibers [8].

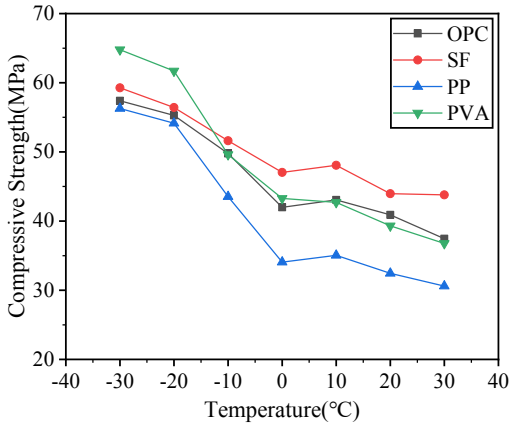

Figure 2：Relationship between concrete compressive strength and temperature

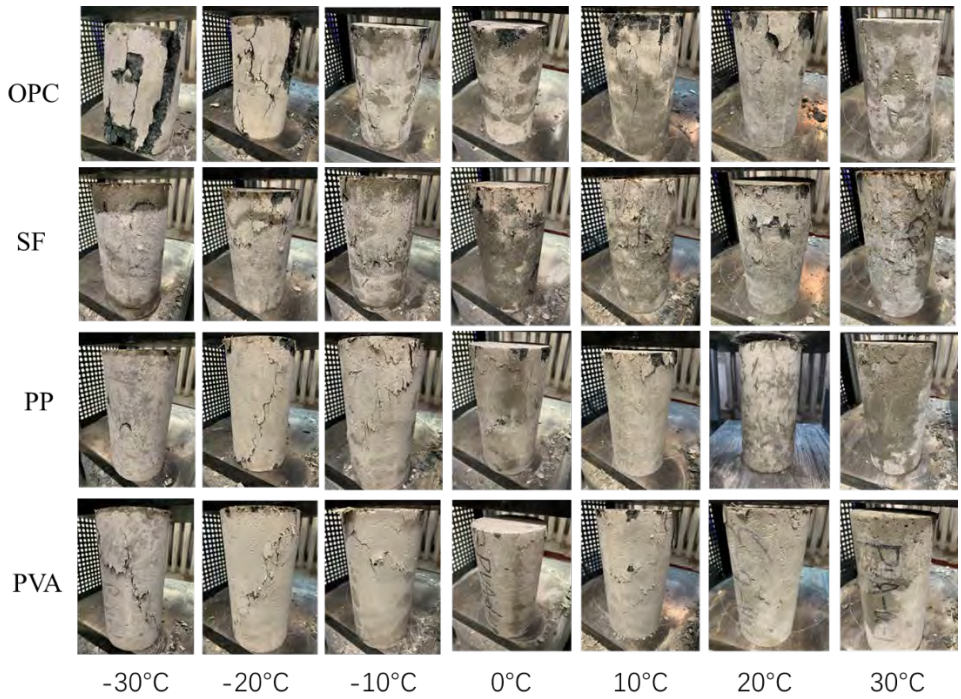

Figure 3: Failure mode of specimens

3.2 Flexural strength

The load deflection curves for specimens at different temperatures are shown in Fig.4. It can be seen that the curves of the three types of FRC have roughly the same trend with temperature and after cracking, FRC still has bearing capacity, while OPC specimen immediately fractures and loses its bearing capacity completely.

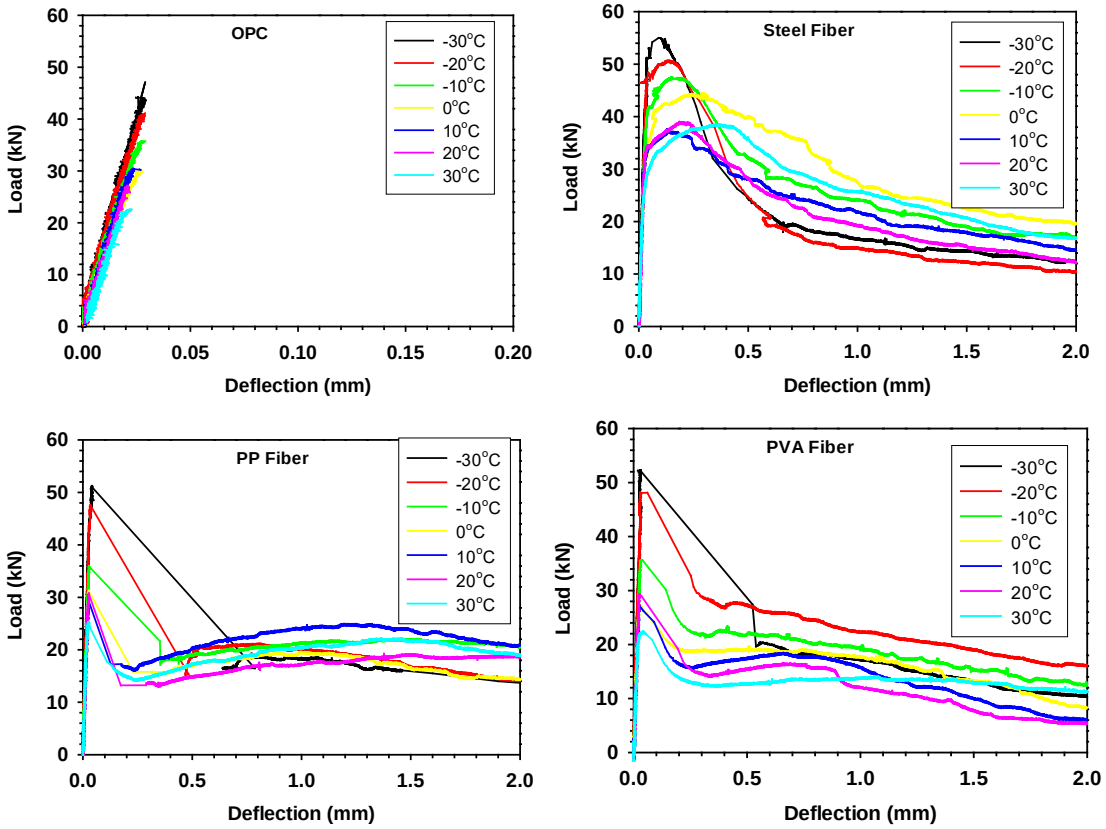

Figure 4：Load deflection curves of FRC at different temperatures

Fig. 5 shows the relationship between flexural strength and temperature for specimens with fiber or not. It indicates that the flexural strength of four kinds of concrete increases with the decrease of temperature. The trends are as follows, 30℃~0℃, the flexural strength increases slowly; 0℃~-30℃, the flexural strength increases greatly and reaches a maximum at -30℃.At this point, the flexural strength of SF reinforced concrete is the largest, 15MPa, closely followed by PVA and PP fiber reinforced concrete at 13.1MPa and 12.3Mpa,and the smallest is OPC, 11.7MPa.As the bonding performance between concrete and fiber plays an important role in improving the strength of FRC [9], and the water in concrete freezes at low temperature, which makes the fine aggregate bond with the coarse aggregate, the specimens have good integrity. In addition, ice can be used as coarse aggregate to bear part of load. The strength and the bonding performance of ice increase with the decrease of temperature, [10,11] which makes the bond between concrete and fiber increase.

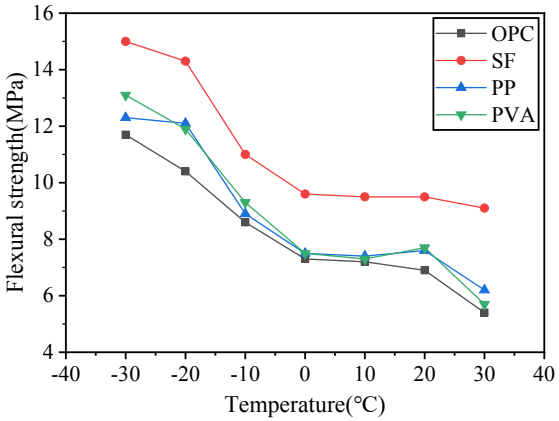

Figure 5: Relationship between flexural strength and temperature

The evolution of residual strength at net deflection of L/150 and flexural toughness for specimens with three types of fibers are presented in Fig. 6 and Fig. 7. It shows in Fig.6 that the residual strength at net deflection of L/150 of SF reinforced concrete decreases with temperature reducing, and reaches the minimum value of 2.62MPa at -30℃, when the flexural toughness is 46.05J. The residual strength at net deflection of L/150 of PP and PVA fiber reinforced concrete increases slightly with temperature reducing, and the residual strength at -30℃ is 3.52MPa and 2.72MPa, the flexural toughness is 47.47J and 45.14J respectively. Fig. 7 shows that the flexural toughness of SF reinforced concrete increases with increasing ambient temperature, while the flexural toughness of PP and PVA fiber reinforced concrete is found to decrease with the increase of temperature, and eventually the three tend to the same stable value. When temperature decreases from 30℃ to -30℃, the flexural toughness of SF reinforced concrete decreases by 18.5%, while that of PP and PVA fiber reinforced concrete increases by 19% and 39%, respectively. This might be attributable to the low-temperature brittleness of steel fiber, whose transition temperature is about -15℃[12].When temperature is lower than -10℃, the toughness of SF reinforced concrete decreases obviously. The transition temperature of PP and PVA fiber are both less than -40℃ and their brittleness increases little in the range of 30℃ to -30℃, but the overall framing effect enhances with the decrease of temperature.

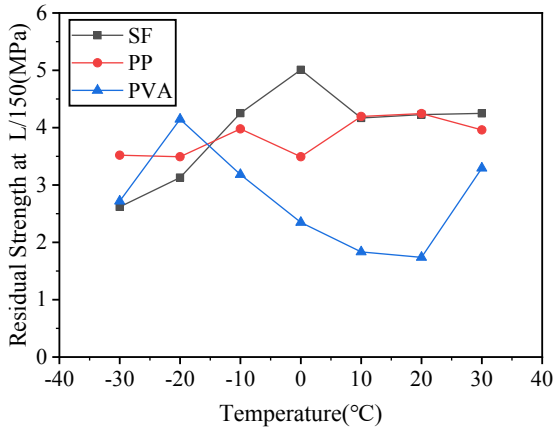

Figure 6: Residual strength of FRC at net deflection of L/150

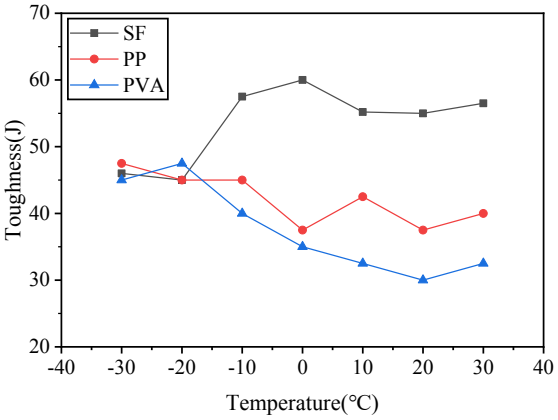

Figure 7: Relationship between toughness and temperature

4. CONCLUSIONS

- The incorporation of fibers limits the generation of cracks and improves the integrity of the concrete under compression and the confine effect on concrete is steel fiber > PVA fiber > PP fiber.
- The compressive strength of FRC increases with the decrease of temperature and the improvement effect on compressive strength is steel fiber > PVA fiber, while the incorporation of PP fiber reduces the compressive strength.
- The flexural strength of FRC increases with the decrease of temperature and the improvement effect on flexural strength is steel fiber > PVA fiber > PP fiber.
- The addition of coarse fibers will improve the flexural toughness of concrete. With the increase of ambient temperature, the toughness of SF concrete increases while that of PP and PVA fiber concrete decreases.

ACKNOWLEDGEMENTS

The authors acknowledge the financial support from Natural Science Foundation of Heilongjiang Province (No. LH2019E036).

REFERENCES

[1] Banthia, N. and Nandakumar, N., 'Crack growth resistance of hybrid fiber reinforced cement composites'. *Cement & Concrete Composites*. **25**(1)(2003)3-9.

[2] Khaloo, A.R. and Afshari, M., 'Flexural behaviour of small steel fibre reinforced concrete slabs'. *Cement and Concrete Composites*. **27**(1)(2005)141-149.

[3] Wasim, K. and Venkatesh, K., 'High Temperature Mechanical Properties of High-Strength Fly Ash Concrete with and without Fibers'. *ACI Materials Journal.* **11**(1)(2012).

[4] Karakoç, M.B,. 'Effect of cooling regimes on compressive strength of concrete with lightweight aggregate exposed to high temperature'.*Construction and Building Materials*. 41 (2013)21-25.

[5] Chao, L., *Experimental study on mechanical properties of concrete at low temperature*. Master's thesis, Beijing: Tsinghua University Press, 2011,51.

[6] ASTM C1609, Standara test method for flexural for flexural performance of fiber reinforced concrete (using beam with third-point loading). West Conshokocken: American Society for Testing and Materials, 2012, 9pages.
[7] ASTM C1074, Standard practice of estimating concrete strength bythe maturity method. Philadelphia: American Society for Testing and Materials, 1998, 8pages.
[8] Zhang, Y. Mechanical and Chloride Permeability Properties of Coarse Fiber Reinforced Concrete. Master's thesis, Harbin: Harbin Engineering University Press, 2019,17-18.
[9] Guozhen, Z. 'Steel fiber concrete structure', Beijing: China Building Industry Press, 1999,45-48.
[10] Montejo, L. and Sloan, O. 'Response of Reinforced Concrete Members at Low Temperatures. J, Coldreg Eng. 22(3)(2008) 79-102.
[11] Lahlou, D., Khenane, A. and Salah, K., 'Behavior of the Reinforced Concrete at Cryogenic Temperatures'. *Cryogenics*. **47**(9)(2007) 517-525.
[12] Ghadban, A. A. ,Wehbe, N. I. and Underberg, M., 'Effect of Fiber Type and Dosage on Flexural Performance of Fiber-Reinforced Concrete for Highway Bridges'. *ACI Materials Journal*. **115**(36)(2018)413-424.

INTERFACE BETWEEN CEMENTITIOUS MATRIX AND FIBRES INFLUENCED BY THE MODIFICATION OF FIBRE SURFACE

Anna Antonova (1), Marika Eik (1), Ville Jokinen (2), Jouni Punkki (1) and Jari Puttonen (1)

(1) Department of Civil Engineering, Aalto University, Finland

(2) Department of Chemistry and Materials Science, Aalto University, Finland

Abstract

The performance of fibre reinforced cementitious composites depends on the interaction between the cementitious matrix and the fibres on the micro-scale. This interaction is affected by the material and surface properties of the fibre and the micro-scale characteristics of the cementitious matrix close to the fibre surface, creating the interfacial transition zone (ITZ). However, the discussions regarding the effect of the fibre surface on the formation of the ITZ and, as a result, the bond strength between the matrix and the fibres are limited. The present paper reports the progress of the ongoing research project, which concentrates on investigating the interface created by the steel fibres with different characteristics of the surface roughness and cementitious matrix. The results of this study can support the development of efficient fibre reinforced cementitious composites.

Keywords: fibre-matrix interface, roughness, wettability, fibre reinforced cementitious composites, pull-out

1. INTRODUCTION

The inclusion of fibres into the cementitious matrix can help to restrict the propagation of cracks and improve the ductile performance of the fibre reinforced cementitious (FRC) composites. However, the behaviour of FRC composites at the structural level depends on the stress transferring from the cement-based matrix to the fibres on the micro-scale. The stress is transferred from the matrix to the fibre by the interfacial contact. This contact is provided by the interfacial transition zone (ITZ), that is known to have porous microstructure with precipitation of calcium hydroxide (CH), whose binding property is lower than that of the calcium-silicate-hydrate (C-S-H) phase [1]. The increased porosity in the ITZ is governed by the poor packing of the cement clinker grains [2]. Since fibre is several orders of magnitude larger than the cement clinker grains, it acts as a wall, and the cement grains that are located at the surface of the fibre cannot efficiently fill the space available. Those empty spaces created between the cement grains also may contribute to increased porosity close to the fibre surface, as it was discussed in [3] by comparing the measured roughness of the fibre and the size of the

particles that can fill the surface grooves. Authors in [4] discussed that the wetting of the fibre surface can affect the distribution of cement hydrates near the fibre. The relation between the wetting and the roughness of the fibre surface and the quality of contact between the fibre and water-based geopolymer matrix was also observed in [5]. At a more general level, the roughness of the surface is known to have an impact on the wetting properties of a material, as was reported in [6, 7]. The ongoing research work is aimed to investigate the influence of the steel fibre roughness on its wetting properties and their mutual effect on the interface characteristics between the steel fibre and the cementitious matrix, such as packing of cement-based matrix around the fibre and mechanical resistance of fibre to the pull-out from a matrix.

2. MATERIALS AND METHODS

2.1 Materials

Steel fibres with a diameter of 1 mm with different surface roughness were examined. The fibres were divided by types of the processing technique applied to receive the different roughness profiles: electro-polished; non-processed; coarsened with sandpaper (Fig. 1). The cement-paste was prepared from the ordinary Portland cement (OPC) CEM I 52,5 N.

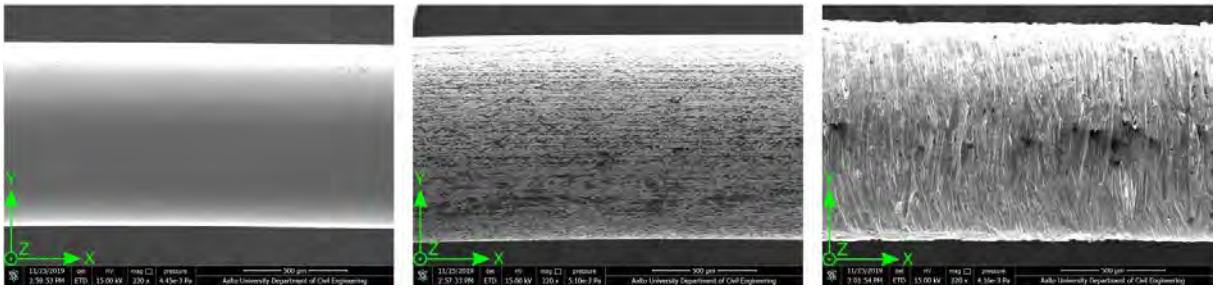

(a) Polished (b) Non-processed (c) Sanded

Figure 1: SEM images of the fibres with different roughness of the surface.

2.2 Methods

The atomic force microscope (AFM) and stylus profilometer were used to quantify the three different surface profiles of the steel fibre. Contact angle goniometry was implied to examine the wetting properties of the steel fibres with different surface roughness by studying advancing (water spreading along the dry surface) and receding (adhesion of the water to the surface) water contact angles of the surface. The cementitious matrix in the vicinity of the fibre was examined with the scanning electron microscope (SEM) by analysing backscattered electron (BSE) images. The performance of the bond between the steel fibres with different surface roughness and the cement-based matrix will be studied with the pull-out test.

3. PRELIMINARY RESULTS AND DISCUSSION

3.1 Roughness profile of the steel fibres

AFM was used to directly measure the roughness of fibres with the polished and non-processed surfaces. The fibres with the sanded surface were measured with stylus profilometer

since the size of this roughness exceeded the measuring limits of the AFM. The measurements were performed in the longitudinal direction of the fibres.

Figure 2 illustrates the surface profiles of the fibres with different types of roughness. The apparent grooves on the surfaces of the non- processed and sanded may contribute to the

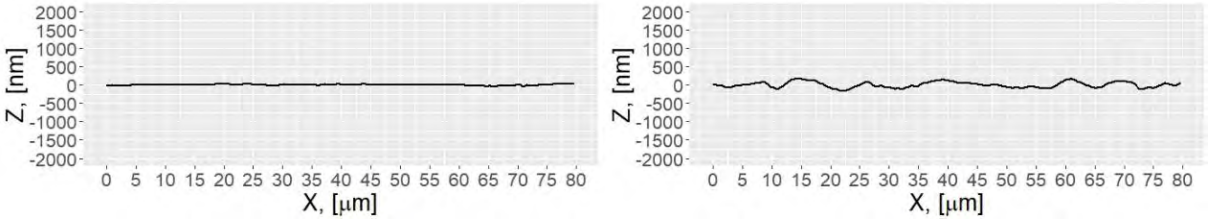

mechanical interlocking between the fibre and the cement-based matrix. The mechanical interlocking between the cement hydrates and the aggregates with a rough surface was noticed previously in [8].

(a) Polished (b) Non-processed

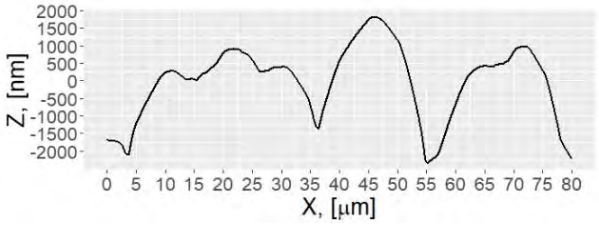

(c) Sanded

Figure 2: The examples of measured surface profiles of the steel fibres with different types of roughness.

The surface irregularities observed on non-processed and sanded fibres may also affect the spreading of the water, that can be captured by the grooves of the surface. The abrupt spreading of the water along the rough surface was explained before in [9] as the "slip-stick" behaviour of the water droplet on the rough surfaces. The peaks of the surface profile work as barriers, which block further movements of the water and capture water in surface grooves. This phenomenon may affect the wetting behaviour of fibres leading to the formation of the uniform water film along the fibre or, in contrary, micro-bleeding. The spreading and sticking of the water at the surface of the steel fibre is crucial for the formation of the hydrates, i.e. packing of the cement-based matrix in the close vicinity to the fibre.

3.2 Packing of the cementitious matrix around the steel fibres

Sufficient packaging of the cementitious matrix around the fibre, especially decreased porosity, promotes lower permeability, thus decreasing the possible corrosion of the steel fibres. In addition, the denser cement-based matrix in the vicinity of the fibre is contributing to better bond between mentioned constituents, therefore increasing the resistance to the cracking of the FRC composite and reducing the subsequent destruction of the material.

In the scope of this study, the packing of the cementitious matrix near the steel fibre was investigated with SEM and backscattered electron (BSE) detector. The pores and unhydrated (UH) cement grains were segmented from the BSE images (Fig. 3(a)) with the automated k-means clustering algorithm, as it is demonstrated in Figure 3(b).

The distributions of pores and UH cement grains were examined within a distance of 100 µm from the fibre surface with the step of 5 µm (Fig. 3(b)).

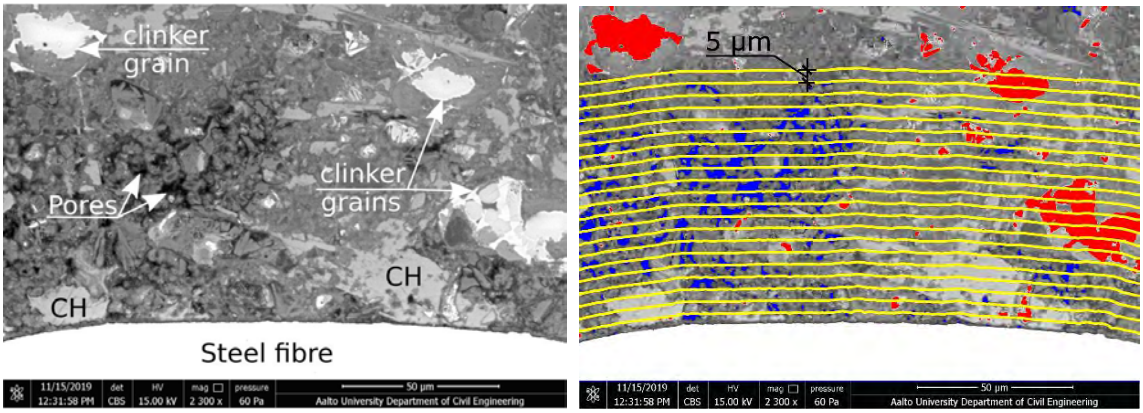

(a) (b)

Figure 3: (a) Example of SEM image. (b) Example of the segmented SEM image. The distributions of pores (blue) and unhydrated clinker grains (red) will be analysed with the step of 5 µm stripe-wise, which are marked with yellow lines.

3.3 Single fibre pull-out test

The quality of the packing of the cementitious matrix around the fibre, i.e. bond, can be also defined with the performance of the pull-out test.

The steel fibre with a total length of 50 mm and the embedded lengths of 30 mm was cast into the cement-paste cylinder with a diameter of 45 mm. The free end of the fibre was fixed from one side and the cement cylinder was fixed from the other side in the loading setup (Fig. 4 (a)). The setup of the pull-out test was designed to eliminate the influence of possible compressive stress, that may occur from the fixation of fibre or cement cylinders. The load was applied with the rate of 0.05 mm/min. Figure 4 (b) illustrates the results of the preliminary pull-out tests of the fibres with three different fibre roughness.

According to the Figure 4 (b) the peak load was increasing with the increase of roughness. This could be influenced by the differences in the microstructure of the ITZ around fibres with different surface roughness, that could be governed by the variations in fibre wetting and cement grains packing near the fibre. In addition, the occurrence of the hardening behaviour was noticed with the sanded fibres after the adhesion breakage. This behaviour may be attributed to the additional mechanical anchorage provided by the roughness of the fibre surface and non-uniform ITZ structure, which result in the interlocking between the cementitious matrix and the steel fibre. This response is typical for the general contact of rough surfaces, that was discussed previously in [10]. The possible occurrence of the slip hardening behaviour during the slippage of fibre from the cementitious matrix was explained in [11] by the nature of the interaction and the damage developed along the interface during the slip.

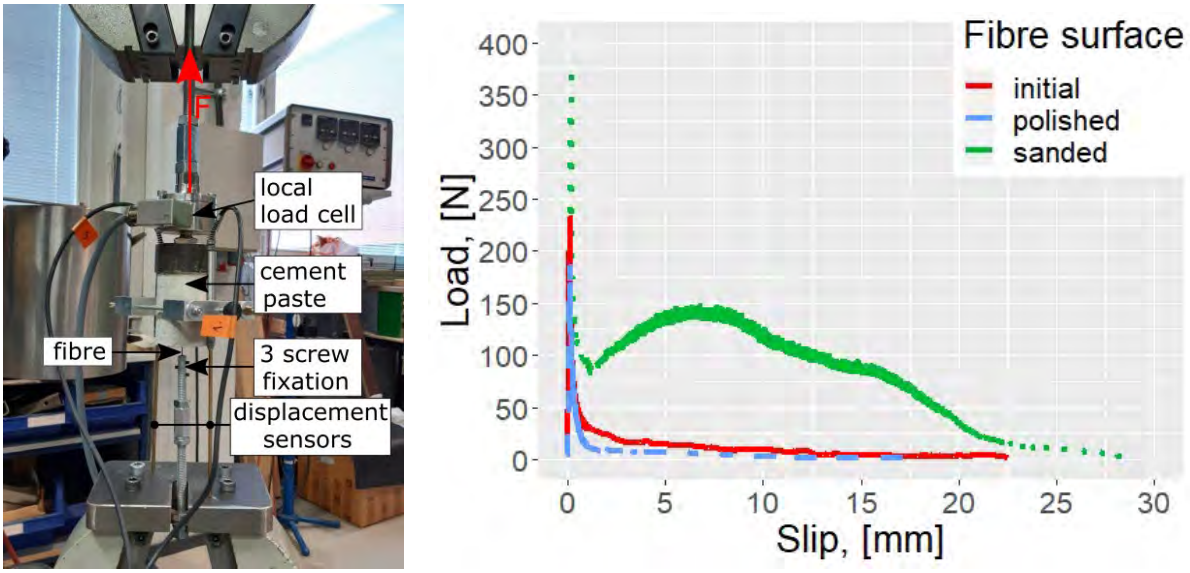

(a) (b)

Figure 4: (a) Setup for single fibre pull-out test. (b) Example of the load-slip curve obtained with single fibre pull-out test of the fibres with different fibre surface treatment.

4. CONCLUDING REMARKS

The combination of several measuring techniques are used in the present study to examine the relation between roughness, packing of the cement-based matrix in the vicinity of the fibre and mechanical performance of the contact between the cement-paste and fibre. This research has the potential to increase understanding of the interaction between the cementitious matrix and steel fibres considering the filling effect and interlocking between the fibre grooves and the cement hydrates and water spreading affected by the roughness of the fibre on the micro-scale.

ACKNOWLEDGEMENTS

The research leading to these results received funding from the Doctoral program of the School of Engineering, Aalto University.

REFERENCES

[1] Lee, S.F., Jacobsen, S. 'Study of interfacial microstructure, fracture energy, compressive energy and debonding load of steel fiber-reinforced mortar'. *Mat. and Str.* **44** (2011) 1451 – 1465.

[2] Scrivener, K. L., Crumbie, A. K. and Laugesen, P. 'The Interfacial Transition Zone (ITZ) Between Cement Paste and Aggregate in Concrete'. *Interface Sci.* **12** (2004) 411 – 421.

[3] Eik, M., Antonova, A. and Puttonen, J. 'Roughness of steel fibre and composition of cement paste close to fibre surface'. *Journal of Adv. Concr. Tech.* **17** (2019) 628 – 638.

[4] Xu, L., Deng, F. and Chi, Y. 'Nano-mechanical behavior of the interfacial transition zone between steel-polypropylene fiber and cement paste.' *Constr. and Build. Mat.* **145** (2017) 619 – 638.

[5] Ranjbar, N., Talebian, S., Mehrali, M., Kuenzel, C., Metselaar, H. S. C. and Jumaat, M. Z. 'Mechanisms of interfacial bond in steel and polypropylene fiber reinforced geopolymer composites'. *Comp. Sci. and Tech.* **122** (2016) 73 – 81.

[6] Wenzel, R. N. 'Resistance of solid surfaces to wetting by water'. *Industrial and Eng. Chem.* **28** (1936) 988 – 994.

[7] Kubiaka, K.J., Wilsona, M.C.T., Mathia, T.G. and Carval Ph. 'Wettability versus roughness of engineering surfaces'. *Wear.* **271** (2011) 523 – 528.

[8] Qudoos, A., Rehman, A. U., Kim, H. G. and Ryou, J. S. 'Influence of the surface roughness of crushed natural aggregates on the microhardness of the interfacial transition zone of concrete with mineral admixtures and polymer latex'. *Constr. and Build. Mat.* **168** (2018) 946 – 957.

[9] Shanahan, M. E. R. 'Simple theory of "stick-slip" wetting hysteresis'. *Langmuir* **11** (1995)1041-1043.

[10] Jiménez, A.-E. and Bermúdez, M.-D. 'Friction and wear'. In: Davim, J. P. (eds.), Tribology for Engineers. Woodhead Publishing, 2011, 33-63.

[11] Bentur, A. and Mindess, S. 'Fibre reinforced cementitious composites'. Crc Press, 2006, 31 – 97.

INTERNAL HYDROPHOBIZATION BY MEANS OF ORGANOSILICON COMPOUNDS

K. Grabowska (1), A. Wieczorek (1), M. Koniorczyk (1)

(1) Department of Building Physics and Building Materials, Lodz University of Technology, Poland

Abstract

The porous structure of building materials significantly affects their properties including their durability. Freezing water, salt crystallization, mold and fungi growths and general deterioration in thermal conditions caused by moisture in building materials lead to shorter life and the sustainability of the material. Internal hydrophobization by means of organosilicon compounds, such as silanes and siloxanes, can significantly improve their durability by increase water resistance and thus extend the application areas. In our paper we investigated the influence of silanes and siloxanes on the aeration, strength characteristics and water absorption of cement mortar. The possible changes in the microstructure of examined mortar was analyzed by mercury intrusion porosimetry (MIP). The heat of cement hydration of cement paste with organosilicon admixtures was studied by using isothermal calorimetry. Internal hydrophobization might be an alternative method to surface treatment. The obtained results showed that it is possible to use organosilicon compounds as admixtures to improve the water resistance, however, it is associated with changes in material properties.

1. INTRODUCTION

In the building industry the used materials are mostly porous especially cementitious one. Their porous structure significantly affects their properties, durability and lifespan. Water and salts dissolved in it might be easily transported by a network of connected capillaries. Water in the material may freeze and salts may crystallize, leading to the destruction of the material and deterioration of its properties. As first, soaps and waxes (e.g., stearates and oleates) were used as hydrophobic agents to protect against water and moisture [1,2]. Since the 50's of the 20th century organosilicon compounds (popularly called "silicones") were used as water-repellents for surface protection of the materials against detrimental effects of water in the industry and construction sectors [3,4]. The most popular hydrophobic agents based on silicon are represented by alkyl siliconates and silanes, siloxanes, polysiloxanes and silicone resins [1,5]. Due to chemical structure and physico-chemical characteristics of the organosilicon compounds and similarity to carbon-based materials organosilicon compounds are considered as very good agents to hydrophobic protection of inorganic, porous building materials (both surface and

volume (internal) hydrophobization). As a result of a chemical reaction, due to the chemical bonds are formed, of organosilicon compounds with cement matrix the permanent connection with the material is formed. Hence, the surface of the pores in cementitious material becomes hydrophobic, and the penetration of liquid water or moisture into the material structure is hinder, but with keeping vapor-permeable properties. The main structure of organosilicon compound is long polysiloxane chain containing oxygen and silicon atoms bonding each other alternately (─Si─O─Si─O─Si─). In addition, their structure includes an organic, alkyl substituent attached to the silicon atoms. Therefore, these compounds are called amphiphilic one. This means that they combine the properties of inorganic silicon-oxygen chain and organic non-polar alkyl groups. These alkyl substituents make interactions with the other organic compounds easier. The main function of alkyl groups, due to their non-polar character, is to give hydrophobic properties. Theoretically it is assumed that longer and higher branching of the alkyl group improves hydrophobic effects. The function of inorganic part of organosilicon compounds (meaning siloxane chain) provide interaction with inorganic substrates (meaning cement phases) [1,5]. In our study we investigated the influence of three commercial admixtures based on poly(dimethylsiloxane) (PDMS) (Fig. 1a) and triethoxyoctylsilane (Fig. 1b). Poly(dimethylsiloxane) is macromolecular, polymeric compound with two methyl groups. Triethoxyoctylsilane, contrary to poly(dimethylsiloxane), is a single monomer with three ethoxy (─O─C_2H_5) groups and one octyl group (─C_8H_{17}). During chemical reactions the ethoxy groups enables hydrolysis the silanes molecules to the silanols. Subsequently polycondensation reactions occur which lead to forming of siloxane chains. Long octyl group is responsible for hydrophobic effects.

The purpose of this preliminary studies is to investigate the functionality of commercially available water-repellents based on organosilicon compounds to internal hydrophobization of porous, cementitious building materials and their impact on the properties of the material, both negative and positive.

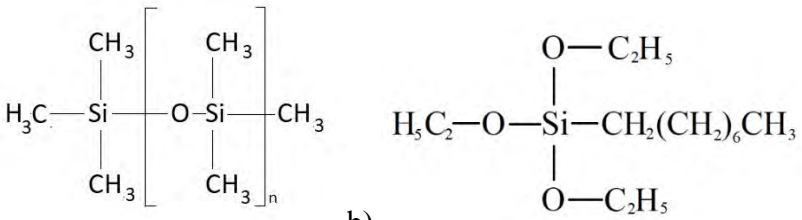

a) b)

Figure 1: Schematic structure of a) poly(dimethylsiloxane) b) triethoxyoctylsilane

2. MATERIALS

The paper shows results of internal hydrophobized cement mortar. Four types of cement mortars were prepared. Reference mortar, which contains only three basic ingredients: cement, water and sand, and three type of cement mortar with organosilicon, hydrophobic admixture. Three different commercially available organosilicon admixture were used. Two of them are based on triethoxyoctylsilane and the third one on poly(dimethylsiloxane). The dosage of the first admixture named OTES A was 0.3%, the second named OTES B was 0.8% and the third one named PDMS was 3%. The amounts of used admixtures were in line with the manufacturers' recommendations and they were dosed per cement mass. All three silicon-based

admixtures are recommended for internal hydrophobization of cement-based materials. OTES B and PDMS types admixtures were added to the batch water before cement. The OTES A type was added just after mixing all basic ingredients. The specific cement mortar compositions are presented in Table 1 and represent amounts of ingredients required for one batch of mortar. Each type of mortar was prepared according to EN 196-1 [6]. The Portland Cement CEM I 42.5 R was used and the water to cement ratio (w/c) was equal to 0.5.

Table 1: Cement mortar composition

	Water repellent agent		
	OTES A	OTES B	PDMS
	0.3%	0.8%	3%
W/C	0.5		
Cement [g]	450		
Water [g]	1350		
Sand [g]	225		
Admixture [g]	1.35	3.60	13.50

3. METHODS

The air content in fresh mortar was determined by the pressure air measurement method according to EN 1015-7 [7] standard. A specially intended for aeration test air entrainment meter was used. A fresh mortar was placed in cylindrical container and compacted in four layers. Mechanical tests of compressive strength have been carried out on the prismatic samples with dimensions 40x40x80 mm (left after flexural strength test) after 28 days of curing according to EN 1015-11 [8] standard. The capillary water absorption test was carried out on six prismatic mortar samples (40x40x80 mm). After 28 days of curing, mortar beams were dried after constant mass were obtained. After removing from the dryer and reaching room temperature, the side walls of all the mortar beams were covered with sealant. After next 24 hours samples were vertically immersed in water to a depth of 1 cm. The weight of samples was examined after 10 min, 30 min, 60 min, 90 min, 2h, 3h, 4h and 24h. The capillary water absorption test was carried out according to the EN 1015-18 [9] standard. By mercury intrusion porosimetry (MIP) we investigated the pore structure of cement mortar. The MIP measurements were carried out with Micromeritics AutoPore IV9500 instrument. Cylindrical samples (6x6 mm) were cut out of the cement mortar. Then they were kept in isopropanol to until the constant mass was achieved and next, they were dried at 30^{o}C in a vacuum dryer. The heat of cement hydration with organosilicon admixtures was measured by isothermal calorimeter TAM Air. The test was carried out on cement pastes with water to cement ratio equal 0.5 and the Portland cement 42.5R was used. The dosage of hydrophobic admixture was the same as in cement mortar. The heat released during cement hydration was measured by 7 days, at temperature T=20°C. For each type of cement paste two samples were prepared.

4. RESULTS AND DISCUSSION

4.1 Air content

The measurement of air content in the fresh mortar showed significant differences between tested organosilicon admixture. The hydrophobic admixtures based on triethoxyoctylsilane do

not caused excessive air entrainment of cement mortar in contrast to poly(dimethylsiloxane), which causes a 2.5-fold increase in aeration of fresh cement mortar (Table 2). It can be safely assumed that this will affect the properties of the hardened mortar. We suppose that excessive air entrainment is caused by methyl groups detaching from the poly(dimethylsiloxane) during admixture – cement interactions and after attaching hydrogen atoms, as gaseous products, caused the increase in aeration.

Table 2: Aeration of fresh mortar

Type of mortar	Aeration
Reference sample	9.5 %
0.3% OTES A	10.5 %
0.8% OTES B	11.5 %
3% PDMS	25.0 %

4.2 Compressive strength

Fig. 2 shows the result of compressive strength test of cement mortar carried out after 28 days of curing. All three hydrophobic admixtures caused a noticeable decrease in mechanical strength. As we assumed the admixture based on PDMS caused the most significant decreased in compressive strength (over 50% according to reference mortar). The admixtures based on triethoxyoctylsilane: OTES A and OTES B decreased the compressive strength by 13% and 25% respectively. In case of PDMS it is probably the result of excessive air entrainment and the structure of poly(dimethylsiloxane) itself. PDMS is a macromolecular, polymeric, most likely spaces, branched structure, which can also hinder and delay cement hydration and thus affect the properties of the cement mortar. As it shown at Fig. 2 triethoxyoctylsilane also decreased compressive strength, but less than PDMS. In case of OTES based admixtures, we assume that the presence of long alkyl groups, such as octyl groups – C_8H_{17}, hinder the cement hydration. The method of adding the hydrophobic admixture into the mortar (with batch water or after mixing all components) might be also important. The obtained results indicate that the addition of admixture later to the fresh mortar mix might soften the influence of admixture on mechanical properties of cementitious materials.

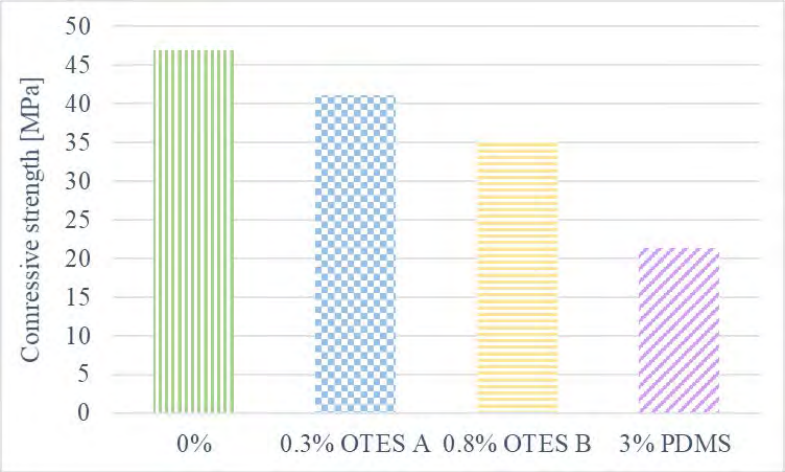

Figure 2: Compressive strength of cement mortar after 28 days of curing

4.3 Capillary water absorption

The capillary water absorption test is a good tool for confirmation of internal hydrophobization by means of organosilicon admixtures. Table 3 and Fig.3 demonstrate the results of capillary water absorption test of cement mortar. Results shown below represent the average value taken over six samples. The results of capillary water coefficient proved that each used in our research silicon-based admixture decreases capillary absorption of cement mortar. The results indicate that the better hydrophobic effect can be achieved by OTES based admixtures. The addition of 3% of PDMS based admixture provided similar capillary water coefficient as OTES A, but the coefficient was bigger and the amount of used admixture was 10 times more. The best hydrophobic effect provided OTES B admixture. The amount of 0.8% of admixture per cement mass caused the decrease of capillary water coefficient by 81% to reference sample. The obtained results clearly indicate that hydrophobic admixture based on silanes, when the reactions of polycondensation occurs during cement hydration, gives better hydrophobic effects. The type of alkyl sidechains is also important in internal hydrophobization. In case of triethoxyoctylsilane the presence of non-polar groups as octyl groups – C_8H_{17} results in better hydrophobization than the presence of methyl groups – CH_3 in poly(dimethylsiloxane). The differences between OTES A and OTES B result primarily from the method of entering the admixture to the fresh mix. The addition of OTES B admixture with batch water provides better integration into the structure of the hydrating cement.

Table 3: Capillary water coefficient

Type of mortar	Capillary water coefficient
Reference sample	0.143
0.3% OTES A	0.068
0.8% OTES B	0.027
3% PDMS	0.072

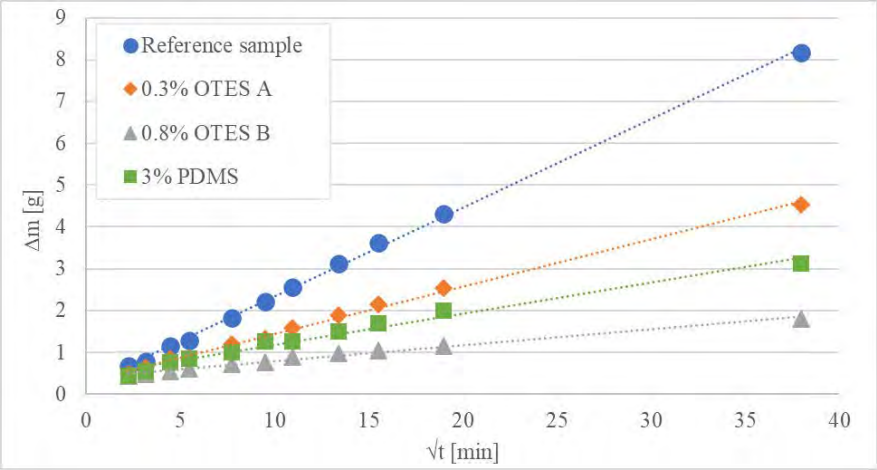

Figure 3: Mass changes of cement mortar during capillary water absorption test.

4.4 Mercury Intrusion Porosimetry

The mercury intrusion porosimetry is a good technique to show the differences in microstructure of cement mortar. Two samples of each type of cement mortar (with three

different organosilicon admixture and reference one) were used to determine the differences in mortar microstructure. The PDMS admixture affects the most on the microstructure of hardened cement mortar (Table 4, Fig. 4). At the Fig. 4 the significant increase in differential pore volume distribution for PDMS samples is noticeable. The highest increase in average pore volume, porosity and total pore area is also prominent for PDMS samples (Table 4). The increase in average pore diameter and porosity and neglectable decrease in total pore area is also visible for OTES based admixtures, but without increase in differential pore volume distribution (Fig. 4). We suspect that such significant changes in the microstructure in cement mortar with poly(dimethylsiloxane) is caused by the macromolecular, polymeric structure of the PDMS which leads to increase in pore diameter and porosity and thus leads to changes in mechanical properties of hardened mortar.

Table 4: Microstructure of cement mortar

Type of mortar	Average pore diameter [nm]	Porosity [%]	Total pore area [m^2/g]
Reference sample	22.1	14.8	12.6
0.3% OTES A	24.4	15.6	12.3
0.8% OTES B	28.8	17.8	12.1
3% PDMS	30.5	23.6	16.3

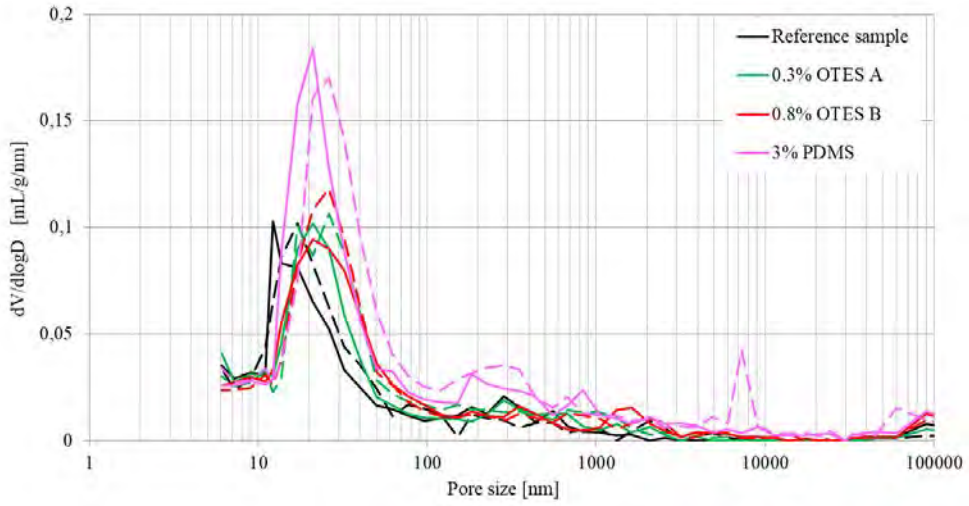

Figure 4: Pore size distribution in cement mortar

4.5 Heat of hydration

By isothermal calorimetry we were able to examined the impact of silicon-based admixtures on Portland cement hydration. As you can see in Table 5 and at Fig. 5 OTES B and PDMS admixtures decreased the heat of cement hydration. Only OTES A admixture did not affect significantly on the amount of released heat during Portland cement hydration. The lowest value of released heat is observed for PDMS admixture which is the most probably associated with the structure of poly(dimethylsiloxane), polymer one. It might hinder the interaction of water with cement phases and thus delay or even stop the cement hydration and thus decrease in mechanical properties of hardened cement mortar. Compared two admixtures based on the same

main compound: triethoxyoctylsilane, it can be concluded that long, non-polar alkyl group such the octyl group, may slow down the hydration if the hydrophobic admixture will be added with batch water.

Table 5: Heat of hydration after 41h

Type of mortar	Average heat of hydration after 41 h [J/g]
Reference sample	206.7
0.3% OTES A	203.9
0.8% OTES B	192.1
3% PDMS	185.1

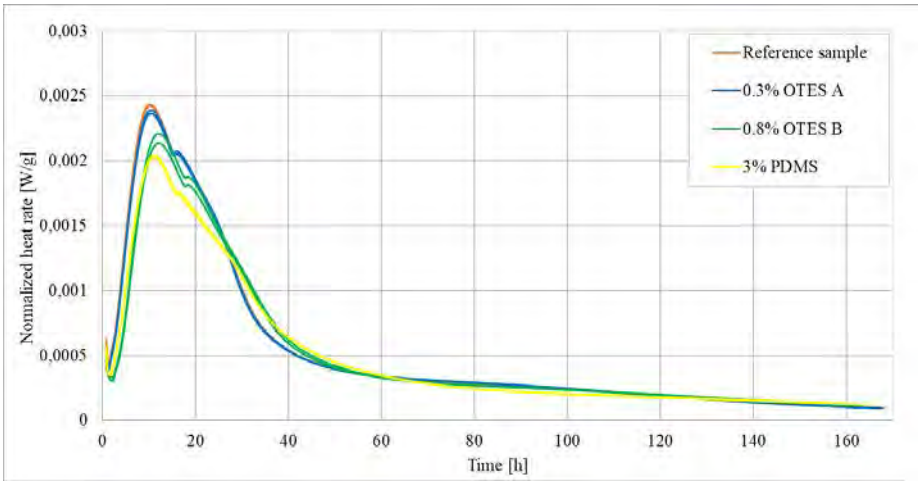

Figure 5: Normalized heat rate during cement hydration.

5. CONCLUSIONS

- The organosilicon admixtures provide effective internal hydrophobization of porous cementitious based materials such as cement mortar.
- The effectiveness of internal hydrophobization is influenced by the type of compound (silane or macromolecular polymer), the type of non-polar, alkyl substituent (octyl or methyl group) and the dosing method (with batch water or after mixing all components).
- Better hydrophobic effects, with less impact on the other properties, provide OTES admixtures. It suggests that if the reaction of polycondensation occurs during cement hydration it provides better internal hydrophobization.
- Due to the fact that the commercially available admixtures were tested it should be undertaken in recognition that the rest of admixture components could also have impact on the material properties.
- The internal hydrophobization by means of silicon-based compounds is a very good alternative to surface hydrophobization. It guarantees decrease in capillary water absorption in porous cement-based materials which lead to improving their durability, but it still has a few drawbacks to keep in mind.

REFERENCES

[1] Barnat-Hunek, D. 'Surface Free Energy as a Factor Affecting Hydrophobisation Effectiveness in Protection of Building Construction' (in Polish), Publishing House Lublin University of Technology, Lublin, Poland, 2016, 39-59.

[2] Ignerowicz, A. and Oleksik, M. 'Hydrophobic admixtures in the production of vibro-pressed products' (in Polish), *BTA*, **4**(2012), 74-76.

[3] Wendler, E., and von Plehwe-Leisen, E. 'Water Repellent Treatment of Porous Materials. A New Edition of the WTA Leaflet'. 5th International Conference on Water Repellent Treatment of Building Materials, Hydrophobe V, Freiburg: Aedificatio Publishers, 2008, 155-168.

[4] Roos, M., König, F., Stadtmüller, S. and Weyershausen B. 'Evolution of Silicone Based Water Repellents for Modern Building Protection'. 5th International Conference on Water Repellent Treatment of Building Materials, Hydrophobe V, Freiburg: Aedificatio Publishers, 2008, 3-16.

[5] Charola, A.E. 'Water Repellents and Other "Protective" Treatments: A Critical Review'. 3th International Conference on Water Repellent Treatment of Building Materials, Hydrophobe III, Aedificatio Publishers, 2001, 3-20.

[6] European Committee for Standardization. EN 196-1:2005 Methods of testing cement – Part 1: Determination of strength. CEN: Brussels, Belgium, 2005.

[7] European Committee for Standardization. EN 1015-7:1998 Methods of test for mortar for masonry – Part 7 : Determination of air content of fresh mortar. CEN: Brussels, Belgium, 1998.

[8] European Committee for Standardization. EN 1015-11:1999 Methods of test for mortar for masonry – Part 11: Determination of flexural and compressive strength of hardened mortar. CEN: Brussels, Belgium, 1999.

[9] European Committee for Standardization. EN 1015-18:2002 Methods of test for mortar for masonry – Part 18: Determination of water absorption coefficient due to capillary action of hardened mortar. CEN: Brussels, Belgium, 2002.

LIGHTWEIGHT AGGREGATE CONCRETE WITH FOAMED BINDER MATRIX FOR SUSTAINABLE APPLICATIONS

Sha Yang (1), Conrad Ballschmiede (1), Albrecht Gilka-Bötzow (1) and Eduardus A.B. Koenders (1)

(1) Institute of Construction and Building Materials, TU Darmstadt, Franziska-Braun-Straße 3, 64287 Darmstadt, Germany

Abstract

Low density load bearing structural concrete members with improved thermal insulation properties, composed of lightweight aggregate (LWA) and foam concrete is investigated, which expands the application range of lightweight structural materials. This study aims to characterize a lightweight aggregate concrete with a foamed cementitious matrix (LWAFC) through its physical properties (dry bulk density, thermal conductivity, compressive strength, and strain) and possible relationships especially linked to the densities. In the experimental studies, samples are prepared by two kinds of LWA with mineral foam with two differing cement mass contents. The resulting densities of the LWAFC in a dry state after 28 days ranged from 427 kg/m³ to 525 kg/m³. The results show that proper mineral foam content introduced into the LWA can greatly improve the thermal conductivity of the mixture. The compressive strength of the LWA used and the bond strength of the aggregate/cement foam in the interface region are important factors influencing the compressive strength of the LWAFC.
Keywords: Foam Concrete, Lightweight Aggregate, Insulation, Compressive Strength

1. INTRODUCTION

In order to reduce heating costs and thus lowering CO_2 emissions, the insulation of buildings is of high priority. To achieve an affordable and in terms of both recycling and construction requirements sensible insulant, a combination of construction and insulation material could be key to a long term solution. While due to its low strength, high tendency to shrinkage and very lightweight, pure mineral foam cannot be used as a construction material, lightweight aggregate concrete with a foamed matrix can be used [1]. Whenever combined with a stiff internal lightweight aggregate (LWA) based skeleton it might also have good insulation properties. This would allow for monolithic building techniques, which guarantee easy recycling and high fire safety [2].

Lightweight aggregates are widely used and can be easily incorporated into concrete or mortar to produce lightweight concrete with a wide range of densities [3][4]. Lightweight concrete (LWC) can be obtained by introducing gas or foam into the concrete cement paste, or by totally or partially replacing standard aggregate fractions with low weight components.

Combining the two materials to a lightweight aggregate foamed concrete (LWAFC) can give full advantage to both properties. Adopting cement foam with similar density to the LWA can make the material homogenous and will enhance the mechanical and building physics properties. For strength and strain, this means an even distribution throughout the concrete and

avoids discontinuities in the load transfer. This was also achieved by the backbone of the framework formed by the LWA, which was used as the basis for the mix designs. The density was kept low as this is favorable in general for construction materials. The lower the density, the lower the resulting mass, and therefore, easier transport of prefabricated components. There is also a clear correlation between low densities of construction materials and their corresponding heat transfer coefficient. Because one of the main goals is to achieve low heat transmission coefficients, a low density is of major importance (acc. with DIN EN 1520:2011).

In view of the various advantages mentioned above, in recent years there have been a large number of studies devoted to LWC and LWAFC. Current research mainly shows that the strength of LAC depends on the strength of the lightweight aggregate and the bond strength between the aggregate/cement paste, representing the interface area [6][7]. Furthermore, the interfacial strength of the LAC depends on the porosity of the LAs surface [8][9]. Ünal et al. found that there was a positive correlation between the thermal conductivity of LAC and the cement content [10]. Weighler and Karl produced LWAFC with a density and compressive strength in the range of 1200-1600 kg/m³ and 12-30 MPa, respectively [11]. Jummat et al. produced reinforced oil palm shell foamed concrete with a density of 1600 kg/m³ and compressive strength of about 20 MPa [12]. Hilal et al. compared the failure mechanism of foam concrete with/without LWA. They showed that LWA leads to an improved ductility of foam concrete [13]. Gilka-Bötzow et al. mentioned that the addition of foam will not only reduce the density, but also improve the thermal conductivity of open-structured lightweight aggregate concretes [14].

According to the above references, the reduction in density can improve the thermal insulation property of the material but adversely may affect the compressive strength as well. All studies have focused on materials with densities larger than 1000 kg/m³, however, materials with lower densities have not been studied. Therefore, the aim of this study was to develop a LWAFC with a target density just below 500 kg/m³ while maintaining a reasonable compressive strength and thermal conductivity. The mixtures were designed for two different cement contents and for two types of coarse aggregates. The cement content was varied because this is a practical way to achieve the target density of the foam (300 kg/m³) and slurry mix, while the different aggregates mainly differed in grain size and raw density. The cement content is also a controlling factor for the strength of the respective mix series which is, a major factor for the applicability of this construction material. In this study the concept of filling the voids between the LWA with lightweight foam concrete. The properties of LWA foamed concrete, including the compressive strength, stress-strain curves, and thermal conductivity were investigated.

2. MATERIALS AND METHODS

2.1 Raw materials

Materials used for this research included Portland cement (CEM I 42.5 R, Heidelberg Zement), hardening accelerator, a stabilizer on basis of melamine resin sulfonate, a shrinkage reducing agent based on a calcium-sulfo-aluminate for the cement paste. The foam was produced with a foaming agent made from hydrolyzed protein. As lightweight aggregate two kinds of expanded aggregate (2B and 2.9E from Liapor) were used, which have grain size range 4/10 and 2/6, respectively (see Figure 1). Fine aggregate (FA) in the form of expanded glass was added with two grain size ranges 0.25/0.5 and 0.5/1.0 (Poraver).

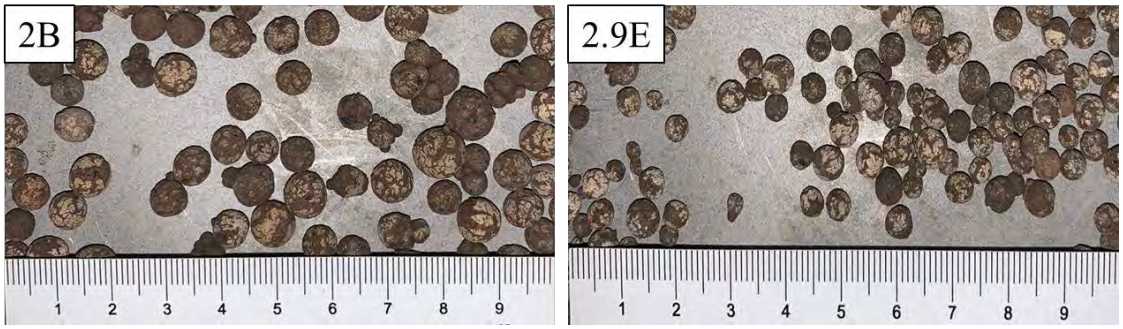

Figure 1: Lightweight aggregate 2B and 2.9E

2.2 Mix design

The mix design was calculated via volume ratios, depending on the pore space created by the coarse LWAs. In order to ensure good workability of fresh concrete, the water-to-binder-ratio (w/b) is determined to be 0.5. Based on the w/b, the volumetric percentage share for the sum of cement paste and foam was 74 % as a share of the created pore space volume (see Figure 2). The foam volume was oriented on the volume of cement and additives. Cement volume was calculated via known w/b and desired cement amount for 1 m³ of foamed concrete. The pre-foaming method was used to prepare the samples. The compositions of the different mix designs referring to the samples are listed in Table 1.

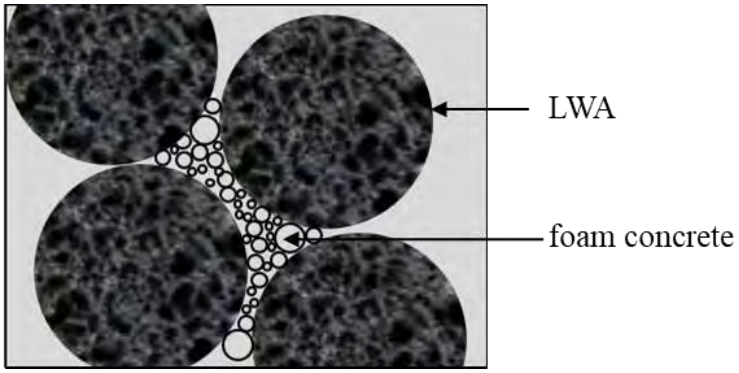

Figure 2: Concept of mix design

Table 1: Mix Design

	LWA	FA (0.25/0.5)	FA (0.5/1.0)	water	cement	foam	hardening accelerator	stabilizing agent	shrinkage reducer
2.9E200	290	35	25	100	200	12	2	2	4
2B200	225								
2.9E180	290	35	25	90	180	12.4	1.8	1.8	3.6
2B180	225								

Note: The unit of all values in the table is kg/m³.

2.3 Production procedure

The mixing sequence was as follows: Before starting any mixing procedure the aggregates (LWA and FA) were moistened to hinder them from destroying the foam or influencing the actual w/b ratio by absorbing water from the mix. The water and stabilizing agent were poured into a colloidal mixer and mixed at 20 Hz. Over the time of 120 s, the cement and solid additives were added and mixed for 60 s at 20 Hz and for another 90 s at 60 Hz. The cement slurry and fine aggregates were mixed thoroughly and the LWA was added and blended into the mortar. This ensures the wetting of the grains' surface area with slurry. The aqueous foam was produced to an aimed density using a foam generator. With a proportional mixer, the foam generator was adjusted to add 2.5 % foaming agent relative to the water. Compressed air flows into the fluid and the kinetic energy is converted to surface energy and subsequently produces foam. The mortar and foam were mixed until a homogenous mass was achieved. The prepared lightweight aggregate concrete with a foamed matrix was moulded and cured in the moulds for 14 days at 20 °C. After 14 days they were demoulded and wrapped in polyethylene foil and cured for another 14 days to obtain a total curing time of 28 days.

2.4 Experimental tests

The experimental program was designed to achieve a better understanding of the relation between compressive strength, density, cement proportion, and thermal conductivity. To be able to examine all the aforementioned parameters the testing program was comprised of compressive strength tests with additional directional recording, heat conductivity tests via transient plane heat source method in accordance with EN ISO 22007-2 and density measurements. The compressive strength tests were conducted with cubic samples with side lengths of 150 mm following the standards from EN 604. The loading rate was set as 20 N/s. The compressive strength tests were conducted for 3 samples per mixture to be able to approach the results statistically. The thermal conductivity tests were performed on samples with 150 mm side length and 80 mm height, which was conducted on a λ-Meter EP500e (guarded hot plate apparatus) in accordance with EN 12667.

3. RESULTS AND ANALYSIS

Figure 3 shows the stress-strain curves for the four mixtures and Figure 4 shows the damage of a sample from mix series 2.9E200 at each stage (A-D). Compared to ordinary concrete and foam concrete, it can be found that the stress-strain curve of LWAFC is closer to that of foam concrete. The curve for the compression process can be divided into four stages:

Stage I (O-A, strain approx. 0 % - 0.5 %): a slow increase in stress with the strain, which is caused by the homogeneous surface structure. The foam matrix on the sample surface is mostly composed of open pore (hemispheres). Therefore, the surface of the sample has a lower bearing capacity and is first crushed.

Stage II (A-B, strain approx. 0.5 % - 2.0 %): the strain continues to increase almost linear with the stress. Under the increased stress, the pores in the foam matrix are gradually compacted. The LW aggregates are displaced between layers, and the joint structure is then destroyed.

Stage III (B-C, strain approx. 2.0 % - 2.5 %): the strain increases oscillating with stress. In this stage, the stress reaches the maximum.

Stage IV (C-D, strain approx. > 2.5 %): the stress begins to decrease. The strain increases slightly until reaching a plateau.

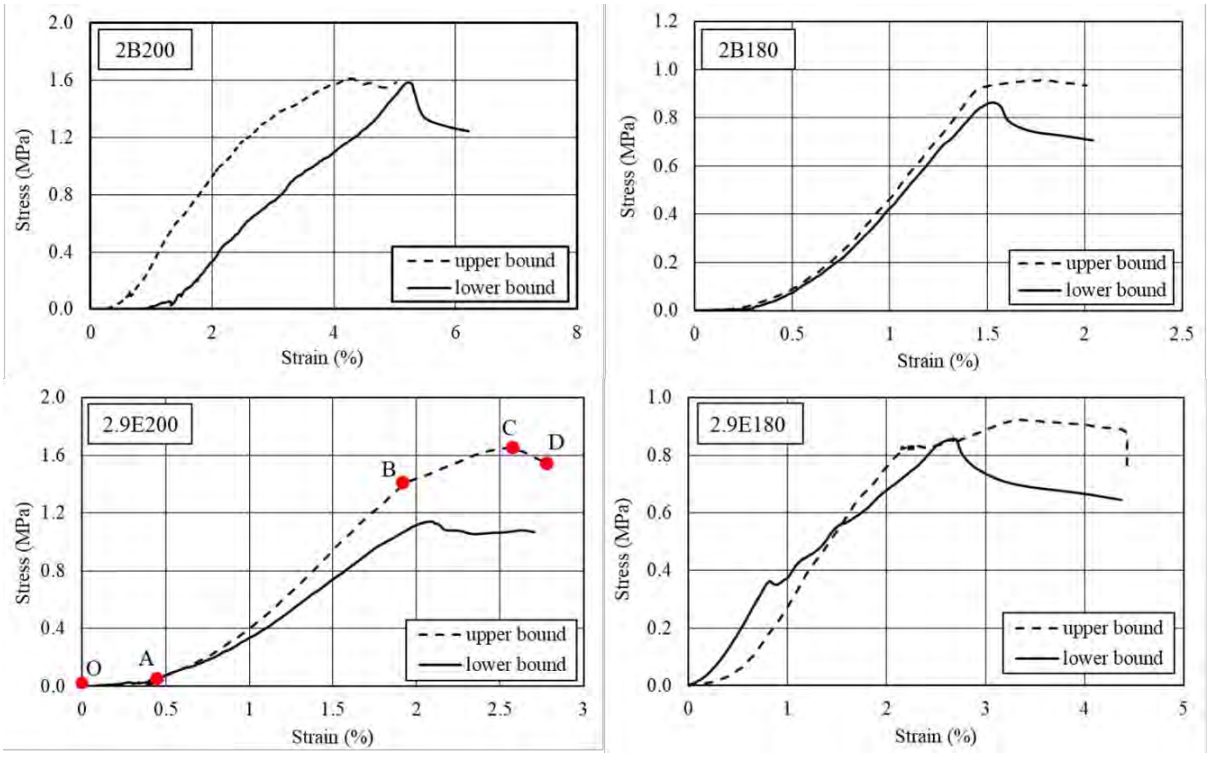

Figure 3: stress-strain curve of LWAFCs

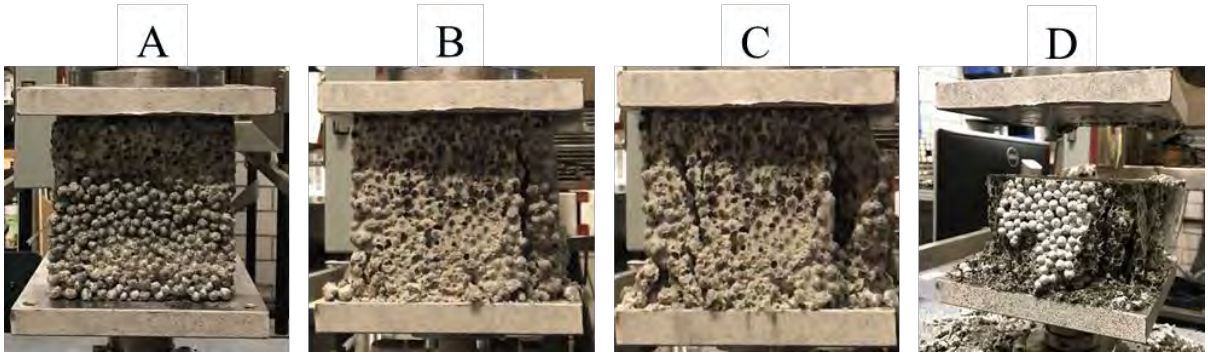

Figure 4: compression fracture mechanism procedure of 2.9E200

As can be seen from Figure 5, the dry bulk density of 2B200 and 2.9E200 is larger than 2B180 and 2.9E180, respectively, because the foam matrix of the former two contains more cement. In addition, the dry bulk density of 2B200 and 2B180 is lower than 2.9E200 and 2.9E180, respectively, which is due to the raw density of the given aggregates of 2B is lower at 420 kg/m³ than that of 2.9E with a raw density of 540 kg/m³.

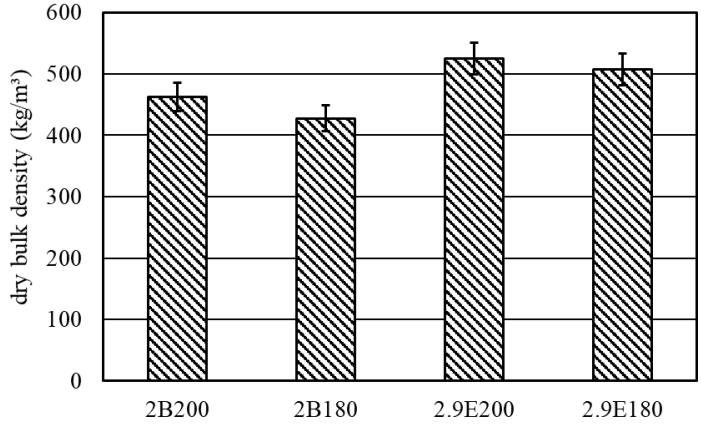

Figure 5: dry bulk density of LWAFCs

When comparing the compressive strength and thermal conductivity of the samples, the density of samples is normalized by the following equation, whereby the influence of the density is eliminated.

$$\sigma_i^* = \frac{\sigma_i}{\rho_a}\rho_i \quad (1)$$

In this equation, σ_i^* is the density-non-normalized compressive strength of sample i, ρ_i is the bulk dry density of sample i, and ρ_a is the average bulk dry density of all samples. Similarly, the same processing is performed on the thermal conductivity.

$$\lambda_i^* = \frac{\lambda_i}{\rho_a}\rho_i \quad (2)$$

where, λ_i^* is the density-non-normalized thermal conductivity of sample i.

From Figure 6, it can be seen that when the density is normalized, 2B200 and 2.9E200 have higher compressive strength, and the values of them are similar. The compressive strength of 2B180 is the lowest, however, it has the best thermal insulation property. In contrast, 2.9E200 and 2.9E180, which have a higher thermal conductivity. The comprehensive comparison of the thermal conductivity and the compressive strength 2B200 was superior to that of the other three.

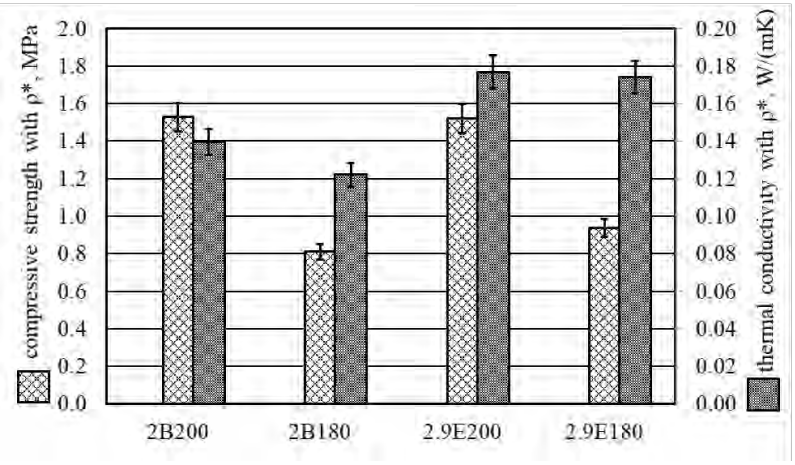

Figure 6: compressive strength and thermal conductivity of LWAFCs with the same density

Figure 7 shows the fracture surface of each sample after the compressive strength test. For samples 2B200 and 2.9E200, fractures occur in the LWA. However, for the samples 2B180 and 2.9E180 only a small amount of LWA cracked, which propagated along the weaker interfacial zone in the cement foam matrix. This is because the first two contain 200 kg/m³ cement, while the latter two contain 180 kg/m³ cement. The higher cement content means that the pore walls are firmer and pore structures are denser [14]. When a crack encounters LWAs, it is forced to propagate through them instead of extending around the aggregate-foam matrix interface.

By comparing the 2B200 and the 2.9E200, it can be found that there is more LWAs fracture in the 2B200. Since the interface toughness is lower than the LWAs, the larger the size of LWAs is, the more tortuous is the crack extension path, and the greater the energy is required to overcome the interfacial bonding. Therefore, for the sample containing lager aggregates (2B200), the compressive strength (1.53 MPa) is slightly higher than 2.9E200 (1.52 MPa). However, it is worth noting, that the 2.9E aggregate has a strength of 0.9 N/mm², while the 2B aggregate has strength only of 0.45 N/mm². When the fracture occurs, the strength of the aggregate plays a major role. Therefore, the difference in compressive strength between the two samples is not obvious.

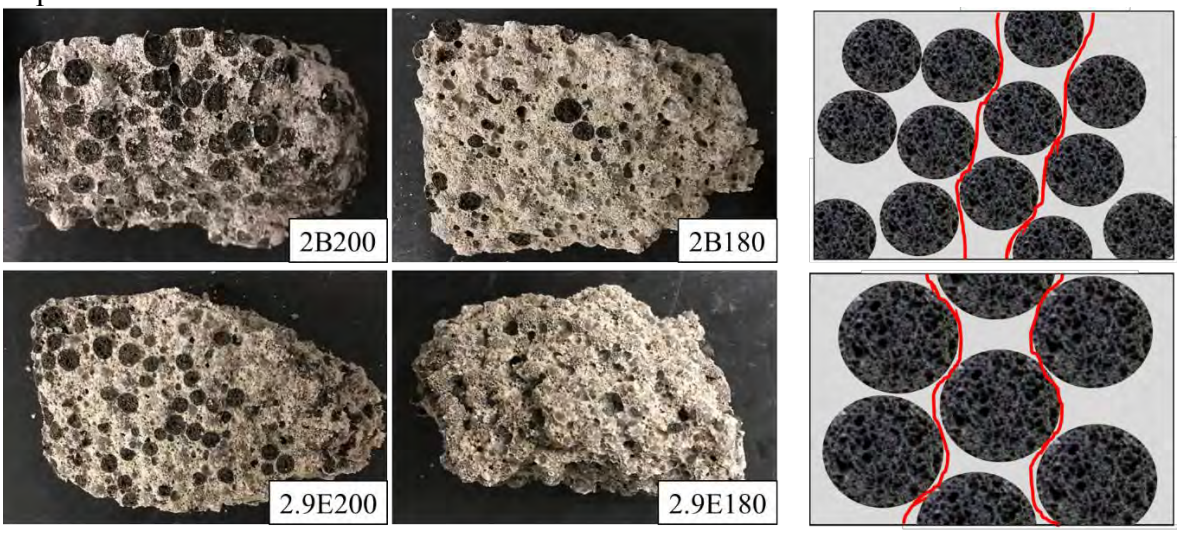

Figure 7: fracture section of LWAFCs

4. CONCLUSIONS

In this study, four different LWAFC mixes with two kinds of LWA were investigated. Their failure mechanism under compressive loading is evaluated and discussed in this study. The relationship between thermal conductivity and dry bulk density is determined. Based on the results and discussions, the following conclusions are drawn:

- Rather than the compressive strength of LWA, their size has a major role in the overall compressive strength of the tested mixtures;
- For higher cement contents, stronger bond strength of the interface developed. When the samples were subjected to compressive loading, cracks occurred mostly in the LWA;
- The higher the cement content of the mixtures, the stronger the bond strength between the interfaces.
- The LWAFC showed a good thermal insulation property with low thermal conductivity in the range of 0.13 W/(mK)-0.16 W/(mK).

5. OUTLOOK

In all the experimental process of this study, the temperature was kept constant (20°C) and the samples were dried for 28 days. However, it would be interesting to examine the weight in the range of temperatures (i.e. 10°C-60°C) and under various humidity conditions. The temperature could influence the thermal conductivity of samples and the stability of the pore structure in the foam matrix. The change in temperature also affects the moisture content in the pores. The optimal balance between these parameters will be the aim of new research in order to effectively improve the performance of the material. This would also mirror more practical orientated conditions and give better insight into actual application possibilities.

ACKNOWLEDGMENTS

The authors would like to thank and acknowledge the Federal Ministry for Economic Affairs and Energy for the project funding, and the contributions of the Laboratory of Institute for Construction and Building Materials, TU Darmstadt.

REFERENCES

[1] Gilka-Bötzow, A. 'Stabilität von ultraleichten Schaumbetonen: Betrachtung instationärer Porenstrukturen', Springer-Verlag, 2017.

[2] Go, Cheer-Germ, et al. 'Fire-resistance property of reinforced lightweight aggregate concrete wall'. *Constr Build Mater*. (30)(2012)725-733.

[3] Lo, Tommy Y., W. C. Tang, and H. Z. Cui. 'The effects of aggregate properties on lightweight concrete'. *Build Environ* **42**(8)(2007)3025-3029.

[4] Short A and Kinniburgh W. 'Lightweight concrete', *Cement Concr Res* **31**(9)(1978)1323-1325.

[5] Spratt, B.H. 'Introduction to lightweight concrete'. No. Monograph, 1980.

[6] Zhang, M.H. and Gjvorv, O.E. 'Mechanical properties of high-strength lightweight concrete'. *Mater Journal* **88**(3)(1991)240-247.

[7] Wang, P. T., Shah, S. P., and Naaman, A. E. 'Stress-strain curves of normal and lightweight concrete in compression'. *Proc* **75**(11)(1978)603-611.

[8] Haque, M. N., Khaiat, H. Al, and Kayali, O. 'Strength and durability of lightweight concrete'. *Cement Concrete Compo* **26**(4)(2004)307-314.

[9] Lo, T.Y., Tang, W. C., and Cui, H. Z. 'The effects of aggregate properties on lightweight concrete'. *Build Environ* **42**(8)(2007)3025-3029.

[10] Ünal, O., Tayfun, U., and Ahmet Y. 'Investigation of properties of low-strength lightweight concrete for thermal insulation'. *Build Environ* **42**(2)(2007)584-590.

[11] Weigler, H., and Karl, S. 'Structural lightweight aggregate concrete with reduced density—lightweight aggregate foamed concrete'. *Int J Cem Compos Lightweight Concr* **2**(2)(1980)101-104.

[12] Jumaat, M.Z., Alengaram, U.J. and Mahmud, H. 'Shear strength of oil palm shell foamed concrete beams'. *Mater Design* **30**(6)(2009)2227-2236.

[13] Hilal, A.A., Thom, N.H. and Dawson, A.R. 'Failure mechanism of foamed concrete made with/without additives and lightweight aggregate'. *J. Adv. Concr. Technol.* **14**(9)(2016)511-520.

[14] Gilka-Bötzow, A., Wetzel, M., Garrecht, H. 'Haufwerksporige leichtbetone (LAC 2) mit minimierter rohdichte', Concrete solutions 55. BetonTage, Neu-Ulm, Germany, 08-10 Februar 2011.

[15] Gilka-Bötzow, A., Yang, S. and Koenders, EAB. 'Ultralight mineral foams for sustainable insulation applications'. Fifth International Conference on Sustainable Construction Materials and Technologies, Kingston University, London, UK, 14-17 July 2019.

MECHANICAL AND CHLORIDE PERMEABILITY PROPERTIES OF COARSE FIBRE REINFORCED CONCRETE

Chenjia Zuo (1), Yixiang Zhang (1), Yudong Tong (1) and Yanbo Liu (1)

(1) College of Shipbuilding Engineering, Harbin Engineering University, China

Abstract

Synthetic fibers have been widely studied as reinforcing materials to increase the mechanical and durability properties of concrete. According to its diameter, fibers can be categorized as micro and macro (or coarse) fibers. As most research focuses on the mechanical properties of fiber reinforced concrete, its chloride permeability properties have been rarely studied. In this investigation, the compressive strength, flexural strength and chloride permeability of concrete with steel fibers (SF) and two types of coarse synthetic fibers, polypropylene (PP) fibers and polyvinyl alcohol (PVA) fibers were studied. It was found that steel fibers are able to improve both the compressive strength and the flexural strength of concrete. Addition of PP and PVA fibers could improve the flexible strength of concrete, with little effect on the compressive strength. Furthermore, test results show that addition of PP fibers slightly increases the chloride permeability of concrete while PVA fibers slightly reduce the chloride permeability.
Keywords: Coarse fibers; Mechanical properties; Chloride permeability; Flexural strength

1. INTRODUCTION

Concrete is the most widely used building material in the world. As concrete is strong in compression and weak is tension, various types of fibers have been added in concrete to improve its ductility properties. Studies have reported that proper addition of fibers are able to enhance the tensile strength, flexural strength, fatigue life, ductility and post-cracking performance of concrete.[1-5] Polyvinyl alcohol (PVA) is a low cost high performance fiber with hydrophilic characteristics which improves the bond between fiber and cementitious matrix. According to the geometrical structure, synthetic fibers can be divided into micro fibers and Macro (coarse) fibers. Compared with micro fibers, macro fibers have been found to enhance the post-cracking response of concrete, improve energy absorption capacity, and reduce the risk of cracking. As most research focuses on the mechanical properties of fiber reinforced concrete, [6-10] the effect of coarse fibers on the chloride permeability of concrete has been rarely studied.

In this investigation, concrete specimens with three types of coarse fibers (SF, PP and PVA) were prepared to study their effects on mechanical and chloride permeability properties of concrete. Compressive strength test and flexibility test (according to ASTM C1609 [11]) were

performed. Chloride permeability tests were performed using rapid chloride migration test (RCM test, NT Build 492 [12]) and electrical resistivity test (AASHTO T 358 [13]).

2. EXPERIMENTAL

2.1 Materials

Thirteen mixes were prepared in this investigation including specimens that contained only ordinary Portland cement (OPC) and specimens with steel, PP and PVA fibers, as shown in Fig.1. The physical and mechanical properties of the coarse fibers are listed in Table 1.

(a) steel fiber (b) PP fiber (c) PVA fiber

Figure 1：Appearance of different coarse fibers

Table1: Physical and mechanical properties of different coarse fibers

Coarse fibers	Density (g/cm^3)	Tensile Strength (MPa)	Elastic Modulus (GPa)	Length (mm)	Diameter (μm)
SF	7.8	1000.0	154.0	50.0	620.0
PP	0.9	530.0	7.1	50.0	910.0
PVA	1.3	254.0	15.9	30.0	646.4

The volume content ranges from 0.6% to 1.5% for steel fibers, 0.9% to 1.8% for PP fibers, and 0.6% to 1.5% for PVA fibers. P·O42.5 cement was used for all the mixes and the *w*/*cm* was 0.4. Additionally, 15% Class I fly ash, 40% Class S slag powder and 1% water reducer were added. Limestone with size ranging from 5 to 20 mm was used as coarse aggregate. River sand from the local Songhua River was used as fine aggregate. Details of the mixture designs are listed in Table 2.

Table 2: Mix properties of concrete.

Mix	Cement (kg/m^3)	Fly Ash (kg/m^3)	Slag (kg/m^3)	Fine agg (kg/m^3)	Coarse agg (kg/m^3)	Fibers		
						Type	Mass (kg/m^3)	Volume Content (%)
OPC	194.0	64.7	172.5	830.8	1015.4	-	-	-
SF6	194.0	64.7	172.5	830.8	1015.4	SF	46.8	0.6

SF9	194.0	64.7	172.5	830.8	1015.4	SF	70.2	0.9
SF12	194.0	64.7	172.5	830.8	1015.4	SF	93.6	1.2
SF15	194.0	64.7	172.5	830.8	1015.4	SF	117.0	1.5
PP9	194.0	64.7	172.5	830.8	1015.4	PP	8.2	0.9
PP12	194.0	64.7	172.5	830.8	1015.4	PP	10.9	1.2
PP15	194.0	64.7	172.5	830.8	1015.4	PP	13.7	1.5
PP18	194.0	64.7	172.5	830.8	1015.4	PP	16.4	1.8
PVA6	194.0	64.7	172.5	830.8	1015.4	PVA	7.8	0.6
PVA9	194.0	64.7	172.5	830.8	1015.4	PVA	11.7	0.9
PVA12	194.0	64.7	172.5	830.8	1015.4	PVA	15.6	1.2
PVA15	194.0	64.7	172.5	830.8	1015.4	PVA	19.5	1.5

2.2 Experimental Methods

In this investigation, prism (10 cm×10 cm×40cm) and cylinder (Φ10 cm×20 cm) specimens were prepared. Each mixture included 3 prism specimens and 12 cylinder specimens. The flexural test was performed on the prism specimens at 28 days age. Compressive test was perform on the cylinder specimens at 7, 14, and 28 days age and electrical resistivity measurements were performed on the cylinders specimens until 28 days age. The RCM test was performed at 28 days age using cylinder specimens.

As the large amount of mineral admixtures added in the concrete reduces the hydration rate, an elevated temperature curing regime was used to accelerate the curing rate of specimens. The specimens were demoulded 48 hours after casting and then immersed in 40°C saturated lime water for curing until the age of 28 days. A maturity method according to ASTM C1074 [14] was employed to calculate the equivalent age of specimens cured at 20°C. The calculated equivalent age is listed in Table 3. It is noted that the concrete age presented in this paper is the actual age but not the equivalent age.

Table 3: Equivalent Age

Curing age at 40°C	Equivalent age at 20°C
7d	49d
14d	99d
28d	197d

3. RESULTS AND DISCUSSION

3.1 Compressive strength

The evolution of compressive strength for various groups are presented in Fig.2. In each plot, the results of OPC specimens were included for comparison. In Fig. 2(a), it shows that addition of steel fibers can significantly increase the compressive strength of concrete, and specimens with 1.5% volume of steel fibers shows the highest compressive strength at 28 days age, which is in agreement with the results from previous researches (P.S. Song 2004). Fig. 2(b) shows that the effect of PP fibers on the compressive strength is almost negligible. Fig. 2(c) shows that addition of PVA fibers could significantly increase the compressive strength of concrete, but

this effect decreases with increasing the volume percentage of PVA fibers and becomes detrimental when the percentage reaches 1.5%.

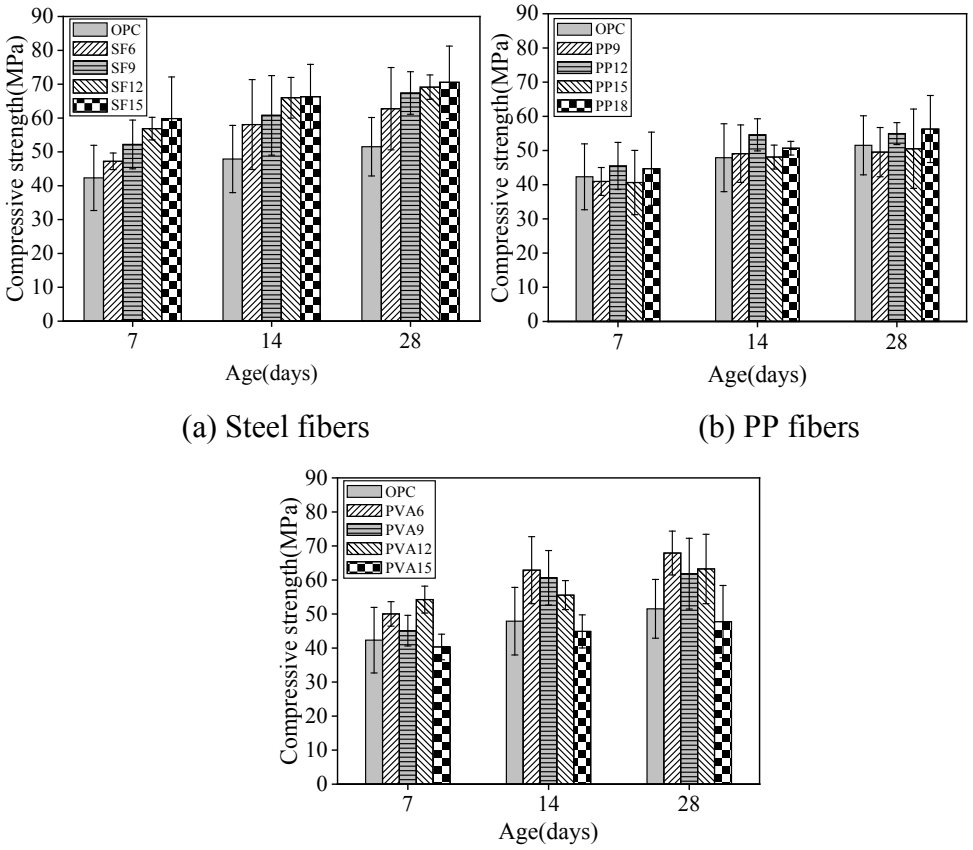

(a) Steel fibers (b) PP fibers

(c) PVA fibers

Figure 2：Compressive strength evolution of concrete

3.2 Flexural strength

The load deflection curves for all the mixtures at the age 28 days are shown in Fig. 3. It shows in Fig. 3(a) that for OPC specimens, they completely crack when deflection reaches about 0.05mm. For specimens with steel fibers, the peak load reaches at the deflection between 0.5 and 1mm. The residue strength of steel fiber reinforced concrete (SFRC) keeps relatively high and decreases as deflection increases. The load deflection curves for the PP and PVA fibers specimens are similar, as shown in Fig.3 (c) and (d). At the same volume percentage, the residual strength of PP fiber reinforced concrete is slightly higher than that of PVA fiber reinforced concrete, which is possibly attributed to the longer length and corrugated surface of PP fibers compared to PVA fibers, despite the hydrophilic characteristics of PVA fibers which could possible increase the bond between fibers and cementitious matrix.

Fig. 4 shows the flexural strength and toughness of the tested specimens. Fig. 4 (a) shows that steel fibers could significantly increase the flexural strength of concrete. At the same volume percentage, the flexural strength of PP and PVA fiber reinforced concrete are similar. However, the results also show that, at the volume percentage of 1.8%, the flexural strength of PVA fiber reinforced concrete is equivalent to that of 1.2% SFRC. Fig.4 (b) shows that in

general the toughness value increases with increasing the volume percentage of fibers. At the same volume percentage, the PP and PVA fiber reinforced concrete shows similar values of toughness.

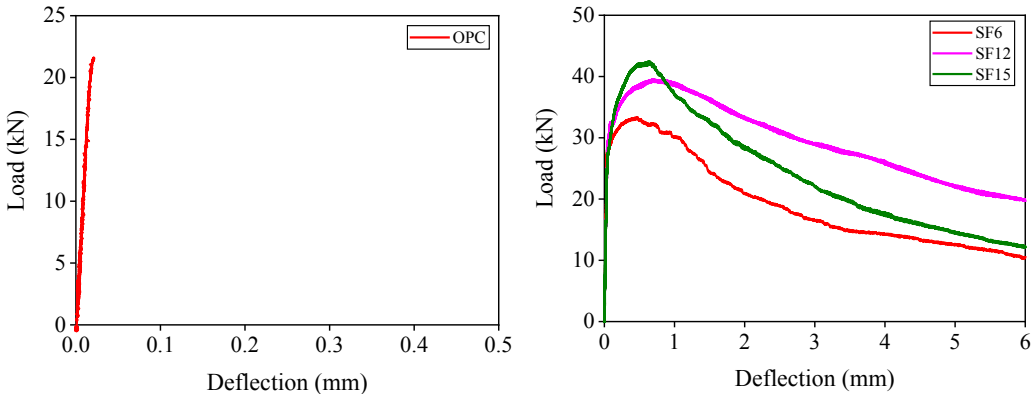

(a) OPC (b) Steel fibers

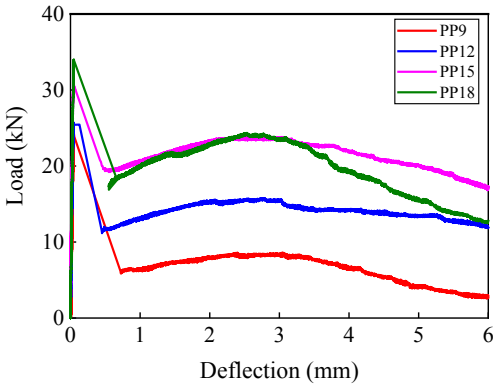

(c) PP fibers (d) PVA fibers

Figure 3：Load-deformation curves of different fiber concrete

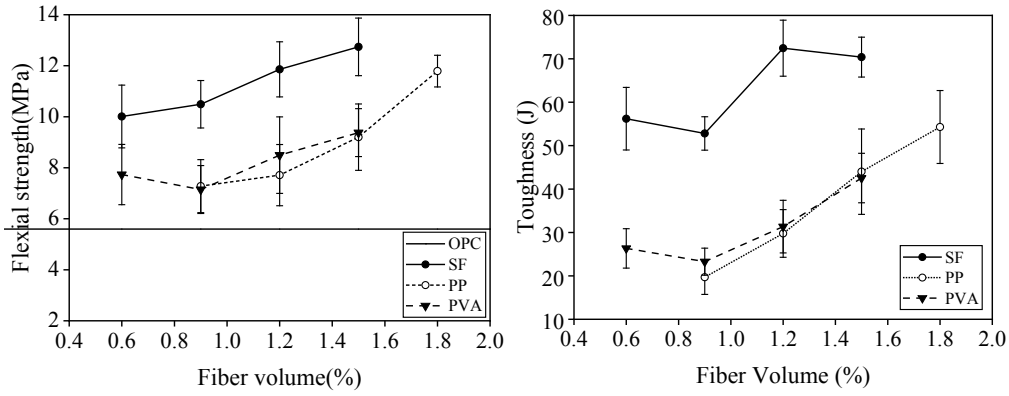

(a) (b)

Figure 4: Flexural strength (a) and toughness (b) at 28 days age.

3.3 Electrical resistivity and chloride migration coefficients

Fig. 5 shows the evolution of electrical resistivity on concrete with different fibers contents. The resistivity vs. content for the different series indicates that the resistivity evolution is significantly different on specimens with different fibers and contents. As can be seen in the figure, the resistivity of all specimens rises with curing age. The 28-day resistivity variation trend of all mixes in Fig. 6 show that the resistivity of SFRC is lower than that of concrete with PP fibers, both are lower than that of OPC and the resistivity of SFRC decreases with the increase of content. Unlike these two kinds of concrete, the resistivity of PVA fibers reinforced concrete rises with increasing content, and is generally higher than that of OPC. This substantial reduction in the resistivity is attributed to the electrical conductivity steel fibers and the hydration products of binding materials cannot completely make up the increased porosity which caused by fibers addition. However, the good affinity and binding property of PVA increase porosity, so resistivity rises along with increase of content.

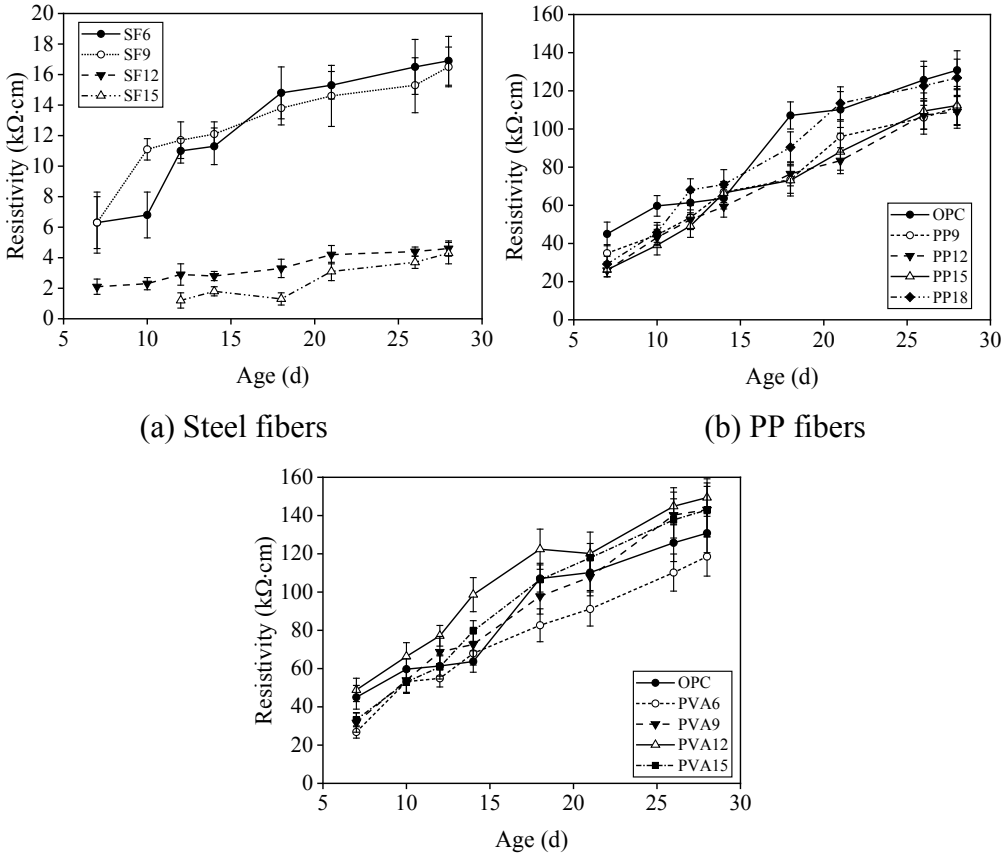

(a) Steel fibers (b) PP fibers

(c) PVA fibers

Figure 5：Resistivity evolution of different fiber concrete

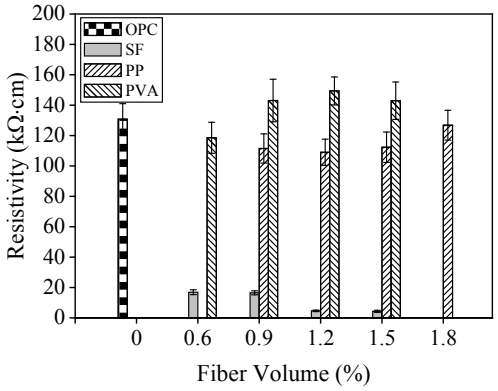

Figure 6：28 days resistivity of different fiber concrete

The 28-day chloride migration coefficients (D_{nssm}) of all mixes are presented in Fig. 7. It shows that D_{nssm} of SFRC is larger than that of OPC test group, and the specimens with 0.9% content are 159.14% higher than OPC test group. But D_{nssm} of the concrete with PP and PVA are similar to that of OPC test group. Compared with the OPC test group, the specimens with 0.9% PP content only increased by $0.2515\times10^{-12}m^2/s$, and the specimens with 0.6% PVA content decreased by $0.074\times10^{-12}m^2/s$.This is attributed to the increase of the weak layer between steel fiber and concrete matrix, which leads to the deterioration of pore structure and the decrease of concrete compactness, thus reducing the chloride penetration resistance. The hydration product of the binding material makes up for the influence of pore structure deterioration to some extent, so D_{nssm} of PP fibers reinforced concrete changes little. The affinity and binding property of PVA fibers make up for the deterioration of pore structure, and even improve the pore structure of concrete, so the chloride resistance permeability is enhanced.

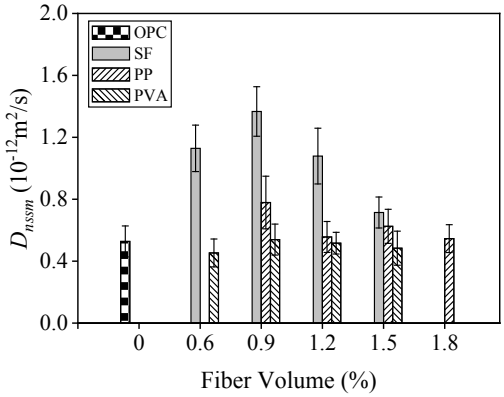

Figure 7: chloride migration coefficients of different fiber concrete

4. CONCLUSIONS

- The compressive strength of concrete is affected by the addition of coarse fibers and the order of improvement effect on compressive strength is steel fibers > PVA fibers > PP fibers.

- The addition of coarse fibers will improve the bending performance of concrete. The flexural strength, remained strength and toughness improve with the increase of fiber content.
- The addition of SF will greatly reduce the resistivity of concrete, while PP fibers and PVA fibers have little effect on it.
- D_{nssm} will increase as the addition of coarse fibers. SFRC has the worst impermeability, while there is no significant difference in impermeability between PP fibers concrete and PVA fibers concrete.

ACKNOWLEDGEMENTS

The authors acknowledge the financial support from Natural Science Foundation of Heilongjiang Province (No. LH2019E036).

REFERENCES

[1] Hamoush, S., Abu-Lebdeh, T., and Cummins, T., 'Deflection behavior of concrete beams reinforced with PVA micro-fibers'. *Construction & Building Materials*.**24**(11)(2010)2285-2293.

[2] Ladanchuk J.D., Nehdi M., 'Fiber Synergy in Fiber-Reinforced Self-Consolidating Concrete'. *ACI Materials Journal*. **101**(6) (2004) 508-517.

[3] Saad, S.A., Abdul, Aziz F.N.A., and Ali, M., 'Effect of Tropical Climate Condition to Compressive Strength and Microstructure Properties of High Performance Fiber Reinforced Concrete (HPFRC)'. *Advanced Materials Research*. 2015,1115: 182-187

[4] Roesler, J.R., Lange, D.A., Altoubat, S.A., et al., 'Fracture of Plain and Fiber-Reinforced Concrete Slabs under Monotonic Loading'. *Journal of Materials in Civil Engineering.* **16**(5) (2004) 452-460

[5] Lee, J.H., 'Influence of Concrete Strength Combined with Fiber Content in the Residual Flexural Strengths of Fiber Reinforced Concrete'. *Composite Structures*. 168(2017) 216-225.

[6] Frazao, C., Camoes, A., Barros, J, et al., 'Durability of steel fiber reinforced self-compacting concrete'. *Construction and Building Materials*. 80(2015) 155-166.

[7] Behfarnia, K., Behravan, A., 'Application of high performance polypropylene fibers in concrete lining of water tunnels'. *Materials & Design*. **55** (6) (2014) 274-279.

[8] Nili, M., Afroughsabet, V., 'Property assessment of steel-fibre reinforced concrete made with silica fume'. *Construction & Building Materials*. **28** (1) (2012) 664-669.

[9] Kakooei, S., Akil, H.M., Jamshidi, M., et al., 'The effects of polypropylene fibers on the properties of reinforced concrete structures'. *Construction & Building Materials*. **27**(1) (2012) 73-77.

[10] Nili, M., Afroughsabet, V., 'The long-term compressive strength and durability properties of silica fume fiber-reinforced concrete'. *Materials Science & Engineering A*. **531** (5) (2012) 107-111.

[11] ASTM C1609, Standard test method for flexural for flexural performance of fiber reinforced concrete (using beam with third-point loading). West Conshokocken: American Society for Testing and Materials, 2012, 9pages.

[12] NTBuild-492, Concrete. Mortar and Cement-Based Repair Materials: Chloride Migration Coefficient from Non-Steady-State Migration Experiments. 1999.

[13] AASHTO T358, Standard method of test for surface resistivity indication of concrete's ability to resist chloride ion penetration. American Association of State Highway and Transportation Officials (AASHTO), 2015, 10pages.

[14] ASTM C1074, Standard practice of estimating concrete strength by the maturity method. Philadelphia: American Society for Testing and Materials, 1998, 8pages.

MICROSTRUCTURAL STUDY OF A UHPFRC INCORPORATING ECAT

A. Abrishambaf (1), C. Costa (2), S. Nunes (3) and M. Pimentel (4)

(1)(3)(4) CONSTRUCT-LABEST, Faculty of Engineering (FEUP), University of Porto, Portugal

(2) High Institute of Engineering of Lisbon (ISEL), Lisbon Polytechnic Institute, Portugal

(1) aminab@fe.up.pt, (2) carla.costa@isel.pt, (3) snunes@fe.up.pt, (4) mjsp@fe.up.pt

Abstract

Ultra-high performance fibre reinforced cementitious composites (UHPFRC) is a family of advanced cementitious materials with optimized matrix packing density, very low water/binder ratio (w/b<0.2) and containing a significant amount of steel fibres. In the development of UHPFRC mixtures, the typically high amount of cement (700-1000 kg/m^3) and silica fume, SF, (as high as 20% of cement content) lead to high production costs and significant autogenous shrinkage deformation.

Spent equilibrium catalyst (ECat) is a by-product material generated by the oil refinery industry. ECat belongs to the aluminosilicate families (SiO_2+Al_2O_3>90%) with high pozzolanic activity similar to SF. The average particle diameter of the ECat is 91.65 μm and they possess a very high internal porosity with high water affinity. Previous results obtained on UHPFRC incorporating ECat showed that this material acts as an internal curing agent reducing the autogenous shrinkage.

This research focuses on the microstructural behaviour of a recently developed UHPFRC incorporating ECat. For this purpose, to quantitatively estimate the influence of ECat particles on the amount of hydration products, thermogravimetric analysis (TGA) was performed on specimens at different ages. Similarly, the influence of ECat particles on the pore structure of the newly developed mixture is also assessed by performing mercury intrusion porosimetry (MIP). The relation between the hydration products and the pore structure is analyzed.

Keywords: Ultra-high performance fibre reinforced cementitious composite, Microstructural behaviour, Thermogravimetric analysis, Mercury intrusion porosimetry, Spent equilibrium catalyst.

1. INTRODUCTION

Ultra-high performance fibre reinforced cementitious composites (UHPFRC) is a family of advanced cementitious materials with significant improvement in matrix packing density, containing a very low water/binder ratio (w/b<0.2), and including a significant amount of high-strength short steel fibres. This combination provides superior mechanical performance and durability [1-3]. In the development of UHPFRC mixtures, the typically high amount of cement (700-1000 kg/m^3) and silica fume, SF, (as high as 20% of cement content) lead to the development of significant shrinkage deformation, during the first days after casting. Unlike conventional concrete, a large part of shrinkage corresponds to the autogenous shrinkage [4].

Spent equilibrium catalyst (ECat) is a by-product generated by the oil refinery industry. ECat belongs to the aluminosilicate families (SiO_2+Al_2O_3>90%), composed of a faujasite-type zeolite (with a highly porous crystalline structure) incorporated in a matrix that contains mainly alumina and other amorphous aluminosilicates compounds. ECat shows high pozzolanic activity close to SF [5]. The average particles' diameter of the ECat is 91.65 μm, and they possess a very high internal porosity with high water affinity. Previous results obtained on UHPFRC incorporating ECat showed that ECat can act as an internal curing agent reducing the autogenous shrinkage [6].

This research focuses on the microstructural behaviour of a recently developed UHPFRC incorporating ECat. For this purpose, to quantitatively estimate the influence of ECat particles on the amount of hydration products, thermogravimetric analysis (TGA) was performed on specimens at different ages. Similarly, the influence of ECat particles on the pore structure of the newly developed mixture is also assessed by performing mercury intrusion porosimetry (MIP). The relation between the hydration products and the pore structure is analyzed.

2. EXPERIMENTAL PROGRAM

Materials and UHPC mixtures

In the preparation of the mixtures, cement CEM I 4.25 R, limestone filler (LF), spent equilibrium catalyst (ECat) and silica fume (SF) with a specific surface area of 437.5, c.a 500, 150070 and 19632 m^2/kg, respectively, were incorporated. Further material chemical and physical properties are presented elsewhere [6]. ECat is generated by Sines Refinery, Portugal, and shows 30% (by mass) of water absorption capacity at 24h on the saturated surface-dry basis. Figure 1 shows the ECat particle morphology and surface obtained by SEM in the secondary electron (SE) mode. A superplasticizer based on polycarboxylate ethers has been used to guarantee the required workability.

The mixture compositions are presented in Table 1. The microstructural analysis was performed on the paste phase of an UHPFRC mixture optimized elsewhere [6] (designated as Mix_Opt) in which ECat was used as an internal curing agent. Furthermore, to better understand the influence of ECat on the microstructural development and its interaction with other cementitious components, some more mixtures were prepared by removing each/both cementitious materials (SF and ECat) from the optimized mixture, as depicted in Table 1. The ECat water absorption was considered and added to the total water in the mixtures incorporating ECat.

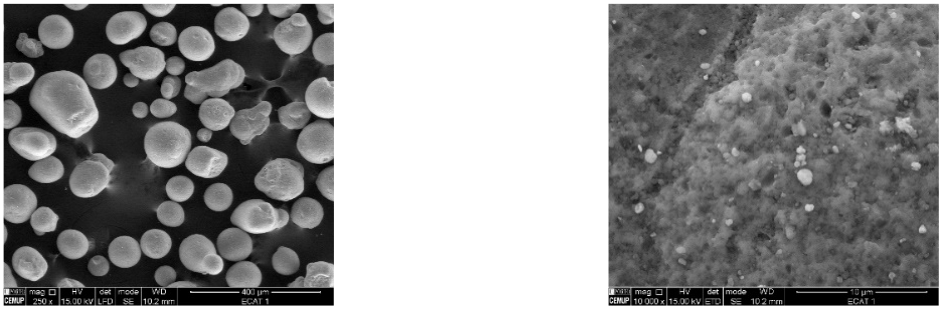

(a) (b)

Figure 1: SEM-SE images of ECat particles: (a) general view of particles morphology and b) particles surface (highly rough porous texture).

Table 1: Compositions of UHPC mixtures for microstructural analysis (kg/m^3).

Mixture	Cement	SF	ECat	LF	Water	SP
Mix_Opt	690.19	33.56	155.45	250.58	203.23(*)	19.48
Mix_woCM	690.19	---	---	250.58	156.60	19.48
Mix_ECat	690.19	---	155.45	250.58	203.23(*)	19.48
Mix_SF	690.19	33.56	---	250.58	156.60	19.48

(*) the absorption water of ECat is included (155.45 (Kg/m^3)× 0.3=46.63(Kg/m^3).

Specimens preparation

The mixing procedure (without the addition of sand) is presented elsewhere [6]. Small cylindrical specimens with a diameter of 8 mm and a height of 25 mm were cast. Microstructural analysis was performed at 1, 7, 28 and 91 days of hydration. After specimens water curing till the desired age, the following strategy was adopted to stop further hydration [7]: 1) specimens immersion inside 99.8% isopropanol alcohol for 7 days, 2) specimens drying inside an oven with 40°C for 48 hours, 3) further specimens drying inside a vacuum chamber for 24 hours.

Thermogravimetric analysis (TGA)

TGA was conducted on a SDT 2960 Simultaneous DSC-TGA (TA Instruments). At the day of testing, 50 mg of the dried specimen was ground to powder, and heated from the room temperature to 1000 °C with a heating rate of 10 °C/min in argon gas flow of 100 ml/min. Then, the decomposition of the hydration products was observed, and the free CH content in the samples was quantified, as discussed in [8]. For each mixture, two specimens were tested.

Mercury intrusion porosimetry (MIP)

The measurements were carried out on an Autopore IV 9h500 instrument (Micromeritics). The mercury intrusion pressure was increased in a stepwise manner from 0.5 to 33000 psi. The contact angle of 140° and surface tension of 485 mN/m were used in the Washburn equation to convert applied pressure to pore diameter. One specimen was tested for each mixture.

3. RESULTS AND DISCUSSION

Thermogravimetric analysis

Figure 2(a-d) shows the differential thermogravimetric (DTG) average curves for the different mixtures. The curves show three major peaks: the first peak (up to 400 °C) is associated to the dehydration of C-S-H, ettringite and AFm phases; the second peak (400°C - 500°C) corresponds to the dehydroxylation of calcium hydroxide (CH); and the third one (500°C - 800°C) is the decarbonation of calcium carbonate.

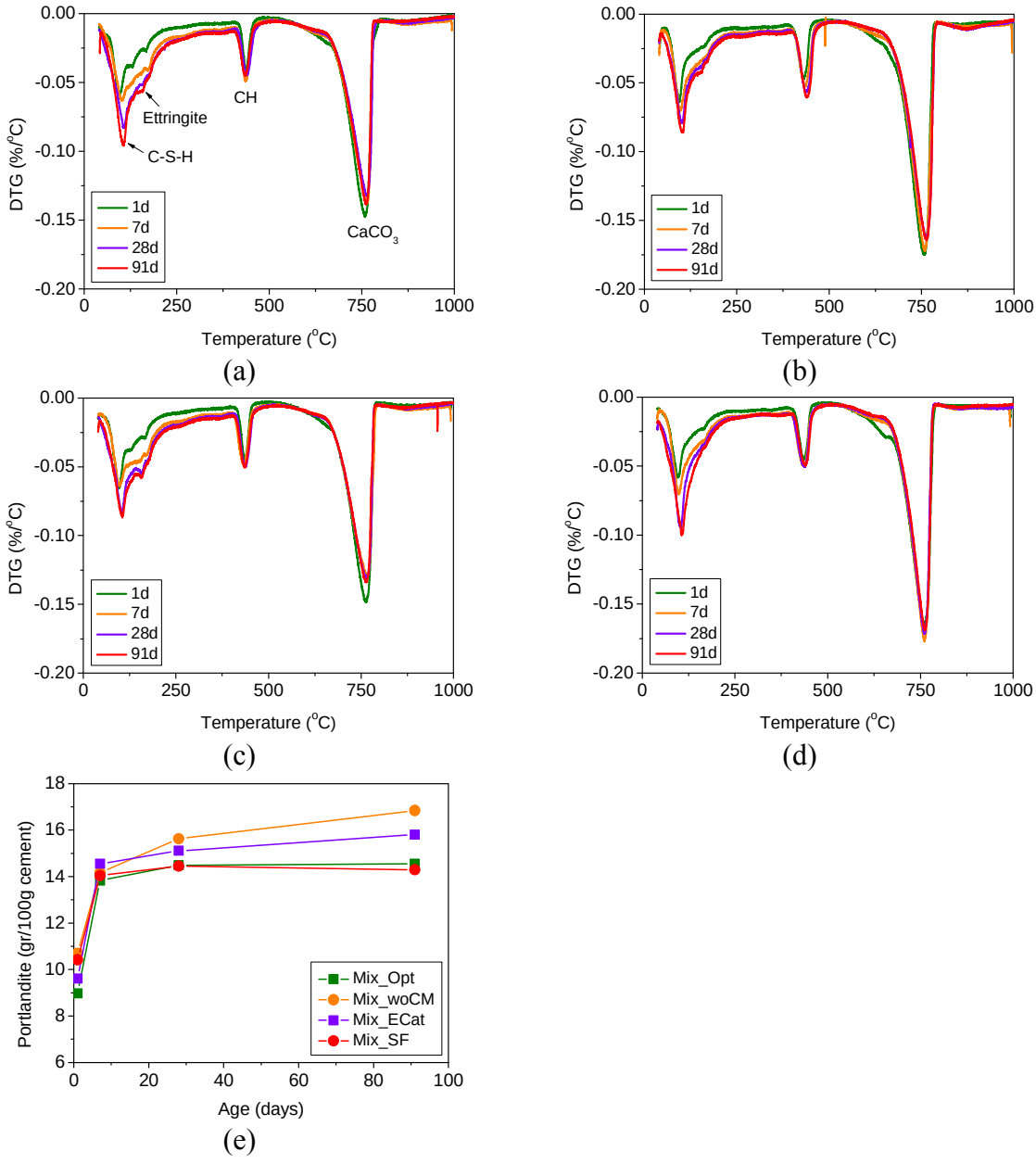

Figure 2: Differential thermal gravimetric curves, DTG, of: (a) Mix_Opt, (b) Mix_woCM, (c) Mix_ECat, (d) Mix_SF, and (e) evolution of calcium hydroxide content.

As seen in Figure 2, in general, the curves show a high peak of calcium carbonate since the mixtures containing a high volume of limestone filler. The first peak showed an increase by extending the curing time, for all mixtures. Figure 2(e) shows the evolution of portlandite in the mixtures normalized per gram of cement. After 1 day, the amount of the portlandite is highest in the mixture without the very reactive SCM (namely, SF and Ecat) and lowest for Mix_Opt. After one day, the amount of the portlandite is highest in the mixture without the very reactive SCM (namely, SFand ECat) and lowest for Mix_Opt. However, after 7 days, the content of CH stays approximately constant in all mixtures except for Mix_woCM which follows an upward trend. This means that CH starts to be gradually consumed by the pozzolanic reactions of SCMs (ECat, SF or both) to form C-S-H. Comparing Mix_ECat and Mix_SF in Figure 2(e), a higher content of CH was consumed by SF than by ECat to form C-S-H. From this assessment, it seems that SF is more pozzolanically reactive than ECat. However, the pozzolanic reactivity of ECat and SF was assessed using the modified Chapelle test method and did not reveal a significant difference between these two SCMs (1540 and 1577 mg of CH consumed per g of ECat and per g of SF) [6]. In Mix_Opt, by combining ECat and SF, a synergetic effect occurs which lead to a higher consumption of CH per gram of SCM during the pozzolanic reaction very similar to that verified in Mix_SF.

Pore structure measurement

Figure 3 shows the cumulative pore volume versus the pore diameter plots for the different mixtures. Figure 4 reveals the relation between the mixture's total porosity and critical pore diameter with age. The critical pore diameter is defined as the pore size where the steepest slope of the cumulative intrusion curve is recorded. In the other words, this can be determined as the pore diameter at the peak of dv/dlog(d) curve (the most probable pore diameter). As expected, the total porosity reduces by increasing the curing time for all mixtures (Figure 4(a)). Likewise, the critical pore diameter decreased gradually when the curing age was prolonged up to 91 days, see Figure 4(b). The highest total porosity was observed for Mix_ECat, followed by Mix_Opt, Mix_woCM and Mix_SF. Thus, mixtures containing ECat showed higher total porosities. However, mixtures with ECat exhibited lower critical pores diameters. For instance, for Mix_Opt, the most probable pore diameter at 91 days was only 0.012 μm. Although this mixture showed a high total porosity, it also showed the most refined pore structure. These results can be attributed to the porous microstructure of unhydrated ECat particles that can also contribute to increasing the total porosity. However, since these particles are not internally connected, it is expected that the transport properties of this mixture should not be affected. On the other hand, the mixture without SCMs showed the largest critical pore diameter value. After 7 days, no improvement was observed in the critical pore diameter of this mixture. Whereas, in the mixtures containing SCMs, the pore structure refined due to the combined filling and pozzolanic effect. This is compatible with the results obtained by TGA in which CH was gradually consumed by pozzolanic reactions to form C-S-H.

The measured pores can be classified into three classes [9]: gel pores of [0.004, 0.1] μm, microcapillary pores [0.1, 4.0] μm and capillary pores [4.0, 80.0] μm. Table 2 presents the pore volumes of each class of pores for the different mixtures. In general, a high percentage of the total porosity belongs to the C-S-H gel pores and only a few microcapillary and capillary pores were observed in all mixtures. This confirms the dense matrix of UHPCs which can lead to a significant improvement in the transport properties. Moreover, in general, although Mix_SF is the mixture that exhibited the lowest total pore volume, mixtures with ECat present denser

matrices since they have higher percentage of gel pores . Moreover, when the curing age was prolonged to 91 days, the microcapillary and capillary pores mainly increased for Mix_SF while for Mix_Opt the pores belonging to these categories remained approximately constant.

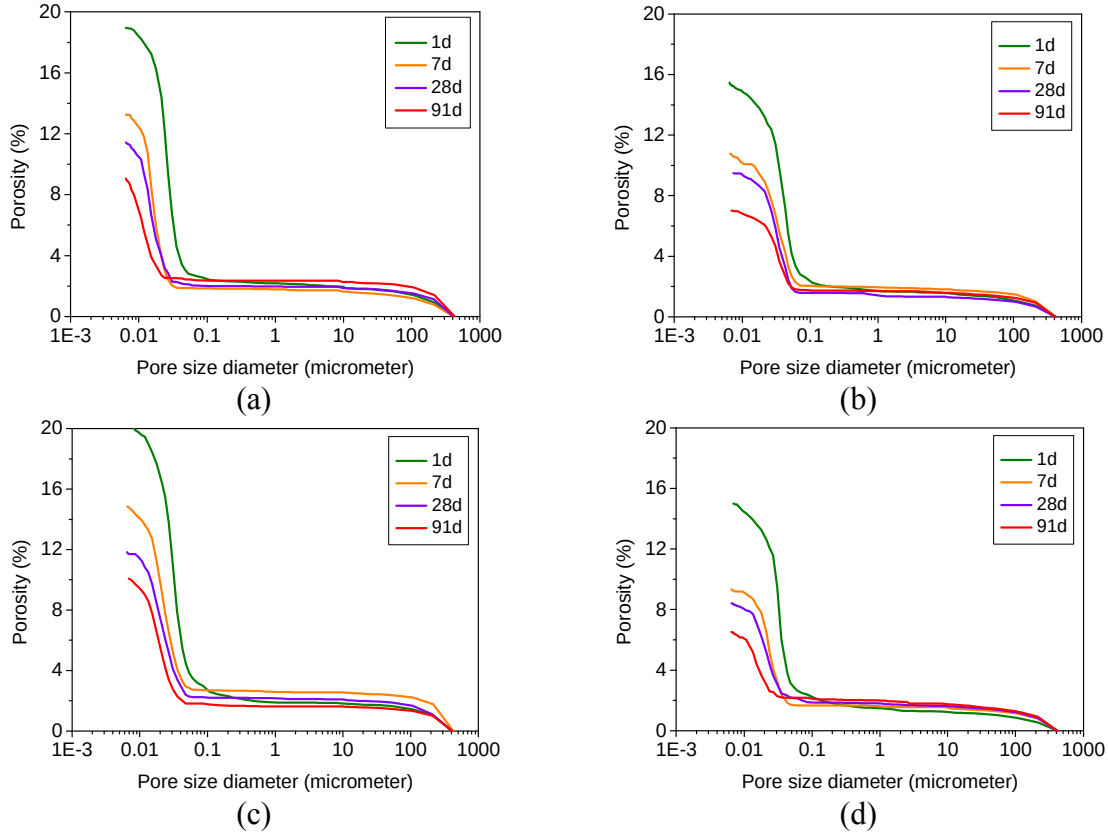

Figure 3: Cumulative pore volume (% of the bulk volume of the sample) for: (a) Mix_Opt, (b) Mix_woCM, (c) Mix_ECat, (d) Mix_SF.

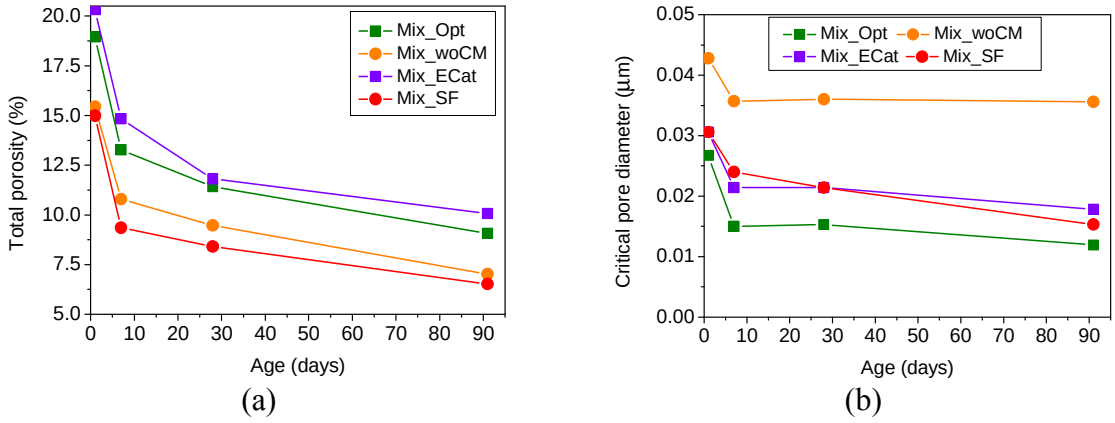

Figure 4: Relation between: (a) total porosity versus age and (b) critical pore diameter versus age.

Table 2: Pore volumes (%, of the bulk volume of the sample) of each pore class [9] for different mixtures.

	Pores' class and diameter (μm)		1 d	7 d	28 d	91 d
Mix_Opt	gel	[0.004, 0.1]	16.55	11.42	9.43	6.70
	microcapillary	[0.1, 4.0]	0.36	0.12	0.06	0.00
	capillary	[4.0, 80.0]	0.63	0.53	0.44	0.45
Mix_woCM	gel	[0.004, 0.1]	13.20	8.73	7.90	5.28
	microcapillary	[0.1, 4.0]	0.65	0.19	0.24	0.09
	capillary	[4.0, 80.0]	0.54	0.39	0.35	0.40
Mix_ECat	gel	[0.004, 0.1]	17.73	12.16	9.62	8.33
	microcapillary	[0.1, 4.0]	0.75	0.12	0.12	0.13
	capillary	[4.0, 80.0]	0.41	0.34	0.41	0.29
Mix_SF	gel	[0.004, 0.1]	12.82	7.67	6.57	4.43
	microcapillary	[0.1, 4.0]	0.89	0.11	0.17	0.31
	capillary	[4.0, 80.0]	0.44	0.44	0.46	0.53

3. CONCLUSIONS

The thermogravimetric analysis results revealed that the amount of portlandite increases for all mixtures at the early ages. After 7 days, the content of calcium hydroxide stays approximately constant for the mixtures containing SCMs, which means the CH was gradually consumed by pozzolanic reactions of SCMs. A higher content of CH was consumed by SF than ECat to form C-S-H, which means SF may present higher pozzolanic reactivity than ECat. However, the optimized mixture revealed a synergetic effect among both SCM with a consumption of CH per gram of pozzolan similar to that of Mix_SF.

The total porosity reduces by increasing the curing time for all mixtures. The highest total porosity was observed for Mix_ECat. In terms of critical pore diameter, Mix_woCM shows the highest value. In the mixtures containing SCMs, the pore structure is more refined due to the combined filling and pozzolanic effect. In particular, mixtures with ECat showed the most refined pore structure. Namely, with both SCM, Mix_Opt presented the smallest critical pore diameter in the range of gel pores. Therefore, the transport properties of this mixture should not be affected by the higher total porosity value.

Thus, besides the advantage of mitigating autogenous shrinkage [6], using ECat in UHPFRC contributes for the efficient re-use of this waste material, turning it into a value-added by-product and to a cleaner production of UHPFRC. Furthermore, ECat in UHPFRC composition may also contribute to improve, or at least do not impair, the durability performance. In this regard, more work is currently underway using other microstructural test methods and correlating with macroscopic properties for a better understanding of ECat role for the UHPFRC performance.

4. ACKNOWLEDGEMENTS

This work was financially supported by: Base Funding - UIDB/04708/2020 and Programmatic Funding - UIDP/04708/2020 of CONSTRUCT -Instituto de I&D em Estruturas

e Construções funded by national funds through the FCT/MCTES (PIDDAC); and by the project PTDC/ECI-EST/31777/2017 – "UHPGRADE - Next generation of ultra-high performance fibre-reinforced cement based composites for rehabilitation and strengthening of the existing infrastructure" funded by FEDER funds through COMPETE2020-Programa Operacional Competitividade e Internacionalização (POCI) and by national funds (PIDDAC) through FCT/MCTES. Collaboration and materials supply by PETROGAL/GALP Energia, Concremat, Secil, Omya Comital, Sika and Bekaert is gratefully acknowledged.

5. REFERENCES

[1] Abrishambaf, A., Pimentel, M., and Nunes, S. 'Influence of fibre orientation on the tensile behaviour of ultra-high performance fibre reinforced cementitious composites'. *Cem. Concr. Res.***97**(2017)28-40.

[2] Abrishambaf, A., Pimentel, M., and Nunes, S. 'A meso-mechanical model to simulate the tensile behaviour of ultra-high performance fibre-reinforced cementitious composites'. *Compos. Struct.***222**(2019)110911.

[3] Charron, J.P., Denarié, E., and Brühwiler, E. 'Permeability of ultra high performance fiber reinforced concretes (UHPFRC) under high stresses'. *Mater. Struct.***40**(2007)269–277.

[4] Fehling, E., Schmidt, M., Walraven, J., Leutbecher, T., and Frohlich, S. 'Ultra-High Performance Concrete UHPC: Fundamentals, Design, Examples'. Berlin, Germany: Wiley, 2014.

[5] Nunes, S., and Costa, C. 'Numerical optimization of self-compacting mortar mixture containing spent equilibrium catalyst from oil refinery'. *J. of Clean. Product.***158**(2017)109-121.

[6] Matos, A.M., Nunes, S., Costa, C., and Barroso-Aguir, J.L. 'Spent equilibrium catalyst as internal curing agent in UHPFRC'. *Cem. Concr. Compos.***104**(2019)103362.

[7] Huang, H., Kazemi-Kamyab, H., Sun, W., and Scrivener, K. 'Effect of cement substitution by limestone on the hydration and microstructural development of ultra-high performance concrete (UHPC)'. *Cem. Concr. Compos.***77**(2017)86-101.

[8] Scrivener, K., Snellings, R., and Lothenbach, B. 'A practical guide to microstructural analysis of cementitious materials'. Taylor & Francis Group, 2016.

[9] Scheydt, J.C., and Muller, H.S. 'Microstructure of Ultra High Performance Concrete (UHPC) and its impact on durability' in 3rd International Symposium on UHPC and Nanothechnology for High Performance Construction Materials, Kassel, Netherlands, 2012.

RESEARCH ON MECHANICAL PROPERTIES AND MICRO-MECHANISM OF GRAPHENE CEMENT-BASED COMPOSITES

Shengtian Zhai (1), Yunsheng Zhang (1)

(1) School of Material Science and Engineering, southeast University, Nanjing 211189, China

Abstract

Graphene cement-based composites have become a hot topic in current research because of its superior comprehensive performance. In this work, incorporation of different content of graphene in cement-based materials can significantly improve its compressive and flexural strength. Meanwhile hydration heat with different graphene content and times was studied by TAM Air, while porosity and pore size with different graphene content were studied by MIP. Indeed, micro-mechanism of graphene cement-based was studied by SEM. The results show that when graphene content is 2.00 wt%, its mechanical properties are the best, and compressive and flexural strength were increased by 29% and 35% respectively in 28 d compared with standard sample. Morever, not only the porosity in the sample is reduced, but also the pore size is refined. Meanwhile the strong nucleation effect of graphene promotes the hydration of cement, but does not change the type of hydration products. In addition, SEM images show that the content of graphene reaches the percolation threshold, the conductive network is formed in the sample, and the distance between graphene particles is closer, and the function improvement is more obvious.

Keywords: Graphene; Cement Based; Mechanical Property; Micro-mechanism

1. INTRODUCTION

To meet the urgent needs of social modernization, building materials should be endowed with multifunction[1, 2] . The new global standards of modern engineering technologies, is driving the development of ultrahigh performance multifunctional construction materials. Therefore, current research is focused on the multifunctional composite structural materials. In addition, as the population grows and environmental deterioration, we seem to face increasing complex environment. Thus, the composite structural materials should exhibit more functionality and intelligence satisfy the needs of human life in the future. The graphene dispersions are obtained through naphthalene water reducer, which is incorporated into cement based materials become a multifunctional and intelligent cement structure material. This composite can be better to satisfy the requirements of modern engineering. According to some research reports,

graphene can not only obviously improve the early compressive strength and pressure sensitivity of mortar [3,4], but also significant improve the electrical and piezoelectric properties of cement-based materials in a certain rang of content [5,6]. Graphene, as a structural material with many excellent properties, is suitable for improving the application of cement-based materials [7,8]. Therefore, in this study, by incorporating graphene with different content in cement-based materials, the mechanical properties, hydration heat, pore structure and micro-mechanism after mixing and curing are systematical studied by different effective testing methods.

2. MATERIALS AND METHODOLOGY

To prepare the different test samples, ordinary Portland cement Type P·Ⅱ52.5, fine dry sand, and the water/cement ratio is 0.45 and the plastic sand ratio is 1:3. The superplasticizer used in the experiments is a polycarboxylic acid type water reducing agent with water reduction of 40%. The chemical composition of the cement is shown in Table 1, while the properties of the graphene is shown in Table 2.

The samples were prepared in a mold to test the compressive and flexural strength. The mortar mixture was prepared in a similar way to the mixture used for mechanical testing. The mortar bars were 16 cm long with a cross-section area of 4×4 cm, whereas the mortar cubes were 10×10×10 cm. The samples were demolded 24 h, then they were cured in water at 20±2℃ for 28 d and allowed to dry for 24 h in ambient conditions prior to their measurements. The tests were performed using standard 3-point bending apparatus supplied by Controls Group, with constant loading on specimens of 100 N $_S$-1.

Mixing time of the mortar batch was 10 min and the molds were taken for 6 min using standard vibrating machine, the mortar bars were 16 cm long with a cross-section area of 4×4 cm. After the bars were demolded 24 h, the samples were cured in water at 20±2℃ for 28 d and allowed to dry for 24 h in ambient conditions. Then the samples were cut into cubes with size of 3 ~ 5 mm, and the cubes were dried for more than 3 d at 50℃ in a blast drying chamber prior to their measurements.

Table 1: Chemical composition of the cement (% wt.)

Composition	CaO	SiO_2	Al_2O_3	Fe_2O_3	MgO	SO_3	R_2O	P_2O_5	MnO	Free CaO
Cement	55.02	20.32	7.83	2.79	0.09	4.74	1.71	5.23	0.01	1.25

Table 2: Properties of the graphene

Specific surface area/ m^2g^{-1}	Thickness/nm	Particle size/μm	Carbon content/%	Powder conductivity/ Sm^{-1}
225.5	<5	7.06	>98.0	5352

3. RESULTS AND DISCUSSION

3.1 Mechanical performance of graphene cement composites

Table 3: Mechanical performance of graphene cement composites with different content for 28 d

No.	Graphene content/%	Compressive strength/MPa	Flexural strength/MPa	Increase of compressive strength/%	Increase of flexural strength%
GM0.00	0.00	55.0	7.8	-	-
GM0.05	0.05	59.7	8.5	9	9
GM0.50	0.50	65.5	8.8	19	13
GM1.00	1.00	69.2	9.7	26	24
GM2.00	2.00	71.0	10.5	29	35
GM4.00	4.00	61.1	9.5	11	22

Table 3 shows the compressive and flexural strength of graphene-cement composites with different graphene content, and these mortar bars were tested and cured for 28 d. On the one hand, from Table 3, it can be observed that the compressive strength of sample shows a first increase and then decrease tendency with the increase of graphene content. Meanwhile the result shows that the compressive strength of sample is 55.0MPa without graphene, which increase by 9% with 0.05 wt.% graphene. when the content of graphene is reach up to 0.5 wt.%, the compressive strength of sample increase to 65.5 MPa. When the content of graphene is 2.00 wt.%, and compressive strength of the sample reaches its maximum is 71 MPa. However, the content is reach up to 4 wt.%, the compressive strength reduced to 61.1 MPa. On the other hand, the result shows that the flexural strength of sample also shows a first increase and then decrease tendency with the increase of graphene content. The flexural strength is 7.8 MPa without graphene, and content is reach up to 2.00 wt.%, the strength is 10.5MPa. However, the flexural strength of sample is decreases when the content of graphene is 4 wt.%.

As we will now discuss, the compressive and flexural strength of mortar sample show an evident increasing trend by incorporation of graphene. But the strength shows a significant decrease trend when the content of graphene is 4.00 wt.%. In order to better understand the strengthening mechanism of graphene, we need to know some basic aspects of this reaction and relevant properties of graphene. Graphene is a two-dimensional carbon nanomaterial with very high strength, high Young 's modulus and a large specific area. And graphene interacts with various elements forming the vast elements C-S-H groups and alters the morphology of the hydration sites, promoting the growth of C-S-H gels along the graphene flakes. This process leads to an increase in the bond strength of cement based materials[9] . As we know that the degree of porosity is a key factor to determine the strength of cement based materials. Therefore, graphene particles can adsorb on the surface of cement hydration products and fine aggregates, the porosity in cement mortar is filled. It can be believed that this tendency is responsible for the poor dispersed of graphene particles, which is prone to agglomeration when the content of graphene beyond a certain range. Thus the result in this work demonstrated the optimum content of graphene is 2.00 wt.%. While the bonding performance of the interface have been greatly improved due to the template effect of graphene. Indeed, the toughness of sample has been significantly improved, and the flexural strength has been greatly increased. The above analysis and results

show that the graphene has a significantly improvement for the strength of cement based material within a certain range of content.

3.2 Hydration Heat of Graphene Cement Composites

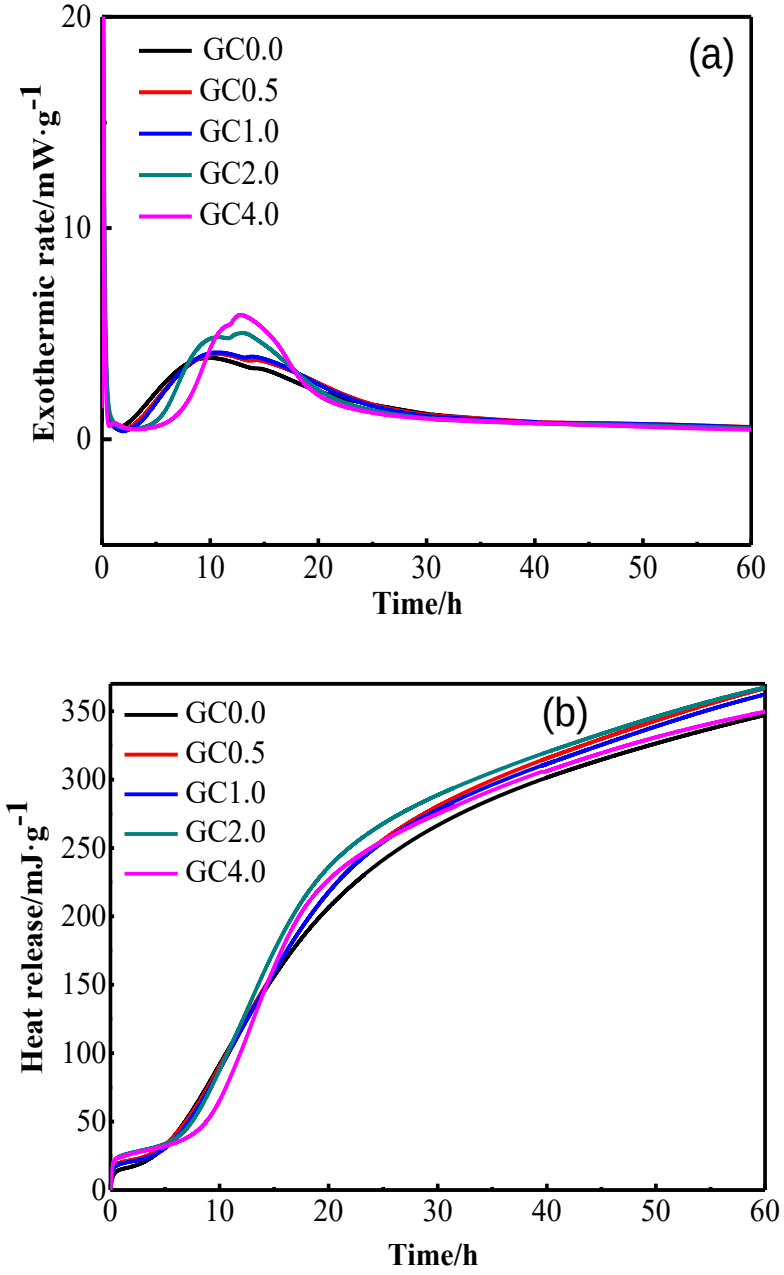

Figure 1: Hydration exothermic curves of graphene-cement composites with different graphene content

The exothermic rate of the sample is gradually increasing with the increase of graphene content. Meanwhile, the peak value is the largest when the content of graphene is 4.00 wt.%, and the content of 2.00 wt.% is lower. However, there is no obvious difference in hydration rate when the cement hydration entered stable stage as shown in Figure 1a). It can be see that this tendency is responsible for the nucleation effect of graphene, which increased contact area between cement and water when graphene particles adsorbed on the surface of cement. In addition, Figure 1b shows that

the total amount of cement hydration heat release first increased and then decreased with the increase of graphene content. The heat release of cement hydration is largest in content of graphene is 2.00 wt.%, but the 4.00 wt.% is lower compared with the other graphene content.

In conclusion, the reason for this result is graphene particles have agglomeration when the content exceeds a certain range. Meanwhile the process of cement hydration has been hindered, and the total amount of cement hydration heat release is also reduced. Moreover, this result is consistent with the results of compressive and flexural strength.

3.3 Pore structure of Graphene Cement Composites

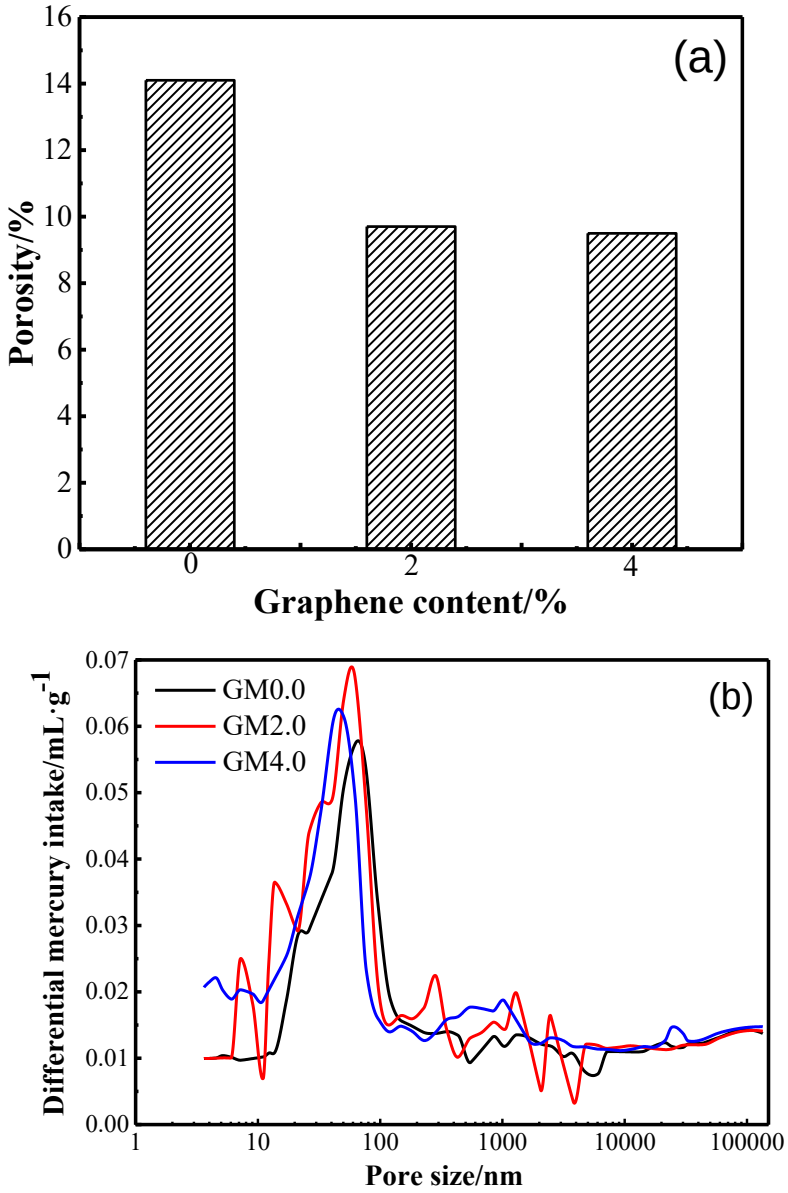

Figure 2: Pore structure of graphene-cement composites with different graphene content

The pore structure is a very important factor for mechanical properties of hardened cement mixture[10]. Therefore, we necessary to study the pore size and distribution in

the hardened mixture. As shown in Figure 2a and b, The porosity of hardened mixture is significantly reduced with the addition of graphene. when the content of graphene is 2.00 wt.%, and the porosity is decreased by 31% compared with standard sample. However, when the graphene content increases to 4.00 wt.%, the porosity is only decreased by 33%. The decreasing trend is not obvious by comparing the two kinds of graphene contents. Therefore, this result can be explained in following two ways, on the one hand, graphene particles are prone to agglomeration when the graphene content exceeds a certain range. While graphene particles are difficult to disperse uniformly, duo to the mass of graphene contained in the dispersion solution is limited. On the other hand, this result demonstrated the optimum content of graphene is about 2.00 wt.%.

To summarize, the small size pore increases first and then decrease, and the large size pore is basically the same. Therefore, this result illustrates that graphene particles are filled in the larger pores of cement paste to form plugging effect, and the number of small pores has increased within a certain range of graphene content. However, its effect on improving the pore structure in hardened paste is no longer obvious, when the graphene content beyond a certain range. In addition, the trend is consistent with that of strength.

3.4 SEM of Graphene Cement Composites

The above results indicate that graphene cement composite through reinforcement with graphene leads to cement based materials with basic mechanical properties, at the same time it extends the range of functionalities. In order to better understand the mechanism of graphene improving the functionality of graphene cement composites, we have measured the SEM of graphene and graphene cement composites with 1.00 wt.% graphene content. As we chose the graphene content is 1.00 wt.%, because it has the best functionality under this conditions.

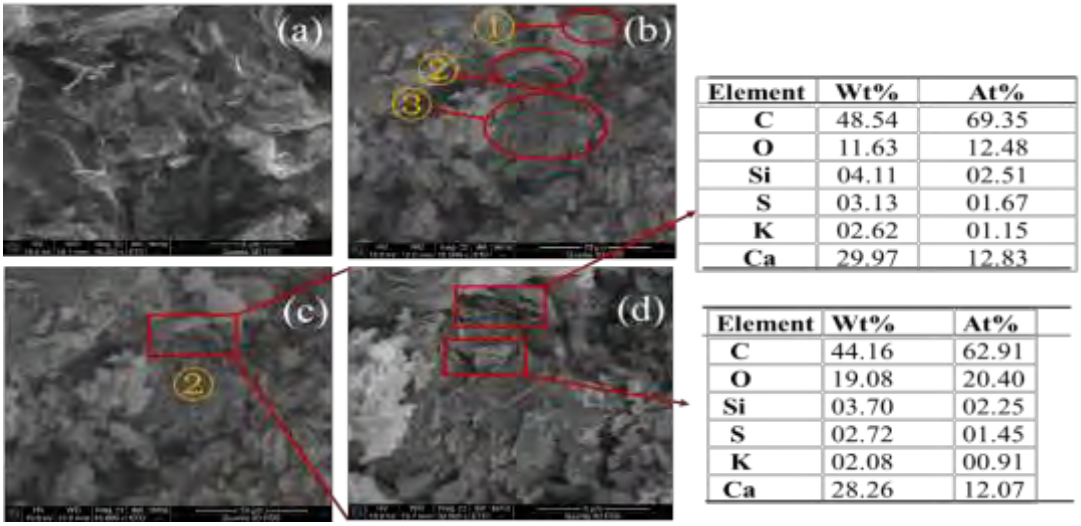

Element	Wt%	At%
C	48.54	69.35
O	11.63	12.48
Si	04.11	02.51
S	03.13	01.67
K	02.62	01.15
Ca	29.97	12.83

Element	Wt%	At%
C	44.16	62.91
O	19.08	20.40
Si	03.70	02.25
S	02.72	01.45
K	02.08	00.91
Ca	28.26	12.07

Figure 3: SEM images of graphene-cement composite with 1.00 wt.% graphene content

As shown in Figure 3 is the SEM of graphene and cement paste with 1.00 wt.% graphene. We can see that the conductive network is formed in the cement paste due to the interconnection of graphene particles. Therefore, the electrons in cement paste more

easily to migrate due to tunnel and contact effects[11, 12], which is the possible reason for the improvement of composites functionality. Meanwhile we believe that electron percolation occurs in the cement paste and reaches its percolation threshold, when the content of graphene is 1.00 wt.%. In addition, graphene significantly improves the thermal conductivity of cement paste sample, which is may be because graphene particles overlap with each other to form heat conduction channels in the cement paste. Graphene also significantly improves the electromagnetic shielding performance of cement paste. We believe that there are two main aspects of the enhancement mechanism. On the one hand, graphene has excellent conductivity, so it has strong dielectric loss ability to electromagnetic wave. Consequently, the dielectric loss performance of composites sample increases with the increase of graphene content.

Thus the electromagnetic shielding performance of composites sample to electromagnetic wave is enhanced. On the other hand, the two-dimensional stacking structure of graphene enlarges the reflective area of which to electromagnetic wave. Therefore, the single reflection loss of composites sample to electromagnetic wave is enhanced, and its shielding efficiency also increases.

4. CONCLUSIONS

Graphene can significantly improve the strength of cement based materials, wherein when graphene content is 2.00 wt%, its mechanical properties are the best. The compressive and flexural strength were increased by 29% and 35% respectively in 28 d. In addition, the network structure and dense internal structure are formed in cement based materials due to the nanoscale and two-dimensional morphological effects of graphene. Thus not only the porosity in the sample is reduced, but also the pore size is refined. Meanwhile the strong nucleation effect of graphene promotes the hydration of cement, but does not change the type of hydration products. Meanwhile, SEM images show that the content of graphene reaches the percolation threshold, the conductive network is formed in the sample, and the distance between graphene particles is closer, and the function improvement is more obvious.

REFERENCES

[1] D'ALESSANDRO A, PISELLO A L, SAMBUCO S, et al. Self-sensing and thermal energy experimental characterization of multifunctional cement-matrix composites with carbon nanoinclusions[M]//Goulbourne N C. Proceedings of SPIE. 2016.

[2] EXARCHOS D A, DALLA P T, TRAGAZIKIS I K, et al. Thermal and electrical behavior of nano-modified cement mortar[M]//Ecke W, Peters K J, Meyendorf N G, et al. Proceedings of SPIE. 2014.

[3] XU J, ZHANG D. Pressure-sensitive properties of emulsion modified graphene nanoplatelets/cement composites[J]. CEMENT & CONCRETE COMPOSITES, 2017,84:74-82.

[4] BIAN X, DING G, WANG Z, et al. Compression and strength behavior of cement-lime-polymer-solidified dredged material at high water content[J]. MARINE GEORESOURCES & GEOTECHNOLOGY, 2017,35(6):840-846.

[5] REHMAN S K U, IBRAHIM Z, MEMON S A, et al. A Sustainable Graphene Based Cement Composite[J]. SUSTAINABILITY, 2017,9(12297).

[6] HAN T, BELOBORODOV R, PERVUKHINA M, et al. Theoretical Modeling of Dielectric Properties of Artificial Shales[J]. GEOFLUIDS, 2018(UNSP 2973181).

[7] CUI X, SUN S, HAN B, et al. Mechanical, thermal and electromagnetic properties of nanographite platelets modified cementitious composites[J]. COMPOSITES PART A-APPLIED SCIENCE AND MANUFACTURING, 2017,93:49-58.
[8] SUN S, DING S, HAN B, et al. Multi-layer graphene-engineered cementitious composites with multifunctionality/intelligence[J]. COMPOSITES PART B-ENGINEERING, 2017,129:221-232.
[9] DIMOV D, AMIT I, GORRIE O, et al. Ultrahigh Performance Nanoengineered Graphene-Concrete Composites for Multifunctional Applications[J]. ADVANCED FUNCTIONAL MATERIALS, 2018,28(170518323).
[10] PANG B, ZHANG Y, LIU G. Study on the effect of waterborne epoxy resins on the performance and microstructure of cement paste[J]. CONSTRUCTION AND BUILDING MATERIALS, 2018,167:831-845.
[11] PAYAKANITI P, PINITSOONTORN S, THONGBAI P, et al. Electrical conductivity and compressive strength of carbon fiber reinforced fly ash geopolymeric composites[J]. CONSTRUCTION AND BUILDING MATERIALS, 2017,135:164-176.
[12] SASMAL S, RAVIVARMAN N, SINDU B S, et al. Electrical conductivity and piezo-resistive characteristics of CNT and CNF incorporated cementitious nanocomposites under static and dynamic loading[J]. COMPOSITES PART A-APPLIED SCIENCE AND MANUFACTURING, 2017,100:227-243.

3D PRINTING OF CEMENTITIOUS MATERIALS WITH SUPERABSORBENT POLYMERS: A DURABLE SOLUTION?

J. Van Der Putten (1)*, D. Snoeck (1), G. De Schutter (1) and K. Van Tittelboom (1)*

(1) Magnel Laboratory for Concrete Research, Ghent University, Tech Lane Ghent Science park, Campus A, Technologiepark-Zwijnaarde 60, 9052, Ghent, Belgium

* Corresponding author: Kim.VanTittelboom@UGent.be

Abstract

Nowadays, 3D printing of cementitious materials is a hot research topic in the construction industry. This construction method is capable of producing complex geometries and large-scale components without the use of expensive formwork. However, due to the lack of molding, more shrinkage will be induced and the amount of cracks will increase. As this phenomenon introduces ingress paths for chemical substances, it will affect the durability of the printed element in a negative way. One potential way to tackle this disadvantage is to include superabsorbent polymers (SAPs) in the cementitious material. As these polymers are able to absorb part of the mixing water and to release it during hardening, they induce internal curing and can mitigate self-desiccation and autogenous shrinkage. Another positive effect of using SAPs is the increased moisture content of the printed surface, enhancing the bond between two subsequent layers. For the aim of this research, two different SAPs were used to fabricate printed elements and the microstructural changes are correlated with their influence on durability and sustainability. First results showed that in general, the addition of superabsorbent polymers decreases the shrinkage in printed materials. They also reduce the nanoporosity in the range of 100 nm to 500 nm and increase the amount of voids with a diameter above 700 nm, resulting in less microcracks and a decreased amount of preferential ingress paths for chemical substances. On the other hand, the total air content increases with the addition of SAPs, proportional to the amount of SAPs added.

Keywords: 3D printing, hydrogels, shrinkage, microstructure

1. INTRODUCTION

3D printing is an innovative way of building with ‘traditional’ concrete. The utmost advantage of this technique – one of the main reasons that it exists, in fact – is the absence of costly formwork. This formwork usually requires a lot of manual labor, translated these days in a huge cost. The second main advantage is the freedom of form of the printed elements. The latter has a similar effect on the projects economy, as does the first: cost reduction [1, 2].

However, prior to revolution in the construction practice, there is a period of study and optimization. Concrete for printing needs to fulfill conflicting requirements. First, there is the

work- or printability that demands a good flow in the printer tubes and nozzle. This means that the material may not settle too fast in the reservoir and blocking in the tubing must be prevented. Second, an adequate buildability is necessary, requiring a material that is viscous enough. It should not set too fast in order to have a good bonding, and not too slow to obtain enough strength for support of the next layer. These demands do not solely depend on the cementitious characteristics but on the printing procedure as well. Time plays a leading role in this performance. Apart from the additional requirements set by the new technology, the concrete faces problems inherent to its mix design, indifferent to the procedure. Due to the lack of molding and the layered end result, shrinkage and void formation are the major issues that need to be counteracted. As both phenomena increase the risk for crack formation, they will affect the durability and mechanical performance of the printed element in a negative way.

In search of possible solutions, scientists have turned to superabsorbent polymers (SAPs) [3, 4]. As these polymers are able to absorb part of the mixing water and to release it during hardening, they induce internal curing and can mitigate self-desiccation and autogenous shrinkage. Another positive effect of using SAPs is the increased moisture content of the printed surface, enhancing the bond between two subsequent layers. In order to correlate the microstructural changes with their durable behavior, two types of SAPs with the same chemical composition but with slightly different size, were added to a reference mixture. The durability of the mixture was evaluated based on shrinkage measurements and correlated with the formation of voids and pores, measured with mercury intrusion porosimetry (MIP) and air void analysis.

2. MATERIALS AND METHODS

2.1. Materials and mix composition

The reference mixture contained an ordinary Portland Cement (CEM I 52.5 N Strong) combined with standard sand with a maximum particle size equal to 2 mm (0/2), water (W/C = 0.35) and a polycarboxylic ether (PCE) with a molecular weight of approximately 4000 g/mol and 35% solids to increase the flowability. An additional $(W/C)_a$ of 0.063 was added to the mixtures with SAPs, following the theory of Poders and Brownyard [5]. The amount of both superabsorbent polymers (type A and P) was obtained after evaluating the flow table test and equals respectively 0.17 and 0.15 mass% of cement weight. The composition of the mixtures with and without the addition of SAPs can be found in Table 1.

Table 1: Mix composition (with and without the addition of SAPs)

Mixture	CEM I 52.5N Strong [kg/m³]	Sand 0/2 [kg/m³]	Water [kg/m³]	SP [woc%]	SAP [moc%]
REF	620.5	1241	226.5	0.15	-
SAP A	620.5	1241	260.6	0.15	A = 0.17
SAP P	620.5	1241	260.6	0.15	P = 0.15

Both polymers have an irregular shape, are bulk-polymerized monovalent salt polyacrylate types and more detailed information can be found in Table 2 [3]. The below mentioned swelling times are measured in demineralised water and are the time needed for a SAP to reach maximal

saturation while being in a vortex. The absorption capacity was obtained through the filtration test after 24h in demineralized water [6].

Table 2: Specifications of the applied superabsorbent polymers (SAPs)

SAP	Type	Company	Size [µm]	Swelling time [sec]	Absorption Capacity [g/g]
A	Copolymer of acrylamide and sodium acrylate	BASF	100 ± 22	10	305 ± 4
P	Cross-linked potassium salt polyacrylate	Evonik Industries	190 ± 61	14	286 ± 1

2.2. 3D printing process

A custom-made apparatus was used to simulate an extrusion-based 3D printing process. The nozzle of the print equipment had an elliptical shape (28 mm x 18 mm) and was capable of printing layers with a maximum length of 300 mm. The height of the layers was manually adjustable. Within this research, two layered specimens were printed, where each layer height equaled 15 mm and the sample width was approximately 30 mm. The printing speed was kept constant at 1.7 cm/s. The effect of an increased interlayer time gap between the layers was not considered within the scope of this research.

2.3. Shrinkage

Shrinkage is one of the mayor obstacles for printed elements and as mentioned before, it will cause unwanted deformations. Especially when the deformations are restrained, for example after printing the second layer, shrinkage may lead to (tensile) stresses and cracking degrading the quality of the printed element. Due to the lack of moulding, mainly drying shrinkage plays an important role. As no standardised techniques are available for measuring the (early age) shrinkage of printed elements, new methods were devised.

An evaluation of the unrestrained shrinkage was based on six different measuring points, placed at the top of a printed layer directly after extrusion and positioning in between two cameras to measure the shrinkage in longitudinal direction. During the first 24h, the pictures were analysed with 20 images at a time every 5 minutes, with a digital mesh of 15 x 15 pixels applied to the surface of interest. The following 6 days, photographs were analysed at 30-minutes intervals, 30 images at a time and with the same pixel size implemented. The earliest photograph was taken as reference for all others, to which the mean technical strain ε_y [µm/mm] was calculated based on Eq. (1):

$$\varepsilon_y\,[\mu m/mm] = \left(\frac{\Delta l}{l_0}\right)_i \quad (1)$$

in which Δl [mm] equals the difference in length of the complete surface and l_0 [mm] is the initial length of the surface. Shrinkage measurements were performed for 168 hours in standardized circumstances (20±3°C, 60±5% RH) and the measurements were executed in triplicate for each mixture.

To exclude autogenous shrinkage from the overall shrinkage, corrugated tubes measurements were performed according to ASTM C1698. For these test, a polyethylene normative corrugated mould was filled and sealed afterwards. The tube was ensured to have an

end-to-end length of 420 mm. The exact initial length was measured manually and used to accurately obtain the lengths at later ages. Afterwards, the tube was placed in an automatic continuous measuring frame with digital dilatometers having a deformation range of 5 mm. Each mix design was observed in triplicate for 7 days, recording the movement every 10 minutes. The linear autogenous strain is obtained as follows (Eq. (2)).

$$\varepsilon_{auto}[\mu m/m] = \left(\frac{L(t) - L(t_{ref})}{L(t_{ref})}\right) \cdot 10^6\ \mu m/m \qquad (2)$$

in which L(t) [mm] is the length of solely the concrete element inside the mould at time t, t_{ref} [s] is the reference time at which the autogenous shrinkage is zeroed out and t [s] is the time instant. As in case of 3D printing, the first 24h are of highest importance, only these results are represented within this paper. Shrinkage graphs are zeroed out at the knee-point t_{kn} [s], which represents the final setting time and is measured by performing automated VICAT measurements for every mix composition.

2.4. Mercury Intrusion Porosimetry (MIP)

The occurrence of capillary pores, with a diameter between 10nm and 10µm, was studied based on Mercury Intrusion Porosimetry (MIP) measurements (PASCAL series 140 and 440, Thermo Fisher Scientific Inc.). For these measurements, cylinders with a diameter of 14 mm were drilled out of a double-layered filament (Figure 1(a)) and freeze-dried at an age of 28 days for 7 days after being put in liquid nitrogen. Afterwards, these cylinders were cut into three equal parts to make a distinction between the porosity of the upper, lower and interlayer zone (Figure 1(b)).

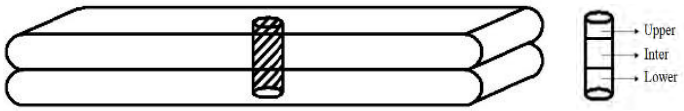

(a) (b)

Figure 1 : (a) Cylindrical specimens (Ø = 14 mm), drilled out a double-layered specimen and (b) indication of the different zones investigated during MIP measurements

2.5. Air void analysis

The air content of hardened double-layered specimens was analysed according to the linear traverse method as described by ASTM C457 by means of a fully automated concrete Experts International RapidAir 457 device. The printed specimens were longitudinally sawn in half (Figure 2) at an age of 28 days and both sides were polished with variable grading. After polishing, the samples were dried for one hour at 35°C and treated with black ink and barium sulphate ($BaSO_4$) to increase the contrast between the air voids and the cement matrix. After scanning the complete surface, the RapidAir 457 device provides the air content A [vol%] based on the number of voids intersected during the scanning procedure T_a [mm] divided by the total chord length T_{tot} [mm] which is according to ASTM C457 equal to 2413mm.

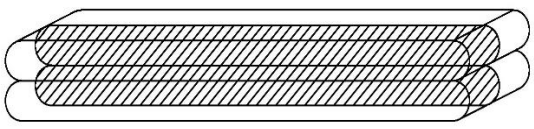

Figure 2: Longitudinal specimens used for air void analysis

3. RESULTS

3.1. Shrinkage

Figure 3 and Figure 4 represent, respectively, the autogenous shrinkage and unprotected shrinkage of the mixtures with and without superabsorbent polymers. Both graphs depict the same trend: in case of a reference mixture shrinkage starts immediately after final setting, while mixtures including SAPs show at first instance a swelling behaviour for approximately 24h. The expansive character of SAP addition is ascribed to the combination of their water mitigation capacity and a chemical swelling present in all mixtures. However, in case of the reference mixture this chemical swelling is not enough to overcome the omnipresent capillary tension. After final setting, the chemical-structural swelling can occur due to the relatively late formation and growth of calcium hydroxide. This will create a crystallisation pressure that counteracts the capillary pore water tension that induces self-desiccation. In case of samples with SAPs, the solid matrix is believed to be more elastic as there is still water supplied to unhydrated cement particles and as such the structuration continues more actively compared to the reference material. Also, the fresh CSH rims that are formed around these unhydrated particles surrounded by water, are larger in volume then their unhydrated counterparts [7].

Once hydration slows down as it reaches its optimum, all mixtures can only shrink under endured evaporation. Comparing the different SAPs, one can also conclude that the swelling behaviour of SAP A lasts longer compared to SAP P and this behaviour can be attributed to the more gradual release of entrapped water while SAP P will release the stored water more quickly [3].

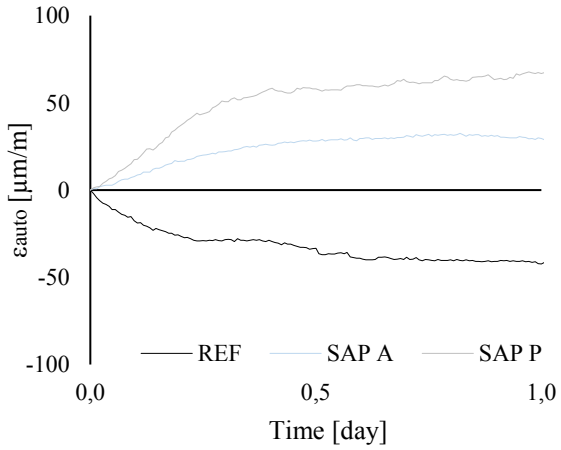

Figure 3: Autogenous shrinkage zeroed out at t_{kn}

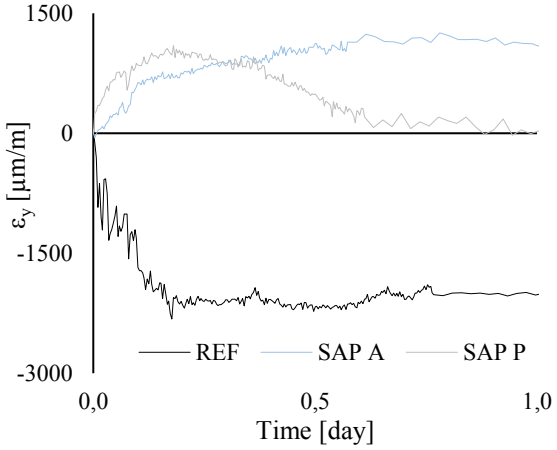

Figure 4: Unprotected shrinkage zeroed out at t_{kn}

3.2. Pore size and pore size distribution

Mercury intrusion porosimetry measurements led to the findings in Table 3 and Figure 4. In general, mixtures with SAPs tend to increase the total nanoporosity in all the layers of the hardened specimens. This confirms with the conclusion stated by Baroghel-Bouny [7]: when the (total) w/c ratio decreases, the nanoporosity decreases as well. This is associated to the denser matrix that results from a reduction in total amount of mixing water.

No conclusive statement can be made about which zone (i.e. upper, inter or lower) has the largest nanoporosity, however there is a clear difference in continuous pore network as

suggested by the distinct variations in derivative intrusion curves (Figure 4). From the median diameters, it is concluded that in general, the bottom layer has the network with the smallest continuous pore diameter. This is ascribed to the densification under additional hydrostatic pressure, exerted by the top layer.

In general, SAPs tend to reduce the amount of nanopores in the range of 100 nm to 500 nm and increase the amount of voids with a diameter above 700 nm. This is ascribed to a better hydration rate around the SAPs, closing up the smaller pores, as well as to their autogenous shrinkage mitigation that reduces the amount of micro cracking [3]. This phenomenon will reduce the amount of ingress paths for chemical substances and result in a more durable material behaviour compared to the reference mix composition.

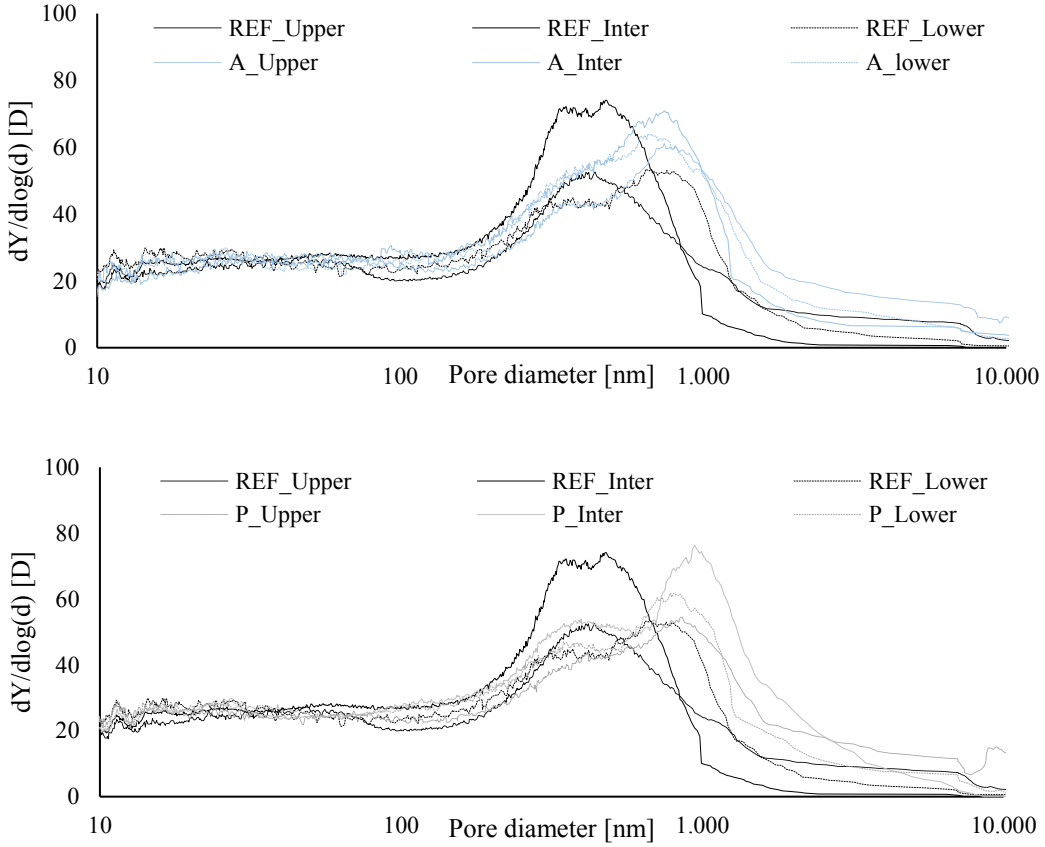

Figure 5 : Derivative intrusion curves obtained for mixtures with and without SAPs

Table 3: Nanoporosity

Sample	Total porosity <10 µm [%]				Median diameter [nm]		
	Upper	Inter	Lower	Overall	Upper	Inter	Lower
REF	15.2	16.2	15.9	16.2	255.6	273.2	246.6
SAP A	19.1	18.4	18.4	18.6	384.4	336.1	327.5
SAP P	17.4	19.9	17.6	18.3	355.1	388.3	299.4

3.3. Air void analysis

Figure 5 depicts the cumulative air content obtained by the RapidAir test. The total air content increases with SAP addition and the exact increase is more or less proportional to the amount of SAPs added. The expected size of the resulting macro pores based on the SAP initial size and absorption capacity of mixing water is 426 $\pm$ 94 µm and 846 $\pm$ 272 µm for SAP A and SAP P, respectively. This is exactly the range as found by RapidAir measurements. Based on a visual inspection of the studied specimens (Figure 6), one can also conclude that the printing process has no influence on the air void distribution within the sample and there is no clear distinction of the interlayer visible. This is already proven in previous research [8] and the results are similar for mixtures including SAPs. The latter research also mentioned the entrapment of air voids at the interlayer in case of increased time gaps. However, as the addition of SAPs increases the moisture content of the surface, further research on the air void distribution in case of different time gaps is required. The higher amount of voids can also affect the mechanical properties (i.e. compressive strength and interlayer bonding strength), but these investigations are not within the scope of this research.

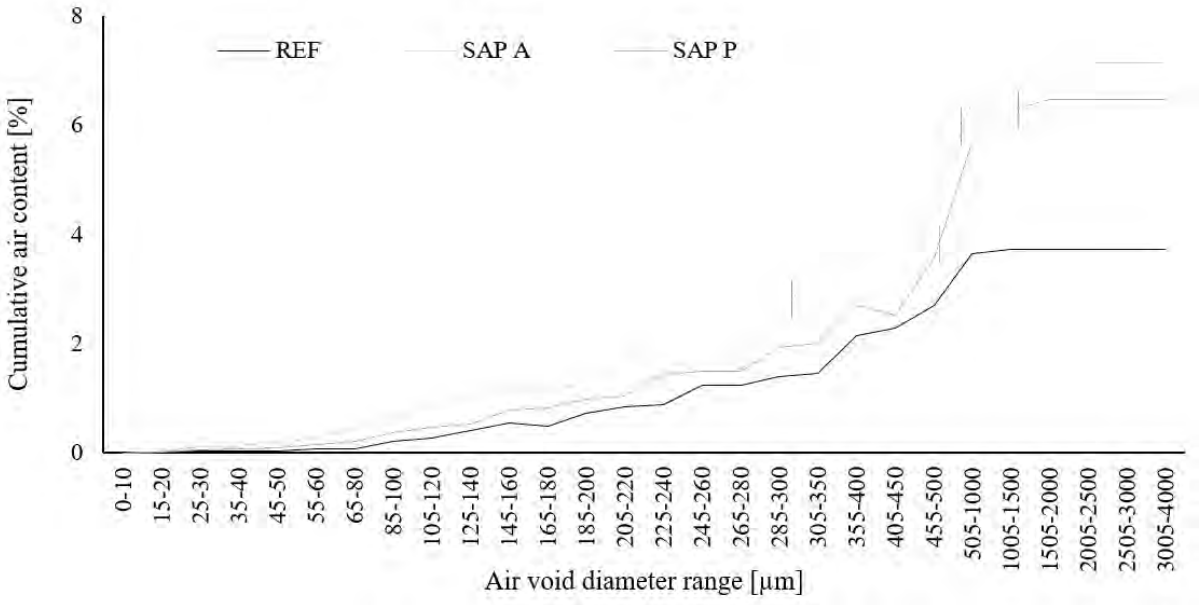

Figure 6: Cumulative air content in hardened specimens

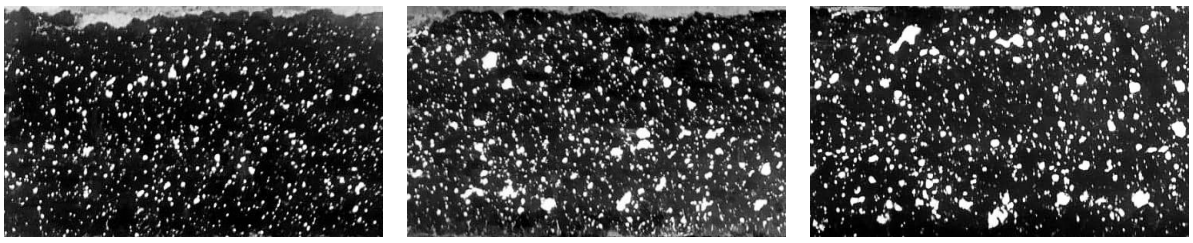

(a) (b) (c)

Figure 7: Studied specimens in RapidAir test : (a) Reference composition, (b) mixtures containing SAP A, (c) mixtures containing SAP P

4. CONCLUSIONS

The effect of two different types of SAPs on the shrinkage behaviour and microstructure of a 3D printed cementitious element is investigated and the following conclusions can be drawn:

- Superabsorbent polymers reduce shrinkage due to internal curing. SAP A shows better properties due a more gradual release of entrained water;
- Both SAPs decrease the nanoporosity in the range of 100 nm to 500 nm. This is ascribed to a better hydration rate around the SAPs, closing up the smaller pores, as well as to their autogenous shrinkage mitigation that reduces the amount of micro cracking resulting in a lower amount of preferential ingress paths for chemical substances;
- The porosity of the different zones within a printed specimen is comparable for all mixture compositions;
- The total air content increase with SAP addition and the exact increase is proportional to the amount of SAPs added.

ACKNOWLEDGEMENTS

J. Van Der Putten would like to acknowledge the support by EFRO for the C3PO-project (B/15100/01). D. Snoeck is a postdoctoral fellow of the Research Foundation-Flanders (FWO) and would gratefully acknowledge for the financial support of project No.12J3620N.

REFERENCES

1. De Schutter, G., et al., *Vision of 3D printing with concrete — Technical, economic and environmental potentials.* Cement and Concrete Research, 2018. **112**: p. 25-36.
2. Bos, F., et al., *Additive manufacturing of concrete in construction: potentials and challenges of 3D concrete printing.* Virtual and Physical Prototyping, 2016. **11**(3): p. 209-225.
3. Snoeck, D., *Self-healing and microstructure of cementitious materials with microfibres and superabsorbent polymers*, in *Faculty of Engingeering and Architecture* 2015, Ghent University.
4. Mechtcherine, V., et al., *Effect of internal curing by using superabsorbent polymers (SAP) on autogenous shrinkage and other properties of a high-performance fine-grained concrete: results of a RILEM round-robin test.* Materials and Structures, 2014. **47**(3): p. 541-562.
5. Mejlhede Jensen, O. and P. Freiesleben Hansen, *Water-entrained cement-based materials: I. Principles and theoretical background*. Vol. 31. 2001. 647-654.
6. Snoeck, D., C. Schröfl, and V. Mechtcherine, *Recommendation of RILEM TC 260-RSC: testing sorption by superabsorbent polymers (SAP) prior to implementation in cement-based materials.* Materials and Structures, 2018. **51**(5): p. 116.
7. Baroghel-Bouny, V., et al., *Autogenous deformations of cement pastes: Part II. W/C effects, micro–macro correlations, and threshold values.* Cement and Concrete Research, 2006. **36**(1): p. 123-136.
8. Van Der Putten, J., et al., *Microstructural Characterization of 3D Printed Cementitious Materials.* Materials, 2019. **12**(18).

Theme 8

Modeling of microstructure, transport, degradation processes and design for durability

A MULTISCALE MODEL FOR PREDICTING THE MECHANICAL PROPERTIES OF CEMENT PASTE

S. Krishnya (1), Y. Yoda (2) and Y. Elakneswaran (1)

(1) Division of Sustainable Resources Engineering, Faculty of Engineering, Hokkaido University

(2) SHIMIZU CORPORATION, Shimizu Institute of Technology, Center for Construction Engineering

Abstract

Mechanical properties of cement paste are indispensable and frequent requirement in structural analysis of concrete and other cement-based materials, and therefore the theoretical predictions have obtained considerable attention in the field of material engineering. Despite of being an active research area, available models for accurately predicting the mechanical characteristics of Ordinary Portland Cement (OPC) are limited, and which remains an imperative requirement in the cement industry. In this paper, a multiscale computational model is proposed for evaluating the basic mechanical properties of cement paste such as compressive strength and Youngs Modulus. The entire model consists of two-phase: hydration model and multi-scale model. The hydration model which has been developed by chemical thermodynamic calculations using coupled PHREEQC is used to quantify the hydration products. Hence the multi-scale analytical scheme is used to predict the mechanical properties of cement paste. In this simulation, a unified procedure based on three hierarchal scales is developed, initiates from Calcium-silicate-hydrate (C-S-H) matrix (consist of two types of C-S-H, monolayer water and gel porous) and progresses consequently up to the cement paste (consist of hydration products, porous and unhydrated cement). Finally, the validity of the proposed multi-scale model is verified with set of experimental data available in the literature. In conclusion, the scheme presented in this paper can accurately predict the Young's modulus and compressive strength accurately with low average relative error.

Keywords: Cement paste, Multiscale model, Calcium-silicate-hydrate (C-S-H), Young's modulus, Compressive strength

1. INTRODUCTION

OPC is one of the prime materials in almost all the construction industries, revealing a versatile scope for wide range of applications. Mechanical characteristics of cement are frequently required in material selections, structural analysis and designing concrete and other

cement-based structures. Therefore, researchers are very intense to explore the cement behaviour, and for this reason, theoretical prediction of the mechanical properties of OPC is being marked as an active area of research. Within the last few decades, many studies have been carried out in this area including numerical predictions, analytical and empirical relationships developed from experimental studies for predicting the characteristics of cement material [1-4]. The numerical predictions are primarily based on the finite element methods with the aid of digital imaging, simulating the microstructure by spherical or real shape particles [4,5]. Most of the previously proposed analytical models are based on the homogenisation method [2, 6], and some of them are simplification of mathematical complexity by introducing reasonable assumptions [7]. For example, cement was frequently assumed to be isotropic elastic material, two-phase composite sphere, etc. In some models, only C-S-H and portlandite were employed as hydration products [4,6,7]; few models ignored the C-S-H, but instead considered the capillary porosity or gel space ratio for the prediction of mechanical properties [1]. Even though the proposed models attempted to represent the approximation of the reality, the assumptions and simplifications limit their application range. It is clearly perceived that due to the complexity in understanding the microstructural characteristics and behaviours, no studies have successfully demonstrated the precise mechanism for effectively predicting the mechanical characteristics of OPC.

Cement paste is comprised of three phases such as the stiff anhydrous cement grains, products of hydration and porosity. Typically, several products are formed during the hydration process of the OPC, and the product that contributes substantially to the mechanical properties is C-S-H (Calcium Silica Hydrate) which has a high specific surface area with a complex pore structure [8]. During the early stage of hydration, a loose-packed (LP) C-S-H forms with an open fractal structure consisting of a random agglomeration of C-S-H globules with relatively a low packing density [9]. With the passage of time, the LP C-S-H densifies to approach a stable jammed packing of globules and nucleates at the surface of unreacted cement grains, leading to the development of soft outer products called low-density (LD) C-S-H. While outer products are continuously formed, fresh C-S-H matrix would start forming within the space confined by the existing C-S-H layer, and this newly formed C-S-H has higher density. It should be noted that, in most of the previous predictions, the C-S-H has been incorporated in single form (in place of three actual forms) with average denseness, led to the increased relative errors in the simulations [1, 5].

This paper proposes a two-phase model for the prediction of the compressive strength and elastic modulus of OPC paste by the means of cement chemistry and nano-micromechanics of cement. The hydration model is employed firstly to predict the fractions of hydration products, and subsequently, the multi-scale model is developed to assess the aforementioned mechanical properties. The multi-scale model initiates at nano-scale, and worth noting that the low-density C-S-H and high-density C-S-H are both taken into account to establish the model more accurately.

2. HYDRATION MODEL

2.1 Existing model: Introduction

The products of hydration and the compositions have the significant role in determining of mechanical properties of cement materials, but very few literatures have quantitatively dealt with those estimations through various mechanisms [3, 10,11]. Recently, Elakneswaran et al

[12] have found a valid thermodynamic model coupled with PHREEQC module to predict the weight assemblage of OPC hydrates, compared with experimental and semi-experimental results and demonstrated the applicability of several cements including OPC, slag-cement and ferrite-rich cement. However, the proposed model has only been established up to the prediction of hydrates by weight. But, as known, the mechanical behaviours of the materials significantly rely on the pores content i.e. the effect of capillary porosity, gel porosity and associated shrinkage. Therefore, in this study, the proposed coupled thermodynamic model is further expanded for the volumetric prediction of hydration products which are the inputs of the subsequent phase of the entire model.

2.2 Model expansion

As discussed earlier, there are two types of C-S-H: the LD C-S-H that tends to form as the outer product and HD C-S-H forms as the inner product of the cement gel. As for the computation of the volumetric fraction of each type of C-S-H, the relationship (Eq. 1) derived experimentally by Tennis and Jennings [8] is adopted herein.

$$M_r = 3.017.\frac{w}{c}.\alpha - 1.347.\alpha + 0.538 \quad (1)$$

where M_r is ratio of the mass of LD C-S-H to the total mass of C-S-H, w/c is water cement ratio and α is degree of hydration. The average densities of both C-S-H used for the calculations are obtained from the literature [13], 2000 kg/m^3 and 1700 kg/m^3 for HD and LD C-S-H respectively.

Volumetric prediction of chemical shrinkage is another important concern, which is typically caused as the molar volume of the products is relatively lower than that of products. The coefficients of chemical shrinkage of cement phases are obtained from the Table 1. The volumetric fraction of both capillary porosity and chemical shrinkage (the sum) can be expressed as given in Eq. (2).

$$V_{cp+cs} = V_i - (V_p + V_{rr}) \quad (2)$$

where, V_{cp+cs} is volume of capillary porosity and chemical shrinkage, V_i is initial volume of cement paste, V_p is volume of products and V_{rr} is volume of remaining reactants.

Table 1: Coefficients for chemical shrinkage [14]

Cement phase	Coefficient (g water/ g solid cement phase)
C_3S	0.0704
C_2S	0.0724
C_3A (Convert all C_3A to ettringite)	0.171
C_3A (Convert all C_3A to Monosulfoaluminate)	0.115
C_4AF (Convert all C_4AF to ettringite)	0.117
C_4AF (Convert all C_4AF to Monosulfoaluminate)	0.086

C-S-H gel, by its internal structure, has the pore spaces and which is generally defined as gel porosity. The porosity of C-S-H gel varies depending on the stiffness of the matrix, leading to the variation in gel porosity of LD C-S-H and HD C-S-H. From the literatures, they were respectively found to be 36% and 26% for LD and HD C-S-H [13].

2.3 Model verification

The expanded model for predicting the volume fractions of hydrates are verified for chemical shrinkage and capillary porosity. For the verification purpose, an independent set of experimental data are collected from the literature [15], which have been made of OPC for the water/cement ratio of 0.55. The computed chemical shrinkage and capillary porosity are shown and compared with the experimental data in Fig. 1-A and Fig. 1-B respectively.

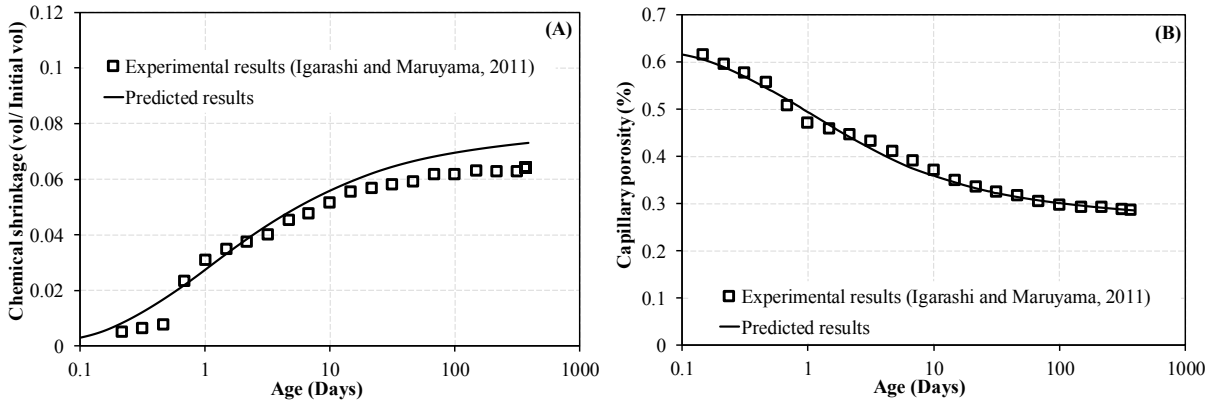

Figure 1: Comparaison of model results with experimental results of (A) chemical shrinkage and (B) capillary porosity for W/C 0.55

It can be seen from Fig. 1-A and Fig. 1-B that the predicted results are in a very good agreement with the experimental results. The predicted chemical shrinkage after 1 day and 320 days are 2.8 % and 7.2 % respectively, and the experimental results are 3.1 % and 6.4 % for the same aging. For the capillary porosity, predicted results after 1 day and 320 days are 49.15 % and 28.7 % while the experimental results are 47.4 % and 28.7 %. It is also observed that the capillary porosity gradually decreases, as expected. Typically, at the very early stage, the matrix could consist of stiff anhydrous cement grains and softer hydrates in a slight suspension form. With the time, due to the consumption of water, hardening of the cement matrix occurs, leading to the decrease in porosity.

3. MULTI-SCALE MODEL

3.1 Model description

In order to compute the compressive strength and Young's modulus of the cement paste, a multi-scale model is proposed. In this analytical scheme, the hydrated cement paste is considered in three levels, initiating at nano-scale C-S-H matrix, expanding to C-S-H foam and finally to cement paste. The volumetric fractions predicted from the hydration model are the inputs of this multi-scale scheme.

In the first level, the Young's modulus and compressive strength of C-S-H matrix is predicted at the characteristic scale of 1-100 nm. At the presence of two types of C-S-H, the Young's modulus of the matrix can be expressed as,

$$E_{CSH} = E_{LD\_CSH} + (E_{HD\_CSH} - E_{LD\_CSH})\Phi_{CSH-HD} \quad (3)$$

where the E_{LD_CSH} and E_{HD_CSH} are found to be 22 GPa and 27.5 GPa [16]. Φ_{CSH-HD} is the volume fraction of HD C-S-H in the total C-S-H, and which was estimated based on the results obtained from hydration model.

For the prediction of compressive strength of C-S-H matrix, the Griffith theory [17] is employed in this study. As the behavior of hydrated cement is brittle, the Griffith strength ratio ($\sigma_c/\sigma_t = 8$, where σ_c is the compressive strength and σ_t is tensile strength) is well applicable, and the compressive strength of C-S-H matrix ($f_{c,CSH}$) is indirectly obtained from its tensile strength ($f_{t,CSH}$). The tensile strength of C-S-H matrix can be expressed in terms of its packing density (η_{CSH}) (Eq. 4) [18].

$$f_{t,CSH} = f_{t,glob}\, exp\left(\frac{1.293(\eta_{CSH}^{13.011} - 1)}{\eta_{CSH}}\right) \quad (4)$$

where $f_{t,glob}$ is the apparent tensile strength of C-S-H globule, and that is found to be 320 Mpa [10]. The packing density of C-S-H matrix (η_{CSH}) can be expressed as follows,

$$\eta_{CSH} = \eta_{LD\_CSH} + (\eta_{HD\_CSH} - \eta_{LD\_CSH})\Phi_{HD\_CSH} \quad (5)$$

where the packing densities of the LD C-S-H (η_{CSH-LD}) and HD C-S-H (η_{CSH-HD}) are obtained from the literatures, which are 0.63 and 0.76 respectively [19].

In the second level, the Young's modulus and compressive strength of C-S-H foam is computed at the characteristic scale of 100 nm-10 μm, and this C-S-H foam consists of C-S-H matrix and capillary porosity. The expression for the Young's modulus of C-S-H foam can be obtained from [10] as

$$E_{CSH\_foam} = E_{CSH}\, exp(A\frac{\Upsilon_{CSH}^{B} - 1}{\Upsilon_{CSH}}) \quad (6)$$

where Υ_{CSH} is C-S-H space ratio, can be expressed as shown in Eq. (7), in which the volume fraction of C-S-H (Φ_{CSH}) and capillary porosity (Φ_{cap}) are obtained from the previous hydration model. A and B are the factors expressed as given in Eq. (8) and Eq. (9) respectively.

$$\Upsilon_{CSH} = \frac{\Phi_{CSH}}{\Phi_{CSH} + \Phi_{Cap}} \quad (7)$$

$$A = 0.82\, exp\,(-4.949\,\frac{\beta^{0.02} - 1}{\beta^{2.8}}) \quad (8)$$

$$B = 1.818\, exp\,(4.310\,\frac{\beta^{0.02} - 1}{\beta^{2.8}}) \quad (9)$$

The compressive strength of C-S-H foam (f_{c,CSH_foam}) can be expressed as shown in Eq. (10) [10].

$$f_{c,CSH\ foam} = f_{c,CSH}\, exp\,(-\frac{C(1 - \Upsilon_{CSH}^{D})}{\Upsilon_{CSH}}) \quad (10)$$

Here, the compressive strength of C-S-H matrix ($f_{c,CSH}$) which has been already computed in first level is implemented for the above calculation. C and D are factors respectively defined by Eq. (11) and Eq. (12).

$$C = 1.101\ exp\ (-\frac{0.296(\beta-1)}{\beta}) \quad (11)$$

$$D = -11.058\beta^{1.987} + 16.191\beta \quad (12)$$

The factor of C-S-H distribution is defined as β. Typically, the distribution factor can be within the range 0.4-1.0, depends on several factors such as heterogeneous nucleation, precipitation of C-S-H and cement finess [10].

In the third level, cement paste is modelled to predict its Young's modulus and compressive strength. The cement paste model comprises the C-S-H matrix, capillary porosity, unreacted clinker and other hydrates at the characteristic scale of 10-100 μm. The Young's modulus of the cement paste (E_{cp}) is predicted from the following expression [10] by implimenting the results obtained from the second level,

$$E_{cp} = E_{CSH\_foam}\ (1 + \Phi_{inclusion}\left(0.0102E_{incl} + 0.278E_{CSH_{foam}}^{0.2}\right)) \quad (13)$$

where $\Phi_{inclusion}$ is the volume fraction of hydrates excluding C-S-H, estimated from the hydration model. E_{incl} is the Young's modulus of solids excluding C-S-H in hydrates. Finally, the compressive strength of the cement paste is derrived from the Eq. (14).

$$f_{c,cp} = f_{c,CSH\ foam}(0.758 + (1 - 0.758)\ exp(-29.3\Phi_{inclusion})) \quad (14)$$

3.2 Model verification

The comparison between the predicted results and experiment results of Maruyama and Igarashi [20] are illustrated in Fig. 2 (A) and Fig. 2 (B) for Young's modulus (Eq. 13) and compressive strength (Eq. 14) respectively. To emphasize the impact of involving two types of C-S-H, predicted results considering the C-S-H as single matrix are compared together in both Fig. 2. From Fig. 2 (A), it can be seen that the predicted Young's modulus increases with the increase in aging, and that fits well with the ultrasonic and loading test results. It can be clearly perceived that when the C-S-H was modelled to be a single matrix, the prediction is approximately 17 % lower than the experimental results after 360 days, which could be attributed to the variation caused in capillary porosity and volume of C-S-H matrix.

Moreover, a good agreement is shown between experiment results and the predicted compressive strength (of LD and HD C-S-H model) (Fig. 2 (B)). For instance, the predicted strength of cement paste reached 42.8 MPa on 28th day and 59 MPa after 360 days, while the experimental results are 45.6 MPa and 58 MPa respectively. It can also be seen that the model slightly underestimates the compressive strength of cement paste at early stage compared to the experimental data. On the other hand, the predicted compressive strength from single C-S-H model shows nearly a 15 % deviation from the experimental results by the end of 360 days hydration.

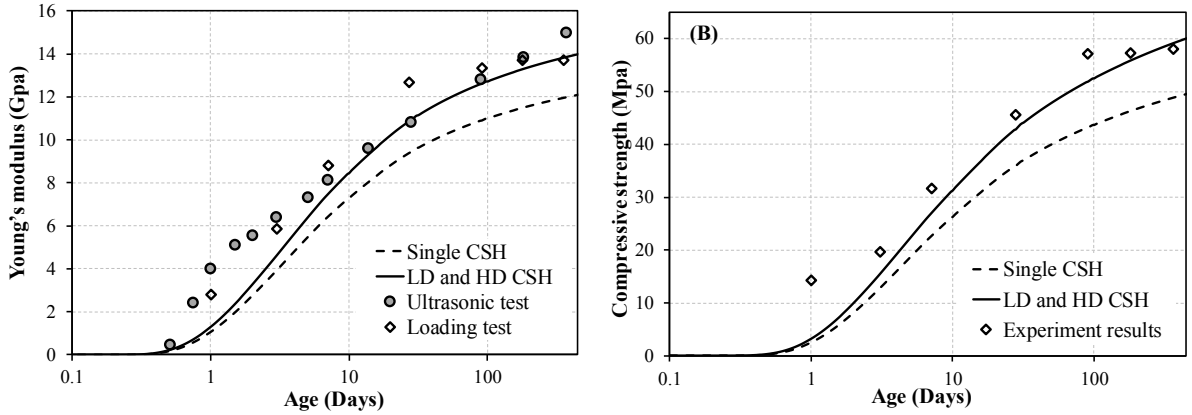

Figure 2:Development of (A) Young's modulus and (B) compressive strength of cement paste for W/C 0.55.

The results demonstrate that the model involved both LD and HD C-S-H could accurately predict the Young's modulus and compressive strength, whereas the conventional approach (C-S-H modelled as single matrix) has been shown to significantly deviate. Generally, the water/cement ratio of cement pastes used in most of the practical use is between the range of 0.4 and 0.6 [7]. In this paper, the proposed model is validated only for the cement paste with high water cement ratio of 0.55. To fully verify the feasibility of this model, further validation is recommended for the cement paste with low water cement ratio (for example, 0.4), and which is left for the future work.

4. CONCLUSIONS

A simple two-phase model has been developed for predicting Young's modulus and compressive strength of the cement paste. The volumetric fractions of hydration products are predicted thermodynamically in the first phase (hydration model), followed by an analytical scheme (multi-scale model) for computing Young's modulus and compressive strength. In this proposed model, the mechanical properties are predominantly related to the C-S-H product, as the C-S-H contributes more to strength development than other hydration products; and that is considered distinctly in the forms of LD C-S-H and HD C-S-H. The validity of the model predictions has been well verified with independent set of experimental data found in the literature. However, to make the proposed model fully feasible, further verifications are essential for different water cement ratios, comparing the predictability with more experimental data.

REFERENCES

[1] Bentz, D. P. 'CEMHYD3D: A Three-Dimensional Cement Hydration and Microstructure Development Modeling Package,' *Autom. Constr.*8 (1999) 227–235.

[2] Bernard, O., Ulm, F.-J., and Lemarchand, E. 'A multiscale micromechanics-hydration model for the early-age elastic properties of cement-based materials,' *Cem. Concr. Res.* 33(9) (2003) 1293–1309.

[3] Stefan, L., Benboudjema, F., Torrenti, J.-M., and Bissonnette, B. 'Prediction of elastic properties of cement pastes at early ages,' *Comput. Mater. Sci.* 47(3) (2010) 775–784.

[4] Mazaheripour, H., Faria, R., Ye, G., Schlangen, E., Granja, J. and Azenha, M. 'Microstructure-based prediction of the elastic behaviour of hydrating cement pastes,' *Appl. Sci.* 8(3) (2018) 442.

[5] Haecker, C. J., Garboczia, E.J., Bullarda, J.W., Bohnb, R.B., Sunc, Z., Shahc, S.P. and Voigt. T. 'Modeling the linear elastic properties of Portland cement paste,' *Cem. Concr. Res.* 35(10) (2005) 1948–1960.

[6] Constantinides, G. and Ulm, F.-J. 'The effect of two types of C-S-H on the elasticity of cement-based materials: Results from nanoindentation and micromechanical modeling,' *Cem. Concr. Res.* 34(1) (2004) 67–80.

[7] Zheng, J., Zhou, X., Shao, L. and Jin, X. 'Simple Three-Step Analytical Scheme for Prediction of Elastic Moduli of Hardened Cement Paste,' *J. Mater. Civ. Eng.* 22(11) (2010) 1191–1194.

[8] Tennis, P. D. and Jennings, H. M. 'A model for two types of calcium silicate hydrate in the microstructure of Portland cement pastes,' *Cem. Concr. Res.* 30(6) (2000) 855–863.

[9] H. Jennings, J. Thomas, J. Gevrenov, G. Constantinides, and F. ULM, "Nanostructure of CSH gel in cement paste as a function of curing conditions and relative humidity," Creep, shrinkage Durab. Concr. Concr. Struct. Proceeding Concreep, vol. 7, no. November, pp. 19–37, 2005.

[10] Hlobil, M., Šmilauer, V. and Chanvillard, G. 'Micromechanical multiscale fracture model for compressive strength of blended cement pastes,' *Cem. Concr. Res.* 83 (2016) 188–202.

[11] S. Krishnya, Y. Yoda, and Y. Elakneswaran, 'A Multi-scale Model for Predicting the Compressive Strength of Ordinary Portland Cement (OPC),' Springer, Singapore, 2020, pp. 9–18.

[12] Elakneswaran, Y., Owaki, E., Miyahara, S., Ogino, M., Maruya, T. and Nawa, T. 'Hydration study of slag-blended cement based on thermodynamic considerations,' *Constr. Build. Mater.* 124 (2016) 615–625.

[13] Jennings, H. M., Thomas, J. J., Gevrenov, J. S., Constantinides, G. and Ulm, F. J. 'A multi-technique investigation of the nanoporosity of cement paste,' *Cem. Concr. Res.* 37(3) (2007) 329–336

[14] Bentz, B. Y. D. P., Lura, P. and Roberts, J. W. 'Mixture proportioning for internal curing,' *Concr. Int.* (2005) 35–40.

[15] Igarashi, G. and Maruyama, I. 'Relationship between mechanical properties and phase composition of hardened cement phase' (In Japanes), *J.Struct. Constr. Eng.* 76(660) (2011) 213–222.

[16] S˘milauer, V. and Bittnar, Z. 'Microstructure-based micromechanical prediction of elastic properties in hydrating cement paste,' *Cem. Concr. Res.* 36(9) (2006) 1708–1718.

[17] Griffith, A. 'Theory of rupture,' *In : C. Biezeno, J. Burgers (Eds.), First International Congress for Applied Mechanics, Delft*, 1924, 55–63.

[18] Nemecek, J., Smilauer, V., Nemecek, J. and Kolarik, F. 'Fracture properties of cement hydrates determined from microbending tests and multiscale modeling,' in*: proceedings of the Conference on Computational Modelling of Concrete and Concrete Structures. Bad Hofgastein, Austria*, 2018, 113–119.

[19] Constantinides, G. and Ulm, F.-J. 'The nanogranular nature of C–S–H,' *J. Mech. Phys. Solids*. 55(1) (2007) 64–90.

[20] Maruyama, I. and Igarashi, G. 'Cement Reaction and Resultant Physical Properties of Cement Paste,' *J. Adv. Concr. Technol.* 12(6) (2014) 200–213.

A PHENOMENOLOGICAL MODEL FOR HYDRATION HEAT EVOLUTION OF A CEMENTED WASTE FORM

Quoc Tri Phung (1), Suresh .C. Seetharam (1), Eduardo Ferreira (1), Joan Govaerts (1), Katrien Hendrix (1) and Elie Valcke (1)

(1) Belgian Nuclear Research Centre (SCK•CEN), 2400 Mol, Belgium

Abstract

This paper presents an extension of an existing phenomenological model for predicting the evolution of hydration heat of a cemented waste form. The cemented waste form is essentially a mixture of blended cement and homogeneous low- and intermediate-level liquid (simulant) radioactive waste (sludge). The motivation stems from the fact that the existing empirical or phenomenological models are not designed to handle the interaction of a blended cement system with the waste sludge. The main objective of the proposed model is to minimize the number of isothermal or semi-adiabatic experiments (and thus the cost) required to design a promising recipe for conditioning the waste form. The paper demonstrates the capability of the model to successfully predict the evolution of hydration heat for various cemented waste form recipes.

Keywords: Hydration heat, Cement, Sludge, Supplementary cementitious materials, Radioactive

1. INTRODUCTION

Blended cements are promising candidates for conditioning of homogeneous low and intermediate-level liquid radioactive waste (very often this is a sludge). The conditioning is typically carried out at industrial scale in disposal containers with a capacity of several hundreds of litres. This means that at the core of such containers, temperature can rise to high levels depending on the formulation of blended cement as well as any additional exothermal heat generated due to cement-waste interaction, and this despite the heat reduction benefit of blended cements. It is therefore important to ensure that the peak temperature in such containers does not rise above a certain threshold (~ 60 °C) to avoid the risk on formation of delayed ettringite and thermal cracking.

The evolution of the hydration heat can be studied via the use of isothermal/semi-adiabatic/adiabatic calorimeters. In this work, a combination of isothermal calorimetric measurements on various blended cements and sludge, and an adapted stoichiometry-based phenomenological hydration heat model [1] is applied to predict the evolution of the hydration heat of a cemented waste form using blended cementitious materials composed of blast furnace

slag, silica fume and ordinary Portland cement. The model has a number of parameters, which are calibrated, in a step-wise manner as in [1], against a specific set of isothermal calorimetric experiments. With the calibrated parameters fixed, the model's performance is examined against several other isothermal experiments.

2. PHENOMENOLOGICAL MODEL FOR HYDRATION HEAT

In a blended cement binder system, the total heat evolution (Q(t)) is attributed to the heat contributions from different exothermic reactions of binders such as ordinary Portland cement (OPC), blast furnace slag (BFS), silica fume (SF), etc. during hydration. Therefore, the enthalpy of reaction of binders $Q_{\infty,i}$ (assumed independent of temperature), weight fraction of binders in the total mixture (f_i), and degree of hydration of each binder (α_i) are needed to compute the total heat evolution. This can be mathematically expressed as:

$$Q(t) = \sum_{i=1}^{n} \dot{\alpha}_i f_i Q_{\infty,i} \quad (1)$$

where $\dot{\alpha}_i$ is the rate of hydration degree of the cemented waste form, which needs to be estimated. In this study, the phenomenological model proposed by Kolani *et al.* [1] (and references therein) is used (Eq. 2). However, an extension is proposed to include the effect of sludge (sludge loading) by introducing an additional variable w_i.

$$\dot{\alpha}_i = A_i g_i \pi_i h_i S_i w_i \quad (2)$$

where $\dot{\alpha}_i$ is the rate of hydration degree, A_i is a constant that needs to be calibrated, g_i is the chemical activation term, which is a function of volumetric concentration of clinker and of water in the cement paste, π_i is a function that accounts for water accessibility of anhydrous clinkers, which is a function of volumetric concentration of hydration phases, anhydrous phase, porosity and free water volumetric concentration in the cement paste, h_i is a function that accounts for temperature effects via Arrhenius equation, and S_i is the delay function to account for the addition of supplementary cementitious materials. Note that in addition to A_i, there are three more calibration parameters associated with the variables of Eq. 2. The strategy for calibrating these parameters is the same as that adopted in [2], *i.e.* the parameters for OPC are first calibrated with the isothermal experiments on pure OPC. These are kept constant and the parameters for BFS are calibrated with the isothermal experiments on OPC-BFS blended system, and so on.

3. CALIBRATION AND VALIDATION

A number of isothermal experiments on pure and blended mixtures, including mixtures with waste sludge have recently become available [3]. Table 1 presents a list of isothermal experiments used for calibration of parameters and validation.

Fig. 1 shows the effects of w/c ratio and BFS replacement level on the cumulative heat release after 7 days of hydration at 20 °C. The heat is normalized by the mass of cement and BFS in each sample. It can be seen that the predicted results are in good agreement with the measured data. Both modelling and experimental results show a small difference in cumulative heat release of samples with w/c ratios of 0.7 and 0.9 (Fig. 1, left). For pure OPC, the two curves overlap during an initial period of around 20 hours. After this period, modelling results show that the sample with lower w/c ratio of 0.7 exhibits a slightly lower heat release, but

experimental data still show the overlapping. It is commonly shown in literature that for low w/c ratio samples (less than 0.45), despite similar cumulative heat release in the initial hydration period, samples with lower w/c ratio produce lower cumulative heat [4, 5]. This phenomenon is typically explained by the reduction in the amount of available water and space for hydration in a system with low w/c ratio. However, if the w/c ratio continues to increase, the effect of w/c ratio on the hydration rate becomes negligible, as seen for the samples with high w/c ratios of 0.7 and 0.9 in this study.

It is not surprising that the addition of BFS reduces the heat release, and the higher the BFS replacement level, the lower the cumulative heat release, as seen Fig. 1 (right). This is consistent with a lower heat release due to the presence of BFS, which is confirmed in the majority of published research [1, 6]. Note that if normalized to the cement content, the heat release is higher with the increase of BFS replacement levels and much high than the one of OPC sample with the same w/b ratio. The heat increase (normalized to cement content) is explained by the acceleration of the clinker hydration in the presence of BFS and the exothermic reaction of BFS itself. Compared to OPC, besides the first (rapid reaction) and the second hydration peak associated to OPC (mainly alite) hydration, a third hydration peak can be recorded for the mixes containing BFS, as shown in Fig. 2. This peak corresponds to the slag reaction in an alkaline environment created by the OPC hydration (e.g. C_2S, C_3S), which liberates a significant amount of calcium hydroxide. The second peak also appears quicker for the BFS mix.

Table 1: Mix formulation

Material	OPC Wt%	BFS (SL) Wt%	Silica Fume (SF) Wt%	Sludge (Slu) V%
Used for calibration				
OPC1(w/c = 0.9)	100	0	0	0
SL 1 (OPC-BFS)	70	30	0	0
SL 1, SF1 (OPC-BFS-SF)	60	30	10	0
SL 1, SF 1, Slu 1 (OPC-BFS-SF-Sludge)	60	30	10	50
Used for validation				
OPC2 (w/c = 0.7)	100	0	0	0
SL 2 (OPC-BFS)	50	50	0	0
SL 2, SF 2 (OPC-BFS-SF)	30	50	20	0
SL 2, SF 2, Slu 2 (OPC-BFS-SF-Sludge)	30	50	20	45

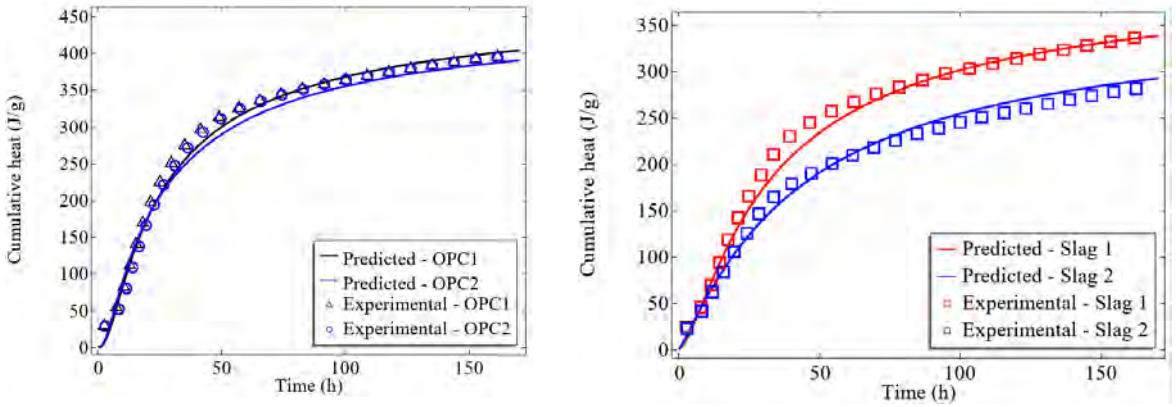

Figure 1: Comparison of experimental results *vs.* prediction for pure OPC formulations (left) and OPC-BFS mix (right)

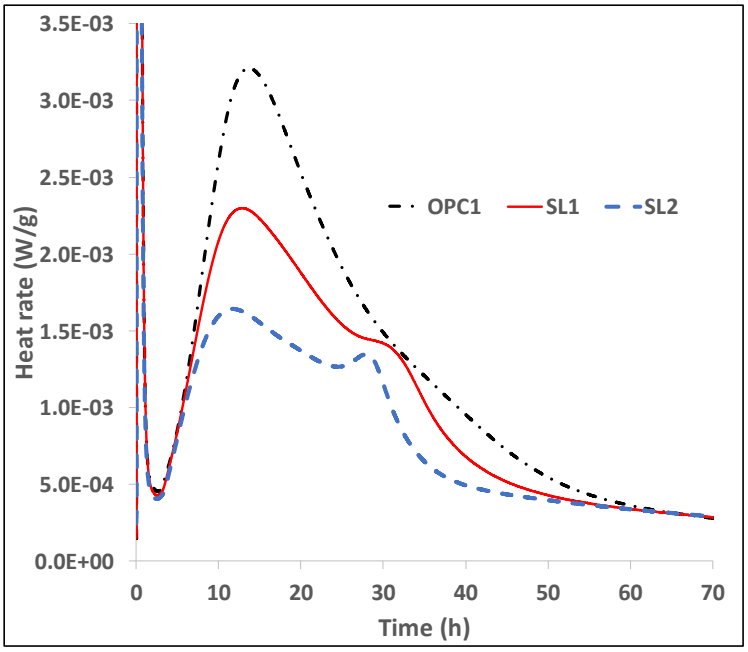

Figure 2: Comparison of experimental heat rate of OPC *vs.* BFS mix

Fig. 3 illustrates the predictive capacity of the model when the system becomes more complicated, e.g. adding 2 supplementary cementitious materials (BFS + SF) and sludge. The model is again able to capture the cumulative heat release for a blended system with or without sludge quite well, except for the case SL2_SF2_SLu2, which is slightly underestimated after 80 hours of hydration. It is also observed that the addition of sludge results in an increase in cumulative hydration heat, due to possible exothermal reactions occurring between the sludge and cementitious matrix, which is well captured by the model.

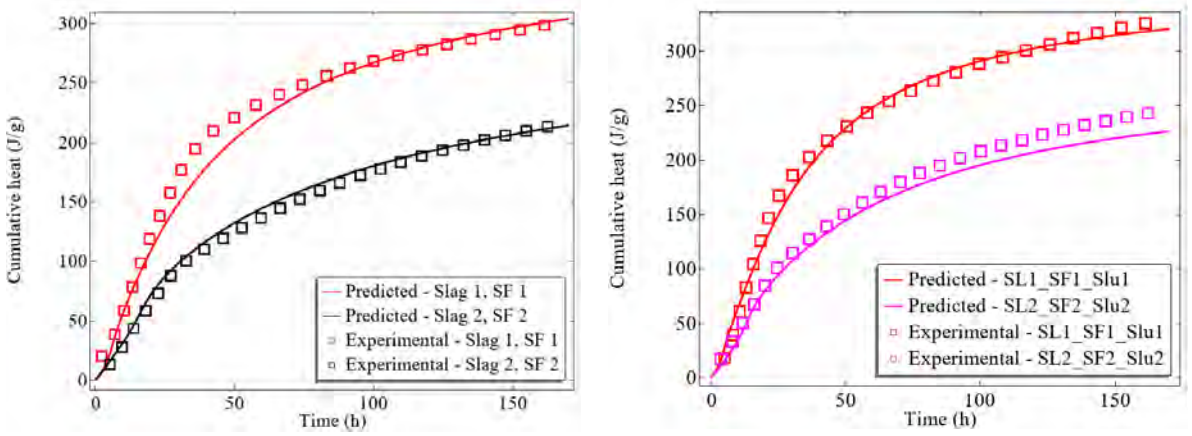

Figure 3: Comparison of experimental results *vs.* predicted solution for OPC-BFS-SF (left) and OPC-BFS-SF-Slu mix (right)

8. CONCLUSIONS

Using a combination of isothermal calorimetric measurements on various blended cements and sludge, and an adapted stoichiometry-based phenomenological hydration heat model, it is possible to predict the evolution of the hydration heat of a cemented waste form. The proposed extension to the stoichiometry-based phenomenological hydration model (multiplicative law) essentially accounts for the additional effect of simulant radioactive sludge to the hydration heat. It is interesting to note that the new model is able to reasonably capture the evolution of hydration heat of various cemented waste form recipes.

REFERENCES

[1] B. Kolani, L. Buffo-Lacarrière, A. Sellier, G. Escadeillas, L. Boutillon, L. Linger, Hydration of slag-blended cements, Cement and Concrete Composites, 34 (2012) 1009-1018.
[2] G. De Schutter, L. Taerwe, General hydration model for portland cement and blast furnace slag cement, Cement and Concrete Research, 25 (1995) 593-604.
[3] Q.T. Phung, E. Ferreira, S.C. Seetharam, E. Valcke, Effects of supplementary cementitious materials on the hydration heat of mortars – applying to cementation of radioactive waste Cement Concrete Comp, (In preparation).
[4] P.Y. Yan, F. Zheng, Z.Q. Xu, Hydration of shrinkage-compensating binders with different compositions and water-binder ratios, J Therm Anal Calorim, 74 (2003) 201-209.
[5] E.-H. Kadri, R. Duval, Hydration heat kinetics of concrete with silica fume, Constr Build Mater, 23 (2009) 3388-3392.
[6] E. Gruyaert, N. Robeyst, N. De Belie, Study of the hydration of Portland cement blended with blast-furnace slag by calorimetry and thermogravimetry, J Therm Anal Calorim, 102 (2010) 941-951.

CONTINUUM PERCOLATION THRESHOLD AND IONIC DIFFUSIVITY OF POROUS MEDIA CONSISTING OF ASYMMETRICAL OVOIDAL PORES

Mingqi Li (1), Huisu Chen(1) and Jianjun Lin (1)

(1)Jiangsu Key Laboratory of Construction Materials, School of Materials Science and Engineering, Southeast University, Nanjing 211189, P.R. China

Abstract

Porous networks provide the main transport channels to the active media, which will damage the microstructure and then lead to a subsequent reduction in the strength, serviceability and aesthetic of porous materials. The connectivity of the porous network plays an essential role in the transport properties of these active media. In statistic physics, the percolation threshold ϕ_c is usually used to describe the formation of long-range connectivity in the system and it has been demonstrated that ϕ_c of porous network is highly depended on the geometrical shape of the pores. However, the previous studies focused on the symmetric pores such as spheres, ellipsoids and spherocylinders, etc. How the particle asymmetry affects the percolation behaviour of the porous network and then influences the transport properties of materials is still undiscovered. In this work, a family of asymmetric ovoids is introduced. By combining the geometric model of ovoid with the Monte Carlo simulation, a series of porous composite composed of congruent overlapping pore of asymmetrical ovoids are modelled. Then, the percolation thresholds ϕ_c of composites are obtained by an excluded volume based approximation formula. Furthermore, a general percolation-based effective-medium approximation is adopted to theoretically study the ionic diffusivities of the two-phase porous composites considering their percolation behaviours. The results shed light on the intrinsic and complex interplay of components, structure and transport properties in composites, which can provide some guidance for the development of percolation theory and the design of composites.

Keywords: Asymmetrical ovoid; Porous composites; Continuum percolation; Ionic diffusivity

1. INTRODUCTION

In the geoscience and engineering fields, porous materials are ubiquitous such as zeolites, wood, concrete, ceramic, etc. From the structural perspective, the porous materials could be assumed as a two-phase systems composed by low permeability solid matrix and high permeability porous network [1]. Porous materials, such as concretes and rocks are exposed to harsh environments yet are often expected to last with little or no repair or maintenance for long periods of time (often 100 years or more). However, the active media in the environment (e.g.,

carbon dioxide, contaminant, ions, fluid, etc.) will penetrate into the porous materials and damage the microstructure of the materials, then lead to a subsequent reduction in the strength, serviceability, and aesthetic of structure [2]. In general, the porous network are the main transport "channels" for those active media and the emergence of system-spanning porous network is the prerequisite of active media transport through the porous materials. Ever since Broadbent and Hammersley [3] modeled the propagation of a fluid in an infinite regular square lattice, the percolation theory has played an abiding role in the study of the connected clusters. The percolation threshold ϕ_c, expressed by critical porosity of porous material, is usually used to characterize the critical emergence of system-spanning path in the system comprising random distributed objects/particles. In the vicinity of percolation threshold, the conductivity, diffusivity and permeability of porous composite materials will have the dramatic changes variation because of the occurrence of the global connectivity. Therefore, accurately obtaining the percolation threshold of porous composites and rigorously incorporating such structural characteristic into the prediction of transport properties of composite is of great significance to illuminate the intrinsic and complex interplay of components, structures and transport properties in porous composites.

From the previous studies [4, 5], it can be concluded that the particle morphology is a very crucial factor for the percolation behavior of the composite. Thus, how to accurately predict the effect of particle shapes on the threshold ϕ_c for different 2D or 3D systems is of great importance for the design of composite. Previous works on the continuum percolation systems mainly focused on symmetrical anisotropic-shaped particles, such as rectangles [5], ellipsoids [6] and spherocylinders [7]. In practice, particulate components in real granular composites are not idealized symmetric particles as mentioned above, as shown in Fig.1. However, how the particle asymmetry affects the percolation behavior of network and then influence the diffusivity of the composite is still undiscovered.

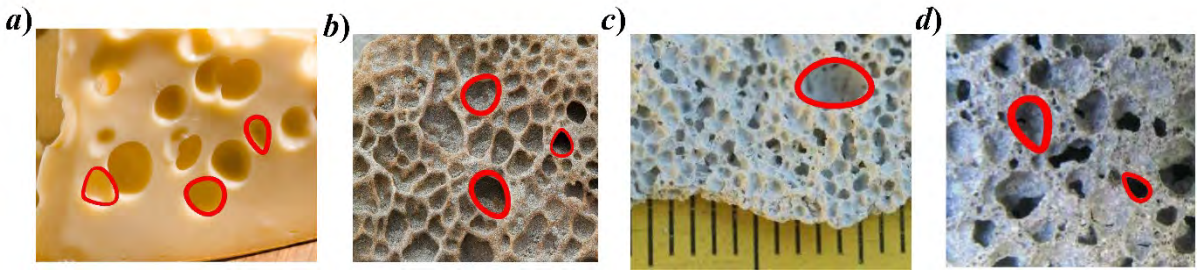

Figure1: The real asymmetrical pores in the porous materials.

To provide a theoretical framework to address this lacuna, a family of single axil asymmetrical ovoids, also known as "tapered ellipsoids", is introduced in this paper. From a geometric modeling perspective, ovoid is a natural extension of the ellipsoid and the surface of ovoid can be expressed by Eq. (1). Fig.2 illustrates the morphologies of ovoids with different c/a and T.

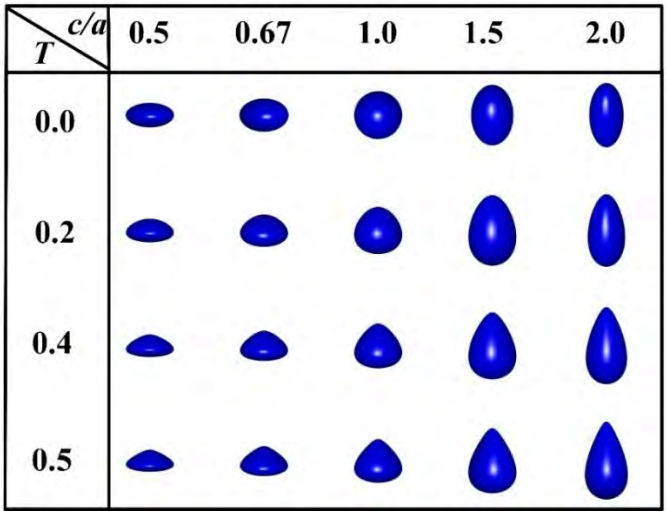

Figure 2: Illustration of the morphologies of ovoids with different *T* and *c*/*a*.

$$F_{ov}(x,y,z)=\left(\frac{1}{T\frac{z}{c}+1}\times\frac{x}{a}\right)^2+\left(\frac{1}{T\frac{z}{c}+1}\times\frac{y}{b}\right)^2+\left(\frac{z}{c}\right)^2-1=0 \quad (1)$$

where a, b and c denote the semi-axis lengths of ovoid in x, y and z directions, and $T\in[0, 0.5]$ is the tapering parameter ($T = 0$ for symmetric ellipsoid).

In this study, the porous systems consist of homogeneous solid matrix and porous network composed of overlapping asymmetric ovoids are generated firstly by combining with the Monte Carlo simulation. Then, the percolation threshold ϕ_c of the congruent overlapping ovoids are obtained by the excluded based approximation formula. To explore the effect of ϕ_c on the diffusivity of systems, the percolation-based generalized effective medium approximation is further applied. Finally, the normalized ionic diffusivity in the saturated porous composite is theoretically predicted and the reliability of the prediction is verified by comparison with the experimental measurements.

2. CONTINUUM PERCOLATION OF OVERLAPPING OVOIDS

In continuum percolation model, the porous composite can be simplified to be the congruent random distributed overlapping asymmetric ovoids, as shown in Fig.3. The porous network is assumed to be the intersected ovoids and the remaining zones are described to be the solid matrix. Once the intersected superovoids long enough to form the system-spanning cluster, the percolation of the porous network is deemed to be realized. In the previous studies [8], we have studied the percolation of ovoids with c/a in [0.5, 2] and an excluded volume based approximation formula is proposed to estimate the effect of shape parameter (i.e., c/a and T) on the threshold ϕ_c, as expressed by Eq. (2).

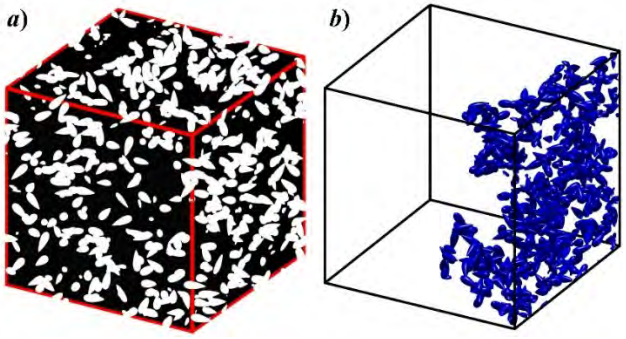

Figure 3: Visualization of *a*) the two-phase porous system consisting of homogeneous solid matrix (black parts) and porous network (white inclusions) composed of overlapping ovoids. *b*) the connected pore cluster in the two-phase porous system.

$$\phi_c = 1 - \exp\left(\frac{-G(c/a,T)}{V_{dex}}\right) \tag{2a}$$

$$G(T,c/a) = 2.730 + 0.037\exp(T) - 0.089\ln(c/a) - 0.025\exp^2(T) - 0.212\ln^2(c/a) + 0.064\exp(T)\ln(c/a). \tag{2b}$$

$$V_{dex} = \frac{V_{ex}}{V} \tag{2c}$$

where V is the volume of the discrete pore and V_{ex} refers to the volume that is inaccessible to other particles as a result of the presence of the first one [9]. To avoid the size effect of the particle, the dimensionless excluded volume V_{dex}, defined as the ratio between the excluded volume and the volume of particle, is usually employed.

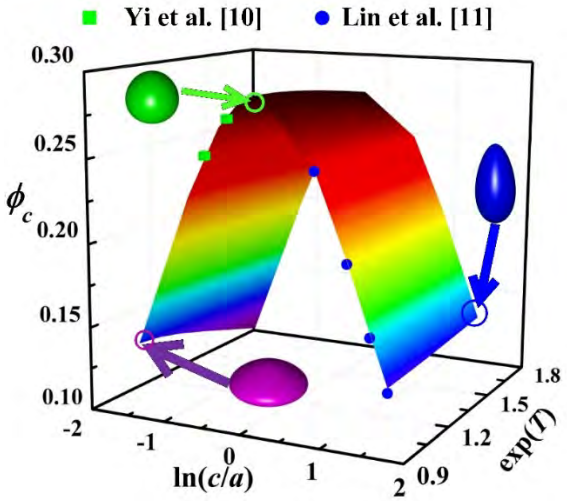

Figure 4: The dereived results of ϕ_c by approximation formula versus the simulated values in Refs. [10, 11].

In this paper, we calculated the V_{dex} of the ovoids with $c/a \in [0.2, 5]$ and the results are shown in Table 1. By combining the V_{dex} in Table 1 with Eq. (2), the thresholds ϕ_c are obtianed. Fig.4 illustrates the thresholds ϕ_c and comparising the theoretical results with the simulated

values in previous researchs [10, 11]. It can be seen that the theoretical results are in weel aggrement with the simulated values, which indicates the reliability of our derived results.

Table 1: The dimensionless excluded volume V_{dex} for ovoids with different *c*/*a* and *T*.

T \ c/a	0.2	0.4	0.6	0.8	1.0	2.0	3.0	4.0	5.0
0.00	15.10	9.95	8.57	8.11	8.00	9.08	10.91	12.96	15.10
0.10	15.24	10.01	8.60	8.13	8.01	9.08	10.90	12.94	15.09
0.20	15.63	10.18	8.70	8.19	8.05	9.07	10.88	12.90	15.03
0.30	16.25	10.45	8.86	8.29	8.12	9.07	10.84	12.84	14.94
0.40	17.06	10.81	9.06	8.42	8.21	9.07	10.79	12.75	14.81
0.50	18.04	11.24	9.32	8.59	8.33	9.06	10.72	12.64	14.66

3. TRANSPORT PROPERTIES OF SATURATED POROUS CEMENT PASTE

For the cement paste, the effective ionic diffusivity D_{eff}, the porosity and diffusivity of porous network are assumed to be ϕ and D_p, and that of solid matrix to be (1- ϕ) and D_m. In this case, McLachlan et al.[12] established the relationship between the effective ionic diffusivity and the percolation threshold of porous materials based on the effective medium approximation and percolation theory, as shown by Eq. (3).

$$\frac{D_{eff}}{D_m}=\left(1-\frac{\phi}{\phi_c}\right)^t \quad \text{for } \phi<\phi_c \tag{3a}$$

$$\frac{D_{eff}}{D_p}=\left(\frac{\phi-\phi_c}{1-\phi_c}\right)^t \quad \text{for } \phi>\phi_c \tag{3b}$$

However, it should be noted that the diffusivity near the percolation threshold cannot be measured by Eq. (3), as illustrated in Fig. 5. To overcome this shortcomings, a generalized effective medium theory (GEMT) [13], as expressed by Eq. (4), is proposed. Then, by combining the thresholds with GEMT, a so called percolation threshold based generalized effective medium approximation (PT-GEMA, see Eq. (5)) is present to link the ionic diffusivity with the percolation behaviors of the cement paste comprising uniform overlapping asymmetrical pores.

$$\frac{\phi(D_p^{1/t}-D_{eff}^{1/t})}{D_p^{1/t}+\frac{1-\phi_c}{\phi_c}D_{eff}^{1/t}}+\frac{(1-\phi)(D_m^{1/t}-D_{eff}^{1/t})}{D_m^{1/t}+\frac{1-\phi_c}{\phi_c}D_{eff}^{1/t}}=0 \tag{4}$$

where t is a transport-percolation coefficient refers to the complexity of the porous networks.

$$\frac{D_{eff}}{D_p}=\left\{\Omega+\sqrt{\Omega^2+\frac{1-\exp\left[-G/V_{dex}\right]}{\exp\left[-G/V_{dex}\right]}\left(\frac{D_m}{D_p}\right)^{\frac{1}{t}}}\right\}^t \tag{5a}$$

$$\Omega=\frac{1}{2}\left\{\left(\frac{D_m}{D_p}\right)^{\frac{1}{t}}-\frac{1-\exp\left[-G/V_{dex}\right]}{\exp\left[-G/V_{dex}\right]}-\frac{\phi}{\exp\left[-G/V_{dex}\right]}\left[\left(\frac{D_m}{D_p}\right)^{\frac{1}{t}}-1\right]\right\} \tag{5b}$$

Afterwards, we utilize PT-GEMA to compute the normalized chloride diffusivity D_{eff}/D_p in cement paste and compare the derived results with the experimental measurements [14, 15]. Referring to the study by Oh et al. [16], the realistic values for t and D_m/D_p are expected to be 2.7 and 2.0E-4 for cement pastes. It can be clearly seen in Fig.5 that the derived results from PT-GEMA are in agreement with the experiment measurements, which indicates that PT-GEMA can accurately predict the ionic diffusivity of cement paste. Moreover, the derived D_{eff}/D_p of cement paste in Fig.5 by the asymmetrical ovoids are closer to the experiment measurements than the results by sphere.

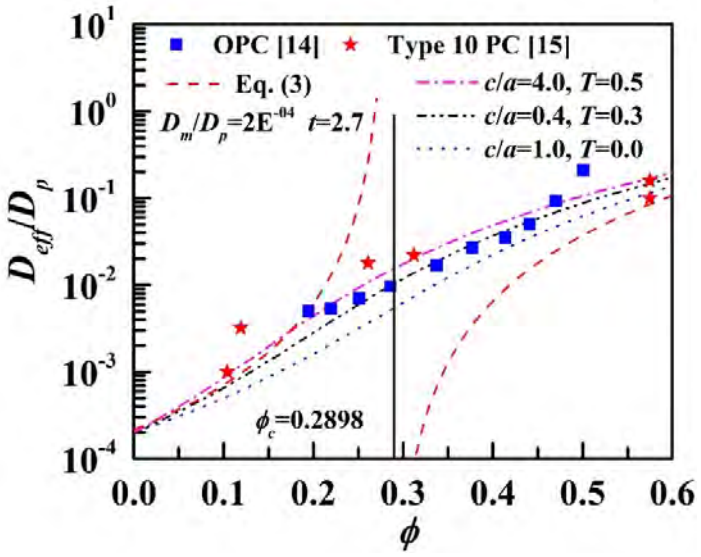

Figure 5: Comparisons of the predicted results of normalized chloride diffusivity from PT- GEMA with experimental data.

4. CONCLUSIONS

The percolation threshold of ovoids with $c/a \in [0.2, 5]$and $T \in [0, 0.5]$ are calculated in this paper. For a constant T in [-0.5, 0.5], ϕ_c shows an initially increasing and then decreasing trend with the increase of c/a and the inflection point located at c/a = 1.0, which is consistent with the previous studies. The ionic diffusivities of the cement paste comprising overlapping

asymmetrical ovoidal pores are theoretically derived by PT-GEMA and the reliability of PT-GEMA is verified by comparing the derived results from PT-GEMA with the experimental measurements. The results demonstrate that the porous systems composed of asymmetrical shaped pores are closer to the realistic porous materials than the systems comprising spherical pores.

ACKNOWLEDGEMENTS

The authors gratefully thanks the financial support from National Natural Science Foundation of China (Grant No.51878152) and Ministry of Science and Technology of China "973 Project" (Grant No. 2015CB655102).

REFERENCES

[1] Qi, L., Chao, X., Tian, W., Ta, W. and Li, H. 'Numerical study of the effects of irregular pores on transverse mechanical properties of unidirectional composites'. *Compos. Sci. Technol.* **159** (3) (2018)142-151.

[2] Liu, L., Wang, X.C., Zhou, J., Chu, H.Q., Shen, D.J., Chen, H.S. and Qin, S.N. 'Investigation of pore structure and mechanical property of cement paste subjected to the coupled action of freezing/thawing and calcium leaching'. *Cem. Concr. Res.* **109** (2018)133-146.

[3] Broadbent, S.R. and Hammersley, J.M. 'Percolation processes: I. Crystals and mazes'. *Math. Proc. Camb. Phil. Soc.* **53** (3)(1957)629-641.

[4] Quintanilla, J., Torquato, S. and Ziff, R.M. 'Efficient measurement of the percolation threshold for fully penetrable discs'. *J. Phys. A: Math. Gen.* **33** (2000)L399-L407.

[5] Li, J.T. and Östling M. 'Percolation thresholds of two-dimensional continuum systems of rectangles'. *Phys. Rev. E* **88** (2013)012101.

[6] Garboczi, E.J., Snyder, K.A. and Douglas, J.F. 'Geometrical percolation threshold of overlapping ellipsoids'. *Phys. Rev. E* **52** (1995)819-828.

[7] Xu, W.X., Su, X.L. and Jiao, Y. 'Continuum percolation of congruent overlapping spherocylinders'. *Phys. Rev. E* **94** (2016)032122.

[8] Li, M.Q., Chen, H.S. and Lin, J.J. 'Efficient measurement of the percolation threshold for random systems of congruent overlapping ovoids'. *Powder Tech.* (2019), doi: https:// doi.org/10.1016/j.powtec.2019.10.044.

[9] Meng, L.Y., Li, S.X., Lu, P., Li, T. and Jin, W.W. 'Bending and elongation effects on the random packing of curved spherocylinders'. *Phys. Rev. E* **81** (2012)061309.

[10] Yi, Y.B. and Sastry, A.M. 'Analytical approximation of the percolation threshold for overlapping ellipsoids of revolution'. *Proc. R. Soc. Lond. A.* **460** (2004)2353-2380.

[11] Lin, J.J., Chen, H.S. and Xu, W.X. 'Geometrical percolation threshold of congruent cuboidlike particles in overlapping particle systems'. *Phys. Rev. E* **98** (2018)012134.

[12] McLachlan, D.S., Blaszkiewicz, M. and Newnham, R.E. 'Electrical resistivity of composites'. *J. Am. Ceram. Soc.* **73** (8)(1990)2187-2203.

[13] McLachlan, D.S. 'An equation for the conductivity of binary mixtures with an isotropic structures'. *J. Phys. C: Solid State Phys.* **20** (1987)865-877.

[14] Christensen, B.J., Coverdale, R.T., Olson, R.A., Ford, S.J., Garboczi, E.J., Jennings, H.M. and Mason, T.O. 'Impedance spectroscopy of hydrating cement-based materials: measurement interpretation and application'. *J. Am. Ceram. Soc.* **77** (11)(1994)2789-2804.

[15] Tumidajski, P.J., Schumacher, A.S., Peron, S., Gu, P. and Beaudoin, J.J., 'On the relationship between porosity and electrical resistivity of cementitious system'. *Cem. Concr. Res.* **26** (4)(1996)539-544.

[16] Balberg, I., Anderson, C.H., Alexander, S. and Wagner, N. 'Excluded volume and its relation to the onset of percolation'. *Phys. Rev. B* **30** (7)(1984)3933-3943

DYNAMIC PACKING MODEL OF 2D FULLY-GRADED ARBITRARY SHAPED CONCRETE AGGREGATE

MU Song (1), XIE Deqing (1), LIU Jianzhong (1) and ZHANG Yunsheng (2)

(1) Jiangsu Sobute New Materials Co., Ltd., Nanjing 211100, China;

(2) College of Materials Science and Engineering, Southeast University, Nanjing 211189, China.

Abstract

The parameter equations of circle, Elliptic and arbitrary polymorphic were deduced by polar coordinates transformation in this paper, and a 2D reconstruction method of irregular particles based on cellular automata theory was introduced, briefly. The particles size and quantity information could be automatic computed by a sectional calculate and residual accumulation algorithm which was developed in this paper. The computed particles size and quantity information had a good agreement with the aggregate actual sieving curve. The corresponding dynamic packing model of 2D fully-graded arbitrary shaped concrete aggregate was further developed, and all kinds arbitrary shaped particles systems' limit accumulation states could be obtained by setting appropriate parameters. The limit packing density of circle particles system was the biggest, up to 79.59%.

Keywords: Concrete aggregate; Fully-graded; Dynamic packing model; Packing density; Numerical simulation

1. INTRODUCTION

As the most widely used civil engineering material, concrete mainly includes coarse aggregate, mortar and interface transition zone (ITZ) from microscopic perspective. The content, size, gradation, and shape of coarse aggregates have crucial effects on ion transport and mechanical properties of hardened concrete. Concrete coarse aggregate reconstruction and placement is a prerequisite for the numerical simulation of concrete. The following scholars at home and abroad have made outstanding contributions in this regard: In 1984 , Wittmann et al.[1] pioneered a multi-sides and multi-angulars random aggregate model. Z.M. Wang and A.K.H Kwan et al.[2] established another method for randomly generating polygon particles based on Monte Carlo method. Xu Wenxiang et al.[3] used the quadratic curve equation to control the production of two-dimensional elliptical particles, and established a corresponding hardened particle accumulation model. Gao Zhengguo and Liu Guangting[4] developed a two-dimensional random aggregate placement algorithm based on aggregate intrusion judgment criteria and aggregate area.

At present, the following problems exist in the numerical simulation of the coarse aggregate reconstruction and placement: (i) The particle size and quantity information cannot be automatically calculated based on the aggregate sieving curve; (ii) The maximum two-dimensional limit bulk density is only 70%[5]; (iii) There are still large discrepancies between round, elliptical, regular polygon particles and the actual crushed stone shape.

This paper develops a " sectional calculate and residual accumulation algorithm " based on C language, which could calculate the particle size and quantity information of the aggregate particles. The computed results had a good agreement with the aggregate actual sieving curve. This paper further establishes a random stacking and dynamic walking model, and all kinds arbitrary shaped particles systems' limit accumulation states could be obtained by setting appropriate parameters. For particle of a particular shape based the real screening curve, the maximum attempts number (N) and maximum walk steps(M) affect the maximum packing density of the " dynamic walking random packing model ". Setting the appropriate parameters, N = 100,000 and M = 1000, the particle system of arbitrary shaped can reach the limit maximum packing density, and the limit value of circular particle system is the highest, up to 79.59% , which is the largest value in related literature.

2. RECONSTRUCT AN ARBITRARY SHAPED AGGREGATE PARTICLE

2.1 Circular and elliptical particle

The key parameters for controlling circular particles are the center coordinate (x_i , y_i) and radius r_i. The governing equations as follows:

$$\begin{cases} x = r_i \times \cos\theta + x_i \\ y = r_i \times \sin\theta + y_i \end{cases} \quad (1)$$

Wherein, θ is the angle parameter [0,2π] of the standard circle .

The key parameters for controlling the ellipse particles are the central coordinates (x_i , y_i), the long semi-axis length F_b, the short semi-axis length F_b, the ratio of long semi-axis to minor semi-axis ratio R_{ab} and the rotated angle β. The governing equations as follows:

$$\begin{cases} x = F_a \times \cos\beta \times \cos\theta - F_b \times \sin\beta \times \sin\theta + x_i \\ y = F_a \times \sin\beta \times \cos\theta + F_b \times \cos\beta \times \sin\theta + y_i \end{cases} \quad (2)$$

Wherein, θ is the angle parameter standard elliptical [0,2π].

2.2. Regular polygon particles

The key parameters of regular polygon particles are the center coordinates (x_i, y_i), the radius of circumscribed circle R, and the number of sides N. The regular polygon particle should be rotated randomly by an angle β as a standard regular polygon has a certain orientation.

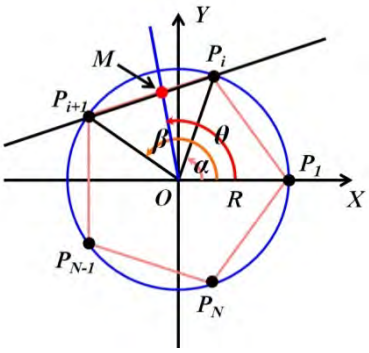

Figure 1: Regular polygon key parameters

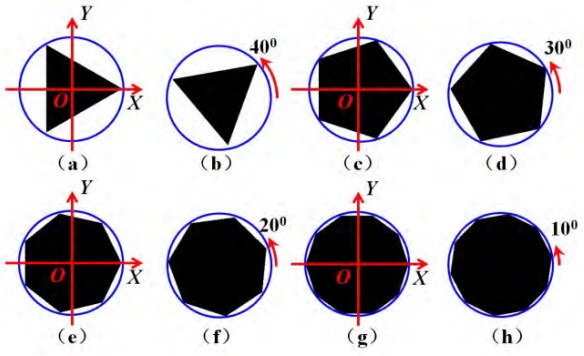

Figure 2: Reconstruction results

However, the inclination of the regular polygon equations could not descripted by a simple formula. The key is to find the parametric equation of point M in Fig. 1, its polar coordinates are (ρ , θ). Based on that the three points including point P_i , point P_{i+1} and point M on the same line, the polar coordinates of point M could be calculated as follows;

$$\begin{cases} x_M = \rho * \cos\theta = \cos\theta * \dfrac{R^2 * \cos\alpha * \sin\beta - R^2 * \cos\beta * \sin\alpha}{(R*\sin\beta - R*\sin\alpha)\cos\theta + (R*\cos\alpha - R*\cos\beta)\sin\theta} \\ y_M = \rho * \sin\theta = \sin\theta * \dfrac{R^2 * \cos\alpha * \sin\beta - R^2 * \cos\beta * \sin\alpha}{(R*\sin\beta - R*\sin\alpha)\cos\theta + (R*\cos\alpha - R*\cos\beta)\sin\theta} \end{cases} \quad (3)$$

Then, the parametric equation of a regular *N*-shaped particle with center coordinates (x_i, y_i), a circumscribed circle radius *R,* and an inclination angle γ is:

$$\begin{cases} x = x_M * \cos\gamma - y_M * \sin\gamma + x_i \\ y = x_M * \sin\gamma - y_M * \cos\gamma + y_i \end{cases} \quad (4)$$

In formulas (3, 4), the only variable is $\theta \in [0,2\pi]$; $\alpha = (i-1)*2\pi/N$、$\beta = i*2\pi/N$, which is controlled by θ .

Fig. 2 shows the regular polygon particles reconstructed by this algorithm. The reconstructed results show that the algorithm can be used to reconstruct rotation any regular polygon rotated by any angle.

2.3 Irregular particles

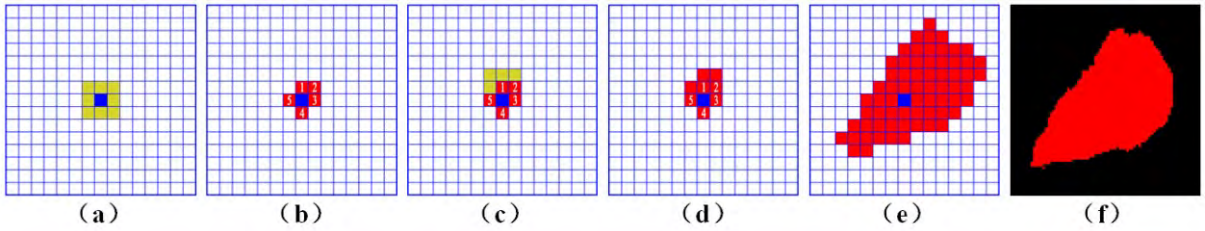

Figure 3: Using "central growth method" to reconstruct an irregular particle

Based on the principle of cellular automata[6] , this paper develops a two-dimensional irregular particle reconstruction rule, which is named "central growth method". The core steps are: Firstly, the coordinates of the first node in the list (i.e., central point) are read and the corresponding pixel is turned into a blue particle pixel, as shown in Fig. 3a. Its eight

neighbouring pixels highlighted in yellow colour are then activated and a set of eight probability values between 0 and 100 are generated for them sequentially based on a Monte Carlo simulation. The eight probability values are then compared with the corresponding characteristic values of the special irregular particles, respectively. If the pointed cell has a probability value smaller than its corresponding characteristic one, the cell would be turned into a part of the particle. As seen in Fig. 3b, five neighbours among the eight neighbouring pixels are turned into cement particle and their coordinates are delivered into the list one by one. Repeating the steps shown in Fig. 3a and b for these five neighbouring pixels, more neighbouring pixels can be classified into the cluster of cement particle, as shown in Fig. 3c and d. These steps are continuously operated on the activated neighbouring pixels until the target area of this particle is achieved. Fig. 3e illustrates an obtained irregular cement particle with 67 pixels, while Fig. 3f illustrates an obtained irregular cement particle with 2021 pixels.

2.4 Periodic boundary conditions

When particles are put into the sample space, the boundary conditions of the sample space need to be set. In this paper, periodic boundary conditions are selected[7]. The periodic boundary means that when the particles intersect with the boundary of the sample space, the particles outside the space need to be compensated to the opposite edge.

3. FULLY GRADED AGGREGATE DYNAMIC STACKING MODEL

3.1 Automatic calculation of aggregate particle information

This paper develops a "sectional calculate and residual accumulation algorithm" based on C language. This algorithm can calculate the particle size and quantity information of the aggregate particles by the real screening curve automatically. The core algorithm as follows: (a) Dividing the coarse aggregate screening curve into different intervals from big to small, as shown in Fig. 4. (b) Using linear screening method to calculate the interval sieve residual percentage. (c) Calculating the quantity of particle in this interval based on the aggregate size and the area of simulated space. (d) The less than one part is accumulated in the next interval.

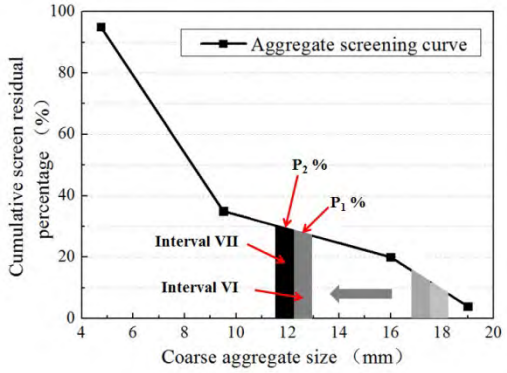

Figure 4: Automatic calculation diagram

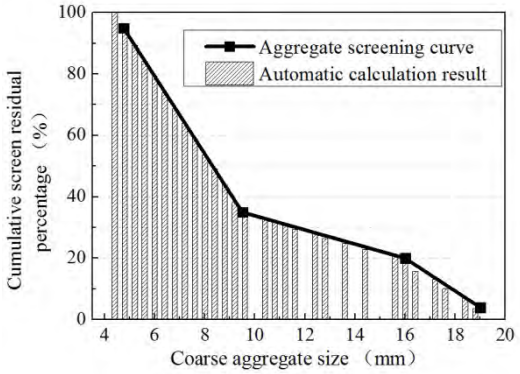

Figure 5: Automatic calculation result

The two-dimensional placement space used in this paper is 500 pixels × 500 pixels, corresponding to an actual size of 100mm × 100mm , each pixel represents 200μm. The specific information of particle size and number using the above algorithm to calculate, when the aggregate content is 80%, the width of the scanning interval is 0.4mm. The cumulative

sieving curve of the calculation results is plotted in Fig. 5, which shows that the particles information agrees well with the actual sieving curve.

3.2 Random stacking and Dynamic walking model

This paper further established a two-dimensional random stacking and dynamic walking model, Fig. 6 shows the flow chart of this model. The specific operation steps are as follows:

(1) Determining the size of the sample space based on the " triple principle " and the " minimum particle principle "[8]. For the coarse aggregate particle size is 4.4 ~ 18.8 mm, the final setting space size is 500 pixels × 500 pixels, corresponding to the actual size of 100 mm × 100 mm with a single pixel size is 200 μm;

(2) Calculating the particle size and quantity information of the aggregate particles based on the "regional calculation and residual accumulation algorithm".

(3) Developing a virtual space of appropriate size and reconstructing a particle of arbitrary shape in the virtual space, from big to small.

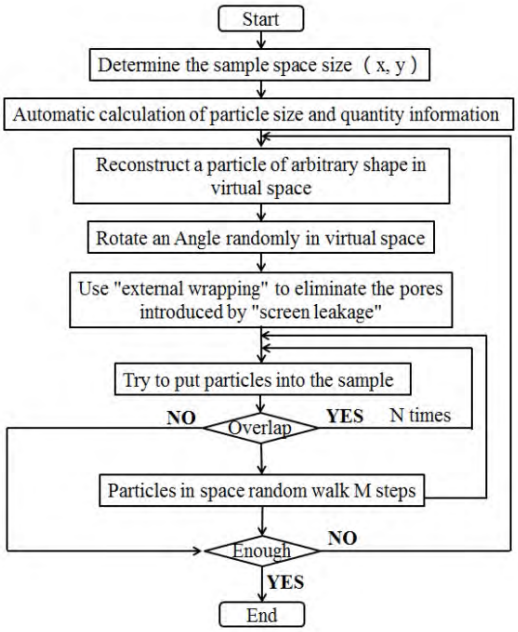

Figure 6: Flow chart of random stacking and dynamic walking model

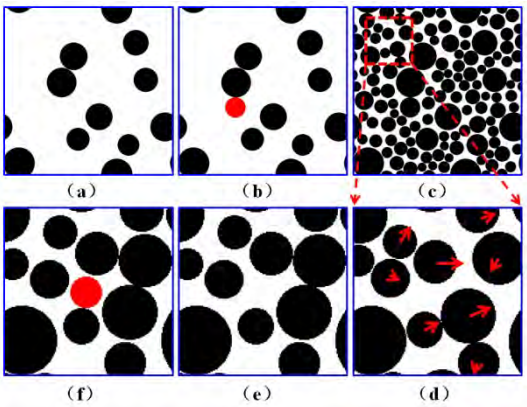

Figure 7: Schematic diagram of key steps

(4) In order to simulate the random distribution of aggregate particle orientation,the particle in the virtual space need to rotate a random angle. Using "out wrapping method" to eliminate internal pores generated during rotation by“ hourglass phenomenon ”[9].

(6) Randomly selecting a coordinate in sample space and throwing the particle at that position. If the particle overlaps with the particle that has been cast, then randomly select a coordinate again and try again. Fig. 7(b) shows that the 12th particle was successfully thrown , and Fig. 7(c) shows that 121particles have been thrown.

(7) When the number of attempts is greater than 100,000 times, it is still impossible to choose a suitable space to accommodate the particles to be dropped. The particles that have been dropped in the sample space need to be randomly moved *N* steps as shown in Fig. 7(d). Then, try to drop the particle again.

(8) When all the particles have been thrown into the space, or the next particles cannot be thrown after the moved particles have moved N steps, the program terminates.

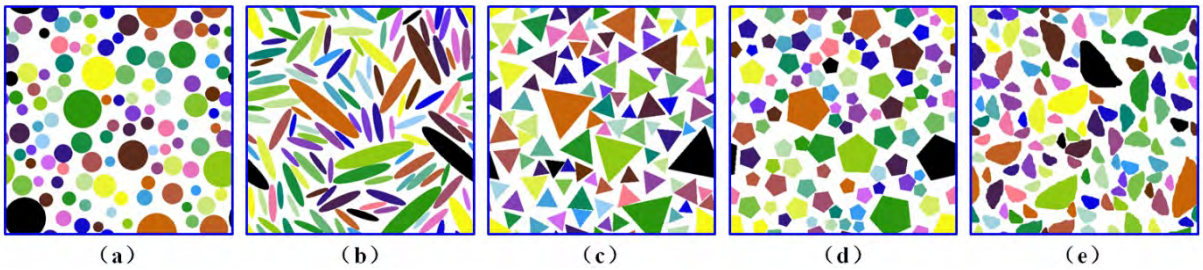

Figure 8: Reconstruction results of fully-graded aggregate particles of various shapes

The aggregate particle systems of different shapes are reconstructed by random stacking and dynamic walking model developed in this paper. The total aggregate content is 50% , which is consistent with the sieving curve in Fig. 4. The reconstruction results are shown in Fig. 8 , (a) circular particle, (b) elliptical particle (the ratio of the long axis to short axis is 5.0), (c) regular triangle, (d) Regular pentagon; (e) irregularly shaped particle. The particle information and the areas of small color particles in different figures are the same. Only the shape of the particles is different. As can be seen from the figure, the random stacking and dynamic walking model can be used to reconstruct arbitrary shape particle systems.

3.3 Maximum packing density

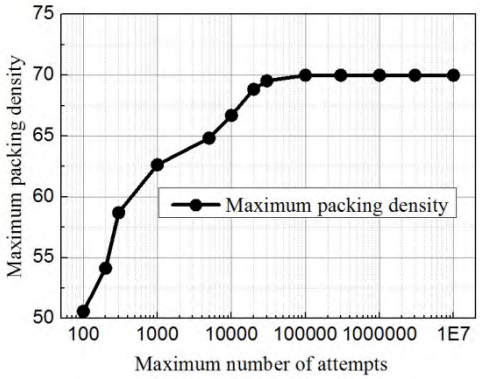

Figure 9: The impact of the maximum attempts number

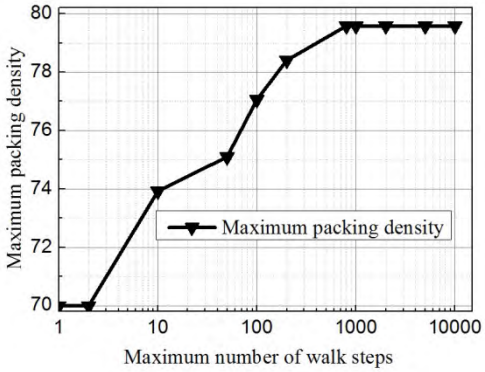

Figure 10: The impact of the maximum walk steps

For circular particle based the real screening curve shown in Fig. 4. The maximum attempts number and maximum walk steps affect the maximum packing density of the " dynamic walking random packing model ". Fig. 9 shows the impact of the maximum attempts number on the maximum packing density. As the maximum attempts number increasing, the maximum packing density increases, but the growth rate increase gradually decreases and there is a limit value. The maximum packing density is stable at the limit value, which is 70.00%, when the maximum attempts number is greater than 100,000. The impact of the maximum walk steps on the maximum packing density show the same pattern. The maximum packing density is stable at the limit value, which is 79.59% shown in Fig. 10, when maximum walk steps are greater than 1,000. Compared with the "static random stacking model", the maximum packing density of "Random stacking and Dynamic walking model"

reached nearly 80% , with the increase was nearly 10% , which is the largest value in related literature.

4. CONCLUSIONS

1. The governing equations of circular, elliptical and regular polygon particle were deduced in this paper. A "central growth method" based on the principle of cellular automata was developed in this paper to reconstruct irregular particle.
2. A sectional calculate and residual accumulation algorithm was developed in this paper was used to calculate the particle size and quantity information of the aggregate particles by the real screening curve automatically. The computed results had a good agreement with the aggregate actual sieving curve.
3. The corresponding dynamic packing model of 2D fully-graded arbitrary shaped concrete aggregate was further developed, and all kinds arbitrary shaped particles systems' limit accumulation states could be obtained by setting appropriate parameters. The limit packing density of circle particles system was the biggest, up to 79.59%.

ACKNOWLEDGEMENTS

This work was financially supported by the National Key Research and Development Project (2017YFB0309904), the Shandong Province United Fund (U1706222), the Scientific Research Project of Jiangsu Provincial Department of Housing and Urban Rural Construction (2018JH017), the Natural Science Foundation of Jiangsu Province (BK20171111, BK20181127).

REFERENCES

[1] Wittmann F H, Roelfstra P E, Sadouki H. Simulation and analysis of composite structures[J]. Materials science and engineering, 1985, 68(2): 239-248.

[2] Wang Z M, Kwan A K H, Chan H C. Mesoscopic study of concrete I: generation of random aggregate structure and finite element mesh[J]. Computers & Structures, 1999, 70(5): 533-544.

[3] XU Wenxiang, Chen Huisu, LV Zhong. A 2D elliptical model of random packing for aggregates in concrete[J]. Journal of Wuhan University of Technology-Mater. Sci. Ed., 2010, 25(4): 717-720.

[4] GAO Zhengguo, LIU Guangting. Two-dimensional random aggregate structure for concrete[J]. Journal of Tsinghua University (Science and Technology), 2004, 43(5): 710-714. (in Chinese)

[5] WU Liang, WANG Jing, MEI Kaihua. Automatic Generation of 2D Mesoscale Models for Fully-Graded Concrete[J]. Journal of Building Materials, 2015, 18(4): 626-632. (in Chinese)

[6] Wolfram S. Statistical mechanics of cellular automata[J]. Reviews of Modern Physics, 1983, 55(3): 601.

[7] Bernard F, Kamali-Bernard S. Predicting the evolution of mechanical and diffusivity properties of cement pastes and mortars for various hydration degrees–A numerical simulation investigation[J]. Computational Materials Science, 2012, 61: 106-115.

[8] Garboczi E J, Bentz D P. Computer simulation and percolation theory applied to concrete[J]. Annual Reviews of Computational Physics VII. 1999: 85.

[9] Jia X, Williams R A. A packing algorithm for particles of arbitrary shapes[J]. Powder Technology, 2001, 120(3): 175-186.

INVESTIGATION ON EFFECT OF TIME DEPENDENT SURFACE CHLORIDE CONCENTRATION ON APPARENT AVERAGE CHLORIDE DIFFUSION COEFFICIENT IN CONCRETE

Jiaqi Zhao (1,2), Zhihong Fan (1) and Jianbo Xiong (1)

(1) CCCC Fourth Harbor Engineering Institute Co., Ltd., Guangzhou, China

(2) School of Civil Engineering and Architecture, Guangxi University, Nanning, China

Abstract

The error function solution of Fick's second law assumes the constant surface chloride concentration, when it is used to calculate the apparent average chloride diffusion coefficient in concrete during the exposure period. However, the surface chloride concentration in concrete often vary with time. The purpose of this study is to investigate the effect of time dependent surface chloride concentration on apparent average chloride diffusion coefficient. A finite element analysis method was employed to simulate the chloride diffusion in concrete, which considering the time dependent surface chloride concentration and instantaneous chloride diffusion coefficient simultaneously. Then the chloride profiles were obtained at various exposure time, by which the apparent average chloride diffusion coefficient would be calculated. Meanwhile, the influences of various kinds of time-varying models of surface chloride concentration on the apparent average chloride diffusion coefficient were investigated. Finally, the rationality of the finite element analysis results was verified by comparing with field exposure test results. Results show that the time dependent surface chloride concentration has significant effect on the apparent average chloride diffusion coefficient.

Keywords: surface chloride concentration, apparent average chloride diffusion coefficient, instantaneous chloride diffusion coefficient

1. INTRODUCTION

The chloride-induced corrosion of steel bars embedded in reinforced concrete structures reduces the service life in chloride environment. It is widely recognized that both surface chloride concentration and chloride diffusion coefficient are two important parameters of quantitative analysis and design for durability of reinforced concrete structures [1].

The error function solution of Fick's second law has been widely to predict the chloride diffusion within concrete. One of the assumptions of the error function solution is constant chloride diffusion coefficient and constant surface chloride concentration [2]. The constant chloride diffusion coefficient is the average diffusion coefficient within a certain period of exposure time, which is different from the instantaneous diffusion coefficient, that is, the

diffusion coefficient at a certain exposure time [3]. The quantitative relationship between average diffusion coefficient and instantaneous diffusion coefficient has been proposed [4]. Unfortunately, the surface chloride concentration at a certain exposure time has been used to describe the boundary condition of chloride diffusion governing equation corresponding to a certain period of exposure time. This mistake will lead to a possible error when average diffusion coefficient was calculated by fitting the error function solution of Fick's second law.

The aim of this study is to investigate the effect of time dependent surface chloride concentration on apparent average chloride diffusion coefficient. A finite element analysis method was employed to simulate the chloride diffusion in concrete, which considering the time dependent surface chloride concentration and instantaneous chloride diffusion coefficient simultaneously. Then the chloride profiles were obtained at various exposure time, by which the apparent average chloride diffusion coefficient would be calculated. Meanwhile, the influences of various kinds of time-varying models of surface chloride concentration on the apparent average chloride diffusion coefficient were investigated. Finally, the rationality of the finite element analysis results was verified by comparing with field exposure test results.

2. FINITE ELEMENT ANALYSIS OF CHLORIDE DIFFUSION IN CONCRETE

2.1 Dual time-dependent Chloride transport model

Fick's second law is commonly used to describe the chloride diffusion within concrete. The assumptions of the error function solution of Fick's second law are constant chloride diffusion and constant surface chloride concentration. However, both the chloride diffusion coefficient and surface chloride vary with time in concrete. Therefore, the governing equation of chloride diffusion within concrete can be correctly expressed as

$$\frac{\partial C(x,t)}{\partial t} = D(t)\frac{\partial^2 C(x,t)}{\partial x^2} \tag{1}$$

where $C(x,t)$ is the chloride concentration (% by weight of concrete) at chloride diffusion depth x and age of concrete t; $D(t)$ is the instantaneous chloride diffusion coefficient.

The boundary conditions and initial conditions of the governing equation are defined as follows

$$C(0,t) = C_s(t); C(x,0) = C_0; C(L,t) = C_0 \tag{2}$$

where C_0 is the initial chloride concentration (% by weight of concrete); C_s is the time-varying surface chloride concentration (% by weight of concrete).

Riding et al. [5] proposed a computational model for surface chloride concentration as a function of t, which can be expressed as

$$C_s(t) = C_s^t \cdot \frac{\alpha \cdot t}{1 + \alpha \cdot t} \tag{3}$$

where C_s^t is the binder factor; α is time coefficient.

Tang and Gulikers [6] showed that instantaneous chloride diffusion coefficient decreased with the age of concrete and can be represented by a power function

$$D(t) = D_0(\frac{t_0}{t})^n \tag{4}$$

where t_0 is the age of concrete initially exposed to chloride environment, which is usually set to be 28 d; D_0 is the instantaneous chloride diffusion coefficient (m^2/s) at t_0, which is usually called initial diffusion coefficient; n is the aging factor of instantaneous chloride diffusion coefficient.

2.2 Finite element formulation of chloride transport model

Using Glaerkin weighted residual method [7], the finite element equation of chloride diffusion is obtained in matrix form for the element as

$$[M]^e\{\dot{c}\}^e+[K(t)]^e\{c\}^e=0 \tag{5}$$

where, $\{c\}^e$ is the element concentration vector, $\{\dot{c}\}^e$ is the derivative of element concentration vector, $[M]^e$ is the element mass matrix, $[K(t)]^e$ is the the element diffusion matrix. $[M]^e$ and $[K(t)]^e$ are given by

$$[M]^e=\int_l[N]^T[N]dx \tag{6}$$

$$[K(t)]^e=\int_l[\frac{dN}{dx}]^T D(t)[\frac{dN}{dx}]dx \tag{7}$$

where, $[N]$ is the shape function matrix. Using Lagrange interpolation function to describe the shape function, one gets

$$N_1(x)=\frac{x-l_e}{-l_e},N_2(x)=\frac{x}{l_e} \tag{8}$$

By substituting Eq. (8) in Eq. (6) and Eq. (7), one gets

$$M_{11}=\frac{l_e}{3},M_{12}=\frac{l_e}{6},M_{21}=\frac{l_e}{6},M_{22}=\frac{l_e}{3} \tag{9}$$

$$K_{11}=\frac{D(t)}{l_e},K_{12}=-\frac{D(t)}{l_e},K_{21}=-\frac{D(t)}{l_e},K_{22}=\frac{D(t)}{l_e} \tag{10}$$

Then, the finite element equation of chloride diffusion for the element can be expressed

$$\frac{l_e}{6}\begin{pmatrix}2&1\\1&2\end{pmatrix}\begin{Bmatrix}\dot{c}_i\\\dot{c}_j\end{Bmatrix}^{(e)}+\frac{D(t)}{l_e}\begin{pmatrix}1&-1\\-1&1\end{pmatrix}\begin{Bmatrix}c_i\\c_j\end{Bmatrix}^{(e)}=\{0\} \tag{11}$$

After element assembly for the entire mesh, a system of finite element equation in the time domain is obtained

$$[M]\{\dot{c}\}+[K(t)]\{c\}=0 \tag{12}$$

This is integrated in time using a finite difference aproximation, and then the iterative calculation format of Eq. (12) is established

$$\left([M]+\theta\Delta t[K]\right)\{C\}^{t+\Delta t}=\left([M]-(1-\theta)\Delta t[K]\right)\{C\}^t \tag{13}$$

where Δt denotes the time increment and θ denotes the relaxation coefficient.

3. EXPERIMENTAL PROCESSES

3.1 Materials and specimens

The cement used was the Ordinary Portland cement (P.O. 52.5). The fine aggregate used in this study was river sand with fineness modulus of 2.51 and the apparent density of 2650 kg/m^3. The coarse aggregate used in this study was crushed granite with the maximum size of 20 mm and the apparent density of 2640 kg/m^3. Water to cement ratios of concretes were varied as 0.45, 0.50 and 0.55. The concrete cube specimens for each mix proportion with the size of 150×150×150 mm were demolded 24 hours after casting, then cured in a standard curing room for 28 days.

3.2 Exposure condition

The specimens were exposured to the tidal zone of the marine site in Zhanjiang, China. Zhanjiang is a coastal city at the southwestern end of Guangdong Province, which is shown in Fig.1. The detailed condition of Zhanjiang exposure site is shown in Fig.2. Chloride in the sea water were ranging from 23.3 to 30.2 g/l. The annual maximum tempreature at this site is 35.9 ℃, the annual minimum tempreature is 4 ℃, and annual average tempreature is 23.3 ℃. The annual average relative humidity is 83.6 %.

Figure 1: Geographical location of the marine site

Fig. 2. Concrete specimens in tidal zone

3.3 Tested program

After exposure period of 3, 5 and 10 year in the tidal zone, the concrete was dry drilled to obtain the concrete power at different depths from the outer surface to the inner. The concrete specimen surface was not sealed with epoxy so that chloride penetration into the concrete specimen at three-dimensional direction. To ensure chloride diffusion in concrete confirms to one-dimensional diffusion law, the sampling areas were at the centre of the cube specimen. The acid-soluble chloride test was performed, according to Chinese Industry Standard JTJ 270-98.

4. RESULTS AND DISCUSSION

4.1 Apparent average diffusion coefficient

Taking $D_0 = 19\times10^{-12}$ m^2/s, $n = 0.1$, $C_s^t = 0.8\%$ and $\alpha = 0.29$ as an example here, the chloride profiles at 0.076a, 0.2a, 0.3a, 0.4a, 0.5a, 1a, 2a, 3a, 5a, 10a were respectively simulated by finite element analysis method (FEM) mentioned above. Furthermore, the apparent average diffusion coefficient D_a and constant surface chloride diffusion coefficient C_s were determined by fitting the chloride profile at arbitrary age t in terms of the error function solution (ERFC)

of Fick's second law. The predicted results of the FEM agree well with the ERFC, as shown in Fig. 3.

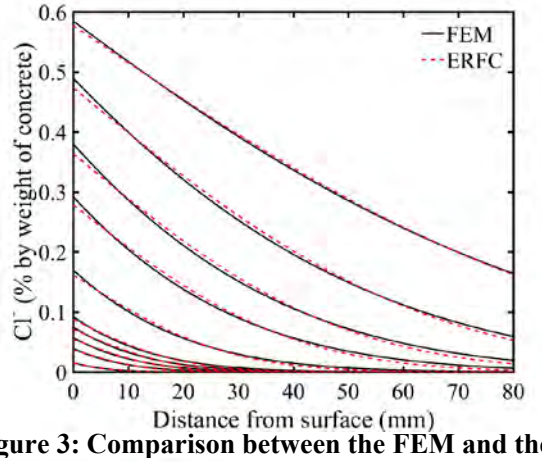

Figure 3: Comparison between the FEM and the ERFC

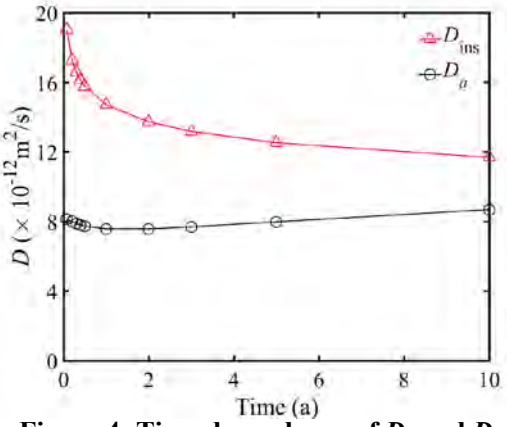

Figure 4: Time dependency of D_a and D_{ins}

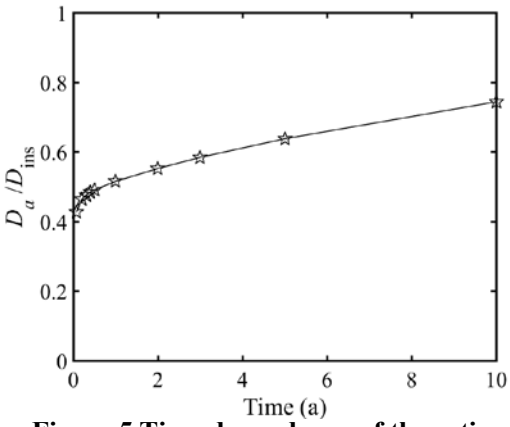

Figure 5 Time dependency of the ratio of D_a to D_{ins}

According to the relationship between instantaneous diffusion coefficient (D_{ins}) and D_0 shown in Eq. (4), D_{ins} at arbitrary age can be obtained. The time dependency of D_a and D_{ins} are given in Fig. 4. As shown in Fig. 4, D_{ins} decreases with the age of concrete, whereas D_a decreases first and then increases with the age of concrete. There are significant differences between the two dependencies. The time dependent relationship between D_a and D_{ins} is shown in Fig. 5. As shown in Fig. 5, the ratio of D_a to D_{ins} is less than 1 and the ratio increases with the age of concrete, which indicates that the value of D_a is almost less than D_{ins} and approaching the D_{ins}.

4.2 Influence of C_s on apparent average chloride diffusion coefficient

In recent years, several C_s models have been developed to investigate the influence of age of concrete on C_s. Petcherdchoo [8] proposed a square root model to describe the time dependent C_s. Arorap et al. [9] adopted exponential fuction to exhibit the time-dependent behavior of C_s. The detailed informance of time-dependent model for C_s are listed in Table 1. The inverse function expressed in Eq. (3) was adopted in the example above.

The parameters of square root model and exponential model were estimated by means of a nonlinear regression analysis of the C_s time-varying curve about time in the example above. The values

of the parameters are illustrated in Table 2. The time-dependent curves of the C_s models above are shown in Fig. 6, which indicates that the curves of both square root model and exponential model are close to the curve of inverse model.

Table 1: Typical time-varying models of C_s

Model type	Expression	Reference
Square root	$C_s(t) = C_s^t \cdot \sqrt{t}$	[8]
Exponential	$C_s(t) = C_s^t \cdot \left(1 - e^{-\alpha \cdot t}\right)$	[9]
Inverse	$C_s(t) = C_s^t \cdot \dfrac{\alpha \cdot t}{1 + \alpha \cdot t}$	[5]

Table 2: Values of parameters for C_s models

Model type	C_s^t	α
Square root	0.194	-
Exponential	0.608	0.327
Inverse	0.800	0.290

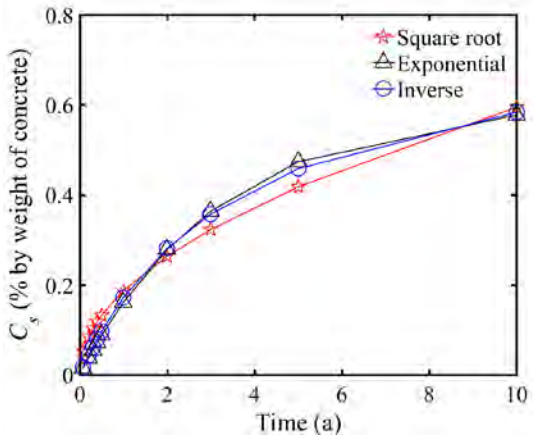

Figure 6: Time-varying behaviour of Cs

Many studies have shown that the time-varying behaviour of chloride diffusion coefficient depends on the aging factor n [10, 11]. A wide range of n was considered in this study, which varies from 0.1 to 0.6. Influences of three kinds of time-varying models of surface chloride concentration on the apparent average chloride diffusion coefficient are shown in Fig. 7. It shows that D_a obtained by the exponential or inverse model first decreases and then increases with increasing age of concrete, when n is equal to 0.1. But D_a decreases with increasing age of concrete, when n is larger than 0.1. In comparison, D_a obtained by the square root model always decreases with increasing age of concrete.

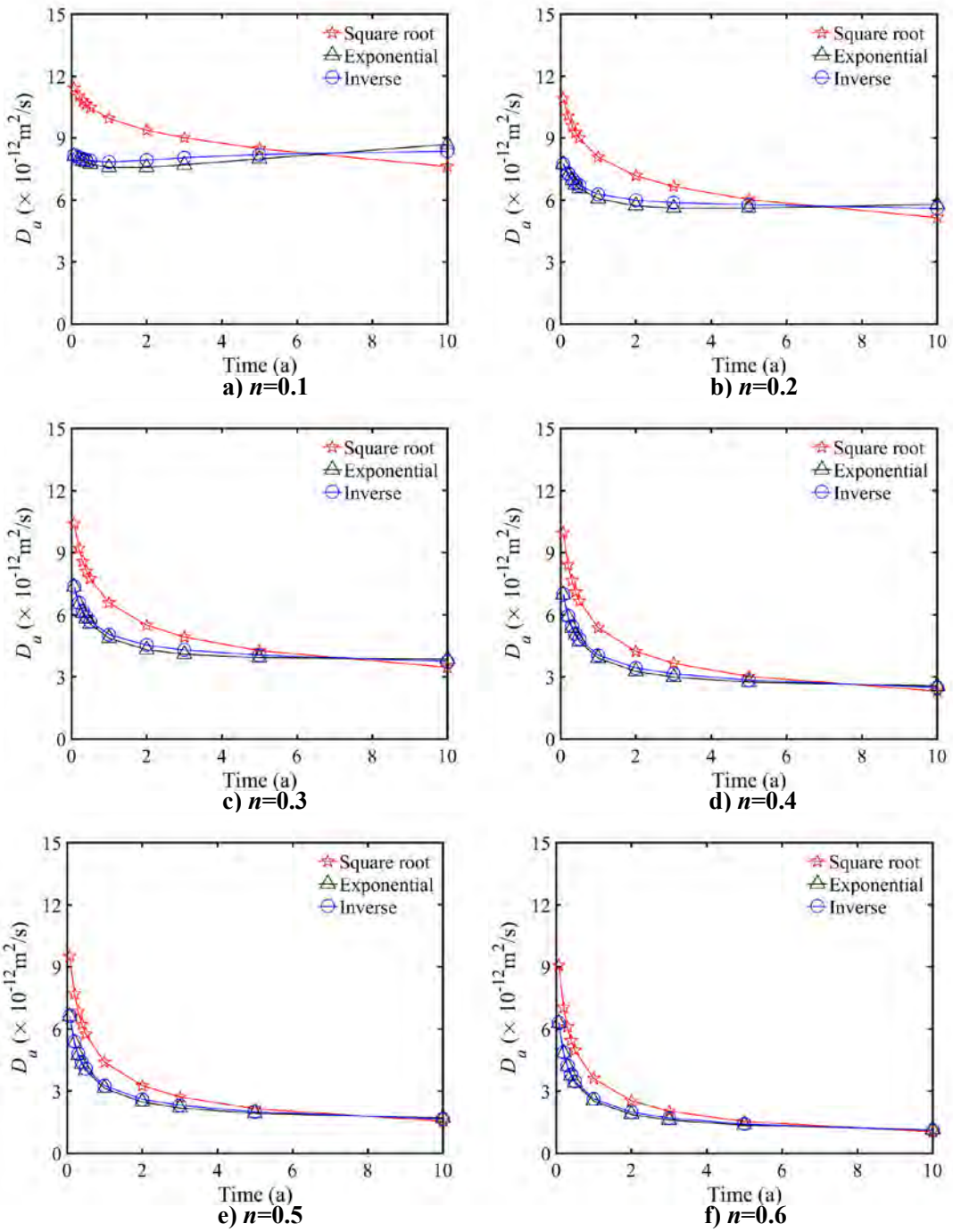

Figure 7: Influence of time-varying behaviour of C_s on D_a

4.3 Comparison between field exposure test results and FEM analysis results

Field data of chloride concentration distribution were employed to determine the apparent average diffusion coefficient D_a in terms of the error function solution (ERFC) of Fick's second law. The concrete mixture proportions and fitted parameters of ERFC are listed in Table 3.

The time-dependent curves of C_s and D_a are shown in Fig. 8. It is clear that C_s increases with increasing age of concrete, which is consistent with the time-varying behaviour of C_s.

When water-to-cement ratio is equal to 0.45, D_a decreases with increasing age of concrete. However, D_a first decreases and then increases with increasing age of concrete, when water-to-cement ratio (W/C) is larger than 0.45. This is due to the fact that n is inversely proportional to W/C [12], and a larger W/C-value will result in a smaller n-value. Hence, the time-varying behavior of D_a obtained by field exposure test results is consistent with FEM analysis results.

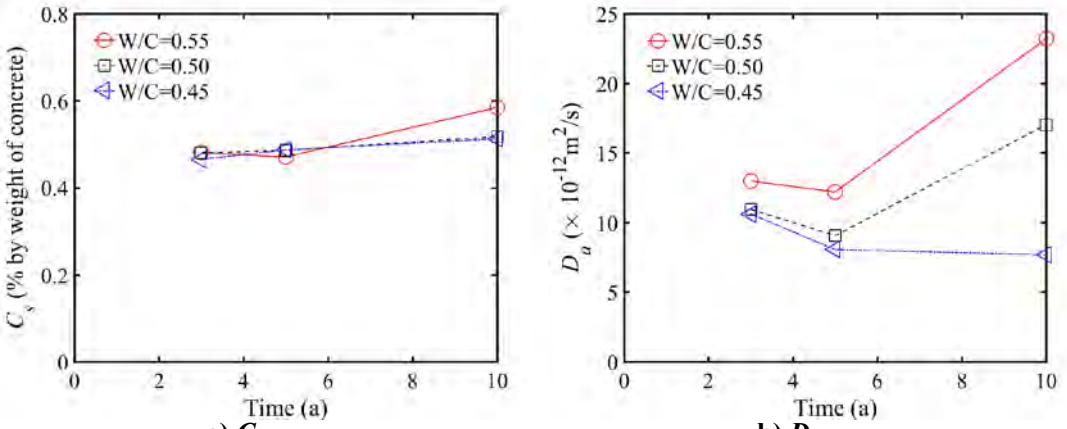

a) C_s **b) D_a**

Figure 8: Time-varying behaviour of C_s and D_a

Table 3: Concrete mixture proportions and fitted parameters of ERFC

No.	D_a			C_s		
	3-year	5-year	10-year	3-year	5-year	10-year
I45	10.62	8.06	7.68	0.465	0.487	0.512
I50	10.94	9.06	17.01	0.479	0.486	0.517
I55	12.97	12.19	23.19	0.481	0.470	0.584

5. CONCLUSIONS

The influences of various kinds of time-varying models of surface chloride concentration on the apparent average chloride diffusion coefficient were investigated. According to analysis results, the following conclusions can be drawn:

- The time dependent surface chloride concentration has significant effect on the apparent average chloride diffusion coefficient at early age of concrete.
- If the value of aging factor is less than 0.1, the apparent average diffusion coefficient first decreases and then increases with increasing age of concrete, which is calculated by using the exponential or inverse model. Otherwise, the apparent average diffusion coefficient decreases with increasing age of concrete. In contrast, the apparent average diffusion coefficient always decreases with increasing age of concrete, which is calculated by using the square root model.

ACKNOWLEDGEMENTS

Thanks for the support by CCCC Fourth Harbor Engineering Institute Co., Ltd., and Guangxi University. The financial support received from the National Natural Science Foundation of China (51678165 and 51668008) is gratefully acknowledged.

REFERENCES

[1] Li K, Chen Z, Lian H. *Concepts and requirements of durability design for concrete structures: an extensive review of CCES01*. Materials and Structures, 2008, 41(4): 717-731.

[2] Yu Z, Ye G. *New perspective of service life prediction of fly ash concrete*. Construction and Building Materials, 2013, 48(11): 764-771.

[3] Song L G, Sun W, Gao J M. *Time dependent chloride diffusion coefficient in concrete*. Journal of Wuhan University of Technology (Materials Science Edition), 2013, 28(2): 314-319.

[4] Stanish K, Thomas M. *The use of bulk diffusion tests to establish time-dependent concrete chloride diffusion coefficients*. Cement and Concrete Research, 2003, 33(1): 55-62.

[5] Riding K A, Thomas M D A, Folliard K J. *Apparent diffusivity model for concrete containing supplementary cementitious materials*. ACI Materials Journal, 2013, 110(6): 705-714.

[6] Tang L, Gulikers J. *On the mathematics of time-dependent apparent chloride diffusion coefficient in concrete*. Cement & Concrete Research, 2007, 37(4):589-595.

[7] Martın-Pérez B, Pantazopoulou S J, Thomas M D A. *Numerical solution of mass transport equations in concrete structures*. Computers and Structures, 2001, 79: 1251-1264.

[8] Petcherdchoo A. *Time dependent models of apparent diffusion coefficient and surface chloride transport in fly ash concrete*. Construction and Building Materials, 2013, 38(1): 497-507.

[9] Arorap P, Popov B N, Haran B, et al. *Corrosion initiation time of steel reinforcement in a chloride environment – A one dimensional solution*. Corrosion Science, 1997, 39(4): 739-759.

[10] Li K, Zhang D, Li Q, et al. *Durability for concrete structures in marine environments of HZM project: Design, assessment and beyond*. Cement and Concrete Research, 2019, 115: 545-558.

[11] Andrade C, Castellote M, Andrea R. *Measurement of ageing effect on chloride diffusion coefficients in cementitious matrices*. Journal of Nuclear Materials, 2011, 412(1):209-216.

[12] Zhang J Z, Zhao J, Zhang Y, et al. *Instananeous chloride diffusioncoefficient and its time dependency of concrete exposed to a marine tidal enviroment*. Construction and Building Materials, 2018, 167: 225-234.

MODELLING COMPRESSIVE BEHAVIOUR OF CEMENT PASTE WITH SUPERABSORBENT POLYMER

Shengying Zhao (1), Xinchun Guan (1) and Guofu Qiao (1)

(1) School of Civil Engineering, Harbin Institute of Technology, China

Abstract

Superabsorbent polymer (SAP) can modify the microstructure and influence the mechanical properties of cement paste in at least two ways: while cavities left by SAP increase the total porosity, water released by SAP affects the hydration degree of the surrounding paste. As a starting point for investigation into the overall effect, this study presents a numerical model comprised of spherical voids, affected zones, and the unaffected matrix. In comparison, a binary model consisting only of the voids and the unaffected matrix is built up. Compressive loads are applied to both paste models. The results show that in either model a considerable negative normal stress (compressive) is typical in the middle part of SAP pore walls. The void-surrounding area subject to positive normal stress seems to be larger in the SAP-containing paste than in the other one. Nevertheless, there is a 10% reduction in maximum principal stress caused by the tougher affected zone.

Keywords: cement paste; superabsorbent polymers; numerical modelling; mechanical behaviour

1. INTRODUCTION

The principle of water entrainment by superabsorbent polymers (SAP) was elucidated on the basis of Power's model [1]. Since then, knowledge of how SAP influences mechanical properties of properties has become critical for the design of SAP-containing cement mortar and concrete. For example, one of the goals of incorporating SAP into concrete is to enhance its frost scaling resistance by means of the air void system. This goal is less likely to achieve if the mature concrete before being subjected to freezing-thawing cycles has too low a strength [2]. Intensive research has thus been revolving around whether SAP compromises the mechanical property of concrete [3–6].

The mechanical property of concrete can be affected by the addition of SAP in at least two ways. On the one hand, SAP particles shrink when releasing water as the hydration of cement goes on. The space once taken by swollen SAP particles partially or fully becomes air voids [7]. As a rule of thumb, every percent of air in concrete reduces the compressive strength by approximately 5% relative to air-free concrete [8]. As there have been numerous comparative studies on the mechanical behaviour of air-free concrete and concrete where air is entrained

by traditional air-entraining agent, the influence of air voids on the mechanical behaviour of concrete is without the scope of the present paper.

On the other hand, the cement paste becomes internally cured by the released water [9]. In a w/c = 0.3 hardened cement paste, the porosity of an internal curing zone (i.e. cement paste within the travel distance of the released water, as distinguished by red dye) is reported to be 55% lower than that of an unaffected zone, and the degree of hydration of an internal curing zone is comparable to that of a w/c = 0.34 paste without SAP [10].

It therefore seems that difference in mechanical behaviour of a SAP-containing cement paste and an air-entrained cement paste lies in the internal curing zone. The aim of this paper is to investigate by numerical approach how this mechanically strengthened zone can make a difference on the mechanical property of an air-entrained cement paste. The mechanical responses under compressive loads are to be observed by comparing two models under numerical compressive load, one with a strengthened zone between the air void and the cement matrix while the other one without.

2. MODELLING APPROACH

2.1 Consideration over material property

Cement paste with SAP comprises three parts: air voids left by SAP, internal curing zone, and matrix unaffected by internal curing. These phases are distinguished by various elastic modulus in this study. By indentation, Wang et al. determined found that the microhardness of the SAP void wall is 1.4 times that of the unaffected matrix [10]. The data regarding the elastic moduli of different phases is not reported, though. However, in non-metallic materials, a large fraction of the indentation deformation is elastic, so microhardness and elastic modulus are not totally independent. A case in point is the almost linear correlation found by Velez et al. between hardness and elastic moduli of pure constituents of Portland cement clinker [11], see Fig. 1. On this basis it is assumed that the elastic modulus, just as microhardness, decreases as the distance from the SAP void increases.

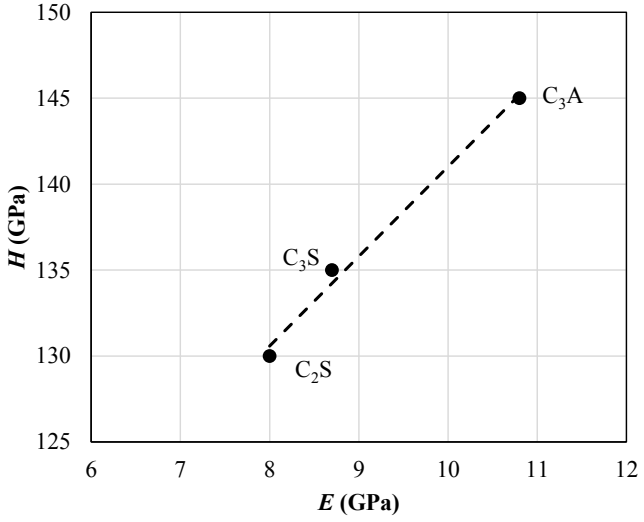

Figure 1: Correlation between hardness *H* and elastic modulus *E* of C_3S, C_2S and C_3A, plotted after data in [11]

2.2 Model set-up

Two cement models are built in commercial software Abaqus. Model 1 is a simulation of cement paste with traditional air-entraining agent. It is built by removing 27 spheres from a 1 mm^3 cube. All the air voids have a diameter of 150 μm and they altogether account for 4.8% of the cube volume.

Model 2 simulates a SAP-containing hardened cement paste. It includes both the air voids and the internal curing zones. A gradient of elastic modulus is generated in the following way. First, 27 spheres each with a diameter of 270 μm are removed from a 1 mm^3 cube, leaving 27 voids. Inside each void, a hollow sphere with outer diameter (D) 270 μm and inner diameter (d) 210 μm is inserted to mimic the outer part of the internal curing zone. Likewise, another hollow sphere (D=210 μm, d=150 μm) is inserted to mimic the inner part of the internal curing zone. This means that the internal curing zone is 60 μm in thickness, which is a typical value, as found by Mönnig [12].

In each model, Possion's ratio is assumed to be 0.25 for each solid phase. The dimension and elastic modulus of each phase are shown in Fig. 2.

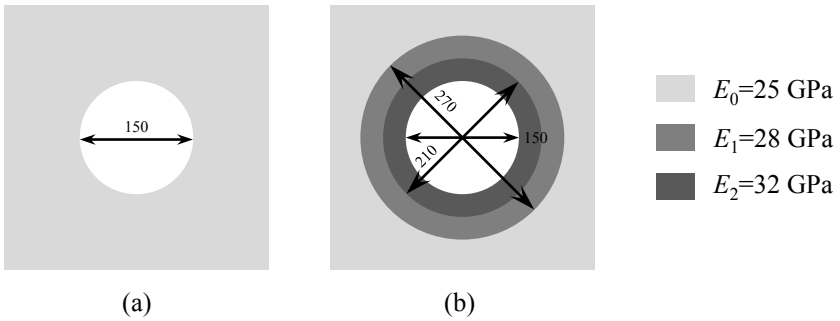

Figure 2: Dimension of SAP voids, dimension of the internal curing zones (in μm) and assigned elastic moduli to solid phases in (a) Model 1 and (b) Model 2

For each model, uniaxial compressive test is performed by applying an evenly distributed load (50 N/mm^2) at one side and fixing the deformation of the opposite side. Fig. 3 shows the boundary condition, loading and meshing of Model 2.

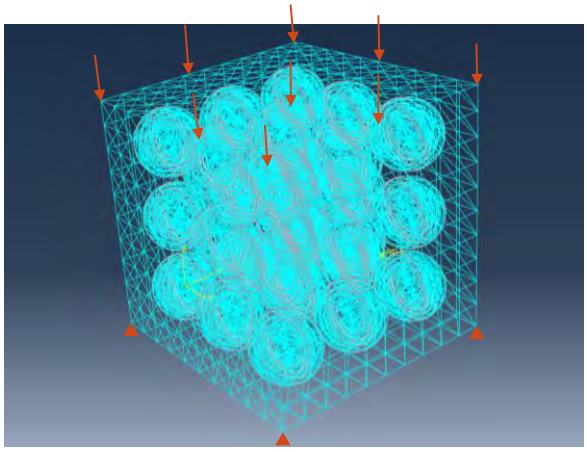

Figure 3: The meshed Model 2, where the surfaces of spheres (D=270 μm) denote the largest distance water released by SAP can travel

3. RESULTS AND DISCUSSION

3.1 Maximum principal stress

The maximum principal stress S is often used as a measure to evaluate the failure strength of brittle materials under one-dimensional compression. The largest S in Model 1 is found to be 44.3 MPa, whereas this value for Model 2 is 40.2 MPa, approximately 10% lower than that in Model 1. Fig. 4 plots the maximum principal stress distribution in Model 2. Both models display a similar pattern of distribution of maximum principal stress. This means that under uniaxial compressive load the crack propagation is alike for air-entrained cement paste and SAP-containing cement paste with the exactly same location, size and number of air voids, and that the SAP-containing model is likely to withstand a larger evenly distributed load due to the strengthened zone between the air voids and the cement matrix.

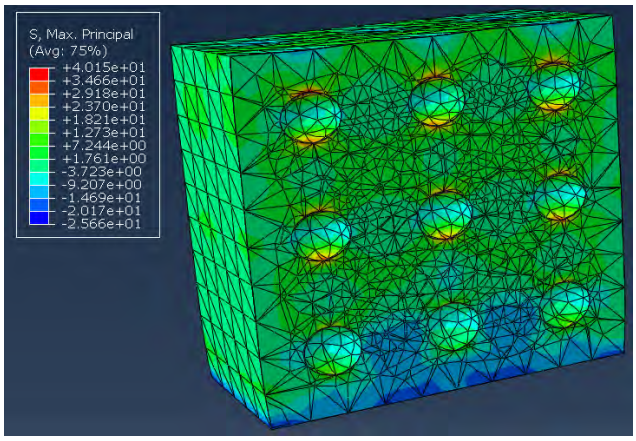

Figure 4: Distribution of maximum principal stress in Model 2 (in MPa). The section in display is parallel to the loading direction.

It should be mentioned the load bearing capacity improvement may vary greatly according to a number of factors. For example, we positioned the SAP voids in such a way that the affected zones of two SAP particles don't overlap. However, when the spacing of air voids is smaller, it is of course possible that a point in the cement matrix is internally cured by water released from more than one SAP particle, and that the elasticity of such a point is even higher than E_2. More cases are to be studied to attain a comprehensive knowledge of how maximum principal stress is affected by air void content, thickness of affected zone, etc.

3.2 Normal stress in the loading direction

Both models are sectioned parallel to the loading direction, and the distribution of the normal stress within the sections in the loading direction S_{yy} is plotted in Fig. 5. In each model, there is a blue band going across the middle of each air void perpendicular to the loading direction, which denotes a compressive stress ($S_{yy}<0$). However, S_{yy} at the top and bottom of each void in each model is above zero, meaning a tensile stress which decreases with the increased y distance from the air void.

Comparing Fig. 5 (a) and (b), it seems that the $S_{yy}>0$ region (in red and yellow) in the vicinity of air voids is larger in volume in Model 2 than in Model 1. Accordingly, the strengthened internal curing zone might increase the volume of region subjected to tensile stress.

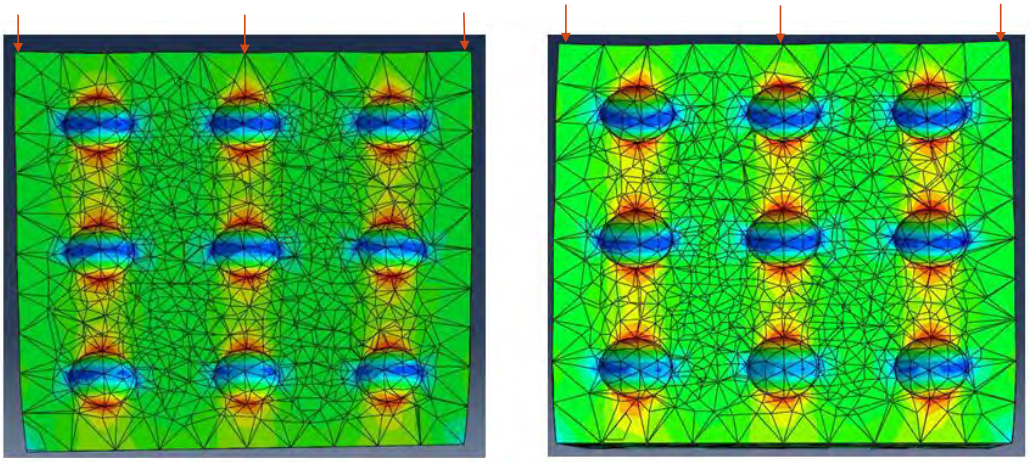

(a) (b)

Figure 5: Distribution of S_{yy} in (a) Model 1 and (b) Model 2

3.3 Comments

The gradient in normal stress sustained by cement paste around an air void is quite pronounced in both models, as shown in Fig. 5. However, there is not much difference in maximum principal stress at an affected zone and at its neighbouring unaffected zone. This implies that results from this study are still not sufficient to determine the fracture behaviour of the internal curing zone or to evaluate the load bearing capacity. Moreover, the maximum-principal-stress criterion postulates that the growth of the crack will occur in a direction perpendicular to the maximum principal stress [13]. As a continuous criterion, it fails to register the discreteness of the numerical modelling of the crack-extension procedure. As such, more detailed investigation concerning how cracks propagate is in need for a better understanding the mechanical behaviour of cement paste with SAP by means of e.g. the lattice fracture model [14–16].

4. CONCLUSIONS

Two numerical models are built for FEM analysis done by Abaqus. One simulates air-entrained cement paste, while the other simulates SAP-containing cement paste. Both models have a porosity of 4.7% and the same loci for the air voids. The only difference between the two models is that in the second one the air voids are encapsulated by two layers of strengthened internal curing zones with elastic modulus higher than the cement matrix. This paper does not conclude if SAP has a positive effect on overall mechanical property of cement paste, but some findings from computational uniaxial loading might be useful:

- The maximum principal stress distribution pattern in the air-entrained cement paste is similar to that in the cement paste with SAP.
- In the present paper, the largest value of maximum principal stress is reduced by 10% in by the increased elastic modulus of the internal curing zone. The reduction is subject to e.g. thickness of affected zone.
- Strengthening the mechanical property of the cement paste near the air voids can increase the volume of zones subject to tensile normal stress along the loading direction.

– It is of further interest to investigate how the mechanical behaviour changes according to air void parameters. Fracture analysis under stepwise loading might be promising towards a better understanding of the deterioration process of cement-based materials with SAP.

ACKNOWLEDGEMENTS

This study is funded by National Key Research and Development Program of China (Grant No. 2018YFC0705404) and National Natural Science Foundation of China (Grant No. 51778189).

REFERENCES

[1] Jensen, O.M. and Hansen, P.F., 2001. Water-entrained cement-based materials: I. Principles and theoretical background. Cement and concrete research, 31(4), pp.647-654.

[2] Valenza II, J.J. and Scherer, G.W., 2007. A review of salt scaling: I. Phenomenology. Cement and Concrete Research, 37(7), pp.1007-1021.

[3] Esteves, L.P., Cachim, P. and Ferreira, V.M., 2007. Mechanical properties of cement mortars with superabsorbent polymers. Advances in Construction Materials 2007 (pp. 451-462). Springer, Berlin, Heidelberg.

[4] Klemm, A.J. and Sikora, K.S., 2013. The effect of superabsorbent polymers (SAP) on microstructure and mechanical properties of fly ash cementitious mortars. Construction and Building materials, 49, pp.134-143.

[5] Farzanian, K., Teixeira, K.P., Rocha, I.P., Carneiro, L.D.S. and Ghahremaninezhad, A., 2016. The mechanical strength, degree of hydration, and electrical resistivity of cement pastes modified with superabsorbent polymers. Construction and Building Materials, 109, pp.156-165.

[6] Hasholt, M.T., Jensen, O.M., Kovler, K. and Zhutovsky, S., 2012. Can superabsorent polymers mitigate autogenous shrinkage of internally cured concrete without compromising the strength?. Construction and Building Materials, 31, pp.226-230.

[7] Justs, J., Wyrzykowski, M., Bajare, D. and Lura, P., 2015. Internal curing by superabsorbent polymers in ultra-high performance concrete. Cement and Concrete Research, 76, pp.82-90.

[8] S. Popovics. Strength and related properties of concrete – a quantitative approach. John Wiley & Sons Inc. (1998)

[9] Hasholt, M.T., Jespersen, M.H.S., Jensen, O.M., 2010. Mechanical properties of concrete with SAP. Part I: Development of compressive strength. In: International RILEM conference on use of superabsorbent polymers and other new additives in concrete. RILEM publications.

[10] Wang, F., Yang, J., Hu, S., Li, X. and Cheng, H., 2016. Influence of superabsorbent polymers on the surrounding cement paste. Cement and Concrete Research, 81, pp.112-121.

[11] Velez, K., Maximilien, S., Damidot, D., Fantozzi, G. and Sorrentino, F., 2001. Determination by nanoindentation of elastic modulus and hardness of pure constituents of Portland cement clinker. Cement and Concrete Research, 31(4), pp.555-561.

[12] S. Mönnig, Superabsorbing additions in concrete: applications, modeling and comparison of different internal water sources, PhD Thesis, University of Stuttgart, Stuttgart, 2009.

[13] Aliabadi, M.H., Boundary element methods in linear elastic fracture mechanics. Comprehensive Structural Integrity, Volume 3, 2003, Pages 89-125

[14] Schlangen, E. and Van Mier, J., 1992. Experimental and numerical analysis of micromechanisms of fracture of cement-based composites. Cement and concrete composites, 14(2), pp.105-118.

[15] Qian, Z., Multiscale modeling of fracture processes in cementitious materials. PhD thesis, Delft University of Technology, Delft, 2012.
[16] Zhang, H., Gan, Y., Xu, Y., Zhang, S., Schlangen, E. and Šavija, B., 2019. Experimentally informed fracture modelling of interfacial transition zone at micro-scale. Cement and Concrete Composites, 104, p.103383.

MODELLING EFFECT OF COARSE AGGREGATES ON OXYGEN TRANSPORT AND CORROSION PRODUCTS PRECIPITATION IN REINFORCED CONCRETE

Zhidong Zhang (1) and Ueli M. Angst (1)

(1) ETH Zurich, Institute for Building Materials, 8093 Zurich, Switzerland

Abstract

The structure of concrete, in particular the microstructure of the steel-concrete interface (SCI), can significantly affect corrosion of rebars. To support corrosion, oxygen needs to diffuse from the ambient environment to the steel surface. Meanwhile, corrosion products transport through the SCI and precipitate in concrete. Transport properties of concrete play an important role in these two processes. However, the effect of the heterogeneous structure of concrete especially coarse aggregates on oxygen transport and corrosion products precipitation in reinforced concrete is rarely studied in the literature. This study employed a numerical model to investigate such effect. Simulation domains in 2D were created with different aggregate contents and sizes. The model included oxygen diffusion, ions diffusion and migration, corrosion products oxidation and precipitation. The simulation results showed that the presence of aggregates significantly reduces oxygen diffusion. It becomes more pronounced for high aggregate contents which lead to more corrosion products formed at the interface. Furthermore, results showed that the interfacial transition zone (ITZ) around aggregates can enhance oxygen diffusion.

Keywords: aggregates, oxygen diffusion, corrosion products, reinforced concrete, kinetic reaction

1. INTRODUCTION

Corrosion of reinforced concrete structures subjected to the natural environment is one of the major concerns about the durability issues. When pH in concrete decreases caused by carbonation, or when chloride penetrates into concrete with liquid water, corrosion is apt to occur at the steel-concrete interface (SCI) (1). To evaluate the degradation of reinforced concrete, the effect of concrete structure, especially the SCI, must be well understood (2).

To construct the concrete structure for numerical modelling, concrete is generally viewed as a composite material with three components, including coarse aggregates, interfacial transition zone (ITZ), and mortar matrix (cement paste with fine aggregates). The mortar matrix is treated as a homogeneous medium. This approach works well for the macroscopic scale, but for the

mesoscopic and microscopic scales, we suggested to obtain the simulation domain from SEM-BSE images of the SCI (3).

In a composite material, coarse aggregates are commonly considered as impermeable and excluded in the simulations. It has been well known that the aggregate content and shape can significantly affect water and ions transport in concrete. Abyaneh et al., (4) used a 3D model to study the effect of the shape and orientation of aggregates on water transport and reported that the transport decreased when spherical aggregate particles were replaced with ellipsoidal particles due to the consequent increase in tortuosity of the cement paste. Liu et al., (5) employed a 2D model to simulate transport of multi-ions in concrete with different aggregate shapes and contents. They concluded that factors such as distribution, shape and content of aggregates have significant impacts on ion transport. Conclusions of these and more studies inspired us to investigate effects of these factors on corrosion of steel in concrete.

The measured thickness of ITZ, mainly based on the measured porosity in an SEM image, varies in different studies. Scrivener and Nemati (6) prepared concrete specimens which were impregnated with a fusible alloy liquid (Wood's metal) and reported that the apparent width of ITZ is 30 – 100 μm, which is wider than the value of 10 – 20 μm by mercury intrusion porosimetry (7). Our recent study determined the thickness of ITZ based on the porosity map converted from SEM-BSE images (8). The thickness is about 5 μm at the upper side of an aggregate and at the underside, the thickness is much wider, more than 70 μm. In the numerical simulations, the ITZ is generally viewed as a uniform thin layer around each aggregate and its thickness depends on the size of the simulation domain. In the study of Du et al. (9), the thickness was assigned as 500 μm because the domain size is above 10 cm so a wider ITZ can be meshed. Abyaneh et al., (4) set an exponential function for the porosity distribution in the ITZ which is about 40 μm wide. The domain size is 7.5 mm so a narrow ITZ can be meshed. Liu et al., (5) set the ITZ thickness as 40 μm as well and the minimum mesh size is about 6.25 μm but their simulation domain is 5 cm, so they reported that the computation was very heavy.

Even though the effect of concrete structure on mass transport have been well studied in the literature, studies on the effect of coarse aggregates on O_2 transport and corrosion products precipitation are rarely found. In this paper, a coupling model with iron oxidation, ions diffusion and migration (see the previous study (10)) was used to simulate transport and precipitation of corrosion products. The 2D simulation domains were created with circular aggregates and different aggregate contents.

2. THE MODEL

2.1 Conceptual model for corrosion products transport and oxidation

Either for the chloride-induced corrosion (11) or the carbonation-induced corrosion (12), corrosion of steel in concrete means the dissolution of iron atoms which is the transition from metallic state to a bivalent oxidation state.

$$\mathrm{Fe} \rightarrow \mathrm{Fe}^{2+} + 2\mathrm{e}^{-} \quad (1)$$

However, in studies characterizing the composition of corrosion products, they always found compounds with ferric iron. This is because there is an intermediate step of oxidation of Fe^{2+} ions, which involves oxygen and hydroxide ion and leads to the final formation of Fe^{3+} (13).

$$\mathrm{Fe}^{2+} \rightarrow \mathrm{Fe}^{3+} + \mathrm{e}^{-} \quad (2)$$

Fe^{3+} oxides and hydroxides are highly insoluble (14,15), but Fe^{2+} hydroxide ($Fe(OH)_2$) can be relatively more soluble (10^{-2} to 10^{-4} M, depending on pH). This means that for corrosion products to precipitate, the Fe^{2+} ions released at the steel surface are either oxidized to Fe^{3+} or to form $Fe(OH)_2$ after the saturation level of Fe^{2+} is reached. Meanwhile, the transport of Fe^{2+} away from the steel surface continues. These processes constantly dilute the Fe^{2+} concentration.

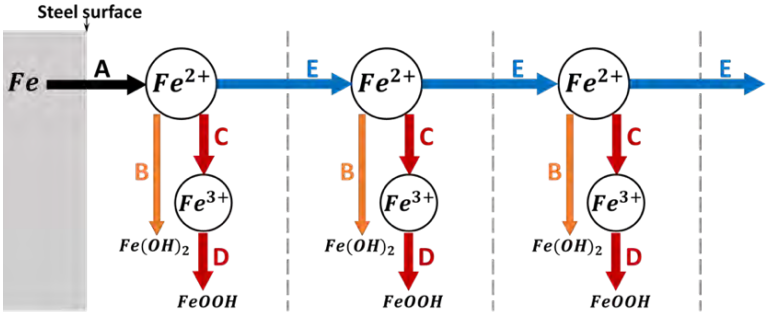

Figure 1: Schematic representation of the reaction path from Fe^{2+} release to formation of solid corrosion products in the water-saturated concrete (adapted from (10)). In the figure, A=Fe^{2+} release, B=$Fe(OH)_2$ precipitation, C=oxidation, D=FeOOH precipitation, E=Fe^{2+} diffusion.

Therefore, a model to describe the fate of Fe^{2+} ions released into a water-saturated concrete during the corrosion process is illustrated in Figure 1. For the uniform corrosion (i.e., carbonation induced) at the macroscopic scale, we assume that the anodic and cathodic reactions occur on the same steel surface. Two half-cell reactions is merged to provide the complete corrosion reaction.

$$2Fe + O_2 + 2H_2O \rightarrow 2Fe^{2+} + 4OH^- \quad (3)$$

As aforementioned, the direct precipitation of Fe^{2+} only occurs when the saturation level of Fe^{2+} is above a certain level (i.e., 10^{-3} M).

$$Fe^{2+} + 2OH^- \rightarrow Fe(OH)_2 \quad (4)$$

The oxidation of Fe^{2+} to Fe^{3+} (to form FeOOH) can be viewed as a kinetic process as the oxidation rate is in competition with the rate of the $Fe(OH)_2$ formation. The Fe^{2+} oxidation by O_2 can be well described by controlling parameters, such as pH and Fe^{2+} (16,17). Some studies showed that if pH is higher than a certain level the oxidation kinetics are not pH dependent (18). Thus, the oxidation rate is only dependent on $[Fe^{2+}]$ and dissolved oxygen $[O_2]_{aq}$.

$$\frac{-d[Fe^{2+}]}{dt} = k[Fe^{2+}][O_2]_{aq} \quad (5)$$

where k is a kinetic constant. Precipitation of FeOOH is here assumed to occur immediately.

2.2 Ion transport

Ion transport in the porous media by diffusion under the concentration gradient and migration under the electrical field is described by the extended Nernst-Planck equation (e.g., (19,20)). The advection is not considered in saturated concrete.

$$\frac{\partial c_i}{\partial t} = \nabla\left(D_i \nabla c_i + z_i F c_i \frac{D_i}{RT} \nabla\psi\right) + R_i \quad (6)$$

where z_i (-) is the charge number, and i represents the ith ion/molecule (see Table 1). c_i (mol/m^3) is the concentration. F is the Faraday constant (9.64846E-4 C/mol). ψ (V) is the local

electrical potential. R_i is the source/sink term which can take into account oxidation/reactions. The effective diffusion coefficient D_i (m^2/s) depends on the pore network so it is described as a function of the tortuosity τ (-) and constructivity δ_i (-) of the pore structure (21).

$$D_i = D_i^0 \frac{\phi \delta_i}{\tau^2} \tag{7}$$

where D_i^0 (m^2/s) is the free diffusion coefficient of species i in pure water. δ_i is species dependent and related to the interaction between species and pore structure.

Poisson's equation is coupled with Eq. (6) to take into account the effect of the electrical potential on the ion transport.

$$\nabla \psi = \frac{F}{\varepsilon_r \varepsilon_0} \sum c_i z_i \tag{8}$$

where ε_r and ε_0 are the relative and vacuum dielectric permittivity of the pore solution.

Ion species in concrete are also considered in the model (see Table 1). Therefore, the presence of these ions can change the potential field and thus affects the transport of Fe^{2+}.

Table 1: Ions/molecules included in modelling

Cations	**Ca^{2+}**	**K^+**	**Na^+**	**H^+**	**Fe^{2+}**
Initial concentration (M)	0.0223	0.0089	0.0039	2e-9	0
D_i^0 ($\times 10^{-9}$ m^2/s)	0.793	1.957	1.33	9.3	0.719
Anions	**Cl^-**	**HCO_3^-**	**SO_4^{2-}**	**S^{2-}**	**OH^-**
Initial concentration (M)	0.013	0.0028	0.0197	0.0011	5E-5
D_i^0 ($\times 10^{-9}$ m^2/s)	2.03	1.1	1.07	0.731	5.3
Molecules	**O_2**	**FeOOH**	**$Fe(OH)_2$**		
Initial concentration (M)	0.00028	0	0		
D_i^0 ($\times 10^{-9}$ m^2/s)	1.97	0	0		

2.3 Modelling

The 2D simulation domains in this study consist of three phases, namely, mortar matrix, coarse aggregates and ITZ. This paper only considered the circular shape of aggregates. Other shapes (e.g., oval) were also investigated which showed higher tortuous effect than the circular aggregates but results are not shown due to the length limit of the paper. Three aggregate/domain ratios (0.45, 0.3 and 0.15) were compared as displayed in Figure *2*.

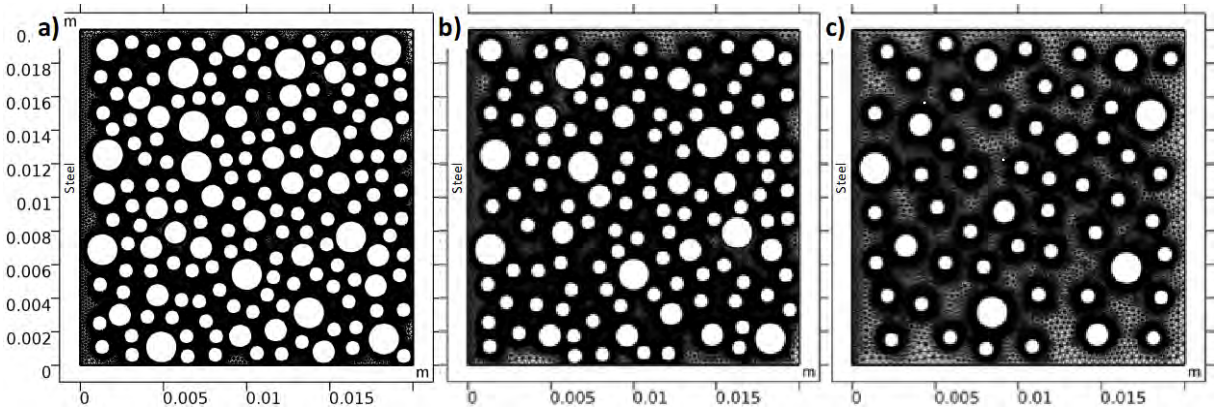

Figure 2: Aggregate content and mesh for three aggregate/domain ratios: a) 0.45, b) 0.3 and c) 0.15.

A simulation domain was set as 2 cm × 2 cm and the maximum diameter of aggregates was about 10 times smaller than the domain size (22). Three aggregate sizes (2, 1.5 and 1 mm) were considered according to the Fuller aggregate gradation. The ITZ for each aggregate was considered as a thin layer around the aggregate with a thickness about 100 μm which is close to the upper limit of measured ITZ thickness (6). The porosity of ITZ is not uniform and decreases from a high value at the aggregate surface to the same as the mortar matrix (see Figure 3). We consider this assumption more realistic than the generally used approach of setting a constant porosity for the ITZ. The finite element method was used to solve the partial differential equations. The minimum size of element is 6 μm so that the ITZ can be well meshed.

3. RESUTLS AND DISCUSSION

As shown in Figure *2*, the left boundary of the domain is the surface of the steel. The release of Fe^{2+} is constant with a corrosion rate of 10 μm/year which is in the range of natural corrosion. According to Eq. (3), with 1 M Fe^{2+} being released, 2 M OH^- is released as well and 0.5 M O_2 is consumed at the steel surface. On the right boundary, the constant oxygen concentration of 0.28 M was applied, meaning that O_2 from air can be quickly dissolved into the pore solution with the consumption of O_2 in the concrete due to corrosion.

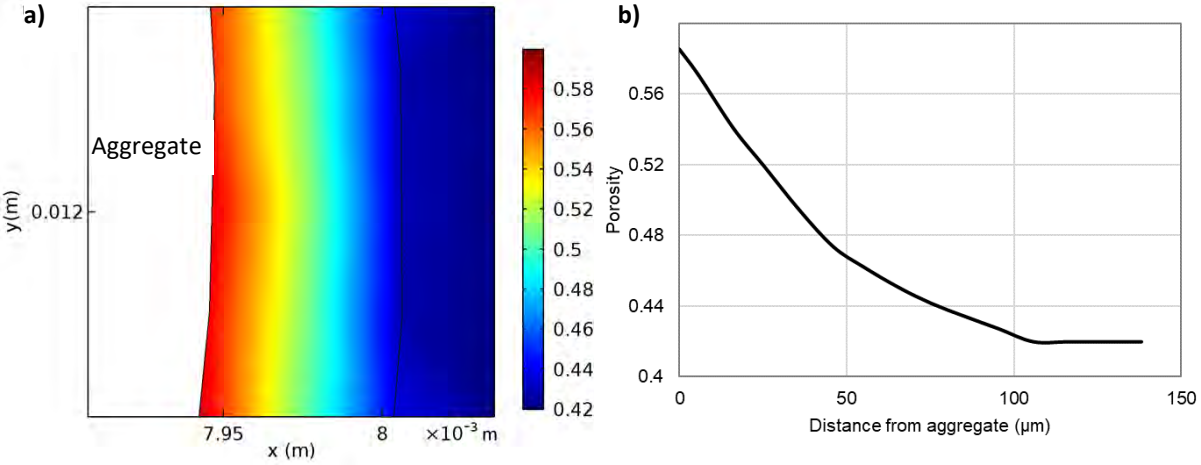

Figure 3: Porosity distribution at ITZ: a) An example in 2D and b) A porosity profile decreasing with the distance from an aggregate.

To investigate the effect of aggregates, simulations were firstly done for a domain without any aggregates. By adjusting δ_{O_2} for O_2, we can make sure that there is always a small amount of O_2 on the steel surface for corrosion (0.00005 M in this study). This means that corrosion can continue almost with infinite time. Then, the same value of δ_{O_2} was used for simulations with aggregates. The simulations stopped if oxygen at any location on the steel surface is zero. Therefore, by comparing the time of O_2 depletion at the steel surface, one can tell how the presence of aggregates affects O_2 diffusion and corrosion products precipitation.

Figure 4 shows an example of O_2 reduction when the presence of aggregates is considered. It is clear that aggregates can significantly reduce O_2 diffusion as O_2 concentration at the steel surface decreases very quick and reduces to zero after just two days (comparing with the infinite time for the domain without aggregates).

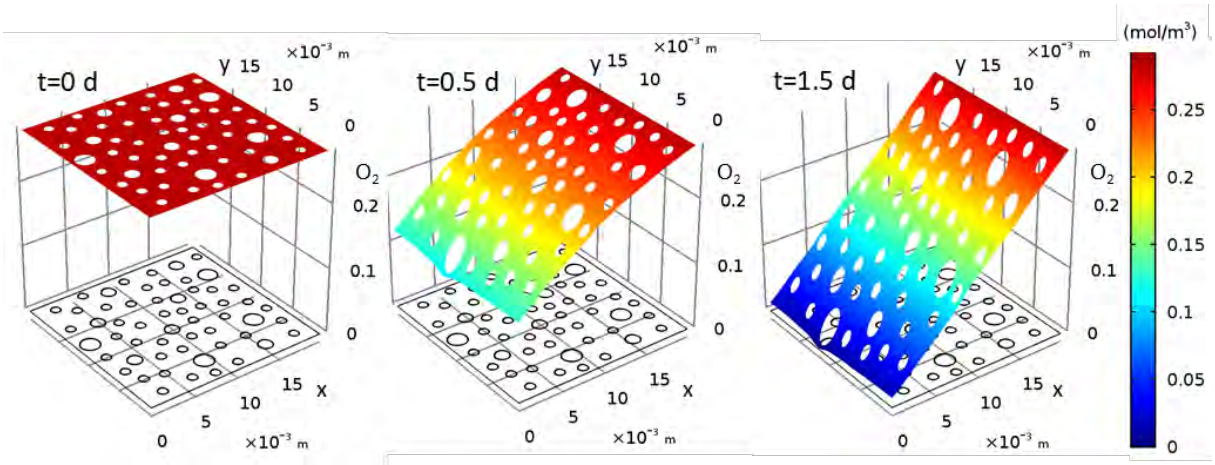

Figure 4: Example of oxygen reduction for the case of aggregate/domain ratio 0.15.

Figure 5 compares O_2 concentration and corrosion products at 0.5 d for three aggregate/domain ratios. It shows that more aggregates has the more pronounced reduction of O_2 diffusion. The amount of $Fe(OH)_2$ is very low but its concentration at the steel surface is slightly higher than 1E-3 M. This means that this concentration difference is not high enough to form a large amount of $Fe(OH)_2$ as the most Fe^{2+} is oxidized to form FeOOH. This agrees with the conclusion of the previous study (10). The concentration of Fe^{2+} at the steel surface decreases slightly with the decreases of the aggregate/domain ratio. This is due to the fact that the high aggregate content reduces the Fe^{2+} diffusion, leading to the accumulation of Fe^{2+} ions at the steel surface. As a result, the concentration of FeOOH at the steel surface increases with the decreases of the aggregate/domain ratio.

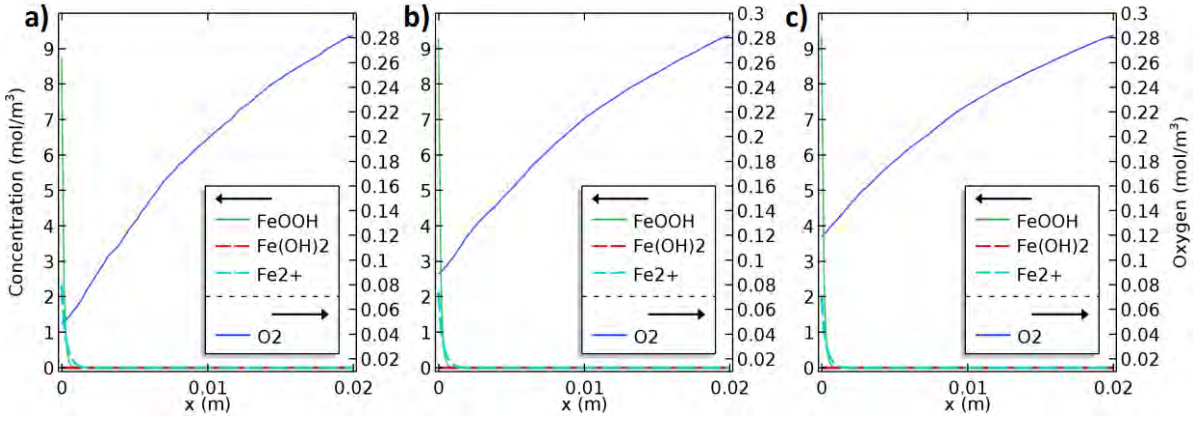

Figure 5: Averaged profiles of oxygen concentration and corrosion productions at 0.5 d for aggregate ratios: a) 0.45, b) 0.3 and c) 0.15.

The cases without ITZ were also simulated in this study. The oxygen depletion time is compared for two cases (with and without ITZ) in Figure 6, which shows that O_2 diffusion is even more reduced if there is no ITZ. The time when O_2 depletion is about 25% lower than the cases with ITZ for all three aggregate/domain ratios, but the effect of ITZ seems less significant than the presence of aggregates, which is in agreement with conclusion in the literature (23).

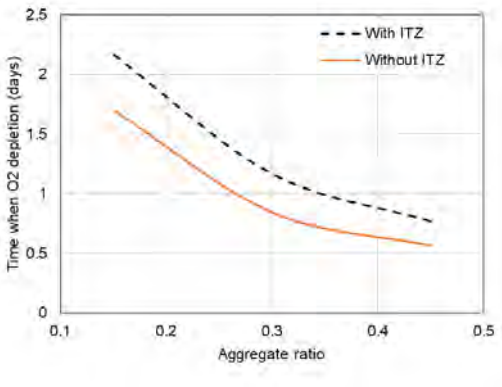

Figure 6: Effect of ITZ on oxygen reduction.

4. CONCLUSIONS

This paper studies the effect of coarse aggregates on O_2 diffusion and precipitation of corrosion products in the reinforced concrete. Numerical simulation results show that

- The presence of aggregates significantly reduce O_2 diffusion. This becomes more pronounced with the increase of aggregate content (up to 0.45 aggregate ratio).
- The high aggregate contents lead to more Fe^{2+} ions accumulating at the steel surface. Consequently, a higher amount of FeOOH is formed but it rapidly drops with the distance from the steel surface.
- The presence of porous ITZ can enhance the diffusion oxygen from the ambient environment to the steel surface.

This paper reports the preliminary simulation results of the effect of coarse aggregates on corrosion in reinforced concrete. More simulations will be performed, including the effects of different aggregate shapes, corrosion rates, etc.

ACKNOWLEDGEMENTS

The authors would thank the Swiss National Science Foundation (SNSF) for the financial support through the ENDURE project (grant number PP00P2-163675).

REFERENCES

1. Angst UM, Geiker MR, Michel A, Gehlen C, Wong H, Isgor OB, et al. The steel--concrete interface. Mater Struct. 2017;50(2):143.
2. Zhang Z, Angst U. A discussion of the paper “Effect of design parameters on microstructure of steel-concrete interface in reinforced concrete.” Vol. 128, Cement and Concrete Research. 2020. p. 105949.
3. Zhang Z, Angst U, Michel A, Jensen M. An image-based local homogenization method to model mass transport at the steel-concrete interface. In: P.A.M.Basheer, editor. Sixth International Conference on the Durability of Concrete Structures. Leeds, UK: Whittles Publishing; 2018. p. 807–14.
4. Dehghanpoor Abyaneh S, Wong HS, Buenfeld NR. Modelling the diffusivity of mortar and concrete using a three-dimensional mesostructure with several aggregate shapes. Comput Mater Sci. 2013;78:63–73.
5. Liu Q, Feng G, Xia J, Yang J, Li L. Ionic transport features in concrete composites

containing various shaped aggregates: a numerical study. Compos Struct. 2017;183(1):371–80.
6. Scrivener KL, Nemati KM. The percolation of pore space in the cement paste/aggregate interfacial zone of concrete. Cem Concr Res. 1996;26(1):35–40.
7. Snyder KA, Winslow DN, Bentz DP, Garboczi EJ. Effects of Interfacial Zone Percolation on Cement-Based Composite Transport Properties. MRS Proc. 1991;245.
8. Zhang Z, Angst UM, Michel A. A framework for modelling corrosion-related degradation in reinforced concrete. In: Caspeele R, Taerwe L, Frangopol DM, editors. IALCCE 2018. Ghent, Belgium: Taylor & Francis; 2019. p. 979–86.
9. Du X, Jin L, Ma G. A meso-scale numerical method for the simulation of chloride diffusivity in concrete. Finite Elem Anal Des. 2014;85:87–100.
10. Stefanoni M, Zhang Z, Angst U, Elsener B. The kinetic competition between transport and oxidation of ferrous ions governs precipitation of corrosion products in carbonated concrete. RILEM Tech Lett. 2018 Sep 14;3:8.
11. Wong HS, Zhao YX, Karimi AR, Buenfeld NR, Jin WL. On the penetration of corrosion products from reinforcing steel into concrete due to chloride-induced corrosion. Corros Sci. 2010;52(7):2469–80.
12. Angst U, Elsener B, Jamali A, Adey B. Concrete cover cracking owing to reinforcement corrosion - Theoretical considerations and practical experience. Mater Corros. 2012;63(12):1069–77.
13. Stratmann M. The Atmospheric Corrosion of Iron - A Discussion of the Physico-Chemical Fundamentals of this Omnipresent Corrosion Process. Berichte der Bunsengesellschaft für Phys Chemie. 1990 Jun;94(6):626–39.
14. Cornell RM, Schwertmann U. The Iron Oxides, Structure, Properties, Reactions, Occurences and Uses. 2003. 1–121 p.
15. Fraser L, Stanger B, Griffin T, Jabri M, Sones G, Steelman M, et al. Seamless Fluids Programs : A Key to Better Well Construction. Oilf Rev. 1996;8(2):42–56.
16. Stumm W, Lee GF. Oxygenation of Ferrous Iron. Ind Eng Chem. 1961;53(2):143–6.
17. Pham AN, Waite TD. Oxygenation of Fe(II) in natural waters revisited: Kinetic modeling approaches, rate constant estimation and the importance of various reaction pathways. Geochim Cosmochim Acta. 2008;72(15):3616–30.
18. Morgan B, Lahav O. The effect of pH on the kinetics of spontaneous Fe(II) oxidation by O2in aqueous solution - basic principles and a simple heuristic description. Chemosphere. 2007;68(11):2080–4.
19. Baroghel-Bouny V, Thiéry M, Wang X. Modelling of isothermal coupled moisture-ion transport in cementitious materials. Cem Concr Res. 2011;41(8):828–41.
20. Jensen MM, Johannesson B, Geiker MR. A Numerical Comparison of Ionic Multi-Species Diffusion with and without Sorption Hysteresis for Cement-Based Materials. Transp Porous Media. 2015;107(1):27–47.
21. Atkinson A, Nickerson AK. The diffusion of ions through water-saturated cement. J Mater Sci. 1984;19(9):3068–78.
22. Wu Z, Wong HS, Buenfeld NR. Influence of drying-induced microcracking and related size effects on mass transport properties of concrete. Cem Concr Res. 2015;68:35–48.
23. Delagrave A, Bigas JP, Ollivier JP, Marchand J, Pigeon M. Influence of the interfacial zone on the chloride diffusivity of mortars. Adv Cem Based Mater. 1997;5(3–4):86–92.

MULTISCALE MODELLING OF CHLORIDE TRANSPORT IN CEMENTITIOUS MATERIALS AT THE ATOMIC AND PORE NETWORK SCALES

Khalil Ferjaoui (1), Fabien Georget (1) and Karen Scrivener (1)

(1) Department of Material Sciencen, Ecole Polytechnique Fédérale de Lausanne, Switzerland

Abstract

To reduce the CO2 footprint of construction materials, concrete producers blend their cement with Supplementary Cementitious Materials (SCMs). And even though such blended systems are eco-friendlier than the Ordinary Portland Cement (OPC), they are required to respect standards. In this context, understanding and predicting the durability of blended concrete is important for optimizing the design of new cementitious materials. Even though chloride ingress is one of the most common problems for reinforced concrete, the quantification of the link between ionic transport and the microstructure is still a challenge. Modelling transport in cementitious materials by Fickian processes usually fails to predict experimental results and particularly those of blended systems. Chloride ingress is thought to be influenced, at the nanoscale, by the adsorption of ions on the hydrates surface due to the formation of an Electrical Double Layer (EDL). Therefore, a multiscale approach will be adapted to model the phenomena arising at different scales. The method for the calculation of ionic diffusivities will couple the Metropolis Monte Carlo algorithm (MC) to the Poisson Nernst-Planck (PNP) equation. First, the Monte Carlo is applied to the Grand Canonical ensemble to determine the ions distributions in the pores as a function of the pore radius. Once the densities of all ionic species are determined, the PNP system is resolved with the Finite Element Method (FEM) and effective diffusion coefficients are calculated as a function of the pore size. The contribution of the microstructure on the transport is to be investigated by developing a consistent microstructural model of the C-S-H, the main hydration product.
Keywords: C-S-H, chloride ingress, multiscale modelling, electrical double layer, diffusion

1. INTRODUCTION

Understanding and modelling ionic transport in hardened cement paste has been shown to be of great impact for the prediction of long-term durability of concrete structures. As a matter of fact, concrete structures are frequently exposed to humid atmosphere or aggressive sources of chloride such as seawater or deicer salts…Hence, chloride ingress is probably the most common reason for steel to corrode leading to the deterioration of the mechanical properties of reinforced structures. Even though ionic transport is not very well understood, a

decent amount of experimental work [1,2,3,4,5] suggests that diffusion of ions in cementitious materials is a complex process that depends upon various factors.

First, the chemical reactions between the solid phases and the solution unavoidably affect the ionic population present in the pores and therefore the way the different species diffuse. Secondly, as the dominant percolating phase, C-S-H constitutes the main pathway for ions to move. C-S-H is also the main hydration product usually characterized with a proportionally high specific surface area of the order of 200-300 m^2/g [6,7]. Surface interactions between C-S-H and the ions have therefore a certain effect at the nanoscale. However, such effects are still not fully understood. And finally, at a coarser scale, the morphology of the porous network (connectivity, tortuosity…).

2. LITERATURE REVIEW

2.1 Binding mechanisms

One of the main hydration products of cement are AFm minerals. It is a phase of aluminate ferrite monosulfates, or Al_2O_3-Fe_2O_3-mono phase which is important in the study of chloride ingress. Indeed, it has been proved that chloride ions get involved in chemical reactions with AFms in order to form Friedel's salt [8] i.e. the chemical binding. Such formed salts are stable products [9] that are supposed to permanently trap chloride ions. Therefore, AFms act as a "sink" for chloride ions and thereby retards diffusion of chloride.

X-ray Diffraction with Rietveld analysis for quantification shows the existence of a non-negligible amount of chloride which is, supposedly, physically bound in the C-S-H phase [10]. Physical binding means that the ion is adsorbed on the surface of solid phases without actually getting trapped in covalent bonds.

So, we might legitimately ask if either of the binding processes is predominant. In order to quantitatively answer the question. Sui et al. [10] computed the total amount of chloride in pastes of different systems. X-ray Diffraction analysis has been conducted to detect chloride in solid phases (Friedel's salt). It was coupled to isopropanol extraction (amount of chloride in free water essentially located at the saturated capillary pores) along with the titration of the ground samples (total chloride content). Results (Fig.1) show the existence of a non-negligible amount of chloride which is physically bound in the C-S-H phase [11,12], supposedly, in the pores of below 10 nm.

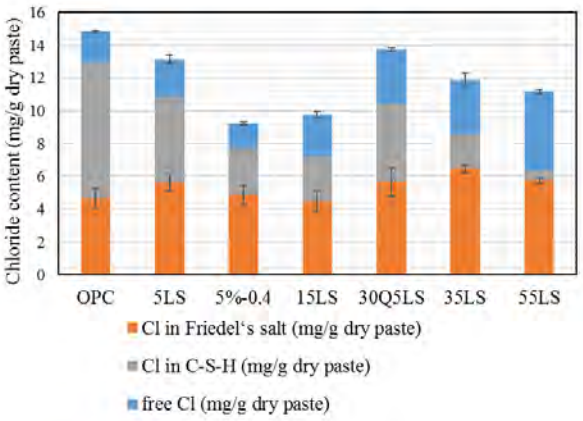

Figure 1: Total chloride proportions in various systems (LS=Limestone) [10]

Therefore, more interrogations arise: Since the "physically bound" chloride ions are still part of the pore solution, how and how much does the physical binding stop or at least delay the chloride ingress?

2.2 A standardized way to characterize and quantify chloride ingress: A macroscopic view

In order to study and quantify the transport of chloride in hydrated cement, scientists reproduce conditions in sea submerged areas. One way to do that consists in conducting bulk diffusion experiments [https://www.astm.org/Standards/C1556.htm]. This experiment consists in leaving mortar or concrete in a known NaCl solution for a certain period (6 months to a few years). After drilling, powder grinding and finally chloride titration of samples obtained at different depths, profile of total chloride content can be plotted as a function of depth. Such work has recently been conducted on a variety of blended systems [10] with results represented in Fig.2.

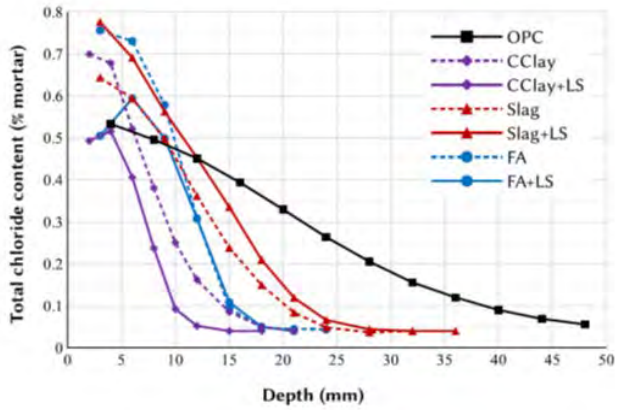

Figure 2: Total chloride content as a function of the depth for blended systems with different SCMs: CClay=Calcined Clay, LS=Limestone, FA=Fly Ash [10]

Given the profiles on Fig.2., it seems that we can, through observation, rank the resistivity of the different systems to the chloride ingress. Nonetheless, a main question before quantitative predictions is: how can we quantitatively classify these systems?

A first empirical modelling approach would rely on the fact that the chloride content curves (Fig.2) look like diffusion profiles. Therefore, a way to quantify the transport is to fit experimental data on a diffusion equation such as the macroscopic Fick's Law of diffusion [13]. Such a method results into the computation of so-called apparent diffusion coefficients which do not represent the diffusion of real diffusion of physical species but can rather be interpreted as the diffusion of the penetration depth.

For a better interpretation, Sui et al. [10] tried to connect transport to microstructure by looking at the relation between the apparent diffusion coefficient and the pore structure parameters: total porosity and critical pore diameter (Fig.3).

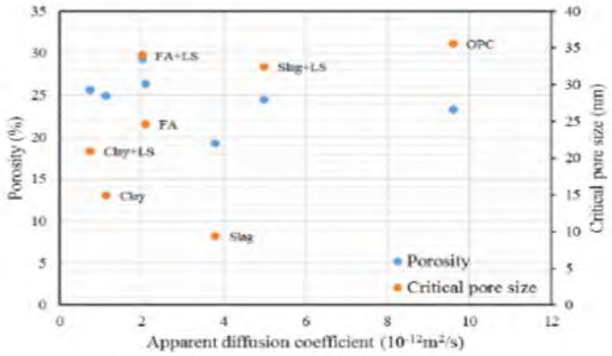

Figure 3: Relationship between apparent diffusion coefficient, porosity and critical pore size [10]

It seems that there is no clear correlation between D_a and porosity which means that either (i) D_a doesn't have any physical meaning or that (ii) it depends on other parameters than the porosity or (iii) both. In fact, when the apparent diffusion coefficient has been compared to the content of alkali in the solutions, as another parameter of the microstructure, a clear trend was remarkably seen (Fig.4).

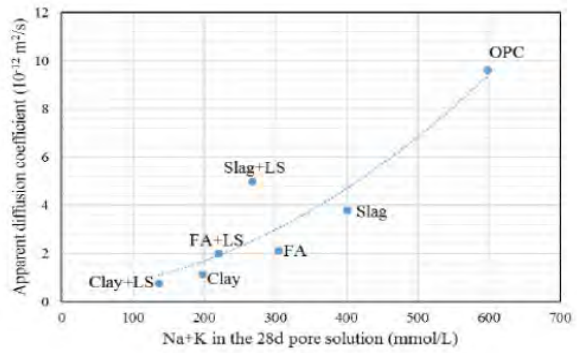

Figure 4: Relationship between apparent diffusion coefficient and alkali ions content in pore solution, the dash line is an indicator of the trend [10]

Even though, such a relationship is not obvious and most probably system-dependent, it at least supports the pore solution effect. Indeed, it has been shown that the pore solution's

content affects chloride transport due to three main phenomena: (a) the non-ideality of the solution, (b) the electroneutrality conservation, and (c) the surface effects.

a) In our case, the ideality of solution is an oversimplifying hypothesis. In fact, due to the non-ideality of the pore solution in cementitious systems, the gradient of chemical potentials is the actual driving force for diffusion. On top of this, pore solutions have usually ionic strengths above 0.5M. This high concentration area is, unfortunately, where most models fail [14].
b) Due to their specific radii and their charges, ions have usually different diffusion coefficients. So according to the local electroneutrality conservation, faster ions are slowed down while slower counter-ions are accelerated. However, the complexity of the pore solution [15, 16,17] makes any prediction of these the effects on chloride transport an actual challenge.
c) Concerning the surface effects, C-S-H has a high specific surface area (~200-300 m²/g) [7,18]. This literally means that a huge proportion of pore solution is in contact with C-S-H's surface. The composition of the solution could influence surface properties [19]. In fact, the presence of alkali can perturbate the adsorption of chloride. However, the influence of C-S-H's surface and its effect on chlorides or alkali is still poorly understood.

Therefore, in order to understand and quantify the effects of the physical binding, it seems inevitable to downscale to the nanoscopic scale where continuity assumptions do not hold, and fundamental interactions arise.

2.3 Nanoscale diffusion: The Electrical Double Layer

In 1853, Helmholtz was the first to discover the formation of a layered structure which forms around a charged solid surface when it interacts with a fluid; the so-called Electrical Double Layer (EDL). In cementitious systems, the pH of the pore solution which is usually beyond values of 12.5 triggers the deprotonation of silanol groups at the surface of the C-S-H. The degree of deprotonation goes up as the pH increases, thus charging negatively the surface of the C-S-H. Relative to the charge on the surface, counter-ions build up near the surface to neutralize the surface charge, and co-ions are depleted in this region due to the effects of entropy and Colombian repulsion.

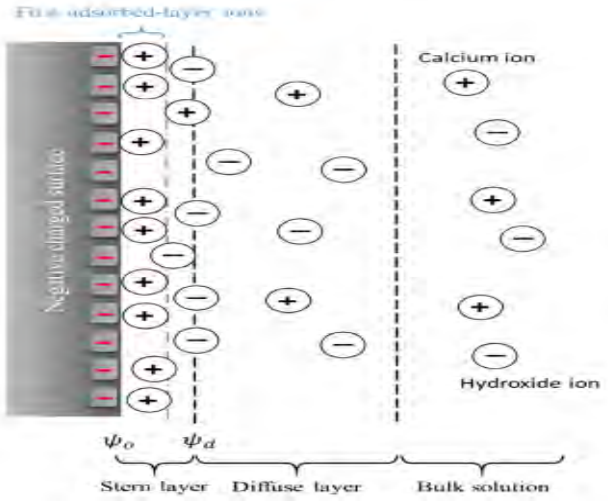

Figure 5: Schematic of the EDL [20]

In the case of C-S-H, it is the EDLs forming at in gel pores (2~10nm) which are assumed to drastically attenuate the diffusivity of chloride anions and amplify that of cations in such a way that chloride gets "almost permanently" physically bound [21]. However, a proper quantification of this physical binding through actual computation of nanoscale ionic diffusivities as function of the pore size or the associated Zeta potential (ζ) is still an object of research.

3. MODELLING APPROACH

3.1 The classical Gouy-Chapman theory

The Gouy-Chapman (GC) theory describes the EDL via the combination of the Poisson equation for electrical potential and the Boltzmann distribution of charge within an electric field next to a planar charged solid surface i.e. the Poisson-Boltzmann equation (Eq. 1). The usual system of equations for a multi-species system is written as follow:

$$\begin{cases} \Delta\Psi = -\frac{\rho}{\epsilon_0 \epsilon} \\ \rho = eN_A \sum_i z_i C_{b,i} \exp(\frac{-z_i e\Psi}{k_B T}) \end{cases} \quad (1)$$

where ε_o is the permittivity of free space, ε is the dielectric constant of the solution, ρ the charge distribution, e is the elementary electrostatic charge, N_A is Avogadro's number, z_i the valence of the species i, $C_{b,i}$ is the concentration in the bulk pore solution of i and k_B is the Boltzmann constant.

This approach treats ions as non-interacting point charges in the vicinity of a single-charged surface in contact with a bulk solution. Stern modified this theory by accounting for the finite size of ions, but the modified GC theory is still limited for modelling most of real systems. In the case of asymmetric electrolytes with divalent counterions, G.M. Torrie et al. [22] showed how the classical theory overestimates the surface potential even at quite low surface charges. Moreover, assuming the only existence of monovalent counterions is a compromising hypothesis given that chloride is adsorbed thanks to the charge reversal due to the accumulation of Ca^{2+} [23]. On the modelling point of view, the main challenge to all EDL modelling is to find out what the charge density function looks like. So, it has also been shown that assuming Boltzmann distributions unavoidably leads to erroneous predictions of the potentials due to neglecting steric and ion-ion correlation effects. Hence, GC theory is inadequate.

In order to remedy the shortcomings of the classical theory, modelers turned toward more complex depictions of the double layer by adopting molecular modelling techniques which have indeed proved themselves very accurate but also computationally costly. The present work focuses on the use of the Grand Canonical Monte Carlo (GCMC) as a better compromise, than Molecular Dynamics, between accuracy and complexity.

3.1 Monte Carlo method

For most adsorption studies, the grand-canonical ensemble is the natural statistical ensemble to use. In this ensemble, the temperature, volume and chemical potential are fixed but the number of the particles is allowed to fluctuate during the simulation. The output of the Grand-Canonical Monte Carlo (GCMC) is the equilibrium number of ions C_i^{GCMC} which translates into the charge density distribution ρ used for the computation of the mean electrostatic potential in eq. (2):

$$\begin{cases} \psi^{GCMC}(x) = -\frac{1}{\epsilon_0 \epsilon} \int_x^{\infty} (t-x)\rho(t)dt \\ \rho = eN_A \sum_i z_i C_i^{GCMC} \end{cases} \quad (2)$$

During the simulation, three types of moves were performed in order to reach the equilibrium configuration: (i) random displacement of one ion, (ii) the addition of an electroneutral pair of ions and (iii) the deletion of an electroneutral pair of ions. The decision of actually making one move or the other depends on the energy difference due to each one of the possible moves. In order to compute that shift, we consider three main energies to characterize the state of our system which are (i) the Coulombic ion-ion interaction, (ii) the Pauli exclusion repulsion force due to the overlapping of the electronic shells and (iii) the interaction with the external charge distribution including both the long-range interaction with ions outside the simulation box and with charged solid-phase walls.

Configurational forces In the model used in this work, each ion i was assigned a charge q_i and a hard sphere radius R_i. The solvent was approximated by a dielectric continuum with the relative permittivity ε_s. Given the elementary charge e and the absolute permittivity of vacuum ε_0, the interaction between two charged species i and j separated by a distance r_{ij} is calculated according to

$$\begin{cases} u^{el}(r_{ij}) = \frac{q_i q_j}{4\pi\epsilon_o\epsilon_s r_{ij}} \\ u^{hs}(r_{ij}) = \infty, \text{if } r_{ij} \leq R_i + R_j \\ u^{hs}(r_{ij}) = 0, \text{if } r_{ij} > R_i + R_j \end{cases} \quad \textbf{(3)}$$

A one-body external field was used to correct for the long-range electrostatic interactions and to account for the cell boundary constraints along the x-direction acting as hard walls (Fig.6.), following the charged sheets method [22, 24]

$$\begin{cases} \nu^{ext}(\mathrm{x}_i) = \infty, \text{ when } \mathrm{x}_i \geq \mathrm{L} \text{ or } \mathrm{x}_i \leq 0 \\ \nu^{ext}(\mathrm{x}_i) = q_i \phi^{ext}(\mathrm{x}_i), \text{ when } 0 < \mathrm{x}_i \leq \mathrm{L} \end{cases} \quad \textbf{(4)}$$

where $\phi^{ext}(x_i)$ is the potential produced by the external charge distribution. The latter is calculated from the mean charge distribution in the slit pore and is updated during the simulation following the method in [22]. The full configurational energy of the system then becomes

$$\mathrm{U}^{conf} = \sum_{i}^{N} \nu^{ext}(x_i) + \sum_{i<j}^{N} u^{el}(\mathbf{r}_{ij}) + u^{hs}(\mathbf{r}_{ij}) \quad \textbf{(5)}$$

where N is the number of mobile ions.

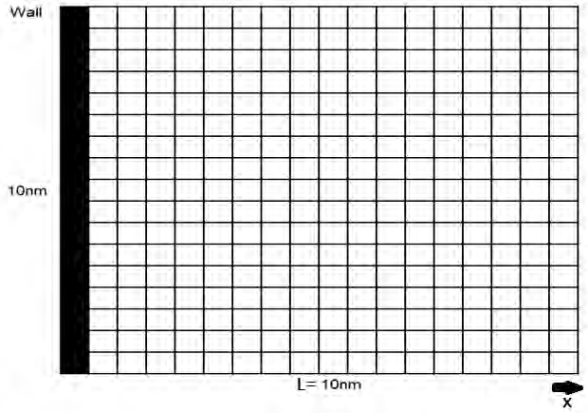

Figure 6: Two-dimensional grid representing the pore space

Surface modelling The surface charged density of C-S-H surface depends on the pH value. Ab initio simulations [20] show that the surface of C-S-H can be represented by titrating surface sites >SiOH with the site density 2.4 sites/nm^2. The sites are distributed in pairs according to the crystal structure of tobermorite.

4. OUTLOOK: RESOLVING THE TRANSPORT EQUATION

Once the charge distribution is determined with the GCMC and the mean electrostatic potential accordingly computed (Eq.2), the numerical resolution of the modified Poisson-Nernst-Planck (PNP) equations (Eq.6) will be conducted with Finite Element Method (FEM). Y. Yang et al. [20], used the potential computed by the MC to define an excess chemical potential μ_i^{ex} which accounts for steric effects in the transport equation:

$$\begin{cases} \frac{\partial C_i}{\partial t} + \nabla \cdot \mathbf{J}_i = 0 \\ \mathbf{J}_i = -D_{i,0}\nabla C_i - D_{i,0}\frac{z_i e C_i}{k_B T}\nabla\phi - D_{i,0}\frac{C_i}{k_B T}\nabla\mu_i^{ex} \end{cases} \quad (6)$$

where C_i, $D_{i,0}$, J_i and z_i denotes the aqueous concentration (mol/m^3), diffusion coefficient in free water (m^2/s), flux (mol.m^{-2}.s^{-1}) and valence of the ith species, respectively. t is time (s), e the absolute charge of electron (C), k the Boltzmann constant (J/K) and T the absolute temperature (K).

Once this partial differential equation resolved, the nanoscopic effective diffusivity of each ion $D_{i,e}^{Micro}$ is computed as follows [20]:

$$D_{i,e}^{Micro} = \frac{\int \mathbf{J}_i dS}{S} \cdot \frac{L}{\Delta C_i} \quad (7)$$

where L is the medium travelled length and ΔC_i the concentration difference that induces the gradient.

References

[1] Page, C., Short, N. R., & El Tarras, A. (1981). Diffusion of chloride ions in hardened cement pastes. *Cement and concrete research*, *11*(3), 395-406.

[2] Goto, S., & Roy, D. M. (1981). Diffusion of ions through hardened cement pastes. *Cement and Concrete Research*, *11*(5-6), 751-757.

[3] Atkinson, A., & Nickerson, A. K. (1984). The diffusion of ions through water-saturated cement. *Journal of materials science*, *19*(9), 3068-3078

[4] Halamickova, P., Detwiler, R. J., Bentz, D. P., & Garboczi, E. J. (1995). Water permeability and chloride ion diffusion in Portland cement mortars: relationship to sand content and critical pore diameter. *Cement and concrete research*, *25*(4), 790-802.

[5] Buenfeld, N. R., & Newman, J. B. (1987). Examination of three methods for studying ion diffusion in cement pastes, mortars and concrete. *Materials and Structures*, *20*(1), 3.

[6] Kantro, D. L., Brunauer, S., & Weise, C. H. (1959). The ball-mill hydration of tricalcium silicate at room temperature. *Journal of Colloid Science*, *14*(4), 363-376

[7] Brunauer, S., Skalny, J., Odler, I., & Yudenfreund, M. (1973). Hardened portland cement pastes of low porosity: VII. Further remarks about early hydration. Composition and surface area of tobermorite gel. Summary. *Cement and Concrete Research*, *3*(3), 279-293.

[8] Birnin-Yauri, U. A., & Glasser, F. P. (1998). Friedel's salt, Ca2Al (OH) 6 (Cl, OH)· 2H2O: its solid solutions and their role in chloride binding. *Cement and Concrete Research*, *28*(12), 1713-1723.

[9] Damidot, D., Birnin-Yauri, U. A., & Glasser, F. P. (1994). Thermodynamic investigation of the CaO-Al~ 2O~ 3-CaCl~ 2-H~ 2O system at 25 C and the influence of Na~ 2O. *Cemento*, *91*, 243-243.

[10] Sui, S., Georget, F., Maraghechi, H., Sun, W., & Scrivener, K. (2019). Towards a generic approach to durability: Factors affecting chloride transport in binary and ternary cementitious materials. *Cement and Concrete Research*, *124*, 105783.

[11] Florea, M. V. A., & Brouwers, H. J. H. (2012). Chloride binding related to hydration products: Part I: Ordinary Portland Cement. *Cement and Concrete Research*, *42*(2), 282-290.

[12] Thomas, M. D. A., Hooton, R. D., Scott, A., & Zibara, H. (2012). The effect of supplementary cementitious materials on chloride binding in hardened cement paste. *Cement and Concrete Research*, *42*(1), 1-7.

[13] Chatterji, S. (1995). On the applicability of Fick's second law to chloride ion migration through Portland cement concrete. *Cement and Concrete Research*, *25*(2), 299-303.

[14] Bethke, C. M. (2007). *Geochemical and biogeochemical reaction modeling*. Cambridge University Press.

[15] Yonezawa, T., Ashworth, V., & Procter, R. P. M. (1988). Pore solution composition and chloride effects on the corrosion of steel in concrete. *Corrosion*, *44*(7), 489-499.

[16] Saremi, M., & Mahallati, E. (2002). A study on chloride-induced depassivation of mild steel in simulated concrete pore solution. *Cement and Concrete Research*, *32*(12), 1915-1921.

[17] Goni, S., & Andrade, C. (1990). Synthetic concrete pore solution chemistry and rebar corrosion rate in the presence of chlorides. *Cement and Concrete Research*, *20*(4), 525-539.

[18] Kantro, D. L., Brunauer, S., & Weise, C. H. (1959). The ball-mill hydration of tricalcium silicate at room temperature. *Journal of Colloid Science*, *14*(4), 363-376.

[19] Viallis-Terrisse, H., Nonat, A., & Petit, J. C. (2001). Zeta-potential study of calcium silicate hydrates interacting with alkaline cations. *Journal of colloid and interface science*, *244*(1), 58-65.

[20] Yang, Y., Patel, R. A., Churakov, S. V., Prasianakis, N. I., Kosakowski, G., & Wang, M. (2019). Multiscale modeling of ion diffusion in cement paste: electrical double layer effects. *Cement and Concrete Composites*, *96*, 55-65.

[21] Friedmann, H., Amiri, O., & Aït-Mokhtar, A. (2008). Physical modeling of the electrical double layer effects on multispecies ions transport in cement-based materials. *Cement and Concrete Research*, *38*(12), 1394-1400.

[22] Torrie, G. M., & Valleau, J. P. (1982). Electrical double layers. 4. Limitations of the Gouy-Chapman theory. *The Journal of Physical Chemistry*, *86*(16), 3251-3257.

[23] Viallis-Terrisse, H., Nonat, A., & Petit, J. C. (2001). Zeta-potential study of calcium silicate hydrates interacting with alkaline cations. *Journal of colloid and interface science*, *244*(1), 58-65.

[24] Jönsson, B., Wennerstroem, H., & Halle, B. (1980). Ion distributions in lamellar liquid crystals. A comparison between results from Monte Carlo simulations and solutions of the Poisson-Boltzmann equation. *The Journal of Physical Chemistry*, *84*(17), 2179-2185.

PREDICTING THE YIELD STRESS OF 3D PRINTING MORTAR BASED ON THE FLOWABILITY OF PASTE AND EXCESS PASTE THICKNESS

C Zhang (1), ZC Deng (1), YM Zhang (1)* and C Chen (1)

(1) Jiangsu Key Laboratory of Construction Materials, College of Material Science and Engineering, Southeast University, Nanjing 211189, P.R. China

Abstract

This paper develops an empirical model to predict the static yield stress of 3D printing mortar based on the flowability of paste and excess paste thickness. The components of the mortar are divided into paste and aggregate. The relation between the yield stress of mortar and the yield stress of paste and the excess paste thickness is investigated. It is found that there is a linear relationship between the yield stress of mortar and that of paste, and the yield stress of mortar also is proportional to the reciprocal of excess paste thickness. Additionally, the yield stress of paste is related to its flowability when the rheological behavior of mortar is modified with different types and dosage of thixotropic agents. Based on the experimental data, an empirical model is built to predict the static yield stress of mortar in accordance with the flowability of paste and excess paste thickness.

Keywords: 3D printing mortar, yield stress, flowability of paste, excess paste thickness

1. INTRODUCTION

With a great success the 3D printing manufacturing achieves in the field of food, biology, aerospace, and so on, this technology also shows excellent prospects in concrete construction. Compared to conventional concrete construction, 3D printing concrete (3DPC) possesses many advantages, like formwork free, less consumption of raw materials, flexible design of structure, etc. [1].

Since the different way of fabricating concrete structure, the workability requirements for 3DPC are also different from conventional concrete. In the processes of printing, 3DPC should be extruded smoothly and continuously through the nozzle of a printer, and meanwhile, have the ability to maintain self-shape stable and sustain subsequently printed concrete layers. Hence, extrudability and buildability are basic printable performance of 3DPC [2]. In fact, the printability of 3DPC is largely dependent on its rheology [3]. For meeting these contradictory performance requirements of extrudability and buildability, 3DPC needs to possess thixotropy and proper yield stress. There is static and dynamic yield stress in the context of thixotropic materials. Only when the shear stress applied on 3DPC exceeds its static yield stress, 3DPC can start to flow and be extruded, which means the static yield stress of 3DPC cannot be too high. In the meanwhile, the printable height of printed structure is related to the static yield stress of 3DPC as well. High static yield stress is conducive to the buildability of 3DPC. Thus, the static

yield stress is a critical rheological parameter, and possessing suitable static yield stress is a precondition for concrete being printable [4]. The preparation of printable concrete is a process of designing the concrete with proper static yield stress. According to the previous researches [5,6], the concrete with the static yield stress in the range of 500 ~ 2500 Pa can basically satisfy the requirements of printability.

Concerning the 3DPC mix design, there is still a lack of relevant criterions to guide the mix design of 3DPC. Researching the influence rule of different raw materials on the printable performance of concrete is a common method to find out the optimum mix proportion of 3DPC, which is a direct and effective method, but with lots of workloads simultaneously, considering that concrete consists of kinds of raw materials. Therefore, it will be very helpful in the mix design of 3DPC if the static yield stress could be predicted in advance just according to some simple parameters regarding the concrete mix. For fixing this problem in the mix design of 3DPC, this paper develops an empirical model in accordance with the investigation on the influence of the yield stress of paste and aggregate content on the static yield stress of mortar respectively, which is verified successful in predicting the static yield of mortar when the static yield stress of mortar is in the range of 500 ~ 2500 Pa.

2. EXPERIMENT

2.1 Materials

In this study, the materials for 3D printing mortar consisted of Portland cement (P. Ⅱ. 42.5 R), China ISO standard sand and one of the two types of rheological modifiers: nano-silica (NS) or micro-attapulgite clay (MAC). Besides, some other kinds of rheological modifiers, including silica fume (SF) and metakaolin (MK), were used in the preparation of cement paste to investigate the relationship between flowability and yield stress of paste. Polycarboxylate superplasticizer (SP) was used to adjust the workability of fresh paste and mortar.

2.2 Mix proportion

In this research, five groups of 3D printing mortar and corresponding cement paste with different content of NS were prepared to investigate the relationship between the yield stress of paste and that of mortar, as shown in Table 1 and Table 2.

Two series of 3D printing mortar with different amount of NS and sand were designed to study the effect of aggregate content on the yield stress of mortar, as listed in Table 3. Each series of mortar had the same content of NS to ensure that the paste of this series of mortar possessed the same yield stress.

Table 1: Mix of paste with different content of NS

Labels	Cement/g	Water/g	W/C	NS
J-NS1.2R0.3	1000	300	0.3	1.2%
J-NS1R0.3	1000	300	0.3	1.0%
J-NS0.8R0.3	1000	300	0.3	0.8%
J-NS0.6R0.3	1000	300	0.3	0.6%
J-NS0.4R0.3	1000	300	0.3	0.4%

Table 2: Mix of mortar with different content of NS

Labels	Sand (g/L)	Cement (g/L)	Water (g/L)	NS (%)	Superplasticizer (%)
B850NS1.2R0.3	1196	849	255	1.2	0.68
B850NS1.0R0.3	1196	849	255	1.0	0.68
B850NS0.8R0.3	1196	849	255	0.8	0.68
B850NS0.6R0.3	1196	849	255	0.6	0.68
B850NS0.4R0.3	1196	849	255	0.4	0.68

Table 3: Two series of 3D printing mortar with different amount of NS and sand

Labels	Sand (g/L)	Cement (g/L)	Water (g/L)	Superplasticizer (g/L)	Nano-silica (g/L)
S-NS0.4R30-1	1247	810	243	5.5	3.24
S-NS0.4R30-2	1277	787	236	5.4	3.15
S-NS0.4R30-3	1307	764	229	5.2	3.06
S-NS0.4R30-4	1337	741	222	5.0	2.96
S-NS0.4R30-5	1367	718	215	4.9	2.87
S-NS1.0R30-1	1082	937	281	6.37	9.37
S-NS1.0R30-2	1112	914	274	6.21	9.14
S-NS1.0R30-3	1142	891	267	6.06	8.91
S-NS1.0R30-4	1172	868	260	5.90	8.68
S-NS1.0R30-5	1202	845	253	5.74	8.45
S-NS1.0R30-6	1232	822	246	5.59	8.22
S-NS1.0R30-7	1262	798	240	5.43	7.98

2.3 Static and dynamic yield stress measurement

In this study, given that 3D printing mortar and corresponding cement paste are thixotropic, yield stress of cement paste and mortar was measured under a constant rotating speed in a Brookfield rheometer. As for static and dynamic yield stress of cement paste test, firstly, about 450 ml of specimen was poured into a 500 ml beaker with a diameter of 95 mm and a depth of 115 mm, and the specimen was sheared with a 30 mm × 60 mm vane spindle. Since the measurement of yield stress usually required a low fixed shearing speed, a constant rotating speed 0.2 s^{-1} was applied in the test; the test duration was 90 s. As for static yield stress of 3DPM measurement, testing processes were similar to the yield stress measurement procedure for cement paste. The distinctions were that the 30 mm × 60 mm vane spindle was replaced by 10 mm × 20 mm one due to the torque limitation of the rheometer, and the test duration was 120 s.

3. RESULTS AND DISCUSSES

3.1 The relationship of yield stress between mortar and paste

The performance, like buildability and extrudability, of 3DPC is relevant to its yield stress. The yield stress of mortar is highly dependent on the yield stress of paste and aggregate content. To quantificationally analyze the relationship between the yield stress of paste and mortar, the five groups of paste with different NS content and the corresponding mortar were prepared to investigate rheological behaviors. Figure 1 shows the rheological behaviors of paste and corresponding mortar with different ns content under a constant shear rate. It can be seen that the static yield stress as well as the dynamic yield stress of paste increases obviously with the rising of NS dosage. Since the aggregate contents of the five groups of mortar are the same, the distinction of yield stress between mortars is totally derived from different properties of paste. Higher the yield stress of paste is, higher the yield stress of corresponding mortar is. Figure 2 show the fitting relationship between the yield stress of mortar and the dynamic and static yield stress of paste. The yield stress of mortar presents good linear relation to not only the static yield stress but the dynamic yield stress of paste.

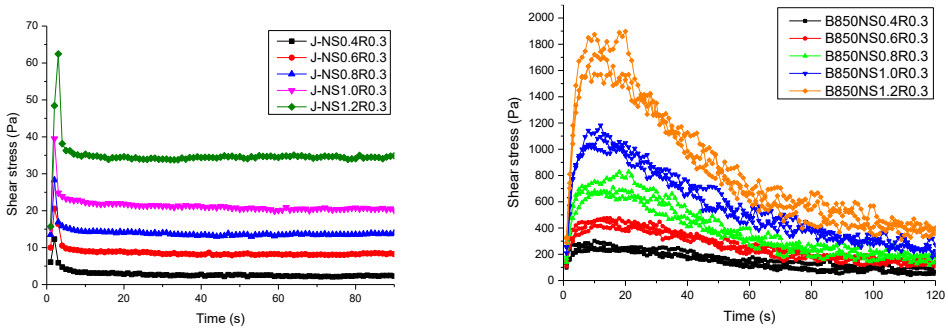

Figure 1: Rheological behaviors of paste and corresponding mortar with different NS content

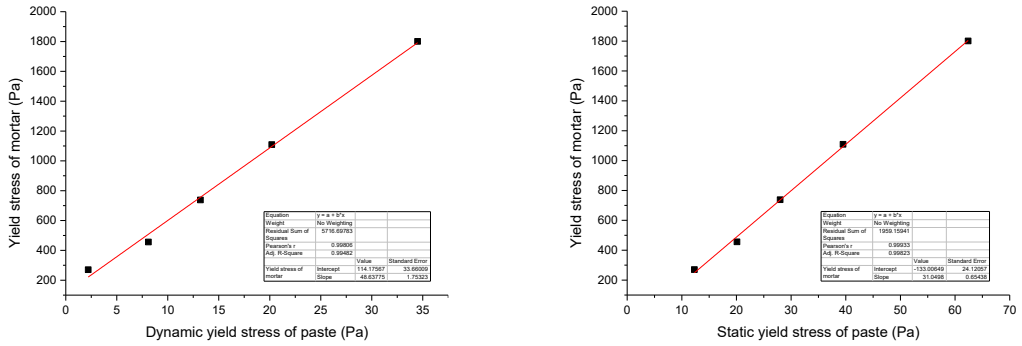

Figure 2: The fitting relationship between the yield stress of mortar and the dynamic and static yield stress of paste

3.2 The relationship between the yield stress of mortar and aggregate content

Except for the yield stress of paste, aggregate content is another crucial factor affecting the yield stress of mortar. To comprehensively investigate the effect of aggregate content on the yield stress of mortar, two kinds of paste with different yield stress, which contain 0.4% and

1.0% NS respectively, were mixed with different content of aggregate to prepare mortar for the yield stress test. Given the printability of mortar, through adjusting the aggregate content, the yield stress of mortar was controlled within 500 ~ 2500 Pa in accordance with [5,6] and the previous experimental experience by the authors. The results of rheological behavior test on mortar were shown in Fig 3. It can be observed that the rising of aggregate content is contributed to increase the yield stress of mortar, which can be explained by the excess paste model. The thickness of excess paste layer that acts as "lubrication" between the aggregate particles decreasing with the rising of aggregate content will lead to the yield stress of mortar increasing. Hence, the thickness of excess paste layer can be as a key parameter to quantificationally analyse the effect of aggregate content on the yield stress of mortar.

Considering the excess paste playing an important role to affect the yield stress of mortar, the thickness of excess paste was selected to replace aggregate content as the vital parameter to investigate the influence of aggregate on the yield stress of mortar. Fig 4 presents the fitting relation between the yield stress of mortar and the reciprocal of excess paste thickness. The yield stress of mortar is linearly related to the reciprocal of excess paste thickness as well.

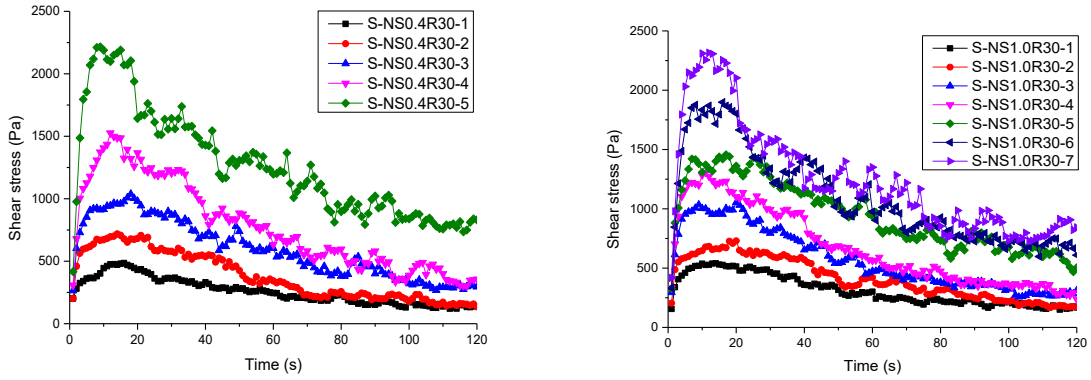

Figure 3: Rheological behaviors of mortar with different NS and sand content

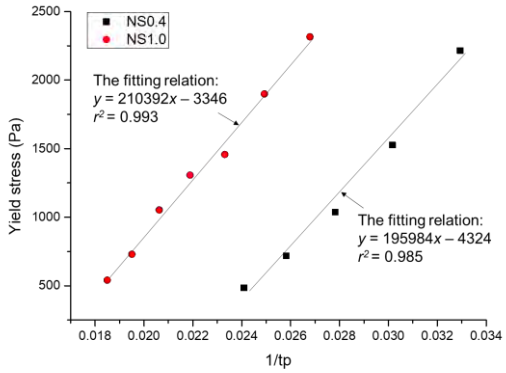

Figure 4: The fitting relation between the yield stress of mortar and the reciprocal of excess paste thickness

3.3 The empirical model to predict the yield stress of 3D printing mortar

For analyzing the slope of fitting lines, it is assumed that the slope is impacted by the yield stress of paste. According to the model of [7,8], the yield stress of mortar τ_m is equal to that

yield stress of paste τ_p is multiplied by the function of aggregate fraction. It can be concluded that the τ_m-to-τ_p ratio is the function of aggregate fraction, while the reciprocal of excess paste thickness is a function of aggregate fraction, which means the τ_m-to-τ_p ratio is the function of reciprocal of excess paste thickness. However, Fig 5 shows that the τ_m-to-τ_p ratio is not the function of reciprocal of excess paste thickness due to the discontinuity of τ_m-to-τ_p ratio. Based on the said analysis to Fig 4, an empirical model can be built, shown as follows:

$$\tau_m = a\times\tau_p+b\times(1/tp)+c \quad (1)$$

This model satisfies the conclusions that the yield stress of mortar τ_m is directly proportional to the yield stress of paste τ_p and the reciprocal of excess paste thickness 1/tp, and the yield stress of paste τ_p governs the intercept rather than the slope of fitting line based on τm and 1/tp. According to the experimental data in Fig 4 and least square method, coefficients in the empirical model Eq (1) are calculated out, and the empirical model is shown as below:

$$\tau_m = 35.9\tau_p+ 203188(1/tp) - 4902.6 \quad (2)$$

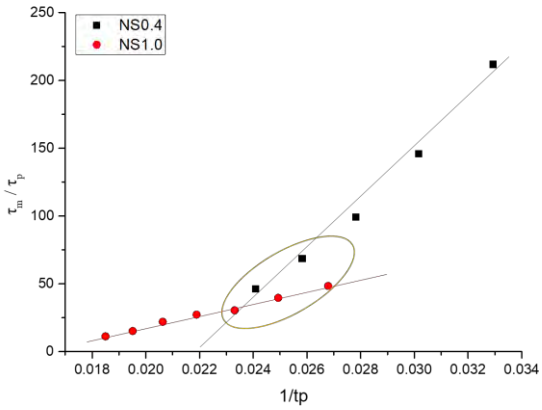

Figure 5: τ_m-to-τ_p ratio of mortar with different NS and sand content

3.4. The relationship between the yield stress and flowability of paste

In the empirical model, there are two essential parameters, the yield stress of paste τ_p and reciprocal of excess paste thickness 1/tp. The 1/tp can be figured out based on the mix proportion and physical properties of aggregate, which is easily obtained without special equipment. While the τ_p test need a rheometer that may not be a common device for some labs or construction site. Aiming to make the empirical model more convenient to use for some engineer and researcher who work in 3D printing construction field, the authors want to use an easier obtained parameter to replace τ_p in the empirical model to predict the yield stress of mortar. It was demonstrated previously that there is a relationship between the yield stress and flowability of paste. Compared to yield stress, flowability is easier to test only with simple tools. Hence, the flowability of paste was employed to take place of τ_p, and the relationship between the yield stress and flowability of paste was investigated in the context of .

So far, many kinds of rheological modifier materials have been developed in the preparation of 3D printing concrete, such as silica fume, nano silica, metakaolin and attapulgite clay. The yield stress and corresponding flowability of paste containing different type and content of rheological modifier materials were measured and presented in Fig 6. It is found that there is a relationship between the flowability of paste and not only dynamic yield stress but also static

yield stress of paste which even contains different kind and content of rheological modifiers. In addition, the results of Fig 6 also demonstrate that superplasticizer dosage makes no difference to the relationship. As a consequent, we can figure out the yield stress of paste based on the flowability and the relationship between the yield stress and flowability of paste even when the paste consists of different materials.

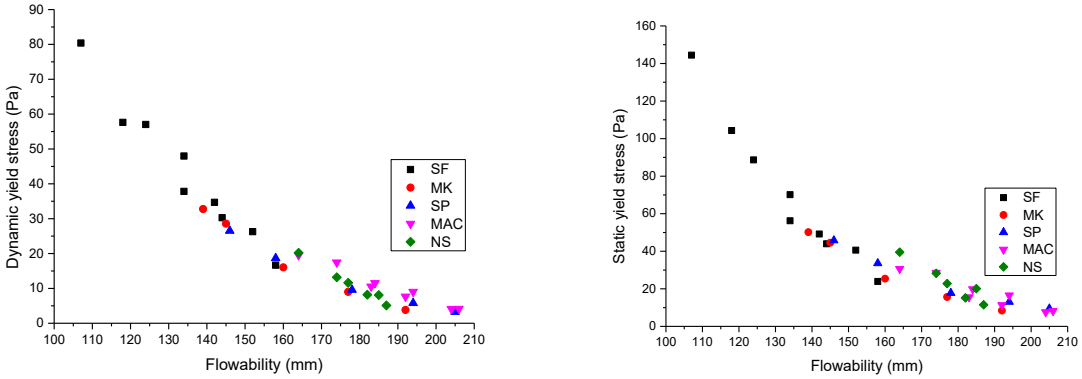

Figure 6: The relationship between the yield stress and flowability of paste

Table 4: Flowability and calculated yield stress of paste for verification

Labels	Flowability (mm)	Calculated Yield stress (Pa)
J-NS0.6R30	167	25
J-NS0.8R30	149	40
J-MAC1.0R30	129	75

Table 5: Mix and corresponding yield stress of mortar for verification

Labels	Sand (g/L)	Cement (g/L)	Water (g/L)	Tested yield stress (Pa)	Calculated yield stress (Pa)	Relative error
S-NS0.6R30-1	1202	845	253	622	729	17.2%
S-NS0.6R30-2	1262	798	240	1166	1437	23.2%
S-NS0.8R30-1	1202	845	253	1273	1269	0.3%
S-NS0.8R30-2	1262	798	240	1829	1977	8.1%
S-MAC1.0R30-1	1022	983	295	1158	1199	3.5%
S-MAC1.0R30-2	1082	937	281	1643	1551	5.6%

3.5. Verification

Some experiment was conducted to verify whether flowability is available to replace the yield stress of paste in the empirical model to predict the yield stress of mortar. The flowability

of three groups of paste with 0.6% NS, 0.8% NS and 1% MAC respectively was measured. According to the value of flowability and the relationship shown in Fig 6, the corresponding yield stress of paste was computed out as presented in Table 4. Each group of paste was mixed with certain content of aggregate to make 3D printing mortar, and the mixes of mortar were shown in Table 5. The reciprocal of excess paste thickness was calculated out in accordance with aggregate content. Based on the reciprocal of excess paste thickness and calculated yield stress of paste, the predicted yield stress of mortar could be figured out by the empirical model, shown as calculated yield stress in Table 5. At the same time, the rheological behavior of mortar was detected, and the tested yield stress was listed in Table 5 as well. It can be observed that relative error between tested and calculated yield stress of mortar is less than 25%, and the relative error of most groups of mortar is within 10%. The results indict that flowability is qualified instead of yield stress of paste to predict the yield stress of mortar.

4. CONCLUSIONS

This paper investigates the effect of paste and aggregate content on the yield stress of mortar and develops an empirical model to predict the yield stress of mortar based on the experimental results. The results obtained in this study can be summarized as the following:

- There is a linear relationship between the yield stress of mortar and that of paste.
- The yield stress of mortar is linearly related to the reciprocal of excess paste thickness.
- The flowability of paste is strong linked to its yield stress and qualified instead of yield stress of paste to predict the yield stress of mortar.

ACKNOWLEDGEMENTS

This work is financially supported by National Key R&D Program of China under 2017YFC0703700 and 2018YFC0705800.

REFERENCES

[1] S. Lim, R.A. Buswell, T.T. Le, S.A. Austin, A.G.F. Gibb, T. Thorpe, Developments in construction-scale additive manufacturing processes, *Autom. Constr.* 21 (2012) 262-268.

[2] V.N. Nerella, M.A.B. Beigh, S. Fataei, V. Mechtcherine, Strain-based approach for measuring structural build-up of cement pastes in the context of digital construction, *Cem. Concr. Res.* 115 (2019) 530-544.

[3] N. Roussel, Rheological requirements for printable concretes, *Cem. Concr. Res.* 112 (2018) 76-85.

[4] R.A. Buswell, W.R. Leal de Silva, S.Z. Jones, J. Dirrenberger, 3D printing using concrete extrusion: A roadmap for research, *Cem. Concr. Res.* 112 (2018) 37-49.

[5] T.T. Le, S.A. Austin, S. Lim, R.A. Buswell, A.G.F. Gibb, T. Thorpe, Mix design and fresh properties for high-performance printing concrete, *Mater. Struct. Constr.* 45 (2012) 1221-1232.

[6] N. Khalil, G. Aouad, K. El Cheikh, S. Rémond, Use of calcium sulfoaluminate cements for setting control of 3D-printing mortars, *Constr. Build. Mater.* 157 (2017) 382-391.

[7] Z. Toutou, N. Roussel, Multi scale experimental study of concrete rheology: From water scale to gravel scale, *Mater. Struct. Constr.* 39 (2006) 189-199.

[8] F. Mahaut, S. Mokéddem, X. Chateau, N. Roussel, G. Ovarlez, Effect of coarse particle volume fraction on the yield stress and thixotropy of cementitious materials, *Cem. Concr. Res.* 38 (2008) 1276-1285.

PREDICTION OF THE CHEMICAL SHRINKAGE OF PORTLAND CEMENT

P. Gao (1) (2), G. Ye (2), J.X. Wei (1), Q.J. Yu (1)

(1) School of Materials Science and Engineering, South China University of Technology, 510640, Guangzhou, People's Republic of China

(2) Microlab, Faculty of Civil Engineering and Geosciences, Delft University of Technology, 2628 CN Delft, The Netherlands

Abstract

Chemical shrinkage is one of the main reasons leading to the early age deformation of concrete. Hence, the prediction of chemical shrinkage is an important issue for evaluating the deformation of concrete and its influence on the durability of concrete structures. There is still room to improve the accuracy for predicting the chemical shrinkage of cement, because some empirical assumptions were involved in traditional methods such as Paulini equation. In this study a discrete algorithm was proposed to deal with the stoichiometry's conversion of tricalcium aluminate (C_3A) and (tetracalcium aluminoferrite) C_4AF with ongoing hydration of cement. Based on this discrete algorithm, the volume evolution of phases in cement paste and the chemical shrinkage of cement were calculated. The chemical shrinkage of cement in W/C 0.3 and W/C 0.4 were simulated using this method and compared with the results of experiments and Paulini equation. It was found that the calculated chemical shrinkage of cement in W/C 0.3 and 0.4 are in good agreement with experiments, respectively. In comparison with Paulini equation, the proposed method was more accurate for predicting the chemical shrinkage of Portland cement, because the nonlinear relationship between the chemical shrinkage and degree of hydration of cement can be simulated by dealing with the stoichiometry's conversion of C_3A and C_4AF with ongoing hydration.

Keywords: Chemical shrinkage, Portland cement, Tricalcium aluminate, Tetracalcium aluminoferrite

1. INTRODUCTION

The products normally occupy less volume than the reactants for the hydration of cement. This volume difference is defined as chemical shrinkage. Generally, chemical shrinkage is one of the main reasons leading to the early age deformation of concrete such as autogenous shrinkage, which increases the cracking risk of concrete structures [1]. Hence, the prediction of chemical shrinkage is an important issue for evaluating the deformation of concrete and its influence on the durability of concrete structures.

In many reports, empirical equations such as Paulini equation [2] were used to calculate the chemical shrinkage of cement. However, because some empirical assumptions were involved in these calculations, there is still room to improve the accuracy for predicting the chemical shrinkage of cement. This study focusses on pure Portland cement system. Since Portland cement mainly consists of tricalcium silicate (C_3S), dicalcium silicate (C_2S), tricalcium aluminate (C_3A), tetracalcium aluminoferrite (C_4AF), the chemical shrinkage of cement could be calculated on condition that the degree of hydration and the stoichiometry of these components in cement are obtained. The degree of hydration of individual component in cement can be predicted using cement hydration models such as CEMHYD3D, HYMOSTRUC3D, μic, and empirical equations [3]. With the development of cement chemistry, many equations were proposed to describe the stoichiometry of individual component in cement (see Figure 1). Generally, the stoichiometry of the hydration of C_3S and C_2S are considered to be constant with ongoing hydration of cement, while that of the hydration of C_3A and C_4AF depend on the actual amount of gypsum ($C\bar{S}H_2$) and ettringite ($C_6A\bar{S}_3H_{32}$) in the system [4,5]. Because not only the actual amount of gypsum and ettringite are dynamic change, but also the hydration rates of C_3A and C_4AF are normally different, it is difficult to determine the stoichiometry of the hydration of C_3A and C_4AF at different ages.

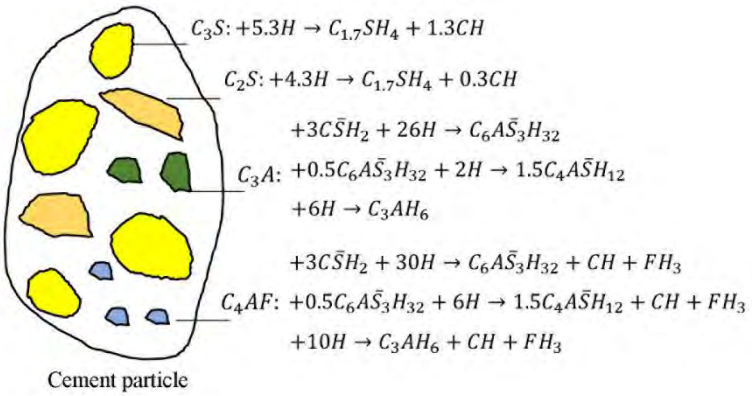

Figure 1: Stoichiometry of the hydration of individual component in cement

This study focused on determining the stoichiometry of the hydration of C_3A and C_4AF with ongoing hydration of cement by proposing a discrete algorithm. Based on this algorithm, the volume evolution of phases in cement paste and the chemical shrinkage of cement were accurately predicted.

2. MODELLING APPROACHES

As presented in Figure 2, the main inputs of this approach included the mineral compositions and particle size distribution of cement, and the water to cement ratio (W/C) of cement paste. The hydration time of cement was divided into several time steps. In each step, the HYMOSTRUC3D model was used to simulate the degree of hydration of individual component in cement. Then, a discrete algorithm was used to determine the stoichiometry of individual component in cement, particularly that of C_3A and C_4AF. Eventually, the volume evolution of phases in cement paste and the chemical shrinkage of cement were calculated.

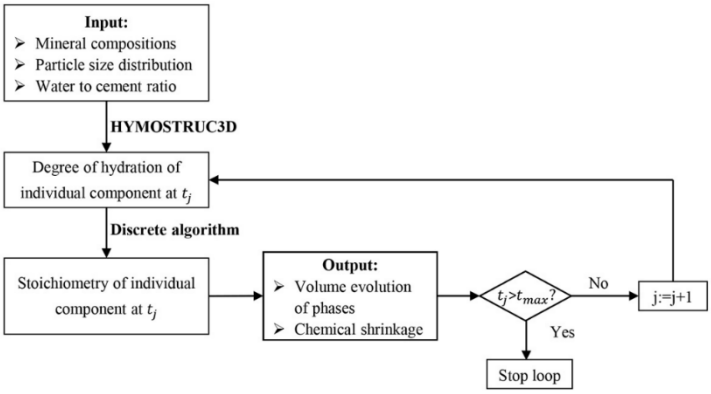

Figure 2: Flowchart of the discrete algorithm for calculating the chemical shrinkage of cement

2.1 Degree of hydration

This study used the HYMOSTRUC3D model to obtain the degree of hydration of individual component in cement at each step. In this model, the reaction rate of cement particles was calculated as a function of the chemical composition and particle size distribution of cement, and the water content and temperature of system. The process of using the HYMOSTRUC3D model to obtain the degree of hydration of individual component in cement can be found in [6].

2.2 *Stoichiometry of cement hydration*

It was assumed that the stoichiometry of the hydration of C_3S and C_2S are constant with ongoing hydration of cement. The stoichiometry of the hydration of C_3A and C_4AF depend on the actual amount of gypsum and ettringite in the system. As schematically shown in Figure 3, three stages were assigned: In stage 1, C_3A and C_4AF reacted with water and gypsum to generate ettringite. In stage 2, all gypsum was consumed, and C_3A and C_4AF reacted water and ettringite to generate AFm ($C_4A\bar{S}H_{12}$). In stage 3, all ettringite was consumed, and C_3A and C_4AF reacted water to generate C_3AH_6.

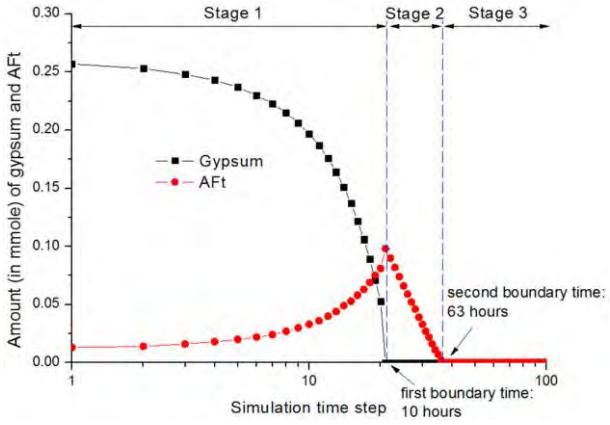

Figure 3: Schematic representation of three stages for determining the stoichiometry's conversion of C_3A and C_4AF

The key point of this discrete algorithm is to determine the degree of hydration of C_3A and C_4AF at the boundary time between different stages.

The condition of the first boundary time is:

$$3.0 \times \left(n_{con,1st,C_3A} + n_{con,1st,C_4AF}\right) = n_{gyp} \quad (1)$$

where $n_{con,1st,C_3A}$ and $n_{con,1st,C_4AF}$ are the amount of reacted C_3A and C_4AF at the first boundary time, respectively.

The above two parameters were related to the degree of hydration of C_3A and C_4AF at the first boundary time, respectively:

$$n_{con,1st,C_3A} = \frac{\alpha_{1st,C_3A} \times f_{C_3A}}{M_{C_3A}} \quad (2)$$

$$n_{con,1st,C_4AF} = \frac{\alpha_{1st,C_4AF} \times f_{C_4AF}}{M_{C_4AF}} \quad (3)$$

where α_{1st,C_3A}, f_{C_3A}, M_{C_3A} and α_{1st,C_4AF}, f_{C_4AF}, M_{C_4AF} are the degree of hydration, weight fraction and molar mass of C_3A and C_4AF, respectively.

In order to solve Eq. (1) to Eq. (3), it is assumed that the ratio of α_{1st,C_3A} to α_{1st,C_4AF} is close to the ratio of α_{C_3A} to α_{C_4AF} at the previous hydration step. Accordingly, it holds that:

$$\alpha_{1st,C_4AF} = \frac{n_{gyp}}{3.0 \times \left(h_{1st,C_3A/C_4AF} \times \frac{f_{C_3A}}{W_{C_3A}} + \frac{f_{C_4AF}}{W_{C_4AF}}\right)} \quad (4)$$

$$\alpha_{1st,C_3A} = h_{1st,C_3A/C_4AF} \times \alpha_{1st,C_4AF} \quad (5)$$

where $h_{1st,C_3A/C_4AF}$ is the ratio of α_{C_3A} to α_{C_4AF} at the previous hydration step for the first boundary time.

The condition of the second boundary time is:

$$n_{re,1st,AFt} - n_{con,2nd,AFt} = 0 \quad (6)$$

where $n_{re,1st,AFt}$ is the amount of ettringite produced in the first stage, and $n_{con,2nd,AFt}$ is the amount of ettringite consumed in the second stage.

Based on Eq. 6, the degree of hydration of C_3A and C_4AF at the second boundary time can be calculated from the ratio of α_{C_3A} to α_{C_4AF} at the previous hydration step for the second boundary time using the similar method in the first stage:

$$\alpha_{2nd,C_4AF} = \frac{\begin{pmatrix} 2 \times n_{re,1st,AFt} + \alpha_{1st,C_3A} \times f_{C_3A}/M_{C_3A} - \\ h_{2nd,C_3A/C_4AF} \times \alpha_{1st,C_4AF} \times f_{C_3A}/M_{C_3A} \end{pmatrix}}{h_{2nd,C_3A/C_4AF} \times \frac{f_{C_3A}}{M_{C_3A}} + \frac{f_{C_4AF}}{M_{C_4AF}}} \quad (7)$$

$$\alpha_{2nd,C_3A} = h_{2nd,C_3A/C_4AF} \times \left(\alpha_{2nd,C_4AF} + \alpha_{1st,C_4AF}\right) - \alpha_{1st,C_3A} \quad (8)$$

where α_{2nd,C_3A} and α_{2nd,C_4AF} are the degree of hydration of C_3A and C_4AF at the second boundary time, respectively. $h_{2nd,C_3A/C_4AF}$ is the ratio of α_{C_3A} to α_{C_4AF} at the previous hydration step for the second boundary time.

(3) The volume evolution *of phases in cement paste and the chemical shrinkage of cement*

Based on the stoichiometry of cement hydration in different stages, the volume evolution of phases in cement paste including reactants: C_3S, C_2S, C_3A, C_4AF, gypsum and capillary water, and hydration products: CSH gel, CH, AFt, AFm, C_3AH_6 and FH_3 were calculated from the degree of hydration of individual component in cement. The chemical shrinkage of cement was calculated as the volume difference of reactants (C_3S, C_2S, C_3A, C_4AF, gypsum and capillary water) to hydration products (CSH gel, CH, AFt, AFm, C_3AH_6 and FH_3).

To validate this model, the chemical shrinkage of cement with a composition of C_3S 56.2%, C_2S 19.61%, C_3A 6.54%, C_4AF 8.91% and gypsum 3.5% was simulated and compared with the experimental data from literature [7]. The particle size distribution of cement can be found in [7], and the W/Cs of cement pastes were 0.3 and 0.4.

3. RESULTS AND DISCUSSIONS

3.1 Degree of hydration

As shown in Figure 4, the simulated degree of hydration of cement in W/C 0.3 is close to that in W/C 0.4 at very early age, while is smaller than that in W/C 0.4 at later age. This is because the influence of W/C on the hydration rate of cement is insignificant at early age. With ongoing hydration, the volume of consumed water is increased, and the hydration rate of cement in the paste with smaller W/C becomes smaller than that in the paste with higher W/C. The above trend is consistent with the experimental data.

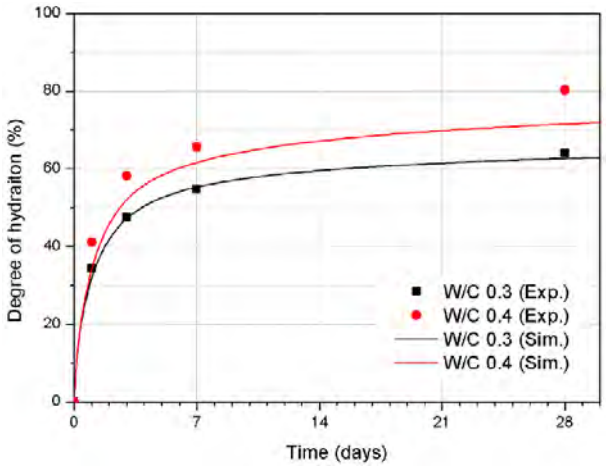

Figure 4: Degrees of hydration of cement in W/C 0.3 and 0.4: simulation (Sim.) *versus* experiment (Exp.)

3.2 Volume evolution of phases

Figure 5a and b show the simulated volume evolution of phases in W/C 0.3 and 0.4, respectively. Table 1 lists the degrees of hydration of C_3A and C_4A at different boundary times. According to Figure 5, the first and second boundary times for W/C 0.4 are earlier than that in W/C 0.3, respectively. As presented in Table 1, however, W/C 0.3 and 0.4 exhibit similar degrees of hydration of C_3A and C_4AF at each boundary time. This is because the boundary times depend on the hydration rates of C_3A and C_4AF, which are earlier in the paste with higher W/C, while the degrees of hydration of C_3A and C_4AF at boundary times depend on the compositions of cement, particularly the amount of gypsum, C_3A and C_4AF (see Eq. (4), (5), (7) and (8)).

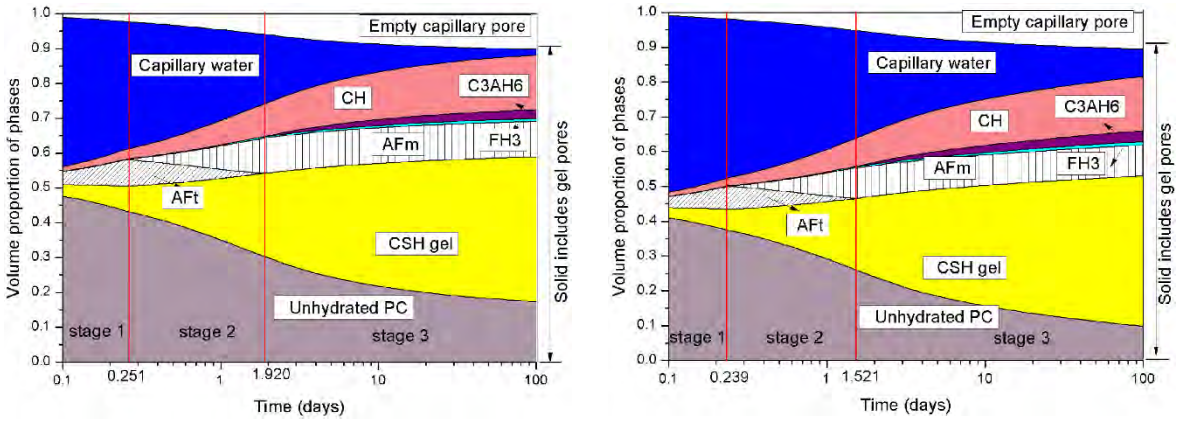

(a) W/C 0.3 (b) W/C 0.4

Figure 5: Simulated volume evolution of phases in W/C 0.3 and 0.4

Table 1 Degree of hydration of C_3A and C_4A at the boundary times

W/C	Boundary times	Time (days)	Degree of hydration (%)	
			C_3A	C_4AF
0.3	first	0.251	24.28	4.87
	second	1.920	69.49	19.00
0.4	first	0.239	24.31	4.83
	second	1.521	69.38	19.15

3.3 Chemical shrinkage of cement

As shown in Figure 6, the simulated chemical shrinkage of cement in W/C 0.3 and 0.4 are in good agreement with the experimental results, respectively. The relationship between the simulated degree of hydration and chemical shrinkage of cement is plotted in Figure 7. As can be seen, the line for the simulated degree of hydration and chemical shrinkage is nonlinear. This is due to the conversion of the stoichiometry of C_3A and C_4AF at different stages. The above trend is close to the experimental data. However, the blue line obtained using Paulini equation [2,7] is linear and different from the experimental data. This is probably because the conversion of the stoichiometry of C_3A and C_4AF at different stages is not considered in Paulini equation.

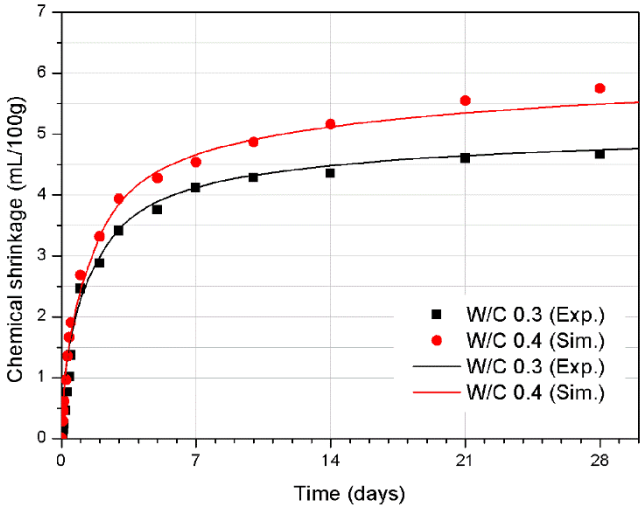

Figure 6: Chemical shrinkage of cement for W/C 0.3 and 0.4: simulation *versus* experiment

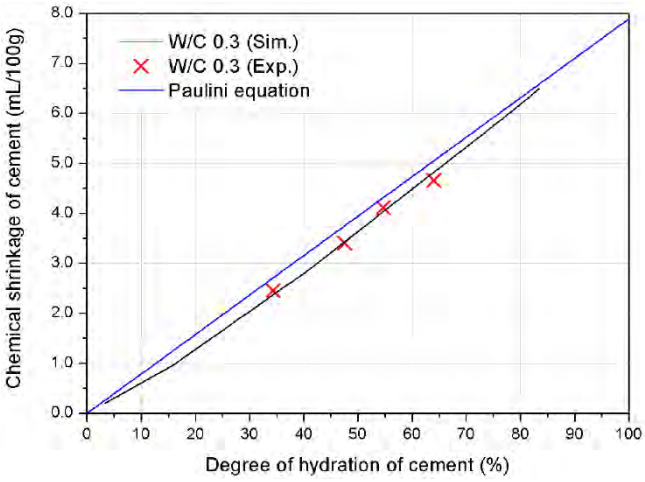

Figure 7: Degree of hydration *versus* chemical shrinkage of cement in W/C 0.3

4. CONCLUSIONS

- A discrete algorithm was proposed to deal with the stoichiometry's conversion of C_3A and C_4AF with progress of the hydration process of cement. Based on this discrete algorithm, the volume evolution of phases in cement paste and the chemical shrinkage of cement were calculated.
- The chemical shrinkage of cement in W/C 0.3 and W/C 0.4 were simulated using this method and compared with the results of experiments and Paulini equation. In comparison with the traditional method for predicting the chemical shrinkage of cement

the proposed method was more accurate, because the nonlinear relationship between the chemical shrinkage and degree of hydration of cement was simulated by dealing with the stoichiometry's conversion of C_3A and C_4AF with ongoing hydration.

ACKNOWLEDGEMENTS

This work was supported by the National key research and development program (2017YFB0310001-02), the National Natural Science Foundation of China (Grant No. 51672084 and 51772103), and the China Postdoctoral Science Foundation funded project (Grant No. 2019M650199).

REFERENCES

[1] Lura, P., Jensen, O.M. and Van Breugel, K. 'Autogenous shrinkage in high-performance cement paste: An evaluation'. *Cem. Concr. Res.*, **33** (2003) 223–232.

[2] Holt, E. 'Early age autogenous shrinkage of concrete', *VTT Publications* **446** (2001), 1-193.

[3] Taylor, H.F.W. 'A method for predicting alkazi ion concentrations in cement pore solutions', *Adv. Cem. Res.*, **1** (1987) 5–17.

[4] Taylor, H.F.W. 'Cement Chemistry'. 2nd ed. London: Thomas Telford Publishing, 1997.

[5] Bentz, D.P., Coveney, P.V., Garboczi, E.J., Kleyn, M.F. and Stutzman, P.E. 'Cellular automaton simulations of cement hydration and microstructure development', *Modell. Simul. Mater. Sci. Eng.*, **2** (1994) 783–808.

[6] Gao, P., Ye, G., Wei, J. and Yu, Q. 'Extension of the HYMOSTRUC3D model for simulation of hydration and microstructure development of blended cements', **64** *Heron*, NO. 1/2.

[7] Zhang, T.S., Gao, P., Luo, R.F., Guo, Y.Q., Wei, J.X., Yu, Q.J. 'Measurement of chemical shrinkage of cement paste: comparison study of ASTM C 1608 and an improved method', *Constr. Build. Mater.*, **48** (2013), 662–669.

SERVICE LIFE PREDICTION OF CONCRETE STRUCTURES UNDER CHLORIDE ENVIRONMENT BASED ON MONTE CARLO METHOD

Chenjia Zuo (1), Yu Liu (1) and Yanbo Liu (1)

(1) College of Shipbuilding Engineering, Harbin Engineering University, China

Abstract

Transport of chlorides is one of the most critical factors determining the service life of concrete structures under ocean environments, and diffusion is usually regarded as the major mechanism for the transport of chloride ions into concrete. As chloride diffusivity is affected by temperature, most existing service life prediction models use the Arrhenius equation to describe the relationship between temperature and chloride diffusivity; however, the variability of activation energy values have rarely been considered. In this investigation, a statistical model using Monte Carlo method is established for the prediction of concrete's service life considering the temperature effect on chloride diffusivity, in which the values of activation energy for diffusivity was determined based on an empirical correlation between diffusivity and activation energy value. The proposed model could theoretically provide a more suitable method for the prediction of concrete's service life under various temperatures.

Keywords: Chloride diffusivity, Activation energy, Monte Carlo method, Service life

1. INTRODUCTION

Corrosion of reinforcing steel is the major cause to the deterioration of concrete structures under marine environment. According to Tutti's model, the service life of reinforced concrete is generally composed of the corrosion initiation period (t_i) and the propagation period (t_p)[1]. The initiation period is the time it takes for the chloride ion to reach the steel surface to a critical value. Most service life prediction models take the initiation period as the dominant factor determining concrete's service life. Compared with traditional service life prediction method, the reliability assessment of structural durability takes into account the randomness of parameters and its necessity has been accepted by many researchers.[2]Based on the statistical properties of the parameters used for service life prediction, Sagues proposed the distributed variables approach.[3] Hartt used this method to explore the evaluation of time-to-corrosion for chloride-exposed reinforced concrete with an admixed corrosion inhibitor, and considered it provided a more realistic representation of what actually transpires.[4] Monte Carlo method is a kind of stochastic simulation method which use random numbers and statistical experiments both based on probability and statistical theory to solve approximate solutions. Due to the accuracy and effectiveness of the calculation results, Monte Carlo based approach has become

one of the most popular methods to solve reliability problems. Before using it to solve stochastic problems, a corresponding probability model should be established according to the characteristics of the stochastic process. And then based on the distribution of random variables in the model, random numbers are generated and a large number of statistical experiments are carried out. The estimate values are calculated from these random numbers and a statistical distribution is obtained in the end [5].

The initiation period is primarily determined by the chloride diffusivity of concrete, therefore, Fick's 2nd law is the most widely used model to calculate initiation period. Diffusion is regarded as the major mechanism for the transport of chloride ions in concrete. It is commonly accepted that chloride diffusivity is affected by temperature and the Arrhenius law is usually employed to describe the correlation between chloride diffusivity and temperature.[6] For example, the activation energy value in the Life-365 model is 35 kJ/mol.[7] Although most service life model employ a constant value of activation energy, researches have shown that the activation energy value is not constant but varies with the diffusivity of concrete.[8] Therefore, using a constant value of activation energy may cause misleading results of service life prediction. In this investigation, a service life prediction model is proposed based on Monte Carlo method considering the variation of activation energy values. The model may theoretically provide a more suitable method for predicting the service life of concrete under various temperatures.

2. MODELS AND METHODS

2.1 Corrosion model

The diffusion of chloride ions in concrete follows Fick's 2nd law, as shown in Eq. (1):

$$\frac{\partial C}{\partial t} = D\frac{\partial^2 C}{\partial x^2} \tag{1}$$

where C is the chloride concentration at depth x and exposure time t, and D is the chloride diffusion coefficient. Assuming the surface chloride content and chloride diffusivity as constants, the solution of Fick's second law is given in Eq. (2):

$$C(x,t) = C_S\left[1 - erf\left(\frac{x}{2\sqrt{Dt}}\right)\right] \tag{2}$$

where *erf* is the error function, C_s is surface chloride content, D is chloride diffusivity, x is depth of rebar and t is the exposure duration.

When the chloride concentration reaches the chloride concentration threshold (C_T), $C(x,t)=C_{T,}$ the steel passive layer is destroyed and steel is corroded. The time of corrosion initiation can be determined by formula Eq. (3) as follows:

$$t_i = \frac{x^2}{4D\left[erf^{-1}\left(1 - \frac{C_T}{C_S}\right)\right]^2} \tag{3}$$

2.2 Monte Carlo method

The reliability analysis of structures is focused on evaluation and the prediction of the probability of reaching certain investigated limit states, which is called failure probability.[9] Monte Carlo method is a popular methods to solve the failure probability of concrete structures. The basic step is to take a large number of random samples of the variables that affect its reliability, and then take these sampling values into the performance function to determine whether they are invalid or not, and the failure probability and the reliability index of structures are obtained in the end. Song used the Monte Carlo simulation technique to analyze the reliability of the concrete tunnel box structure directly exposed to seawater with regard to the time to corrosion initiation of steel embedment.[10] In addition, Monte Carlo method is also used to build corrosion models. Kirkpatrick developed a Monte Carlo-based approach to modeling corrosion damage to explore the service life of bridge decks under chloride-induced corrosion and achieve better results.[11]

In this paper, it is assumed that C_T is constant, x, C_S and D all obey the probability distribution. According to the known distribution conditions, N random sampling tests are carried out for x, C_S and D. One random number is generated for each parameter in each test, and the service life of concrete structure is calculated by these generated random numbers. At the same time, the number of the initiation period (t_i) appearing in time t and expressed in n, is recorded. Ratio of n to N (the total number of tests) is the probability of concrete structures reaching service life at time t.

2.3 Distribution variables approach

A study [3] reported an approach to corrosion damage forecasting of the parallel twin-Escambia bay bridges. The deterioration model, which is the ratio of corrosion elements to total number, can be expressed as Eq. (4).

$$\frac{Nd(t)}{N}=\frac{1}{\sum_i N_i}\sum_i N_i\int_{Dli}^{Dhi}\int_{Csli}^{Cshi}P_{cumli}\left[2\sqrt{D(t-t_{pi})}erf^{-1}\left(1-\frac{C_T}{C_S}\right)\right]P_{Csi}(C_S)P_{Di}(D)\,dC_S dD \quad (4)$$

Where D_{li}, C_{Sli} and D_{hi}, C_{Shi} represent the lowest and highest values. Nd(t) is the number of units whose chloride concentration achieves C_T in time t. The tidal range area (i=1) with the most serious corrosion damage to the substructure of the bridge round piles is calculated in this investigation. A summary of the random variables for the model is given in Table 1.[3]

Table 1: Escambia Bay Bridges Parameters

Parameter	Distribution	Mean	Standard Deviation
D,m^2/s	Normal	2.13×10^{-13}	1.4×10^{-13}
C_S,kg/m^3	Normal	25.02	12.1
x,m	Normal	0.0279	0.0063
C_T,kg/m^3	Determine	4.8	

Fig. 1 shows a comparison of damaged probability based upon the above two approaches and the Table 1 parameters. It indicates that predict results from Monte Carlo method are basically consistent with the distributed variables approach. Moreover, 100,0000 of random

variables for each parametric value were achieved through the Monte Carlo Simulation. A large number of random experiments make the prediction results more accurate.

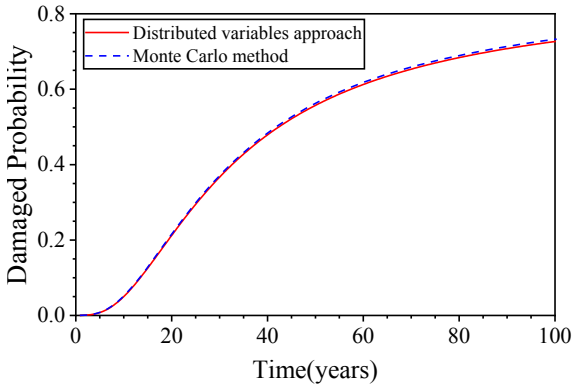

Figure1: Comparison between the results of two approaches

2.4 Statistical model

The relationship between temperature and chloride diffusion is usually described by the Arrhenius equation, as shown in Eq. (5):

$$D(T) = D_0 \exp\left[\frac{E_a}{R}\left(\frac{1}{T_0} - \frac{1}{T}\right)\right] \tag{5}$$

where $D(T)$ is the diffusion coefficient at temperature T and D_0 is the diffusion coefficient at the reference temperature T_0. R is the gas constant and E_a is the activation energy of the diffusion process. E_a is treated as a constant and its value is 35kJ/mol in Life-365's service life prediction model.[7] Liu developed the correlation between non-steady-state migration coefficients (D_{nssm}) at 21℃ and E_a ,[12] as given in Eq. (6):

$$E_a = -4.46 \ln\left(D_{nssm,\,21^\circ C}\right) + 27.92 \tag{6}$$

The chloride diffusion coefficient usually is regarded as a time dependent random variable and Life-365 uses the following relationship to account for time-dependent changes in diffusion [9]:

$$D(t) = D_0 \left(\frac{t_0}{t}\right)^m \tag{7}$$

where D_0 is diffusion coefficient at reference time t_0 (usually 28 days) and m is attenuation coefficient. However, it is unreasonable for the chlorine diffusion coefficient to decrease with time indefinitely. Therefore, it is usually assumed that the diffusion coefficient will not decrease when the exposure time is longer than n years. For example, Life-365 states that the relationship shown in Eq. (7) is only valid up to 25 years. Beyond this time, the value of chlorine diffusion coefficient at 25 years calculated from Eq. (7) is assumed to be constant throughout the rest of the analysis period.[7] For durability design in the Hong Kong-Zhuhai-Macao (HZM) Bridge project, the power law in the above equation is truncated at the end of 30 years and it is assumed that the chloride diffusion coefficient will be stable after 30 years' exposure.[13] so the value of n is 30. In this case, Eq. (7) can be expressed as:

$$D(t)=\begin{cases} D_0\cdot\left(\dfrac{t_0}{365\cdot n}\right)^m, n<30 \\ D_0\cdot\left(\dfrac{t_0}{365\cdot 30}\right)^m, n\geq 30 \end{cases} \quad (8)$$

The value of non-steady-state migration coefficients (D_{nssm}) is considered equal to the value of diffusion coefficient (D).Based on the relationship shown in Eq. (2), a statistical model introducing temperature variable is obtained from Eq. (5), Eq. (6) and Eq. (8), as given in Eq. (9).

$$t_i=\frac{x^2}{4\cdot D_{21^\circ C}\cdot\left(\dfrac{t_0}{365\cdot 30}\right)^m\cdot\exp\left[\dfrac{\left[-4.46\ln\left[D_{21^\circ C}\cdot\left(\dfrac{t_0}{365\cdot 30}\right)^m\right]+27.92\right]\cdot 1000}{R}\left(\dfrac{1}{T_{21^\circ C}}-\dfrac{1}{T}\right)\right]\cdot\left[erf^{-1}\left(1-\dfrac{C_T}{C_S}\right)\right]^2} \quad (9)$$

3. RESULTS AND DISCUSSION

This paper takes the HZM project as an example to predict the service life of concrete structure in splash zones at different temperatures. The reference temperature is assumed to be 21℃. Studies have reported that temperature range of this sea area is between 15℃ and 29℃.[14] In order to explore the effect of temperature in a wider range, 5℃ is taken as an interval to take values ranges from 10℃ to 35℃. A summary of the random variables for the corrosion models adopted in this work is listed in Table 2[14]. The length of the initiation period of concrete is predicted by using the model of introducing temperature variable.

Table 2: Distribution Parameters for Variables

Parameter	Distribution	Mean or α	Standard Deviation or β
D_{28d} ,m^2/s	Normal	3.0×10^{-12}	0.6×10^{-12}
C_S,%	Lognormal	5.76	0.87
C_T,%	Beta	0.22	0.36
x,mm	Normal	80	0.00526
m	Normal	0.471	0.0286

Fig. 2 shows comparisons of damaged probability, which is the probability of concrete structures reaching service life in time t, at different temperature based upon the Life-365 model and the statistical model both using Monte Carlo method and the parameter values from Table 2.

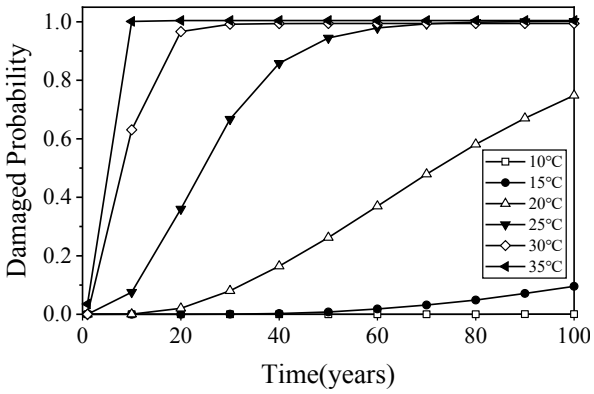

(a) E_a=-4.46ln($D_{nssm,21}$)+27.92

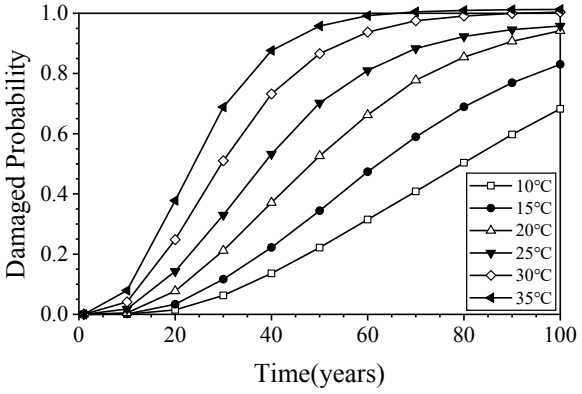

(b) E_a=35kJ/mol

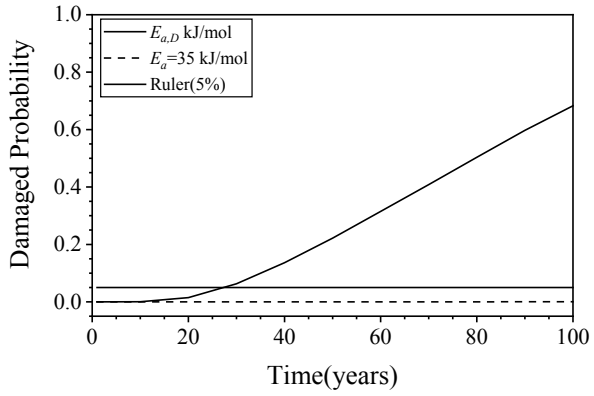

(c) 10℃

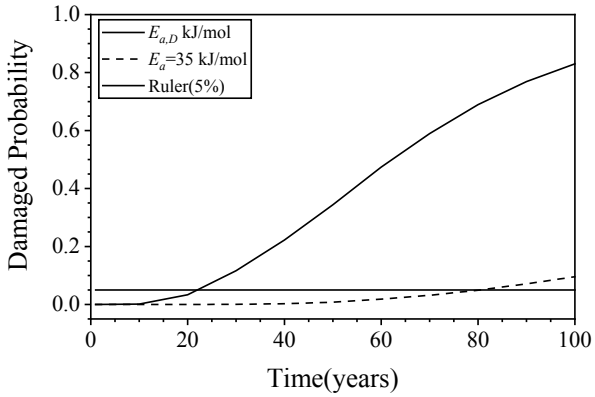

(d) 15℃

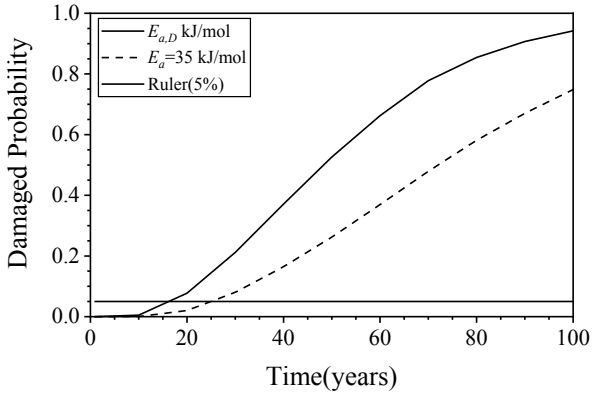

(e) 20℃

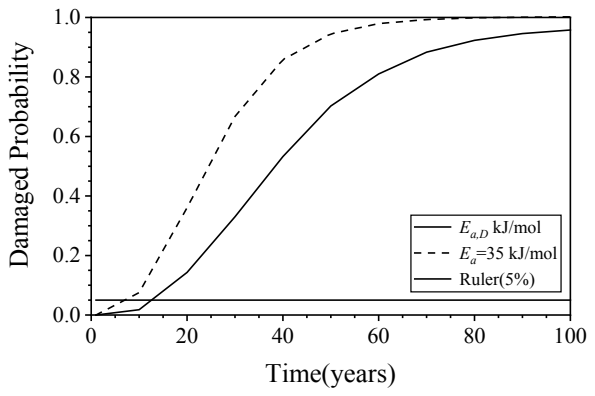

(f) 25℃

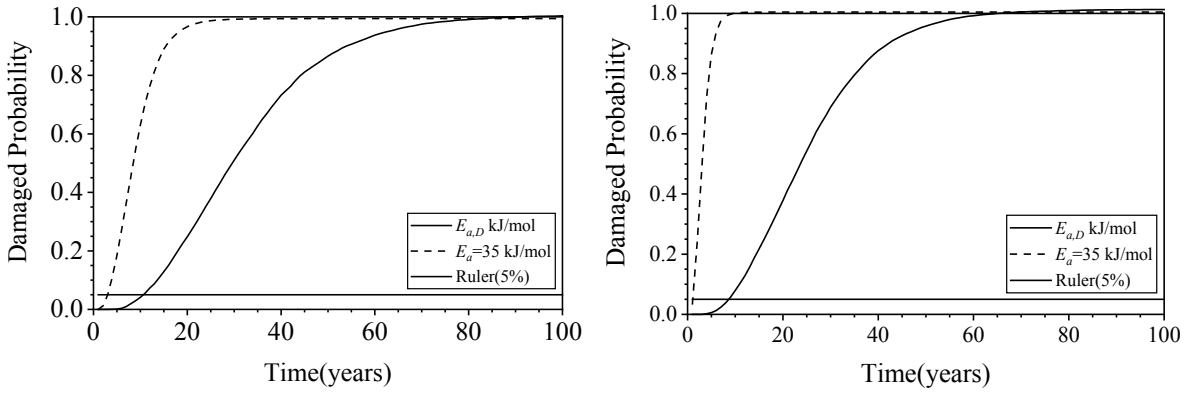

(g) 30℃ (h) 35℃

Figure 2: Comparison of damaged probability at different temperatures

5% is assumed to be the maximum probability that concrete structures are allowed to reach the chloride concentration threshold within time *t* in this paper, which is called the probability limit. Fig.2 (a) and Fig.2 (b) show the variation trend of the probability of reaching service life of two models with time at different temperatures. It is found that there is a difference in time t between the statistical model and the Life-365 prediction model, in which E_a is 35 kJ/mol, when the probability is the same. Likewise, the slopes of both probability curves are markedly elevated as the temperature increases. The comparison of probability changes at different temperatures are shown in Fig.2 (c) to Fig.2 (h). It appears to suggest that with the temperature rising, the time to reach the probability limit decreases, which illustrates the service life of concrete structures is shorten with increasing temperature, and when the ambient temperature is 10 ℃, the service life predicted by the above two models are the longest in this investigation. The time gap between these two models to reach the probability limit reduces first and then increases with the rise of temperature, and the predicted results are basically the same at a certain temperature between 20 ℃ and 25 ℃. This is because E_a at various temperatures calculated by Eq. (6) differ from that in Life-365 life prediction model, which results in a large difference between the mean value and standard deviation of chloride diffusion coefficient of the two models calculated by Arrhenius equation. Therefore, the time for structures to reach the probability limit of service life are also not same. This illustrates that the temperature sensitivity of this model is greater than that of the Life-365 model, which may provide a reference for predicting the service life of concrete structures under different temperatures theoretically.

4. CONCLUSIONS

- The results predicted by Monte Carlo method fit well with those predicted by distributed variable method, and are more accurate and easier to understand.
- The service life of concrete is affected by temperature, and the service life of concrete structures is shortened with increasing temperature
- There is a difference between the service life predicted by the model in the paper and the life-365 life prediction model and with the increase of temperature, the difference decreases and then increases.

- Based on the model developed in this study which introduces the correlation between $D_{nssm,21℃}$ and E_a, it will provide a reference for the durability design to extend the service life of marine concrete structures.

ACKNOWLEDGEMENTS

The authors acknowledge the financial support from Natural Science Foundation of Heilongjiang Province (No. LH2019E036).

REFERENCES

[1] Tutti, K., 'Corrosion of Steel in Concrete'. Stockholm： Swedish Cement and Concrete Research Institute. **82**(4)(1982)469-478.

[2] Vořechovská, D., Teplý, B,.and Chromá, M., 'Probabilistic assessment of concrete structure durability under reinforcement corrosion attack'. *Journal of Performance of Constructed Facilities*. **24**(6)(2010) 571-579

[3] Sagüés, A.A., 'Modelling the effects of corrosion on the lifetime of extended reinforced concrete structures'. *Corrosion*. **58**(10)(2003)854-866.

[4] Hartt, W.H., 'Service Life Projection for Chloride-Exposed Concrete Reinforced with Black and Corrosion-Resistant Bars', *Corrosion*. **68**(8)(2012)754-761.

[5] Kalos, M.H., and Whitlock P.A., 'Monte Carlo Methods, Volume 1: Basics'. *Technometrics*, **31**(2)(1989)269-270.

[6] Amey, S.L., Johnson, D.A., Miltenberger, M.A., and Farzam, H., 'Predicting the service life of concrete marine structures: an environmental methodology'. *ACI Structural Journal*, **95**(2)(1998)205-214.

[7] Benz, E.C., Thomas, M.D.A., and Ehlen, M.A., 'Life-365 Service Life Prediction Model for Reinforced Concrete Exposed to Chlorides'. 2012.

[8] Page, C.L., Short, N. R., and Tarras, A. EI., 'Diffusion of Chloride ions in Hardened Cement Pastes'. *Cement and Concrete Research*. **11**(3)(1981) 395-406.

[9] Li, X.M., Liu,Z,J., and Tang.Y., 'Reliability analysis of the security and stability control device based on the Monte Carlo method'. *Energy Procedia*. 145(2018) 9-14.

[10] Song, H.W., Pack, S.W., Ann, K.Y., et al. 'Probabilistic assessment to predict the time to corrosion of steel in reinforced concrete tunnel box exposed to sea water'. *Construction & Building Materials*. **23**(10)(2009)3270-3278.

[11] Kirkpatrick, T. J., Weyers, R.E., and Anderson-Cook, C.M., et al. 'Probabilistic model for the chloride-induced corrosion service life of bridge decks'. *Cement and Concrete Research*. **32** (2002) 1943-1960.

[12] Liu, Y., and Presuel-Moreno, F., 'A Laboratory Study on the Temperature Dependence of Chloride Transport in Concrete', in 'The Seventh International Conference on Concrete under Severe Conditions Environmental and Loading', Nanjing, September, 2013.

[13] Li,Q.W.,Li,K.F.,Zhang, Zhou,X.G., Q.M.,and Fan, Z.H., 'Model-based durability design of concrete structures in Hong Kong-Zhuhai-Macau sea link project'. *Structural Safety*. **53**(2015) 1-12.

[14] Wang, S.N., Li, K.F., Fan, Z.H., Su, Q.K., and Xiong, J.B., 'Durability strategy for main concrete structure of Hong Kong-Zhuhai-Macao Bridge with designed service life of 120 years'. *Port & Waterway Engineering*.3(2015)78-84.(in Chinese)

SULFATE DIFFUSIVITY ALTERED BY PORE CRYSTALLIZATION DUE TO CHEMICAL SULFATE ATTACK OF CEMENT-BASED MATERIALS

Bo Ran (1,2), Othman Omikrine Metalssi (2), Teddy Fen-Chong (2), Patrick Dangla (3), Kefei Li (1)

(1) Department of Civil Engineering, Tsinghua University, Beijing, 100084, P.R. China

(2) Université Paris-Est, MAST, FM2D, IFSTTAR, France

(3) Université Paris-Est, Laboratoire Navier (UMR 8205), CNRS, Ecole des Ponts ParisTech, IFSTTAR, France

Abstract

Three models are proposed for the sulfate diffusivity change due to the pore clogging by crystallization from the chemical sulfate attack of cement-based materials. The averaging model takes a linear relationship between the crystallization quantity and diffusivity change while the constriction model takes an inverse linear form and the self-consistent scheme model lies in between. These models are integrated into a diffusion-reaction model for chemical sulfate reactions in cement-based materials and solved numerically. The results show that all the three models can capture the rapid self-deceleration of sulfate ingress by fitting different relative kinetic coefficients k/D_0 and reduction parameters θ.

Keywords: cement, external sulfate attack, pore crystallization, pore refinement

1. INTRODUCTION

Sulfate attack is one of main durability concerns for concretes in saline-soil and marine environments. It leads to material expansion and spalling of cover concrete[1] thus accelerates the penetration of other aggressive agents. The cause of expansion is widely recognized to be ettringite formation. However, recent works show that the ettringite crystals formed in pores not only cause expansion but also induce pore refinement, which decelerates the sulfate ingress[2,3] and chloride diffusion for concrete under combined actions of sulfates and chlorides[4]. This paper attempts to quantify the sulfate diffusivity decrease in terms of pore clogging by crystallization. To this purpose, three conceptual models are proposed and solved numerically to demonstrate their respective capacities to account for this change.

2. SULFATE DIFFUSIVITY CHANGE BY PORE CRYSTALLIZATION

2.1 Pore structure change by pore crystallization

According to Clifton et al. [5], the effective diffusivity of sulfate ions through cement-based materials is three to five orders of magnitude smaller than the diffusivity in water D^{γ}. Particularly, the pore structure reduces the diffusivity through the following mechanisms: the solid skeleton lowers the diffusion volume; the tortuosity of diffusion path increases the diffusion path length; the constricted regions offers higher diffusion resistance.

During the sulfate reactions the ettringite crystals are formed in pores, altering the pore structure and the diffusivity for subsequent ion transport, cf. Figure 1(a), (b). In terms of the above effects, the crystals will decrease globally the diffusion area and increase the constricted regions. The tortuosity can be assumed unchanged during crystallization due to the unchanged path length. The sulfate diffusivity in the liquid film, between the crystal and the solid pore wall, is judged much smaller than D^{γ} values due to the electrical double layer effect[6] and the structured water molecules in liquid film[8,9]. The former is due to the building-up of a repulsion potential barrier from solid surface (crystal or pore wall), and latter is attributed to the much higher viscosity of liquid film in the layered structure of water molecules in liquid film. A reduction parameter θ (<1) is adopted for the diffusivity in liquid film compared to D^{γ}.

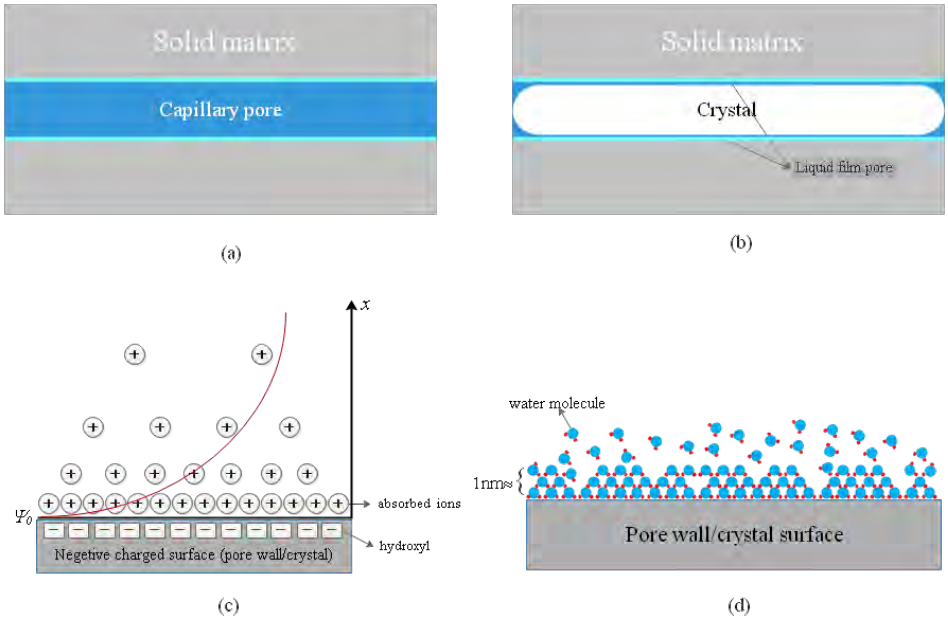

Figure 1: Diffusion path before crystallization (a), diffusion path during crystallization (b), electrical double layer on the surface (c)[7] and layer structure of water film (d)

Accordingly, the porosity during reactions can be divided into capillary porosity ϕ_{cap} (liquid), liquid film porosity ϕ_{film} (liquid but structured) and crystal porosity ϕ_{AFt} (solid). Assume further that the deformation is negligible during the crystallization process, we can write,

$$\phi_0 = \phi_{cap} + \phi_{film} + \phi_{AFt} \quad (1)$$

where ϕ_0 is the initial porosity. In a single cylinder pore, cf. Figure 1(b), the ratio of liquid film and crystal volumes writes,

$$\alpha = \frac{\phi_{\text{film}}}{\phi_{\text{AFt}}} = \frac{4d\delta - 4\delta^2}{d^2 - 4d\delta + 4\delta^2} \text{ and } \phi_0 = \phi_{\text{cap}} + (1+\alpha)\phi_{\text{AFt}} \tag{2}$$

where d is pore diameter and δ the thickness of film. Depending how the change of pore structure is considered for the diffusivity change, three models are proposed in the following.

2.2 Three models for diffusivity change

The first model, averaging model, considers the contribution of liquid phase, ϕ_{cap} and ϕ_{film}, on an average basis, and neglects the constriction effect. Thus, the resulted sulfate diffusivity writes,

$$D^{\text{avg}} = \phi_{\text{cap}} D^{\gamma} + \phi_{\text{film}} \theta D^{\gamma} = D^{\gamma}\left[\phi_0 - \left(1+\left(1-\theta\right)\alpha\right)\phi_{\text{AFt}}\right] \tag{3}$$

The initial diffusivity before crystallization D_0 equals to $D^{\gamma}\phi_0$ under the premise that all the pores are capillary pores before reaction. And the ratio between the initial sulfate diffusivity and the changed diffusivity is,

$$\frac{D^{\text{avg}}}{D_0} = 1 - \left[1+\left(1-\theta\right)\alpha\right]\frac{\phi_{\text{AFt}}}{\phi_0} \tag{4}$$

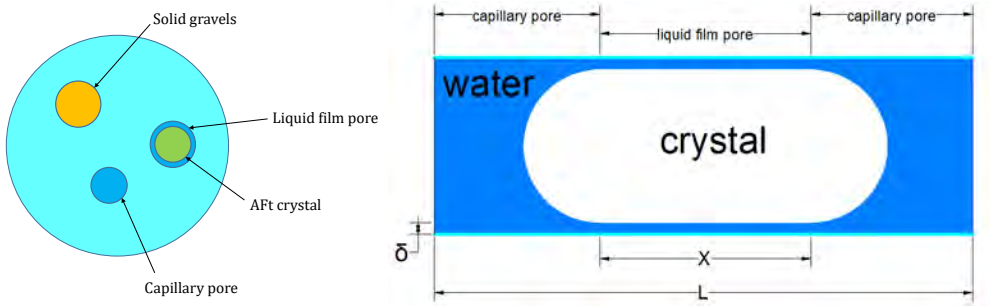

(a) (b)

Figure 2: Material REV (a) and constriction effect by crystallization (b)

The self-consistent scheme model considers the same contribution to diffusivity but employs a homogenization scheme to describe the diffusivity change. The pores and the phases in pores are considered as the inclusions embedded in the homogeneous matrix. Taking the available results for thermal conductivity[10], the diffusivity can be expressed as[8],

$$D^{\text{hom}} = \overline{DA} = \overline{D_i}\,\overline{A_i} = \sum(\phi_i D_i \overline{A_i}) \tag{5}$$

where i represents the different phases in the representative elementary volume (REV), ϕ_i, D_i and A_i represents volume fraction, diffusivity and average concentration tensor of phase i. The average concentration tensor is referred to shape geometry and spatial distribution of inclusions[9]. Further, we assume spherical capillary pores (cap), spherical AFt crystals (AFt), and annular liquid film (film) enfolding AFt crystals and spherical solid matrix (S), cf. Figure2(a), with the diffusivity for each phase:

$$D_{\text{cap}} = D^{\gamma},\ D_{\text{AFt}} = D_S = 0,\ D_{\text{film}} = \theta D^{\gamma} \tag{6}$$

The average concentration tensors were solved by Yang[8] and that the homogenized diffusivity D^{hom} is,

$$D^{\text{hom}} = D^{\gamma}\frac{\phi_{\text{cap}}A_{\text{cap}} + \alpha\theta\phi_{\text{AFt}}A_{\text{film}}}{\phi_{\text{cap}}A_{\text{cap}} + (3/2+\alpha)\phi_{\text{AFt}}A_{\text{film}} + (1-\phi_0)A_S} \tag{7}$$

with,

$$A_S = \frac{3}{2},\ A_{\text{AFt}} = \frac{3}{2}A_{\text{film}},\ A_{\text{cap}} = \frac{3D_{\text{hom}}}{D^{\gamma}+2D_{\text{hom}}},\ A_{\text{film}} = \frac{3D_{\text{hom}}(\phi_{\text{AFt}}+\phi_{\text{film}})}{(3\phi_{\text{AFt}}+2\phi_{\text{film}})D_{\text{hom}} + \phi_{\text{film}}\theta D^{\gamma}} \tag{8}$$

Note that the initial diffusivity without crystallization can be obtained from Eq.(7) letting $\phi_{\text{cap}}=\phi_0$ and $\phi_{\text{AFt}}=0$. Then, the diffusivity ratio between without and with crystals is expressed as,

$$\frac{D^{\text{hom}}}{D_0} = \frac{\phi_{\text{cap}}A_{\text{cap}} + \alpha\theta\phi_{\text{AFt}}A_{\text{film}}}{\phi_{\text{cap}}A_{\text{cap}} + (3/2+\alpha)\phi_{\text{AFt}}A_{\text{film}} + (1-\phi_0)A_S}\cdot\frac{\phi_0 A_{\text{cap}} + (1-\phi_0)A_S}{\phi_0 A_{\text{cap}}} \tag{9}$$

The third model, constriction model, takes into account the constriction effect of the pores filled by solid crystals (AFt), cf. Figure 2(b). Assuming the pore geometry as cylindrical, the constriction effect for diffusion can be described through connected series pores of capillary (liquid) and liquid film (semi-liquid), and the resulted diffusivity writes,

$$\frac{\phi_0}{D^{\text{csr}}} = \frac{1}{D_0}\left[\phi_{\text{cap}} + \frac{(\phi_{\text{AFt}}+\phi_{\text{film}})^2}{\theta\phi_{\text{film}}}\right] \tag{10}$$

and the diffusivity ratio between without and with crystals can be deduced as,

$$\frac{D^{\text{csr}}}{D_0} = \left[1 + \frac{(1+\alpha)}{\alpha\theta}\left(1+\alpha(1-\theta)\right)\frac{\phi_{\text{AFt}}}{\phi_0}\right]^{-1} \tag{11}$$

2.3 Comparison among the three models

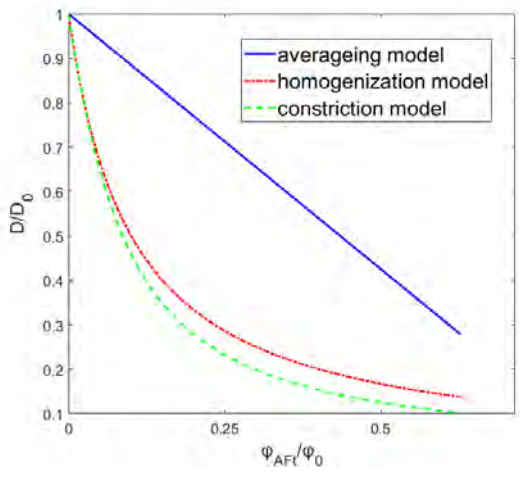

Figure 3: Comparison of three models for diffusivity change

The relations between the crystal porosity and the diffusivity ratio are illustrated in Figure 3 using Eqs.(4), (9), (11) from the three models. The averaging model shows a linear crystallization-diffusivity relation while the construction model predicts an inversely proportional relation and the self-consistent scheme model lies in between. The inversely proportional relation from constriction model indicates that a small amount of crystals can lead to a large reduction of diffusivity, which means the deceleration of sulfate ingress takes place in the very early stage of sulfate attack.

3. DIFFUSION-REACTION MODELLING FOR SULFATE ATTACK

3.1 Diffusion-reaction modelling

The diffusion-reaction model, in one dimension, is written through the mass conservation of sulfate ions in liquid phase of pores,

$$\frac{\partial c}{\partial t} = \frac{\partial}{\partial x}\left(D\frac{\partial c}{\partial x} \right) - kc \tag{12}$$

where c, D are respectively the aqueous concentration of SO_4^{2-} ion (mol/L) and its diffusivity (m^2/s), k is kinetic coefficient for the crystal formation (s^{-1}). This equation assumes that the mass change of sulfate ions in pores caused by the diffusion and the crystal formation or dissolution. The crystal porosity change, $d\phi_{AFt}$, is assumed to be proportional to the consumed sulfates ions kc in crystallization,

$$d\phi_{AFt} = \nu kc dt \tag{13}$$

where ν represents the volumetric increase associated with pore crystallization of ettringite (L/mol). The diffusion coefficient of sulfate ions in Eq.(12) will consider the impact of pore crystallization, discussed in the previous section through Eqs.(4), (9) and (11).

The Eq.(12) is solved numerically through an explicit finite difference method for the fixed value boundary condition for $c(x=0, t>0)= c_0$. The algorithm is described as follows: the time-space domain $R=\{(x,t):0\le x\le L, 0\le t\le T\}$ is discretized into a grid of m-1 by n-1 mesh with sizes $h=L/m$ and $\tau=T/n$. For a fixed position, $x=ih$, the sulfate concentration at the instant, $t=(j+1)\tau$, is calculated through the explicit difference scheme,

$$\frac{c_i^{j+1}-c_i^j}{\tau} = \frac{1}{h}\left[\frac{(D_{i-1}^j + D_i^j)}{2}\frac{(c_{i-1}^j - c_i^j)}{h} - \frac{(D_i^j + D_{i+1}^j)}{2}\frac{(c_i^j - c_{i+1}^j)}{h} \right] - kc_i^j \tag{14}$$

where c_i^j, D_i^j are respectively the sulfate concentration and its diffusivity at the point ($x=ih$, $t=j\tau$). Then the crystal porosity can be calculated based on the discrete scheme of Eq.(13) and substitute it into Eq(4), (9) and (11) to obtain the changed diffusivity.

3.2 Modelling results from simulations

The volume increase ratio ν is taken as 0.165[11], and the initial porosity ϕ_0 is 0.35[2]. Then it is assumed that the average pore diameter is 20nm and thickness of liquid film is 1nm, α equals to 0.23. In a thin water channel with 1nm size, the double layer effect reduces the diffusivity to about 0.1 times of D^{γ}[6], and the increased viscosity results in a 20% reduction in the diffusivity[9]. Accordingly the reduction parameter θ should be less than 0.1.

By fitting two unknown parameters, relative kinetic coefficient k/D_0 and reduction parameter θ, the experimental results of relative ettringite amount in Ref. [2] can be represented through diffusion-reaction model combined with three diffusivity models in Figure 4. The fitting parameters are shown in Table 1. The values of relative kinetic coefficient k/D_0 are 0.48-1.67mm^{-2}. The θ values from the last two models are close to 0.1. The possible reason why they exceed 0.1 is that the gel pores (liquid film pores) in C-S-H are ignored. However, to reproduce the rapid decrease of sulfate adsorption in Ref. [2] for linear crystallization-diffusivity relation from the first model, the reduction parameter should be as small as 10^{-4}.

As aforementioned, the reduction parameter is to characterize the reduction of diffusivity in liquid film pores. It depends on pore diameter and solid surface materials. And the kinetic coefficient is referred to the solution ions and the temperature.

Certainly the obtained values for these two parameters are only for model comparison purpose. To obtain the true values of these two parameters, more kinetics-based data are expected for the diffusivity change and the ettringite formation.

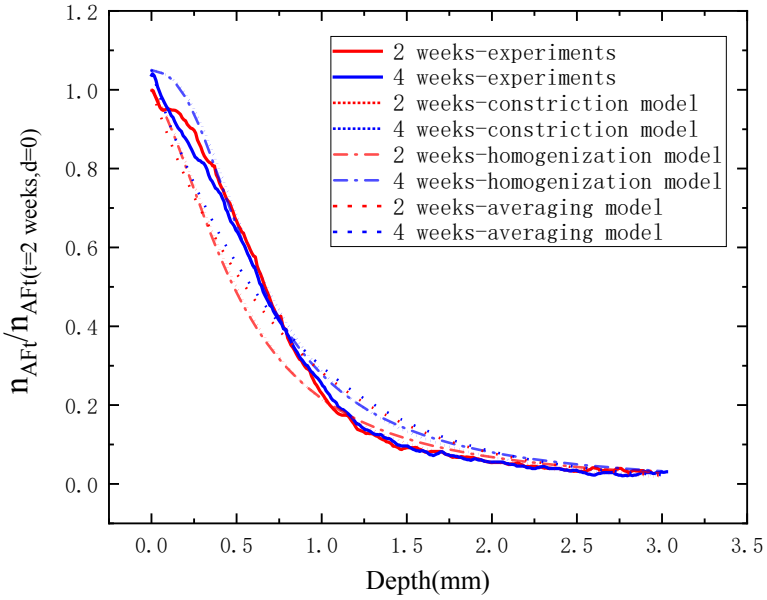

Figure 4: Relative ettringite amount in hardened cement paste in terms of diffusion depth at 2, 4 weeks of sulfate exposure. The parameters are retained as follows in the numerical simulations: ϕ_0=0.35[3], α=0.23, ν=0.165[11], c_0=0.3 M[2].

Table 1: Relative kinetic coefficient and reduction parameter in three models

Diffusivity change model	k/D_0 (mm^{-2})	θ
Averaging	1.67	0.0001
Homogenization	0.48	0.15
Constriction	0.95	0.35

4. CONCLUSIONS

- The change of sulfate diffusivity of cement-based materials by pore crystallization during chemical sulfate attack is addressed through three models: the averaging model, self-consistent scheme model and constriction model. All these models can describe the diffusivity decrease by pore crystallization and the constriction model gives most rapid decrease with the AFt formation.
- From a conceptual diffusion-reaction model for chemical sulfate attack, the rapid decrease of sulfate adsorption observed in experiments can be explained by the reduction of diffusivity in three proposed models. And a further study should be conducted to measure the kinetic coefficient and reduction parameter.

ACKNOWLEDGEMENTS

The research is supported by National Key R& D Program of China (No. 2017YFB0309904).

REFERENCES

[1] Mehta, P. K.; and Monteiro, P. J. M., 'Concrete: Microstructure, properties, and materials', 2nd Edn (1993).
[2] Naik, N., Sulfate attack on portland cement-based materials: Mechanisms of damage and long-term performance, Ph.D. thesis, Georgia Institute of Technology, 2003.
[3] Ragoug, R. , Metalssi, O. O. , Barberon, F. , Torrenti, J. M. , Roussel, N. , & Divet, Loïc, et al. 'Durability of cement pastes exposed to external sulfate attack and leaching: physical and chemical aspects'. *Cement and Concrete Research*, 116 (2019), 134-145.
[4] Cao, Y. , Guo, L. , & Chen, B. , 'Influence of sulfate on the chloride diffusion mechanism in mortar'. *Construction and Building Materials,* 197(2019), 398-405.
[5] Clifton, J. R., Bentz, D. P. & Pommersheim, J.M., 'Sulfate diffusion in concrete', NISTIR 5361, Building and Fire Research Laboratory, National Institute of Standards and Technology, 1994.
[6] Yang, Y. K.; Patel, R.A.; Churakov, S.V.; Prasianakis, N.I.; Kosakowshi, G.; Wang, M.R. 'Multiscale modeling of ion diffusion in cement paste: Electrical double layer effect'. *Cem. Concr. Compos*, 96(2019), 55–65.
[7] C. Labbez, B. Jönsson, I. Pochard, A. Nonat, B. Cabane, 'Surface charge density and electrokinetic potential of highly charged Minerals: experiments and Monte Carlo simulations on Calcium silicate hydrate', *J. Phys. Chem*. B 110 (18) (2006) 9219-9230.
[8] Yang, R. W. Contributions to micromechanical modelling of transport and freezing phenomena within unsaturated porous media. Ph.D. thesis, Université Paris-Est, 2013.
[9] Li, T. D., Gao, J., Szoszkiewicz, R., Landman, U., & Riedo, E., 'Structured and viscous water in subnanometer gaps'. *Physical Review B*, 75.11(2007), 115415.
[10] Gruescu, C., Giraud, A., Homand, F., Kondo, D. & Do, D. P., 'Effective thermal conductivity of partially saturated porous rocks'. *International Journal of Solids and Structures*, 2007, 44(3-4), 811-833.
[11] Atkinson, A. & Hearne, J. A., 'Mechanistic model for the durability of concrete barriers exposed to sulphate-bearing groundwaters'. *MRS Online Proceeding Library Archive,* 176(2011).

THE ROLE OF THE MICRON-SCALE IN REACTIVE TRANSPORT PROCESSES

Fabien Georget (1), William Wilson (1), Wioletta Soja (1), Junjie Zheng (1,2), and Karen Scrivener (2)

(1) École polytechnique fédérale de Lausanne (EPFL), Lausanne VD, Switzerland

(2) CCCC Fourth Harbor Engineering Institute Co., Ltd., Guangzhou, China

Abstract

Quantitative predictions for durability issues are necessary to adapt the formulations of cement blends with novel supplementary cementitious materials. These predictions are usually carried out with reactive transport models which are solved at the macroscopic scale. Upscaling laws are necessary to ensure that effective transport properties represent the lower scales properties. Therefore, to define reasonable laws, we need to understand the mechanisms at lower scales.

In this work, we focus on the impact of the micron-scale on reactive transport models. We employ the *edxia* framework to investigate chemical mappings of samples subjected to macroscopic durability tests (obtained with energy dispersive spectroscopy in a scanning electron microscope). The samples investigated are (1) a carbonating cement paste sample, (2) a specimen of 16-year old concrete exposed to sea water, and a cement paste subjected to chloride electro-migration. We demonstrate that both profiles and quantitative chemistry of phases can be readily obtained to characterize reactive transport processes at the micron scale. The results are used to discuss the definition of the representative elementary volume in the case of carbonation and chloride ingress. In addition, we demonstrate that we can quantify the AFm solid solution along the depth of the sample.

Keywords: Durability,Carbonation,Chloride Ingress,SEM-EDX,edxia

1. INTRODUCTION

To improve the sustainability of cementitious material, the best compromise must be found between the environmental footprint of the initial materials and the durability of the concrete. Modeling and simulations are promising methods to accelerate the discovery and the standardization of new formulations, but they need to be fully validated before quantitative predictions can be claimed. This is a difficult challenge as it necessitates to decouple the transport and chemical driving forces. Most experimental protocol only provides macroscopic profiles. However most simulations lacks both the effective diffusion properties and precise information about the phase assemblage. Therefore, fitting these profiles to obtain the properties depends on many assumptions. It was recently shown that many of these assumptions often breaks when many systems are compared together [1].

More advanced characterization techniques can be used. For example Morandeau et al. [2], used gamma-densimetry, TGA and XRD to analyse the change in phase assemblage during carbonation. However, their measure average over a large volume (5mm in depth) and their analysis depends on strong assumptions (e.g., no density changes due to drying). Maltais et al. [3] presented microprobes analysis and qualitative SEM-EDX analysis to study chloride ingress and sulfate attack. Although it was shown that it can improve the validation of models, the lack of quantification and phase identification means that the mechanisms cannot be independently validated.

In this paper we present practical examples of advanced microstructure characterization of carbonation and chloride ingress experiments initially performed at the macroscopic scale. Chemical mappings are analysed using the *edxia* framework to identify phases, quantify their chemistry and determine profiles of elemental concentrations and phase chemistry.

2. MATERIALS AND METHODS

2.1 Carbonation sample

Cement pastes were prepared from an ordinary Portland cement at w/b=0.4 using a vacuum mixer and cast in plastic cylindrical moulds (diameter 32mm). After one day of sealed curing, the pastes were demolded and exposed at the relative humidity (RH) of 95 % until the age of 28 days. Cylinders were cut with a slow speed saw allowing to obtain thin slices with a thickness of 1mm. The slices were exposed to natural carbonation environment at 400ppm of CO2 and 70% RH. Moreover, reference samples were exposed to CO2-free atmosphere and 70% RH [7].

2.2 Bulk diffusion sample

Concrete samples were prepared with an OPC cement blended with 30% Fly Ash. In a 10x10x10 cm molds. The samples were demolded at 1 day and cured for 28 days. They were then exposed in an industrial facility for 16 years in the tidal zone. The total chloride profile was obtained by grinding the samples layer by layer and titrating the chloride content following the ASTM C1152 [11].

2.3 Electro-migration sample

ement pastes were prepared from an ordinary Portland cement at w/b=0.4 using a vacuum mixer and cast in plastic cylindrical moulds (diameter 32mm). After one day of sealed curing, the pastes were demolded and cured in small amount of water with crushed samples to avoid leaching. Cylinders were cut with a slow speed saw allowing to obtain thin slices with a thickness of 10mm. The samples were subjected to an electro-migration test as described in Wilson et al. [12].

2.4 SEM-EDS sample preparation and acquisition

After the analysis, the samples were dried using the solvent exchange method: isopropanol was changed two times during the first 24 hr, then the sample was removed after 5–7 days of immersion and placed in a desiccator for at least 48 hr. A piece of the sample was then impregnated using a low viscosity epoxy resin. The sample's surface was polished using diamond suspensions (9 μm, 3 μm and 1 μm) [13].

SEM-EDS for the carbonation and the bulk diffusion sanples were carried out with a Quanta 200 scanning electron microscope equipped with a tungsten filament and operated at an accelerating voltage of 15 kV, the working distance was 12.5 mm. A Bruker AXS Microanalysis XFlash 4030 silicon drift detector was used as the EDS detector. The electron migration sample was studied using a Zeiss Cross Beam FEI equipped with an Oxford Ultim Max 170 energy-dispersive spectrometer. The EDS analyses were calibrated with standard reference materials (CaCO3 for C, CaSiO3 for O & Ca, Jadeite for Na, MgO for Mg, Al2O3 for Al, SiO2 for Si, CaSO4 for S, KCl for Cl & K, TiO2 for Ti, and Fe2O3 for Fe).

2.5 SEM-EDS maps analysis

The maps were analyzed with the *edxia* framework [10,14]. Quantitative maps are used as input. Representative points are extracted from the maps using a SLIC segmentation of a Si-Al-Ca composite image. These points are then analyzed using ratios plots similar to the EDS point analysis workflow[13]. The composition of the AFm was found by using the Cl/Ca vs. Al/Ca ratio plots as described by Sui et al. [6], i.e. the composition of the pure AFm is given by the extrapolation of the mixture line between the C-S-H and the AFm to Al/Ca=0.5. The C-S-H were found by plotting the points in the Al/Ca vs Si/Ca. The Cl/Ca were found by averaging the Cl/Ca of the points identified as C-S-H.

3. RESULTS

3.1 Characterization of the carbonation front

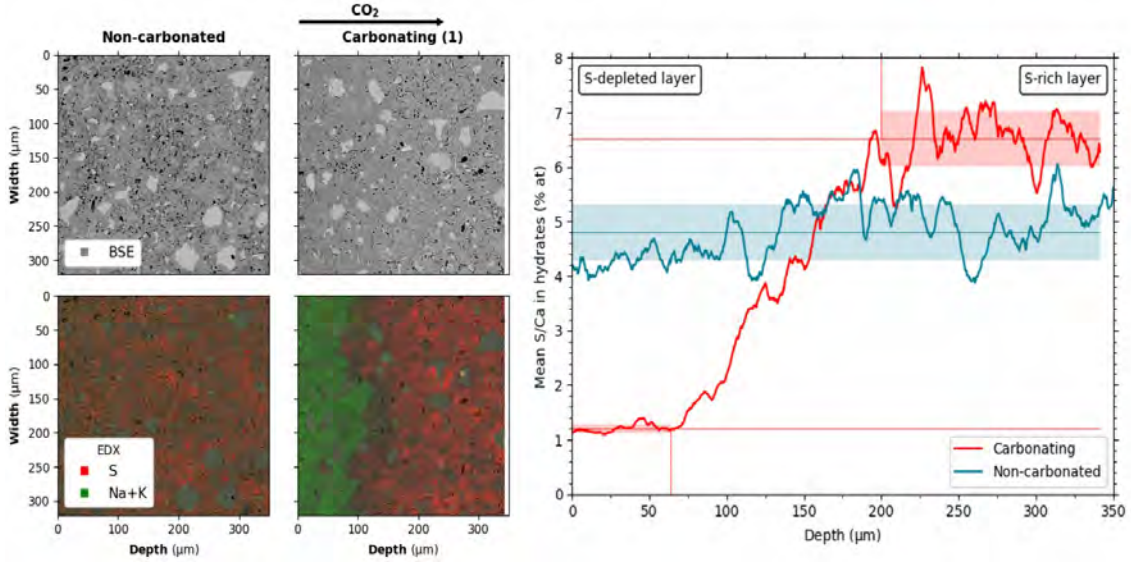

Figure 1: Identification of the carbonation front by SEM-EDX: sulfur concentration accross the carbonation front

Figure 1 presents the BSE and an EDS composite map as well as the mean S/Ca in the hydrates in a carbonated sample and a similar sample subjected to a carbon-free atmosphere. In the non-carbonated sample, the S/Ca is mostly constant across the sample. But the

carbonated sample present a clear gradient with a sulfate-depleted layer at the surface and a sulfate enrichment in the core. This sulfate diffusion was hypothesized by Georget et al. [4] and verified experimentally by De Weerdt et al. [5]. This is an independent validation of this intrinsic mechanisms of carbonation. It should be noted that few models consider this effect that may have drastic effect on the porosity [4].

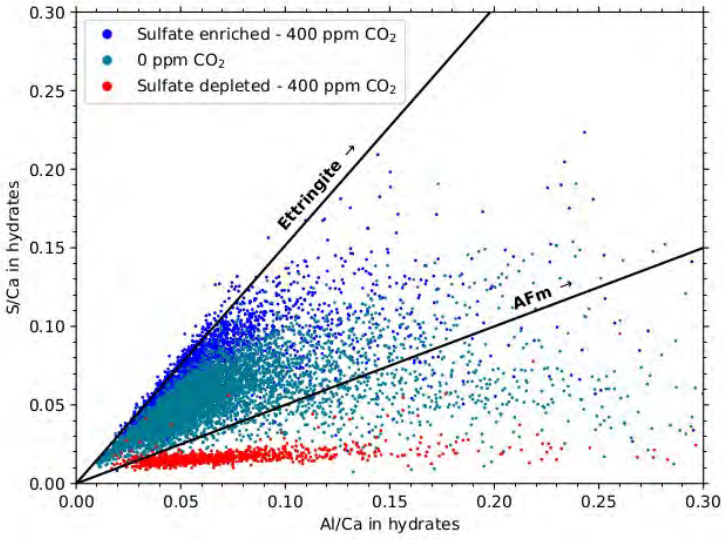

Figure 2: Phase identification accross the carbonation front: the higher sulfate concentration in the non-carbonated layer is due to the precipitation of ettringite.

Using thermodynamic arguments, it can be hypothesized that the sulfate enrichment is due to the precipitation of ettringite. Our methods can demonstrate it. Figure 2 shows the S/Ca ratio versus the Al/Ca ratio in sampling points situated in the hydrates. The points from the non-carbonated samples shows the typical profile where the C-S-H point are mixed in-between the ettringite and the AFm mixture lines. In the sulfate-depleted layer, the S/Ca is greatly decreased without significant change to the Al/Ca. This indicates that the other main elements do not diffuse with sulfur. On the opposite side of the sample, the S/Ca is significantly increased and the points align better with the portlandite-ettringite mixture line. This is a demonstration of the higher content of ettringite in the non-carbonated layer of the carbonated sample.

3.2 Characterization of bulk diffusion profiles

A similar chemical characterization can be performed for chloride bulk diffusion sample. Figure 3 presents the total chloride content profile for a fly ash concrete. These type of profile is hard to validate because it mixes many mechanisms: diffusion of chloride, leaching, chemical binding in AFm and chemical binding in C-S-H. Using quantitative SEM-EDS maps acquired along the depth of the sample, it is possible to separate these effects. Thus, Figure 3 also present the Cl/Ca ratio in the C-S-H gel and in the Afm, as well as the portlandite volume

fraction. The Cl/Ca ratio provides the binding affinity for these phases. With the quantification of these phases, it is possible to quantify the total binding capacity provided by these phases [6]. The portlandite volume fraction provides an indication of the leaching. Although the signal-to-noise ratio is high, there is a clear indication of leaching in the first 10mm of the sample.

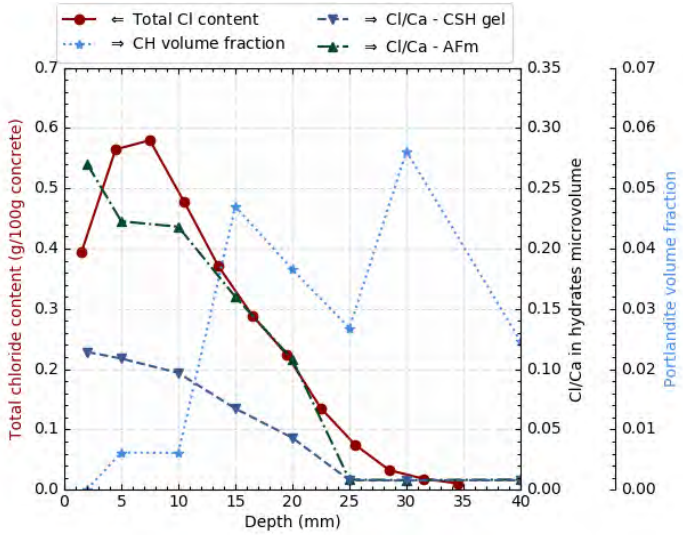

Figure 3: Characterization of the bulk diffusion profilein fly ash concrete samples: Cl/Ca in AFm and C-S-H gel microvolume and the portlandite volume fraction.

3.3 Characterization of electro-migration profile

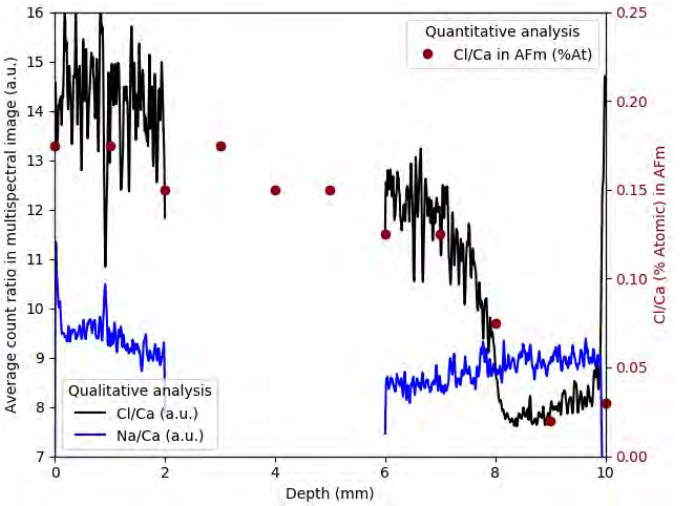

Figure 4: Characterization of the electro-migration front: Cl/Ca in AFms and sodium gradient

Figure 4 presents the chloride front as seen by the Cl/Ca ratio in counts, as observed in qualitative EDS maps, at day 6 of the experiment. A clear drop is observed around 8mm. On the opposite, the Na/Ca is flatter, with a small increase on the side of the samples. On the upstream side, the Cl/Ca profile is relatively flat even the chloride content is slightly higher at the surface. To complement this analysis, quantitative EDS maps were acquired along the depth of the sample.

4. DISCUSSION

4.1 The representative elementary volume

The resolution of SEM-EDS maps is typically around the micrometer. This size is limited by the interaction of the electron beam with the sample [8] . It is however smaller than most other methods available such as XRD and TGA. It is also smaller than the characteristic length of transport as seen in our profiles. As such it allows us to investigate the details of the front.

These analysis can be used to define a representative elementary volume characteristic for the durability problem. This can be used to identify the main mechanisms at play. For example, in the case of carbonation the advancement at 6 months is limited to the first hundreds of micrometers. However, the apparent carbonation front is also a hundred micrometers. This is only an apparent carbonation front, because the front is narrower if it is observed directly on the EDS composite maps (figure 1). Locally it can be seen that the front is at most 50 micrometer. However, the front is non-sharp and tortuous. This micrometer scale tortuosity creates a wider apparent diffusion coefficient. This tortuosity should be considered when identifying the representative elementary volume.

However, Figure 1 shows that no clean representative elementary volume can be defined for this experiment since the scale of the heterogeneities is close to the scale of the front. It means that no single effective diffusion coefficient can be defined, instead a distribution of diffusion coefficient needs to be defined. This distribution of diffusion coefficient will widen the front even if local thermodynamic equilibrium is assumed [7].

The same problem does not impact as strongly the chloride diffusion. The diffusion profiles are wider (a few millimeters) and the microstructure is more homogeneous at the millimeter scale. Therefore, a correct representative volume can be defined, as well as a unique chloride diffusion coefficient in the cement paste. However, it should be noted that the aggregates still create large scale heterogeneities. For example, it can be seen on figure 3 that the Cl/Ca ratio in AFm and in CSH is null at 25mm. However, the total chloride content is not 0. The total chloride content is measured over a much larger volume that the EDS maps. This higher content is probably due to the heterogeneities caused by the aggregates which widen the apparent diffusion profile.

4.2 The chloride solid solution

The wide front of the bulk diffusion problem is assumed to be due to the solid solution between the AFm and the friedels' salt, where the total content of chloride in AFm is

increasing with the chloride concentration in solution. Most chloride ingress models assume a monosulfate based solid solution. However, most OPC contains at least 2 % limestone which is sufficient to transform all sulfate-AFm into carbonate-AFm [8]. However, this solid solution is less known and the necessary data for proper validation is lacking [6]. Our method provides the amount of chloride in the solid solution along with the bulk diffusion profiles, or the electromigration front. This is an important information as it allows to decouple the chemical and the transport mechanisms when validating reactive transport models. In particular it can be noted in figure 5 that only a fraction of the maximum binding capacity in AFm is reached in this electro-migration experiment (Cl/Ca = 0.15 <0.5). In the bulk diffusion profile, higher values are reached however they are still half of the maximum value.

5. CONCLUSIONS

Validating reactive transport models on profiles of macroscopic experiments is challenging for cementitious materials due to the different mechanisms occurring simultaneously. The use of the *edxia* framework for quantitative image analysis of SEM-EDS maps provides comprehensive and complementarity information on the microstructure:

- The phases formed can be identified;
- The composition of these phases can be measured;
- The analysis can be done along the depth of the sample and compared to standardized macro-scale measurements.

For example, the fate of sulfur was studied in carbonating sample. In addition to validating mechanisms seen in simulations [4], this study provided some insight on the representative elementary volume necessary to define the effective transport properties. Large heterogeneities exist at the scale of the front and creates a sharp but tortuous front which could be misinterpreted as kinetically-controlled reaction. For chloride ingress, we demonstrated that we can obtain crucial information on the chloride binding (usually neglected in assumptions). This information is key to decouple the transport and chemical mechanisms.

Future studies will focus on coupling this method with complementary methods to study the microstructure, and on applying these results to validate reactive transport modelling of chloride ingress.

ACKNOWLEDGEMENTS

Wioletta Soja thesis was funded by the Swiss National Science Fundation(SNF) under the project no 154026: “Formulation, use, and durability of con-crete with low clinker cement.”. This support is most gratefully acknowledged.We would also like to thanks LafargeHolcim for providing some materials for this study.

REFERENCES

[1] Sui, Shiyu, Georget, Fabien, Maraghechi, Hamed, Sun, Wei, Scrivener, Karen: Towards a generic approach to durability: Factors affecting chloride transport in binary and ternary cementitious materials , Cement and Concrete Research 124, 105783, 2019
[2] Morandeau, A., Thiéry, M., Dangla, P.: Investigation of the carbonation mechanism of CH and C-S-H in terms of kinetics, microstructure changes and moisture properties , Cement and Concrete Research 56(0), 153–170, 2014
[3] Maltais, Y., Samson, E., Marchand, J.: Predicting the durability of Portland cement systems in aggressive environments—Laboratory validation , Cement and Concrete Research 34(9), 1579–1589, 2004, H. F. W. Taylor Commemorative Issue
[4] Georget, Fabien, Prévost, Jean H., Huet, Bruno: Impact of the microstructure model on coupled simulation of drying and accelerated carbonation , Cement and Concrete Research 104, 1–12, 2018
[5] Weerdt, K. De, Plusquellec, G., Revert, A. Belda, Geiker, M.R., Lothenbach, B.: Effect of carbonation on the pore solution of mortar , Cement and Concrete Research 118, 38–56, 2019
[6] Sui, Shiyu, Wilson, William, Georget, Fabien, Maraghechi, Hamed, Kazemi-Kamyab, Hadi, Sun, Wei, Scrivener, Karen: Quantification methods for chloride binding in Portland cement and limestone systems , Cement and Concrete Research 125, 105864, 2019
[7] Georget Fabien, Wioletta Soja, Karen Scrivener, Characteristic lengths of the carbonation front in naturally carbonated cement pastes: implications for reactive transport models, Cement and Concrete Research (submitted)
[8] Lothenbach, Barbara, Saout, Gwenn Le, Gallucci, Emmanuel, Scrivener, Karen: Influence of limestone on the hydration of Portland cements , Cement and Concrete Research 38(6), 848–860, 2008
[9] William Wilson, Luca Sorelli, Arezki Tagnit-Hamou, Automated coupling of NanoIndentation and Quantitative Energy-Dispersive Spectroscopy (NI-QEDS): A comprehensive method to disclose the micro-chemo-mechanical properties of cement pastes, Cement and Concrete Research, Volume 103, 2018, Pages 49-65,
[10] Fabien Georget, & William Wilson. (2019, June 15). edxia (Version 0.1.0). Zenodo. http://doi.org/10.5281/zenodo.3246902
[11] ASTM C1152-12, Standard Test Method for Acid-Soluble Chloride in Mortar and Concrete. West Conshokocken: American Society for Testing and Materials, 2012, 4pages
[12] Wilson, W., Gonthier, J.N., Georget, F. and Scrivener, K.L., 'Tortuosity as a Key Parameter of Chloride Diffusion in LC3 Systems'. In: Bishnoi, S. (eds.), 3rd International Conference on Calcined Clays for Sustainable Concrete III. New Delhi, India: RILEM Bookseries by Springer, 2019, 13-20, accepted.
[13] Scrivener, K., Snellings, R., and Lothenbach, B., 'A Practical Guide to Microstructural Analysis of Cementitious Materials Edited', 2016.
[14] Georget, F., Wilson, W. and Scrivener, K., 'Comprehensive microstructure phase characterization from quantified SEM-EDS maps in cementitious materials' (In preparation)

WILL ORTHO-ENRICHED WATER INCREASE THE DURABILITY OF CONCRETE?

Kai Yang (1), Guang Ye (2), Geert De Schutter (1)

(1) Magnel Laboratory for Concrete Research, Ghent University, Belgium

(2) Microlab, Section of Materials and Environment, Delft University of Technology, Netherlands

Abstract

Water molecules exist as two spin isomers, differing by the relative orientation of the nuclear spins of the two hydrogen atoms: either antiparallel (para-water, S=0) or parallel (ortho-water, S=1) [1]. The transition between these nuclear spin states can be achieved through magnetic symmetry breaking via a field gradient across the spins applied by a suitably placed magnetic moment for a sufficiently long time [2]. The contradictory mechanisms of interaction between water or an aqueous solution and magnetic field were reviewed, especially the one expanded on Dynamically Ordered Liquid Like Oxyanion Polymers (DOLLOP) [3]. Then the state of art agreements that have been proved by reproductive experiments or theories were discussed. A new hypothesis for the magnetic effects on the interconversion of nuclear spin isomers of water at the interface of water-O_2 was proposed, as well as its applicability in the structure modification of C-S-H.

Keywords: magnetic field, nuclear spin isomers, water, DOLLOP

1. INTRODUCTION

Magnetism is one of the key physical properties of materials and every material has its own magnetism. It is a dream of chemists and physicists to use this physical property for controlling chemical and physical processes [4], including engineers in concrete technology. In 1962, Wulachoufuski and Alnanina in Russia started research on using magnetized water to mix concrete for military structures [5]. Similar research was also conducted in Japan, Europe, and China confirming that magnetized water could increase concrete strength by 10% [5, 6]. Besides, various studies have shown that usage of magnetic field treated water in the concrete field can increase the workability [7], accelerate the hydration reaction, improve the impermeability and freeze/thaw resistance [8] and early-age shrinkage cracking resistance [9]. Meanwhile, the effects of the magnetic field on the physicochemical [1] properties of water or aqueous solutions and morphology of mineral precipitation, like $CaCO_3$ [10] have been the most controversial issue for at least over a century [11, 12].

Objectively, according to a large number of related publications, patents, commercial devices, and published tests, there is no doubt that magnetized water exists. But even so, it is difficult to fully understand this "new material" since the nature of the magnetization mechanism of water is still very controversial. In order to better understand, when experiments on magnetic effects on water or aqueous solution are conducted, the following information should be carefully considered:

(1). The distribution of the magnetic field, including the strength, gradient, and frequency,
(2). The preparation of water, i.e. deionization, degassing, distillation,
(3). The gas dissolved in water or aqueous solution during the treatment and the tests,
(4). The temperature during the treatment and the tests,
(5). The exposure time in the field and the time needed to finish the tests,
(6). The cleaning procedures and possible contamination sources,
(7). The applied statistical methods.

Based on these criteria, a review was performed on magnetic effects as studied in recent decades to clear the inextricable links of the interconversion of nuclear spin isomers of water and the nature of magnetized water.

As a consequence of the Pauli principle, the wave function of a water molecule is antisymmetric under the exchange of its two protons, which is written as a product of a rotational state and a nuclear spin state [13]. Our hypothesis is that at room temperature the ratio of ortho/para water at the interface of O_2-H_2O is not 3.0 and that the water molecules stay at Triplet-Singlet-Imbalance (TSI) states. In an external magnetic field, oxygen dissolved in water catalyses the TSI states to the equilibrium state with the ratio of ortho/para to be 3.0. Meanwhile, metastable complexes form at the interface of O_2-H_2O that can last a relatively long time in the absence of external destructive perturbations, including alcohol, sonication or heat transfer, etc.

2. MECHANISMS FOR THE MAGNETIC EFFECTS

The unrepeatability of data is one of the main reasons why skepticism appears whenever the magnetic effects are discussed. Therefore, above all, it is necessary to clarify why the magnetic effects are always so doubtful.

In magnetic field – aqueous solution interactions, some observations can be perfectly understood with thermodynamics. In a highly inhomogeneous magnetic field, a magnetic force acts on a material with magnetic susceptibility χ, which can be utilized in synthesizing high-quality protein crystals [14], flying frogs [15] or aligning silicate-surfactant composites for preparing macroscopic structurally ordered silica [16]. However, not all of the magnetic effects can be perfectly understood in that scale, like the separation of nuclear spin isomers of water in the elegantly designed magnetic field with high vertical gradient [1], where quantum mechanics theory has to be used. In spin dynamics, the energy split by the magnetic field is several magnitudes lower than thermal energy, but they may nevertheless make a significant difference.

The correlation of magnetic flux density (B) and the involved effects is not linear. By increasing *B* from 0.1 to 1 T, a transition of magnetodesorption-to-magnetoadsorption of H_2O onto certain solids was observed. [17]. When the reduced coagulation rate constant was taken as an indicator for the magnetic effects, the capability of static magnetic field on promoting coagulation reached a "saturation level" at 0.4 T [18]. On the other hand, following the variation

of Zeta potential of TiO_2 and $CaCO_3$ suspensions in water, both the adsorption and the dissipation of the energy occur in an oscillatory manner [19].

It is an open question whether the magnetic effects can be recorded when the aqueous solution is relatively stationary with the field in time and space. The first proof of the existence of magnetized water supports that the water is magnetized only when water dissolved O_2 and B changed [20]. But it worth noting that, in microscale, both the water molecules and the dynamically ordered liquid-like oxyanion polymers (DOLLOPs) move randomly and rapidly at ambient temperature [21]. Moreover, the lifetime of water molecules is limited to several milliseconds due to the proton transfer [13]. Most of the time they are dissociated OH^--H^+ ionic pairs [22].

2.1 The mechanisms based on Lorentz force

The nature of the interaction between aqueous solution (including pure water) and the magnetic field is so complicated that there is no agreement even after decades of endless debate. Generally, the most popular mechanisms can be classified as ion mechanism and surface mechanism [11], in both of which, Lorentz force is supposed to increase the mobility of ion cluster.

Inspired by Michael Faraday as early as 1830, claiming that when a magnetic field flux is crossed by flow ions or conductive material, electrical current is induced, electromagnetic devices are installed in the cooling system to recycle and treat hard water [23]. The force is given by the vector product

$$\boldsymbol{F} = q(\boldsymbol{E} + \boldsymbol{v} \times \boldsymbol{B})$$

Where $\boldsymbol{F}$ is the force, q the charge, $\boldsymbol{E}$ the electric field, $\boldsymbol{v}$ the velocity, and $\boldsymbol{B}$ the magnetic induction. The force is perpendicular to both the velocity and the magnetic induction, thus the work is 0 and hence the energy is unchanged [24]. It has been proved that the Lorentz force on moving ions in solution is far too weak to affect a crystallization process to any measurable degree, even if it is realized that $\boldsymbol{v}$ is the instantaneous and not the drift velocity [3, 25]. Even allowing for a high dielectric constant, the induced electric dipole moment will be pitifully small [3]. This also applies to other kinds of motion, e.g. the proton in the O-H stretching vibration. And any perturbation of the electron structure of the ions may be ruled out as well since it is known that Zeeman effect requires high-resolution spectra to be detected [25].

Besides, the Lorentz force failed to explain the surface tension decrease of pure water due to the magnetic field [20] and other magnetic effects by static treatment [18, 26-30].

2.2 Agreements when interpreting magnetic effects

(1) “Memory effects”

The magnetic effects persist minutes or hours or days after the water treatment, which is uniquely known as the “magnetic memory of water” [31]. Both anecdotal and scientific evidence suggests that the effect is not ephemeral, but continues for some time after the field has been applied [32]. These “memory effects” have been recorded for decades and supported by a large number of published results.

(2) Proton transfer

The proton transfer was firstly proposed by H.E. Lundager Madsen in 1995 to explain the unusual magnet effects on precipitation of some inorganic salts. He found that increased nucleation and crystal growth rates in a 0.27 T static magnetic field only happened for carbonates and phosphates with diamagnetic metal ions [25]. Subsequently, it was proved that

at high pH and when heavy water was used as a solvent, the magnetic effects were suppressed, which confirmed the importance of proton transfer [33].

(3) Gas-liquid interface

The discovery that the main "receptor" of electromagnetic radiation or magnetic field is gas-water interface was published, for the first time, by Miroslav Colic and Dwain Morse in 1998 [34]. A helical resonator was used to stimulate triply distilled water, aqueous solution and colloidal silica, that has been degassed or not [34-36]. Although the results were not always fully reproducible and difficult to analyse statistically, they insisted that the magnetic effects can only be recorded in the samples without degassing. Subsequently, Sumio Ozeki, et al. concluded that only when water contains dissolved O_2, the water is magnetized by changing B over the water [20]. From the publications on "magnetized water", we should realize that the role of O_2 (or more generally, the air) dissolved in aqueous solutions has been overlooked.

2.3 DOLLOPs mechanism

This mechanism was offered by Coey, based on the non-classical nucleation mechanism for subsaturated calcium carbonate solutions. Bicarbonate ions, the predominant carbonate species in solution at neutral pH, are considered to park next to each other on one side of a polar nucleation cluster and form a negatively charged surface. The other, positive side is occupied by Ca^{2+} ions. For the cluster to grow on the negatively charged surface, protons in the HCO_3^- must be replaced by Ca^{2+} ions. An inhomogeneous magnetic field promotes the exchange of singlet and triplet states of the proton spin dimers next to the HCO_3^- layer and facilitates the attachment of Ca^{2+}, by spin-dephasing. It was estimated that for most of the magnet devices, the minimum magnetic gradient required is 100 T/m [3]. But, as usual, the gas-liquid interfaces are neglected in literature.

This mechanism successfully explained the "memory effects" and the proton transfer considered in the nucleation quantitatively. An increased formation of nm-sized prenucleation clusters due to the exposure to the magnetic field (0.2 T/m) was observed in tap water which is believed to be consistent with Coey's theory [21]. However, the critical criteria for this theory, a quantitative relationship between the magnetic gradient and these nm-sized clusters are missing in the discussion. In other words, the magnetic gradient in the same order of magnitude has been involved in nearly all of the experiments related to the magnetic effects and promotion on nucleation can be easily found in most of them. But these records cannot be the proof for Coey's theory, because the reasoning on proton transfer and a comparison with varying magnetic gradient have always been omitted.

2.4 A new mechanism based on the interconversion of ortho-para water

The foundation of this new mechanism is the interconversion of nuclear spin isomers of water, which can be catalysed by molecular O_2 in an inhomogeneous extra magnetic field.

(1). The ratio of ortho-para water in a liquid phase at ambient temperature

By terahertz time-domain spectroscopy, in-room temperature for water vapor, the ratio was found to be humidity-dependent. When the humidity approaches 50%, the ratio is around 1.0 due to the preferential formation of dimers and clusters at increasing concentrations [37]. For liquid water, via ^{1}H-NMR[38, 39], four-photon laser spectroscopy [38, 40] and Raman spectrum [41], Pershin, S. M, et al. found that the ratio varies in a wide range. In distilled water, the ratio is 1.0 due to hydrogen bonds. By comparing the proton density via ^{1}H-NMR with that

of distilled water, increased content of ortho water was observed [38]. Coincidentally, the ratio will relax to 3.0 rapidly when increasing the temperature or by sonication [42].

(2). The paramagnetic spin catalyst with molecular oxygen

O_2 has been proved to be a perfect paramagnetic spin catalyst for the conversion of $H_2@C_{60}$ and $H_2O@C_{60}$ at present [2, 43, 44]. In 2017, based on the concept of paramagnetic spin catalysis of H_2, the interconversion of ortho-para water was proved in H_2O and O_2 collisional complexes in an external magnetic field, which was believed to be the nature of "magnetized water" [45]. Now the paramagnetic catalyst theory is sufficiently developed to predict experimental results.

(3). Acceleration on the interconversion of nuclear spin isomers due to extra magnetic field

Different from the mechanism of ortho-para H_2 conversion on the magnetic surface [46, 47], an extrinsic magnetic field accelerates the interconversion, which was first observed in 1968 in the presence of Cr_2O_3 catalyst [48]. There was no consistent explanation until 1999 when the electron-nucleus resonant mechanism was proposed by E. Ilisaca and S. Paris [49, 50]. Besides, the influence of an external homogeneous magnetic field on nuclear spin conversion in CH_3F was predicted in 1997. The effects arose either from the Zeeman splitting or from the magnetic shielding of the molecular nuclei [51].

In liquid water, at ambient temperature, the dissolved oxygen, present as nanobubbles and surrounded by water molecules, forms clathrate-like complexes [52]. At this O_2-H_2O interface, the water is highly structured and each of them is in the Singlet or Triplet state. Without a magnetic field, there can be no coordination between the S or the T states of different water molecules, hence they cannot be correlated and induced to form part of the S or the T state of the overall clathrate. However, in an inhomogeneous magnetic field, protons process at different Larmor frequencies with promoted proton transfer rate. As a consequence, a clathrate with all co-directional water molecules develops a T eigenstate (where the ratio of ortho-para water is 3:1). When the magnetic field is removed, these clathrate complexes, in T eigenstate, being "frozen", serve as a nucleus for a potential crystallite in the bulk. In an electrolyte solution, cations favor the O_2-H_2O interfaces which become negatively charged. Dissociation of water molecules and proton transfer enhanced the solvation of cations, developing more cation-water complexes.

The comprehensive quantum mechanics explanation was first given by S. Srebrenik, et al. to explain the "memory effect" of magnetically treated water, via $Ca(H_2O)_n$ [53]. Afterwards, it was referred to by Sumio Ozeki in interpreting the magnetic-field-induced adsorption and desorption (MAD) and transient oxygen clathrate-like hydrates in pure water with dissolved O_2 induced by a magnetic field [17, 54, 55].

The formation of C-S-H follows a complex two-step pathway. In the first step, amorphous and dispersed spheroids are formed, whose composition is depleted in calcium compared to C−S−H and charge compensated with sodium [56]. It is possible that these "frozen" clathrate-like complexes act as nucleation sites to promote the formation of the spheroids. ^{1}H-NMR magnetic resonance relaxometry revealed four different populations of pore water in cement paste: C−S−H interlayer water (confined in about 1 nm spaces between the backbone C−S−H sheets), water confined in gel pores (spaces of a few nanometres between the stacks of the C−S−H sheets), and interhydrate (8-10 nm) and capillary pore water. At the interface of C-S-H sheets-water, water molecules dissociate to produce an OH^--H^+ ionic pair and form Si-OH and Ca-OH. This interface is controlled by protons transfer. In the polymerization of silica, Sumio Ozeki found that the magnetic field suppressed the formation of pores below 30 nm. Thus, it

can be inferred that the pore structure in C-S-H might be modified by the magnetic field. Related experiments on the structure of C-S-H and the possible improvement on the durability in microscale are in progress.

3. CONCLUSIONS

- The mechanisms based on the Lorentz force for interpreting the magnetic effects on aqueous solutions are reviewed generally and revealed to be doubtful.
- The interface of gas-liquid was neglected in the DOLLOPs mechanism and the related experiments cannot support the theory strongly.
- A new mechanism based on the interconversion of nuclear spin isomers of water at the O_2-H_2O interface was proposed and it is possible to use these clathrate-like complexes to promote the nucleation of C-S-H.

REFERENCES

[1] Kravchuk, T., et al., A Magnetically Focused Molecular Beam of Ortho-Water. Science, 2011. **331**(6015): p. 319-321.

[2] Chen, J.Y.C., et al., *Nuclear spin isomers of guest molecules in H-2@C-60, H2O@C-60 and other endofullerenes.* Philosophical Transactions of the Royal Society a-Mathematical Physical and Engineering Sciences, 2013. **371**(1998).

[3] Coey, J.M.D., *Magnetic water treatment – how might it work?* Philosophical Magazine, 2012. **92**(31): p. 3857-3865.

[4] Yamaguchi, M. and Y. Tanimoto, *Magneto-Science Magnetic Field Effects on Materials: Fundamentals and Applications*. 2006.

[5] Afshin, H., M. Gholizadeh, and N. Khorshidi, *Improving Mechanical properties of high strength concrete by magnetic water technology.* Scientia Iranica, 2010. **17**(1 A): p. 74-79.

[6] Su, N. and C.-F. Wu, *Effect of magnetic field treated water on mortar and concrete containing fly ash.* Cement and Concrete Composites, 2003. **25**(7): p. 681-688.

[7] Esfahani, A.R., M. Reisi, and B. Mohr, *Magnetized Water Effect on Compressive Strength and Dosage of Superplasticizers and Water in Self-Compacting Concrete.* Journal of Materials in Civil Engineering, 2018. **30**(3): p. 7.

[8] Choi, M.S., et al., *Effects of an externally imposed electromagnetic field on the formation of a lubrication layer in concrete pumping.* Construction and Building Materials, 2014. **61**: p. 18-23.

[9] Wei, H., Y. Wang, and J. Luo, *Influence of magnetic water on early-age shrinkage cracking of concrete.* Construction and Building Materials, 2017. **147**: p. 91-100.

[10] Coey, J.M.D. and S. Cass, *Magnetic water treatment.* Journal of Magnetism and Magnetic Materials, 2000. **209**(1-3): p. 71-74.

[11] Chibowski, E. and A. Szczes, *Magnetic water treatment A review of the latest approaches.* Chemosphere, 2018. **203**: p. 54-67.

[12] Alabi, A., et al., *Advances in anti-scale magnetic water treatment.* Environmental Science: Water Research & Technology, 2015. **1**(4): p. 408-425.

[13] Meier, B., et al., *Spin-Isomer Conversion of Water at Room Temperature and Quantum-Rotor-Induced Nuclear Polarization in the Water-Endofullerene H2O@C-60.* Physical Review Letters, 2018. **120**(26).

[14] Yan, E.-K., et al., *An Overview of Hardware for Protein Crystallization in a Magnetic Field.* International journal of molecular sciences, 2016. **17**(11): p. 1906.

[15] Simon, M.D. and A.K. Geim, *Diamagnetic levitation: Flying frogs and floating magnets (invited).* Journal of Applied Physics, 2000. **87**(9): p. 6200-6204.

[16] Tolbert, S.H., et al., *Magnetic field alignment of ordered silicate-surfactant composites and mesoporous silica.* Science, 1997. **278**(5336): p. 264-268.
[17] Ozeki, S., et al., *Water-Solid Interactions under Steady Magnetic Fields: Magnetic-Field-Induced Adsorption and Desorption of Water.* J. Phys. Chem., 1996. **100**(10): p. 4205-4212.
[18] Higashitani, K., K. Okuhara, and S. Hatade, *Effects of magnetic fields on stability of nonmagnetic ultrafine colloidal particles.* Journal of Colloid And Interface Science, 1992. **152**(1): p. 125-131.
[19] Chibowski, E. and L. Holysz, *Changes in zeta potential of TiO2 and CaCO3 suspensions treated with a radiofrequency electric field as measured with a Zeta Plus instrument.* Colloids and Surfaces a-Physicochemical and Engineering Aspects, 1995. **105**(2-3): p. 211-220.
[20] Otsuka, I. and S. Ozeki, *Does Magnetic Treatment of Water Change Its Properties?* The Journal of Physical Chemistry B, 2006. **110**(4): p. 1509-1512.
[21] Sammer, M., et al., *Strong Gradients in Weak Magnetic Fields Induce DOLLOP Formation in Tap Water.* Water, 2016. **8**(3): p. 79.
[22] Manzano, H., et al., *Confined water dissociation in microporous defective silicates: mechanism, dipole distribution, and impact on substrate properties.* J Am Chem Soc, 2012. **134**(4): p. 2208-15.
[23] Zaidi, N.S., et al., *Magnetic Field Application and its Potential in Water and Wastewater Treatment Systems.* Separation and Purification Reviews, 2014. **43**(3): p. 206-240.
[24] Madsen, H.E.L., *Theory of electrolyte crystallization in magnetic field.* Journal of Crystal Growth, 2007. **305**(1): p. 271-277.
[25] Madsen, H.E.L., *Influence of magnetic-field on the precipitation of some inorganic salts*. Journal of Crystal Growth, 1995. **152**(1-2): p. 94-100.
[26] Higashitani, K., et al., *Effects of a magnetic field on the formation of CaCO3 particles.* Journal of Colloid And Interface Science, 1993. **156**(1): p. 90-95.
[27] Higashitani, K., et al., *Magnetic Effects on Zeta Potential and Diffusivity of Nonmagnetic Colloidal Particles.* Journal of Colloid And Interface Science, 1995. **172**(2): p. 383-388.
[28] Higashitani, K., J. Oshitani, and N. Ohmura, *Effects of magnetic field on water investigated with fluorescent probes.* Colloids and Surfaces a-Physicochemical and Engineering Aspects, 1996. **109**: p. 167-173.
[29] Higashitani, K. and J. Oshitani, *Measurements of magnetic effects on electrolyte solutions by atomic force microscope.* Process Safety and Environmental Protection, 1997. **75**(2): p. 115-119.
[30] Higashitani, K. and J. Oshitani, *Magnetic effects on thickness of adsorbed layer in aqueous solutions evaluated directly by atomic force microscope.* Journal of Colloid and Interface Science, 1998. **204**(2): p. 363-368.
[31] Colic, M. and D. Morse, *The elusive mechanism of the magnetic 'memory' of water.* Colloids and Surfaces A: Physicochemical and Engineering Aspects, 1999. **154**(1): p. 167-174.
[32] Baker, J.S. and S.J. Judd, *Magnetic amelioration of scale formation.* Water Research, 1996. **30**(2): p. 247-260.
[33] Madsen, H.E.L., *Crystallization of calcium carbonate in magnetic field in ordinary and heavy water.* Journal of Crystal Growth, 2004. **267**(1-2): p. 251-255.
[34] Colic, M. and D. Morse, *Mechanism of the long-term effects of electromagnetic radiation on solutions and suspended colloids.* Langmuir, 1998. **14**(4): p. 783-787.
[35] Colic, M. and D. Morse, *Effects of amplitude of the radiofrequency electromagnetic radiation on aqueous suspensions and solutions.* Journal of Colloid and Interface Science, 1998. **200**(2): p. 265-272.
[36] Colic, M. and D. Morse, *Influence of resonant rf radiation on gas/liquid interface: Can it be a quantum vacuum radiation?* Physical Review Letters, 1998. **80**(11): p. 2465-2468.

[37] Miao, X., et al., *Determining the Humidity-Dependent Ortho-to-Para Ratio of Water Vapor at Room Temperature Using Terahertz Spectroscopy.* Applied Spectroscopy, 2018. **72**(7): p. 1040-1046.
[38] Pershin, S.M., et al., *Water enrichment by H2O ortho-isomer: Four-photon and NMR spectroscopy.* Laser Physics, 2009. **19**(3): p. 410-413.
[39] Pershin, S.M., *Effect of quantum differences of ortho and para H2O spin-isomers on water properties: Biophysical aspect.* Biophysics, 2013. **58**(5): p. 723-730.
[40] Pershin, S., *Ortho-para spin conversion of H2O in aqueous solutions as a quantum factor of the Konovalov paradox.* Biophysics, 2015. **59**: p. 986-994.
[41] Bunkin, A.F., S.M. Pershin, and L.N. Rashkovich, *Changes in the Raman spectrum of OH stretching vibrations of water in an ultrasonic cavitation field.* Optics and Spectroscopy, 2004. **96**(4): p. 512-514.
[42] Pershin, S.M. and A.F. Bunkin, *Temperature evolution of the relative concentration of the H2O ortho/para spin isomers in water studied by four-photon laser spectroscopy.* Laser Physics, 2009. **19**(7): p. 1410-1414.
[43] Turro, N.J., et al., *The Spin Chemistry and Magnetic Resonance of H2@C60. From the Pauli Principle to Trapping a Long Lived Nuclear Excited Spin State inside a Buckyball.* Accounts of Chemical Research, 2010. **43**(2): p. 335-345.
[44] Li, Y.J., et al., *A Magnetic Switch for Spin-Catalyzed Interconversion of Nuclear Spin Isomers.* Journal of the American Chemical Society, 2010. **132**(12): p. 4042-+.
[45] Valiev, R.R. and B.F. Minaev, *Influence of Molecular Oxygen on Ortho-Para Conversion of Water Molecules.* Russian Physics Journal, 2017. **60**(3): p. 485-493.
[46] Petzinger, K.G. and D.J. Scalapino, *Para- to Ortho-Hydrogen Conversion on Magnetic Surfaces.* Physical Review B, 1973. **8**(1): p. 266-279.
[47] Ilisca, E., *theoretical calculation of a new effect in ortho-para h2 conversion on magnetic surfaces.* Physical Review Letters, 1970. **24**(15): p. 797-&.
[48] Misono, M. and P.W. Selwood, *Extrinsic field acceleration of the magnetic parahydrogen conversion.* Journal of the American Chemical Society, 1968. **90**(11): p. 2977-2978.
[49] Selwood, P.W., *The Effect of a Magnetic Field on the Catalyzed Nondissociative Para hydrogen Conversion Rate*, in *Advances in Catalysis*. 1979. p. 23-57.
[50] Ilisca, E. and S. Paris, *Magnetic field acceleration of the ortho-para H_2 conversion on transition oxides.* Physical Review Letters, 1999. **82**(8): p. 1788-1791.
[51] Bahloul, K., et al., *Magnetic field effect in CH3F nuclear spin conversion.* Chemical Physics Letters, 1997. **279**(1-2): p. 29-34.
[52] Temesgen, T., et al., *Micro and nanobubble technologies as a new horizon for water-treatment techniques: A review.* Advances in Colloid and Interface Science, 2017. **246**: p. 40-51.
[53] Srebrenik, S., S. Nadiv , and I.J. Lin, *Magnetic Treatment of Water–A Theoretical Quantum Model.* Magnetic and Electrical Separation, 1993. **5**(2): p. 71-91.
[54] Ozeki, S., C. Wakai, and S. Ono, *Is a magnetic effect on water adsorption possible?* The Journal of Physical Chemistry, 1991. **95**(26): p. 10557-10559.
[55] Ozeki, S. and I. Otsuka, *Transient Oxygen Clathrate-like Hydrate and Water Networks Induced by Magnetic Fields.* J. Phys. Chem. B,, 2006. **110**(100): p. 20067-20072.
[56] Krautwurst, N., et al., *Two-Step Nucleation Process of Calcium Silicate Hydrate, the Nanobrick of Cement.* Chemistry of Materials, 2018. **30**(9): p. 2895-2904.

THERMODYNAMIC MODELING OF THE REACTIONS OF SELF-HEALING AGENTS AND THE CHEMICAL BINDING OF AGGRESSIVE IONS IN SEA WATER

Xintong Wu (1), Haoliang Huang (1), (2)*, Hao Liu (1), Jie Hu (1), (2), Jiangxiong Wei (1), (2), Qijun Yu (1), (2)

(1) School of Materials Science and Engineering, South China University of Technology, Guangzhou China

(2) France Guangdong Low Carbon Technologies Engineering Center for Building Materials, Guangzhou, China

Abstract

In this study, a new concept on self healing of cracks that the ingressive ions in the crack is chemically bound to improve the self-healing efficiency was proposed for cracked cementitious materials in a marine environment. Thermodynamic modeling was performed to determine the appropriate masses and ratio of Ca^{2+} and Al^{3+} provided by chemical agents for a good efficiency of self-healing and chemical binding of Cl^-, SO_4^{2-}, and Mg^{2+} ions from sea water. It was found that when CaO-$NaAlO_2$ and CaO-metakaolin are used as self-healing agents, Friedel's salt, kuzel's salt, ettringite and hydrotalcite can be formed and, thus, Cl^-, SO_4^{2-} and Mg^{2+} from sea water are chemically bound. Moreover, the volume of phase assemblages becomes larger, which facilitates the self-healing of cracks. For a ratio of 0.3 between the mass of self-healing agent to the mass of sea water, the removal efficiency of Cl^- ions for CaO-$NaAlO_2$ agent with a Ca/Al of 5 reaches the maximum value, i.e. 87%, while for CaO-metakaolin agent the removal efficiency of Cl^- ions reaches the maximum when the Ca/Al is 3. The chemical binding of Mg^{2+} and SO_4^{2-} ions is hardly influenced by Ca/Al when it is larger than 2 and the removal efficiency approximates 100%.

Keywords: thermodynamic modeling, ion binding, marine environment, self-healing

1. INTRODUCTION

In order to make rebars withstand bending loading appropriately, occurrence of cracks with a certain width is usually expected in reinforced concrete elements. In the concrete structures in marine environments, cracks usually become pathways for ingression of ions, such as Cl^-, SO_4^{2-}, and Mg^{2+}, and cause deterioration of reinforced concrete structures. It was encouraging to find that concrete was able to heal cracks autogenously. Self-healing of cracks can be a potential solution to the durability problem caused by cracks in reinforced concrete in marine environments.

Self-healing of cracks in cementitious material has attracted great attention in recent years

[1-5]. It was found that environmental factors, in particular extra ions from the environment, presented significant impacts on the self-healing process and efficiency[1]. It was reported that autogenous self-healing of cracks in a marine environment was promoted by Mg^{2+} in the sea water [6, 7]. Compared to autogenous self-healing in fresh water, the closure ratio of a surface crack with an initial width of 400 μm increases by 37% for a healing period of 7 days in sea water [7]. However, it must be emphasized that there are multiple aggressive ions in the marine environments, such as Cl^-, SO_4^{2-}, and Mg^{2+}. These aggressive ions can obviously decrease the durability performance of reinforced concrete, particularly cracked reinforced concrete [8-10]. It is conceivable that once cracks appear, aggressive ions immediately invade through the cracks. Therefore, in order to improve the durability performance of cracked reinforced concrete in a marine environment, the self-healing of cracks not only can block the crack to prevent from the further ingression of aggressive ions, but also be able to "capture" the aggressive ions already exist in the cracks .

According to the literature [11-13] , Cl^-, SO_4^{2-}, and Mg^{2+} in concrete can be chemically bound in Friedel's salt ($3CaO \cdot Al2O_3 \cdot CaCl_2 \cdot 10H_2O$), ettringite ($3CaO \cdot Al_2O_3 \cdot 3CaSO_4 \cdot 32H_2O$), and hydrotalcite ($4MgO \cdot Al_2O_3 \cdot 10H_2O$) in cement paste respectively. It can be seen that these minerals are composed of calcium and aluminum. From the thermodynamics point of view, if adequate concentrations of Ca^{2+} and Al^{3+} are present in the crack solution, Friedel's salt, ettringite and hydrotalcite can be formed, which means that chemical binding of Cl^-, SO_4^{2-}, and Mg^{2+} in the crack can take place. Simultaneously, the crack can be filled by the precipitates. Calcium is one of the main elements in cement-based materials. According to the previous study [14], when portlandite having a high solubility is present in the matrix, there will be quantities of Ca^{2+} ions diffusing into the crack. In addition, Al^{3+} ions can be supplied by Al-rich materials, such as slag and metakaolin, which can be added by directly blending or after encapsulation. It is interesting to quantify the binding efficiency of Cl^-, SO_4^{2-}, and Mg^{2+} and the volume of precipitates formed in sea water as a function of the masses and the ratio of Ca^{2+} and Al^{3+} ions.

In this study, in order to determine the propriate masses and ratio of Ca^{2+} and Al^{3+} ions for the self-healing of cracks and the chemical binding of Cl^-, SO_4^{2-}, and Mg^{2+} ions from sea water, thermodynamic modeling was performed. The volume of relevant precipitates and the corresponding binding efficiency of the aggressive ions in sea water as a function of the masses and ratio of Ca^{2+} and Al^{3+} ions were predicted. The Ca^{2+} and Al^{3+} ions are supposed to be provided by $CaO\text{-}Al_2O_3$ and $CaO\text{-}SiO_2\text{-}Al_2O_3$ agents with various masses and Ca/Al ratios.

2. THERMODYNAMIC MODELING

Thermodynamic modeling was performed with software GEMS 3.5, in which Gibbs energy minimization was used to calculate the mass and volume of equilibrium phase assemblages and the equilibrium ion concentrations from the total bulk elemental composition. The databases used were CEMDATA18 database [15] particularly for cementitious materials.

In this study, two series of self-healing agents, $CaO\text{-}NaAlO_2$ and CaO-metakaolin, were chosen to provide additional Ca^{2+} and Al^{3+} ions for the binding of aggressive ions in sea water and the self-healing of cracks. These agents can be used to manufactured artificial aggregates and added into concrete deliberately, as described in previous study [7]. The concentration of the main ions in synthetic sea water was listed in Table 1. In the calculation in this study, the

volume of sea water was set as 100 ml.

Table 1: Ions concentrations in synthetic sea water

Ion	Concentration [g/L]
Cl^-	19.36
Mg^{2+}	1.266
SO_4^{2-}	2.69
Ca^{2+}	0.40
Na^+	1.34
K^+	0.39

3. RESULTS AND DISCUSSION

3.1 Phase assemblages of self-healing agents mixed with sea water

As shown in Fig. 1, Friedel's salt, ettringite, hydrotalcite and portlandite are the main precipitates formed when the ratio between the mass of $CaO\text{-}NaAlO_2$ agent to the mass of sea water was less than a criteria, i.e. 0.08 for Ca/Al (by mole) =3 and 0.12 for Ca/Al (by mole) =5, respectively. As the ratio between the mass of $CaO\text{-}NaAlO_2$ agent to the mass of sea water increases, the volume of precipitates increases and the mineralogy changes. For the $CaO\text{-}NaAlO_2$ agent has a Ca/Al of 3, ettringite disappears and the volume of Friedel's salt decreases while kuzel's salt forms as the ratio between the mass of $CaO\text{-}NaAlO_2$ agent to the mass of sea water increases from 0.08 to 0.24. Similar phenomenon occurs in the mixture of sea water and $CaO\text{-}NaAlO_2$ agent with a Ca/Al of 5. Moreover, for the $CaO\text{-}NaAlO_2$ agent has a Ca/Al of 3, C_4AlH_{19} is formed when the ratio between the mass of $CaO\text{-}NaAlO_2$ agent to the mass of sea water is larger than 0.18 and SO_4_OH-AFm also presents when the ratio increases to 0.22. The percentage of portlandite in the mixture of sea water and $CaO\text{-}NaAlO_2$ agent with a Ca/Al of 5 is larger than that with a Ca/Al of 5.

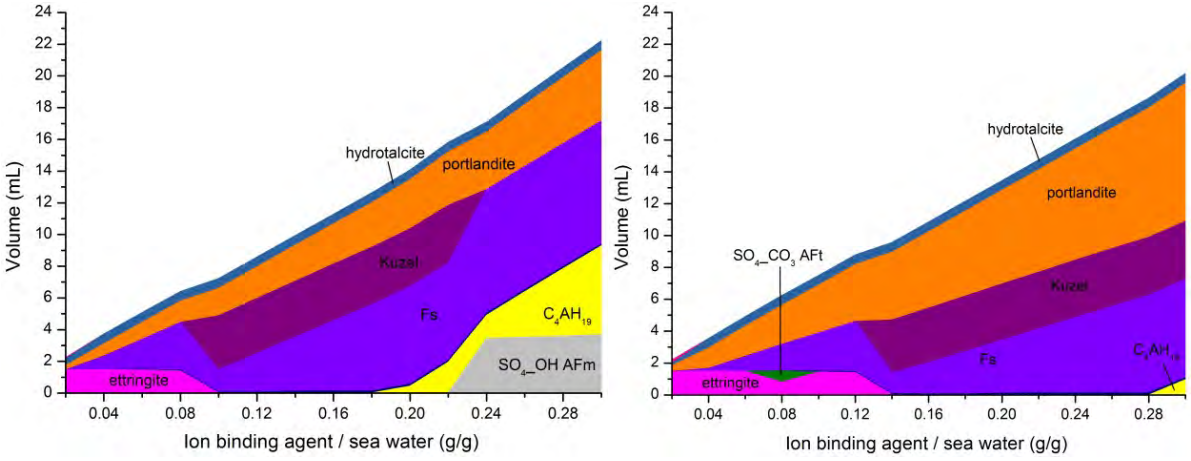

Figure 1: Phase assemblages in the mixture of $CaO\text{-}NaAlO_2$ and 100 ml sea water: (a) with Ca/Al molar ratio of 3; (b) with Ca/Al molar ratio of 5

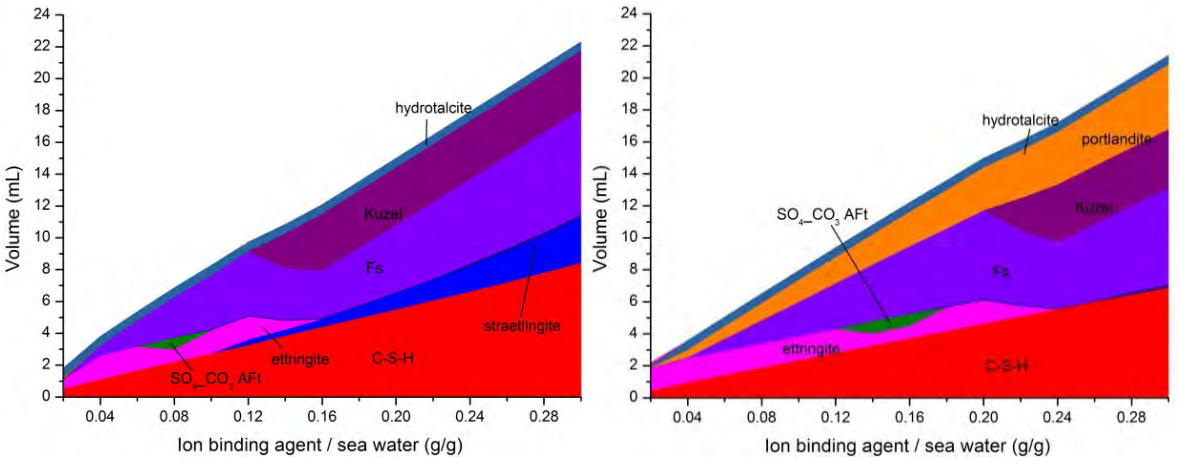

(a) **(b)**

Figure 2: Phase assemblages in the mixture of CaO-metakaolin and 100 ml sea water: (a) with Ca/Al molar ratio of 3; (b) with Ca/Al molar ratio of 5

For the mixture of CaO-metakaolin agent and sea water, besides Friedel's salt and ettringite, C-S-H and straetlingite ($CaAl_2Si_2O_8$) can be formed as well. It is worth noting that when the Ca-to-Al molar ratio is 3 (see Fig. 2 (a)) portlandite is absent, while when the Ca-to-Al molar ratio increases to 5 (see Fig. 2 (b)) portlandite occurs.

According to the results discussed above, the Ca/Al in the self-healing agent has significant effect on the mineralogy of the phase assemblages, thus on the binding of aggressive ions in sea water. Therefore, it is of significance to determine the phase assemblages changing with the Ca/Al in the self-healing agents. From Figure 3, it can be seen that the mineral composition of the reaction products changes with Ca/Al molar ratio in the self-healing agents. In general, the increase of Ca/Al means a larger amount of Ca and smaller amount of Al provided to the system. Therefore, the volume percentage of phases containing Al decreases and the volume of portlandite increases with the increase of Ca/Al. For CaO-$NaAlO_2$, the volume of reaction products reaches the maximum when Ca/Al = 3. In comparison, for CaO-metakaolin the volume of reaction products reaches the maximum when Ca/Al = 2.

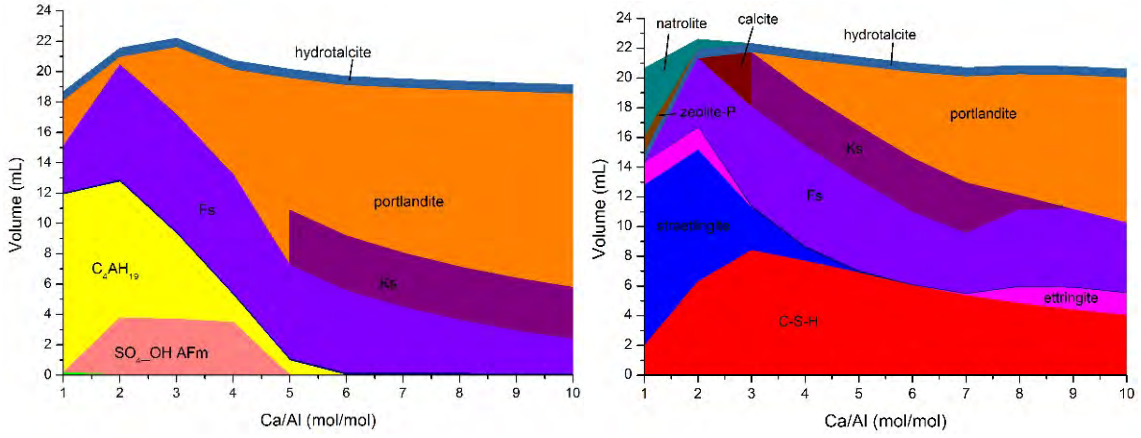

(a) **(b)**

Figure 3: Phase assemblages in the mixture of 100 ml sea water and 30 g self-healing agents with various Ca/Al: (a) CaO-$NaAlO_2$; (b) CaO-metakaolin

3.2 Mass ratios of ingressive ions to self-healing agent.

Figure 4 shows the ratio between the mass of ingressive ions bond and the mass of self-healing agent as a function of the ratio between the mass of agent to the mass of sea water. The relative content of Cl^- for unit mass of binding agent keeps increasing significantly when the ratio between the mass of binding agent to the mass of sea water ranges from 0.02 to 0.12. When the ratio between the mass of binding agent to the mass of sea water increases further, the relative content of Cl^- becomes stable or even decreases for $CaO\text{-}NaAlO_2$ agent with Ca/Al of 3. In comparison, the relative contents of SO_4^{2-} and Mg^{2+} decrease with the increase of the ratio between the mass of binding agent to the mass of sea water. This is because SO_4^{2-} and Mg^{2+} are of low concentrations in sea water. As a result, they are almost chemically bond even the ratio between the mass of binding agent to the mass of sea water is very low. Therefore, with further addition of the binding agents, the relative contents of SO_4^{2-} and Mg^{2+} decrease.

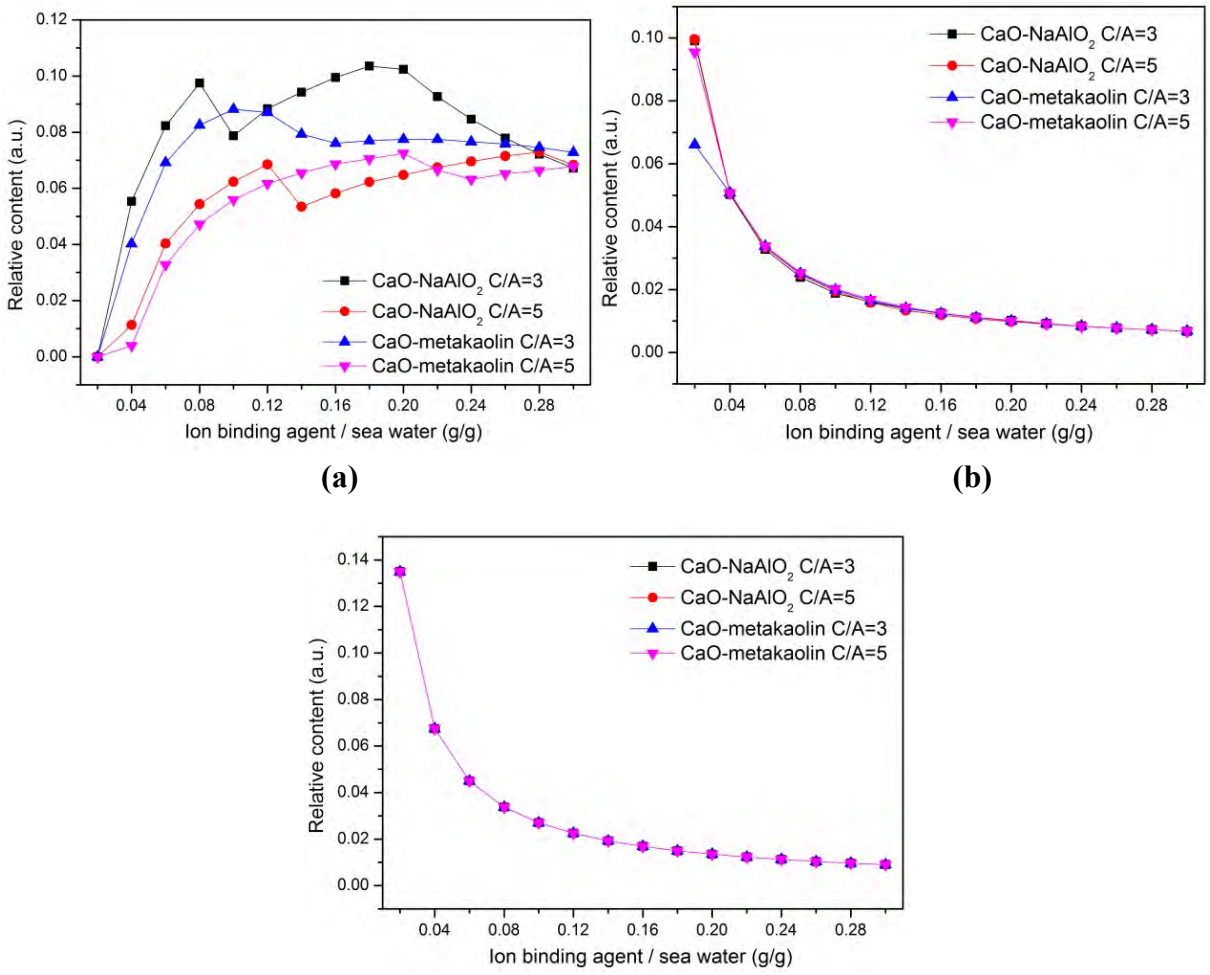

Figure 4: Ratio between the mass of ingressive ions and the mass of the self-healing agent: (a) Cl^-; (b) SO_4^{2-}; (c) Mg^{2+}.

3.3 Ion removal of Cl^-, SO_4^{2-}, and Mg^{2+} in solution.

As shown in Figure 5 (a), the removal efficiency of Cl^- ions from sea water increases linearly with the increase of the amount of self-healing agents. The slope of the lines corresponding to the Ca/Al of 3 is larger than that of 5. It means that the increase rate of the removal efficiency of Cl^- ions by these two self-healing agents with Ca/Al of 3 is larger than that with Ca/Al of 5. It should be mentioned that the removal efficiency of Cl^- ions reaches the maximum, i.e. 80%, when the ratio between the mass of CaO-$NaAlO_2$ agent with Ca/Al of 3 to the mass of sea water reaches 0.2.

As shown in Figure 5 (b) and (c), the removal of SO_4^{2-} and Mg^{2+} can reach 100% even with a low ratio between the mass of self-healing agent and the mass of sea water. It reveals that SO_4^{2-} and Mg^{2+} show greater potential to be bond compared with Cl^-. Besides, there is a "valley" in the removal efficiency curve of SO_4^{2-} in the four series of self-healing agent (see Figure 5 (b)). It is interesting to find that the positions of valleys are always consistent with that of transition of ettringite to the Kuzel's salt shown in Figure 1 and 2, which demonstrates that when ettringite is transferred to kuzel's salt a part of SO_4^{2-} is released to the solution again.

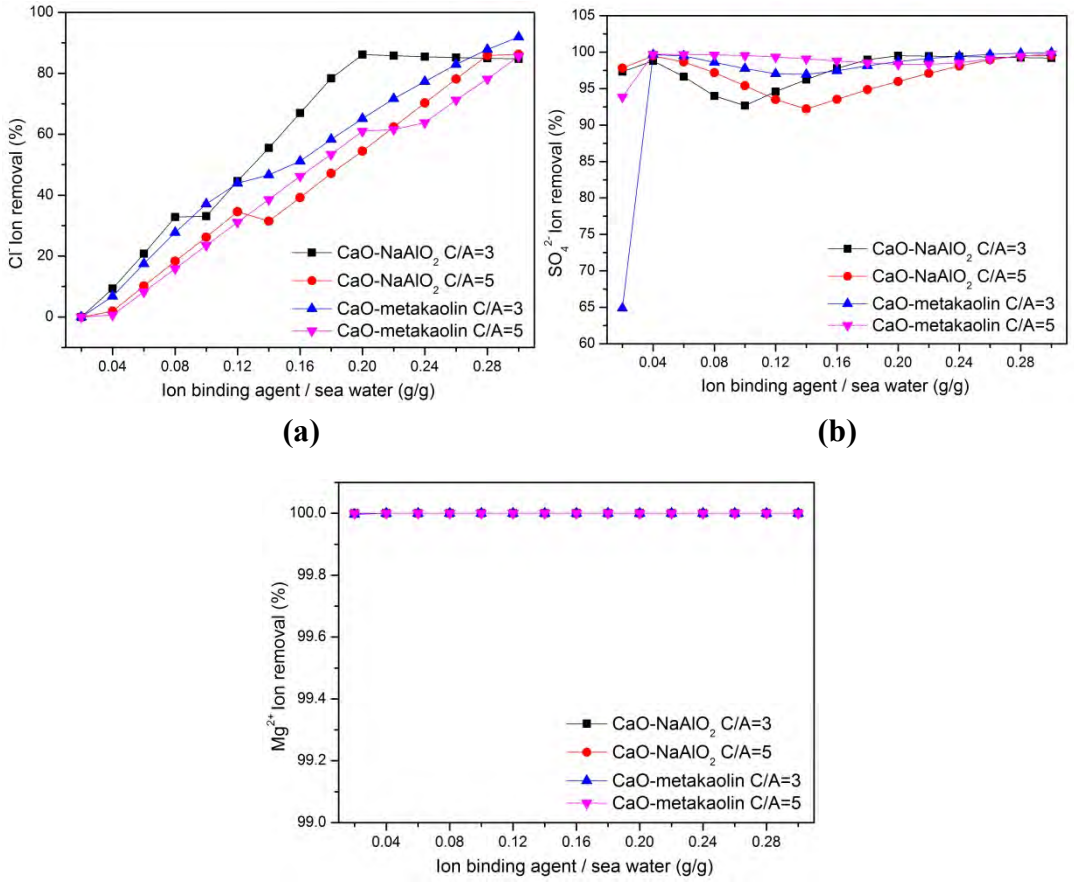

Figure 5: Removal efficiency of ions: (a) Cl^-; (b) SO_4^{2-}; (c) Mg^{2+} in sea water. C/A means Ca/Al molar ratio.

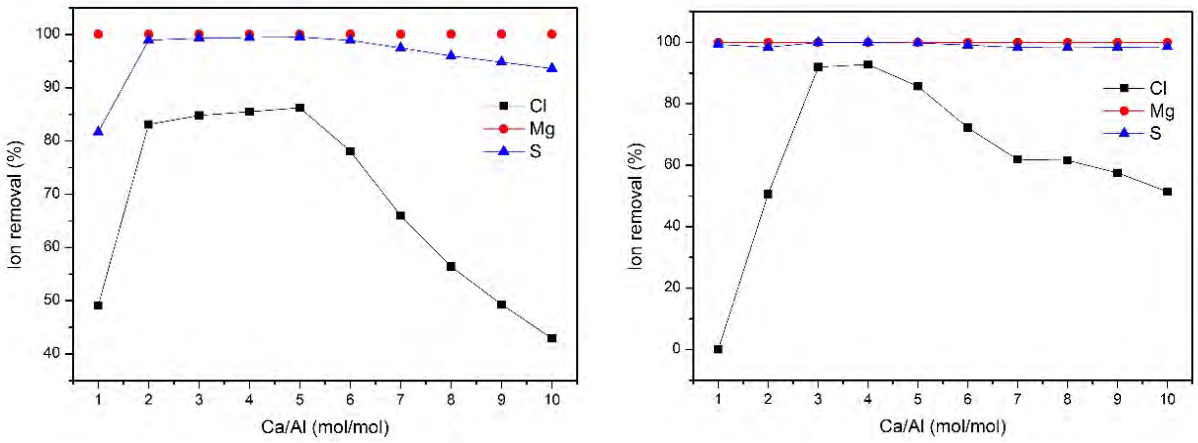

Figure 6: Removal efficiency of ions in sea water as a function of Ca/Al in self-healing agent: (a) CaO-$NaAlO_2$ agent; (b) CaO-metakaolin. The ratio between the mass of self-healing agent and the mass of sea water is 0.3.

Figure 6 presents the removal efficiency of ions in sea water as a function of Ca/Al molar ratio in CaO-$NaAlO_2$ and CaO-metakaolin agents. The ratio between the mass of self-healing agent and the mass of sea water is 0.3. It is found that both for CaO-$NaAlO_2$ and CaO-metakaolin agents the removal efficiency of Cl^- ions firstly increases and then decreases with Ca/Al, while the removal efficiency of Mg^{2+} ions is hardly influenced by Ca/Al and approximates 100%. The removal efficiency of Cl^- ions for CaO-$NaAlO_2$ agent reaches the maximum value, i.e. 87%, when the Ca/Al is 5, while for CaO-metakaolin agent the removal efficiency of Cl^- ions reaches the maximum when the Ca/Al is 3. The removal efficiency of SO_4^{2-} ions for CaO-$NaAlO_2$ agent increases from about 80% to 100% when the Ca/Al increases from 1 to 2, and decreases slightly when the Ca/Al increases further to be larger than 6. In comparison, the removal efficiency of SO_4^{2-} ions for CaO-metakaolin agent is hardly influenced by Ca/Al.

4. CONCLUSIONS

In this study, thermodynamic modeling was performed to determine the propriate masses and ratio of Ca^{2+} and Al^{3+} ions for the self-healing of cracks and the chemical binding of Cl^-, SO_4^{2-}, and Mg^{2+} ions from sea water. Based on the thermodynamic modeling results, the following conclusions can be drawn:

(1) As the ratio between the mass of self-healing agent to the mass of sea water increases, the volume of precipitates increases and the mineralogy changes. Due to the formation of Friedel's salt, kuzel's salt, ettringite and hydrotalcite, Cl^-, SO_4^{2-} and Mg^{2+} in sea water are chemically bound when the self-healing agents provide Ca^{2+} and Al^{3+} ions.

(2) The relative content of Cl^- for unit mass of binding agent keeps increasing when the ratio between the mass of binding agent to the mass of sea water ranges from 0.02 to 0.12.

(3) For a ratio of 0.3 between the mass of self-healing agent to the mass of sea water, the removal efficiency of Cl^- ions for CaO-$NaAlO_2$ agent reaches the maximum value, i.e. 87%, when the Ca/Al is 5, while for CaO-metakaolin agent the removal efficiency of Cl^- ions reaches the maximum when the Ca/Al is 3. The removal efficiency of Mg^{2+} and SO_4^{2-} ions is

hardly influenced by Ca/Al when it is larger than 2 and the removal efficiency approximates 100%.

ACKNOWLEDGEMENTS

The financial support of the Ministry of Science and Technology of the People's Republic of China (No. 2017YFB0309904), National Natural Science Foundation of China (No. 51602050 and No. 51872097) is greatly appreciated.

REFERENCES

[1] Huang H, Ye G, Qian C, Schlangen E. Self-healing in cementitious materials: Materials, methods and service conditions. Materials & Design. 2016;92:499-511.
[2] Van Tittelboom K, De Belie N. Self-healing in cementitious materials—A review. Materials. 2013;6(6):2182-217.
[3] Li W, Dong B, Yang Z, Xu J, Chen Q, Li H, et al. Recent Advances in Intrinsic Self-Healing Cementitious Materials. Advanced materials. 2018;30(17):e1705679.
[4] Jonkers HM. Self healing concrete: a biological approach. Self healing materials: Springer; 2007. p. 195-204.
[5] Seifan M, Samani AK, Berenjian A. Bioconcrete: next generation of self-healing concrete. Applied microbiology and biotechnology. 2016;100(6):2591-602.
[6] Liu H, Huang H, Wu X, Peng H, Li Z, Hu J, et al. Effects of external multi-ions and wet-dry cycles in a marine environment on autogenous self-healing of cracks in cement paste. Cement and Concrete Research. 2019;120:198-206.
[7] Wu X, Huang H, Liu H, Zeng Z, Li H, Hu J, et al. Artificial aggregates for self-healing of cement paste and chemical binding of aggressive ions from sea water. Composites Part B: Engineering. 2019:107605.
[8] Otieno M, Beushausen H, Alexander M. Chloride-induced corrosion of steel in cracked concrete–Part I: Experimental studies under accelerated and natural marine environments. Cement and Concrete Research. 2016;79:373-85.
[9] Van Belleghem B, Kessler S, Van den Heede P, Van Tittelboom K, De Belie N. Chloride induced reinforcement corrosion behavior in self-healing concrete with encapsulated polyurethane. Cement and Concrete Research. 2018;113:130-9.
[10] Valencia Saavedra WG, Angulo DE, Mejia de Gutierrez R. Fly ash slag geopolymer concrete: Resistance to sodium and magnesium sulfate attack. Journal of Materials in Civil Engineering. 2016;28(12):04016148.
[11] Shi Z, Geiker MR, De Weerdt K, Østnor TA, Lothenbach B, Winnefeld F, et al. Role of calcium on chloride binding in hydrated Portland cement–metakaolin–limestone blends. Cement and Concrete Research. 2017;95:205-16.
[12] Kunther W, Lothenbach B, Skibsted J. Influence of the Ca/Si ratio of the C–S–H phase on the interaction with sulfate ions and its impact on the ettringite crystallization pressure. Cement and concrete research. 2015;69:37-49.
[13] Machner A, Zajac M, Haha MB, Kjellsen KO, Geiker MR, De Weerdt K. Limitations of the hydrotalcite formation in Portland composite cement pastes containing dolomite and metakaolin. Cement and Concrete Research. 2018;105:1-17.
[14] Huang H, Ye G, Damidot D. Characterization and quantification of self-healing behaviors of microcracks due to further hydration in cement paste. Cement and Concrete Research. 2013;52:71-81.
[15] Lothenbach B, Kulik DA, Matschei T, Balonis M, Baquerizo L, Dilnesa B, et al. Cemdata18: A chemical thermodynamic database for hydrated Portland cements and alkali-activated materials. Cement and Concrete Research. 2019;115:472-506.

COMPARISON OF NUMERICAL PREDICTIONS FOR EARLY-AGE CREEP

Z. Hu (1), M. Wyrzykowski (1) and P. Lura (1)(2)

(1) Concrete/Construction Chemistry Laboratory, Empa, Dübendorf CH-8600, Switzerland

(2) Institute for Building Materials, ETH Zurich, Zurich CH-8092, Switzerland

Abstract

Creep at early ages significantly affects the volumetric deformation of cementitious materials. Efficient modelling of early-age creep is a challenging task, mainly due to continuously evolving material properties (hydration) and other phenomena (e.g. autogenous shrinkage) taking place in parallel. Various methods were introduced during the past decades to achieve a successful prediction. However, few comparisons between different methods are available until now.

This study re-examines different numerical predictions for creep of cement pastes before 28 days. The investigated predicting methods include the recently proposed incremental rheology model [1], fictitious time (age) model [2] and solidification theory [3–5]. To compare the performance of these predictions, experimental creep results of cement pastes with water to cement ratio of 0.35 were used. Creep results under separate loading/unloading cycles were used to calibrate the parameters in the different methods, while creep results under sequential loading were used to validate their predictions. The advantages and disadvantages of each method are discussed. This study provides an assessment of the different methods and clarifies their requirements.

Keywords: Creep, Early age, Models, Comparisons

1. INTRODUCTION

Concrete manifests stress- and age- dependent behavior, e.g. creep and relaxation [6,7]. The viscoelastic deformation (creep) has significant impact on durability and service life of concrete structures [8]. Comprehensive experimental investigations and reliable predictions of creep are topics of concrete research with immediate practical interest. Extensive studies confirm that cement paste is the source of the viscoelastic behavior of concrete, which is instead restrained by elastic aggregates [1,9]. To understand long-term deformation of concrete, a good understanding and a robust prediction of the (aging) viscoelastic deformation of cement paste is paramount.

A sophisticated prediction of creep is impeded by the difficulties in estimating creep of hardening cement pastes. Specifically, the simultaneous changes of the creep kinetics and the material microstructure in hydrating materials is the utmost challenge. Despite extensive studies being carried out in recent years, no agreement has been reached until now on approving one type of model to be the most comprehensive one among all the models in the literature [10–12]. Creep models, e.g., solidification model [3,4], microprestress-solidification model [13], fictitious time models [2,14] and incremental rheology models [1,12], can be classified into either phenomenological or mechanistic. Another classification divides models into those based on the experimental creep curves without explicit physical meaning [1,4,12] and into other models based on a model of the microstructure of the material that includes a creep mechanism [15,16]. In this paper, we focus on models that are based exclusively on the measured creep curves. It is noticed that most models that have been proposed in the literature either lack verification by extensive and systematic experimental results or lack comparison with other models.

This paper verifies different models in the literature (chosen among the most common and easy to implement) for creep at early ages with the most recent experimental aging creep results on cement pastes. A systematic comparison among different models is presented, namely: incremental rheology models equipped with aging algorithms [1], solidification model [4] and fictitious time/degree of hydration model [2]. The parameters in the three models were first determined with creep results of cement paste with water to cement ratio (w/c) of 0.35 under constant loads at different ages, recently published in [1]. The models were then applied on the creep results of the same cement paste under sequential loading with time span from 20 h to 28 d to test their predictive power on the same materials but on separate experiments. The stress-to-strength ratio in the experiments was controlled to be 0.1 to ensure linear viscoelastic behavior.

2. MODELS USED IN THE STUDY

2.1 Solidification model

Solidification theory was first introduced as a mechanism for aging creep in concrete by Bažant [3] in the late 80s with the attempt to better guarantee the thermodynamic restrictions. This model is not only proposed to describe the mechanism but also to model the viscoelastic deformation of hardening cementitious materials. With 50 years' development, it was extended from the original solidification model to the microprestress-solidification model and with a particular focus on including the effect of relative humidity and temperature [3,13,17]. It has been implemented into the B3 and B4 models, which are widely used in practice [18,19].

The constitutive law in the model defines the aging creep as follows: the aging behavior is induced by the volume growth of the non-aging hydration products at different hydration time. The most prominent assumption in the model is that the hydration products are generated at stress free states and that they are intrinsically viscoelastic. These assumptions still hold in many microstructural models proposed more recently.

The deformation of the load-bearing hydration products from the moment of applying loads can be formulated with simple stress-strain relationships, e.g. the double power law. The aging effect is thereafter only associated with the volume fraction of the hydrates. In this study, we

followed the equations derived in [4], the formulation for creep strain ε(*t*) at time *t* (instantaneous strain is not considered in the equation) is shown in Eq.(1):

$$\varepsilon(t)=\int_0^t J(t,t')\frac{\partial\sigma(t')}{\partial t'}dt' \quad (1)$$

where:

$$J(t,t')=\int_0^t\left(\frac{\dot{\Phi}(\tau-t')}{v(\tau)}+\frac{1}{\eta(\tau)}\right)d\tau$$

In which, $J(t,t')$ is the creep compliance function, σ is the stress applied at loading age *t'*, $\dot{\Phi}$ is the derivative of the microscopic creep compliance with respect to the time under load (*t-t'*), *v* is the volume fraction of the hydration products and η is the viscosity.

The microscopic creep compliance is a non-aging function that depends on the load duration. In the original work on the solidification model, the authors showed a possible fit to the experimental data with four parameters, considering either power-law or log-time evolution [4]. In their further work, they also confirmed the possibility for using rheology models (chains) for estimating the compliance [20]. In this study, we applied three Kelvin-Voigt units for fitting and the aging evolution was characterized with the volume fraction of the hydration products. For simplicity, only viscoelastic deformation was considered (without the viscous part).

2.2 Fictitious time/degree of hydration model

The fictitious time model, also called equivalent time method was proposed by Acker et al. [21]. Based on the equivalent time principle, De Schutter and Taerwe developed the fictitious degree of hydration method [2]. This method was validated and considered to be applicable for predicting the early-age creep, particularly for creep under step-wise loading [14].

The basic idea of this method is: at a subsequent time, when a new load is applied, the corresponding creep response can be considered as creep of the material starting from a fictitious time (t_f)/degree of hydration (α_f). t_f and α_f are between the previous loading time/degree of hydration and the current loading time/degree of hydration. In [2], the basic creep curve of materials under constant load was estimated with the following expression:

$$\varepsilon(\alpha,\alpha',\sigma)=a(\alpha',\sigma)\cdot\left(\frac{\alpha-\alpha'}{1-\alpha'}\right)^{b(\alpha',\sigma)} \quad (2)$$

in which, α and α' are the degree of hydration (as a function of time) and degree of hydration at the loading time, respectively. ε and σ are the creep strain and the stress applied at the loading time. The regression parameters *a* and *b* depend on the degree of hydration and the applied stress at the loading time.

The critical step in the creep prediction with the fictitious degree of hydration model is to estimate the fictitious time/degree of hydration (t_f and α_f). An equation was suggested in [2,14] to determine the α_f:

$$\varepsilon(\alpha)=\varepsilon_o(\alpha_f,s_f)\cdot\varphi_c(\alpha,\alpha_f) \quad (3)$$

in which, s_f is the stress-to-strength ratio, i.e. the stress applied per unit compressive strength of the material at the loading time; ε_o is the instantaneous strain and φ_c is the creep coefficient, which

only depends on the degree of hydration and the fictitious degree of hydration. Based on the experimental creep results, the estimation of the α_f and of the creep coefficient is possible. Thereafter, Eq.(2) and Eq.(3) are applied to complete the prediction with the fictitious degree of hydration method.

2.3 Rheology model with age-dependent parameters

A recent study [1] provided a method relying on rheology units with age/degree of hydration dependent parameters for predicting creep at early ages. Incremental rheology models were used widely in the literature for creep simulation [22,23]. The essential advantage of the current rheology model (generalized Kelvin-Voigt model) is the early-age creep prediction by considering the age-dependent parameters (the evolution relies on the properties of the material, e.g. stiffness of the springs and viscosity of the dashpots in the units). The constitutive formulas were derived by considering the degree of hydration and porosity dependent parameters, see [1,12].

The employed generalized Kelvin-Voigt model is composed of three Kelvin-Voigt units and one additional dashpot. The Kelvin-Voigt units account for the short-term creep, while the additional dashpot accounts for the long-term creep. The units have springs with stiffness of $E_n(t)$ and dashpots with viscosity of $\eta_n(t)$, n represents the number of the units, t is the time in days and τ_n stands for the characteristic time. The viscosity of the additional dashpot is represented by η_0. The incremental basic creep strain at early ages can be calculated based on Eqs (4-6) (a detailed derivation can be found in [1,12]):

$$\Delta\varepsilon_n^i=\frac{\sigma_n^i}{k_n^i}\cdot\left(1-e^{-\frac{\Delta t_i}{\bar{\tau}_n^i}}\right)+(\sigma_n^{i+1}-\sigma_n^i)\cdot\frac{1}{k_n^i}\cdot\left(1-\frac{\eta_n^i}{k_n^i\cdot\Delta t_i}\cdot\left(1-e^{-\frac{\Delta t_i}{\bar{\tau}_n^i}}\right)\right) \tag{4}$$

where k_n is equal to $E_n+\dot{E}_n\times\tau_n$ and $\bar{\tau}_n$ equal to $\tau_n/\left(1+\dot{E}_n/(E_n\cdot\tau_n)\right)$

$$\sigma_n^{i+1}=\eta_n^{i+1}\cdot\left(\frac{\sigma_{n\eta}^i}{\eta_n^i}\cdot\left(1-\frac{k_n^i\cdot\Delta t_i}{E_n^i\cdot\tau_n^i}\right)+\frac{\dot{\sigma}_n^i}{\eta_n^i}\cdot\Delta t_i\right) \tag{5}$$

$$\Delta\varepsilon_{am}=\frac{\sigma_n^{i+1}+\sigma_n^i}{2}\cdot ln\left(\frac{t_{i+1}}{t_i}\right)/\left(\frac{\eta_\infty}{1-\sqrt{(1-p_0)\cdot(1-\alpha)}}\right) \tag{6}$$

where ε_{am} is the strain in the additional dashpot in the rheology model; $\sigma_{n\eta}$ is the stress in the dashpots in the Kelvin-Voigt units; p_0 is the initial porosity.

In this study, the abovementioned three models were applied to experimental basic creep results of cement pastes with w/c of 0.35 [1,24]. The autogenous shrinkage measured with corrugated tubes was subtracted from the total strain to obtain the basic creep. Detailed information on the materials and the equipment used to measure creep can be found in [1,24]. Together with the creep results, the degree of hydration and other properties of the microstructure were systematically measured in [1,24] and can be used to determine all parameters involved in the models. Concretely, the degree of hydration in the fictitious degree of hydration method, the evolution of the volume fraction of hydration produces and the degree of hydration and porosity in the rheology model are

required. To better show the impact of aging and stepwise loading, the experimental results were compared not only with the predictions from the three models but also with the superposed results of the cement pastes under constant loads.

3. RESULTS AND DISCUSSION

3.1 Measured early-age creep of cement pastes

The early-age creep strains of cement pastes with w/c of 0.35 under two types of loading schemes are shown in Fig.1: under constant loading and under stepwise (sequential) loading. The loading time for the constant loading was: 20h-3d; 42h-7d;3d-18d; 14d-28d and 28d-56d. The loads added in the stepwise loading were first at 20 h and further loads were added at 42 h, 3d and 14 d on the same specimens. All applied loads were removed at 28d. Duplicated specimens were measured.

The basic creep strain in Fig.1 demonstrates a clear evolution as a function of time and a similar evolution was observed in duplicate specimens under the same loading process. Comparing the creep strain under constant loads at different ages, reduced instantaneous strain part and creep kinetics were evident at later loading time. The gradually decreased instantaneous strain is mainly due to the increase of the elastic modulus of the material during hydration. The change of the creep kinetics indicates the aging effect. Considering the creep strain under stepwise load, reduced creep kinetics at later loading time was also observed. The creep strain was only partly reversible, since the creep recovery was much lower than the creep.

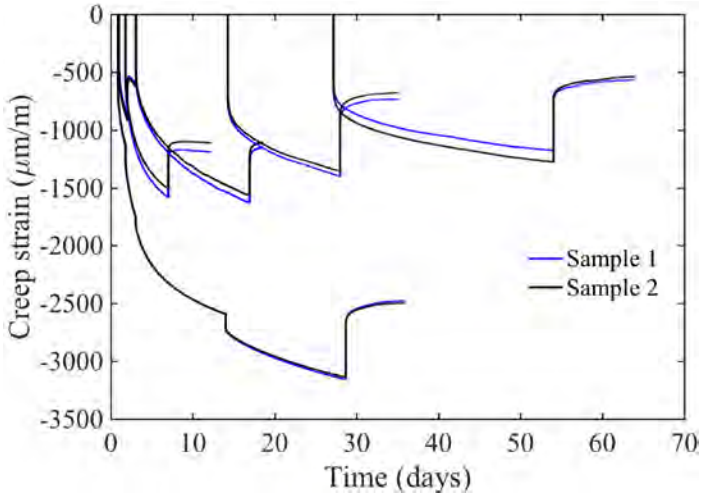

Figure 1: Basic creep strain and creep recovery measured on cement pastes with w/c 0.35, adapted from [1,24]

3.2 Creep prediction with different models

Incremental rheology model

In the incremental rheology model, the evolution of $E_n(t)$ is a function of $E_n(t=\infty)$ and normalized degree of hydration $\bar{\alpha}$. The value of the parameters involved in the generalized Kelvin-Voigt model are listed in Table 1, adapted from [1]. The parameters were determined by fitting to the experimental creep results of the material under constant loads. The value of $E_n(t=\infty)$ was obtained by fitting to the creep results of the material loading at 28d. The characteristic time was 0.001, 0.1 and 3.0 days and $E_n(t=\infty)$ were 99, 93 and 85 MPa.

Table 1: Parameters in the generalized Kelvin-Voigt model obtained by fitting to the creep results under constant loads, adapted from [1]

Parameters	Chain 1	Chain 2	Chain 3
τ_n (days)	0.01	0.1	3.0
$E_n(t=\infty)$ (MPa)	99	93	85
η_∞ (MPa)	20		

Fictitious degree of hydration model

Based on the description in Section 2.2, Eq.(2) yields relatively good agreement with the experimental basic creep results of materials under constant loading at 20 h, 42 h and 14 d. Therefore, with a regression process, the values found for parameters *a* were: 0.249, 0.231, 0.237 and for *b* were: 0.406, 0.409 and 0.395. The creep results of materials under constant loading at 3 d were excluded from the calculation. The reason is that the obtained regression parameters at this age were completely different with the overall trend of values from other ages. Using Eq.(3), the calculated strain at the loading time and the fictitious degree of hydration during the three loading steps are determined, see Table 2.

Table 2: Calculated fictitious degree of hydration and the strain at the loading time using the fictitious degree of hydration model

Loading time	α' (-)	Calculated ε at a' (μm/m)	Calculated α_f (-)
20 h	0.30	-	-
42 h	0.45	0.41	0.41
3 d	0.53	0.64	0.46
14 d	0.63	0.88	0.57

Solidification model

In the solidification model, three Kelvin-Voigt units with characteristic times of 0.1,1.0 and 35 days and stiffness of 5, 3, 1.5 MPa were constructed and used to represent the creep strain under constant loads. In a certain system, the evolution of the volume fraction of the hydration products

has the same kinetics as the evolution of the degree of hydration. Therefore the degree of hydration was used to replace the volume fraction in Eq.(1). Instead of following a power law expression with three regression parameters as in [4], the evolution of the volume fraction used directly the measured value of the degree of hydration multiplied with an empirical constant.

The experimental creep strain of the cement paste under stepwise load is used to verify the three predictions. The comparison of the predictions and the measurements is plotted as a function of time (Fig.2) and as a function of degree of hydration (Fig.3). Note that the autogenous shrinkage was subtracted from the total strain, while the instantaneous strain was added in the figure.

In Fig.2, before about 7 days, all the predictions underestimated the measured creep strain. The non-satisfactory fit of the creep results at early ages, especially in the case of the solidification model, leads to this underestimation. Considering the predicted results at 28 days, the prediction with the incremental rheology model agreed the best with the measurements. The calculation with the superimposed creep results of the material under constant loads overestimated the creep strain by about 450 μm/m. This overestimation is to be expected, since this approach does not take into account the loading history.

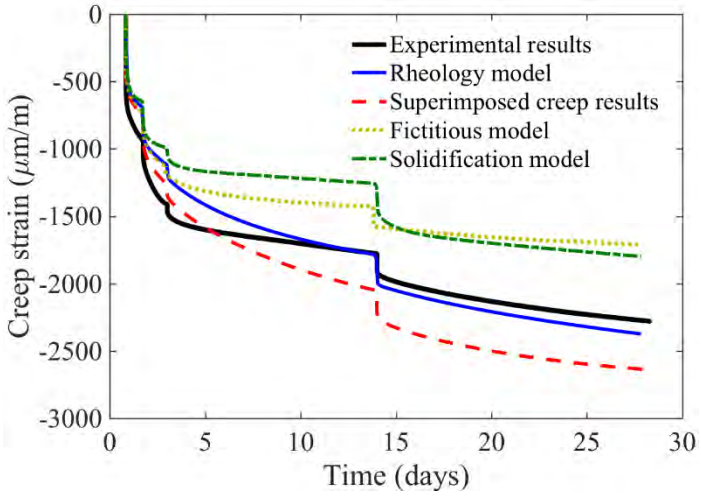

Figure 2: Comparison of predicted results from different creep models and experiments as a function of time

Both the fictitious degree of hydration model and the solidification model underestimated the creep strain. At 28 days, the underestimation was about 500 μm/m for both approaches. Despite the clear underestimation, the kinetics of the predicted creep strain after 3 days using the solidification model was in line with the kinetics of the measured creep. Therefore, the underestimation is mainly caused by the inaccurate prediction of creep under the first two loads. This situation can be seen more obviously against the degree of hydration in Fig.3. The creep kinetics of cement paste with degree of hydration lower than 0.5 was better predicted by the incremental rheology model and the superimposed results. However, when the degree of hydration

was higher than 0.5, a better prediction was obtained by the fictitious degree of hydration model and by the solidification model.

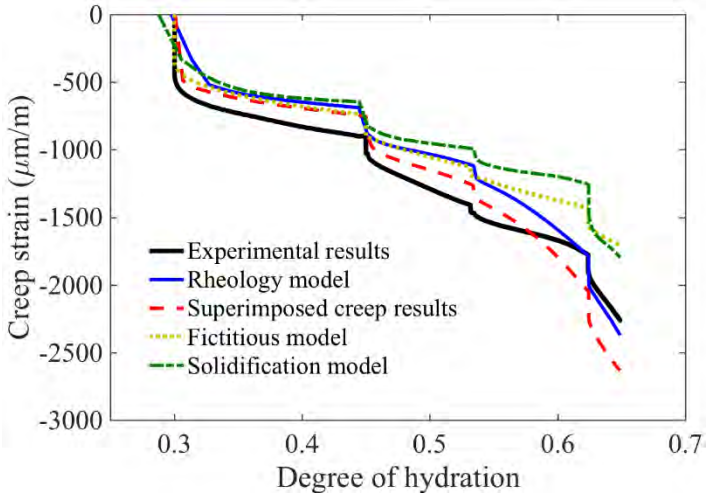

Figure 3: Comparison of predicted results from different models as a function of degree of hydration

4. CONCLUSION

In this paper, the principle of three different numerical predictions of early-age creep, incremental rheology model, fictitious degree of hydration model and solidification model, were briefly reviewed. The three models were applied to predict the creep results of a cement paste with w/c of 0.35 under stepwise loading. The comparison was made as a function of time and degree of hydration, respectively. All the models capture the aging effect of creep at early ages when compared with the superimposed creep results under constant loads. It can be seen that different models have advantages when estimating different parts of the measured creep curves. In this specific case (only a single system was considered in this study), all the models underestimated the creep strain under stepwise loads, in particular at early ages (before 7 d, with degree of hydration below 0.5). Besides, all the models are phenomenological and extensively dependent on the fitting results of the experimental data, especially when the fitting results covering a long time duration. More systematic experimental results are necessary for a better assessment of different creep predictions.

REFERENCES

[1] Hu, Z., Hilaire, A., Wyrzykowski, M., Lura, P. and Scrivener, K. 'Visco-elastic behavior of blended cement pastes at early ages'. *Cem. Concr. Compos.* **107** (2020) 103497.

[2] De Schutter, G. and Taerwe, L. 'Fictitious degree of hydration method for the basic creep of early age concrete'. *Mater. Struct.* **33** (2000) 370–380.

[3] Bažant, Z.P. and Prasannan, S. 'Solidification theory for aging creep'. *Cem. Concr. Res.* **18** (1988) 923–932.

[4] Bažant, Z.P. 'Solidification theory for concrete creep. i: formulation'. *Engineering.* **115** (1989) 1691–1703.
[5] Bažant, Z.P. and Santosh,P. 'Solidification theory for concrete creep'. *J. Eng. Mech.* **115** (1989) 1691–1703.
[6] Brooks, J. J. 'Creep, shrinkage and durability mechanics of concrete and other quasi-brittle materials'. in: Proc. Sixth Int. Conf., 2001.
[7] Neville, A.M., Dilger, W.H. and Brooks, J.J. 'Creep of plain and structural concrete', Construction Press, London, 1983.
[8] Acker, P. 'Micromechanical analysis of creep and shrinkage mechanisms'. in: F.-J. Ulm, Z.P. Bažant, F.H. Wittmann, T.C. Powers (Eds.), Creep, Shrinkage Durab. Mech. Concr. Other Quasi-Brittle Mater. Proc. Sixth Int. Conf. CONCREEP-6, Elsevier, Cambridge (MA), USA, 2001: 811.
[9] Wyrzykowski, M., Scrivener, K. and Lura, P. 'Basic creep of cement paste at early age - the role of cement hydration'. *Cem. Concr. Res.* **116** (2019) 191–201.
[10] Li, X., Grasley, Z.C., Bullard, J.W. and Garboczi, E.J. 'Computing the time evolution of the apparent viscoelastic/viscoplastic Poisson's ratio of hydrating cement paste'. *Cem. Concr. Compos.* **56** (2015) 121–133.
[11] Bažant, Z.P., Kim, J.K. and Panula, L. 'Improved prediction model for time-dependent deformations of concrete: Part 1-Shrinkage'. *Mater. Struct.* **24** (1991) 327–345.
[12] Hilaire, A., Benboudjema, F., Darquennes, A., Berthaud, Y. and Nahas, G. 'Modeling basic creep in concrete at early-age under compressive and tensile loading'. *Nucl. Eng. Des.* **269** (2014) 222–230.
[13] Bažant, Z.P. and Jirásek, M. 'Microprestress-solidification theory and creep at variable humidity and temperature'. in: Creep Hygrothermal Eff. Concr. Struct. Solid Mech. Its Appl., Springer, Dordrecht, 2018: 455–498.
[14] Jiang, W., De Schutter, G. and Yuan,Y. 'Degree of hydration based prediction of early age basic creep and creep recovery of blended concrete'. *Cem. Concr. Compos.* **48** (2014) 83–90.
[15] Pichler, C., Lackner, R. and Mang, H. A. 'A multiscale micromechanics model for the autogenous-shrinkage deformation of early-age cement-based materials'. *Eng. Fract. Mech.* **74** (2007) 34–58.
[16] Li, X., Rahman, S. and Grasley, Z.C. 'Computationally implemented modeling of creep of composite materials caused by phase dissolution'. *Comput. Mater. Sci.* **125** (2016) 61–71.
[17] Bažant, Z.P., Cusatis, G. and Cedolin, L. 'Temperature Effect on Concrete Creep Modeled by Microprestress-Solidification Theory'. *J. Eng. Mech.* **130** (2004) 691–699.
[18] RILEM 'Creep and shrinkage prediction model for analysis and design of concrete structures-model B3'. *Mater. Struct.* **3** (1995) 357–365.
[19] Hubler, M.H., Wendner, R. and Bažant, Z.P. 'Statistical justification of Model B4 for drying and autogenous shrinkage of concrete and comparisons to other models'. *Mater. Struct.* **3** (2015) 797–814.
[20] Granger, L.P. and Bažant, Z.P. 'Effect of composition on basic creep of concrete and cement paste'. *J. Eng. Mech.* **121** (1995) 1261.
[21] Acker, P., Lau, M.Y. and Collet, F. 'Comportement différé du béton: validation expérimentale de la méthode du temps équivalent'. *Bulletin de Liaison des Laboratoires des Ponts de Chaussées*. **163**(1989) 31–39.
[22] Carol, I. and Bažant, Z.P. 'Viscoelasticity with aging caused by solidification of nonaging constituent'. *J. Eng. Mech.* **119** (1993) 2252–2269.
[23] Shahidi, M., Pichler, B. and Hellmich, C. 'Interfacial micromechanics assessment of classical rheological models. II: Multiple interface sizes and viscosities'. *J. Eng. Mech.* **142** (2016) 04015093.
[24] Hu, Z., Hilaire, A., Ston, J., Wyrzykowski, M., Lura, P. and Scrivener, K. 'Intrinsic viscoelasticity

of C-S-H assessed from basic creep of cement pastes'. *Cem. Concr. Res.* **121** (2019) 11–20.

REINFORCED AND PLAIN GEOPOLYMER CONCRETE SPECIMEN CROSS-SECTION COMPOSITION INFLUENCE ON CREEP STRAINS

R. Gailitis (1), A. Sprince (1), L. Pakrastins (1), K. Korniejenko (2) and T. Kozlovskis (1)

(1) Riga Technical University Riga, Latvia

(2) Cracow University of Technology, Cracow, Poland

Abstract

Low calcium alkaline solution activated cement composite, or geopolymer concrete has been around for about 40 years. The main benefit of this material - it is partially made by utilising waste products, such as fly-ash, slags and others. It has been claimed that the manufacturing of various geopolymer binder produces up to 6 times less CO2 than the production of Portland cement. Because of the nature of the binding process of the geopolymer concrete, there are some differences in the cause of the shrinkage. Because of this aspect, the long-term property development mechanism is slightly different, and the microstructure of the specimen could be different than for ordinary Portland cement.

Although the researches regarding the geopolymer concrete composition and mechanical properties have significantly been reviewed in the previous couple of years, there has been a lack of investigations regarding the long-term properties and the conditions affecting and influencing long-term properties of the geopolymer concrete.

Two geopolymer concrete mixes are the test subject for this article - plain geopolymer and reinforced geopolymer with 1% waste steel fibers that have been subjected to creep and shrinkage tests. Waste steel fibers are the by-product of the car tire recycling process. The steel industry is not willing to take them, but if recycle these products they can be used as fiber reinforcement. The microstructure analyses with SEM were done by analysing specimens polished sections. Afterward acquired images of specimen cross-sections were analysed by determining the amount of fiber, geopolymer binder, filler, and air void amount in analysed cross-section. The results were cross-referenced with creep and shrinkage test results of analysed specimens.

The aim of this article is to determine the loading influence and geopolymer concrete microstructure influence on long-term properties by evaluating polished specimen sections.
Keywords: Geopolymer concrete, polished section micro-analysis, long-term properties

1. INTRODUCTION

In recent years there has been increased interest in low carbon footprint materials such as geopolymer concrete. Geopolymer concrete is a novel three-dimensional inorganic material that

is formed due to a silicon and aluminium reaction that is activated by hydroxide silicates from sodium and potassium alkali activating solution. There are several beneficial properties such as low CO_2 emissions, low cost, low density and remarkable mechanical properties [1–4]. As the mechanical properties are similar to Portland cement concrete geopolymer concrete main advantage in this scope is its environmental contribution. If geopolymer matrix fully replaces the Portland cement the carbon emission for this material drops from 26 to 46% and reduction in costs varies from 7% less up to 39 % higher than for material with Portland cement as a binder [4, 5].

In terms of sustainable and effective resource management, it is critical to recycle and reuse industrial waste as much as possible so that the fraction of recycled material that goes to landfills is as little as possible. Furthermore, produced materials from recycled products should have new added value [6, 7]. Every year approximately 17 million tons of old tires are created, that have no further use [8]. This waste is a serious contaminant to the environment, so it is extremely important to recycle them.

Creep is an essential factor in human-made materials, especially to concrete and similar materials. Stress and deformation distribution throughout the cross-section of the specimen is affected by creep. The main creep affecting factors are the temperature of the surrounding environment, relative humidity, and applied stress level [9, 10].

As the shrinkage strains appear simultaneously to creep strains, it is crucial to measure shrinkage throughout the time of creep testing. Geopolymer shrinkage appears mainly due to water loss while curing reaction and evaporation and pore structure relevant factors, for example, alkaline activator, water content, binder material, and curing conditions. The pores develop during the polymerisation process [11].

This study shows the microstructure difference of waste steel cord reinforced and plain geopolymer concrete that has/has not been subjected to load.. And further, the microstructure composition results have been tried to link to achieved creep strains.

2. MATERIALS AND METHODS

Geopolymer cylindrical specimen matrix was based on fly ash sourced from the power plant in Skawina city (Poland). This fly ash is suitable for geopolymers because of its physical and chemical properties. The fly ash contains spherical aluminosilicate particles as well as it is rich with oxides such as SiO_2 (47.81%), Al_2O_3 (22.80%). The high value of SiO_2 and Al_2O_3 gives advantages for polymerisation [12].

Geopolymer specimens were prepared using sodium promoter, fly ash, sand (ratio sand and fly ash – 1:1). The process of activation has been made by 10M NaOH solution combined with the sodium silicate solution (at a ratio of 1:2.5). To make the composite the technical NaOH as flakes were used and water solution of sodium silicate R–145. Tap water was used instead of the distilled one. The alkaline solution was prepared by pouring the aqueous solution of sodium silicate and water over solid sodium hydroxide. The solution was mixed and leftover the night until its temperature is stabilised, and the concentrations equalised. The fly ash, sand, and alkaline solution were mixed for about 15 minutes by using a low-speed mixing machine (to receive the homogenous paste). Then half of the specimens were reinforced with 5% by mass of steel cords from recycled car tires. Then the mix was poured into the plastic moulds as it is shown in Fig.1. The specimens were hand-formed and then the air bubbles were removed by vibrating them. Moulds were heated in the laboratory dryer for 24h at 75 °C. Then, the

specimens were unmolded. All the geopolymer specimen preparation was done at Cracow University of Technology (CUT), Poland.

(a) (b)

Figure 1: Plain geopolymer (a) and recycled tire steel cord reinforced geopolymer (b) concrete

All specimens were prepared according to RILEM recommendations [13]. The dimensions of the specimens were Ø 46 x 190 mm or ¼ diameter to height ratio respectfully.

For creep deformation tests, 6 aluminium plates (10 x 15 mm) were glued to each specimen in pairs. Afterward, strain gauges were attached to those plates. For the shrinkage specimens, 1 aluminium plate was glued to the top and bottom part of the specimen. Afterward, shrinkage specimens were placed in the measuring stand to measure the shrinkage throughout testing time. All the specimen preparatory work was done at Riga Technical University (RTU), Latvia.

Creep and shrinkage strains were monitored for the first two weeks every day, afterward-every two days. During creep tests, specimens were subjected to constant load throughout the whole creep testing period. The load that specimens were subjected to was equivalent to 20% of the ultimate compressive strength, which was determined in compressive strength tests. Specimens were loaded gradually by 25% of the determined load in a short period (within 5 minutes). Creep test was carried out on tests stands shown in Fig.2.

(a) (b)

Figure 2: Specimen testing to creep strains

After creep and shrinkage tests cylinders middle parts (where the creep strain measurements were recorded) cut to disc shape specimens with a thickness of 5mm. The surfaces of specimens

were saturated with polyester resin to make specimens more durable for surface polishing cycles.

(a) (b) (c)

Figure 3: Specimen polishing stages (a, b) and the result (c)

Afterward, for all specimens, their surfaces were polished by various grade sandpapers and polishing compounds. The process is shown in Fig.3. Polishing was done according to the sequences shown in Table 1.

Table 1: Specimen surface polishing steps

Polishing stage number	Polishing compound (sandpaper or paste grade) type	Polishing cycle time, minutes	Compression force to specimen polishing surface, daN
1.	P180	2	2.5
2.	P320	2	2.5
3.	P600	2	2.5
4.	P1000	2	2.5
5.	3µm	4	2.5

Afterward, specimens were delivered to Cracow University of Technology (CUT) where they were carbon plated and surface images at 25-time magnification made.

To get the optimal amount of the specimen cross-section data and images, the reviewed cross-section is divided into zones that represent the centre, middle and outside areas of the specimen. The adopted principle is shown in Fig.4.

Figure 4: Specimen cross-section division into zones

The achieved SEM images from each examined specimen's cross-section were joined together in Adobe Photoshop CC to get a full cross-section image. The next step was cross-section image dividing into layers based on what partition of cross-section (matrix, filler, air voids or reinforcement) is visible in it and RGB tone allocation. The process is shown in Fig. 5. The process step order is shown by the numbers. The layer dividing starts with the filler layer, then void layer, reinforcement fiber layer and finished with the matrix layer.

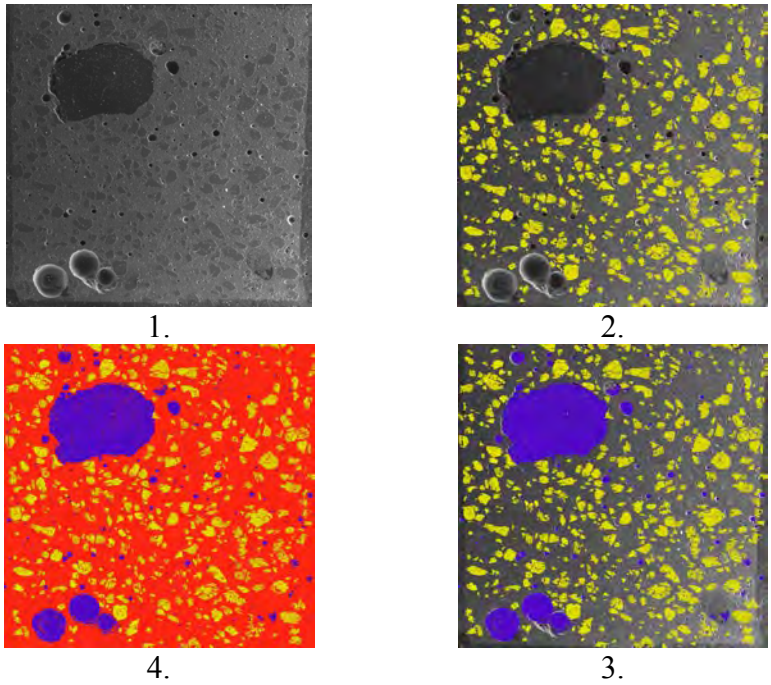

Figure 5: Image dividing sequence in layers and tone allocation

When the image was divided into layers, and the RGB tone allocated the specific tone pixel amount was divided by the number of image pixels. In doing so, the amount of particular partition of the cross-section was achieved.

3. RESULTS AND DISCUSSION

The compressive strength of the tested specimens at the beginning of the test is shown in Table 2. The specimens in the creep test were subjected to a load that was calculated from Table's 2 compressive strength values.

Table 2: Compressive strength values of 7days old cylinder specimen

Specimen material	Average compressive strength, MPa
Plain geopolymer concrete	30.37
Tire steel cord reinforced geopolymer concrete	44.52

After the initial compressive strength test, the creep and shrinkage tests were carried out for 90 days (approximately 3 months). The creep and shrinkage strain measurements are shown in Fig. 6.

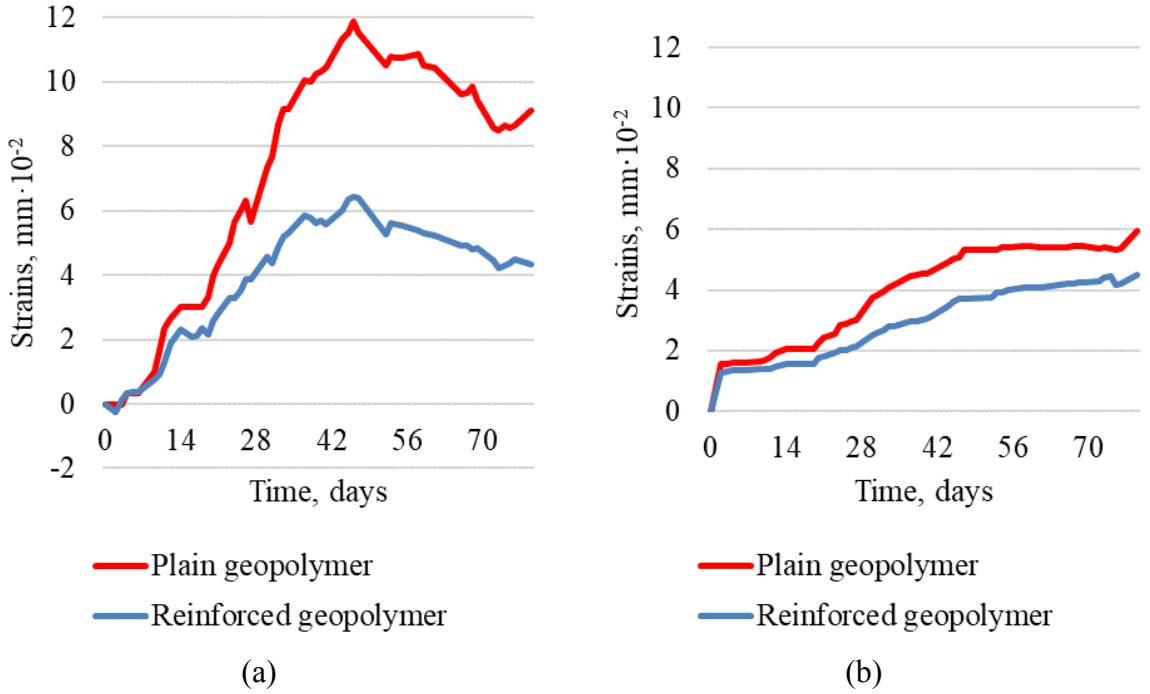

Figure 6: Shrinkage (a) and creep (b) strains

Figure 6 has shown shrinkage and creep strain curves. It is easy to determine that geopolymer concrete specimens reinforced with steel cords have significantly (~50%) less shrinkage and a bit smaller (~30%) creep properties than plain geopolymer concrete. Furthermore, it is visible that cord reinforced specimens have a slight delay in shrinkage strains to plain geopolymer specimens. That leads to thinking that steel cords from old tires have a significant restraining quality to shrinkage introduced strains.

The cross-section composition values of plain and waste steel cord reinforced geopolymer concrete is shown in Table 3.

Table 3: Average values of specimen cross-section composition

Test type	Geopolymer concrete type	Matrix amount in cross-section, %	Filler amount in cross-section, %	Air void amount in cross-section, %	Steel cord amount in cross-section, %
Shrinkage	Plain	78.96	16.91	4.13	-
	Reinforced	77.11	13.81	6.39	2.69
Creep	Plain	76.17	19.22	4.61	-
	Reinforced	77.79	15.43	5.22	1.56

From the cross-section composition values presented in Table 3, it is clear that specimens reinforced with waste tire steel cords have a significantly larger amount of air voids than plain geopolymer specimens. Also, filler distribution to creep and shrinkage specimens is uneven for both geopolymer types. For plain geopolymer, the difference is 2.31% and for reinforced specimens 1.62%. The filler amount difference in specimen cross-section composition depending on specimen type on average is 3.45% in favour of plain geopolymer. The difference is up to 2.26% for specimens that have not been subjected to load and 0.61% for those that have been loaded. This result leads to the conclusion that relatively large fiber incorporation into a geopolymer mix leads to foaming up process.

It is also apparent that the void amount for steel cord reinforced specimens that have been loaded is 19% lower than those that have not been loaded. The reason for this can be because steel cord reinforced specimens in contrast to plain ones have 32% higher compressive strength and they carried by the same amount greater load during creep tests than plain geopolymer concrete keeping the load value 20% from compressive strength load value. Therefore, the reinforcement is restraining the deformations but matrix and voids in it in this instance is the subject that is deformed for these specimens.

4. CONCLUSIONS

- The quantitative image analysis of the plain and recycled tire steel cord reinforced geopolymer concrete cross-sections shows that on average the plain geopolymer concrete specimens have from 1% up to 2.26% less amount of air voids than steel cord reinforced specimens.
- Further analysis shows that if the reviewed cross-section part is more to the centre of the specimen, then the level of the air voids decreases from 4.2% to 5.4% for plain geopolymer and from 4.7% up to 10.3% for steel cord reinforced geopolymer concrete. This could be due to insufficient vibrating to the specimens.
- Examining shrinkage and creep strain curves and cross-referencing them to achieved specimen cross-section composition, there is no direct link that cross-sections of specimens have significant flaws that would affect creep properties.
- For shrinkage strains, it is determined that for reinforced specimen greater porosity, the shrinkage strain remains lower mainly because reinforcement is restraining and delaying the strains to happen.

- Further testing and analysis are needed for specimen upper and lower parts to determine what loading influence is to specimen parts where the stress distribution is not homogeneous.

ACKNOWLEDGEMENTS

1. This work has been supported by the Latvian Council of Science within the scope of the project 'Long term properties of innovative cement composites in various stress-strain conditions' No. lzp-2018/2-0249.
2. This publication was supported by Riga Technical University's Doctoral Grant programme.
3. This work has been supported by the European Regional Development Fund within the Activity 1.1.1.2 "Post-doctoral Research Aid" of the Specific Aid Objective 1.1.1 "To increase the research and innovative capacity of scientific institutions of Latvia and the ability to attract external financing, investing in human resources and infrastructure" of the Operational Programme "Growth and Employment" (No.1.1.1.2/VIAA/3/19/401).

REFERENCES

[1] A. Mehta and R. Siddique, "Sulfuric acid resistance of fly ash based geopolymer concrete," *Constr. Build. Mater.*, vol. 146, pp. 136–143, 2017.
[2] S. Yan *et al.*, "Effects of high-temperature heat treatment on the microstructure and mechanical performance of hybrid C f -SiC f -(Al 2 O 3p) reinforced geopolymer composites," *Compos. Part B Eng.*, vol. 114, pp. 289–298, 2017.
[3] M. Łach, D. Mierzwiński, K. Korniejenko, and J. Mikuła, "Geopolymer foam as a passive fire protection," *MATEC Web Conf.*, vol. 247, pp. 1–6, 2018.
[4] E. Linul *et al.*, "Quasi-Static Mechanical Characterization of Lightweight Fly Ash-Based Geopolymer Foams," *IOP Conf. Ser. Mater. Sci. Eng.*, vol. 416, no. 1, 2018.
[5] L. Sele, D. Bajare, G. Bumanis, and L. Dembovska, "Alkali Activated Binders Based on Metakaolin," vol. 1, pp. 200–204, 2015.
[6] G. Mucsi, Á. Szenczi, and S. Nagy, "Fiber reinforced geopolymer from synergetic utilization of fly ash and waste tire," *J. Clean. Prod.*, vol. 178, pp. 429–440, 2018.
[7] V. Vishwakarma and D. Ramachandran, "Green Concrete mix using solid waste and nanoparticles as alternatives – A review," *Constr. Build. Mater.*, vol. 162, pp. 96–103, 2018.
[8] M. Łach, A. Kiszka, K. Korniejenko, and J. Mikuła, "The Mechanical Properties of Waste Tire Cords Reinforced Geopolymer Concretes," *IOP Conf. Ser. Mater. Sci. Eng.*, vol. 416, 2018.
[9] S. Liang and Y. Wei, "Methodology of obtaining intrinsic creep property of concrete by flexural deflection test," *Cem. Concr. Compos.*, vol. 97, no. April 2018, pp. 288–299, 2019.
[10] A. Sprince, L. Pakrastins, and R. Gailitis, "Long-Term Parameters of New Cement Composites BT - 3rd International Conference on the Application of Superabsorbent Polymers (SAP) and Other New Admixtures Towards Smart Concrete," 2020, pp. 85–94.
[11] Y. Ling, K. Wang, and C. Fu, "Shrinkage behavior of fly ash based geopolymer pastes with and without shrinkage reducing admixture," *Cem. Concr. Compos.*, vol. 98, no. October 2018, pp. 74–82, 2019.
[12] K. Korniejenko, M. Łach, M. Hebdowska-Krupa, and J. Mikuła, "The mechanical properties of flax and hemp fibres reinforced geopolymer composites," *IOP Conf. Ser. Mater. Sci. Eng.*, vol. 379, no. 1, 2018.
[13] P. Acker *et al.*, "RILEM TC 107-CSP: CREEP AND SHRINKAGE PREDICTION MODELS: PRINCIPLES OF THEIR FORMATION Recommendation Measurement of time-dependent strains of concrete," *Mater. Struct.*, vol. 31, pp. 507–512, Oct. 1998.

Special session 1

Alkili-activated Materials/DuRSAAM midterm workshop

A REVIEW: THE STRENGTH INFLUENCE FACTORS OF SLAG AND FLY ASH BASED ALKALI ACTIVATED MATERIALS

Beibei Sun (1), Guang Ye (1), and Geert De Schutter (1)

(1) Ghent University, Department of Structural Engineering, Magnel Laboratory for Concrete Research, Technologiepark-Zwijnaarde 60, 9052 Ghent, Belgium

Abstract

Alkali-activated materials(AAM) are known to be environmentally friendly alternatives to cement-based materials because they can potentially reduce greenhouse gas emissions and reutilize industrial by-products. However, the application of AAM is still limited by the lack of mixture design regulation. Unlike cement, the very different chemical composition of the precusors and alkaline activators may result in a very fluctuating strength. In order to study the factors influencing the strength of slag and fly ash-based alkali-activated materials (BFS/FA-AAM), and clarify their reaction mechanism, this paper reviews current knowledge about the mechanical properties and the reaction mechanisms of BFS/FA-AAM. The control factors of strength are BFS/binder ratio, Na_2O/binder ratio, and SiO_2/Na_2O ratio. The ion concentrations, determined by these control factors, play a decisive role in the development of strength. Generally, the strength is proportional to the BFS/binder ratio. The best strength could be obtained at the optimum values of Na_2O/binder ratio, and SiO_2/Na_2O ratio. The optimum values of the SiO_2/binder ratio of BFS-AAM and FA-AAM are between 5.5%-8% and between 7-10%, respectively. The optimal values of the SiO_2/Na_2O ratio of BFS-AAM and FA-AAM are between 0.85-1.4 and between 0.6-1, respectively. For BFS/FA-AAM, the optimum ratio is still unknown. Further study is needed to investigate the effect of control factors on the mechanical properties of BFS/FA-AAM.

Keywords: slag and fly ash based alkali-activated materials, reaction mechanism, strength control factors

1. INTRODUCTION

It is known that cement production is associated with high energy consumption and the emission of a considerable amount of greenhouse gas[1]. For the sake of the environment protection, alkali-activated materials (AAM) have attracted attention as a potential replacement for ordinary Portland cement concrete (OPC)[2][3][4]. AAM possesses a lot of advantages, such as rapid strength gaining, low thermal conductivity, high volume stability, fire resistance, and chemical erosion resistance[5][6][7][8].

Typically, AAM is produced by the alkali activation of silica and alumina-rich materials using alkaline activators. The most popular precursors of AAM are blast furnace slag (BFS) and fly ash (FA). Blast furnace slag based alkali-activated materials (BFS-AAM) have poor workability and short setting time, while fly ash based alkali-activated materials (FA-AAM) characterizes with a slow strength development. Based on previous research, A good synergy between mechanical strength and durability could be obtained by adding BFS in FA-AAM[9][10] [11][12] [13].

Although FA/BFS-AAM has good application prospects, the lack of mixture design regulation still limits the application of these materials. Currently, limited research has been conducted on mix design of FA/BFS-AAM[14][15][16][17]. The study of mix design mainly involves 3 difficulties. Firstly, the codes that are used for conventional concrete are not applicable for AAM. Secondly, the chemical composition and particle size of raw materials are not uniform. Thirdly, limited research has been conducted to study the mechanical properties of BFA/FA-AAM. Besides, a large number of them have focused on the effect of confusing factors, such as alkali activators/ precursor ratio, $NaOH/Na_2SiO_3$ ratio on mechanical properties of BFS/FA-AAM, which results in nonrepeatable mix proportion, because the modulus of Na_2SiO_3 varies a lot and the alkali concentration is unclear.

A literature study on the effect of the control factors on the strength and reaction process of BFS/FA-AAM has been looked though in this paper. The reaction product at different ages is closely related to the concentration of ions and the reaction mechanism in the system. In addition, any change of Na_2SiO_3 modulus and $NaOH/Na_2SiO_3$ ratio in mix design is indeed changing the control factors (the ion concentration). The main propose of this study is to understand the control factors influencing the strength of BFS/FA-AAM and to clarify their effect mechanism. Thus, it could provide a theoretical foundation for the mix design of BFS/FA-AAM.

2. REACTION MECHANISM OF BFS/FA-AAM

2.1 Reaction process

A theoretical heat evolution rate curve is shown in Fig. 1(a). The reaction mechanism of BFS and FA alkali-activated by NaOH and Na_2SiO_3 could be divided into 5 stages based on isothermal calorimetry study[18][19][20], as shown in Fig. 1(b). In literature, the optimum value and occurrence time vary, and different stages may emerge, appearing as another type of curve. This is due to the effect of control factors on the reaction process, which will be discussed later.

In the initial stage, the undersaturation degree of modifying elements is very large, So a large amount of reaction elements is released. Previous research has shown that among the reaction ions, the Si-O-Si bonds are stronger than Si-O-Al, the bonds between network forming species and network modifying species are the weakest[21][22][23]. Because BFS contains a more substantial amount of Ca and Mg and less Al than FA. Therefore, the dissolution of BFS is faster than that of FA. The first heat evolution rate is mainly caused by the dissolution of BFS.

In the second stage, the formation of CASH is characterized by the second heat evolution peak. During the dissolution, the FA particles could act as nuclea sites, capturing the reaction ions released by BFS. Therefore, CASH gel is not only formed on the surface of BFS, but also on the surface of FA. The formation of CASH gel consumes ions, leading to a rapid increase of the undersaturation degree and promoting the release of reaction ions before a Si layer could be created on the surface of BFS. In the third stage, a period of reduced heat production rate occurs.

The accumulation of reaction products on the surface of BFS forms shells and prevents the further reaction of unreacted BFS. The dissolution of BFS is gradually stopped. In the meantime, the FA particle is still mainly under the destruction period. The reaction ions releasing rate is faster than the reaction products forming rate, because of its relatively lower reactivity and the amber curing temperature.

After the induction periods, sufficiently high content of reaction ions exist in the solution around FA particles in the fourth stage, leading to the polycondensation of a large amount of NASH gels. The generated NASH and CASH gels have different structures than those in a single precursor system, because they do not develop separately but interact with each other in the further reaction process[21]. An exchange of Al and Ca ions proceeds in the restructuration of CASH and NASH gels. In the fifth stage, the reaction produces shell gradually formed on the surface of the FA particle, and the dissolution is therefore ceased. A thermodynamically stable CASH gel will be created if time is long enough[21].

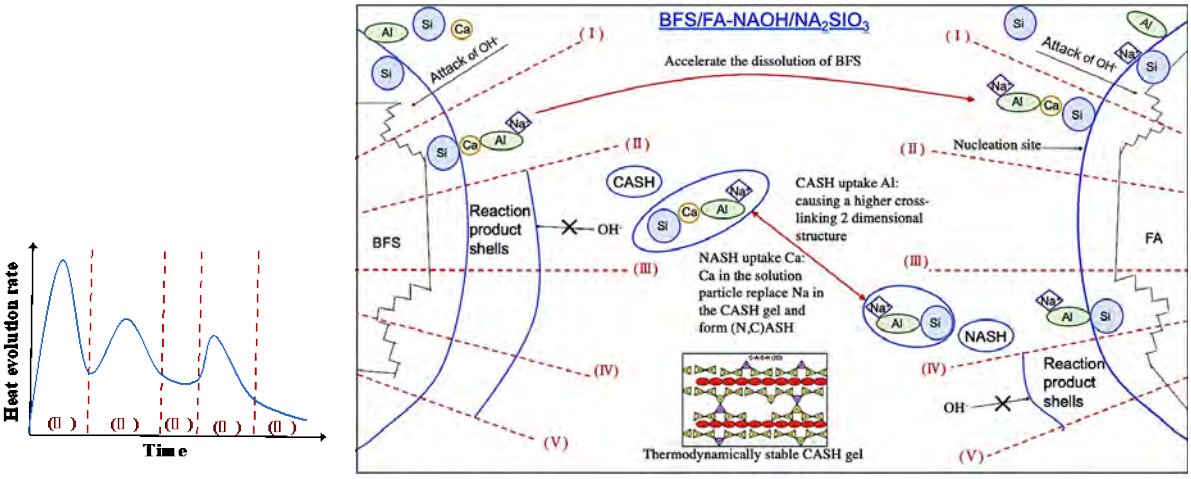

Figure 1: (a) A theoretical heat evolution rate curve of BFS/FA-AAM; (b) Reaction process of BFS/FA-AAM

2.2 Reaction products

Both micro and nanostructure research has shown that a complex mix of amorphous CASH and NASH gels are formed at an early age (28d) [5][25]. The results from NMR analysis show that the higher content of FA is associated with higher polymerization. More Q^4 and Q^3 units are detected when the BFS/binder ratio was 10% (binder refers to the sum of the mass of BFS and FA). While reaction products with Q^1 and Q^2 units, but without Q^3 and Q^4 units were observed when the BFS/binder ratio was 30-50%[26].

When the pH is higher than 12, CASH gels are preferentially formed instead of NASH gels. As time goes by, the Ca in the solution gradually distorts the Si-O-Al bonds and create new Si-O-Ca bonds, because of the polarizing effect. Therefore, higher Ca content and lower Al content is gradually found in the structure. As a result, NASH turns into (N,C)ASH gel with a more depolymerized structure. On the other hand, the released Al form NASH is taken up by CASH in bridge positions to build a 2-dimensional structure with higher cross-linking. Ultimately, a single CASH gel (most thermodynamically stable) could be formed[27]. A series of secondary products with crystalline phase are accompanied, such as hydrotalcite, tetracalcium aluminate

hydrate, katoite, stratlingite and zeolitic phase (including hydroxysodalite, zeolite P, Na-chabazite, zeolite Y and faujasite)[28][29][30][31][32][33].

3. CONTROL FACTORS AND MECHANISMS

3.1 BFS/binder ratio

As shown in Fig. 2(a), There is a strong linear relationship between the BFS/b ratio and 28 d strength[34][35][36][37]. The results indicate that the higher the content of BFS, the higher the strength. It seems that FA has little help on the development of strength. This is probably because of the low reactivity of FA. As discussed in the reaction mechanism, the formation of NASH gels is later than the formation of CASH gels. In this age, the hollow sphere particle of FA create lots of pore in the materials, since the time is insufficient for the precipitate of reaction products to fill the hollow space. The pores created by FA cause stress concentrations in the material and thus result in a decrease of strength. 90d of curing age is suggested for BFS/FA-AAM.

The effect of the BFS/binder ratio on the reaction process is shown in Fig. 2(b). The increase of the content of BFS is associated with an increase of Ca and a decrease of Al in the reaction system. Since the Ca-O-Si bonds are weaker than Al-O-Si bonds. It may lead to faster dissolution and a higher value of the first peak. As the reaction process advances, an induction period may occur before the second peak, because the number of nuclei sites is reduced, and the Si layer may form on the surface of BFS, which hinders the further dissolution of reaction ions. The induction period between the second and the third peak may be shortened or may even disappear. Because less NASH is formed, the value of the third peak may decrease.

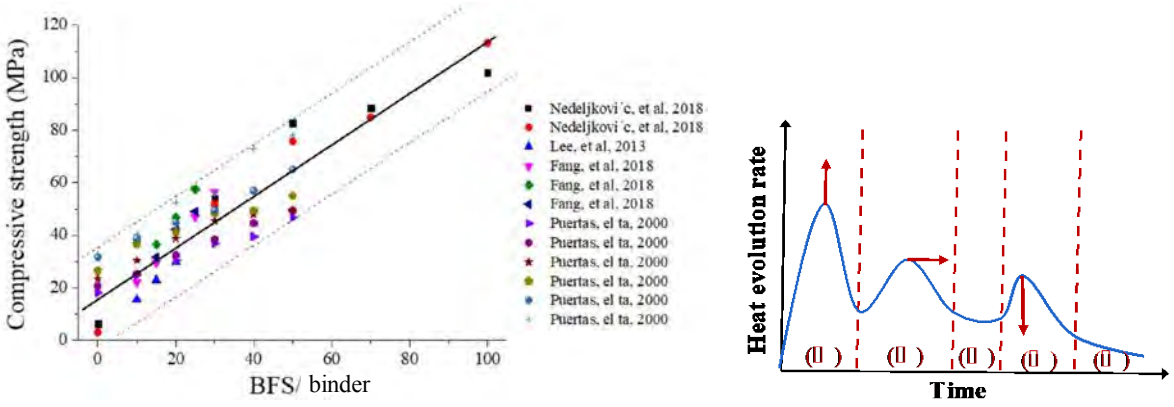

(a) (b)

Figure 2: Effect of BFS/binder ratio on BFS/FA-AAM: (a) effect on strength; (b) effect on reaction process

3.2 Na_2O/binder ratio

The effect of Na_2O/binder ratio on BFS/FA-AAM is shown in Fig. 3[38][39][40]. The strength first increases and then decreases with the Na_2O/binder ratio. Higher content of OH^- increases the dissolution of BFS and FA, associated with a higher value of the first peak. At the same time, a higher amount of free ions and a high amount of catalyzer (Na^+) improve the formation rate of CSH gels. The second peak may be advanced or may even merge with the first peak.

The destruction coagulation period of NASH is accelerated since the higher content of released monomers has a higher tendency to be connected. To a certain extent, the third peak may increase with the Na_2O/binder ratio.

However, when the Na_2O/binder ratio exceeds a specific value, the third peak may begin to decrease. When the concentration of OH^- is high, the dissolution of $Ca(OH)_2$ is reduced, and a thin layer of $Ca(OH)_2$ is formed on the surface of BFS particles. So Ca is less capable of reacting with Al and Si and forming the CASH gels. What is more, excess OH^- causes Al-Si gel precipitation at the very early stage on the surface of the FA particles, so the subsequent polymerization is hindered, and the strength is therefore decreased. Excess Na may also cause efflorescence and reduce the strength to some extent. To obtain the highest strength, the optimum value of Na_2O/binder ratio in BFS-AAM and FA-AAM is 5.5%-8% and 7%-10%, respectively, while the optimum value of Na_2O/binder ratio in BFS/FA-AAM is still unknown.

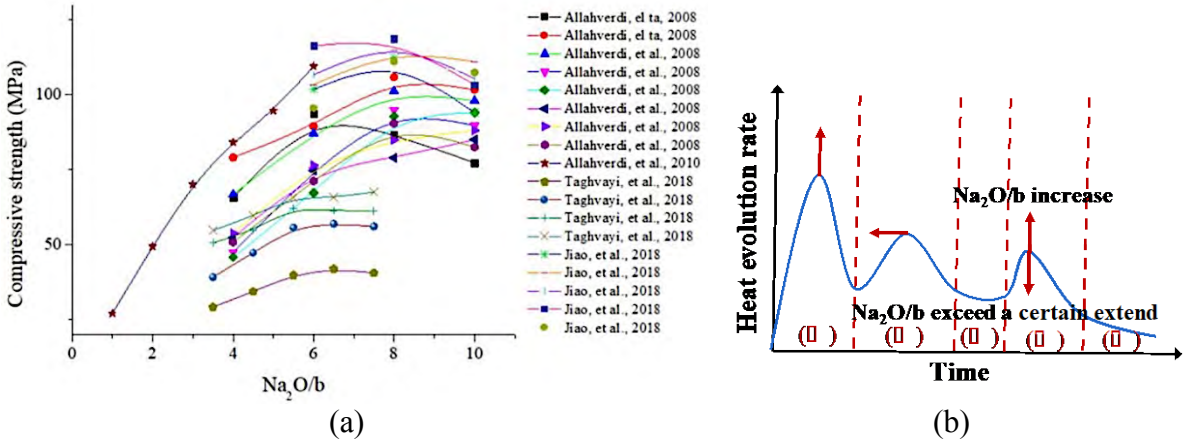

Figure 3: Effect of Na_2O/b ratio on BFS/FA-AAM: (a) effect on strength; (b) effect on reaction process

3.3 SiO_2/Na_2O ratio

The effect of the SiO_2/Na_2O ratio on BFS/FA-AAM is shown in Fig. 4[38][39][40][41]. With the increase of SiO_2/Na_2O, the strength first increases, then decreases. The first peak may decrease because the undersaturation degree of Si is lower in the solution, and the dissolution of Si is hindered. The second peak may increase because with more structure-forming element (Si) available in the solution, the reaction products could not only form on the surface of BFS particles, but also in the solution. Therefore, a denser microstructure could be generated. The third peak may be advanced because the dissolved Al is absorbed by Si in the solution, instead of being precipitated on the surface of FA particles. The dissolution of reaction ions is accelerated, and the formation of NASH gels advanced with more monomers for polymerization. More Si-O-Si bonds are formed, which are stronger than Si-O-Al bonds, leading to a higher degree of polymerization.

However, when the SiO_2/Na_2O ratio exceeds a particular value, the strength begins to decrease. Excess SiO_2/Na_2O could hinder the further dissolution of reaction ions since the Si layer may form on the surface of the precursor particles. Less dissolution of reaction ions eventually prevents the formation of CASH. On the other hand, excess SiO_2 species could form polymerized SiO_4 and precipitation, which may depress the precipitation of zeolite crystals and hinder the polymerization of FA in the subsequent process. To obtain the highest strength, the

optimum value of SiO_2/Na_2O ratio in BFS-AAM and FA-AAM is 0.85-1.4 and 0.6-1, respectively, while the optimum value of SiO_2/Na_2O ratio in BFS/FA-AAM is still unknown.

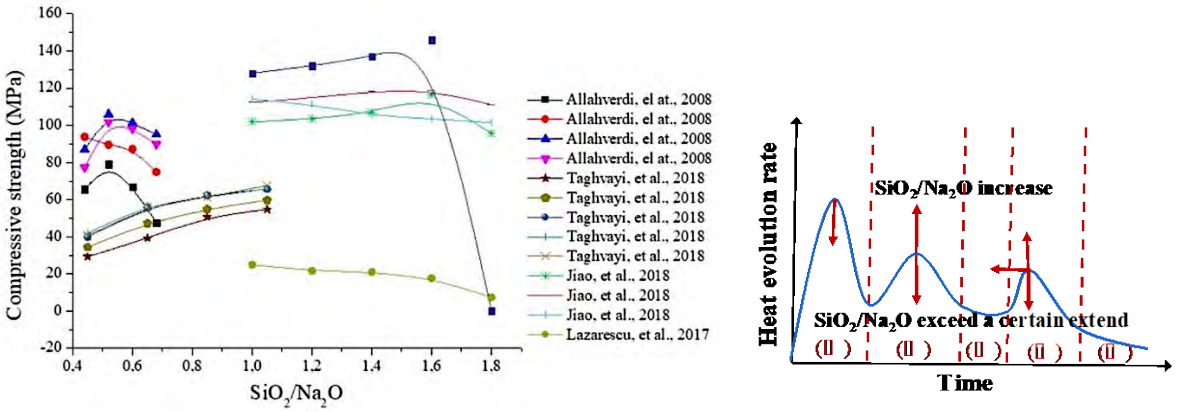

(a) (b)

Figure 4: Effect of SiO_2/Na_2O ratio on BFS/FA-AAM: (a) effect on strength; (b) effect on reaction process

3.4 Other factors

The relationship between the l/b ratio (the mass ratio of alkaline activated solution and binder) and the compressive strength and workability is shown in Fig. 5[34][36][42][43]. The study indicates that l/b has little effect on the strength of AAM. One significant difference between OPC and AAM is that the formation of reaction products requires no water. Water nearly reacts during the creation of CASH. In FA-AAM, water is consumed in the dissolution stage while release again in the polymerization process. Obviously, water is not chemically bound to the structure of the matrix[44]. From the reaction mechanism point of view, less water leads to a slightly higher compressive strength. But its effect is negligible, compared with the effect of control factors on the strength.

Nevertheless, water content is still an important factor in considering the workability of BFS/FA-AAM. With the increase of the l/b ratio, the dimensional flowability is increased. Water demand is affected by several factors, including particle size and shape distribution and specific surface area[45]. It is recommended to use the w/b ratio (the mass ratio of water and binder) instead of the l/b ratio to obtain more precise results for further study.

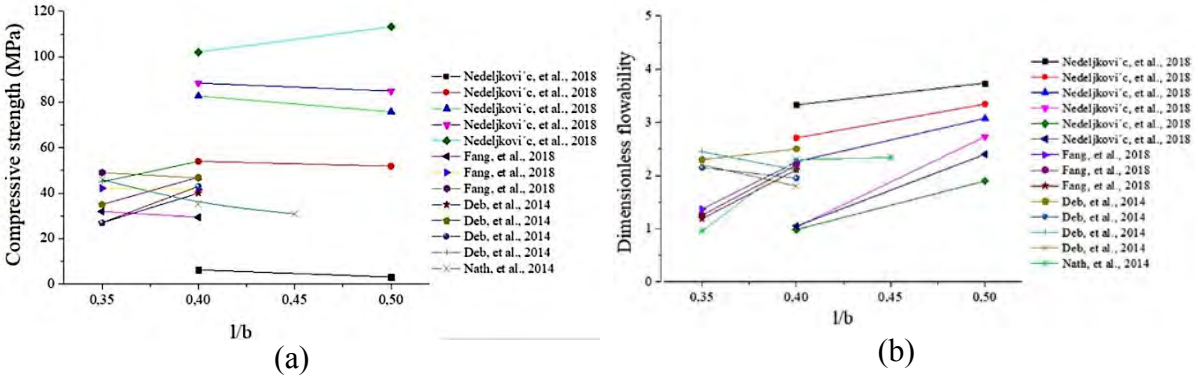

(a) (b)

Figure 5: Effect of l/b ratio on BFS/FA-AAM: (a) effect on strength; (b) effect on flowablity

4. CONCLUSIONS

In this paper, a theoretical foundation of the strength development of BFS/FA-AAM is built. The demonstration of the effect of control factors on the strength and reaction process could provide some guidance for the mix design of BFS/FA-AAM. For further study of mix design, a quantitative relationship between these factors and strength is required.

ACKNOWLEDGEMENTS

The first author also would like to gratefully acknowledge the China Scholarship Council (Grant Number 201806370216).

REFERENCES

[1]. Davidovits, J. 'Geopolymer cements to minimize carbon-dioxide greenhouse warming'. Conference: Proceedings of the Advances in Cement and Concrete, eds M.W. Grutzeck & S. L. Sarkar, Durham,1994.
[2]. Habert, G. J.B. d'Espinose de Lacaillerie, N. Roussel. 'Environmental evaluation of geopolymer based concrete production: reviewing current research trends'. Journal of Cleaner Production. 19(2011)1229-1238.
[3]. Turner, L.K, Collins, F.G. 'Carbon dioxide equivalent (CO_2-e) emissions: a comparison between geopolymer and OPC cement concrete'. Construction and Building Materials.43(2013)125-130.
[4]. Jannie, S.J. van Deventer, Provis. J.L, Duxson. P, Brice. D.G. 'Chemical Research and climate change as drivers in the commercial adoption of alkali activated materials'. Waste Biomass Valorization.1(2010)145-155.
[5]. Fernandez-Jimenez. A.M, Palomo, A., Lopez-Hombrados, C. 'Engineering properties of alkali-activated FA concrete' ACI Materials Journal.103 (2)(2006)106-112.
[6]. Sofi, M., Jannie, S.J. 'Engineering properties of inorganic polymer concretes (IPCs)'. Cement and Concrete Composites.37(2007)251-257.
[7]. Rashad, A.M, 'A comprehensive overview about the influence of different admixtures and additives on the properties of alkali-activated FA', Material Design.53(2014)1005-1025.
[8]. Yusuf, M.O., Johari, M.A.M, Ahmad, Z.A., Maslehuddin, M. 'Evolution of alkali activated ground blast furnace slag-ultrafine palm oil fuel ash based concrete'. Material Design.55(2014)387-393.
[9]. Nedeljković, M., Arbi, K., Zuo, Y.B., Ye, G. 'Microstructure and mineralogical analysis of alkali activated FA-slag pastes'. Conference: the 3nd International RILEM Conference on Microstructure Related Durability of Cementitious Composites, Nanjing, China, 2016.
[10]. Nedeljković, M., Arbi, K., Zuo, Y.B., Ye, G. 'Physical properties and pore solution analysis of alkali activated FA-slag paste'. Conference: International RILEM Conference on Materials, Systems and Structures in Civil Engineering, August 2016
[11]. Nedeljković, M., Zuo, Y.B., Arbi, K, Ye, G. 'Natural carbonation of alkali-activated FA and slag pastes'. Conference: Fib Symposium 2017 (high tech concrete): Where technology and engineering meet!), At Maastrich, the Netherlands, June 2017.
[12]. Arbi, K., Nedeljković, M., Zuo, Y.B., Ye, G. 'Durability of alkali-activated FA and slag concrete'. Conference: 9th International Concrete Conference 2016 Environment, Efficiency and Economic Challenges for Concrete, At Dundee, Scotland, UK, July 2016.

[13]. Ma, Y.J., Hu, J., Ye, G. 'The effect of activating solution on the mechanical strength, reaction rate, mineralogy, and microstructure of alkali-activated FA'. Journal of Materials Science.47(11)(2012)4568-4578.
[14]. Anuradha, R., Sreevidya, V., Venkatasubramani, R., Rangan, B.V. 'Modified guidelines for geopolymer concrete mix design using Indian Standard'. Asian Journal of Civil Engineering and Building House.13 (3)(2012)353-364.
[15]. Ferdous, M.W., Kayali, O., Khennane, A. 'A detailed procedure of mix design for FA based geopolymer concrete'. In: Fourth Asia-Pacific Conference on FRP in Structures, Australia. 2013, 11-13.
[16]. Lloyd, N.A., Rangan, B.V. 'Geopolymer concrete with FA'. In: Second International Conference on Sustainable Construction Materials and Technologies, Ancona, Italy. 2010.
[17]. Ferdous, M.W., Kayali, O., Khennane, A. 'A detailed procedure of mix design for FA based geopolymer concrete'. Fourth Asia-Pacific Conference on FRP in Structures, Australia. 2013,11-13.
[18]. Zuo, Y.B. Experimental Study and Numerical Simulation of the Reaction Process and Microstructure Formation of Alkali activated Materials. Ph.D. Thesis, Delft: Delft University Press, 2018, 42-59.
[19]. Chithiraputhiran, S., Neithalath, N. 'Isothermal reaction kinetics and temperature dependence of alkali activation of slag, fly ash and their blends'. Construction and Building Materials. 45 (2013) 233-242.
[20]. Gao, X., Yu, Q., Brouwers, H. 'Reaction kinetics, gel character and strength of ambient temperature cured alkali activated slag–fly ash blends, Constr. Build. Mater., 80 (2015) 105-115.
[21]. Hamilton J. P., Brantley S. L., Pantano C. G., etc, ''Dissolution ofNepheline, Jadeite and Albite Glasses: Toward Better Models for Aluminosilicate Dissolution,'' Geochim. Cosmochim. Acta, 65 [21] 3683–702 (2001).
[22]. Blum A. E., Lasaga A. C., ''The Role of Surface Speciation in the Dissolution of Albite,'' Geochim. Cosmochim. Acta, 55 [8] 2193–201 (1991).
[23]. Oelkers E. H., Gislason S. R., ''The Mechanism, Rates and Consequences of Basaltic Glass Dissolution: I. An Experimental Study of the Dissolution Rates of Basaltic Glass as a Function of Aqueous Al, Si and Oxalic Acid Concentration at 251Cand pH53 and 11,'' Geochim. Cosmochim. Acta, 65 [21] 3671– 81 (2001).
[24]. Garcia-Lodeiro, I., Palomo, A., Fernández-Jiménez, A. 'Crucial insights on the mix design of alkali-activated cement-based binders'. Handbook of Alkali-Activated Cements, Mortars and Concretes, Oxford: Woodhead Publishing, 2015, 49-73.
[25]. Yip C.K., Lukey G.C., Deventer J.S.J. 'The coexistence of geopolymeric gels and calcium silicate hydrate at the early stage of alkaline activation'. Cement and Concrete Research 35 (2005) 1688-1697.
[26]. Lee N.K., Lee H.K. 'Reactivity and reaction products of alkali-activated, FA/slag paste'. Construction and Building Materials. 2015, 81:303-312.
[27]. Garcia-Lodeiro I., Palomo A., Fernández-Jiménez A., Macphee D.E. 'Compatibility studies between N-A-S-H and C-A-S-H gelss. Study in the ternary diagram Na2O–CaO–Al2O3–SiO2–H2O'. Cement and Concrete Research 41 (2011) 923-931.
[28]. Wang, S.D. and Scrivener, K. L., 'Hydration products of alkali activated slag cement', Cem. Concr. Res. 25 (3) (1995) 561-571.

[29]. Myers, R.J., Lothenbach, B., Bernal, S.A. and Provis, J.L., 'Thermodynamic modelling of alkali-activated slag cements', Appl. Geochem. 61 (2015) 233-247.
[30]. Richardson, I.G., Brough, A. R., Groves, G.W. and Dobson, C.M., 'The Characterization of Hardened Alkali-Activated Blast-Furnace Slag Pastes and the Nature of the Calcium Silicate Hydrate (C-S-H) Phase', Cem. Concr. Res. 24 (5) (1994) 813-829.
[31]. Palomo, A., Grutzeck, M. W. and Blanco, M. T., 'Alkali-activated FAes - A cement for the future', Cem. Concr. Res. 29 (8) (1999) 1323-1329.
[32]. Duxson, P., Fernández-Jiménez, A., Provis, J., Lukey, G., Palomo, A. and Van Deventer, J., 'Geopolymer technology: the current state of the art', J. Mater. Sci. 42 (9) (2007) 2917-2933.
[33]. Criado, M., Fernández-Jiménez, A., Palomo, A., Sobrados, I. and Sanz, J., 'Effect of theSiO2/Na2O ratio on the alkali activation of FA. Part II: 29Si MAS-NMR Survey', Micropor Mesopor Mat.109 (1–3) (2008) 525-534.
[34]. Nedeljkovi´c, M., Li, Z.M. and Ye, G. 'Setting, Strength, and Autogenous Shrinkage of Alkali-Activated Fly Ash and Slag Pastes: Effect of Slag Content'. Materials.11(2018) 2121
[35]. Lee, N.K., Lee, H.K., 'Setting and mechanical properties of alkali-activated fly ash/slag concrete manufactured at room temperature'. Construction and Building Materials 47 (2013) 1201-1209.
[36]. Fang, G.H., Ho, W.K., Tu, W.L., Zhang, M.Z. 'Workability and mechanical properties of alkali-activated fly ash-slag concrete cured at ambient temperature'. Construction and Building Materials 172 (2018) 476- 487.
[37]. Puertas, F., MartõÂnez-RamõÂrez, S., Alonso, S., VaÂzquez, T. 'Alkali-activated fly ash/slag cement Strength behaviour and hydration products'. Cement and Concrete Research 30 (2000) 1625-1632
[38]. Allahverdi, A., Najafi Kani, E., Esmaeilpoor, S. 'Effects of Silica Modulus and Alkali Acttivated Concentration on Activation of Blast-Furnace Slag'. Iranian Journal of Materials Science and Engineering, 5(2)(2008) 32-35
[39]. Taghvayi, H., Behfarnia, K., Mohammadbagher, K. 'The Effect of Alkali Concentration and Sodium Silicate Modulus on the Properties of Alkali-Activated Slag Concrete' Journal of Advanced Concrete Technology. 16(2018) 293-305.
[40]. Jiao, Z.Z., Wang, Y., Zheng, W.Z., Huang, W.X. 'Effect of Dosage of Alkaline Activator on the Properties of Alkali-Activated Slag Pastes'. Advances in Materials Science and Engineering. (2018) 1-12.
[41]. Lăzărescu, A. V., Szilagyi, H., Baeră, C., Ioani, A.' The Effect of Alkaline Activator Ratio on the Compressive Strength of Fly Ash-Based Geopolymer Paste'. IOP Conf. Ser.: Mater. Sci. Eng. 2017.
[42]. Deb, P.S., Pradip, N., Sarker, P.K. 'The effects of ground granulated blast-furnace slag blending with fly ash and activator content on the workability and strength properties of geopolymer concrete cured at ambient temperature'. Materials and Design 62 (2014) 32-9.
[43]. Pradip, N., Sarker, P.K. 'Effect of GGBFS on setting, workability and early strength properties of fly ash geopolymer concrete cured in ambient condition'. Construction and Building Materials 66 (2014) 163-171.
[44]. Xu, H., Deventer, J.S.J., Jannie, S.J. 'The effect of alkali metals on theformation of geopolymeric gelss from alkali-feldspars'. Colloid Surf.216(2003)27-44.
[45]. Hewlett, P., Lea's Chemistry of Cement and Concrete, Butterworth-Heinemann, Oxford, 2003.

DRYING SHRINKAGE OF ALKALI-ACTIVATED SLAG CONCRETE WITH NATURAL/RECYCLED AGGREGATES

H. Dong (1), X. Yao (1) (2), S. Burgmann (3), G. Ye (1) (4)

(1) Microlab, Delft University of Technology, The Netherlands

(2) School of Energy and Power Engineering, Shandong University, China

(3) Construction Material Technology, University of Kaiserslautern, Germany

(4) Magnel Laboratory for Concrete Research, Ghent University

Abstract

Each year a large amount of construction and demolition waste (CDW) is generated in the European Union. For sustainability development the CDW is recycled and re-used. To promote the use of CDW, recycled aggregates from CDW were incorporated in alkali-activated concrete (AAC), which mainly consisted of secondary materials or industrial by-products. This study investigated the influence of recycled aggregates on workability, compressive strength and drying shrinkage of slag-based AAC. Properties of conventional concrete with natural/recycled aggregates were also tested for comparison. The results showed that the pre-saturated recycled aggregates only slightly affected the workability of conventional concrete or AAC. Recycled aggregates reduced compressive strength of both conventional concrete and AAC due to extra water for pre-saturation of the recycled aggregates. The mass loss of the concrete specimens upon drying was greater for low-strength concrete than for moderate strength concrete. The recycled aggregates increased the mass loss and drying shrinkage of AAC. For conventional concrete, low-strength concrete had a higher drying shrinkage compared with moderate strength concrete. On the contrary, for AAC in this study, low-strength concrete had a lower drying shrinkage compared with moderate strength concrete.

Keywords: recycled aggregates, conventional concrete, alkali-activated concrete, compressive strength, drying shrinkage

1. INTRODUCTION

Concrete is the most essential material for buildings and infrastructure due to its good performance and economical characteristic. Each year a huge amount of concrete is produced worldwide, while the global cement production increased from 1.4 billion tons in 1995 to 4.1 billion tons in 2019 [1]. Depending on applications the designed service life of concrete structures mainly ranges from 50 years to 100 years [2]. After the service life or premature failure, concrete structures need to be demolished. According to Eurostat [3], 345 million tons

mineral waste from construction and demolition was generated in the European Union in 2016. For sustainability development, the construction and demolition waste (CDW) is being recycled and reused. The recovery rate of CDW in the EU had reached 89% in 2016 [3]. In the annual review 2018-2019 reported by European Aggregates Association, recycled/re-used aggregates takes up 12% of the total amount of aggregates used in construction [4]. By using recycled aggregates in concrete, the burden of extracting primary natural resources (e.g., gravels) is alleviated. A comprehensive review on recycled aggregate in conventional concrete has been published, in which the fresh properties, mechanical properties, long-term performance and design codes are discussed in detail [5].

To further promote sustainability, secondary materials or industrial by-products need to be used to a large extent in concrete production. For that purpose, alkali-activated concrete (AAC) has emerged as a solution. The AAC is cement free and can be made with industrial by-products, like blast furnace slag (BFS) and fly ash (FA) as precursors, NaOH and water glass as alkali activators, and aggregates [6]. Concerning that 70% - 80% of the volume of concrete is made of aggregates, attempts have also been made to incorporate recycled aggregates from CDW in AAC [7-14]. These studies mainly focused on workability, mechanical properties and durability (e.g., water absorption, chloride resistance, sulfate resistance and freeze-thaw resistance). Investigation on drying shrinkage, which is a common critical issue for AAC [16], is still scarce for AAC with recycled aggregate. This study mainly investigated the influence of recycled aggregates on drying shrinkage of slag-based AAC. Meanwhile, workability and compressive strength of the AAC with natural/recycled aggregates were tested and compared with that of conventional concrete.

2. MATERIALS AND EXPERIMENTS

3.1 Raw materials

Concrete with two strength classes were prepared, namely low strength (i.e., C30) and moderate strength (C50). For each strength class, both conventional concrete and AAC were prepared. Conventional concrete was prepared with cement (CEM III/B 42,5 N), quartz sand, natural/recycled coarse aggregates. AAC was prepared based on RILEM mixtures [17], with BFS as precursor, NaOH pellets (Honewell) and water glass (PQ Corporation) as activators, quartz sand, natural aggregates or recycled aggregates. The chemical compositions of CEM III/B 42.5 N [18] and BFS [19] are listed in Table 1. BFS had a particle size of 0.1 - 50 μm and a d_{50} of 18.3 μm. The quartz sand had a modulus of 3.4. The natural aggregates were pebbles with a size of 4-16 mm. The recycled aggregates from CDW mainly consisted of crushed concrete (77 % by weight) and unbound stone (18% by weight), with a size of 4-16 mm, a saturated surface dry density of 2400 kg/m^3, and a water absorption capacity of 5.2%. The recycled aggregates were pre-saturated with water before use.

Table 1: Chemical compositions of cement and BFS [wt %]

	SiO_2	Al_2O_3	CaO	MgO	Fe_2O_3	SO_3	K_2O	TiO_2	Other	LOI
CEM III/B 42,5 N	30.0	11.0	45.0	7.0	1.3	1.9	0.5	0.9	2.3	0.1
BFS	31.8	13.3	40.5	9.3	0.5	1.5	0.3	1.0	0.5	1.3

3.2 Mix design and methodology

Mix designs of conventional concrete and AAC are listed in Table 2. The natural and recycled aggregates were pre-saturated before mixing. 150 mm × 150 mm × 150 mm specimens and 100 mm × 100 mm × 400 mm specimens were cast for tests on compressive strength and drying shrinkage. All specimens were demoulded after 2 days because 2 days curing was needed for demoulding AAC specimens with recycled aggregates. The specimens were subjected to sealed curing at 20 ℃ until testing. The compressive strength of the 7-day and 28-day old specimens was determined according to NEN 5988. For drying shrinkage measurements, the specimens were stored at 50% relative humidity and 20 ℃. The measurements of drying shrinkage started at 3 days and last for 28 days, according to NEN-EN 12390-16. During the drying process at 50% relative humidity and 20 ℃, mass loss of the specimens was also recorded.

Table 2: Mix design of conventional concrete and AAC [kg/m^3]

	Low strength concrete				Moderate strength concrete			
	Conventional concrete		AAC		Conventional concrete		AAC	
	C30	C30-RA	S1b	S1b-RA	C45	C45-RA	S3a	S3a-RA
CEMIII/B 42,5N	335	335	-	-	383	383	-	-
BFS	-	-	357	357	-	-	375	375
NaOH	-	-	10,7	10,7	-	-	15	15
$Na_2O{\cdot}2SiO_2$	-	-	4,8	4,8	-	-	10,1	10,1
Sand	826	826	734	734	786	786	729	729
Natural aggregate	1017	-	1101	-	1010	-	1093	-
Recycled aggregate	-	915	-	990	-	908	-	983
Water	184	184	156	156	163	163	153	153
W/B	0,55	0,55	0,42	0,42	0,425	0,425	0,382	0,382

3. RESULTS AND DISCUSSION

3.1 Workability

The slump of all mixtures is listed in Table 3. In general, concrete mixtures with recycled aggregates had lower slump values than that with natural aggregates. This can be explained by the angular shape of the recycled aggregates, in comparison with the rounded natural aggregates used in this study. It is known that for a given paste volume, mixtures made with angular coarse aggregate can have lower deformability, thus a smaller slump value [20].

Table 3: Slump of fresh conventional concrete and AAC [mm]

C30	C30-RA	S1b	S1b-RA	C45	C45-RA	S3a	S3a-RA
160	100	175	155	65	60	165	160

3.2 Compressive strength

Fig. 1 shows the 7 days and 28 days compressive strength of conventional concrete (i.e., low-strength: C30 and C30-RA, moderate-strength: C45 and C45-RA) and AAC (i.e., low-strength: S1b and S1b-RA, moderate-strength: S3a and S3a-RA). The low-strength concrete C30 and S1b had a 28 days compressive strength of 34 MPa and 30 MPa, respectively. The moderate-strength concrete C45 and S3a had a 28 days compressive strength of 44 MPa and 45 MPa, respectively. The incorporation of recycled aggregates reduced compressive strength of both conventional and AAC, which was in accordance with reported work [7]. Porous and cracked structure of recycled aggregates were believed to be one of the causes of reduction of concrete strength. Besides, the extra water for pre-saturation of recycled aggregates diluted the alkali solution, and thus reduced the concrete strength. Note that the negative effect of recycled aggregates on compressive strength was smaller for low-strength concrete than for moderate-strength concrete. It is known that the mortar matrix plays a greater role for low-strength concrete, while the influence of coarse aggregates becomes bigger for high-strength concrete [21, 22].

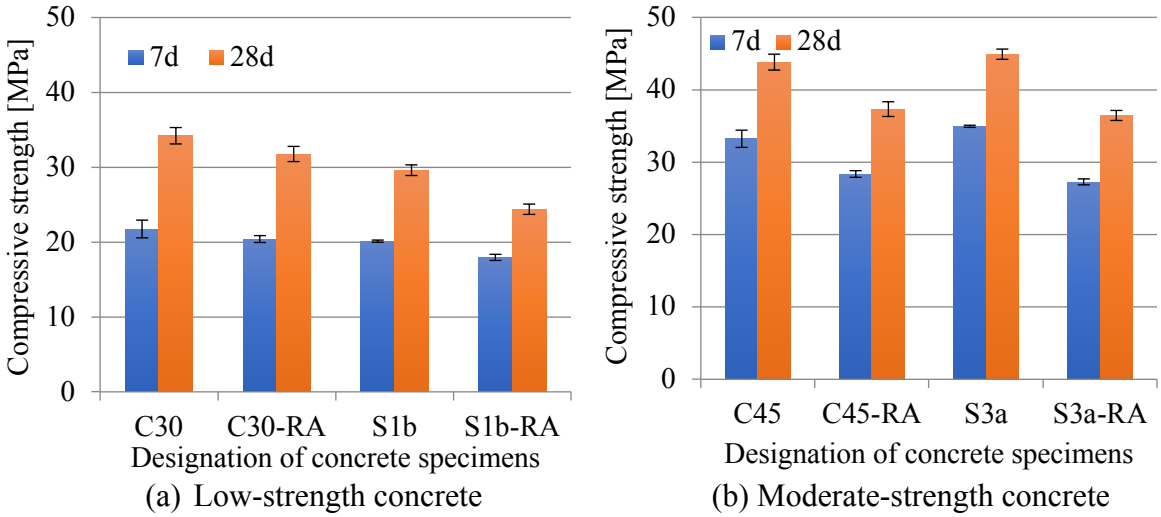

Figure 1: Compressive strength of conventional concrete and AAC

3.3 Drying shrinkage and mass loss

Fig. 2 shows the mass loss and drying shrinkage of conventional concrete and AAC. In general, the mass loss of the specimens upon drying was greater for low-strength concrete (e.g., C30 and S1b) than for moderate strength concrete (e.g., C45 and S3a). The mass loss of the specimens was also greater for concrete with recycled aggregates (e.g., S1b-RA and S3a-RA) than for concrete with natural aggregates (e.g., S1b and S3a).

The incorporation of recycled aggregate in AAC increased the drying shrinkage, in accordance with the findings by Alonso et al. [23] who applied recycled fine aggregates from CDW in alkali-activated slag mortar. The increase in paste content in concrete due to the incorporation of recycled aggregate was identified as the main reason for the increase of drying shrinkage [24, 25]. For conventional concrete, low-strength concrete had a higher drying shrinkage compared with moderate strength concrete. It can be explained by the fact that low-strength concrete had a higher porosity and a coarser pore structure, leading to a faster moisture

loss compared with moderate-strength concrete. On the contrary, for AAC, low-strength concrete had a lower drying shrinkage compared with moderate strength concrete. The causes are more complicated than that for conventional concrete. One possible reason can be related to the alkali activators of the AAC. In this study, moderate-strength AAC was prepared with a higher concentration (i.e., NaOH and $Na_2O{\cdot}2SiO_2$) and a higher modulus (i.e., SiO_2/Na_2O) of the alkali solution. The higher concentration of alkali activator was reported to increase the drying shrinkage of AAC [26]. Besides, a higher modulus of alkali solution resulted in finer pore structure. The finer pores increase the tensile stresses imposed by pore solution to capillary pores under drying, and consequently the drying shrinkage rates increase [27].

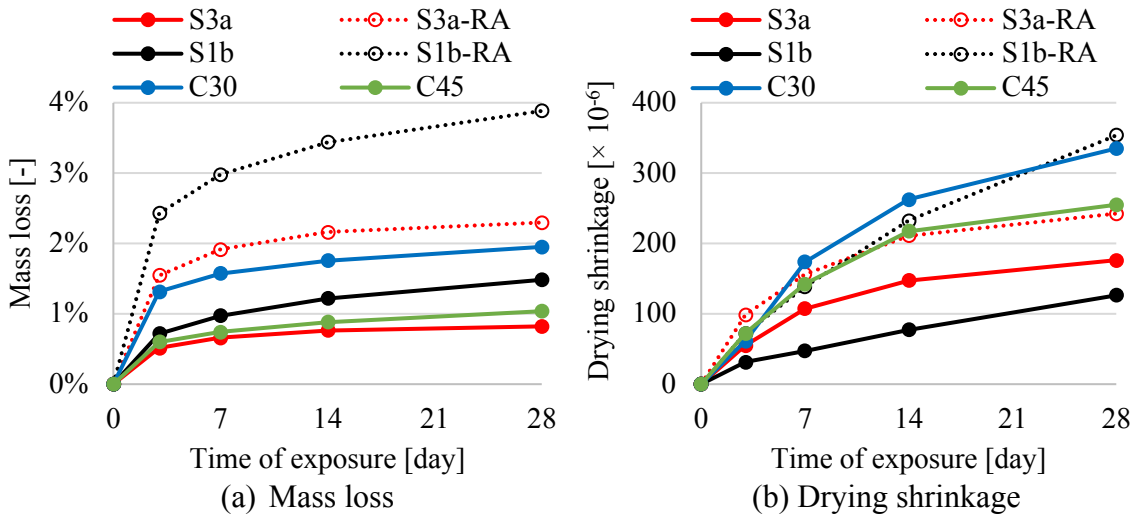

Figure 2: Mass loss and drying shrinkage of conventional concrete and AAC. After 3 days sealed curing, the concrete specimens were subjected to drying for 28 days.

Fig. 3 shows the relationship between mass loss and drying shrinkage of conventional concrete and AAC. For concrete with natural aggregates, moderate-strength concrete (i.e., C45, S3a and S3a-RA) exhibited a steeper curve of drying shrinkage with respect to mass loss compared with low-strength concrete (i.e., C30, S1b and S1b-RA). This result is in accordance with the findings for conventional concrete in [28]. At a certain mass loss, the smaller drying shrinkage of low-strength concrete can be explained by the fact that the water loss mainly took place in large capillary pores, thus lower tensile stresses were generated in the pores [29]. It is also interesting to note that the curves of C30 and C45 almost coincided with that of S1b and S3a, respectively. It indicates that for concrete with natural aggregates there existed a correlation between the compressive strength and the drying shrinkage-mass loss relation. For concrete with natural aggregates in this study, it is implied that reaching a certain drying shrinkage was a matter of time, depending on the point when a certain mass was lost. For AAC, the drying shrinkage-mass loss curves of S1b and S3a were steeper than that of S1b-RA and S3a-RA, respectively. This can be explained by the extra water for pre-saturation of recycled aggregates, which diluted the alkali activators and resulted in lower geopolymerization of AAC [7]. The lower geopolymerization indicates a coarser pore structure of AAC. With the coarser pore structure, smaller tensile stress was generated in capillary pores at a certain mass loss, leading to a smaller drying shrinkage of S1b-RA and S3a-RA.

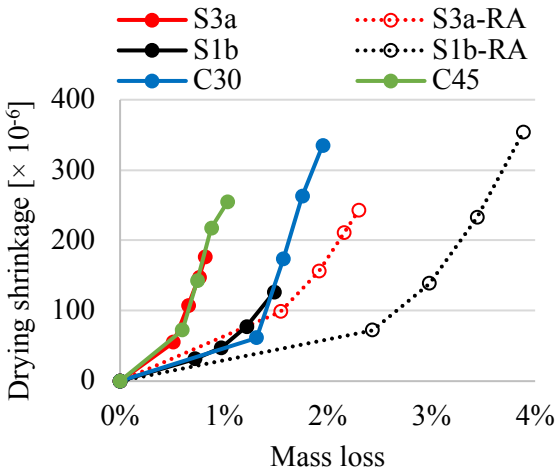

Figure 3: Relationship between mass loss and drying shrinkage of conventional concrete and AAC. After 3 days sealed curing, the concrete specimens were subjected to drying for 28 days.

4. CONCLUSION

This study evaluated the influence of recycled aggregates from construction and demolition waste on workability, compressive strength and drying shrinkage of conventional and alkali-activated concrete (AAC). The following conclusions can be drawn:

- Incorporation of pre-saturated recycled aggregates only slightly affects the workability of conventional concrete or AAC. The slightly reduced workability of concrete with recycled aggregates was due to the angular shape of the recycled aggregates compared with the rounded natural aggregates.
- Recycled aggregates showed a similar effect on compressive strength of both conventional concrete and AAC. The reduction of compressive strength of concrete with recycled aggregates was caused by the extra water for pre-saturation of the recycled aggregates that diluted alkali activators. Porous and cracked structure of recycled aggregates was believed to be another cause of concrete strength reduction.
- The mass loss of the specimens upon drying was greater for low-strength conventional concrete or AAC than for moderate-strength conventional concrete or AAC. The recycled aggregates increased the mass loss of AAC compared with natural aggregates.
- Recycled aggregate increased the drying shrinkage of AAC, explained by the increase in paste content in concrete due to the incorporation of recycled aggregate. For conventional concrete, low-strength concrete had a higher drying shrinkage compared with moderate strength concrete. On the contrary, for AAC in this study, low-strength concrete had a lower drying shrinkage compared with moderate strength concrete. It was explained by the higher concentration and modulus of alkali solution of AAC.

ACKNOWLEDGEMENTS

Support by the European Regional Development Fund for the Interreg project URBCON is gratefully acknowledged.

REFERENCES

[1] USGS, M.C.S. 'Cement Statistics and Information'. US Geological Survey, Washington, DC, 2019. https://www.usgs.gov/centers/nmic/cement-statistics-and-information.

[2] Amey, S., et al. 'Service-Life Prediction—State-of-the-Art Report'. ACI Committee 365. American Concrete Institute, 2000.

[3] Eurostat, 'Generation of waste by waste category, hazardousness and NACE rev. 2 activity'. 2016. https://ec.europa.eu/eurostat/web/products-datasets/-/env_wasgen.

[4] Association, E.A. 'A sustainable industry for a sustainable Europe'. UEPG, 2019. https://rmis.jrc.ec.europa.eu/?page=rm-profiles#/Aggregates.

[5] De Brito, J. and Saikia, N. 'Recycled aggregate in concrete: use of industrial, construction and demolition waste'. Springer Science & Business Media, 2012.

[6] Provis, J.L. and Van Deventer, J.S. 'Alkali activated materials: state-of-the-art report, RILEM TC 224-AAM'. Springer Science & Business Media, Vol. 13, 2013.

[7] Abdollahnejad, Z., et al., 'Construction and Demolition Waste as Recycled Aggregates in Alkali-Activated Concretes'. *Materials.* **12**(23)(2019)4016.

[8] Nuaklong, P., Sata, V. and Chindaprasirt, P. 'Properties of metakaolin-high calcium fly ash geopolymer concrete containing recycled aggregate from crushed concrete specimens'. *Constr Build Mater*. **161(2018)**365-373.

[9] Parthiban, K. and Mohan, K. S. R. 'Influence of recycled concrete aggregates on the engineering and durability properties of alkali activated slag concrete'. *Constr Build Mater*. **133**(2017)65-72.

[10] Shaikh, F.U.A. 'Mechanical and durability properties of fly ash geopolymer concrete containing recycled coarse aggregates'. *Int J Sustain Built Environ*. **5**(2)(2016)277-287.

[11] Rao, K.N.H.S. 'A Review on Strength and Durability Studies on Geopolymer Concrete Produced with Recycled Aggregates'. *Int J Sci Res*. **4**(07)(2016).

[12] Nuaklong, P., Sata, V. and Chindaprasirt, P. 'Influence of recycled aggregate on fly ash geopolymer concrete properties'. *J Clean Prod*, **112**(2016)2300-2307.

[13] Sata, V., Wongsa, A. and Chindaprasirt, P. 'Properties of pervious geopolymer concrete using recycled aggregates'. *Constr Build Mater*, **42**(2013)33-39.

[14] Pacheco-Torgal, F., et al. 'Are geopolymers more suitable than Portland cement to produce high volume recycled aggregates HPC?' *Constr Build Mater*. **36**(2012)1048-1052.

[15] Commission, E. 'EU Construction & Demolition Waste Management Protocol'. 2016.

[16] Mastali, M., et al. 'Drying shrinkage in alkali-activated binders – A critical review'. *Constr Build Mater*. **190**(2018)533-550.

[17] Provis, J.L. and Winnefeld, F. 'Outcomes of the round robin tests of RILEM TC 247-DTA on the durability of alkali-activated concrete'. in MATEC Web of Conferences. EDP Sciences, 2018.

[18] Nedeljković, M., et al. 'Effect of curing conditions on the pore solution and carbonation resistance of alkali-activated fly ash and slag pastes'. *Cem. Concr. Res.* **116**(2019)146-158.

[19] Li, Z., et al., 'Mitigating the autogenous shrinkage of alkali-activated slag by metakaolin'. *Cem. Concr. Res.* **122**(2019)30-41.

[20] Aïssoun, B.M., Hwang, S. D. and Khayat, K.H. 'Influence of aggregate characteristics on workability of superworkable concrete'. *Mater Struct*. **49**(1-2)(2016)597-609.

[21] Özturan, T. and Çeçen, C. 'Effect of coarse aggregate type on mechanical properties of concretes with different strengths'. *Cem. Concr. Res.* **27**(2)(1997)165-170.

[22] Hansen, T.C. and Boegh. E. 'Elasticity and drying shrinkage concrete of recycled-aggregate'. in Journal Proceedings. 1985.

[23] Alonso, M., dríguez, A. and Puertas, F. 'Viability of the use of construction and demolition waste aggregates in alkali-activated mortars'. *Mater Construcc*. **68**(331)(2018)164.

[24] Kou, S. C., Poon, C. S. and Agrela, F. 'Comparisons of natural and recycled aggregate concretes prepared with the addition of different mineral admixtures'. *Cem Concr Compos*. **33**(8)(2011)788-795.
[25] Limbachiya, M., Leelawat, T. and Dhir, R. 'Use of recycled concrete aggregate in high-strength concrete'. *Mater Struct*. **33**(9)(2000)574.
[26] Vijayakumar, R.M. 'Evaluating shrinkage of fly ash-slag geopolymers'. Ph.D. Thesis, University of Illinois at Urbana-Champaign, 2013.
[27] Taghvayi, H., Behfarnia, K. and Khalili, M. 'The Effect of Alkali Concentration and Sodium Silicate Modulus on the Properties of Alkali-Activated Slag Concrete'. *J Adv Concr Technol*. **16**(7)(2018)293-305.
[28] Bissonnette, B .T., Pierre, P. and Pigeon, M. 'Influence of key parameters on drying shrinkage of cementitious materials'. *Cem. Concr. Res.* **29**(10)(1999)1655-1662.
[29] Neville, A.M. 'Properties of concrete'. John Wiley & Sons, 1996.

INFLUENCE OF MIX DESIGN PARAMETERS ON REACTIVITY AND SETTING OF ALKALI-ACTIVATED MATERIALS

Marcello Mutti (1), Shiju Joseph (1) and Özlem Cizer (1)

(1) Department of Civil Engineering, KU Leuven, Belgium

Abstract

The mix design of alkali-activated materials (AAMs) is developed by taking into account several interdependent parameters. Therefore, the optimization of these to achieve a robust composition might represent a great challenge. The aim of this study is to investigate and compare the influence of some key parameters on the reactivity and setting of AAMs. The effects of alkali-modulus (Ms), water to binder (w/b) and solution to binder (s/b) ratios are assessed on a binder made from 50% blast furnace slag and 50% fly ash activated with a combination of NaOH and water glass in which Na_2O and SiO_2 are tuned according to the chosen mix design. Results show that each parameter leads to significant effects in the investigated aspects. Although the heat release is significantly influenced by w/b ratio at early ages, this appears to be more influenced by Ms and s/b ratio at 7 days. Nevertheless, the w/b ratio exhibits a significantly higher impact on setting time.

Keywords: alkali-activated materials, setting, reactivity

1. INTRODUCTION

Alkali-activated materials (AAMs) are generally obtained from the hydration of (calcium)aluminosilicates in high alkaline conditions. A wide range precursors and activators, the alkaline solution used to promote the hydration, can be used in the formulation of AAMs' mixes. The suitable precursors are classified based on their chemical composition, specifically on the amount of CaO. Common binders, belonging respectively to the class of high calcium and low calcium binders, are blast furnace slag (BFS) and fly ash (FA) while sodium hydroxide and sodium silicate represent the most common activators [1,2]. Typical AAMs are made by combining all these four starting materials and the resulting mix design is characterized by several interdependent parameters that make its optimization a challenging task. Moreover, each of these parameters can significantly affect aspects such as reactivity, microstructure, setting, and mechanical properties. It is known that AAMs suffer from several shortcomings, such as fast setting and autogenous shrinkage, which hinder their practical application but those might be overcome by a conscious design. Among all the parameters, some, like the BFS/FA ratio and the alkali modulus (SiO_2/Na_2O, Ms) have been extensively investigated while others, such as the water to binder (w/b) and solution to binder (S/b) ratio,

and their influence on AAMs are less known. By decreasing the BFS/FA ratio it is possible to prolong the setting while also reducing the autogenous shrinkage, but this comes at the cost of reduced strength [3,4]. Similarly, higher Ms enhances the mechanical properties exhibited by the material and it also delay the setting but it drastically reduces the workability [5]. The w/b ratio, despite being deeply investigated for OPC-based systems, has not been directly addressed by many studies. Recently, it has been observed that high water contents lead to a faster structuration of the material while also delaying the setting [6]. In AAMs, changes in this parameter not only influence the pore structure, and thus the mechanical properties, but also significantly affect the reaction kinetics by altering the alkalis' concentration. For this reason, it might be preferable to formulate AAMs in terms of S/b rather than w/b. Some similarities have been found between the influence of S/b ratio on AAMs and those of w/b ratio on OPC [7]. In both cases decreasing the ratio leads to higher compressive strength while also lowering the drying shrinkage. Nevertheless, the S/b ratio represents a difficult parameter to optimize due to its effects on the reaction process. In fact, the dissolution of the binder is promoted in presence of high amount of solution but, in this condition, a reduced polycondensation rate has been observed [8]. The aim of this study is, therefore, to investigate the influence of three parameters, Ms, w/b, and S/b, on the early age reactivity and setting of AAMs. This is done by comparing the early age reactivity, measured by isothermal calorimetry, with the setting process evaluated by ultrasonic P-wave velocity measurements and by Vicat-needle tests.

2. MATERIALS AND METHOD

2.1 Materials and mix design

The BFS and FA used in this study were purchased from Ecocem and BauMineral respectively. Their chemical composition retrieved from X-ray fluorescence spectrometry are reported in Table 1. Technical grade sodium hydroxide pellets (≥97%), purchased from VWR chemicals and sodium silicate(aq), purchased from abcr, were used to prepare the activating solutions. Due to the heat released during the preparation of the solutions those were prepared beforehand and let cool down to room temperature.

Table 1: Chemical composition by mass % of BFS and FA

	Oxides	CaO	SiO_2	Al_2O_3	MgO	SO_3	K_2O	Na_2O	Fe_2O_3
BFS	wt. %	39.8	36.2	12.4	7.3	-	0.5	-	0.6
FA		3.5	54.5	26.5	2.0	1.3	2.9	1.0	6.6

A reference composition was chosen based on previous unpublished study and three different series, each made by the reference and two additional compositions, were designed to investigate the influence of Ms, S/b and w/b ratios on setting and hardening. The complete mix design is reported in Table 2.

Table 2: Mix compositions

Sample ID	BFS/FA ratio	Solution/binder ratio (S/b)	Water/binder ratio (w/b)	Water/solid ratio	Na_2O %	SiO_2 %	Ms
Ref	1	0.55	0.42	0.37	5.26	7.56	1.44
HS	1	0.70	0.53	0.45	6.69	9.63	1.44
LS	1	0.48	0.36	0.32	4.54	6.53	1.44
HW	1	0.65	0.51	0.45	5.26	7.56	1.44
LW	1	0.50	0.37	0.32	5.26	7.56	1.44
HMs	1	0.53	0.41	0.37	4.02	7.56	1.88
LMs	1	0.52	0.41	0.37	5.26	5.26	1

*H=high, L=low, S=solution/binder, W=water/binder, Ms=alkali modulus, Ref=reference composition

2.2 Testing procedure

2.2.1 Reaction kinetics

The reaction kinetics was evaluated on paste specimens through the hydration heat by means of a TAM Air isothermal calorimetry set at 20°C. Approximately 10 g of paste were poured in a glass ampoule immediately after mixing and the measurement started in a couple of minutes. Due to the focus on setting the heat flow curves are reported up to 4 hours.

2.2.3 Ultrasonic P-wave measurements

The solidification process was monitored on paste specimens, using IP-8 ultra-sonic measuring instrument (Ultra Test), according to standard EN 1250-4. To prevent solvent evaporation and subsequent drying during the measurements the moulds were covered with plastic films immediately after casting.

2.2.4 Setting time

Initial and final setting time were evaluated according to standard EN-196-3 using an automatic recording Vicat needle apparatus. Initial setting is determined as the time occurring between the moment in which the binder was mixed with the activating solution (t0) and the time at which the penetration depth of the needle reaches 6±3 mm from the baseplate. Final setting is determined when the penetration depth reaches 0.5mm. In this study the standard consistency was not used in the paste preparation and thus the evaluated setting times cannot be defined as standard setting times.

3 RESULTS AND DISCUSSION

The isothermal calorimetry heat flow of Ref, reported in Fig.1 (a) (solid line), shows a behaviour typically observed in cementitious materials with two well distinct peaks, one occurring in the very first moments after mixing, here around 30 min, and the other occurring at a later stage, here around 20 hours. Similarly, also in the UPV curve, the dotted line in Fig.1(a), it is possible to observe two distinct acceleration periods occurring in time frames comparable to those of the two heat flow peaks. Therefore, both heat release and UPV curves can be divided into four stages, corresponding to: pre-induction (I), induction (II), acceleration (III), and deceleration (IV).

Fig. 1(b) reports the heat flow's first peak of each samples. This peak is commonly associated to physical phenomena, especially to the heat of wetting, rather than chemical ones.

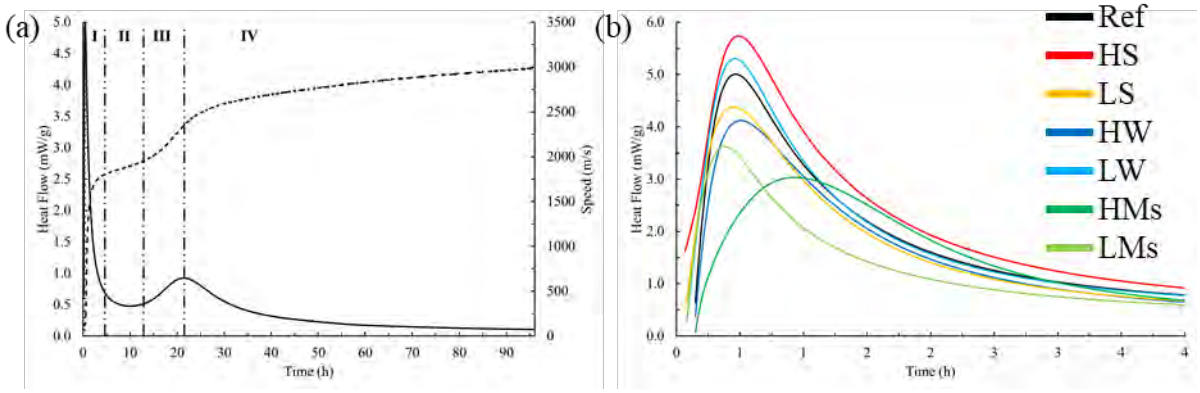

Nevertheless, it is in this stage that the dissolution of the starting materials begins and the hydrolysis of T-O (T = Si, Al) and M-O (M = Ca, Mg) bonds leads to the release of ions

Figure 1: (a) Isothermal calorimetry heat flow curve and UPV speed of Ref. measured up to 96h and divided into five different stages. (b) Heat flow curves of the investigated compositions, up to 4 hours.

and monomeric units in solution [9]. The effectiveness of this process is mainly related to the availability of hydroxyl moieties, introduced with the activating solution. The only significant shift in the peak position can be observed focusing on the effect of the alkali modulus. At higher Ms, the peak shows a considerable shift, moving from ~30 minutes to ~1 hour. In contrast, lowering Ms moves the peak at around 24 min. These shifts might be inferred to the different viscosity of the solutions. Although the S/b and w/b ratios do not induce any valuable shifts in the peak position, they influence the intensity. Among these series, HS and LW exhibit the highest heat release. In LW this can be inferred to the higher concentration, obtained by lowering the w/b ratio while keeping Na_2O and SiO_2 constant. That leads to a slightly faster dissolution rate when compared to Ref. Despite the constant concentration of alkalis also higher S/b ratio are reported to promote the hydrolysis of the binder [8].

Table 3: Vicat initial and final settings compared with corresponding UPV and cumulative heat release

Sample ID	Initial Setting			Final Setting		
	Time (min)	Speed (m/s)	Heat (J/g)	Time (min)	Speed (m/s)	Heat (J/g)
Ref	50	911	10.30	70	1354	14.22
HS	60	600	14.64	95	1460	16.80
LS	40	916.5	7.29	60	1509	11.42
HW	75	1320	13.00	135	1537	19.36
LW	40	617	8.49	60	1475	13.26
HMs	40	518	3.51	65	1487	7.99
LMs	60	820	6.00	100	1366	9.51

Table 3 reports the experimental results from Vicat testing. Both initial and final setting times are delayed by increasing the S/b and w/b ratios while the opposite is obtained by increasing the Ms. Despite this substantial difference, Ms and S/b exhibit the lowest influence on setting. The results obtained for HS and LS are very similar to those obtained for LMs and HMs. On the other hand, the w/b ratio is the parameter that exhibits the highest influence on the setting.

While the estimation of setting times by Vicat-needle test is quite straightforward, in the case of UPV two different strategies are often adopted. One of those considers the time necessary to reach a certain speed while the other relies on the inflection points of the UPV curve, inferred to specific microstructural changes. Fig. 2 reports the comparison between heat flow (solid line), acceleration of the P-waves (dotted line), and Vicat setting times (vertical dotted lines). A strong acceleration of the P-waves velocity is observed in correspondence of the first heat flow peak. This trend is generally associated to the initial formation of a percolating network and thus to the evolution of the system from a suspension towards a porous solid [10]. The occurrence of the initial setting corresponds well to this initial structural build-up of the material except for HW and LMs. The behaviour observed in the w/b series, earlier acceleration at higher ratio, was already reported in a recent study [6] and it was attributed to an increased rate of polycondensation driven by the weakening of binding between ionic species in diluted conditions [11]. Nevertheless, this hastened gel formation does not lead to faster setting due to the very diluted condition of the system that presumably remains in a suspension state longer than the other compositions. Similarly, the delayed setting of LMs, compared to the timing of the P-wave acceleration, might be explained considering the lower viscosity of the pore solution, poor in SiO_2. On the other hand, in a high viscous system such as HMs the initial setting is reached before the acceleration peak. Although the final setting is mostly reached far from the acceleration peak, it occurs while the speed is still increasing, even if at a lower rate, due to the continuous condensation reactions occurring both at the solid-liquid interface and between adjacent aluminosilicate units [12]. Table 3. also compares the initial and final setting time evaluated from Vicat-needle test with the speed and the cumulative heat recorded at the corresponding time. Although similar speeds are observed at the occurrence of the final setting, all between 1350 and 1550 m/s, those observed during the initial setting significantly differs from each other.

4. CONCLUSION

This study aims to investigate and compare the effect of S/b, w/b, and Ms on the early age reactivity and setting of AAMs. Based on the results the following conclusions can be drawn:

- All the investigated parameters seem to influence the particles' wetting and initial dissolution but only in the case of Ms it is possible to observe substantial shifts in the position of the peak associated to these events.
- Among the investigated compositions, the highest variations in terms of setting time, evaluated from Vicat-needle test, are those belonging to the w/b series.
- The estimation of setting by defining certain speed thresholds does not seem feasible in AAMs. Although similar speed values are obtained in correspondence of the Vicat

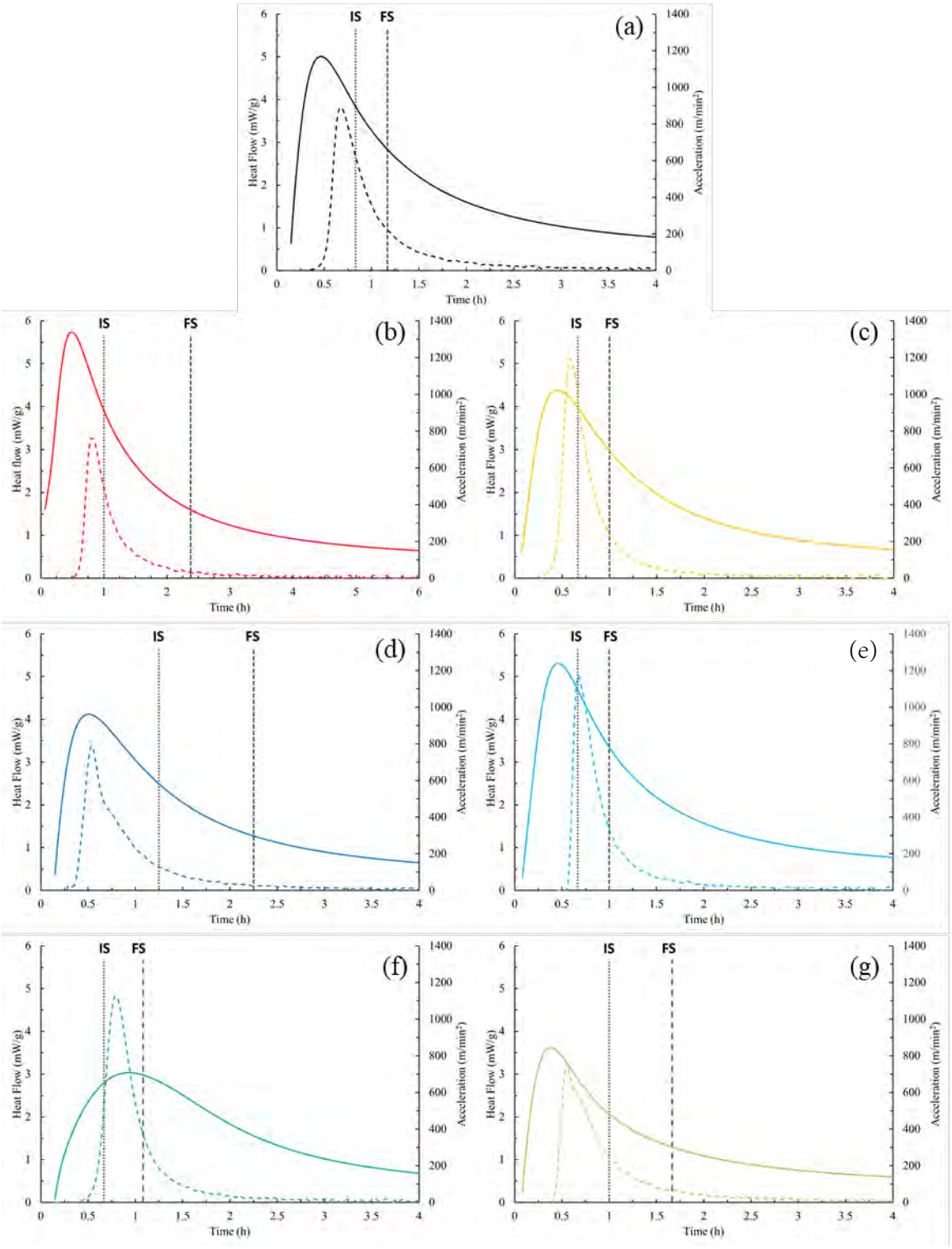

Figure 2: Initial setting time (IS), final setting times (FS) heat flow curves (solid line) and UPV acceleration (dotted line) during the first 4 hours. (a) Ref, (b) HS, (c) LS, (d) HW, (e) LW, (f) HMs, and (g) LMs

- final setting time, those associated to the initial setting exhibit substantial differences. Moreover, the comparison of the results reported in this study with those available in literature highlights how the speed reached in correspondence of setting strongly depends on the mix compositions and it is not possible to identify common thresholds [12].
- The initial setting times estimated through the inflection points of UPV curves does not always fit those from Vicat-needle tests. While in most cases the initial setting corresponds to the initial formation of the percolating network those two events do not seem to be correlated in diluted and less viscous systems (i.e HW and LMs).

ACKNOWLEDGEMENTS

This work is supported by the EOS-programme (The Excellence of Science) through research project 30439691.

REFERENCES

[1] I. Ismail, S.A. Bernal, J.L. Provis, R. San Nicolas, S. Hamdan, J.S.J. Van Deventer, Modification of phase evolution in alkali-activated blast furnace slag by the incorporation of fly ash, Cem. Concr. Compos. 45 (2014) 125–135. https://doi.org/10.1016/j.cemconcomp.2013.09.006.

[2] M. Chi, R. Huang, Binding mechanism and properties of alkali-activated fly ash/slag mortars, Constr. Build. Mater. 40 (2013) 291–298. https://doi.org/10.1016/j.conbuildmat.2012.11.003.

[3] N.K. Lee, J.G. Jang, H.K. Lee, Shrinkage characteristics of alkali-activated fly ash/slag paste and mortar at early ages, Cem. Concr. Compos. 53 (2014) 239–248. https://doi.org/10.1016/j.cemconcomp.2014.07.007.

[4] M. Hojati, A. Radlińska, Shrinkage and strength development of alkali-activated fly ash-slag binary cements, Constr. Build. Mater. 150 (2017) 808–816. https://doi.org/10.1016/j.conbuildmat.2017.06.040.

[5] X. Ouyang, Y. Ma, Z. Liu, J. Liang, G. Ye, E ff ect of the Sodium Silicate Modulus and Slag Content on Fresh and Hardened Properties, Minerals. 10 (2020).

[6] X. Dai, S. Aydin, M.Y. Yardimci, K. Lesage, G. de Schutter, Influence of water to binder ratio on the rheology and structural Build-up of Alkali-Activated Slag/Fly ash mixtures, Constr. Build. Mater. 264 (2020) 120253. https://doi.org/10.1016/j.conbuildmat.2020.120253.

[7] M. Chi, Effects of the alkaline solution/binder ratio and curing condition on the mechanical properties of alkali-activated fly ash mortars, Sci. Eng. Compos. Mater. 24 (2017) 773–782. https://doi.org/10.1515/secm-2015-0305.

[8] C. Ruiz-Santaquiteria, J. Skibsted, A. Fernández-Jiménez, A. Palomo, Alkaline solution/binder ratio as a determining factor in the alkaline activation of aluminosilicates, Cem. Concr. Res. 42 (2012) 1242–1251. https://doi.org/10.1016/j.cemconres.2012.05.019.

[9] X. Gao, Q.L. Yu, H.J.H. Brouwers, Reaction kinetics, gel character and strength of ambient temperature cured alkali activated slag-fly ash blends, Constr. Build. Mater. 80 (2015) 105–115. https://doi.org/10.1016/j.conbuildmat.2015.01.065.

[10] R. Cao, S. Zhang, N. Banthia, Y. Zhang, Z. Zhang, Interpreting the early-age reaction process of alkali-activated slag by using combined embedded ultrasonic measurement, thermal analysis, XRD, FTIR and SEM, Compos. Part B Eng. 186 (2020) 107840. https://doi.org/10.1016/j.compositesb.2020.107840.

[11] J.L. Provis, J.S.J. van Deventer, Geopolymerisation kinetics. 2. Reaction kinetic modelling, Chem. Eng. Sci. 62 (2007) 2318–2329. https://doi.org/10.1016/j.ces.2007.01.028.

[12] S. Uppalapati, L. Vandewalle, Ö. Cizer, Monitoring the setting process of alkali-activated slag-fly ash cements with ultrasonic P-wave velocity, Constr. Build. Mater. (2020) 121592. https://doi.org/10.1016/j.conbuildmat.2020.121592.

INFLUENCE OF THE MS-MODULUS ON THE EARLY AGE VOLUME CHANGE AND HEAT RELEASE OF SLAG AND FLY ASH PASTES ACTIVATED BY SODIUM HYDROXIDE AND SODIUM SILICATE

B. Delsaute (1), J. Gambacorta (1) and S. Staquet (1)

(1) BATir, Université Libre de Bruxelles, Belgium

Abstract

Blended pastes composed of slag and fly ash (ratio 50:50) are used with sodium hydroxide and sodium silicate as precursors. Each composition has the same solution to binder ratio (S/B) and the Ms-modulus varies between 1.04 and 1.58. All the experiments were conducted at a constant temperature of 20°C. The physical mechanisms related to the volume change in sealed condition are studied by means of repeated thermal variation using an adapted Autoshrink device, a new testing protocol and by means of isothermal calorimetry tests. From these tests, the autogenous strain, the coefficient of thermal expansion (CTE) and the heat release are determined. It is observed from the results, that an increase of the Ms-modulus causes a decrease of the autogenous shrinkage and the CTE. A linear relationship is observed between the autogenous shrinkage and the heat release by the binder. Thus, the development of the autogenous shrinkage seems to be mainly driven by one major mechanism in case of slag and fly ash paste activated by sodium hydroxide and sodium silicate.

Keywords: Alkali-activated materials, Ms-modulus, heat release, autogenous shrinkage, CTE

1. INTRODUCTION

Alkali-activated materials (AAM) are considered as a new alternative to Ordinary Portland cement, and are obtained by the reaction of calcium-silicates or alumino silicate-rich solid precursor with an alkaline solution. As a result of the chemical and microstructural properties of AAMs, they offer several potential advantages as compared to OPC. They are characterized by high strength development at early-age and an enhanced resistance to acid and sulphate attacks [1]. Despite these advantages, AAMs possess a crucial shortcoming, which is rapid hardening, resulting in very short setting times and large shrinkage deformations which can be up to seven times larger than that in OPC [2]. This induces a high risk of early-age cracking, which, in turn, endangers mechanical properties and durability performance [3,4].

The research of this paper is done in the context of the Interact project (INTERdisciplinary multiscale Assessment of a new generation of Concrete with alkali activated maTerials). The link of the website is https://interact.ulb.be/. Four universities (ULB, KULeuven, UGent, TU Wien) and one institution (VITO) are currently working on the subject of AAMs within the

framework of this project. Each university/institution works on a precise field and the ULB mainly tackles the problem of the volume stability and mechanical behavior. The objective of this paper is to experimentally investigate the influence of the silica modulus (Ms) on the autogenous shrinkage, the coefficient of thermal expansion (CTE) and the heat release of AAMs pastes. This paper is divided in two parts. First, there is a description of the materials used, as well as the experimental methods. Secondly, the results will be presented. In the first place, there is an analysis of the heat release. After that, results of the autogenous shrinkage and the CTE will be analyzed.

2. MATERIALS AND METHODS

2.1 Materials and mixture proportions

This study considers pastes obtained by alkali-activation of fly ash and GGBFS. Two activators are considered: a sodium silicate solution (Na2O+ SiO2) and a sodium hydroxide solution 8M (NaOH). The sodium silicate solution is made with 18% in mass Na2O, 28.5% SiO2 and 53.5% H2O. The density is 1.37 g/mL. The silica modulus is the mass ratio between SiO2 and Na2O and will vary between 1.04 and 1.58.

4 different AAFS pastes were tested and were prepared according to the European Standard EN 196-1:2016 [5]. There is the same amount of fly ash and slags (50:50) and the 2 activators are used with deionized water. Compositions T1 to T4 have the same S/B (0.55) but Ms is changed between 1.04 and 1.58. Those compositions are presented in Table 1. All the tests are performed at an average temperature of 20°C.

Table 1: Mix proportion of the AAFS pastes

Mix	S/B	W/B	Ms	GGBFS (g)	FA (g)	Sodium silicate (g)	NaOH 8M (g)	H2O (g)
T1	0.55	0.45	1.04	50	50	22.9	11.1	21.5
T2		0.44	1.24			24.9	6.4	23.9
T3		0.42	1.44			26.5	2.5	25.9
T4		0.42	1.58			27.5	0.1	27.2

2.2 Experimental methods

Monitoring of the autogenous strain and the coefficient of thermal expansion

The original version of the auto-shrink device allows measuring the autogenous deformation as a function of time in an environment where the temperature remains constant. But this device was improved at the Université Libre de Bruxelles (ULB) in order to be able to apply controlled temperature variations to the samples [35]. These temperature changes allow determining the CTE by imposing a variation of -3°C to +3°C to the system. This change is produced by the thermal regulation system composed of a thermostatic bath and a convolution system as shown in Figure 1. The device is isolated from the environment by an insulated box in order to improve the thermal regulation. Hence, care is taken to the control of the temperature. In addition to all of this, the auto-shrink device contains 3 samples in the same test to ensure the repeatability of the results obtained [50, 51]. The picture from Figure 1 shows the auto-shrink device from the ULB. On this photo are present the different elements: the thermal regulator, 3 corrugated tubes, the insulator and the digital gauge.

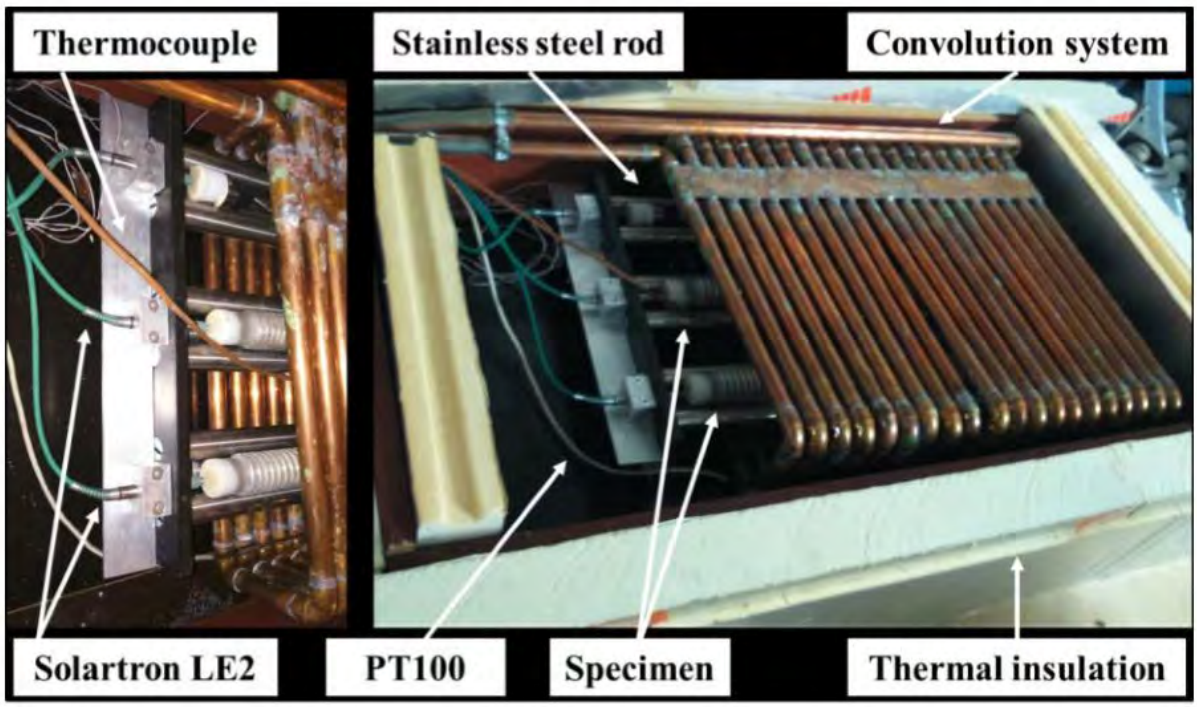

Figure 1: Adaptation of the Autoshrink device for the simultaneous determination of the CTE and the autogenous strain.

A complete and detailed presentation of the experimental setup, the test protocol and the data treatment can be found in [6,7].

Isothermal calorimetry

The heat release is determined with the TAM Air micro-calorimeter device [8]. This device is composed of 8 channels. Each channel is composed of two ampoules. One is filled with the paste (approximately 8g of paste), the other one is the reference filled with sand. For each test, it is necessary to use 2 channels in order to measure the heat release of 2 pastes for the repeatability of the results. The data acquisition consists of the heat release in function of the time. The test usually lasts 2 weeks because after that, the rate of heat flow is very low and the device is not accurate enough to monitor precisely the heat flow [7,8].

3. RESULTS AND DISCUSSION

3.1 Heat release

Figures 2 to 3 present the results of the different isothermal calorimetry tests. Results presented here correspond to the average of two tests. The heat flow is plotted in function of the equivalent age and 2 peaks are observed. The first one corresponds to the early dissolution of the FA and BFS. The second one corresponds to the acceleration of the formation of the reaction products, the C-N-A-S-H gels. The decrease between the two peaks is called "induction period" and is due to the fluid-solid transition time [9]. Globally, the Ms-modulus does not have a major influence on the heat release on long duration. At an equivalent age of 100h, the heat

release is higher when the Ms-modulus is lower, but this tendency is not exactly the same later. The second peak of the heat flow is higher when the Ms-modulus is lower, and the induction period decreases.

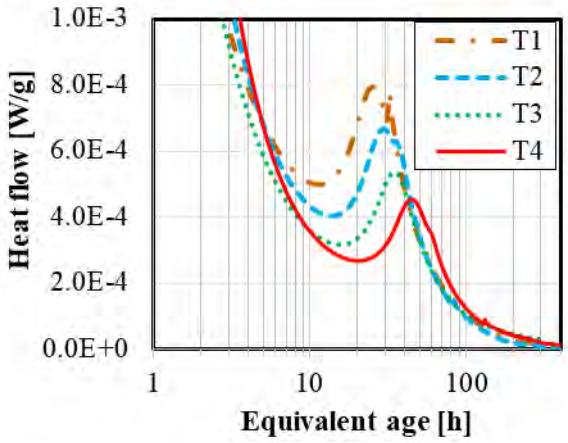

Figure 2: Heat flow

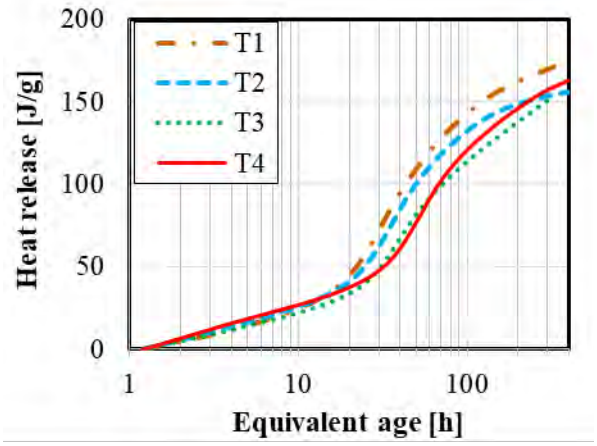

Figure 3: Heat release

3.2 Autogenous strain

Figure 4 shows the development of the autogenous shrinkage of AAFS pastes over a period of two weeks. Each results presented correspond to the average of two tests. Globally, the autogenous strain increases when the Ms-modulus decreases. A smaller Ms also means more NaOH in the composition. As for the results obtained with the heat release, this higher amount lead to a higher pH in the solution and may be at the source of the higher autogenous shrinkage. Similar trend was found by D. Kumarappa [10].

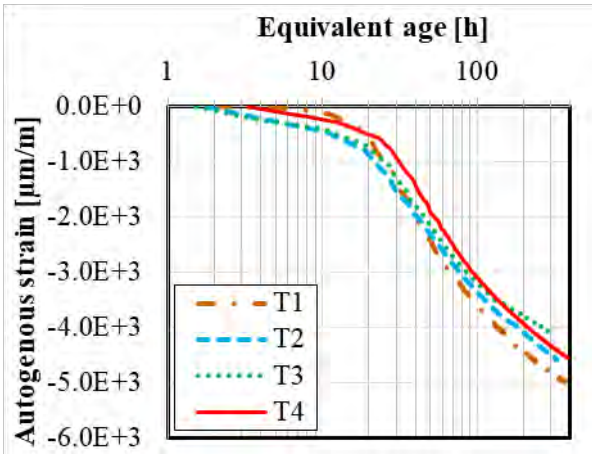

Figure 4: Autogenous shrinkage in function of the equivalent age

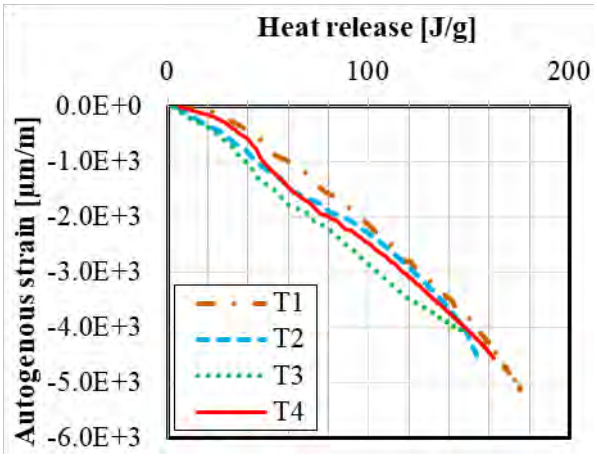

Figure 5: Autogenous shrinkage in function of the heat release

The development of the autogenous shrinkage is associated to the hydration process (formation of capillary pores) and thus the heat release [11]. Several mathematical expressions were developed in the literature to link both parameters. Power law and sinusoidal law were generally used [12]. In Figures 5, the development of the autogenous shrinkage is plotted

according to the heat release. It is observed that the autogenous shrinkage evolved linearly according to the heat release. This suggests that there is one major reaction occurring and that induces autogenous deformations when slag and fly ash react with both NaOH and sodium silicate. The slope of this linear trend increases when the silica modulus decreases. The end is less linear. This is probably due to the precision of the isothermal calorimeter. The rate of heat flow is really low at the end of the test and the device will not monitor accurately this heat flow. When Ms is plotted in function of the slope (Figure 6), there is a parabola that is formed. This means that there is an optimum value of Ms to minimize the shrinkage.

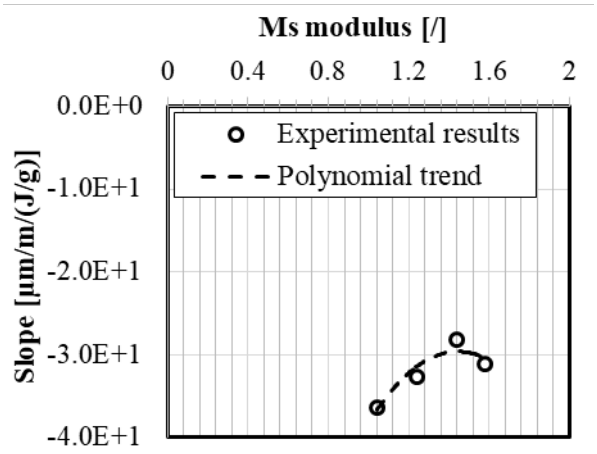

Figure 6: Ms in function of the slope of the linear relation observed in Figure 5 between the autogenous strain and the heat release

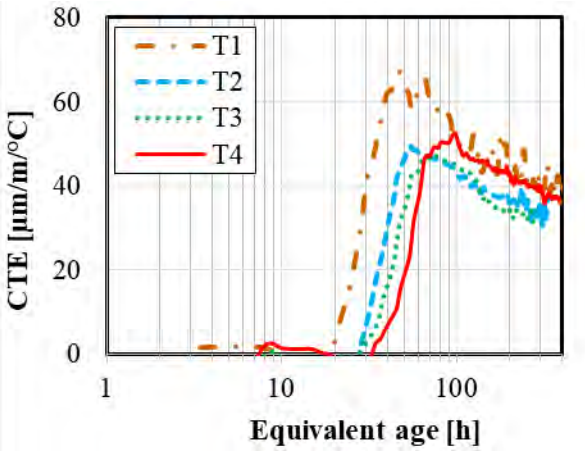

Figure 7: Coefficient of thermal expansion

3.3 Coefficient of thermal expansion

Figure 4 shows the development of the coefficient of thermal expansion of AAFS pastes over a period of two weeks. Each results presented correspond to the average of two tests. The development of the CTE and the magnitude of the CTE are both related to the Ms-modulus. For each composition, the evolution of the CTE can be divided in 3 stages. Firstly, the value of the CTE is very low during the first hours after setting (around 3µm/m/°C). Secondly, an increase of the CTE is observed till a maximum value between 50 and 65 µm/m/°C. This increase starts sooner for pastes with a lower Ms-modulus. This maximum value of the CTE is reached first for pastes with lower Ms-modulus at an equivalent age between 50 and 90 hours and is higher in case of low Ms-modulus. Thirdly, the CTE decreases till a value between 30 and 40 µm/m/°C at an age of 2 weeks. No specific trend is obtained between the Ms-modulus and the CTE reached at an equivalent age of 2 weeks. This can be explained by the fact that, when the Ms-modulus decreases, there is a small increase of the W/B ratio. Water has a CTE value higher than the one of solids. This means that when there is less water, the CTE is decreased. This can explain the fact that CTE of AAM pastes decreases as the W/B ratio decreases [13]. However, the E-modulus of the solid skeleton has also an influence on the CTE. In case of lower E-modulus, the pressure applied by the water for a temperature change causes higher volume change. Both properties should be considered simultaneously to interpret the results of the CTE obtained at later ages.

4. CONCLUSIONS

Based on the different experiments conducted in this paper, some conclusions can be drawn on the influence of the Ms-modulus on the early age volume change and heat release of slag and fly ash pastes activated by sodium hydroxide and sodium silicate.

The heat release increases when the Ms decreases. The study of the autogenous shrinkage highlighted the influence of the Ms-modulus. A higher Ms will decrease the autogenous shrinkage. It also confirmed the higher value for AAMs paste compared to OPC paste. And while plotting it in function of the cumulative heat release, a linear trend was discovered. This suggests that only one mechanism linked to the hydration is the main driver of the development of the autogenous shrinkage. The exact reason could not be identified and will have to be the object of further work where the chemical shrinkage will have to be characterized, as well as the evolution of the porosity (total quantity as well as pore distribution). Also the development of hydrates is also a data to be known. However, this information is not easy to determine, as a chemical shrinkage test cannot be carried out as for cement pastes, the pore size is so small compared to OPCs that it may not be possible to correctly determine the porosity distribution as well as the total pore quantity. A review and validation of a suitable method is therefore surely necessary.

The coefficient of thermal expansion was also studied and was found to be higher compared to an OPC paste. A smaller Ms increases the CTE at early age while at later ages no clear trend is observed between the magnitude of the CTE and the Ms-modulus.

ACKNOWLEDGEMENTS

This paper is the result of research actions performed in the framework of the FNRS-FWO-EOS project 30439691 ‘INTERdisciplinary multiscale Assessment of a new generation of Concrete with alkali- activated maTerials’ (INTERACT). The financial support by FNRS-FWO-EOS is gratefully acknowledged.

REFERENCES

[1] J.L. Provis, Geopolymers and other alkali activated materials: why, how, and what?, Mater. Struct. 47 (2014) 11–25. doi:10.1617/s11527-013-0211-5.

[2] T. Bakharev, J.. Sanjayan, Y.-B. Cheng, Effect of admixtures on properties of alkali-activated slag concrete, Cem. Concr. Res. 30 (2000) 1367–1374. doi:10.1016/S0008-8846(00)00349-5.

[3] A.Z. Bendimerad, B. Delsaute, E. Rozière, S. Staquet, A. Loukili, Advanced techniques for the study of shrinkage-induced cracking of concrete with recycled aggregates at early age, Constr. Build. Mater. 233 (2020) 117340. doi:10.1016/j.conbuildmat.2019.117340.

[4] B. Delsaute, S. Staquet, Testing Concrete Since Setting Time Under Free and Restrained Conditions, in: Adv. Tech. Test. Cem. Mater., 2020: pp. 177–209. doi:10.1007/978-3-030-39738-8_6.

[5] EN 196-1, En 196-1, 2016.

[6] B. Delsaute, S. Staquet, Monitoring of the Thermal and Autogenous Strain, in: 2020: pp. 135–176. doi:10.1007/978-3-030-39738-8_5.

[7] B. Delsaute, New approach for Monitoring and Modelling of the Creep and Shrinkage behaviour of Cement Pastes , Mortars and Concretes since Setting Time, Université Libre de Bruxelles (BATir) and Université Paris Est (IFSTTAR), 2016.

[8] T. Instruments, Tam air isothermal calorimetry, (2017) 23. http://www.tainstruments.com/pdf/brochure/TAM AIR brochure.pdf (accessed February 14,

2017).
[9] G. Fang, H. Bahrami, M. Zhang, Mechanisms of autogenous shrinkage of alkali-activated fly ash-slag pastes cured at ambient temperature within 24 h, Constr. Build. Mater. 171 (2018) 377–387. doi:10.1016/j.conbuildmat.2018.03.155.
[10] D. Ballekere Kumarappa, S. Peethamparan, M. Ngami, Autogenous shrinkage of alkali activated slag mortars: Basic mechanisms and mitigation methods, Cem. Concr. Res. 109 (2018) 1–9. doi:10.1016/j.cemconres.2018.04.004.
[11] O.M. Jensen, P.F. Hansen, Autogenous deformation and RH-change in perspective, Cem. Concr. Res. 31 (2001) 1859–1865. doi:10.1016/S0008-8846(01)00501-4.
[12] B. Delsaute, S. Staquet, Decoupling Thermal and Autogenous Strain of Concretes with Different Water/Cement Ratios During the Hardening Process, Adv. Civ. Eng. Mater. 6 (2017) 22. doi:10.1520/ACEM20160063.
[13] E.J. Sellevold, · Ø Bjøntegaard, Coefficient of thermal expansion of cement paste and concrete: Mechanisms of moisture interaction, Mater. Struct. 39 (2006) 809–815. doi:10.1617/s11527-006-9086-z.

MICROSTRUCTURE AND PROPERTIES OF HYBRID COAL GANGUE-BASED ALKALI-ACTIVATED CEMENT

Bruna J. FRASSON (1), Malik CHERIAF (2) and Janaíde C. ROCHA (2)

(1) Civil Engineering, CTC, Federal University of Santa Catarina, Brazil

(2) Department of Civil Engineering, CTC, Federal University of Santa Catarina, Brazil

Abstract

Addition of Portland cement in low-calcium aluminosilicate-based alkali-activated materials can provide rapid hardening at room temperature, thus modifying microstructure and mechanical properties. In the present study, the effect of Portland cement addition on alkali-activated materials, cured at room temperature, was analysed by mechanical strength test, FT-IR and electrochemical impedance spectroscopy. The results showed samples hardening at room temperature after 24 hours and compressive strength of 26 MPa (7 days) for 5% of OPC addition. Hybrid alkali-activated cements presented higher sorptivity and lower electrical resistance than alkali-activated cement without OPC addition which can be related to more connected pores. The analysis of EIS spectrum highlights continued formation of microstructure over the ages of alkali-activated cement and can be related to mechanical properties and sorptivity.

Keywords: hybrid, alkali-activated, coal gangue, compressive strength, sorptivity.

1. INTRODUCTION

Synthesis of Alkali-activated binders (AAM) occurs by chemical reaction between aluminosilicate sources and alkaline reagents. The process consists basically of dissolution, agglomeration and polymerization [1], thus amorphous aluminosilicate gel (Me-A-S-H) is the main reaction product [2]. Low-calcium aluminosilicate-AAM generally presents slow hardening and long setting time at room temperature, hence thermal cure is required to accelerate the reaction process [3].

Portland cement addition (OPC) in AAM is an alternative to accelerate chemical reaction and provide hardening at room temperature, therefore, forming hybrid cements. OPC addition increases internal temperature during reaction [4] and provides formation of complex microstructure, where N-A-S-H and C-A-S-H precipitate [5]. Industrial by-products and calcined clay, such as fly ash, slag and metakaolin are the main aluminosilicates studied [1]. Mining wastes red mud [2] and coal gangue [6, 7] have been used as aluminosilicate to produce AAM.

In Brazil, coal mining industry in southern region, extracts around 6 million tons per year [8]. However, about 60% are impurities generated by the washing process. Fine wastes go through neutralization and decantation processes, forming sludge from decantation basin (CS). Coal mining wastes contain Al_2O_3, SiO_2 and low Fe_2O_3 [9, 10, 11], in mineralogical phases such as quartz and kaolinite. Dehydroxylation of kaolinite occurs at calcination temperature between 500ºC and 700ºC making it more reactive [9] and calcination also provides the burn organic. However, during calcination, CO_2 and SO_2 are released, and pyrite transformation is the main cause of SO_2 release [12].

Microstructure development can be observed by electrical parameters, obtained by means of electrochemical impedance spectroscopy (EIS). There is little research for the use of EIS, in alkali-activated materials, the main analyzes are related to reaction kinetics [13, 14], transport properties [15, 16] and microstructure development [17].

This study aimed to analyze the effect of Portland cement addition in microstructure and mechanical properties of hybrid alkaline cements by means of compressive strength, FT-IR and electrochemical impedance technique.

2. MATERIALS AND METHODS

2.1 Materials

The coal sludge (CS) was used as aluminosilicate, oven dried at 100°C for 24 hours and ball milled for 30 minutes. Coal sludge was calcined at 700°C for 1 hour and then designated as CST. Early high strength Portland cement replaced wastes in 5 wt% and 10 wt%. Chemical and mineralogical composition of materials were performed in a previous work [18]. However, calcination of CS provided reduction of volatile material, sulfur and kaolinite dehydroxylation.

Sodium hydroxide (97% Na_2O) and sodium silicate (12.7% Na_2O, 30.4% SiO_2 and 56.9% H_2O) were used to prepare alkaline solution (AS). NaOH (solid) was dissolved in sodium silicate to obtain the SA with a silica modulus (SiO_2 / Na_2O) of 1.5.

2.2 Methods

Alkali-activated cements were prepared by pre-mixing OPC and wastes, then added to AS at a 1:1 mass ratio, the water to binder ratio was 0.75. Cylindrical samples of 2 x 4 cm (diameter x height) were filled, hermetically sealed and cured at room temperature (25°C), after 24 hours were demolded and sealed with PVC film. Table 1 shows binders' compositions, the CST-0 was heat-cured in oven at 50°C for hours.

Compressive strength test was performed at 7 and 28 days in Instron press with 50 kN static load cell and at 7000 N/min loading speed. Fragments of cements were submerged in acetone for 24 hours, filtered, oven dried at 50°C for 24 hours and grounded to particles less than 150 μm. FT-IR spectra were obtained in Agilent Carry 600, averaging 32 scans, in transmission mode, ranging from 4000cm $^{-1}$ to 400cm $^{-1}$, and 4cm $^{-1}$ resolution, the powders were prepared with KBr.

Alkali-activated hybrid mortars were prepared for EIS and capillary water absorption tests. Mortars were prepared by mixing the binders with sand to binder ratio of 3 (mass). Cylindrical samples of 5 x 10 cm (diameter x height) were filled, sealed and cured at room temperature, except the CST-0, which was thermally cured. Electrochemical Impedance Spectroscopy (EIS) was performed in 100 MHz bandwidth digital oscilloscope (Tektroniz

TDS 3014C), function generator (AFG 3102) and current gauges (P6022). The data was measured at 7, 14 and 21 days then analyzed in the EISA software [19] using Complex Nonlinear Least Squares – CNLS algorithm. ErroX was determined by simplex method [20]. Capillary water absorption test was performed at 28 days, the samples were dried in oven at 50° C for 72 hours before the water absorption test, that was performed over 24 hours, as described by Santos et al [21].

Table 1: Mix proportions and molar ratio

Designation	Waste (g)	OPC (g)	SiO_2/Al_2O_3 (mol/mol)	Na_2O/Al_2O_3 (mol/mol)	% CaO
CST-0	100	0	3.35	0.99	1.05
CST-5	95	5	3.40	1.04	6.15
CST-10	90	10	3.46	1.10	11.25
CS-5	95	5	4.94	3.09	7.86
CS-10	90	10	5.11	3.27	12.87

3. RESULTS AND DISCUSSIONS

3.1 Cements compressive strength and microstructure formation

Fig. 1 shows visual aspect of cements at 28 days, efflorescence appears in CS-systems which is related to presence of free alkaline cation (Na^+) and lower reactivity of coal sludge. Alkaline cation percolate through connected pores and reacts with CO_2, yielding sodium carbonates on material surface. Mechanical strength of alkali-activated cement is shown in Fig. 2, in general there is an increase in compressive strength over the ages, except for CST-10.

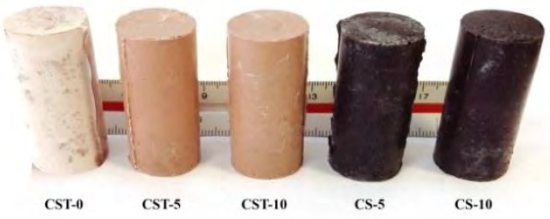

Figure 1: Alkali-activated cements at 28 days

Hardening and compressive strength of alkali-activated cements cured in room temperature are influenced by OPC addition. CST-5 and CST-10 present hardening at 24 hours and increase of 45% and 108% respectively in compressive strength over CST-0. Reaction kinetics and microstructure formation can be accelerated by addition of calcium sources, which implies strength development [7] and an increase of stiffness. Compressive strength of CS-systems is 40% lower than CST-systems and it was not influenced by different OPC addition. CS mineralogical and chemical composition may affect microstructure development and the mechanical properties.

FT-IR spectra of aluminosilicates materials and AAM at 28 days are presented in Fig. 3. Vibration bands at 3620 cm^{-1} to 3696 cm^{-1} related to presence of hydroxyl groups and at 1033 cm^{-1} and 1016 cm^{-1} of Si-O bonds, and 912 cm^{-1} 1538 cm^{-1} of Al-OH and Si-O-Al respectively, point kaolinite content in CS. Kaolinite dehydroxylation and break of Al-OH and Si-O-Al were observed from CST-spectra, which was evidenced by the disappearance of hydroxyl bands and the absence of 912 cm^{-1} and 538 cm^{-1} [22].

Alkaline activation alters the main vibration band (1000-1100 cm^{-1}) to lower frequencies, related to asymmetric T-O vibration (T: Si or Al), amorphous aluminosilicate gel is evidenced by changes in this vibration band range [23]. In CST systems the peak shifts from 1052 cm^{-1} to 1027 cm^{-1}, 1024 cm^{-1} and 1016 cm^{-1} for CST, CST-0, CST-5 and CST-10 respectively (Fig. 3b). OPC addition provides slight displacement of the main band of CST-5 (-3 cm^{-1}) and CST-10 (-11 cm^{-1}) compared to CST-0. Between CS-5 and CS-10 no changes were observed which is in agreement to the mechanical strength.

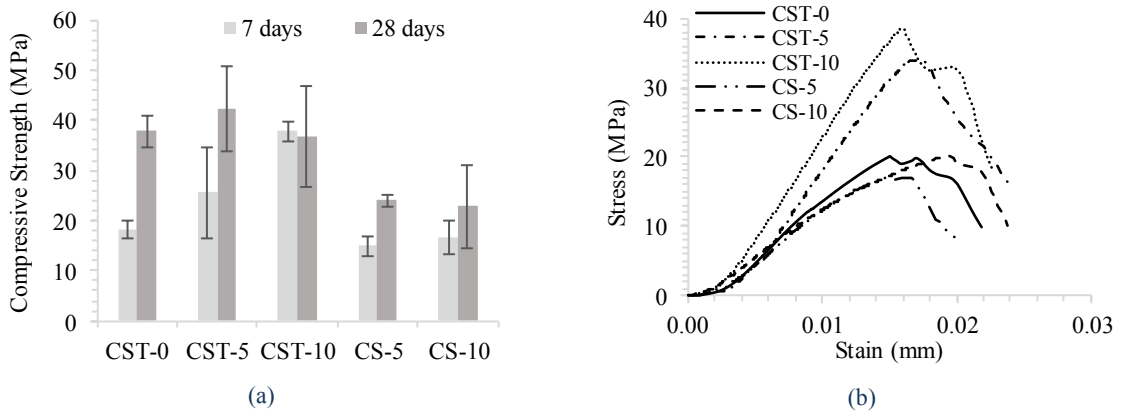

Figure 2: Alkali-activated cements (a) compressive strength; (b) stress x strains plot at seven days.

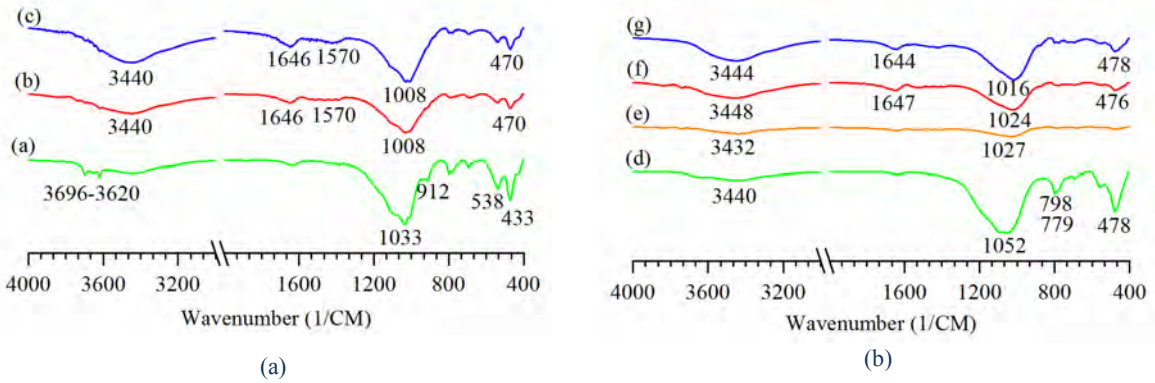

Figure 3: FT-IR spectrogram of aluminosilicate and alkali-activated cements (a) CS-powder; (b) CS-5; (c) CS-10; (d) CST-powder; (e) CST-0; (f) CST-5; (g) CST-10.

3.2 Mortar impedance spectroscopy and sorptivity

Electrochemical impedance spectroscopy presents a complex graph, which the abscissa axis is related to the real component and the ordinate to imaginary. Electrical parameters and equivalent electrical circuits were obtained by means of EISA software. Voight type reactive circuit and blocking circuit were simulated according to the scheme of Fig.4. The complex equations are present below. Wherein Z: Electrochemical Impedance (Ω), R_1: electrolyte/ohmic Resistance (Ω), R_2: charge transfer Resistance (Ω), ω is frequency (Hz) and C_p: double layer Capacitance (Farad).

$$Z = R_1 - [1/(i\omega C_p)] - \text{Blocking circuit} \quad (1)$$

$$Z = R_1 + 1/[(i\omega C_p) + 1/R_2] - \text{Voight circuit} \quad (2)$$

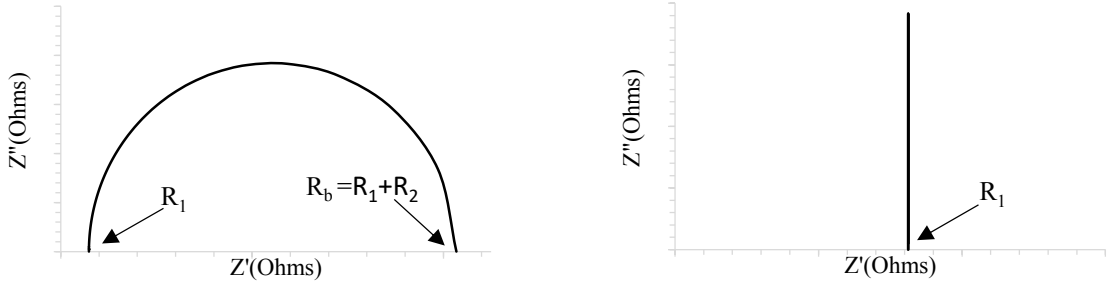

Figure 4: Simulated (a) Reactive circuit – Voight; (b) blocking circuit;

Nyquist arc increases over the time for all CST mortars and indicates continuous microstructure formation, which is correlated to the mechanical strength increase. Electrical parameters are shown in Table 2 and complex plots for all sample in the Fig. 5. CST-0 electrical resistance parameter (R_1 and R_2) is higher than other mortars at all ages analyzed. CST-0 electrical parameters and Nyquist plot (Fig. 5a) indicates acceleration of reaction mechanisms due to thermal cure (50˚C for 24 hours), which will consume alkaline ions and evaporate free water.

CST-5 presents at seven days a blocking circuit (Eq. 1 and Fig. 5b), although at 14 and 21 days the Nyquist arc is formed, related to the Voight circuit (Eq. 2), and suggests a delay in the reaction process. CST-10 presents at seven days Nyquist arc formation (reactive circuit Eq. 2 and Fig. 5c), and increase in the electrical resistance over the time. Portland cement content influenced the impedance spectra and the R_2, which may relate to the quick reaction provided by the hydration of OPC particles.

However, at 21 days CST-5 and CST-10 show similar electrical parameters (R_1, R_2 and C_p). These analyzes may be correlated to results of mechanical resistance, where at seven days is higher for CST-10 than for CST-5, but similar at 28 days. Reaction rates at early ages (seven ages) influences mortars electrical parameters and the reaction kinetics are affected by OPC addition, leading to hardening and microstructure formation. Therefore, at older ages (more than 7 days) electrical parameters are controlled by aluminosilicate chemical reactions [24].

Table 2: Electrical parameters and sorptivity results

Mortar	Age	R_1 (Ω)	R_2 (Ω)	C_p (pF)	Error Simplex	Sorptivity (μm/s$^{1/2}$)
CST-0	7 days	215.6	2406.4	101.18	14.30	5.6 [18]
	14 days	225.9	2826.7	74.46	16.21	
	21 days	294.1	3841.9	60.07	18.92	
CST-5	7 days	326.3	-	-	0.76	9.48
	14 days	393.1	46.4	1410.30	1.72	
	21 days	364.1	750.9	111.06	5.62	
CST-10	7 days	286.4	559.3	99.52	6.64	8.57
	14 days	310.6	758.9	95.99	7.25	
	21 days	409.9	853.4	123.54	5.64	
CS-10	7 days	161.1	-	-	12.74	4.28
	14 days	140.7	-	-	0.35	
	21 days	138.0	-	-	0.17	

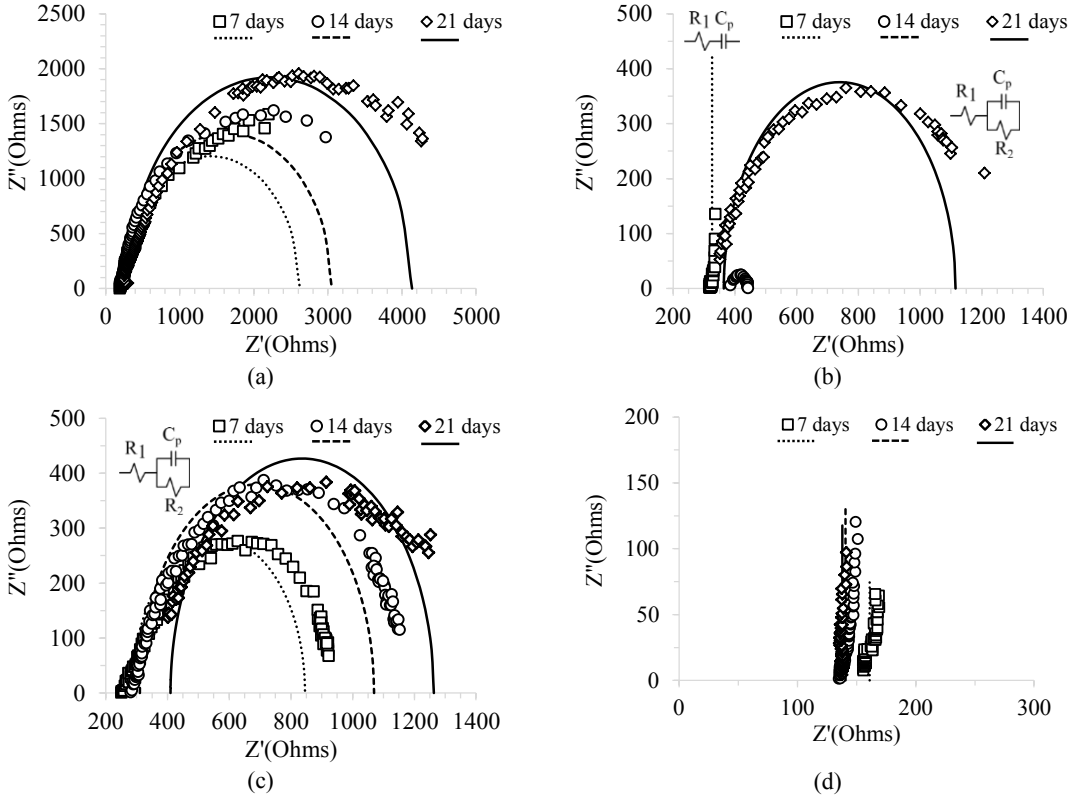

Figure 5: Nyquist plot to mortars (a) CST-0; (b) CST-5; (c) CST-10; (d) CS-10.

Mortar sorptivity are present in Table 2, the results suggest higher connected pore structure for CST-10 than to CST-0 and CST-5. The results of CST-0 are presented in previous studies [18] but are included here for comparative analysis with other mortars. CST-0 was thermal cure, which allows acceleration of microstructure formation thus indicates denser microstructure, with smaller pores and a more tortuous network [24]. However, higher permeability of CST-5 and CST-10 did not influence mechanical strength; the results were similar in all CST-systems at 28 days. Sorptivity can be related to the electrical parameters, the lower sorptivity the higher electrical resistance (R_b=R_1+R_2) and the lower capacitance.

Blocking circuit are evidenced in CS-10 mortars, at test ages, and indicates ideally polarizable electrode [25]. Poor microstructure formation and high free alkaline cation can be related to this behavior, which leads to higher electrical conductivity. CS-10 presents lower sorptivity than CST-10 and CST-5; physical, chemical and mineralogical characteristics of CS may affect porous structure.

4. CONCLUSIONS

The main conclusions obtained from the experimental analyses are listed below:

- Aluminosilicate replacement for Portland cement increased compressive strength and stiffness of hybrid alkali-activated pastes at seven days. Formation of N-A-S-H as the main reaction product is evidenced by FT-IR;
- EIS highlights the continued formation of microstructure in CST systems over time. Calcium contents affected the development of the microstructure at seven days (early ages), this effect is evidenced by the formation of complex arc and the parameter of electrical resistance (R_2);
- Sorptivity was higher for hybrid mortars than for CST-0, which may be related to the formation of different microstructures. The addition of Portland cement modified porous structure and influenced the permeability; however, mechanical strength was similar at 28 days for CST-systems;
- The mortar produced with CS presents different behavior than CST; it was evidenced low microstructure formation (EIS), despite lower sorptivity than the other mortars. Complementary tests are necessary for a better understanding of the CS system.

ACKNOWLEDGEMENTS

This study was financed in part by the Coordenação de Aperfeiçoamento de Pessoal de Nível Superior - Brasil (CAPES) – Finance Code 001.

REFERENCES

[1] Provis, J. L.; Palomo, A. and Shi, C. ‘Advances in understanding alkali-activated materials’. *Cement Concrete Res.* **78**(2015)110–125.

[2] Shi, C.; Fernández-Jiménez, A. and Palomo, A. ‘New cements for the 21st century: The pursuit of an alternative to Portland cement’. *Cement Concrete Res*., **41**(2011) 750–763.

[3] Cheng, Y.; Hongqiang, M.; Hongyu, C.; Jiaxin, W.; Jing, S.; Zonghui, L. and Mingkai, Y. ‘Preparation and characterization of coal gangue geopolymers’. *Constr. Build. Mater.* **187**(2018)318–326.

[4] Garcia-Lodeiro, I.; Fernandez-Jimenez, A. and Palomo, A. ‘Hydration kinetics in hybrid binders: Early reaction stages’. *Cement Concrete Comp.*, **39**(2013)82–92, 2013.

[5] Provis, J. L.; Palomo, A. and SHI, C. 'Advances in understanding alkali-activated materials'. *Cement Concrete Res.*, **78**(2015)110–125.
[6] Cheng, Y.; Hongqiang, M.; Hongyu, C.; Jiaxin, W.; Jing, S.; Zonghui, L. and Mingkai, Y. 'Preparation and characterization of coal gangue geopolymers'. *Constr. Build. Mater.* **187**(2018)318–326.
[7] Huang, G.; Ji, Y.; Li, J.; Hou, Z. and Dong, Z. 'Improving strength of calcinated coal gangue geopolymer mortars via increasing calcium content'. *Constr. Build. Mater*. **166**(2018)760–768.
[8] Carvão Mineral - SieceSC. *Informações sobre o carvão mineral em SC.* November 2019, http://www.siecesc.com.br/siecesc/informacoes-sobre-o-carvao-mineral-em-santa-catarina.
[9] Cao, Z.; Cao, Y.; Dong, H.; Zhang, J. and Sun, C. 'Effect of calcination condition on the microstructure and pozzolanic activity of calcined coal gangue'. *Int. J. Mineral Process.* **146**(2016) 23–28.
[10] Dong, Z.; Xia, J.; Fan, C. and Cao, J. 'Activity of calcined coal gangue fine aggregate and its effect on the mechanical behavior of cement mortar'. *Constr. Build. Mater*. **100**(2015)63–69.
[11] Cheng, Y.; Hongqiang, M.; Hongyu, C.; Jiaxin, W.; Jing, S.; Zonghui, L. and Mingkai, Y. 'Preparation and characterization of coal gangue geopolymers'. *Constr. Build. Mater.* **187**(2018)318–326.
[12] Zhang, Y.; Ge, X.; Nakano, J.; Liu, L.; Wang, X.; Zhang, Z. 'Pyrite transformation and sulfur dioxide release during calcination of coal gangue'. *RSC Adv.* **4**(2014)42506-42513.
[13] Provis, J. L.; Walls, P. A. and Van Deventer, J. S. J. 'Geopolymerisation kinetics. 3. Effects of Cs and Sr salts'. *Chem. Eng. Sci.*, **63**(18)(2008)4480–4489.
[14] Mccarter, W. J.; Chrisp, T. M. and Starrs, G. 'Early hydration of alkali-activated slag: Developments in monitoring techniques'. *Cement Concrete Comp*., **21**(4)(1999) 277–283.
[15] Nguyen, Q. H.; Lorente, S.; Duhart-Barone, A. Lamotte, H. 'Porous arrangement and transport properties of geopolymers'. *Constr. Build. Mater.*, **191**(2018)853–865.
[16] Ravikumar, D. and Neithalath, N. 'An electrical impedance investigation into the chloride ion transport resistance of alkali silicate powder activated slag concretes'. *Cement Concrete Comp.*, **44**(2013)58–68
[17] Zeng, S. and Wang, J. 'Characterization of mechanical and electric properties of geopolymers synthesized using four locally available fly ashes'. *Constr. Build. Mater.*, **121**(2016)386–399.
[18] Frasson, B. J.; Pinto, R. C. A. and Rocha, J. C. 'Influence of different sources of coal gangue used as aluminosilicate powder on the mechanical properties and microstructure of alkali-activated cement'. *Mater. Construcc.* **69**(336)(2019)1-18.
[19] Bandarenka, A. S.; Ragoisha, G. A. *In progress in chemometrics research*. New York, 2005. http://www.abc.chemistry.bsu.by/vi/analyser.
[20] Keddam, M.; Takenouti, H.; Nóvoa, X. R.; Andrade, C.; Alonso, C. 'Impedance measurements on cement paste'. *Cement Concrete Res.*, **27(**8)(1997)1191–1201.
[21] Santos, F. I. G.; Rocha, J. C. and Cheriaf, M. 'Influence of bottom ash replaced natural aggregate and air-entraining agent in moisture transfer mechanisms in mortars'. *Revista Matéria.* **12**(2)(2007) 253–268.
[22] Guo, W.; Zhu, J.; Li, D.; Chen, J. and Yang, N. 'Early hydration of composite cement with thermal activated coal gangue'. *J. Wuhan University of Technology*. **25**(1)(2010)162–166.
[23] Garcia-Lodeiro, I.; Palomo, A.; Fernández-Jiménez, A. and MacPhee, D. E. 'Compatibility studies between N-A-S-H and C-A-S-H gels. Study in the ternary diagram Na2O-CaO-Al2O3-SiO 2-H2O'. *Cement Concrete Res*. **41**(9)(2011)923–931.
[24] Noushini, A. and Castel, Arnaud. 'The effect of heat-curing on transport properties of low-calcium fly ash-based geopolymer concrete'. *Constr. Build. Mater*. **112**(2016)464–477.
[25] Vladikova, Daria. 'The technique of the differential impedance analysis part i: basics of the impedance spectroscopy'. *Advanced Techniques for Energy Sources Investigation and Testing*, (2004).

STRENGTH AND MICROSTRUCTURE OF ALKALI-ACTIVATED PHOSPHOROUS SLAG BINDER: EFFECTS OF ACTIVATOR TYPE/ DOSAGE AND PHOSPHOROUS SLAG CHEMICAL COMPOSITION

Z. Huang (1), Q. Wang (1)

(1) Department of Civil Engineering, Tsinghua University, China

Abstract

In this paper, the influence of sodium hydroxide and water glass of various modulus, as activators, on the compressive strength, microstructure and hydration products of two alkali-activated phosphorous slag (AAPS) with different chemical composition were studied. Water glass activation shows relatively higher later compressive strength when the slag with a higher Ca content is activated. Phosphorous slag with higher Ca content shows a faster strength development. Heat evolution shows that the alkalinity of the paste determines the intensity of early reaction and the Si content of the paste determines the development of later reaction. X-ray diffraction depicts a well-organized crystal structure in both two phosphorous slags activated by sodium hydroxide. Hydrotalcite formation is also observed in these groups. The main hydration product C-S-H in alkali-activated phosphorous slag with higher Ca content exhibits a higher crystallinity due to the increase of paste's alkalinity. ^{29}Si and ^{27}Al MAS NMR spectroscopy reveals that the alkalinity plays important role on the disorder of the product. The disorder of the product decreases with the increase of the alkalinity.

Keywords: Phosphorous slag, Alkali-activated material, Isothermal calorimetry, XRD, NMR

1. INTRODUCTION

Alkali-activated materials(AAMs) have been widely considered as a promising alternative to Portland cement [1]. Different types of precursors of AAMs are well described in the recent studies including [2,3]. Most investigation of the waste precursor of AAMs is granulated blast furnace slag (GBFS) due to its good hydraulic activity [4-6].

Phosphorus slag (PS) is the waste produced in the production of yellow phosphorous by electric furnaces. Compared to the GBFS few studies have been made to investigate the alkali-activated PS [7-9]. Phosphorous slag is mainly composed of amorphous phase with a low aluminum content, which is expected to have a potential hydraulic property. Although different kinds of precursors with different chemical component are well investigated, such as GBFS with high Ca content and fly ash with low Ca content, the precursor with low Al content has not been fully studied. Phosphorous slag is a kind of waste precursor with relatively low Al

content, which makes phosphorous slag become a suitable material to explore the low Al alkali-activated system.

This paper studies the mechanical property, hydration activity, crystalline phase and amorphous phase structure of two kinds of phosphorous slag with different chemical component activated by different type and dosage of the activator. Compressive strength, isothermal calorimetry, XRD , ^{29}Si and ^{27}Al MAS NMR spectroscopy were tested.

2. EXPERIMENT

3.1 Materials

Two different quenched granulated phosphorous slag (PS) was used in this study (P1 and P3. The Blaine specific surface areas of P1 and P3is 435 m^2/kg and 443 m^2/kg respectively. Chemical compositions of P1 and P3 determined by XRF are shown in Table 1.

Table 1: Chemical compositions of two kinds of phosphorous slag wt. %

Material	CaO	SiO_2	Al_2O_3	P_2O_5	F	MgO	Fe_2O_3
P1	43.12	38.27	5.33	4.62	2.46	1.69	0.291
P3	55.75	30.76	2.71	3.05	1.89	2.18	1.43

X-ray diffraction patterns of PS1 and PS2 are shown in Fig. 1. The amorphous phases are the main component of phosphorous slag, which can be reflected by the broad peaks from 17° to 37° in the XRD patterns. Few crystalline phases were found in phosphorous slag which means the chemical composition determined by XRF are almost the chemical components in the phosphorous phase. This means two kinds of phosphorous slag are consisting of similar amorphous phase with different Ca/Si (in modulus) ratios (1.2 for P1; 1.94 for P3).

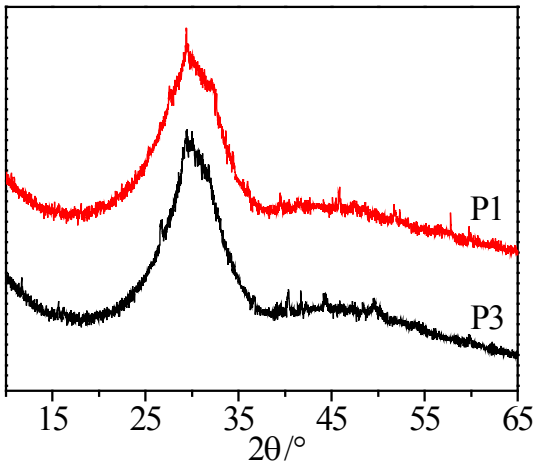

Figure 1: X-ray diffraction of two kind of phosphorous slag

NaOH solution and water glass was chosen to activate the phosphorous slag. Na_2O-to-slag weight ratio were 4% for all activator. Three modules were set for water glass 1, 1.5 and 2. Four experimental groups were recorded as N, 1, 1.5, 2. The alkali hydroxide solutions were prepared by dissolving sodium hydroxide pellets (99.9% purity) in deionized water. Water glass with different modulus was prepared by adding the sodium hydroxide pellets into industrial water

glass (initial Ms=3.3). The solution-to-slag ratio used for all paste and mortar in this study was 0.50 and the slag-to-sand ratio for mortar was 1:3 in this study.

3.2 Methods

The paste and mortar specimens were both cured under the standard curing conditions of 20 ±2℃ and 95% RH. Motar samples were prepared to test the compressive strength by mixing the raw materials with a planet mixer. The fresh mortars were cast in 40mm×40mm×160mm molds and cured under the standard curing conditions of 20±2℃ and 95% RH until testing. Paste samples were prepared to use the same planet mixer and cast in the polymer pipes 10cm in height and 1cm in diameter.

Heat evolution was measured using an 8 channel isothermal calorimeter (TA Instruments, USA). Preliminary tests were conducted to make sure that homogeneous pastes could be achieved for each reaction system even at the lowest liquid-to-solid ratio. Compared with the reaction heat, heat disturbance caused by the mixing could be neglected. The mixing procedure lasted 3 mins and the calorimetric data.

Crystalline phases of two kinds of phosphorous slag were tested by X-ray diffraction (XRD) with CuKα X-rays. Sample were tested from 5° to 65° with 0.02°and 2s per step. Paste were crushed into small pieces and grinded with agate mortar until the particle diameter is less than 38 μms.

^{29}Si and ^{27}Al Magic Angle Spinning (MAS) NMR spectroscopy was performed on the unreacted phosphorous slag and the pastes activated by different activators after 28 days curing. The sample preparation process is the same as XRD. The resonance frequency was 119MHz and 156MHz for ^{29}Si and ^{27}Al respectively. And the mass frequency is 12kHz.

3. RESULT AND DISSCUSSION

3.1 Compressive strength

The compressive strength differs when different phosphorous slag was activated (Fig. 2). Different activators exhibit approximately similar 28 days' compressive strength when the PS with a lower Ca content (P1) was activated (Fig. 2a) while the slag with a higher Ca content (P3) exhibit a higher compressive strength when water glass was used as activator (Fig. 2b). This might due to the silica in water glass reduce the total Ca/Si ratio in the paste and promote the long-term development of the reaction.

Up to 28 days, the compressive strength shows no significant difference between two slags activated by NaOH. But the PS3 shows a faster compressive strength development than the P1 due to the high Ca content increase the alkalinity of P3.

With three modules, compressive strength of alkali-activated P3 is higher than P1 at 28 days. This illustrates that water glass is more suitable for phosphorous with high Ca content. Besides due to the high alkalinity, PS3 also exhibits a faster strength development in the early age.

As for alkali-activated phosphorous system, the compressive strength result depicts that high Ca content will lead to a fast growth of compressive strength, but the long-term or middle-term strength mainly depends on Si content.

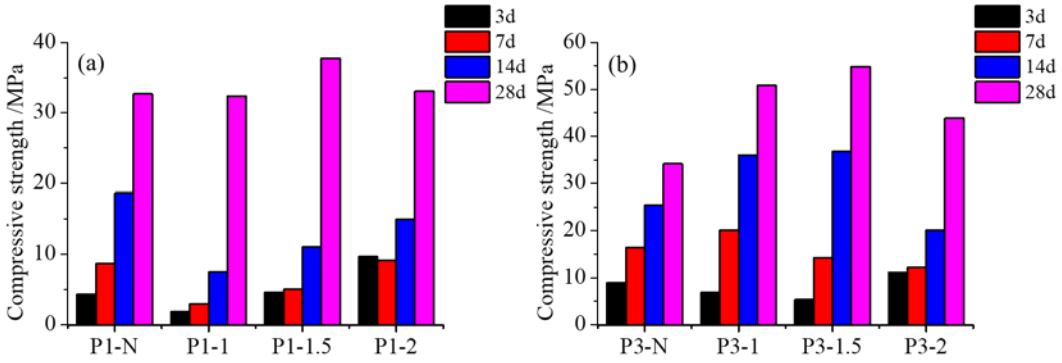

Figure 2: Compressive strength of two alkali-activated PS

3.2 Isothermal calorimetry

Isothermal calorimetry was carried out to evaluate the early reaction kinetic of alkali-activated phosphorous slag. An exothermic peak occurs immediately when the solution is added into the phosphorous. This peak can be interpreted as wetting and the initial dissolution of the precursor [11]. Induction period and accelerate period was observed in all groups although the potential chemical reaction may be different [12].

Due to the high alkalinity, P3 shows intenser hydration activity. The induction period of the P3 group is shorter than P1, and the broad exothermic peak followed by indution period is intenser than P1 when same activator was used. The induction period is supposed to be the time needed for concentration growing up in cement hydration for nucleation[12]. Thus the second exthermic peak is mainly contributed by the precipitation of early reaction products [13], such as C-A-S-H nucleus or C-S-H nucleus when there isn't enough Al content in the system.

Short induction period of the P3 activated by water glass can be explained as there are sufficient ions in the early system for nucleus to grow compared to P1. A fast dissolution of the Ca^{2+} and the silicate anions provided by water glass make the early nucleation more rapid. In water-glass-activated-P1 system, although there is enough silicate for nucleation, the lower alkalinity due to the low Ca content limits the early dissolution rate, and thus slow down the necleation rate. Longer induction period and milder second exthermic peak were observed when high modulus water glass were chosen. This is due to the alkalinity of water glass decreases with the increase of modulus, which slow down the dissolution rate of early Ca^{2+} from the slag and prolong the indution period. For NaOH activated system, the second exothermic occur faster than water glass system. The noticeable peak after the initial peak is widely reported as condensation [14]. The intensity of the second exothermic peak in NaOH-activated P1 is slightly stronger than P3. This is also due to the higher alkalinity induced by the higher Ca content in P1.

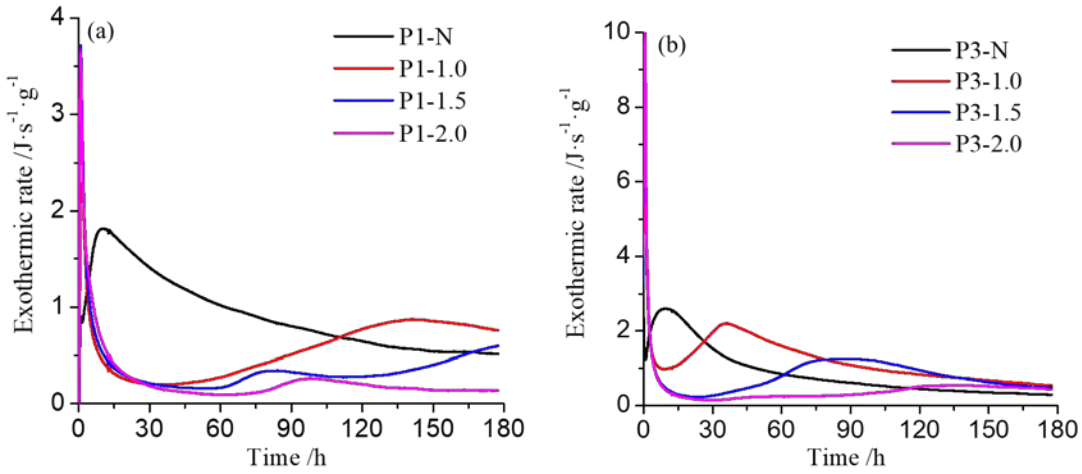

Figure 3: Heat evolution of alkali-activated (a) P1; (b) P3 with NaOH and water glass

Fig. 4 depicts the total heat release of the reaction. Significant differences were observed when water glass was used. The accumulative heat curves of alkali-activated P3 are higher than alkali-activated P3 when different modulus was chosen within 180 hours. This is consistent with the strength result (fig. 2), P3 exhibit higher compressive strength and fasted strength development in the early age. This is also due to the high alkalinity of the P3 and thus result in a better hydraulic activity. The total heat release decreases with the increase of modulus which is consistent with the exothermic curves. Alkalinity played an important role in early hydration. The total heat release of the NaOH activated system is similar between P1 and P3. But the curve's slope of different phosphorous slag is different at 180 hours. The hydration heat curve of P3-N (fig. 4b) is flattering than P1-N (fig. 4a), which indicate that P1 has better reaction development corresponding to the strength development (fig. 2). This is caused by the high Si content and low alkalinity in P1. The continuous dissolution of silica in P1 extends the later reaction. On the other hand, the high alkalinity of the P3 accelerates the dissolution and result in a fast percipitation. This may hinder the dissolution and diffusion of the ions which finally restrict the later reaction.

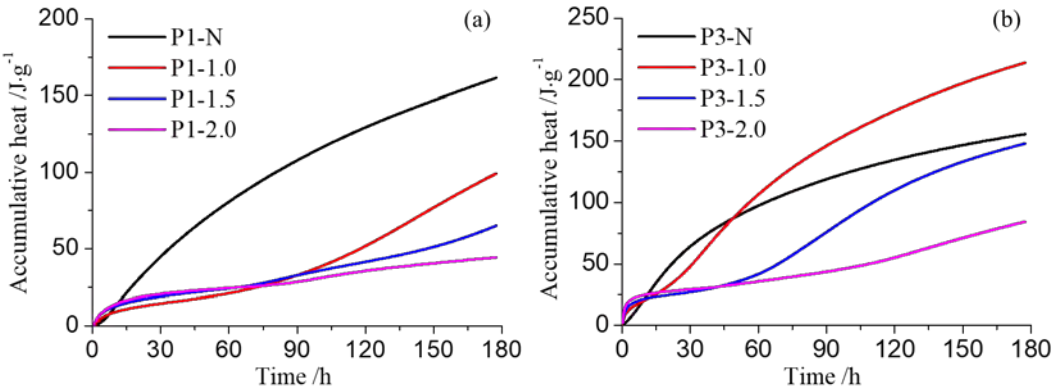

Figure 4: Accumulative heat of alkali-activated (a) P1; (b) P3 with NaOH and water glass

3.3 X-ray diffraction (XRD)

The mineralogical composition of pastes is shown in Fig. 5. Hydrotalcite (PDF 01-089-0460) C-S-H (PDF 00-033-0306) was observed in all paste, while the crystallinity of C-S-H is different when using different activator. A little gismondine (PDF 00-20-0452) was found in alkali-activated P3.

Semi-crystalline C-S-H is the main product in NaOH activated system. For both two phosphorous slags, the crystallinity of C-S-H is lower than the NaOH activated system and decrease with the increase of modulus. According to the recent reported [15], this is due to a higher pH will change the amorphous C-S-H into semi-crystalline.

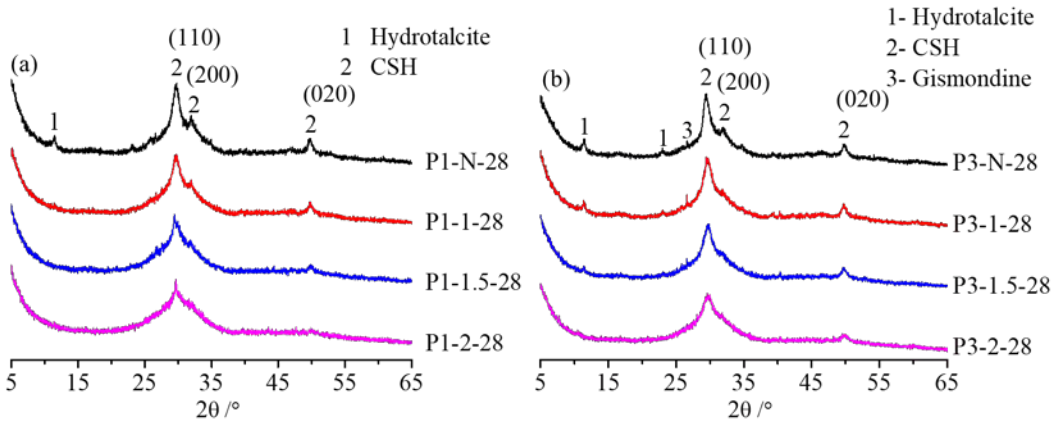

Figure 5: XRD spectra of alkali-activated (a) P1, (b) P3 at 28 days.

Hydrotalcite is second phase in NaOH activated system. For water-glass-activated P1, no hydrotalcite was found (Fig. 5b), which is contrary to the higher Al content of P1 (Table 1). While in water-glass-activated P3 paste, weak but observable hydrotalcite peak was found in the paste activated by modulus of 1 and 1.5 (Fig. 5b). This can be interpreted as the lower alkalinity results in a lower pH of the solution to the paste decrease the crystallinity of the hydrotalcite [16]. NaOH system provides a higher pH in the solution, which leads to the high hydrotalcite crystallinity. Therefore, a higher hydrotalcite crystallinity is observed in P3, though a lower Al content may affect the formation of hydrotalcite.

3.4 NMR spectroscopic

3.4.1 ^{29}Si MAS NMR spectra

Fig. 6 shows the ^{29}Si MAS NMR and ^{27}Al MAS NMR of two kinds of phosphorous slag. No significance difference is observed which means the structure of amorphous phase in two slags is similar.

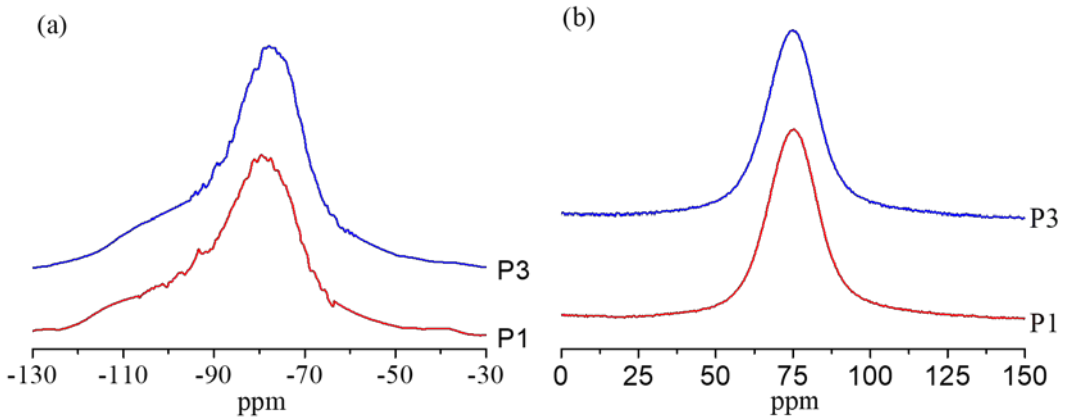

Figure 6: (a) ^{29}Si NMR and (b) ^{27}Al NMR spectrum of two kinds of phosphorous slag

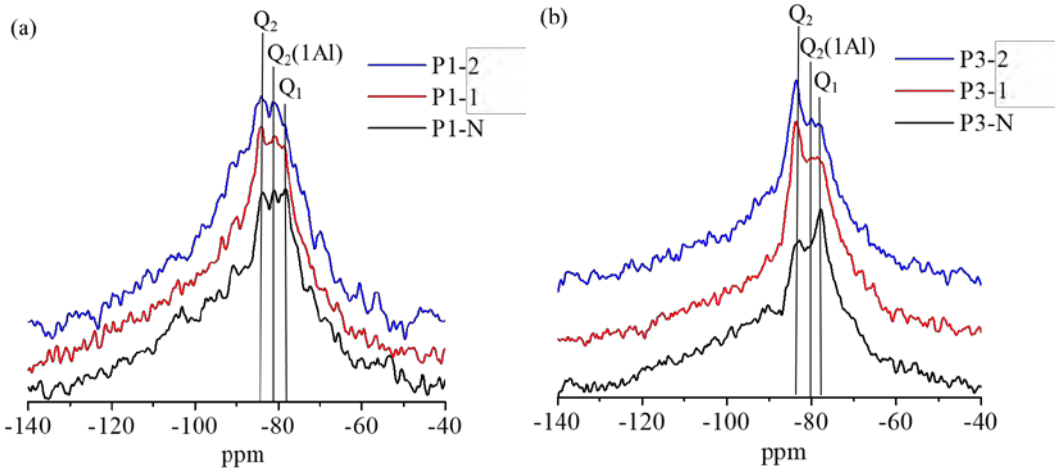

Figure 7: ^{29}Si MAS NMR spectrum of alkali-activated (a) P1, (b) P3.

The paste was tested for NMR after 28 days curing. The ^{29}Si MAS NMR spectrum is shown in Fig. 7. Compared to origin spectrum three new intense peaks can be observed. Those three peaks can be assigned to Q_2 (~84 ppm), Q_2(1Al) (~81 ppm) and Q_1(~79 ppm) according to [17-18]. Fig. 7 shows that the higher silica concentration in the activator is , the less Q_1 and more Q_2 will be. This can be explained as more silica participated in forming C-S-H gel, and thus increase the content of Q_2. This phenomenon is more obvious in P3 (Fig. 7b), this due to the Si content is lower in P3 and thus the rising of modulus has a greater impact on the C-S-H structure. On the other hand, due to the high alkalinity, C-S-H formed in alkali-activated P3 paste has a better crystallinity, which also result in the sharper peak. Fig. 7a shows more Al content participate into the C-S-H gel in P1 compared to P3 (Fig. 7b) which can be attributed to the higher Al content in original slag.

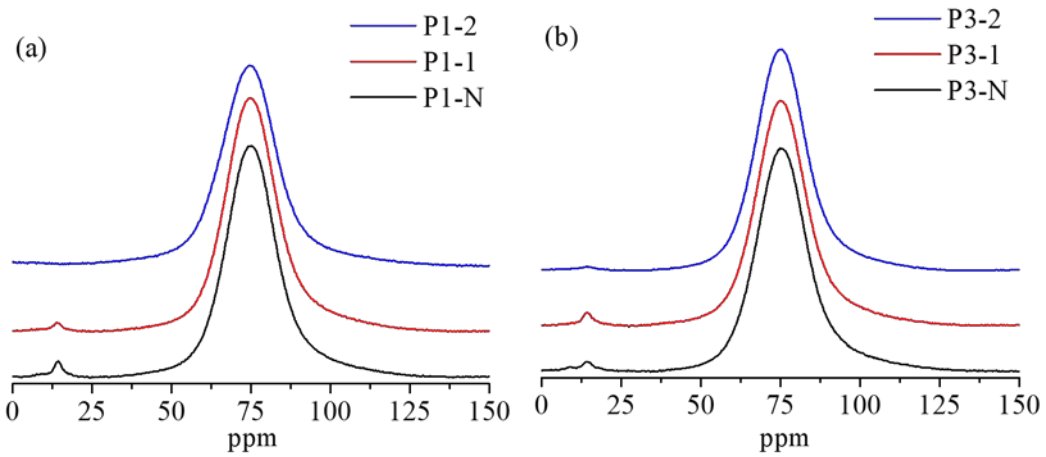

Figure 8: ^{27}Al MAS NMR spectrum of alkali-activated (a) P1, (b) P3.

Fig. 8 show the ^{27}Al MAS NMR spectrum of two different alkali-activated phosphorous slag. The broad peak range from 50 ppms to 100 ppms is attributed to the conbination of Al(IV), Al(V) and Al(VI) in the amorphous which cannot be separated as independent peak [19-20]. The new peak at 14.5 ppm can be assigned to hydrotalcite phases with Al(V) [21] which is consistent with the result of XRD (Fig. 5). The intensity of this peak is lower with the increasing of the modulus due to the reduction of alkalinity. An imperceptible peak at 14.5 ppms can be obsereved in curve P3-2 (Fig. 8b), while no peak is found in P1-2 (Fig. 8a). This also due to the high alkalinty of the P3 which result in a better crystallinity of hydrotalcite.

4. CONCLUSSION

Different phosphorous slag with a lower Al content was activated by NaOH and water glass with different modulus. Mechanical property, hydration activity, crystalline phase and amorphous phase structure was carried out by compressive strength, isothermal calorimetry, XRD and NMR spectroscopic. The main conclusion can be drawn out as follows :

- Water glass show a better activation of the phosphorous slag with higher Ca content while NaOH are more suitable for the phosphorous slag. High Ca content result in a fast strength growth in compressive strength while high Si content extend the development process of the strength.
- High origin Ca content, NaOH, and low modulus water glass with the high alkalinity will increase the early reaction. High origin Si content and water galss with high modulus will extend the later reaction.
- The crystallinity of the hydration products is highly depends on the alkalinity of the system. The higher the alkalinity is, a better crystallinity products will form.

REFERENCES

[1] Provis, J.L. Alkali-activated materials. *Cem. Concr. Res.***114** (2018)40-48.
[2] Provis J.L. and van Deventer J.S.J., 'Alkali-Activated Materials: State-of-the-Art Report, RILEM TC 224-AAM', Dordrecht: Springer/RILEM, 2014
[3] Provis J.L and Palomo A, Shi C. Advances in understanding alkali-activated materials. *Cem. Concr. Res.***78**(2015)110-125.

[4] Fernández-Jiménez A., Palomo J.G. and Puertas F. Alkali-activated slag mortars: mechanical strength behaviour. *Cem. Concr. Res.***29**(8)(1999)1313-1321.
[5] Barnett S. J., Soutsos M. N. and Millard S. G. Strength development of mortars containing ground granulated blast-furnace slag: Effect of curing temperature and determination of apparent activation energies. *Cem. Concr. Res.***36**(3)(2006)434-440.
[6] Aydin S. and Baradan B. Mechanical and microstructural properties of heat cured alkali-activated slag mortars. *Mater. Design.***35**(2012)374-383
[7] You D. Preparation and properties of alkali-activated cement containing phosphorous slag and fly ash. *Ceram. Silikaty*.**60**(1)(2016)63-67.
[8] Mehdizadeh H. and Najafi Kani E. Rheology and apparent activation energy of alkali activated phosphorous slag. *Const.r Build. Mater.***171**(2018)197-204.
[9] Cheng L, Zhu C and Sheng G. Mechanical properties and microstructures of alkali-activated phosphorous slag cement. *J. Chin. Ceram. Soc*.**34**(5)(2006)604-609.
[10] Ben Haha M., Le Saout G. and Winnefeld F. Influence of activator type on hydration kinetics, hydrate assemblage and microstructural development of alkali activated blast-furnace slags. *Cem. Concr. Res.***41**(2011) 301-310.
[11] Shi C., Krivenko P.V. and Roy D.M. 'Alkali-Activated Cements and Concretes', Abingdon. UK: Taylor & Francis, 2006.
[12] Dolado J.S. and Breugel K.V. Recent advances in modeling for cementitious materials. *Cem. Concr. Res.***41**(7) (2011)711-726.
[13] Chithiraputhiran S. and Neithalath N. Isothermal reaction kinetics and temperature dependence of alkali activation of slag, fly ash and their blends. *Cem. Concr. Res.***46**(2013) 233-242.
[14] Sun, Z. andVollpracht A. Isothermal calorimetry and in-situ XRD study of the NaOH activated fly ash, metakaolin and slag. *Cem. Concr. Res.***103**(2018)110-122.
[15] Kanchanason V. and Plank, J. Role of pH on the structure, composition and morphology of CSH–PCE nanocomposites and their effect on early strength development of Portland cement. *Cem. Concr. Res.***102**(2017)90-98.
[16] Wang Q., Tay H.H., Guo Z., et al. Morphology and composition controllable synthesis of Mg-Al-CO_3 hydrotalcites by tuning the synthesis pH and the CO2 capture capacity. *Appl Clay Sci*.**55**(2012)0-26.
[17] Bernal S.A., Provis J.L., and Walkerly B., et al., Gel nanostructure in alkali-activated binders based on slag and fly ash, and effects of accelerated carbonation, *Cem. Concr. Res.***53**(2013) 127–144.
[18] Bernal S.A., Nicolaset R.S., Myers R.J., MgO content of slag controls phase evolution and structural changes induced by accelerated carbonation in alkali-activated binders, *Cem. Concr. Res.***57**(2014)33–43.
[19] Palomo A., Alonso S., Fernandez A., et al. Alkaline activation of fly ashes: NMR study of the reaction products. *J. Am. Ceram. Soc*.**87**(6)(2004)1141–1145
[20] Merwin L.H., Sebald A., RagerH ., et al. ^{29}Si and ^{27}Al MAS NMR spectroscopy of mullite, *Phys. Chem. Miner.***18**(1991)47–52.
[21] Wang S.D. and Scrivener K.L. ^{29}Si and ^{27}Al NMR study of alkali-activated slag, *Cem. Concr. Res.***33**(5)(2003)769–774.

UTILIZATION OF BIOMASS FLY ASH IN ALKALI-ACTIVATED MATERIALS

Xuhui Liang (1), Hua Dong (1), Zhenming Li (1), Marc Brito van Zijl (2), and Guang Ye (1)

(1) Section of Materials and Environment (Microlab), Faculty of Civil Engineering and Geoscience, Delft University of Technology, Delft, the Netherlands

(2) Mineralz, Loswalweg 50, Rotterdam, the Netherlands

Abstract

This paper investigated the feasibility of using biomass fly ash (BFA) to prepare alkali-activated slag and fly ash paste. The reference mixture was alkali-activated slag and coal fly ash (CFA) paste with a slag-to-coal fly ash ratio of 50/50. In other mixtures, coal fly ash was replaced at 40% and 100% with BFA, respectively. The results showed that the incorporation of BFA accelerated the setting of the paste, while its impact on the compressive strength was minor. XRD and FTIR results indicated that the BFA participated in the reaction process. BFA showed potential use as CFA replacement in synthesizing alkali-activated materials, which would pave a way for the valorisation of BFA.

Keywords: biomass fly ash, alkali-activated materials, waste

1. INTRODUCTION

Fossil fuels are currently the most dominant resource for energy production. Besides the high expenses and irreversibility of fossil fuels, their burning process releases a large quantity of greenhouse gases, causing negative impact on the environment [1]. It has been agreed that by 2030, EU shall reduce the CO_2 emission by 40%. The energy industries take great responsibility and have to shift their focus to clean energy [2]. Thus, the desire for alternative fuels is greater than ever before. Bioenergy, derived from the biomass incineration, stands out for its superior characteristics with cheap resources and minor environmental impact. It is believed that biomass is carbon-neutral fuel, where CO_2 emissions during biomass combustion could be compensated through photosynthesis process [3, 4]. Therefore, the biomass is praised with bright prospects. Up to now, biomass has been applied as the fourth most used fuels for energy production, contributing to 10-14 % of total energy production worldwide [5, 6]. It is proposed that an increasing amount of biomass will be used in the coming decades [2].

During the incineration process of biomass for bioenergy production, by-products will be generated. Biomass fly ash (BFA) is the main residue from incineration process. The unburnt fine particles are carried by flue gas and eventually collected through bag filters or electrostatic

filters. Currently, most of BFA is landfilled or disposed directly, resulting in serious environmental problems. Recycling BFA and using it in building materials will benefit the environment and prompt the development of clean bioenergy. However. BFA is prohibited to be used in Portland cement concrete according to EN 450-1 [7], which requires the fly ash for concrete use should derived from coal combustion.

Apart from Portland cement, alkali-activation could be a possible way for BFA valorisation. Alkali-activated materials (AAM) is one type of cement clinker free binder and a promising alternative to Portland cement [8]. In recent years, intensive investigations have been carried out on AAMs. AAMs have high compatibility with raw materials [8]. Multiple industrial aluminosilicates wastes were used as precursors for AAMs preparation [9-12]. AAMs made of blast furnace slag (BFS) and coal fly ash (CFA) have shown good mechanical properties and workability [13, 14]. However, studies on BFA in AAM are scarce. The aim of this paper, therefore, is to investigate the possibilities of using BFA as precursor for producing AAM, where the BFA was used to partially replace the coal fly ash in alkali-activated slag and fly ash system.

2. MATERIALS AND METHODS

2.1 Materials

Biomass fly ash was collected from an energy plant in the Netherlands, where multiple biomass was used as fuel. Ground granulated blast furnace slag (GGBFS) and CFA were supplied by Ecocem Benelux BV (the Netherlands) and Vliegasunie BV (the Netherlands), respectively.

The particle size distribution of the raw materials was measured by laser diffraction analyser (DIPA 2000). Particle sizes of BFA were all below than 55 μm and close the GGBFS, while CFA showed bigger particle sizes, as shown in Fig. 1. The chemical and mineralogical compositions were determined through X-ray fluorescence (XRF) and X-ray diffraction (XRD), respectively.

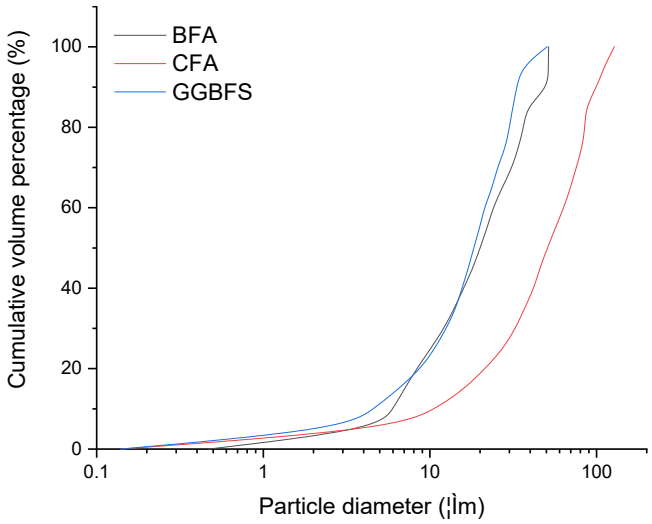

Figure 1: Particle size distribution of raw materials

According to the chemical composition, BFA contained higher amount of calcium oxide (CaO) compared with CFA (Tab. 1), and can be regarded as the Class C fly ash. The XRD pattern of BFA was almost flat with crystalline peaks, showing minor amount of glassy phases. There was a broad hump between 20-30 degrees for CFA, which represented the amorphous phases. The slag consisted of typical glassy phases almost without crystalline phases.

Table 1 Chemical composition of raw materials

	SiO_2	Al_2O_3	CaO	Fe_2O_3	K_2O	SO_3	Na_2O	Cl
BFA	50.92	12.53	17.16	7.70	2.18	3.77	0.27	0.12
CFA	52.60	26.37	5.46	9.52	1.55	0.85	-	-
BFS	32.19	13.43	41.04	0.52	0.34	1.51	-	-

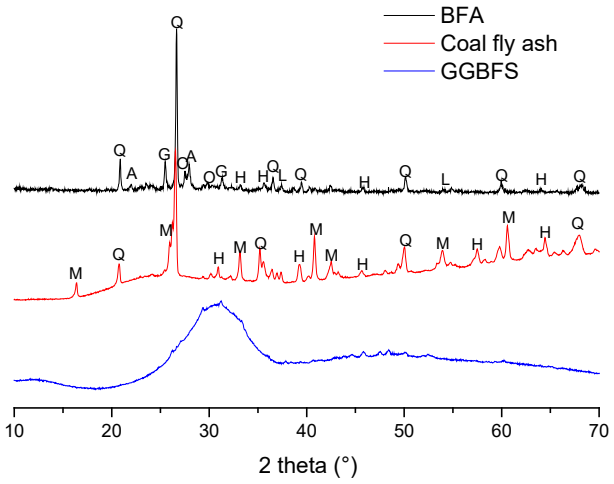

Figure 2: XRD patterns of raw materials
(Q: quartz, M: mullite, H: hematite A: albite, O: orthoclase, G: gypsum, L: lime)

The alkaline activator was a mix of sodium hydroxide (analytical reagent, >98% purity) and water glass solution (Na_2O: 8.25 wt%, SiO2: 27.50 wt%). The molar ratio of SiO_2 to Na_2O of the activator was 1.5 and the mass ratio of Na_2O to binder was 4.5%.

2.2 Methods

Three kinds of alkali-activated paste were prepared with the mixture proportion shown in Tab 2. All the raw materials were premixed in the mixer for 2 min to reach a homogenous state, then the activator was gradually added and the mixing continued for another 2 min. The paste was cast into cubes ($4 \times 4 \times 4$ cm^3) and compacted on the vibration table. Afterwards, the specimens were covered with plastic films to avoid water evaporation. Specimens were demoulded after one day, sealed in plastic bags and placed in the curing room at 20 ^oC until the compressive strength tests [15].

Table 2: Mixture proportion of alkali-activated slag and fly ash paste

Mixture	BFS(.wt%)	CFA(.wt%)	BFA(.wt%)	Liquid/Solid
B0	50	50	0	0.5
B20		30	20	
B50		0	50	

Setting time was determined using an automatic Vicat apparatus (VICAMATIC 2). The experiment was conducted at 20 ºC and 50 % RH following EN 196-3 [16]. Isothermal calorimetry test was carried out to study the hydration process of pastes at 20 ºC. Compressive strength test was conducted at a loading speed of 2.4 kN/s following EN 196-1 [17]. Five specimens were tested for each mixture, and the average compressive strength was calculated. After the compression tests, interior fragments of the specimens were collected and subjected to grinding and hydration stoppage for XRD and FTIR tests. The procedures for hydration stoppage could be found in ref [18].

XRD technique was applied to study the characteristics of hydration products in different pastes. Powder samples were prepared and their XRD patterns were determined by Philips X'Pert diffractometer. Scanning was conducted with Cu Kα radiation, the 2 theta increased from 10 º to 70º with a step size 0.03º. FT-IR (Spectrum TM 100 Optical ATR-FTIR) was applied for measuring the chemical bonds of molecules in raw materials and hydration products.

3. RESULTS AND DISCUSSION

3.1 Setting time and calorimetry

The setting time of the pastes was shown in Tab 3. It shows that the initial and the final setting time decreased with the increasing amount of BFA.

Table 3: Setting time of the pastes

Mixture	Initial setting (min)	Final setting (min)
B0	51	86
B20	29	57
B50	16	35

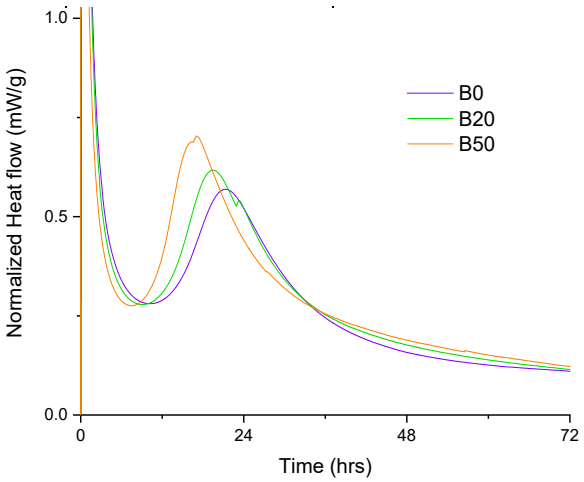

Figure 3: Heat flow of the pastes

It is believed that setting time could be linked to the hydration rate of early age pastes. Shorter setting time indicates faster chemical reaction in the pastes. The reasons for the acceleration of hydration can be explained by two facts. 1). From the chemical composition point of view, the amount of calcium in BFA is higher than that in coal fly ash. When mixed with alkaline solution, a higher amount of calcium in BFA would be released, which was beneficial for C-(A)-S-H precipitation [19]. 2). The finer particles of BFA have a nucleation effect and account for the faster setting [20].

Fig 3 presents the heat realise rate of pastes. The first peak in the heat release curve is related to the dissolution of precursors, and the second peak is for the formation of reaction products. With the incorporation of BFA, the second peak appeared earlier with higher intensity, which suggested an accelerated formation of C-(A)-S-H gel at early stage.

3.2 Compressive strength

The compressive strength of alkali-activated slag and coal/biomass fly ash at 1d and 7d was shown in Fig 4. Despite the acceleration of hydration, the incorporation of BFA did not improve the compressive strength at 1d. The compressive strength at 1d of all specimens was close to 20 MPa. With the proceeding hydration, the strength increased to nearly 65 MPa at 7d. A slight improvement of compressive strength was observed with the incorporation of BFA.

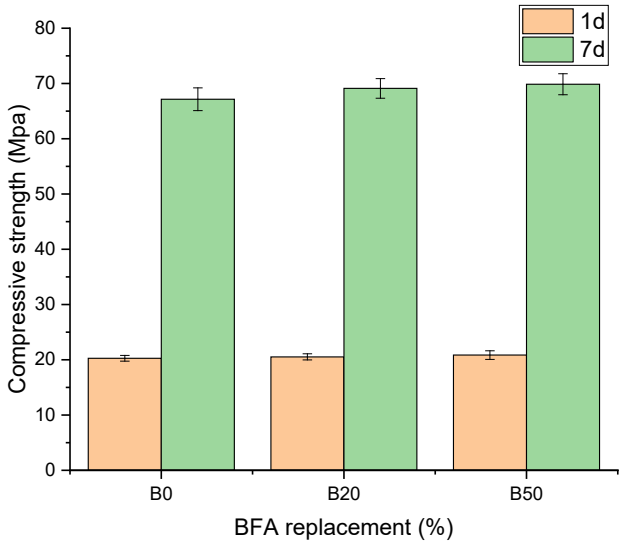

Figure 4: Compressive strength of alkali-activated slag and coal/biomass fly ash

3.3 XRD analysis

The XRD results of B50 at 1 day and 7 days, and B0 at 7 days were shown in Fig 5. Unreactive phases such as quartz and hematite, etc. remained in the XRD patterns after 1 and 7 d of reaction in B50 samples. It can be found that the peak at 2 theta angle of 25.5^{o}, which represents anhydrite in BFA, disappeared after alkali activation. The intensity of peaks at 2-theta angle of 28^{o} representing albite comparatively decreased from 1d to 7d. These could be explained by the dissolution of BFA in alkaline solution. Meanwhile, XRD spectrum for all samples presented a peak at 2 theta angle of around 29^{o}, which is associated with the formation of C-(A)-S-H gel [21]. The intensity of C-(A)-S-H peak in B50 increased from 1d to 7d, indicating more reaction products were formed, which contributed to the strength development.

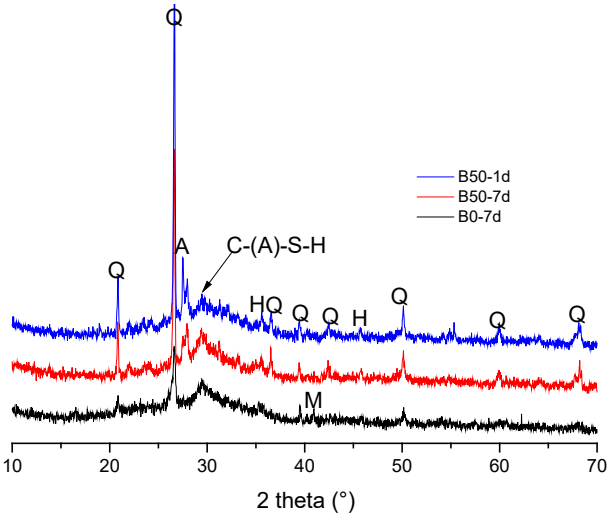

Figure 5: XRD patterns of hardened paste (Q: quartz, M: mullite, H: hematite A: albite)

3.4 FT-IR analysis

Fig 6 showed the FT-IR spectra of CFA, BFA, B0 at 7d and B50 at 7d. For CFA and BFA, the main bands around 1100 cm^{-1} were related with Si(Al)-O-Si [22, 23]. The tiny difference in wavenumbers at the main band (1097^{-1} and 1050 cm^{-1}) between CFA and BFA was the results of aluminium substitution in silicon tetrahedral position [23, 24]. Calcium sulphate was also observed for BFA at 678 cm^{-1} and 611 cm^{-1}, in agreement with the XRD results of the presence of anhydrite. Broad bands presented at 3400 cm^{-1} and 1625 cm^{-1} in B0-7d and B50-7d samples represented the vibration of hydroxyl (water) [22]. The main band at 945 cm^{-1} indicated the existence of C-(A)-S-H, which was the dominant hydration products for both B0 and B50 [25]. Generally, the spectrums for hydration products in B0 and B50 were similar. The band representing sulphate in the raw materials BFA disappeared after hydration, which confirmed that the sulphate dissolved in alkali activation and participated in reaction process.

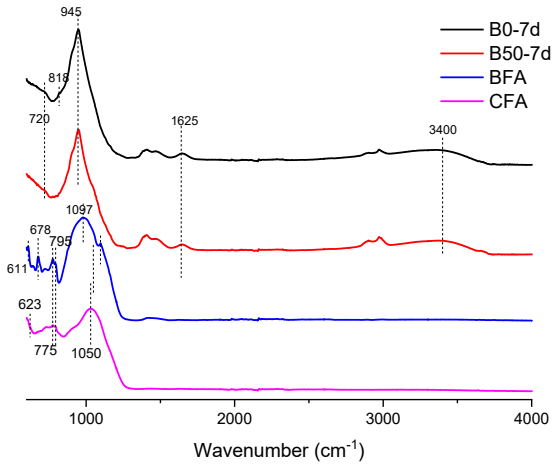

Figure 6: FT-IR spectra of precursors and pastes

4 CONCLUSIONS

Based on the results, the following conclusions can be drawn:

- Due to the high soluble calcium salts and fine particle size of BFA, the incorporation of BFA accelerated the setting of alkali-activated slag and fly ash paste, while showing minor impact on compressive strength at early age.
- BFA could dissolve in alkaline activation, which was confirmed through the dissolution of anhydrite, lime and albite determined through XRD and FTIR.
- BFA showed potential as a precursor for synthesizing alkali activated materials, which could be a promising routine for its valorisation.

ACKNOWLEDGEMENT

Xuhui Liang acknowledges the financial support from China Scholarship Council (No.201806050051). Zhenming Li acknowledges the financial support from China Scholarship Council (No.201506120072). Mineralz was acknowledged for the financial support of the experiments.

REFERENCES

1. Energy, I.G., *Global Energy & CO_2 Status Report: The Latest Trends in Energy and Emissions in 2018.* International energy agency iea, 2019: p. 1.
2. Commission, E.E., *GREEN PAPER-a 2030 framework for climate and energy policies.* COM (2013), 2013. **169**.
3. Agrela, F., et al., *2 - Biomass fly ash and biomass bottom ash*, in *New Trends in Eco-efficient and Recycled Concrete*, J. de Brito and F. Agrela, Editors. 2019, Woodhead Publishing. p. 23-58.
4. Johnson, E., *Goodbye to carbon neutral: Getting biomass footprints right.* Environmental Impact Assessment Review, 2009. **29**(3): p. 165-168.
5. McKendry, P., *Energy production from biomass (part 1): overview of biomass.* Bioresource Technology, 2002. **83**(1): p. 37-46.
6. Islas, J., et al., *Chapter Four - Solid Biomass to Heat and Power*, in *The Role of Bioenergy in the Bioeconomy*, C. Lago, N. Caldés, and Y. Lechón, Editors. 2019, Academic Press. p. 145-177.
7. EN, B., *450-1, Fly Ash for Concrete—Definition, Specifications and Conformity Criteria.* British Standards Institution, 2012.
8. Provis, J.L., *Alkali-activated materials.* Cement and Concrete Research, 2018. **114**: p. 40-48.
9. Fořt, J., et al., *Application of waste brick powder in alkali activated aluminosilicates: Functional and environmental aspects.* Journal of Cleaner Production, 2018. **194**: p. 714-725.
10. Palmero, P., et al., *Valorisation of alumino-silicate stone muds: From wastes to source materials for innovative alkali-activated materials.* Cement and Concrete Composites, 2017. **83**: p. 251-262.
11. He, J., et al., *Synthesis and characterization of red mud and rice husk ash-based geopolymer composites.* Cement and Concrete Composites, 2013. **37**: p. 108-118.

12. Bernal, S.A., et al., *Management and valorisation of wastes through use in producing alkali-activated cement materials.* Journal of Chemical Technology & Biotechnology, 2016. **91**(9): p. 2365-2388.
13. Nedeljković, M., Z. Li, and G. Ye, *Setting, Strength, and Autogenous Shrinkage of Alkali-Activated Fly Ash and Slag Pastes: Effect of Slag Content.* Materials, 2018. **11**(11): p. 2121.
14. Yousefi Oderji, S., et al., *Fresh and hardened properties of one-part fly ash-based geopolymer binders cured at room temperature: Effect of slag and alkali activators.* Journal of Cleaner Production, 2019. **225**: p. 1-10.
15. Nedeljković, M., et al., *Effect of curing conditions on the pore solution and carbonation resistance of alkali-activated fly ash and slag pastes.* Cement and Concrete Research, 2019. **116**: p. 146-158.
16. BSI, *BS EN 196-3: Methods of testing cement–Part 3: Determination of setting times and soundness*. 2005, BSI London, UK.
17. EN, T., *196-1. Methods of testing cement–Part 1: Determination of strength.* European Committee for standardization, 2005. **26**.
18. Snellings, R., et al., *RILEM TC-238 SCM recommendation on hydration stoppage by solvent exchange for the study of hydrate assemblages.* Materials and Structures, 2018. **51**(6): p. 172.
19. Song, W., et al., *Effect of steel slag on fresh, hardened and microstructural properties of high-calcium fly ash based geopolymers at standard curing condition.* Construction and Building Materials, 2019. **229**: p. 116933.
20. Scrivener, K.L., P. Juilland, and P.J.M. Monteiro, *Advances in understanding hydration of Portland cement.* Cement and Concrete Research, 2015. **78**: p. 38-56.
21. Zuo, Y., M. Nedeljković, and G. Ye, *Pore solution composition of alkali-activated slag/fly ash pastes.* Cement and Concrete Research, 2019. **115**: p. 230-250.
22. Zhang, Z., H. Wang, and J.L. Provis, *Quantitative study of the reactivity of fly ash in geopolymerization by FTIR.* Journal of Sustainable Cement-Based Materials, 2012. **1**(4): p. 154-166.
23. Mozgawa, W., et al., *Investigation of the coal fly ashes using IR spectroscopy.* Spectrochimica Acta Part A: Molecular and Biomolecular Spectroscopy, 2014. **132**: p. 889-894.
24. Flanigen, E.M., H. Khatami, and H.A. Szymanski, *Infrared Structural Studies of Zeolite Frameworks*, in *Molecular Sieve Zeolites-I*. 1974, AMERICAN CHEMICAL SOCIETY. p. 201-229.
25. Li, Z., et al., *Mitigating the autogenous shrinkage of alkali-activated slag by metakaolin.* Cement and Concrete Research, 2019. **122**: p. 30-41.

EFFECT OF PORLAND CEMENT ADDITION ON INITIAL DISSOLUTION OF COAL GANGUE BASED ALKALI-ACTIVATED CEMENT

Bruna J. Frasson (1), Janaíde C. Rocha (2)

(1) Civil Engineering, CTC, Federal University of Santa Catarina, Brazil

(2) Civil Engineering Department, CTC, Federal University of Santa Catarina, Brazil

Abstract

Release of silicon and alumina from aluminosilicate occurs at early stages of alkaline reaction. Alkalinity and different aluminosilicate could influence dissolution of particles and modify microstructure of alkali-activated systems. However, there is a lack of study regarding the effects of Portland cement (OPC) addition on alkali-activated systems. This paper investigates alkaline dissolution of aluminosilicate by leaching experiments, varying Portland cement content. Chemical stability of AA-hybrid pastes was determined by water immersion and compressive strength at 28 days. Hybrid alkali-activated cement was produced with coal sludge (CS) and coal gangue (CG). Portland cement was added in 10 wt% and 20 wt% of precursor, and the water to binder ratio was of 0.75. Compressive strength increased in hybrid alkali-activated materials after chemical stability test, and leached solutions have a peak of pH and electrical conductivity at seven days. Chemical analysis of leached solutions detected contents of SiO_2, SO_3, K_2O, Fe_2O_3 and CaO. Portland cement addition increased alkaline dissolution of Si and Al from aluminosilicate at initial stages of chemical reaction with a synchronized behaviour. Dissolution efficiency was according to the material reactivity, following CST>CG>CS.

Keywords: alkali-activation, coal gangue, dissolution, chemical stability.

1. INTRODUCTION

Synthesis of alkali-activated cement involves chemical reaction between aluminosilicates and alkaline reagents. Basically, chemical reaction consists of dissolution, condensation and polymerization [1]. Dissolution of aluminosilicate can be influenced by alkalinity $[OH]^-$ [2, 3], temperature [4], aluminosilicate characteristic [2, 5] and calcium content [6]. Aluminum is more readily to dissolves than silicon, since Al-O bonds are weaker than Si-O bonds [4]. Sagoe-Crentsil and Weng [7] suggested that the process of condensation occurs in two stages: quick condensation between $[Al(OH)_4]^-$ and $[SiO_2(OH_2)]^{2-}$, and slow condensation of silicate

species. Factors as higher partial charge, larger atomic size and four hydroxyl groups are attributed to higher activity of $[Al(OH)_4]^-$ [3].

Reaction products of alkali-activated cements are amorphous aluminosilicate gel and/or zeolites [1]. Chemical stability of alkali-activated cements (AAM) is related to microstructure formation. Continuous immersion in water can weaken Si-O-Si bonds and increase capillary pore pressure, which implies in the reduction of compressive strength [8].

Fly ash, metakaolin and slags are main aluminosilicate used in AAM [9], however, there are advances in use of mining wastes, such as coal gangue. Cheng et al [10] observed that, the higher alkalinity, the higher the compressive strength of coal gangue alkali-activated cements, reaching a plateau at 12 M. Granulated blast furnace (GBFS) addition in CG-based alkali-activated material can improve the compressive strength; the main reaction products evidenced were C-A-S-H and C-S-H [11].

Low-calcium aluminosilicates based AAM, generally presents difficulty to hardening at room temperature, thus thermal cure is required to accelerate the reaction processes [12]. Synergy between heat released by hydration of Portland cement and presence of alkalis, in hybrids alkaline cements, provide dissolution of aluminosilicate particles [13].

Coal gangue are composed by silicon and aluminum oxides, and lower iron content, whereas the main crystalline phases are quartz and kaolinite [14]. Calcination heat at 500ºC and 700ºC is applied, in order to burn organic material [15] and can induce to kaolinite dehydroxylation [16]. However, this process can release significant levels of CO_2 and SO_2 [15], which may limit large-scale application as a building material.

Effect of Portland cement addition on the alkaline dissolution of calcined and non-calcined coal mining waste were analyzed in this work. Compressive strength and chemical stability test were implemented to observed the influence of OPC in mechanical properties of AAM.

2. MATERIALS AND METHODS

2.1 Materials

Two different coal mining wastes were used as aluminosilicates, (i) coal sludge (CS) and (ii) granular coal gangue (CG); they were oven dried at 105°C for 24 hours and ball milled for 30 minutes. Part of CS was calcined at 700°C for 1 hour, then designated by CST. Portland cement replaced wastes in 10 wt% and 20 wt%. Chemical and mineralogical wastes characteristic were explained in a previous work [17] and are summarized in Table 1. Alkaline solution (AS) was prepared by dissolving NaOH (97% Na_2O – solid) in sodium silicate (12.7% Na_2O, 30.4% SiO_2 and 56.9% H_2O - solution), to obtain silica modulus (SiO_2/Na_2O) of 1.5.

2.2 Methods

Alkali-activated paste was prepared by pre-mixing OPC and wastes (dry-mix), adding AS with AS/solid of 1: 1 by weight, and 0.75 (wt) water to binder ratio. Cylindrical samples, 2 x 4 cm (diameter x height), were cast and hermetically sealed. Three series of AAM were studied, using different aluminosilicate, (i) CS, (ii) CG and (iii) CST. OPC replaced aluminosilicate in contents of zero wt% (control groups), 10 wt% and 20 wt%. Hybrid-AA were cured at room temperature (25°C). Control groups (CST-0, CS-0 and CG-0) were heat-cured in 50ºC for 24 hours, due to its non-hardening, until seven days at room temperature. CST series were demolded after 24 hours, but hybrid-CS and hybrid-CG after 48 hours.

Samples were sealed with PVC film, until test ages. Compressive strength test was implemented at 7 and 28 days in Instron press with 50 kN static load cell and 7000 N/min loading speed.

Chemical stability test was performed by immersed samples (at 7 days) in distilled water, 1: 4 (by weight) over 21 days. Samples were weighed and the contact solution was subjected to electrical conductivity, pH and chemical analysis, at intervals of one hour, 7 days, 14 days and 21 days. Compressive strength test was performed after 21 days of immersion. Chemical analyzes were implemented in X-Ray fluorescence Shimadzu 7000.

Alkaline dissolution test consists of: weigh one gram of powder (waste and OPC), add 25 g of NaOH (10.3M) and mix it on a magnetic stirrer for 10 and 60 minutes. The solution is vacuum filtered with a quantitative filter (8 μm), diluted with 50 ml distilled water and acidified (HNO_3 - pH <2). The concentration (mg/l) of dissolved aluminum and silicon was analyzed by atomic absorption (AA).

Table 1: Main Chemical and mineralogical characterization

Characterization	CST	CS	CG	OPC
SiO_2	60.0	28.8	47.1	17.2
Al_2O_3	30.4	10.2	21.03	-
Fe_2O_3	2.5	8.0	4.2	0.1
CaO	0.7	1.9	0.22	68.7
L.O.I	1.9	24.8	19.35	0.9
Others	26.3	4.5	8.1	9.2
Main crystalline phases	Quartz Muscovite	Quartz Kaolinite Muscovite	Quartz Kaolinite Pyrite	-

3. RESULTS AND DISCUSSION

3.1 Alkaline dissolution

Alkaline dissolution test was performed, at 10 and 60 minutes, to analyze OPC influence in Al and Si dissolution from coal mining wastes. Since the initial formation of AAM involves dissolution of aluminosilicate, which yields aluminates and silicates species, and they will hydrolyze to form monomers, those process can occur simultaneously [7].

Table 2 shows that Si and Al dissolution from coal wastes increase over the time. CST series show higher ions dissolution than the others series (CS and CG). OPC addition increases the dissolution of Si at 60 minutes for all samples, but does not affect the Al dissolution in CS and CG series. Dissolution of Si and Al seem to have a synchronized behavior in CST series, the Si/Al molar ratio have range from 1.0 to 1.8 at 60 minutes, the CST are composed mainly by quartz and metakaolin. Although the CS series and CG, due to their mineral composition, can have different degree of dissolution, thus, varying the

dissolution of aluminosilicates, the CS and CG series have range of Si/Al molar ratio from 1.3 to 3.6, at 60 minutes.

Transformation of kaolin during calcination leads to a metastable phase, metakaolin, and can be related to higher leaching of Si and Al, from CST series. Silicon and aluminum amorphous have lower bond energy and higher degree of ion dissolution [18]. Sagoe-Crentsil and Weng [7] by means of partial charge model evidenced aluminates species are consumed by condensation with silicates species, alongside with continuous dissolution and hydrolysis, which can result in hardening and setting of AAM.

The presence of more silicon species, provided by OPC addition, may justify the hardening of hybrid cements at room temperature, since the condensation occurs between silicates and aluminates species, and silicates species only [7]. Therefore, the results show Portland cement content, wastes chemical composition and crystalline phases influence dissolution of Al and Si, which will imply in AAM hardening.

Table 2: Si and Al concentration (ppm) after alkaline dissolution

Description	Si		Al	
	10 min.	60 min.	10 min.	60 min.
CST-0	128.4	210.2	-	205.0
CST-10	218.9	230.5	65.7	177.6
CST-20	186.2	362.8	73.5	192.8
CG-0	57.1	136.5	54.2	70.0
CG-10	78.8	161.4	53.7	70.3
CG-20	232.7	294.3	55.0	78.9
CS-0	53.2	117.4	53.2	87.4
CS-10	95.7	148.1	62.0	80.4
CS-20	145.9	214.3	70.6	88.1

3.2 Mechanical Properties

Fig. 1 shows compressive strength at 7 and 28 days, and after the chemical stability test (water). CST samples present higher mechanical strength than the other materials. Portland cement addition induce hardening at room temperature and increased mechanical strength. CS-0 and CG-0 systems did not harden at either oven cure, or room temperature, so demold was not possible.

Hybrid cements show increase in compressive strength after chemical stability test. Compressive strength may be affected by continued hydration of anhydrous OPC particles immersed in water. CS-20 and CG-20 present an increase of about 67% after chemical stability test in compressive strength, which is more significant than CST-series. However, CS-10 and CG-10 show, after the chemical stability test, a decrease in compressive strength and volumetric expansion, this behavior can be related to the oxidation of sulfates such as pyrite.

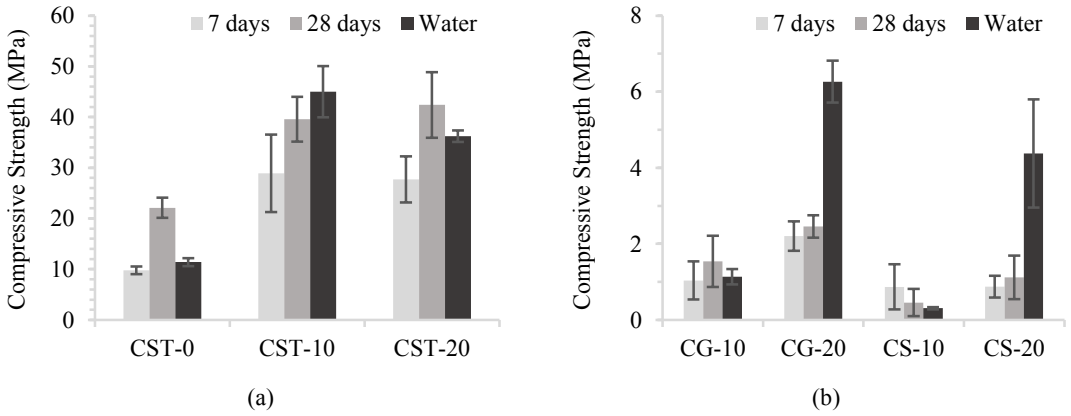

Figure 1: Compressive Strength (a) burnt waste; (b) unburnt wastes.

Fig. 2 shows the correlation between ions alkaline dissolution at 60 minutes and compressive strength. The data was linearly normalized, as Eq. 1, wherein the L is normalized values (MPa/MPa or ppm/ppm), X_i is value (MPa or ppm) to be normalized, X_{min} is minimum values of each series (MPa or ppm) and X_{max} is maximum values of each series (MPa or ppm). Alkaline dissolution of Al and Si can be an indicator of mechanical development, the higher initial ions dissolution, the greater compressive strength. The r-square are higher than 0.90, evidencing a higher linear correlation.

The alumina dissolution at early stages of reaction plays a role in development of initial mechanical strength, due to cross-linked gel. However, the silicon contribution in mechanical strength occurs in later stages of microstructural development [19]. Hardening of alkali-activated cement can be influenced by the presence of more reactive Al and the heat released from hydration of OPC particle. CST raw material is more reactive in an alkaline medium than CS and CG, thus, the results shows that the mechanical properties and initial microstructure formation seem to be influenced by reactivity of raw materials and OPC content.

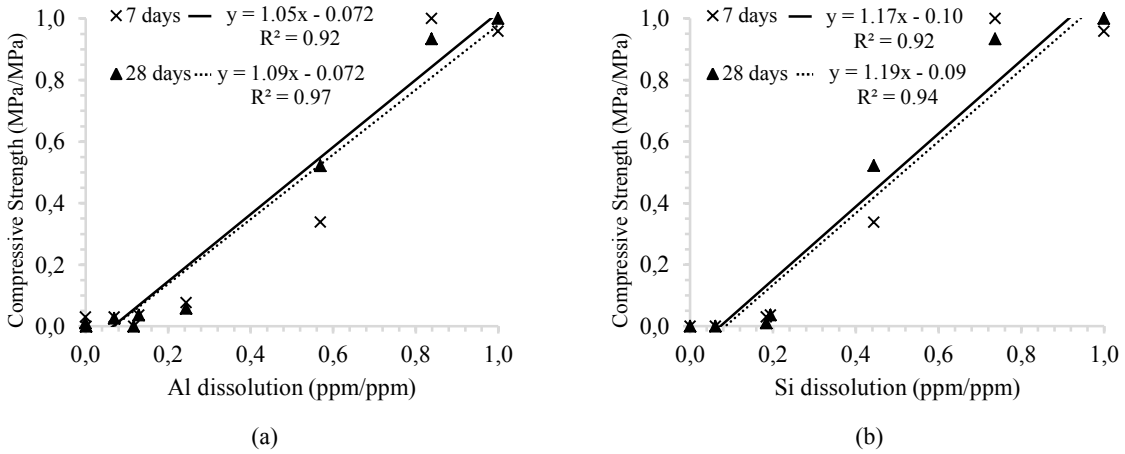

Figure 2: Normalized compressive Strength by (a) normalized Al dissolution; (b) normalized Si dissolution CST-systems.

$$L = (X_i - X_{min})/(X_{max} - X_{min}) \quad (1)$$

3.3 Chemical Stability

Salt solubility in aqueous medium can be analyzed by electrical conductivity (EC), the higher ion concentration, the higher the EC. EC and pH were measured in aqueous solution after chemical stability test, at intervals of 60 minutes, 7, 21 and 28 days. Fig. 3 presents pH and EC variation over time.

CS and CG systems present higher EC and pH values at seven days, which indicates that alkalis and metal ions did not participate of the alkaline reaction, and are free to leach. CST systems have lower EC and pH values, thus, the development of more stable microstructure. Hybrids CST-systems present higher values of EC at seven days than the CST-0, probably due to the OPC addition which leads to an increase in leached calcium ion.

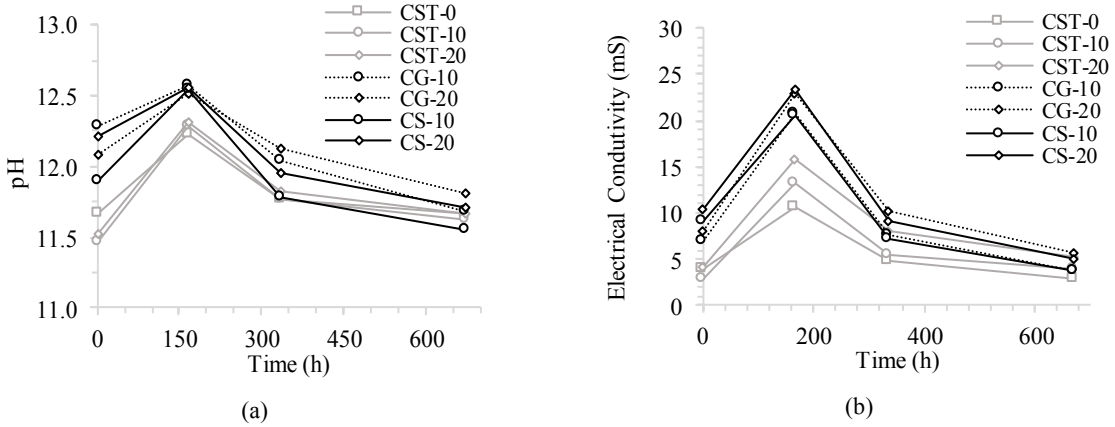

Figure 3: Chemical stability test (a) pH; (b) electric conductibility.

Table 3 shows that during the chemical stability test, SiO_2 leached more from materials than the other oxides. OPC addition decrease the SiO_2 released, and the CST samples have the lowest values. Therefore, factors such as waste reactivity and calcium content can induce formation of stable microstructure, which results in less leached silica oxide. The higher SiO_2 leachate the lower compressive strength after water immersion, as evidenced in CST systems.

Table 3: Total leaching oxides (mol/kg) from chemical stability test;

Description	SiO_2	Fe_2O_3	K_2O	CaO	SO_3
CST-0	3.74	0.08	0.37	-	1.17
CST-10	2.91	0.13	0.65	0.10	1.11
CST-20	2.39	0.09	0.58	0.56	1.42
CG-10	4.82	0.02	0.11	0.11	0.16
CG-20	4.52	0.02	0.13	0.09	0.33
CS-10	5.86	0.02	0.02	-	0.20
CS-20	5.04	0.04	0.17	0.12	0.30

Highest leached SiO_2 was for CST-0, which did not show increase in compressive strength after chemical stability test. Water immersion may have inhibited the continuous alkaline reaction in CST-0, so there was no increase in mechanical strength compared to seven days. Water weakens Si-O-Si bonds and capillary action induces pore wall pressures, affecting microstructure and mechanical properties [8].

Correlation between compressive strength, EC and pH are present in Fig. 3, exponential correlation is evidenced, EC and pH values are from 60 minutes after water immersion. Electric conductivity and pH values can be indicators of mechanical development, when performed at early ages.

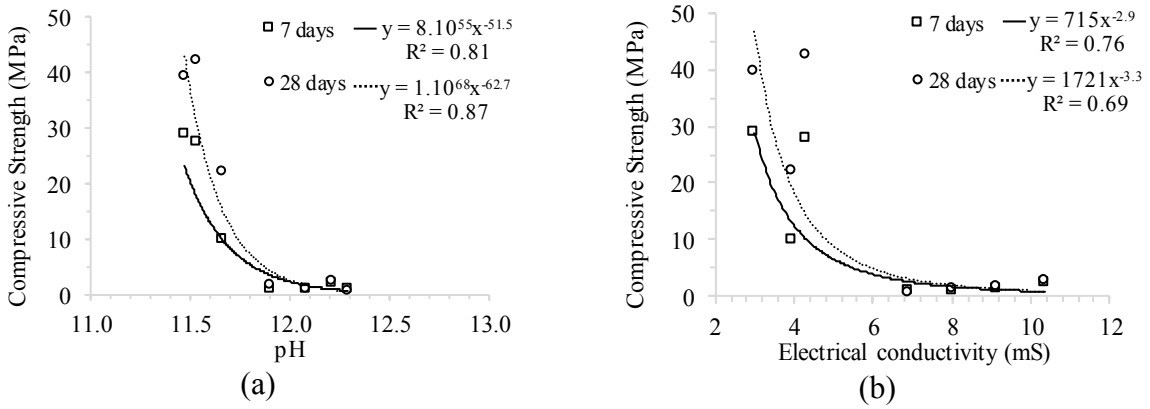

Figure 4: Chemical stability test exponential fit of (a) pH, (b) electrical conductivity.

4. CONCLUSIONS

The main conclusions obtained from the experimental results are listed below:

- Portland cement addition influenced alkaline dissolution of Si and Al ions, for all samples analyzed. The higher OPC addition, the greater dissolution of Al and Si ions. Concentration of aluminum dissolution at 60 minutes can be an indicator of mechanical development;
- Hybrids cement presents an increase in compressive strength after chemical stability test excepting CST-0. Hydration of anhydrous OPC particles may have positively affected hybrids cement. Whilst, CST-0 was negatively affected by internal pore pressure and weakened bonds of Si-O-Si;
- Electrical conductivity and pH were lower for CST-systems which may be related to formation of more stable microstructure. EC and pH values of chemical stability after 60 minutes of immersion, may be an indicator of mechanical strength as evidenced by exponential correlation.

ACKNOWLEDGEMENTS

This study was financed in part by the Coordenação de Aperfeiçoamento de Pessoal de Nível Superior - Brasil (CAPES) – Finance Code 001, and CNPq.

REFERENCES

[1] Shi, C.; Fernández-Jiménez, A. and Palomo, A. 'New cements for the 21st century: The pursuit of an alternative to Portland cement'. *Cement. Concrete Res*. **41**(2011) 750–763.

[2] Panagiotopoulou, C.; Kontori, E.; Perraki, T.; Kakali, G. 'Dissolution of aluminosilicate minerals and by-products in alkaline media'. *J. Mater. Sci*. **42**(9)(2007)2967–2973.

[3] Weng, L.; Sagoe-Crentsil, K. 'Dissolution processes, hydrolysis and condensation reactions during geopolymer synthesis: Part I-Low Si/Al ratio systems'. *J. Mater. Sci*. **42(**9)(2007)2997–3006.

[4] Granizo, N.; Palomo, A.; Fernandez-Jiménez, A. 'Effect of temperature and alkaline concentration on metakaolin leaching kinetics'. *Ceram. Int.* **40**(7)(2014)8975–8985.

[5] Hajimohammadi, A.; Provis, J. L.; van Deventer, J. S. J. 'The effect of silica availability on the mechanism of geopolymerisation'. *Cement and Concrete Res*. **41**(3)(2011)210–216.

[6] Zeng, S.; Wang, J. 'Characterization of mechanical and electric properties of geopolymers synthesized using four locally available fly ashes'. *Constr. Build. Mater*, **121**(2016)386–399.

[7] Sagoe-Crentsil, K.; Weng, L. 'Dissolution processes, hydrolysis and condensation reactions during geopolymer synthesis: Part II. High Si/Al ratio systems'. *J. Mater. Sci*. **42**(9)(2007)3007–3014.

[8] Slaty, F.; Khoury, H.; Wastiels, J.; Rahier, H. 'Durability of alkali activated cement produced from kaolinitic clay'. *Appl. Clay Sci*. **104**(2015)229–237.

[9] Koshy, N.; Dondrob, K.; Hu, L.; Wen, Q.; Meegoda, J. N. 'Synthesis and characterization of geopolymers derived from coal gangue, fly ash and red mud'. *Constr. Build. Mater*. **206**(2019) 287–296.

[10] Cheng, Y.; Hongqiang, M.; Hongyu, C.; Jiaxin, W.; Jing, S.; Zonghui, L. and Mingkai, Y. 'Preparation and characterization of coal gangue geopolymers'. *Constr. Build. Mater.* **187**(2018)318–326.

[11] Huang, G.; Ji, Y.; Li, J.; Hou, Z. and Dong, Z. 'Improving strength of calcinated coal gangue geopolymer mortars via increasing calcium content'. *Constr. Build. Mater*. **166**(2018)760–768.

[12] Samson, G.l; Cyr, M.; Gao, X. X. 'Formulation and characterization of blended alkali-activated materials based on flash-calcined metakaolin, fly ash and GGBS'. *Constr. Build. Mater.* **144**(2017)50–64.

[13] Garcia-Lodeiro, I.; Fernandez-Jimenez, A. and Palomo, A. 'Hydration kinetics in hybrid binders: Early reaction stages'. *Cement Concrete Comp.* **39**(2013)82–92, 2013.

[14] Cao, Z.; Cao, Y.; Dong, H.; Zhang, J. and Sun, C. 'Effect of calcination condition on the microstructure and pozzolanic activity of calcined coal gangue'. *Int. J. Mineral Process*. **146**(2016) 23–28.

[15] Zhang, Y.; Ge, X.; Nakano, J.; Liu, L.; Wang, X.; Zhang, Z. 'Pyrite transformation and sulfur dioxide release during calcination of coal gangue'. *RSC Adv.* **4**(2014)42506-42513.

[16] Guo, W.; Zhu, J.; Li, D.; Chen, J. and Yang, N. 'Early hydration of composite cement with thermal activated coal gangue'. *J. Wuhan University of Technology*. **25**(1)(2010)162–166.

[17] Frasson, B. J.; Pinto, R. C. A. and Rocha, J. C. 'Influence of different sources of coal gangue used as aluminosilicate powder on the mechanical properties and microstructure of alkali-activated cement'. *Mater. Construcc.* **69(** 336)(2019)1-18.

[18] Li, H.; Sun, H.; Tie, X.; Xiao, X. 'Dissolution properties of calcined gangue'. *Journal of University of Science and Technology Beijing: Mineral Metallurgy Material*, **13**(6)(2006)570–576.

[19] Hajimohammadi, A.; Provis, J.; van Deventer, J. 'Effect of alumina release rate on the mechanism of geopolymer gel formation'. Ch*em. Mat. 22(18)(2010)5199-5208.*

EFFECT OF PRECURSORS AND WATER TO BINDER RATIOS ON THE WATER PERMEABILITY OF ALKALI-ACTIVATED MORTARS

Thi Nhan Nguyen (1,2), Quoc Tri Phung (2), Lander Frederickx (2), Diederik Jacques (2), Alexandre Dauzeres (3), Jan Elsen (1), Yiannis Pontikes (1)

(1) Department of Materials Engineering, KU Leuven, 3001 Leuven, Belgium

(2) Institute for Environment, Health, and Safety, Belgian Nuclear Research Centre (SCK CEN), Boeretang 200, 2400 Mol, Belgium

(3) IRSN, BP 17, 92262 Fontenay-aux-Roses, France

Abstract

This work investigates the water permeability of alkali-activated materials (AAMs), which is one of the key transport properties beside the diffusivity to assess the material durability. The AAMs were produced from granulate blast furnaces slag (BFS) and metakaolin (MK) with various water/binder ratios of 0.35, 0.45, 0.55, and 0.75, 0.85, 0.95 for BFS and MK based AAMs, respectively. Herein, a direct method using a constant flow controlled by a syringe pump, which has been successfully applied on conventional concrete, was used to measure the permeability of the AAMs. Data was then compared with the OPC mortars with similar w/b ratios. The results reveal that the permeability of BFS activated mortars is comparable to the one of OPC mortars. Both BFS and MK based AMMs are highly sensible with the changes in w/b ratio. The higher the w/b ratio, the higher the permeability. The extent in changing permeability with w/b ratio is stronger for BFS compared to MK based AMMs. Furthermore, a correlation between water permeability and microstructure obtained by nitrogen adsorption of the investigated AAMs is highlighted, which indicates that the permeability of MK based mortars is mostly controlled by capillary pores, while gel pores significantly affect the permeability of BFS based mortars.

Keywords: Alkali-activated materials, granulated blast furnaces slag, metakaolin, water permeability, w/b ratio

1. INTRODUCTION

The performance of AAMs under several aggressive conditions has been intensively investigated such as acid attack, carbonation, chloride penetration, and efflorescence [1]. These degradation processes are caused by the mass transport of aggressive liquids, gases and ions from external environment through the material matrix [2, 3]. As a result, the degradation of materials is significantly affected by the transport properties, which define how fast the mass transport through the pore structure could be. Besides diffusivity, under an advective regime,

permeability is the key parameter to assess the durability of construction and building materials exposed to an aggressive environment [4, 5].

Unlike classical cementitious materials with a numerous studies on the permeability, the permeability data for AAMs is limited based on our knowledge [4, 6]. Furthermore, such reported permeability is also incomparable, stretching in a large range with water permeability coefficient k (hereafter expressed as hydraulic conductivity) from 10^{-3} - 10^{-4} m/s in alkali-activated concretes (with coarse aggregate) to 10^{-9} - 10^{-13} m/s in alkali-activated mortars, due to the variety in examined precursors, activators, w/b ratio, and curing time [4, 7-10]. Probably the reported permeability for alkali-activated concretes is too high due to uncertainty in measurements (e.g. leaking) or the coarse aggregates are permeable. Specially, even with the similar material parameters, the permeability results are still different because of the difference in methods used to determine the permeability as illustrated by the permeability measurement on alkali-activated slag (AAS) using head constant pressure (direct method) reported by Shi compared to using beam-bending method in Blyth and Vichit's studies [4, 7, 11]. Therefore, there is a need to perform a comprehensive study on permeability of AAMs to provide additional data complimentary with the available data to build a permeability dataset for these newly developed materials. A short review of water permeability of AAMs is presented below in order to have an overview of the permeability of AAMs in comparison with OPC system.

1.1. Existing water permeability data of AAMs

Several studies have been conducted on the water permeability of AAMs as summarized in Table 1. The study of Shi et al. is considered as one of the first intensive research on permeability of AAMs in general and alkali-activated slag (AAS) in particular [7]. He measured the water permeability on OPC and AASs activated by sodium silicate/sodium carbonate using a head constant pressure. The results indicated that both AAS types had a lower water permeability than OPC. The permeability were 10^{-14} and 10^{-13} m/s for sodium silicate activated BFS, sodium carbonate activated BFS, respectively, compared to 5×10^{-10} m/s for OPC sample. The lower permeability of AAS compared to OPC was also reported by Mithun [12]. However, few other studies showed a higher permeability in AAS than in OPC [13, 14]. It might be explained by the specific pore structure of examined materials, which directly controlled the permeable capacity. The pore structure of AAMs is not only affected by the water to binder ratio (w/b), but also by various factors including the precursor behaviours, activators, curing conditions. Therefore, it has been reported that the AAMs produced from low-calcium precursors such as fly ash and metakaolin (geopolymers) have elucidated a higher water permeability than OPC [8, 10], which is attributed to the more porous structure of these geopolymers compared to OPC matrix with the same w/b ratio.

Two main factors influencing the gel structure of materials and thereby the water permeability are the precursors used and the water to binder ratio. In terms of precursor, as shown in Table 1, N-A-S-H gel, which is formed by the activation of fly ash or metakaolin results in a higher water permeability due to its more porous structure compared to the one of C-A-S-H gel formed by the activation of slag. In the alkali-activated slag/fly ash blended materials, the increase of fly ash substitution leads to increase porosity and reduces tortuosity (because of more N-A-S-H is formed) as shown in the studies of Gao and Provis [15, 16]. Ismail also reported that fly ash content significantly affects the volume of permeable voids (VPV) of alkali-activated slag/fly ash blended mortars. The results showed that there is a limited change of VPV when fly ash content is lower than 50%, but VPV is significantly increased when the fly ash content exceeds 50% [17]. Besides, water permeability is remarkably influenced by w/b ratio. Higher w/b ratio leads to a larger permeability due to the larger pore volume and pore

size. The increase of w/b ratio in low-calcium fly ash based geopolymers results in a higher VPV and thereby a higher the water permeability. With low w/b ratios between 0.20 – 0.23, Olivia revealed that the permeability coefficient is in the range from 2.46×10^{-11} to 4.67×10^{-11} m/s corresponding to the VPV varying from 8.2% to 13% [18]. In case of geopolymer concrete produced from blends of rice husk-bark ash and fly ash, it exhibits a reasonably high water permeability of 6.79×10^{-9} m/s for w/b ratio of 0.82 [8]. Besides, the water permeability is also affected by the interfacial transition zone (ITZ) between the matrix and aggregates. Ismail reported a higher VPV, thereby the permeability, of alkali-activated slag/fly ash blended concretes than mortars despite the fact that the paste volume fraction of mortars is higher than the one of concrete [17]. This implies that a coarser ITZ in concretes compared to mortars. Additionally, other factors such as curing time and temperature also may contribute to the permeability of AAMs like OPC because these factors affect the development of pore structure as well as the formation of cracks during polymerization, which significantly influence the water transport [19].

Table 1: A summary of water permeability of AAMs reported in literatures

Precursors	Types of materials	w/b ratio	Curing time, days	Permeability (m/s)	Ref.
Rice husk-bark ash + fly ash	Concrete, (Fine aggregate)	0.6-0.8	28, 90	$10^{-10} \div 6\times10^{-9}$	[8]
BFS	mortar	0.485	7, 28	$\sim10^{-13}$	[7]
Fly ash	mortar	0.4	7, 28, 90, 180	$10^{-13} \div 10^{-10}$	[10]
Metakaolin (MK) BFS MK+BFS	concrete	0.38 0.6 0.4	7	BFS's: $1.3 \times10^{-3} \div 3\times10^{-4}$ MK's: $1.4 \times10^{-3} \div 3\times10^{-4}$ (MK+BFS)'s: $1.6 \times10^{-3} \div 4\times10^{-4}$	[13]
Fly ash	concrete	0.35 0.40 0.45	7	$2\div 6 \times10^{-3}$	[9]
Fly ash	concrete	0.3	7	$0.6 \div 1.3 \times10^{-3}$	[20]
Fly ash (high calcium)	concrete	0.45	7	$0.7 \div 1.2 \times10^{-3}$	[21]

1.2 The current state and perspectives

Despite the importance of water permeability to evaluate durability of AAMs, there is only a limited dataset on permeability available as discussed above. The existing data is also not consistent and does not allow to establish any correlation between water permeability and gel/micro structure (e.g. porosity, pore size, tortuosity) as the case of cementitious materials [22, 23]. Therefore, there is a need to perform comprehensive studies and provide additional datasets which allows to correlate the microstructure and permeability of AAMs.

Most of existing techniques to measure permeability of cementitious materials could be used for AAMs as their similar characteristics with respect to the transport of fluids. The direct method with a constant water head pressure commonly used for OPC systems could be a relevant method for geopolymers because of the consistently obtained permeability on both

OPC materials and AAMs [6-8, 10]. Recently, beam-bending technique has been used to study on AAS and showed the similar permeability to OPC and lower values compared to AAS measured by the direct method in other studies [4]. The difference in permeability due to using various techniques once again elucidates the necessity of building a dataset for AAMs' permeability, which can be used as an important input for the prediction of durability of AAMs.

Considering limited dataset of AAM permeability available in literature, the main objective of the present study is to improve the knowledge on the effects of w/b and precursors on the permeability of AAMs. A novel constant flow was used to determine the permeability of AAS and alkali-activated metakaolin with different w/b ratios (i.e. 0.35-0.55 for AAS and 0.75-0.95 for alkali-activated metakaolin). Furthermore, the pore structure accessed by nitrogen adsorption are highlighted and used to correlate with the water permeability AAMs.

2. MATERIALS AND TEST SETUP

2.1. Raw materials and mixtures

The chemical compositions of BFS and MK used in the study are shown in **Table 2**. Sodium hydroxide 10 N and sodium trisilicate solution with 64.25% water were used as an activating solution. The fine river sand (d_{max} = 2 mm) was used as a small fraction of 20% by volume. Tap water was used for mixing in this study. Three w/b ratios of 0.35, 0.45, 0.55 and 0.75, 0.85, 0.95 were investigated of AAS and MK-based geopolymers, respectively. Note that such w/b ratios were chosen in the context of immobilisation of radioactive liquid wastes, which is not discussed in this study. The binders here are referred to the total amount of precursor, solid sodium trisilicate and sodium hydroxide. The mix designs are presented in **Table 3**.

AAS and MK-based geopolymers specimens were produced by mixing BFS/MK with the activating solution, additional water and sand in a mortar mixer within around 10 minutes. The fresh geopolymers were then cast in cylindrical PVC tubes with the inner diameter of 97.5 mm. Herein, BFS 0.35, BFS 0.45, and BFS 0.55 denote for alkali-activated slag with w/b of 0.35, 0.45, and 0.55; while MK 0.75, MK 0.85, and MK 0.95 denotes for MK-based geopolymers with w/b of 0.75, 0.85, and 0.95, respectively. After casting, the specimens were sealed and cured at temperature of 20°C and relative humidity of 95% in a curing bench for 28 days.

Table 2: Chemical composition of BFS and MK (wt.%)

Oxides	SiO_2	Al_2O_3	Fe_2O_3	CaO	MgO	K_2O	Na_2O	TiO_2	SO_3	LOI
BFS	32.4	11.1	0.60	43.40	7.77	0.53	0.27	1.01	2.41	2.08
MK	52.08	44.27	0.45	0.03	0.08	0.17	0.26	1.68	0.03	0.83

Table 3: Mix compositions of BFS and MK-based geopolymers

w/b	BFS	MK	Silicate solution	Sodium solution	Additional water	Sand
	kg/m^3	kg/m^3	kg/m^3	kg/m^3	kg/m^3	kg/m^3
0.35	955.5		63.3	249.4	109.0	519.4
0.45	863.6		57.2	225.4	190.6	519.4
0.55	790.1		52.3	206.2	258.7	519.4
0.75		863.6	637.9	389.8	127.7	519.4
0.85		790.1	583.6	356.7	222.0	519.4
0.95		735.0	542.9	331.8	304.2	519.4

2.2. Water permeability measurements

After 28 day curing, the samples were cut into small disks with the thickness of 25 mm by a diamond saw. The specimen were then saturated under vacuum water within 24 hours before embedding into a permeability cell. The sample preparation for the testing is described in details in a previous study on cement-based materials [6]. A photo and a schematic view of the experimental setup are shown in **Figure 1**.

a) **b)**

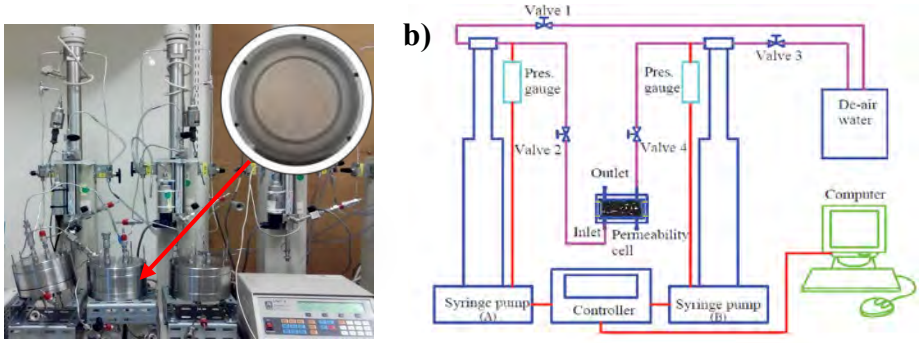

Figure 1: A picture (a) and schematic view (b) of permeability setup adapted from [24]

The testing procedure started from checking the leakage as well as removing entrapped air between lids and embedded samples by applying a water flow on each side of the permeability cell. Then, a pressure gradient was applied, which depends on each types of examined samples and their w/b ratios in order to ensure a high flow rate for high accuracy measurement but not create cracks in the samples due to high applied pressure. In all cases, the applied pressure was lower than 5 bar. Once a stable in-flow was achieved under a constant applied pressure, the testing system was switched to constant flow mode, and pressure was monitored until the difference in pressure between 2 measurements within 24 hours is smaller than 10%. The average pressure recorded within the last 24 hours was then used to calculate the water permeability coefficient using Darcy's law as follows [25].

$$K_w = \frac{Q \times H \times g \times \rho}{(A \times dP)}$$

where K_w= water permeability coefficient, m/s; Q = rate of water flow, m^3/s; H = thickness of the specimen, 0.025 m; g = acceleration due to gravity, 9.81 m^2/s; ρ = density of the water, 1000 kg/m^3; A = the area exposed to water, 0.007462 m^2 (with diameter of 0.0975 m); dP = average pressure gradient, Pa.

2.3. Characterization of microstructure

Nitrogen adsorption technique was used to define the specific surface area and quantify the pore sizes in the range from 3 to 70 nm. Samples after 28 days of curing were freeze-dried and then sieved at 500-800 µm before testing. The measurement was carried out with the TriStar 3020 device at temperature of 77K. The specific surface area was quantified by using BET method, which is applied to the adsorption isotherm, while the pore size distribution was

determined by the Barret-Joyner-Halenda (BJH) method for the desorption isotherm.

In addition, the water porosity was determined using a traditional saturation method.

3. RESULTS AND DISCUSSION

3.1. Water permeability results

The water permeability coefficients of examined AAMs are shown in **Figure 2**. As expected, the permeability decreases with the decrease of w/b ratios in both types of mortars activated from MK and BFS. Generally, higher w/b ratio results in a coarser pore structure of AAMs (i.e. higher porosity and larger pore size) [18, 26]. Especially, the capillary porosity, which controls the permeability of mortar due to composing of a plenty number of large and connected pores [10, 27], is also expected to be significantly increased with the increase of w/b ratio. Regarding to the influence of precursor, although the permeability of MK-based geopolymers is approximately 5 orders of magnitude higher than of AASs (i.e. 10^{-8} m/s compared to 10^{-13} m/s). The difference is attributed to not only the difference in precursor types but also the variation in w/b ratios. However, the latter is expected to largely contribute to permeability of the samples because much higher w/b ratios were used for activating MK than BFS.

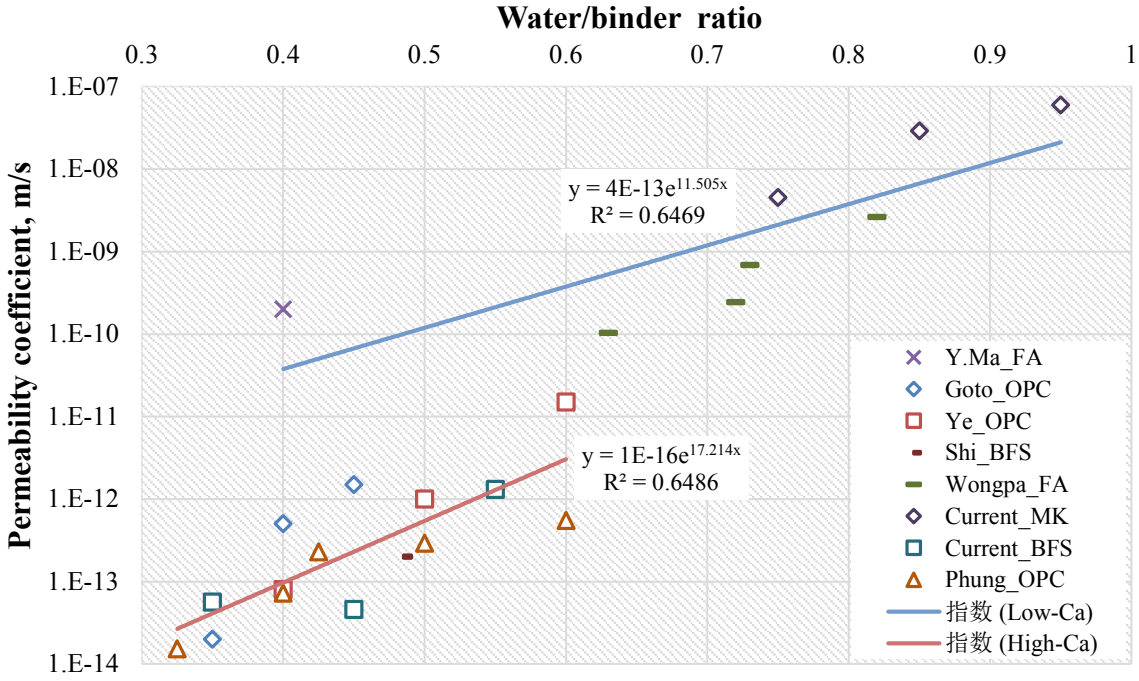

Figure 2: Water permeability of current AAMs and from literature

Figure 2 also shows the comparison of permeability measured in this study and data reported in the literature using direct methods [7, 8, 10, 27, 28]. In general, the current results are consistent with reported data, especially with AAS samples compared to results of Shi's study [7], which also examined with similar AASs and used a traditional testing method for permeability measurement. Besides, the permeability of AAS is very close to that of OPC materials, evidenced by a relatively high R^2 value of 0.65 for high calcium system including AAS and OPC (high-Ca). This indicates that the matrix of AAS can be as dense as that of OPC with the same w/b ratio. The results of obtained MK-based geoplymers are also in agreement with the data reported by Ma et al. and Wongpa et al. [8, 10], which examined with fly ash (FA) at a lower w/b range. There exhibits a slightly lower permeability of FA-based geopolymers

compared to MK-based geopolymers (this study), which can be attributed to the difference precursor behaviours such as its reactivity and pore size particles as well as the synthesis conditions leading to the difference in the extent of geopolymerization and thereby their pore structure. In addition, the higher Ca in FA than in MK may contribute to the denser structure of FA-based geopolymers compared to MK-based geopolymers [29]. Within a similar w/b ratio, it can be observed that the geopolymers produced from low-calcium precursors (e.g. MK and FA) exhibit a higher permeability than high-calcium ones (e.g. BFS). The difference can be up to 2-3 orders of magnitude depending on the w/b ratio. This can be explained by the more porous structure of N-A-S-H (from low-Ca precursors) compared to C-(A)-S-H structure produced from high-Ca precursors resulting in a higher porosity and lower tortuosity in N-A-S-H gel and higher VPV if BFS is substituted by FA in activated BFS/FA blend as reported in [15, 16].

3.2. Correlation between the water permeability and microstructure of AAMs

As mentioned above, the pore structure plays as a key role governing the water permeability of AAMs. Herein, the pore volume, pore size distribution, specific surface area (SSA), porosity obtained from N_2 adsorption tests are shown in Table 4. The pore volume, SSA and porosity as indicated here is mainly characterized for gel pores within the range of 3-70 nm. It is clearly shown in Figure 3 that the higher the w/b ratio of alkali-activated slag, the higher the pore volume. The water porosity, which is characterized for a wider pore size range, is also consistently increased with the increase of w/b ratio of AAS. The higher pore volume results in an increase in the water permeability which is consistent with the trend of permeability in all AASs discussed previously in section 1.1. Additionally, the pore size distribution of these samples slightly shifts to the larger pore size range with the increase of w/b ratio. The specific surface area obtained from BET method and porosity from BJH, presented in Table 4, also increase with the increase of w/b ratio.

Table 4: Summary results from N_2 adsorption and water porosity test

Samples	BFS 0.35	BFS 0.45	BFS 0.55	MK 0.75	MK 0.85	MK 0.95
SSA (BET), m^2/g	5	15	21	11	7	3
Porosity (BJH), %	2.4	3.6	6.5	5.2	3.3	2.1
Water porosity, %	29.5	33.0	37.2	45.5	46.0	50.2

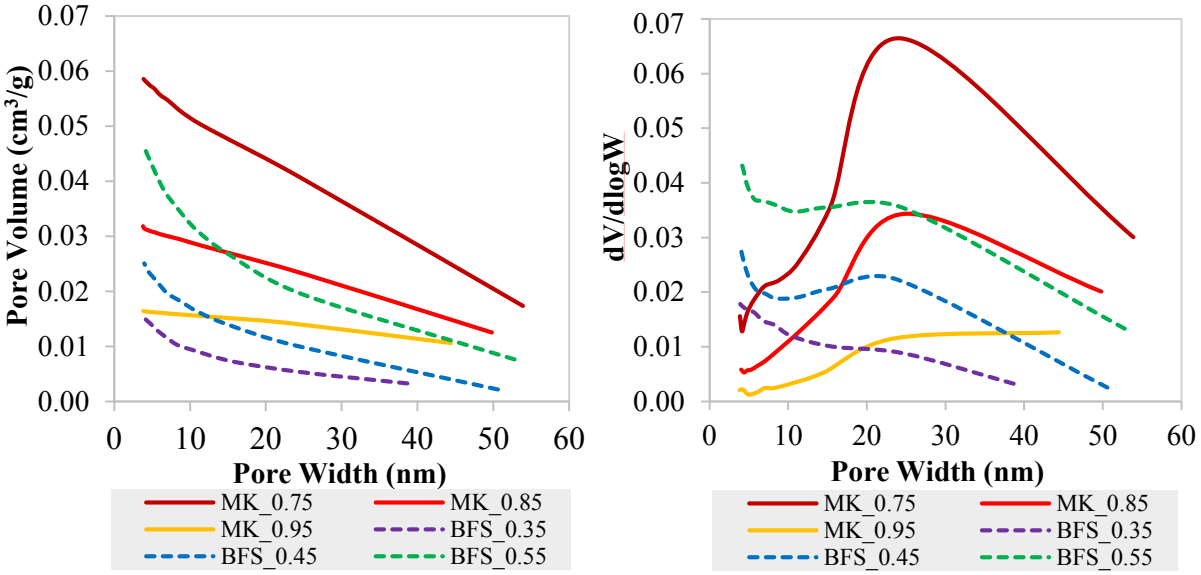

Figure 3: Pore volume (a) and pore size distribution (b) of AAMs determined by N_2 adsorption

In contrast to AAS, it is observed that the MK-based geopolymer with w/b ratio of 0.75 has the highest pore volume, SSA, and porosity (BJH), while showing the lowest water permeability. The permeability was 4.52×10^{-9}, 2.90×10^{-8}, 6.23×10^{-8} m/s for samples with w/b ratio of 0.75, 0.85, 0.95, respectively. The effect of w/b ratio on the microstructure of low calcium geopolymers is not consistently reported in the literatures. Maricela et al. [30] showed an increase in water porosity with the increase in w/b ratio of MK-based geopolymers with a low water content, while Oliver et al. [31] reported a reduction in the gel pore volume (smaller than 30 nm) with the increase of w/b ratio for MK/FA-based geopolymers with a low water content. In addition, an increase in water porosity with the increase of w/b ratio was observed for MK-based geopolymers with high water content. In this study, we also observed a higher water porosity for higher w/b ratio geopolymers. However, the higher the w/b ratio, the lower the BJH porosity as shown in Table 4. Perhaps in a higher water content system as the case in this study, the dissolution of precursor and the mobility of alkali are increased with the increase of w/b ratio resulting in a higher N-A-S-H gel formation, which reduces the porosity at nano-scale. However, more water in the system would increase the capillary pore volume in hardened geopolymers. Furthermore, the gel porosity is significantly smaller compared to the water porosity. Therefore, the water permeability of MK-based geopolymers may be dominated by capillary pores rather than gel pores detected by N_2 adsorption [10].

4. CONCLUSIONS

In this study, the influence of precursors (i.e. metakaolin and BFS) and w/b ratios on the water permeability of alkali-activated mortars were elucidated. The results show that both factors have a significant effect on the water permeability of AAMs. AAS mortar exhibits a similar permeability compared to OPC system indicating a similar pore structure for both types of materials with the same w/b ratio. Higher w/b ratio results in a larger gel pore volume and total porosity determined by saturation method for BFS-based activated mortars. N_2 adsorption also indicates that the permeability of AAS is significantly controlled by gel pores. The higher the gel pore volume, the larger the water permeability. In contrast, MK-based mortars show an increase in the gel pore with the increase of w/b ratio, though the water porosity is still higher with the higher w/b ratio in MK-based mortars. The water permeability of MK-based mortars is also followed the same trend (i.e. higher w/b ratio results in higher permeability) as for AAS mortars, however, the extent in changing permeability with w/b ratio is stronger for BFS compared to MK-based AMMs. This implies that the permeability of MK-based mortars is mostly controlled by capillary pores. However, further analysis on pore structure (on-going work), which covers a wider pore size ranges (e.g. combined with mercury intrusion porosimetry and scanning electron microscopy) is needed to confirmed this hypothesis.

ACKNOWLEDGEMENTS

This study has been funded by the Belgian Nuclear Centre (SCK CEN) and Institute for Radiological Protection and Nuclear Safety (IRSN).

REFERENCES

1. Hu, X., et al., *Compressive strength, pore structure and chloride transport properties of alkali-activated slag/fly ash mortars.* Cement and Concrete Composites, 2019. **104**.
2. Albitar, M., et al., *Durability evaluation of geopolymer and conventional concretes.* Construction and Building Materials, 2017. **136**: p. 374-385.
3. Hossain, M.M., et al., *Durability of mortar and concrete containing alkali-activated binder with pozzolans: A review.* Construction and Building Materials, 2015. **93**: p. 95-109.
4. Blyth, A., et al., *Impact of activator chemistry on permeability of alkali-activated slags.* Journal of the American Ceramic Society, 2017. **100**(10): p. 4848-4859.
5. Guang, Y., *The microstructure and permeability of cementitious materials. PhD thesis*, in *Delft University of Technology, Delft*. 2003.
6. Phung, Q.T., et al., *Determination of water permeability of cementitious materials using a controlled constant flow method.* Construction and Building Materials, 2013. **47**: p. 1488-1496.
7. Shi, C., *Strength, pore structure and permeability of alkali-activated slag mortars.* Cement and Concrete Research, 1996. **26**(12): p. 1789-1799.
8. Wongpa, J., et al., *Compressive strength, modulus of elasticity, and water permeability of inorganic polymer concrete.* Materials & Design, 2010. **31**(10): p. 4748-4754.
9. Tho-in, T., et al., *Pervious high-calcium fly ash geopolymer concrete.* Construction and Building Materials, 2012. **30**: p. 366-371.
10. Ma, Y., J. Hu, and G. Ye, *The pore structure and permeability of alkali-activated fly ash.* Fuel, 2013. **104**: p. 771-780.
11. Vichit-Vadakan, W. and G.W. Scherer, *Measuring Permeability of Rigid Materials by a Beam-Bending Method: III, Cement Paste.* Journal of the American Ceramic Society, 2002. **85**(6): p. 1537-1544.
12. Mithun, B.M. and M.C. Narasimhan, *Performance of alkali-activated slag concrete mixes incorporating copper slag as fine aggregate.* Journal of Cleaner Production, 2016. **112**: p. 837-844.
13. Sun, Z., X. Lin, and A. Vollpracht, *Pervious concrete made of alkali-activated slag and geopolymers.* Construction and Building Materials, 2018. **189**: p. 797-803.
14. Bernal, S.A., et al., *Effect of binder content on the performance of alkali-activated slag concretes.* Cement and Concrete Research, 2011. **41**(1): p. 1-8.
15. Gao, X., Q.L. Yu, and H.J.H. Brouwers, *Assessing the porosity and shrinkage of alkali-activated slag-fly ash composites designed applying a packing model.* Construction and Building Materials, 2016. **119**: p. 175-184.
16. Provis, J.L., et al., *X-ray microtomography shows pore structure and tortuosity in alkali-activated binders.* Cement and Concrete Research, 2012. **42**(6): p. 855-864.
17. Ismail, I., et al., *Influence of fly ash on the water and chloride permeability of alkali-activated slag mortars and concretes.* Construction and Building Materials, 2013. **48**: p. 1187-1201.
18. Olivia, M. and H. Nikraz, *Strength and Water Penetrability of Fly Ash Geopolymer Conrete.* Journal of Engineering and Applied Sciences, 2011. **6**(7): p. 70-78.
19. Zhang, J., et al., *Durability of alkali-activated materials in aggressive environments: A review on recent studies.* Construction and Building Materials, 2017. **152**: p. 598-613.
20. Zaetang, Y., et al., *Use of coal ash as geopolymer binder and coarse aggregate in pervious concrete.* Construction and Building Materials, 2015. **96**: p. 289-295.
21. Sata, V., A. Wongsa, and P. Chindaprasirt, *Properties of pervious geopolymer concrete using recycled aggregates.* Construction and Building Materials, 2013. **42**: p. 33-39.
22. Phung, Q.T., et al., *Determination of water permeability of cementitious materials using a controlled constant flow method.* Construction and Building Materials, 2013. **47**(0): p. 1488-1496.
23. Phung, Q.T., et al., *Water permeability of cementitious materials: outstanding issues on measurement and modelling approaches*, in *2nd International RILEM/COST Conference on*

Early Age Cracking and Serviceability in Cement-based Materials and Structures EAC-02. 2017: Brussels, Belgium. p. 521-526.
24. Phung, Q.T., et al., *Effect of limestone fillers on microstructure and permeability due to carbonation of cement pastes under controlled CO2 pressure conditions.* Construction and Building Materials, 2015. **82**: p. 376-390.
25. Q.T. Phung, N.M., D. Jacques, G. De Schutter, G. Ye, *Effects of W/P ratio and limestone filler on permeability of cement pastes*, in *International RILEM Conference on Materials, Systems and Structures in Civil Engineering*. 2016.
26. Okada, K., et al., *Water retention properties of porous geopolymers for use in cooling applications.* Journal of the European Ceramic Society, 2009. **29**(10): p. 1917-1923.
27. Phung, Q.T., et al., *Investigation of the changes in microstructure and transport properties of leached cement pastes accounting for mix composition.* Cement and Concrete Research, 2016. **79**: p. 217-234.
28. Ye, G., P. Lura, and K. van Breugel, *Modelling of water permeability in cementitious materials.* Materials and Structures, 2006. **39**(9): p. 877-885.
29. Dombrowski, K., A. Buchwald, and M. Weil, *The influence of calcium content on the structure and thermal performance of fly ash -based geopolymers.* Journal of Materials Science, 2006. **42**(9): p. 3033-3043.
30. Lizcano, M., et al., *Effects of Water Content and Chemical Composition on Structural Properties of Alkaline Activated Metakaolin-based Geopolymers.* Journal of the American Ceramic Society, 2012. **95**(7): p. 2169-2177.
31. Vogt, O., et al., *Reactivity and Microstructure of Metakaolin -based Geopolymers: Effect of Fly Ash and Liquid/Solid Contents.* Materials (Basel), 2019. **12**(21).

CHLORIDE DIFFUSION OF ALKALI-ACTIVATED FLY ASH/SLAG CONCRETE

Jingxiao Zhang (1)(2), Yuwei Ma (1)(2), Jiazheng Zheng (1)

(1) Guangzhou University - Tamkang University Joint Research Centre for Engineering Structure Disaster Prevention and Control, Guangzhou University, China

(2) Centre for Future Materials, University of Southern Queensland, Australia

(3) School of Materials Science and Engineering, South China University of Technology, China

Abstract

The widespread application of alkali-activated fly ash/slag (AAFS) concrete requires satisfaction of a series of performance criteria both from its early age properties (e.g. workability, strength) and long-term stability. In this study, long-term (till 180 days) natural chloride diffusion tests were conducted to evaluate the chloride diffusion in AAFS concretes prepared with different slag content, water-binder (w/b) ratio, alkali content, and sand-aggregate ratio. The results revealed that the free chloride diffusion coefficient (D_f) of AAFS concretes was between 0.4-1.8×10^{-12} m^2/s. The slag content and w/b were found as dominant parameters affecting the long-term chloride transport in AAFS concretes, while the sand-aggregate ratio presented a limited effect. MIP results indicated that capillary pores in AAFS reached percolation and became disconnected after 180 days. The long-term chloride diffusivity of AAFS concretes was closely related to the threshold pore diameter and volume of pores > 5 nm. The more larger pores, the higher chloride diffusion coefficient was.
Keywords: Alkali-activated concrete, Natural chloride diffusion tests, Chloride diffusion coefficient, Pore structure

1. INTRODUCTION

Alkali-activated materials (AAMs), manufactured by the reaction between alkaline activator and solid aluminosilicate powders, i.e. fly ash (FA), ground granulated blast furnace slag (GGBFS) and calcined clay, have attracted much interest in academic and industrial fields over the past decades [1, 2]. AAMs present comparable mechanical properties and considerably lower CO_2 emission, thus are regarded as a promising alternative to ordinary Portland cement (OPC) [3-5]. To overcome the shortcomings of AAMs based on single raw material, alkali-activated fly ash/slag binary system (AAFS) is proposed to satisfy the performance criteria for concrete, and this binary system is also applied in real construction in Australia. Except for

early age properties, another technical issue that raises wide concern is the chloride resistance of AAFS and its efficient to protect steel bars in reinforced AAFS concrete.

This study presents a comprehensive investigation on the chloride diffusion of AAFS concretes with different mixing parameters by using natural chloride diffusion test at long term (till 180 days). Chloride transport was assessed according to the free chloride diffusion coefficient (Df). The effects of various parameters, including slag content, water–binder ratio, alkali content, and sand–aggregate ratio, were evaluated. The pore structures of AAFS mixtures were characterized by mercury intrusion porosimetry (MIP). Then, the relationship of pore structures and chloride diffusion properties was discussed.

2. MATERIALS AND METHODS

2.1 Materials

Fly ash (Zhongshan Power Station, Guangdong, China) classified as Class F according to ASTM C618, and ground granulated blast furnace slag (Shaoguan Steel Group Company Limited, Guangdong, China) were used as solid precursors to manufacture AAFS concrete. The chemical compositions of FA and GGBFS determined by XRF techniques are listed in Table 1.The alkaline activator used in this study was a mixture of NaOH and sodium silicate solution. Analytic grade NaOH pellets were dissolved in distilled water to prepare NaOH solution. NaOH solution, sodium silicate solution (Na_2O = 82.19 wt.%, SiO_2 = 28.18 wt.%) and tap water were then mixed in proportions to prepare alkaline activator solution with different Na_2O and SiO_2 contents. The alkaline activator was prepared 24 hours before concrete casting. Natural river sand with a maximum size of 0.5 mm was used as fine aggregates. Coarse aggregates were prepared by mixing crushed basalt with medium size (10–20 mm) and small size (5–10 mm) in a ratio of 60:40.

Table 1: Chemical composition of FA and GGBFS

	SiO_2	Al_2O_3	CaO	Fe_2O_3	MgO	SO_2	Na_2O	K_2O	LOI
FA	50.59	25.55	9.84	6.92	1.12	1.12	1.45	1.19	2.22
GGBFS	34.36	16.89	38.13	0.36	6.23	2.3	0.24	0.41	1.08

AAFS concretes with different slag content, w/b, Na_2O content and sand-aggregate ratio were prepared in a single horizontal shaft concrete mixer. Table 2 presents the mixture proportions of AAFS concretes, which (Table 2) were denoted as: slag% (SL), w/b (W), Na_2O% (N) and sand-aggregate ratio (S). Na_2O content was designed as low as possible with the consideration of concrete cost. The unit weight of AAFS concrete was designed in the range of 2350-2450 kg/m^3 and the binder content was 400 kg/m^3. Firstly, sand, coarse aggregates and precursor materials (FA and GGBFS) were dry-mixed for 2 mins. Subsequently, the alkaline activator was added into the mixture and mixed for another 2 mins. Fresh concrete was then cast into cube moulds (100 mm × 100 mm × 100 mm). After 24 hours curing at 20 °C, specimens were cured in a curing chamber (relative humidity of 95% and temperature of 20 °C ± 2°) before tests.

Table 2: Mixture proportions of AAFS concrete

Sample	FA	GGBFS	Na_2O[b]	SiO_2[b]	Sand	CA	w/b	s/a
SL30	**280**	**120**	4%	6%	720.3	1080.4	0.45	0.40
SL50[a]	**200**	**200**						
SL70	**120**	**280**						
SL100	**0**	**0**						
W40	200	200	4%	6%	720.3	1080.4	**0.40**	0.40
W45[a]							**0.45**	
W50							**0.50**	
N4	200	200	**4%**	4%	720.3	1080.4	0.45	0.40
N5			**5%**					
N6			**6%**					
S36	200	200	4%	6%	648.3	1152.5	0.45	**0.36**
S38					684.3	1116.5		**0.38**
S40[a]					720.3	1080.4		**0.40**
S42					756.3	1044.5		**0.42**
S44					792.3	1008.5		**0.44**

[a] SL50, W45 and S40 are the same mix proportion

[b] $Na_2O\% = Na_2O/(FA + GGBFS)$ (%) and $SiO_2\% = SiO_2/(FA + GGBFS)$ (%)

2.2 Methods

Natural diffusion test was performed according to a slightly modified form of ASTM C1543. After curing for 28 days, surfaces of AAFS concrete specimens were sealed with water-resistant paraffin wax and only the bottom surface was exposed to the testing solution to ensure one-dimensional diffusion [6]. Subsequently, sealed specimens were immersed in 3.5% NaCl solution for another 90 and 180 days. The solution was renewed every 30 days, and the container was sealed with a lid to avoid water evaporation. At the end of each testing age, concrete specimens were taken out from NaCl solution and ground into powder layer by layer. After removing the surface paraffin wax, concrete specimens were fixed on the DRB-H1 concrete grinding machine. 10 layers were ground for each concrete specimen and each layer was kept in 2 mm. The grinded powder was then sieved with a 0.6 mm sieve-mesh, dried in an oven (55 °C ± 5°) for 2 hours, and put in a desiccator to cool to 20 °C [7]. For statistical reliability, 3 × 2 specimens were ground to powder for each concrete mixture with two testing ages (90 days and 180 days).

After that, the free chloride content of grinded powder was measured in accordance with JTJ270-98. 2 g concrete powder (*G*) was put in 50 ml distilled water (*V1*). After shaking for 20 min and standing for 24 hours, suspension liquid was filtered. Subsequently, 20 ml filtered solution (*V2*) was pipetted into an Erlenmeyer flask with 2 drops of phenolphthalein. Diluted H_2SO_4 solution was then used to neutralize until the solution became colorless. Afterwards, 10 drops of K_2CrO_4 solution were added and 0.02 mol/L $AgNO_3$ solution was used to titrate until the solution become red. The volume of consumed $AgNO_3$ solution (*V3*) was recorded. The free chloride content was calculated based on Equation 1 [7]:

$$C = \frac{C_{AgNO_3} V_3 \times 0.03545}{G \times \frac{V_2}{V_1}} \times 100\% \qquad (1)$$

Where:

C is free chloride content in concrete powder; C_{AgNO3} is content of $AgNO_3$ solution, 0.02 mol/L; *G* is weight of concrete powder, 2 g; V_1 is volume of water used to dissolve concrete powder, 50 ml; V_2 is volume of filtrate, 20 ml; V_3 is volume of $AgNO_3$ solution for titration. For statistical reliability, each grinded powder was assessed three times; and the average result was calculated.

The D_f was determined by fitting Fick's second law as expressed in Equation 2 to the measured free chloride profile:

$$C(x,t) = C_0 + (C_S - C_0)\left(1 - \mathrm{erf}\left(\frac{x}{2\sqrt{Dt}}\right)\right) \quad (2)$$

Where:

$C(x,t)$ is chloride content at depth x and time t; C_0 is initial chloride content of the concrete; C_s is chloride content at exposure surface; *erf* is error function.

MIP was used to determine the total porosity and pore size distribution of AAFS mortar specimens. Mortar with a size of 2 mm × 2 mm × 2 mm was obtained from concrete specimens (after immersion for 180 days). Coarse aggregates were eliminated and the mortars were then immersed in ethanol for 2 weeks to stop further reaction. Afterwards, mortar samples were put in freeze-dryer for another 2 weeks of drying process. Micrometritics Poresizer 9500 was applied for the MIP measurement (0.485 N/m, 130°).

3. RESULTS AND DISCUSSION

3.1 Chloride diffusion

Figure 1 shows the D_f of AAFS concrete with different FA/GGBFS, w/b, Na_2O content and sand-aggregate ratio after 90 and 180 days of immersion. The w/b exhibited the most prominent effect on the D_f of AAFS concretes. As shown in Figure 1, the D_f increased from 1.1×10^{-12} m^2/s to 3.2×10^{-12} m^2/s as the w/b increased from 0.4 to 0.5 at 90 days. Such results were different from the findings in AAS concrete [8], where they claimed that excess water was not affecting the pore structure and chloride penetration. However, in their study [8], a considerably higher w/b (from 0.55 to 0.7) and higher NaCl concentration (165 g/L) were applied, under which condition the real D_f cannot be correctly reflected. In fact, the extra water in the alkaline activator acted as capillary pores in the concrete matrix, particularly around the ITZ [9, 10]. At longer age (180 days), the D_f of W50 reduced to 1.3×10^{-12} m^2/s, indicating a significantly pore refinement between 90 to 180 days.

For AAFS concrete with higher slag content, the D_f decreased from 1.8×10^{-12} m^2/s (SL30) to 0.4×10^{-12} m^2/s (SL100), which was consistent with the findings from previous researches [11-13]. Compared with N-A-S-H gels, C-A-S-H gels could incorporate water into their crystalline structure during hydration process [14]. As a result, pores were filled and the chloride resistance of AAFS concrete was improved. However, the decrease of D_f was more pronounced with age for SL30 and SL50, which indicated that after 90 days, the continuous reaction of AAFS concrete was dominated by fly ash.

The D_f of AAFS concretes gradually decreased with increased Na_2O content. Such findings were different from the results by Babaee and Castel [11], in which they noted increasing Na_2O content increased the D_f of AAFS. They ascribed it to the high alkaline environment that hinder the diffusion of calcium from slag. However, in their experiments, the SiO_2 content increased

as the Na_2O content increased in order to keep a constant modulus (SiO_2/Na_2O). The SiO_2 content is known to decrease the overall pH of activator, leading to a lower degree of reaction. With a constant SiO_2 content, higher Na_2O content was expected to promote a more rapid dissolution of raw materials and reduce chloride transport in AAFS. However, the effect of Na_2O content was relatively small compared with FA/GGBFS and w/b.

Compared with other parameters, the sand-aggregate ratio had no significant effect. AAFS concrete with different sand-aggregate ratio presented similar D_f both at 90 days and 180 days, which is consistent with the findings in prior work [15].

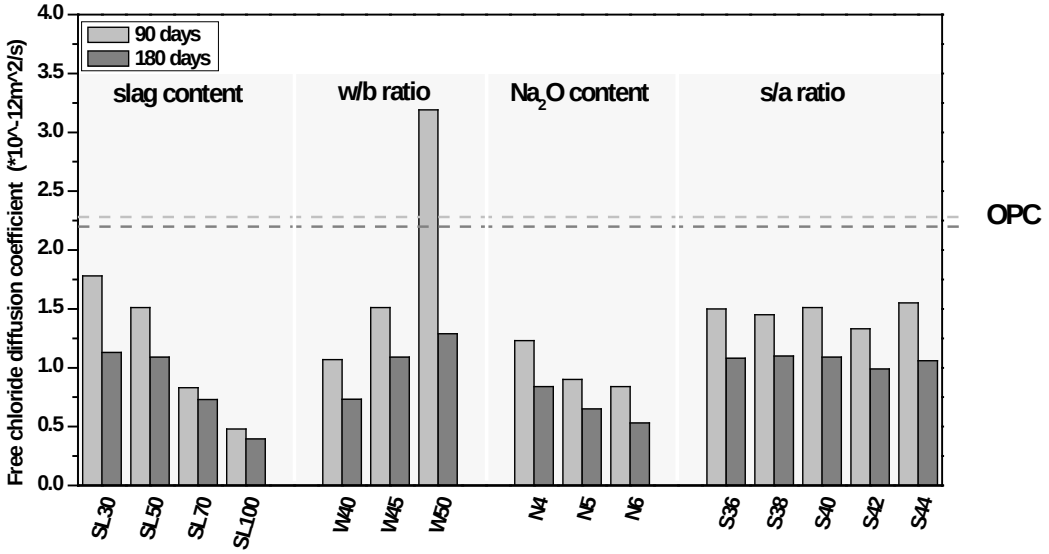

Figure 1: Free chloride diffusion coefficients of AAFS concrete with different FA/ GGBFS, w/b, Na_2O content and sand-aggregate ratio after 90 and 180 days of immersion

3.2 Pore structure

Figure 2 presents the pore size distribution and differential pore size distribution of AAFS mortar with different slag content, w/b and Na_2O content at the age of 180 days. Generally, AAFS with higher slag content, lower w/b and higher Na_2O content showed lower total porosity. However, SL50, SL70 and SL100 (Figure 2A), W40 and W45 (Figure 2B), N4 and N5 (Figure 2C) presented similar total porosity. Therefore, further study and discussion are required

The peak in differential curve was also corresponded to pore system in AAFS. In view of the ion diffusion characteristic, the pore diameter corresponding to the peak (also known as threshold pore diameter) was regarded as the minimum diameter of pores that form a continuous network throughout materials [16]. AAFS mixtures with lower threshold pore diameter had a smaller and denser pore system under the similar total porosity. For example, SL50 displayed a distinct peak at larger pore diameter (20 nm), while the peaks for SL70 and SL100 were at 4 nm (SL70 had bimodal curve) (Figure 2a). W40, with w/b of 0.4, presented two peaks at 5 nm and 15 nm, while W45 exhibited only one peak at around 20 nm (Figure 2b). N4 presented two peaks at 5 nm and 10 nm, while N5 exhibited only one peak at around 5 nm (Figure 2c).

From the above analyses, the pore structure of AAFS was closely related not only to total porosity, but also to threshold pore diameter. AAFS mixtures with higher slag content, lower

w/b and higher Na_2O content showed lower total porosity and/or lower threshold pore diameter, which means they had more excellent pore structure.

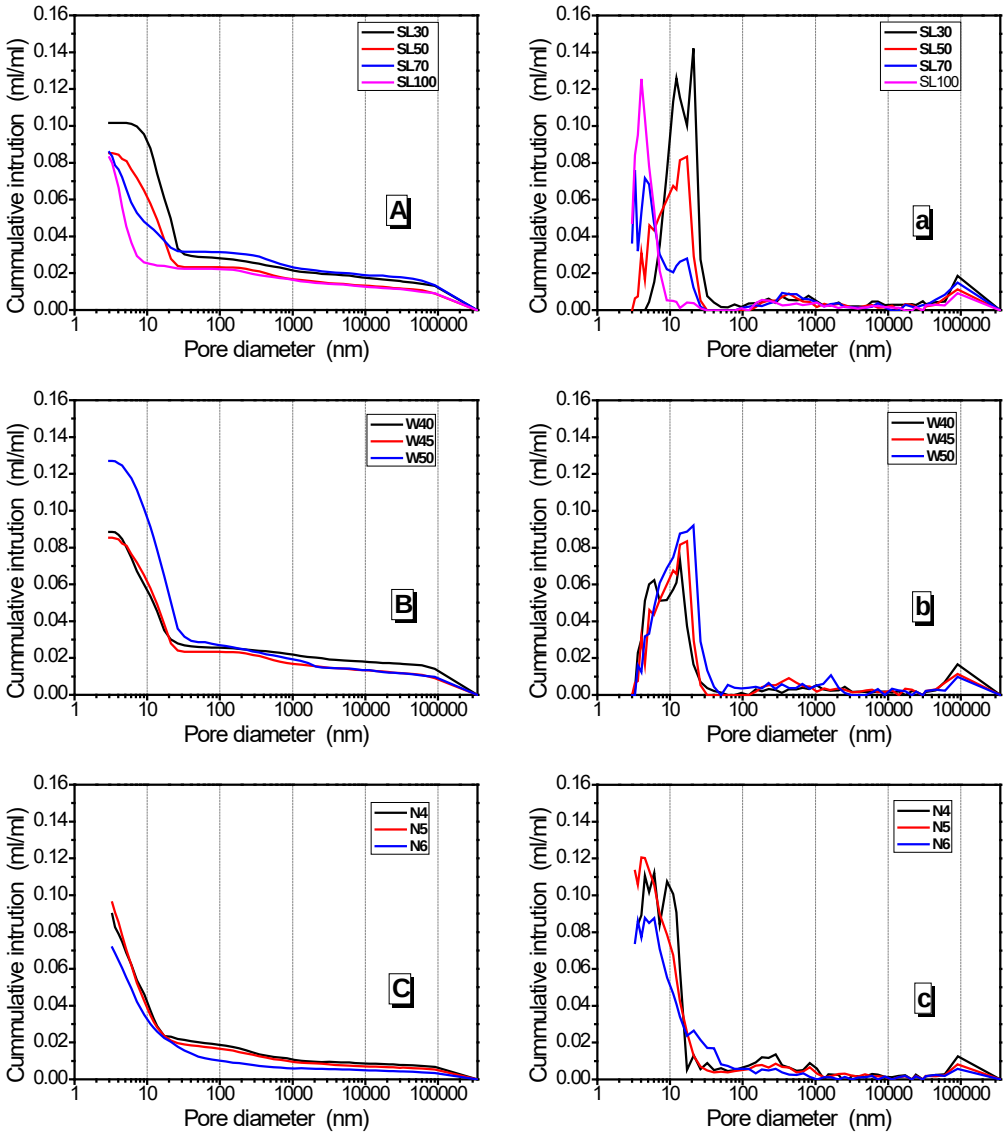

Figure 2: Porosity and pore size distribution with different FA/GGBFS (A), w/b (B) and Na_2O content (C) at 180 days

3.3 Pore structure vs. chloride diffusion

The D_f of AAFS depended not only on total porosity, but also on pore size distribution. It was observed that total porosity could not fit well with the D_f (Figure 3a), while a good correlation was obtained between the D_f and porosity of pores larger than 5 nm (Figure 3b). It was reported by Powers et al.[17] that capillary pores (pores > 10 nm) were regarded as disconnected when the capillary porosity reduced to 18%-20%. It implied that the transportation of ions in material was mainly depended not only on capillary pores, but also on a part of gel pores. Therefore, the threshold pore diameter of gel pores became vital to the ion transportation.

In this study, all the AAFS mixtures had total porosity lower than 18% (Figure 3a), and the minimum threshold pore diameter was around 5 nm. It is likely that capillary pores and gel pores larger than 5 nm contributed to ion transportation in AAFS. Therefore, the D_f exhibited a well correlation with the pores larger than 5 nm.

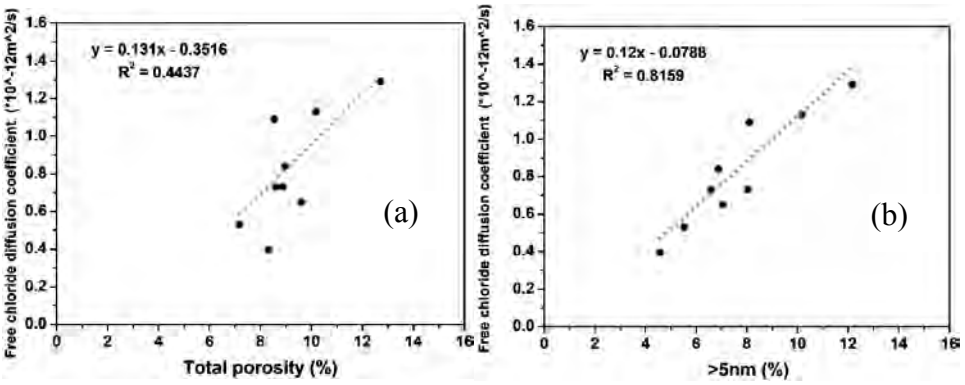

Figure 3: Relationship between free chloride diffusion coefficient (D_f) and total porosity (a); free chloride diffusion coefficient (D_f) and porosity of pores larger than 5 nm (b).

4. CONCLUSIONS

This study investigated the chloride diffusion and pore structure of AAFS concretes prepared with different parameters, including FA/GGBFS, w/b, Na_2O content and sand-aggregate ratio. Then the relationship between pore structure and chloride diffusion was explored. The main conclusions from the experimental work can be summarized as follows:

1. FA/GGBFS and w/b had a more prominent effect on the chloride diffusivity resistance of AAFS concretes than the effect of Na_2O and sand-aggregate ratio both at 90 days and 180 days. More C-A-S-H gels (by increasing slag content) and lower w/b (≤0.45) were preferred for durable AAFS concretes. The D_f gradually increased with increasing Na_2O content, while sand-aggregate ratio had no obvious effect.
2. AAFS mixtures with higher slag content, lower w/b and higher Na_2O content showed lower total porosity and/or lower threshold pore diameter, which means achieving more excellent pore structure
3. At 180 days, the capillary pores in AAFS reached its percolation and became disconnected. The chloride transportation was mainly depended on capillary pores and a part of gel pores. Therefore, the D_f of AAFS was closely related to the volume of pores > 5 nm.

ACKNOWLEDGEMENTS

The authors thank the Pearl River S&T Nova Program of Guangzhou (201806010004), Australian Research Council Discovery Project (1006016), National Natural Science Foundation of China (51561135012) and State Key Laboratory of Silicate Materials for Architectures Foundation (SYSJJ2017-05) for funding the project.

REFERENCES

[1] M.A. Longhi, B. Walkley, E.D. Rodríguez, A.P. Kirchheim, Z. Zhang, H. Wang, New selective dissolution process to quantify reaction extent and product stability in metakaolin-based geopolymers, Composites Part B: Engineering 176 (2019) 107172.

[2] N. Li, C. Shi, Z. Zhang, H. Wang, Y. Liu, A review on mixture design methods for geopolymer concrete, Composites Part B: Engineering (2019) 107490.

[3] Y. Ma, X. Yang, J. Hu, Z. Zhang, H.J.C.P.B.E. Wang, Accurate determination of the "time-zero" of autogenous shrinkage in alkali-activated fly ash/slag system, 177 (2019) 107367.

[4] G. Liang, H. Zhu, Z. Zhang, Q. Wu, J. Du, Investigation of the waterproof property of alkali-activated metakaolin geopolymer added with rice husk ash, Journal of Cleaner Production 230 (2019) 603-612.

[5] Z. Zhang, Y. Zhu, T. Yang, L. Li, H. Zhu, H. Wang, Conversion of local industrial wastes into greener cement through geopolymer technology: a case study of high-magnesium nickel slag, Journal of cleaner production 141 (2017) 463-471.

[6] C. Hall, Water movement in porous building materials—I. Unsaturated flow theory and its applications, Building and Environment 12(2) (1977) 117-125.

[7] Y. Wang, Y. Cao, P. Zhang, Y. Ma, T. Zhao, H. Wang, Z. Zhang, Water absorption and chloride diffusivity of concrete under the coupling effect of uniaxial compressive load and freeze–thaw cycles, Construction and Building Materials 209 (2019) 566-576.

[8] D. Bondar, Q. Ma, M. Soutsos, M. Basheer, J.L. Provis, S. Nanukuttan, Alkali activated slag concretes designed for a desired slump, strength and chloride diffusivity, Construction and Building Materials 190 (2018) 191-199.

[9] H. Zhu, Z. Zhang, Y. Zhu, L. Tian, Durability of alkali-activated fly ash concrete: chloride penetration in pastes and mortars, Construction and Building Materials 65 (2014) 51-59.

[10] A. Elsharief, M.D. Cohen, J. Olek, Influence of aggregate size, water cement ratio and age on the microstructure of the interfacial transition zone, Cement and Concrete Research 33(11) (2003) 1837-1849.

[11] M. Babaee, A. Castel, Chloride diffusivity, chloride threshold, and corrosion initiation in reinforced alkali-activated mortars: Role of calcium, alkali, and silicate content, Cement and Concrete Research 111 (2018) 56-71.

[12] D. Bondar, M. Basheer, S. Nanukuttan, Suitability of alkali activated slag/fly ash (AA-GGBS/FA) concretes for chloride environments: Characterisation based on mix design and compliance testing, Construction and Building Materials 216 (2019) 612-621.

[13] X. Hu, C. Shi, Z. Shi, L. Zhang, Compressive strength, pore structure and chloride transport properties of alkali-activated slag/fly ash mortars, Cement and Concrete Composites 104 (2019) 103392.

[14] J. Provis, J. Van Deventer, What controls the durability of geopolymer binders and concretes?, Sixth International Conference on Concrete under Severe Conditions: Environment and LoadingCentro de Investigacion y de Estudios Avanzados del IPN, Unidad MeridaConsejo Nacional de Ciencia y Tecnologia, CONACyTUniversidad Autonoma de YucatanGobierno del Estado de YucatanH Ayuntamiento de la Ciudad de MeridaH Ayuntamiento de la Ciudad de ProgresoAsociacion Latinoamericana de Control de Calidad, Patologia y Recuperacion de la Construccion, ALCONPAT MexicoCEMEX Concretos SA de CVWR GRACE Holdings SA de CVPENMAR SA de CVSIKA Mexicana SA de CVBASF Mexicana SA de CV, 2010.

[15] D. Bondar, S. Nanukuttan, J.L. Provis, M. Soutsos, Efficient mix design of alkali activated slag concretes based on packing fraction of ingredients and paste thickness, Journal of cleaner production 218 (2019) 438-449.

[16] G. Ye, Experimental study and numerical simulation of the development of the microstructure and permeability of cementitious materials, (2003).

[17] T.C. Powers, L.E. Copeland, H. Mann, Capillary continuity or discontinuity in cement pastes, 1959.

CHLORIDE-INDUCED CORROSION OF STEEL REINFORCEMENT IN ALKALI-ACTIVATED SLAG/ METAKAOLIN BLENDED CONCRETES

Juan Pablo GevaudanE (1), Susan A. Bernal (1)

(1) Civil Engineering Department, University of Leeds, United Kingdom

Abstract

The aim of this study is to understand the corrosion mechanism of steel embedded in alkali-activated slag/metakaolin blended concretes via electrochemical testing after 407 days of exposure to a 3.5 wt.% NaCl solution, with an emphasis on characterising the material prior to the onset of corrosion. In order to accurately depict the material's state, the importance of time-dependent stability of the corrosion potential (E_{corr}) is discussed in the context of both two-electrode cell set-up on a carbon-steel exposed to basic solutions (0.8 M NaOH and 0.8 M NaOH + 1.2 M NaCl) and reinforced alkali-activated concretes. When carbon-steel is exposed to NaOH solutions, the E_{corr} values did not attain a logarithmic equilibrium or passive condition prior to 72 hours of exposure. At the same NaOH concentration, and in the presence of chlorides, E_{corr} values fluctuated as a consequence of localised corrosion activity at the metal surface. In order to circumvent the instability caused by chlorides, both direct-current (linear polarization resistance) and alternating-current (electrochemical impedance spectroscopy) techniques were utilized to determine and cross-validate the polarization resistance (Rp) in steel-reinforced alkali-activated concretes. With a 0.6% difference in Rp values, results demonstrate excellent agreement by utilizing both techniques. Thus, results demonstrate that these concretes do not initiate corrosion activity before 158 days of aggressive exposure to chloride. These results demonstrate some stability of the oxide films forming in alkali-activated concretes, and highlight the need for long duration testing of these materials to truly understand how corrosion might take place in reinforced concretes.

Keywords: alkali-activated cements, corrosion, electrochemistry, corrosion potential

1. INTRODUCTION

When compared to conventional portland cement concrete, alkali-activated concrete (AAC) materials (an alternative class of construction materials) have attracted global attention due to their reduced chloride permeability and increased chloride binding potential. A recent study observing the corrosion behaviour of AACs over a period of 500 days identified that the chloride-ingress rate and observed corrosion was lower than that of portland cement materials

[1]. Similarly, Tittarelli et al. [2] found that these materials often outperform portland cement ones with similar compressive strength. The low chloride permeability is attributed to a highly disconnected porous structure as also observed in historical precedents from 30 year-old AACs [3]. It is expected that a reduction in chloride permeability may also be due to the formation of chloride binding phases, such as Mg-Al and Ca-Al layered double hydroxides [4].

However, it is believed that the high alkalinity of the pore solution achieved in alkali activated materials, might induce high corrosion activity of steel [5]. Recent reviews have discussed the effect of precursor type and activator chemistry on the phase assemblages evolution, and consequently the overall properties of these materials, leading to various corrosion mechanisms [6], [7]. These reviews highlighted the little existing understanding of how corrosion might take place in these systems, and the factors influencing performance of steel reinforced AACs, particularly when exposed to chloride rich environments.

Electrochemical testing limitations, such as time-dependent stability of the corrosion potential (E_{corr}), often obfuscate a mechanistic understanding. In this study, the corrosion mechanism of metakaolin/slag AACs is analysed via electrochemical testing after 407 days of 3.5 wt.% NaCl exposure. Special importance is placed on the analysis of the state of the concrete material prior to the onset of corrosion. In order to accurately depict the material's state, the importance of time-dependent stability of the E_{corr} is demonstrated via both two-electrode cell solution and reinforced metakaolin/slag AAC materials. In order to circumvent demonstrated E_{corr} stability limitations, the study leverages both direct-current and alternating-current electrochemical tests to cross-validate the polarization resistance values of embedded reinforcement over time.

2. EXPERIMENTAL PROGRAM

2.1 Materials

In order to test carbon-steel exposed to basic solutions, carbon-steel metal (X65, 625 mm^2) was utilized and exposed to NaOH (Honeywell, #58045) and NaCl (Sigma Aldrich) solutions prepared with deionized water.

In order to produce concrete specimens, granulated blast furnace slag (GBFS), sourced from Acerías Paz del Río (Colombia), and metakaolin (MK), generated via calcination of kaolin as discussed in [8], were utilized as aluminosilicate precursors; see chemical composition in Table 1. The specific gravity, Blaine fineness, and particle size range of GBFS were 2900 kg/m^3, 399 m^2/kg, and 0.1–74 μm (d50 = 15 μm), respectively. The particle size range of the MK is 1.8–100 μm, with a d50 of 12.2 μm and 10% of particles finer than 4 μm. Alkali activating solutions were composed of a combination of commercial sodium silicate solution (SiO_2: 32.4 wt.%, Na_2O: 13.5 wt.%, and H_2O: 54.1 wt.%) with a M_s of 2.4 and NaOH solutions (50% wt.). Concrete specimens were produced with a sourced crushed gravel and river sand as coarse and fine aggregates, respectively. Structural 1018 carbon-steel bars of 6.35 mm diameter were used as reinforcement, according to ASTM A 706-08 Standard.

Table 1: Chemical composition of precursors determined by X-ray fluorescence

Precursors	Oxide (wt.%)							
	SiO_2	Al_2O_3	CaO	Fe_2O_3	MgO	TiO_2	Others	LOI*
GBFS	32.29	16.25	42.45	2.35	2.87	0.5	1.38	1.91
MK	50.72	44.63	2.69	–	–	–	0.94	1.02

*LOI – loss on ignition determined at 1000 °C

2.2 Concrete sample preparation

Concrete samples were produced with a total binder (GBFS + MK) content of 400 kg/m^3 with a mix design shown in Table 2. The total Si:Al ratio and Na_2O activator concentration were 2.0 and 11.6 wt.%, respectively. Cylindrical reinforced concrete specimens (76.2 mm diameter and 76.2 mm length) were cast for electrochemical testing. The steel bar was symmetrically embedded after the fresh concrete was cast. The rebars were coated with an epoxy painting leaving an active surface area of 9.97 cm^2. Epoxy resin was applied in the upper surface of the tested specimens in order to prevent localised corrosion due to differential aeration, as well as to avoid penetration of chloride solution or other aggressive agents for the duration of the immersion in the chloride rich solution.

Specimens were cured at a relative humidity = 90% and 25 ± 5 °C, for 28 days. This curing regime was selected with the aim to prevent drying shrinkage effects or leaching of the alkali-activator. Detailed mechanical and physical characterisation of these concretes can be found in [8]. After 28 days of curing, specimens were submerged in 3.5 wt.% NaCl solutions for 64, 158, 276, and 335 days.

Table 2: Mixture proportions for concrete specimens

Components	kg/m^3 of fresh concrete
GBFS	360
MK	40
Sodium Silicate solution	136
NaOH solution	72
Coarse aggregate	816
Sand	816
Free water	124

2.3 Electrochemical characterisation of steel rebars

An Ivium potentiostat (Ivium-n-Stat) with two independent channels (5A/10V) was utilized to determine the corrosion potential (E_{corr}), otherwise also known as the open circuit potential, over time of carbon-steel exposed to both 0.8 M NaOH and 0.8 M NaOH + 1.2 M NaCl solutions. Steel samples were mounted in epoxy with soldered wires attached to each metal piece and wet-polished using a No.600 grit paper. The electrochemical cell (1L capacity) was filled with 700ml ± 25ml of either a 0.8M NaOH solution (Cl-/OH- = 0.0) or a 0.8M NaOH with 1.2M of NaCl (Cl-/OH- = 1.50). A MettlerToledo Oxidation-Reduction Potential (ORP) Ag/AgCl sensor (ARGENTHALTM) was used as a reference electrode.

2.4 Electrochemical characterization of concrete samples

A Gamry model PCI 4 workstation with a general 3-electrode configuration was utilised to monitor the E_{corr}, as well as perform all electrochemical tests, such as linear polarization resistance (LPR), and electrochemical impedance spectroscopy (EIS). The steel reinforcement bar was used as a working electrode, an external graphite bar as a counter electrode, and a silver/silver chloride (Ag/AgCl) as a reference electrode. E_{corr} monitoring, as well as LPR and EIS tests, were performed in a saturated surface dry condition.

E_{corr} of the steel reinforcement in concrete specimens was monitored for 600 seconds before LPR or EIS non-destructive testing. Linear polarization was conducted ±20 mV from E_{corr} at a scan rate of 0.166 mV/s and a sample period of 2 seconds. Linear resistance (Rp) values were calculated utilizing regression analysis ±10 mV from the E_{corr} value; ensuring that Rp values were linearly derived. Electrochemical impedance spectroscopy was conducted in potentiostatic mode (±10 mV) from an initial high frequency of 0.1 MHz to 10 mHz by taking 3 points per decade. Gamry Echem Analyst software was utilized to analyze all collected data and, in the case of EIS data, fit appropriate equivalent circuits.

3. RESULTS AND DISCUSSION

3.1 Time-variability of corrosion potential (E_{corr})

3.1.1 Behaviour in simulated pore solutions

The E_{corr} value of a carbon-steel metal exposed to high pH solutions does not reach an equilibrium, or stability, prior to 72 hours, as seen in Figure 1. In absence of chlorides the equilibrium process follows a logarithmic behaviour as also observed for other chemical equilibria. Thus, indicating that the metal has changed and is now reaching an average surface chemistry. These changes are most likely due to the development of an oxide surface film, which can behave as a cathodic site.

In the presence of chlorides, for over 140 hours of testing, twelve localized corrosion events are identified and characterised by a sudden drop of potential, likely due to anodic dissolution followed by a recovery (i.e., increase in potential). These localized corrosion events are responsible for the instability and sudden changes in E_{corr}.

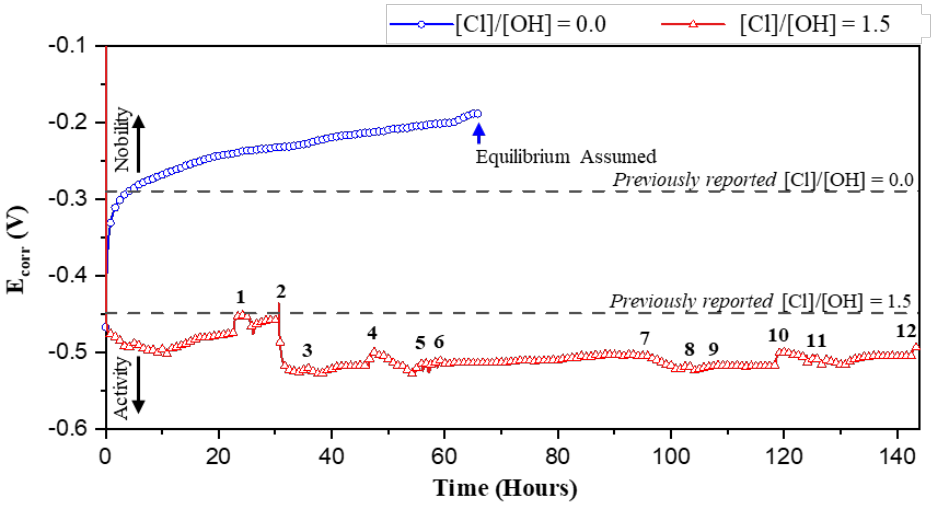

Figure 1: Corrosion potential (E_{corr}) of carbon-steel as a function of time (hours) in a two-electrode electrochemical cell. Dashed lines correspond the E_{corr} reported in [9].

In the majority of corrosion studies, not just for evaluating alkali-activated materials but other cementitious systems as well, E_{corr} stabilisation criteria is either not reported, given as 0.016 mV/s or shown as a time (e.g., 30 minutes) prior to performing an electrochemical test [10]–[12]. E_{corr} stabilisation is important as it is the starting potential utilized in direct-current (DC) polarization-based electrochemical tests, such as linear polarization resistance, anodic polarization, or cyclic voltammetry. If the E_{corr} value changes (drifts) at the time of performing polarization tests, particularly in absence of chlorides, then electrochemical results will be difficult to interpret or can mislead the identification of the mechanisms of corrosion taking place in the tested specimens. Further studies interrogating the E_{corr} stabilisation times, in conditions relevant to alkali-activated systems, need to be performed in order to standardise testing protocol for evaluation of corrosion resistance of steel rebars embedded in these materials.

In subsequent sections, the E_{corr} behaviour will be evaluated for alkali-activated slag/metakaolin blended concretes.

3.1.2 Behaviour in concrete materials

In specimens immersed in a 3.5% NaCl chloride solution, an increased exposure time led to significant reduction in the E_{corr} values (Figure 2), likely indicating that the steel is in an active state. This is particularly noticeable for the first 200 days of testing, when a nearly three-fold drop of the E_{corr} was observed, compared with the value obtained in saturated samples prior chloride exposure. These fluctuations cannot be solely attributed to corrosion of steel occurring during testing, as differentials in saturation degrees of the concretes, particularly from the start of the test, after 200 days of immersion in the chloride solution will induce significant variations in the E_{corr} values. This has been observed in portland cement systems [13].

Between 200 and 300 days of testing, small changes in the E_{corr} are observed, however after 276 days an increase of the E_{corr} (becoming less negative) followed, but a decrease in the E_{corr} after 335 days was observed. Hence indicating that corrosion events take place in the presence of chlorides at high pH, in alkali-activated materials even after a stable oxide layer has been formed. Moreover, the E_{corr} values recorded in this concrete lie between 0.3 to -0.5 V, however, a likelihood of corrosion cannot be inferred via application of the criteria reported in ASTM C876. Here, E_{corr} values represent an average potential over the reinforcement bar surface, hence not resembling a macro-cell set up. Thus, the average potential of the steel rebar at 400 days stabilizes at nearly -0.5 V.

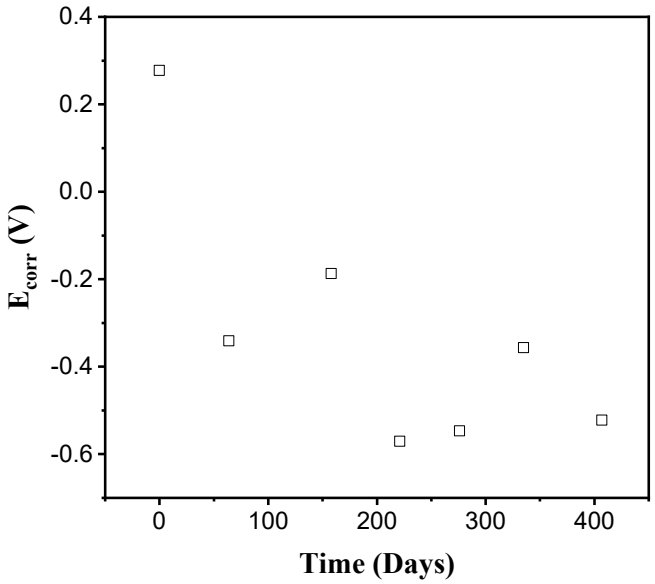

Figure 2: Corrosion potential (E_{corr}) of embedded carbon-steel reinforcement as a function of time (days) in MK/Slag AACs.

3.2 Polarization resistance (Rp) of embedded carbon-steel reinforcement

3.2.1 Cathode/Anode polarization

The Rp collected over a time length of 247 days indicated that corrosion activity initiates after 158 days in MK/Slag AAC materials. As seen in Figure 3, there is an increase in Rp during 158 days of 3.5 wt.% NaCl exposure, indicating an increased steel corrosion resistance, which is consistent with the observed E_{corr} values (Figure 1). Recent research by others, such as [2], [12], have reported similar Rp values as those reported here. After 158 days, however, chlorides initiate corrosion at the steel-concrete interface (SCI) indicated by a sharp decrease in Rp values. This observation correlates well with the low E_{corr} values observed in Figure 1, approaching -0.6 V. Thus, relating the likely presence of chlorides and anodic dissolution to low Rp and E_{corr} values.

However, as previously discussed, the changes over time of E_{corr} (fluctuations) may prevent accurate assessment of corrosion mechanisms. As a result, EIS data will be analysed to cross-validate and confirm proper analysis of Rp values.

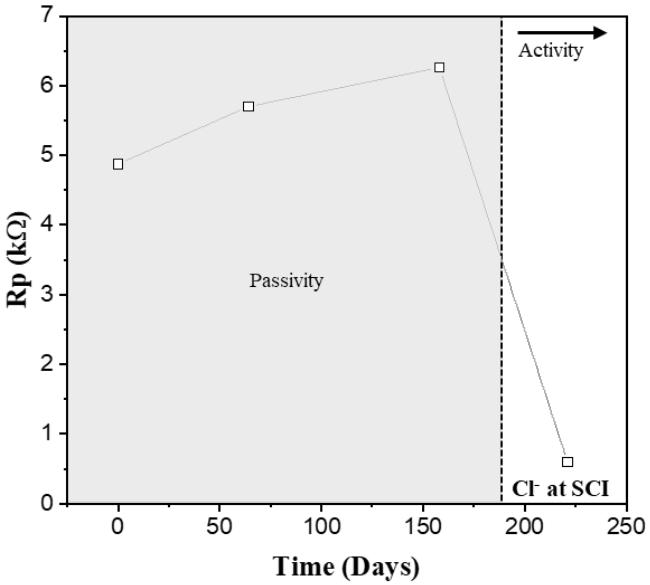

Figure 3: Polarization resistance values (Rp) of embedded carbon-steel reinforcement as a function of time (days) in MK/Slag AACs.

3.2.2 Electrochemical impedance spectroscopy

Figure 4 shows the collected EIS data and the fitted impedance circuit model for a MK/Slag AAC specimen exposed to 3.5 wt.% NaCl for 158 days, prior to expected corrosion initiation (Figure 3). The well-fitted model (χ^2 value of $1.23e^{-4}$) describes the physical concrete components affecting the corrosion process [14] and has been selected to represent the two-time constants experimentally observed in both Bode phase and Nyquist plots (**Figure 4**). The equivalent circuit model was chosen to physically represent the formed passive oxide film in the AAC concrete as provided by [15]. It is shown that due to the high NaCl exposure of 3.5 wt.%, the solution resistance (R_Ω) is very low (14 Ω). The Wardburg diffusion phase component ($1.68e^{-3}$ $S*S^{0.5}$) represents a semi-infinite linear diffusion of chlorides within the AAC matrix. This physical component accounts for both the tortuous pore network and chloride binding capacity of the concrete, which delay the diffusion of aggressive chloride ions.

The total corrosion resistance (6,338 Ω) of the embedded reinforcement is a result of both the charge transfer resistance generated by both the metal (1,350 Ω) as well as that of the oxide film formed (4,988 Ω), as described in [15]. Hence, the corrosion resistance is a function of steel conditions (e.g., microstructural features, geometry, surface conditions, oxide film), while the concrete resistance, in this case, is mainly a function of the concrete pore solution chemistry and the diffusion of ionic species through the porous network, represented by the Warburg diffusion coefficient.

The constant-phase element, used as an alternative to a pure capacitor, is associated with the heterogeneity of the electrical double layer formed at the interface of the reinforcement [16]. The large constant-phase element values indicate the local concentration of ionic species forming the electrical double layer at this interface located at the steel-concrete interface – an area for further research.

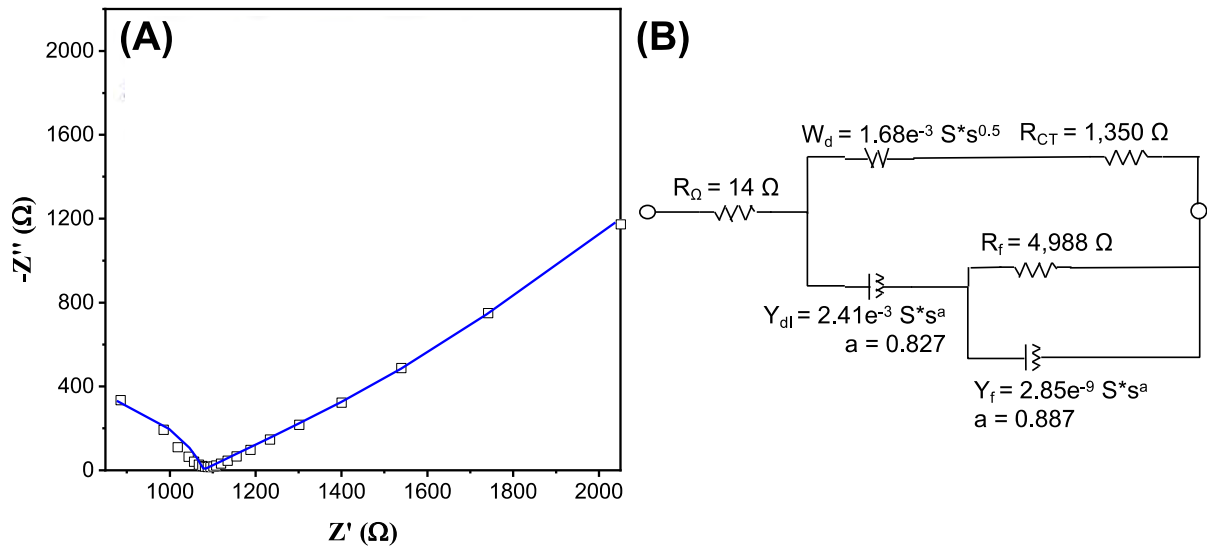

Figure 4: EIS of MK/Slag AACs after 158 days of chloride exposure. (A) data and model fit are shown ($\chi^2 = 1.23e^{-4}$); (B) equivalent circuit utilized to model fit EIS data.

In order to ensure accurate analysis of both EIS and LPR measurements, Rp values are cross-validated and demonstrate good agreement (s = 26.8 Ω). As described above, EIS measurements is not only important to understand the different components participating in the corrosion of embedded reinforcement, but also to circumvent testing limitations of DC-based testing. In order to circumvent earlier discussed limitations on the OCP stabilization, EIS can be performed in galvanostatic mode. Moreover, EIS allows the determination of R_Ω which, as discussed earlier, can impact the total value collected for Rp values. Here we use EIS to cross-validate the appropriate interpretation of Rp values, which are critical for the determination of accurate corrosion rates in reinforced concrete materials. Rp values obtained by both show good agreement and yield a value of 6,319 Ω ± 26.8 Ω. Thus, confirming the accurate analysis of both electrochemical tests to interpret the corrosion mechanisms occurring in AAC materials.

4. CONCLUSIONS

The stability of E_{corr} values of a carbon-steel metal exposed to high pH solutions does not reach an equilibrium, or stability, prior to 72 hours. In the presence of chlorides and a high pH, E_{corr} values are instable due to localized corrosion activity, which is expected. This highlights the need to performing further studies evaluating the stability and nature of the oxide layer forming in steel reinforced in conditions relevant to alkali-activated materials, as the presence of chlorides in these systems will influence its stability.

Linear polarization demonstrate that corrosion activity initiates in MK/Slag AAC materials after 158 days of exposure to a 3.5% NaCl solution. The results were cross validated by analysing the EIS data at 158 days of chloride exposure. A well-fitting model was achieved ($\chi^2 = 1.23e^{-4}$) and, hence, Rp values of 6,319 Ω ± 26.8 Ω we obtained. It was found that prior to corrosion initiation the corrosion resistance provided by MK/slag AACs was about 21% of the total corrosion resistance. Thus, confirming the valuable role of concrete properties, such as isolated pore structure, chloride binding, and pore solution chemistry, as well as both the concrete-steel interface and steel properties to resist the corrosion of embedded reinforcement.

ACKNOWLEDGEMENTS

This project has received funding from the European Union's Horizon 2020 research and innovation programme under the Marie Skłodowska-Curie grant agreement No 839436. Participation of S.A. Bernal in this study was partially funded by EPSRC through ECF EP/R001642/1.

REFERENCES

[1] C. Tennakoon, A. Shayan, J. G. Sanjayan, and A. Xu, "Chloride ingress and steel corrosion in geopolymer concrete based on long term tests," *Materials & Design*, vol. 116, pp. 287–299, Feb. 2017, doi: 10.1016/j.matdes.2016.12.030.

[2] F. Tittarelli, A. Mobili, C. Giosuè, A. Belli, and T. Bellezze, "Corrosion behaviour of bare and galvanized steel in geopolymer and Ordinary Portland Cement based mortars with the same strength class exposed to chlorides," *Corrosion Science*, vol. 134, pp. 64–77, Apr. 2018, doi: 10.1016/j.corsci.2018.02.014.

[3] J. L. Provis *et al.*, "Will geopolymers stand the test of time?," presented at the Ceramic Engineering and Science Proceedings, 2007, vol. 28, pp. 235–248.

[4] X. Ke, S. A. Bernal, and J. L. Provis, "Uptake of chloride and carbonate by Mg-Al and Ca-Al layered double hydroxides in simulated pore solutions of alkali-activated slag cement," *Cement and Concrete Research*, vol. 100, pp. 1–13, Oct. 2017, doi: 10.1016/j.cemconres.2017.05.015.

[5] M. Basheer, Q. Ma, S. Nanukuttan, J. Provis, and K. Yang, "Are alkali activated slag concretes suitable for reinforced concrete in chloride environments?," presented at the Structural Faults & Repair 2018 and European Bridge Conference 2018, Edinburgh, Scotland, May 2018, p. 11.

[6] S. Mundra *et al.*, "Steel corrosion in reinforced alkali-activated materials," *RILEM Tech Lett*, vol. 2, pp. 33–39, Dec. 2017, doi: 10.21809/rilemtechlett.2017.39.

[7] J. Osio-Norgaard, J. P. Gevaudan, and W. V. Srubar, "A review of chloride transport in alkali-activated cement paste, mortar, and concrete," *Construction and Building Materials*, vol. 186, pp. 191–206, Oct. 2018, doi: 10.1016/j.conbuildmat.2018.07.119.

[8] S. A. Bernal, R. Mejia de Gutierrez, and J. L. Provis, "Engineering and durability properties of concretes based on alkali-activated granulated blast furnace slag/metakaolin blends," *Construction and Building Materials*, vol. 33, pp. 99–108, 2012, doi: 10.1016/j.conbuildmat.2012.01.017.

[9] S. Mundra, M. Criado, S. A. Bernal, and J. L. Provis, "Chloride-induced corrosion of steel rebars in simulated pore solutions of alkali-activated concretes," *Cement and Concrete Research*, vol. 100, pp. 385–397, 2017.

[10] M. Stefanoni, U. M. Angst, and B. Elsener, "Kinetics of electrochemical dissolution of metals in porous media," *Nature materials*, p. 1, 2019.

[11] M. Criado and J. L. Provis, "Alkali activated slag mortars provide high resistance to chloride-induced corrosion of steel," *Frontiers in Materials*, vol. 5, Jun. 2018, Accessed: Nov. 27, 2019. [Online]. Available: https://doi.org/10.3389/fmats.2018.00034.

[12] M. Babaee and A. Castel, "Chloride diffusivity, chloride threshold, and corrosion initiation in reinforced alkali-activated mortars: Role of calcium, alkali, and silicate content," *Cement and Concrete Research*, vol. 111, pp. 56–71, Sep. 2018, doi: 10.1016/j.cemconres.2018.06.009.

[13] J. A. González, A. Cobo, M. N. González, and E. Otero, "On the effectiveness of realkalisation as a rehabilitation method for corroded reinforced concrete structures," *Materials and Corrosion*, vol. 51, no. 2, pp. 97–103, 2000, doi: 10.1002/(SICI)1521-4176(200002)51:2<97::AID-MACO97>3.0.CO;2-3.

[14] M. Grossi and B. Riccò, "Electrical impedance spectroscopy (EIS) for biological analysis and food characterization: a review," *Journal of Sensors and Sensor Systems*, vol. 6, pp. 303–325, 2017, doi: 10.1016/j.corsci.2008.08.049.

[15] J. R. Scully, “Polarization Resistance Method for Determination of Instantaneous Corrosion Rates,” *CORROSION*, vol. 56, no. 2, pp. 199–218, Feb. 2000, doi: 10.5006/1.3280536.
[16] J. Shi, J. Ming, and W. Sun, “Electrochemical performance of reinforcing steel in alkali-activated slag extract in the presence of chlorides,” *Corrosion Science*, vol. 133, pp. 288–299, Apr. 2018, doi: 10.1016/j.corsci.2018.01.043.

INVESTIGATION OF POROSITY AND CARBONATION DEPTH IN ALKALI-ACTIVATED GGBS MORTAR

S. Tavasoli (1) and W. Breit (1)

(1) Institute for Construction Material Technology, University of Kaiserslautern, Germany

Abstract

The effect of type of activator on porosity and CO_2 penetration of the alkali activated ground granulated blast furnace slag (GGBS) mortar is an important behavior which is required for designing a durable concrete mixture. This research article investigates the influence of three types of activators consisting of NaOH, $Na_2.nSiO_2$ and $K_2.nSiO_2$ on the porosity, pore size and distribution, as well as carbonation depth in activated GGBS mortar which will affect the compressive strength, shrinkage, water penetration and durability of the concrete incorporating these types of pastes. It was observed that the GGBS activated by NaOH showed higher porosity than the other activators, while mixtures with $Na_2.nSiO_2$ and $K_2.nSiO_2$ demonstrated lower porosity, respectively. The results of carbonation depth were also coincident with the porosity of specimens, in which the one activated by NaOH was fully carbonated. In contrast, the least affected mortar was activated by $K_2.nSiO_2$. This trend was also observed for the compressive strength, while $K_2.nSiO_2$ provided the highest compressive strength stored in the air, although its rate of reduction due to CO_2 exposure was also the highest among other activators.

Keywords: Porosity, carbonation, GGBS, alkali-activated slag, mortar

1. INTRODUCTION

Alkali activated binders as one of the replacement alternatives for Ordinary Portland cement (OPC) has become more popular over the last 60 years. Different behaviors of this type of binders are proposed to be investigated by researchers [1]. In spite of its practices in China, Russia and Ukraine, there are uncertainties about the long-term and durability of concrete using this types of binders [2].

Several test methods are using for measuring the carbonation in concrete and mortar. One of the specific procedure for mortar specimens was described in RILEM TC56-MHM by using phenolphthalein spray on the cutting section of mortar prism [3]. The unclear point in this testing procedure is the method of splitting or cutting the specimens. Wet cutting always will influence the phenolphthalein procedure in comparison with dry splitting procedure and subsequently will give different results for OPC mortar.

The Portland cement carbonation occurred due to the reaction of CO_2 in atmosphere with $Ca(OH)_2$ and/or Ca rich C-S-H gels to form calcium carbonate (CO_2 could be dissolved in rain

drops or in the water inside the concrete pores) [4,5]. Alkali-activated binders are low in calcium content, in contrast its gel structure is enriched in aluminum and alkalis. Therefore, different mechanisms should be expected from these types of binders depending on their source materials and activators. Moreover, the rate of both natural carbonation, as well as, accelerated carbonation should be influenced by source materials. The carbonation process of the Portland cement exposed to 3 % CO_2 is almost similar to the corresponding process with 0.03 % CO_2 [5], although no other proof for change of carbonation mechanism was found yet, specifically for the higher concentrations of carbon dioxide.

The accelerated carbonation is a method of specimen's carbonation exposure that it could be influenced by CO_2 in the condition including higher concentration of CO_2. Shi et al stated the rate of natural carbonation in alkali silicate-activated binders are lower than 1 mm/year [2]. On the other hand, another experimental investigation declared that the carbonation depth in alkali-activated concrete will be between 13 mm to 25 mm after 240 hours exposure to 7 % CO_2 [6].

A study performed by Bernal et al showed that the carbonation progress is highly dependent to the CO_2 concentration, as well as difference of total and capillary porosity of hardened concrete [5,8].

The hydroxide activators have different effect on the CO_2 absorption in comparison with other types of activators, since hydroxide activators are well known in carbon dioxide absorption in CO_2 flow or air [4,9].

The accelerated carbonation has completely different effect on the behavior of the alkali-activated concrete in comparison with the natural condition carbonation which provided far more damaging condition for steel corrosion in reinforced concrete elements than in the natural carbonation condition. Actually, in natural carbonation of alkali-activated binders no considerable reduction could be observed in PH value of pore solution, while in accelerated condition the PH of pore solution decreased sharply [4].

The sorptivity of geopolymer concrete increases with the age of concrete, while the sorptivity of OPC concrete decreases by age which shows the opposite behavior during the long-term reaction. Moreover, the porosity of geopolymer concrete increases by exposing to the carbonation field [10].

2. EXPERIMENTAL PROCEDURE

2.1 GGBS

The GGBS used in this research was including the following chemical composition, listed in Table 1. The activity indexes of the GGBS were 1.02 and 1.25 at 7 and 28 days, respectively, based on EN 450-1 [12]. Moreover, the density of mentioned GGBS determined 2.5 g/cm^3 by pycnometer test method and the blain of 4,050 cm^2/g was measured according to EN 196-6 [13].

Table 1: Chemical composition of ground granulated blast furnace slag (GGBS)

	Fe	Mn	MnO	SiO_2	TiO_2	Al_2O_3	CaO	MgO	S	Na_2O	K_2O
GGBS	0.24	0.12	0.16	36.62	0.91	11.34	42.13	6.48	1.42	0.3	0.53

2.2 Aggregates

The aggregates which were used for the production of mortar, were standard reference sand according to EN 196-1 [14].

2.3 Activators

Three types of activators were used in this research that all were solutions in water. Two types of water glasses including $Na_2.nSio_3$ (Betol 52) and $K_2.nSiO_2$ (Geosil 14,517) which contained the 45 % concentration of solid material in the solution having density of 1.55 g/cm^3 and 1.50 g/cm^3 and molar ratio (SiO_2/Na_2O) of 2.1 and 1.7, respectively. The other activator was sodium hydroxide which was solved in water with the concentration of 16 mol/L and 24 hours before preparing the mortar in order to equalize the temperature of solution with the room temperature.

2.4 Mixture design

In this study more than 20 mixtures designs with water to binder ratio (W/B) of 0.5 were provided based on EN 196-1 in order to evaluate the effect of activator type on the GGBS paste separately and combination of two or three of them on the GGBS as binder. However, five mixtures compositions which were more highlighted are presented in this article, listed in Table 2. Regarding the previous studies, the final compressive strength of the alkali-activated GGBS could be reached by curing the specimens in 60°C for 24 hours due to the acceleration of hydraulic reaction. Thus, the specimens in this study cured for 24 hours in 60°C in order to obtain their final strength, then exposed to the accelerated CO_2 condition.

Table 2: Mixture composition

Mixture	Sand (g)	GGBS (g)	Water (g)	NaOH (g)	$Na_2.nSiO_3$ (g)	$K_2.nSiO_3$ (g)	A.A./Binder (%)
1	1,350	450	203	-	40	-	4
2	1,350	450	203	-	-	40	4
3	1,350	450	203	40	-	-	4
4	1,350	450	184	14	30	30	8
5	1,350	450	182	19	-	60	8

2.5 Sampling and curing

The mortar mixture was produced according to EN 196-1. Then, the mortar was poured in the triple prismatic mold having the dimensions of 160×40×40 mm and it was put on the vibrating table for two minutes to be compacted. Thereafter, the filled mold was covered by a glass plate and cured for (24 ± 1)°C hour in a climate chamber having (92 ± 2) % humidity and (20 ± 1)°C as well as (60 ± 1)°C temperature regarding the experiment plan respectively. The specimens were demolded after 24 hours and for alkali-activated specimens, they were wrapped in cling film in order to keep the humidity of the specimens constant until the considered curing time reached.

2.6 Carbonation test

The provided mortar specimens were tested according to the RILEM TC56-MHM (CPC-18 Measurement of hardened concrete carbonation depth). Based on the mentioned recommendation, the mortar specimens must be produced in 160×40×40 mm prisms and exposed to the target condition. While in RILEM recommendation CPC-18 that is proposed to consider the natural carbonation condition (0.03 % CO_2 concentration) [3], based on the previous studies on the accelerated carbonation of Portland cement paste, the mechanism of

carbonation will be similar to the natural condition when the specimens are exposed to 3 % carbon dioxide concentration [5]. Therefore, the 3 % concentration of CO_2 was considered for this study to apply carbonation on the provided specimen.

After the specific period of time of exposure, the specimens were cut into the slices having 2 cm thickness. Then, the cross sections of specimens were sprayed with the 1 % phenolphthalein solution in 70 % ethyl alcohol. The dark pink parts of the sprayed area showing the non-carbonated part having PH value of higher than 9 and the carbonated areas will be colorless. The depth of carbonation was determined by measuring the depth of colorless parts from the edge of the specimen with 0.5 mm precision. Moreover, the compressive strength of specimens after a period of time exposure to carbon dioxide was measured based on the EN 196-1.

2.7 Mercury intrusion porosimetry

In order to evaluate the volume of capillary pores, as well as its distribution, the mercury intrusion porosimetry method according to ISO 15901 was used [15]. For this purpose, the Pascal 140/440 (low/high pressure porosimetry) was used to measure the porosity of carbonated, as well as non-carbonated parts in mixture 1-4. In this experiment, the 3-4 gram of dried specimen in vacuum desiccator was prepared to put in the equipment canister to start the test by increasing the mercury pressure up to 200 MPa. Subsequently, the pores distributions graph was drawn by calculating the volume mercury penetration at specific pressure.

2.8 Compressive strength

Compressive strength of produced mortars in this research was tested according to EN 196-1 [14].

3. RESULTS AND DISCUSSION

The capillary porosity of the mortar as one of the most effective criteria in rate of carbonation, as well as other durability hazards is considered. By increasing the capillary porosity, specifically the larger pores the probability of CO_2 penetration will be increased that leads to increase the carbonation occurrence through the specimens.

In Fig. 1 the cumulative pore volume distribution, as well as relative pore volume is demonstrated with respect to the variation of pore size. It could be clearly observed that more than 85 % of the pores are smaller than 1 μm and the rest of 15 % are smaller than 0.1 mm. The total volume of the pores in the GGBS mortar using $Na_2.nSiO_2$ activator was 93.85 mm^3/g measured. Another mixture which was activated by another type of silicate based activator, $K_2.nSiO_2$ was tested in mercury intrusion apparatus and the results are shown in Fig. 2. This type of activator made lower porous structure 82.36 mm^3/g in the mortar of alkali-activated GGBS which had a considerable influence on the mechanical, as well as the durability properties of these types of binders. The distribution of pore size also showed the lower pore diameter than the first mixture which was stating the lower penetration potential for the penetration of the fluids through the mortar or concrete matrix.

The effect of NaOH as an activator on the porosity of alkali-activated GGBS is moderately different from the two previous silicate based activators, specifically in pore size distribution which included larger pores than the two previous mixtures, shown in Fig. 3. The pore volume of alkali-activated GGBS with NaOH was 99.88 mm^3/g measure that with respect to activated mortar with $Na_2.nSiO_2$ showed 8 % increase and with $K_2.nSiO_2$ demonstrates 21 %

enhancement. On the other hand, the dispersion of the pores according their sizes is completely different as for sodium and potassium silicate based activated GGBS 18 % and 16 % of the pores volume were larger than 1 µm, respectively, whereas in NaOH activated GGBS mortar, 28 % of pores were larger than 1µm.

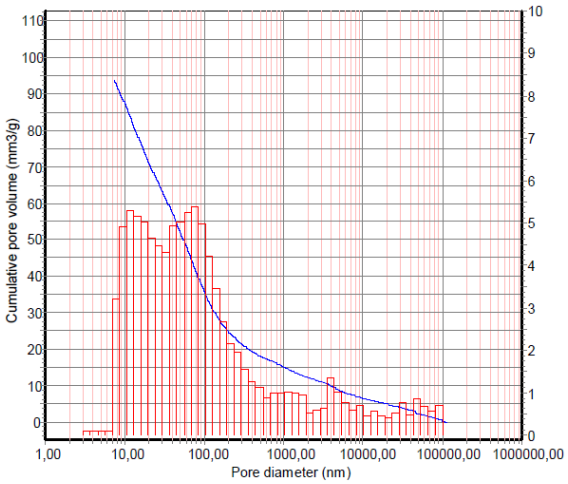

Figure 1: Pore volume distribution of GGBS activated by $Na_2.nSiO_2$ with respect to pore size

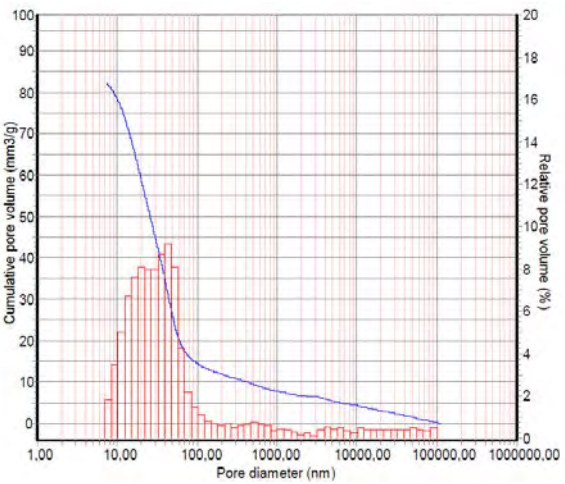

Figure 2: Pore volume distribution of GGBS activated by $K_2.nSiO_2$ with respect to pore size

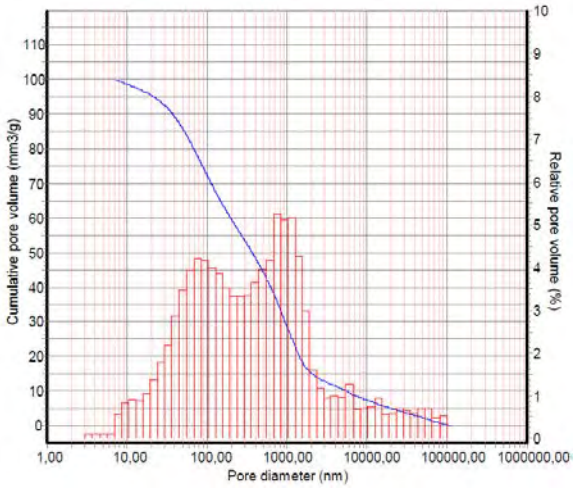

Figure 3: Pore volume distribution of GGBS activated by NaOH with respect to pore size

The photos of the mortar prisms after exposing to the CO_2 (Bottom) as well as natural air condition (Top) with (Left) and without spraying phenolphthalein (Right) are shown in Fig. 4-6. By comparing the cross section of mixture 1 (Fig. 4) and mixture 2 (Fig. 5) which were the activated GGBS with $Na_2.nSiO_2$ and $K_2.nSiO_2$ respectively, it could be concluded that the sodium silicate based activator was highly affected by CO_2 than potassium silicate based activator. Apart from chemical composition of both activators, the higher porosity of the $Na_2.nSiO_2$ can be one of the main reasons for the higher depth of carbonation in the similar

condition. It can also be observed from the cross section of the specimens that the gray parts are already carbonated or affected by carbonation and the green parts are not influenced by the carbonation mechanism yet.

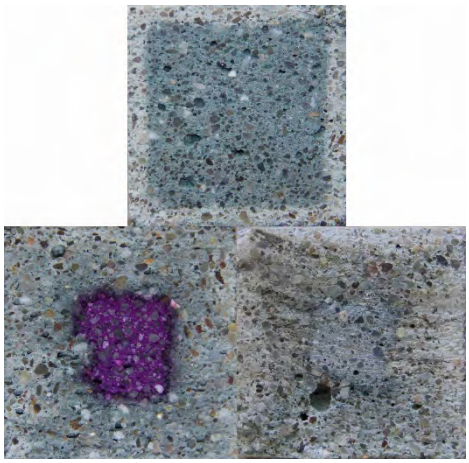

Figure 4: The cross section of activated GGBS mortar specimen with $Na_2.nSiO_2$ exposed to room condition (Top) and 3 % CO_2 condition phenolphthalein sprayed (Left) without phenolphthalein (Right)

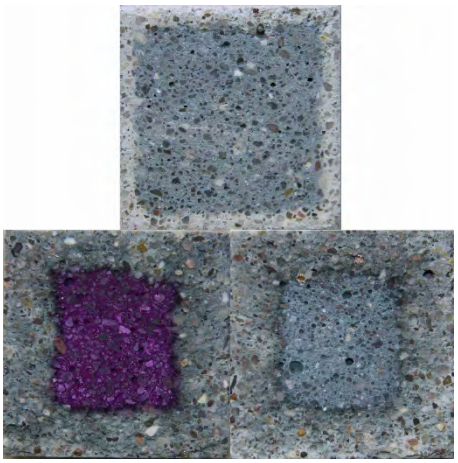

Figure 5: The cross section of activated GGBS mortar specimen with $K_2.nSiO_2$ exposed to room condition (Top) and 3 % CO_2 condition phenolphthalein sprayed (Left) without phenolphthalein (Right)

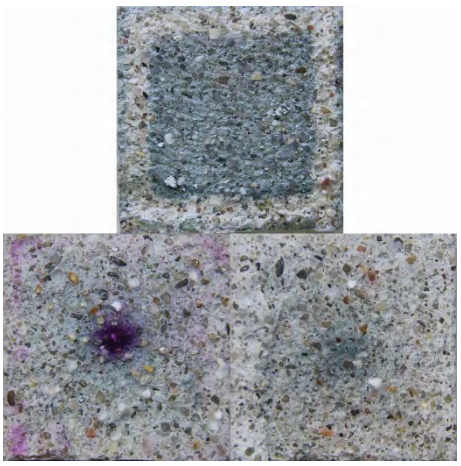

Figure 6: The cross section of activated GGBS specimen with NaOH exposed to room condition (Top) and 3 % CO_2 condition, with (Left) and without phenolphthalein (Right)

The carbonation depth in Fig. 6 which is showing the carbonation through alkali-activated GGBS specimen using NaOH as activator is completely different from the other mixtures using silicate based activators, shown in Fig. 4 and Fig. 5.

By comparing the depth of carbonation after 7 days, it can state that the depth of carbonation in mixture 4 does not have a considerable difference with mixture 2 including $K_2.nSiO_2$ which is the main reason of resistance against carbonation in alkali-activated GGBS (Fig. 7). Whereas

the corresponding porosity of mixture 4 that was considerably lower than mixture 2, is not highly affecting the carbonation mechanism in alkali-activated GGBS. The compressive strength of alkali-activated GGBS specimens after 7 days in room condition ((21 ± 1)°C, relative humidity of (55 ± 5) %) and also 3 % carbon dioxide are represented in Fig. 8. The highest reduction in compressive strength was experienced 33 % decrease by activated GGBS with $K_2.nSiO_2$.

The compressive strength in mixture 1 and 2 using NaOH and $Na_2.nSiO_2$ decreased up to 30 % and 27 % respectively. Although the corresponding carbonation depth of activated GGBS with NaOH was the highest among the other two silicate based activators, the compressive strength reduction of $K_2.nSiO_2$ activated GGBS mortar was higher than NaOH activated GGBS mortar. Interestingly, the compressive strength of mixture 4 having 8 % activator showed 18 % reduction which was a little (about 1.5 %) lower than that of mixture 5 activated by 6 % $K_2.nSiO_2$ + 2 % NaOH instead of 3 % $K_2.nSiO_2$ + 3 % $Na_2.nSiO_2$ + 2% NaOH. It can be concluded that using potassium based silicate activator leads to higher decreases in compressive strength of alkali-activated GGBS mortar due to exposure to 3 % CO_2 condition.

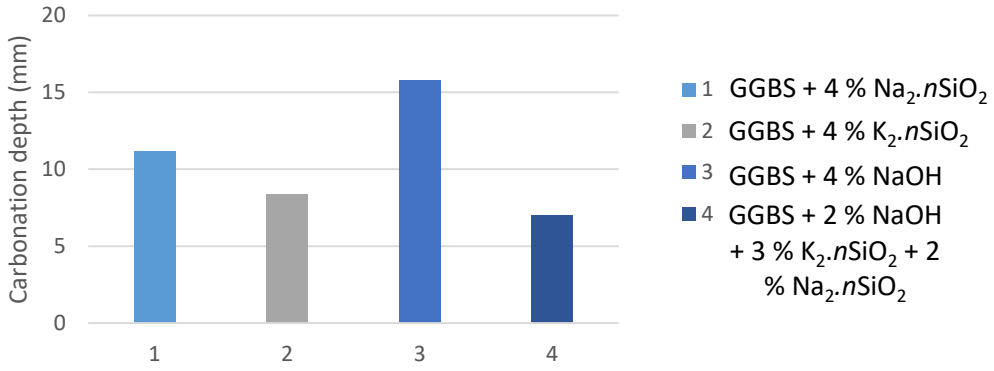

Figure 7: Carbonation depth of alkali-activated GGBS mortar mixtures 1-4, exposed to 3 % CO_2 after 7 days

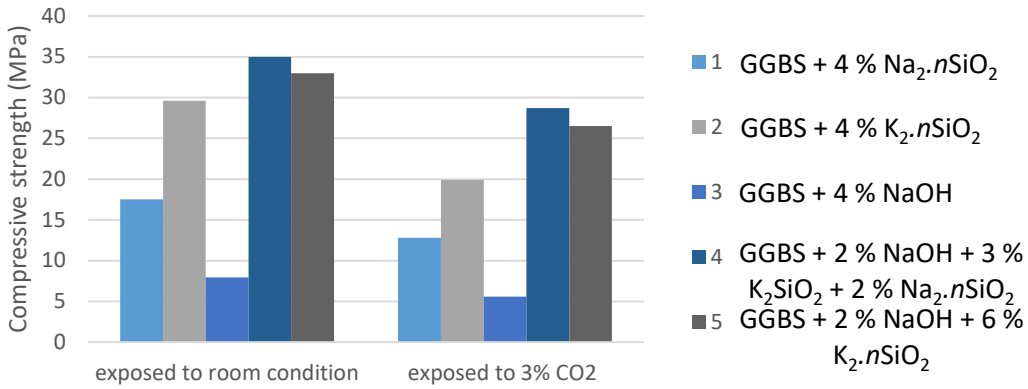

Figure 8: Compressive strength of alkali-activated GGBS mortar mixtures 1-5, exposed to room condition and 3 % carbon dioxide condition for 7 days

4. CONCLUSIONS

- Due to the higher absorption feature of CO_2 by NaOH activator, activated GGBS mortar using this type of activator shows highest porosity, as well as carbonation depth than $K_2.nSiO_2$ and $Na_2.nSiO_2$.
- Increasing the dosage of alkali activator improves porosity and in contrary reduces the carbonation depth, although the rate of decrease in carbonation depth is not linearly related to the porosity.
- The carbonation mechanism has lower effect on the reduction of compressive strength in alkali-activated GGBS with NaOH and $Na_2.nSiO_2$ than $K_2.nSiO_2$, although the compressive strength of $K_2.nSiO_2$ activated GGBS has considerably higher value than the two other activators. It means that the compressive strength of alkali-activated GGBS with $K_2.nSiO_2$ is the most affected mixture by carbonation.

ACKNOWLEDGEMENTS

This research was carried out as part of the European joint research project INTERREG North-West Europe URBCON (By-products for sustainable concrete in the urban environment). The tests were carried out at the Institute for Construction Material Technology at the University of Kaiserslautern, Germany.

REFERENCES

[1] Bernal, S.A., Provis, J.L., Walkley, B., San Nicolas, R., Gehman, J.D., Brice, D.G., Kilcullen, A.R., Duxson, P. and van Deventer, J.S. 'Gel nanostructure in alkali-activated binders based on slag and fly ash, and effects of accelerated carbonation'. *Cement and Concrete Research***53**, (2013)127–144, 10.1016/j.cemconres.2013.06.007.

[2] Shi, C., Roy, D. and Krivenko, P. 'Alkali-activated cements and concretes', CRC press, 2003.

[3] RILEM TC 'CPC-18 Measurement of hardened concrete carbonation depth (1988)'. In: RILEM Recommendations for the Testing and Use of Constructions Materials, E& FN SPON, 1994, 56-58, doi: 10.1617/2351580117.026.

[4] Bernal, S.A., Provis, J.L., Brice, D.G., Kilcullen, A., Duxson, P. and van Deventer, J.S. 'Accelerated carbonation testing of alkali-activated binders significantly underestimates service life: The role of pore solution chemistry'. *Cement and Concrete Research***42**(10)(2012)1317–1326, 10.1016/j.cemconres.2012.07.002.

[5] Castellote, M., Fernandez, L., Andrade, C. and Alonso, C. 'Chemical changes and phase analysis of OPC pastes carbonated at different CO_2 concentrations'. *Materials and Structures***42**(4)(2009)515–525, 10.1617/s11527-008-9399-1.

[6] Rodríguez, E.D., Bernal, S., de Gutiérrez, R.M. and Puertas, F. 'Alternative concrete based on alkali-activated slag'. *Materiales de Construcción***58**(291)(2008)53-67.

[7] D.W.S., Ho., R.K., Lewis. 'Carbonation of concrete and its prediction'. *Cement and Concrete Research***17**(3)(1987)489–504, 10.1016/0008-8846(87)90012-3.

[8] Bernal, S.A., Provis, J.L., de Gutiérrez, R.M. and van Deventer, J.S. 'Accelerated carbonation testing of alkali-activated slag/metakaolin blended concretes: effect of exposure conditions'. *Materials and Structures***48**(3)(2015)653–669, 10.1617/s11527-014-0289-4.

[9] Payne, J.W. and Dodge, B.F. 'Rate of absorption of carbon dioxide in water and in alkaline media'. *Industrial & Engineering Chemistry***24**(6)(1932)630–637.

[10] Bernal, S.A., de Gutiérrez, R.M., Pedraza, A.L., Provis, J.L., Rodriguez, E.D. and Delvasto, S. 'Effect of binder content on the performance of alkali-activated slag concretes'. *Cement and Concrete Research***41**(1)(2011)1–8, 10.1016/j.cemconres.2010.08.017.

[11] Pasupathy, K., Berndt, M., Sanjayan, J., Rajeev, P. and Cheema, D.S. 'Durability Performance of Precast Fly Ash–Based Geopolymer Concrete under Atmospheric Exposure Conditions'. *Journal of Materials in Civil Engineering***30**(3)(2018)4018007, 10.1061/(ASCE)MT.1943-5533.0002165.

[12] EN 450-1, Fly ash for concrete - Part 1: Definition, specifications and conformity criteria, 2012.

[13] EN 196-6, Methods of testing cement - Part 6: Determination of fineness, 2018.

[14] EN 196-1, Methods of testing cement - Part 1: Determination of strength, 2016.

[15] ISO 15901, Evaluation of pore size distribution and porosity of solid materials by mercury porosimetry and gas adsorption - Part 1: Mercury porosimetry, 2016.

INFLUENCE OF CURING CONDITIONS ON ALKALI-ACTIVATED MORTARS INTENDED FOR CONCRETE REPAIR

Ivana Krajnović (1) Stijn Matthys (1)

(1)Magnel-Vandepitte Laboratory, Department of Structural Engineering and Building Materials, Faculty of Engineering and Architecture, Ghent University, Technologiepark-Zwijnaarde 60, 9052, Belgium

Abstract

Repair mortars are costly materials with high level of Portland cement and various additives which questions their eco-efficiency. In this respect, cement free material solutions such as alkali-activated mortars based on ground granulated blast furnace slag (BFS) are gaining interest for structural repair. The aim of this research is to study blast furnace slag as a precursor for producing ambient cured alkali-activated repair mortars. To achieve this purpose, a total of four mixtures were prepared using four different molar ratios of the silicate solution. The fresh and hardened properties of the produced mortars including flow retention, dry density, compressive and flexural strength are studied comparing ambient-cured and sealed-cured specimens. Furthermore, the tensile bond strength between the repair mortars and a grit blasted concrete substrate was verified (after 7 days sealed + 21 days ambient curing). The results demonstrate, for the tested configurations, the feasibility of the alkali-activated repair mortar, including a good adherence. Given the limited scope of the tests, more work is needed to confirm the observations further.

Keywords: Alkali-activated materials, Geopolymers, Repair mortars, Tensile pull-off bond strength, Curing conditions

1. INTRODUCTION

Over the last century the development of concrete as a building material and its usage exploded, changing the landscapes of the entire planet. Most of the contemporary infrastructure is made of concrete and designed for a life span of 50 to 100 years. A vast amount of these structures reach the end of service life, in a condition more suitable for repair or upgrading, rather than for replacement. Furthermore, concrete structures often experience various environmental attacks, accidental events, lack of maintenance and other actions, which can result in need for repair during their service life. For all of these reasons, in recent years, developed countries often are investing more in rehabilitation and repair than in new construction.

Alkali-activated materials (AAMs) are emerging as future-proof technology of concrete production, as they combine utilisation of industrial by-products and omission of ordinary Portland cement (OPC), hence maximizing environmental benefits of concrete [1]. In some parts of the world, this technology has been utilised in the last century due to shortages of OPC, and in the western world it has been extensively researched over the last 20 years [2]. AAMs typically have rapid strength development, good fire resistance, good bond with OPC substrate, fast setting time, and good acid resistance which makes them attractive as repair mortars [2,3]. This combined with environmental benefits justifies recent increase in development of AAMs in concrete repair [4].

The purpose of this research is to develop alkali-activated repair mortar based on locally available industrial by-products and furthermore to check its potential for structural strengthening of concrete structures by means of textile reinforced mortar (TRM). A previously published repair mortar mix design based on the ground granulated blast furnace slag [3,5] was chosen as a starting point, due to its high flexural and compressive strength and relatively low shrinkage and compatibility of the materials. Concerns had been raised that proper adhesive bond between this repair mortar configuration and old concrete substrates might be an issue, as the delamination of mortar from substrate was reported in the original study [3,5]. Keeping in mind that the adhesive bond is sensitive to the pre-treatment of the concrete substrate and the application procedure [6,7], authors had decided in favour of replication and further investigation. This paper reports on a verification of the feasibility of BFS based AAM repair mortar according to EN 1504-3 [8], looking into different molar ratios of the silicate activator solution, as well as into curing conditions. Behaviour in terms of workability, strength and bond interaction with concrete substrates are considered.

2. EXPERIMENTAL PROGRAM

As a precursor for alkali-activated repair mortars, locally available BFS, provided by Ecocem Benelux is used. The chemical composition of the BFS is determined by X-ray fluorescence (XRF), and presented in Table 1. Particle size distribution (PSD) and specific surface area of BFS is obtained with laser diffraction. Results are shown in Table 2. Commercially available sodium silicate solution (type Crystal 112), with molar ratio of the silicate solution (MS) of about 2; sodium hydroxide flakes with purity higher than 99%; and demineralized water are used to create the aqueous alkali solution. Standard CEN sand compliant with EN 196-1 [9] was used as the aggregate. The mortars are prepared with an aggregate to precursor ratio of 2.42, water to precursor ratio of 0.45 and Na_2O content (present in the alkali solution) of 5 % per weight of precursor. The MS of the alkali solution is tailored by blending the sodium silicate and sodium hydroxide, while the concentration of the Na_2O per weight of the precursor was kept the same. Solutions with MS = 0.24 as in [3], MS = 0.46 analogue to [10] and MS = 0.7 and MS = 1 were used as activators.

Table 1: Content of important oxides in binder constituents

	Na_2O	SiO_2	CaO	Al_2O_3	SO_3	Fe_2O_3	MgO
BFS [wt%]	-	31.1	40.9	13.7	2.3	0.4	9.2
Sodium silicate [wt%]	15	29.75	-	-	-	-	-

Activators were created by mixing water, sodium silicate and sodium hydroxide 24 hours in advance, while precursors and sand were stored in laboratory condition together with mixing equipment. Mortars were prepared in a 3l mixer (type Hobart) that complies with EN 196-1 [9]. The aggregate and precursors were added in the mixing bowl and mixed for at least 180 seconds at low speed (140 rpm), then the alkaline solution was added to the mixing bowl slowly over the period of 60 seconds, while mixing at low speed. For the next 30 seconds, the mixing speed is increased to 285 rpm, after which mixing is stopped for 90 seconds; 30 for scraping the material from bowl's bottom and edges with a plastic scoop and another 60 seconds for the mixture to stabilize and rest; than the mixture is again mixed at high speed (285 rpm) for 60 seconds more. Five minutes after mixing, a flow test is conducted to determine consistency of the mortars according to EN 13395-1 [11] (and repeated after 10 and 30 minutes for the determination of the flow retention). Mortars were casted into moulds, which are subdivided into three prisms with following dimensions: length - 160 mm, width and height of 40 mm. The casting process is done in two layers. Every layer is compacted with at least 10 strokes with a tamper after which the mould is vibrated for 15-30 seconds to avoid air cavities.

Table 2: Particle size distribution and specific surface area of the BFS obtained with laser diffraction

	Particle size distribution			**Specific surface area**
	d_{10} (μm)	d_{50} (μm)	d_{90} (μm)	[m^2/g]
BFS	1.238	7.117	20.485	0.655

After mixing, moulds are covered with plastic sheet and stored for 24 hours. During which specimens were demoulded, 3 of each was tested, and the rest is stored in the following way: part of the specimens was stored at so-called ambient curing (AC), meaning uncovered in a large climate room at 20°C and RH of 60%, and part of the specimens was stored in sealed conditions at the constant temperature of 20°C. The bulk density of mortars, flexural and compressive strengths were determined according to EN196-1 [9]. At least 3 specimens were tested for each time and curing condition. Specimens for testing bond strength of repair mortars are prepared and carried out according to EN 1542 [12]: all mix configurations were applied to a concrete substrate type MC(40) according to EN 1766 [13]. The substrates, 300x300x100 mm, were at least three months old, grit blasted to the roughness of 0.45 mm, thoroughly cleaned and every batch passed quality control in terms of compressive and tensile pull-off strength [14]. Wooden formwork was glued to the concrete to ensure thickness of the overlay of 20 mm. The surface was prewetted 30 minutes before the application (yet moist-dry at the surface), and the mortar was hand-applied, with special attention to the creation of the interface layer between old and new material, and covered with plastic sheet. After 24 hours, wooden formwork is removed, specimens were sealed with plastic sheet for 6 more days, after which they were stored at ambient curing. 21 days after casting, 5 cores were drilled in every specimen and 28 days after casting every specimen was subjected to the tensile pull-off tests according to EN 1542 [12]. This bond test comprises direct pull-off of a steel dolly glued to the top of the core repair mortar previously cored through mortar and substrate until 15 mm in the substrate.

3. RESULTS AND DISCUSSION

The initial configuration MS 0.24 was designed [3] as a stiff, thixotropic trowel grade mortar suitable for application on vertical surfaces, but with increase of the MS ratio the initial flow increased to the value more characteristic to self-compacting mortars (Figure 1). However, the flow retention in terms of final setting was not influenced by the increase of MS ratio, all configurations were not workable after 30 mins, as previously reported in [3,5].

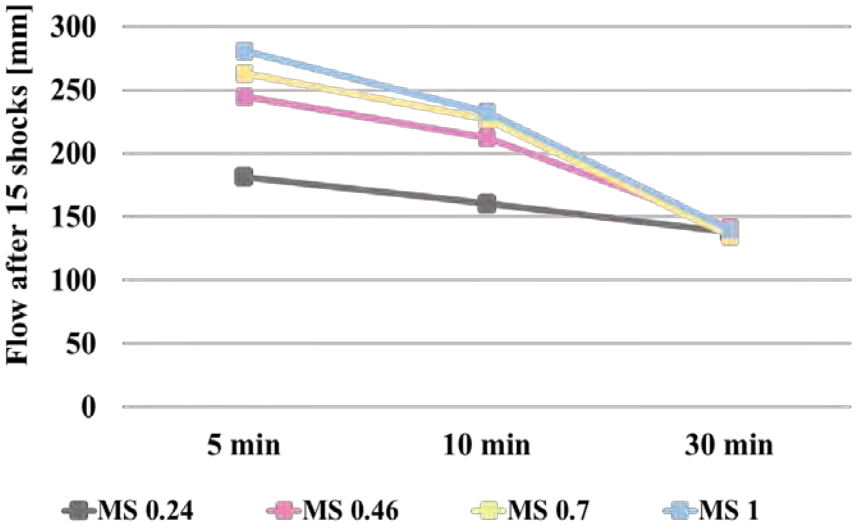

Figure 1: Flow values of different mortar configurations

The bulk densities of the mortars, are given in Figure 2, and range between 2220 and 2380 kg/m^3. With the increase of MS ratio, the bulk density increases, which is probably due to increase in the microstructural density of the reaction products in the alkali-activation process [15]. Since bulk density was measured each time on a different set of specimens, no conclusions on weight loss could be drawn, but it is worth mentioning that AC specimens have lower density than their sealed counterparts. This difference is the most prominent on the 28 days old specimens of each configuration.

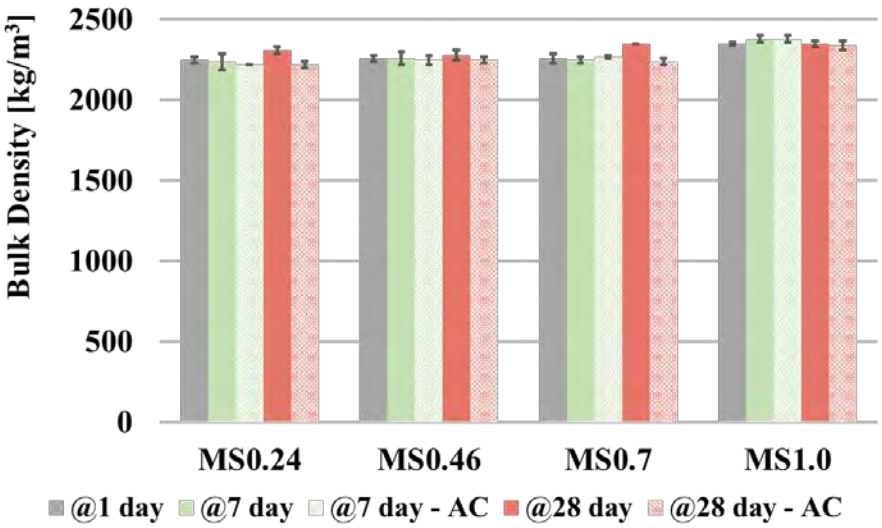

Figure 2: Bulk densities of tested mortar configurations

Compressive strength of tested configurations and curing regiments are presented in Figure 3. All configurations showed compressive strength above 45 MPa, which is the minimal strength for R4 repair mortars according to EN 1504-3 [8]. With the increase of the molar ratio of the silicate solution, compressive strength increases, from about 45 for MS 0.24 to around 94 MPa for MS 1. The curing condition does not affect the compressive strength of the mortars, with differences between sealed and AC specimens within margins of standard deviation. It does, however, affect flexural strength in all configurations.

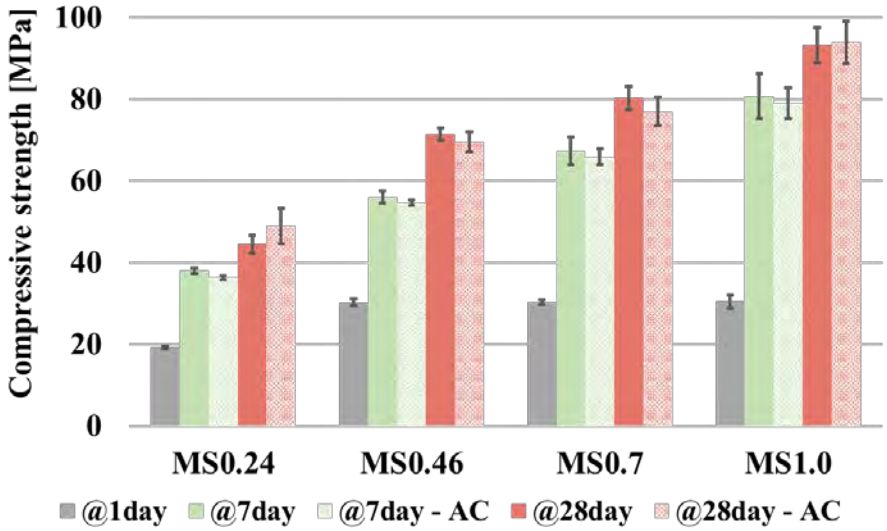

Figure 3: Compressive strengths of tested mortar configurations

Ideally, for high-end structural repair mortars, flexural strength of 8 MPa is required [14]. For the reference mix MS 0.24 after 28 days sealed curing, this is approached with 7,5 MPa. This value was lower than 11.4 MPa reported in the original study [3] for the same age and same curing conditions.

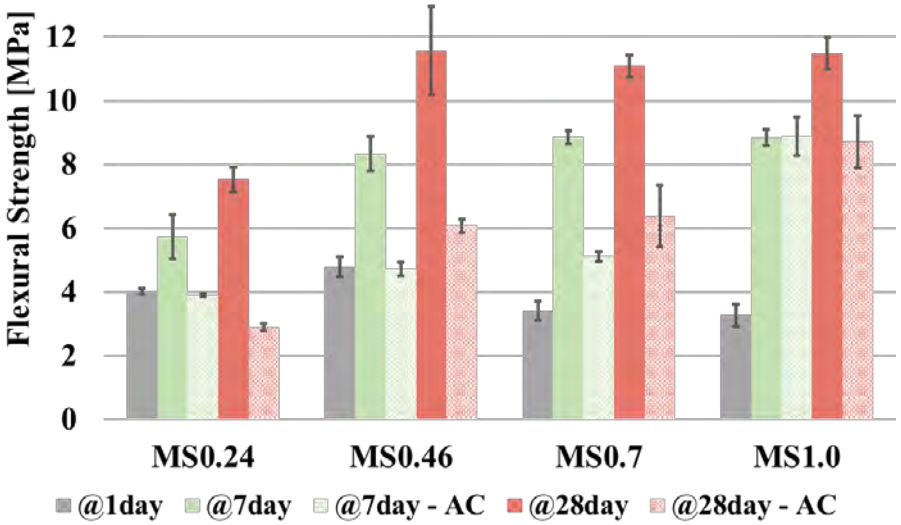

Figure 4: Flexural strengths of tested mortar configurations

By increasing the MS, flexural strength of sealed specimens generally increased, yet not necessarily already after 1 day. A 28 days flexural strength of 11,5 MPa was obtained for MS1.0, for sealed curing.

When cured at unsealed ambient conditions, the flexural strength was significantly affected, sometimes with strength reductions of 50% with respect to their sealed counter parts. Only mortar with MS 1.0 achieved value above 8 MPa, while configurations MS 0.46 and MS 0.7 showed values above 6 MPa (Figure 4).

To study the adhesive bond between the repair mortar and an OPC concrete substrate, the 4 mixes were tested further. The failure aspect of the specimens are shown in Figure 5 and bond strengths results are presented in Table 3.

Specimen MS 0.24 had no visible cracks or delaminations before testing. An average pull-off strength of 2.5 MPa was obtained fulfilling criteria for R4 class mortar from EN 1504-3 [8]. It was observed that failure is either on the interface between mortar and concrete or in the substrate itself. This indicates that the bond capacity was close to the tensile strength of the substrate. The clear difference between this and previously reported results, might come from various factors. Time and manner in which the wooden formwork removed might play a role, since it can damage material if removed too early, or constrain shrinkage/expansion and induce microcracks in the interface zone. Treatment of the substrate's surface can also play a role, as the grit-blasted surface facilitates mechanical interlocking between old concrete and repair mortar and prewetting minimises substrate's adsorption of the alkaline solution needed for the alkali-activation of the mortar. However, all of this is speculative and could be further investigated.

Table 3: Results of the pull-off tensile test

Configuration	**MS 0.24**	**MS 0.46**	**MS 0.7**	**MS 1**
Adhesive bond strength, mean value [MPa]	2.5	≥ 2.1	n.t.*	≥ 1.7

Standard deviation	0.27	0.31	n.t.*	0.30
Failure mode, cumulative for all tests	80% mortar-concrete interface 20% concrete	90% concrete, 10% mortar concrete interface	n.t.*	100% concrete

*not tested

Specimen MS 0.46 had an average tensile bond strength of 2.1 MPa with no single value lower than 75% of the minimal requirement which fulfils requirement for R4 repair mortar [8]. There was no visible cracking of delamination observed on this specimen either.

Specimen MS 0.7 showed some minor surface cracks that appeared after 7 days, but it was mishandled during the preparation of cores and was excluded from the analysis. This, however, demonstrates the importance of proper preparation of specimens, and subsequently, the importance of handling concrete repairs with care, competence and skill.

Specimen MS1.0 showed surface cracks that appeared after 7 days, yet no delamination was observed. This specimen reached an average pull-off strength of 1.7 MPa, going hand in hand with tensile failure in the concrete substrate. Note that dolly #3 failed during drilling and could not be tested further. Given the fact that the substrate's tensile strength in this case was the weakest part of this system and lower than required by the standard (in spite of the batch passing quality control), no further conclusion can be made of the bond capacity of the repair mortar MS. Tentatively, in reference to a tensile bond strength of minimum 1.7 MPa, this would correspond with at least an R3 class repair mortar. More extensive testing is however needed to come to further conclusions.

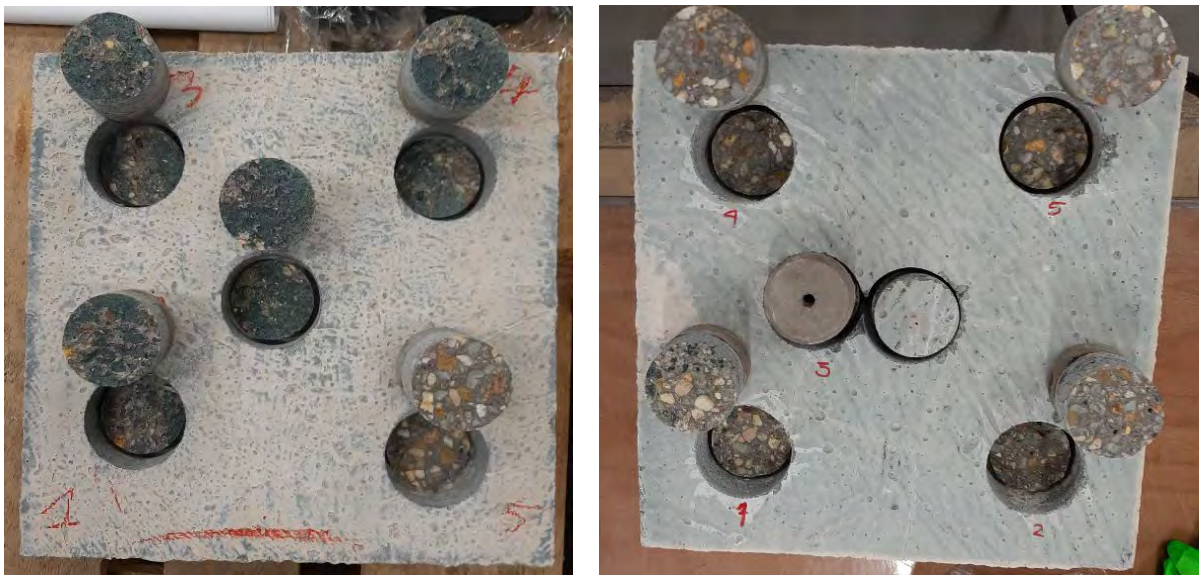

Figure 5: Pull-off bond test specimens of the configuration MS 0.24 and MS 1

4. CONCLUSIONS AND FUTURE WORK

All mortar configurations showed mechanical properties that are putting them at least in class R3 repair mortars according to EN 1504-3 [8], even when cured in ambient conditions.

In terms of the flow and flow retention, all configurations performed as expected. With the increase of MS ratio, the initial flow of the mixtures increased, with no effect on final setting time. None of the mortars were sufficiently workable after 30 minutes. This remains as a challenge for future work.

Compressive strength was almost not affected by curing conditions, which might indicate that Na_2O content of 5% per weight of precursor might be the right concentration for BFS based AAMs. In boundary conditions (MS 0.24 and MS 1), AC specimens showed slightly higher compressive strength, still within margins of standard deviations.

Flexural strength is the most affected by the curing condition. Restrained internal shrinkage effects, and associated microcracking in the material, might be a possible cause for this phenomena. This stresses the importance of establishing proper protocols when AAM repair mortars would be applied in practice, and the need for application robust AAM repair mortar mix designs in this respect.

By looking at the results of the pull-off tests, the good bond was observed, even in cracked specimen, indicating suitability of slag-based AAMs for concrete repair and the application in TRM systems. Shrinkage mitigation and evaluation of other durability properties according to EN 1504-3 [8] remains as a challenge for further work.

ACKNOWLEDGEMENTS

This project has received funding from the European Union's Horizon 2020 research and innovation programme under grant agreement No 813596 DuRSAAM.

REFERENCES

[1] Habert, G., and Ouellet-Plamondon, C., Recent update on the environmental impact of geopolymers, *RILEM Tech. Lett.* **1** (2016) 17.

[2] Provis, J. L., and van Deventer, J. S. J., *Alkali Activated Materials State-of-the Art Report RILEM TC 224-AAM*, 2014).

[3] Kramar, S., Šajna, A., and Ducman, V., Assessment of alkali activated mortars based on different precursors with regard to their suitability for concrete repair, *Constr. Build. Mater.* **124** (2016) 937–944.

[4] Fahim Huseien, G., Mirza, J., Ismail, M., Ghoshal, S. K., and Abdulameer Hussein, A., Geopolymer mortars as sustainable repair material: A comprehensive review, *Renew. Sustain. Energy Rev.* **80** (2017) 54–74.

[5] Ducman, V., Kramar, S., and Šajna, A., Alkali activated repair mortars based on different precursors, in *Eco-Efficient Repair Rehabil. Concr. Infrastructures*, 2018).

[6] Yazdi, M. A., Dejager, E., Debraekeleer, M., Gruyaert, E., Van Tittelboom, K., and De Belie, N., Bond strength between concrete and repair mortar and its relation with concrete removal techniques and substrate composition, *Constr. Build. Mater.* **230** (2020) 116900.

[7] Courard, L., Bissonnette, B., Garbacz, A., Vaysburd, A. M., and Von Fay, K. F., Guidelines for concrete surface preparation: 10 years research and experience, *MATEC Web Conf.* **199** (2018).

[8] NBN EN 1504-3 - Products and systems for the protection and repair of concrete structures - Definitions, requirements, quality control and evaluation of conformity - Part 3: Structural and

non-structural repair, (2005).
[9] NBN EN 196-1:2016 - Methods of testing cement - Part 1: Determination of strength, (2016).
[10] Provis, J. L., Arbi, K., Bernal, S. A., Bondar, D., Buchwald, A., and Castel, A., RILEM TC 247-DTA Round Robin Test : Mix design and reproducibility of compressive strength of alkali-activated concretes, *Mater. Struct.* **59** (2019) 1–22.
[11] EN 13395-1 - Products and systems for the protection and repair of concrete structures - Test methods - Determination of workability - Part 1: Test for flow of thixotropic mortars, (2002).
[12] NBN EN 1542 - Products and systems for the protection and repair of concrete structures - Test methods - Measurement of bond strength by pull-off, (2003).
[13] NBN EN 1766 - Products and systems for the protection and repair of concrete structures - Test methods - Reference concretes for testing, (2000).
[14] Belgian Construction Certification Association, PTV 563: Technische Voorschriften Voor Herstelmortels Voor Beton, (2007) 1–59.
[15] Aydin, S., and Baradan, B., Effect of activator type and content on properties of alkali-activated slag mortars, *Compos. Part B Eng.* **57** (2014) 166–172.

STRAIN HARDENING BEHAVIOUR OF PVA FIBRE REINFORCED GEOPOLYMER COMPOSITES

Yi Wang (1), Mingzhong Zhang (1)

(1) Department of Civil, Environmental and Geomatic Engineering, University College London, London, WC1E 6BT, UK

Abstract

Strain hardening geopolymer composites (SHGC) as a tailored group of fibre reinforced geopolymer composites are featured by large tensile strain capacity with multiple micro-cracks. This paper experimentally investigates the strain hardening behaviour of SHGC in terms of flexural stress-deflection response, failure mode and cracking, flexural strength and toughening mechanisms. SHGC specimens were prepared using fly ash and slag with a weight ratio of 80:20 as the binder, a combination of NaOH and Na_2SiO_3 as the alkaline activator with the activator/binder ratio of 0.4. The effects of PVA fibre content (0, 1%, 1.5%, and 2%) and micro-silica sand content (0, 10%, 20%, 30%, and 40%) on strain hardening behaviour of SHGC specimens were estimated. The toughening mechanisms (fibre bridging, rupture, and pull-out) and features of micro-cracks (number and width) distributed over the tensile side of specimens under four-point bending were characterised using digital microscope.

Results indicate that all fibre reinforced specimens exhibited strain hardening behaviour with large deflection and multiple micro-cracks. The addition of PVA fibres up to 2% improved the strain hardening behaviour of SHGC and increased the flexural strength by 126% compared to SHGC specimen without fibre because of fibre bridging effect. The incorporation of micro-silica sand up to 20% enhanced the flexural strength by 38.3% but further adding sand to 40% reduced the flexural strength of SHGC specimens. Overall, the SHGC specimen containing 2% PVA fibre and 20% micro-silica sand achieved the optimum strain hardening behaviour.

Keywords: Alkali-activated materials, Engineered geopolymer composites, Fibre reinforced concrete, Flexural behaviour, Toughness

1. INTRODUCTION

In the past decades, geopolymers sourced from industrial by-products such as fly ash (FA), ground granulated blast-furnace slag (GGBS) have emerged as a promising alternative to ordinary Portland cement (OPC), because geopolymers can help enhance the mechanical properties and reduce the environmental impact of concrete. The production of one tonne OPC generates 0.7-1.1 tonne of carbon emission to the environment, and the construction industry consumes 4.3 billion tonnes of OPC annually as the binder for concrete [1]. It has been proved

that the use of geopolymers as binder for concrete can result in a reduction in carbon emission by 80%-90% compared to OPC [2]. However, geopolymers are brittle and prone to cracking, which would decrease the strength and durability of geopolymers. To overcome these drawbacks, short fibres such as steel, basalt, and polyvinyl alcohol (PVA) fibres are incorporated into geopolymers to produce fibre reinforced geopolymer composites (FRGC), which have higher cracking resistance and improved overall properties, such as mechanical strengths, ductility, toughness, and drying shrinkage.

As a tailored group of FRGC, strain hardening geopolymer composites (SHGC), also called engineered geopolymer composites (EGC), are featured by large tensile strain capacity and multiple micro-cracks distributed over the specimens. In recent years, an increasing number of studies have been focused on properties of either FA- or GGBS-based SHGC. Shaikh [3] investigated the deflection hardening behaviour of FA-based SHGC containing mono steel or PVA fibre and hybrid steel-PVA fibre. Specimens all exhibit strain hardening behaviour and multiple micro-cracks similar to that of strain hardening cementitious composites. Lee et al. [4] studied the feasibility of producing GGBS-based SHGC and found that the produced specimens achieve the tensile strain up to 4.7%, whereas the GGBS mortar without fibre only has a tensile strain of 0.02%. However, heat curing is required for FA-based SHGC to gain early strength, and the GGBS-based SHGC has low flowability, short setting time and significant drying shrinkage. Therefore, an increasing number of researches address these drawbacks by using blended FA-GGBS as the binder to produce SHGC that has optimum workability and mechanical properties under ambient curing conditions. Ling et al. [5] investigated the effect of GGBS replacement ratio on the mechanical properties of FA-GGBS blended SHGC and concluded that increasing GGBS content enhances the strength but adversely affects the ductility. However, the strain hardening behaviour of FA-GGBS based SHGC cured at ambient conditions considering the effects of fibre and sand has not been systemically studied yet.

The main purpose of this paper is to experimentally investigate the effects of PVA fibre content (0, 1%, 1.5%, and 2%) and micro-silica sand content (0, 10%, 20%, 30%, and 40%) on the strain hardening behaviour of blended FA-GGBS based SHGC under ambient curing conditions. Strain hardening behaviour of SHGC was evaluated and discussed in terms of flexural stress-deflection response, failure mode and cracking, flexural strength and toughening mechanism, based on which the optimal mix proportion of SHGC was proposed.

2. EXPERIMENTAL PROGRAMME

2.1 Raw materials

In this study, the low calcium FA (equivalent to ASTM Class F) and GGBS, supplied by Drax power station, UK and Hanson, UK, respectively, were used as precursor to produce SHGC specimens. Table 1 shows the chemical compositions of FA and GGBS. Micro-silica sand sourced from a quarry in Cheshire, UK was used as the aggregate. Fig. 1 shows the particle size distribution of FA, GGBS, and micro-silica sand. The alkaline activator was prepared by mixing the sodium hydroxide (NaOH) solution with the molarity of 10 and sodium silicate (Na_2SiO_3) solution with modulus of 2.0. The modified polycarboxylate-based superplasticiser (SP), Sika® ViscoFlow® 2000 was used to improve the workability of geopolymer matrix. Short PVA fibres supplied by Kuraray Co., Ltd., Japan was incorporated to reinforce SHGC specimens. The fibre used in this work has a length of 12 mm, density of 1.3 g/cm^3, tensile strength of 1560 MPa, and elongation of 6.5%.

Table 1: Chemical compositions (wt.%) of FA and GGBS

	SiO_2	Al_2O_3	CaO	MgO	K_2O	Fe_2O_3	TiO_2	Na_2O	SO_3
FA	49.80	25.08	4.65	1.67	3.30	11.67	1.24	0.66	1.35
GGBS	36.77	13.56	37.60	7.45	0.55	0.41	0.79	0.25	1.82

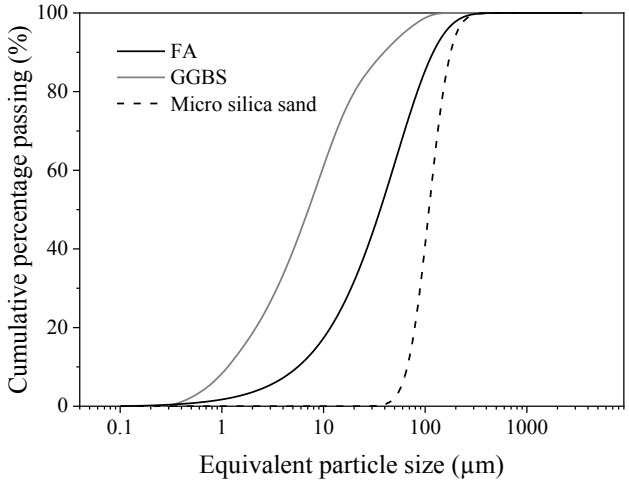

Figure 1: Particle size distribution of FA, GGBS and micro-silica sand

2.2 Specimen preparation

Eight SHGC mixes were prepared to investigate the effects of PVA fibre content and micro-silica sand content on the strain hardening behaviour of SHGC specimens. The mix proportions were determined based on a previous study [6]. The SHGC specimens were named in terms of fibre content represented by "F" and micro-silica sand content denoted by "S", as shown in Table 2.

Table 2: Mix proportions of SHGC specimens

Mix no.	FA	GGBS	Activator/binder	SP/binder	Sand /binder	Fibre (vol.%)
SHGC_S0F0	0.8	0.2	0.4	0.01	0	0
SHGC_S0F1	0.8	0.2	0.4	0.01	0	1
SHGC_S0F1.5	0.8	0.2	0.4	0.01	0	1.5
SHGC_S0F2	0.8	0.2	0.4	0.01	0	2
SHGC_S10F2	0.8	0.2	0.4	0.01	0.1	2
SHGC_S20F2	0.8	0.2	0.4	0.01	0.2	2
SHGC_S30F2	0.8	0.2	0.4	0.01	0.3	2
SHGC_S40F2	0.8	0.2	0.4	0.01	0.4	2

A Hobart HSM 10 was used to mix all samples, and the whole mixing process typically took around 8 min. In the beginning, FA, GGBS, and micro-silica sand were added in the mixer and dry mixed for 1 min. The alkaline activator was gradually added into the mixer and mixed for another 1 min, and SPs were then added into the binder to ensure flowability and mixed for further 1 min. Lastly, short PVA fibres were gradually added to avoid multifilament forms. After mixing, fresh SHGC was poured into moulds immediately and vibrated for around 5 min using a vibration table. All samples were covered with the plastic sheet to prevent water evaporation and stored in an ambient environment. After 24 h, samples were demoulded and covered with the plastic sheet and then placed in the curing room with an average temperature and relative humidity of 20±2 °C and 60±5% respectively until testing at 28 d.

2.3 Test method

Four-point bending test was conducted on an Instron 3345 with a loading capacity of 5 kN to evaluate the flexural strength and strain hardening behaviour of SHGC specimens as per ASTM C1609-05 [7]. Fig. 3 shows the loading set up with a loading rate of 1.6 mm/min. The vertical displacement of specimens was recorded automatically by the machine. Flexural strength was determined by the average value of three prismatic specimens with a dimension of 400×100×20 mm. Immediately after the test before unloading, Dino-Light microscopy was used to capture the cracks and fibres in SHGC specimens to analyse features of micro-cracks and toughening mechanism. The flexural strength of SHGC specimens can be calculated as:

$$\sigma_f = \frac{Pl}{bd^2} \quad (1)$$

where σ_f represents the ultimate strength of the specimen (MPa), P is the ultimate load of the specimen (kN), l is the test span of the specimen (300 mm in this case), b is the width of the specimen (mm), and d is depth of the specimen (mm).

3. RESULTS AND DISCUSSION

Table 3 lists the detailed test results of SHGC specimens under four-point bending, including average ultimate flexural strength and deflection, crack number and average crack width.

Table 3: Flexural properties of SHGC specimens at 28 d

Mix no.	Average ultimate flexural strength (MPa)	Average ultimate flexural deflection (mm)	Crack number	Average crack width (μm)
SHGC_S0F0	2.87	0.68	-	-
SHGC_S0F1	4.61	11.49	21	431.90
SHGC_S0F1.5	5.73	25.02	80	62.28
SHGC_S0F2	6.48	24.20	93	68.2
SHGC_S10F2	8.64	27.36	132	58.6
SHGC_S20F2	8.97	24.80	98	80.0
SHGC_S30F2	8.85	26.87	89	91.9
SHGC_S40F2	7.55	22.74	50	124.1

3.1 Stress-deflection curves

Fig. 2 displays the typical stress-deflection curves of all mixtures. Except for SHGC_S0F0 without fibre, all SHGC specimens exhibited strain hardening behaviour: the flexural stress-deflection curve initiated with a linear elastic stage until the first crack was generated and continued with a higher rate in deflection until reaching the ultimate load capacity of the specimen, followed by the final failure of the specimens.

Fig. 2a shows the influence of fibre content on flexural stress-deflection curves of SHGC specimens. The addition of PVA fibre improved the strain hardening behaviour of specimens. The specimen without fibre (SHGC_S0F0) presented a brittle behaviour: the specimen failed immediately when it reached the ultimate flexural strength and only had an ultimate deflection of 0.68 mm. The incorporation of 1% fibre (SHGC_S0F1) allows the specimen to exhibit strain hardening behaviour and increased the deflection by 1589.7% compared to SHGC_S0F0. A serrated line can be observed in the post peak stage, which indicated sharp brittle cracks due to insufficient fibre bridging effect. Further incorporation of PVA fibre up to 2% (SHGC_S0F1.5 and SHGC_S0F2) significantly enhanced the strain hardening behaviour of SHGC specimens, showing a relatively smoother line in the post peak stage and the doubled deflection capacity compared to SHGC_S0F1.

The effect of micro-silica sand content on flexural stress-deflection curves of SHGC specimens is illustrated in Fig. 2b. All specimens exhibited strain hardening behaviour and were marginally influenced by the increase of micro-silica sand content. The ultimate flexural strength of all SHGC specimens was approximately twice of first crack flexural strength. The average ultimate flexural deflection of specimens ranged from 24.20 mm (SHGC_S0F2) to 27.36 mm (SHGC_S10F2).

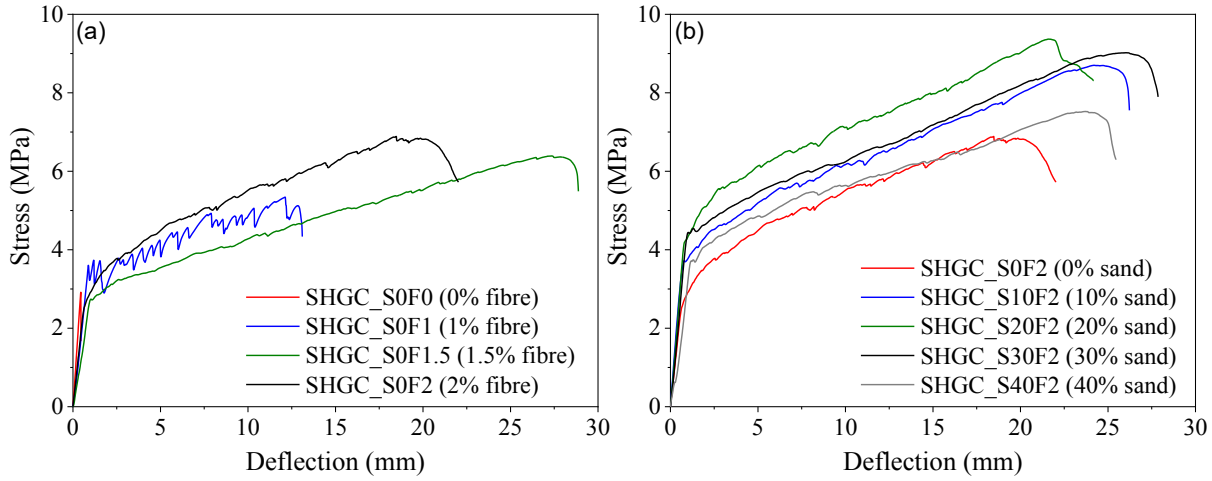

Figure 2: Typical stress-deflection curves of SHGC specimens: (a) effect of fibre content, and (b) effect of sand content

3.2 Failure mode and cracking

Fig. 3 shows the typical failure mode of the SHGC specimens with a large deflection and multiple micro-cracks distributed over the tensile side of the specimen under four-point bending. The content of PVA fibre exhibits a significant influence on the fracture behaviour of SHGC specimens. As seen in Table 3, the addition of PVA fibre increased the crack number but

reduced the average crack width of SHGC specimens. SHGC_S0F0 failed into two parts (or three parts) immediately when the specimen reached the ultimate flexural strength following a brittle failure mode. The specimen with the incorporation of 1% fibre (SHGC_S0F1) only had 21 cracks and an average crack width of 431.90 μm, respectively. Further addition of fibres up to 2% significantly increased the crack number by 342.8% but reduced the average crack width by 84.2% compared to SHGC_S0F1. The incorporation of fibres into SHGC specimens restrained the growth of cracks but increased the crack number under four-point bending because of fibre bridging effect, as explained in Section 3.4, which contributes to the enhanced deflection capacity, as shown in Fig. 2. On the other hand, increasing the micro-silica sand content reduced the crack number but increased the average crack width of SHGC specimens. SHGC mortar with 10% micro-silica sand (SHGC_S10F2) had 132 cracks and an average crack width of 58.60 μm. Further addition of micro-silica sand up to 40% reduced the crack number by 62.1% but increased the average crack width by 111.8% compared to SHGC_S10F2. The excessive incorporation of micro-silica sand can adversely affect the interaction between fibre and matrix in the SHGC specimens and further reduce the fibre bridging effect, which can result in the impaired fracture resistance and strain hardening behaviour [8].

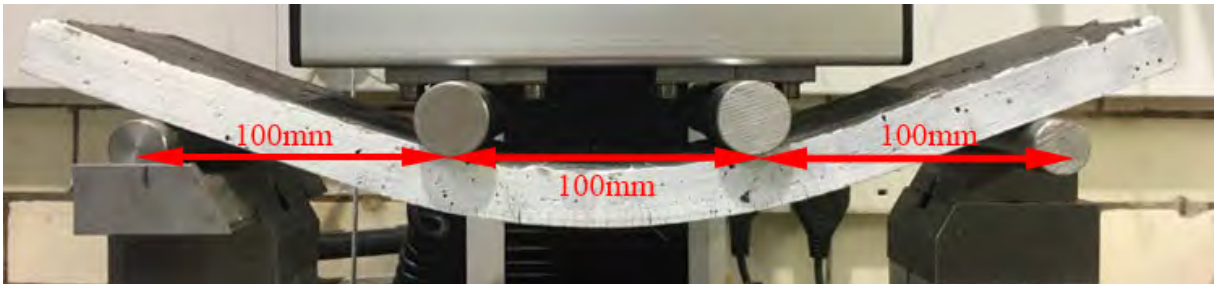

Figure 3: Loading set up and typical failure mode of SHGC specimen with micro-cracks

3.3 Flexural strength

Fig. 4 illustrates the effects of fibre content and micro-silica sand content on the flexural strength of SHGC specimens. The flexural strength of SHGC specimens was increased with the addition of PVA fibres. SHGC without fibre (SHGC_S0F0) had a flexural strength of 2.87 MPa. As compared with SHGC_S0F0, the increase of fibre content by 1%, 1.5%, and 2% enhanced the flexural strength of SHGC specimens by 60.6%, 99.7%, and 125.8%, respectively. The improvement of flexural strength of SHGC specimens can be attributed to the improved fibre bridging effect. In addition, SHGC specimens containing micro-silica sand (SHGC_S10F2, SHGC_S20F2, SHGC_S30F2, and SHGC_S40F2) all had a higher flexural strength than SHGC paste (SHGC_S0F0, SHGC_S0F1, SHGC_S0F1.5, and SHGC_S0F2), which is consistent with the findings by Nematollahi et al. [9]. In comparison with SHGC_S0F2, the addition of 10% micro-silica content (SHGC_S10F2) significantly increased the flexural strength by 33.3%, but further increasing micro-silica sand content by 20% (SHGC_S20F2) marginally enhanced the flexural strength by 3.8% compared to SHGC_S10F2. However, SHGC specimens containing 30% (SHGC_S30F2) and 40% (SHGC_S40F2) micro-silica sand had reduced flexural strengths by 1.3% and 15.8%, respectively, compared to SHGC_S20F2. Such reduction in flexural strength can be ascribed to fibre corrugation caused by the interaction between matrix and fibre [8].

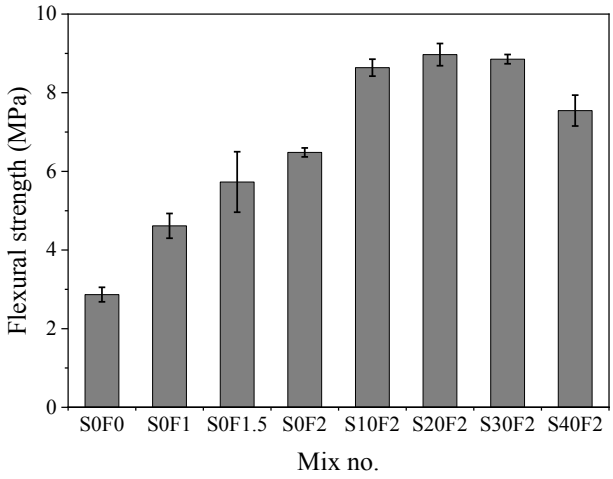

Figure 4: Flexural strength of SHGC specimens

3.4 Toughening mechanisms

Fig. 5 exhibits the toughening mechanisms of SHGC specimens, including fibre rupture, fibre pull-out and fibre bridging.

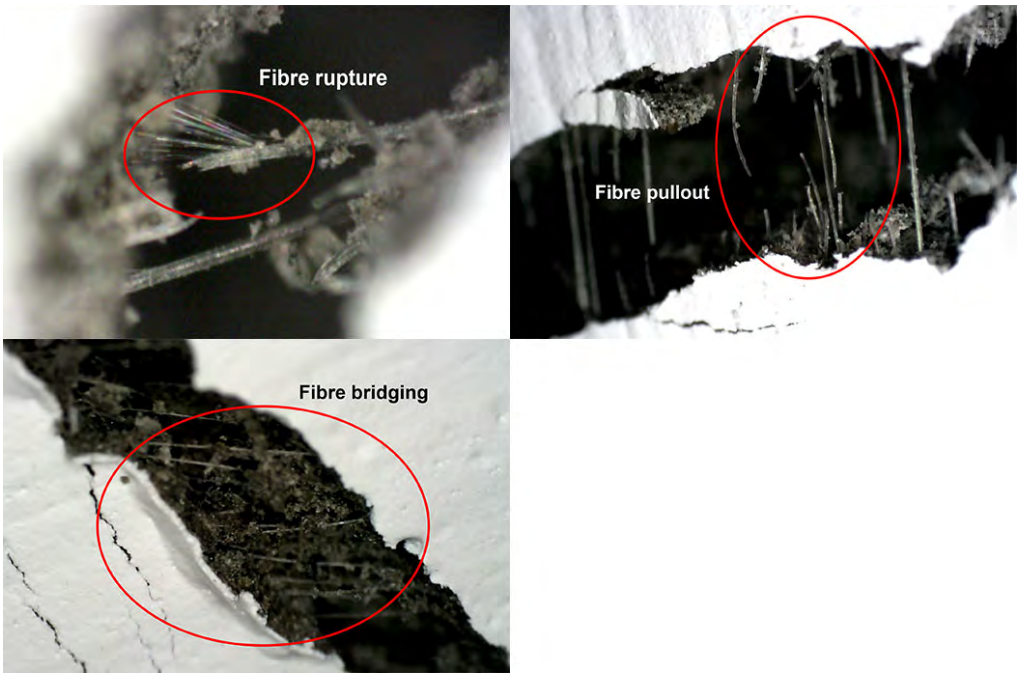

Figure 5: Toughening mechanisms of SHGC specimens

The development of strain hardening behaviour of SHGC specimens can be ascribed to fibre bridging effect. As described in Sections 3.1 and 3.2, SHGC with low fibre content (SHGC_S0F1) experienced sharper brittle cracks and exhibited less cracks with larger average crack width, while SHGC specimens containing higher fibre content (SHGC_S0F1.5 and SHGC_S0F2) presented smoother strain-deflection curves and contained more cracks with

smaller average crack width. Once the crack was initiated, the flexural stress was transferred to other parts of the specimens because of fibre bridging effect that prevents the sudden failure at crack region. When the fibre at crack region cannot resist the flexural stress, fibre rupture occurs, while fibre pull-out happens when the flexural stress exceeds the bond strength between fibre and matrix [10].

4. CONCLUSIONS

This paper experimentally investigated the strain hardening behaviour of FA-GGBS based SHGC cured at ambient conditions under four-point bending considering various PVA fibre content (0%, 1%, 1.5%, and 2%) and micro-silica sand content (0%, 10%, 20%, 30%, and 40%). All fibre reinforced specimens exhibited strain hardening behaviour with large deflection and multiple micro-cracks distributed over the tensile side of specimens. It was indicated that the SHGC specimen incorporated with 20% micro-silica sand and 2% PVA fibre presented the optimum strain hardening behaviour among all mixtures.

ACKNOWLEDGEMENTS

The authors gratefully acknowledge the financial support of the Engineering and Physical Sciences Research Council (EPSRC) via grant EP/R041504/1 “Development of a Novel Self-Healing Composite for Sustainable and Resilient Concrete Infrastructure”.

REFERENCES

[1] Bosoaga, A., Masek, O. and Oakey, J.E. ‘CO_2 capture technologies for cement industry’. *Energy Procedia* 1(1)(2009)133-140.

[2] Lehne, J. and Preston, F. ‘Making concrete change: innovation in low-carbon cement and concrete’. London: The Royal Institute of International Affairs, 2018.

[3] Shaikh, F.U.A. ‘Deflection hardening behaviour of short fibre reinforced fly ash based geopolymer composites’. *Mater. Design* 50(2013)674-682.

[4] Lee, B.Y., Cho, C.G., Lim, H.J., Song, J.K., Yang, K.H. and Li, V.C. ‘Strain hardening fiber reinforced alkali-activated mortar - A feasibility study’. *Constr. Build. Mater.* 37(2012)15-20.

[5] Ling, Y., Wang, K., Li, W., Shi, G. and Lu, P. ‘Effect of slag on the mechanical properties and bond strength of fly ash-based engineered geopolymer composites’. *Compos. Part B Eng.* 164(2019)747-757.

[6] Fang, G., Ho, W.K., Tu, W. and Zhang, M. ‘Workability and mechanical properties of alkali-activated fly ash-slag concrete cured at ambient temperature’. *Constr. Build. Mater.* 172(2018)476-487.

[7] ASTM C1609-05, Standard Test Method for Flexural Performance of Fiber-Reinforced Concrete (Using Beam with Third-Point Loading). West Conshokocken: American Society for Testing and Materials, 2012, 9 pages.

[8] Akkaya, Y., Peled, A., Picka, J.D. and Shah, S.P. ‘Effect of sand addition on properties of fiber-reinforced cement composites’. *ACI Struct. J.* 97(2000)393-400.

[9] Nematollahi, B., Sanjayan, J. and Shaikh, F.U.A. ‘Matrix design of strain hardening fiber reinforced engineered geopolymer composite’. *Compos. Part B Eng.* 89(2016)253-265.

[10] Ranjbar, N. and Zhang, M. ‘Fiber-reinforced geopolymer composites: A review’. *Cement Concrete Comp.* 107(2020)103498.

LATTICE BOLTZMANN SIMULATION OF CHLORIDE TRANSPORT IN ALKALI-ACTIVATED SLAG

Zhiyuan Xu (1), Yibing Zuo (2), Guang Ye (1)

(1) Microlab, Section of Materials and Environment, Faculty of Civil Engineering and Geosciences, Delft University of Technology, Delft 2628 CN, the Netherlands

(2) School of Civil Engineering and Mechanics, Huazhong University of Science and Technology, Wuhan, China

Abstract

In this work, a numerical model is proposed to study chloride transport in alkali-activated materials. This model is based on multiple-relaxation-time lattice Boltzmann method, where particle distribution function is introduced to simulate the chloride binding and diffusion. This model takes into account diffusion, homogenous reaction between chloride ions and diffusive solid, and heterogeneous reaction between chloride ions and non-diffusive solid. The accuracy of the model is confirmed by a benchmark simulation of transient reactive transport problem. As a demonstration, this model is then applied to simulate chloride transport in alkali-activated slag paste with varying alkaline activators. The influence of alkali content, silica content, curing age and chloride binding on the chloride transport property is briefly discussed.

Keywords: lattice Boltzmann method, chloride transport, alkali-activated slag, chloride binding

1. INTRODUCTION

Chloride ingress from external sources, e.g., marine environment or de-icing salts, is the dominant cause for the steel rebar corrosion in the reinforced concrete. The steel rebar is protected by a layer of iron oxide formed on its surface, which results from the high alkaline environment provided by the cement paste. However, a sufficient amount of chloride ions penetrated onto the surface of the steel rebar will break down the passive layer and then initiate the rebar corrosion, which in the end may lead to the structure failure [1].

Alkali-activated materials (AAMs), synthesized by the reaction between aluminosilicate precursor and alkaline activators, have emerged as promising alternatives with low carbon footprint and comparable compressive strength to Portland cement [2]. Although the growing technology of AAMs is drawing a lot of attention in the engineering and research fields [3], only a few experimental studies focused on the chloride transport [3-5] and no numerical study has been carried out in this aspect.

The simulation of chloride transport is significantly dependent on the microstructure of cementitious material. Recently, Zuo developed a numerical framework to simulate the hydration and microstructure formation of alkali-activated materials, called GeoMicro3D [6]. It is composed of four modules, parking of precursors, dissolution of precursors, formation of reaction products, nucleation and growth. All the modules were validated through experimental results, showing the numerical framework can fairly predict the reaction process and microstructure development. Over the last two decades, the lattice Boltzmann method has attracted considerable attention due to its simplicity and accuracy in solving problems with complex boundaries such as fluid flow and convective diffusion in porous media. A detailed introduction and implementation are presented in the next section.

The aim of this study is to present a numerical model to simulate the chloride transport in the alkali-activated materials. The simulation is based on the microstructure generated from GeoMicro3D and lattice Boltzmann method. The numerical model is firstly validated by a benchmark case and then applied to chloride transport in the alkali-activated slag paste.

2. NUMERICAL METHOD

2.1 Lattice Boltzmann method for reactive diffusion

Chloride transport in the cementitious materials is a reactive transport problem. The governing equation for this process can be written as

$$\frac{\partial \phi C}{\partial t} = \nabla \cdot \left(\phi D_p \nabla C \right) + R_{\text{hom}}, \tag{1}$$

where C is the chloride concentration, ϕ is local voxel porosity, D_p is the local chloride diffusivity and R_{hom} is the homogenous reaction caused by chloride binding. Many studies have used lattice Boltzmann method to solve reactive transport problem [7, 8]. Different from conventional numerical methods such as finite volume method, lattice Boltzmann method solves the governing equation by tracking the evolution of particle distribution function $g_i(\mathbf{x},t)$. The evolution of the $g_i(\mathbf{x},t)$ follows the lattice Boltzmann equation

$$g_i\left(\mathbf{x}+\mathbf{e}_i\delta t, t+\delta t\right) - g_i(\mathbf{x},t) = \Omega_i\left(\mathbf{x},t\right) + Q_i\left(\mathbf{x},t\right), \tag{2}$$

where Ω_i is the collision operator, Q_i is the source term due to homogenous reaction and $\mathbf{e}_i$ is the discrete velocity in *i*th direction. The obtained particle distribution function g_i will be used to calculate the macroscopic variable, which is $\phi C = \sum_i g_i$ in this reactive transport problem. In three-dimension, a lattice structure of 19 velocity directions (D3Q19) is usually adopted in fluid mechanics. However, it is reported that the velocity directions can be decreased from 19 to 7 (D3Q7) without compromising the numerical accuracy in the pure diffusion process without convective term [9]. Thus the lattice structure of D3Q7 is employed in the present model to avoid unnecessary computation. The discrete velocity $\mathbf{e}_i$ is given as $\mathbf{e}_0 = (0,0,0)$, $\mathbf{e}_{1,2} = (\pm 1,0,0)$, $\mathbf{e}_{3,4} = (0,\pm 1,0)$ and $\mathbf{e}_{5,6} = (0,0,\pm 1)$. There are several different collision operators available in the framework of lattice Boltzmann method. Bhatnagar-Gross-Krook (BGK) operator is probably most frequently used due to its simplicity. However, BGK operator is criticized for the dependence of numerical results on the relaxation parameter [10]. To

eliminate such artificial results, multiple-relaxation-time (MRT) scheme is adopted in the present model, which has been demonstrated more suitable, in terms of accuracy and stability, to study transport problem [10, 11]. The basic process of MRT scheme is to project the particle distribution function g_i onto the seven-dimensional vector space, where each component corresponds to a physically relevant moment of g_i, then relax the moments to equilibrium with different relaxation coefficients and finally project the relaxed moments back onto the original space. Mathematically, the collision operator Ω_i in MRT scheme is given by

$$\Omega_i\left(\mathbf{x},t\right)=-\left(\mathbf{M}^{-1}\mathbf{S}\mathbf{M}\right)_{ij}\left[g_j(\mathbf{x},t)-g_j^{(eq)}(\mathbf{x},t)\right], \tag{3}$$

where g_i^{eq} is the equilibrium particle distribution function, **M** is the transformation matrix and **S** is a diagonal relaxation matrix. To recover the governing equation from lattice Boltzmann equation, the equilibrium distribution function is designed as follows [7],

$$g_i^{eq}=w_iC, \tag{4}$$

where ω_i is the weight factor and is defined as,

$$\omega_i=\begin{cases}\dfrac{c_\phi}{2}, & i=1,\ldots,6\\ \phi-3c_\phi, & i=0\end{cases}. \tag{5}$$

c_ϕ is an adjustable parameter and is set as $\min(\phi)/3.5$ [7]. To contain certain physically relevant moments, e.g., ion amount, ion flux, the transformation matrix **M** is designed as [12]

$$\mathbf{M}=\begin{bmatrix}1&1&1&1&1&1&1\\0&1&-1&0&0&0&0\\0&0&0&1&-1&0&0\\0&0&0&0&0&1&-1\\6&-1&-1&-1&-1&-1&-1\\0&2&2&-1&-1&-1&-1\\0&0&0&1&1&-1&-1\end{bmatrix}. \tag{6}$$

The diagonal relaxation matrix **S** is expressed as $\mathbf{S}=diag\left(s_0,s_1,s_1,s_1,s_2,s_2,s_2\right)$, where s_i is relaxation coefficient for each particle distribution function g_i. The relaxation coefficient s_0 is related to conserved moment ϕC and does not affect the numerical results. In the present model, s_0 is set as 0 for simplicity. Comparing the governing equation and the recovered equation from classic multi-scale Chapman-Enskog analysis, it is found s_1 is related to diffusion coefficient by [7]

$$D_p=\frac{c_\phi}{\phi}\left(\frac{1}{s_1}-\frac{1}{2}\right). \tag{7}$$

s_2 corresponds to the second-order moment and has a significant influence on the accuracy of MRT scheme. It is reported that $s_2=2-s_1$ can eliminate discrete effect of boundary condition,

which can generate a more accurate result [11]. The source term Q_i is introduced to incorporate the homogenous reaction R_{hom}. It is expressed by [13]

$$Q_i = \left[\mathbf{M}^{-1} \left(\mathbf{I} - \frac{\mathbf{S}}{2} \right) \mathbf{M} \right]_{ij} \omega_i R_{\text{hom}}, \tag{8}$$

where **I** is the unit matrix. The macroscopic variable should be recalculated by

$$\phi C = \sum_i g_i \left(\mathbf{x}, t \right) + \frac{1}{2} R_{\text{hom}}, \tag{9}$$

in order to correctly recover the term of homogenous reaction in the governing equation.

2.2 Implementation of numerical method

The microstructure used for chloride transport simulation in this study is generated from GeoMicro3D [6], which is a numerical framework for simulating hydration and microstructure formation of alkali-activated materials. Figure 1 (a) shows the simulated microstructure of alkali-activated slag paste at 28 days. The size of the microstructure is 125 μm ? 125 μm ? 125 μm at the resolution of 1 μm ? 1 μm ? 1 μm per voxel. The microstructure is composed of liquid, unhydrated slag, C-(N-)A-S-H gel and crystalline reaction products. The chloride ions are diffusive in liquid and C-(N-)A-S-H gel and non-diffusive in the rest of the phases. Each voxel can be filled by any combination of these 4 phases. Based on the numerical test, a voxel is considered non-diffusive if the non-diffusive solid volume fraction is larger than 0.688 [6]. Figure 1 (b) shows the distribution of diffusive and non-diffusive area. For diffusive voxel, it can consist of different phases, which generates three cases, shown in Figure 2. The local chloride diffusivity is estimated based on these three cases, by differential effective media theory [14]. In Figure 2 (a), the voxel is composed of one diffusive phase and one non-diffusive phase. The local diffusivity is given as [15]

$$D_p = D_B \phi_B^{5/3}, \tag{10}$$

providing that the non-diffusive inclusions are prolate spheroids. For Figure 2 (b), the diffusive Phase A is considered as spherical inclusions in diffusive Phase B. Thus the local diffusivity can be computed as [15]

$$\left(\frac{D_A - D_p}{D_A - D_B} \right) \left(\frac{D_B}{D_p} \right)^{1/3} = \varphi_B. \tag{11}$$

Three phases, non-diffusive solid and two diffusive phases, form the voxel in Figure 2 (c). The determination of such local diffusivity can combine previous two formulas. Phase A and C can be considered as diffusive Phase AC and the diffusivity is calculated by Eq.(10). Then the local voxel diffusivity is calculated by Eq.(11) considering Phase AC and Phase B as two diffusive phases. The equation is shown as [6]

$$D_{AC} = D_A \left(\frac{\phi_A}{\phi_A + \phi_C} \right)^{5/3}, \quad \left(\frac{D_{AC} - D_p}{D_{AC} - D_B} \right) \left(\frac{D_B}{D_p} \right)^{1/3} = \varphi_B. \tag{12}$$

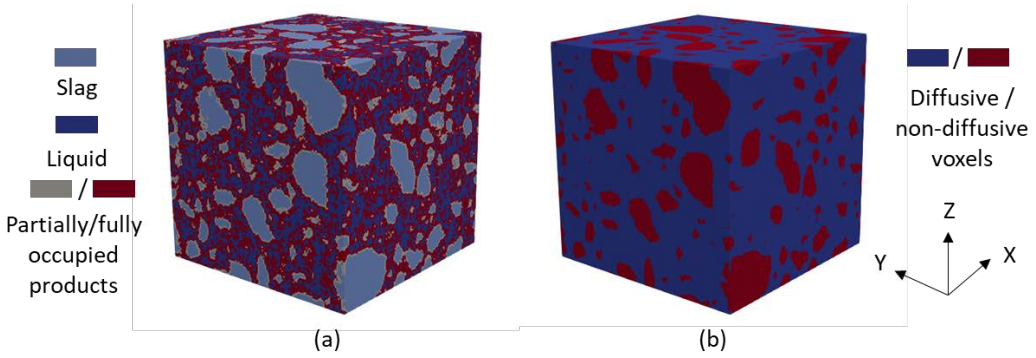

Figure 1: Simulated microstructure of alkali-activated slag paste at 28 days

Since the insufficient knowledge on the transport property of C-(N)-A-S-H gel, the C-(N)-A-S-H gel is considered as the same properties of C-S-H gel. The diffusivity of C-S-H gel is usually obtained indirectly. The reported relative diffusivity of the C-S-H gel ranges from 0.001 [6] to 0.00775 [16]. In the present simulation, the relative diffusivity of C-(N-)A-S-H gel is chosen as 0.002 and the diffusivity of chloride ions in capillary pores is set as 1.5×10^{-10} m^2/s [17]. The porosity of C-(N-)A-S-H is set as 0.3 as the porosity of high-density and low density C-S-H is 0.24 and 0.37 respectively [18]. When the chloride ions transport in the paste, the chloride ions can be bound by reaction products such as C-(N-)A-S-H gel, hydrotalcite (LDH) and strätlingite (AFm). Ke et al. [19] reported that LDH and AFm can bind a great amount of chloride ions and measured their binding capacities. To demonstrate that the present model is able to simulate the chloride transport coupled with chloride binding, the C-(N-)A-S-H gel, LDH and AFm are considered as binding phases and their chloride binding capacities are set as 20 mg/g, 160 mg/g and 130 mg/g respectively [20].

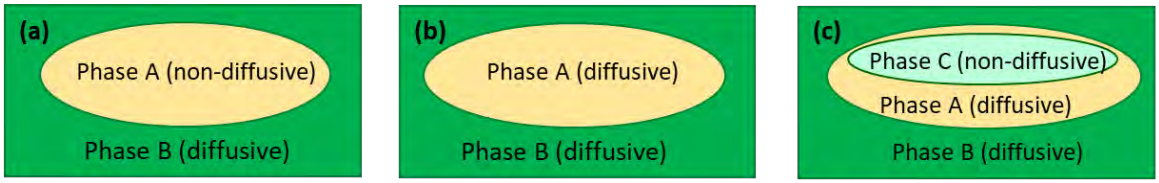

Figure 2: Three cases for local diffusivity

In the simulation, four boundary conditions are implemented, i.e., non-diffusive solid boundary, constant concentration boundary and heterogeneous reactive boundary and periodic boundary. The non-diffusive solid boundary is implemented by half-way bounce-back scheme. The constant concentration is realized by bounce-back scheme at two ends in the x direction, seen in Figure 1. The unknown $g_{\bar{i}}$ entering from outside is determined by exiting g_i and constant boundary concentration C_w, shown as

$$g_{\bar{i}}\left(\mathbf{x},t+\delta t\right)=-g_i^{\dagger}\left(\mathbf{x},t\right)+c_{\phi}C_w. \tag{13}$$

The constant boundary concentration C_w at $x=0$ μm and $x=125$ μm is set as 0.5 mol/L and 0 mol/L respectively, where 0.5 mol/L is chloride concentration in typical seawater. In reality, the chloride binding does not occur instantaneously. It takes at least several hours for reaction

products and chloride ions to reach equilibrium. Kayali et al. [21] showed that 70% binding capacity of hydrotalcite takes place within an hour and the rest binding capacity happens in the next 24 hours. Since the majority of chloride binding occurs in the very beginning, the present numerical model takes the assumption that the binding happens instantaneously, which means chloride ions are removed immediately if the binding capacity of the reaction products is not reached yet. The homogenous reaction R_{hom} is set based on this assumption. For binding phases locating at the non-diffusive solid in contact with the liquid site, i.e., the heterogeneous reactive boundary, the solid site is set as 0 mol/L constant concentration before the binding capacity is reached. The periodic boundary is used in y and z directions, where the exiting particle distribution functions enter from the opposite side.

3. VALIDATION OF NUMERICAL METHOD

To validate the effectiveness and accuracy of the present model, one benchmark case is simulated and the numerical and analytical results are compared. The chosen benchmark case is a transient reactive transport problem in a homogenous porous structure, described by the following equation

$$\frac{\partial \phi C}{\partial t} = \frac{\partial C}{\partial x}\left(\phi D \frac{\partial C}{\partial x}\right) + k_r\left(C_{eq} - C\right), \tag{14}$$

where k_r is the reaction rate constant, C_{eq} is the equilibrium concentration. The porosity ϕ and diffusivity D are constant. This transient problem is also subjected to initial and boundary conditions, which are expressed as

$$C\left(x, t=0\right) = C_{eq}\ ,\ C\left(x=0, t\right) = C_0\,. \tag{15}$$

For this problem, an analytical solution exists and is given by

$$C\left(x,t\right) = C_{eq} - \frac{C_{eq} - C_0}{2}\left(e^{-qx}\operatorname{erfc}\left(\frac{x - \sqrt{b}t/\phi}{2\sqrt{Dt}}\right) + e^{qx}\operatorname{erfc}\left(\frac{x + \sqrt{b}t/\phi}{2\sqrt{Dt}}\right)\right), \tag{16}$$

where b and q can be expressed as $b = 4k_r\phi D$, $q = \sqrt{b}/2\phi D$ respectively.

To simulate this problem, the computational domain is set as $100 \times 20 \times 20\,\text{mm}^3$, where the porosity, diffusivity and reaction rate on each lattice site are constants and set as 0.6, 0.17 mm^2/s and 0.0001 mm/s respectively. The domain initially is filled with solute at equilibrium concentration C_{eq} = 5 mol/L. The left boundary x=0 maintains the constant concentration with C_0 = 10 mol/L and the right boundary is set as open boundary to realize the infinite extension in the right direction. For the above setting, the higher concentration on the boundary will lead to the diffusion of solute downstream and this further results in the reaction of solute due to higher concentration than the equilibrium concentration. The diffusive and reactive process will become steady after a period of time. The present model is used to simulate this reactive transport problem. The comparison of simulated result and analytical result [22] is shown in Figure 3. This figure clearly shows that the present model can accurately predict the transient

concentration distribution in a reactive transport process, which indicates that it can be used in the study of chloride transport.

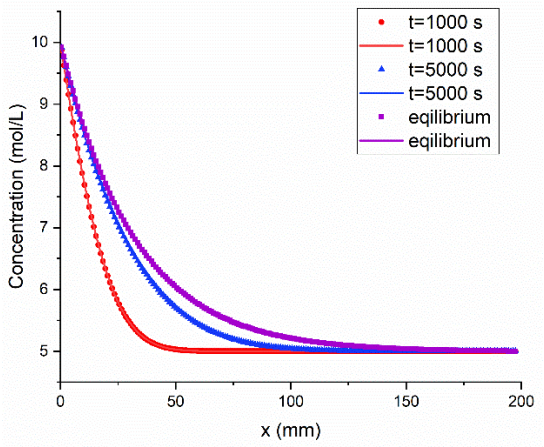

Figure 3: The comparison of solute concentrations between simulated and analytical results. The lines are analytical results and the isolated symbols are simulated results.

4. RESULTS AND DISCUSSIONS

The present model is employed to study chloride transport in the alkali-activated slag paste. Three different pastes are used in this study, i.e., N4S0, N6S0 and N6S5.4. N and S represent Na_2O and SiO_2 and the number behind indicates its weight percentage with respect to the precursor. The water-to-precursor ratio is fixed at 0.4 in all mixtures. The chloride transport simulation is carried out in cubic samples with curing age varying from 12 hours to 28 days. Figure 4 (a) shows the evolution of effective diffusivity as a function of curing age in all three mixtures. Since no effective diffusivity in the alkali-activated slag paste was reported in the literature, the simulated effective diffusivity cannot be quantitatively verified. However, some studies have reported the effective diffusivity in the alkali-activated concrete [3, 4]. As the effective diffusivity in paste should be smaller than that in concrete due to the high porosity of interfacial transitional zone in the concrete, the concrete effective diffusivity can be used to qualitatively verify the simulated results of alkali-activated pastes. The reported effective diffusivity in alkali-activated slag concrete after 28 days is in the range of 10^{-12} to 10^{-11} m^2/s [3, 4]. The simulated effective diffusivity in all three paste mixtures is between 6×10^{-13} and 5×10^{-12} m^2/s, which is reasonable compared to the values reported in the concrete.

As shown in Figure 4 (a), the effective diffusivity decreases as expected with the increase of curing age, due to the ongoing reaction and gradually formed denser microstructure. Figure 4 (a) also shows the influence of sodium content and silica content. Since the average pore size decreases considerably with the increase of sodium content [23], the effective diffusivity is also reported decreasing with more Na_2O content [3]. In the numerical simulation, the effective diffusivity decreases from 5×10^{-12} to 1×10^{-12} m^2/s at 28 days when Na_2O content rises from 4% to 6%, which roughly conforms to the experimental findings. The influence of silica content displayed in the simulation is also consistent with the trend in experiments where increasing silica content at low silica modulus will enhance the resistance to chloride transport [3]. Based on above discussion all the trend shown in the simulation is reasonable and consistent with the experiment.

The present numerical model is also used to study the influence of chloride binding. Figure 4 (b) shows that the chloride concentration is lower when the chloride binding by C-(N-)A-S-H gel, LDH and AFm is considered. This numerically proves that chloride binding can reduce the chloride penetration depth and thus retard the initialization of rebar corrosion.

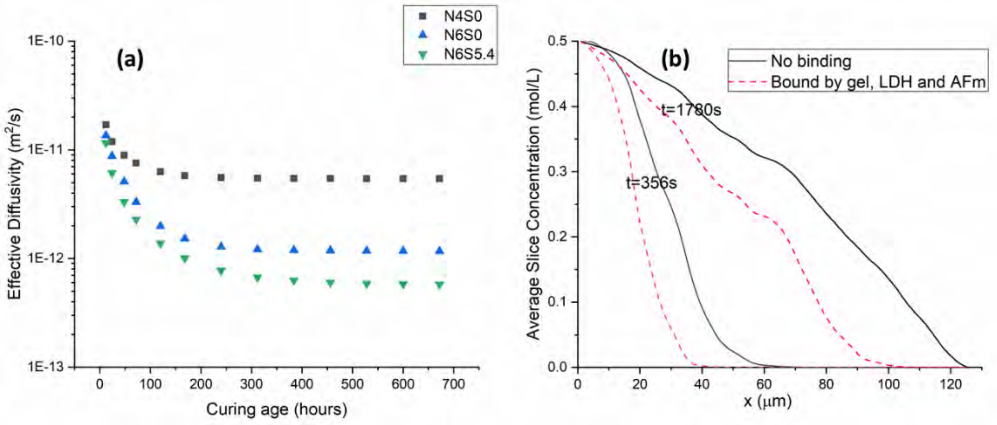

Figure 4: (a) Effective diffusivity in alkali-activated paste with respect to curing age (b) Influence of chloride binding

5. CONCLUSION

In this paper, a lattice Boltzmann method for simulating chloride transport in alkali-activated materials is presented. The numerical model is demonstrated as effective and accurate by simulating a transient reactive transport process. This model then is applied to study chloride transport in a cubic sample of alkali-activated slag paste. The simulated results are compared qualitatively with available experimental results, showing that the current numerical method is a promising numerical tool to predict the chloride transport in alkali-activated materials.

ACKNOWLEDGEMENTS

This work is financially supported by the European Commission through project "PhD Training Network on Durable, Reliable and Sustainable Structures with Alkali-Activated Materials".

REFERENCES

1. Neville, A. *Chloride Attack of Reinforced-Concrete - an Overview.* Materials and Structures, 1995. **28**(176): p. 63-70.
2. Provis, J.L. and S.A. Bernal *Geopolymers and Related Alkali-Activated Materials.* Annual Review of Materials Research, 2014. **44**: p. 299-327.
3. Ma, Q.M., S.V. Nanukuttan, P.A.M. Basheer, Y. Bai, and C.H. Yang *Chloride transport and the resulting corrosion of steel bars in alkali activated slag concretes.* Materials and Structures, 2016. **49**(9): p. 3663-3677.
4. Dehghan, A., K. Peterson, G. Riehm, and L.H. Bromerchenkel *Application of X-ray microfluorescence for the determination of chloride diffusion coefficients in concrete chloride penetration experiments.* Construction and Building Materials, 2017. **148**: p. 85-95.
5. Ismail, I., S.A. Bernal, J.L. Provis, R.S. Nicolas, D.G. Brice, A.R. Kilcullen, S. Hamdan, and J.S.J. van Deventer *Influence of fly ash on the water and chloride permeability of alkali-activated slag mortars and concretes.* Construction and Building Materials, 2013. **48**: p. 1187-1201.

6. Zuo, Y. and G. Ye *GeoMicro3D: A novel numerical model for simulating the reaction process and microstructure formation of alkali-activated slag.* Cement and Concrete Research, 2021. **141**: p. 106328.
7. Patel, R.A., J. Perko, D. Jacques, G. De Schutter, G. Ye, and K. Van Breugel *A three-dimensional lattice Boltzmann method based reactive transport model to simulate changes in cement paste microstructure due to calcium leaching.* Construction and Building Materials, 2018. **166**: p. 158-170.
8. Kang, Q.J., P.C. Lichtner, and D.X. Zhang *Lattice Boltzmann pore-scale model for multicomponent reactive transport in porous media.* Journal of Geophysical Research-Solid Earth, 2006. **111**(B5).
9. Jeong, N., D.H. Choi, and C.L. Lin *Estimation of thermal and mass diffusivity in a porous medium of complex structure using a lattice Boltzmann method.* International Journal of Heat and Mass Transfer, 2008. **51**(15-16): p. 3913-3923.
10. Chai, Z.H., C.S. Huang, B.C. Shi, and Z.L. Guo *A comparative study on the lattice Boltzmann models for predicting effective diffusivity of porous media.* International Journal of Heat and Mass Transfer, 2016. **98**: p. 687-696.
11. Cui, S.Q., N. Hong, B.C. Shi, and Z.H. Chai *Discrete effect on the halfway bounce-back boundary condition of multiple-relaxation-time lattice Boltzmann model for convection-diffusion equations.* Physical Review E, 2016. **93**(4).
12. Yoshida, H. and M. Nagaoka *Multiple-relaxation-time lattice Boltzmann model for the convection and anisotropic diffusion equation.* Journal of Computational Physics, 2010. **229**(20): p. 7774-7795.
13. Chai, Z.H. and T.S. Zhao *Nonequilibrium scheme for computing the flux of the convection-diffusion equation in the framework of the lattice Boltzmann method.* Physical Review E, 2014. **90**(1).
14. Phan-Thien, N. and D.C. Pham *Differential multiphase models for polydispersed spheroidal inclusions: thermal conductivity and effective viscosity.* International Journal of Engineering Science, 2000. **38**(1): p. 73-88.
15. Patel, R.A. *Lattice Boltzmann Method Based Framework for Simulating Physico-Chemical Processes in Heterogeneous Porous Media and Its Application to Cement Paste*. 2016, Ghent University.
16. Ma, H.Y., D.S. Hou, J. Liu, and Z.J. Li *Estimate the relative electrical conductivity of C-S-H gel from experimental results.* Construction and Building Materials, 2014. **71**: p. 392-396.
17. Zheng, J.J., X.Z. Zhou, and Z.M. Wu *A simple method for predicting the chloride diffusivity of cement paste.* Materials and Structures, 2010. **43**(1-2): p. 99-106.
18. Ulm, F.J., G. Constantinides, and F.H. Heukamp *Is concrete a poromechanics material? - A multiscale investigation of poroelastic properties.* Materials and Structures, 2004. **37**(265): p. 43-58.
19. Ke, X., S.A. Bernal, and J.L. Provis *Uptake of chloride and carbonate by Mg-Al and Ca-Al layered double hydroxides in simulated pore solutions of alkali-activated slag cement.* Cement and Concrete Research, 2017. **100**: p. 1-13.
20. Ke, X. *Improved Durability and Sustainability of Alkali-Activated Slag Cements*. 2017, University of Sheffield: Sheffield.
21. Kayali, O., M.S.H. Khan, and M.S. Ahmed *The role of hydrotalcite in chloride binding and corrosion protection in concretes with ground granulated blast furnace slag.* Cement & Concrete Composites, 2012. **34**(8): p. 936-945.
22. Lichtner, P.C. *Continuum formulation of multicomponent-multiphase reactive transport.* Reactive Transport in Porous Media, 1996. **34**: p. 1-81.
23. Ravikumar, D. and N. Neithalath *Electrically induced chloride ion transport in alkali activated slag concretes and the influence of microstructure.* Cement and Concrete Research, 2013. **47**: p. 31-42.

MITIGATING THE AUTOGENOUS SHRINKAGE OF ALKALI-ACTIVATED SLAG BY INTERNAL CURING

Zhenming Li (1), Mateusz Wyrzykowski (2), Hua Dong (1), Shizhe Zhang (1), Pietro Lura (2,3) and Guang Ye (1,4)

(1) Faculty of Civil Engineering and Geoscience, Delft University of Technology, the Netherlands

(2) Concrete/Construction Chemistry Laboratory, Empa, Swiss Federal Laboratories for Materials Science and Technology, Switzerland

(3) Institute for Building Materials, ETH Zurich, Switzerland

(4) Magnel Laboratory for Concrete Research, Department of Structural Engineering, Ghent University, Belgium

Abstract

Alkali activated slag (AAS) has shown promising potential to replace ordinary Portland cement as a binder material. Synthesized from industrial by-products, AAS can show high strength, thermal resistance and good durability. However, AAS has been reported to exhibit high autogenous shrinkage. Autogenous shrinkage is a critical issue for building materials since it can induce micro- or macro-cracking when the materials are under restrained conditions. Hence, this work aims at mitigating the autogenous shrinkage of AAS by means of internal curing. The influences of internal curing on microstructure formation and autogenous shrinkage are investigated. The results show that internal curing provided by superabsorbent polymers is a promising way to reduce the autogenous shrinkage of AAS.

Keywords: Internal curing, autogenous shrinkage, alkali-activated materials, slag, superabsorbent polymers (SAP)

1. INTRODUCTION

Alkali-activated slag (AAS) has emerged as an eco-friendly alternative to ordinary Portland cement (OPC) as a binder material. Compared with cement production, the production of AAS entails around 25-50% lower CO_2 emissions and more than 40% lower embodied energy [1,2]. AAS is typically prepared by mixing alkali solution with ground granulated blast-furnace slag (GGBFS), a by-product of the iron ore smelting industry [3]. When used as a binder material, AAS shows high strength, good chemical resistance and fire resistance [4–6]. However, several drawbacks of $NaOH/Na_2SiO_3$ activated slag, such as the fast setting and the large autogenous shrinkage, limit a wide application of this material in engineering practice. It has been reported in the literature that mixtures based on AAS can

exhibit several times higher autogenous shrinkage than mixtures based on OPC [7]. The high autogenous shrinkage of AAS can increase the risk of early-age cracking of the concrete [8].

Internal curing by SAP has been widely reported to have beneficial effects on mitigating the self-desiccation and the consequent autogenous shrinkage of Portland cement and blast-furnace slag cement pastes [9–14]. In AAS systems, the pore pressure resulting from self-desiccation is also an important driving force of autogenous shrinkage according to Collins and Sanjayan [15] and Ye and Radlińska [16]. Therefore, SAP should have potential in reducing the autogenous shrinkage of AAS. Despite this potential and the preliminary results reported in [17–20], studies in this field are still limited.

This study aims at exploring the effectiveness of internal curing by SAP in mitigating the autogenous shrinkage of $NaOH/Na_2SiO_3$ activated slag. The autogenous shrinkage of the plain and internally cured pastes were measured. X-ray computed tomography (CT) scan and scanning electron microscope (SEM) were utilized to observe the liquid desorption from the SAP and microstructure of the SAP-containing mixtures, respectively.

2. MATERIALS AND METHODS

2.1 Materials

The precursor used in this study was ground granulated blast-furnace slag (hereinafter termed slag) supplied by Ecocem Benelux. The chemical composition determined by X-ray fluorescence (XRF) is given in Table 1. The loss of ignition of the slag was determined according to ASTM D7348-08. The density of the slag is 2.89 g/cm3. The particle size range, determined by laser diffraction, was 0.1-50 μm, with a d_{50} of 18.3 μm.

Table 1: Chemical compositions of slag

Oxide	SiO_2	Al_2O_3	CaO	MgO	Fe_2O_3	TiO_2	SO_3	K_2O	MnO	**Other**
Slag	31.77	13.25	40.50	9.27	0.52	0.97	1.49	0.34	0.36	1.52

The alkaline activator was prepared by mixing anhydrous pellets of sodium hydroxide, deionized water and commercial sodium silicate solution (27.5 wt.% SiO_2, 8.25 wt.% Na_2O). The solution was then allowed to cool for 24 h before mixing with the precursor and dry SAP. The concentrations of Na_2O and SiO_2 in the activator were 9.5 wt.% (corresponding to 3.8 M) and 13.8 wt.%, respectively.

Solution-polymerized SAP of irregular particle shape and particle sizes of up to about 200 μm in the dry state were used.

2.2 Mixtures

The basic liquid/binder ratio (l/b) of the plain AAS paste is 0.5 (the control mixture). The absorption capacity of the SAP in the activator is 20g/g. The basic dosage of the SAP is 0.26%. The total l/b of AAS paste with SAP is therefore 0.552. Higher amounts of SAP (0.5% and 1%) and correspondingly higher amounts of internal curing activator are also applied (we assume that the SAP absorb the same amount, 20 g/g, of activator in mixtures with higher l/b). For each total l/b, a mixture without SAP is also set as reference. All mixtures compositions are shown in Table 2.

Table 2: Mixture compositions of AAS pastes with and without SAP (by mass proportion)

Mixture	AAS0.5	AAS0.552	AAS0.552SAP	AAS0.6	AAS0.6SAP	AAS0.7	AAS0.7SAP
Slag	1	1	1	1	1	1	1
Activator	0.5	0.552	0.552	0.6	0.6	0.7	0.7
SAP	-	-	0.0026	-	0.005	-	0.01

2.3 Measurement of initial and final set

The time of initial and final set was measured by an automatic Vicat setup with a measurement interval of 5 min. The samples were covered with a plastic film during the measurement in order to limit the evaporation from the surface [12].

2.4 Linear autogenous shrinkage

The linear autogenous shrinkage of the pastes was measured by the corrugated tube method [21], in which three sealed corrugated tubes about 425 mm long and Ø 28.5 mm were used for each mixture. After mixing, the fresh paste was carefully cast into the corrugated tubes and sealed by plugs. The length changes were automatically measured on three specimens in parallel placed on a stainless-steel bench (immersed in a temperature-controlled silicone-oil bath) by linear variable differential transformers (LVDTs) until 7 days. A detailed description of the method can be found in [22]. The strains are referenced to the length of the sample at the time of final set determined by Vicat needle on the corresponding paste in parallel tests, where the samples were protected from evaporation by means of a plastic film. The automatic measurements show a low scatter for triplicate samples, with the relative standard error in the range of 1–2% after the final set of the materials.

2.5 X-ray microcomputed tomography

To study the absorption and desorption behavior of SAP in AAS paste, the mixture AAS0.552SAP was scanned using CT scan through a Phoenix Nanotom CT scanner. The paste was first cast into a small plastic container with a diameter of 4 mm and a height of 6 mm. Immediately after casting, the container was sealed by paraffin film and put into the CT scanner. During the first week after casting, the same sample was scanned at the age of 1 hour, 8 hours, 1 day and 7 days, respectively. The duration of each scan was one hour. The spatial resolution was 5 μm. 3D Reconstruction was carried out with VG Studio Max.

2.6 SEM analysis

The fracture surface of internally cured paste and the voids left by the SAP were observed using SEM. The paste AAS0.552SAP was cast into a PVC cylinder bottle with a diameter of 24 mm and a height of 50 mm. At the age of 7 days, the sample was taken out from the bottle and crushed into pieces with a size of around 1 cm^3. These pieces were then immersed in isopropanol for a week to stop the reaction. During that period, the isopropanol was replaced every two days. Afterwards, the samples were put into a moderate vacuum as obtained by an aspirator pump until a constant weight (<0.1%) was obtained. After carbon coating, the

samples were imaged with an environmental scanning electron microscope (Philips- XL30-ESEM) in secondary electron mode in high vacuum.

3. RESULTS AND DISCUSSION

3.1 Setting time

The times of initial and final set are shown in Table 3. The initial and final set occur later for pastes with higher l/b without SAP. However, for pastes with SAP, the time of initial set is similar to that of the control mixture AAS0.5, which is likely due to the similar basic l/b of these mixtures. The times of final set of SAP-containing pastes are longer than for the control mixture but shorter than for the non-SAP mixtures with the same total l/b.

Table 3: Times of initial and final set for AAS pastes with and without SAP

Mixture	AAS0.5	AAS0.5 52	AAS0.5 52SAP	AAS0.6	AAS0.6 SAP	AAS0.7	AAS0.7 SAP
Initial set (min)	25	36	24	40	25	55	35
Final set (min)	35	51	39	65	56	80	70

3.2 Autogenous shrinkage

Figure 1 shows the linear autogenous shrinkage of the plain and internally cured AAS pastes in the first week of reaction. It can be seen that the shrinkage of the control mixture AAS0.5 develops rapidly after setting, reaching 3630 µm/m at 1 day and around 6600 µm/m at 7 days. Increasing the liquid content without adding SAP reduces the autogenous shrinkage slightly. By adding 0.26 wt. % SAP, the autogenous shrinkage is dramatically reduced. Increasing the SAP dosage (together with the corresponding absorbed liquid amount) to 0.5% or 1% does not lead to any significant change in the measured shrinkage.

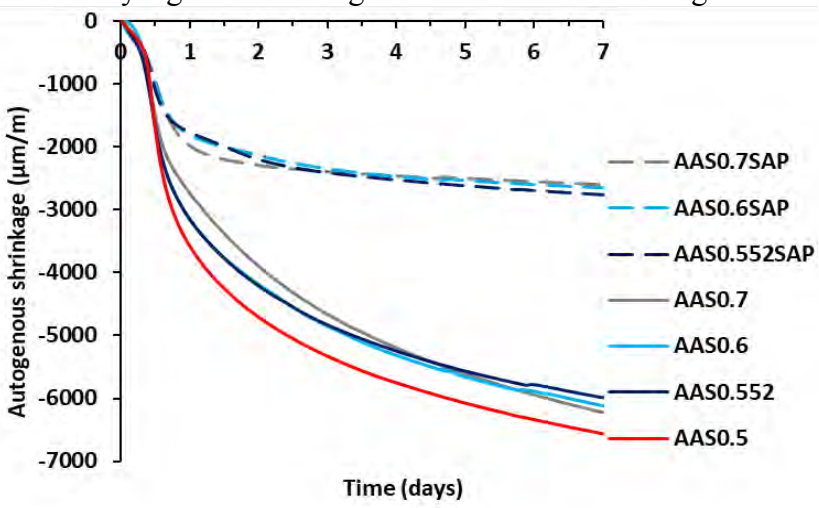

Figure 1: Autogenous shrinkage of AAS pastes with different l/b and different amounts of SAP. Each curve shows the average result of three samples.

3.3 X-ray micro-computed tomography analysis

The evolution of a horizontal cross-section of AAS0.552SAP obtained from the CT scan is shown in Figure 2. Based on the grey levels, several phases can be distinguished within the paste, including unreacted slag particles (white), SAP with liquid (dark grey), entrapped air (black and spherical) and newly formed voids/pores (black, marked by the arrows) within the SAP-originated voids.

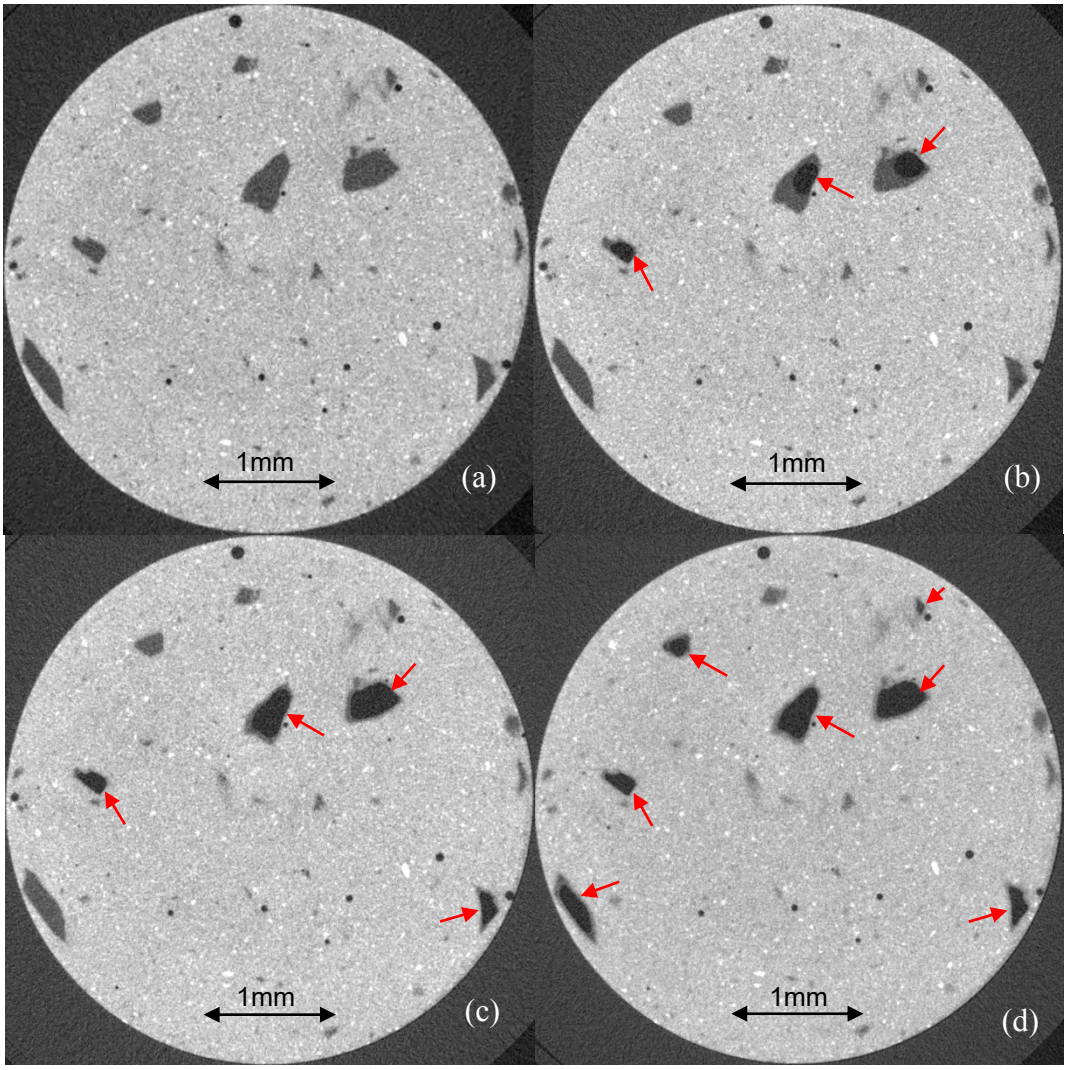

Figure 2: A representative cross-section of AAS0.552SAP paste obtained by X-ray microtomography at the curing age of (a) 1 hour, (b) 8 hours, (c) 1 day and (d) 7 days.

Figure 2 (a) shows the randomly distributed swollen SAP particles in the paste, indicating a successful absorption of liquid by SAP. The size of SAP in the paste can reach more than 0.5 mm. At the age of 8 h (Figure 2 (b)), air voids have already formed within the voids originally occupied by the swollen SAP, indicating the liquid release from SAP to the surrounding paste, i.e. internal curing. At the age of 1 day, the area of newly formed voids increases, indicating more liquid is released from the SAP. At the age of 7 days, most of the

SAP particles located at the chosen cross-section have been emptied, but some of them still have liquid stored inside, which could be distinguished by the dark grey colour of these SAP-originated voids. This part of liquid can be useful to compensate the self-desiccation occurring after 7 days. At the given resolution, no reaction products forming inside the SAP voids could be identified.

Figure 3 (a) and 3 (b) show two representative SEM images of the microstructure of AAS0.552SAP paste cured for 7 days. Figure 3 (c) shows a representative interface between SAP and the surrounding paste. From the images, the dry SAP and the surrounding paste can be clearly distinguished based on their surface features: SAP have a locally porous microstructure while the paste is dense and homogenous. The SAP particle shown in Figure 3 (a) has a big void inside, with a smooth curved surface, which is consistent with the CT scan observations in Figure 2. Figure 3 (b) shows a void that is filled with SAP. This can be due to either that the liquid inside the SAP particle has not been consumed yet at the moment of hydration stoppage or that the liquid has been consumed but the dry SAP particle left agglomerates into the void shown in Figure 3 (b). In both Figure 3 (a) and (b), a rim of paste can be observed surrounding the SAP particle, with a relatively smoother surface and fewer unreacted slag particles embedded. This could be due to the liquid released from the SAP particle resulting in a local increase of l/b in the rim.

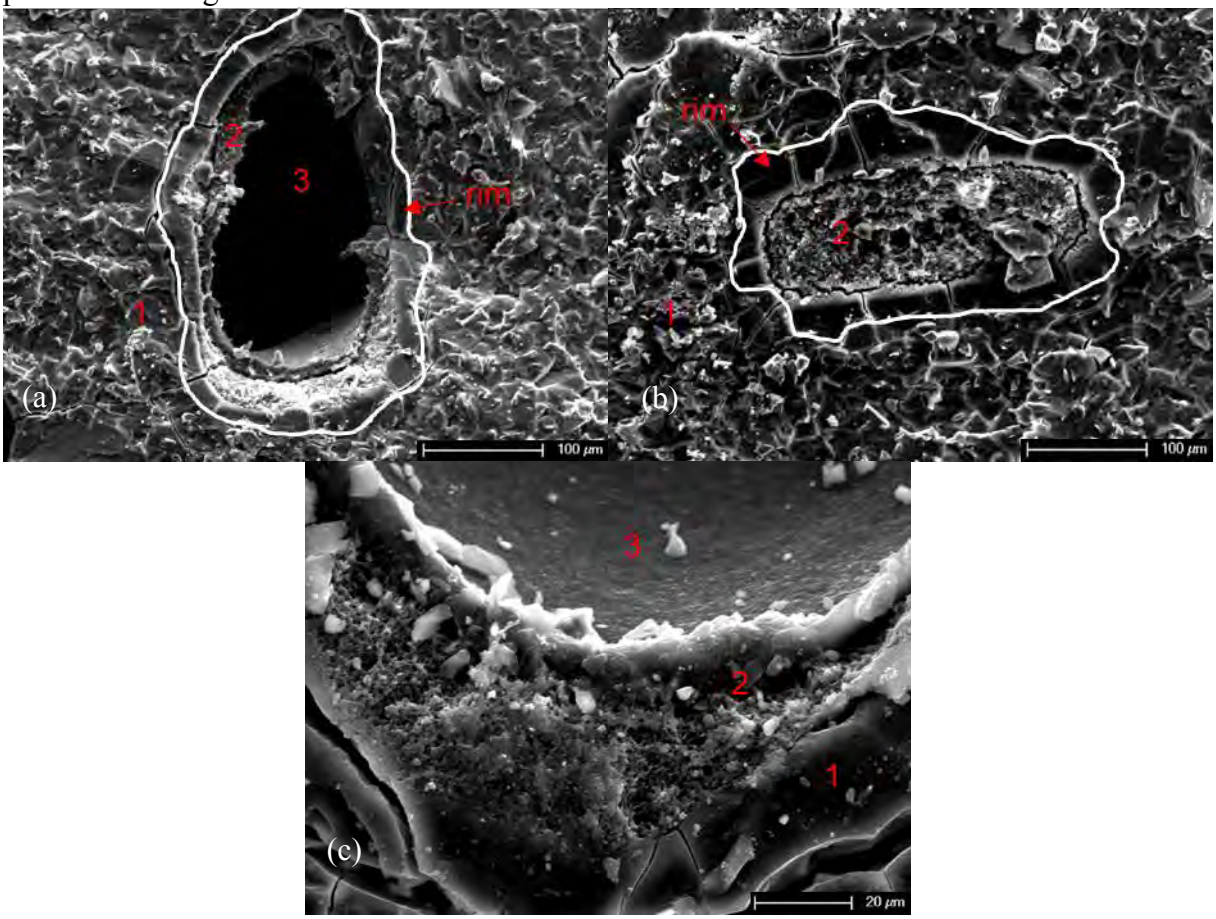

Figure 3: SEM images of the SAP-originated voids in paste AAS0.552SAP cured for 7 days. (a) and (b) shows a void that is partly and fully filled by dry SAP, respectively. (c)

shows an interface between SAP and surrounding paste. 1 indicates the paste, 2 indicates the dry SAP and 3 indicates the SAP-originated voids

4. CONCLUSOINS

Based on the results and discussion, the following conclusions can be drawn:

- Internal curing by SAP delays the times of initial and final set.
- Internal curing by SAP can largely mitigate the autogenous shrinkage of $NaOH/Na_2SiO_3$ activated slag. This is beneficial for tackling the problem of large autogenous shrinkage of AAS in practical applications. Larger amounts of SAP than 0.26 wt.% do not bring further mitigation of autogenous shrinkage of the AAS paste studied.
- In the internally cured sample, the SAP are observed to release liquid to the surrounding paste starting from before 8 h. After the first week, there is still a certain amount of liquid left in SAP for mixture AAS0.552SAP, indicating a further internal curing potential for later reactions.

ACKNOWLEDGEMENTS

This work is supported in part by the scholarship from China Scholarship Council (CSC) and the grant from the Netherlands Organisation for Scientific Research (NWO). The short visit at Empa by the first author was supported by STSM project from COST Action TU1404 “Towards the next generation of standards for the service life of cement-based materials and structures”

REFERENCES

[1] R.J. Thomas, H. Ye, A. Radlinska, S. Peethamparan, Alkali-activated slag cement concrete, Concr. Int. 38 (2016) 33–38.

[2] P. Duxson, J.L. Provis, G.C. Lukey, J.S.J. van Deventer, The role of inorganic polymer technology in the development of “green concrete,” Cem. Concr. Res. 37 (2007) 1590–1597. doi:10.1016/j.cemconres.2007.08.018.

[3] C. Shi, A.F. Jiménez, A. Palomo, New cements for the 21st century: The pursuit of an alternative to Portland cement, Cem. Concr. Res. 41 (2011) 750–763. doi:10.1016/j.cemconres.2011.03.016.

[4] J.L. Provis, J.S.J. Van Deventer, Geopolymers: structures, processing, properties and industrial applications, Woodhead, Cambridge, UK, 2009.

[5] K. Arbi, M. Nedeljković, Y. Zuo, G. Ye, A Review on the Durability of Alkali-Activated Fly Ash/Slag Systems: Advances, Issues, and Perspectives, Ind. Eng. Chem. Res. 55 (2016) 5439–5453. doi:10.1021/acs.iecr.6b00559.

[6] M.C.G. Juenger, F. Winnefeld, J.L. Provis, J.H. Ideker, Advances in alternative cementitious binders, Cem. Concr. Res. 41 (2011) 1232–1243. doi:10.1016/j.cemconres.2010.11.012.

[7] Z. Li, M. Nedeljkovic, Y. Zuo, G. Ye, Autogenous shrinkage of alkali-activated slag-fly ash pastes, in: 5th Int. Slag Valoris. Symp., Leuven, 2017: pp. 369–372.

[8] Z. Li, A. Kostiuchenko, G. Ye, Autogenous shrinkage-induced stress of alkali-activated slag and fly ash concrete under restraint condition, in: ECI (Ed.), Alkali Act. Mater. Geopolymers Versatile Mater. Offer. High Perform. Low Emiss., Tomar, 2018: p. 24.

[9] V. Mechtcherine, M. Gorges, C. Schroefl, A. Assmann, W. Brameshuber, A.B. Ribeiro, D. Cusson, J. Custódio, E.F. Da Silva, K. Ichimiya, S.I. Igarashi, A. Klemm, K. Kovler, A.N. De Mendonça Lopes, P. Lura, V.T. Nguyen, H.W. Reinhardt, R.D.T. Filho, J. Weiss, M. Wyrzykowski, G. Ye, S. Zhutovsky, Effect of internal curing by using superabsorbent polymers (SAP) on autogenous shrinkage and other properties of a high-performance fine-grained concrete: Results of a RILEM round-robin test, Mater. Struct. Constr. 47 (2014) 541–562. doi:10.1617/s11527-013-0078-5.

[10] O.M. Jensen, P.F. Hansen, Water-entrained cement-based materials - I. Principles and theoretical background, Cem. Concr. Res. 31 (2001) 647–654. doi:10.1016/S0008-8846(01)00463-X.

[11] P. Lura, F. Durand, O.M. Jensen, Autogenous strain of cement pastes with superabsorbent polymers, Proc. Internaltional RILEM Conf. Vol. Chang. Hardening Concr. Test. Mitig. C (2006) 57–66. doi:10.1617/2351580052.007.

[12] J. Justs, M. Wyrzykowski, D. Bajare, P. Lura, Internal curing by superabsorbent polymers in ultra-high performance concrete, Cem. Concr. Res. 76 (2015) 82–90. doi:10.1016/j.cemconres.2015.05.005.

[13] D. Snoeck, O.M. Jensen, N. De Belie, The influence of superabsorbent polymers on the autogenous shrinkage properties of cement pastes with supplementary cementitious materials, Cem. Concr. Res. 74 (2015) 59–67. doi:10.1016/j.cemconres.2015.03.020.

[14] M. Wyrzykowski, P. Lura, Reduction of autogenous shrinkage in OPC and BFSC pastes with internal curing, in: Proc. XIII Int. Conf. Durab. Build. Mater. Components, São Paulo, Brazil, 2014: pp. 2–5.

[15] F. Collins, J.. Sanjayan, Effect of pore size distribution on drying shrinking of alkali-activated slag concrete, Cem. Concr. Res. 30 (2000) 1401–1406. doi:10.1016/S0008-8846(00)00327-6.

[16] H. Ye, A. Radlińska, Shrinkage mechanisms of alkali-activated slag, Cem. Concr. Res. 88 (2016) 126–135. doi:10.1016/j.cemconres.2016.07.001.

[17] A.R. Sakulich, D.P. Bentz, Mitigation of autogenous shrinkage in alkali activated slag mortars by internal curing, Mater. Struct. 46 (2013) 1355–1367. doi:10.1617/s11527-012-9978-z.

[18] S. Oh, Y.C. Choi, Superabsorbent polymers as internal curing agents in alkali activated slag mortars, Constr. Build. Mater. 159 (2018) 1–8. doi:10.1016/j.conbuildmat.2017.10.121.

[19] C. Song, Y.C. Choi, S. Choi, Effect of internal curing by superabsorbent polymers – Internal relative humidity and autogenous shrinkage of alkali-activated slag mortars, Constr. Build. Mater. 123 (2016) 198–206. doi:10.1016/j.conbuildmat.2016.07.007.

[20] W. Tu, Y. Zhu, G. Fang, X. Wang, M. Zhang, Internal curing of alkali-activated fly ash-slag pastes using superabsorbent polymer, Cem. Concr. Res. 116 (2019) 179–190. doi:10.1016/j.cemconres.2018.11.018.

[21] ASTM C1968, Standard Test Method for Autogenous Strain of Cement Paste and Mortar, (2013) 1–8. doi:10.1520/C1698-09.2.

[22] M. Wyrzykowski, Z. Hu, S. Ghourchian, K. Scrivener, P. Lura, Corrugated tube protocol for autogenous shrinkage measurements: review and statistical assessment, Mater. Struct. 50 (2017) 57. doi:10.1617/s11527-016-0933-2.

Special session 2: Carbonation

ACCELERATED CARBONATION OF ORDINARY PORTLAND CEMENT PASTE AND ITS EFFECTS ON MICROSTRUCTURE AND TRANSPORT PROPERTIES

Claudia Romero Rodriguez (1), Rui Ye (1,2), Aikaterini Varveri (3), Emanuele Rossi (1), Giovanni Anglani (2), Paola Antonaci (2), Erik Schlangen (1) and Branko Šavija (1)

(1) Microlab, Department of Materials, Mechanics, Management and Design, Delft University of Technology, the Netherlands

(2) DISEG, Politecnico di Torino, Italy

(3)Pavement Engineering, Department of Concrete Structures, Delft University of Technology, the Netherlands

Abstract

Coupling of carbonation and chlorides ingress mechanisms is very common in concrete under certain exposure conditions such as coastal environments. The aggravation/ mitigation of corrosion by the existence of carbonation lies on the fact that microstructural changes due to carbonation result in changes on the transport properties of the material. In this study we investigate and quantify evolving transport properties of ordinary Portland cement paste, such as porosity, tortuosity and intrinsic permeability. Dual X-ray micro computed tomography (micro CT) is used for the quantification of porosity. Furthermore Dynamic Vapour Sorption (DVS) measurements are carried out to resolve water retention and relative permeability curves. The authors expect to provide insights into the mechanisms of accelerated carbonation in both types of cement paste, as well as data for input and validation of numerical and analytical models on this degradation phenomenon.
Keywords: transport properties cement, dual X-ray microcomputer tomography, DVS, carbonation, blended cement

1. INTRODUCTION

Concrete is the most common used material for construction all over the world [1]. However, the microstructure of concrete, which determines most of its properties such as strength and durability, does not remain constant over time. In fact, the microstructure of concrete still develops during its service life; however, deterioration due either to external or to internal factors can alter the microstructure properties as well, and consequently its durability. According to ACI Committee 201 [1], the durability of concrete is defined as its ability to withstand the deterioration process caused by its interaction with the environment.

Generally, all degradation mechanisms in concrete involve three main factors [2]. First of all, the presence of moisture, which is capable of caring aggressive ions within the concrete

and moreover needed for various internal concrete degradation processes themselves. Secondly, the rate of degradation largely depends on the transport properties of concrete, which in turn is strictly related to the pore structure of the hydrated cement paste such as porosity and connectivity of the pore network; lastly, the presence of aggressive ions: air, in fact contains carbon dioxide and oxygen, and the latter is required for the corrosion of the reinforcing steel. All these parameters are also capable of evolving with time, making the durability of concrete challenging to predict [3].

Nowadays, durability characteristics of construction materials are continuously gaining more importance, also due to its high economic impact on society. The repair and maintenance costs of existing structures require about 40% of the total resources of the construction industry and keep growing every year [4]. Carbonation is one of the degradation mechanisms responsible for the corrosion of reinforcing steel, and the latter is one of the major causes of concrete damage. It was reported by the U.S. Department of Transportation that 90 billion dollars were spent in 1991 for repairing damage caused by corrosion of reinforcing steel [4]. In summary, carbonation of the hardened Portland cement paste reduces the pH of the pore solution from approximately 13.5 to a value of about 9 [5], leading to removal of the steel passivation layer which covers and protect the steel rebar from corrosion. In addition, carbonation of Portland cement pastes alters its microstructure with consequent changes in transport properties which in turns may result in the initiation of other degradation phenomena.

Although carbonation in concrete has been widely studied experimentally, there is still the need for models that can correctly predict its evolution in real structures. For the development of such predictive models complete sets of data are needed. Unfortunately, the foci of existing experimental studies are not aligned with the need formulated earlier.

This study investigated the effects of the carbonation on the microstructure and transport properties of ordinary Portland cement pastes, and its evolution after carbonation. The main aim is to provide experimental data for further research as well as for modelling purposes.

2. METHODOLOGY

Ordinary Portland cement pastes were prepared with 0.6 water-binder ratio and CEM I 52.5R from ENCI, the Netherlands. The pastes were cast in polypropylene cylindrical moulds and sealed with plastic film and lids and rotated for 24 hours around their generatrix at 5-7 rpm as used in [6] to prevent bleeding. Subsequently they were stored at laboratory temperature (20°C) to cure. At age 90 days the samples where demoulded and cut into 1 cm side prims for preconditioning at the same temperature and 65% RH in order to reach the optimal internal condition for accelerated carbonation as suggested in [7].

Prior to the accelerated carbonation exposure, dual micro Computed X-ray Tomography (dual CT) as described in a previous paper from the authors [8], Thermogravimetric Analysis (TGA) and Dynamic Vapor Sorption (DVS), as described in a previous paper from the authors [9], were performed in order to assess porosity, hydrated phases composition, and water vapour sorption isotherms respectively. Moreover, by means of the water vapour sorption isotherms, the unsaturated permeability coefficient and capillary pressure curve were obtained. All the properties assessed directly or indirectly at this stage describe the noncarbonated state. Successively carbonation of the samples was done under accelerated condition at laboratory temperature (20°C) and 65% RH at a CO_2 concentration of 5%. All

the properties measured prior to carbonation are repeated after 22 days of accelerated exposure. At each carbonation step, the samples were taken out from the carbonation chamber and analysed as follows: dual scan to obtain the spatial distribution and magnitude of porosity, TGA for quantification of portlandite (CH) and carbonates content, and DVS to obtain water vapour sorption isotherms. Moreover, both TGA and DVS were performed at different depths of the sample from the exposed surface, namely 3, 6, 9 mm.

3. RESULTS AND DISCUSSIONS

The parameters of the water-retention and relative permeability curves were obtained by fitting the Van Genuchten and Mualem formulations [10, 11] (equation 1 and 2) with the data obtained from the DVS. Furthermore, from dual CT scans total and spatial distribution of porosity were resolved. These values are listed in Table 1 for the studied cement paste before and after 22 days of accelerated carbonation.

$$p_c(S_r) = a\left(S_r^{-1/m} - 1\right)^{1-m} \quad (1)$$

$$k_{rl}(S_r) = \sqrt{S_r}\left(1 - (1 - S_r^{1/m})^{m}\right)^2 \quad (2)$$

Table 1: Summary of measured properties before and after 22 days of accelerated carbonation

Property	Uncarbonated	Carbonated
Porosity [%]	50.1	41.3
Parameter ‘a’ from Van Genuchten [-]	73.3	66.47
Parameter ‘m’ from water-retention and relative permeability curves [-]	0.617	0.6

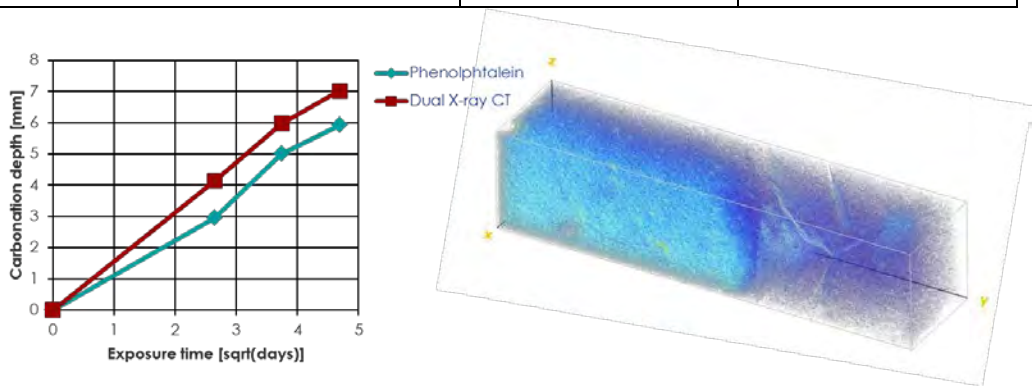

Figure 1: Carbonation depth as measured from dual CT in comparison to phenolftalein indicator.

It can be evinced from Table 1 that the dual CT methodology can quantify decreases in total porosity after carbonation, as well as locally, as shown in Figure 1. In the latter, it is

observed that there exists an underestimation of the carbonation depth, maybe due to the changes in pore structure at the carbonation front where pH has not been yet modified, similar findings were shown in [6] through TGA results and shown also in the TGA results shown in Figure 2. Regarding relative permeability, parameter m seems to change very literally which confirms what has been previously shown in literature for pastes with different water-to-cement ratio, regarding the independence of relative permeability from pore structure [12]. On the other hand, the parameter of the water-retention curve named 'a' decreases in value as found from DVS results.

Figure 2 shows the portlandite and carbonate contents at different depths from exposed surface in a 22 days carbonated paste.

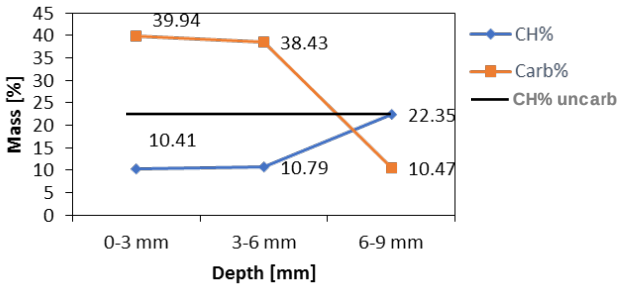

Figure 2: Portlandite and carbonate contents at different depths from exposed surface after 22 days.

It can be observed that after 22 days the carbonated area shows a nearly constant CH content approximately at 10.6%, whereas carbonates are not constant in the same area. This is an indication of the ongoing carbonation of the CSH gel after depletion of CH available for carbonation.

4. CONCLUSIONS

The following conclusions can be drawn out of the study presented herein:

- Dual CT scans can successfully be used to monitor local changes in porosity in cement paste samples.
- After accelerated carbonation the relative permeability function does not change but the water-retention curve parameter related to pore structure does decrease.
- Depletion of portlandite by carbonation was complete after 15-22 days of accelerated carbonation. Nevertheless, carbonates content are seen to vary within the carbonate region which indicates ongoing carbonation of CSH gel.

ACKNOWLEDGEMENTS

The first author acknowledges the financial support from the Construction Technology Research Program funded by the Ministry of Land, Infrastructure and Transport of the Korean Government under the grant 17SCIP-B103706-03.

REFERENCES

[1] ACI Committee 201, ACI 201.2R-16, Guide to Durable Concrete, 2016

[2] Mario Collepardi, Silvia Collepardi, Roberto Troli, Il nuovo calcestruzzo (sesta edizione), 2014, pag. 153-154.
[3] Baroghel-Bouny, V., 'Water vapour sorption experiments on hardened cementitious materials, Part I: Essential tool for analysis of hygral behaviour and its relation to pore structure', *Cem. Concr. Res.* 37(3), 414-437.
[4] Kumar Mehta, P., Monteiro P. J. M., 'Concrete: Microstructure, Properties, and Materials'. 2006.
[5] Neville, A. M. 'Properties of concrete', 6th Edition, Pearson Education Limited, 2011.
[6] Wu, B., and Guang Ye. 'Development of porosity of cement paste blended with supplementary cementitious materials after carbonation.' Construction and Building Materials 145 (2017): 52-61.
[7] Roy, S. K., K. B. Poh, and D. O. Northwood. 'Durability of concrete—accelerated carbonation and weathering studies.' Building and environment 34.5 (1999): 597-606.
[8] Romero Rodriguez, C., Zhang, H., Schlangen, E., Šavija, B. 'Resolution effect on permeability and tortuosity measurements through dual micro computed X-ray tomography.' Manuscript in preparation (2020).
[9] Romero Rodriguez, C., Ye, R., Anglani, G., Varveri, A., Antonaci, P., Schlangen, E., Šavija, B. 'Evolution of microstructure, porosity and transport properties in ordinary and slag-blended cement pastes during accelerated carbonation.' Manuscript in preparation (2020).
[10] Van Genuchten, M.T., 'A closed-form equation for predicting the hydraulic conductivity of unsaturated soils I', Soil science society of America journal 44 (5) (1980) 892-898.
[11] Mualem, Y.. 'A new model for predicting the hydraulic conductivity of unsaturated porous media', Water resources research 12 (3) (1976) 513-522.
[12] Baroghel-Bouny, V., 'Water vapour sorption experiments on hardened cementitious materials. Part II: Essential tool for assessment of transport properties and for durability prediction', Cem. Concr. Res. 37 (3) (2007) 438-454.

CARBONATION RATES OF ALKALI-ACTIVATED AND CEMENT-BASED CONCRETES

Marija Nedeljković (1, 2), Kamel Arbi (3), Guang Ye (1)

(1) Microlab, Department of 3MD, Faculty of Civil Engineering and Geosciences, Delft University of Technology, The Netherlands

(2) TNO Buildings, Infrastructure & Maritime Delft, The Netherlands

(3) Delta Concrete Consult B.V. Vianen, The Netherlands

Abstract
The reduction of pH from ~12.5 to ~9 by carbonation of the pore solution of reinforced cement-based concrete structures results in the reinforcement corrosion. The rate of carbonation is an important input for design of the concrete cover depth and the service life prediction of reinforced concrete structures because the initiation of reinforcement corrosion is usually considered as the end of service life of concrete infrastructure. The information from the field carbonation of alkali activated concrete is in most cases limited and related to exposure shorter than 40 years. In this paper, a comparative study regarding accelerated and natural carbonation of alkali-activated concretes and cement-based concretes has been carried out. The pH and carbonation depths are periodically measured. The results show that, despite the low porosity of alkali-activated concrete with 50 wt. % slag, these concretes must have an appropriate curing in order to be used in exposure classes where carbonation is an issue, due to their lower carbonation resistance compared to cement-based concrete. Regardless the exposure conditions, the pH of carbonated alkali-activated concrete was maintained above 9. Finally, recommendations for alkali activated concrete applications and their improved carbonation resistance are given.
Keywords: Alkali activated concrete, Carbonation, Natural test, Accelerated test, pH

1. INTRODUCTION

Structural application of alkali activated concrete is still argued worldwide due to lack of data regarding long-term performance [1]. Additionally, the prediction of the service life of structures made with alkali activated concrete is not reported in the literature. This largely impedes the standardization process of alkali activated concrete for the building industry. Furthermore, it is still unknown whether the carbonation is responsible for corrosion of

reinforcing steel in alkali-activated concretes or whether some other carbonation-induced structural deterioration of the alkali-activated binder has to be envisaged.

Carbonation of cement-based concrete results in a decrease of the pH of the pore solution, initiating the corrosion of reinforcing steel. Beside carbonation of the pore solution, the carbonation of $Ca(OH)_2$ and C-S-H gel result in the formation of $CaCO_3$ and amorphous silica gel, respectively. Figure 1 demonstrates influence of key parameters on the carbonation mechanism for two concrete domains, i.e. pore solution and microstructure. The comparative study of cement and alkali activated concretes includes the following parameters:

a) pore solution (NaOH/KOH). Carbonation initially occurs in the pore solution of the concrete. Hence, NaOH/KOH as a dominant species in the pore solution plays a buffer role for the carbonation reactions;
b) $Ca(OH)_2$ in the microstructure;
c) Ca/Si in the microstructure.

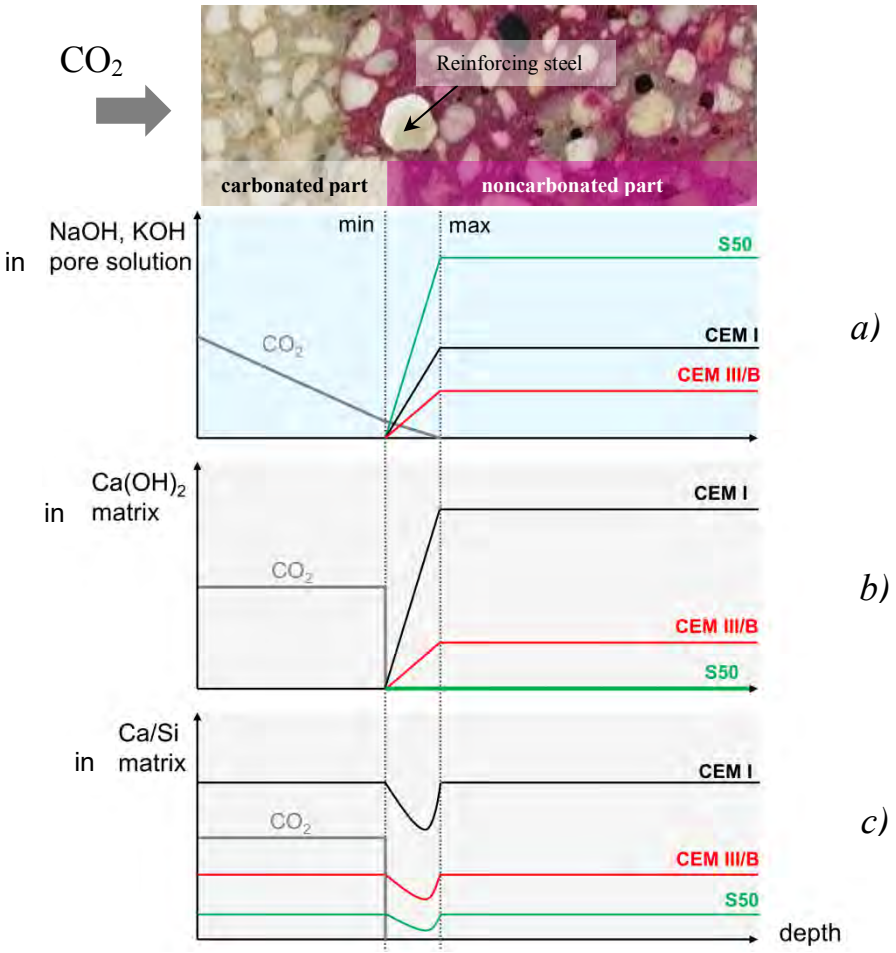

Figure 1: Domains (pore solution, microstructure) and parameters (NaOH/KOH, $Ca(OH)_2$ content, Ca/Si ratio) for comparative study between CEM I and CEM III/B concretes and alkali activated concrete S50. The comparison includes the following:

a) Pore solution (NaOH/KOH). Carbonation initially occurs in the pore solution of the concrete. Therefore, NaOH/KOH as a dominant species in the pore solution plays a buffer role for the carbonation reactions.
b) $Ca(OH)_2$ in microstructure. Concrete CEM I has the highest content of $Ca(OH)_2$.
c) Ca/Si in the microstructure. Concrete CEM I has the highest Ca/Si ratio.

A full understanding of the effects of these parameters on deterioration of concrete is a key step in modelling of the carbonation rate in alkali activated materials, as shown by Nedeljković [2]. According to Bernal et al. [3], the accelerated carbonation of the pore solution leads to significantly larger pH reduction (two pH log units lower) compared to natural carbonation. The pH in case of natural carbonation remains above 10. The reason why the pH is so high, is that the Na^+ content remains constant regardless the partial pressure of CO_2 [4]. The significant reduction of the pH in accelerated conditions is attributed to a higher fraction of bicarbonate ions (HCO_3^-), which conditions are more acidic compared to carbonate ions (CO_3^{2-}). This indicates that carbonation of the pore solution of alkali activated slag concrete would not be a problem in service conditions. However, there are no experimental measurements to validate numerical predictions. Furthermore, other mixtures than alkali activated slag concrete are not taken into account. To experimentally evaluate the effects of these parameters, in this paper the pH and carbonation depths are measured in alkali activated fly ash (FA) and ground granulated blast furnace slag (GGBFS) concrete and compared to cement-based concretes.

2. MATERIALS AND METHODS

2.1 Materials and sample preparation

Nedeljković et al. [5] shown that pastes with 100 wt.% GGBFS have a high resistance to carbonation due to their dense microstructures. It is of interest to study binders and concretes with lower slag content in the binder than 100 wt.%. For that purpose, the concretes with 50 wt.% GGBFS and 50 wt.% fly ash (FA) were cast (named S50 in the further text). Cement-based concretes were prepared with CEM I and CEM III/B. The details of mixtures proportions are listed in Table 1.

Table 1: Mixture designs for alkali activated concretes and cement-based concretes [m^3].

	FA [kg]	GGBFS [kg]	CEM I [kg]	Aggregate [0-4 mm]	Aggregate [4-8 mm]	Aggregate [8-16 mm]	Activator [kg]	liquid/ binder
Density [kg/m^3]	2440	2890	3000	2640	2650	2650	1250	[-]
Mix 1 S50	200	200	0	789.14	439.81	524.69	200	0.5
Mix 2 S50	130	130	0	789.14	439.81	524.69	156	0.6
Mix 3 CEM I	0	0	400	789.14	439.81	524.69	200 (water)	0.5
Mix 4 CEM III/B	0	280	120	789.14	439.81	524.69	200 (water)	0.5

In the absence of European standards for performance testing of alkali activated concrete, assessment for carbonation resistance are followed the EN 206-1 [6]. The assessment of carbonation resistance of alkali activated concrete with 260 kg/m^3 and 400 kg/m^3 of FA+GGBFS was performed to investigate conformity of an alkali activated concrete with minimum binder content for exposure class XC1 and XC3 [6], respectively.

The concrete samples were beams (1500×100×150 mm^3), which were cured in unsealed conditions (in curing room with 99% RH) for 28 days. After 28 days curing, the beams were sawn into 187.5-mm-wide samples (see Figure 2), sealed at the lateral sides and preconditioned for additional 28 days under laboratory conditions (55% RH, 20°C, 0.04% v/v CO_2). After preconditioning, samples were exposed to different carbonation conditions (Table 2).

Table 2: Exposure conditions for carbonation of concretes.

	Natural laboratory	Natural outdoor	Accelerated carbonation
CO_2 concentration	0.04% v/v	0.04% v/v	1% v/v
Relative humidity	55%	80-98%	60%
Temperature	20°C	0-20°C	20°C

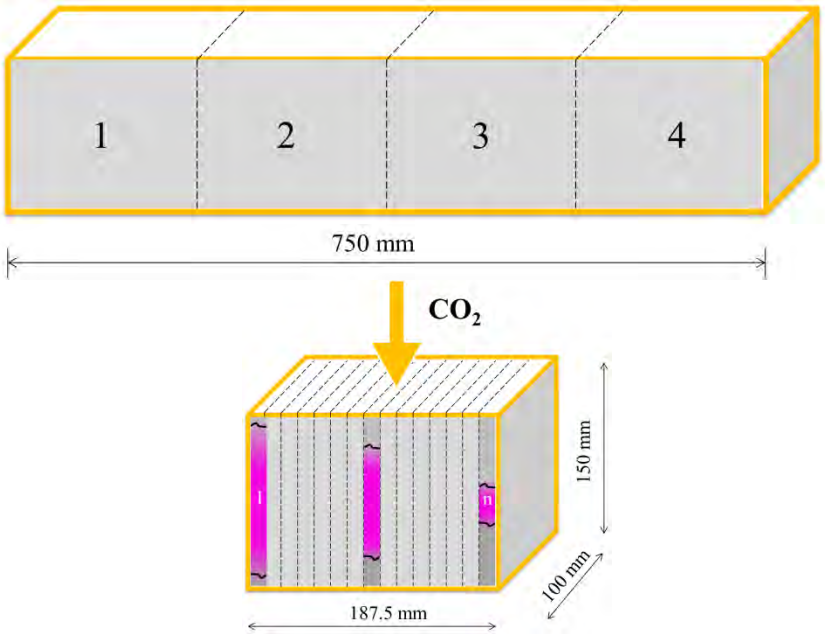

Figure 2: Geometry of the prepared concrete samples for each of the mixtures. After a certain period of exposure, a slice (width equal to 1 cm) of each of the prisms was cut (slices denoted as 1, …, n). Subsequently, the slice surface was sprayed with phenolphthalein spray for measurement of the carbonation depth. The noncarbonated part is indicated by the pink colour.

2.2 Experimental methods

2.2.1 Compressive strength

Compressive strength was measured for each concrete mixture at 1 day, 7, 28, 56, 180, 365, 548 days according to the NEN 5988 on three cubes with dimension of 150×150×150 mm^3. The mean values and standard deviations were calculated for each set of the data.

2.2.2 Carbonation depth

Carbonation depths were measured after 0, 14, 28, 42, 56, 114, 193, 236, 365, 548 days of exposure in accelerated conditions. In natural indoor and outdoor conditions, the carbonation depths were measured after 0, 28, 240, 365, 548. Slices with a thickness of 10-15 mm were cut from the concrete prisms by sawing (Figure 2). The fresh surface was sprayed with a 1 wt. % phenolphthalein aqueous solution. On average, 10 to 15 measurements were made per slice. Then the standard deviations were calculated for each set of the data.

2.2.3 pH of the pore solution

Direct extraction of the pore fluid from carbonated concrete samples was not possible due to the presence of aggregates and sample size that is needed for pore solution extraction. Therefore, pH measurements were carried out on simulated pore solutions, by equilibrating 1 g

of powdered sample with 10 ml of de-ionized water during 15 minutes at ambient temperature while stirring with a magnetic bar. Subsequently, the pH of the suspension was measured with a pH meter 827 Metrohm.

3. RESULTS AND DISCUSSION

3.1 Compressive strength

The compressive strength results and standard deviations for alkali activated concretes S50 (l/b=0.5), S50 (l/b=0.6), cement-based concretes made of CEM I (w/c=0.5) and CEM III/B (w/c=0.5) are shown in Figure 3. The compressive strength of concretes was measured during curing, preconditioning and exposure. Afterwards, the concrete samples were placed in outdoor sheltered conditions, where development of the compressive strength was monitored from 56 days to 548 days.

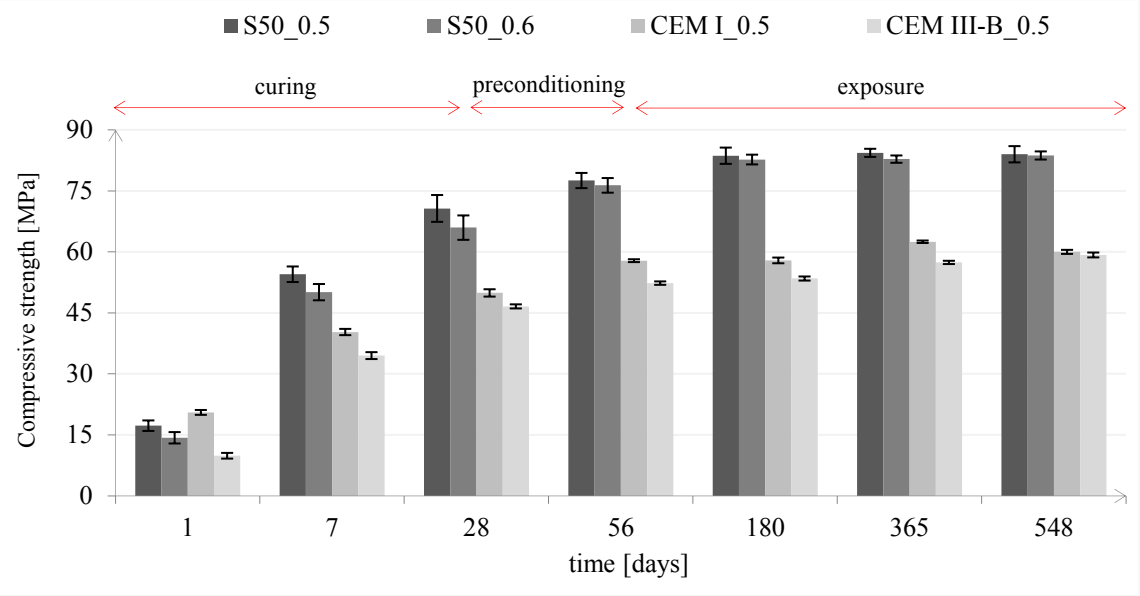

Figure 3: Compressive strength development in cement-based and alkali-activated concretes (samples (150×150×150 mm^3) were cured in the curing room for 28 days, preconditioned for additional 28 days (28-56 days) at 55% RH and then exposed to natural outdoor sheltered conditions (56-548 days)).

Figure 3 shows that the strength of alkali-activated concrete samples is higher than that of cement-based concrete samples. Furthermore, when comparing compressive strength of S50 mixture with precursor content (GGBFS+FA) of 400 kg/m^3 (l/b=0.5) with S50 mixture with precursor content of 260 kg/m^3 (l/b=0.6), there is no significant difference, specifically at the later ages (180, 365, 548 days). This suggests that for reaching high strength in alkali-activated concrete, the binder content can be optimized, i.e. reduced. Exposure in natural outdoor conditions did not cause drop in compressive strength of the studied concretes.

3.2 Carbonation depth

The propagation rate of the carbonation front was monitored for three exposure conditions: natural (outdoor (sheltered) and indoor) and accelerated carbonation conditions (Figure 4 (A), (B), (C)). Propagation of the carbonation front in concrete was monitored from the age of 56 days.

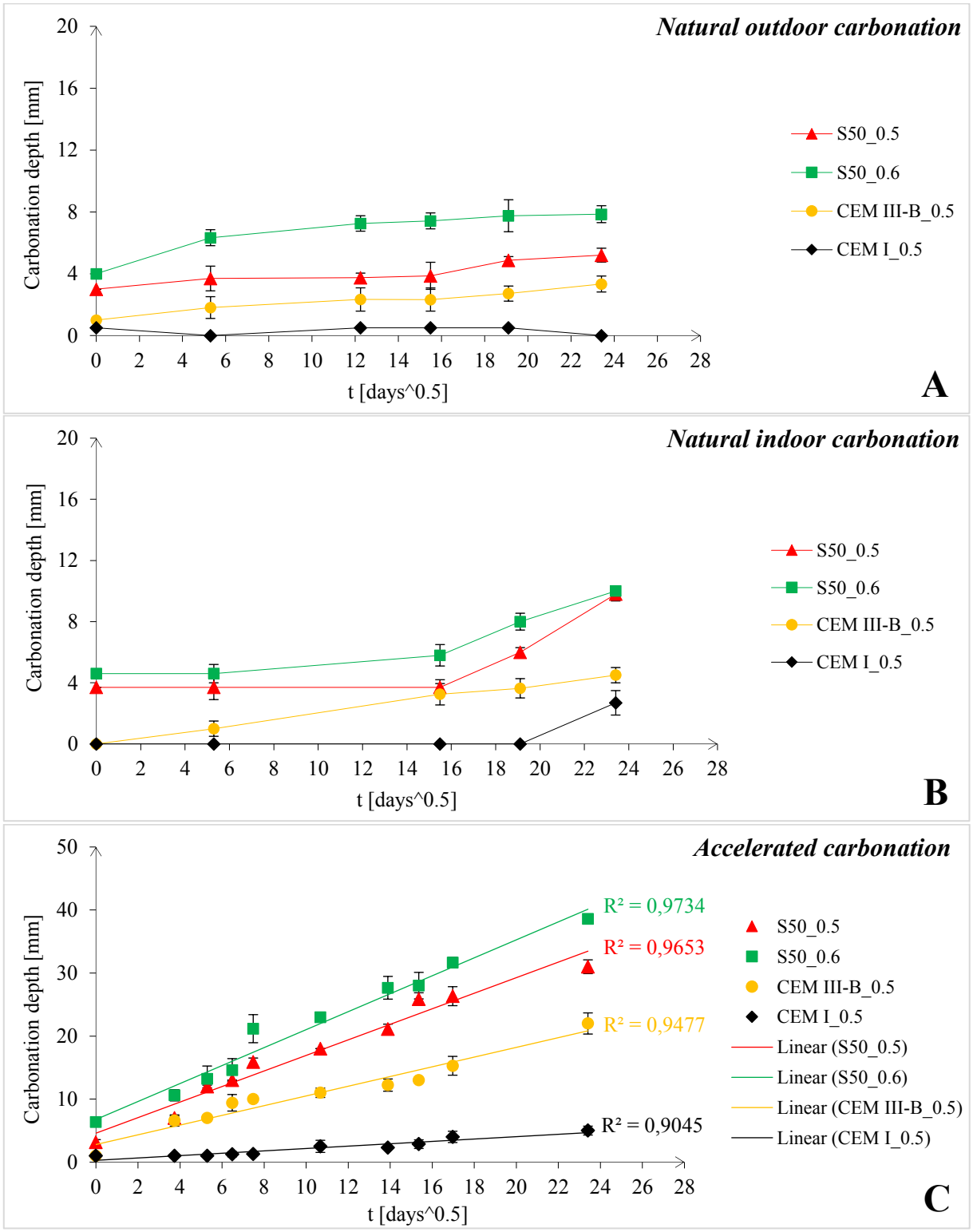

Figure 4: Carbonation depth versus time in natural outdoor (sheltered), indoor and accelerated carbonation conditions. At 56 days measurements of the carbonation depth in concretes started and, therefore 56th day is regarded as t=0. Since at 56 days carbonation depth was already measured, the fitted curves do not pass through the origin of the plots.

Figure 4 (A) demonstrates that carbonation did not proceed in the CEM I concrete in natural outdoor (sheltered) conditions. This is due to the large hydroxide alkalinity of the CEM I concrete. In contrast, the carbonation proceeds in CEM III/B and alkali activated concretes. For natural indoor conditions, sudden increase of carbonation depths can be seen after an age of 240 days (Figure 4(B)). The internal RH gradient over the cross section of the concrete sample at earlier stages can be an explanation for delayed carbonation of internal layers of the samples (4-12 mm).

Figure 4(C) indicates that in case of accelerated carbonation conditions, the propagation of the carbonation front is the fastest for the S50 (l/b=0.6) mixture, followed by the S50 (l/b=0.5), CEM III/B and CEM I. The carbonation is faster for S50 0.6 concrete, as l/b ratio is higher and the binder content is lower. CEM I 42.5 N concrete shows a high resistance to carbonation. Carbonation resistance decreases with decreasing clinker content, i.e. for CEM III/B 42.5 N concrete due to lower $Ca(OH)_2$ content, as shown by [7].

3.3 pH

The pH was also monitored for three different exposure conditions: natural (outdoor (sheltered) and indoor) and accelerated carbonation conditions (Figure 5 (A), (B), (C)). The pH of the pore solution in carbonated alkali-activated concrete is around 10, earlier than in cement-based concrete due to the absence of $Ca(OH)_2$. However, the phenolphthalein indicator shows that a gradual color change of phenolphthalein from fuchsia to colorless upon pH changes from 10 to 8.2. Therefore, it cannot be stated that the pore solution of alkali-activated concrete is neutralized to 8.2, since it can also be reduced to maximum pH 10 and again it appears as colourless. The pH of the carbonated alkali-activated concrete in accelerated test is found to be higher than 9. Due to the absence of $Ca(OH)_2$ in alkali-activated concretes, the CO_2 diffusion and CO_2 binding capacity of the mixture S50, are the subsequent mechanisms for faster propagation of the carbonation front compared to the cement-based concretes. In the case of natural carbonation (indoor and outdoor), the pH values are very close for all concretes (see Figure 5 (A), (B)).

According to the pH values, after 548 days of exposure, three stages can be distinguished for alkali activated concretes in case of accelerated carbonation (see Figure 5 (C)):

(1) from 0 mm to 15 mm, the pH of concrete surface decreases to 9.2, where the alkalis are fully depleted. This zone is fully carbonated;

(2) from 30 mm to15 mm, the pH of concrete decreases from 10.20 to 9.6. This suggests that the alkalis are partially depleted. This zone is partially carbonated;

(3) from 30 mm to 40 mm, the pH of concrete is above 10. This zone is noncarbonated.

In case of natural carbonation, only stages (1) and (3) are observed. This indicates slow progress of the carbonation process in natural conditions. Nevertheless, the pH in stage (1) in natural conditions is similar to stage (1) for accelerated carbonation. The pH in stage (1) and (2) of carbonated alkali activated concrete corresponds well with the pH of alkali activated pastes after 500 days of accelerated carbonation, as shown by Nedeljković et al. [8].

The pH of the CEM I concrete is maintained around 10.5. This value, however, is not a true pH especially not for the carbonated cement-based concrete (Figure 5 (C)). Some $Ca(OH)_2$ remains after carbonation and it dissolves when the suspension is made. Therefore, the pH evaluation using suspension method is not appropriate for CEM I concrete.

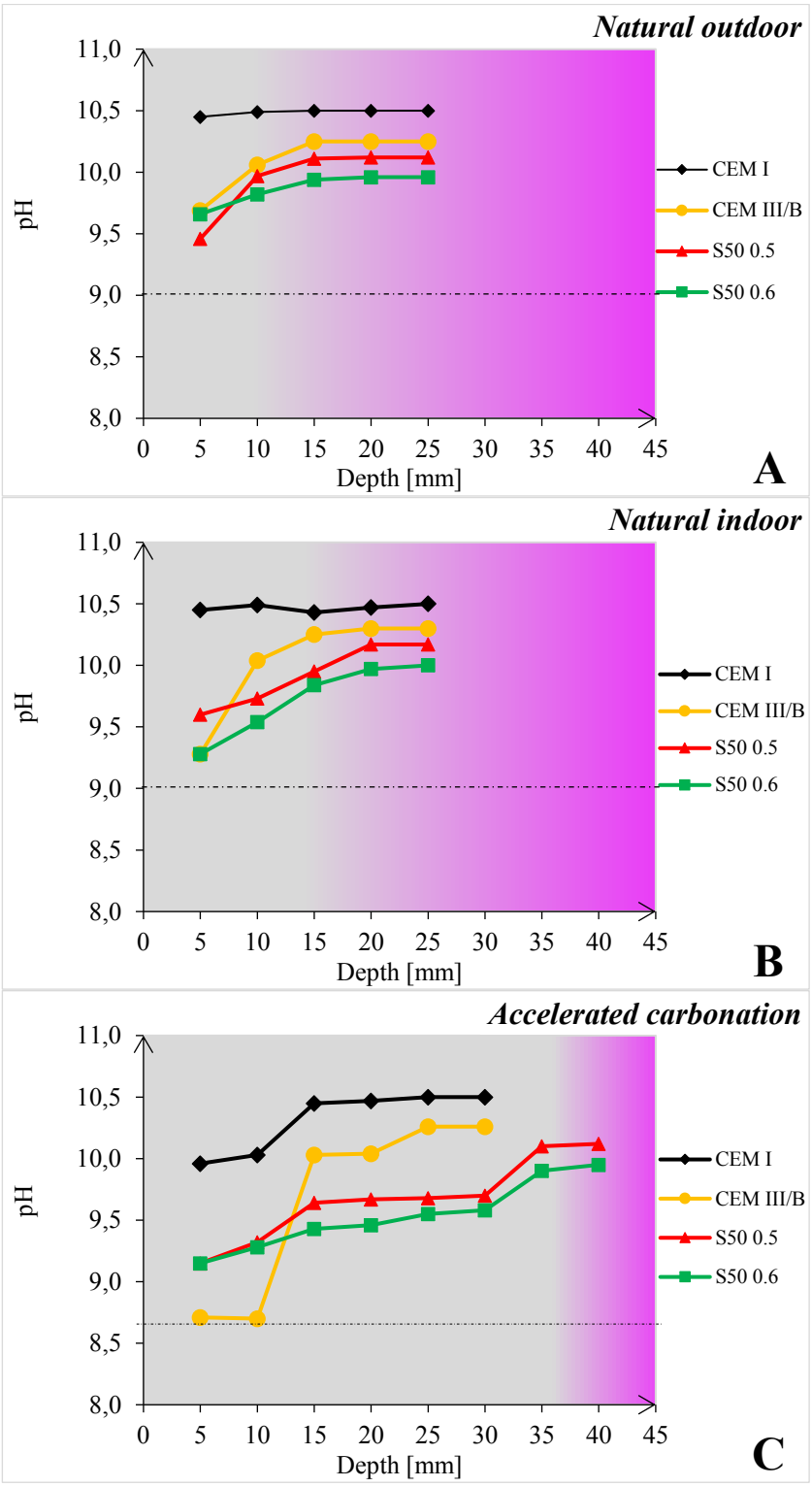

Figure 5: pH along carbonation path measured after 548 days of exposure in natural (indoor and outdoor (sheltered)) and accelerated carbonation conditions. (In the graphs, pink colour indicates noncarbonated zone and grey colour indicates the carbonated zone.)

For CEM III/B concrete, the results reflect the real reduction of the pH under carbonation. $Ca(OH)_2$ in CEM III/B concrete is mainly consumed by the pozzolanic reaction of GBFS. Therefore, the only source of alkalis after carbonation of this type of concrete are Na^+ and K^+. Under accelerated carbonation conditions, the carbonated CEM III/B concrete has a pH below 9, while in the noncarbonated part a pH >10 is measured. In natural indoor and outdoor conditions of exposure, the pH of carbonated CEM III/B concrete is above 9.

The pH of all carbonated alkali-activated S50 concretes was above the pH 9, which is reported as a threshold value for an initiation of the carbonation induced reinforcement corrosion in the OPC-based binders [9]. The pH of the noncarbonated alkali-activated concretes S50 was above 10.

4. CONCLUSIONS

- The higher propagation rate of the carbonation front in the alkali-activated GGBFS+FA concrete, despite its higher compressive strength and finer pore structure compared to cement-based concrete, is due to absence of $Ca(OH)_2$, different pore solution chemistry (alkalinity buffer), lower calcium content in the gel phases, hence lower content of the carbonatable phases.
- From all above factors, the carbonation rate is the most influenced by the alkalinity of the alkali activated concretes. This implies that the total alkalinity of the material might be used in future to predict the carbonation depths. It should be noted that the carbonation depth for alkali activated concrete is the domain where alkalinity is reduced and microstructure is deteriorated.
- Improved carbonation resistance of the alkali-activated concrete S50 can be achieved by higher GGBFS content (70, 100 wt.%) and by applying the sealed curing.
- Future modeling studies are needed to consider the synergy between reduced alkalinity and deterioration of concrete microstructure under different exposure conditions.

REFERENCES

[1] Arbi, K., Nedeljković, M., Zuo, Y. and Ye, G. 'A review on the durability of alkali-activated fly ash/slag systems: advances, issues, and perspectives'. *Ind. Eng. Chem. Res.*, **55**(19)(2016) 5439-5453.

[2] Nedeljković, M. *Carbonation mechanism of alkali-activated fly ash and slag materials: In view of long-term performance predictions*. Ph.D. Thesis, Delft: Delft University Press, 2019.

[3] Bernal, S. A., Provis, J. L., Brice, D. G., Kilcullen, A., Duxson, P. and van Deventer, J. S. 'Accelerated carbonation testing of alkali-activated binders significantly underestimates service life: The role of pore solution chemistry.' *Cem. Concr. Res.***42**(10)(2012) 1317-1326.

[4] Bernal, S. A., de Gutierrez, R. M., Provis, J. L. and Rose, V. 'Effect of silicate modulus and metakaolin incorporation on the carbonation of alkali silicate-activated slags.' *Cem. Concr. Res.***40**(6)(2010) 898-907.

[5] Nedeljković, M., Zuo, Y., Arbi, K. and Ye, G. 'Carbonation resistance of alkali-activated slag under natural and accelerated conditions.' *Journal of Sustainable Metallurgy* **4**(1)(2018), 33-49.

[6] EN 206-1 Concrete - Part 1: Specification, performance, production and conformity (CEN, 2013).

[7] Nedeljković, M., Ghiassi, B., Melzer, S., Kooij, C., van der Laan, S. and Ye, G. 'CO_2 binding capacity of alkali-activated fly ash and slag pastes.' *Ceram. Int.* **44**(16)(2018), 19646-19660.

[8] Nedeljković, M., Ghiassi, B., van der Laan, S., Li, Z. and Ye, G. 'Effect of curing conditions on the pore solution and carbonation resistance of alkali-activated fly ash and slag pastes' *Cem. Concr. Res.***116**(2019) 146-158.

[9] Bertolini, L., Elsener, B., Pedeferri, P., Redaelli, E. and Polder, R. 'Carbonation-Induced Corrosion' in Corrosion of Steel in Concrete, Wiley-VCH Verlag GmbH & Co. KGaA, 2013, 79-92.

EFFECT OF CA BACTERIA ON THE CARBONATION PROCESS OF γ-C_2S

Peng Jin(1,2), Ruixing Wang(1,2)*, Siyi Zhang(1,2), Hua Dong(1,2), Chun Chen(1,2)

1. College of Materials Science and Engineering, Southeast University, China

2. Jiangsu Key Laboratory of Construction Materials, Southeast University, China

*Corresponding author: e-mail addresses: ruixing@seu.edu.cn.

Abstract

Carbonation has been proven to be a promising way to improve the mechanism properties and durability of steel slag products. CA bacteria can promote the hydration of CO_2. In this study, one kind of alkali-resistant CA bacteria was chosen to investigate its effects on the carbonation process of γ-C_2S. Results showed that bacteria could increase the compressive strength of carbonized γ-C_2S by 19.0%. Main products of carbonized γ-C_2S were vaterite, calcite and SiO_2 gel. The addition of bacteria could only accelerate the deposition of calcium carbonate, while hardly changing the types and properties of the carbonation products. Additionally, accelerated carbonation makes it harder for the carbon dioxide to diffuse inward, leading to the decline of accelerating carbonation effect. However, CA bacteria could change the morphology of calcium carbonated during the carbonation process of β-C_2S and further accelerate the hydration process of β-C_2S. The pore structure can also be refined with the incorporation of bacteria.

Keywords**:** γ-C_2S; β-C_2S; CA bacteria; Carbonation products; Pore structure;

1. INTRODUCTION

γ-dicalcium silicate (γ-C_2S), which has little hydration activity according to some relevant research[1, 2], was one of the most important ingredients in some types of steel slag[3]. However, it is worth noting that γ-C_2S has relatively high carbonation activity, which makes it possible to be applied in carbon dioxide capture and storage. Carbonation process of γ-C_2S has been studied from many aspects. Chang et al.[4] thought that γ-C_2S had higher carbonation reactivity than β-C_2S; calcium carbonate and silica gel were the main products of the carbonized γ-C_2S. It remains controversial whether the crystal product is calcite or vaterite calcium carbonate. Saito et al.[5] thought that vaterite was the main crystal product of carbonized γ-C_2S because coordination number and Ca-O bond length of Ca ion in γ-C_2S and vaterite were similar to each other. γ-C_2S could not react with water and it reacted directly with H_2CO_3 as shown in

Eq.(1) and (2) and it was the deposition of calcium carbonate that made this reaction continuously proceed. However, Goto et al.[6] thought that the main crystal products were calcite. Therefore, this study payed attention to the products of carbonized γ-C_2S as well.

$$CO_2+H_2O\rightarrow H_2CO_3 \quad (1)$$

$$2CaO\cdot SiO_2+2H_2CO_3\rightarrow 2CaCO_3+SiO_2+2H_2O \quad (2)$$

There is an increasing interest in the microbe-induced calcium carbonate precipitation (MICP), which is also a process of calcium carbonate deposition. Traditional MICP technique takes advantage of urease bacteria to hydrolyze urea and obtains carbon dioxide and NH^{4+}, which can increase the pH value of the solution and promote the formation of CO_3^{2-} and then induce the deposition of calcium carbonate[7]. In recent years, a new kind of bacteria has been studied to realize MICP with brand-new mechanisms[8-11]. This kind of carbonic anhydrase (CA) bacteria could speed up the hydration process of CO_2 about 10^7 times[12]. The catalysis of CO_2 hydration is initialized by the nucleophilic attack on the carbon atom of CO_2 by zinc-bound OH^-, and bicarbonate ($EZnHCO_3^-$) is formed, zinc in which is then replaced by a water molecule[9, 13].

The hydration of CO_2 is also one of the crucial steps of carbonation process. However, few studies focused on the interaction between MICP and carbonation. In this study, γ-C_2S was synthesized and exposed to CO_2 with incorporation of bacteria to study the effects of CA bacteria on the carbonation process of γ-C_2S. Carbonation process of β-C_2S was also studied as a contrast.

2. MATERIALS AND METHODS

2.1 Raw materials

Analytical pure $CaCO_3$ and SiO_2 with a molar ratio of 2:1 were heated for the sintering of γ-C_2S. The purity of the sample is 92.4%, containing some impurities of β-C_2S.

A kind of carbonic anhydrase bacteria powder was used in this experiment which consisted of spores of bacteria, spherical carriers and a certain amount of organic matter. It is determined that the best content of bacteria powder is 1wt.% of γ-C_2S through the preliminary test.

2.2 Sample preparation and the accelerated carbonation process

Cylindrical specimens with a diameter of 20mm and a height of 15mm were used for the characterization of degree of carbonation. Before carbonation, samples were cured under a relative humidity higher than 95% at 25℃ for 22h. γ-C_2S specimens were carbonized in a chamber which was vacuumed to -0.1MPa first and then filled with carbon dioxide with a purity higher than 99.9%. The partial pressure of the carbon dioxide was 0.25MPa.

2.3 Degree of carbonation, carbonation products and pore structure

Characterization of carbonation degree was conducted by X-ray-CT test. Software such as VG Studio Max and ImageJ were utilized to process 3D images and 2D images respectively. X-ray diffraction analysis (XRD) was utilized to study different kinds of crystal products during

carbonation process. Fourier infrared spectrometer was used for further characterization of carbonation products with a testing range from 4000cm^{-1} to 400cm^{-1}. Scanning electron microscope (SEM) test was conducted to observe the micromorphology of carbonation products. BET and MIP methods were carried out to study the effect of CA bacteria on the pore structure of carbonized C_2S. The absorbate gas of BET method was nitrogen.

3. RESULTS AND DISCUSSION

3.1 Effects of bacteria on degree of carbonation

Fig. 1 shows the 3D images of C_2S pastes reconstructed from X-ray-CT data by using VG Studio Max software. Blue color represented the uncarbonized part while blank space represented the carbonized part. It was clear that the blank space of the sample without bacteria was larger than that of the sample with bacteria. For a quantitative comparison, ten 2D images of each sample were selected with equal distance from the top surface to calculate the ratio of carbonized volume to total volume of the sample, whose average value was referred to as degree of carbonation. Samples carbonized without bacteria had a carbonation degree of 51.1% and that of samples with bacteria was only 45.7%.

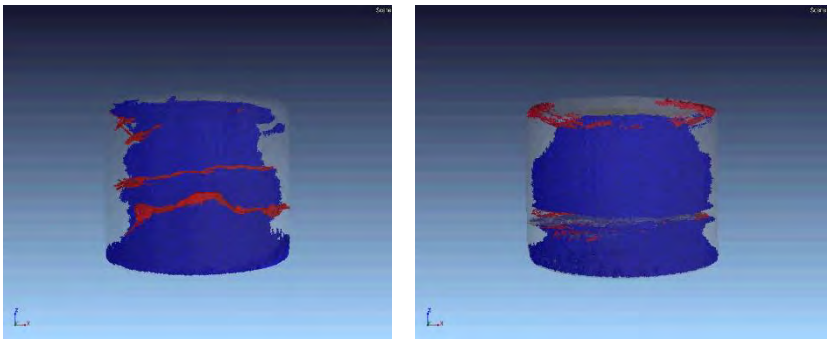

(a) Without bacteria **(b)With bacteria**

Figure 1: 3D images of γ-C_2S samples reconstructed by X-ray-CT

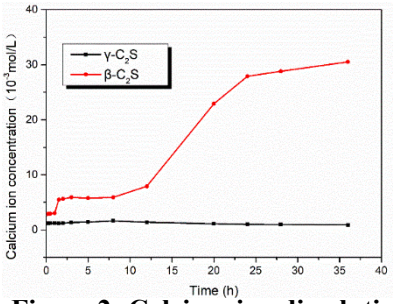

Figure 2: Calcium ion dissolution properties of γ-C_2S and β-C_2S

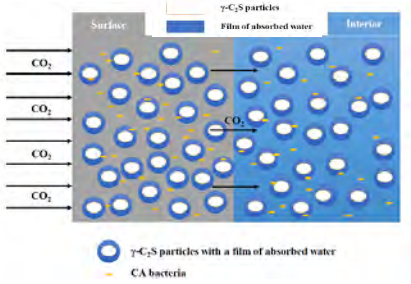

Figure 3: The influence of bacteria on diffusion of CO_2 into the samples

Further research about the calcium ion dissolution characteristics of γ-C_2S was conducted to explain such phenomenon. Calcium ion dissolution characteristics of β-C_2S was studied as well for comparison. As illustrated in **Fig. 2**, it was easy for β-C_2S powder to dissolve calcium ions in deionized water, which could account for its relatively high hydration activity. As the

hydration process proceeded, more and more portlandite was generated and calcium ion concentration kept increasing. On the contrary, γ-C_2S could not dissolve calcium ions quickly, which was consistent with its low hydration characteristics. However, γ-C_2S has a strong ability to absorb water. The carbonation reaction takes place in this film of absorbed water. Based on those results, an assumption was put forward to explain why bacteria could accelerate the early carbonation rather than the late carbonation process. CA bacteria accelerate the carbonation process by promoting the hydration of CO_2, and they were evenly distributed in the solution consisting of free water and the absorbed water film. As shown in **Fig. 3**, with the addition of bacteria, more CO_2 dissolved in the pore solution on the surface of the samples. However, only CO_2 dissolving in the film of absorbed water could react with γ-C_2S directly, whose amount was relatively limited. And it was a great waste for too much CO_2 to dissolve in the free water, causing less CO_2 to spread inside, leading to the decrease in carbonation degree of samples with bacteria.

3.2 Characteristics of carbonation products

Fig. 4 illustrates the XRD patterns of carbonized γ-C_2S powder with or without bacteria. It indicates that the main crystal product was calcium carbonate with two different crystal forms, which were calcite and vaterite. Samples with bacteria had a higher relative peak intensity of calcium carbonate. However, no brand-new products were generated were generated in the γ-C_2S pastes with bacteria. Comparing with the XRD pattern of β-C_2S shown in **Fig. 5**, portlandite was absent from the carbonation products, which represented that carbonation process of γ-C_2S was not accompanied by the hydration process. Moreover, the presence of vaterite could further confirm that carbonation reaction of γ-C_2S was not like that of β-C_2S, which was a chemical reaction occurring in solution by the combination of Ca^{2+} and CO_3^{2-} and formed calcite calcium carbonate. However, γ-C_2S reacted directly with carbon dioxide and formed vaterite because of the similarities of crystal structure between γ-C_2S and vaterite. Water served as reaction medium during the whole process. Calcite was also observed among the carbonation products of γ-C_2S mainly because of the instability of vaterite and it was prone to crystal transition with the change of temperature, relative humidity, gas pressure and so on.

Fig. 6 shows the FT-IR spectrum of γ-C_2S powder, carbonized γ-C_2S with and without bacteria. Before carbonation, a broad characteristic band from 900cm^{-1} to 950cm^{-1} represented asymmetric stretching (ν^3) of Si–O bond, corresponding to the island silicate structure of γ-C_2S. After carbonation, new bands were located around 1423 cm^{-1}, 874 cm^{-1} and 713 cm^{-1}, which represented asymmetric stretching (ν^3) of C–O bond, out-of-plane bending vibration (ν^4) of C–O bond and in-plane bending vibration (ν^2) of C–O bond present respectively. These were all characteristics of calcite calcium carbonate and bands at 850 cm^{-1}, 815 cm^{-1} and 669cm^{-1} were due to the presence of vaterite calcium carbonate, which was consistent with the results of XRD test. Moreover, it was worth noting that the broad characteristic peak from 900cm^{-1} to 950cm^{-1} migrated to higher wavenumbers and had a decrease in the intensity. The band at 1060 cm^{-1} was due to the formation of Si-O-Si bond, which was usually present in SiO_2 or C-S-H gel. Since no crystal SiO_2 was found in XRD patterns, it was more likely that SiO_2 gel was generated

during the carbonation of γ-C_2S. Taking bacteria into consideration, it had little effect on the species and crystal forms of carbonation products.

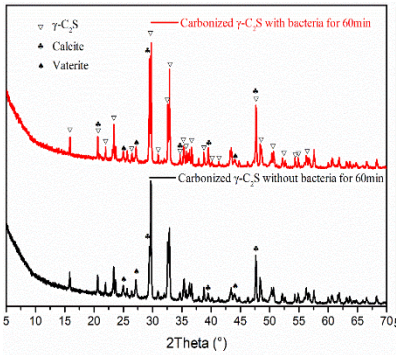

Figure 4: XRD patterns of carbonized γ-C_2S

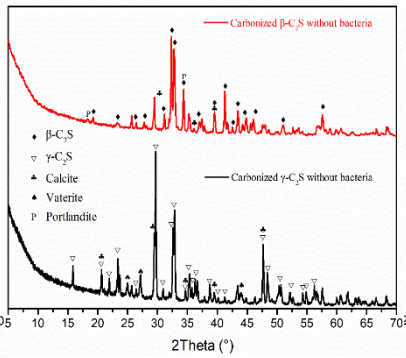

Figure 5: XRD patterns of carbonized γ-C_2S and β-C_2S

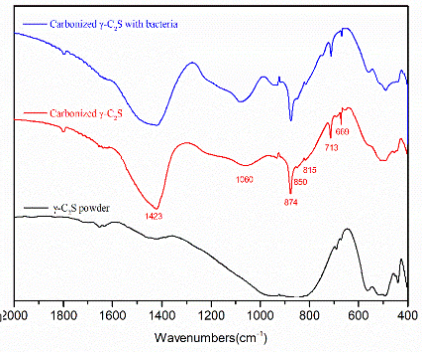

Fig. 6. FT-IR spectrum γ-C_2S

3.4 Morphology of hydration products

The microstructure morphology of different samples was observed under SEM. As shown in **Fig. 7(a)** and **Fig. 7(b)**, the structure of the uncarbonized sample was loose and porous. However, the loose particles were connected by amorphous products after carbonation, and a denser structure was formed. **Fig. 7(c)** shows the magnified micrographs of carbonized γ-C_2S without bacteria. No obvious calcium carbonate particles were found, which were different from the carbonation products of β-C_2S shown in **Fig. 7(e)**. And taking results of FT-IR into consideration, the flocculent substance adhering to the surface of the particle was likely to be SiO_2 gel. It was plausible that uncarbonized γ-C_2S was enveloped by silica gel, and calcium carbonate was embedded in silica gel to fill the pore of the system. The morphology of carbonized β-C_2S was quite different from that of carbonized γ-C_2S because it was easy for β-C_2S to dissolve calcium ions into pore solution and the carbonation process happened in pore solution. Hence, it was much easier to find individual particles of calcium carbonate in pore structure of carbonized β-C_2S.

As shown in **Fig. 7(d)**, with the addition of CA bacteria, morphology of crystal carbonation products had less obvious change. However, the surface of particles was covered with more reticular gelatinous material, which was mainly composed of carbon, oxygen, silicon and calcium by EDS test. Carbon, oxygen and calcium might come from deeper particles because the electron beam used for detection has a certain penetrability. Therefore, higher silicon content could indicate that more silica gel was formed during carbonation process with the incorporation of CA bacteria. Such accelerated carbonation effect was consistent with other results like compressive strength, mass gain rate and degree of carbonation. Differently, CA bacteria could change the morphology and particle size of calcium carbonate crystal generated in carbonation process as shown in **Fig. 7(e)** and **Fig. 7(f)**. Cube-like calcium carbonate was formed with a size of 3-10μm. While with the addition of CA bacteria, calcium carbonate particles with much smaller size were generated and bound together by some substance such as silica gel or C-S-H gel, forming a spherical structure. It is indicated that the appearance of

calcium carbonate induced by bacteria might be affected. However, it is indicated that the significant effect exists only when calcium carbonate deposition reaction takes place in solution. This might be the reason for the fact that bacteria could not change the morphology of calcium carbonate produced by the carbonation of γ-C_2S.

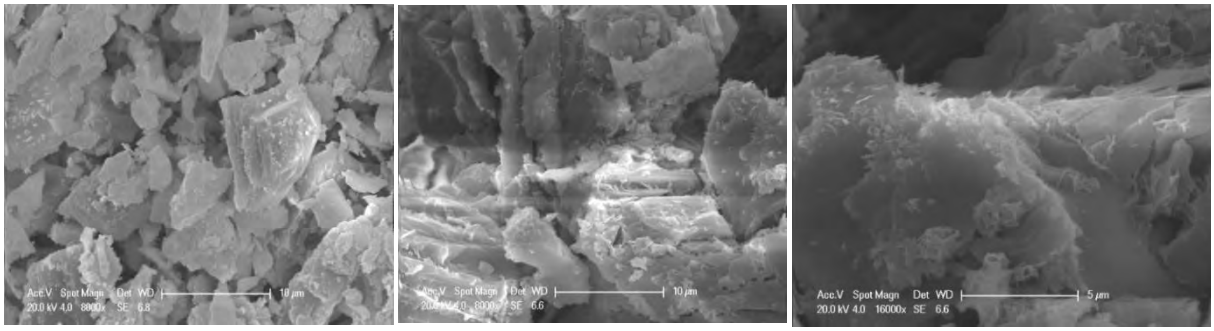

(a) Uncarbonized γ-C_2S powder (b) Carbonized γ-C_2S powder (c) Carbonized γ-C_2S without bacteria

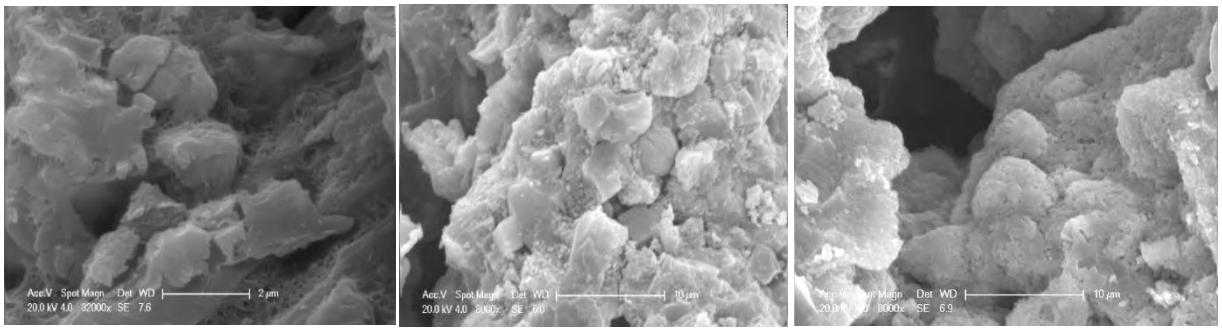

(d)γ-C_2S with bacteria (e) d β-C_2S without bacteria (f) β-C_2S with bacteria

Figure 7: SEM micrographs of C_2S with different carbonation conditions and magnification

3.5 Characterization of pore structure

MIP method and BET method were both used for comprehensive description of pore structure development of carbonized γ-C_2S. Results of MIP method show that the total porosity of carbonized γ-C_2S without bacteria was 29.4%, which decreased to 27.0% with the incorporation of CA bacteria. As for β-C_2S samples, porosity of carbonized samples was about 23%, which decreased to 20% with the addition of CA bacteria. Carbonized β-C_2S samples had a denser internal structure with lower porosity when compared with carbonized γ-C_2S, which mainly resulted from higher hydration activity of β-C_2S. The carbonation process of β-C_2S was along with the accelerated hydration process[13], especially in the presence of CA bacteria. Nanoscale calcium carbonation induced by bacteria acted as a nucleus, which could accelerate the formation of C-S-H gel and further promote the hydration process of β-C_2S.

Detailed pore size distribution of samples was illustrated in **Fig. 8**. As shown in **Fig. 8(a)**, it is worth noting that carbonized samples had slightly higher amount of gel pores in the range of 1nm to 10nm, which increased obviously with the addition of bacteria. It means that participation of bacteria could further promote the carbonation process and generate more gel material, which is consistent with the results of SEM. **Fig. 8(b)** shows the results of pore size distribution determined by MIP test, it is obvious that pores in the range of 100nm to 2μm

decreased greatly and pores in the range of 10nm to 100nm increased in samples carbonized with bacteria. As mentioned before, larger pores were filled with carbonation products and formed smaller pores. Relevant research[14] also agrees that the increase in pores ranging from 20nm to 70nm could indicate that the cement-based material was well-carbonized. Denser pore structure could further confirm the assumption that it was difficult for CO_2 to diffuse inward in the late carbonation process with the addition of bacteria. Besides, it is worth noting that large pores ranging from 2μm to 4μm showed a slightly increase. In addition to errors in sample preparation process, it might result from cracks generated during the accelerated carbonation process, which requires detailed research.

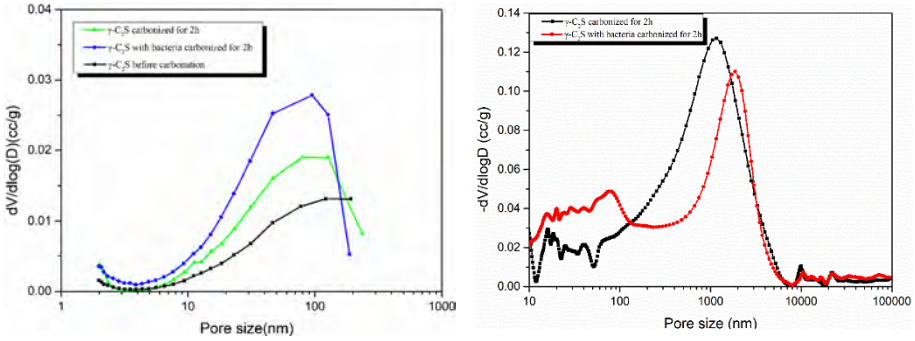

(a) BET methods **(b) MIP methods**

Figure 8: Pore size distribution of γ-C_2S samples

4. CONCLUSION

Through a series of characterization methods, accelerated carbonation characteristics of γ-C_2S were investigated. Carbonized β-C_2S was also studied for comparison. Some conclusions can be drawn as follows:

- CA bacteria can further accelerate the carbonation process during the early age of carbonation. However, such acceleration effect diminishes because accelerated carbonation process densifies the surface of samples quickly, making it hard for carbon dioxide to diffuse inward.
- Carbonation products of γ-C_2S are composed of vaterite calcium carbonate, calcite calcium carbonate and SiO_2 gel. CA bacteria can promote the deposition of calcium carbonate by accelerating the dissolution and hydration of CO_2. However, compared with the effects of bacteria on β-C_2S, it cannot change the crystal phase, morphology or size of particles of calcium carbonate of carbonized γ-C_2S. CA bacteria cannot affect the properties of calcium carbonate unless the deposition process happens in solution.
- Carbonation process of γ-C_2S is along with the process of refining the pore structure. Calcium carbonate and SiO_2 gel are generated on the surface of γ-C_2S particles, leading to the volume expansion and filling the pore structure. As for β-C_2S, nanoscale calcium carbonate can act as nucleus and promote the formation of C-S-H gel, improving the pore structure greatly.

ACKNOWLEDGEMENTS

The authors would like to appreciate the financial support from National Nature Science Foundation of China (Grant No.51738003) and National Nature Science Foundation of China (Grant No. 51872046).

REFERENCES

[1] Q.Q. Wang, H. Manzano, Y.H. Guo, I. Lopez-Arbeloa, X.D. Shen, 'Hydration Mechanism of Reactive and Passive Dicalcium Silicate Polymorphs from Molecular Simulations', *J Phys Chem C*.**119**(34) (2015) 19869-19875.

[2] L. Kriskova, Y. Pontikes, F. Zhang, O. Cizer, P.T. Jones, K. Van Balen, B. Blanpain, 'Influence of mechanical and chemical activation on the hydraulic properties of gamma dicalcium silicate', *Cement Concrete Res*.**55** (2014) 59-68.

[3] M. Bodor, R.M. Santos, L. Kriskova, J. Elsen, M. Vlad, T. Van Gerven, 'Susceptibility of mineral phases of steel slags towards carbonation: mineralogical, morphological and chemical assessment', *Eur J Mineral*.**25**(4) (2013) 533-549.

[4] J. Chang, Y.F. Fang, X.P. Shang, 'The role of beta-C2S and gamma-C2S in carbon capture and strength development', *Mater Struct*.**49**(10) (2016) 4417-4424.

[5] T. Saito, E. Sakai, M. Morioka, N. Otsuki, 'Carbonation of gamma-Ca2SiO4 and the Mechanism of Vaterite Formation', *J Adv Concr Technol*.**8**(3) (2010) 273-280.

[6] S. Goto, K. Suenaga, T. Kado, M. Fukuhara, 'Calcium Silicate Carbonation Products', *J Am Ceram Soc*.**78**(11) (1995) 2867-2872.

[7] W. De Muynck, N. De Belie, W. Verstraete, 'Microbial carbonate precipitation in construction materials: A review', *Ecol Eng*.**36**(2) (2010) 118-136.

[8] G.M. Bond, J. Stringer, D.K. Brandvold, M.G. Medina, F.A. Simsek, G. Egeland, 'Development of integrated system for biomimetic CO2 sequestration using the enzyme carbonic anhydrase.', *Abstr Pap Am Chem S*.**220** (2000) U395-U395.

[9] P. Mirjafari, K. Asghari, N. Mahinpey, 'Investigating the application of enzyme carbonic anhydrase for CO(2) sequestration purposes', *Ind Eng Chem Res*.**46**(3) (2007) 921-926.

[10] Y.L. Su, J.H. Feng, P. Jin, C.X. Qian, 'Influence of bacterial self-healing agent on early age performance of cement-based materials', *Constr Build Mater*.**218** (2019) 224-234.

[11] M. Ferraroni, S. Tilli, F. Briganti, W.R. Chegwidden, C.T. Supuran, K.E. Wiebauer, R.E. Tashian, A. Scozzafava, 'Crystal structure of a zinc-activated variant of human carbonic anhydrase I, CA I Michigan 1: Evidence for a second zinc binding site involving arginine coordination', *Biochemistry-Us*.**41**(20) (2002) 6237-6244.

[12] R.W. Heck, S.M. Tanhauser, R. Manda, C.K. Tu, P.J. Laipis, D.N. Silverman, 'Catalytic Properties of Mouse Carbonic-Anhydrase-V', *J Biol Chem*.**269**(40) (1994) 24742-24746.

[13] P. Jin, R. Wang, Y. Su, H. Dong, Q. Wang, 'Study on carbonation process of β-C2S under microbial enzymatic action', *Constr Build Mater*.**228** (2019) 117110.

[14] B. Johannesson, P. Utgenannt, 'Microstructural changes caused by carbonation of cement mortar', *Cement Concrete Res*.**31**(6) (2001) 925-931.

A CONTINUUM MODEL FOR CARBONATION CURING OF FIBER-CEMENT COMPOSITES

S.C. Seetharam(1), Q.T. Phung(1), B. Kottititum(2), N. Maes(1), T. Srinophakun(2)

(1) Belgian Nuclear Research Centre (SCK•CEN), 2400 Mol, Belgium

(2) Department of Chemical Engineering, Kasetsart University, Bangkok, Thailand

Abstract

Accelerated carbonation curing of cellulose fiber-cement composites is known to improve their durability in the form of decreased porosity and increased mechanical properties. In addition, because carbonation results in a decrease in the alkalinity of cement paste, it makes cement less aggressive towards the cellulose fibers. The properties of the composite can be controlled by adjusting carbonation curing time, carbonation curing pressure as well as mechanical rolling pressure. In this context, a continuum model is proposed that couples the process of hydration of cement with heat, moisture and CO_2 transport, including precipitation of $CaCO_3$, change of porosity because of hydration as well as carbonation and water release and consumption. Experimental data on carbonation curing of a cellulose fiber-cement composite has recently become available, which serves to validate the model. Preliminary results indicate that the model is able to predict within reasonable accuracy the depth of carbonation.

Keywords: Carbonation, Hydration, Fiber-cement composites, Modelling, Early age

1. INTRODUCTION

The carbonation process in hardened cement-based materials is typically considered as a deterioration phenomenon because it results in a pH decrease, which accelerates the corrosion of reinforcing bars in concrete. On the other hand, carbonation also results in beneficial effects such as decrease in transport properties, refined pore structure of cement-based materials [1, 2], and enhanced mechanical properties, which is frequently applied to improve the performance of fiber-cement composites properties. Typically, fiber-cement composites have high porosity resulting in low physical and mechanical properties. Accelerated carbonation of fiber-cement matrix during the curing period significantly enhances their durability [3]. The extent of modification in microstructure and hence mechanical properties significantly depends on carbonation conditions (e.g. CO_2 concentration, relative humidity, applied CO_2 pressure) and cement types (e.g. OPC or blended systems) and the age of materials. The reduction of transport properties is a result of the precipitation of carbonation products in the pore structure, which leads to a significant reduction of the total porosity [4].

Typically, hydration is not considered in carbonation models because the hydration is nearly stable in hardened materials (after 28-day curing), which is not the case for early age carbonation curing of fiber-cement composites (carbonation typically initiated few hours after casting). In a previous study [5], the authors have successfully developed a comprehensive 1D reactive transport model accounting for both advective and diffusive transports under CO_2 pressure gradients for hardened cement pastes. This model enables to predict carbonation depth and changes in permeability, diffusivity, and porosity due to carbonation. In this study, an improved model is proposed that couples the process of hydration of cement with heat, moisture and CO_2 transport in order to investigate the key parameters including curing time, curing pressure, rolling pressure and initial physical properties of fiber-cement composites on the carbonation efficiency. The performance of the model is explored by simulating an accelerated carbonation curing experiment reported in [6].

2. COUPLED MODEL

2.1 Hydration of fiber-cement composites

This study considers reactions of four main cement clinker phases (i.e. C_3S, C_2S, C_3A, C_4AF) with water as shown in Table 1. Fibers and limestone filler are considered as inert ingredients. The rate equations are based on Papadakis et al. [7], which are empirical. The effect of temperature is also considered by correcting the hydration rate constant using Arrhenius equation.

Table 1: Hydration and carbonation reactions considered in the model

Hydration reactions	
$3CaO.SiO_2 + 4.3H_2O \xrightarrow[r_{H,C3S}]{} 1.7CaO.SiO_2.3H_2O + 1.3Ca(OH)_2$	(1)
$2CaO.SiO_2 + 3.3H_2O \xrightarrow[r_{H,C2S}]{} 1.7CaO.SiO_2.3H_2O + 0.3Ca(OH)_2$	(2)
$3CaO.Al_2O_3 + 3CaSO_4.2H_2O + 26H_2O \xrightarrow[r_{H,C3A,S}]{} 3CaO.Al_2O_3.3CaSO_4.32H_2O$	(3)
$4CaO.Al_2O_3.Fe_2O_3 + 2Ca(OH)_2 + 2(CaSO_4.2H_2O) + 18H_2O \xrightarrow[r_{H,C4AF,S}]{} 6CaO.Al_2O_3.Fe_2O_3.2CaSO_4.24H_2O$	(4)
$3CaO.Al_2O_3 + Ca(OH)_2 + 12H_2O \xrightarrow[r_{H,C3A}]{} 3CaO.Al_2O_3.Ca(OH)_2.12H_2O$	(5)
$4CaO.Al_2O_3.Fe_2O_3 + 2Ca(OH)_2 + 22H_2O \xrightarrow[r_{H,C4AF}]{} 6CaO.Al_2O_3.Fe_2O_3.2Ca(OH)_2.24H_2O$	(6)
Carbonation reactions	
$3CaO.SiO_2 + 3CO_2(aq) + (H_2O) \xrightarrow[r_{C3S}]{} SiO_2 + (H_2O) + 3CaCO_3$	(7)
$2CaO.SiO_2 + 2CO_2(aq) + (H_2O) \xrightarrow[r_{C2S}]{} SiO_2 + (H_2O) + 2CaCO_3$	(8)
$1.7CaO.\ SiO_2.3H_2O + 1.7CO_2(aq) \xrightarrow[r_{CSH}]{} 1.7CaCO_3 + SiO_2.1.8H_2O + 1.2H_2O$	(9)
$3CaO.Al_2O_3.3CaSO_4.32H_2O + 3CO_2(aq) \xrightarrow[r_{AFt}]{} 3CaCO_3 + 3CaSO_4.2H_2O + 2Al(OH)_3 + 9H_2O$	(10)
$Ca(OH)_2(aq) + CO_2(aq) \xrightarrow[r_{CH}]{} CaCO_3 + H_2O$	(11)

2.2 Carbonation at early age under CO_2 curing

Among the hydration products, calcium silicate hydrate (C-S-H), portlandite (CH), and ettringite (AFt) undergo carbonation. Furthermore, two main clinkers (i.e. C2S and C3S), which have not yet hydrated, are also carbonated as shown in Table 1. The carbonation reactions occur in the aqueous phase, which involve both dissolution of solid phases and their reaction with dissolved CO_2. The kinetics of these carbonation reactions are therefore expressed using a first

order rate equation comprising dissolved CO_2 concentration and exposed surface area of reactive solid phases [8].

2.3 Transport of heat, moisture and CO_2

The formulation for coupled heat and moisture (liquid and vapour) transport is based on Thomas and Ye [9] and references therein, with the deviation that the moisture transport is recast in terms of relative humidity (RH) as the primary variable. Note that heat convection is ignored. As heat is generated because of hydration, the heat transfer equation additionally considers a heat source term [9]. The formulation for two-phase transport of CO_2 (gaseous and aqueous) is based on Phung et al. [5] and references therein. The water release due to carbonation and water consumption due to hydration (Table 1) is incorporated as a sink/source term in the moisture transport equation [9].

2.5 Evolution of porosity during hydration and carbonation

The change in porosity is obtained from the change in solid phases produced by the hydration of cement clinkers and carbonation of hydration products and unhydrated clinkers (C_2S, C_3S). The total porosity, ϕ, of a sample during carbonation is expressed as follows:

$$\phi = \phi_0 - \sum([i]_0 - [i])\,\Delta\bar{V}_{H,i} - \sum(CC_i)\,\Delta\bar{V}_{CC,i} \tag{12}$$

where ϕ_0 is the initial total porosity. i_0 and i are the concentration of cement species at initial and any time step during hydration. CC_i is the concentration of calcium carbonate attributable to reactant i during carbonation. $\Delta\bar{V}_{H,i}$ and $\Delta\bar{V}_{CC,i}$ are the change in volume per mole of reactant i during hydration and carbonation, respectively. The carbonation of hydration product might partially contribute to the capillary porosity change, especially under accelerated conditions. Following the previous study [5], the capillary porosity is calculated as follows:

$$\phi_c = \phi_h + 0.5\sum(CC_i)\,\Delta\bar{V}_{CC,i} \tag{13}$$

where ϕ_h is the capillary porosity due to hydration, which can be estimated based on hydration degree.

3. APPLICATION

3.1 Accelerated carbonation curing experiments

A dry mixture of fiber-cement composites consisted of 75% OPC type I cement, 20% limestone filler, 3% cellulose fiber, and 1% synthetic fiber PVA. The water to cement ratio was initially controlled at 0.62, which reduced to 0.45 and 0.45 after passing through the Hatschek rolling machine at rolling pressure of 2.5 bar and 9 bar, respectively. After 3 hours since casting, the fiber-cement composite samples (70 mm × 210 mm × 5 mm) were placed in a carbonation chamber under semi-adiabatic conditions for 3, 5, and 9 h at different CO_2 pressures (1 and 3 bar). After that, they were kept in air saturated curing condition (i.e., sealed in plastic bags) under 25 °C until 3, 7, 14, and 28 days of age. CO_2 of approximately 99.5% purity was injected to the carbonation chamber, which contained a stack of 15 samples. Temperature and relative humidity inside the chamber were measured during carbonation. Details of the experiments are available in [6].

After carbonation, a number of post-analysis methods were used to qualitatively and quantitatively analyse the carbonated samples including the physical properties (porosity, bulk density) and mechanical properties (not shown in this paper). Furthermore, the carbonated

sample was sawn and sprayed by phenolphthalein solution to determine the phenolphthalein carbonation depth [2]. For simulation purposes, the experiment with a rolling pressure of 9 bar and 9 h carbonation curing is considered.

Table 2: Salient material parameters

Parameter	**Value used and source**
Moisture retention	$S = [1 + (-\varepsilon \ln(RH))^{1/(1-\gamma)}]^{-\gamma}$ [5] ε = 5.72; γ = 0.444
Intrinsic permeability	$k_{int} = \zeta_p d_{cr}^2 \phi_c^{2.5}/(1-\phi_c)$ (m^2) [10] ζ_p = 0.0118; d_{cr} = 9×10^{-8} (m)
Hydraulic conductivity	$k_l = k_{int} k_{rl} (g\rho/\mu)$ (m/s) [5] $k_{rl} = S^p\left[1-\left(1-S^{1/q}\right)^q\right]^2$; p = 5.5; q = 0.56
Thermal conductivity	2.5 (W/m/K) [11]
Diffusivity of CO_2	For dissolved CO_2: $D_l = D_{l0} k_{Dl}^*(\phi,\tau) k_{Dl}(S)$ (m^2/s) [5] $k_{Dl}^*(\phi,\tau) = (1-0.7d_c) k_{Dl}(\phi,\tau)$ $k_{Dl}(\phi,\tau) = 0.001 + 0.07\phi_c^2 + 1.8H(\phi_c - 0.18)(\phi_c - 0.18)^2$ $k_{Dl}(S) = S^\alpha$; D_{l0} = 1.94×10^{-9} (m^2/s); α = 3.3 For CO_2 gas: $D_g = D_{g0} k_{Dg}^*(\phi,\tau) k_{Dg}(S) k_{Knu}$ (m^2/s) [5] $k_{Dg}^*(\phi,\tau) = (1-0.7d_c) k_{Dg}(\phi,\tau)$ $k_{Dg}(\phi,\tau) = \phi^\beta$ $k_{Dg}(S) = (1-S)^\alpha$ $k_{Knu} = 1/(1+\Re dc)$ $\Re = 5$; $\beta = 1.33$; d_c = 1 if portlandite = 0, otherwise d_c = 0
Carbonation rate constants	Phases — Rate constants C_3S — 10^{-8} (m/s) C_2S — 10^{-9} (m/s) CSH — 10^{-9} (m/s) CH — 3.58×10^{-2} (1/s) AFt — 10^{-9} (m/s)
Hydration rate constants	$Ae^{(-E_a/RT)}$ Phases — A (1/s); derived from [12] — E_a (kJ/mol) C_3S — 34.39 — 36.3 C_2S — 166.98 — 45 C_3A — 0.70 — 25 C_4AF — 17.24 — 35

3.2 Modelling methodology

Numerical analysis have been carried out in a step-wise manner to follow the experimental protocol. In particular, the analysis have been carried out in three steps: (i) first, the hydration reactions of a single sample are modelled assuming equilibrium with ambient conditions (fixed RH and temperature at the boundary of the sample), (ii) second, the combined hydration and carbonation reactions of a stack of 15 samples are modelled assuming a 2D geometry as shown in Figure 1, and (iii) third, only hydration is modelled post carbonation assuming thermal equilibrium with the surroundings and no moisture flux in/out of the sample. The initial conditions for each step is obtained from the preceding step. As for boundary conditions in step 2, zero flux is imposed at the chamber boundary for both CO_2 and moisture, and convective heat loss is allowed at the boundary.

Salient material parameters are principally extracted from literature as shown in Table 2. It is worthwhile to note that no parameters are calibrated in this study.

3.3 Results

This section mainly focusses on the discussion of results for the carbonation step. Figure 1 shows 2D contours of temperature and RH fields at around 6 hours, which corresponds to the simulated peak temperature as shown in Figure 2. The results are consistent with typical experimental observations with the maximum temperature predicted at the centre of the domain due to hydration heat of the samples, and minimum temperature at the walls of the curing chamber. The RH results are consistent with the temperature field. The initial RH in the chamber is initially roughly around 75%, which increases progressively because of water release from carbonation reactions and also from the hydrating samples (high initial moisture content) due to both RH and temperature gradient. The model shows condensation at the inner walls of the chamber, which was also visually observed during the dismantling of the chamber. Figure 2 shows a comparison of simulated and experimental results of the evolution of temperature and RH variables. Note that the simulated values are averaged over the void space in the modelled chamber. The results are qualitatively consistent with the experimental data. Quantitative discrepancy is attributed to the 2D simplification of the problem, averaging of the temperature and RH values in the void space although these fields are not uniform as seen from Figure 1, and any uncertainty in the material parameters.

Figure 3 shows simulated carbonation depth at the end of the curing period (12 hours). The carbonation depth is here assumed to be the region where CH is almost completely consumed. The experimental measurements showed an average carbonation depth of 0.5 mm. The simulated results corresponds well with this value (Figure 3, right).

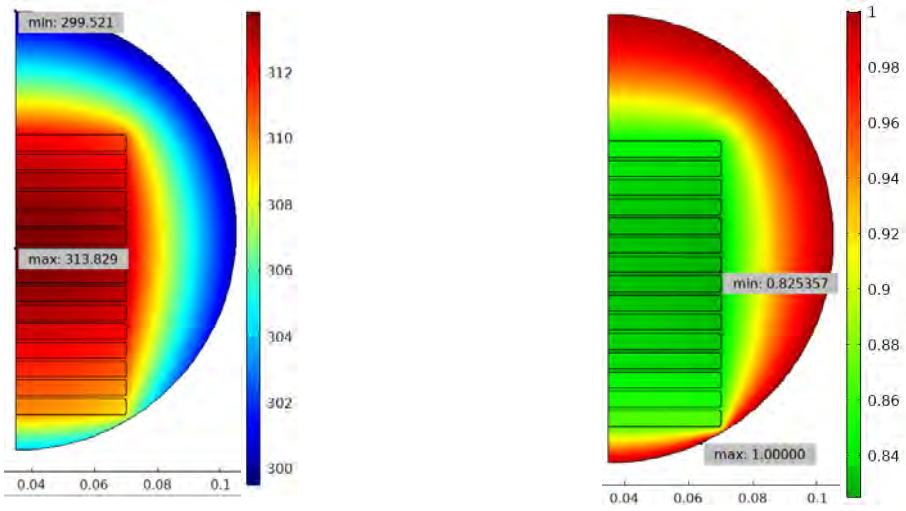

Figure 1: Predicted temperature (left) and RH (right) snapshots at ≈6 hours (simulated peak temperature, see Figure 2)

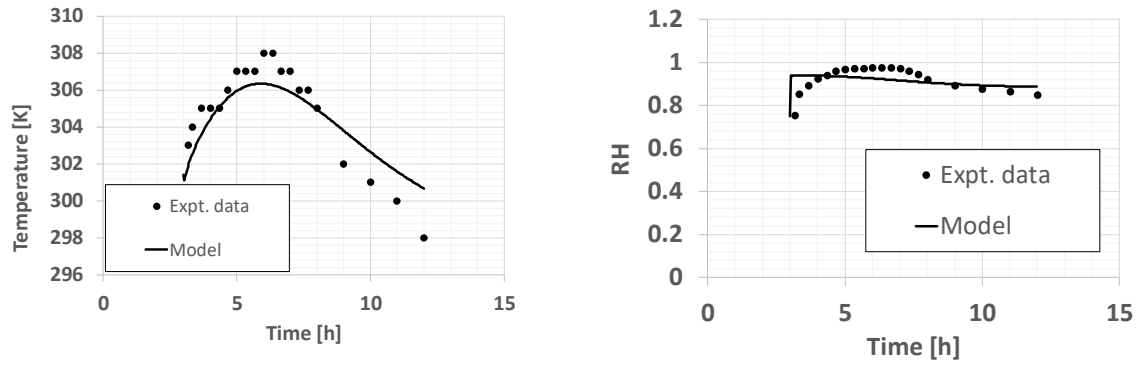

Figure 2: Comparison of experimental *vs.* predicted results of temperature (left) and RH (right)

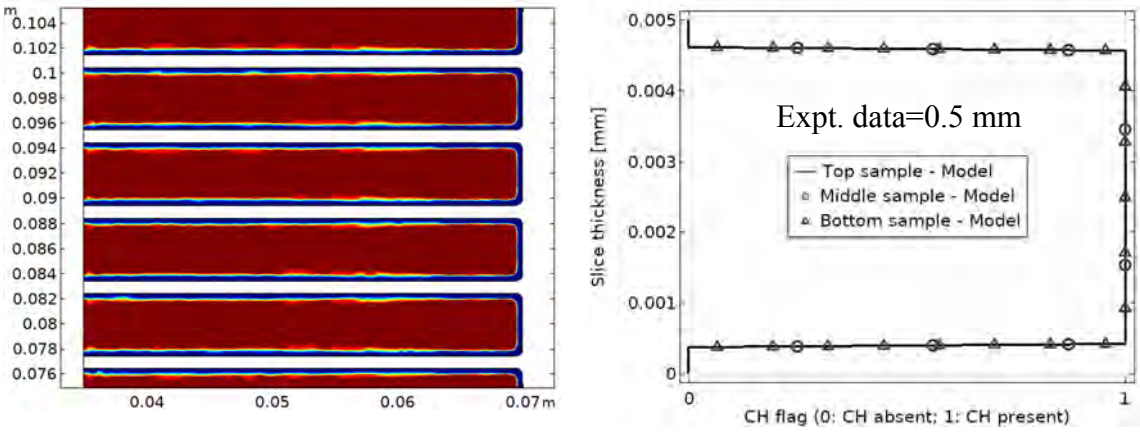

Figure 3: Carbonation penetration depth (equivalent to complete CH consumption)

4. CONCLUSIONS

An improved continuum model is proposed that couples the process of hydration of cement with heat, moisture and CO_2 transport, including precipitation of $CaCO_3$, change of porosity because of hydration as well as carbonation and water release and consumption. This serves as an invaluable tool to study the influence of key parameters such as curing time, curing pressure, rolling pressure and initial physical properties of fiber-cement composites on the carbonation efficiency. The performance of the model was tested by simulating an accelerated carbonation curing experiment. Qualitatively consistent results were obtained with respect to temperature and RH fields. The model was also able to predict within reasonable accuracy the depth of carbonation. At this point, the main challenge lies in dealing with the uncertainty in the significant number of material parameters in the continuum model.

ACKNOWLEDGEMENTS

This work is supported by SCK•CEN as part of their internal RD&D program on concrete durability.

REFERENCES

[1] Q.T. Phung, N. Maes, D. Jacques, G.d. Schutter, G. Ye, Effect of Limestone Fillers on Ca-Leaching and Carbonation of Cement Pastes, Key Engineering Materials, 711 (2016) 269-276.

[2] Q.T. Phung, N. Maes, D. Jacques, E. Bruneel, I. Van Driessche, G. Ye, G. De Schutter, Effect of limestone fillers on microstructure and permeability due to carbonation of cement pastes under controlled CO2 pressure conditions, Constr Build Mater, 82 (2015) 376-390.

[3] G. Tonoli, S. Santos, A. Joaquim, H. Savastano Jr, Effect of accelerated carbonation on cementitious roofing tiles reinforced with lignocellulosic fibre, Construction and Building Materials, 24 (2010) 193-201.

[4] Q.T. Phung, Effects of Carbonation and Calcium Leaching on Microstructure and Transport Properties of Cement Pastes, in: Department of Structural Engineering, Ghent University, Belgium, 2015, pp. 249.

[5] Q.T. Phung, N. Maes, D. Jacques, G. De Schutter, G. Ye, J. Perko, Modelling the carbonation of cement pastes under a CO2 pressure gradient considering both diffusive and convective transport, Constr Build Mater, 114 (2016) 333-351.

[6] B. Kottititum, Q.T. Phung, N. Maes, W. Prakaypan, T. Srinophakun, Early Age Carbonation of Fiber-Cement Composites under Real Processing Conditions: A Parametric Investigation, Applied Sciences, (2018) 21.

[7] V.G. Papadakis, C.G. Vayenas, M.N. Fardis, Fundamental Modeling and Experimental Investigation of Concrete Carbonation, Aci Mater J, 88 (1991) 363-373.

[8] M. Peter, A. Muntean, S. Meier, M. Böhm, Competition of several carbonation reactions in concrete: A parametric study, Cement and Concrete Research, 38 (2008) 1385-1393.

[9] H.R. Thomas, Y. He, Analysis of coupled heat, moisture and air transfer in a deformable unsaturated soil, 45 (1995) 677-689.

[10] Q.T. Phung, N. Maes, D. Jacques, G.D. Schutter, G. Ye, EFFECTS OF W/P RATIO AND LIMESTONE FILLER ON PERMEABILITY OF CEMENT PASTES, in: O.M. Jensen, K. Kovler, N.D. Belie (Eds.) International RILEM Conference Materials, Systems and

Structures in Civil Engineering 2016, RILEM Publications S.A.R.L., Lyngby, Denmark, 2016, pp. 141-151.
[11] P.K. Mehta, P.J.M. Monteiro, Concrete: microstructure, properties, and materials, McGraw-Hill, 2006.
[12] V.G. Papadakis, C.G. Vayenas, M.N. Fardis, A Reaction Problem of Engineering Approach to the Concrete Carbonation, Aiche J, 35 (1989) 1639-1650.

Special session 3: Alkali Silica Reactions

ANALYTICAL STUDY ABOUT THE EXPANSION PROGRESS OF CONCRETE EXPOSED TO COMBINED ALKALI SILICA REACTIONS AND FREEZING THAWING CYCLES

Yuya Takahashi (1), Fuyuan Gong (2) and Koichi Maekawa (3)

(1) Department of Civil Engineering, The University of Tokyo, Japan

(2) College of Civil Engineering and Architecture, Zhejiang University, China

(3) Department of Civil Engineering, Yokohama National University, Japan

Abstract

Using numerical simulations, this study investigated the concrete expansion damage caused by the coupled action of freeze-thaw cycles (FTC) and alkali silica reactions (ASR). In the authors' previous experiments, it was shown that a preceding ASR definitely accelerated the succeeding expansion by FTC. Further, even if the specimens have sufficient entrained air to prevent expansion by sole FTC action, they can expand under the combination of ASR and FTC. The presence of air voids in specimens has little effect on the single ASR expansion rates. These observed experimental trends were analyzed by numerical simulations. Authors have proposed the mixed pore pressure and concrete expansion models for coupled ASR and FTC, and a non-linear finite element system for concrete structures was used to analyze them. These models were used to work out the factors governing the experimental trends. By comparing the experiments and simulations, it appears the air voids contribution can be the key factor on the coupled ASR and FTC expansion process. With effective modeling of microscopic ASR-gel and ice formations inside air voids, the experimental trends can successfully be reproduced numerically.

Keywords: Combined deterioration, Alkali silica reaction, Freezing thawing cycles

1. INTRODUCTION

Concrete structures in service have to endure various environmental actions simultaneously and the deterioration process of concrete is highly complicated. For example, on road structures in colder regions, anti-freezing salt used to reduce freeze-thaw cycle (FTC) damage can accelerate expansion by alkali silica reaction (ASR) and additional damage. The deterioration process is not easily explained by a single deterioration mechanism, and is expressed more effectively as coupled action deterioration. Previous research [1,2] conducted combined FTC and ASR action experiments on concrete, and increased discussion of these detailed mechanisms is needed to predict future behavior of these complicated phenomena.

Authors [3] have been developing models that consider the combined FTC and ASR deterioration on concrete. This study focuses on the expansion progress of concrete under combined FTC and ASR and the characteristic behaviors observed in previous experiments [4] using the developed numerical models tried to be understood.

2. REFERENTIAL EXPERIMENT

In the authors' previous papers [4], a combined FTC and ASR experiment was conducted with different water-to-cement (W/C) ratios, air contents, and sequences of ASR/FTC actions. Table 1 presents the experimental series and mix proportions. Six concrete specimen series were prepared with two different target air contents (1% and 6%), and three different W/C ratios (35%, 50%, and 60%). Ordinary Portland cement was used. Fine aggregate is not reactive during ASR, while coarse aggregate acts as the reactive andesite. Sodium chloride was added to the specimens to accelerate ASR expansion and the total alkali content in terms of Na_2O_{eq} was 10.0 kg/m^3. Four series of deterioration processes (single FTC, single ASR, FTC after ASR, and ASR after FTC) were implemented and two 10×10×40 cm prism specimens were prepared for each case to measure expansion progress. After hardening the air contents and air bubble spacing coefficients were measured and those values are listed in Table 1. In the target 1% air content cases, the air content of fresh mortar was approximately 2% and subsequently became approximately 1% after hardening, leading to higher air bubble spacing coefficients. The target 6% air content cases have more than 6% air content in fresh mortar, but they decreased to less than 5% after hardening.

Figures 1 and 2 show the measured expansion progress of the specimens with the target 1% and 6% air contents, respectively [4]. The figure sequences, (i) – (iv) show the single FTC expansions, the ASR expansions after FTC, the single ASR expansions, and the FTC expansions after ASR, respectively. The length changes are plotted by considering a length of zero before each deterioration action, and the results of two specimens are expressed in the legend as xx-x-1 and xx-x-2.

Among the single FTC process cases (Figs. 1(i) and 2(i)), the expansion in the 35-6 case was minimal, which indicates high resistance against FTC action. The specimens with higher air contents and lower W/C were confirmed to have higher FTC resistance due to the entrained air resistance against FTC actions and ice pressures. For the single ASR acceleration process, the lower the W/C, the larger the expansion after 13 weeks of ASR

Table 1: Series of specimens and mix proportions [4]

	Air (%)	W/C (%)	W	C	S	G	NaCl	water-reducing agent	AE	Air of fresh mortar (%)	Slump (cm)	Air after curing (%)	bubble spacing coeff. (μm)
35-1	1	35	175	500	717	914	17.17	C×0.7%	20T	1.7	5.5	1.3	1156
50-1		50	175	350	836	999	18.87	C×1.0%	20T	2	6	0.9	1422
60-1		60	175	292	839	1044	19	C×1.0%	20T	1.9	4.1	0.8	1154
35-6	6	35	175	500	736	845	17.17	C×0.7%	4.0A	6.6	16.5	4.3	273
50-6		50	175	350	777	928	18.87	C×0.9%	6.0A	6.2	11.2	2.7	336
60-6		60	175	292	781	971	19	C×1.0%	8.5A	6.5	15.4	4.8	302

accelerations. Furthermore, no significant difference exists between the 1% and 6% air content cases. Entrained air is therefore considered as having little buffering contribution to expansion pressure caused by ASR.

Figures 1(iv) and 2(iv) show that all cases have rapid expansion. As mentioned earlier, minimal expansion occurred in the 35-6 case during the single FTC process; however, significant expansion occurred during the FTC after the ASR process. Even if the preceding ASR expansion is small, such as in the 60-6 case (Fig. 2(iii)), the subsequent FTC expansion after ASR (Fig. 2(iv)) occurs much faster than the single FTC (Fig. 2(i)). The preceding ASR did have an effect on the subsequent FTC progress. The effective ability of entrained air to resist FTC damage can be impaired by a preceding ASR. In the case of ASR after FTC, the expansion rates (Figs. 1(ii) and 2(ii)) showed no significant difference from that of a single ASR action case (Figs. 1(iii) and 2(iii)).

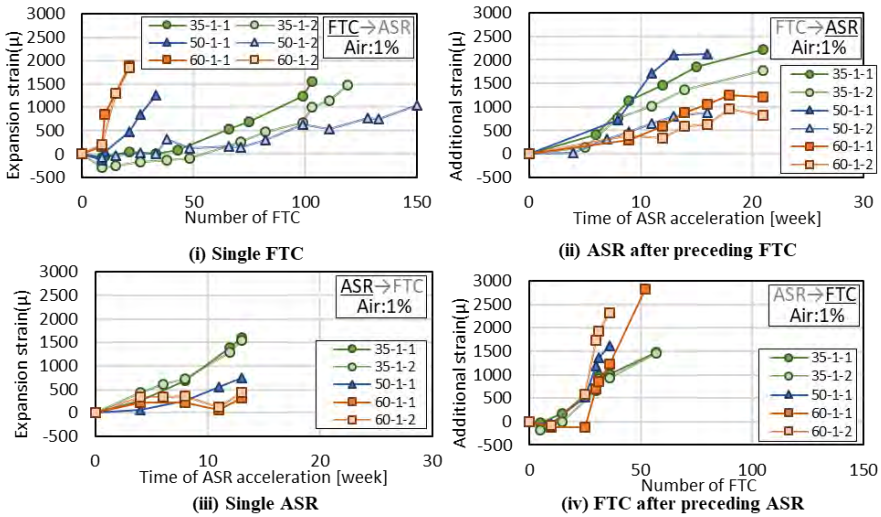

Figure 1: Sequential expansion of ASR and FTC for non-air entrained concrete [4]

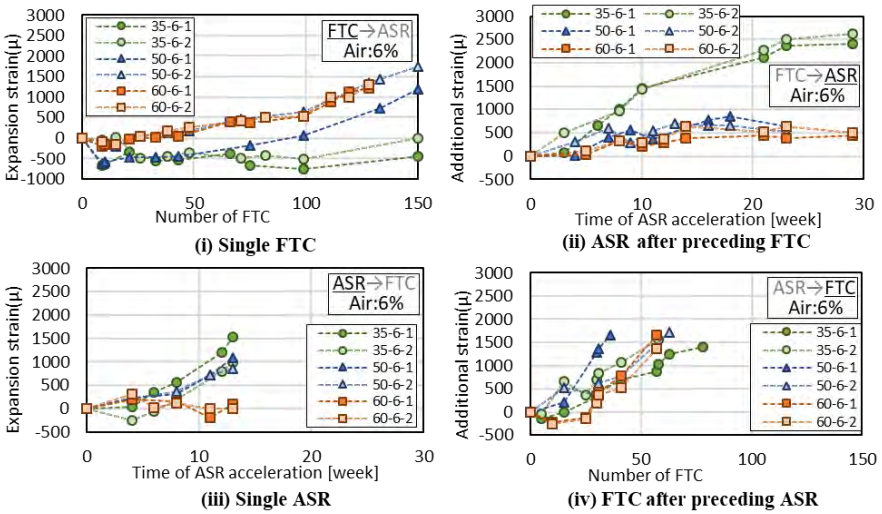

Figure 2: Sequential expansion of ASR and FTC for air entrained concrete [4]

3. PORO-MECHANICAL SIMULATION MODELS

The authors have been developing an analytical scheme to simulate concrete deterioration by combined FTC and ASR actions [3]. The models considering the internal pressures and deformations of ASR gel and ice inside cracks or voids are formulated based on the poro-mechanics, and they are implemented in the multi-scale chemo-hygral analytical scheme named DuCOM-COM3 [5]. The formulation details can be referenced in the previous paper [3]. The volume formulations of ASR gel and ice are summarized as follows:

The effective ASR gel volume (V_{ASR}) and ice expansion volume (V_{ICE}) that can contribute to the poro-mechanical expansion are expressed as Eqs. (1) and (2) [3].

$$V_{ASR} = V_{ASR\_TOTAL} - (S_{ASR} + V_{ASR \rightarrow AIR}) \quad (1)$$

$$V_{ICE} = 0.09 S_{ICE} - max\,(0.1 Air - V_{ASR \rightarrow AIR}, 0.0) \quad (2)$$

where V_{ASR_TOTAL} is the total created ASR gel volume formulated as a function of the alkali concentration, updated free water, and the reactive aggregate content [6], S_{ASR} and S_{ICE} are the volume of spaces occupied by ASR-gel and ice in the pore sized cement paste distribution, respectively, as shown in Fig. 3, and Air is concrete air content. $V_{ASR \rightarrow AIR}$ is the ASR gel volume absorbed to air bubbles and is formulated as follows:

$$\dot{V}_{ASR \rightarrow AIR} = k_{AIR} \cdot (1.0 - \beta_{ASR \rightarrow AIR}) \cdot p_{ASR} \cdot Air \quad (3)$$

where k_{AIR} is a constant determining the gel intrusion speed to air bubbles, $\beta_{ASR \rightarrow AIR} = (V_{ASR \rightarrow AIR}/Air)$ is the ASR gel occupying ratio in the air bubbles (0.0-1.0) and p_{ASR} is the ASR gel pressure. As formulated in Eq. (1), some created ASR gel potions can be absorbed in capillary pores (equivalent to S_{ASR}) and air bubbles (equivalent to $V_{ASR \rightarrow AIR}$) and they do not contribute to the ASR expansion. Ten percent of existing air bubbles and capillary pores larger than the minimum freezing radius (r_{ICE}) excluding inkbottle pores (S_{ink}) are available for ice formation, except the space pre-occupied by ASR-gel (S_{ASR} and $V_{ASR \rightarrow AIR}$). The k_{AIR} value is provisionally set as 2.0E-9 $Pa^{-1}s^{-1}$ in the previous study, but the proper value is discussed in the following chapter.

V_{ASR} and V_{ICE} are considered in the dynamic equilibrium equations of the concrete skeleton and each pore substance in cracks and the concrete expansion can be calculated.

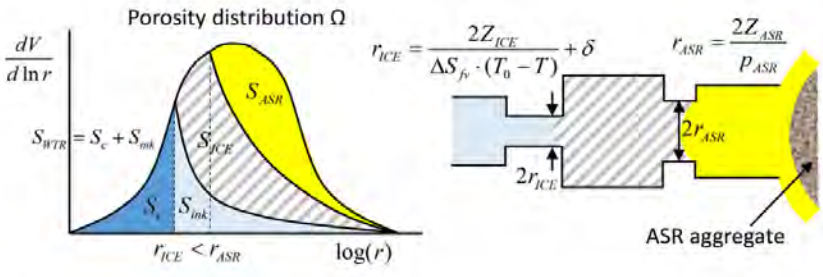

Figure 3: ASR gel intrusion and ice formation in pores [3]

4. ANALYTICAL STUDIES

4.1 Single ASR cases

Using the previous chapter's summarized analytical scheme, simulation of the reference experiments [3,4] was attempted. Prism-shaped meshes of 10-10-40 cm are prepared and the

same mix proportions, curing conditions, and environmental conditions are entered. The simulated single ASR case results are shown in Fig. 4.

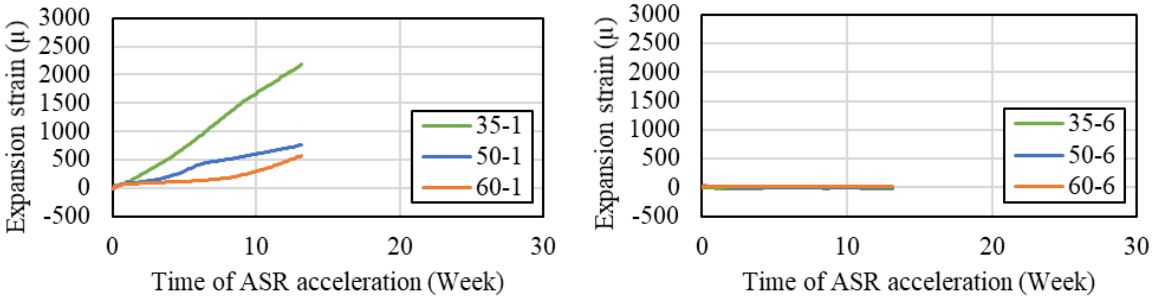

(i) Air 1% cases (ii) Air 6% cases

Figure 4: Simulated expansion progresses for single ASR cases (k_{air}=2.0E-9)

It can be observed in Fig. 4 that the 1% air cases agree well with the experiments (Fig. 1(iii)), while no expansion occurs in all 6% air cases. The calculated V_{ASR}, V_{ASR_TOTAL} and (S_{ASR}+$V_{ASR\rightarrow AIR}$) for the 50-6 case are plotted in Fig. 5. Here, not only in the k_{AIR} = 2.0E-9 case (Fig. 5(i)), but also for the k_{AIR} = 5.0E-9 and 1.0E-10 cases are simulated and plotted. All generated ASR gels are absorbed to air bubbles and capillary pores in the k_{AIR} = 2.0E-9 case, but lower k_{AIR} values reduces the gel absorption to voids and increases the effective ASR gel volumes. Figure 6 shows the expansion progress of the 50-6 case under various k_{AIR} values, and shows that the expansion progress corresponds to V_{ASR} increases. With a low enough value (k_{AIR} =1.0E-10), the calculations for 6% air cases were conducted again (Fig. 7) and the simulations properly reproduce the experimental trends (Fig. 2(iii)). The ASR gel intrusion behavior into voids is influential in the ASR expansion progress calculations.

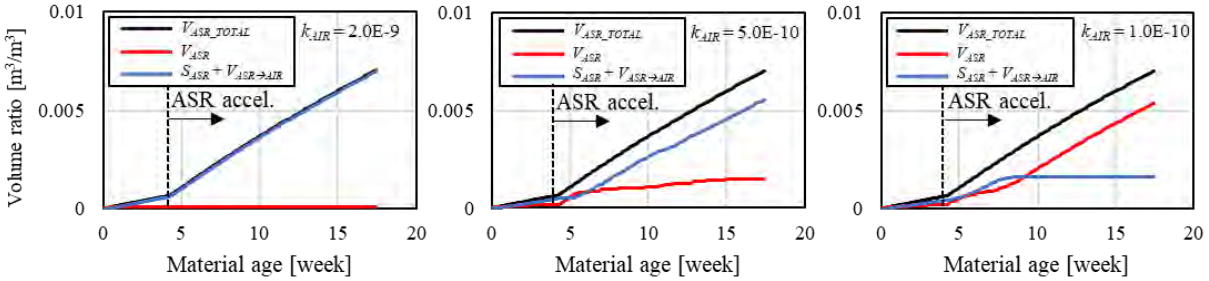

(i) k_{AIR} = 2.0E-9 (ii) k_{AIR} = 5.0E-10 (iii) k_{AIR} = 1.0E-10

Figure 5: ASR gel volumes simulated in 50-6 case with different k_{AIR} values

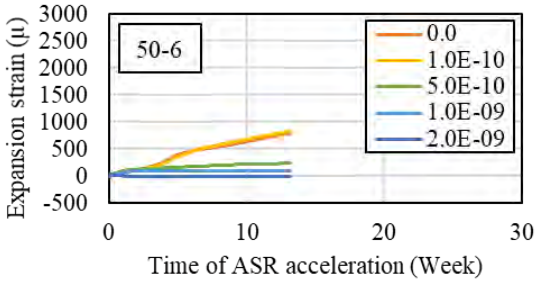

Figure 6 : Expansion progress of 50-6 case with various k_{AIR} values

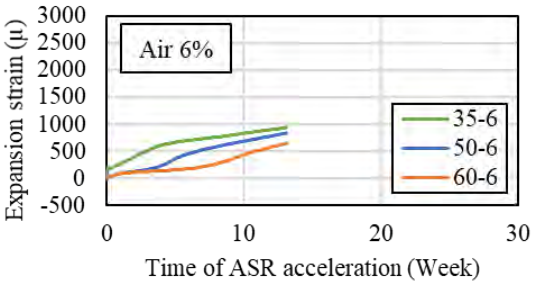

Figure 7 : Expansion progress for single ASR cases with k_{AIR} = 1.0E-10

4.2 Single FTC case

The air content and air bubble size distributions after hardening are quite influential parameters in the FTC deterioration processes, and it is difficult to control them precisely as designed (as shown in Table 1). This is one reason for the large data scattering in FTC deterioration experiments. In both the model and simulations, results can differ greatly due to entered air content, and proper air content values should be determined to reproduce each experimental result. For this study's reference experiments, the values are determined by sensitivity analyses of input air contents; 2.0%, 2.6%, 1.0%, 6.0%, 4.2% and 4.95% can be proper air content values for 35-1, 50-1, 60-1, 35-6, 50-6, 60-6 cases, respectively. The simulated single FTC action expansion progress with determined input air contents are shown in Fig. 8.

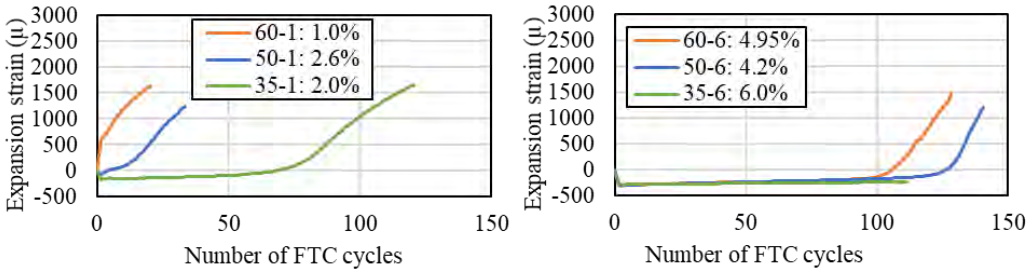

(i) Air 1% cases (ii) Air 6% cases

Figure 8: Expansion progress for single FTC actions

With appropriate input air content values, the resistivity differences between FTC actions can be reproduced. The frost damage resistivity should be determined not only by air content, but also by air bubble size distribution (or air bubble spacing factors). Future investigations should seek integrated ways to input resistivity against frost damage appropriately, considering bubble size distribution. The determined input air content values here are used in the following study simulations as the provisional values.

4.3 Combined FTC and ASR cases

In the reference experiment, the subsequent FTC expansions are accelerated even if the preceding ASR expansion is quite small, as seen in the 60-6 case (Fig. 2). This could mean that ASR gel can be intruded to entrained air even if there is little expansion, and impairs the effective ability of the entrained air to resist FTC damage. Here, $V_{ASR \rightarrow AIR}$ should be a critical factor governing the expansion progress and accordingly the effect of k_{AIR} is investigated for the ASR → FTC case.

The simulations of preceding ASR expansion and subsequent FTC expansion for the 50-6 case are conducted with different values of k_{AIR}, i.e., 1.0E-9, 5.0E-10 and 1.0E-10. Figure 9 shows the calculated volume graphs of ASR gels during ASR acceleration, and expansion progresses during preceding ASR and succeeding FTC actions. As mentioned in the previous section, inputted air content is 4.2%, expressing the proper frost damage resistance of the experiments.

With larger values of k_{AIR} such as 1.0E-9 (Fig. 9(i)), subsequent FTC expansion is accelerated compared to the single FTC case (Fig. 8). This is because the air bubbles are occupied by ASR gels, while there is little expansion during the preceding ASR period because most portions of generated ASR gels are absorbed to the air voids and capillary pores.

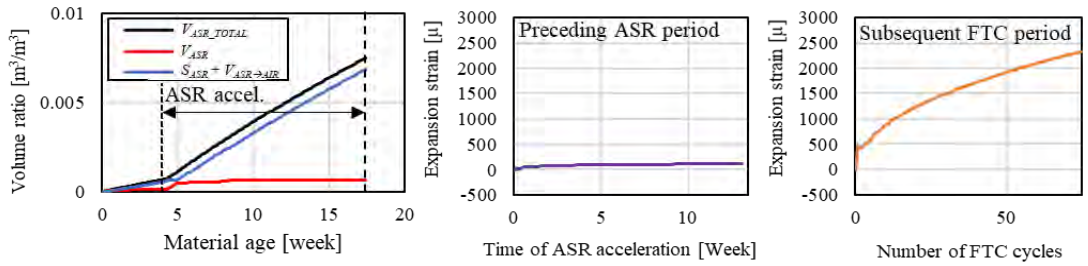

(i) ASR→FTC calculation with k_{AIR}=1.0E-9

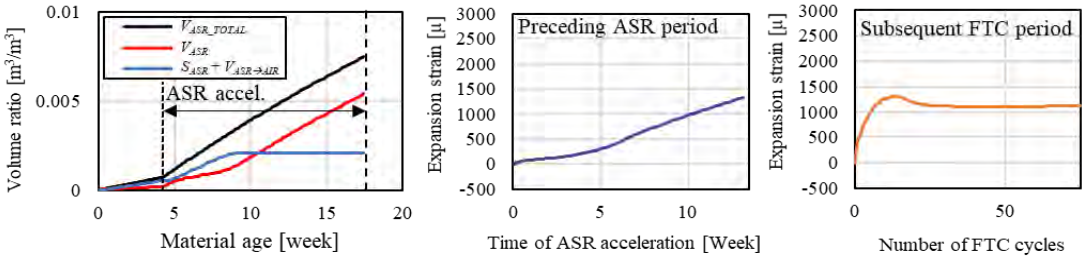

(ii) ASR→FTC calculation with k_{AIR}=5.0E-10

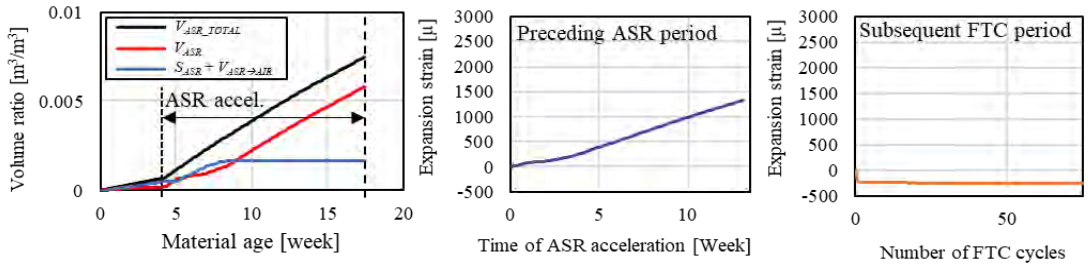

(iii) ASR→FTC calculation with k_{AIR}=1.0E-10

Figure 9 : Simulated results for ASR → FTC actions of 50-6 case

On the other hand, with smaller values of k_{AIR} such as 1.0E-10 (Fig. 9(iii)), expansion occurs during the ASR acceleration period due to less gel absorption to air and pores, but the smaller occupation of air voids by ASR-gel fails to accelerate the subsequent expansion by FTC actions. Only with the intermediate value such as k_{AIR} = 5.0E-10, expansion occurs during the ASR acceleration period and acceleration of subsequent FTC expansions can also be observed. It is understood that the time-dependent multiphase behavior inside air bubbles is important in realizing the expansion behavior during combined effects of FTC and ASR on concrete. With the determined value of k_{AIR} (5.0E-10), 6% air cases are simulated, and the results are shown in Fig. 10. With all air contents, the subsequent FTC expansions are accelerated compared to the single FTC case (Fig. 8(ii)), while the expansion rate of subsequent FTC differs from experimental results (Fig. 2(iv)). Also, k_{AIR} = 5.0E-10 still seems larger for the 35-6 case because there is no expansion in the preceding ASR acceleration period.

The role of air voids in concrete for the combined actions of FTC and ASR is realized in this study. However, it is still difficult to predict all experimental results with the limited factors appearing in this study. Further model investigations should be completed for combined ASR and FTC actions based on the microscopic multiphase phenomena inside air bubbles. The FTC → ASR case is even more difficult to predict. Figure 11 shows the succeeding ASR expansion of 6% air cases simulated after the FTC deteriorations shown in Fig. 8 (ii). The succeeding ASR is affected by preceding FTC in simulations, while little experimental influence is seen. The mechanisms responsible for the small effect of FTC on ASR progress should be studied.

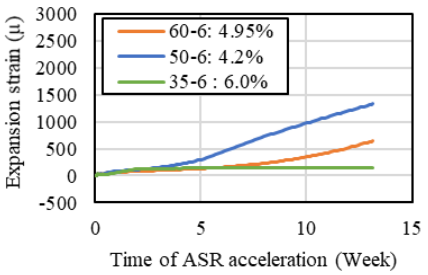

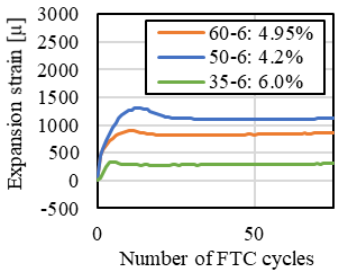

Figure 10: Simulation results for ASR → FTC actions for air 6% case (k_{AIR} =5.0E-10)

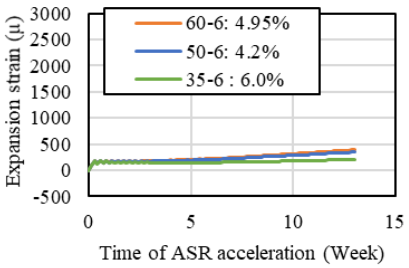

Figure 11: FTC → ASR simulations for air 6%

5. CONCLUSIONS

This study investigates the process of concrete expansion damage by the coupled actions of FTC and ASR focusing on the role of air bubbles in the concrete. Based on the poro-mechanical models, the referenced experiments of the combined FTC and ASR effects were attempted by simulation. In the single ASR action simulations, it is realized that enough low ASR-gel absorption rate to air bubbles should be considered to predict the expansion progress of high air entrained concrete accurately. In the coupled ASR and FTC simulations, the intermediate rate of gel absorption to air allows both the maintaining of preceding ASR expansions higher and the subsequent acceleration of FTC expansion. The detailed multiphase behavior inside air bubbles during coupled FTC and ASR actions is needed for quantitative prediction of deterioration behavior caused by these coupled actions.

ACKNOWLEDGEMENTS

This study was financially supported by the National Key R&D Program of China (2017YFC0806100), the Fundamental Research Funds for the Central Universities (2019QNA4032) and JSPS KAKENHI grant number 18H01507.

REFERENCES

[1] Bérubé, M., Chouinard, D., Pigeon, M., Frenette, J., Boivert, L. and Rivest, M. 'Effectiveness of Sealers in Counteracting Alkali-silica Reaction in Plain and Air-Entrained Laboratory Concretes Exposed to Wetting and Drying, Freezing and Thawing, and Salt Water', *Canadian Journal of Civil Engineering*, **29** (2002) 289-300.

[2] Deshenes, R.A., Giannini, E.R., Drimalas, T., Fournier, B. and Micah Hale, W. 'Effects of Moisture, Temperature, and Freezing and Thawing on Alkali-Silica Reaction', *ACI Materials Journal*, **115**(4) (2018) 575-584.

[3] Gong, F., Takahashi, Y. and Maekawa, K. 'Multi-scale computational modeling for concrete damage by mixed pore pressures -case of coupled alkali-silica reaction and cyclic freeze/thaw', *Engineering Computations*, **35**(6) (2018) 2367-2385.

[4] Segawa, I., Takahashi, Y., Gong, F. and Maekawa, K. 'Expansions and damage processes of concrete due to coupled alkali silica reactions and freeze-thaw cycles', In: Proceedings of the 8th International Conference of Asian Concrete Federation, 2018, 649-658.

[5] Maekawa, K., Ishida, T. and Kishi, T. 'Multi-Scale Modeling of Structural Concrete', Taylor and Francis, 2008.

[6] Takahashi, Y., Ogawa, S., Tanaka, Y. and Maekawa, K. 'Scale-Dependent ASR expansion of concrete and its prediction coupled with silica gel generation and migration, *Journal of Advanced Concrete Technology*, **14**(8) (2016) 444-463.

CHARACTERIZATION OF ASR PRODUCTS FORMED IN CONCRETE AGGREGATES

Andreas Leemann (1), Jan Lindgård (2)

(1) Empa, Swiss Federal Laboratories for Materials Science and Technology, Dübendorf, Switzerland

(2) SINTEF, Building and Infrastructure, Trondheim, Norway

Abstract

ASR products formed in various aggregates of two different concrete mixtures tested both at 38 °C and 60 °C with the concrete prism test have been analysed by scanning electron microscope with energy dispersive X-ray spectroscopy. Additionally, Raman spectra of ASR products have been acquired.

The variations in the chemical composition of ASR products formed in individual aggregates is relatively small. This applies as well to the average composition of ASR products formed in the concrete tested at 38 and 60 °C. However, the Raman spectra of crystalline ASR products formed at 38 °C differ from the ones formed at 60 °C. The first correspond to ones obtained in aggregates of concrete structures, while the later is identical to synthesized shlykovite.

Keywords: concrete, microstructure, ASR, composition

1. INTRODUCTION

Concrete damages due to alkali silica reaction (ASR) occur world wide [1]. The expansion causing the damage is the result of the reaction between the alkaline concrete pore solution and SiO_2 in aggregates causing the subsequent formation of ASR products. The first ASR products are formed in existing porosity of the aggregate close to the cement paste. With ongoing reaction ASR products ingress into the aggregates as a front. This ingress goes together with a simultaneous stress generation eventually leading to aggregate cracking. Many of these newly formed cracks are not restricted to the aggregates and continue into the cement paste with a concurrent extrusion of ASR product. In a recent study, the use of caesium as a tracer incorporated in ASR products has made it possible to follow this sequence of reaction down to a nanometre scale [2]. After the initial crack formation, the mostly empty cracks in the aggregates start to fill with ASR products again forming a front from the periphery of the aggregate moving inwards. In contrast to the initial phase of reaction, where the ASR products seem to be amorphous, the second stage is characterized by the formation of primarily crystalline ASR products. In the concrete prism test (CPT) a temperature of either 38 or 60 °C is used to accelerate ASR. It is not clear if these temperature conditions influence the

composition, mineralogy and morphology of the ASR products formed. For both exposure temperatures the prisms are stored in sealed containers over water securing a relative humidity (RH) close to 100 %.

In this study, ASR products formed in two different concrete mixtures both tested with the concrete prism test at 38 °C and 60 °C are investigated. The chemical composition of amorphous and crystalline ASR products formed in the aggregates is investigated by scanning electron microscopy (SEM) with energy-dispersive X-ray spectroscopy (EDS) on impregnated and polished samples. Raman microscopy and SEM are used to characterize the structure of the crystalline ASR products and their morphology, respectively, on broken samples.

2. MATERIALS AND METHODS

2.1 Materials

Concrete C1 and C2 were produced with a cement content of 440 kg/m^3 and a w/c of 0.45. The Na_2O-equivalent of the cement was 1.26 mass-%. For concrete C1 the aggregate used was a natural gravel with low reactivity, mainly consisting of granite and feldspatic rocks. The aggregate employed to produce concrete C2 was a medium reactive natural gravel, consisting of various rock types. Of the about 25 % potential reactive rock types present in the gravel, sandstone, mylonite/cataclasite and siltstone/silt-claystone/meta-marl constituted about 20 %. Three prisms (100 x 100 x 450 mm^3) of both concrete mixtures were produced for the Norwegian concrete prism test at 38 °C [3] and three prisms (70 x 70 x 280 mm^3) for the concrete prism test at 60 °C [4]. The expansion determined in the tests and on field exposed cubes (300 x 300 x 300 mm^3) are shown in Table 1.

Table 1: Expansion of the different concrete mixtures.

	CPT 38 °C	CPT 60 °C	Natural exposure
concrete C1	*C1-38:* 0.12 % /110 weeks	*C1-60:* 0.40 % / 155 weeks	0.01 % / 9 years[1] -0.01 % / 8 years[2]
concrete C2	*C2-38:* 0.23 % / 110 weeks	*C2-60:* 0.29 % / 150 weeks	0.04 % / 9 years[1] 0.16 % / 8 years[2]

[1] *Exposed at SINTEF's field exposure site in Trondheim, Norway*

[2] *Exposed at LNEC's field exposure site in Lisbon, Portugal*

Samples of all concrete mixtures were cut after the tests and locations of interest were identified. Areas close to the surface of the samples were discarded, as they may have been affected by alkali leaching [5] or carbonation. The samples for SEM were dried for three days at 50 °C, impregnated with epoxy resin, polished and carbon coated.

Samples for Raman microscopy and SE-imaging in the SEM were separated from cut concrete sections using chisel and hammer. After isolating aggregates containing cracks with ASR products, they were split along these cracks. Samples for Raman were stored in a dry cabinet and samples for SEM were dried at 50 °C for a day and then carbon coated. Due to the little amount of ASR products present in concrete C1-38 it was not possible to prepare samples.

2.2 Methods

Two different SEM were used. The Nova NanoSEM 230 FEI was used in the high vacuum mode (3.0-5.0 × 10^{-6} Torr) with an acceleration voltage of 12 kV, a spot size of 4.5 and a beam

current of 90–100 μA. An Qxford SSD detector (80 mm^2) and INCA Energy software with ZAF correction were used for the EDS analysis. With the FEI Quanta 650 an acceleration voltage of 8-12 kV, a spot size from 3.0-4.5 and a pressure of 3.0-5.0 × 10^{-6} Torr were applied depending on the detector used (back-scattering electron (BSE) or secondary electron (SE) detector). Chemical analysis was performed by energy-dispersive X-ray spectroscopy (EDS) with a Thermo Noran Ultra Dry 60 mm^2 detector and Pathfinder X-Ray Microanalysis Software. For the polished samples a back-scattering electron detector (BSE) detector was used in combination with EDS and for the broken samples the secondary electron (SE) detector was deployed to acquire images. Composition of ASR products formed in aggregates were performed on 6-9 aggregates per concrete and testing condition resulting in a total of about 2400 points analysed with EDS.

A Raman Bruker Senterra microscope was used for spectra acquisition. The laser wavelength was 532 nm, operating power 20 mW and lens magnification 50x. The instrument was equipped with a Peltier-cooled CCD detector and operated with Opus 6.5. 20-40 spectra with a resolution of 3-5 cm^{-1} were collected for each sample. The spectra were baseline corrected, averaged and smoothed by a running mean of 11. The designation of the specific Raman bands are based on Balachandran et al. [6] and Leemann [7].

3. RESULTS

3.1 Scanning electron microscopy

3.1.1 Chemical composition of the ASR products

Not taking into account O the ASR products formed in aggregates of the two concrete mixtures mainly consist of Si with an about equal amount of alkalis and calcium lower by a factor of 4 compared to Si (Table 2). Other elements like Mg, Al and Fe are only present as traces.

There is some variation in composition of the ASR products formed in the different aggregate particles. These differences are easiest visible in ratio-plots (Figs 1 and 2). In concrete C1-38 atomic Ca/Si-ratio and (Na+K)/Si of different aggregates vary between 0.19-0.25 and 0.18-0.27, respectively. While the variations are in an identical range for the atomic (Na+K)/Si-ratio in concrete C1-60, the variation of the atomic Ca/Si-ratio is smaller with 0.20-0.22. The same applies to the ASR products formed in the aggregate particles of concrete C2: identical variation in the (Na+K)-ratio and smaller variation of the Ca/Si-ratio in concrete C2-60. In both concrete mixtures the average values for the Ca/Si-ratio are slightly lower and the average (Na+K)/Si-ratio slightly higher at a testing temperature of 60°compared to 38 °C.

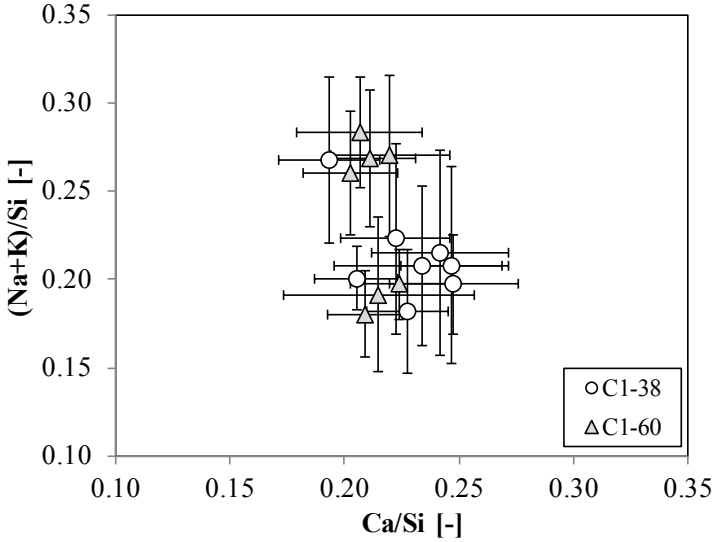

Figure 1: Atomic (Na+K)/Si-ratio as a function of atomic Ca/Si-ratio of the ASR products formed in aggregate particles of concrete C1 tested at 38 and 60 °C.

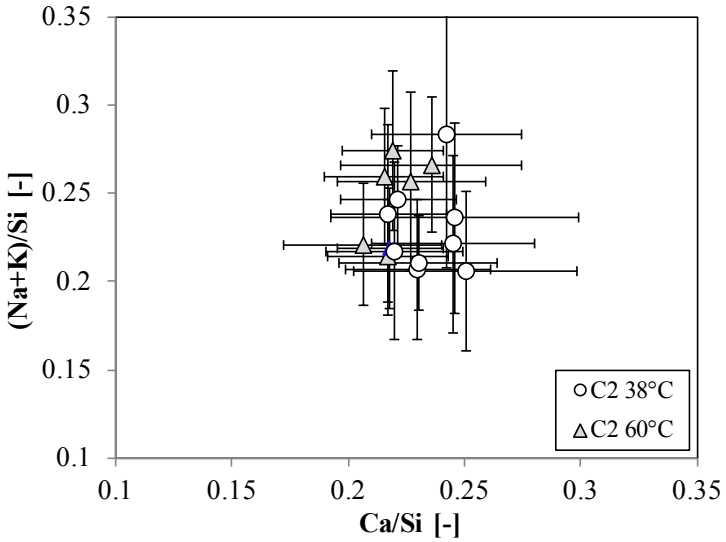

Figure 2: Atomic (Na+K)/Si-ratio as a function of atomic Ca/Si-ratio of the ASR products formed in aggregate particles of concrete C2 tested at 38 and 60° C.

Table 2: Average composition of ASR products formed in the aggregates of concrete C1 and C2.

Sample	Elements								
	O	Na	Mg	Al	Si	S	K	Ca	Fe
	[atom-%]								
C1-38	69.4 ±2.5	0.9 ±1.4	0.0 ±0.1	0.5 ±1.8	20.7 ±2.3	0.0 ±0.1	3.9 ±1.5	4.3 ±1.8	0.1 ±0.3
C1-60	69.3 ±2.3	1.1 ±0.9	0.0 ±0.1	0.4 ±1.0	21.1 ±1.7	0.0 ±0.1	3.4 ±1.0	4.6 ±0.9	0.1 ±0.3
C2-38	70.9 ±1.9	1.1 ±0.8	0.0 ±0.1	0.1 ±0.5	19.8 ±2.0	0.0 ±0.1	3.4 ±0.6	4.6 ±1.0	0.1 ±0.4
C2-60	69.0 ±2.4	0.8 ±0.8	0.0 ±0.2	0.0 ±0.2	20.8 ±2.1	0.0 ±0.1	4.3 ±1.1	4.8 ±1.3	0.2 ±0.3

3.1.2 Morphology of the crystalline ASR products

Crystalline ASR products formed in aggregates are mostly packed tightly (Fig. 3). The small gaps between the platy mineral bundles are the result of drying before epoxy impregnation. In some locations along the split aggregate particles crystals were able to grow without restraint in space showing their idiomorph form (Fig. 4). All the studied samples including the one of a bridge used as reference show thin platelets. The ones formed in the reference and the crystals formed in concrete C2-38 are wider than the ones formed in concrete C1-60 and C2-60.

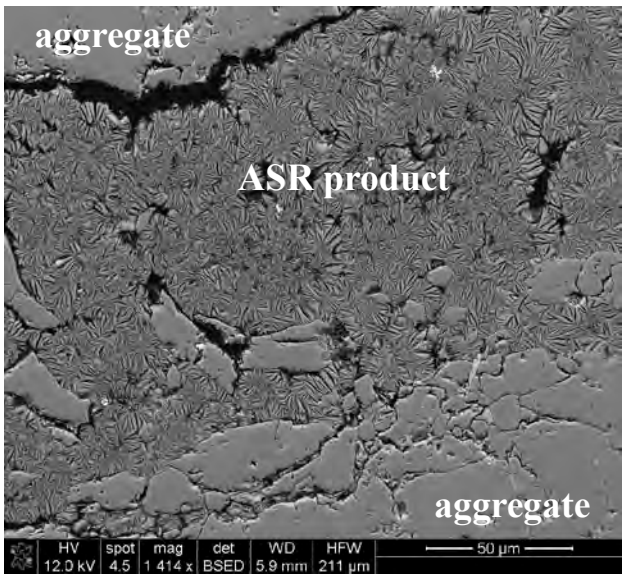

Figure 3: Tightly packed crystalline ASR product formed in an aggregate particle of concrete C2-38. HWF is 211 µm.

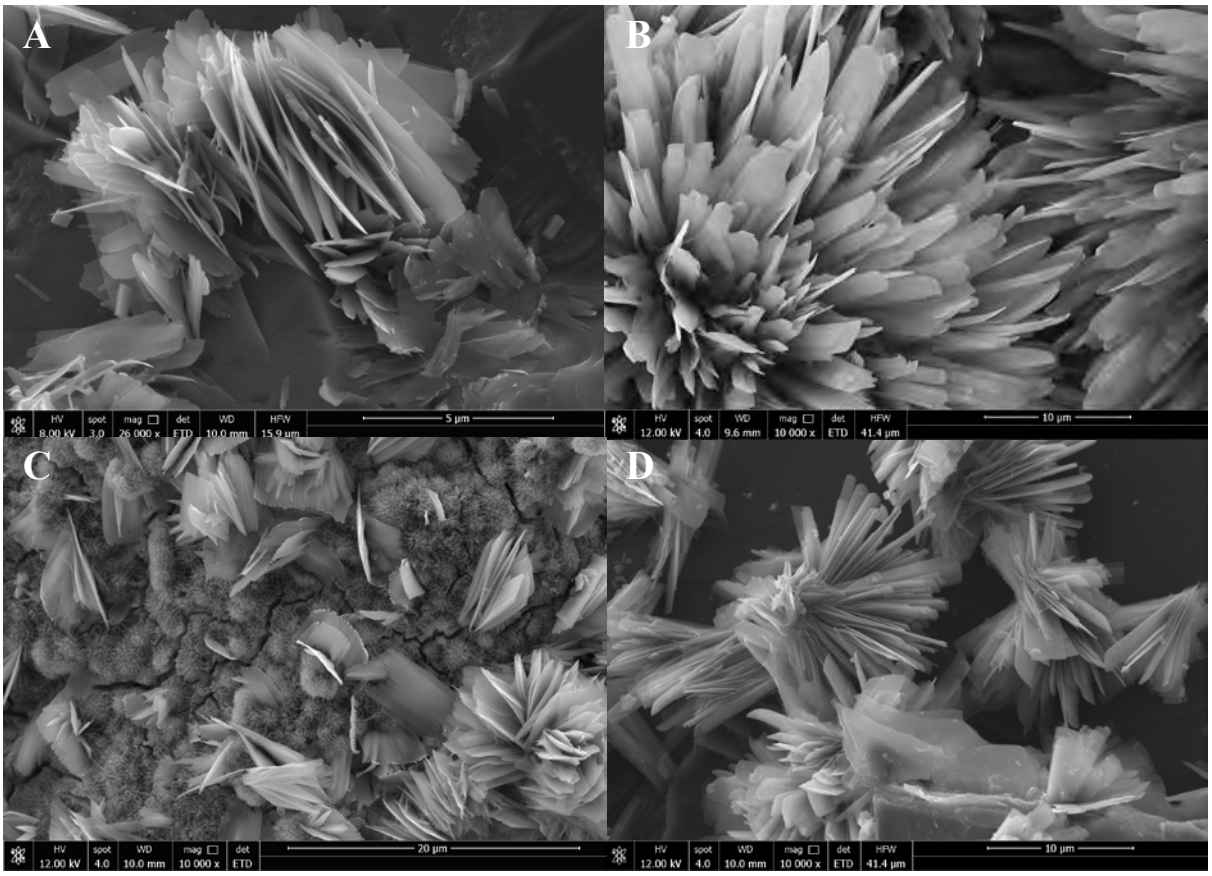

Figure 4: Crystalline ASR product formed in aggregate particles: concrete of a bridge (A), concrete C1-60 (B), C2-38 (C) and C2-60 (D). Horizontal width of field (HWF) is 15.9 µm (A) and 41.4 µm (B, C, D).

3.2 Raman microscopy

Raman spectra in concrete C1-60 match the ones in concrete C2-60 (not shown). Both differ from the spectrum obtained in concrete C2-38 (Fig. 5). While the intense band of Si-O-Si bending vibrations attributable to Q_3-sites at about 600 cm^{-1} is nearly at the same position in the studied concrete mixtures tested at 38 and 60 °C, the Q_3 band in the Si-O-Si stretching vibration range differs clearly. In concrete C2-60 it is located at 1087 cm^{-1} with a relative intensity of 32%, while it is located at 1110 cm^{-1} with a relative intensity of 100 % in concrete C2-38 and the reference. The band located between 1021-1026 cm^{-1} attributable to Si-O-Si stretching vibration of Q_2–sites is very similar in all concrete mixtures.

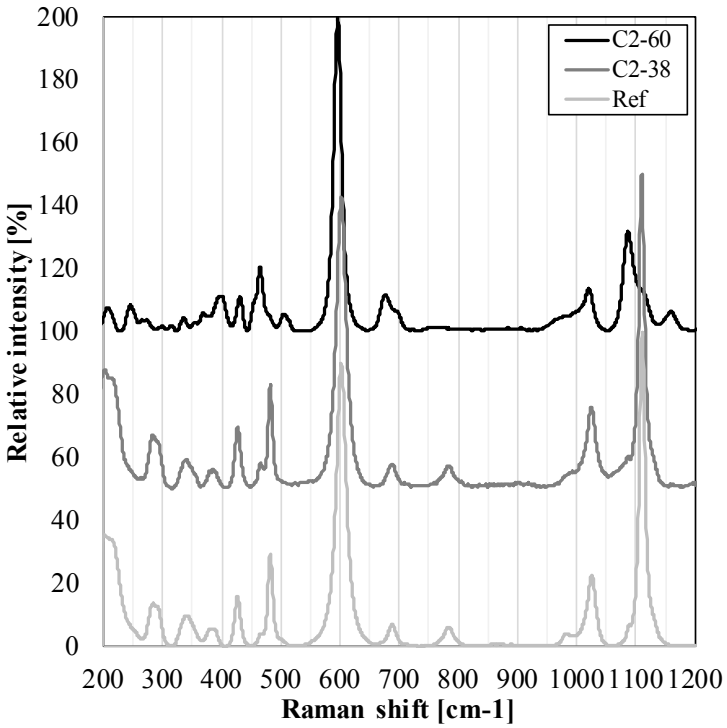

Figure 5: Raman spectra of the crystalline ASR product formed in aggregate particles from a concrete structure [7] and from concrete C2 tested at 38 and 60°C.

4. DISCUSSION

There is a certain variation in the ASR products formed in different aggregate particles of the same concrete, but the compositions are very close. Possible causes of the observed differences may be attributable to alkali leaching from feldspars present in the aggregate particles. ASR products formed in concrete C1-60 and C2-60 display a slightly higher average alkali content than their counterparts tested at 38 °C ((Na+K)/Si-ratio of 0.24 to 0.21 in both concrete mixtures). As K and Na concentration in the pore solution increase with increasing temperature, both in pure PC systems and systems blended with fly ash [8,9] and the composition of the pore solution affects the composition of ASR products [10], this is reasonable. As Ca concentration in the pore solution decreases with increasing alkali concentration, the lower Ca/Si-ratio of the ASR products formed at the 60 °C makes sense. In general, the composition of the ASR products as determined is in line with other studies [11,12].

Although the composition of ASR products formed at 38 and 60 °C are very similar, Raman microscopy proves that the crystalline ASR product formed at 60°C has a different crystal structure than the one formed at 38 °C. The spectra are similar but not identical. Synthesis of ASR products at 80 °C can result in a phase that matches XRD patterns of natural shlykovite as shown in a recent study [13]. The Raman spectra of the synthesized shlykovite matches the crystalline ASR product formed in concrete C1-60 and C2-60. The Raman spectrum of the crystalline ASR product formed in concrete C2-38 and the reference does not agree with any known mineral.

5. CONCLUSIONS

- The composition of ASR products formed in different aggregates of the same concrete vary in a relatively small range with an atomic Ca/Si-ratio in the range of 0.19-0.25 and an atomic (K+Na)/Si-ratio of 0.18-0.27.
- ASR products formed in aggregates of concrete tested at 60 °C display a slightly higher K and Na content and a lower Ca content than concrete tested at 38 °C agreeing with the increasing alkali and decreasing Ca content of the pore solution at increasing temperature.
- The Raman spectrum of crystalline ASR product formed in the concrete tested at 38 °C agrees with the of crystalline ASR product formed in concrete of structures.
- The crystalline ASR product formed at 60 °C is different to the one formed at 38 °C. It matches the Raman spectrum of synthesized shlykovite.

REFERENCES

[1] De Mayo Bernardes, H. and Hasparyk, N.P. (Eds.). Proceeding of the 15th International Conference on Alkali-Aggregate Reaction, Sao Paolo/Brasil, 2016.

[2] Leemann, A. and Münch, B. 'The addition of caesium to concrete with alkali-silica reaction: Implications on product identification and recognition of the reaction sequence'. *Cem. Concr. Res.* **120**(2019)27-35.

[3] Norwegian Concrete Association, NB, Alkali–aggregate reactions in concrete, Test methods and Requirements to Test Laboratories, NB Publication No. 32, 2005, 39 pages.

[4] Nixon, P. J. and Sims, I. (Eds.). 'RILEM Recommended Test Method: AAR-4.1 - Detection of Potential Alkali-Reactivity - 60° C Test Method for Aggregate Combinations Using Concrete Prisms'. In: RILEM Recommendations for the Prevention of Damage by Alkali-Aggregate Reactions in New Concrete Structures. Springer, Dordrecht, 2016, pp. 99-116.

[5] Lindgård, J., Thomas, M. D., Sellevold, E. J., Pedersen, B., Andiç-Çakır, Ö., Justnes, H. and Rønning, T. F. 'Alkali–silica reaction (ASR)—performance testing: influence of specimen pre-treatment, exposure conditions and prism size on alkali leaching and prism expansion'. *Cem. Concr. Res* **53**(2013)68-90.

[6] Balachandran, C., Muñoz, J.F. and Arnold, T. 'Characterization of alkali silica reaction gels using Raman spectroscopy'. *Cem. Concr. Res.* **92**(2017)66-74.

[7] Leemann, A. 'Raman microscopy of alkali-silica reaction (ASR) products formed in concrete'. *Cem. Concr. Res.* **102**(2017)41-47.

[8] Lothenbach, B., Winnefeld, F., Alder, C., Wieland, E. and Lunk, P. 'Effect of temperature on the pore solution, microstructure and hydration products of Portland cement pastes'. *Cem. Concr. Res* **37**(2007)483-491.

[9] Deschner, F., Lothenbach, B., Winnefeld, F. and Neubauer, J. 'Effect of temperature on the hydration of Portland cement blended with siliceous fly ash'. *Cem. Concr. Res.* **52**(2013)169-181.

[10] Leemann, A. and Lothenbach, B. 'The influence of potassium–sodium ratio in cement on concrete expansion due to alkali-aggregate reaction'. *Cem. Concr. Res **38***(2008)1162-1168.

[11] Thaulow, N., Hjorth Jakobsen, U. and Clark, B. 'Composition of alkali–silica gel and ettringite in concrete railroad ties: SEM-EDX and X-ray diffraction analyses'. *Cem. Concr. Res.* **26**(1996) 309–318.

[12] Leemann, A. and Merz, C. 'An attempt to validate the ultra-accelerated microbar and the concrete performance test with the degree of AAR-induced damage observed in concrete structures'. *Cem. Concr. Res.* **49**(2013)29-37.

[13] Shi, Z., Geng, G., Leemann, A. and Lothenbach, B. 'Synthesis, characterization, and water uptake property of alkali-silica reaction products'. *Cem. Concr. Res* **121**(2019)58-71.

EFFECT OF REACTIVE AGGREGATE ON THE EARLY AGE REACTION OF WATER-GLASS ACTIVATED SLAG/FLY ASH MORTARS

Wei Wang* (1) , Shizhe Zhang (2), Ye Guang (2), Takafumi Noguchi (1)

(1). Department of Architecture, Graduate School of Engineering, The University of Tokyo, Tokyo, 113-8654, Japan.

(2). Microlab, Section Materials and Environment, Faculty of Civil Engineering and Geosciences, Delft University of Technology, Stevinweg 1, 2628 CN Delft, the Netherlands.

* Corresponding author: wangwei@bme.arch.t.u-tokyo.ac.jp

Abstract

Alkali activated materials (AAMs) have received worldwide attention due to its lower embodied energy and environmental impact than that of traditional cementitious materials. However, the activators with high alkalinity may raise the risk of alkali silica reaction (ASR) induced deterioration when reactive aggregates are used, which thereby limits the commercial use of AAMs. Not speaking the ASR induced long-term expansion, the early-age reaction of AAMs prepared with reactive aggregates is largely unknown. In this paper, isothermal calorimetry, thermogravimetry (TG) and mercury intrusion porosimetry (MIP) were adopted to study the heat evolution, mineralogical changes and pore structures of early-age ordinary Portland cement (OPC) mortar and water-glass activated slag/fly ash mortars. In each system, emphasis were made to understand the differences between mixtures prepared with standard inert quartz sands and reactive fine aggregates. The results show that the mortars prepared with reactive aggregates generated more heat in the wetting and dissolution stage. Particularly, the water-glass activated slag mortar presented the highest heat flow peak. Meanwhile, the results of TG illustrate that higher amount of reaction products were formed in water-glass activated mortars prepared with reactive aggregates than that with inert quartz sands. These findings suggest that the reactive aggregates are evidently involved in the early-age alkaline reaction of AAMs system.

Keywords: Alkaline activation; Alkali-silica reaction; Early-age; Heat evolution; Pore structure.

1. INTRODUCTION

Alkali-silica reaction (ASR), known as “concrete cancer”, is one of the main durability problems of reinforced Ordinary Portland concrete structures. ASR is a chemical reaction between alkalis in pore solution and reactive silica in aggregates [1–3]. The reaction product from ASR is a gel which will expand when it comes in contact with water. This expansion can

cause cracks in the aggregate and surrounding cement matrix [4], thereby decreasing the durability and service life of structures. Thus, it is essential to pay attention to this issue and make some precautions when reactive aggregates are used to prepare AAMs.

Up till now, a few studies have been carried out to address this potential risk of ASR in AAMs [5–13]. Although the research related to ASR in AAMs is relatively less than that of OPC system, the findings about the ASR in AAMs are always contradictory due to the different mix designs [14]. In some cases [12,14,15], the ASR-induced expansion of AAMs was very low during the standard test duration of accelerated method which was developed for traditional cementitious materials, but continued to increase if the test time was extended. This may lead to underestimating the ASR expansion of AAMs. Mahanama et al. [14] investigated the ASR-induced expansion of water-glass activated fly ash/slag blends (50 wt.% fly ash + 50 wt.% slag) by monitoring the expansion up to 150 days under accelerated condition and observed a small shrinkage in initial 21 days, followed by an exponential growth of expansion. Therefore, some researchers recommended to extend the test duration to 180 days [8].

Most of the existing researches mainly focused on the long-term ASR behaviour in AAMs, however, the role of reactive aggregates in the early-age reaction of AAMs is somehow neglected. The reactive aggregate may participate in the alkaline activation in the early-age due to the initial high alkalinity activators [8,16], and could consequently lead to differences between the long-term ASR behaviour of AAM and OPC system. The aforementioned delayed ASR expansion in AAMs may attributed to this early-age consumption of reactive aggregates. Moreover, compared to the discrepancies in the results of long-term ASR behaviour, much is unknown about the early-age reaction of AAMs mixed with reactive aggregates. Therefore, it is necessary to investigate the early-age reaction of AAMs prepared with reactive aggregates, and consequently to improve the understanding of ASR behaviour in AAMs.

In this work, the effects of reactive aggregates on the early-age reaction of OPC mortar and water-glass activated slag or fly ash were studied in terms of reaction kinetics, products and pore structures. The main aim is to investigate and to compare the role of reactive aggregates in the early-age reaction within OPC system and AAMs system. This work provides further insights for the early age ASR in AAMs and contributes to the understanding of long-term ASR behaviour in AAMs.

2. MATERIALS AND METHODS

2.1. Materials

The solid precursors used in this study were commercial ordinary Portland cement (OPC), slag (SL) and fly ash (FA), and their chemical are presented in Table 1. The mineral composition and particle size distribution of precursors are shown in Fig. 1 and Fig 2, respectively. The activator used was water-glass with a silicate modulus of 1.5 (Ms=SiO_2/Na_2O by mass), which was prepared by mixing the industrial grade NaOH pellets (purity>98.5%) with industrial grade sodium silicate (Ms=3, water content=60±1%) conformed to Japanese industrial standard [17]. The activators were pre-mixed with water 24 h prior to casting to remove the effect of heat release during dilution [18].

The reactive aggregate used in this study was provided by Marushin Shitake Construction from Toyama ken in Japan. Meanwhile, the standard quartz sand per Japanese industrial standard [19] was used as inert aggregate for reference. Their chemical compositions were presented in Table 1, and mineral composition are shown in Fig. 3, respectively. The XRD patterns suggest that the reactive aggregate mainly consisted of albite; cristobalite, biotite,

clinochlore and quartz, and the amorphous content acquired by Rietveld refinement method [20] was 34.7%. The aggregates were sieved to almost same particle size distribution as shown in Fig. 4, and the D_{50} of the reactive aggregate and inert aggregate are 838.6 μm and 839.7 μm, respectively.

Table 1: Chemical composition of OPC, SL, FA and aggregates (%)

Ingredients	OPC	SL	FA	NA	RA
CaO	62.16	43.63	3.66	0.20	4.87
SiO_2	17.11	31.07	61.89	98.40	58.97
Al_2O_3	4.45	12.40	23.60	0.40	17.28
Fe_2O_3	3.00	0.32	4.50	0.40	12.02
MgO	0.83	5.45	0.94	-	2.02
Na_2O	0.39	0.25	0.04	0.01	0.71
K_2O	0.26	0.34	1.14	0.01	1.79
Na_2Oeq	0.56	0.47	0.79	0.01	1.89
MnO	0.09	0.18	0.04	-	0.18
TiO_2	0.28	0.51	1.07	-	1.01
P_2O_5	0.41	0.01	0.08	-	0.04
SO_3	2.87	1.85	0.36	-	-
Loss on ignition	2.27	0.37	2.16	0	0.89

Note: RA=Reactive aggregate; NA=inert quartz sand; Na_2Oeq=%Na_2O+0.658%K_2O.

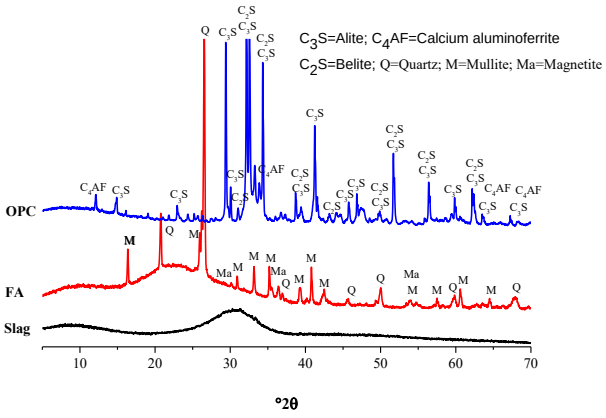

Figure 1: XRD patterns of OPC, FA and SL

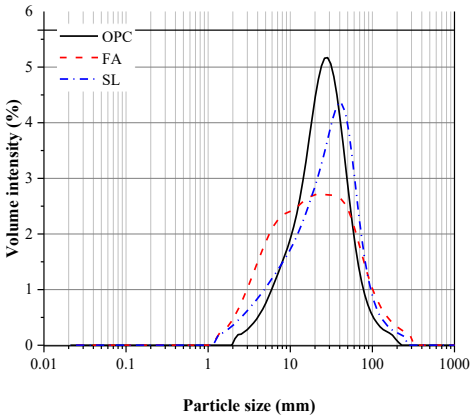

Figure 2: Particle size of solid precursors

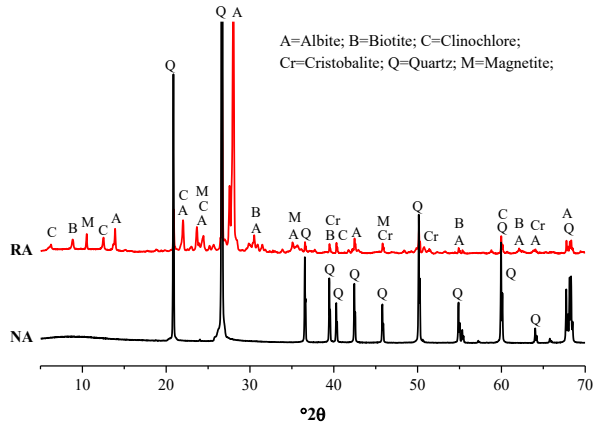

Figure 3: XRD patterns of RA and NA

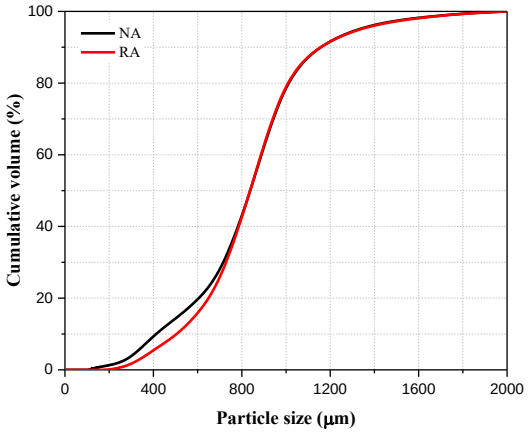

Figure 4: Pore size distribution of NA and RA

2.2. Mix design

The mix design of samples used in this study are presented in Table 2. The water to binder ratio for OPC mortars was 0.5, while the water to binder ratio of SL and FA mortars were 0.34 and activator to binder ratio were 0.5, respectively. For each group, amount of binder, water or activator were the same, only the aggregate was the variable. After casting, the specimens were cured in a climate chamber (T=20°C, RH>95%). The specimens were demoulded after 24h and were kept in the chamber until the prescribed day.

Table 2: Mixture proportions of mortars

Sample ID	Precursor	Aggregate	Aggregate/precursor	Water/cement	Activator/cement
OPC-NA	OPC	NA	1	0.5	-
OPC-RA	OPC	RA		0.5	-
SL-NA	SL	NA		0.34	0.5
SL-RA	SL	RA		0.34	0.5
FA-NA	FA	NA		0.34	0.5
FA-RA	FA	RA		0.34	0.5

Note: SL-NA represents the mixture of water-glass activated slag prepared with non-reactive aggregate; SL-RA represents the mixture of water-glass activated slag prepared with reactive aggregate. The whole of SL-NA and SL-RA were taken as AAS group, while FA-NA and FA-RA were taken as AAFA group in the following section.

2.3. Testing methods

To characterize the hydration and microstructures of mortars prepared with RA, the following instruments and methods were used. The samples used for thermogravimetry (TG) and mercury intrusion porosimetry (MIP) were cut into small pieces and immersed in alcohol for 3 days to stop hydration, followed by vacuum pumping before testing [20].

2.3.1. Heat evolution measurement

The heat evolution of different mixtures were tested using a TAM air isothermal calorimeter. The preliminary tests using internal mixing method identified the problem of clogging inside the ampoules due to the high viscosity and fast setting of AAS. Additionally, it is hard to guarantee the homogeneity of mortars by internal mixing. Therefore, the samples were mixed outside and then loaded into the TAM air isothermal calorimeter immediately after mixing. For the external mixing, it is important that the mixing time was kept the same to ensure the comparability between different specimens. The calibration was conducted at temperature of 20 °C, 48h prior to the test. The heat evolution of reaction for all mixtures were recorded for 48h.

2.3.2. Thermogravimetry (TG) analysis

TG analysis was performed using TG-DTA 2000SA system to study the amount of amorphous main hydration products in mortars at 1, 3 and 7 days. To guarantee the representativeness of samples, about 5 g samples were ground with agate mortar and approximately 50 mg powder samples were loaded in an aluminum oxide crucible. The samples were heated from 30 °C to 600 °C at a rate of 10 °C /min under 100 ml/min flow speed of nitrogen gas atmosphere.

2.3.3. Pore structures measurement

Although the MIP method has some limitations, it is still considered as an invaluable technique to study the pore structure of cementitious materials [20]. In this study, Micromeritics AutoPore III was used to investigate the pore structures of mortars prepared

with reactive aggregates or inert aggregates at 1, 3 and 7 days. The range of intruding pressure of this machine is from 3.654 kPa to 414MPa, the surface tension of mercury is 0.485N/m and the contact angle is 130°, respectively. Thus, according to the Washburn equation [21], the pore radius can be detected ranges from 1.5 nm to 170 μm.

3. RESULTS AND DISCUSSION

3.1. Heat evolution

The effect of reactive aggregate on the early-age heat evolution of OPC, AAS and AAFA system are shown in Fig. 5. In general, the heat evolution curve can be divided into five stages [20,22], namely, initial reaction, induction period, accelerating period, decelerating period and the continued slow reaction period. As shown in Fig. 5a, for OPC system, the trend of the heat evolution curves with different aggregates are similar. This demonstrated that the effect of reactive aggregate on the early-age reaction of OPC is negligible. This may be related to the pH (approximately 12) of the pore solution in OPC system, which is mainly buffered by $Ca(OH)_2$, and the amount of $Ca(OH)_2$ in the early-age is relatively low. Therefore, the dissolution rate of silica from reactive aggregate remains low and thereby the reaction kinetic of OPC system was scarcely influenced.

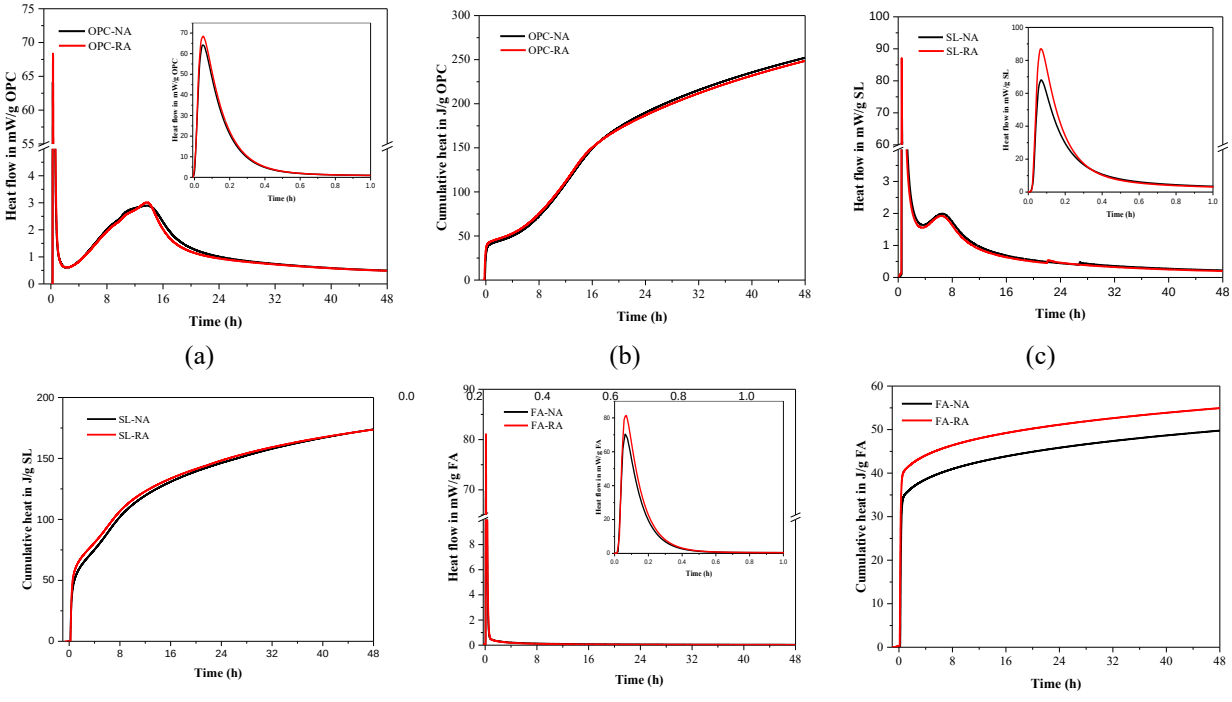

Figure 5: Heat evolution of OPC, AAS and AAFA mortars mixed with NA or RA. (AAS=waterglass activated slag; AAFA=water-glass activated fly ash)

In contrast to Fig. 5a, the first peak of heat flow curves in Fig. 5c and e were significantly affected by the reactive aggregate. For AAMs, this first peak is mainly caused by the wetting and dissolution of solid materials [23], which is similar to the initial reaction period of OPC system, but the potential physicochemical reactions are totally different. Thus, the evident increment of this peak indicated that the reactive aggregates obviously dissolved in this stage, which would influence the following chemical reaction processes and products. Meanwhile,

the heat evolution process of AAFA in Fig. 5e are different from OPC and AAS in Fig. 5a and c, it only has one peak, and no other distinct heat peak can be found. This is owing to the slow gelation and polymerization process of AAFA, which is consistent with the previous researches [24]. Additionally, very low compressive strength of early-age AAFA cured at room temperature was also reported [25,26]. As such, comparing with AAS system, the cumulative heat of AAFA after the dissolution increases only gradually and does not show tremendous increase until 48h. Nevertheless, for AAS, the heat evolution curves are similar to that of OPC system. It also has two peaks, one is before the induction period and the other is after the induction period, which is due to the high pH values (pH=14.6) of the activator used in this study [23]. However, the position and magnitude of these two peaks are different from that of OPC system as a result of different reaction mechanisms between two systems. Compared to AAFA system, it can be seen that, as time goes on, the effect of reactive aggregate on the cumulative heat of AAS gradually weaken. It is possible that the effect of reactive aggregates on the heat evolution of AAS samples might be two-edged. On the one hand, incorporating reactive aggregates prompt the dissolution heat response. On the other hand, the excessive consumption of OH^- in the dissolution stage led to the insufficient OH^- for the destruction of the bonds of other glassy phases [27] and accordingly prolonged the induction period and the corresponding heat release. This phenomenon is very similar to the effect of activator-to-slag ratio on reaction heat of AAS [23,27], which suggests that incorporating reactive aggregate acts as the role of increasing the binder content and thereby the activator-to-slag ratio of the mixture decreased. Therefore, the reaction kinetics of AAS were further influenced.

3.2. Thermogravimetric analysis

The TG and differential thermogravimetric (DTG) curves of all samples after 1, 3 and 7 days curing are presented in Fig. 6. For OPC system, there are two major peaks in the DTG curves, which is consistent with previous studies [20]. The first peak from 30 °C to 300 °C corresponds to absorbed water and the decomposition of C-S-H. The second peak between 380 °C and 500 °C is attributed to the decomposition of portlandite (CH). It is also shown that, at 1day, the weight loss of OPC-NA and OPC-RA from 30 °C to 600 °C is almost equal, and correspondingly the TG curves are almost similar. However, after 3 days curing, the difference between the curves of OPC-RA and OPC-NA were non-inevitable. This may have something to do with the amount of OH^- in pore solution of OPC system. Although the amount of CH increased with age, the solubility of CH is relatively low and thereby the pH of pore solution changes little. Therefore, the effect of reactive aggregate on hydration of OPC system is still limited.

Compared to Fig. 6a, there are only a single peak in the DTG curves of Fig 6b and c due to absence of CH in the alkali activated system [4, 36]. Previous literature suggested that this peak is mainly caused by the loss of interlayer water and dehydration of C-(N)-A-S-H type gels for AAS [29] and N-A-S-H for AAFA [30]. Therefore, that is to say, the amount of main reaction products in AAS and AAFA can be roughly reflected by the weight loss from the 105 °C to 300 °C of the TG curves in Fig. 6b and c. For AAS system, the sequence of weight loss isSL-RA-7D (4.14%) > SL-NA-7D (3.72%) > SL-RA-3D (3.37%) > SL-NA-3D (3.29%) > SL-RA-1D (2.98%) > SL-NA-1D (2.93%). For AAFA system, the sequence of weight loss is FA-RA-7D (1.51%) > FA-RA-3D (1.38%) > FA-NA-7D (1.26%) > FA-RA-1D (1.07%) >

FA-NA-3D (1.00%) > FA-NA-1D (0.75%). It clearly shows that the reactive aggregate had noticeable influence on the reaction process and promoted the gel formation.

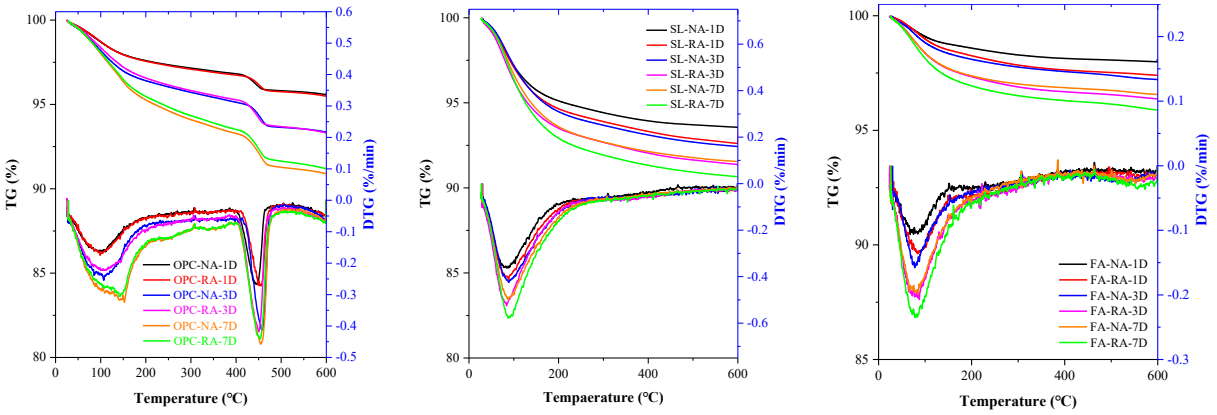

(a) OPC (b) AAS (c) AAFA

Figure 6: TG and DTG curves of OPC, AAS and AAFA mortars mixed with NA or RA.

3.3. Porosity and pore size distribution

The effect of reactive aggregate on the porosity and pore size distribution of all specimens are given in Fig. 7. With the increase of curing time, the porosity of all samples decreased gradually, except for FA-RA-3D sample. As shown in Table 3, the total porosity of FA-RA-1D and FA-RA-3D were 30.2263% and 31.0282%, respectively. The abnormal phenomenon will be explained in the following text. Meanwhile, the pore size distribution also shows refinement of pores with an increase in curing time.

For OPC system, the porosity of OPC-RA samples at 1 and 3 days were higher than that of OPC-NA, while the porosity of OPC-RA-7D was lower than that of OPC-NA-7D. In contrast to OPC, the porosity of AAS or AAFA prepared with reactive aggregate from 1 to 7 days are always greater than that of samples mixed with non-reactive aggregates. Meanwhile, the total porosity shows a strong negative correlation with the amount of reaction products. The more reaction products are, the higher total porosity is. At room temperature, the dissolution of silica from reactive aggregate is negligible [31], while it can react with the high alkaline solution in AAMs over time [32]. This may relate to the alkalinity of pore solution in corresponding samples, and this effect might be bilateral. On one hand, the high amount of OH^- in the first few days accelerates the dissolution of poorly crystallized silica in reactive aggregate, and the dissolved reactive silica participated in the early-age reaction and thereby facilitated formation of reaction products. On the other hand, the dissolution of reactive aggregate leaves the hollows in the surface of aggregate, and consequently lead to the increase of total porosity [33,34]. Since the amount of OH^- in OPC system is relative lower than that of AAMs [35], the reactive aggregate in AAMs were attacked more than that of OPC and thereby result in higher porosity in AAMs prepared with reactive aggregates. Particularly for AAFA, whose reaction speed is low and cannot make up the hollows in time, the results that the total porosity of FA-RA-3D was bigger than that of FA-RA-1D further reflected this effect.

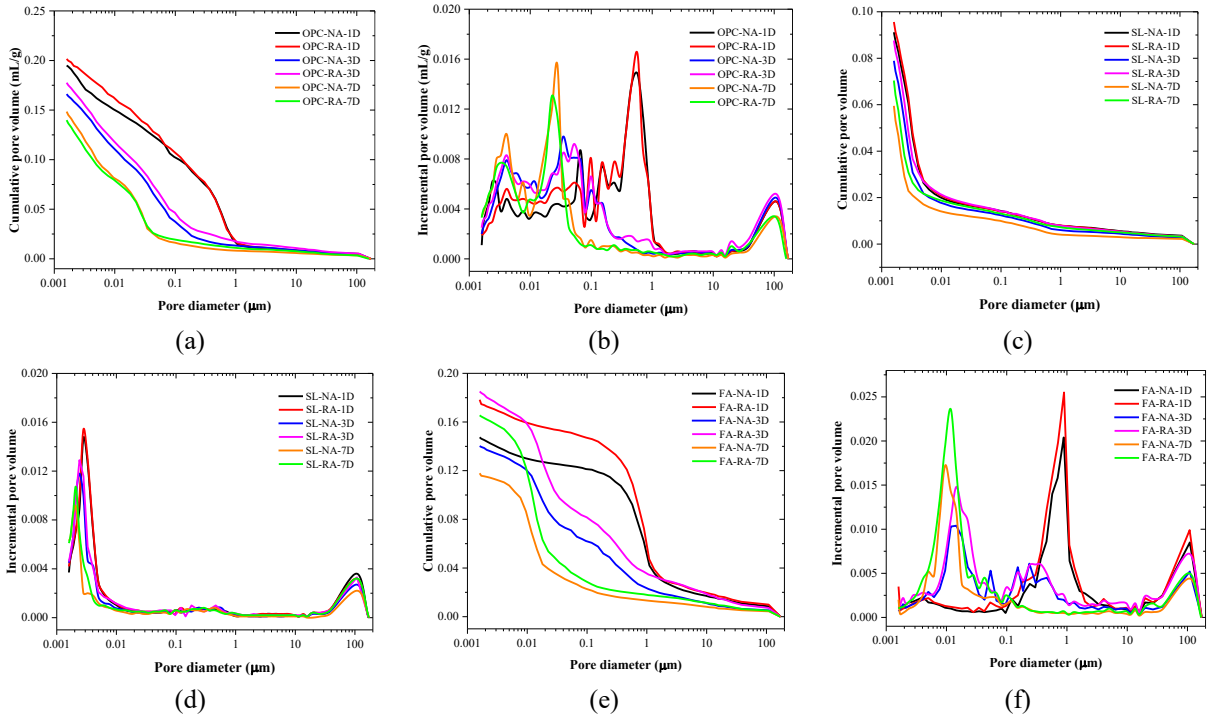

Figure7: Cumulative and incremental pore volume of OPC, AAS and AAFA mortars mixed with NA or RA

Table 3: Total porosity of samples

Sample ID	1 day	3 days	7 days
	Total porosity (%)	Total porosity (%)	Total porosity (%)
OPC-NA	34.9816	29.8330	27.6005
OPC-RA	35.4872	31.4117	25.7926
FA-NA	27.3188	26.2142	22.4827
FA-RA	30.2263	31.0282	29.1259
SL-NA	18.7866	16.4220	13.5995
SL-RA	19.3866	17.7266	14.4044

4. CONCLUSIONS

This study investigated the effect of reactive aggregates on the early-age reaction of OPC, AAS and AAFA. Based on the experiments and discussion, the following conclusions can be drawn:

(1) This study suggested that the effect of reactive aggregate on the early-age reaction of OPC, AAS and AAFA are different with each other.

(2) Compared to OPC system, the reactive aggregates in AAS and AAFA system were easier to dissolve due to the high alkaline activator and thereby generated more heat in the dissolution stage in calorimetry study.

(3) The dissolved reactive aggregate participated in the early-age reaction of AAS and AAFA, and facilitated the gel formation, which were further confirmed by TG analysis.

(4) The total porosity of AAS mortar and AAFA mortar made of reactive aggregates showed negative correlation with the amount of reaction products in early-age. The refinement of pore structure with time was also observed.

(5) The possibility of explaining the long-term ASR behavior of AAMs in terms of early-age reaction was confirmed in this study. Further cross-checking work is needed for better bridging the knowledge gap.

ACKNOWLEDGEMENT

This research is supported by Japan Society for the Promotion of Science (JSPS) and China Scholarship Council (CSC).

REFERENCES

[1] F. Rajabipour, E. Giannini, C. Dunant, J.H. Ideker, M.D.A. Thomas, Alkali-silica reaction: Current understanding of the reaction mechanisms and the knowledge gaps, Cem. Concr. Res. 76 (2015) 130–146. doi:10.1016/j.cemconres.2015.05.024.

[2] J. Lindgård, Ö. Andiç-Çakir, I. Fernandes, T.F. Rønning, M.D.A. Thomas, Alkali-silica reactions (ASR): Literature review on parameters influencing laboratory performance testing, Cem. Concr. Res. 42 (2012) 223–243. doi:10.1016/j.cemconres.2011.10.004.

[3] B. Fournier, M.-A. Bérubé, Alkali-aggregate reaction in concrete: a review of basic concepts and engineering implications, Can. J. Civ. Eng. 27 (2000) 167–191. doi:10.1139/l99-072.

[4] J.H.M. Visser, Fundamentals of alkali-silica gel formation and swelling: Condensation under influence of dissolved salts, Cem. Concr. Res. 105 (2018) 18–30. doi:10.1016/j.cemconres.2017.11.006.

[5] I. García-Lodeiro, A. Palomo, A. Fernández-Jiménez, Alkali-aggregate reaction in activated fly ash systems, Cem. Concr. Res. 37 (2007) 175–183. doi:10.1016/j.cemconres.2006.11.002.

[6] T. Williamson, M.C.G. Juenger, The role of activating solution concentration on alkali-silica reaction in alkali-activated fly ash concrete, Cem. Concr. Res. 83 (2016) 124–130. doi:10.1016/j.cemconres.2016.02.008.

[7] P. Krivenko, R. Drochytka, A. Gelevera, E. Kavalerova, Mechanism of preventing the alkali – aggregate reaction in alkali activated cement concretes, Cem. Concr. Compos. 45 (2014) 157–165. doi:10.1016/j.cemconcomp.2013.10.003.

[8] C. Shi, Z. Shi, X. Hu, R. Zhao, L. Chong, A review on alkali-aggregate reactions in alkali-activated mortars/concretes made with alkali-reactive aggregates, Mater. Struct. 48 (2015) 621–628. doi:10.1617/s11527-014-0505-2.

[9] Z. Shi, C. Shi, S. Wan, Z. Zhang, Effects of alkali dosage and silicate modulus on alkali-silica reaction in alkali-activated slag mortars, Cem. Concr. Res. 111 (2018) 104–115. doi:10.1016/j.cemconres.2018.06.005.

[10] R. Tänzer, Y. Jin, D. Stephan, Effect of the inherent alkalis of alkali activated slag on the risk of alkali silica reaction, Cem. Concr. Res. 98 (2017) 82–90. doi:10.1016/j.cemconres.2017.04.009.

[11] Y. Chen, X. Pu, C. Yang, Q. Ding, Alkali aggregate reaction in alkali slag cement mortars, J. Wuhan Univ. Technol. Sci. Ed. 17 (2002) 60–62.

[12] A. Fernández-Jiménez, F. Puertas, The alkali-silica reaction in alkali-activated granulated slag mortars with reactive aggregate, Cem. Concr. Res. 32 (2002) 1019–1024. doi:10.1016/S0008-8846(01)00745-1.

[13] R. Pouhet, M. Cyr, Alkali-silica reaction in metakaolin-based geopolymer mortar, Mater. Struct. 48 (2015) 571–583. doi:10.1617/s11527-014-0445-x.

[14] D. Mahanama, P. De Silva, T. Kim, A. Castel, M.S.H. Khan, Evaluating Effect of GGBFS in Alkali-Silica Reaction in Geopolymer Mortar with Accelerated Mortar Bar Test, J. Mater. Civ. Eng. 31 (2019) 1–11. doi:10.1061/(ASCE)MT.1943-5533.0002804.

[15] T. Bakharev, J.G. Sanjayan, Y.B. Cheng, Resistance of alkali-activated slag concrete to alkali-aggregate reaction, Cem. Concr. Res. 31 (2001) 331–334. doi:10.1016/S0008-8846(03)00125-X.
[16] A. Hajimohammadi, T. Ngo, J. Vongsvivut, Interfacial chemistry of a fly ash geopolymer and aggregates, J. Clean. Prod. 231 (2019) 980–989. doi:10.1016/j.jclepro.2019.05.249.
[17] Japanese industrial standard, Sodium silicate, 1966. doi:10.1136/jnnp.45.7.644.
[18] Z. Shi, C. Shi, J. Zhang, S. Wan, Z. Zhang, Z. Ou, Alkali-silica reaction in waterglass-activated slag mortars incorporating fly ash and metakaolin, Cem. Concr. Res. 108 (2018) 10–19. doi:10.1016/j.cemconres.2018.03.002.
[19] Japanese industrial standard, Physical testing methods for cement, Japanese Standards Association, Japan, 2015.
[20] K. Scrivener, R. Snellings, B. Lothenbach, A Practical Guide to Microstructural Analysis of Cementitious Materials, 2016. doi:10.1201/b19074.
[21] W. Gardner, The dynamics of capillary flow, Phys. Rev. 17 (1921) 273–283. doi:10.1103/PhysRev.18.206.
[22] J. Hu, Z. Ge, K. Wang, Influence of cement fineness and water-to-cement ratio on mortar early-age heat of hydration and set times, Constr. Build. Mater. 50 (2014) 657–663. doi:10.1016/j.conbuildmat.2013.10.011.
[23] C. Shi, D. Roy, P. Krivenko, Alkali-activated cements and concretes, CRC press, 2003.
[24] Z. Sun, A. Vollpracht, Isothermal calorimetry and in-situ XRD study of the NaOH activated fly ash, metakaolin and slag, Cem. Concr. Res. 103 (2018) 110–122. doi:10.1016/j.cemconres.2017.10.004.
[25]J.L. Provis, A. Palomo, C. Shi, Advances in understanding alkali-activated materials, Cem. Concr. Res. 78 (2015) 110–125.
[26] M.H. Samarakoon, P.G. Ranjith, T.D. Rathnaweera, M.S.A. Perera, Recent advances in alkaline cement binders: A review, J. Clean. Prod. 227 (2019) 70–87. doi:10.1016/j.jclepro.2019.04.103.
[27] D. Khale, R. Chaudhary, Mechanism of geopolymerization and factors influencing its development: A review, J. Mater. Sci. 42 (2007) 729–746. doi:10.1007/s10853-006-0401-4.
[28] S. Zhang, A. Keulen, K. Arbi, G. Ye, Waste glass as partial mineral precursor in alkali-activated slag/fly ash system, Cem. Concr. Res. 102 (2017) 29–40. doi:10.1016/j.cemconres.2017.08.012.
[29] X. Gao, Q.L. Yu, H.J.H. Brouwers, Reaction kinetics, gel character and strength of ambient temperature cured alkali activated slag-fly ash blends, Constr. Build. Mater. 80 (2015) 105–115. doi:10.1016/j.conbuildmat.2015.01.065.
[30] A. Fernández-Jiménez, A. Palomo, J.Y. Pastor, A. Martín, New cementitious materials based on alkali-activated fly ash: Performance at high temperatures, J. Am. Ceram. Soc. 91 (2008) 3308–3314. doi:10.1111/j.1551-2916.2008.02625.x.
[31] R.K. Iler, The chemistry of silica: solubility, polymerization, colloid and surface properties and biochemistry., Wiley Online Library, New York, 1979.
[32] J.L. Provis, J.S.J. Van Deventer, Alkali activated materials: state-of-the-art report, RILEM TC 224-AAM, Springer Science & Business Media, 2013.
[33] T. Kim, M.F. Alnahhal, Q.D. Nguyen, P. Panchmatia, A. Hajimohammadi, A. Castel, Initial sequence for alkali-silica reaction: Transport barrier and spatial distribution of reaction products, Cem. Concr. Compos. 104 (2019) 103378. doi:10.1016/j.cemconcomp.2019.103378.
[34] O. Copuroglu, Effect of silica dissolution on the mechanical characteristics of alkali-reactive aggregates, J. Adv. Concr. Technol. 8 (2010) 5–14. doi:10.3151/jact.8.5.
[35] Y. Zuo, M. Nedeljković, G. Ye, Pore solution composition of alkali-activated slag/fly ash pastes, Cem. Concr. Res. 115 (2019) 230–250. doi:10.1016/j.cemconres.2018.10.010.

SYNTHESIS OF ALKALI-SILICA REACTION (ASR) PRODUCTS AND THE ROLE OF AL AND LI IN MITIGATING ASR

Zhenguo Shi (1), Barbara Lothenbach (1) (2)

(1) Laboratory for Concrete & Construction Chemistry, Swiss Federal Laboratories for Materials Science and Technology (Empa), 8600 Dübendorf, Switzerland

(2) Department of Structural Engineering, Norwegian University of Science and Technology (NTNU), 7491 Trondheim, Norway

Abstract

Using Al-rich supplementary cementitious materials to partially replace Portland cement is a well-established empirical approach to mitigate expansion of concrete caused by alkali-silica reaction (ASR). However, the mechanisms behind it are still not completely understood. Synthesis of ASR products in the laboratory provides a unique opportunity to better understand the conditions and mitigation mechanism of ASR. This study focusses on the synthesis of an 10.8 Å ASR product, which is structurally identical to the ASR product formed in concrete. The effect of Al and Li on formation of the 10.8 Å ASR product is studied. The results show that Al does not prevent the formation of the 10.8 Å ASR product, whereas the formation of the 10.8 Å ASR product is supressed in presence of Li. At low initial Li/Si an amorphous product is formed and a crystalline lithium silicate at high initial Li/Si ratio.

Keywords: Alkali-silica reaction, Mitigation, Synthesis, Aluminium, Lithium

1. INTRODUCTION

Alkali-silica reaction (ASR) can cause substantial damage in concrete structures. The reaction occurs between the reactive silica in the aggregates and alkalis from the pore solution of concrete. In addition, some calcium is needed to generate expansion, although the expansion mechanism behind is still unclear. For new concrete structures, ASR can be prevented by adding Al-rich supplementary cementitious materials (SCMs) or lithium salts. However, these mitigation measures are mainly based on empirics.

Understanding the mechanism of ASR and their mitigation measurements within concrete are difficult, since direct monitoring of the reaction and the characterization of the reaction products are difficult by conventional laboratory techniques such as X-ray diffraction (XRD) analysis, Nuclear Magnetic Resonance (NMR), thermogravimetric analysis (TGA). An alternative approach to fill these knowledge gaps is to synthesize ASR products in large quantity. Syntheses of ASR products which are structurally similar to those formed in field concrete were recently achieved at 80 °C [1]. Based on this approach, also solubility products of ASR products

could be obtained, and thus the conditions for formation of ASR products predicted [2,3]. Moreover, some structural differences were observed between ASR products synthesized at 80 °C and ASR products formed at lower temperature in field concrete, indicating the needs to synthesized ASR products at relatively lower temperature.

In this study, synthesis of ASR product at 40 °C is attempted. In addition, the effect of Al and Li on formation of the ASR product is also investigated. The obtained products have been characterized by XRD. The results are expected to help understanding the formation and mitigation mechanism of the ASR products in concrete, which is an important step to further evaluate the long-term efficiency of Al and Li in mitigating ASR.

2. SAMPLES AND METHODS

The samples with a constants Ca/Si ratio of 0.25 and K/Si ratio of 0.5 were prepared with different Al/Si ratios (i.e., 0, 0.1 and 0.3) and Li/Si ratios (i.e., 0, 0.2 and 0.4). For all samples, amorphous silica (hydrophilic silica (SiO_2), surface area 200 m^2/g, from EVONIK industries) was mixed with freshly burnt CaO (obtained by burning calcium carbonate for 12 h at 1000 °C) and KOH pellet at designated portions. In addition, a certain amount of aluminium hydroxide powder ($Al(OH)_3$, from Sigma-Aldrich) with 63-67 wt.% Al_2O_3 was added into two of the samples, while lithium hydroxide monohydrate ($LiOH \cdot H_2O$, purity 98.5 wt.%) was added for another two samples to obtained the designated molar ratios as shown in Table 1. The water contents were adjusted for the samples containing Li in order to better disperse the materials.

All materials were mixed in hard polyethylene (PE-HD) bottles and shaken by hand. Afterwards, all samples were reacted in an incubator at 40 °C. Samples were filtrated after 160 days and 210 days for the Al-series and the Li-series, respectively. The solids were rinsed first with approximately 50 mL of 1:1 water-ethanol solution and then with 50 mL 94% ethanol solution in the N_2 filled glove box. The obtained solids were then vacuum dried for three days, and stored in N_2 filled desiccators at 35% RH with CO_2 absorbent to prevent carbonation.

Table 1: Starting materials and mix proportions for the samples.

	SiO_2	CaO	$Al(OH)_3$	$LiOH \cdot H_2O$	KOH	H_2O	Ca/Si	K/Si	Al/Si	Li/Si
	g	g	g	g	g	mL	mol/mol			
SKCA_0	6.0	1.4	0		2.8	50	0.25	0.5	0	
SKCA_0.1	6.0	1.4	0.78		2.8	50	0.25	0.5	0.1	
SKCA_0.3	6.0	1.4	2.35		2.8	50	0.25	0.5	0.3	
SKCL_0	6.0	1.4		0	2.8	50	0.25	0.5		0
SKCL_0.2	6.0	1.4		0.85	2.8	54.1	0.25	0.5		0.2
SKCL_0.4	6.0	1.4		1.70	2.8	50.8	0.25	0.5		0.4

The phases in the solids were determined by a conventional X-ray powder diffraction (XRD, PANalytical X'pert Pro) with CoKα radiation in a θ–θ configuration. The samples were scanned with a step size of 0.017° 2θ between 5 and 90° 2θ with the X'Celerator detector during 150 min.

3. RESULTS AND DISCUSSION

3.1 Effect of the initial Al on ASR

The XRD patterns of the samples with different initial Al/Si ratios after 160 days of reaction are shown in Figure. 1. The samples were stored in desiccator at 35% RH prior to the XRD measurements. The results show that a crystalline phase with a basal spacing of 10.8 Å is observed in the sample without addition of $Al(OH)_3$ powder. A detailed characterization of this product and its comparison with that formed in field concrete has recently been made [4]. It was concluded that the synthesized 10.8 Å ASR product is structurally identical to crystalline ASR product formed in the field concrete aggregates.

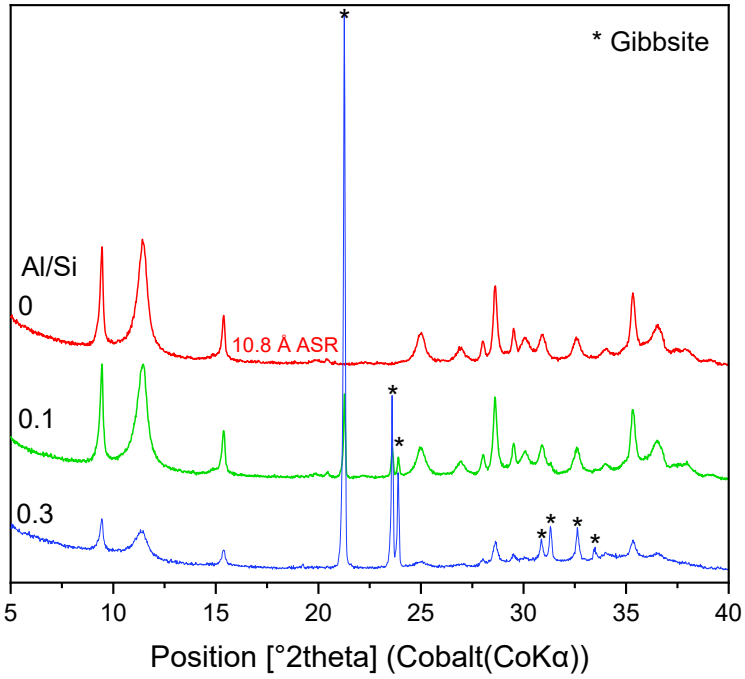

Figure 1: XRD patterns for the samples with different Al/Si ratios after reaction for 160 days

When $Al(OH)_3$ powder is added in the samples, the formation of gibbsite is observed as shown in Figure. 1, while the 10.8 Å ASR product is also observed with their intensity of the XRD patterns reduced with the increase of Al/Si ratio, which could indicate the formation of less crystalline ASR product; however with the same structure as the XRD peaks were not shifted. The addition of Al neither prevents ASR nor alters the crystal structure of the ASR product. Thus, it is most likely that mitigation of ASR by using Al-rich supplementary cementitious materials (SCMs) is associated with the fact that Al can slow down the dissolution of reactive silica and thus reaction kinetics as proposed by previous studies [5, 6, 7, 8]. This observation suggests that precautions should be taken for the long-term efficiency of the Al-rich SCMs in mitigating ASR in field concretes.

3.2 Effect of initial Li ratio on ASR

The effect of LiOH on mitigating ASR is also investigated after 210 days of reaction as shown in Figure 2. The samples were also dried at 35% RH prior to XRD measurements. In contrast to the samples containing $Al(OH)_3$, the addition of LiOH in the samples prevented the formation of 10.8 Å ASR product. Instead, an amorphous phase is observed in the samples with initial Li/Si ratios of 0.2 and 0.4. Crystalline lithium silicate (Li_2SiO_3) is also observed at higher initial Li/Si ratio of 0.4. Several studies [9, 10, 11] proposed that mitigation ASR by Li was attributed to the hypothesis that the Li ions facilitate the formation of a physical barrier on the surface of reactive silica, which prevent further attack on the reactive sites by hydroxyl ions. This is not necessarily the true as our observation shown in Figure 2, indicate that all the amorphous silica had reacted without forming a crystalline ASR product.

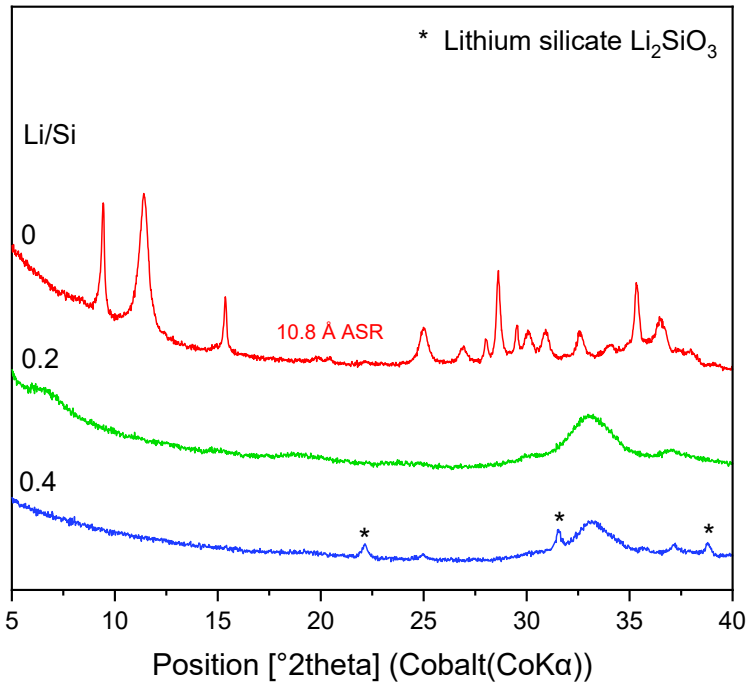

Figure 2: XRD patterns for the samples with different Li/Si ratios after reaction for 210 days

4. CONCLUSIONS

In this study, the 10.8 Å ASR product is synthesized at 40 °C. In addition the effects of Al and Li on ASR are also investigated. Based on the XRD results, the following conclusions can be drawn:

- Al does not prevent the formation of ASR product. Thus, the ASR mitigation mechanism by Al-rich SCMs is most likely related to the slowdown of the dissolution rate of reactive silica and the lower pH. Thus, the long-term effect of Al-rich SCMs in mitigating ASR in field concretes should be further studied.

- In presence of Li, formation of the crystalline ASR product can be prevented, while formation of an amorphous product or crystalline lithium silicate is observed instead at low or high initial Li/Si ratio. The hypothesis proposed in earlier studies on the formation of physical barrier due to precipitation of lithium containing reaction products is not necessary the mechanism for Li in mitigating ASR.

ACKNOWLEDGEMENTS

The authors would like to thank the SNF Sinergia: Alkali-silica reaction in concrete (ASR), grant number CRSII5_17108. The EMPAPOSTDOCS-II programme has received funding from the European Union's Horizon 2020 research and innovation programme under the Marie Skłodowska-Curie grant agreement number 754364.

REFERENCES

[1] Shi, Z., Geng, G., Leemann, A., & Lothenbach, B. 'Synthesis, characterization, and water uptake property of alkali-silica reaction products'. Cem. Concr. Res., **121**(2019), 58-71.

[2] Shi, Z., & Lothenbach, B. 'The role of calcium on the formation of alkali-silica reaction products'. Cem. Concr. Res., **126**(2019), 105898.

[3] Shi, Z., & Lothenbach, B. 'The combined effect of potassium, sodium and calcium on the formation of alkali-silica reaction products'. Cem. Concr. Res., **127**(2020), 105914.

[4] Shi, Z., Leemann, A., Rentsch, D., & Lothenbach, B. 'Synthesis of alkali-silica reaction product structurally identical to that formed in field concrete'. (2020) Manuscript submitted.

[5] Chappex, T., & Scrivener, K. L. 'The influence of aluminium on the dissolution of amorphous silica and its relation to alkali silica reaction'. Cem. Concr. Res., **42**(12) (2012), 1645-1649.

[6] Chappex, T., & Scrivener, K. 'Alkali fixation of C–S–H in blended cement pastes and its relation to alkali silica reaction'. Cem. Concr. Res., **42**(8) (2012), 1049-1054.

[7] Chappex, T., & Scrivener, K. L. 'The effect of aluminum in solution on the dissolution of amorphous silica and its relation to cementitious systems'. J. Am. Ceram. Soc., **96**(2) (2013), 592-597.

[8] Leemann, A., Bernard, L., Alahrache, S., & Winnefeld, F. 'ASR prevention—Effect of aluminum and lithium ions on the reaction products'. Cem. Concr. Res., **76**(2015), 192-201.

[9] Kim, T., & Olek, J. 'The effects of lithium ions on chemical sequence of alkali-silica reaction'. Cem. Concr. Res., **79**(2016), 159-168.

[10] Feng, X., Thomas, M. D. A., Bremner, T. W., Folliard, K. J., & Fournier, B. 'New observations on the mechanism of lithium nitrate against alkali silica reaction (ASR)'. Cem. Concr. Res., **40**(1)(2010), 94-101.

[11] Leemann, A., Lörtscher, L., Bernard, L., Le Saout, G., Lothenbach, B., & Espinosa-Marzal, R. M. Mitigation of ASR by the use of $LiNO_3$—characterization of the reaction products. Cem. Concr. Res., **59**(2014), 73-86.

ANALYSIS OF THE POROSITY OF ALKALI-SENSITIVE AGGREGATES FOR THE ASSESSMENT OF MICROSTRUCTURE-DEPENDENT SOLUBILITY IN THE CONTEXT OF ASR

Tyler Oesch (1), Frank Weise (1), Heidi Marx (1), Mario Kositz (2) and Klaus-Juergen Huenger (2)

(1) Bundesanstalt für Materialforschung und –prüfung (BAM - Federal Institute for Materials Research and Testing), Germany

(2) Brandenburgische Technische Universität (BTU) Cottbus-Senftenberg, Germany

Abstract

Intensified Alkali-Silica Reaction (ASR) damage has occurred on German roadways in recent years, leading to requirements for compulsory pre-construction investigation of aggregate alkali sensitivity using concrete tests with external alkali supply. However, since these tests are time-consuming and cost-intensive, there is interest in replacing them with a solubility test on pure aggregate in 0.1 M KOH solution at 80°C with a defined NaCl content (1wt.-%). In this context, the influence of aggregate pore structure on SiO_2 and Al_2O_3 solubility was investigated in this project. This paper compares the results of porosity studies with X-ray Computed Tomography (3D-CT) and the Brunauer-Emmett-Teller (BET) method on individual quarried and river gravel granules of both rhyolite and greywacke. For visualization and quantification of both externally accessible and fully enclosed surfaces of granules using X-ray 3D-CT, special software tools were developed. The results demonstrated that the river gravel granules had significantly larger externally accessible surfaces than the quarried granules. BET measurements on individual stones showed, as expected, that measured surfaces were about three orders of magnitude larger than those from the X-ray 3D-CT analyses due to the higher spatial resolution of BET. There was no apparent correlation between the X-ray 3D-CT and BET surface areas. Mercury porosimetry measurements indicate that this may be due to the presence of significant porosity below the spatial resolution of the X-ray 3D-CT. A comparison of SiO_2 and Al_2O_3 solubility measurements with the X-ray 3D-CT and BET surface area data resulted only in weak, inconclusive correlations, indicating the need for further experimental investigation.

Keywords: X-ray Computed Tomography (CT), Brunauer-Emmett-Teller (BET) Method, Alkali-Silica Reaction (ASR), Porosity, Solubility

1. INTRODUCTION

1.1 Alkali-Silica Reaction (ASR)

For more than 15 years, extensive research has been carried out in Germany on alkali-silica reaction (ASR). The need for such research into limiting the impact of ASR was

demonstrated by the Federal Highway Research Institute (BASt) analysis in 2012, which found that ASR was suspected in about 1,500 km of roadway [1]. Stark et al. [2] have suggested that during ASR, reactive SiO_2 within the aggregate granules reacts, in the presence of water, with alkalis (supplied from cement paste or externally) to form swelling alkali-silicate hydrates (ASR gels). When calcium also present, this can result in the swelling pressures up to 8.7 N / mm² [3], which is much higher than the tensile capacity of the concrete used in most conventional roadways and leads inevitably, therefore, to cracking.

The most important starting point for avoiding the ASR damage to concrete pavements is the exclusion of the alkali-sensitive aggregate prior to construction. For this purpose, experiments are generally carried out in which concrete prisms are subjected to various climatic and alkaline environmental conditions and the alkali sensitivity of the aggregates is assessed on the basis of elongation within the specimens [4, 5]. These experimental methods are, however, very time-consuming, cost-intensive and conservative. They also do not separately consider overlapping effects of multiple-simultaneous damage processes, such as secondary ettringite formation and freeze-thaw.

A useful supplement or alternative to conventional ASR test methods is the modified BTU-SP test [6, 7], which relies on solubility tests of individual aggregate granules for two months in 0.1 M potassium hydroxide solution at 80 °C. However, the influence of the externally accessible pore structure of the aggregate on the solubility behaviour of silicon and aluminium is not sufficiently understood.

1.2 X-ray Computed Tomography (3D-CT)

The visualization and quantification of the crack structures and pores extending from the outer granule surface into the granule was of central interest in this study and was investigated using X-ray 3D-CT (Figure 1). The X-ray 3D-CT measuring arrangement consists of a radiation source, in this case an X-ray tube, the test object on a turntable and a detector. The measurement principle is based on the X-ray irradiation of the test object from different viewing angles over its entire circumference. The test object is rotated step-by-step on a turntable, with one or more radiographic images acquired by the detector at each position. From these, the spatial distribution of the X-ray attenuation coefficients in the test object is calculated using reconstruction algorithms [8]. The X-ray attenuation, which is roughly correlated with density, of individual component materials within the specimen can then be identified and objects, such as pores and cracks, can be visualized. For the X-ray 3D-CT examinations described in this paper, a custom-built micro X-ray 3D-CT system equipped with a 225 kV X-ray source manufactured by X-ray WorX GmbH and a 2048x2048 pixel detector manufactured by Perkin Elmer, Inc was used.

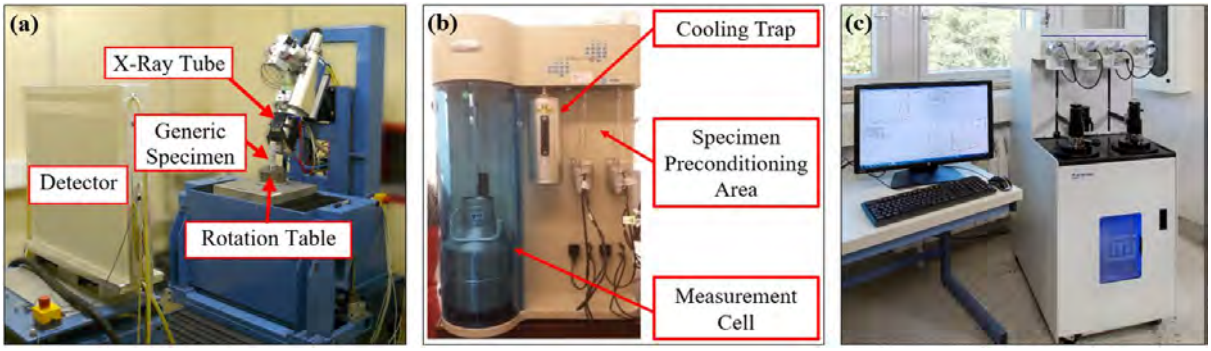

Figure 1: X-ray 3D-CT (a), BET (b) and mercury porosimetry (c) systems used

1.3 Brunauer-Emmett-Teller (BET) Method

As an alternative and supplement to X-ray 3D-CT, the specific surface area of the individual granules was also measured using high-resolution gas adsorption [9]. This method is based on determining the amount of adsorbate or used adsorbent required to cover the outer surface and the accessible inner pore surface of a solid with a complete adsorbate monolayer at a defined temperature. For the adsorbent, gases are used that are adsorbed by physisorption with weak interaction forces (Van der Waals forces) on the solid surface and desorbed rapidly by lowering the pressure. As a rule, nitrogen (boiling temperature: 77.3 K) is used for this purpose. Alternatively, krypton (boiling temperature: 119.93 K) is used for objects with small specific surfaces (<1 m^2/g). The adsorbate monolayer capacity is determined from the adsorption isotherm using the BET evaluation method developed by Brunauer, Emmett, and Teller [10]. For this study, an autosorb iQ instrument from Quantachrome Instruments (Figure 1) and the analysis software ASiQwin was used.

1.4 Mercury Porosimetry

To assess the relevance of the externally-accessible surface areas measured using X-ray 3D-CT and BET, the pore size distribution was determined for individual granules using mercury porosimetry [11]. This method is based on the measurement of the volume of mercury intrusion into a porous solid as a function of the applied pressure. Only pores are detected, into which mercury can penetrate when pressure is applied. This is because mercury is a non-wetting liquid (the contact angle, ϑ, between mercury and most solids is between 135° and 142°) and, thus, penetrates into a porous material only under pressure. The applied pressure is inversely proportional to the opening width of the pores. For cylindrical pores, the relationship between pore radius and pressure is described by the Washburn equation [11]. The mercury porosimetry measurements in this study were completed using an AutoPore V device from Micromeritics (Figure 1).

2. EXPERIMENTS

2.1 Specimens

The goal of this project was to quantitatively verify the influence of the externally accessible granule surface on ASR for aggregates with different alkali sensitivities. The full results from this project can be found in [12]. Within the framework of the full research project, granules within the size ranges 2 to 5 mm, 5 to 8 mm, 8 to 16 mm and 16 to 22 mm

were examined for four different aggregate types. It was found that for aggregate types with more homogeneous granules, the SiO_2 and Al_2O_3 solubility tends to increase with decreasing granule diameter due to the increasing specific surface area. This is often not the case, however, for aggregate types with heterogeneous granules.

Given these known granule size dependencies, the research presented in this paper, involving X-ray 3D-CT examinations of the microstructural state of the individual granules, focuses exclusively on granules within the size range of 8 to 16 mm, as this size range represents a compromise between desired solubility characteristics and resolution of the resulting X-ray 3D-CT images. This paper will also only present results for quarried and river gravel granules of both rhyolite and greywacke. River gravels are typically characterized by significant mineralogical deterioration when compared to quarried stones due to naturally occurring weathering processes. Ten individual granules were selected from each of these aggregate types for subsequent analysis. Following non-destructive investigation of externally accessible surface area using X-ray 3D-CT (Section 2.2) and BET (Section 2.3), the individual granules were subjected to (destructive) solubility experiments (Section 2.5). Separate granules from the same aggregate batches were also selected for pore size distribution analysis using mercury porosimetry (Section 2.4).

2.2 X-ray 3D-CT Investigations

During all X-ray 3D-CT scans, 130 kV acceleration voltage and 180 µA tube current were used. The X-ray beam was passed through a 0.5-mm-thick copper plate positioned between the X-ray source and the granule to filter out unwanted low-energy X-rays. During each scan, 2D projection images were collected at 3000 equally spaced rotation increments with an exposure time for each image of 1 second. This resulted in voxel sizes of 11.2 µm (quarried granules) and 21.1 µm (river gravel granules) in the resulting image reconstructions. Quarried granule images had smaller voxel sizes because, given the typically lower aspect ratio of these granules, their radiographic projections could be magnified on the X-ray detector.

Evaluation of the resulting 3D image reconstructions was challenging because the available conventional programs for this purpose did not meet all the requirements. The segmentation of the pores and cracks in the individual granules needed to be as automated and reproducible as possible. For this reason, a separate, modular, expandable MATLAB evaluation algorithm was developed. The details of that algorithm are beyond the scope of this paper but have already been described in detail in a previous publication [13].

The results of this analysis are presented in Figure 2. By providing specific surface areas (i.e. relative to mass), the variations due to differences in stone size are partially removed. In Figure 3, visualizations of selected individual granules have been created from X-ray 3D-CT images in order to provide insight into the internal microstructures of the aggregates.

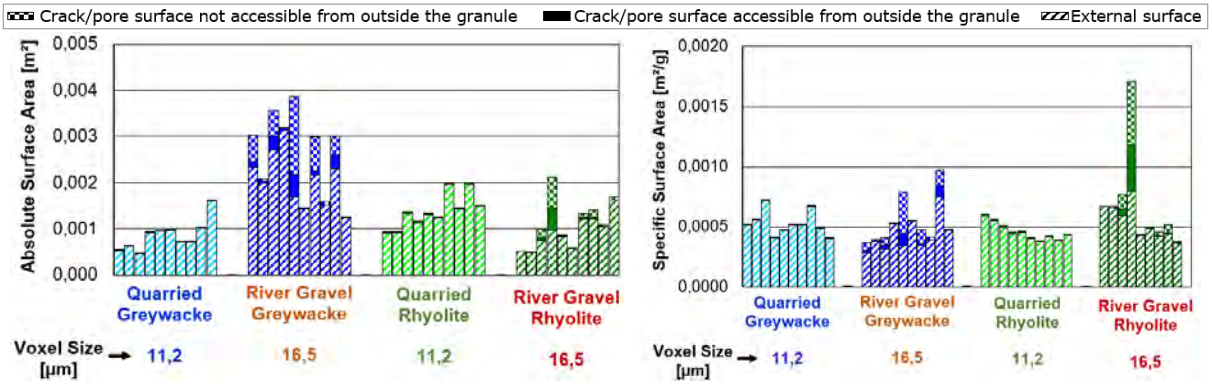

Figure 2: X-ray 3D-CT surface analysis results for individual granules

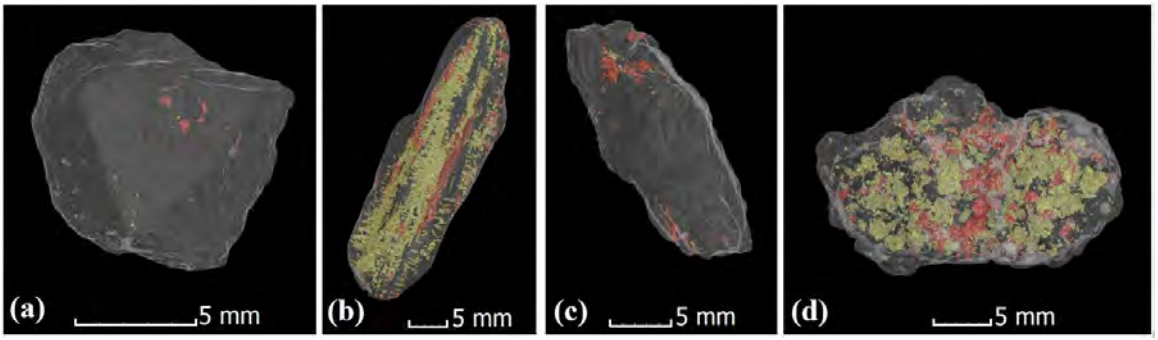

Figure 3: Visualization of selected individual granules using X-ray 3D-CT images; a) quarried greywacke, b) river gravel greywacke, c) quarried rhyolite, and d) river gravel rhyolite. Cracks and pores that emanate from the granule surface are coloured red. Cracks and pores not accessible from outside of the granule are coloured yellow.

The granules with the highest measured internal pore and cracking surface areas for each aggregate type have been selected for visualization in Figure 3. In these visualizations, the solid material of the individual granules is displayed semi-transparently. This enables a better spatial depiction of the cracks and pores. It is clear from Figure 2 that much higher internal surface areas (both accessible and inaccessible to the outer surface) are present for river gravel granules than for quarried granules. This is in spite of the fact that the X-ray 3D-CT images of the river gravel granules had larger voxel sizes, which would be expected to reduce the measurable crack and pore surface areas compared to the quarried granule images. The higher internal surface areas of the river gravel granules are also qualitatively confirmed by the individual granule visualisations in Figure 3. For the river gravel greywacke granule visualized in Figure 3b, for instance, a stratification is recognizable within the mineral structure and the pore and crack surface area that is inaccessible from the outer surface appears to be significantly larger than that which is accessible from the outer surface. Given the consistent and significant observable qualitative and quantitative differences between the cracking and pore characteristics of the different stone types, these the X-ray 3D-CT results were considered to provide a relatively good representation of the characteristics of each stone type.

2.3 Brunauer-Emmett-Teller (BET) Investigations

The limiting factor for determining the externally accessible and inaccessible surface areas in a single granule with X-ray 3D-CT is the voxel size. Thus, it was of interest to also determine the specific surface areas of the individual granules using the BET method in order to record smaller structures (≥ 0.3 nm). During this project, granule pre-treatment was performed uniformly by heating at 10 K/min to 200 °C. This temperature was maintained for 72 hours under an applied vacuum, followed by cooling the granule to room temperature, all while preventing granule exposure to external moisture. Krypton was used as an adsorptive agent and nitrogen was used as the coolant for the Dewar flask. The adsorption isotherm was determined at several gas pressure stages.

The results of the surface analyses with BET and X-ray 3D-CT are presented and compared in Figure 4. The X-ray 3D-CT surfaces in this figure include both the external granule surface and the surface of externally accessible pores and cracks. In this figure, it is observable that BET-measured specific surface areas are about three orders of magnitude larger than the X-ray 3D-CT measured values. This is due to the limited spatial resolution of X-ray 3D-CT. No clear relationship between the measured BET and X-ray 3D-CT values can be observed, which is an indication that significant porosity is likely to exist at smaller length-scales than the X-ray 3D-CT system is capable of measuring.

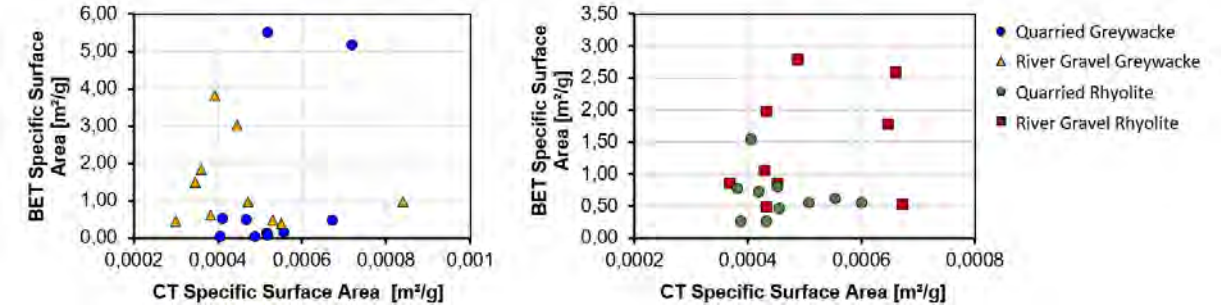

Figure 4: Comparison of the results of surface analyses with BET and X-ray 3D-CT on the individual granules

2.4 Mercury Porosimetry Investigations

In order to better understand the relationship between the BET and X-ray 3D-CT measurements and their relevance for assessing ASR resistance, a mercury porosimetry analysis was carried out on two further individual granules for each aggregate type (Figure 3). It is notable that for each of the different aggregate types, local maxima occur length-scales below the spatial resolution of the X-ray 3D-CT. It is not yet known which pore size ranges are most relevant for the transport and solubility processes in the BTU test or for ASR in general. This remains an area with a need for further research. It is assumed, however, that due to the high temperature of the elution medium in the solubility tests (80 °C), transport and solubility processes take place in very small pores and cracks (<100 nm). These observations indicate that the specific surface areas measured by means of BET are likely to be of greater relevance for the solubility processes than those measured by means of X-ray 3D-CT.

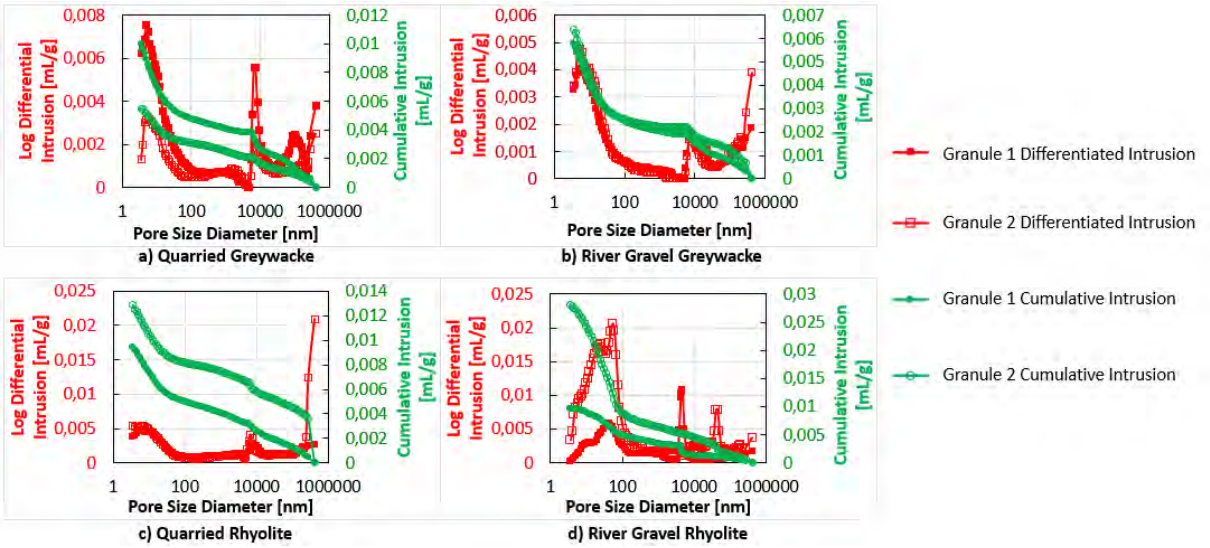

Figure 5: Differential and cumulative mercury intrusion into individual granules as a function of pore diameter

2.5 Solubility Investigations

After the characterization of the aggregates using X-ray 3D-CT and BET, solubility experiments on a few of the individual granules were carried out in 0.1 M KOH solution at 80 °C with a NaCl content of 1.0 wt.-%. In Figure 6, a comparison of the measured SiO_2 and Al_2O_3 concentrations in the eluate after 56 days of solubility testing with the externally accessible surface areas measured using BET and X-ray 3D-CT (including the external granule surfaces) is provided.

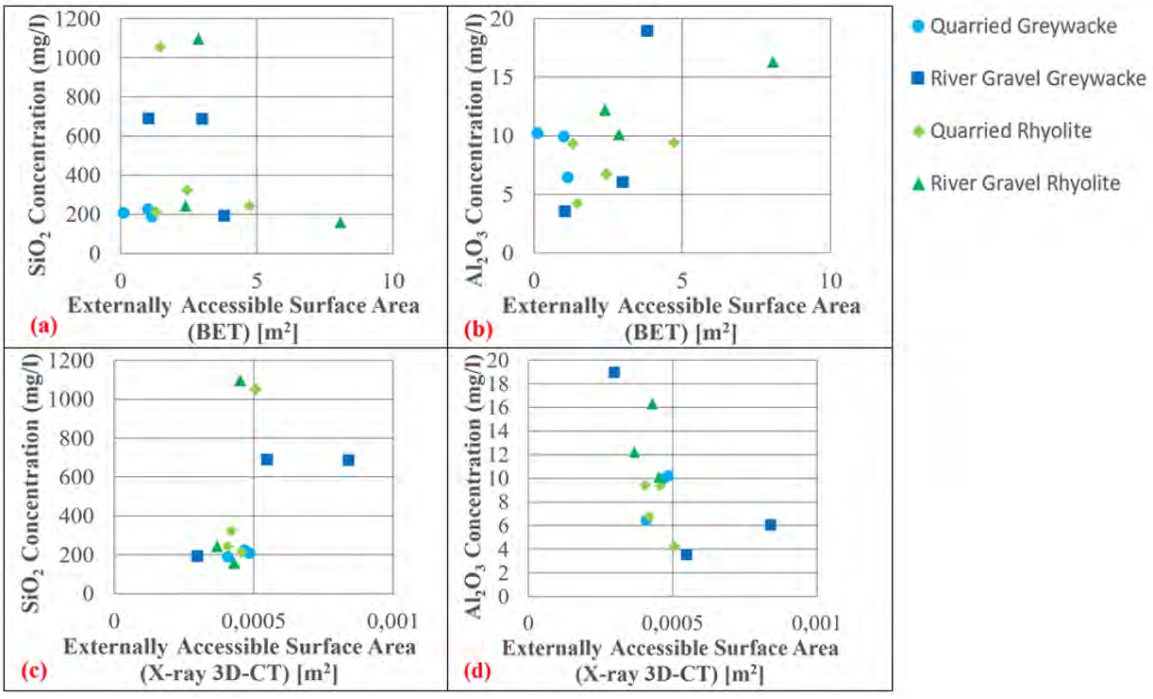

Figure 6: Comparison of SiO_2 and Al_2O_3 solubility experiment results (56 d) with the externally accessible surface areas measured using BET and X-ray 3D-CT

During solubility tests of the granules in 0.1 M KOH solution at 80°C, the SiO_2 excess in the solution is of central interest. In accordance with the method recommended in [14], the SiO_2 excess is calculated by subtracting the SiO_2 portion bound as an aluminosilicate by the total dissolved Al_2O_3 ($Al_2O_{3,\ total}$) from the total SiO_2 concentration ($SiO_{2,\ total}$) in the solution using the following equation:

$$SiO_{2,\ excess} = SiO_{2,\ total} - 1.4 * Al_2O_{3,\ total} \quad (1)$$

Given its roll in calculating the excess SiO_2 in the solution, the determination of the Al_2O_3 content in the eluate is, thus, mandatory. The choice of temperature and molarity of the KOH solution for the solubility tests is based on the fact that the results of the solubility tests under these boundary conditions show the best correlation with the strain measurements in the standard 40 °C concrete elongation test [6, 7, 15].

In previous systematic solubility tests on groups of individual aggregates without X-ray 3D-CT investigations, NaCl contents of 0.5, 1.0, 2.0, 3.0 and 10.0 wt.% were used with the 0.1 M KOH solution. Comparisons of the results of the solubility tests with the strains determined in the standard 60°C concrete elongation test with external alkali supply show that the addition of 1.0 wt.% NaCl to the 0.1 M KOH solution provides the best correlation between the two tests [5, 12]. For this reason, a 1.0 wt.% NaCl content was used for all the solubility experiments reported in Figure 6. This results in an Na/K-ratio of 0.87.

A mass ratio of granule to test solution of 1:100 was used during the solubility experiments and 3.0 ml of the eluate was removed after 4, 14, 28 and 56 days and filtered with a 0.2 µm membrane filter. The analysis of the filtered eluate was carried out using inductively coupled plasma optical emission spectrometry (ICP-OES), which provided measurements of the concentrations of the dissolved silicon and aluminium ions.

The conclusiveness of the results in Figure 6 is significantly limited due to the low number of samples. From a theoretical standpoint, it would be reasonable to expect higher levels of dissolved SiO_2 and Al_2O_3 for larger reactive surfaces (i.e. larger externally accessible surface areas). It is, however, clear from viewing this data that there is a large amount of scatter and that no definitive conclusions about relationships between surface area and solubility can be drawn without results from a significantly larger number of samples.

Despite these drawbacks, some trends are visible within the data. Analysis of SiO_2 concentration comparisons in Figure 6a has shown, for instance, that when a linear regression for each stone type is calculated, contrary to expectations, all resulting lines have negative slopes, albeit with very low certainty (mean of the four R^2 values of only 0.25). Similar calculations for Figure 6c, however, result in lines that all exhibit the expected positive slopes (mean of the four R^2 values still only 0.60). The findings from these two analyses may result purely from scatter within the data but merit further investigation in future testing programs.

As expected for Al_2O_3 concentrations, linear regression calculations for each of the stone types in Figure 6b result in lines exhibiting positive slopes, with the exception of quarried greywacke, which exhibited a negative sloping line. Contrary to expectations, linear regression calculations for each of the stone types in Figure 6d resulted in negative sloping lines, again with the exception of quarried greywacke, which exhibited a positive sloping line. Given the small number of samples and high scatter within the data, investigations of a significant number of additional samples will be needed before definitive conclusions about the correlation between Al_2O_3 concentrations and crack surface areas can be drawn.

It must be clearly acknowledged that important parameters of the single granules chosen here for solubility experiments are unknown. Such parameters are the chemical and, especially, the mineralogical composition of each granule, which influences the solubility behaviour considerably. Additionally, the quartz characteristics within each of the granules are not identical, they vary from granule to granule, especially in the granule crystallite sizes and structures. The determination of these values by X-ray diffraction (XRD) or by chemical analysis would, however, require the destruction of the single granules, which can be performed only at the end of the project.

4. CONCLUSIONS

This research has demonstrated the importance and difficulty of identifying and measuring pore and crack surface area characteristics within the most relevant size range for ASR-related solubility processes. A series of measurement methods were used in this research to measure pore size distribution, the surface areas of cracks and pores and to visualize crack and pore structures in individual granules. Mercury porosimetry measurements indicated that for the granules studied, much of the inner porosity occurs within a size range significantly below the measurement capabilities of the X-ray 3D-CT system used. This indicates that BET may be more useful for evaluating surface area characteristics in these materials relevant to ASR-related solubility processes. The X-ray 3D-CT images were still, however, very useful for identifying and visualizing the internal structure of porosity, such as stratification and fracture patterns. No apparent correlation was visible between the X-ray 3D-CT and BET measurements, which can be attributed to the large difference in the sensitive size ranges for BET and X-ray 3D-CT.

Comparison of X-ray 3D-CT and BET measurements of externally accessible surface area with the results from solubility experiments yielded highly scattered data. Although some weak trends within this data were identifiable, these trends were contradictory and to some extent counterintuitive. This may be an indication that other factors, such as chemical and mineralogical compositions and crystalline structure effects, play also an important role in understanding the solubility behaviour relative to the externally accessible surface area. Clearly, however, a large body of additional experimental data is necessary before definitive conclusions about the effects of reactive surface area on ASR-related solubility processes can be confidently drawn.

ACKNOWLEDGEMENTS

Dieser Präsentation liegen Teile der im Auftrag des Bundesministeriums für Verkehr und digitale Infrastruktur, vertreten durch die Bundesanstalt für Straßenwesen, unter FE-Nr. 06.0108/2014/BRB durchgeführten Forschungsarbeit zugrunde. Die Verantwortung für den Inhalt liegt allein beim Autor. (This presentation is based on parts of the research project carried out at the request of the Federal Ministry of Transport and Digital Infrastructure, represented by the Federal Highway Research Institute, under research project No. 06.0108/2014/BRB. The author is solely responsible for the content.)

The authors would also like to thank Ms. Zimathies from the BAM for carrying out the mercury porosimetry experiments.

REFERENCES

[1] F. Weise, T. Kind, L. Stelzner, M. Wieland, Dunkelfärbung der Betonfahrbahndecke im AKR-Kontext - Ursachenanalyse mit innovativer Prüftechnik, Beton- und Stahlbetonbau 113(9) (2018) 647-655.
[2] J. Stark, D. Erfurt, E. Freyburg, C. Giebson, K. Seyfarth, B. Wicht, Alkali-Kieselsäure-Reaktion, F. A. Finger-Instituts für Baustoffkunde, Weimar, Germany, 2008.
[3] Y. Qi, W. Ziyun, Study of expansion mechanism of A.S.R. using sol-gel expansion method, in: T. Mingshu, D. Min (Eds.) 12th ICAAR, Beijing, China, 2004, pp. 226–229.
[4] FGSV, Technische Prüfvorschriften für Verkehrsflächenbefestigungen – Betonbauweisen - TP B-StB 14: Widerstand gegen Alkali-Kieselsäure-Reaktion von Beton bei Alkalizufuhr von außen (FIB-Klimawechsellagerung) (Draft), Forschungsgesellschaft für Straßen- und Verkehrswesen e.V., Cologne, Germany, 2016.
[5] FGSV, Technische Prüfvorschriften für Verkehrsflächenbefestigungen – Betonbauweisen - TP B-StB 14: Widerstand gegen Alkali-Kieselsäure-Reaktion von Beton bei Alkalizufuhr von außen (60 °C-Betonversuch mit Alkalizufuhr von außen) (Draft), Forschungsgesellschaft für Straßen- und Verkehrswesen e.V., Cologne, Germany, 2016.
[6] R. Bachmann, Über das Zusammenspiel chemischer und physikalischer Gesteinsparameter zum besseren Verständnis des Ablaufs einer schädigenden Alkali-Kieselsäure-Reaktion, Doctoral Thesis, Brandenburgische Technische Universität Cottbus - Senftenberg, 2014.
[7] J. Kronemann, Untersuchung der zeitlichen Abhängigkeit von Löseprozessen in hochalkalischen Lösungen zur Charakterisierung der Alkaliempfindlichkeit von Gesteinskörnungen, Doctoral Thesis, Brandenburgische Technische Universität Cottbus - Senftenberg, 2015.
[8] L.A. Feldkamp, L.C. Davis, J.W. Kress, Practical cone-beam algorithm, J. Opt. Soc. Am. A 1(6) (1984) 612-619.
[9] ISO, Determination of the specific surface area of solids by gas adsorption – BET method, ISO 9277, International Organization for Standardization, 2010.
[10] S. Brunauer, P.H. Emmett, E. Teller, Adsorption of gases in multimolecular layers, Journal of the American Chemical Society 60 (1938) 309-319.
[11] ISO, Pore size distribution and porosity of solid materials by mercury porosimetry and gas adsorption — Part 1: Mercury Porosimetry, ISO 15901-1, International Organization for Standardization, 2016.
[12] F. Weise, M. Kositz, T. Oesch, K.-J. Huenger, G. Wilsch, S. Sigmund, Analyse des gefügeabhängigen Löslichkeitsverhaltens potenziell AKR-empfindlicher Gesteinskörnungen, Bundesanstalt für Straßenwesen (BASt), Schlussbericht FE 06.0108/2014/BRB, Bergisch Gladbach, DE, 2019.
[13] T. Oesch, F. Weise, G. Bruno, Detection and Quantification of Cracking in Concrete Aggregate through Virtual Data Fusion of X-ray Computed Tomography Images, Materials (Basel) 13(18) (2020).
[14] S. Hill, Zur direkten Beurteilung der Alkaliempfindlichkeit präkambrischer Grauwacken aus der Lausitz anhand deren Kieselsäure- und Aluminiumlöseverhalten, Brandenburgische Technische Universität Cottbus - Senftenberg, 2004.
[15] DAfStb, Vorbeugende Maßnahmen gegen schädigende Alkalireaktion im Beton (Alkali-Richtlinie), Deutscher Ausschuss für Stahlbeton, Beuth Verlag GmbH, Berlin, Germany, 2013.

MODELLING OF MICROSTRUCTURE OF ASR INFLUENCED CEMENT-BASED MATERIALS

Xiujiao Qiu (1), Jiayi Chen (2), Guang Ye(2) and Geert De Schutter (1)

(1) Department of Structural Engineering and Building Materials, Ghent University, 9052 Gent, Belgium.

(2) Department of Materials, Mechanics, Management & Design, Delft University of Technology, 2628 CN Delft, The Netherlands.

Abstract

ASR (alkali-silica reaction) is one of the toughest durability problems in engineering. However, the damage induced by ASR is still fairly unpredictable due to the lack of microstructural information of cement-based materials affected by ASR, while the microstructure determines the global performance. In order to fill this gap, a multiscale simulation model of ASR is under development. The basic theory and assumptions about this multiscale model can be found in [8]. This paper illustrates how the microstructure evolution of cement-based materials induced by ASR is achieved by this model. In the model, the entire chemical process including dissolution of reactive aggregate, nucleation and growth of ASR products (alkali silicate complex, calcium alkali silicate complex), is quantitatively simulated based on the kinetic and thermodynamic parameters. Furthermore, the 3D heterogeneous aggregate is numerically simulated using stereology based on the data from 2D thin-section. As a result, the dissolution degree of aggregate, the amount and location of ASR products and the porosity change can be traced. These micro parameters can be used for the simulation of crack formation in mesoscale. Similarly, the macroscale damage can be predicted based on the simulation results from mesoscale.

Keywords: ASR; microstructure; multi-scale modelling; heterogeneous aggregate; kinetics and thermodynamics;

1. INTRODUCTION

The famous deleterious chemical reaction between pore solution and reactive aggregate in existing concrete structures was firstly named alkali-silica reaction (ASR) by Stanton in 1940s [1]. One of the reaction products, ASR gel, is a kind of hydrophilic expansive product, which causes extensive cracking in concrete. Numerous concrete structures, such as dams and bridges, have been suffering from durability and safety issues due to ASR. Modelling is needed to analyse the behaviour of ASR-affected structures, thus evaluating the safety level, providing

suggestions about the reinforcement of the degraded structures, and also in view of preventative measures for to-be-built structures.

The global mechanical performance of a structure is determined by the structure of its constituents on micro-scale. Therefore, there are two basic aspects involved when simulating the ASR process in concrete: 1) the modelling of the chemical reaction and diffusion process at micro-scale, and 2) the modelling of mechanical response including expansion and cracking of concrete at macro-scale. The first aspect determines the microstructure change of concrete induced by ASR and the resulting expansion. The second aspect illustrates how the material and the structure degrade. A comprehensive ASR model should combine these two aspects. Unfortunately, due to the complexity of the influencing factors of ASR (reactivity of silica in aggregate, humidity, alkali amount etc.), such a model is missing now. Instead, theoretical [2, 3], semi-empirical [4, 5] and numerical models [6, 7] have been mainly developed depending on the observed response of ASR-affected concrete or laboratory experiments at a mesoscopic or a macroscopic scale. Most of these models either introduce too many parameters or the chemical reaction mechanism is simplified as a single parameter, which is far from reality.

In order to construct such a comprehensive model, a multiscale simulation model of ASR is under development in Ghent University in cooperation with Delft University of Technology. The basic theory and method of this comprehensive model are introduced in the conference paper [8]. In this paper, the simulation of the first aspect - the chemical reaction and diffusion process at micro-scale is described. The output of this model is the evolution of the microstructure of concrete induced by ASR including the porosity change, the amount and location of ASR products, and the change of the pore solution properties. These results will be used as input parameters in the future mesoscale model to simulate the cracking progress and to further obtain the whole crack pattern induced by ASR at macroscale. However, due to the lack of accurate input parameters (under experiments) as discussed in section 2.3, no comparable simulation results are stated. The paper mainly focuses on how to implement such a numerical model based on the proposed theory and method.

2. METHODOLOGY

As we know, ASR is a chemical reaction happening between pore solution in concrete and reactive silica in aggregates. Thus, at microscale, the initial simulation domain is composed of three parts as shown in Fig.1: 1) cement paste, 2) ITZ between cement paste and aggregate, and 3) heterogeneous aggregate at microscale. The microstructure of cement paste including ITZ is simulated using a new numerical cement hydration model developed by TU Delft [9]. The microstructure of heterogeneous aggregate is simulated based on the 3D crystal size distribution of reactive silica.

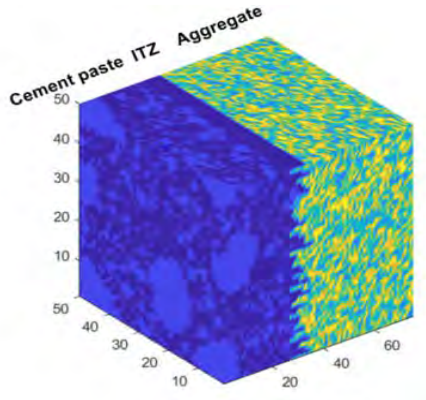

Figure 1: Illustration of the simulation domain at the initial state(unit:).

The simulation flow chart is given in Fig 2. Firstly, the aggregate microstructure domain is simulated as detailed in section 2.2. Secondly, the reactive silica will be dissolved once the alkalis are present on the site through transportation, which results in the ion concentration change in the pore solution. Once the supersaturated condition is reached, nucleation will start. Finally, mass ASR products will be formed by the growth of the formed nucleus.

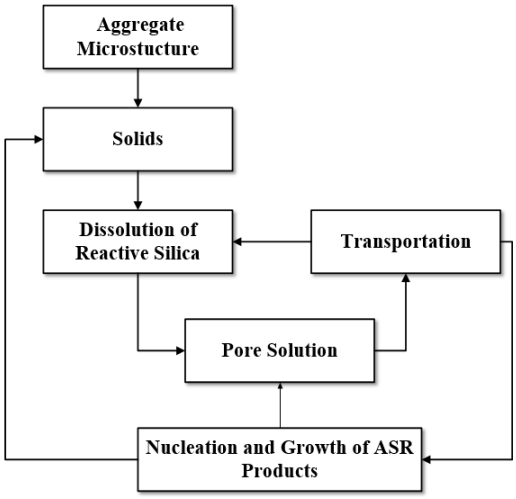

Figure 2: The simulation flow chart

2.1 Initialization

In the microscale model, the microstructure of aggregate, especially the distribution of reactive silica phases, is a fundamental input parameter to the model. In this model, The microstructure of aggregate at microscale will be simulated and introduced into the model as the initial step of the simulation. A brief introduction of this method is given in the following paragraph.

When considering 3D microstructure, CT scans are often a good choice. However, it is not applicable in the case of ASR based on mainly two reasons: 1) The resolution of CT scan is not always high enough to capture all the microstructural information of the reactive silica such as the cryptocrystalline silica (crystal size is less than 4 μm). 2) It is difficult to obtain a representative sample for a specific kind of aggregate. A big amount of aggregates need to be scanned, which causes a big time and economic burden.

An alternative way to obtain the 3D reactive silica distribution is by numerical simulation. Firstly, 2D particle distribution (with clear particle outline, sometimes the outline of the cluster of crystal particles when the particle size is too small) images should be acquired through thin sections or SEM-BSE images as shown in Fig.3. Based on these images, we are able to not only identify the reactive silica phases but also obtain the quantitative particle size distribution including the maximum ellipse length and the number of reactive silica particles using image software. Inputting these 2D data into a 3D stereology model CSD [10], the 3D crystal size distribution per unit volume of the reactive silica or other minerals can be calculated and corrected based on the 2D particle size distribution. The microstructure of aggregate can then be simulated. The shape of the crystal is assumed as an irregular one, which is more realistic. The roadmap of this method is shown in Fig.4. Using this method, lots of aggregates can be sampled and tested at the same time. With the help of image software, it is easy to obtain sufficient microstructure information. However, the localization of the reactive silica cannot be obtained through this method. In this model, particles are randomly parked in the aggregate domain.

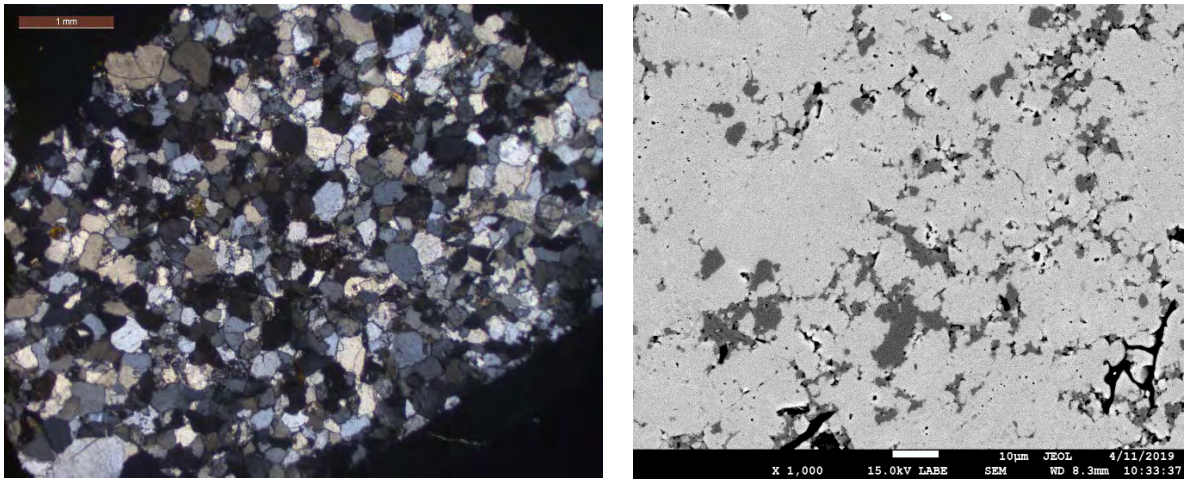

(a) (b)

Figure 3: (a) A thin section of sandstone; (b) A SEM-BSE image of siliceous limestone (grey: cluster of silica particles, white: calcium carbonate).

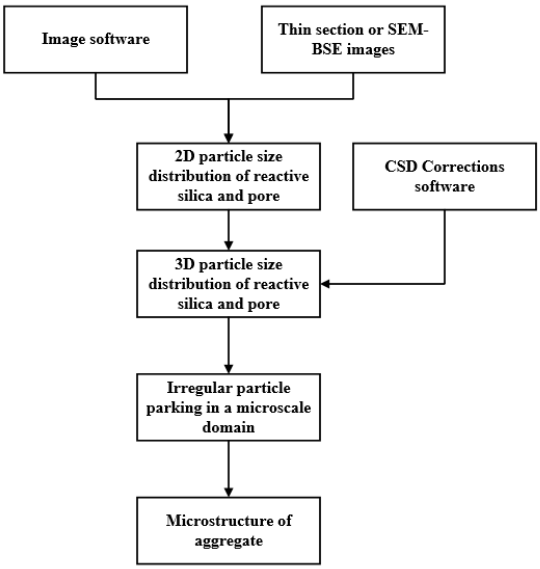

Figure 4:Roadmap about how to simulation an aggregate

2.3 Input Parameters

As stated before, this model is to mimic the entire chemical process of ASR including the dissolution of reactive silica, nucleation and growth of the products. The input parameters include the kinetic rates of the above processes respectively. More details can be found in [8].

2.3.1 Dissolution of reactive silica

ASR starts from the dissolution of reactive silica, which is influenced by the silica surface area, the temperature, pH, ionic strength and under saturation degree. The dissolution rate of silica is calculated according to the comprehensive equation proposed in [11] as shown below.

$$R_{diss} = \left(A_s \mathrm{A} e^{-E_A/RT_K}\right)(a_{OH})^{0.5}(I)^{0.2}\left(1-\frac{Q}{\mathrm{K}}\right) \quad (1)$$

Where A_s is the mineral area of the reactive silica (mm^2); A is the Arrhenius pre-exponential factor ($mole/mm^2/s$); E_A is activation energy (kJ / mole); R is gas constant (8.314J /K / mole); T_K is absolute temperature (K); a_{OH} is the activity of hydroxide ions; I is the ionic strength; Q is the reaction activity quotient; K is the dissolution equilibrium constant of reactive silica.

According to equation (1), the kinetic parameters need to be determined for dissolution are E_A, A and K respectively. Based on the microstructure disorder, there are mainly seven silica phases namely well-crystallized quartz, crypto to microcrystalline quartz, chalcedony, cristobalite, tridymite, opal, amorphous silica in order of increasing reactivity. The activation energies of these silica phases can be found in the literature [12], which is in the range from 46 kJ / mole to 96 kJ/mole. The Arrhenius pre-exponential factor of silica dissolution in base solution is around 0.01 $mole/mm^2/s$ [11]. For the dissolution equilibrium constant, lots of data can be used from a thermodynamic database, such as the LLNL database [13]. The value of $\log K$ of these silica phases lies between -2.71 and -4. The thin section results reveal which reactive silica phases are contained in the aggregate. The microstructure of the aggregate is simulated based on the crystal size distribution results of each reactive silica phase. The

dissolution rate calculated according to the above equation can be assigned to each node in the domain.

2.3.2 Nucleation and growth of ASR products

As stated in [8], the nucleus is assumed to be formed independently, the probability of forming a nucleus in the solution can be calculated via Poisson distribution. According to this assumption, the probability $P_{\geq 1}$ that at least 1 nucleus has formed in a time interval t can be calculated with equation (2)-(4).

$$J = AS\exp\left(-\frac{B}{ln^2 S}\right) \quad (2)$$

$$N = JVt \quad (3)$$

$$P_{\geq 1} = 1 - exp(-N) \quad (4)$$

Where J is the nucleation rate; S is the saturation degree; A and B are kinetic and thermodynamic parameters for nucleation, respectively; N is the average number of nucleus formed in a time interval t. V is the volume of the solution.

In these equations, the input parameters are the equilibrium constants of ASR products to calculate the saturation degree, A and B for ASR products respectively. In this model, the ASR products are divided into two types: alkali-silica gel and calcium-alkali silica gel. The equilibrium constants are obtained from [11]. For A and B, unfortunately, there is no such nucleation data in the literature. Experiments are needed to be done. In conformity with equation (2), $\ln(J/S)$ should be a linear function of $1/ln^2 S$. The thermodynamic parameter B can be estimated from the slope of the best-fit straight line, while the kinetic parameter A can be derived from the intercept to that line. Lots of methods can be used to get the nucleation rate such as by detecting the turbidity change or electricity change of the solution. In this research, the yellow molybdate method is used to determine the nucleation rate J based on the silica polymerization theory. More details can be found in [14].

According to the silica polymerization theory, the nucleation rate of silica is mainly influenced by the temperature, saturation degree, pH and ionic strength. In our model, the temperature is set as 298.15K. And A and B should be different at different pH or ionic strength. Experiments are designed considering the saturation degree, pH and ionic strength. A compiled table about A and B at different pH and ionic strength corresponding to the pore solution properties in concrete will be acquired in the end.

For the growth of silica, except the four influential factors stated above, the formed nanoparticle size also affects the growth rate, which makes it hard to do the experiments. However, lots of research proved that the rate-limiting step of ASR is the dissolution of silica. Therefore, the growth rate of ASR products can be obtained assigning directly as the dissolution rate of silica or via experiments. On the other way, all of these parameters can also be determined by parameter studying.

2.3.3 Ions transport and boundary conditions

The transport of ions will be simulated via the Lattice Boltzmann method [15]. In this model, the ions include $K^+, Na^+, OH^-, H_2SiO4^{2-}, H_4SiO_4,$ and Ca^{2+}. The input parameters are the diffusion coefficients. The cement paste domain is simulated with the simplification that the domain is saturated with water during the simulation. Hereinafter, the diffusion coefficients are the effective coefficients in the liquid phase and porous phase. The fluid flow is ignored. The

diffusion coefficients of these ions in different phases are used from [16] as shown in Table 1 . The diffusion coefficients in the high density phases such as aggregate and low density such as alkali-silica gel are reduced by a factor of 80 and 720, respectively.

Table 1: Diffusion coefficients of ASR related ions in different phases, $\times$ $^{-9}$

m^2/s Ions	K^+	Na^+	OH^-	H_2SiO4^{2-}	H_4SiO_4	Ca^{2+}
Water	1.8	1.33	5.3	0.7	0.53	0.71
[a]HD CSH; Calcium-alkali gel; Unhydrated cement; Aggregate; [c]Other hydration products	1.8/80	1.33/80	5.3/80	0.7/80	0.53/80	0.71/80
[b]LD CSH; Alkali-silica gel	1.8/720	1.33/720	5.3/720	0.7/720	0.53/720	0.71/720

a: high density CSH
b: low density CSH
c: CH, $Ca_4Al_2(SO_4)(OH)_{12}6H_2O$, $Ca_3Al_2(OH)_2$

A periodic boundary condition is applied for the ion transport in the simulation.

3. MICROSTRUCTURE OUTPUT

The entire microstructure data file can be printed in a full or as a system summary sheet. Specific characteristics, such as the percentage of silica reacted, pore volume, amount of the ASR products, and ions concentration change can all be calculated and plotted vs time. The microstructure can also be represented graphically. A 2D or 3D distribution map of different phases can be represented by different colors.

An important point is that the data file contains information about the system which can be retrieved and refined in many ways. In future, the simulated cement-based microstructure induced by ASR can be compared to a real microstructure.

4. CONCLUSION

ASR is one of the toughest durability problems in concrete engineering. The model discussed in this paper describes the chemical reaction process including the dissolution of the reactive silica, nucleation and growth of the products of ASR in three-dimensional space. It has the potential for predicting the microstructure change induced by ASR from a wide variety of reaction conditions. The output is the basic parameters for the multiscale model towards the goal of simulating the entire cracking process resulting from ASR in concrete.

The model provides a means for studying the implications of various assumptions about the alkali silica reactions by comparing the results of model calculations with the results of laboratory experiments. The model can be continuously updated to accommodate new experimental and theoretical developments and thus it will be a concise representation of the current state of knowledge.

REFERENCES

[1]. Stanton, T.E. Expansion of concrete through reaction between cement and aggregate. *ASCE Transactions*.107(1)(1942)54-84.

[2]. Bazant, Z.P. and Steffens, A. Mathematical model for kinetics of alkali-silica reaction in concrete. *Cem. Concr. Res.* **30**(3)(2000)419-428.

[3]. Hobbs, D.W. The alkali-silica reaction-a model for predicting expansion in mortar. Magazine of Concrete Research.**33**(117)(1981) 208-220.

[4]. Herrador, M.F., Martinez-Abella, F., and Fernandez-Gago, R.D. Mechanical behavior model for ASR-affected dam concrete under service load: formulation and verification. *Mater. Struct.* **42**(2)(2009)201-212.

[5]. Pietruszczak, S. On the mechanical behaviour of concrete subjected to alkali-aggregate reaction. *Comput. Struct.***58**(6)(1996)1093-1097.

[6]. Comby-Peyrot, I., Bernard, F., Bouchard, P.O., Bay, F., and Garcia-Diaz, E. Development and validation of a 3D computational tool to describe concrete behaviour at mesoscale: application to the alkali-silica reaction. *Comput. Mater. Sci.* **46**(4)(2009)1163-1177.

[7]. Dunant, C.F. and Scrivener, K.L. Micro-mechanical modelling of alkali-silica-reaction-induced degradation using the AMIE framework. *Cem. Concr. Res.* **40**(4)(2010)517-525.

[8]. Qiu, X.J., Chen, J.Y., Schlangen, E., Ye, G. and Schutter, G.D.' Introduction of a multiscale chemo-pyshical simulation model of ASR'. In: Gemrich, J.(eds.), Proceedings of 15th International Congress on the Chemistry of Cement. Prague: Research Institute of Binding Materials Prague Publisher, 2019.

[9]. Chen, J.Y., Liu, X., and Ye, G. ' Numerical simulation of cement hydration coupling transport and thermodynamics part i: theory and implementation'. Workshop on Concrete Modelling and Materials Behaviour in Honor of Professor Klaas van Breugel. Delft, 2018, 42-47.

[10]. Higgins, M. D. Measurement of crystal size distributions. *Am. Mineral.* 85(9)(2010)1105-1116.

[11]. Kim, T. *Alkali-silica reaction: chemical mechanism, thermodynamic modelling, and effects of lithium ions*. Ph.D. Thesis, West Lafayette: Purdue University Press, 2013.

[12]. Brady, P. and Walther, J. Kinetics of quartz dissolution at low temperature. *Chem. Geol.* 82(1990)253-264.

[13]. Bethke, C.M. and Yeakel, S. The Geochemist's Workbence® Release 8.0. Urbana, Illinois: Hydrogeology Program, Department of Geology, University of Illinois; 2010. http://www.gwb.com/documentation.php.

[14]. Icopini, G.A., Brantley, S.L. and Heaney, P. Kinetics of silica oligomerization and nanocolloid formation as a function of pH and ionic strength at 25ºC. *Geochim. Cosmochim. Acta.* 69(2)(2005)293-303.

[15]. Mohamad, A.A. 'Lattice Bolzmann Method Fundamentals and Engineering Applications with Computer Codes'. London: Springer Press, 2019.

MULTI-PHASE MODELLING OF MULTI-SPECIES TRANSPORT IN CONCRETE: IN CASE OF ELECTROCHEMICAL PROTECTION FOR BOTH ASR AND CHLORIDE ATTACK

Qing-feng Liu (1), Li-xuan Mao (2) and Zhi Hu (3)

(1) State Key Laboratory of Ocean Engineering, Shanghai Jiao Tong University, P. R. China

(2) School of Marine Science and Engineering, University of Plymouth, UK

(3) School of Architecture, Building and Civil Engineering, Loughborough University, UK

Abstract

Existing reinforced concrete structures experience severe durability degradation when subjected to alkali–silica reaction (ASR) and chloride attack. A special electrochemical rehabilitation treatment, containing lithium compound anolyte, has been developed to drive lithium ions into concrete as well as remove chlorides simultaneously, for mitigating both the ASR-induced cracks and the chloride-induced corrosion. Good performance of introduced lithiums in controlling ASR-induced expansion has already been proved. Unfortunately, the migration mechanism of lithium in concrete under an external electric field is seldom investigated in existing literature. In this study, with help of the "double-multi" model, the efficiency of impregnation of lithium ions and simultaneously the removal of chloride ions through a specific electrochemical treatment are numerically evaluated, which results into the distribution profiles of all typical ionic species. The heterogeneous concrete model examines the aggregate effect, especially on the interaction with lithiums which are supposed to mitigate ASR. The ionic interaction between different species and the electrochemical reaction at electrodes are also considered. Through a relative thorough modelling of multi-phase and multi-species, a systemic parametric analysis based on a series of significant factors during electrochemical treatment (e.g., current density, treatment time, temperature, cathode position and concentration of lithium solution) reveals some important tendencies of ionic electromigration in concrete, which are supposed to guide the field application.

Keywords: Electrochemical Rehabilitation, Chloride, Alkali–Silica Reaction, Lithium, Multi-species

1. INTRODUCTION

Existing reinforced concrete structures experience severe durability degradation when subjected to chloride-induced corrosion and alkali–silica reaction (ASR). The former is due to the destruction of passive film surrounding a steel-rebar when adjacent chlorides reach a

threshold concentration [1]. The latter is a chemical reaction between reactive siliceous compounds in aggregates and alkali ions in pore solution, producing a hygroscopic gel, which absorbs water from mortar and swells inducing cracks in the concrete [2], [3]. As a result, the ASR affected concrete becomes more vulnerable to chloride attack and making the corrosion of rebar easier. Worse still, the risk of ASR will also increase when treating the chloride-induced corrosion of reinforcement, especially during the process of electrochemical rehabilitation.

Electrochemical rehabilitation techniques originally developed for treating reinforced concrete structures about to suffer or already suffered from chloride attack [4,5,13] has been proposed to drive lithium ions into concrete to avoid ASR [16-21]. During this migration process, not only the lithium ions can be impregnated into concrete to anti-ASR but also chloride ions will be removed out to mitigate the chloride-induced corrosion of reinforcing steel. This combined treatment of ELM & ECR (i.e., electrochemical lithium migration and electrochemical chloride removal) involves setting an auxiliary anode surrounded by a lithium-based electrolyte solution on the surface of the concrete and applying a direct current (DC) density between the anode and the embedded rebar acting as a cathode.

There have been a set number of numerical studies on ionic transport in concrete materials, however, very limited works have been paid on the interaction of different factors on the transport of each individual ionic species. The accurate electro-chemical-physical mechanism of ELM & ECR is not fully understood. In this study, with help of the "double-multi" model [5-12], the efficiency of impregnation of lithium ions and simultaneously the removal of chloride ions through a specific electrochemical treatment are numerically evaluated, which results into the distribution profiles of all typical ionic species. The heterogeneous concrete model examines the aggregate effect, especially on the interaction with lithiums which are supposed to mitigate ASR. The ionic interaction between different species and the electrochemical reaction at electrodes are also considered. Through a relative thorough modelling of multi-phase and multi-species, a systemic parametric analysis based on a series of significant factors during electrochemical treatment (e.g., current density, treatment time, temperature, cathode position and concentration of lithium solution) reveals some important tendencies of ionic electromigration in concrete, which are supposed to guide the field application.

2. MULTI-COMPONENT IONIC TRANSPORT IN ELECTROLYTES

The pore solution in concrete involves many ionic species including hydroxyl, sulphate, sodium, potassium, calcium etc., among which the hydroxyl has the highest concentration, followed by the potassium and sodium. The transport of ions in a saturated concrete is mainly by two driving forces, known as the diffusion and migration. The former is due to the concentration gradient of the species itself; the latter is due to the electrostatic potential generated by an externally applied electric field and/or the internal charge imbalance between different species in the solution. The charge imbalance is caused by opposite-direction movement of cations and anions as well as different travel speeds of ions. The exact effect of charge imbalance on the transport of ions in concrete is dependent on the external electric field applied and the difference of diffusion coefficients between ionic species. In general, the effect of charge imbalance on the ionic transport increases with the external electric field and the difference of diffusion coefficients between ionic species. Mathematically, the flux of an

ionic species in a multi-component electrolyte solution can be expressed in terms of Nernst-Planck equation as follows.

$$\mathbf{J}_k = -D_k \nabla C_k - D_k C_k \frac{z_k F}{RT} \nabla \Phi \quad (1)$$

where Jk is the flux, Ck is the concentration, Dk is the diffusion coefficient, zk is the charge number, F = 9.648×10-4 Cmol-1 is the Faraday constant, R = 8.314 J mol-1K-1 is the ideal gas constant, T = 298 K is the absolute temperature, Φ is the electrostatic potential, and the subscript k represents the k-th ionic species. Eq. (2) is required for each ionic species involved in the solution owing to the mass conservation in unit volume of electrolyte solution,

$$\frac{\partial C_k}{\partial t} = -\nabla \cdot \mathbf{J}_k \quad (2)$$

where t is the time. Substituting Eq. (1) into (2), it yields,

$$\frac{\partial C_k}{\partial t} = \nabla (D_k \nabla C_k) + \nabla \left[\left(\frac{z_k D_k F}{RT} \right) C_k \nabla \Phi \right] \quad (3)$$

Note that if the electrostatic potential, Φ, in Eq. (3) is purely determined in terms of the externally applied electric field without taking into account the internal charge imbalance between ionic species, that is , then the concentration of each ionic species can be calculated independently by using Eq. (3). Otherwise, the electrostatic potential has to be determined using Poisson's equation as follows,

$$\nabla^2 \Phi = -\frac{F}{\varepsilon_0 \varepsilon_r} \sum_{k=1}^{N} z_k C_k \quad (4)$$

where εo = 8.854×10^{-12} CV^{-1}m^{-1} is the permittivity of a vacuum, εr = 78.3 is the relative permittivity of water at temperature of 298 K, and N is the total number of species involved in the solution. The use of Poisson's equation creates two difficulties. One is the coupling of Eq. (3) between different ionic species, since Φ is now dependent on not only the boundary conditions governed by the externally applied electric field, but also the concentrations of all ionic species involved in the solution. The other is the nonlinearity and numerical difficulty which involves calculations of large and small numbers that need be handled carefully. Nevertheless, Eqs. (3) and (4) plus initial and boundary conditions can be used to determine the electrostatic potential, Φ, and the concentrations of individual ionic species, C_k (k =1,2,…,N), at any point and any time in the solution domain.

3. IONIC TRANSPORT IN THE MEDIUM OF MULTI-PHASES

As aforementioned, concrete can be treated as a composite with aggregate-, cement paste- and ITZ-phases. Compared with the cement paste and ITZs, aggregates are much denser and have much high resistance to the transport of ions and therefore, in the present study they are assumed to be the impermeable material. The cement paste- and ITZ-phases can be treated as two individual porous materials with different transport properties. When applying the ionic transport equations from an electrolyte solution to a porous material, one has to consider the effects of porosity and tortuosity of the pore structure as well as the adsorption/desorption of ions at pore surfaces on the ionic transport in the porous material. The former is usually to be incorporated into the diffusion coefficient and the latter is often represented using ionic binding models. In this case, Eq. (2) need be modified as follows,

$$\frac{\partial(\varphi C_k)}{\partial t}+\frac{\partial[(1-\varphi)S_k]}{\partial t}=-\varphi\nabla\cdot\mathbf{J}_k \tag{5}$$

where φ is the porosity of the porous material and S_k is the concentration of bound ions. To eliminate φ and S_k in Eq. (5), the following Langmuir isotherm is often used to link the concentrations of bound and free ions,

$$\frac{(1-\varphi)S_k}{\varphi}=\frac{\alpha_k C_k}{w(1+\beta_k C_k)} \tag{6}$$

where w is the content of the water in which ionic transport takes place, expressed per unit weight of cement, α_k and β_k are the constants which can be determined experimentally. Note that other chloride binding isotherms such as the linear and Freundlish isotherms could also be used, which will result in Eq. (6) to have different expressions. The use of Eqs. (1) and (6) in Eq. (5), yields,

$$(1+\lambda_k)\frac{\partial C_k}{\partial t}=\nabla(D_k\nabla C_k)+\nabla\left[\left(\frac{z_k D_k F}{RT}\right)C_k\nabla\Phi\right] \tag{7}$$

where $k > 0$ is a dimensionless parameter for the k-th species defined as follows,

$$\lambda_k=\frac{\alpha_k}{w(1+\beta_k C_k)^2} \tag{8}$$

Eqs. (7) and (4) can be used to determine the electrostatic potential, Φ, and the concentrations of individual ionic species, C_k (k =1,2,…,N), at any point and any time in the domain of the porous material. Note that when Eqs. (4) and (7) are applied to the concrete material of aggregates, ITZs, and cement paste phases, one has to use different transport properties for aggregates, ITZs, and cement paste, whereas continuous conditions are imposed for ionic concentrations and ionic fluxes at the interfaces between different phases. The details of the geometric modelling of the concrete of multi-phases will be given in following section.

4. MODELING ON ELECTROCHEMICAL REHABILITATION

The concretes modelled in previous studies [5-12] as well as the presented work are treated as a heterogeneous composite structure with three phases consisting of mortar matrix, coarse aggregates and ITZs. Fig.1 shows a series of the 2-D concrete numerical models with the same size of 50×50 mm and the volume fraction of Vagg = 0.5. In the figure the circular areas represent the impermeable aggregates with the radii ranging from 1.5 mm to 10 mm. Outside each aggregate, there is an aureole ITZ shell of tiny scale (40 μm) wrapping the aggregate. Outside the ITZs, the remaining part of the concrete model represents the mortar matrix. The location of the aggregates was randomly generated using a MATLAB program.

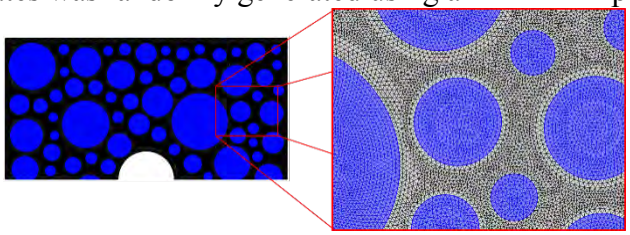

Figure 1: Finite element mesh of the two phases concrete model (Va=0.5)

The model described above is mainly used to simulate the ELM&ECR treatment of concrete. Fig. 2 graphically displays the simulated test, in which there are multi-component species governed by Eqs. (4) and (7). Due to the symmetry of the geometry of the specimen and the cathode settings, only a half of the specimen (50 mm × 25 mm) is modelled for simplifying calculation (as shown in Fig. 3). The initial and boundary conditions employed in the simulations are given in Table.1 [4].

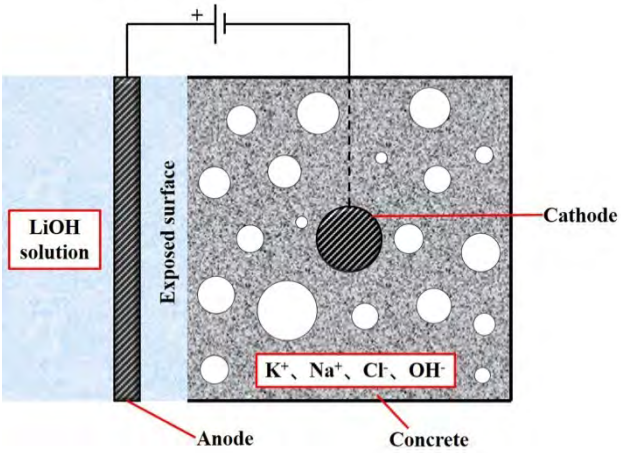

Figure 2: Schematic representation of simulated ELM & ECR set up

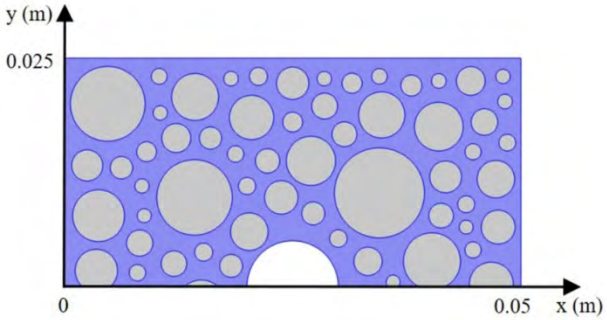

Figure 3: The geometry of two phases mesoscale concrete model (Va=0.5)

Assuming that the volume of the electrolyte reservoir at anode is much larger than that of the concrete sample, the concentration of lithium in electrolyte is assumed to be constant C_{Li0}. By considering both the ionic electro-coupling interactions and heterogeneous nature of cement-based materials, the "multi-phase, multi-species" transport models for concrete, which is so-called “double multi” model, can be obtained.

Table 1: Information about five ionic species considered during modelling (25 ºC)

Field variables	Potassium	Sodium	Chloride	Hydroxide	Lithium
Charge number	1	1	-1	-1	1
Diffusion coefficient in mortar phase, $\times 10^{-11}$ m^2/s	3.900	2.700	10.20	52.80	3.700
Diffusion coefficient in aggregate phase, $\times 10^{-11}$ m^2/s	0.039	0.027	0.102	0.528	0.037

Boundary concentration, mol/m3 (at anode, x=0)	5	5	10	1000	1000
Initial concentration in mortar phase, mol/m^3	100	900	380	620	0

5. SIMULATION OF ELM & ECR

By using of the "double multi" model, one can solve a set of mechanism problems along the line of concrete durability study: ionic electro-coupling effect, diffusivity prediction, binding effect, EDL effect, cracking effect, ITZs, aggregate morphology, etc. This study shows a typical example of using this model, which is the simulation of ELM&ECR as mentioned.

The distribution contours of five ionic species (Cl^-, K^+, Na^+, OH^-, Li^+) for specimens after 4-, 8- and 12-weeks treatment with a constant current density of 2A/m2 are depicted in Figs. 4-8, respectively. In these 3-D plots, x and y coordinates show the change of the position in the model and the vertical coordinate represents the value of concentration. It can be seen from these plots that the profiles of each species have its own unique characteristics.

Fig. 4 shows a concave formed around the cathode for chloride under the external electric field. It can be observed that the chloride concentration gradually decreases from the initial value of 380 mol/m^3 to only 219 mol/m^3 (maximum value in concrete after 12-week treatment), which means ECR &ELM achieves a good performance of removing chlorides from concrete. Additionally, the chloride concentration near right boundary always reaches peak value, which demonstrates that the dominant process of ionic transport is still diffusion in the region out of the two electrodes, which makes the removal of chlorides harder. A closer observation also shows that there is a funnel-like pit around each aggregate since the great ionic diffusivity difference between aggregates and mortar.

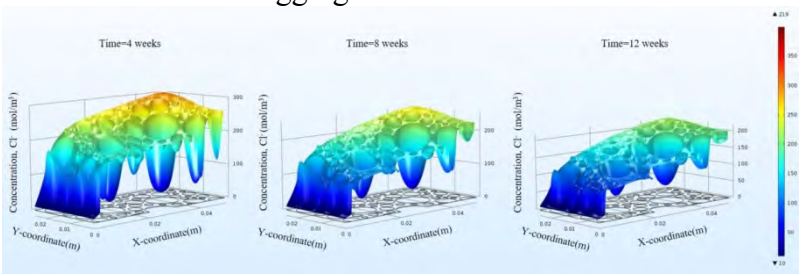

Figure 4: Distribution profiles of chloride concentration at 4 weeks, 8 weeks and 12 weeks

The positively charged potassium ions gradually gather around the rebar with time as shown in Fig. 5. The sodium ions also move towards rebar like potassium ions under the driving of the external current, therefore the distribution profiles of sodium are qualitatively similar with those of potassium as shown in Fig. 6. The peak values of sodium concentration are far greater than potassium, owing to its higher initial concentration in specimen. The accumulation of Na^+ and K^+ is of advantages for protecting rebar at cathode by locally increasing the pH and thus stabilizing the passive layer.

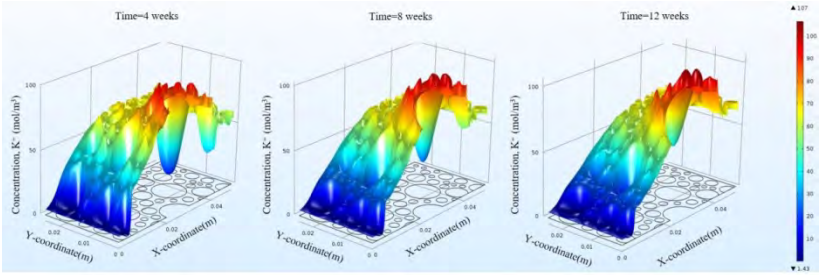

Figure 5: Distribution profiles of potassium concentration at 4 weeks, 8 weeks and 12 weeks

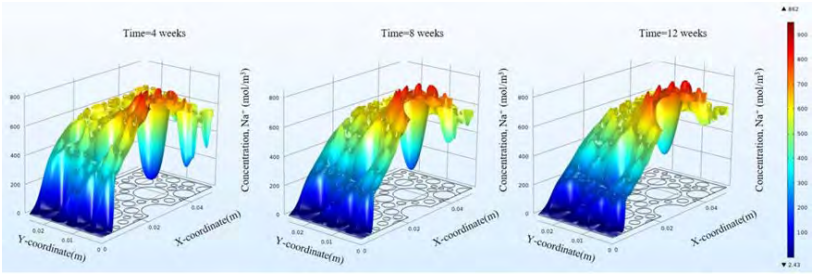

Figure 6: Distribution profiles of sodium concentration at 4 weeks, 8 weeks and 12 weeks

As shown in Fig. 7, the concentration around the cathode forms as convex for hydroxide ions, which is similar with the performances of two cations (i.e. potassium and sodium) rather than the negatively charged chlorides. This is because of that the electrochemical reactions taken place at the rebar surface provides an inward flux for the hydroxide ions. Notably, hydroxide ions concentration inside of whole concrete specimen gradually built up with the treatment time, which demonstrates that the hydroxide ions generated at the cathode are more than those move towards anode. Such behavior of hydroxides creates an alkaline environment in specimen, which is beneficial to protect rebar from corrosion.

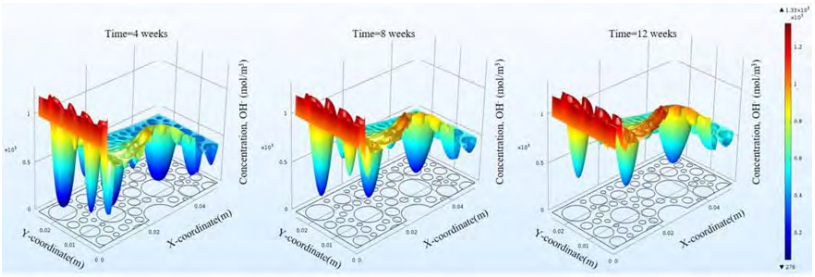

Figure 7: Distribution profiles of hydroxide concentration at 4 weeks, 8 weeks and 12 weeks

It can be seen from the Fig. 8 that the contents and penetrations of lithiums in the specimen are built up with treatment time, which are meaningful to control ASR. It confirms that ECR & ELM is a very promising technique in driving lithiums into the concrete and reducing local chloride concentration in the vicinity of cathodes, which has been experimentally investigated by Ueda et al. [19] and theoretically verified by Venglovska et al. [21]. From the contour plots, it can be noted that the lithium content is still very low behind the cathode after 12-week treatment, as limited current flow exists in this range, thereby the transport of lithiums driven

by the electric field is much slower. The simulations of all ionic species agree well with the obtained shapes by Ueda et al. [19,20] and exhibit the characteristics of each ionic species.

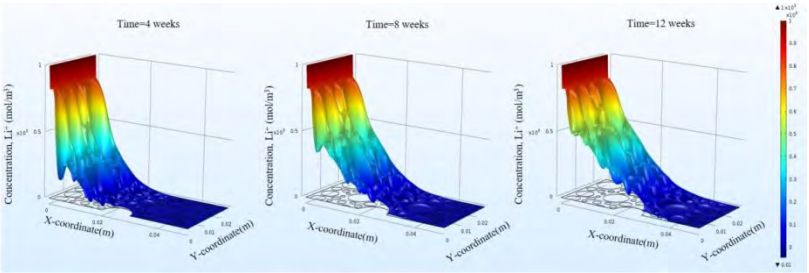

Figure 8: Distribution profiles of lithium concentration at 4 weeks, 8 weeks and 12 weeks

In order to further verify the reliability of the modelling, a simulated dummy test case is conducted by using the presented model with the parameters provide by Ueda's et al experiment [20]. The normalized lithium concentration in concrete (C_{Li}/C_{Li0}) from numerical model after 8-week and the results from experiments are shown in Fig. 9, where C_{Li} is the lithium concentration in concrete and C_{Li0} is the concentration in electrolyte. It is clear that the numerical predictions agree well with the experimental data. The normalized lithium concentrations in concrete from modelling are higher than those of experiments in the range of 0-25 mm depth. This is because of the assumption of constant concentration at boundaries during simulation based on partial differential equations (PDEs). However, it is apparent from the comparison that the tendency of the results from these two methods fits very well and most of the data points from the experiments after 8-week lie nearby or on the modelling results curve. The small fluctuation in the curve is mainly caused by the tortuosity variation due to the local distribution of aggregate particles.

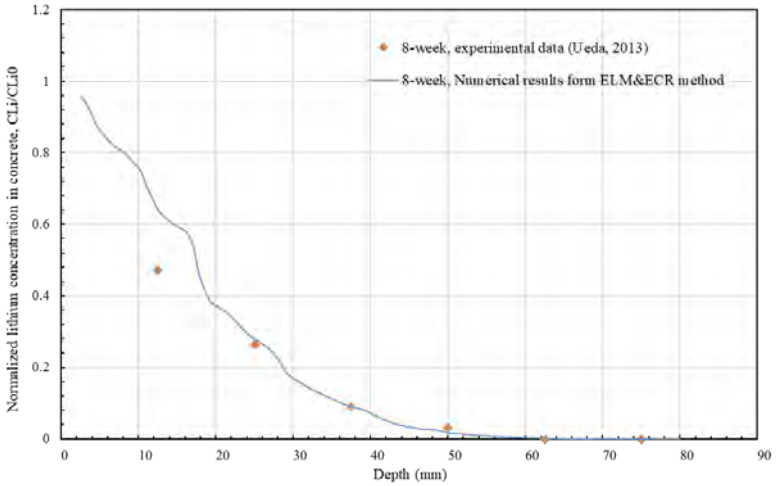

Figure 9: Comparisons of the lithium concentration obtained from ELM & ECR model and experimental data

ACKNOWLEDGEMENTS

This work was funded by the Natural Science Foundation of China [51978396] and the Shanghai Rising-Star Program, China [19QA1404700]. The authors also would like to thank the supports from Young Elite Scientists Sponsorship Program by CAST [2018QNRC001],

the State Key Laboratory of High Performance Civil Engineering Materials [2018CEM006] and the State Key Laboratory of Structural Analysis for Industrial Equipment [GZ18119].

REFERENCES

[1] Bazant, Z.P. (1979). Physical model for steel corrosion in concrete sea structures-application. Journal of Structural Divison. 105:6, 1155-1166.

[2] Buenfeld, N.R., Glass, G.K., Hassanein, A.M., & Zhang, J.Z. (1998). Chloride transport in concrete subjected to electric field. Journal of Materials in Civil Engineering. 10:4, 220-228.

[3] Geng, J., Easterbrook, D., Liu, Q.F, & Li, L.Y. (2016). Effect of carbonation on release of bound chlorides in chloride-contaminated concrete. Magazine of Concrete Research. 68:7, 353-363.

[4] LI, L.Y. & PAGE, C.L. (2000). Finite element modelling of chloride removal from concrete by an electrochemical method. Corrosion Science. 42, 2145-2165.

[5] LIU, Q.F., XIA, J., EASTERBROOK, D., YANG, J. & LI, L.Y. (2014). Three-phase modelling of electrochemical chloride removal from corroded steel-reinforced concrete. Construction and Building Materials. 70, 410-427.

[6] HU, Z., MAO, L.X., XIA, J., LIU, J.B., GAO, J., YANG, J. & LIU, Q.F. (2018). Five-phase modelling for effective diffusion coefficient of chlorides in recycled concrete. Magazine of Concrete Research. 70, 583-594.

[7] JIANG WQ, SHEN XH, XIA J, MAO LX, YANG J, LIU QF. (2018): A numerical study on chloride diffusion in freeze-thaw affected concrete. Construction and Building Materials, 179, 553–565.

[8] LIU, Q.F., EASTERBROOK, D., YANG, J. & LI, L.Y. (2015a). A three-phase, multi-component ionic transport model for simulation of chloride penetration in concrete. Engineering Structures. 86, 122-133.

[9] LIU, Q.F., FENG, G.L., XIA, J., YANG, J. & LI, L.Y. (2018). Ionic transport features in concrete composites containing various shaped aggregates: a numerical study. Composite Structures. 183, 371-380.

[10] LIU, Q.F., LI, L.Y., EASTERBROOK, D. & YANG, J. (2012). Multi-phase modelling of ionic transport in concrete when subjected to an externally applied electric field. Engineering Structures. 42, 201-213.

[11] MAO LX, HU Z, XIA J, FENG GL, AZIM I, YANG J, LIU QF. (2019): Multi-phase modelling of electrochemical rehabilitation for ASR and chloride affected concrete composites. Composite Structures, 207, 176–189.

[12] LIU, Q.F., YANG, J., XIA, J., EASTERBROOK, D., LI, L.Y. & LU, X.Y. (2015b). A numerical study on chloride migration in cracked concrete using multi-component ionic transport models. Computational Materials Science. 99, 396-416.

[13] LIU, Y. & SHI, X. 2012. Ionic transport in cementitious materials under an externally applied electric field: Finite element modeling. Construction and Building Materials, 27, 450-460.

[14] MARTINEZ, I., ROZAS, F., RAMOS-CILLAN, S., GONZáLEZ, M. & CASTELLOTE, M. (2015). Chloride Electroremediation in reinforced structures: preliminary electrochemical tests to detect the steel repassivation during the treatment. Electrochimica Acta, 181, 288-300.

[15] JIANG, W.Q., SHEN, X.H., HONG S., WU, Z.Y., LIU, Q.F.. (2019): Binding capacity and diffusivity of concrete subjected to freeze-thaw and chloride attack: a numerical study. Ocean Engineering, 186C (2019) 106093.

[16] PAGE, C. & YU, S. (1995). Potential effects of electrochemical desalination of concrete on alkali–silica reaction. Magazine of concrete research. 47, 23-31.

[17] POWERS, T. & STEINOUR, H. (1955). An interpretation of some published researches on the alkali-aggregate reaction Part 1-The chemical reactions and mechanism of expansion. Journal Proceedings. 497-516.
[18] RAJABIPOUR, F., GIANNINI, E., DUNANT, C., IDEKER, J.H. & THOMAS, M.D. A. (2015). Alkali–silica reaction: Current understanding of the reaction mechanisms and the knowledge gaps. Cement and Concrete Research, 76, 130-146.
[19] UEDA, T., BABA, Y. & NANASAWA, A. (2013). Penetration of lithium into ASR-affected concrete due to electro-osmosis of lithium carbonate solution. Construction and Building Materials. 39, 113-118.
[20] UEDA, T., KUSHIDA, J., TSUKAGOSHI, M. & NANASAWA, A. (2014). Influence of temperature on electrochemical remedial measures and complex deterioration due to chloride attack and ASR. Construction and Building Materials. 67, 81-87.
[21] VENGLOVSKA, S., PEL, L. & ADAN, O. C. G. (2016). Electromigration of lithium ions into cementitious materials as observed by NMR. International RILEM Conference on Materials, Systems and Structures in Civil Engineering.